



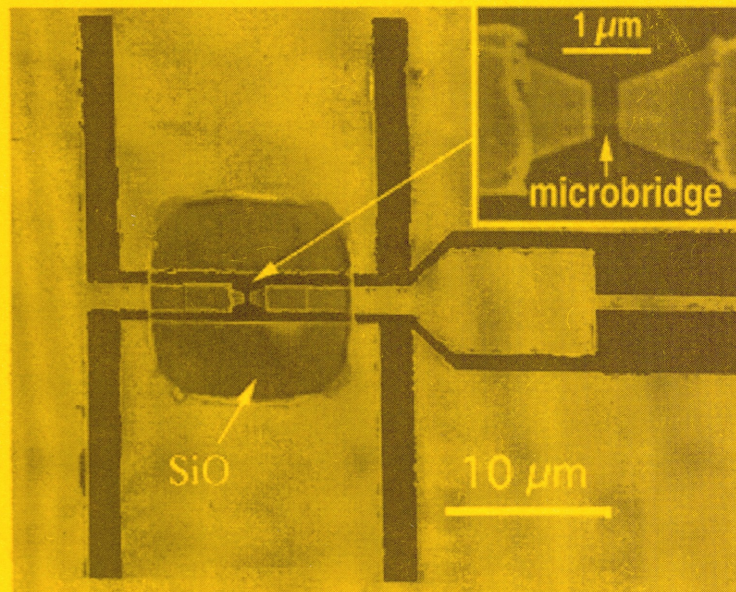
Ninth International Symposium on Space Terahertz Technology



17 - 19 March 1998
Pasadena Hilton
Pasadena, California, USA



PROCEEDINGS



Broadband 1.5 - 2.5 THz HEB Mixer

Sponsored and organized by the Center for Space Microelectronics Technology;
Jet Propulsion Laboratory, California Institute of Technology;
and National Aeronautics Space Administration Office of Space Science

PROCEEDINGS
of the
NINTH INTERNATIONAL SYMPOSIUM ON
SPACE TERAHERTZ TECHNOLOGY

Tuesday - Thursday, March 17 - 19, 1998

Pasadena Hilton Hotel
Pasadena, California, USA

Sponsored by: NASA Office of Space Science.

Organized by: The Jet Propulsion Laboratory,
California Institute of Technology

Organizing Committee: Rob McGrath (JPL)

PREFACE

The Ninth International Symposium On Space Terahertz Technology was held at the Pasadena Hilton Hotel, Pasadena, California, on March 17 - 19, 1998. The Symposium was attended by 150 scientists, engineers, and program managers from around the world. The theme of the Symposium was similar to previous years and centered on the detection, generation, and manipulation of radiation in the terahertz spectral region for ground-based, aircraft, balloon, and spaced-based applications including astronomy, planetary science, and remote-sensing of Earth's atmosphere. The Abstract Booklet contained 68 abstracts, and the program was divided into 11 oral sessions, plus, for the first time, a poster session covering a wide variety of topics including HEB mixers; Schottky diode mixers and fabrication; SIS mixers, receivers and devices; multiplier and fundamental sources; and detectors and backends. In addition, there were invited presentations that outlined the status of programs for the NASA Stratospheric Observatory for Infrared Astronomy (SOFIA) and that discussed the heterodyne instrument for the ESA Far Infrared and Submillimeter Space Telescope (FIRST).

In an attempt to design the Symposium in future years to meet the needs and desires of the participants, a survey was conducted to determine the preferred format for accommodating an increasing number of papers submitted to the Symposium. Of the four options--(a) increase the symposium to 4 days, with no parallel sessions; (b) keep the symposium at 3 days, but add parallel sessions; (c) keep the symposium at 3 days, but add more poster sessions; and (d) reject enough papers (using tighter reviewing criteria) to keep the symposium at its current size--by far the most popular option was (c) keep the symposium at 3 days, but add more poster sessions. This year we added one poster session for the first time, and it was very well received. It provided a great opportunity for increased interaction between the presenters and the audience.

The Symposium was sponsored by the NASA Office of Space Science, and the Center for Space Microelectronics Technology at the Jet Propulsion Laboratory which also organized the event. I would like to thank these organizations for their support. I would also like to thank everyone who helped to make the Symposium a success: Anders Skalare, Boris Karasik, and Imran Mehdi for setting up the technical program and organizing the lab tours; Wenonah Green and Pat McLane and her staff for handling the local arrangements and making small miracles happen; the session chairs for keeping us on schedule; and everyone who attended or contributed a presentation. Also an additional thanks to Wenonah for putting this Proceedings together, and to Tim Brice for assisting with the graphics on the Abstract Booklet.

Rob McGrath

The Tenth International Symposium On Space Terahertz Technology will be held in Charlottesville, Virginia, on March 16 - 19, 1999, and will be hosted by the University of Virginia. For more information on the next Symposium, please contact:

Dr. Thomas W. Crowe
University of Virginia
Department of Electrical Engineering
Charlottesville, VA 22903
Tel: 804-924-7693
Fax: 804-924-8818
E-mail: twc8u@virginia.edu

NINTH INTERNATIONAL SYMPOSIUM ON SPACE TERAHERTZ TECHNOLOGY

March 17 - 19, 1998
Pasadena Hilton Hotel
Pasadena, California, USA

Sponsored by: NASA Office of Space Science.

Organized by: The Jet Propulsion Laboratory, California Institute of Technology

CONTENTS

DAY 1 - TUESDAY, MARCH 17			Page
Opening Session			
Welcome	C. Kukkonen	JPL	1
SOFIA--A Versatile Facility for Infrared and Submillimeter Astronomy in the New Millennium [abstract]	M. Morris	UCLA	15
<hr/>			
Session 1: HEB MIXERS I	Chair: K. Jacobs	U. Koln	
Noise Performance of Diffusion Cooled Hot-Electron Bolometers: Theory vs. Experiment	P. J. Burke, R. J. Schoelkopf, I. Siddiqi, D. E. Prober, A. Skalare, B. S. Karasik, M. C. Gaidis, W. R. McGrath, B. Bumble, H. G. LeDuc	Yale JPL	17
First Light with an 800 GHz Phonon-Cooled HEB Mixer Receiver	J. Kawamura, R. Blundell, C.-Y. E. Tong, D. C. Papa, T. R. Hunter, G. Gol'tsman, S. Cherendichenko, B. Voronov, E. Gershenson	CIT H-SCA MSPU	35
Quasioptical Phonon-Cooled NbN Hot-Electron Bolometer Mixers at 0.5-1.1 THz	S. Svechnikov, A. Verevkin, B. Voronov, E. Menschikov, E. Gershenson, G. Gol'tsman	MSPU	45
Low Noise NbN Phonon-Cooled Hot-Electron Bolometer Mixers at 810 GHz	C. Roesch, T. Lehnert, C. Schwoerer, M. Schicke, K. H. Gundlach, K. F. Schuster, F. Schaefer	IRAM MPIfR	53

Session 2: HEB MIXERS II		Chair: A. Kleinsasser	JPL	
Resistive Behaviour of Nb Diffusion-Cooled Hot Electron Bolometers	D. W. Floet, J. J. A. Baselmans, J. R. Gao, T. M. Klapwijk		U. Groningen SRON	63
Optimal Choice of Material for HEB Superconducting Mixers	B. Karasik, W. McGrath		JPL	73
A Large Signal Model for Phonon-Cooled Hot-Electron Bolometric Mixers for THz Frequency Applications	H. F. Merkel, E. L. Kollberg, K. S. Yngvesson		CUT	81
Capacitively Coupled Hot-Electron Microbolometer as a Perspective IR and Sub-mm Wave Sensor	L. S. Kuzmin		CUT	99
Session 3: HEB MIXERS III		Chair: B. Karasik	JPL	
Measured Results for NbN Phonon-Cooled Hot Electron Bolometric Mixers at 0.6-0.75 THz, 1.56 THz, and 2.5 THz	E. Gerecht, C. F. Musante, H. Jian, K. S. Yngvesson, J. Dickinson, J. Waldman, G. N. Gol'tsman, P. A. Yagoubov, B. M. Voronov, E. M. Gershenson		U. Mass. MSPU	105
Measurements with a Diffusion-Cooled Nb Hot-Electron Bolometer Mixer at 1100 GHz	A. Skalare, W. R. McGrath, B. Bumble, H. LeDuc		JPL	115
NbN Hot-Electron Mixer at Radiation Frequencies Between 0.9 THz and 1.2 THz	Y. P. Gousev, H. K. Olsson, G. N. Gol'tsman, B. M. Voronov, E. M. Gershenson		RIT MSPU	121
Quasioptical NbN Phonon-Cooled Hot Electron Bolometric Mixers with Low Optimal Local Oscillator Power	P. Yagoubov, M. Kroug, H. Merkel, E. Kollberg, G. Gol'tsman, A. Lipatov, S. Svechnikov, E. Gershenson		CUT MSPU	131
Gain-Bandwidth Characteristics of High-Tc Superconducting Millimeter-Wave Hot-Electron Bolometer Mixers	C.-T. Li, B. Deaver, Jr., R. M. Weikle, II, M. Lee, R. A. Rao, C.-B. Eom		U. VA Duke U.	141

DAY 1 - TUESDAY, MARCH 17 (continued)

Page

Session 4: SCHOTTKY DIODE MIXERS	Chair: T. Gaier	JPL	
2.5 THz GaAs Monolithic Membrane-Diode Mixer-- <i>A New Planar Circuit Realization for High Frequency Semiconductor Components</i>	P. H. Siegel, R. P. Smith, M. Gaidis, S. Martin, J. Podosek, U. Zimmermann	JPL	147
On the Design and Measurement of a 2.5 THz Waveguide Mixer	C. M. Mann, D. N. Matheson, B. N. Ellison, M. L. Oldfield, B. P. Moyna, J. J. Spencer, D. S. Wilsher, B. J. Maddison	RAL	161
A Discussion of Power Coupling Bandwidth Limitations of Planar Schottky Diodes at Submillimeter Wavelengths	J. L. Hesler, B. Gelmont	U. VA	173
A High Performance, 318 GHz Subharmonic (x3) Balanced Mixer	I. Galin	Aerojet	181
Quasi-Integrated Planar Schottky Barrier Diodes for 2.5 THz Receivers	T. Suzuki, C. Mann, T. Yasui, H. Fujishima, K. Mizuno	Photodyn. RIEC RAL	187

DAY 2 - WEDNESDAY, MARCH 18

Session 5: SIS MIXERS AND RECEIVERS I	Chair: V. Belitsky	CUT	
A Tunerless SIS Mixer for 200-280 GHz with Low Output Capacitance and Inductance	A. R. Kerr, S.-K. Pan, A. W. Lichtenberger, H. H. Huang	NRAO U. VA	195
A 350 GHz Finline Mixer Fed by a Horn-Reflector Antenna	G. Yassin, S. Withington, M. Buffey, K. Jacobs, S. Wulff	U. Koln	205
An Integrated Sideband Separating SIS Mixer for 200-280 GHz	A. R. Kerr, S.-K. Pan, H. G. LeDuc	NRAO JPL	215
Experimental Results of SIS Mixer with Distributed Junction Arrays	S.-C. Shi, T. Noguchi, J. Inatani, Y. Irimajiri, T. Saito	NRO TSC CRL MELSC	223
Doubled Shot Noise in Niobium SIS Mixers	P. Dieleman, J. R. Gao, T. M. Klapwijk	U. Groningen SRON	235

Session 6: SIS MIXERS AND RECEIVERS II	Chair: H. van de Stadt	SRON	
Low Noise Fixed Tuned 490 GHz SIS Mixers Made of Epoxy Resin [abstract]	M. Sahr, D. Hottgenroth, S. Haas, K. Jacobs, C. E. Honingh	U. Koln	243
A Low-Noise, 9-Element Micromachined SIS Imaging Array	G. de Lange, K. Konistis, Q. Hu, R. Robertazzi, D. Osterman	MIT Hypres	245
Results of the PIROG 8 Balloon Flight with an Embarked Experiment Based on a 425/441 GHz SIS Receiver for O2 Search	A. Deschamps, P. Encrenaz, P. Febvre, H. G. Floren, S. George, B. Lecomte, B. Ljung, L. Nordh, G. Olofsson, L. Pagani, J. R. Pardo, I. Peron, M. Sjoekvist, K. Stegner, L. Stenmark, J. Tauber, C. Ullberg	DEMIRM Stockholm Ob. SSC ACRE AB ESTEC	253
Recent Progress on the Superconducting Imaging Receiver at 500 GHz	S. V. Shitov, A. B. Ermakov, L. V. Filippenko, V. P. Koshelets, W. Luinge, A. M. Baryshev, J.-R. Gao, P. Lehtikoinen	RAS SRON U. Groningen HUT	263

Session 7: SIS MIXERS AND DEVICES	Chair: R. LeDuc	JPL	
Terahertz NbN/AlN/NbN Mixers with Al/SiO/NbN Microstrip Tuning Circuits	Y. Uzawa, Z. Wang, A. Kawakami	KARC	273
Low-Loss NbTiN Films for THz SIS Mixer Tuning Circuits	J. Kooi, J.A. Stern, G. Chattopadhyay, H. LeDuc, B. Bumble, J. Zmuidzinas	Caltech JPL	283
Fabrication of Nb/Al-Nx/NbTiN Junctions for SIS Mixer Applications Above 1 THz	B. Bumble, H. G. LeDuc, J. A. Stern	JPL	295
Fabrication and DC-Characterization of NbTiN Based SIS Mixers for Use Between 600 and 1200 GHz	J. A. Stern, B. Bumble, H. G. LeDuc, J. W. Kooi, J. Zmuidzinas	JPL Caltech	305

POSTER SESSION	Chair: R. Wyss	JPL	
A 4x1 GHz Array Acousto-Optical Spectrometer for Air- and Spaceborne Observations in the Submm Region	J. Horn, C. Macke, F. Schloeder, F. Schmuelling, O. Siebertz, R. Schieder	U. Koln UCLA	315
Comparative Study of the Bandwidth of Phonon-Cooled NbN Hot-Electron Bolometers in Submillimeter and Optical Wavelength Ranges	K. S. Il'in, S. I. Cherednichenko, G. N. Gol'tsman, M. Currie, R. Sobolewski	MSPU U. Rochester	323
Normal Metal Hot-Electron Microbolometer with Andreev Mirrors for THz Space Applications	D. Chouvaev, L. Kuzmin, M. Tarasov, P. Sundqvist, M. Willander, T. Claeson	CUT RAS	331
Single Sideband Mixing at Submillimeter Wavelengths	J. Inatani, S.-C. Shi, Y. Sekimoto, H. Masuko, S. Ochiai	NSDA NRO U. Tokyo CRL	337
Noise and Conversion Efficiency of High-Tc Superconductor Josephson Mixers	O. Harnack, S. Beuven, M. Darula, H. Kohlstedt, M. Tarasov, E. Stepantsov, Z. Ivanov	RC Julich CUT	347
Design of 100-900 GHz AlGaAs/GaAs Planar Heterostructure Barrier Varactor Frequency Triplers	J. Stake, L. Dillner, S. H. Jones, C. Mann, E. Kollberg	CUT U. VA RAL	359
A Compact 500 GHz Planar Schottky Diode Receiver with a Wide Instantaneous Bandwidth	B. J. Maddison, R. J. Martin, M. L. Oldfield, C. M. Mann, D. B. Matheson, B. N. Ellison, J. Thornton, W. J. Hall, D. M. Lamarre	RAL MMS UK ESTEC	367
Computer Controlled, Phase-Locked 126-147 GHz Transferred Electron Oscillator System	T. Ye, S. Jones, J. Carlstrom, R. Weikle	U. VA U. Chicago	373
Series Connection of Resonant Tunneling Diodes for Eliminating Spurious Oscillations	T. Fujii, O. Boric-Lubecke, J. Bae, K. Mizuno	IPCR Tohoku U.	381
Electromagnetic Modeling of Objective Lenses in Combination with Integrated Lens Antennas	M. J. M. van der Vorst, P. J. I. de Maagt, M. H. A. J. Herben	EUT ESTEC	389
A Novel Radio-Wave Alignment Technique for Millimeter and Sub-Millimeter Receivers	C.-Y. E. Tong, M. T. Chen, D. C. Papa, R. Blundell	H-SCA Acad. Sinica	397
Spectroscopic Measurements of Optical Components Around 1 Terahertz	D. J. Benford, J. W. Kooi, E. Serabyn	Caltech	405

DAY 2 - WEDNESDAY, MARCH 18 (continued)

Page

POSTER SESSION (continued)

A Simple Millimeter/Submillimeter-Wave Blackbody Load Suitable for Spaceborne Applications	P. H. Siegel, R. H. Tuffias, P. Goy	JPL Ultramet AB Mm	415
Practical Micromachining Techniques for High Aspect Ratio Submillimeter Wave Components	V. M. Lubecke, C. M. Mann, K. Mizuno	RIKEN RAL Tohoku U.	425
A Supra THz SIS Heterodyne Receiver Using Waveguide/Membrane Technology [abstract]	M. Salez, Y. Delorme, I. Peron, J.-M. Munier, D. Rovera, J.-C. Villegier, V. Larrey	DEMIRM DANOF CEA	431
Design of Mixer Elements for the HHT 345 GHz Heterodyne Array Receiver	G. Narayanan, C. K. Walker, H. Knoepfle, J. Capara	U. AZ	433
Low Noise Single Sideband SIS Mixers for MM and Submillimeter Radio Astronomy [abstract]	A. Karpov, J. Blondel, M. Voss, D. Billon-Pierron, P. Pasturel, K. H. Gundlach	IRM	443
A High-Power Frequency-Stabilized Tunable Two-Frequency Diode Laser System for Generation of Coherent Terahertz-Wave by Photomixing	S. Matsuura, G. Blake, P. Chen, J. C. Pearson, H. M. Pickett	Caltech JPL	445

DAY 3 - THURSDAY, MARCH 19

Invited Talk	Chair: A. Skalare	JPL	
The Focal Plane Unit of the Heterodyne Instrument for FIRST: <i>HIFI</i>	N. D. Whyborn, Th. de Graauw, H. van de Stadt, V. Belitsky, R. Kruisinga, S. Torchinsky, H. Visser, K. Wildeman	SRON CUT	453
Session 8: MULTIPLIER SOURCES	Chair: A. Raisanen	HUT	
A Local Oscillator System for the FIRST Heterodyne Instrument	G. W. Schwaab, J. C. Pearson, N. D. Whyborn	DLR Inst. JPL SRON	463
Wideband High Efficiency Planar Diode Doublers	N. Erickson	U. Mass.	473

Session 8 (continued)

A Broadband Frequency Tripler for SIS Receivers	S. Mahieu, C. M. Mann, J. Stake, L. Dillner, S. H. Jones, E. Tong, J. Thornton	RAL CUT U. VA Smithsonian U. Oxford	481
A 430.5 GHz Quasi-Optical HBV Frequency Tripler	P. Arcioni, M. Bozzi, G. Conciauro, H. L. Hartnagel, L. Perreggini, E. Sacchi, M. Shaalan, J. Weinzierl	U. Pavia Darmstadt UT	493

Session 9: SCHOTTKY DIODE FABRICATION Chair: H. Eisele

U. MI

Planar Schottky Mixer Development to 1 THz and Beyond	S. M. Marazita, J. L. Hesler, R. d Feinaugle, W. L. Bishop, T. W. Crowe	U. VA ISST	501
Quartz-Based GaAs Schottky Diodes--Lifetime and Failure Analysis	R. Lin, A. Pease, R. Dengler, D. Humphrey, T. Lee, S. Kayali, I. Medhi	JPL	511
Physical Properties of the Potential Barrier of Pt/n-GaAs Schottky Mixer Diodes	H.-W. Hubers, H. P. Roser	DLR	521

Session 10: FUNDAMENTAL SOURCES I Chair: J. Pearson

JPL

Photomixing in Low-Temperature-Grown GaAs	S. Verghese, K. A. McIntosh, S. M. Duffy, E. R. Brown, S. Calawa, K. Molvar, W. F. Dinatale, T. M. Lyszczarz	MIT	529
A Coherent, Tunable, FIR Source	J. H. Brownell, M. F. Kimmitt, J. C. Swartz, J. E. Walsh	Dartmouth	537
Electrical Generation of Terahertz Current Oscillations in Ballistic Devices	A. N. Korshak, V. V. Mitin	Wayne S. U.	543
Generation of CW-Terahertz Radiation Using a Two-Longitudinal-Mode Laser Diode	P. Gu, M. Tani, K. Sakai, T. Hidaka	Kansai ARC Shonan I. T.	553
2.5 THz Laser Local Oscillator for the EOS CHEM 1 Satellite	E. R. Mueller, W. E. Robotham, Jr., R. P. Meisner, R. A. Hart, J. Kennedy, L. A. Newman	DeMaria EOS	563

Session 11: FUNDAMENTAL SOURCES II	Chair: S. Verghese	MIT	
A W-Band HEMT Based Power Amplifier Module for Millimeter-Wave LO Multipliers	I. Mehdi, T. Gaier, J. Kooi, B. Fujiwara, R. Lai	JPL Caltech TRW	573
Transient Simulation of Harmonic TEO Circuits	G. B. Tait, S. H. Jones	VC U.	579
GaAs TUNNETT Diodes and InP Gunn Devices for Efficient Second-Harmonic Power Generation Above 200 GHz	H. Eisele	U. MI	587

Session 12: DETECTORS AND BACKENDS	Chair: J. Kawamura	Caltech	
A Non-Bolometric Model for a Tunable Antenna-Coupled Intersubband Terahertz (TACIT) Detector	C. L. Cates, G. Briceno, M. S. Sherwin, K. D. Maranowski, A. C. Gossard	UCSB	597
Superconducting Correlators for Radio Astronomy	M. J. Feldman	U. Rochester	607
WASP: A Wideband Analog Autocorrelation Spectrometer	K. G. Isaak, A. I. Harris, J. Zmuidzinas	U. MD U. Mass. Caltech	615

Authors and Registered Participants Listing			625
--	--	--	------------

Welcome and Introduction

Ninth International Symposium on Space Terahertz Technology

Carl Kukkonen

Director, Center for Space Microelectronics Technology

JPL

March 17-19, 1998

SUBMILLIMETER AND THZ DRIVERS

- **ASTROPHYSICS**

**Long awaited major observation platforms, SOFIA, and
FIRST now close to reality.**

- **EARTH ATMOSPHERIC CHEMISTRY**

EOS-MLS now in Phase C/D

- **PLANETARY AND COMETARY SCIENCE**

- **LABORATORY SPECTROSCOPY**

Terahertz Astrophysics Observing Platforms

- **Far Infrared Submillimeter Telescope (FIRST) - ESA Mission**

Proposal submitted for heterodyne instrument, February 15, 1998
Joint European / US Instrument Team

Baseline Capabilities

- Passively cooled 3.8 m telescope
- 480-1250 GHz SIS mixers
- 1.4-1.9 THz and 2.4-2.7 THz HEB mixers
- High resolution spectroscopy 85-600 μm , photoconductor and bolometer arrays
- Broad band photometry 85-900 μm bolometer arrays

NASA Contributions

- Orbit: Increase observing time and sensitivity
- 3.8 m telescope
- 3 receiver bands: SIS 1.0-1.2 THz; HEB 1.4-1.9 THz, & 2.4-2.7 THz
- MMIC Power amps for LO system
- InP HEMT's for IF system

Terahertz Astrophysics Observing Platforms

The Stratospheric Observatory for Infrared Astronomy (SOFIA)

- **Joint US / German Project**
- **2.5 m aperture airborne telescope for wavelengths between 0.3 μm and 1.6 mm, with emphasis on submillimeter and far-IR**
- **First round of instruments selected and under construction
(A Submillimeter and Far-Infrared Heterodyne Receiver)**
- **First flights in 2001**
- **20 year lifetime**
- **USRA, Raytheon E-Systems, United Airlines**

Terahertz Astrophysics Observing Platforms

- **Submillimeter Wave Astronomy Satellite (SWAS)**
 - Small Explorer Mission
 - Heterodyne receivers near 480 and 560 GHz
 - Observe interstellar water, oxygen, and carbon
 - Launch date 1998
- **Antarctic Submillimeter Telescope and Remote Observatory (AST/RO)**
 - South Pole Observatory operational this year funded by NSF
 - 1.7 m aperture for 0.5 mm wavelengths
 - Built, running and taking data
- **Heinrich Hertz / Submillimeter Telescope Observatory (HHT/SMTO)**
 - Located on Emerald Peak of Mt. Graham, approximately 75 miles north-east of Tucson, Arizona
 - 10 m aperture for wavelengths between 1.3 mm and 350 microns
 - Joint University of Arizona / Max-Planck Institut fur Radioastronomie project
 - Operational and taking data

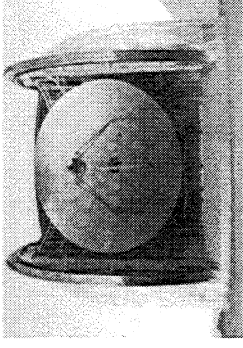
Terahertz Astrophysics Observing Platforms

- **NRAO - Millimeter Array in Chile**
 - 32 Telescopes (64 with European collaboration)
 - 10 m diameter (12 m with European collaboration)
 - Construction start 2001
 - Operational 2007
 - Frequency: 30 -950 GHz
- **South Pole 10 m Telescope**
 - Operational 2003
 - AST/RO - NSF Funded Program
 - SIS & Bolometers up to 1.5 THz

Terahertz Astrophysics Observing Platforms

- **Microwave Instrument for the Rosetta Orbiter (MIRO)**
 - Approved for the Rosetta Orbiter - Launch 2003
 - Currently in Phase B: Proto-flight models under development
 - Two channel continuum and spectroscopic heterodyne receiver system
 - Submillimeter Wave Receiver - Frequency: 540 GHz
 - Millimeter Wave Receiver - Frequency: 190 GHz
 - RFP for flight subsystems in 1998
- **Submillimeter Array (SMA)**
 - Harvard Smithsonian Center for Astrophysics
 - 6 telescopes, upgrade to 8
 - 6 m diameter
 - On Mauna Kea, Hawaii
 - Operational 2000
 - Operational frequency range: 200 - 800 GHz

Terahertz Astrophysics Observing Platforms



- **Caltech Submillimeter Observatory**
 - A cutting-edge facility for astronomical research and instrumentation development
 - Located on "submillimeter ridge" near the summit of Mauna Kea, Hawaii
 - 10 m Telescope
 - Frequencies: 230 - 950 GHz



- **Owens Valley Radio Observatory**
 - Largest university-operated radio observatory in the world
 - Located five hours north of Pasadena, near the Sierra Nevada range
 - Six 10m telescopes
 - Frequency ranges 80-116 GHz and 210-270 GHz
 - 40m Telescope
 - 5m Telescope
 - Two 27m Telescopes

Status of NASA Submillimeter Sensors Astrophysics Program

- **Superconducting Mixers**
 - Nb SIS Mixers meet needs of FIRST for frequencies up to 1 THz
 - Challenge is to improve performance to 1250 GHz
 - Approach: NbTiN SIS mixers
 - Above 1.4 THz: Use Hot Electron Bolometer Mixers
 - Approach: Diffusion Cooled (Nb, Al)
- **Solid State Local Oscillator Sources**
 - Multiplier chains meet power requirements of FIRST for frequencies up to about 1.2 THz
 - Challenge is to provide
 - Wide bandwidth with fixed tuning
 - Reliability
 - Higher Power and Stable Photomixer L.O. (1-3 THz)

NASA Terahertz Space Missions for Earth Observations

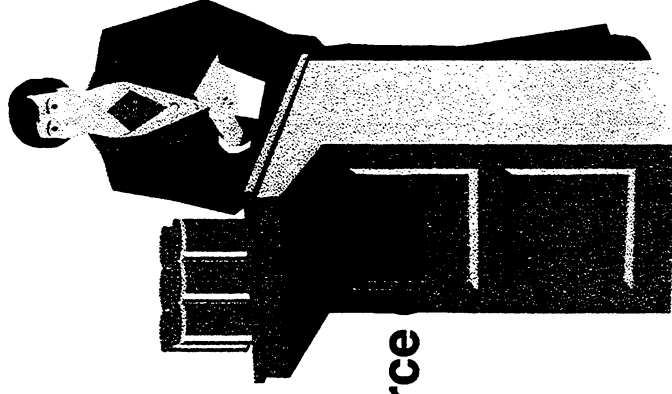
- **Earth Observing Satellite Microwave Limb Sounder**
Study of chemistry of stratospheric ozone on a global scale
 - 118 GHz
 - Temperature and Pressure
 - 190 GHz
 - Continuity with UARS MLS for O₃, ClO, and H₂O
 - 240 GHz
 - O₃, CO - Temperature and Pressure
 - 640 GHz
 - Ozone chemistry (O₃, HCl, ClO, NO₂ and others)
 - 2.5 THz
 - Ozone chemistry (OH), Temperature and Pressure
- **Approved mission, Phase C/D began January 1998;
instrument engineering model build in 1998**
- **Launch date 2002**

Status of NASA Submillimeter Sensors Earth Remote Sensing Program

- **EOS Microwave Limb Sounder is beginning Phase C/D Receiver Engineering Models to be delivered 1998.**
- **Major development thrust areas include:**
 - **Planar Schottky diode waveguide harmonic mixers up to 640 GHz**
 - **Planar Schottky diodes & integrated mixer circuitry for 2.5 THz**
 - **Planar varactor diode waveguide multipliers up to 320 GHz**
 - **Superconducting high- T_c diffusion cooled bolometer mixers**
 - **Laser diode pumped photomixers for THz LO generation**
 - **CO₂ pumped gas lasers for high power THz LO generation**
 - **High frequency GUNN oscillators**
 - **Low power digital autocorrelators**
 - **1-20 GHz ultra low noise HEMT amplifiers**
 - **MMIC power amplifiers**

Kukkonen Challenge 1993

- **First SIS mixer with**
 - Frequency > 1 THz
 - $T_{\text{sys}} < 1000 \text{ K DSB}$
- **First Solid State Local Oscillator Source**
 - Frequency > 1 THz
 - Output power > 100 microwatts
(100 GHz Bandwidth) Unclaimed



Awarded 1995

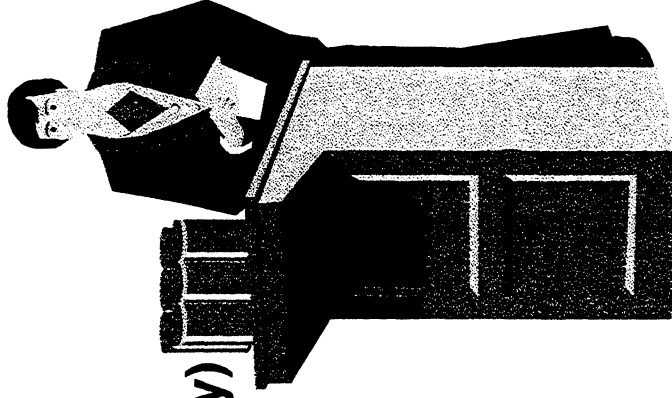
1997 Kukkonen Challenge

Local Oscillator

Frequency: 1-3 THz (500 GHz Tunability)

Power: 10-50 μ watts

Unclaimed



SOFIA -- A Versatile Facility for Infrared and Submillimeter Astronomy in the New Millenium

Mark Morris

Department of Physics and Astronomy
University of California, Los Angeles, CA

SOFIA, The Stratospheric Observatory for Infrared Astronomy, is a joint US and German project to develop and operate a 2.5-meter infrared telescope in an airborne platform, a Boeing 747-SP. NASA has contracted with the Universities Space Research Association (USRA), teamed with Raytheon E-Systems and United Airlines, to build and operate the observatory. The telescope assembly is being provided by a consortium of German companies led by MAN-GHH. Work has been under way for over a year on both the telescope and the aircraft, and first science flights are expected to begin in 2001. Observations and instrument development will proceed through the 20-year lifetime of the observatory, with 20% of the observing time (and a similar fraction of the instrument development) being assigned to German investigators. SOFIA will be used for observations from the UV to submillimeter wavelengths (0.3 microns to 1.6mm), with particular emphasis on mid and far-infrared, and submillimeter. The initial complement of instruments has been selected, and will be discussed, as will the broad scientific themes which SOFIA will be used to address. The prospects for THz astronomy are particularly exciting, and will be featured. Unlike its predecessor, the Kuiper Airborne Observatory, SOFIA will have facility instrumentation in addition to more specialized instruments built by selected principal investigator teams.

Noise performance of diffusion cooled hot-electron bolometers: theory vs. experiment

P.J. Burke, R.J. Schoelkopf, I. Siddiqi, and D.E. Prober

*Departments of Applied Physics and Physics, Yale University, 15 Prospect St., New Haven, CT
06520-8284*

A. Skalare, B.S. Karasik, M.C. Gaidis, W.R. McGrath, B.Bumble, and H.G. LeDuc

*Center for Space Microelectronics Technology, Jet Propulsion Laboratory, Caltech, Pasadena, CA
91109*

We have measured the spectrum of the output noise and the conversion gain from 0.1-7.5 GHz under identical conditions for both diffusion and phonon-cooled Nb bolometers, using a 20 GHz LO on a variety of devices varying in length from 0.08 μm to 3 μm , where the gain-bandwidth varies between 100 MHz and > 6 GHz. In this paper, we will present systematic comparison between theory and experiment for the devices measured. We find the frequency dependence of the device conversion efficiency and noise is well described by a simple thermal model. We have used two methods of inferring dR/dT , and describe the predictions for the magnitude of the efficiency and noise based on these. Neither method provides consistent quantitative predictions of the magnitude of device performance for a variety of operating conditions. Thus the device performance, while excellent, must continue to be investigated experimentally. We have therefore begun a series of experiments on lower T_c devices made of Al, which may have improved performance.

I. INTRODUCTION

Recent research on hot-electron bolometer mixers has enhanced the prospect of achieving quantum-noise-limited performance ($T_Q = h\nu/k$) in heterodyne receivers at THz frequencies. Hot-electron bolometer mixers of both the phonon cooled [1] and diffusion cooled [2-4] type have already shown excellent noise performance. We have recently predicted [5] and shown [2,6] that for Nb devices diffusion cooling provides much larger intermediate frequency (IF) gain bandwidth than can be obtained with phonon cooling, due to faster thermal response. We have also recently shown [7-9] that the spectrum of the device output noise obeys a simple thermal model, consisting of frequency-dependent thermal fluctuation noise plus a white background (Johnson noise). There, it was shown that there is a frequency scale associated with the dominant part of the output noise that scales with device length as it does for the gain bandwidth. In this paper, we present detailed comparisons of the zero IF magnitude of the conversion efficiency and output noise with theoretical predictions.

II. THEORY

For a lumped thermal element, theoretical calculations have already been performed which relate the device conversion efficiency and output noise to the dc current, LO power, device resistance, thermal conductance, temperature, and change of resistance with temperature (dR/dT) [10-12]. In this section, these lumped-element calculations are summarized in order to allow comparison with theory. A diffusion cooled device should properly be modeled as

a distributed thermal system. The results of our calculations for the distributed system are given later in this section and related to the lumped element approach calculations already available in the literature. A more microscopic approach which treats the spatial distribution of the superconducting energy gap in the presence of strong ac and dc self-heating, such as that being developed in [13], is desirable. We use the normal state heating results as a guide until a more complete theory can be developed.

A. Lumped Element Predictions

1. Conversion efficiency

The coupled conversion efficiency, defined as the power out at the IF over the power in at the rf, can be predicted in terms of the dc current I_{dc} , the LO power P_{LO} , the thermal conductance to the bath G , the resistance $R \equiv V_{dc}/I_{dc}$, and the change in resistance with temperature dR/dT as [10–12]

$$\eta(\omega) = \eta_{IF} \frac{P_{LO}}{2R} \left(\frac{I_{dc}(dR/dT)}{G_{eff}} \right)^2 \frac{1}{1 + (\omega\tau_{eff})^2} \quad (1)$$

$$= \eta(0) \frac{1}{1 + (\omega\tau_{eff})^2}, \quad (2)$$

where ω is the IF. This is the single-sideband (SSB) efficiency. We define the “gain bandwidth” as the IF at which the conversion efficiency drops by 3 dB relative to its low IF value. Thus, from Eq. 1, the gain bandwidth is given by $f_{3dB,gain} = 1/(2\pi\tau_{eff})$. Here τ_{eff} is the effective thermal time constant and G_{eff} the effective thermal conductance to the bath. The effective thermal conductance and time constant are related to the “bare” thermal conductance G and time constant τ_{th} by

$$\tau_{eff} \equiv \tau_{th}/(1 - \alpha), \quad (3)$$

$$\tau_{th} \equiv C/G, \quad (4)$$

$$G_{eff} \equiv G(1 - \alpha), \quad (5)$$

$$\alpha \equiv \frac{I_{dc}^2 dR/dT}{G} \left(\frac{R_L - R}{R_L + R} \right) \quad (6)$$

$$= \alpha_0 \left(\frac{R_L - R}{R_L + R} \right) \quad (7)$$

$$\alpha_0 \equiv \frac{I_{dc}^2 dR/dT}{G}, \quad (8)$$

where C is the (electronic) heat capacity, and R_L the load resistance at the IF, i.e., the input resistance of the IF amplifier, which is typically 50 Ω . The effect of the electro-thermal feedback between the electron temperature and the dc bias supply is described quantitatively by the parameter α . If α is small (due to small current or small dR/dT), then the effect of electro-thermal feedback is small, and the effective time constant τ_{eff} is equal to the “bare” thermal time constant τ_{th} , and the effective thermal conductance G_{eff} is equal to the bare thermal conductance G . The IF load resistance tends to suppress electro-thermal feedback if the device resistance R is comparable to the load resistance R_L . This is the case for the devices studied in this work.

The factor η_{IF} is defined as

$$\eta_{IF} \equiv \frac{4RR_L}{(R + R_L)^2}, \quad (9)$$

where R_L is the IF load resistance. This factor is not a standard mismatch factor in the usual sense, since the device impedance depends on frequency, whereas Eq. 9 is independent of frequency. The factor results from a more rigorous calculation of the effect of a finite load impedance at the IF on the electron dynamics [10,12]. The parameter varies between zero and one, and is one when the device resistance is equal to the input impedance of the IF amplifier.

2. Output Noise

In hot-electron bolometers, the important noise sources are expected to be thermal fluctuation noise and Johnson noise. The prediction for the output noise due to thermal fluctuations T_{TF} is given by [10–12]:

$$T_{TF}(\omega) = \left(I_{dc} T_e (dR/dT) \right)^2 \frac{1}{RG_{eff}(1-\alpha)} \frac{1}{1 + (\omega\tau_{eff})^2} \eta_{IF} \quad (10)$$

$$= T_{TF}(0) \frac{1}{1 + (\omega\tau_{eff})^2}, \quad (11)$$

where η_{IF} is the IF mismatch factor in Eq. 9, and T_e the electron temperature.

In addition to affecting the thermal fluctuation noise, electro-thermal feedback also affects the Johnson noise. The resultant expression for the Johnson output noise is given by [14,12]:

$$T_{John} = T_e \frac{1}{(1-\alpha)^2} \left(\frac{1 + (\omega\tau_{th})^2}{1 + (\omega\tau_{eff})^2} \right) \eta_{IF}. \quad (12)$$

This should be added to T_{TF} to get the total output noise, i.e.

$$T_{out}(\omega) = T_{John} + \frac{T_{TF}(0)}{1 + (\omega\tau_{eff})^2} \quad (13)$$

3. Mixer noise

The single-sideband (SSB) *mixer noise* $T_{mix} \equiv T_{out}/\eta$ is the noise referred to the input. (The double-sideband mixer noise is one half of the SSB mixer noise.) The mixer noise can now be calculated on the basis of the above calculations. The result is [12]:

$$T_{mix}(\omega)(SSB) = \frac{2T_e^2 G}{P_{LO}} + \frac{2RT_e G^2}{P_{LO} I_{dc}^2 (dR/dT)^2} \left(1 + (\omega\tau_{eff})^2 \right). \quad (14)$$

The first term is due to the thermal fluctuation noise, while the second term is due to the Johnson noise. The second term is dependent on the IF. This is simply due to that fact that Johnson noise is white, whereas the conversion efficiency decreases as the IF is increased. As a result of this, the *gain bandwidth* (i.e., the IF at which the conversion efficiency drops

by 3 dB) is not necessarily equal to the *noise bandwidth*, $f_{3dB,noise}$, which we define as the frequency at which the *mixer noise* increases by a factor of two. In fact, using Eq. 14, it is simple to show that [15]:

$$\frac{f_{3dB,noise}}{f_{3dB,gain}} = \sqrt{\frac{T_{John} + T_{TF}(0)}{T_{John}}} \quad (15)$$

B. Distributed system predictions

For a distributed non-superconducting system, the output noise temperature due to Johnson noise is predicted to be the average temperature along the length of the bridge. However, a quantitative theory for the conversion efficiency and thermal fluctuation noise which treats the device as a distributed system has not yet been developed¹. Therefore, in this section we will take the average temperature to determine the Johnson noise. We calculate the temperature profile under conditions of uniform dissipation of dc and ac power and attempt to relate the distributed system approach to the lumped element approach by deriving an effective time constant and thermal conductance between the electrons and the bath. These quantities can then be used in the theory of section II A as an approximation to expected device performance.

The impedance of the device at frequencies above the energy gap frequency (≈ 700 GHz in bulk Nb) is constant and equal to the normal state impedance. Therefore, if a high frequency signal is applied above the energy gap frequency, then the dissipation of power is uniform. However, if the frequency of the applied signal is less than the energy gap frequency, then it is possible that the dissipation of power varies spatially, since the temperature and hence resistance vary spatially. At T_c the energy gap vanishes, suggesting that the dissipation of power may still be uniform at all frequencies.

1. DC heating, no electron-phonon interaction

In the steady state, the flow of heat and the electron temperature are governed by the time-independent heat-diffusion equation. It can be shown [16,17] that the electron temperature along the length of the device is given by

$$T_e(x) = T_b \sqrt{1 + \frac{x}{L} \left(1 - \frac{x}{L}\right) \frac{PR}{T^2 L}}. \quad (16)$$

Here P is the power dissipated, T_b the bath temperature, and L the Lorenz number. The temperature profile is not directly measured in this work. To relate the above calculation more directly to measurements, we need to calculate the average temperature rise as a function of input power. The result is [18,17]:

¹The case of a lumped element connected to a bath *through* a distributed system was considered in [14] and [12].

$$\langle T_e \rangle = \frac{T_b}{2} + \left[T_b^2 \sqrt{\frac{\mathcal{L}}{PR}} + \frac{1}{4} \sqrt{\frac{PR}{\mathcal{L}}} \right] \arcsin \left(\sqrt{\frac{PR}{4T_b^2 \mathcal{L} + RP}} \right) \quad (17)$$

2. AC heating, no electron-phonon interaction

When the source of heating is time-dependent, as in most of the experiments in this work, the equation that governs the temperature profile is the time-dependent generalization of the heat diffusion equation. We have solved for the electron temperature $T_e(x, t)$ and find for a time dependent input power given by $P(t) = P_0 + P_\omega e^{i\omega t}$ that the electron temperature averaged along the length of the device is given by:

$$\begin{aligned} \langle T_e(x, t) \rangle_x = & T_b + P_0 \frac{L^2}{C} \\ & + e^{i\omega t} P_\omega \frac{8}{\pi^2} \frac{\tau_0}{C} \sum_{n=0}^{+\infty} \frac{1}{(2n+1)^4} \frac{1}{1+i\omega\tau_n}, \end{aligned} \quad (18)$$

where C is the heat capacity (the specific heat c times the volume), and τ_n is defined as

$$\tau_n \equiv \frac{L^2}{\pi^2 D (2n+1)^2}; \quad (19)$$

the diffusion constant D is equal to the thermal conductivity K divided by the specific heat c . The second term in Eq. 18 simply gives the dc rise in the average temperature. This allows a dc thermal conductance to be calculated from

$$\langle T_e \rangle_x = \frac{P_0}{C/L^2} = \frac{P_0}{\mathcal{L}T_b/R/12}. \quad (20)$$

Thus, the resultant "effective" dc thermal conductance is given by

$$G = \frac{\mathcal{L}T_b}{R/12}. \quad (21)$$

(This results in an effective resistance of $R/12$ derived by one of us in [5].) The third term in Eq. 18 is the ac component of the average temperature rise. To a good approximation, a lumped element approach can still be used, provided an effective thermal time constant of

$$\tau_{th} = \frac{L^2}{\pi^2 D} \quad (22)$$

is used. This time constant is *not* equal to the heat capacity C divided by the dc thermal conductance G , defined in Eq. 21. (Ref. [5] had used $\tau_{th} = C/G$; we now see that choice was in error by $\sim 20\%$. We choose to express the results in this work in terms of $R/12$, since that quantity was defined as "*Effective*" in ref. [5].) The diffusion time constant is equal to τ_{e-ph} when the bridge length is equal to πL_{e-ph} . Therefore, the crossover from phonon-cooled to diffusion-cooled behavior occurs at $L = \pi L_{e-ph}$.

3. Spatially distributed temperature fluctuations, no electron-phonon interaction

In section II A 2, the fluctuations in the temperature of a single thermal element connected through a thermal conductance to the thermal bath were considered. In a distributed system, fluctuations in the flow between nearest neighbors are postulated, and the magnitude of forcing function must be calculated. A generalized Langevin equation can be derived [19–21] for this process. In this work, we consider the solution to that equation with boundary conditions that the temperature at the ends is fixed. We find the following for the resultant spectral density of the temperature fluctuations:

$$\left(\langle \delta T_e(x, \omega) \rangle_x\right)^2 = \frac{4k_B T_e^2}{\frac{\tau_0}{C} \frac{\pi^2}{8}} \sum_{n=0}^{+\infty} \frac{1}{(2n+1)^4} \frac{1}{1 + (\omega\tau_n)^2}. \quad (23)$$

This equation was derived when no external power is applied, so that T_e is well defined, and equal to the bath temperature. The first term in Eq. 23 is the dominant term, and so the lumped element approximation can still be used to a very good approximation, provided an effective thermal time constant given by Eq. 22 is used. Finally, the low-frequency limit of Eq. 23 is:

$$\lim_{\omega \rightarrow 0} \left(\langle \delta T_e(x, \omega) \rangle_x\right)^2 = \frac{4k_B T_e^2}{C \frac{L^2}{12D}} = \frac{4k_B T_e^2}{\mathcal{L}T_b \frac{R}{12}}. \quad (24)$$

Thus, the lumped element prediction for the thermal fluctuation noise (eq. 10) can be used, provided the dc effective thermal conductance of $\mathcal{L}T_b \frac{R}{12}$ (eq. 21) is used.

4. DC heating with electron-phonon interaction

In the presence of electron-phonon interaction, the diffusion equation contains a “sink” term for the heat flow: power can flow from the electron system directly to the phonon system. The power flow density depends on the electron temperature and the phonon temperature, as well as the electron mean-free-path. There is no theoretical prediction that accounts for the strength of the electron-phonon coupling in Nb, so empirical results must be used. Experimentally [22], the electron-phonon coupling is given by:

$$p_{out} = A(T_e^4 - T_{ph}^4), \quad (25)$$

where p_{out} is the electron-phonon power flow per unit volume, and $A = 1 - 2 \times 10^{10} \text{ W m}^{-3} \text{ K}^{-4}$ for $D = 1 \text{ cm}^2/\text{s}$.

5. AC heating in the presence of electron phonon interaction; strong AC heating

Based on the above results, we can come to the following conclusions regarding the temperature profile: For very long devices, in the presence of weak or strong dc or ac heating, the behavior should be that of a lumped element with a single time constant, τ_{e-ph} . For devices much shorter than πL_{e-ph} in the presence of weak ac heating, a lumped element is a good approximation, with a single time constant of $L^2/\pi^2 D$. A similar conclusion is expected to hold in the case of strong ac heating, without electron-phonon interactions; this has not yet been calculated. A numerical calculation of the time-dependent diffusion

equation in the presence of electron-phonon interactions would be required to quantitatively evaluate the behavior between the two regimes. However, we expect that the cooling rates should approximately add, and this approximation will be used in the remainder of this paper.

C. Voltage dependence of conversion efficiency and noise; α from I-V curve

When dc and ac power are applied to the device, the electron temperature is heated above the bath temperature to somewhere near the critical temperature. However, the temperature of the electron system is difficult to predict accurately. This makes predictions of the conversion efficiency and output noise difficult, since dR/dT depends sensitively on the electron temperature near T_c . There is, however, a way to determine the value of α from the measured I-V curve which allows predictions of the output noise and efficiency. An increase in bias voltage increases the power dissipated, which raises the electron temperature. This in turn causes an increase in resistance. Based on this physical principle, a derivation is given in [11] for the following formula:

$$I_{dc}^2 dR/dP = I_{dc}^2 (dR/dT)/G = \frac{(dV/dI) - R}{(dV/dI) + R} \equiv \alpha_0. \quad (26)$$

Therefore, the measured dc I-V curve can provide a measurement of α_0 . (It is straightforward to calculate α from the dc I-V curve once α_0 is known.) The predictions of Eqs. 1 and 10 can be rewritten in terms of α and α_0 as

$$\eta(\omega_{IF}) = \frac{P_{LO}}{2 P_{dc}} \frac{\alpha_0^2}{(1 - \alpha)^2} \frac{1}{1 + (\omega_{IF}\tau_{eff})^2} \eta_{IF}, \quad (27)$$

$$T_{out} = \frac{T_e^2 G}{P_{dc}} \frac{\alpha_0^2}{(1 - \alpha)^2} \frac{1}{1 + (\omega_{IF}\tau_{eff})^2} \eta_{IF}. \quad (28)$$

The values of P_{dc} , P_{LO} , G , and T_e can be estimated with reasonable accuracy, so a prediction of device performance from the measured I-V curve is possible.

III. EXPERIMENTAL TECHNIQUE

A. Device Fabrication

The devices studied were all fabricated from the same thin (100 Å) Nb film, deposited on a quartz substrate. The patterned film has a transition temperature of $T_c \approx 5$ K, transition width $\Delta T_c \sim 0.5K$, and sheet resistance $\approx 33 \Omega$. The length of the bridge was defined by the normal metal (1000 Å thick Au) contacts using direct write e-beam lithography in a self-aligned process [23]. The length and width of the devices measured in this work were determined by inspecting the SEM image of different devices with the same design length in the same fabrication run. The estimated error using this technique is approximately $\pm 0.05 \mu m$. The devices measured in this work were not measured in an SEM, in order to avoid electrical damage. The device dc properties are summarized in Table I. The measured resistance vs. temperature curves are plotted in Fig. 1.

TABLE I. Device geometries and dc resistances.

Device:	Length (μm)	Width (μm)	R_N (Ω)	dR/dT^a (Ω/K)
A1	0.08	0.08	56	140
A2	0.08	0.08	56	-
B	0.16	0.08	80	200
C	0.24	0.08	96	250
D	0.6	0.2	93	-
E	3	1	86	-

^aFor this table, dR/dT is evaluated at the steepest point on the R vs. T curve.

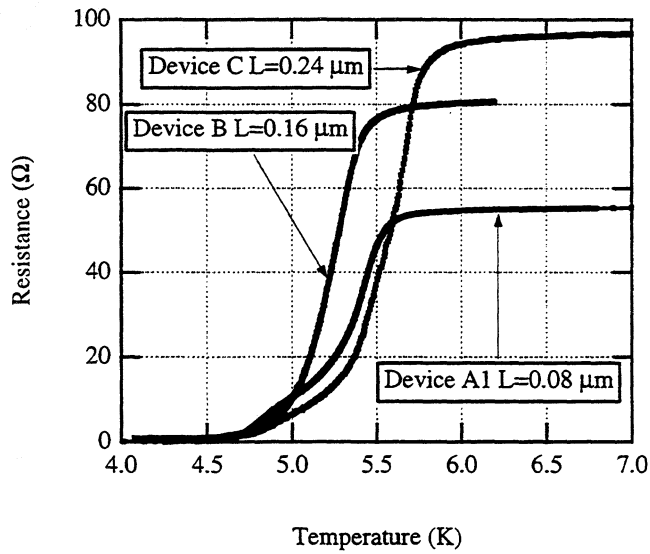


FIG. 1. Resistance vs. temperature curves for diffusion-cooled devices.

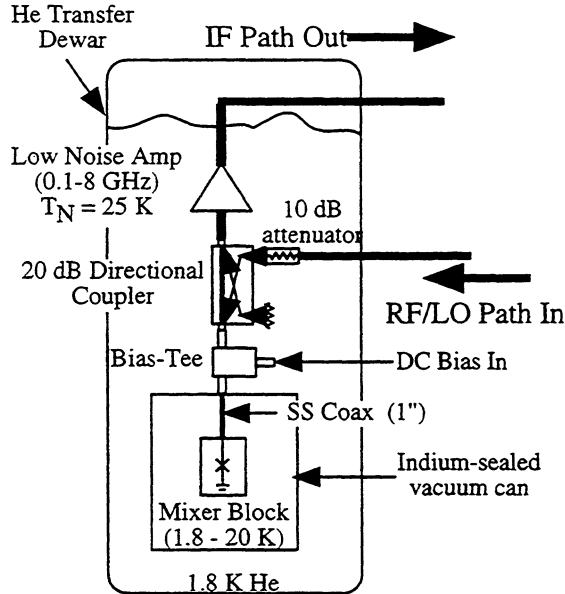


FIG. 2. Schematic of experimental setup.

B. Measurement technique and calibrations

Each device was mounted at the end of a section of 50Ω microstrip, using a “flip-chip” configuration to assure a broadband match. A cooled directional coupler was used to weakly couple in the rf and LO. The through port was connected to a cooled, low noise (≈ 25 K), broadband amplifier. The cable losses, amplifier gain, and coupler performance were each measured at 2 K. The mixer conversion efficiency as a function of intermediate frequency was thus measured to ± 2 dB. The amplifier chain noise and gain were calibrated *in-situ* to the plane of the device by heating the device above T_c and using it as a variable temperature load. This calibration applies for a source impedance given by R_n . Some measurements were performed with an isolator to confirm that impedance mismatch effects were not significantly affecting the calibration. Additional measurements of the return loss of the devices were performed in order to determine the impedance mismatch in the intermediate state. The coupling was 90% or better over the frequency range measured for all the devices, except device E. Therefore, the lack of an isolator should not significantly modify the calibration constants of the amplifier gain and noise which were determined when the device was in the normal state. A schematic of the experimental setup is shown in Fig. 2.

IV. EXPERIMENTAL RESULTS

A. Conversion efficiency and Noise

The measured conversion efficiency, output noise, and mixer noise all depend on several parameters under experimental control for a given device. We first discuss the dependence

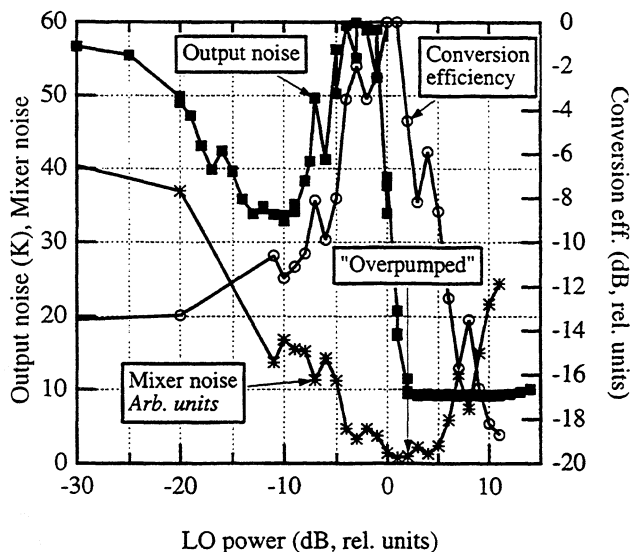


FIG. 3. Efficiency, output noise, and mixer noise vs. LO power for device A1.

on LO power, then on dc power, then on the IF. The measurements of the conversion efficiency and noise were all performed at a bath temperature of 2 K.

1. Conversion efficiency and noise vs. LO power

The (relative) conversion efficiency, output noise, and mixer noise are plotted as a function of LO power for fixed dc voltage in Fig. 3 for device A1. There are two cases of LO power which are of interest. We refer to the LO power required to maximize the (coupled) conversion efficiency as the “optimum efficiency” case. Note that the conversion efficiency and output noise peak at different LO powers, for a fixed bias voltage. However, the *mixer* noise is relatively constant near its minimum, even though the efficiency and output noise are changing very rapidly with LO power there. The second qualitative case is the “overpumped” case, where the critical current is suppressed. In that case, the output noise is drastically suppressed relative to its maximum value. The conversion efficiency is also somewhat lower than its maximum value. However, the mixer noise does not change much between the “optimum efficiency” case and the “overpumped” case. The overpumped case is of practical interest because the output noise and efficiency are less sensitive to the dc bias voltage, which will be discussed next. The general behavior indicated in Fig. 3 was observed in all the devices measured. For all the devices measured, the *mixer* noise in the overpumped case at the dc bias that minimized the mixer noise was lower than the mixer noise in the optimum efficiency case at the dc bias that minimized the mixer noise.

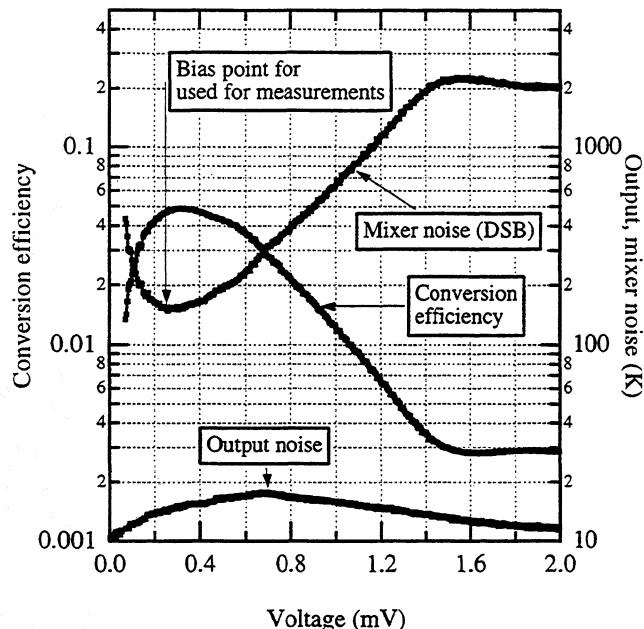


FIG. 4. Efficiency, output noise, and mixer noise vs. voltage for device B in overpumped case. IF=125-215 MHz.

2. Conversion efficiency and noise vs. dc power

In order to investigate the dependence of the conversion efficiency and noise on dc bias, the output noise and conversion efficiency were measured as a function of dc bias for two different LO powers (optimum efficiency, and overpumped) for each device. The resultant mixer noise was calculated by taking the ratio of the output noise to the conversion efficiency. The measurements were done at an IF that is low enough to be representative of the zero IF limit of the device performance. The results for a typical device (device B) are plotted in Figs. 4 and 5. The immediate conclusion in these graphs is that the mixer noise is *very low*, ≈ 200 to 300 K (DSB). In the overpumped case, the conversion efficiency, output noise, and mixer noise are seen to depend smoothly on the dc bias.

The results of the measurements of the frequency dependence and magnitude of the conversion efficiency and output noise are summarized in Table II. The relative spectrum of the output noise behaves similarly with frequency as the conversion efficiency, as can be seen by comparing the fitted time constant for the conversion efficiency and output noise. This implies that the 3 dB noise bandwidth is larger than the 3 dB gain bandwidth, which is also indicated by comparing the two quantities in Table II.

B. Comparison with theory

In this section, we compare the measured results of the coupled output noise and coupled conversion efficiency with the theoretical predictions presented in section II. The predicted

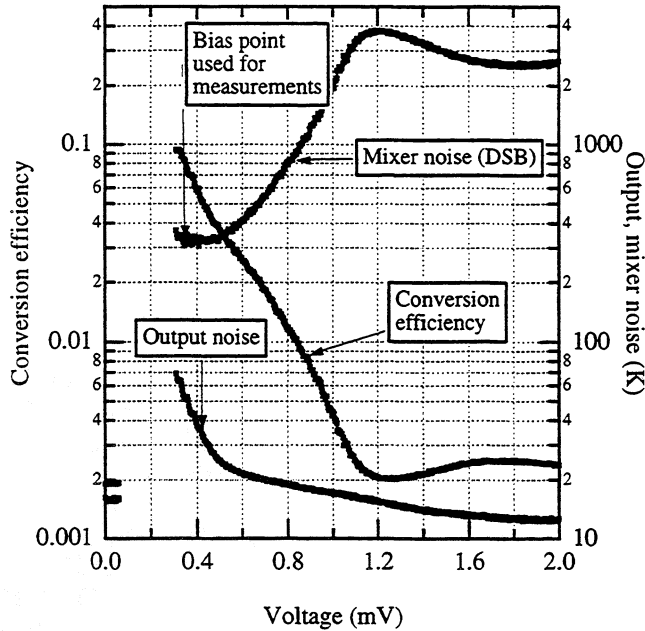


FIG. 5. Efficiency, output noise, and mixer noise vs. voltage for device B in optimum efficiency case. IF=125-215 MHz.

TABLE II. Device parameters and output noise; top half: optimum efficiency case; bottom half: overpumped case.

Dev.	L (μm)	$\eta(0)$ (dB)	$(2\pi\tau_{th})^{-1}$ (GHz)		$T_{TF}(0)$ (K)	T_J (K)	Noise BW (GHz)	$T_{mix}(0) \equiv T_{out}(0)/2\eta(0)$ (K, DSB)
			from fit of $\eta(f)$ to Eq. 2	from fit of $T_{out}(f)$ to Eq. 13				
A1	0.08	-5.6	≥ 6	2.3	49	25	> 6	120
A2	0.08	-	≥ 6	-	-	-	-	-
B	0.16	-11	2.4	1.4	34	23	3.9	320
C ^a	0.24	-8	1.5	-	-	-	-	200
D	0.6	-4.1	0.3	0.13	262	19	0.73	120
E	3	-2 ^b	0.08	0.13	223	8	0.75	530
A1	0.08	-7	≥ 6	≥ 6	-	-	> 6	≤ 100
B	0.16	-13.5	2.25	2.3	6	10	3.1	170
C	0.24	-12.7	1.5	-	-	-	-	160
D	0.6	-10.4	0.38	0.11	33	16	0.53	120
E	3	-11.7	0.064	0.045	62	7	0.16	310

^aDevice C was electrically damaged before the noise spectrum could be measured.

^bThe lowest efficiency measured was only -4 dB, but the fit returned a value of -2 dB because the lowest IF measured for this particular experiment was only 100 MHz.

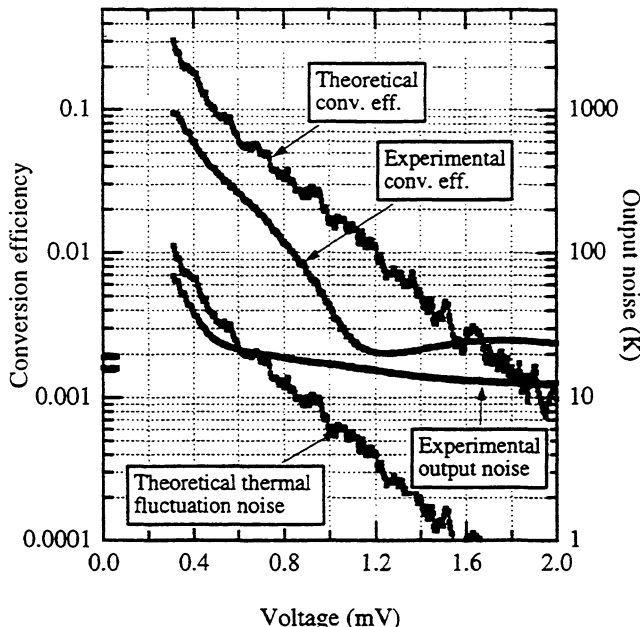


FIG. 6. Theoretical and experimental conversion efficiency and output noise for dev. B, optimum efficiency case. The predicted Johnson noise is not plotted, but is of order $T_c \approx 5.5$ K.

conversion efficiency and output noise based on Eqs. 1 and 10 was calculated for each device by using the maximum value of dR/dT measured with small bias current and no LO power. This method is expected to predict an upper limit for η and T_{TF} since the electron temperature may not be at a point where dR/dT is maximized under operating conditions. A "local" value of dR/dT can be estimated by inferring the electron temperature from $R \equiv V_{dc}/I_{dc}$, and evaluating dR/dT at the inferred electron temperature from the measured R vs. T curve. This method was carried out for the dc bias voltages which minimized the mixer noise in both the overpumped and optimum efficiency cases. The parameters for the theoretical calculations are shown in the Appendix A, Table IV. The results of the calculated conversion efficiency based on this method are presented in Table III.

The method to determine dR/dP (which we call method 2) and hence η and T_{out} directly from the measured I-V curve was described in section II C. This procedure has also been carried out, and the resulting theoretical predictions for the conversion efficiency and noise are compared to the experimental results for a typical device (B) measured in the optimum efficiency and overpumped cases in Figs. 6- 7. Since the predictions depend on the calculated values of α and α_0 , these are also plotted with the I-V curve for device B in Appendix B, Fig. 8. The results of the calculated conversion efficiency based on this second method are also in Table III for all the devices.

For devices B and C the second method gives reasonable agreement between theory and experiment. Since the length of device A is comparable to the electron-electron length ($\sqrt{D\tau_{ee}}$, with τ_{ee}^{-1} the electron-electron scattering rate), a local equilibrium temperature cannot be well defined and the simple thermal model may not apply quantitatively to this device. We have also calculated the predicted output noise and conversion efficiency as a function of dc bias using method 2 (Eq. 26) for all the devices studied in both the optimum

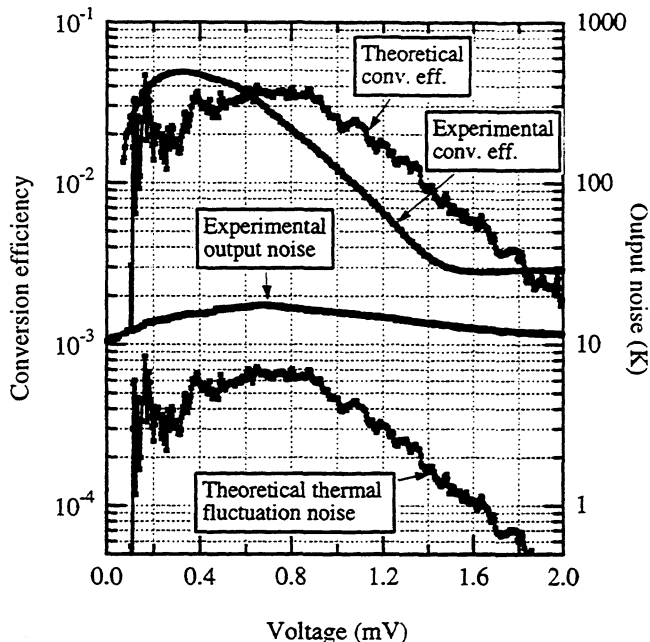


FIG. 7. Theoretical and experimental conversion efficiency and output noise for dev. B, overpumped case. The predicted Johnson noise is not plotted, but is of order $T_c \approx 5.5 K$.

efficiency and overpumped cases [8]. We find qualitative agreement between the theoretical and experimental dc bias dependence of the output noise and efficiency for all devices except device A. However, neither method provides consistent quantitative predictions of device performance for a variety of operating conditions. Thus, device performance cannot yet be quantitatively predicted from first principles and must continue to be investigated experimentally. We find it to be excellent. Lower T_c devices made of Al may have improved performance.

ACKNOWLEDGMENTS

We thank A. Kozhevnikov for assistance with the experiments. This research was supported by the NSF and by the NASA Office of Space Science. Funding for PJB was provided by a NASA Graduate Student Fellowship as well as a Connecticut High Technology Fellowship.

APPENDIX A: DEVICE PARAMETERS

APPENDIX B: DYNAMIC AND ABSOLUTE RESISTANCE, α , AND α_0

TABLE III. Predicted and experimental conversion efficiency and output noise; top half: optimum efficiency case; bottom half: overpumped case.

Dev.	$\eta(0)$ (dB)			$T_{\text{out}}(0) = T_{TF}(0) + T_J$ (K)		
	calc. from eq. 1 max./local dR/dT used	calc. from eq. 27	expt.	calc. from eq. 10 max./local dR/dT used	calc. from eq. 28	expt.
A1 ^b	+1.0/-5.3	-17.5	-5.6	237.5/60.5	9	37
B	+0.2/-3.2	-7	-11	389.5/180.5	78.5	51
C	+0.7/+0.2	-9.4	-9.9	671.5/223.5	20.5	44
D ^c	+0.3/-	-0.5	-5.4	365.5/-	179.5	118
E ^c	+0.3/-	0.0	-8.6	695.5/-	409.5	105
A1 ^b	+2.3/0.0	-31	-7	165.5/91.5	5.6	14
B	-2.2/-4.0	-17.2	-13.5	115.5/78.5	9	14
C	+0.7/+0.2	-13.8	-12.7	330.5/145.5	7.8	17
D ^c	0.0/-	-8.8	-10.4	92.5/-	17.5	26
E ^c	-7.0/-	-3.7	-20	42.5/-	83.5	10

^aA value of 5.5 K was assumed for T_J in the theoretical prediction.

^bThe output noise for device A quoted in this table was measured under slightly different operating conditions than that plotted in Fig. 1.

^cThe low frequency limit of the noise and efficiency is not well-determined for devices D and E, so the experimental value at 125-175 MHz is quoted in this table.

TABLE IV. Device parameters; top half: optimum efficiency case; bottom half: overpumped case

Dev.	V_{dc} (mV)	P_{dc} (nW)	P_{LO} (nW)	dR/dT (Ω/K) loc./max.	G^a (nW/K) Exp. (thy.)	α_0	α	η_{IF}
A1	0.45	9	13	68/140	40 (29)	0.16	0.06	0.86
B	0.35	5.5	5	135/200	30(20)	0.56	0.22	0.85
C	0.46	6.4	8	144/250	-(17)	0.41	0.086	0.95
D	0.38	5.6	15	-/250 ^b	44(-)	0.66	0.24	0.87
E	0.65	39	85	-/250	520(-)	0.71	0.46	0.58
A1	0.5	9	26	103/140	40 (29)	-0.025	-0.007	0.92
B	0.25	2.3	10	163/200	30(20)	0.095	0.028	0.92
C	0.4	4.3	16	164/250	-(17)	0.15	0.021	0.98
D	0.23	1.9	30	-/250	48(-)	0.13	0.037	0.92
E	0.2	2.9	170	-/250	520(-)	0.13	0.076	0.68

^aMeasured value at 6 K or 6.5 K extrapolated to 5.5 K. (Theoretical value calculated using $LT/(R_N/12)$.) G was determined experimentally using noise thermometry measurements in the normal state.

^bNot actually measured. Estimated based on device C, which has the same normal state resistance as devices D,E.

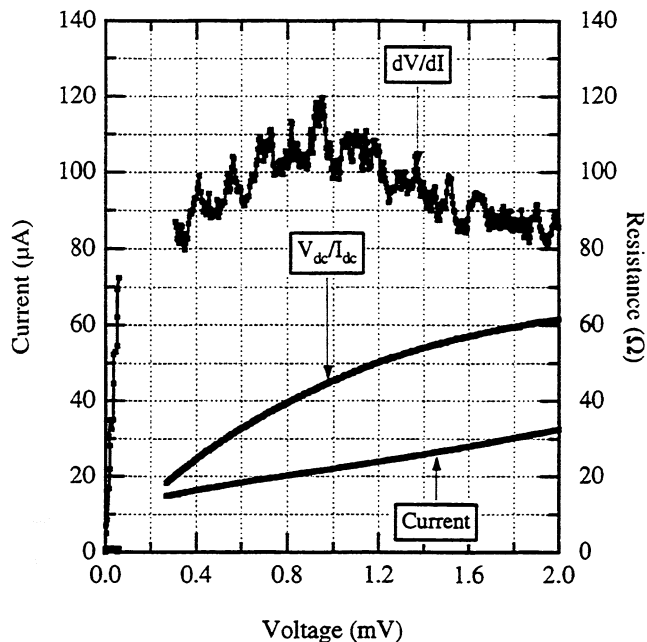


FIG. 8. IV curve, dynamic and absolute resistance for device B, optimum efficiency case.

- [1] J. Kawamura, R. Blundell, C. Y. Tong, G. Gol'tsman, E. Gershenzon, and B. Voronov, *Applied Physics Letters* **70**, 1619 (1997).
- [2] A. Skalare, W. R. McGrath, B. Bumble, H. G. LeDuc, P. J. Burke, A. A. Verheijen, R. J. Schoelkopf, and D. E. Prober, *Applied Physics Letters* **68**, 1558 (1996).
- [3] A. Skalare, W. McGrath, B. Bumble, and H. G. LeDuc, *IEEE Transactions on Applied Superconductivity* **7**, 3568 (1997).
- [4] B. S. Karasik, M. C. Gaidis, W. R. McGrath, B. Bumble, and H. G. LeDuc, *Applied Physics Letters* **71**, 1567 (1997).
- [5] D. E. Prober, *Applied Physics Letters* **62**, 2119 (1993).
- [6] P. J. Burke, R. J. Schoelkopf, D. E. Prober, A. Skalare, W. R. McGrath, B. Bumble, and H. G. LeDuc, *Applied Physics Letters* **68**, 3344 (1996).
- [7] P. J. Burke, R. J. Schoelkopf, D. E. Prober, A. Skalare, B. S. Karasik, M. C. Gaidis, W. R. McGrath, B. Bumble, and H. G. LeDuc, *Applied Physics Letters* **72**, 1516 (1998).
- [8] P. J. Burke, Ph.D. thesis, Yale University, 1997, available from authors.
- [9] P. J. Burke, R. J. Schoelkopf, D. E. Prober, A. Skalare, B. Karasik, M. Gaidis, W. McGrath, B. Bumble, and H. LeDuc, (1998), to be submitted to *Journal of Applied Physics* (in preparation).
- [10] F. Arams, C. Allen, B. Peyton, and E. Sard, *Proceedings of the IEEE* **54**, 612 (1966).
- [11] H. Ekström, B. Karasik, E. Kollberg, and K. Yngvesson, *IEEE Transactions on Microwave Theory and Techniques* **43**, 938 (1995).
- [12] B. Karasik and A. Elantev, in *Proceedings of the 6th International Symposium on Space Terahertz Technology*, edited by J. Zmuidzinas and G. Rebiez (CalTech, Pasadena, CA, 1995), pp. 229–246. See Ref. [24].
- [13] D. W. Floet, J. Baselmans, J. Gao, and T. Klapwijk, in *Proceedings of the 9th International Symposium on Space Terahertz Technology*, edited by W. McGrath (Caltech, Pasadena, CA, 1998).

- [14] J. C. Mather, *Applied Optics* **21**, 1125 (1982).
- [15] E. Gershenzon, M. Gershenzon, G. Gol'tsman, A. M. Lyul'kin, A. Semenov, and A. Sergeev, *Soviet Physics: Technical Physics* **34**, 195 (1989).
- [16] A. Mittal, 1995, personal communication.
- [17] M. J. M. de Jong, Ph.D. thesis, Leiden University, 1995.
- [18] A. Skalare, 1994, personal communication.
- [19] L. D. Landau and E. M. Lifshitz, *Statistical Physics Part 2* (Pergamon, Oxford, 1980).
- [20] K. M. van Vliet and J. R. Fassett, in *Fluctuation Phenomena in Solids* (Academic Press, New York, 1965), Chap. Fluctuations Due to Electronic Transitions and Transport in Solids.
- [21] R. F. Voss and J. Clarke, *Physical Review B* **13**, 556 (1976).
- [22] E. Gershenzon, M. Gershenzon, G. Gol'tsman, Lyul'kin, A. Semenov, and A. Sergeev, *Journal of Experimental and Theoretical Physics* **70**, 505 (1990).
- [23] B. Bumble and H. G. LeDuc, *IEEE Transactions on Applied Superconductivity* **7**, 3560 (1997).
- [24] in *Proceedings of the 6th International Symposium on Space Terahertz Technology*, edited by J. Zmuidzinas and G. Rebiez (CalTech, Pasadena, CA, 1995).

First Light with an 800 GHz Phonon-cooled HEB Mixer Receiver

Jonathan Kawamura¹

California Institute of Technology and Harvard-Smithsonian Center for Astrophysics

Raymond Blundell, C.-Y. Edward Tong, D. Cosmo Papa, Todd R. Hunter
Harvard-Smithsonian Center for Astrophysics

Gregory Gol'tsman, Sergei Cherednichenko, Boris Voronov, Eugene Gershenzon
Moscow State Pedagogical University

Abstract

Phonon-cooled superconductive hot-electron bolometric (HEB) mixers are incorporated in a waveguide receiver designed to operate near 800 GHz. The mixer elements are thin-film niobium nitride microbridges with dimensions of 4 nm thickness, 0.2 to 0.3 μm in length and 2 μm in width. At 780 GHz the best receiver noise temperature is 840 K (DSB). The mixer IF bandwidth is 2.0 GHz, the absorbed LO power is $\sim 0.1 \mu\text{W}$. A fixed-tuned version of the receiver was installed at the Submillimeter Telescope Observatory on Mt. Graham, Arizona, to conduct astronomical observations. These observations represent the first time that a receiver incorporating any superconducting HEB mixer has been used to detect a spectral line of celestial origin.

Introduction

Superconducting HEB mixers look to become the technology of choice for heterodyne detection above 1 THz. This technology has thus far fulfilled, in the laboratory at least, all the basic requirements for efficient astronomical observing at submillimeter wavelengths: low-noise performance, low local oscillator power requirement and large intermediate frequency bandwidth. However, performance in the laboratory is often a poor substitute for performance in the field. Even with the detection of molecular lines in the laboratory with this type of receiver, many people, in particular potential users, remain cautiously skeptical about whether or not this new technology will be useful in practice. In order to address this final concern directly, we have aimed our efforts in the past six months to build a complete receiver system employing a superconducting HEB mixer to take to a submillimeter telescope facility and test its performance definitively.

Our receiver employs a phonon-cooled HEB mixer [1] fabricated from niobium nitride [2]. The mixer elements are thin-film microbridges with typical thickness of 4 nm fabricated on crystalline quartz substrates. The critical temperature, T_c , is ~ 9 K, with a transition width of ~ 1 K. The sheet resistance ranges from 1000 to 2000 Ω .

Over the course of our experiments [3], we have learned that all of our mixers fabricated using conventional optical photolithography require more local-oscillator power

¹ present address: Caltech 320-47, Pasadena, CA 91125

than can be conveniently provided by frequency multiplied solid-state sources, especially at the highest frequencies. For example, we were able to pump an 800 GHz mixer at only two frequency points. Furthermore, with optical lithography it is difficult to make a mixer that has simultaneously a low impedance and low LO power requirement. Since our goal was to build a receiver for a telescope, we absolutely needed to be able to pump the mixer continuously across the operating band of the receiver. Also, we desired to lower the mixer impedance from about 400 Ω or so, which was typical of optically fabricated mixers, to about 100 Ω . For a phonon-cooled mixer the optimal LO power simply scales with the volume of the microbridge. With the thickness fixed, the area of the mixer can be flexibly adjusted in order to give a wide range in impedance and in the level of local-oscillator power. We have therefore fabricated NbN microbridges defined by electron beam lithography that have in-plane areas ~ 10 times smaller than those manufactured for our previous studies. Such mixers have LO power requirement reduced by 10 dB compared to that of larger mixers. The mixers also have favorably lower impedance. In this paper we state the performance of our HEB receiver, and show results of its operation on a telescope.

Receiver Performance

A current-voltage curve of a mixer is shown in Figure 1. This mixer is 2 μm wide and 0.3 μm long, with a normal room-temperature resistance of 90 Ω . The general shape of the IV curve is similar to the larger mixers. One major difference, however, is that the voltage scale is compressed in the voltage-total IF power curve, which is also plotted in the figure. This difference is a clue that the new mixer will require less local-oscillator power and dc power to reach the optimal operating point. Incidentally, this difference also has interesting consequences for the mixer saturation level, which is discussed below.

The mixer is incorporated in a waveguide block with a mechanically driven backshort. The block was designed to accommodate an SIS mixer, the details of which can be found in [4]. The corrugated feed illuminates a cold off-axis paraboloid and an optical flat before exiting the cryostat. Several layers of porous Teflon provides near-infrared filtering, and a 0.5 mm Teflon window seals the cryostat. The local-oscillator is a multiplied solid-state source, and a Martin-Puplett diplexer is used to combine the local-oscillator and signal beams.

Receiver noise temperature

The sensitivity of the receiver was measured using the standard Y -factor technique of alternatively placing a room temperature load and a cold load at the temperature of liquid nitrogen at the input of the receiver. No corrections were made. We were able to make a continuous measurement of the receiver noise temperature across the operating band of the local-oscillator source. The noise performance across the 800 GHz band is plotted in Figure 2, and across the band, the noise temperature is always less than 2 K GHz⁻¹. The best noise temperature at 780 GHz is 850 K, where we estimate that the conversion loss is 14 dB and that $T_{mix} = 750$ K. The receiver will actually work all the way down to the cut-off frequency of the waveguide, which is near 600 GHz.

IF bandwidth

We have measured the intermediate frequency bandwidth of a representative mixer from the same batch of mixers at a signal frequency of 20 GHz. The measurement is shown in Figure 3, which shows that the -3 dB roll-off in the gain occurs at 2.0 GHz. This is very similar to the bandwidth we have measured in a number of previous batches. Unfortunately, this value falls considerably short of the 10 GHz predicted for NbN-based mixers, and we attribute this to the quality of the film that can be grown on the chosen substrate [2]. For our present purposes, 2.0 GHz is sufficient; but, for such applications as extragalactic observations and interferometry, it will be necessary to have more bandwidth.

Gain compression and LO power

The LO power level and the linearity of the 800 GHz mixers were measured using a technique described in [5]. In this method, a second local-oscillator is coupled to the receiver at the signal port. The input power from the second source is calibrated against the receiver's response to the hot and cold loads. The technique assumes equivalence between the receiver's response to broad-band noise and monochromatic radiation. Using this technique, we determined that the LO incident at the receiver is $1 \mu\text{W}$. The 1 dB compression point occurs about -25 dB below the LO power, which corresponds to an input power of 3 nW. This result is quite different from our result with the larger mixer, in which the 1 dB compression point was -6 dB below the LO power. We conclude that the saturation is occurring at the IF output of the receiver rather than at the RF input. That this might be the case can be simply argued: from Figure 1, we estimate that the maximum IF voltage swing in which there is constant conversion gain is about 0.1 mV. If the IF load resistance is 50Ω , then the IF output power with maximum swing voltage is 0.1 nW. From our estimate of the conversion loss for this mixer, about 16 dB, we see that the power at the input of the mixer is 4 nW, in good agreement with the actual measured value. Thus, the mixer saturates when there is 3 nW of power incident on the receiver within a bandwidth given the IF bandwidth. In terms of load temperature, this represents $\sim 5 \times 10^4$ K. Thus, our Y-factor measurements were made well within the linear regime of the mixer.

From the constant temperature assumption, we measure that the absorbed LO power is about $\sim 0.1 \mu\text{W}$. Thus, there is a 10 dB loss in the LO path. From FTS measurements we know that we are losing about 3 dB in gain from the peak response near 600 GHz. Also, the losses in the diplexer and filters is maximally about 4 dB. Thus there appears to be about 3 dB of power that is lost. This may simply be the power being absorbed to heat the lattice. Further investigation is necessary to understand these losses.

Astronomical observations

The receiver was installed at the 10 m Submillimeter Telescope Observatory (SMTO) on Mt. Graham, Arizona in March, 1998. The primary task of the run was to use the HEB mixer receiver to detect known submillimeter lines of astronomical importance in order to prove that it works as a practical instrument. The mixer was mounted in a fixed-tuned block of the type developed for the SMA receivers [4], and is fixed so that over the operating band the mixer sees a real impedance of about 110Ω . The receiver IF bandpass is

centered at 1.5 GHz, and useable bandwidth of the receiver, measured after the facility spectrometer, is 600 MHz. The noise temperature at an LO frequency of 810 GHz is 1300 K, which is actually 15% noisier than the receiver's performance in the laboratory at sea level. We attribute this degradation to the cooler bath temperature at high altitude. The noise temperature at an LO frequency of 690 GHz was 650 K. The receiver noise temperature as a function of IF is shown in Figure 4. The LO was a conventional frequency multiplied solid-state Gunn oscillator. The LO was coupled to the signal beam with a Martin-Puplett diplexer employing free-standing wire grids. The stability of the receiver system was primarily determined by the changes in the LO power level. The receiver setup is identical an SIS-based system, with the exception that it is not necessary to provide a magnetic field to the mixer. Our brief experience with the HEB receiver on a telescope shows that it is easier to use than an SIS receiver.

We observed several bright sources to test the receiver under reasonably favorable sky opacities. For example, we made a five-point map of IRC+10216 in CO ($J=7\rightarrow 6$) at 805 GHz, shown in Figure 5, which beautifully illustrates that the beam of the telescope is, as expected, about 10 asec. With the same receiver, we were also able to observe the CO ($J=6\rightarrow 5$) at 690 GHz and the fine-structure transition of neutral carbon at 809 GHz.

Conclusion

We have developed a waveguide receiver employing a phonon-cooled superconductive HEB mixer, and have conducted astronomical observations with it. The receiver has sufficient bandwidth, reasonable noise performance, and is generally a very useable, practical system. We anticipate that in the coming year that we will optimize the receiver design, and make its performance competitive to SIS receivers now in operation.

Acknowledgments

We thank P. Strittmatter of Steward Observatory for allocating valuable observing time to us at the SMTO. The staff of the SMTO facility gave us indispensable help in setting up the receiver and assisting our observations. In particular, F. Patt helped us to set up all the hardware and sorted out all the interconnections between the telescope and the receiver. We are indebted to M. Smith for his meticulous work on many components of our receiver, most notably the mixer block. The rest of the SAO receiver laboratory staff built a viable system on very short notice. J. K. acknowledges support from the Smithsonian Institution Short-term Visitor program. Research at M.S.P.U. is supported by the Russian Program of Condensed Matter (Superconductivity division) under grant No. 98062.

References

- [1] E. M. Gershenzon et al. 1990, *Sov. Phys. Superconductivity* 3, 1583
- [2] Y. P. Gousev et al. 1994, *J. Appl. Phys.* 75, 3695; Cherednichenko et al. 1997, *Proc. 8th Int. Symp. Space Terahertz Tech.*, Cambridge, Massachusetts.
- [3] J. Kawamura et al. 1997, *Proc. 8th Int. Symp. Space Terahertz Tech.*, Cambridge, Massachusetts and references therein.
- [4] R. Blundell et al. 1995, *IEEE Trans. Microwave Theory Tech.* 43, 933
- [5] C.-Y. E. Tong et al, 1996, *IEEE Trans. Microwave Theory Tech.* 44, 1548

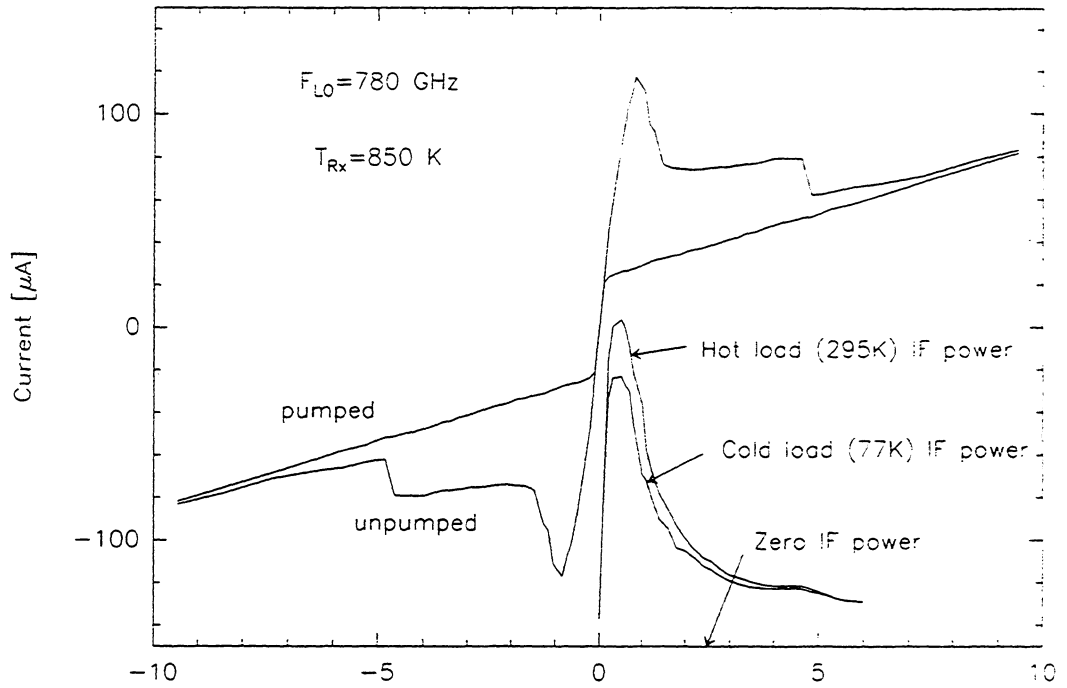


Figure 1. Current-voltage characteristic of a mixer 2 mm wide and 0.3 mm long measured at 4.2 K. At an LO setting of 780 GHz, the receiver noise temperature is 850 K (DSB). The operating bias point is 0.7 mV.

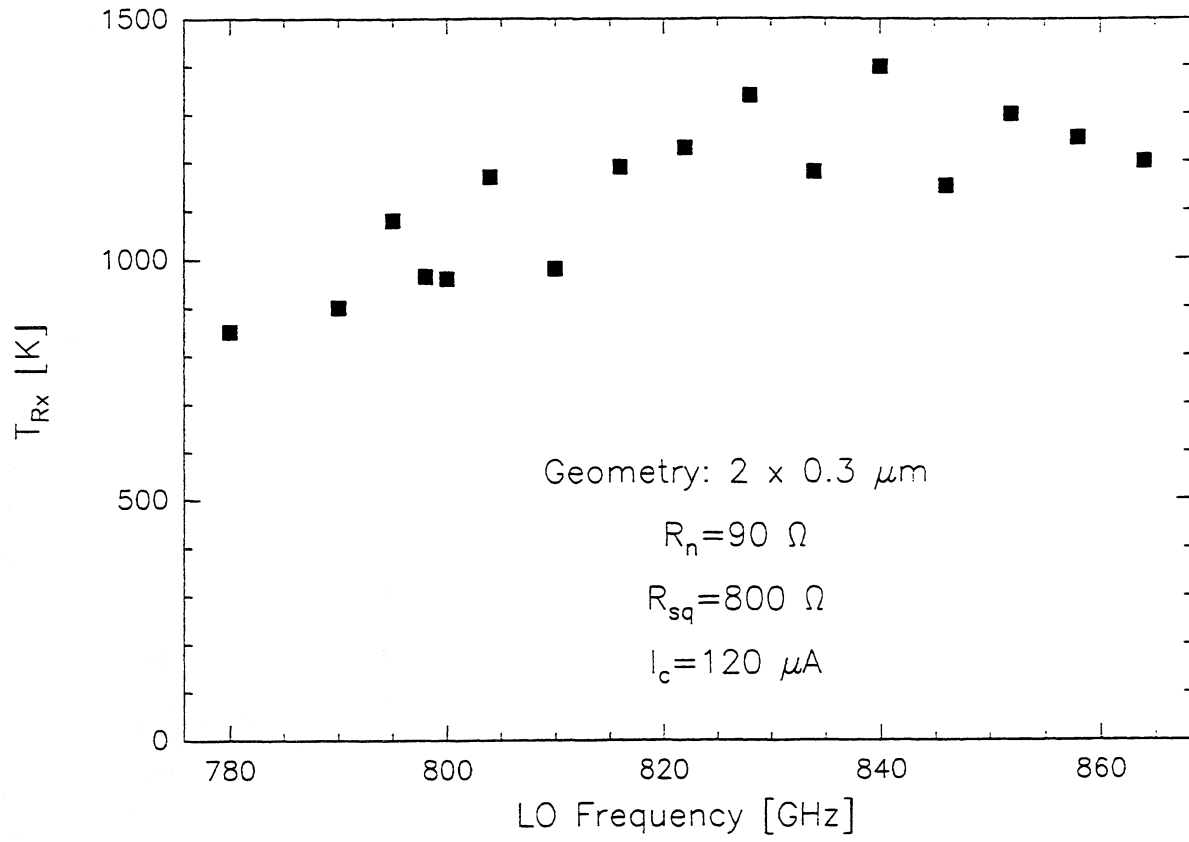


Figure 2. The receiver noise temperature across the operating band of the local-oscillator source.

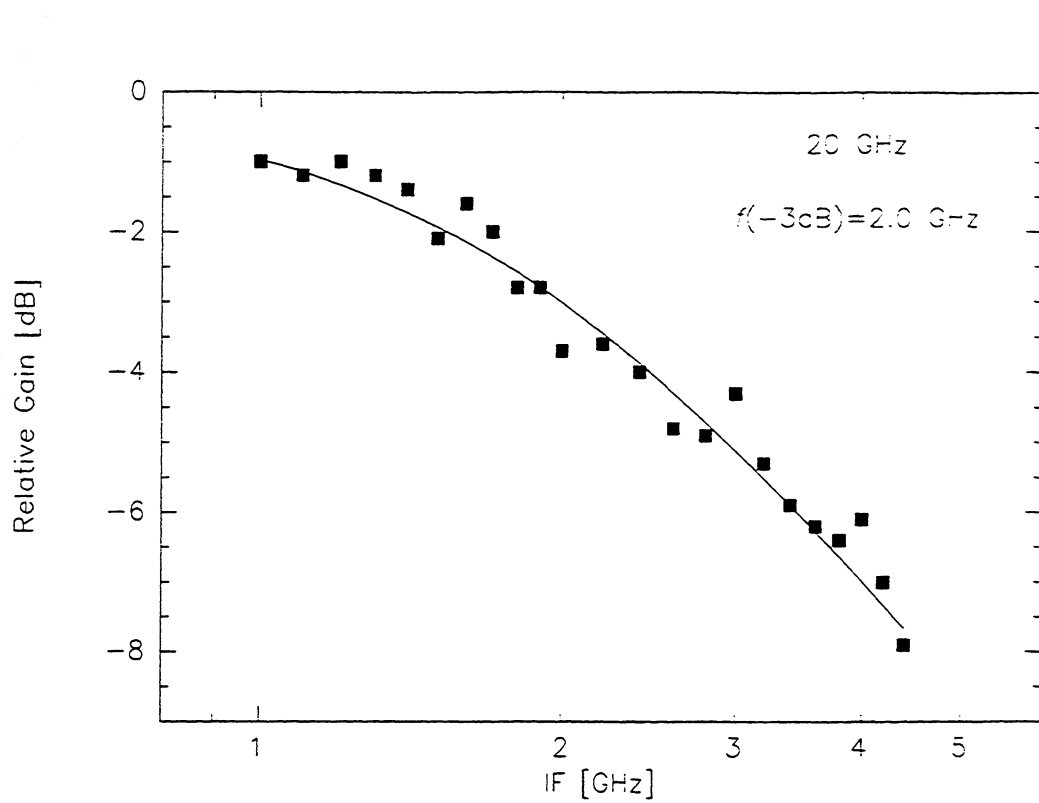


Figure 3. The IF gain bandwidth measured at a signal frequency of 20 GHz. The data are fitted to the formula $(1+(f/f_c)^2)^{-1}$, where $f_c=2.0$ GHz.

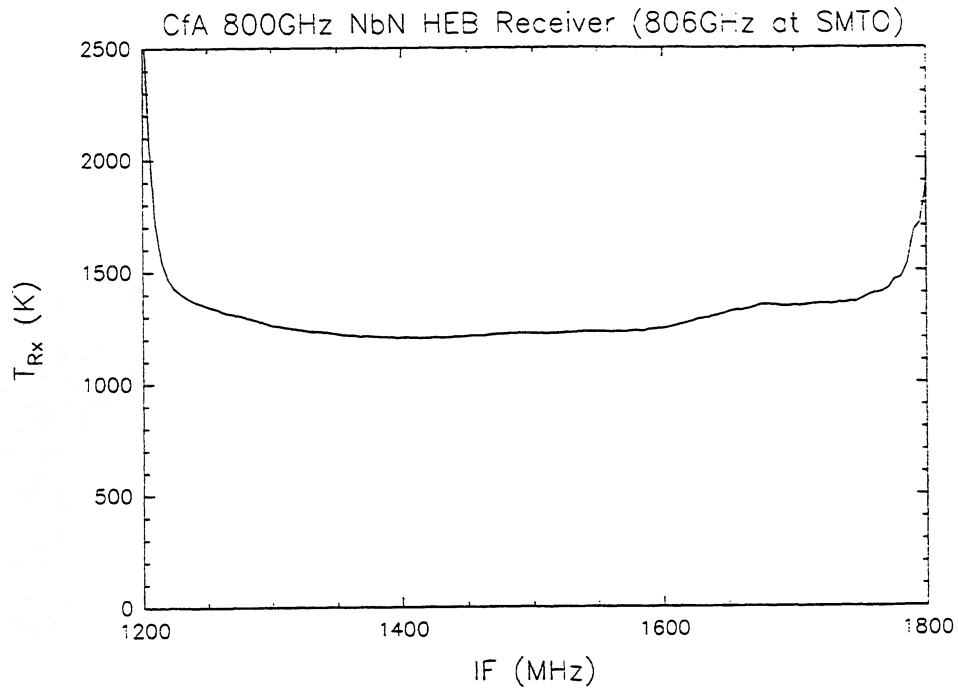


Figure 4. The receiver noise temperature measured as a function of IF for the mixer used at the telescope. This is computed after the AOS. The useful bandwidth is roughly 600 MHz, and there apparently is no degradation in the noise at the highest IF. The slight rise at 1.7 GHz is due to the response of the isolator following the mixer.

CO(7-6) in IRC+10216
 CfA NbN phonon-cooled HEB at SMT0

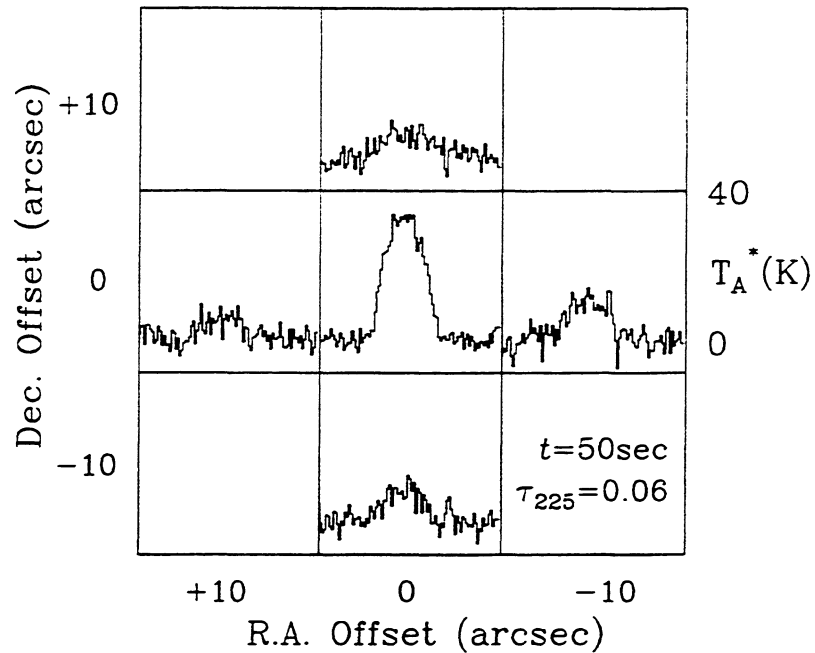


Figure 5. A five-point map of IRC+10216 in CO(7-6). The LO frequency for this measurement is 805 GHz. Each panel represents a spectra taken at different sky offsets from the central position, and within each panel, the amplitude is given in antenna temperature and the frequency span is about 100 MHz.

Quasioptical phonon-cooled NbN hot electron bolometer mixers at 0.5-1.1 THz

S. Svechnikov, A. Verevkin, B. Voronov, E. Menschikov, E. Gershenzon, and G. Gol'tsman

Physics Department, Moscow State Pedagogical University, Moscow 119435, Russia.

Abstract

The noise performance of a receiver incorporating spiral antenna coupled NbN phonon-cooled superconducting hot electron bolometric mixer is measured from 450 GHz to 1200 GHz. The mixer element is thin (thickness ~ 3.5 nm) NbN $1.5 \mu\text{m}$ wide and $0.2 \mu\text{m}$ long film fabricated by lift-off e-beam lithography on high-resistive silicon substrate. The noise of the receiver temperature is 1000 K at 800-900 GHz, 1200 K at 950 GHz, and 1600 K at 1.08 THz. The required (absorbed) local-oscillator power is ~ 20 nW.

Introduction

Over the last few years, hot electron bolometric (HEB) mixers have become a rapidly developing field of terahertz technology. Two types of HEB mixers are currently developed: so-called phonon-cooled HEB mixers [1-6] and diffusion-cooled HEB mixers [7-11]. Both mixer types have produced impressive results during the last year. For the former, the following values of receiver noise temperature were obtained: 410 K (430 GHz) [2,3], 480 K (636 GHz) [3], 600 K (700-800 GHz), 850 K (910 GHz), and 1200 K (1.1 THz) [4]. The conversion bandwidth was 4 GHz [5], and the noise bandwidth reached 8 GHz [6]. The optimal local oscillator power was of the order of $P_{\text{LO}} \sim 1 \mu\text{W}$. The latter type of HEB mixers showed a noise temperature of 650 K (533 GHz) [8], 1880 K (1267 GHz) [9], 2700 K (2.5 THz) [10], and a noise bandwidth of about 2 GHz [9,10], and a conversion bandwidth of up to 6 GHz was achieved for the shortest bridges at 20-40 GHz frequency, as reported in [11]. The optimal local oscillator power for the diffusion-cooled HEB mixers was 10-100 nW [9-11]. One of the differences between the performances of the two kinds of mixers was the order of magnitude of their local oscillator power. A lower P_{LO} may prove necessary at terahertz frequencies, where the absence of solid-state sources of a considerable power is an important factor contributing to a wider scope of application.

At the same time, the optimal P_{LO} for the phonon-cooled HEB mixers may show a considerable variance, since it is proportional to the volume of the superconducting film. The dimensions of the film are not a critical parameter for this kind of HEB mixers, unlike the diffusion-cooled HEB mixers, where the small length of the superconducting film located between normally conducting contacts determines the size of the mixer bandwidth. Typical P_{LO} values so far obtained for the phonon-cooled HEB mixers are of an order of few

microwatts, as determined by the facilities of photolithography: the characteristic film size in plane is 1 μm . A decrease in the optimal P_{LO} value means a shift to electron-beam lithography and to submicron dimensions, although they need not be so small as those required for the diffusion cooled HEB mixers. The results of the present work show that the P_{LO} for a NBN film of $1.5 \times 0.2 \times 0.003 \mu\text{m}^3$ is about 20 nW. It is important that the noise temperature and conversion losses drop with a decrease in size. For one of the spiral antenna coupled HEB mixers presented in this paper, the noise temperature of the receiver is about 1000K at 800-900 GHz, 1200K at 950 GHz, and 1600K at 1.08 THz. A decrease in the superconducting film volume may result in a decrease of the optimal local oscillator power and a notable drop of the noise temperature but may bring about certain negative effects. One of these is a narrowing of the dynamic range. Another effect, which may be not so self-evident, is a possible increase of the direct detection contribution into the response manifested in Y-factor measurements. Indeed, the responsivity of a HEB is inversely proportional to the volume of the film [1], whereas the heterodyne response shows a much weaker growth with the decrease in the volume. As a result, the direct detection response to black body radiation from hot and cold loads may become comparable with the heterodyne response. In this paper, we have made an attempt at an assessment of this contribution.

Devices and fabrication

To manufacture spiral antenna coupled HEB mixers, a layer of thin (30-35 Å) NbN film was deposited onto a Si high-resistive (with a resistivity of 5 k Ωcm) 350 μm thick substrate using reactive magnetron sputtering. The process of sputtering the NbN film is described in detail in [5].

The central part of the spiral antenna was formed using lift-off electron lithography based on metallization of 800 Å thick Cr-Au layer. The dimensions of the gap that opened the active NbN film in the antenna were 0,2-0,4 μm by 1,0-2,0 μm . To remove the NbN layer from the chip field, a repeated lift-off electron lithography with alignment was used, in the course of which the whole central spiral was covered by an Al mask, which duplicated the topology of the Cr-Au spiral antenna, but overlapped the gap. The NbN which was not protected by the Al mask was then removed using ion milling in an Ar atmosphere, and after that Al was chemically removed in a selective etchant, not affecting Au and NbN.

The final operations included deposition of a relatively thick (the thickness of the Au layer was 0.5 μm) Ti-Au metallization of the peripheral part of the antenna; direct lithography over this metallization using alignment marks, which provided alignment of the external and the internal spirals; ion milling of Au; chemical etching of Ti; and, finally, partitioning the wafer by scribing it into separate chips. Fig. 1 shows a SEM photo of a completed device.

Experiment and discussion

The substrate on which the device and antenna are integrated, is glued to an extended hyperhemispherical silicon lens with a diameter of 4.2 mm. The mixer is mounted in a liquid He-cooled vacuum cryostat equipped with a 1-mm-thick Teflon window and a 380 μm Zitex G 115 IR radiation filter. We use three backward wave oscillators (BWO) as local oscillator sources with a common frequency range 450÷1250 GHz. The radiation from the LO is focused by a Teflon lens and combined with the signal by a 20- μm -thick Mylar beamsplitter. For dc bias and IF signal output the device is attached to a coplanar 50 Ω line soldered to a SMA connector, and connected to a bias-T. The receiver sensitivity is measured using the Y-factor method of alternately placing a hot load at 295 K and a cold load at 77 K at the input of the receiver. The receiver noise temperatures T_r reported are not corrected to account for losses. The sensitivity refers to the double-sideband receiver noise temperature.

Fig.2 shows three IV curves: an unpumped one, one pumped by optimal LO power, and another one pumped by optimal LO power reduced by a factor of $\alpha=0.8$ dB. To calculate the optimal LO power absorbed by NbN film, we use a conventional technique common for the bolometers. Supposing that the resistance of the film in the resistive state only depends on electron temperature, we can draw the isotherm as a straight line that crosses the last two IV-curves in the points 1 and 2 (fig.2) and calculate the absorbed LO power:

$$P_{\text{abs}} = \frac{\alpha}{\alpha - 1} (I_2 V_2 - I_1 V_1) \quad (1)$$

The precision of this procedure appears to be better if the isothermal line corresponds to a resistance much higher than that observed at the working point of the mixer. In this case, the resistive state is more uniform, which validates the assumption of the crucial role played in the resistance by the electron temperature. This assumption is accurate in a normally conducting state, but in such a case the resistance hardly shows any dependence on the temperature, and the precision of $I_1 V_1$ and $I_2 V_2$ products prove to be utterly insufficient. Calculations by (1) yield an absorbed optimal P_{LO} of 20nW, and for the given working point of the mixer $P_{\text{dc}} = I_0 V_0 = 15$ nW (fig.2). It should be emphasized that the dependence of the noise temperature of the receiver on P_{LO} and P_{dc} over quite a wide range is very weak. This can be seen from the same figure, which also shows the dependence of T_r on bias voltage. The bias voltage may vary from $V_0=0.3$ mV to $V_0=1.5$ mV, while T_r only shows a 20% change. The same figure shows the bias current range where the noise temperature varies within the same limits with the change of P_{LO} . Here, P_{LO} shows a 4dB change, i.e., it changes from 15 nW to 32 nW.

It is interesting to make a theoretical estimation of the required local oscillator power. The simplest way to do this is to ignore the heating of the lattice and to perform the calculations for a pure hot electron bolometer [1, 12]. In this case, for NbN

$$P_{\text{dc}} + P_{\text{LO}} = AV(\theta^{3.6} - T^{3.6}), \quad (2)$$

where $A=C_e(T)/3.6\tau_{\text{eph}}(T)T^{2.6}\approx 3\cdot 10^4 \text{ W}\cdot\text{cm}^{-3}\text{K}^{-4}$ for NbN, V is the NBN film volume, θ is the electron temperature. Assuming that $T_e=8 \text{ K}$, we will obtain $P_{\text{dc}}+P_{\text{LO}}=36\text{nW}$, while experimentally assessed values of $P_{\text{dc}}+P_{\text{LO}}$ may vary from 25 to 55 nW without any significant increase of T_r .

Fig. 3 shows the dependence of the noise temperature of the receiver on the frequency for a HEB mixer studied at $T=4.5\text{K}$. In the 800-900 GHz range, T_r does not vary and is equal to 1000 K, but at frequencies $F<750 \text{ GHz}$ and $F>950 \text{ GHz}$ it shows a smooth growth. The atmospheric absorption makes a considerable contribution to the measured $T_r(F)$ dependence at high frequencies. A rather significant line of water absorption can be observed around the 1.18 THz mark and a much smaller line can be seen near the 730 GHz mark.

There are a great variety of factors that contribute to the frequency dependence of the noise temperature, which are still difficult to distinguish. They include the frequency dependence of the NbN film impedance ($h\nu<2\Delta$ for NbN in the used frequency range), and hence its mismatch with the antenna, the frequency dependence of the silicon lens reflection, etc. One of the principle ways to increase the noise performance of NbN HEB mixers made by e-beam lithography is the advancement of manufacturing processes. The purpose of this is to achieve in the final product a high critical current density, high critical temperature, and a small width of the superconducting transition, which has been attained for thin NbN films (and for NbN HEB mixers made by photolithography).

Another important aspect of the measurements deserves special attention. As was noted above, if for a HEB mixer T_r is measured using the Y-factor technique, an additional error may appear due to the contribution of direct detection. When the input of the receiver is switched from hot to cold load, one can observe that the IV-curve shifts a little into the region of higher currents (see Fig.2). At an optimal local oscillator power and bias voltage, the current shift is $\sim 0.3 \mu\text{A}$ (points 3 and 4 in Fig.2). To assess a possible contribution of direct detection to the measured Y-factor, we have measured, in addition to the output noise power P_{out} for hot and cold loads (after amplification they were $102 \mu\text{W}$ and $85 \mu\text{W}$, respectively), another two values of P_{out} for two different local oscillator powers, one being optimal for conversion gain ($P_{\text{out}}=102 \mu\text{W}$) and another one, reduced by a factor $\alpha=0.8 \text{ dB}$ ($P_{\text{out}}=88 \mu\text{W}$). These two states of the HEB mixer are marked with points 3 and 5 in IV-curves of Fig.2 In these measurements, bias voltage remained the same, and a hot load was located at the input of the receiver. Since the P_{LO} varies only a little from point 3 to point 5 (the change is 0.8dB), we can approximate the dependence of the output noise power from the bias current in this area by a linear function. This will permit us to estimate the P_{out} value at point 4 in Fig.2 as $100 \mu\text{W}$. Thus, when the receiver input is switched from hot to cold load, a small part of the measured Y-factor is due to direct detection. The adjusted value of the noise temperature at a frequency of 880 GHz may be estimated as 1170 K. Note that the obtained correction of the

noise temperature of the receiver is only a little higher than the measurement error. At the same time, if the volume of the superconducting film of the HEB mixer is reduced further, or if the frequencies are used at which the heterodyne response drops, the contribution to the direct detection into the measured Y-factor may become considerable. This effect could be seen in Fig.3 in the center of the absorption line located near 1.18 THz frequency point. Assuming complete absorption at this frequency point one can expect that only direct detection contributes to the Y-factor value here. Indeed, this value coincides with the direct detection signal estimated above (Fig.3).

Acknowledgments

The authors would like to thank A.Lipatov for his contribution to antenna design and A.Dzardanov and P.Kouminov for their assistance in measurements.

This work has been supported by Russian program on Condensed matter (Superconductivity Division) under Grant No.98062.

References

- [1] E.M.Gershenson, G.N. Gol'tsman, I.G.Gogidze, Y.P.Gousev, A.I.Elant'ev, B.S.Karasik, and A.D. Semenov, *Sov.Phys.Semicond.* 3, 1582 (1990).
- [2] J.Kawamura, R. Blundell, C.-Y.E. Tong, G.N. Gol'tsman, E. Gershenson, B. Voronov, *Appl.Phys.Lett.*70, 1619 (1997).
- [3] J.Kawamura, R. Blundell, C.-Y.E. Tong, G.N. Gol'tsman, E. Gershenson, B. Voronov, and S.Cherednichenko, *Proceedings of the 8th International Symposium on Space Terahertz Technology*, Harvard University, 1997, pp.23-26.
- [4] P.Yagoubov, M.Kroug, H.Merkel, E.Kollberg, G.N.Gol'tsman, A.Lipatov, S.Svechnikov, and E.M.Gershenson, presented at the 9th Int. Symp. on Space Terahertz Technology, Pasadena, USA, March 1998, this issue.
- [5] S.Cherednichenko, P.Yagoubov, K.II'in, G.Gol'tsman, and E.Gershenson, *Proceedings of the 8th International Symposium on Space Terahertz Technology*, Harvard University, 1997, pp.245-252.
- [6] H.Ekström, E.Kollberg, P.Yagoubov, G. Gol'tsman, E. Gershenson, and S. Yngvesson, *Appl.Phys.Lett.* 70, 3296 (1997).
- [7] D.E.Prober, *Appl.Phys.Lett.* 62, 2119 (1993).
- [8] A.Skalare, W.R.McGrath, B.Bumble, M.G.LeDuc, B.J.Burke, A.A.Verheijen, R.J.Schoelkopf, and D.E.Prober, *Appl.Phys.Lett.* 68 (11), 1558 (1996).
- [9] A.Skalare, W.R.McGrath, B.Bumble, and H.G.LeDuc, *IEEE Transactions on Appl. Supercond.* 7 (2), 3568 (1997).
- [10] B.S.Karasik, M.C. Gaidis, W.R. McGrath, B. Bumble, and H.G. LeDuc, *Appl.Phys. Lett.* 71, 1567 (1997).
- [11] P.J.Burke, R.J.Schoelkopf, D.E.Prober, A.Skalare, W.R.McGrath, B.Bumble, and H.G.LeDuc, *Appl.Phys.Lett.* 68 (23), 3344 (1996).
- [12] B.S.Karasik and A.I.Elantiev, *Applied Physics Letters*, 68 (6), 853 (1996).

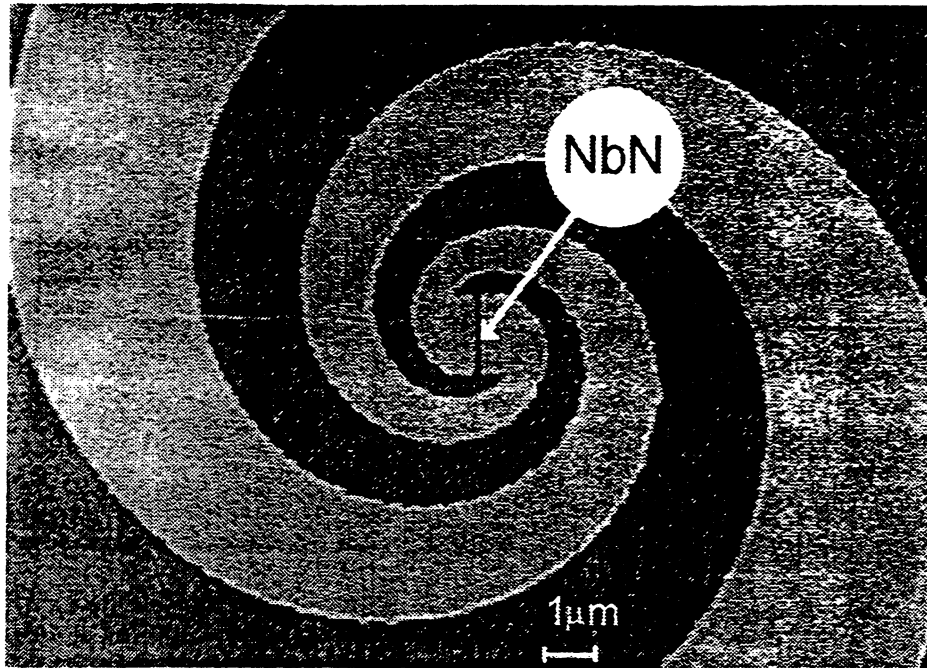


Fig.1. SEM photo of the 0.2 μm by 1.5 μm NbN HEB device integrated into spiral antenna.

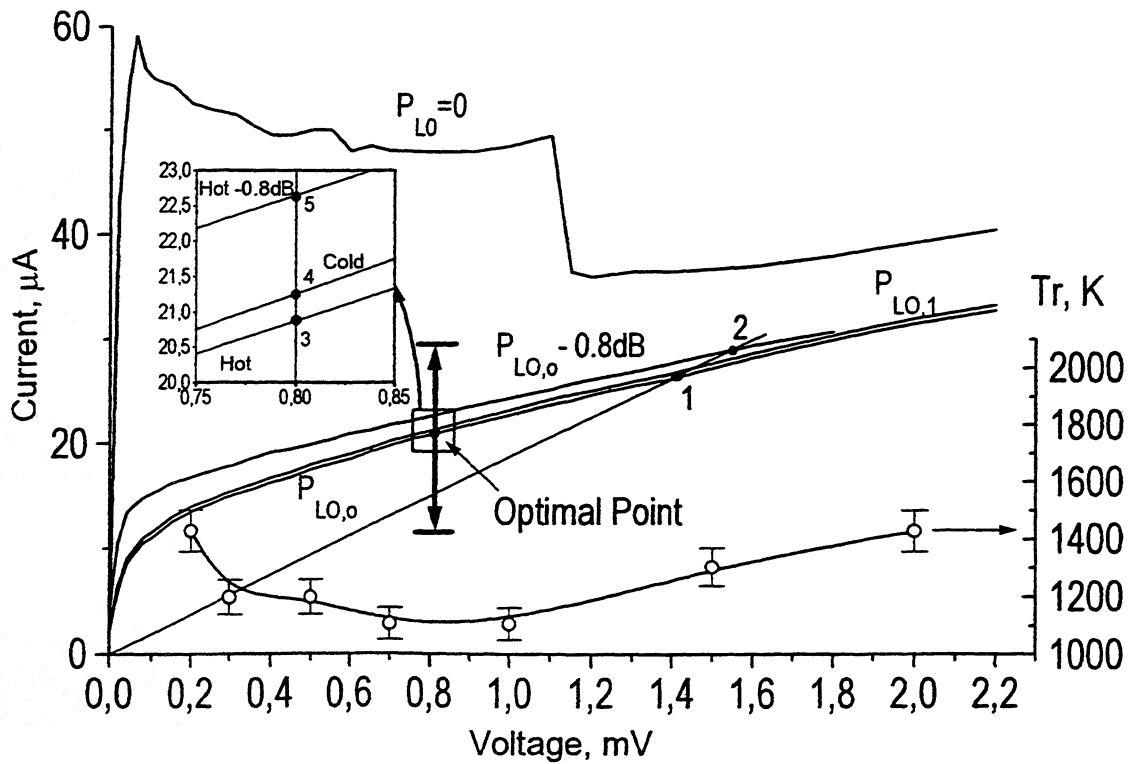


Fig.2. Unpumped and pumped IV-curves at 880 GHz and the receiver noise temperature versus bias voltage.

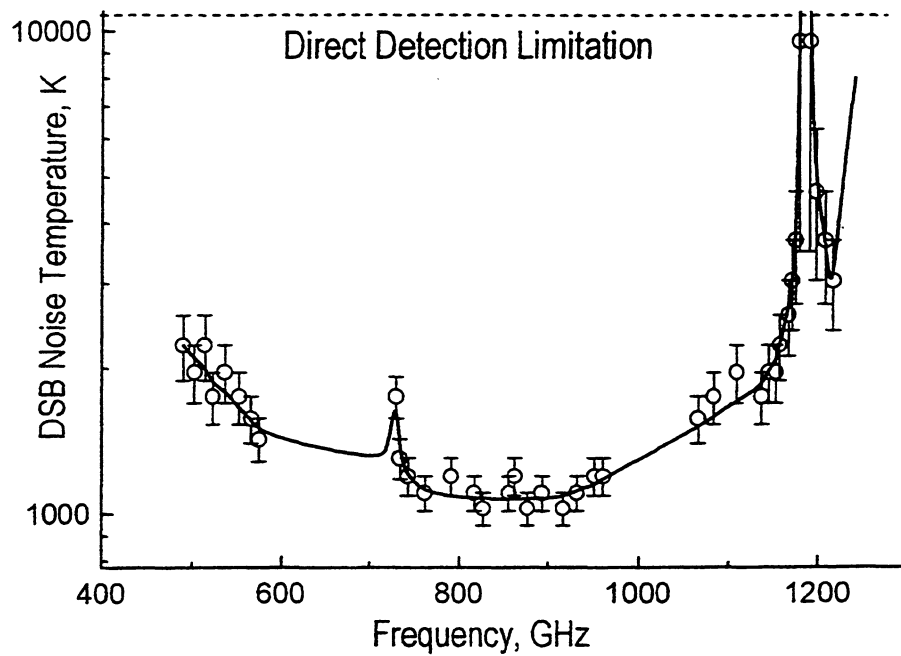


Fig.3. Noise temperature for the NbN HEB mixer receiver within frequency range 450-1200 GHz.

LOW-NOISE NbN PHONON-COOLED HOT-ELECTRON BOLOMETER MIXERS AT 810 GHz

C. Rösch *, T. Lehnert, C. Schwoerer,
M. Schicke, K. H. Gundlach, K. F. Schuster

*Institut de Radio Astronomie Millimétrique
300 rue de la Piscine, Domaine Universitaire de Grenoble
38406 St. Martin d'Hères, France*

Frank Schäfer
*Max-Planck-Institut für Radioastronomie
53121 Bonn, Germany*

Abstract

NbN phonon-cooled superconducting hot-electron bolometric mixers with quasi-optical coupling were fabricated in a self-aligned process by means of e-beam-lithography. The mixer element consists of a 5 nm thick NbN film sputtered on a fused quartz substrate. Noise performance was investigated in the frequency range of 798 to 813 GHz for intermediate frequencies from 1.0 to 1.75 GHz. Uncorrected double sideband receiver noise temperatures of about 900 K were measured at an intermediate frequency of 1000 MHz with a 50 MHz bandpass filter.

The gain bandwidth was determined by superposing two local oscillator signals and measuring the height of the discrete line at the intermediate frequency output. A 3dB-roll-off-frequency of some 1.3 GHz was obtained.

1. Introduction

Superconductor-insulator-superconductor (SIS) mixers have nearly replaced Schottky-diode mixers in millimeter and submillimeter astronomical studies. Presently, the first choice for low-noise receivers up to nearly 1.2 THz are Nb SIS junctions with Al embedding circuits [1, 2, 3]. The frequency limit $f_l = \frac{4\Delta}{h}$ is set by the energy gap of niobium $\Delta(Nb) \simeq 1.4$ meV. The higher energy gap of NbN $\Delta(NbN) \simeq 2.4$ meV suggests to employ NbN junctions

*email: roesch@iram.fr

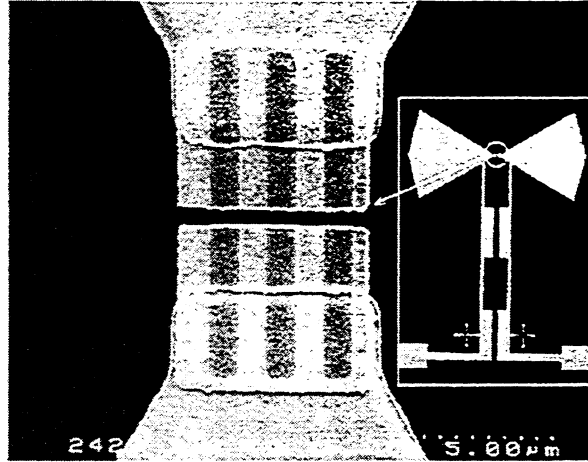


Figure 1: Microbridges integrated in the center of an dipole-antenna

with Al embedding circuits for frequencies up to 2 THz. So far, the relatively large leakage current and the high specific capacity conflicts with the desired low-noise performance [4, 5].

While superconducting hot-electron bolometers (HEB) can compete with SIS-mixers at 1 THz they are supposed to be superior at higher frequencies. Since the mixing mechanism in a HEB utilizes the temperature dependence of the resistance near the transition temperature T_c , this device is not limited by the energy gap of the superconductor as SIS mixers, and is therefore expected to have a good performance up to several terahertz [6]. Schottky mixers which also work in the THz region are noisier and require orders of magnitude more local oscillator (LO) power.

Two types of bolometers are known, differing in their cooling mechanism. While the cooling mechanism in Nb bolometers [7, 8, 9] is based on the fast out-diffusion of hot electrons and requires extremely short bridges, NbN bolometers [10, 11, 12, 13] are mainly cooled by electron-phonon interaction. Very thin NbN films ensure that the phonons immediately escape into the substrate.

2. Device Fabrication

We fabricated the second type of hot-electron bolometers using thin NbN films. Our devices consist of three parallel lines integrated in the center of a dipole antenna. (See fig. 1)

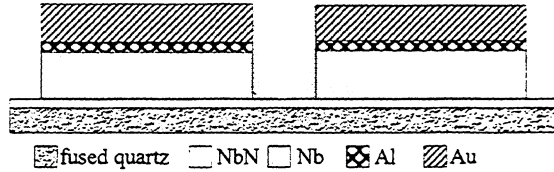


Figure 2: Sectional view of the microbolometer

The thin films for the devices were sputtered on a fused quartz substrate beginning with a blank NbN deposition of 5 nm. Optimized sputter parameters are described elsewhere [14].

Subsequently, the antenna and the rf-filters, consisting of 100 nm Nb, 8 nm Al and 50 nm Au are patterned by means of optical lithography. The length of the microbridges is defined by two rectangular pads at the center of the antenna, using e-beam lithography. For these pads either 100 nm Au or 100 nm Nb is used indicating no major difference when operated at 810 GHz. Also by means of e-beam lithography three parallel Al lines, defining the microbridges, are patterned across the Au (Nb) contact pads. Al serves as etch mask and will be removed afterwards. Since the effective length of the microbridge is determined by the distance of the two contact pads only, the length of the Al-lines can be chosen arbitrarily, avoiding alignment problems. After reactive ion etching of the NbN layer with CF_4 the Al can be removed easily in a base.

A sectional view of the device is shown in fig. 2. The distance of the two rectangular pads is about $0.5 \mu\text{m}$ and was chosen to match the resistance of the antenna, which is as low as 100Ω . Even shorter bridges are feasible with the used technology providing the possibility to reduce the film thickness without increasing the resistance. The shortest bridges produced so far were $0.2 \mu\text{m}$ long. The width of the microstrips is about $1 \mu\text{m}$ each (see fig. 1).

3. Experimental Setup

The double sideband (DSB) receiver noise temperature T_{rec} is determined by the usual Y-factor method.

Therefore the device is glued to a hemispherical lens of crystal quartz and mounted in a LHe-cooled cryostat. A Gunn diode followed by a varistor

doubler and tripler is used as local oscillator. This assembly provides an LO power of about $80 \mu\text{W}$ in the range from 798 to 813 GHz [15], which is superposed with the signal of the load using a $19 \mu\text{m}$ polyester foil as beam splitter. The intermediate frequency (IF) signal was matched to the 50Ω input of a cryogenic HEMT amplifier by a quarter-wave line. Furthermore the IF-chain consists of two other amplifiers operating at room temperature and a bandpass filter of 50 MHz bandwidth tunable between 1000 and 1750 MHz.

4. Results

With this setup noise temperatures were measured for a range of bias voltages, LO power levels, IF and LO frequencies. The results for the Y-factor are found between 1.155 and 1.225 corresponding to noise temperatures between 890 and 1330 K.

Extreme care has been taken to ensure that no direct bolometric response to ambient thermal radiation occurred. Therefore current/voltage (I/V) curves were recorded with hot as well as with cold load. No difference between these two curves has been observed indicating that the operating point is not altered when switching between hot and cold load. Using the isothermic method first proposed by Ekström [16] an LO power of some 80 nW was obtained.

Fig. 3 shows a typical result of these measurements. The pumped I/V curve is plotted as well as the IF conversion curves for hot and cold load. The unpumped I/V curve which has the typical hysteretic behaviour is not shown in the figure. The critical current for increasing bias voltage is $230 \mu\text{A}$ and the drop-back current for decreasing bias voltage is $70 \mu\text{A}$.

Best bias points are obtained when the LO power is sufficiently high to suppress the hysteresis. The performance of the device was found to deteriorate by the application of higher or lower LO power. Fig. 4 shows the noise temperature as a function of IF and as a function of the LO frequency.

Heterodyning of similar devices was already shown in [10]. Lehnert et al. have superposed two free running solid state oscillators at similar frequencies. One served as pumping-LO and the other one as signal source. The IF signal was observed by a spectrum analyzer. The same setup is used to get a first notion of what the IF bandwidth might be. Therefore the signal height is measured for different intermediate frequencies. The IF is changed by tuning the pumping-LO. The signal-LO is not touched and the signal power remains

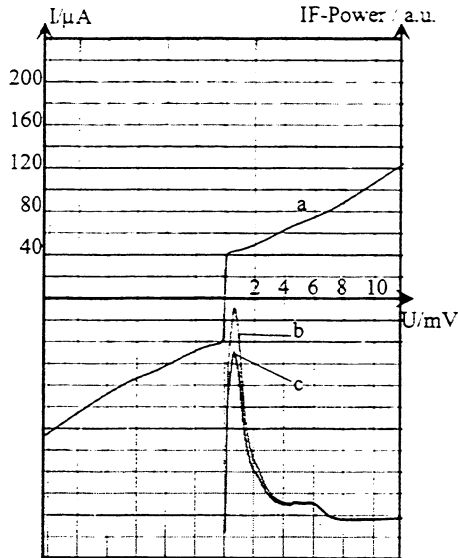


Figure 3: a) pumped I/V curve of the device and conversion curves for b) hot and c) cold load.

constant during the whole measurement. Therefore the dependency of the power level from the frequency does not influence the results. As far as the pumping-LO is concerned, the incident power is kept constant using the I/V curve. After tuning the frequency the output level of this LO is changed until the initial I/V curve is recovered. Whenever the same bias curve is attained the absorbed LO power is assumed to be the same. In Fig. 5 the output signal is shown as a function of the IF. The data points are lying in the range from 500 MHz to 3.3 GHz and reaching a maximum value of about 20 dB above noise. An IF bandwidth of $\omega_{3dB} = 1.3$ GHz can be estimated.

5. Conclusion

We succeeded in fabricating the phonon-cooled version of superconducting hot-electron bolometers integrated in a quasi-optical receiver. Since the fabrication process is free of difficult alignment, a high degree of reproducibility can be attained. With these devices DSB receiver noise temperatures and IF bandwidth were determined at an LO frequency of about 800 GHz.

While the IF bandwidth of 1.3 GHz remains relatively small best DSB receiver noise temperatures are as low as 900 K at an IF of 1000 MHz. The

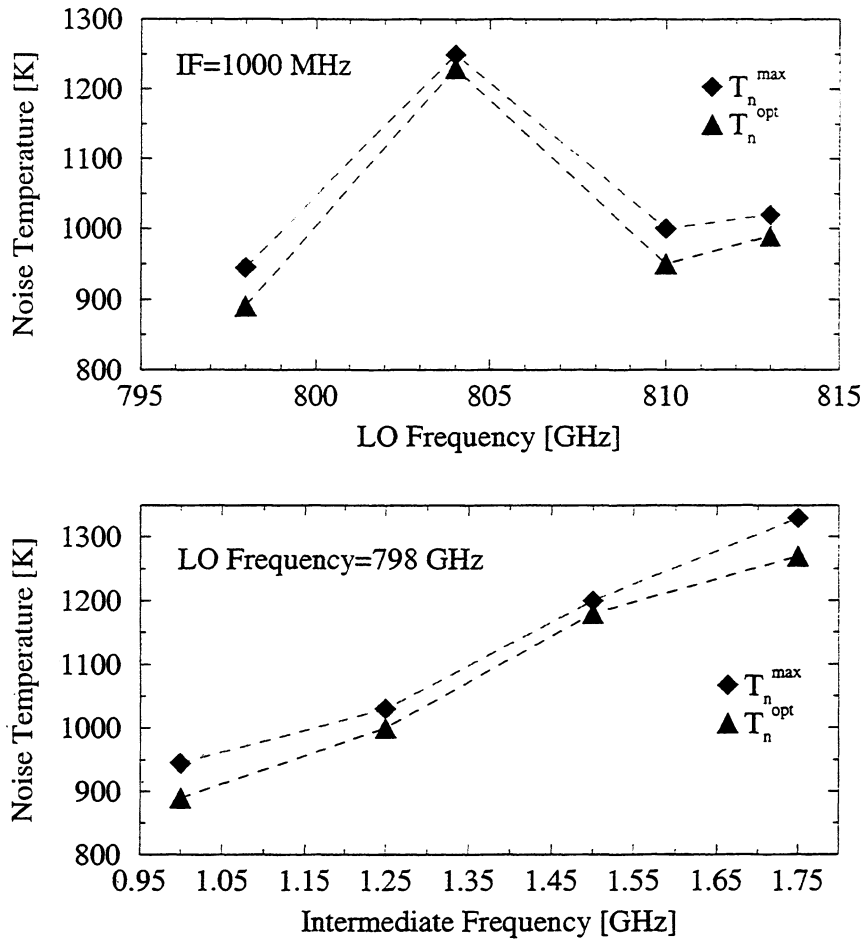


Figure 4: Noise temperatures for a range of LO frequencies (upper part) and different IF (lower part). T_n^{max} is measured at the maximum of the conversion curve while T_n^{opt} is measured at slightly higher voltages.

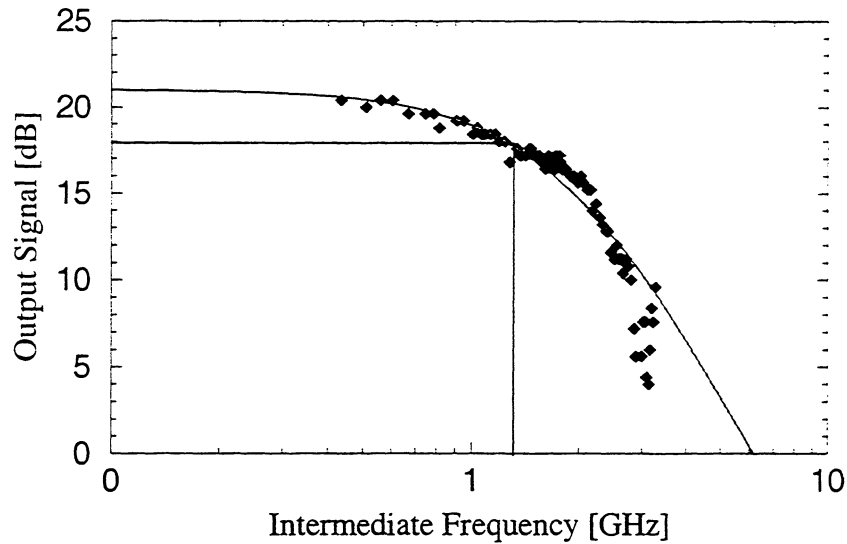


Figure 5: Output signal for different intermediate frequencies. An IF bandwidth of about 1.3 GHz can be estimated.

noise temperature increases to only 1300 K at 1750 MHz. It should be emphasized that the present quasi-optical receiver was initially designed for the 350 GHz frequency band [17]. With a somewhat more sophisticated antenna, an antireflection coated lens and windows optimized for the operating frequency considerably better noise temperatures can probably be achieved at 800 GHz.

Crystalline quartz substrates might also be advantageous because of their approximately 10 times higher thermal conductivity and experiments are planned to see whether the use of these substrates results in a higher IF bandwidth. These results demonstrate that NbN hot electron bolometers can compete with well-established SIS-technology at 800 GHz and represent a promising tool for the detection in the THz range.

6. Acknowledgements

The authors like to thank Dr. H. Rothermel for the receiver as well as for his substantial help.

References

- [1] M. Bin et al. Low-noise 1 THz niobium superconducting tunnel junction mixer with a normal metal tuning circuit. *Appl. Phys. Lett.*, 68:1714; 1996.
- [2] D. Maier et al. Submicron Nb-Al/Al oxide-Nb tunnel junctions sandwiched between Al films. *Physica C*, 268:26 – 40, 1996.
- [3] F. Schäfer et al. A quasioptical SIS receiver with normal metal tuning for the 800-900 GHz band. In *8th International Symposium on Space Terahertz Technology*, pages 566 – 569, Cambridge, USA, 1997.
- [4] P. Dieleman et al. Performance limitations of NbN SIS junctions with Al striplines at 600 - 850 GHz. In *8th International Symposium on Space Terahertz Technology*, pages 291 – 298, Cambridge, USA, 1997.
- [5] M. Schicke et al. NbN tunnel junctions with Al tuning circuits and hot-electron transition-edge bolometers for THz mixing. In *ISEC'97*, volume 3, pages 150 – 152, Berlin, Germany, 1997.
- [6] D. E. Prober. Superconducting terahertz mixer using a transition-edge microbolometer. *Appl. Phys. Lett.*, 62:2119 – 2121, 1993.
- [7] B. S. Karasik et al. Low noise in a diffusion-cooled hot-electron mixer at 2.5 THz. *Appl. Phys. Lett.*, 71(11):1567 – 1569, 1997.
- [8] A. Skalare. Large bandwidth and low noise in a diffusion-cooled hot-electron bolometer mixer. *Appl. Phys. Lett.*, 68:1558 – 1560, 1996.
- [9] K. Fiegle, D. Diehl, and K. Jacobs. Diffusion-cooled superconducting hot electron bolometer heterodyne mixer between 630 and 820 GHz. *IEEE Trans. Appl. Supercond.*, 7:3552, 1997.
- [10] T. Lehnert, H. Rothermel, and K. H. Gundlach. Low-noise heterodyne mixing with NbN microbolometers at 800 GHz. *J. Appl. Phys.*, to be publ. in the 15 March 1998 issue, 1998.
- [11] H. Ekström et al. Gain and noise bandwidth of NbN hot-electron bolometric mixers: *Appl. Phys. Lett.*, 70(24):3296 – 3298, 1997.

- [12] S. Svechnikov et al. Spiral antenna NbN hot-electron bolometer mixer at submm frequencies. *IEEE Trans. Appl. Supercond.*, 7:3395, 1997.
- [13] J. Kawamura et al. Low noise NbN lattice-cooled superconducting hot-electron bolometric mixers at submillimeter wavelengths. *Appl. Phys. Lett.*, 70:1619 – 1621, 1997.
- [14] B. Plathner et al. A niobiumnitride mixer with niobium tuning circuit. *Appl. Phys. Lett.*, 69:4102 – 4104, 1996.
- [15] *Radiometer Physics GmbH, Meckenheim, Germany.*
- [16] H. Ekström et al. Investigation of a superconducting hot electron mixer. *Proc. 5th Int. Symp. on Space Terahertz Technology*, pages 169 – 175, 1994.
- [17] H. Rothermel, M. Voss, and K.-H. Gundlach. In *SPIE Proceeding Series*, volume 2211, page 396, 1994.

RESISTIVE BEHAVIOUR OF Nb DIFFUSION-COOLED HOT ELECTRON BOLOMETERS

D. Wilms Floet^{a,1}, J.J.A. Baselmans^a, J.R. Gao^{ab}, and T.M. Klapwijk^a

^aDepartment of Applied Physics and Materials Science Center,
University of Groningen, Nijenborgh 4, 9747 AG Groningen,
The Netherlands

^bSpace Research Organisation of the Netherlands, PO Box 800, 9700 AV Groningen,
The Netherlands

Abstract.

We present a new model for the description of the resistive transition of Nb diffusion-cooled hot electron bolometer mixers. The device is a thin (12 nm) microbridge with a length and width of 220 nm, attached to large Au banks. Heterodyne mixing experiments in a 700 GHz waveguide receiver yield a receiver noise temperature (DSB) of 2200 K at 3.3 K and an IF of 1.4 GHz. We show that the $R(T)$ is an intrinsic property of a superconducting microbridge, connected to normal conducting cooling pads. The essential ingredients of our model are the superconducting proximity effect, charge imbalance and Andreev reflection. Our conclusion is that the resistive transition is not related to the conditions under which the device is operated as a mixer. We propose a mixing mechanism in terms of a normal electronic hotspot of which the length and consequently, the resistance oscillates at the intermediate frequency.

I. Introduction and motivation

The increasing demand for sensitive heterodyne receivers in the terahertz frequency range has largely stimulated the development of hot electron bolometer (HEB) mixers. These devices are being considered as promising candidates for this frequency range, because their noise performance is predicted to not degrade with increasing frequency. Indeed, recent experimental work on HEB mixers has not shown a significant increase of the mixer noise up to 2.5 THz. Also, the intermediate bandwidth of a HEB can be several GHz, which is large enough for many practical applications [1-5].

Several authors have discussed in theoretical models the factors that limit the sensitivity of both diffusion-cooled and phonon-cooled HEBs [6, 7]. They derive expressions for the noise contributions from both Johnson noise and thermal fluctuation noise in terms of the critical temperature T_c of the microbridge, the width of the transition ΔT_c , the radiation coupling factor and the operating temperature T . In these models the $R(T)$ of the microbolometer is represented by a so-called broken-line transition model i.e. $dR/dT = R_N/\Delta T_c$, where R_N is the normal state resistance of the microbridge. It is shown that the noise contribution from thermal fluctuations forms the dominant contribution to the mixer noise and its minimum value does not depend on the width of the transition, as long as ΔT_c is small compared to T_c . Moreover, for a large conversion gain, one desires a narrow transition and a high T_c .

From these points it is clear that in our present understanding of operation of the HEB, the resistive transition plays a crucial role in the sensitivity of the device. On the other hand, a clear physical picture describing the finite transition width of a HEB is not available yet. Here we present a new model which describes the superconducting transition in a Nb diffusion-cooled HEB. We show that the width of the transition is an intrinsic property of a microbridge attached to normal conducting contactpads and also related to the length of the bridge. The paper is organized as follows. In Section II we give an overview of device

¹ electronic mail: wilms@phys.rug.nl

fabrication, DC characterisation and heterodyne performance. In Section III we present a model for the resistive transition in terms of the superconducting proximity effect, charge imbalance and Andreev reflection. The model is compared to measurements of the resistive transition on test-samples. In Section IV we discuss the resistive behaviour of the device when it is operated as a mixer and we propose a mechanism for the mixing process in terms of an oscillating electronic hotspot.

II. Device fabrication and characterization

II.A Device fabrication

We have fabricated Nb diffusion-cooled hot electron bolometers for a 700 GHz waveguide heterodyne receiver by a two step electron beam lithography (EBL) process [8]. First, a 12 nm Nb film is DC sputtered over the whole area of a 200 μm thick fused quartz substrate. The Au cooling pads are defined by EBL using a standard lift-off process. Then, the RF filter and electrical contacts are defined by optical lithography (lift-off). The filter is an in-situ sputtered Nb-Au bilayer. As a last step the bridge between the Au pads is defined by reactive ion etching (RIE). The etch mask (PMMA) is defined using EBL (fine structure) and deep UV exposure (large areas). The R(T) measurements described in Section III are performed on devices where the RF filter is replaced by large electrical contacts (Au).

II.B DC measurements

As a first characterization of the samples, the DC resistance as a function of the temperature is measured using a standard lock-in technique and low current bias conditions (1 μA) in order to avoid self-heating. A typical result for a 220 nm long microbridge is shown in Fig. 1a. Transitions are observed around 6.1 K and 5.4 K. This behaviour was also observed for devices which were produced with optical lithography [9]. Between the two transitions the resistance changes gradually with temperature. It is worth mentioning that R(T) measurements on (large) thin Nb films always show a narrow transition with ΔT_c never larger than 0.1 K.

II.C Heterodyne measurements

We have performed heterodyne measurements with hot and cold loads to determine the DSB receiver noise temperature of the devices. The length and the width of the device under test are both 220 nm and the normal state resistance just above the transition is 24 Ω . We have used a waveguide receiver set-up which was originally designed for Nb SIS mixers around 700 GHz. The device is connected via an isolator to the IF amplifier chain with 80 dB gain at 1.1 GHz and 60 MHz bandwidth. The LO is provided by a carcinotron and is coupled into the mixerblock via a 55 μm thick Mylar beamsplitter.

Fig. 1b shows the IF output powers for hot (295 K) and cold (77 K) input loads as a function of the bias voltage together with unpumped and pumped curves. The measurement is performed at a LO frequency of 735 GHz, a bath temperature of 3.3 K and an IF of 1.1 GHz. The maximum measured Y-factor is 0.22 dB, corresponding to a receiver noise temperature T_{REC} of 2200 K after correction for the beamsplitter loss (0.2 dB). The noise temperature at 4.7 K was 3400 K. No significant variation of the Y-factor is observed when the IF signal is tuned within the gain bandwidth of the amplifier chain (1.1-1.7 GHz), indicating a IF roll-off of at least 1.5 GHz. By calculating the difference in DC power dissipation on a constant resistance line in the pumped and unpumped IV curves we have estimated the coupled LO power to the device. We find a value of 35 ± 5 nW. We have estimated the noise of the mixer

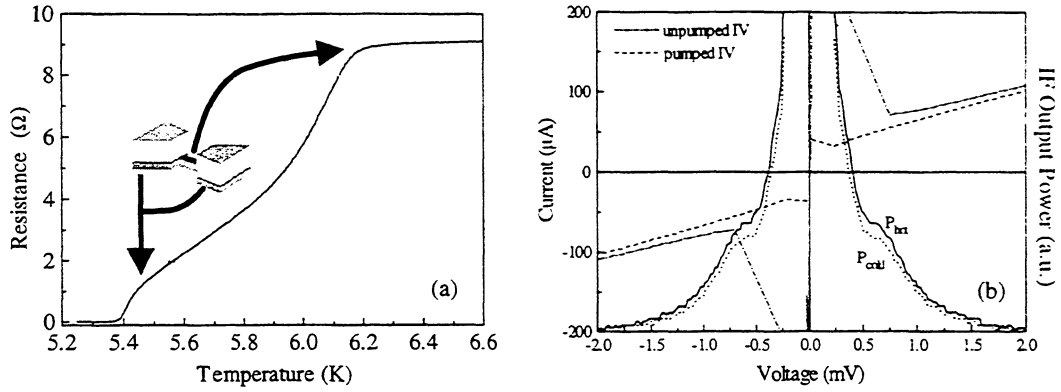


Figure 1 : (a) Resistance as a function of temperature of a Nb HEB. (b) AC IF Output power as a function of bias voltage with hot and cold loads together with pumped and unpumped IV curves. Measurements are carried out at 735 GHz and a bath temperature of 3.3 K. The intermediate frequency is 1.1 GHz.

itself by correcting the receiver noise temperature for the gain and noise contributions of the RF optics and IF amplifier chain using the relation (see also Table 1):

$$T_{\text{rec}} = T_{\text{RF}} + \frac{T_{\text{MIX}}}{G_{\text{RF}}} + \frac{T_{\text{IF}}}{G_{\text{RF}}G_{\text{MIX}}}. \quad (1)$$

with T_{RF} , T_{IF} , and T_{MIX} the noise contributions from the RF-optics, IF amplifier chain and bolometer mixer, respectively, and G_{RF} , G_{IF} and G_{MIX} the corresponding gains. It follows that the mixer noise temperature is 900 K. In the calculation we have not included the mismatch between the mixer and IF amplifier chain. Further improvement of device performance is expected by lowering the bath temperature to 2 K and using a device with a higher resistance i.e. $R_{\text{N}} \sim 50 \Omega$.

	<i>RF Optics</i>	<i>IF Chain</i>	<i>HEB Mixer</i>
Gain	-1.1 dB	80 dB	-24 dB
T_{N}	24 K	3.2 K	-

Table 1: Gain and noise contributions of the RF optics and the amplifier chain.

III. A model for the resistive transition: proximity effect, charge imbalance generation and Andreev reflection

In this section we will present a model which describes the resistive transition. First we will shortly address the observation of two transitions. In the second part of the section we will develop a microscopic model based on charge-imbalance and Andreev reflection, which explains the resistive behaviour at temperatures close to T_{c} .

The observation of two transitions in the $R(T)$ curve of the device is due to the superconducting proximity effect: the parts of the Nb which are covered with Au will have a lower critical temperature (see also Fig. 1a). In previous work [9] we compared the reduced critical temperature with calculations based on a model by Werthamer, but no satisfactory agreement was found. To correctly calculate the actual value of the critical temperature of the thin film as a function the normal metal thickness in N-S sandwiches one has to take into account the electronic properties of both materials and finite transparency of the interface

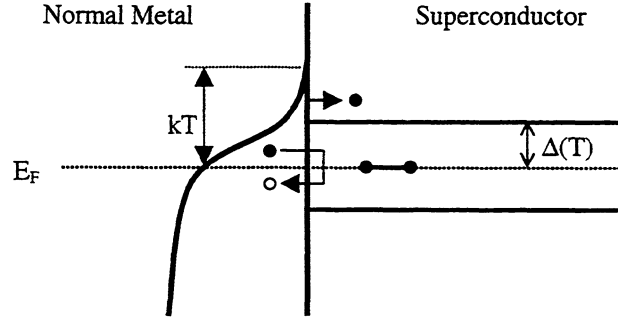


Figure 2: Schematic representation of transport processes near a N-S interface. Electrons with energies $E > \Delta$ are injected as quasi-particles, whereas Andreev reflection occurs for energies $E < \Delta$.

between the two layers, caused by the mismatch in Fermi-velocities in both materials and the possible presence of a potential barrier due to contaminations or interfacial oxides. We have performed measurements and calculations of the critical temperature of Nb-Au bilayers and find good agreement. Details have been described elsewhere [10], but are beyond the scope of this paper.

A second observation is that the resistance is decreasing gradually as a function of temperature in between the two transitions. We show that the observed behaviour can be understood in terms of generation of charge imbalance inside the Nb microbridge. The model allows a description of the $R(T)$ of a fully superconducting microbridge connected to normal electrodes. The resistance is a function of both temperature and bridgelength. Measurements show reasonable agreement with our predictions.

If, at low temperatures, a current is passed through a N-S interface, the normal current is gradually converted into a supercurrent by means of Andreev reflection; an incident electron ($E < \Delta$) is converted into a Cooper pair and a hole is reflected, retracing the path of the electron. This process occurs over a distance ξ , the coherence length of the superconductor and is schematically represented in Fig. 2. However, at temperatures of interest i.e. near T_c , the energy gap Δ becomes smaller than kT and a substantial fraction of the incident electrons enters the superconductor as a quasi-particle, leading to an antisymmetric distribution of the quasi-particles inside the superconductor and consequently to an imbalance of the quasi-particle charge density [11]. To compensate this excess charge, the electrochemical potential of the quasi-particles and Cooper pairs shift in opposite directions, which leads to a measurable (chemical) potential difference given by [12]:

$$\mu_n - \mu_s = \frac{Q^*}{2N_0} . \quad (2)$$

Here Q^* is the excess charge and N_0 the density of states per spin at the Fermi energy. Charge imbalance relaxation can occur via inelastic scattering processes i.e. electron-phonon or electron-electron scattering and its characteristic time, the branch-mixing time, is given by

$$\tau_{Q^*}(T) = \left(\frac{4kT}{\pi\Delta(T)} \right) \tau_{E-E} . \quad (3)$$

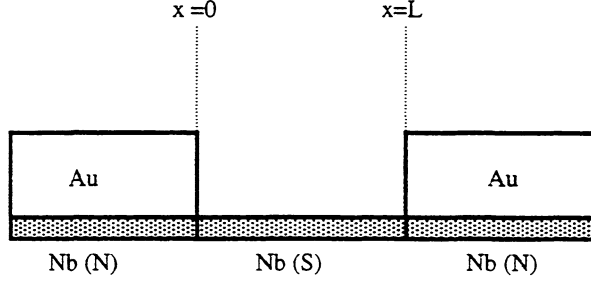


Figure 3: *Schematic cross-section of the HEB as used in the model. The parts of Nb which are covered by Au are normal conducting [Nb (N)], whereas the bridge is a fully superconducting state [Nb(S)].*

Here τ_{E-E} is the inelastic electron scattering time at the Fermi energy. The associated diffusion length is given by

$$\Lambda_{Q^*}(T) = \sqrt{D\tau_{Q^*}(T)} , \quad (4)$$

where D is the electronic diffusion constant.

Let us now consider the situation where a superconducting microbridge of length L is attached to two normal conducting pads (Fig. 3). If the relaxation time τ_{Q^*} is independent of position, this leads to the following differential equation [13]:

$$\frac{d^2(\mu_n(x) - \mu_s)}{dx^2} = \frac{\mu_n(x) - \mu_s}{[\Lambda_{Q^*}(T)]^2} . \quad (5)$$

Assuming that the current is fixed by the source, we use the as boundary condition for $x=0$ and $x=L$:

$$\left. \frac{d(\mu_n(x) - \mu_s)}{dx} \right|_{x=0,L} = \frac{j_n e}{\sigma} . \quad (6)$$

Here σ is the normal state conductivity of the microbridge and j_n is the quasi-particle current which enters the superconductor. With these conditions it is possible to calculate the potential drop across the microbridge, and thus the resistance. We find that

$$R_{\text{bridge}}(T) = \frac{2F^*(T)R_{\text{sq}}}{w} \Lambda_{Q^*}(T) \left[1 - \cosh\left(\frac{L}{\Lambda_{Q^*}(T)}\right) \right] \sinh^{-1}\left(\frac{L}{\Lambda_{Q^*}(T)}\right) . \quad (7)$$

R_{sq} is the square resistance of the Nb microbridge and w is the width of the bridge. The factor $F^*(T)$ takes into account that not all current is injected as quasi-particle current, but is partially converted to Cooper pair current by means of Andreev reflection. For $F^*(T)$ we use a result from Blonder, Tinkham and Klapwijk [14] for the N-S interface in the zero-barrier limit. The reason for this is that in our device the actual interface is formed between superconducting and normal conducting Nb (see Fig. 3), so in principle no barrier is expected. Fig. 4 shows the result of the calculation of the normalised resistance as a function of temperature for microbridges with different lengths. In the calculation we have assumed that the inelastic scattering rate is dominated by electron-electron interaction. We have approximated the scattering time by [15]

$$(\tau_E)^{-1} = 10^8 R_{\text{sq}} T . \quad (8)$$

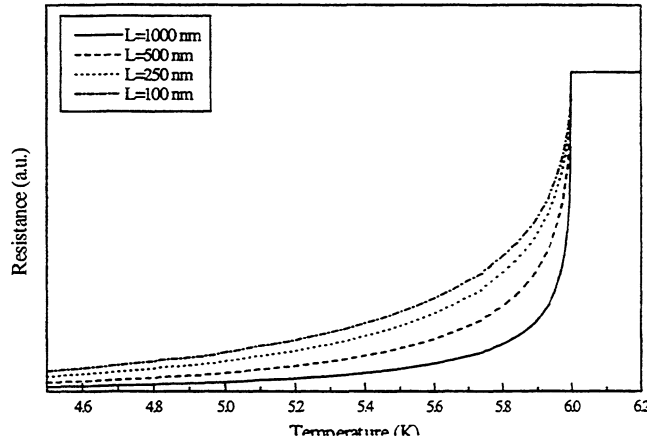


Figure 4: Normalised resistance as a function of temperature for a Nb HEB. The calculation is performed for different lengths of the microbridge.

From the calculation it is clear that the contribution of charge imbalance is depending not only on temperature, but also on the length of the microbridge. Its relative contribution becomes larger with decreasing length.

We have compared the results of the model with $R(T)$ measurements of Nb microbridges with varying length contacted by Au pads. The results are shown in Fig. 5. Fig. 5a shows both measurement and calculation of a 160 nm long microbridge. Reasonable agreement between experiment and model is found, except for temperatures above 5.7 K. Also, below ~ 4.7 K, the Nb under the Au pads is becoming superconducting, so the total resistance drops to zero. Fig. 5a shows the *measured* $R(T)$ of a short (160 nm) and long (1900 nm) bridge. From this figure it is clear that the $R(T)$ depends on the length of the bridge as predicted by our model (see Fig. 4). We have normalised both curves with respect to the normal state resistance and to T_c in order to make the comparison more straightforward. T_c is defined here as the temperature where the resistance has dropped to 90 % of the normal state resistance

Several factors can contribute to the observed differences between model and measurements. In the model it is assumed that there is no spatial variation of the energy gap of the superconductor along the bridge. This assumption is correct, except for temperatures close to T_c , where the coherence length diverges. In this situation it is possible that charge imbalance does not only relax via inelastic scattering, but also via elastic scattering processes [16]. If the last process becomes the dominant one near T_c , one might expect a slower

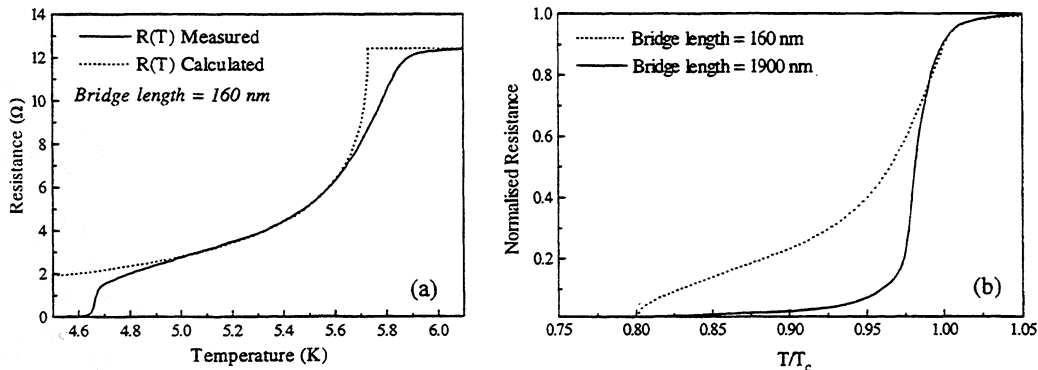


Figure 5: (a) Comparison of the model with experimental data. The figure shows the measured and calculated curve for a 160 nm long microbridge. (b) Experimental $R(T)$ of a long (1900 nm) and short (160 nm) bridge. The data are normalised to T_c and to the normal state resistance.

increase of the resistance. Also, at temperatures close to T_c , we often observe a rounding of the $R(T)$ curve. The physical reason for this is not clear, but superconducting fluctuations can for instance play a role. The rounding makes the estimation of T_c for the calculation somewhat arbitrary. Moreover, in our model it is assumed that the intrinsic superconducting phase transition of Nb can be described by a step-function i.e. $\Delta T_c = 0$. In general we always observe some finite width, although it is usually smaller than 0.1 K.

IV. Resistive behaviour and mixing

The main conclusion from the above presented model is that the resistive transition of a Nb hot electron bolometer is an intrinsic property of a superconducting microbridge connected to normal conducting banks. However, heterodyne mixing experiments are usually performed at temperatures well below the (lowest) transition of the bolometer in order to reduce conversion losses. In this situation the Nb under the Au is superconducting, so charge-imbalance generation does no longer determine the resistance. The high current density inside the microbridge due to LO and DC signals will lead to high dissipation inside the bridge. The Nb/Au banks remain superconducting since the current density there is much lower. It is therefore clear that there exists no direct relation between the DC measured $R(T)$ curve and the resistive behaviour when the device is operated as a mixer.

A naturally resulting question is what the physical state of the microbridge is at its (optimum) operating point i.e. with both DC and LO power dissipation. The Nb/Au banks are superconducting and the microbridge is in a resistive state, thus the situation is in principle analogous to a S-N-S system. It has been shown by Skocpol, Beasley and Tinkham (SBT) that the electrical behaviour of superconducting microbridges at low temperatures can be well described in terms of a localised hotspot, maintained by self-heating [17]. The formation of a hotspot is also the main cause of the observation of hysteresis in the $I(V)$ curve of microbridges at low temperatures. Josephson coupling between the banks (the S-parts) can be important in the description of the $I(V)$ behaviour, but in our case this does not play a role because the coherence length (at low temperature) in the microbridge is much smaller than the bridge length ($\xi \sim 6 \text{ nm} \ll L \sim 200 \text{ nm}$).

The length of the hotspot L_H is directly related to the temperature profile in the microbridge and therefore depends on the amount of dissipated power; larger dissipation will lead to an increase of the size of the hotspot. In the SBT-model equilibrium between the electrons and phonons is assumed. Here we transfer this model to an *electronic hotspot*, in which case the equations are given by:

$$-K \frac{d^2 T}{dx^2} + \frac{c_{el}}{\tau_{e-ph}} (T - T_b) = j^2 \rho \quad (\text{for } |x| < L_H) \quad (9)$$

and

$$-K \frac{d^2 T}{dx^2} + \frac{c_{el}}{\tau_{e-ph}} (T - T_b) = 0 \quad (\text{for } |x| > L_H) \quad (10)$$

Here K is the thermal conductivity of the microbridge and assumed to be the same for superconducting and normal parts and independent of temperature, j is the current density and c_{el} is the electronic heat capacity. In taking this formulation we can use the analytical solutions of SBT at the expense of ignoring the temperature dependence in K and in the heat transfer between electrons and phonons. It is convenient to introduce a thermal healing length $\eta = (D\tau_{e-ph})^{1/2}$, being a measure of the strength of the coupling between the (hot) electrons and the phonons [18]. The relaxation of electrons is dominated by coupling to the phonons if $\eta/L < 1$, whereas diffusion to the normal conducting pads is the dominant relaxation mechanism when $\eta/L > 1$.

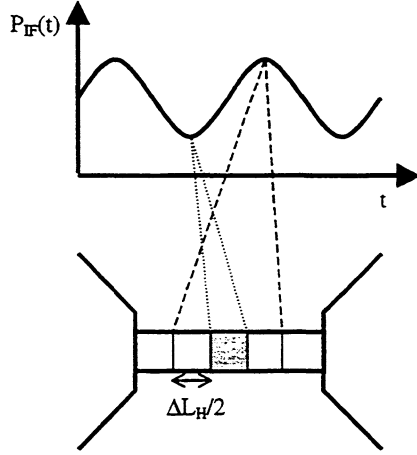


Figure 6: Schematic representation of the mixing process due to the modulation of the size of a hotspot. The grey areas schematically represent the hotspot in case of minimum and maximum power dissipation at the IF frequency. The white parts of the microbridge are superconducting.

In the situation where the device is operated as a mixer, the RF power dissipation is modulated at the intermediate frequency and, as a consequence, the size of the electronic hotspot is modulated. Since the hotspot is a normal (resistive) region, it implies that the resistance of the microbridge is also modulated at the intermediate frequency. Hence, the non-linear response of the device is due to the variation in length of the normal domain with input power. This situation is schematically depicted in Fig. 6. The change of the resistance due to a change in the length of the hotspot (or: change in dissipated power) is given by

$$\Delta R = \left(\frac{R_{sq}}{w} \right) \Delta L_H = \left(\frac{R_{sq}}{w} \right) \left(\frac{dL_H}{dP} \right) \Delta P. \quad (11)$$

Here R_{sq} is the square resistance of the microbridge, L_H the length of the hotspot and P the power dissipated in the hotspot. The voltage responsivity is defined as the change in voltage drop per Watt of absorbed signal power and thus given by

$$S = I \left(\frac{\Delta R}{\Delta P} \right) = I \left(\frac{R_{sq}}{w} \right) \left(\frac{dL_H}{dP} \right), \quad (12)$$

where I is the bias current.

We have calculated $S(V)$ on basis of the heat balance equations given by Eqs. 10 and 11. Fig. 7 shows the result of the calculation. Plotted are the responsivity as a function of bias voltage and the corresponding $I(V)$ curves for along (1000 nm, $\eta/L < 1$) and short (200 nm, $\eta/L > 1$) microbridge. The calculation predicts an increasing sensitivity with decreasing bias voltage, which is in general observed experimentally (Fig. 1b). In practice, however, it is difficult to find a stable bias point on the negative differential part of the $I(V)$, due to relaxation oscillations.

There are a few remarks to be made with respect to the limitations of the calculation. To start with, it is assumed that the absorption of power takes place only in the normal conducting parts. This is true for DC dissipation and RF dissipation, as long as the RF frequency is well below the gap frequency of the superconducting parts (~ 450 GHz). At higher frequencies there is also absorption in the superconducting parts of the bridge and therefore the right term in Eq. 12 is no longer zero, but equals αP_{LO} . Here α is the relative part

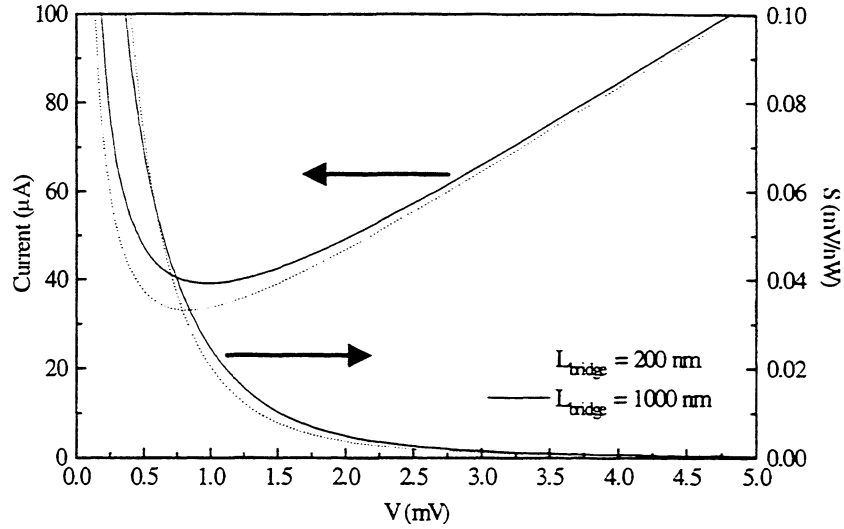


Figure 7: Calculation of the voltage responsivity (see text for definition) as a function of bias voltage together with the corresponding $I(V)$ curve. The calculation is performed in case $L_{\text{bridge}} = 1000 \text{ nm}$ ($\tau/L < 1$, phonon-cooled) and $L_{\text{bridge}} = 200 \text{ nm}$ ($\tau/L > 1$, diffusion-cooled).

of the bridge which is in a superconducting state. Consequently, a term $(1-\alpha)P_{\text{LO}}$ should be added to the right hand side of Eq. 11. Also, the thermal conductivity is taken to be independent of temperature and the same for superconducting and normal state. This is not true in general: the temperature and thermal conductivity are related to each other via the Wiedemann-Franz law and the thermal conductivity is expected to be much lower for the parts which are superconducting. In this case, however, it is not possible to find an analytical solution of the differential equations. Numerical simulations including these factors are in progress. As a last remark we note that in the analysis the N/S interface is sharply defined. Possible effects of non-equilibrium near the interface have not been included. Despite the above limitations of the calculation, we believe that it contains the essential physics.

Conclusions

In conclusion, we have presented a model which describes the resistive transition of Nb diffusion-cooled HEBs. We have shown that it is due to the dissipation in a superconducting microbridge connected to normal conducting heatsinks. We find that by using the concepts of the proximity effect, charge imbalance and Andreev reflection, a satisfactory agreement is found between the model and experimental observations. It follows from the analysis that the (DC measured) resistive transition is not related to the situation where the device is operated in a heterodyne mixing experiment i.e. under the application of DC and LO power. We propose a new mixing mechanism in terms of a (normal conducting) electronic hotspot of which the size oscillates at the intermediate frequency.

Acknowledgements

Helpful ideas, discussions and general assistance from A.A. Golubov, P. de Korte, H. van de Stadt, W.F.M. Ganzevles, E. Miedema and D. Nguyen are acknowledged. This work is financially supported in part by the Stichting voor Technische Wetenschappen and in part by the European Space Agency under contract No. 11738/95/NL/PB.

References

- [1] A. Skalare, W.R. McGrath, B. Bumble, H.G. LeDuc, P.J. Burke, A.A. Verheijen, R.J. Schoelkopf, and D.E. Prober *Appl. Phys. Lett.* 68, 1558 (1996)
- [2] H. Ekström, E. Kollberg, P. Yagoubov, G. Gol'tsman, E. Gershenzon, and S. Yngvesson *Appl. Phys. Lett.* 70, 3296 (1997)
- [3] A. Skalare, W.R. McGrath, B. Bumble, and H.G. LeDuc *IEEE Trans. Appl. Supercond.* 7, 3568 (1997)
- [4] B.S. Karasik, M.C. Gaidis, W.R. McGrath, B. Bumble, and H.G. LeDuc *IEEE Trans. Appl. Supercond.* 7, 3580 (1997)
- [5] P.J. Burke, R.J. Schoelkopf, D.E. Prober, A. Skalare, W.R. McGrath, B. Bumble, and H.G. LeDuc *Appl. Phys. Lett.* 68, 3344 (1996)
- [6] D. E. Prober *Appl. Phys. Lett.* 62, 2119 (1993)
- [7] B.S. Karasik and A.I. Elantiev *Appl. Phys. Lett.* 68, 853 (1996)
- [8] D. Wilms Floet, J.R. Gao, W. Hulshoff, H. van de Stadt, T.M. Klapwijk, and A.K. Suurling *Appl. Supercond.* 1997 401 (1997)
- [9] J.R. Gao, M. E. Glastra, R. H. Heeres, W. Hulshoff, D. Wilms Floet, H. van de Stadt, T.M. Klapwijk, and Th. de Graauw *Proc. 8th Int. Symp. On Space Terahertz Technology*, 36 (1997)
- [10] J. J. A. Baselmans, M. Sc. Thesis, University of Groningen, the Netherlands (1998) and references therein.
- [11] M. Tinkham, *Introduction to Superconductivity*, 2nd edition, McGraw-Hill, Inc. New York, Chapter 11 (1996)
- [12] M. Tinkham and J. Clarke *Phys. Rev. Lett.* 28 1366 (1972)
- [13] M. Stuiyinga, C. L. G. Ham, T. M. Klapwijk, and J. E. Mooij *J. Low Temp. Phys.* 53 (5/6) 633 (1983) and references therein
- [14] G.E. Blonder, M. Tinkham, and T.M. Klapwijk *Phys. Rev. B* 25(7) 4515 (1982)
- [15] P. Santhanam and D. E. Prober *Phys. Rev. B* 29 3733 (1984)
- [16] T. Y. Hsiang and J. Clarke *Phys. Rev. B.* 21 945 (1980)
- [17] W.J. Skocpol, M. R. Beasley, and M. Tinkham *J. Appl. Phys.* 45 (9) 4054 (1974)
- [18] M. Stuiyinga, T. M. Klapwijk, J. E. Mooij, and A. Bezuijen *J. Low Temp. Phys.* 53 (5/6) 673 (1983)

Optimal Choice of Material for HEB Superconducting Mixers

Boris S. Karasik* and William R. McGrath

*Center for Space Microelectronics Technology,
Jet Propulsion Laboratory, California Institute of Technology,
Pasadena, CA 91109*

We demonstrate that a potential distinction in ultimate performance of phonon-cooled and diffusion-cooled HEB mixers is not due to the cooling mechanisms but rather due to the different properties of available superconductors. The only available material for a phonon-cooled mixer with sufficiently large IF bandwidth (~4 GHz) is NbN, whereas a variety of clean materials (e.g., Nb, NbC, Al) are suitable for a diffusion-cooled mixer. For a readily achievable device length of 0.1 μm for example, the IF bandwidth can be ≥ 10 GHz. The requirement of low local oscillator (LO) power can also be more easily met in diffusion-cooled devices by selection of a material with lower critical temperature and low density of electron states. In contrast, the parameters in the NbN-based mixer cannot be widely varied because of the high resistivity and high transition temperature of the material and the necessity of using ultrathin films. Given the limited availability of LO power from compact solid-state sources at frequencies above 1 THz, a diffusion-cooled mixer based on aluminum is a very attractive choice for low-background radioastronomy applications.

1. INTRODUCTION

Hot-electron bolometric (HEB) superconducting mixers are becoming the desirable choice for use in radioastronomy heterodyne receivers at frequencies above 1 THz. The development effort of the last several years has resulted in the achievement of excellent device characteristics both for phonon-cooled and diffusion-cooled mixers. HEB receivers hold the low-noise record, by a wide margin, at 2.5 THz [1] and successfully compete with SIS mixers at frequencies around 1 THz (see Fig. 1) [2].

In addition to the noise temperature, the local oscillator (LO) power and the mixer IF bandwidth are the most important characteristics which must meet certain requirements set by a specific application and or availability of sufficiently powerful LO sources. A typical amount of LO power absorbed in the device is approximately 50-100 nW for many HEB mixers. One should account for 5-10 dB of embedding circuit and optical losses typical for terahertz mixers. While this LO requirement is lower than any competing device technology, there are nonetheless no tunable solid state sources available to pump HEB mixers at frequencies above 1.5 THz.

* Electronic mail: karasik@merlin.jpl.nasa.gov

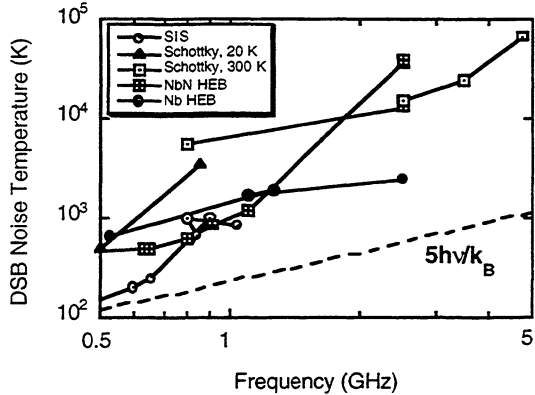


Fig. 1. Noise temperature of State-Of-The-Art THz heterodyne receivers [2]. The dashed line shows the fivefold quantum limit for comparison.

Though an instant bandwidth of ~ 4 GHz seems to be sufficient for many practical spectroscopy applications, the unavailability of tunable THz LO sources may require much larger bandwidth for an HEB mixer. This is because a CO_2 -pumped FIR laser may be the only option for an LO, and most often the available laser emission lines are many GHz separated from the particular spectral line of interest.

Currently LO source technology is not as well developed as mixer technology and this puts further demands for improvement of HEB mixers in terms of decreasing the LO power requirements and increasing the IF bandwidth. Also, since theoretically the HEB mixers can achieve quantum limited noise performance, it is of practical interest to find a way to achieve this limiting performance. In general, there is always a tradeoff between mixer characteristics when one attempts to optimize a particular characteristic of the mixer. The relationships between the mixer characteristics depend on the

cooling mechanism dominating in the HEB device. A proper choice of the device material can create a more optimal combination of mixer parameters. In the present paper we evaluate several superconducting materials with the goal of achieving optimal mixer performance and show what limitations are set by the cooling mechanism.

2. COOLING MECHANISMS IN HEB DEVICES

Any HEB mixer device is a strip of superconducting film deposited onto a dielectric substrate between two normal-metal contacts. Depending on the device size, either phonon or diffusion cooling dominates in the thermal energy removal from a hot-electron bolometer. The first mechanism takes place in relatively large devices with a length $L > \sqrt{D\tau_{e-p}}$ (D is the electron diffusion constant, τ_{e-p} is the electron-phonon interaction time). In this case the energy deposited into the electron subsystem by radiation or dc current is removed by means of electron-phonon collisions and consequent escape of nonequilibrium phonons into the substrate. The characteristic time of the phonon escape (proportional to the film thickness), τ_{es} , must be much shorter than the phonon-electron energy transfer time $\tau_{p-e} \approx \tau_{e-p}c_p/c_e$ (c_e , c_p are the electron and phonon specific heats respectively). At helium temperatures $\tau_{p-e} < \tau_{e-p}$ and the film must be very thin in order that all

the energy will be transferred from electrons to the substrate. An intense “back and forth” exchange of energy between electrons and phonons will result in effective slowing down of the relaxation process, decrease of required LO power for the mixer, and increase of the noise temperature. In fact, the case when $\tau_{es} > \tau_{p-e}$ is typical for conventional low- T_c superconducting bolometers which are not used as heterodyne mixers, and for high- T_c superconducting HEB mixers (more details on the latter case can be found in [3]). For operation of the low- T_c hot electron bolometer as a mixer one should avoid this situation and make sure that $\tau_{es} \ll \tau_{p-e}$. This case was successfully implemented in Nb films with thickness $d < 10$ nm [4,5]. However, the electron-phonon time in Nb is too long to be useful for most practical applications (see Fig. 2). The same applies for many other superconducting materials. The only known material which has a sufficiently short electron-phonon time to provide the bandwidth of several GHz is NbN [6]. It will be described in greater detail in the following section.

Another cooling mechanism for HEB mixers proposed by Prober [7], uses electron diffusion in submicron size devices for fast removal of heat from the microbridge. If one assumes total absorption of nonequilibrium electrons in the normal-metal contacts, then the relaxation time is given by $\tau_{dif} = L^2 / (\pi^2 D)$, where L is the device length. This expression

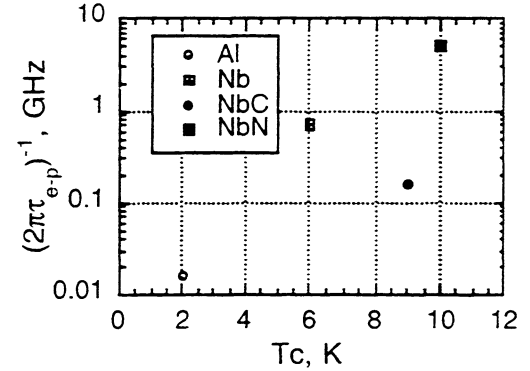


Fig. 2. Typical values of electron-phonon relaxation time for various superconducting films. The data points are shown at the critical temperatures of the materials. NbN could theoretically provide an effective bandwidth of ≈ 10 GHz, however the effect of a finite phonon escape time slows down the relaxation in these films. See explanation in Section 3.

should be strictly valid only for a normal metal bridge. In real superconducting bridges driven into the resistive state by a dc current and LO power, the resistance is distributed non-uniformly along the bridge and there is also a finite healing length in the contacts. Therefore this “lumped model” giving a functional dependence of the diffusion time on the length and diffusivity is only approximately valid, and the experimental values of τ_{dif} are often higher than predicted by this simple approximation.

In general, both cooling mechanisms can coexist and the dominance of one over the other is a matter of the device size, material and temperature. Figure 3 illustrates how the crossover from the electron-phonon to the diffusion-cooled regime occurs in NbC devices made from a film with $D \approx 10$ cm²/s [8]. For a 100- μ m-long device, the electron-phonon

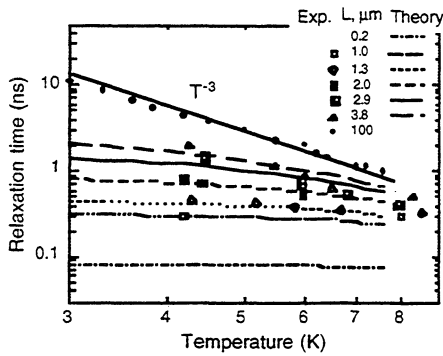


Fig. 3. The crossover from phonon cooling to diffusion cooling in NbC HEB devices of Ref. 8. The data points following the T^{-3} law represent the electron-phonon time in a long device. The relaxation time in shorter devices has much weaker temperature dependence since the contribution of electron diffusion is larger.

interaction dominates at all temperatures and the relaxation time follows the T^{-3} dependence typical for clean material. For shorter devices, the temperature dependence saturates at lower temperatures where the diffusion time becomes shorter than the electron-phonon time. For very short devices, diffusion dominates and the relaxation time is temperature independent.

3. BANDWIDTH

The diffusion cooling regime can be achieved in most materials as long as the device is made sufficiently short. It is simpler to observe however when the diffusion constant $D \geq 1 \text{ cm}^2/\text{s}$. For smaller diffusivities, the device length needs to be less than $0.1 \text{ } \mu\text{m}$ in order to provide a practical (ie: $> 1 \text{ GHz}$) bandwidth. Such short device sizes are difficult to achieve. Fortunately, there is a variety of

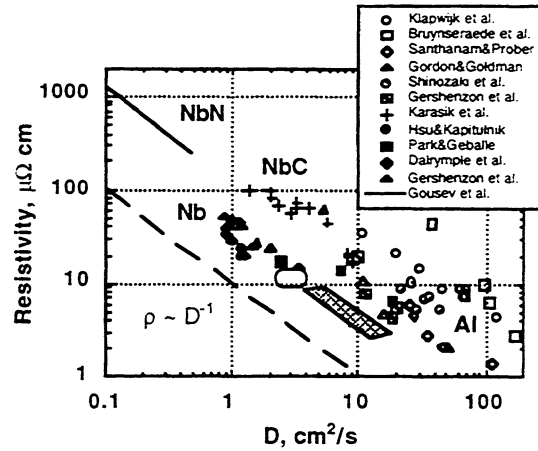


Fig. 4. The resistivity vs diffusivity data for different superconducting films. The following references were used: for Al films (open symbols) Klapwijk et al. [9], Bruynseraede et al. [10], Santhanam&Prober [11], Gordon&Goldman [12], Shinozaki et al. [13], Gershenson et al. [14]; for NbC films Karasik et al. [8], for Nb films (closed symbols) Hsu&Kapitulnik [15], Park&Geballe [16], Dalrymple et al. [17], Gershenson et al. [4]; for NbN films Gousev et al. [6]. The shaded tetragonal is an extrapolation for some low-resistive Nb film (diffusivity was not measured), the oval represents the range for Nb films used at JPL [18].

materials where large diffusivities can be easily obtained. As seen in Fig. 4, Nb, NbC, and Al all have $D \geq 1 \text{ cm}^2/\text{s}$. Many data points have been obtained for Nb microdevices with $D \approx 1\text{-}2 \text{ cm}^2/\text{s}$. The data for the devices of different length made from the same film approximately follow the expected L^{-2} as shown in Fig. 5. This dependence was previously shown at microwave frequencies below 20 GHz [19], and we show here the first confirmation at submillimeter frequencies. Thus for $L = 0.1 \text{ } \mu\text{m}$ one can expect a bandwidth of 10 GHz or greater.

For $D = 10 \text{ cm}^2/\text{s}$ (a typical value for aluminum) and $L = 0.1 \text{ } \mu\text{m}$, the calculated diffusion time is $\approx 1 \text{ ps}$ which corresponds to

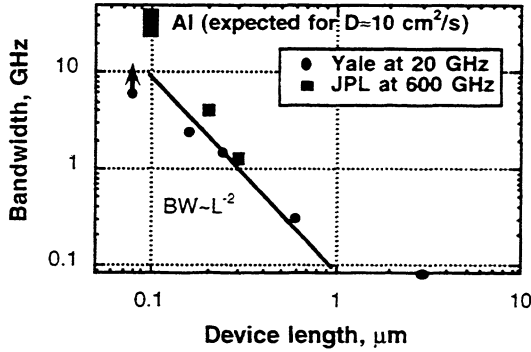


Fig. 5. The bandwidth data for Nb HEB devices fabricated at JPL [18]. The Yale data are from Ref. 19. The JPL data point for $L = 0.2 \mu\text{m}$ was measured for the device made from a less resistive film than others.

an effective mixer bandwidth of 160 GHz. Even taking into account the difference between the theory and experiment, a bandwidth of several tens GHz seems to be quite possible.

A large range of diffusion constants gives flexibility in adjusting the mixer resistance to a desirable value. Indeed, if one tries to increase the bandwidth by using very clean film, it may happen that the resistivity will be so low that the mixer device will be mismatched with the planar antenna impedance. Such a situation is more likely in Nb which has a higher density of electron states N_e ($\rho^{-1} = N_e e^2 D$) than Al and NbC where the density of states is three times lower than in Nb (see Fig. 4) Therefore one can use cleaner films (= larger bandwidth) of these materials, while maintaining at the same time a suitable resistance for matching to rf embedding circuits.

Niobium nitride is the only material which has a short enough electron-phonon time and, therefore, is useful for fabrication of HEB mixers. There is indirect evidence that the

intrinsic bandwidth set by the electron-phonon relaxation time at the critical temperature of 8-9 K is ~ 10 GHz [6]. The corresponding relaxation time $\tau_{e-p} \approx 13$ ps [20] is very short and since $c_e = 0.3c_p$ the phonon-electron relaxation time $\tau_{p-e} \approx 40$ ps. Even for the thinnest NbN films used in the recent experiments [20,21] the phonon escape time is also 40 ps. It means that the phonons do not remove the thermal energy from the film but rather exchange it with electrons. As a result, the relaxation slows down and the apparent bandwidth is smaller than that implied by τ_{e-p} , i.e. 4 GHz instead of 10 GHz. This situation can be adequately described by introduction of both electron and phonon temperatures different from the temperature of substrate. Any further increase of bandwidth in NbN seems to be problematic because: (a) it is hardly possible to fabricate even thinner (< 3 nm) high quality NbN films; and (b) electron diffusion still does not play a role in the relaxation since $D \approx 0.2 \text{ cm}^2/\text{s}$.

4. ULTIMATE NOISE PERFORMANCE AND LOCAL OSCILLATOR POWER

According to theory [22] the best HEB mixer performance takes place when the thermal fluctuation noise dominates over the Johnson noise. This is a case of a strong self-heating in the mixer device which is possible if the device has a sharp superconducting transition and large critical current density. Under these circumstances assuming that the

device operates at temperature $T \ll T_c$, the SSB mixer noise temperature, T_M , is given by the following expression:

$$T_M = (n+2)T_c, \quad (1)$$

where n is the exponent in the temperature dependence of the electron temperature relaxation time. For phonon-cooled devices it is an electron-phonon time: $n = 1.6$ for NbN, $n = 2$ for Nb, $n = 3$ for NbC. For diffusion cooled devices $n = 0$. The limits given by Eq. 1 are shown in Fig. 6 (horizontal lines). One can see that the theoretical limit for Al is many times lower than that for NbN. The theory of Ref. 22 does not consider any quantum phenomena though the quantum noise limit will be important at THz frequencies. A simplistic empirical correction can be made by adding one quantum contribution, $h\nu/k_B$, to the limit of Eq. 1. As a result the difference in T_M between Al and NbN HEB mixer becomes smaller but is still significant.

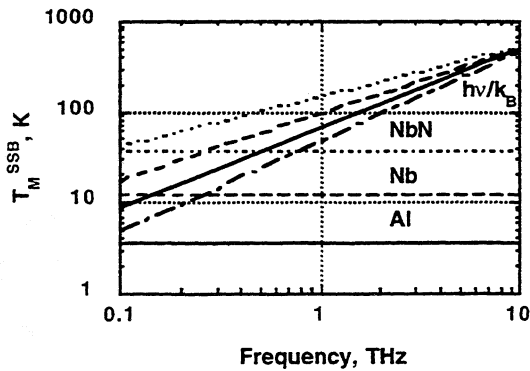


Fig. 6. Theoretical noise temperature limits for different mixer materials. The dash-and-dot line is the quantum limit.

The theory also predicts that under optimal conditions the local oscillator power should be much larger than the DC Joule power. The following equations apply in this case:

For NbN [20,23]:

$$P_{LO} = c_e(T_c)V(T_c^n - T_p^n) / [nT_c^{n-1}\tau_{e-p}(T_c)] \quad (2a)$$

$$c_e(T_c)V(T_c^n - T_p^n) / [nT_c^{n-1}\tau_{e-p}(T_c)] = c_p(T_p) / \tau_{es}(T_p - T). \quad (2b)$$

For a diffusion-cooled HEB mixer [24]:

$$P_{LO} = 4\mathcal{L}(T_c^2 - T^2) / R, \quad (3)$$

where R is the device resistance, and \mathcal{L} is the Lorenz constant.

The results of calculations using Eqs. 2 and 3, are shown in Fig. 7. We used $R = 20 \Omega$ for diffusion-cooled Al, Nb and NbC bolometers and $V = 0.15$ (length) \times 1.5 (width) \times 0.003 (thickness) μm^3 for an NbN phonon-cooled bolometer.

A further reduction of the local oscillator power might be achieved in a

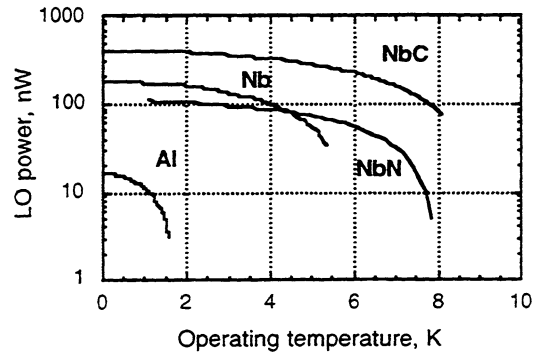


Fig. 7. Local oscillator power for optimized diffusion-cooled (Nb, NbC and Al) and phonon-cooled (NbN) HEB mixers.

phonon-cooled mixer by reduction of the volume. However, in the case of NbN, the large resistivity of the material requires the use of ~ 0.1 square size devices to ensure a reasonable match of the device resistance to a planar antenna impedance. Therefore, the NbN device of Fig. 7 is close to the optimum. In the case of diffusion-cooled mixers one has a choice of materials with lower values of critical temperature. For $T^2 \ll T_C^2$, $P_{LO} \propto T_C^2$, and one can see from Fig. 7, that Al with its low T_C (≈ 1.6 K) requires very low LO power compared to other materials. The bandwidth does not suffer however since it is temperature independent, in contrast to that in phonon-cooled devices.

5. PERFORMANCE TRADEOFFS

As can be seen from the above considerations, for a phonon-cooled HEB mixer, the IF bandwidth depends on the electron-phonon interaction time which is temperature dependent. Since a material with a relatively high T_C such as NbN is required, a wide bandwidth means higher noise temperature (Eq. 1) and higher LO power (Eqs. 2). Thus these mixer characteristics must be traded against each other to optimize the performance for this type of mixer.

For a diffusion cooled HEB mixer, the IF bandwidth is independent of temperature. Relatively lower T_C materials, such as Al, can be chosen to reduce mixer noise and LO power

requirements without sacrificing IF bandwidth. This type of mixer thus provides more flexibility in optimization for a particular application.

6. CONCLUSION

We have shown that both phonon-cooled and diffusion-cooled HEB mixers are predicted to give quantum limited noise performance. However, due to the characteristic properties of commonly used superconducting thin films, diffusion-cooled HEB provide more flexibility to meet the various needs of practical applications in regards to LO power, bandwidth, and noise. Developing HEB devices with lower critical temperature may allow the mixer to more readily reach quantum-limited noise performance at THz frequencies and meet the power requirements for the state-of-the-art tunable solid state LO sources. In particular, aluminum films appear to possess desirable and necessary qualities for optimization of HEB mixers for use in demanding radioastronomy applications.

ACKNOWLEDGMENT

The research described in this paper was performed by the Center for Space Microelectronics Technology, Jet Propulsion Laboratory, California Institute of Technology, and was sponsored by NASA, Office of Space Science.

REFERENCES

- [1] B.S. Karasik, M.C. Gaidis, W.R. McGrath, B. Bumble, and H.G. LeDuc, *Appl. Phys. Lett.* **71**, 1567 (1997).
- [2] These data are borrowed from different sources: Schottky diode data are taken from the Proc. 7th Int. Symp. on Space Terahertz Technology (STT-7), University of Virginia, Charlottesville, VA, March 1996; SIS data are from STT-7; NbN HEB data are from STT-7, STT-8, Ref. 21, J. Kawamura et al., *J. Appl. Phys.* **80**, 4232 (1996); *Appl. Phys. Lett.* **70**, (1997), A.D. Semenov et al. *Appl. Phys. Lett.* **69**, 260 (1996), G.W.Schwaab, 1998 SPIE Int.Symp. Astronomical Telescopes and Instrum. (communication); Nb HEB data are from A.Skalare et al. *Appl. Phys. Lett.* **68**, 1558 (1996), *IEEE Trans. Appl. Supercond.* **7**, 3568 (1997) and Ref. 1.
- [3] B.S. Karasik, W.R. McGrath and M.C. Gaidis *J. Appl. Phys.* **81**, 1581 (1997).
- [4] E.M. Gershenzon, M.E. Gershenzon, G.N. Gol'tsman, A.M. Lyul'kin, A.D. Semenov, and A.V. Sergeev, *JETP* **70**, 505 (1990).
- [5] E.M. Gershenzon, G.N. Gol'tsman, I.G. Gogidze, Yu.P. Gousev, A.I. Elant'ev, B.S. Karasik and A.D. Semenov, *Superconductivity* **3**, 1582 (1990).
- [6] Yu.P. Gousev, A.D. Semenov, G.N. Gol'tsman, A.V. Sergeev, and E.M. Gershenzon, *Physica B* **194-196**, 1355 (1994).
- [7] D.E. Prober, *Appl.Phys.Lett.* **62**, 2119 (1993).
- [8] B.S. Karasik, K.S. Il'in, E.V Pechen', and S.I. Krasnosvobodtsev. *Appl. Phys.Lett.* **68**, 2285 (1996).
- [9] T.M. Klapwijk, P.A. v.d. Plas, and J.E. Mooij, *Phys.Rev.B* **33**, 1474 (1986).
- [10] Y. Bryunseraede, M. Gijs, C. van Haesendonck, and G. Deutscher, *Phys.Rev.Lett.* **50**, 277 (1983).
- [11] P. Santhanam and D.E. Prober, *Phys.Rev.B* **29**, 3733 (1984).
- [12] J.M. Gordon and A.M. Goldman, *Phys.Rev.B* **34**, 1500 (1986).
- [13] B. Shinozaki, T. Kawaguti, Y. Fujimori, *J. Phys. Soc. Japan* **61**, 3678 (1992).
- [14] E.M. Gershenzon, G.N. Gol'tsman, V.D. Potapov, and A.V. Sergeev, *Solid State Com.* **75**, 639 (1990).
- [15] J.W.P. Hsu and A. Kapitulnik, *Phys.Rev B* **45**, 4819 (1992).
- [16] S.I. Park and T.H. Geballe, *Phys.Rev.* **135B**, 108 (1985)
- [17] B.J. Dalrymple, S.A.Wolf, A.C. Enrich, and D.J. Gillespie, *Phys.Rev.B* **33**, 7514 (1986).
- [18] B. Bumble and H.G. LeDuc, *IEEE Trans. Appl. Supercond.* **7**, 3560 (1997).
- [19] P.J.Burke, R.J. Schoelkopf, D.E. Prober, A. Skalare, W.R. McGrath, B. Bumble, and H.G. LeDuc, *Appl. Phys. Lett.* **68**, 3344 (1996).
- [20] S. Cherednichenko, P. Yagubov, K. Il'in, G. Gol'tsman, and E. Gershenzon. *Proc. 8th Int. Symp. on Space Terahertz Technol.*, p.245, 1997.
- [21] P. Yagubov, M. Kroug, H. Merkel, E. Kollberg, G. Gol'tsman, A. Lipatov, S. Svechnikov, and E. Gershenzon.
- [22] B.S. Karasik and A.I. Elantev, *Appl. Phys. Lett.* **68**, 853 (1996); *Proc. 5th Int.Symp. Space Terahertz Technol.*, p.229, 1995.
- [23] R.S. Nebosis, A.D. Semenov, Yu.P. Gousev, and K.F. Renk. *Proc. 7th Int. Symp. Space Terahertz Technol.*, p.601, 1996.
- [24] P.J. Burke. Ph.D. Dissertation, Yale University, 1997.

A LARGE SIGNAL MODEL FOR PHONON-COOLED HOT-ELECTRON BOLOMETRIC MIXERS FOR THZ FREQUENCY APPLICATIONS

Harald F. Merkel, Erik L. Kollberg, K. Sigfrid Yngvesson

Department of Microelectronics
Chalmers University of Technology
S 412 96 Göteborg
SWEDEN

Phone: +46-31-772-1848

Fax: +46-31-164 513

Email: harald@ep.chalmers.se

Abstract

Phonon cooled hot electron bolometers (HEB) show smaller noise temperatures in mixer applications above 1THz compared to Schottky diodes or SIS devices. To determine the optimal bias point for maximum IF bandwidth and lowest noise of a HEB detailed understanding of the current-voltage characteristic is indispensable.

A complete nonlinear model for a hot electron bolometric (HEB) mixer is derived. The dynamic resistance of a superconducting film is calculated under strong demagnetization conditions. The resistance is modeled due to vortex flow and phase slip lines. Self heating gives rise to normal domains in the film. In addition the resistance due to thermally activated flux creep and thermal fluctuations is taken into account. All these relations form a large signal model for the iv-characteristics and the bias points of the device. A small signal linearization yields then conversion gain and noise temperatures. Furthermore a quality measure for HEB devices is set up by deriving the thermal coupling of the film to the substrate and the achieved critical current density from measured current-voltage characteristics.

Introduction

A hot electron bolometer (HEB) is characterized by its resistance as a function of film temperature ($R(T)$ curve) and current-voltage (iv-)characteristics. Typically an iv curve (c.f. Figure 1 and 2) shows a very small resistance at very low voltages until a critical current is reached, increasing the device voltage further a region with very small or even negative differential resistance is encountered. Then for even higher voltages the device becomes complete normal resistive and the iv-curve exhibits then the slope of the normal resistance. Several phenomenological models have been proposed to approximate the resistive behavior of a HEB. Karasik et al. [2] proposed a broken-line model to model the device noise [11]. There the resistive transition starts with a given critical current and the resistance increases linearly until the normal resistance is reached at another experimentally determined current. With this model a different set of fitting parameters has to be applied for every substrate temperature. The sharp separation between positive and negative differential resistance regions which occurs in some devices cannot be modeled correctly. Vendik et al.[18] proposed a refinement of this model by fitting a parabola to the superconducting-resistive transition which rounds the obtained iv-curves somewhat. Recently an expansion of the temperature derivative of the $R(T)$ curve in terms of gaussian functions has been proposed [15]. There the resistance expansion is used in a heat balance equation to calculate iv curves with self heating. This model approximates iv curves reasonably well but modeling negative resistance regions quantitatively correct requires the introduction of correction terms to the device current.

Measured current-voltage characteristics

Typical measured unpumped current-voltage characteristics for hot electron bolometers (HEB) with the film temperature as a parameter are shown below. Figure 1 shows a complete current-voltage characteristic beginning with a Meissner state area for very small voltages. Exceeding a critical current vortex flow becomes remarkable leading to the formation of phase slip lines. If one exceeds the critical voltage for hot spot formation the characteristics shows a small positive differential resistance determined by hot spot growth. Increasing the voltage further drives the device to normal state (not shown , at about 25 mV)

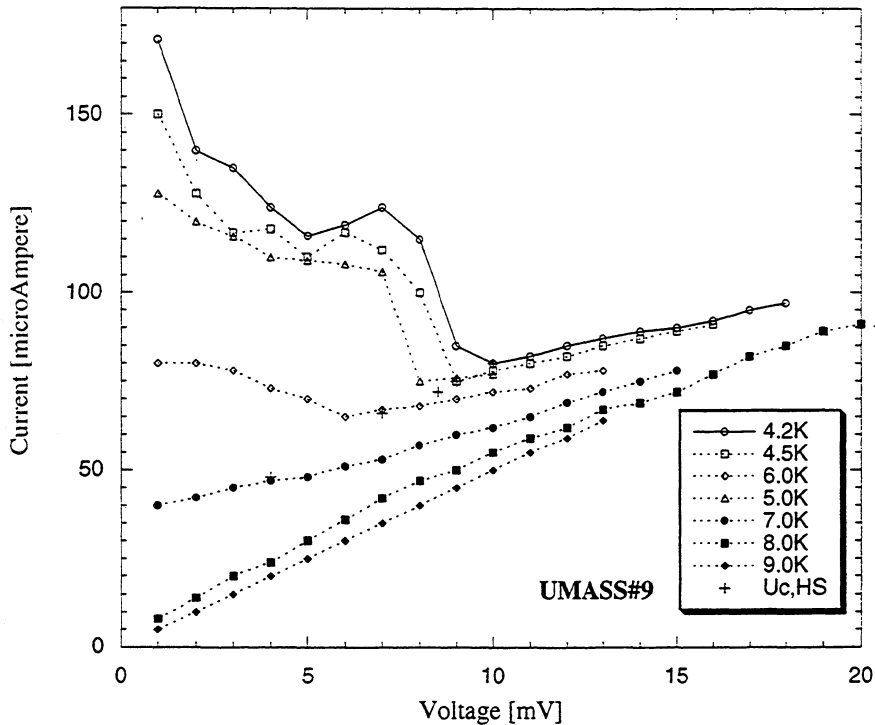


Figure 1: Unpumped current-voltage characteristic (device #9 from UMASS) for different film temperatures. The iv-curves for low temperatures (<5.0K) show a negative differential resistance behavior due to vortex flow and the formation of phase slip centers. For higher device voltages a hot spot is formed which grows until it covers the complete device. For temperatures above 9K the device becomes completely normal conducting. The crosses indicate theoretical results of the critical voltage for hot-spot formation.

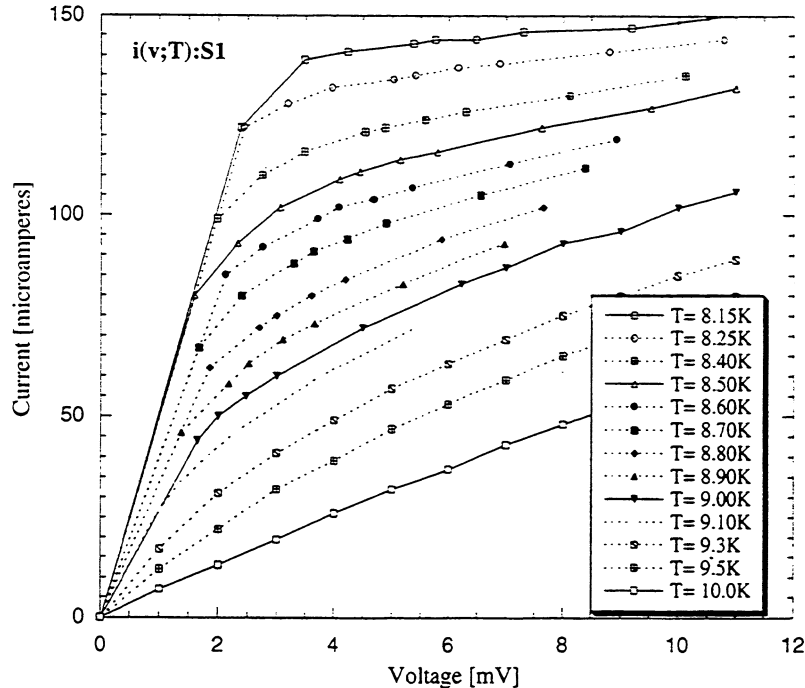


Figure 2: Unpumped current-voltage characteristic (device S1#5) for different film temperatures. The iv-curves for lower temperatures ($<7.6\text{K}$) show a negative differential resistance. In the bias voltage and temperature interval shown here the device is in the resistive zone as soon as the curve departs from the superconducting straight line. For temperatures above 9.9K the device becomes completely normal conducting.. The best (lowest noise and maximum bandwidth) bias points for this device is located at $8.8\text{K}/7\text{mV}$. The normal resistance at 20K is about 230Ω

A typical bias point in a HEB mixer is located in the hot spot growth region. There the device is unconditionally stable (since the differential resistance is positive) but at the same time the device sensitivity to power changes is maximal. The sensitivity in the unstable region is larger than in the hot spot growth area but due to the negative differential resistance no stable operating point can be realized. Choosing the bias point close to the normal conducting state the sensitivity is very low.

In the following the device resistance will be modeled as a function of film temperature, voltage and dissipated electrical power. This requires the analysis of resistance-voltage (rv-) curves. These rv-characteristics are easily derived from the iv-characteristics in Figures 1 and 2. Figures 3 and 4 show the resistance-voltage characteristics for the devices CTH:S1 and UMASS#9. Assuming hot spot growth as the crucial resistance mechanism one has to solve a thermal power balance equation on the strip. For film temperatures in vicinity of the critical temperature this power balance can be linearized. Solving this equation the length of the hot spot is determined. The resistance of such a hot spot shows then a slope which is proportional to the difference between the film temperature and the temperature where the device becomes normal conducting. Data of device S1 exhibits this behavior: its resistance-voltage curves are almost parallel straight lines (c.f. Figure 3). Extrapolating the resistance curves to zero currents (and zero voltages) yields the resistance without any self heating. There the hot spot disintegrates and a set of vortices is left over. The vortices are still present because the resistance curves are linearly extrapolated for zero heat dissipation without changing the basic resistive effects.

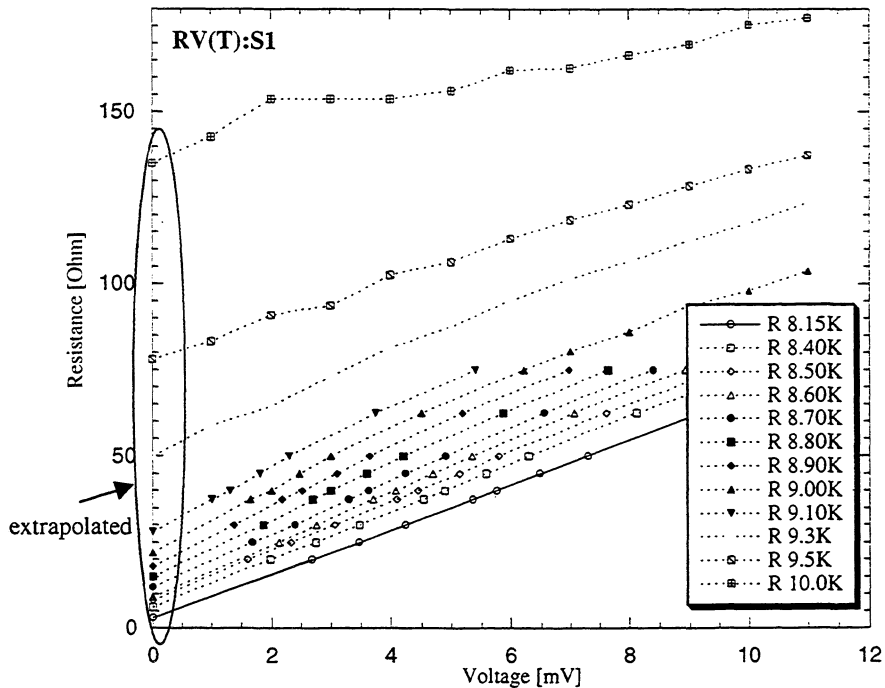


Figure 3: Unpumped resistance-voltage characteristics (device S1 , belongs to the current-voltage characteristic shown in Figure 1) for different film temperatures. The device is in hot spot growth regime. The temperature was chosen close to the critical temperature (9.9K). So no negative differential resistance region is observed. (In the measurement negative differential resistance was encountered at a film temperature of below 7.6K). The best bias points for this device is located at 8.8K/7mV

The resistance-voltage characteristics for device UMASS#9 shows a transition from the purely superconducting state (zero resistance , Meissner state) to a vortex flow / phase slip state (negative resistance region, unstable operation of the device). The resistance-voltage characteristics for the vortex state are straight lines intersecting the coordinate origin. No residual resistance is thus observed there until the film temperature is very close to the critical temperature. Then a sharp transition to normal state is observed (c.f residual resistance in Figure 5 denoted by dotted line). The instability will prevail until a hot spot is formed. Then the differential resistance becomes slightly positive.

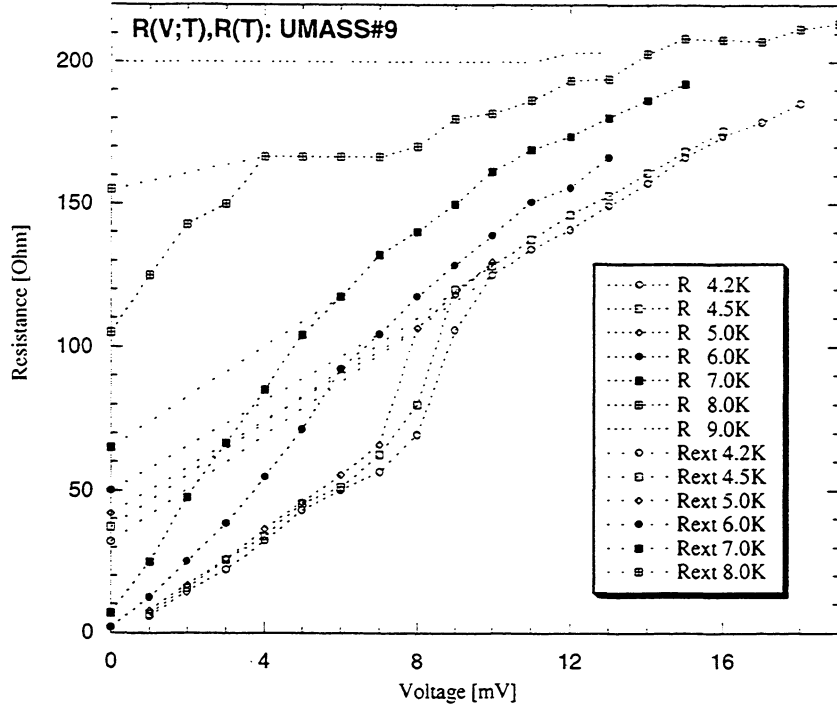


Figure 4 Device resistance as a function of device voltage for different film temperatures. The extrapolated values for the residual resistance under hot spot growth conditions (shown in Figure 5 as solid rectangles) are indicated on the y-axis. The interpolation line segments are indicated as sparse dotted lines. The interpolation of the vortex flow resistance

Device model outline

The resistance of a HEB depends on transport current, substrate temperature and heat dissipation in the superconducting film. Expanding the resistance in a power series with respect to dissipated power p and current I one obtains the following decomposition:

$$R(T, I, p) = R(T, I) \Big|_{p=0} + \sum_{\mu=1}^{\infty} \frac{1}{\mu!} p^{\mu} \frac{\partial^{\mu}}{\partial p^{\mu}} R(T, I, p) \Big|_{p=0} = R(T, I) \Big|_{p=0} + \Delta R(T, I, p) \quad (1)$$

In Equation (1) the cold resistance (obtained for $p=0$) is separated in a “current free-cold” resistance and a “dynamic resistance”.

$$R(T, I) \Big|_{p=0} = R(T) \Big|_{p=0, i=0} + R(I; T) \Big|_{p=0} \quad (2)$$

In the subsequent text the following terms for resistances will be used:

$R(T, I) \Big|_{p=0} = R_{cold}(T, I)$ This isothermal “cold” resistance excludes all self-heating effects. Thus the remaining resistive effects are due to the film temperature without any current and due to the transport current (dynamic resistance).

$R(T)_{p=0,i=0} = R_T(T)$	denotes the current-free resistance which only depends on temperature. This resistive contribution is due to thermal fluctuations and due to thermally activated vortex flow.
$R(I;T)_{p=0} = R_D(I;T)$	is the dynamic resistance due to transport current flow which contains the film temperature as a parameter. This resistance is caused by vortex creep / vortex flow and phase slip formation.
$\Delta R(T, I, p)$	denotes the resistance change due to self-heating. It is obtained explicitly by solving a heat balance equation on the HEB strip.

Self heating is included by solving a heat balance equation based on the “cold” resistance where the dissipated heat due to RF and bias acts as a heat source. Its solution yields an updated film temperature. Self heating results in the formation of hot spots and normal domains.

The model can be greatly simplified for the region of special interest for HEB mixer operating points: There the relevant current dependent resistive effect is hot spot growth. The “zero-current” temperature dependent resistance is determined by thermally activated flux creep.

Investigating the dynamic resistance of a superconducting strip under voltage bias the film properties will change at distinct voltages. Such a critical voltage drives a critical current at the device resistance. Assume that the device resistance jumps from a value R_{lo} to R_{hi} if the critical current is exceeded. Increasing the bias voltage to reach the critical voltage the film current will increase too and the critical current is reached. Then the resistance is increasing and which diminishes the current to a value below the critical one. Obviously a stable mixed state is reached at the voltage which drives the critical current at R_{lo} . This mixed state is stable until the voltage exceeds the voltage for which the critical current is driven even for the higher resistance R_{hi} . Above the upper critical voltage the film state becomes homogenous again.

The current-dependent resistive transition, “dynamic resistance”

As a well known fact type II superconductors allow penetration of magnetic fields in the form of localized flux quanta [5], [13], [14] if the inner magnetization exceeds the lower critical magnetic field. Demagnetization effects reduce the critical transport current needed to sustain this vortex flow. Since the mixers investigated here are operated under constant voltage conditions the critical currents have to be translated to critical voltages. Following the behavior of a superconducting film under increasing device voltage one obtains a complete Meissner state starting at very low voltages: Assuming a perfect magnetic shielding the only magnetic field present is induced by the transport current in the superconductor. The extrinsic voltage measured at the mixer pads is determined by the pad resistance only.

$$U_{c,Meissner} = R_{pad} \cdot I_{c1} = R_{pad} \cdot B_{c1} \cdot \frac{d\pi^2}{\mu_0} \cdot \left[1 - \left(\frac{T}{T_c} \right)^2 \right] \quad (3)$$

If this extrinsic voltage is exceeded the lower critical current is reached and vortices penetrate the film. Usually if no shielding is provided the earth’s magnetic field is sufficient to exceed the lower critical field so vortices will be present even then.

Phase slip line formation

Since there is always an impurity at the film surface where vortices are predominantly formed the vortices will not be equally distributed. Assume the extreme case that all vortices are generated at the same point on the film a normal conducting well will be formed perpendicular to the transport current direction if the mean distance of the vortices in this cross section becomes equal to the vortex diameter. For a phase slip line to form the vortex density (given by Equation B5 in Appendix B) the following relation must hold:

$$n_{vortex}(I_{c,PSL}) = \frac{1}{4 \cdot \xi^2} \cdot \left(\frac{\lambda_{London}}{l_{Film}} \right)^2 \quad (4)$$

Equation (4) is used to derive a relation for the minimum current needed to sustain a phase slip. If the current exceed the phase slip critical current the film exhibits a normal conducting barrier with the resistance:

$$R_{PSL} = R_N \cdot \frac{2\xi}{l_{film}} \quad (5)$$

A phase slip will lead to an intrinsic voltage drop which in turn reduces the transport current below the critical current leading to phase slip dissolution. The superconducting film will thus exhibit a mixed state between vortex-free regions and a weak phase-slip line which adjusts the film resistance pinning the transport current to the critical current for vortex formation. This mixed state will vanish if the (extrinsic) voltage is large enough to drive the lower critical current if the device resistance equals the phase slip line resistance:

$$U_{c,PSL} = (R_{pad} + R_{PSL}) \cdot I_{c1} = (R_{pad} + R_{PSL}) \cdot B_{c1} \cdot \frac{d\pi^2}{\mu_0} \cdot \left[1 - \left(\frac{T}{T_c} \right)^2 \right] \quad (6)$$

Phase slip line resistance

According to the phase slip line (PSL) model given in [6, vol.iii , p.57] the resistance of a superconducting film carrying phase slip lines is given as:

$$R_{PSL,\infty} = R_N \frac{I_{c2}}{I} \cdot \left(\frac{I - I_{c1, film}}{I_{c2} - I_{c1, film}} \right)^2 \quad (7)$$

This relation is applicable to infinitely long films and requires the presence of more than one phase slip line whose distance depends on the device current. The films investigated here are far too short to sustain more than one phase slip line. Therefore the resistance due to phase slippage is the resistance of a single PSL.

Model for the “cold” device resistance

The device resistance is now modeled as a function of the extrinsic voltage. Thereby no self-heating effects are taken into account. The only resistance in the Meissner state is the pad resistance. The first mixed state occurs between the phase slip formation and the Meissner critical voltage. There the device resistance is at first order linearly dependent on the voltage since the transport current is pinned to the lower critical current. Exceeding the critical voltage for the phase slip line the resistance remains constant supposed that the film is short enough not to support more than one phase slip line. One obtains for the cold device resistance Equations (3,5,6,7):

$$R_{cold}(U, T, T_s) = \begin{cases} R_{pad} & U_{c,Meissner} > U \\ R_{pad} + R_{PSL} \cdot \frac{R_{pad} \cdot (U - U_{c,Meissner})}{U_{c,PSL} - U_{c,Meissner}} & U_{c,PSL} > U \geq U_{c,Meissner} \\ R_{pad} + R_{PSL} & U \geq U_{c,PSL} \end{cases} \quad (8)$$

The temperature-dependent resistive transition, “zero-current resistance”

Under idealized conditions the dc-resistance of a superconductor is identically zero below the critical temperature and jumps to its normal resistance if the critical temperature is exceeded. The transition between normal and superconducting state is broadened due to thermal effects (suppressed superconductivity and diffusion of excess electrons into the strip do not play a significant role because the bridge is quite long [15]):

Below the critical temperature: Thermally activated vortex creep and thermal fluctuation

Pinned vortices present in the film will be excited thermally and will start creeping. In addition thermal fluctuations will increase the resistance below the critical temperature. Among other approximations for the current-free resistance for different temperatures [5] the best coincidence to experimental results is realized by the following relation:

$$R_T = \alpha_{flux\ creep} \cdot R_N \cdot e^{\frac{T-T_c}{\Delta T}} \quad (9)$$

The effective flux creep factor varies from device to device. Values for the parameters (and the hot spot length due to voltage variation needed for Equation (15)) for some devices are given in the table below .

Device	β [Ω / mV]	$\alpha_{flux\ creep}$ [1]	R_N [Ω]	T_c (dipstick) [K]	ΔT [K]
CTH, S1	6.6	0.5	270	9.9	0.425
UMASS #9	6.0	1.2	185	9.0	0.43
CTH, C2 #1	6.2	1.0	150	8.5 (from iv-curve)	0.5

Table 1: Parameters for the thermally activated vortex creep resistance given by Equation (9). The data of the device UMASS#9 were measured by K.S. Yngvesson at University of Massachusetts.

To obtain the “zero current ” resistance the measured data have to be extrapolated for vanishing transport currents. Measuring at currents large enough to provide vortex flow the extrapolation will yield the influence of vortex creep. If the measurement is performed at currents smaller than the lower critical current no vortex will penetrate the film and the obtained resistive transition will become very sharp.

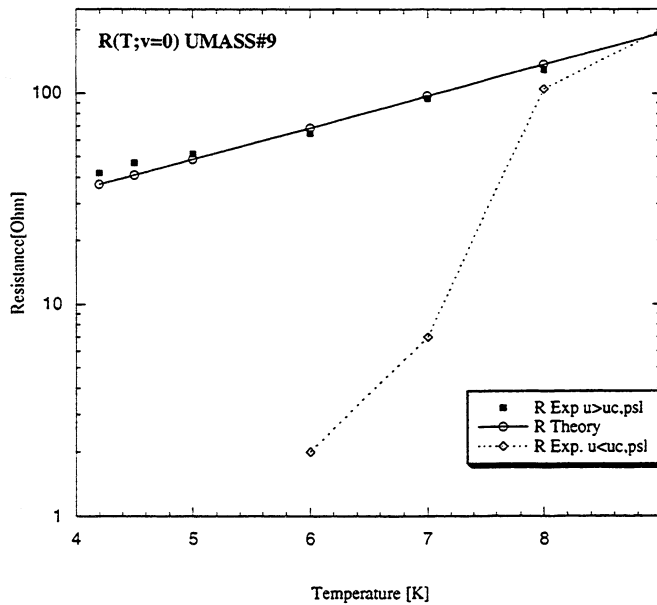


Figure 5 Logarithmic plot of the extrapolated (zero current) device resistance as a function of film temperature for the device UMASS #9. The black squares indicate extrapolated values from the hot spot growth area (c.f. Figure 3). The carets are extrapolated values for the vortex flow/phase slip region.

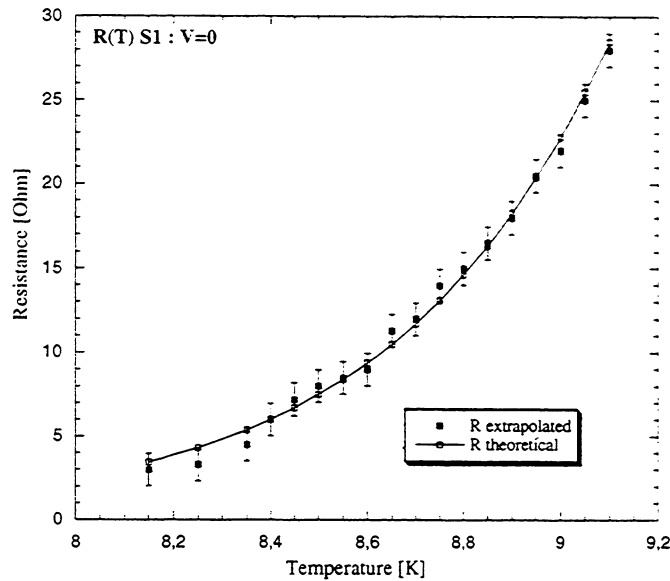


Figure 6: Device resistance as a function of temperature extrapolated for zero voltage. The theoretical curve is obtained under the assumption that thermally activated vortex flow is the only resistive process. Denote that the extrapolation to zero currents (and zero voltage) yields a "cold" resistance where self heating processes are not present. The functional relation for the theoretical curve is given by Equation [9] the needed parameters are found in the uppermost row of Table 1

Above the critical temperature: Finite lifetime of Cooper pairs, Thermal fluctuation

Above but in close vicinity of the critical temperature the measured conductivity of a superconducting thin film exceeds the normal resistance. Stochastic thermal fluctuation enable Cooper pairs to exist for a finite lifetime even above the critical temperature. These pairs will provide an additional resistance free electron transport channel and increase the macroscopically measured film conductivity. Since the HEB is typically operated in the hot-spot growth region temperatures above T_c are only reached in extended hot-spot regions. The extrapolated values of typical zero current resistances are all below the critical temperature and fit perfectly to the activated vortex creep curves.

Film self-heating

Since vortex flow and the pad resistance are quite small their contribution to device heating is negligible. Almost the whole device resistance is due to phase slip lines. Phase slip lines require the penetration of the film by vortices entering the film at a weak point. If the power dissipated in the resistor generated by the phase slip is large enough to heat the phase slip line volume to the critical temperature a stable normal domain is generated. Such a domain is called a hot spot [13]. Referring to the above steady state power balance one obtains for the minimum voltage needed to sustain a hot spot where b denotes the normalized thermal coupling:

$$\frac{U_{c,HotSpot}^2}{R_{PSL}} - b \cdot [T^\gamma - T_{substrate}^\gamma] = 0 \quad (10)$$

Solving Equation (10) for the voltage one is left with the minimum voltage needed to sustain a hot spot:

$$U_{c,HotSpot} = \sqrt[2]{\frac{2bR_n\xi}{l_{film}} (T_c^\gamma - T_{substrate}^\gamma)} \quad (11)$$

Theoretically obtained values of the critical hot spot voltage are depicted in Figure 1. They should coincide with the end of the negative differential resistance region of the device. Obviously the agreement with the behavior of measured iv-curves is fairly good.

Film Temperature	$U_{c,HotSpot}(T_c=7.7)$	Measured UMASS#9
4.2K	9.503mV	9.6mV
4.5K	9.325mV	9.0mV
5.0K	8.942mV	8mV
6.0K	7.730mV	6mV (+/- 0.5mV)
7.0K	5.395mV	5mV(+/- 0.7mV)

Table 2: Theoretical and measured critical voltages for hot-spot generation This critical voltage is determined by the upper end of the unstable region in the current-voltage characteristics. The beginning stabilization is attributed to the formation of a hot spot which exhibits a much slower time constant than phase slip lines or vortex fluids.

Device voltages exceeding the critical voltage for hot spot formation will heat the normal domain even more and broaden it. Finally the complete film becomes normal conducting. A rough estimate for this voltage is obtained by assuming that the film temperature is uniform and equal to the critical temperature of the film. One obtains then:

$$\frac{U_{c,Normal}^2}{R_n} - b \cdot [T^\gamma - T_{substrate}^\gamma] = 0 \quad (12)$$

$$U_{c,Normal} = \sqrt[2]{\frac{bR_n}{l_{film}} (T_c^\gamma - T_{substrate}^\gamma)} \quad (13)$$

Model for the device resistance

The device resistance is now modeled as a function of the extrinsic voltage. The only resistance in the Meissner state is the pad resistance. The first mixed state occurs between the phase slip formation and the Meissner critical voltage. There the device resistance is at first order linearly dependent on the voltage since the transport current is pinned to the lower critical current. Exceeding the critical voltage for the phase slip line the resistance remains constant supposed that the film is short enough not to support more than one phase slip line. Increasing the applied voltage further the power dissipated in phase slip line is sufficient to heat the phase slip line area to the film's critical temperature. A hot spot is formed. Exceeding the critical voltage for hot spot formation the hot spot will broaden until it covers the complete film. In a last step the resistance due to thermal activation is added to the device resistance and in the calculation of the critical voltages Finally one obtains for the device resistance:

$$R(U, T) = \begin{cases} R_{pad} + R_{PSL} \cdot \frac{R_{pad}}{U - U_{c,Meissner}} + R_T(T) & U_{c,Meissner} > U \\ R_{pad} + R_{PSL} + (R_n - R_{PSL} - R_T(T)) \cdot \frac{U - U_{c,HotSpot}}{U_{c,Normal} - U_{c,HotSpot}} + R_T(T) & U_{c,PSL} > U \geq U_{c,Meissner} \\ & U_{c,HotSpot} > U \geq U_{c,PSL} \\ & U_{c,Normal} > U \geq U_{c,HotSpot} \\ & U \geq U_{c,Normal} \end{cases} \quad (14)$$

Simplified model for typical mixer applications

Operating a HEB mixer in the hot spot growth region one typically finds resistance-voltage curves consisting of a set of almost parallel trajectories as depicted in Figure 7.

This set of parallel resistance trajectories can be explained under several assumptions:

Assume the substrate temperature to be close to the critical temperature. This allows to linearize the heat loss terms due to a temperature difference between the film and the substrate.

Secondly the differential resistance in this region is small. Since the slope of these curves is small the current is almost constant and therefore the power becomes proportional to the device voltage. Then the hot spot length becomes essentially proportional to the dissipated power.

Under this assumptions an increase in bias voltage will prolong the hot spot a certain amount which is independent of substrate temperature.

Extrapolating the resistance curves to zero currents (and zero voltages) yields the resistance without any self heating. There the hot spot disintegrates and a set of vortices is left over. The vortices are still present because the resistance curves are linearly extrapolated for zero heat dissipation without changing the basic resistive effects. The relation for the device resistance based on these assumptions becomes then :

$$R(V, T) = \alpha_{fluxcreep} \cdot R_N \cdot e^{\frac{T-T_c}{\Delta T}} + \beta \cdot V \cdot \left(T_c + \frac{1}{2} \Delta T - T \right) \quad (15)$$

The values for the parameters $\alpha_{fluxcreep}$ and β are listed in Table 1. Here $\alpha_{fluxcreep}$ denotes the efficiency to unpin a vortex in the film where β is a proportional to the (linearized) thermal coupling of the film to the substrate and describes the change of the hot spot length under voltage variations. Extrapolating this relation for zero voltage results in the residual resistance given in Equation (9).

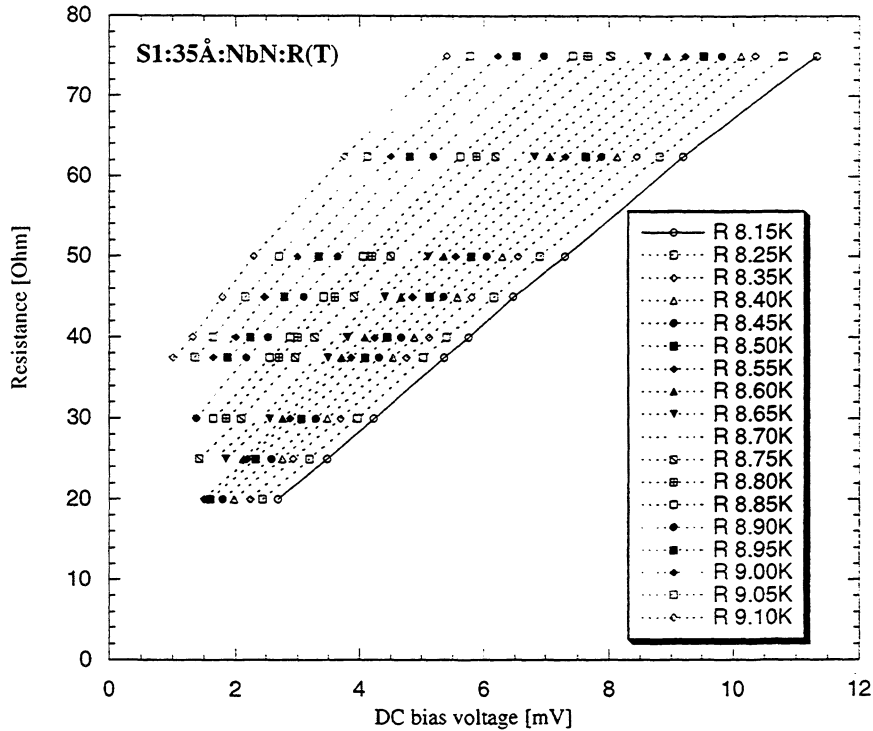


Figure 7: Unpumped resistance-voltage characteristics (device S1#4) for different film temperatures in the interval 8.15K to 9.1K. The device completely is in hot spot growth regime. This plot is a part of Figure 3 and contains the temperature interval which is most interesting for mixer operation.

Comparison to experimental data of demagnetized lower critical currents

In Figure 8 the theoretical values for a bolometer strip for a critical temperatures of 10.2K and 7.7 K are compared to measured values for a 10.2K NbN made by CTH and a 7.7K NbN (UMASS #9) HEB from University of Massachusetts.

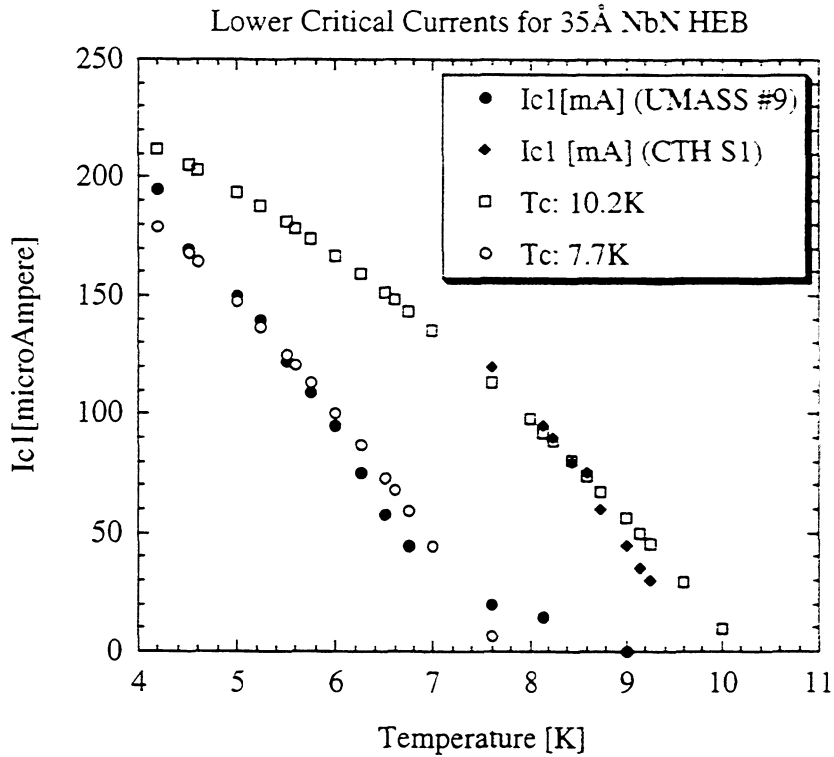


Figure 8: Critical current for the devices UMMASS#9 (measured: filled circles , theoretical: empty circles) and CTH S1 (measured: filled carets , theoretical: empty squares). The data is taken from measurements of umpumped iv-characteristics for various substrate temperatures.

In the following table the theoretical and experimentally obtained values for critical currents of a NbN bolometer strip are listed for 4.2K and 8.15 K substrate temperature. The critical current for vortex flow is considerably larger than the current for phase slip line formation which leads to the direct transition from Meissner state to phase slip lines.

Critical value	$T_{\text{substrate}}=4.2\text{K}$	$T_{\text{substrate}}=8.15\text{K}$	$T_{\text{substrate}}=8.15\text{K, measured}$
I_{c1} (Equation 3)	194.2 μA	96.0 μA	95 μA
$U_{c,\text{Meissner}}$ (Equation 3)	10.8 μV	6.2 μV	not observable
$U_{c,\text{PSL}}$ (Equation 6)	162.2 μV	91 μV	0.1mV
$U_{c,\text{HotSpot}}$ (Equation 11)	11.94 mV	4.95 mV	5 mV
$U_{c,\text{Normal}}$ (Equation 13)	168.9 mV	59 mV	>55 mV

Table 3: Theoretical critical currents and critical voltages for vortex flow, phase slip line and hot-spot formation for the device CTH:S1 for different temperatures and a comparison with data obtained from measurements.

Conclusion

In contrast to previous models for the iv-characteristic of hot-electron bolometers the resistive transition obtained directly from the physical behavior of the film and is not fitted to the experimental data. Furthermore there is a clear distinction between the “equilibrium” heating due to thermal heating and bias power which is dissipated via vortex scattering and the “nonequilibrium” heating acting on the electrons of the film only which are thermally coupled to the film phonons which in turn transfer energy to the film material. In addition the bolometer temperature is no longer assumed to be constant throughout the film. The large signal behavior of a phonon-cooled hot-electron bolometer can therefore be described using only one model parameters besides geometric and physical parameters: the thermal loss coefficient per unit square of the film to the surrounding (needed for the lateral power balance Equation (12)).Both parameters are independent of geometry and a characteristic for the film quality and the films thermal coupling to the substrate.

The knowledge of the lateral distribution of the film temperature allows the model to take the frequency behavior of the RF absorption mechanisms completely into account. The RF absorption takes place only in the film regions where the quasiparticle bandgap is smaller than the photon energy. This limits the active area where Cooper pair dissociation occurs to a frequency dependent fraction of the film explaining the curvature change of pumped iv-curves with frequency. In addition the device noise model is refined. Now vortex shot noise, Nyquist noise for the normal domains and thermal fluctuation noise are easily included because the resistance as a function of current, voltage and dissipated power is explicitly known.

Acknowledgements

The authors are deeply indebted to Dr. Pavel Yagoubov for fruitful discussions on the device physics and for the data of a complete parametric measurement for the devices CTH S1#5 and CTH C2.

Appendix A: Demagnetization and vortex flow in a type II superconducting film

Demagnetization effects

The formation of vortices is determined by the magnetic field inside the material. The magnetization at the sample surface shield a part of the applied magnetic field. The surface magnetization depends on the sample geometry. For ellipsoids (including degenerate ellipsoids like discs, rods) it can be shown [5: p.420 (applying duality theorems)] that external fields in the ellipsoids’ main axes lead to collinear demagnetization fields. Therefore the influence of surface magnetization is conveniently described by demagnetization factors in the main axes.

$$\vec{B}_{outer} \cdot \hat{x} = \vec{B}_{inner} \cdot \hat{x} - N_x \cdot (\vec{M} \cdot \hat{x}) \quad (A1)$$

Since the surface magnetization vanishes when integrated over the whole surface, the sum of the demagnetization factors is unity. Let us consider now the case of a thin film. Applying a magnetic field normal to the film surface gives rise to a very big area which will carry depolarization currents compared to a magnetic field normal to the film edge. The demagnetization factor for a normal field is approximated by:

Defining the magnetic susceptibility of a material according to

$$(1 + \chi) \cdot \mu_0 = \mu \quad (A2)$$

one obtains for the magnetic flux density and the magnetization in a demagnetizing geometry in terms of the applied field B_{app} :

$$B_{inner} = B_{app} \cdot \frac{1 + \chi}{1 + \chi \cdot N} \quad (A3)$$

$$M = B_{app} \cdot \frac{1}{\mu_0} \cdot \frac{\chi}{1 + \chi \cdot N} \quad (A4)$$

A type II superconductor in Meissner state is a perfect diamagnet with $\chi \equiv -1$ if the inner magnetic field does not exceed the first critical magnetic field

$$\mu_0 \cdot H_{inner} = |\mu_0 \cdot M| \leq B_{c1} \quad (A5)$$

In samples with non demagnetizing geometries ($N = 0$), the magnetization leads to a flux density which cancels the applied field inside the superconductor. For thin films the demagnetization factor normal to the film surface are almost unity. The magnetization in the material sample for a film with the thickness d and width w becomes then:

$$\mu_0 M = -B_{app} \cdot \frac{1}{1 - N} \approx -B_{app} \cdot \frac{2}{\pi} \frac{w}{d} \quad (A6)$$

In ultrathin and wide films the magnetization and the inner field strength reaches very big values. The applied field needed to reach the critical magnetic field in the film is reduced by $1 - N$.

$$B_{c1, demagnetized} = (1 - N)B_{c1} \Rightarrow B_{c1, film} = B_{c1} \cdot \frac{\pi d}{2 w} \ll B_{c1} \quad (A7)$$

Typical film dimensions for HEB bridges are 35 \AA thick and a few microns wide which leads to three orders of magnitude in reduction of the lower critical field. The upper critical field remains essentially unaffected by demagnetization effects since the susceptibility of the film in normal state is close to zero.

Lower critical transport current for vortex generation in a thin film

Based on the above equation and the relation between the total film current and its magnetic field the lower critical transport current is obtained by setting the current induced magnetic flux density equal to the lower critical flux density in a thin film assuming a square law temperature dependence of the critical fields [5:p.52]

$$I_{c1, film} \approx \pi^2 \cdot B_{c1, 0K} \cdot \left(1 - \left[\frac{T}{T_c} \right]^2 \right) \cdot \frac{d}{\mu_0} \quad (A8)$$

This current is obtained by the current where the unpumped i - v -characteristic departs from the pad resistance line. Sometimes the superconducting part of an unpumped i - v -characteristic looks like a parabola. This is attributed to a transition resistance between the normal conducting cover layer (typical 100 nm Au film) and the superconducting bottom layer. In these cases a the lower critical current must be estimated by the point where the curve begins to deviate from the parabola. Comparison between theory and experiment obtained for 35 \AA NbN films are shown in Figure 8.

Appendix B: A scaling model for the susceptibility

A simple scaling model for the susceptibility of a type II superconductor is obtained as follows:

$$\chi = \begin{cases} -1 & B_{app} \leq B_{c1, film} \\ -1 + \left(\frac{B - B_{c1, film}}{B_{c2} - B_{c1, film}} \right)^{\frac{1}{2}} & B_{c1, film} < B_{app} \leq B_{c2} \\ 0 & B_{app} < B_{c2} \end{cases} \quad (B1)$$

The susceptibility for the mixed state can be simplified by applying Ginzburg-Landau's relation between the critical fields [1:p.270] for a high-kappa approximation:

$$\frac{B - B_{c1, film}}{B_{c2} - B_{c1, film}} = \frac{2\kappa^2 \frac{B}{B_{c2}} - (1 - N) \cdot \ln \kappa}{2\kappa^2 - (1 - N) \cdot \ln \kappa} \approx \frac{B}{B_{c2}} - (1 - N) \frac{\ln \kappa}{2\kappa^2} \quad (B2)$$

In a superconductor in mixed state the magnetic flux is penetrating the superconductor in flux quanta whereas the remaining material excludes the field completely. Assuming that the whole internal magnetic field is carried by flux quanta their number density is given by the difference between the magnetization obtained for the Meissner state ($\chi = -1$) and the actual mixed state ($\chi > -1$) divided by the flux quantum. For fields not exceeding the upper critical field one obtains for the number density of vortices:

$$n = \begin{cases} 0 & B_{app} \leq B_{c1, film} \\ \frac{B_{app}}{\mu_0 \cdot \Phi_0} \cdot \left(\frac{\chi}{1 + \chi \cdot N} + \frac{1}{1 - N} \right) & B_{c1, film} < B_{app} \end{cases} \quad (B3)$$

It is more convenient to express the vortex number in terms of transport current instead of lateral magnetic fields. Vortices will enter the film if there is a point where the lower critical magnetic flux is exceeded. This requires a minimum transport current through the strip which is denoted as lower critical current:

$$I_{cF1} = 2\pi w \frac{B_{c1}}{\mu_0} \approx \frac{B_{c1, bulk}}{\mu_0} \pi^2 \cdot d \cdot \left(1 - \left[\frac{T}{T_c} \right]^2 \right) \quad (B4)$$

After a lengthy but straightforward calculation one is left with the following expression for the vortex number density as a function of the transport current supposed that the current does not drive the complete film into normal state (i.e. the upper critical field is not exceeded):

$$n = \begin{cases} 0 & B_{app} \leq B_{c1, film} \\ \frac{B_{app}}{\mu_0 \cdot \Phi_0} \cdot \left(\frac{\chi(B_{app})}{1 + \chi(B_{app}) \cdot N} + \frac{1}{1 - N} \right) & B_{c1, film} < B_{app} \end{cases} \quad (B5)$$

This relation is used to determine the critical current for phase slip line formation and the resistance due to vortex flow. The vortices travel with a collision-dominated speed and give rise to a voltage drop:

$$V_{vortex flow} = n \cdot v_{saturation} \cdot \frac{\Phi_0}{4\pi\xi^2} \quad (B6)$$

Applying a relation between the transport current and the applied field the resistance due to vortex flow can be calculated.

References

- [1] B.S. Karasik, A.I. Elantev: Analysis of the Noise Performance of a Hot Electron Superconducting Bolometer Mixer 6.th Intl. Symposium on Space Terahertz Technology Proc.: p.229
- [2] H. Ekström, B.S. Karasik: Electron Temperature Fluctuation Noise in Hot Electron Superconducting Mixers Appl. Phys. Lett. 66 (23) June 1995
- [3] B.S. Karasik, A.I. Elantev: Noise Temperature limit of a superconducting hot-electron bolometer mixer, Appl. Phys. Lett. 68 (6) February 1996 p.853
- [4] S. Maas Nonlinear Microwave Circuits IEEE Press 1996

- [5] C.P.Poole, H.C. Farach, R.J. Creswick "Superconductivity" Academic Press 1996
- [6] O.Vendik,I.Vendik,High Temperature Superconductor Devices for Microwave Signal Processing .
Scladen , St. Petersburg 3 volumes 1996
- [7] E. Gerecht, C. F. Musante, K. S. Yngvesson, "Optical Coupling and Conversion Gain for NbN HEB Mixer at THz Frequencies" Proceedings of the 1997 Int. Semiconductor Device Research Symposium, Charlottesville, VA., pp. 47-50, 1997.
- [8] B. S. Karasik, M. C. Gaidis, W. R. McGrath, B. Bumble, H. G. LeDuc. "Low Noise in a Diffusion Cooled Hot-Electron Mixer at 2.5 THz", Appl. Phys- Lett., vol. 71, pp. 1567-1569, 1997
- [9] A. Skalare, W.R. McGrath, B. Bumble, H.G. LeDuc (1997), "Noise and RF bandwidth measurements of a 1.2THz HEB heterodyne receiver" Proc. for the 8th Int. Symp. on Space Terahertz Technology, Cambridge MA, 1998
- [10] A. Skalare, W.R. McGrath, B. Bumble, H.G. LeDuc, P.J. Burke, A.A. Verheijen, and D.E. Prober (1995) A heterodyne receiver at 533 GHz using a diffusion cooled superconducting hot electron mixer, "IEEE Trans. on Applied Superconductivity, vol. 5, March 1995.
- [11] H. Ekström, B. Karasik, E. Kollberg, and K.S. Yngvesson (1995) Conversion Gain and Noise of Niobium Superconducting Hot-Electron-Mixers, IEEE Transactions on Microwave Theory and Techniques, vol. 43, 938-947
- [12] H. Merkel, E. Kollberg, "A power balance model for hot-electron bolometric mixers based on phase slip center and hot-spot formation" to appear in Proc. for the 9th Int. Symp. on Space Terahertz Technology, Pasadena, USA, 1998
- [13] A. V. Gurevich and R. G. Mints (1987) Self-heating in normal metals and superconductors, Reviews of Modern Physics, vol. 59, 841-999,
- [14] R. P. Huebener (1979) Magnetic flux Structures in Superconductors. Berlin: Springer.
- [15]. H. Merkel, P. Yagoubov, E. Kollberg, "A Power Balance Model for Hot-Electron Bolometer Mixers at THz Frequencies, Proceedings of the 1997 Int. Semiconductor Device Research Symposium, Charlottesville, VA., pp. 489-492, 1997.
- [16]. D. Wilms Floet, J. Baselmans, J.R. Gao, and T.M. Klapwijk, Abstract for 9th Int. Symp. on Space Terahertz Technology, Pasadena, USA, 1998
- [17] H. Ekstrom, E. Kollberg, P. Yagoubov, G. Gol'tsman, E. Gershenson and S. Yngvesson, "Gain and noise bandwidth of NbN hot-electron bolometric mixers", Appl. Phys. Lett., 70(24), 1997.
- [18] O. Vendik and E. Kollberg, "Conversion Loss of a Resistive State Superconductor Mixer", Proceedings of the 8th Int. Symp. on Space Terahertz Technology,, Boston, 1997.

CAPACITIVELY COUPLED HOT-ELECTRON MICROBOLOMETER AS A PERSPECTIVE IR AND SUB-MM WAVE SENSOR

Leonid S. Kuzmin

Department of Physics, Chalmers University of Techn., S-41296 Gothenburg, Sweden
kuzmin@fy.chalmers.se

ABSTRACT

A novel concept of the normal-metal hot-electron bolometer using capacitive coupling of the absorber to antenna (NHEB-CC) has been proposed. The concept is based on the normal metal hot-electron microbolometer with Andreev mirrors (NHEB-A) using a SIN junction as a temperature sensor [1-3]. The NHEB-A technology brings a possibility to fabricate the sub-mm wave receiver for space applications with a noise equivalent power NEP about $3 \times 10^{-18} \text{ W/Hz}^{1/2}$ at 100 mK. However, the Andreev mirrors could give certain frequency limitations for using this bolometer for higher frequencies with the energy quantum hf higher than the energy of a superconducting gap Δ . The NHEB-CC technology with capacitive coupling of the absorber to antenna avoids these problems. The effective high frequency coupling of the external signal in NHEB-CC is achieved by a low impedance of the coupling capacitances. At the same time, the capacitance gives reliable protection against escaping the hot electrons from the absorber. Usual tunnel junctions with proper thickness of the barrier can be used as capacitors. In such realization, we keep the main advantage of the NHEB technology - very small thermal conductance between electrons and phonons due to small volume of an absorber (typical value of G is $2 \times 10^{-13} \text{ W/K}$ for $T=100 \text{ mK}$) in combination with frequency independent protection of the absorber against thermal leak to the antenna.

I. INTRODUCTION

Ultra low noise bolometers are required for space - based astronomical observations. The most sensitive and fast bolometer for infrared and millimeter wave region is a normal metal hot-electron microbolometer (NHEB-A) with Andreev mirrors and an SIN junction as a temperature sensor [1,2]. A schematic of the NHEB-A is shown in Fig. 1a.

The NHEB-A technology is based on a weak coupling between electrons and phonons in

normal metal strip at low temperatures (so called "hot electron effect") to produce a large

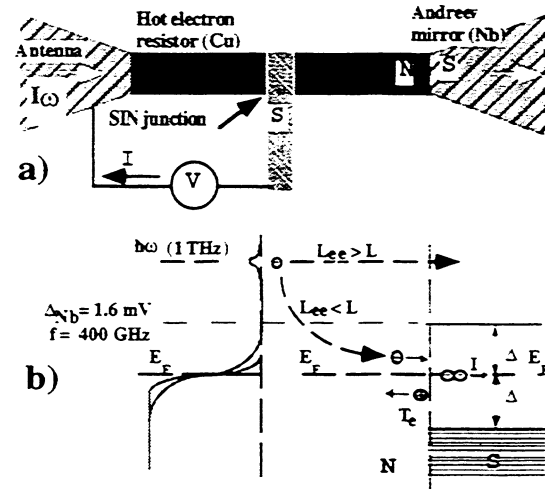


Fig. 1. A schematic of the normal metal hot-electron microbolometer (NHEB-A) with Andreev mirrors (a) and illustration of possible problems with escaping the high-energy electrons through the SN interface for higher frequencies (b).

temperature rise of electrons T_e for small absorbed power P

$$T_e = \left(T_{ph}^5 + \frac{P}{\Sigma V} \right)^{1/5}$$

where V is volume of the strip, Σ is material constant and T_{ph} is the phonon temperature. A very elegant approach is using the Andreev reflection for *thermal insulation* at SN interface between a metal absorber and a superconducting antenna. Simultaneously, the SN interface provides a perfect *electrical contact* to the superconducting antenna (Fig. 1b).

The NHEB-A technology brings possibility to fabricate the sub-mm wave receiver for space applications with a noise equivalent power NEP about $3 \times 10^{-18} \text{ W/Hz}^{1/2}$ at 100 mK and $3 \times 10^{-17} \text{ W/Hz}^{1/2}$ at 300 mK with a time constant better than $20 \mu\text{s}$ [2]. However, the Andreev mirrors could give certain frequency limitation for using this

bolometer. The problem can arise for higher frequencies when the photon energy hf becomes higher than the energy of a superconducting gap Δ [5] as it is demonstrated in Fig. 1b. For example, the Nb gap $\Delta=1.6$ meV corresponds to the frequency 400 GHz. Really, the probability of photon absorption can be considerable only at an energy level corresponding to interband transitions [6]. For copper, for example, this level of energy corresponds to 2 eV. Thus the photon absorption process should be really important only at frequencies considerably higher than 1 THz. Thermalization of the excited electrons depends on relation between an electron-electron inelastic scattering length L_{ee} and length of the absorber L . In the case of $L_{ee} > L$, there is no effective thermalization at the length of absorber and electrons can come to SN interface roughly with the same energy as after excitation. In this case, the Andreev SN interface would not be an effective mirror for these hot electrons and thermal conductance can be increased.

Another problem at higher frequencies can arise due to increasing resistance of the superconducting antenna for frequencies higher than 2Δ . Resistance increase can lead to heating the antenna and decreasing the effective superconducting gap at SN interface. For example, the Nb double gap corresponds to the frequency 800GHz. To avoid this problem, the main part of antenna can be covered by normal metal with good conductivity except a part near the SN interface to keep Andreev reflection for hot electrons of an absorber. Thus, discussed problems are complicated and can lead to suppression of the device parameters at higher frequencies. This situation has stimulated search for new configurations of the microbolometer where these problems will not limit the operation of the device.

A novel concept of the normal-metal hot-electron bolometer using capacitive coupling of the absorber to the antenna (NHEB-CC) has been proposed to avoid the frequency limitation of the NHEB-A and for technological improvements.

II. HOT ELECTRON BOLOMETER WITH CAPACITIVE COUPLING

The idea of this device is to use the capacitance for thermal isolation of the normal-metal absorber instead of the Andreev SN mirrors (Fig. 2a).

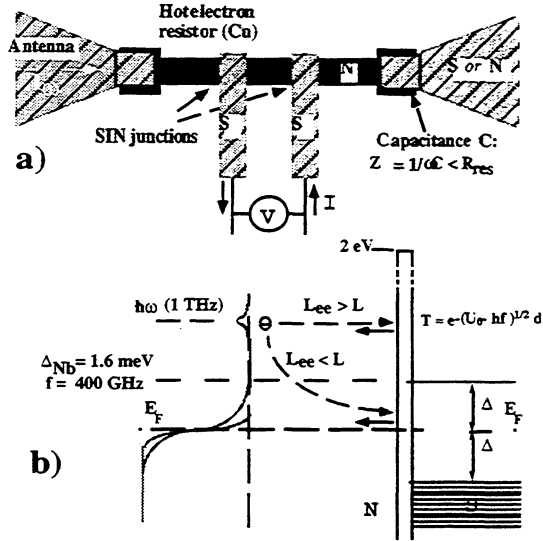


Fig. 2. (a) A schematic of the normal metal hot-electron microbolometer with capacitive coupling to the antenna (NHEB-CC) and (b) energy diagram for illustration of protection of an absorber against escaping the high-energy electrons for higher frequencies by high potential barrier.

In this case, the effective high frequency coupling of the external signal in the NHEB-CC can be achieved by the low impedance of coupling capacitances between the absorber and the antenna. For an absorber resistance $R_{abs} = 100$ Ohm and a frequency 1 THz it is enough to have $C = 15$ fF to get the impedance of the capacitance equal to 10 Ohm that would provide good coupling. Such capacitance can be easily realized by overlap $0.5 \times 0.5 \mu\text{m}^2$. The antenna can be made of both superconducting or normal metal.

The insulation barrier of the capacitors gives perfect thermal protection of absorber in the NHEB-CC configuration. A more universal and effective approach for this device is to use the tunnel junctions as capacitors. More than that, it is possible to use tunnel junctions made in the same vacuum circle as tunnel junctions for temperature measurements but of different area. The transparency of a

barrier is exponentially dependent on the thickness of the barrier d

$$T \approx e^{-(U_0 - hf)^{1/2} d}$$

and for typical $d=12 \text{ \AA}$ and $U_0 = 2 \text{ eV}$, $T \approx 4 \times 10^{-8}$. For all frequencies with energy hf well below the height of the potential barrier U_0 (corresponding to $5 \times 10^{14} \text{ Hz}$) the transparency will be negligibly small.

In such realization, we keep the main advantage of the NHEB technology - very small thermal conductance between electrons and phonons due to the small volume of the absorber (typical value of G is $2 \times 10^{-13} \text{ W/K}$ for $T=100 \text{ mK}$) in combination with reliable protection of the absorber against thermal leak to the antenna.

Impedance matching. The NHEB-CC configuration uses the dimensions of the absorber much smaller than the wavelength of a signal and a planar antenna structure can be used to provide efficient coupling in this case [1]. To our experience the optimal choice is a very broad-band (over a decade) log-periodic complementary antenna having a frequency independent real impedance

$$Z_{\text{ant}} = 377[2(1+\epsilon)]^{1/2}$$

where ϵ is dielectric constant of the substrate [7]. For Si substrate $Z_{\text{ant}} \approx 80 \Omega$.

For high frequency coupling of the bolometer to the antenna, we have to match the impedances of these parts. The impedance of the bolometer has three components

$$Z_{\text{bol}} = Z_C + Z_L + Z_{\text{abs}},$$

where Z_C is the impedance of two coupling capacitances

$$Z_C = (2/j\omega C),$$

Z_L is the impedance due to geometrical inductance of the absorber [6]

$$Z_L = 2 \times 10^{-7} j \omega l \left[\ln \frac{l}{(w+t)} + 1.19 + 0.22 \frac{(w+t)}{l} \right]$$

where l - length, w - width, and t - thickness of the absorber. For typical parameters of the absorber [2,3]: $l = 6 \mu\text{m}$, $w = 3 \mu\text{m}$, and $t =$

$0.05 \mu\text{m}$, - one can get for inductance component:

$$Z_L = 8 \times 10^{-13} j \omega l,$$

with a length of the absorber l in μm .

Taking into account that the log-periodic antenna has a real impedance Z_{ant} , there is an optimal way to compensate the inductive component Z_L by the capacitive component Z_C . For typical length of absorber $l = 6 \mu\text{m}$ [2,3], the estimated Z_L is 30Ω . For compensation Z_L , the capacitive component $Z_C = Z_L$ gives at $f = 0.8 \text{ THz}$ the value of the capacitance $C = 13 \text{ fF}$ that can be easily realized by tunnel junctions with an area of $0.5 \times 0.5 \mu\text{m}^2$.

As a result, using the NHEB-CC configuration we have even improvement of coupling to the antenna due to compensation of the inductive impedance of an absorber by the capacitive impedance of coupling junctions.

Double-layer technology. One more advantage of the NHEB-CC is that the same type of SIN tunnel junctions as for a temperature sensor but of larger area can be used for capacitive coupling. In this case we can use double-layer technology with one vacuum circle that would considerably simplify fabrication of the bolometer in comparison with triple-layer technology [2,3].

The inconvenience of the NHEB-CC is absence of possibility to calibrate the bolometer using dc current measurements: such calibration can be made only using a high frequency signal.

Two SIN junctions for measurements. The NHEB-CC technology suggests using two SIN junctions for temperature measurement in comparison with one junction used in Refs. [1,2]. This necessary step should only improve the performance of the device due to increase of output signal by a factor of 2 (and noise of the junctions only by a factor of $2^{1/2}$) that is important for the amplifier-noise limited bolometer.

The optimal configuration. Taking into account that the same tunnel junctions are used for capacitive coupling to antenna as for temperature measurement, we can combine these two functions in one pair of junctions. The simplest configuration is shown in Fig. 3.

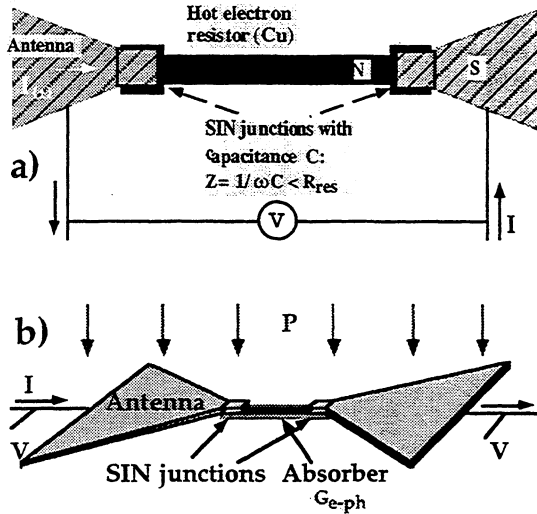


Fig. 3. a) The optimal simplest configuration of the NHEB-CC comprising an absorber and two tunnel junctions. The tunnel junctions carry out three functions: temperature measurements, capacitive coupling to antenna, and thermal isolation of the absorber. b) The high frequency coupling of the NHEB-CC.

The measuring junctions are placed in series with the absorber and bias electrical contacts are made to the antenna. Taking into account that typical resistance of the junctions ($\approx 20 \text{ k}\Omega$) is considerably higher than the resistance of the absorber ($\approx 80 \text{ }\Omega$) we would have still correct measurements of the junction voltage in this configuration.

Electronic microrefrigeration. The additional advantage of using tunnel junctions for capacitive coupling is a possibility to use these junctions for electronic microrefrigeration [9-11]. For electronic cooling, the tunnel junctions should be made of larger area that coincides with a purpose of capacitive coupling. The SIN junctions for temperature measurements are located in the center of the strip as in usual configuration (Fig. 2a). The whole

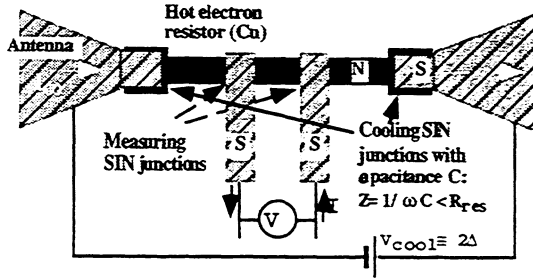


Fig. 4. A schematic of the NHEB-CC with possible electronic cooling through coupling SIN junctions.

configuration becomes to be simpler than the NHEB-A configuration with possible cooling discussed in Ref. 9.

III. CONCLUSIONS

Finally, the NHEB-CC technology seems very worthwhile and can help to overcome the possible frequency limitation of the NHEB technology with Andreev mirrors.

Simplification of the fabrication technology using two layers (instead of three layers in NHEB-A configuration) is especially attractive. Due to compensation of the inductive impedance of an absorber by the capacitive impedance of coupling junctions, the NHEB-CC configuration gives improvement of coupling to the antenna.

The obligatory two SIN junctions for measurements (instead of one in the NHEB-A) can improve a noise figure by a factor of two for the case of the amplifier-noise-limited microbolometer. The simplest configuration consisting of an absorber and two junctions for coupling with antenna and temperature measurements looks optimal for applications requiring arrays of microbolometers.

The fruitful discussions with D. Golubev, I. Devyatov, M. Tarasov, D. Chouvaev, and T. Claeson are gratefully acknowledged.

REFERENCES

- [1] M.Nahum, P.Richards, C.Mears. IEEE Trans.on Appl. Superc., 3, 2124 (1993)
- [2] M.Nahum, J.M.Martinis, Appl. Phys. Lett., v. 63, N 22, pp. 3075-3077 (1993).
- [3] D.Chouvaev, L.Kuzmin, M.Tarasov, P. Sundquist, M. Willander, T.Claeson, this conference.

- [4] A. F. Andreev, Sov. Phys. JETP, **46**, N5, 1823 (1964).
- [5] A. Zaitsev, private communication.
- [6] N.W. Ashcroft and N.D. Mermin, Solid State Physics (Saunders College Publishing, 1976).
- [7] D. B. Rutledge, D.P. Neirkirk, and D.P. Kasilingam, "Integrated circuit antennas," *Infrared and Millimeter Waves, New York: Academic, 1983, vol. 10.*
- [8] F. E. Ternman, Radio Engineers Handbook (McGrow-Hill, New York, 1943).
- [9] M.Nahum, J.M.Martinis, Appl. Phys. Lett., v. 65, N 23, 3123 (1994).
- [10] M.Leivo, J.Pecola and D.Averin. Appl. Phys. Lett., v. 68, 1996 (1996).
- [11] L.Kuzmin, I.Devyatov, subm. to the 4th Int. conf. on submm waves, San-Diego, July 1998

MEASURED RESULTS FOR NbN PHONON-COOLED HOT ELECTRON BOLOMETRIC MIXERS AT 0.6-0.75 THz, 1.56 THz, AND 2.5 THz

E. Gerecht, C. F. Musante, H. Jian, and K. S. Yngvesson

Department of Electrical and Computer Engineering, University of Massachusetts,
Amherst, MA 01003

J. Dickinson and J. Waldman

Submillimeter Technology Laboratory, University of Massachusetts at Lowell Research Foundation,
Lowell, MA 01854

G.N. Gol'tsman, P.A. Yagoubov, B.M. Voronov, and E.M. Gershenzon

Department of Physics, Moscow State Pedagogical University,
Moscow, Russia

I. INTRODUCTION

NbN Hot Electron Bolometric (HEB) mixers represent a promising approach for achieving receiver noise temperatures of a few times the quantum noise limit at frequencies above 1 THz. These HEB mixers have so far demonstrated a DSB noise temperature as low as 500 K at 630 GHz [Kroug et al., 1997; Kawamura et al., 1997], and 980 K at 900 GHz [Kroug et al., 1997]. Noise temperatures of about 1000 K or less can be expected for frequencies above 1 THz in the future. NbN HEB mixers have been shown to have sufficient bandwidths for the anticipated applications such as future receiver frontends for THz astronomical observation from space. A receiver noise bandwidth of 5 GHz and conversion gain bandwidth of 3 GHz were measured by [Ekström et al., 1997]. The LO power required is typically 100 nW, which makes the NbN HEB mixers suitable for use with future solid state tunable THz sources. However, the LO power is not at such a low level that its operating point is affected by input thermal noise power. This paper describes the development of THz HEB mixers for the 1 THz to 2.5 THz frequency range. The HEBs employ NbN as the bolometric material. We present our first results from measurements with these mixers at frequencies of 0.6 THz to 0.75 THz, 1.56 THz, and 2.52 THz. We have measured a DSB receiver noise temperature of $5,800^{+1400}_{-1000}$ K at 1.56 THz. In a separate experiment, we measured a conversion gain of 3 dB ± 2 dB at the same frequency.

II. DEVICE DESIGN AND FABRICATION

NbN Films

The NbN films were fabricated on silicon substrates at Moscow State Pedagogical University (MSPU) by magnetron reactive sputtering in an argon/nitrogen gas mixture. For this work we have primarily used films of thickness 3.5-4 nm in order to maximize the conversion gain bandwidth. The production of such thin films is still an evolving technology, but recent films on both sapphire and silicon substrates have shown much improved properties [Cherednichenko et al., 1997]. The optimum thickness, based on the sap-

phire work, appears to be close to 3.5-4 nm. The films used in these measurements have $T_c = 7.5 - 9$ K, the transition width is about 1 K, and the critical current density is 2×10^6 A/cm².

Optical Design

Optical design considerations are crucial for efficiently coupling LO and signal power into the device. Quasi-optical coupling to the device is most common for frequencies above 1 THz. We chose to use an extended hemispherical silicon lens coupled to a self-complementary log-periodic antenna (see Figure 1), as successfully demonstrated and analyzed at 250 GHz and 500 GHz by [Filipovic et al, 1993]. The log-periodic antenna is convenient since it can be used over a very wide frequency range; later versions will employ twin-slot or twin-dipole antennas tuned to smaller frequency bands. We scaled the dimensions of the lens and the antenna used in the 250 GHz setup by a factor of ten, resulting in a lens diameter of 1.3 mm. We chose an extension length, beyond the hemispherical lens, of 0.33 times the lens radius. We can predict the amount of beam-scan which would be caused by misalignment of the center of the antenna with respect to the center of the lens: a 20 micrometer misalignment results in a 5 degree beam scan. This makes it imperative to use an accurate alignment procedure, which will be described below. We are not employing a matching layer for the lens at this stage.

Device Fabrication

Devices have been fabricated at MSPU as well as at UMASS/Amherst. The processes are somewhat different at the two locations, but in what follows we will emphasize the UMASS process. The gold log-periodic antenna is fabricated using liftoff. After the pattern has been defined in the photoresist, a 40 nm thick layer of Nb is applied by sputtering. Next, 20 nm of Ti and 100 nm of Au are deposited by E-beam evaporation, and the lift-off is performed. The NbN strips are then defined and etched using Reactive Ion

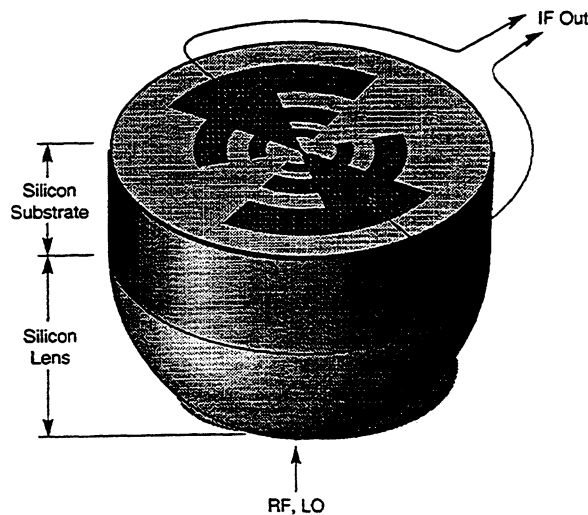


Figure 1: Log-periodic antenna fabricated on an extended hemispherical lens.

Etching (RIE). The substrate is thinned by lapping to a thickness equal to the lens extension length. The position of a square alignment window for the lens is defined in a photoresist layer on the opposite side of the substrate from the antenna and device, using an infrared mask aligner, whereupon the alignment window is etched by RIE to a depth of 100 nm. The lens is attached to the silicon substrate using purified bees wax. The final dimensions of the device strips are about 0.6μ long by 1.0μ wide. The number of strips is from one to three. The mask also has a different pattern for which all teeth are larger by a factor of two, i.e. the smallest teeth determine a highest frequency of the antenna of about 1.25 THz. This antenna can have up to five strips.

III. EXPERIMENTAL SETUP

Receiver Configuration

The integrated antenna/HEB device and lens are attached to a copper post, which is thermally anchored at the other end to the liquid helium reservoir of an IRLAB dewar (see Figure 2 and Figure 3). The antenna is connected to the IF and bias system via a microstrip/semirigid coax line and bias tee. A cooled HEMT amplifier with isolator input is also used inside the dewar (Figure 3). This IF amplifier has a bandwidth from 1250 to 1750 GHz, with noise temperature of about 10K.

Optical Setup

The optical coupling loss as well as the receiver noise temperature are measured with a CO_2 laser pumped FIR methanol laser as the LO source. The laser setup is illustrated in Figure 4. Mylar beam split-

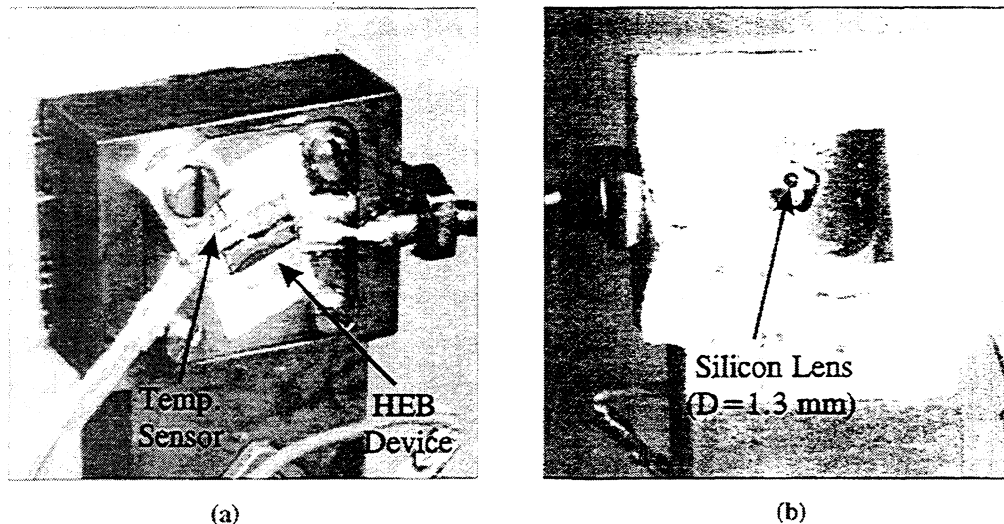


Figure 2: Photographs of the OFHC copper pedestal: (a) close-up of the device mount and contacts, (b) close-up of the opposite side of the pedestal showing the silicon lens.

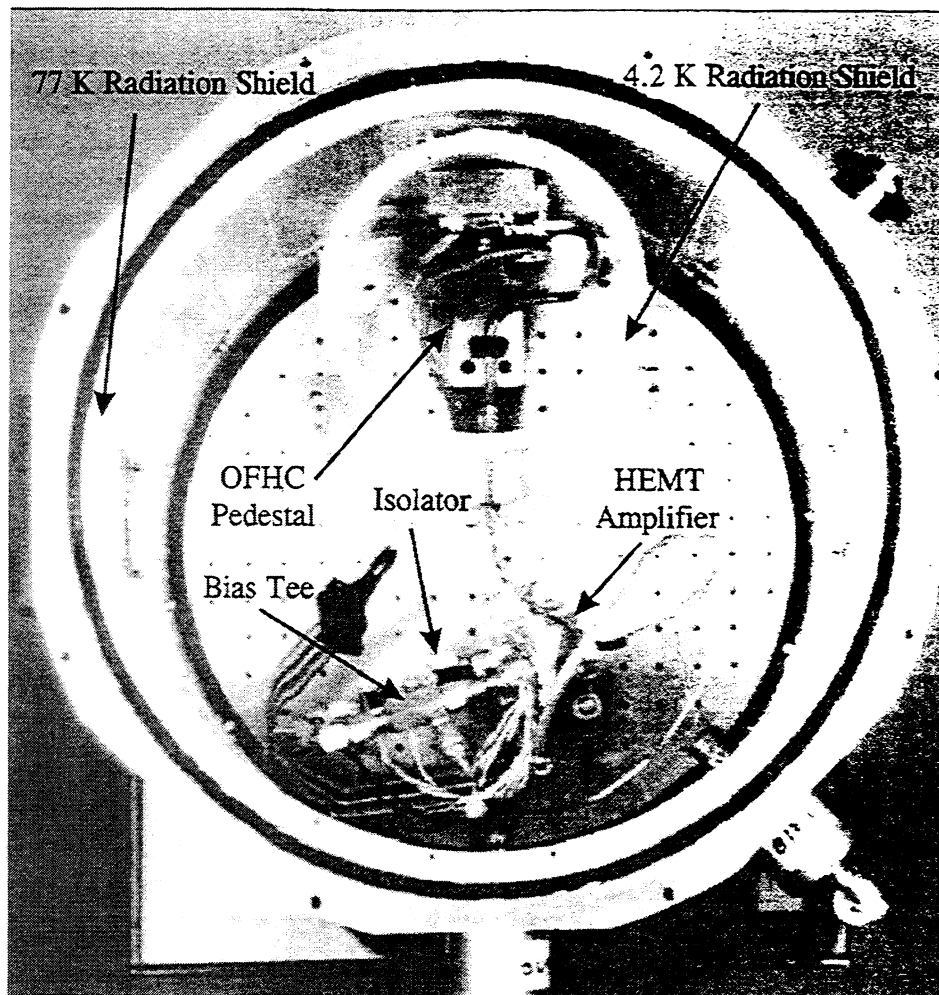


Figure 3: Top view of the IRLAB dewar showing the *dc* and *IF* connections.

ters with a thickness of 6, 12.5, and 25 micrometers, respectively, act as diplexers between the LO and a chopped hot/cold noise source. The radiation is focussed by an offset paraboloidal reflector or a TPX lens. In order to measure the conversion gain directly, we employ two lasers at UMASS/Lowell as shown in Figure 5. The active medium of these lasers is difluoromethane, and the frequency 1.56 THz. The lasers were slightly detuned and produced an IF of 600 kHz. The gain bandwidth of NbN HEB devices at the IF cannot be easily measured at THz frequencies. At present, we measure the mixer gain bandwidth at 94 GHz instead. Since the LO power required is so low, the same optical configuration (including the lens), can be used at 94 GHz also, although the antenna response does not extend this low in frequency.

Noise temperature measurements at 0.6 THz to 0.75 THz were also performed at Chalmers University in a setup which used a BWO as LO source and a 12.5 μm beam splitter. The experimental arrangement was as described in [Ekström et al., 1997].

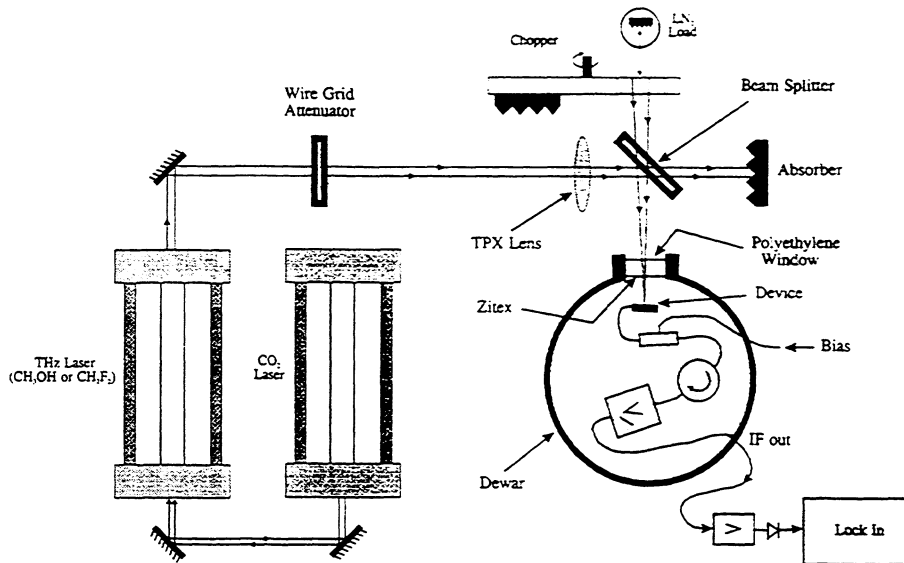


Figure 4: Optical setup for measurement of optical coupling loss and receiver noise temperature.

FTS Spectra of the Device Response

Fourier Transform Spectra were obtained at Chalmers University by employing the device as a detector, at a temperature close to T_c .

IV. RESULTS AND DISCUSSION

FTS Spectra of the Device Response

Figure 6 shows the spectra obtained for a NbN device integrated with the larger version of the log-periodic antenna described above. The device was mounted in two perpendicular orientations in order to elucidate the frequency-dependence of its optimum polarization. [Kormanyos et al., 1993] showed that the polarization for optimum response varies periodically with frequency at an amplitude of $\pm 22.5^\circ$. This is consistent with the spectra we observed, in which dips in the response occur at frequencies which are one octave apart. As the orientation of the device was changed by 90 degrees, peaks appear where dips occur for the perpendicular orientation. The highest frequency peak corresponds to when the second smallest tooth is one quarter wavelength long when considering the effective dielectric permittivity of the silicon medium. In order to utilize self-complementary log-periodic antennas, one has to be aware of their sensitivity to the incident polarization. The power available, when lasers are used as the LO sources, is in general sufficiently large such that a polarization rotator can be used to produce the optimum polarization. This was confirmed in our experiments at both 1.56 THz and at 2.52 THz.

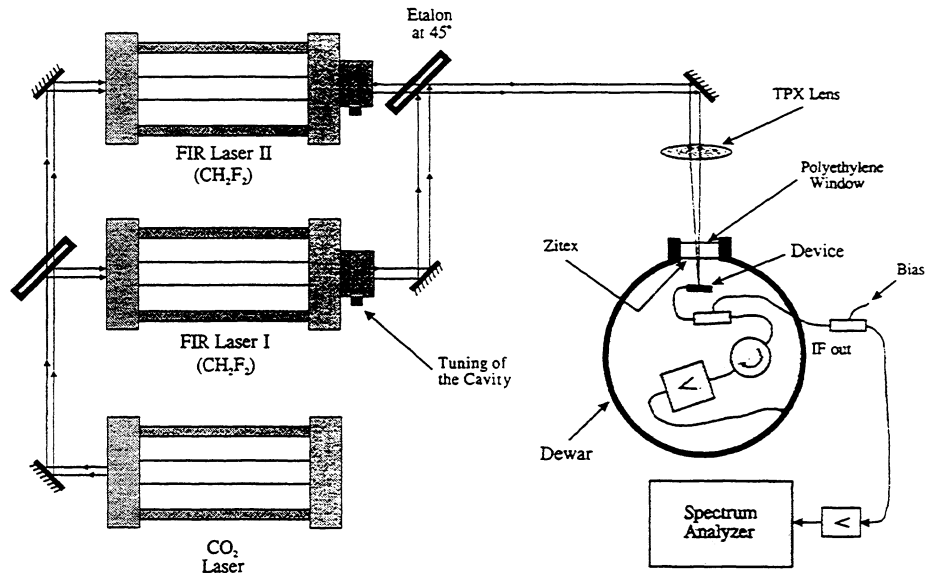


Figure 5: Optical setup for measurement of conversion gain.

Noise Temperature Measurements

Our results from the noise temperature and conversion loss measurements at different frequencies are summarized in Table I below.

Table I: Noise Temperature and Conversion Loss Summary

f (GHz)	T_{DSB} (K)	T_{out} (K)	T_{IF} (K)	T_{mix} (K)	$L_{c,tot}$ (dB)	$L_{c,i}$ (dB)	$L_{c,opt}$ (dB)
94	NA	NA	NA	NA	NA	9	NA
600-750	900	105	24	730	12.7	7.7	5
1,560	5,800	10	13	2,500	27	18-20	7-9

The Y-factor was measured by inserting a liquid nitrogen cooled absorber by hand into the path of the beam several times. In the 1.56 THz experiment, the IF output power was recorded on a chart recorder, and the results of many individual Y-factor measurements were averaged. The Y-factor was determined to be 0.155 dB \pm 0.03 dB, which yields a DSB receiver noise temperature of 5,800⁺¹⁴⁰⁰₋₁₀₀₀ K. The fact that it was possible to perform the Y-factor measurement at this noise temperature level without the use of a rotating chopper is a tribute to the excellent amplitude stability of the UMass/Lowell laser used for this experiment. The stability is also evident in the I-V curves recorded by our fast (about 1 ms) computerized recording system. Figure 7 shows the optimum operating point of the device in the noise temperature measurement. Near

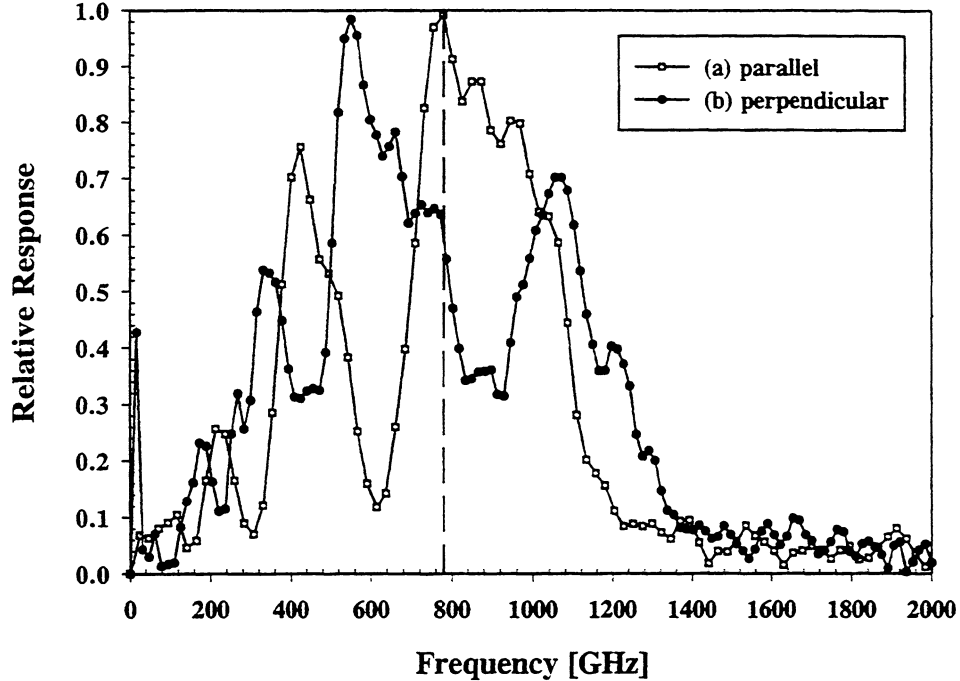


Figure 6: FTS spectra of the device for (a) device orientation parallel to the FTS polarization, and (b) perpendicular to the FTS polarization.

the optimum operating point (0.97 mV, 38 μ A), the device is very sensitive to variations in LO power. Nevertheless, only very small variations are evident in this recording. In contrast, the I-V curve obtained with the free-running 2.52 THz laser shows large fluctuations in the sensitive region of the I-V curve (see Figure 8). The antenna/lens combination clearly performed well at 1.56 THz, as evidenced by the fact that during a chopped noise measurement on the system, it was possible to blank out essentially the entire signal by blocking the cold source with a piece of absorber of a size equal to the predicted beamwidth, about 8 degrees at this frequency. The LO power absorbed by the device was 240 nW (for the 600-750 GHz device it was about 100 nW). There was no measurable change in the DC operating point when the input load of the mixer was changed from room temperature to liquid nitrogen temperature.

Table I shows the estimated break-down of the total conversion loss into components. We assume that the optical coupling loss is essentially given by the known losses of different components, such as the polyethylene window, the Zitex thermal radiation filter, the reflection loss of the lens, etc.. The remaining loss to be accounted for by the mixer itself, the intrinsic conversion loss, including IF output mismatch, is about 18-20 dB for the 1.56 THz mixer. This somewhat high intrinsic loss can be explained by the HEB theory [Ekström et al., 1995] and the specific I-V curve for this device when irradiated by the 1.56 THz LO, taking into account the IF output mismatch. Nevertheless, a detailed explanation will have to await the completion of a new, more complete, theoretical model for the HEB device [Merkel et al., 1998]. It is interesting to compare the I-V curves recorded with LO power at different frequencies in Figure 8, however. Radiation at both 1.56 THz and 2.52 THz should be above the bandgap frequency of the NbN film, and thus it

would be expected that both frequencies should be uniformly absorbed by the device. Yet, the I-V curves differ noticeably when the device is irradiated by 1.56 THz and 2.52 THz. The curves with 356 GHz and 94 GHz radiation are quite different from the higher frequency curves and also differ among themselves. Note that all I-V curves were recorded for the same device without changing the device configuration. Neither of the I-V curves in Figure 8 agrees with curves recorded without LO power at higher device temperatures, which gives another indication that the HEB model needs to be refined. HEB mixer theory predicts a 10 dB intrinsic conversion loss with an LO at 94 GHz which is in good agreement with the measured value of 9 dB (Table I). The exact shape of the I-V curve thus is very important for the actual performance of the device in terms of conversion loss. Note that different devices (phonon-cooled or diffusion-cooled, operated at different frequencies) often differ drastically in terms of the intrinsic conversion loss as well as the output noise level from the devices. Both conversion loss and output noise are relevant in establishing the receiver noise temperature and a comparison of the ultimate potential receiver noise performance of different types of devices will require the more detailed understanding of the device models we refer to above. It should be clear, however, that receiver noise temperatures of HEB mixers at THz frequencies are likely to progressively get lower. Our own measurement of 5,800 K at 1.56 THz was for a single device, the only one tested so far. Experience at the lower frequencies has already shown that refinement in the receiver configuration, as well as in device fabrication, will gradually lead to lower noise temperatures.

Measurement of Conversion Gain

The intrinsic (device only) *conversion gain* at 1.56 THz was measured in the two-laser setup to be +3 dB, with a probable error of ± 2 dB. The device used for this measurement was fabricated in Moscow

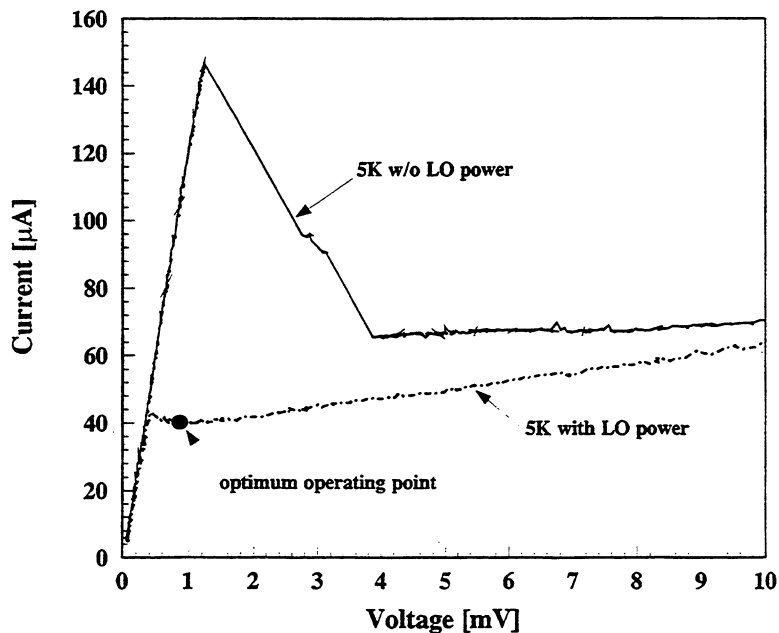


Figure 7: I-V curve for the device used in the 1.56 THz noise temperature measurement.

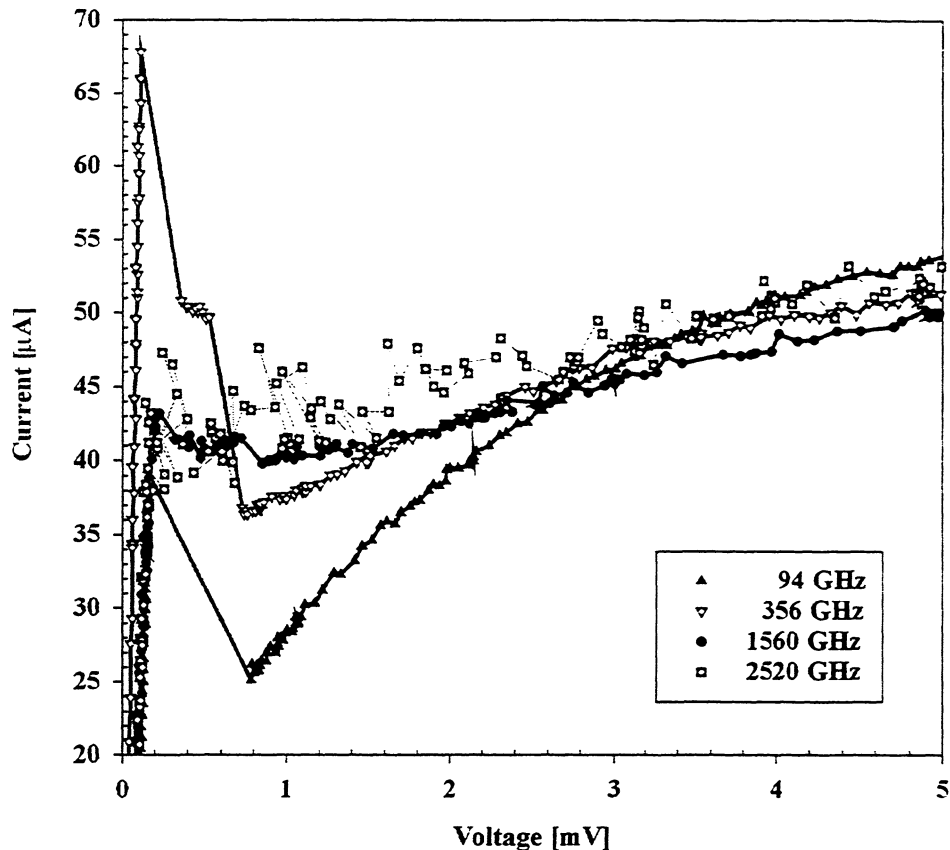


Figure 8: I-V curves of the device irradiated by four different frequencies.

and utilized an equiangular spiral antenna. The absorbed power from the RF laser was obtained by the technique we employed for the absorbed LO power at a high enough RF power level to make this possible. Calibrated attenuators were then used to lower the RF power until the mixer was shown to be operating in its linear region. The IF power was observed on a spectrum analyzer and the IF voltage was measured directly on an oscilloscope. The optical coupling loss was estimated to be about 33 dB in this case. Note that HEB mixer theory allows actual conversion gain to be realized. The conversion gain at higher IF frequencies may be somewhat lower; so far, the best intrinsic conversion gain of any HEB THz mixer at about 1 GHz IF, inferred from noise measurements, is about -6 dB (Kroug et al., 1997). The apparent difference in conversion loss at different IF frequencies indicates another area in which our present device models are inadequate.

V. CONCLUSION

We have demonstrated receiver noise temperatures of 900 K at 600-750 GHz, and 5,800 K at 1.56 THz for a NbN HEB device, coupled through a silicon lens and a log-periodic antenna. The very small LO power required by such devices when optimally matched (as low as 100 nW) has been verified. We have also demonstrated 3 dB conversion gain of an HEB mixer device at 1.56 THz, for a 600 kHz IF frequency.

We expect that measured receiver noise temperatures of NbN HEB mixers will continue their downward trend at frequencies above 1 THz in the future. NbN HEB THz mixers are especially advantageous in the following respects:

- Submicron size is not required
- Can be operated at 4.2 K; Al devices require He3 cooling
- LO power 100 nW, smaller for submicron devices
- Present receiver noise temperatures are as low as for diffusion-cooled mixers up to 1 THz
- Operating point not sensitive to 300 K radiation

ACKNOWLEDGEMENTS

This work was supported by the Russian Program on Condensed Matter (Superconductivity Division) under Grant No.93169, as well as grants from the National Science Foundation (ECS-96128), The National Research Council, and NASA (NRA 93-OSSA-06). Lasertron, Inc. provided access to their IR mask-aligner. We gratefully acknowledge their assistance with this crucial step in our fabrication process. We would also like to thank Dr. Neil Erickson for lending us the multiplier source used for the 356 GHz measurements, and Dr. A. Verevkin for help with experiments at UMASS/Amherst.

VII. REFERENCES

- S. Cherednichenko et al., "Large Bandwidth of NbN Phonon Cooled Hot Electron Bolometer Mixers on Sapphire Substrates," *8th Intern.Symp.Space THz Technol.*, Cambridge, MA, March 1997.
- H. Ekstrom, E. Kollberg, P. Yagoubov, G. Gol'tsman, E. Gershenson, and K.S. Yngvesson, "Gain and Noise Bandwidth of NbN Hot Electron Bolometric Mixers," *Appl. Phys. Lett.*, **70**, 3296, 1997.
- H. Ekstrom, B. Karasik, E. Kollberg and S. Yngvesson, "Conversion Gain and Noise of Niobium Hot-Electron Mixers," *IEEE Trans.Microw.Theory Techniques*, MTT-43, 938 (1995)
- D.F. Filipovic et al., "Double-Slot Antennas on Extended Hemispherical and Elliptical Dielectric Lenses," *IEEE Trans.Microwave Theory Techniques*, MTT-41, 1738, 1993.
- J. Kawamura, R. Blundell, C.-Y.E. Tong, G. Gol'tsman, E. Gershenson, B. Voronov, and S. Cherednichenko, "Phonon-Cooled NbN HEB Mixers for Submillimeter Wavelengths," *8th Intern.Symp.Space THz Technol.*, Cambridge, MA, March 1997.
- B.K. Kormanyos et al., "A Planar Wideband 80-200 GHz Subharmonic Receiver," *IEEE Trans. Microw.Theory Techniques*, MTT-41, 1730 (1993).
- M. Kroug, P. Yagoubov, G. Gol'tsman and E. Kollberg, "NbN Quasioptical Phonon Cooled Hot Electron Bolometric Mixer at THz Frequencies," *EUCAS'97*, Eindhoven, The Netherlands, June 29-July 3, 1997.
- H. Merkel and E. Kollberg, "A Large Signal Model for Phonon-Cooled Hot-Electron Bolometric Mixers for THz Applications", this symposium.

Measurements with a Diffusion-Cooled Nb Hot-Electron Bolometer Mixer at 1100 GHz

A. Skalare, W.R. McGrath, B. Bumble, H. LeDuc

Center for Space Microelectronics Technology,
Jet Propulsion Laboratory, California Institute of Technology,
Pasadena, CA 91109

Abstract

In this paper we report receiver sensitivity measurements with a diffusion-cooled niobium hot-electron bolometer around 1100 GHz. The lowest receiver noise temperature was 1670 K DSB, with approximately 40 nW of local oscillator power being dissipated in the device. The intermediate frequency bandwidth of this device, due to its short length (0.15 μm) and low normal resistance (43 Ω), exceeded the 1.8 GHz bandwidth of the measurement setup. The receiver was used to detect the sulfur dioxide gas absorption line at 1102 GHz in a heterodyne mode.

Introduction

In the last few years, superconducting Hot-Electron Bolometers (HEB's) [1-3] have emerged as the detectors of choice for low-noise heterodyne receivers at frequencies exceeding 1 THz. Funding has already been allocated, and receiver development has begun within both airborne (National Aeronautics and Space Administration's SOFIA) and spaceborne (European Space Agency's FIRST) projects. Critical issues to this technology, in addition to achieving low receiver noise temperatures, are the RF and IF bandwidths and the very limited amount of local oscillator (LO) power that would likely be available in a spaceborne mission.

Our earlier measurements [4] have shown that a relatively low receiver noise temperature, 1880 K DSB at 1267 GHz, can be achieved with an HEB using as little as 6 nW of dissipated LO power. For the same reason that this device required such low LO power,

namely its high resistance (140 Ω), it also showed some effects of direct detection in the receiver Y-factor measurements. The purpose of the experiments reported here is to confirm the older measurements with a lower resistance device that does not exhibit these direct detection effects.

The Device

The bolometer was a 0.15 μm long and 0.15 μm wide strip of niobium of with an approximate thickness of 10 nm on a Z-cut crystal quartz substrate. The device was fabricated with normal metal (gold) contacts in a self-aligned process [5]. A similar device is shown in Fig.1. Fig.2 shows the resistance versus temperature curve for the device used in the measurements. As can be seen, the normal state resistance was approximately 43 Ω . The critical current of the device was 200 μA at 4.2 K ambient

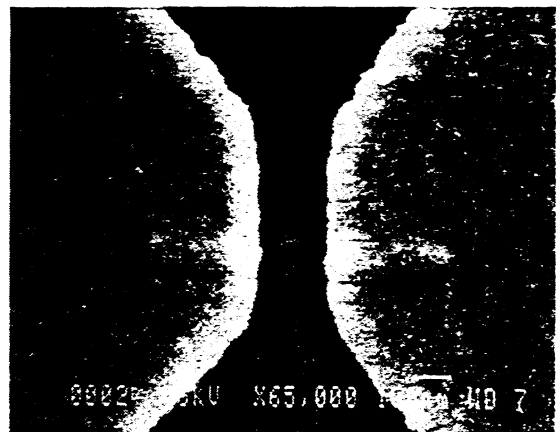


Fig. 1; SEM of an HEB device similar to the one used in the reported measurements.

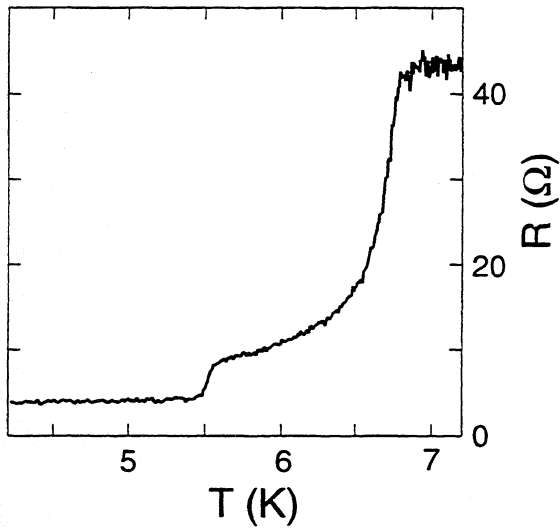


Fig. 2; Resistance versus temperature curve for the HEB mixer.

temperature. A gold planar double-dipole antenna with a center frequency of 1 THz was integrated on-chip with the HEB device [6-7].

Measurement of Receiver Noise

The HEB chip was glued to the back of a hyperhemispheric crystal quartz lens with a diameter of 13 mm. A hyperbolic polyethylene lens in front of this quartz lens was used to increase the f-number of the antenna beam. To eliminate the back lobe of the dipole antenna, a quarter-wavelength thick crystal quartz chip with a gold mirror was glued on top of the HEB chip. The device was shunted in the DC bias circuit by a 17 Ω resistor. The DC shunt current through this resistor has been subtracted in the diagrams in this paper.

The fixture holding the device/lens assembly was placed in a liquid-helium cooled vacuum cryostat, that was connected to an evacuated box containing a 0.5 mil Mylar™ beamsplitter, a 295 K “hot” calibration load, an 82 K “cold” load that was cooled by liquid nitrogen, and a switch/chopper that allowed one or the other of the loads to be seen by the mixer, as shown in Fig.3. The calibration loads were made of Eccostock MF 116

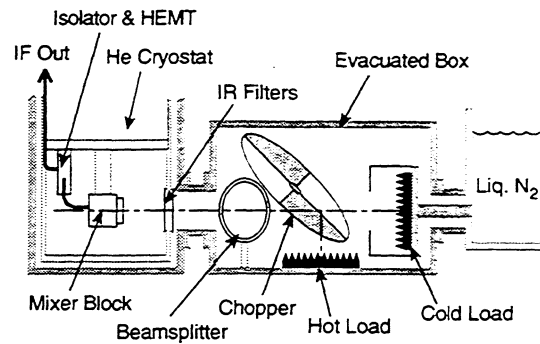


Fig. 3; Schematic of the cryostat containing the mixer and of the measurement box with the hot and cold calibration loads. There are no windows between the cryostat and box, but there are two Zitex™ infrared filters in the optical path.

microwave absorber with the surface machined into pyramids. The cold load also had several baffles coated with an absorbing paint to reduce room-temperature thermal radiation influx to the load, and to eliminate any scattering off the microwave absorber. A backward-wave oscillator (BWO) was used as the local oscillator. An isolator and an L-band cooled HEMT amplifier with a combined input noise temperature of 6.3 K were used as the first stage in the intermediate frequency (IF) system. A bandpass filter in the room temperature part of the amplifier-chain defined the IF bandwidth in the Y-factor measurements to about 300 MHz, centered around 1.4 GHz.

The receiver equivalent noise temperature was determined through a Y-factor measurement by switching between the hot and cold calibration loads. At a mixer ambient of 4.2 K, the lowest measured receiver noise temperature was 3050 K double-sideband (DSB) at a local oscillator (LO) frequency of 1107 GHz. No corrections for beamsplitter losses or other losses were made in calculating the receiver noise, but the thermal radiation from the calibration loads was assumed to be in the Rayleigh-Jeans limit. The local oscillator power that was absorbed in the device was estimated from the DC current-voltage (IV) characteristic to be 20 nW. In a separate Y-factor measurement, the mixer ambient temperature was reduced to 1.9 K, resulting in a lowest receiver noise

temperature of 1670 K DSB at an LO frequency of 1103.5 GHz. This data is shown in Fig.4 . This receiver noise temperature includes an IF system contribution of 470 K DSB, referred to the receiver input. The conversion loss was approximately 18 dB DSB, including an estimated 5 to 8 dB of RF coupling losses. No significant level of direct detection was evident in the measurements at either 1.9 K or 4.2 K.

The niobium film quality in the tested device was very high, and as a result the critical current was comparatively large. At 1.9 K the critical current of the unpumped device was too high to be measured, due to protection diodes and resistors in the DC bias network. Therefore the absorbed LO power could not be directly deduced by comparison of the pumped and unpumped IV curves. A rough estimate of 40 nW, however, could be made from the estimated LO power at 4.2 K, and by using the analytic expression for the temperature distribution in the microbridge. This approach assumes that the electron temperature at the center of the bridge is close to the critical temperature, and takes into account that the measured DC dissipated power at the optimum LO pump level was approximately 20 nW at both 1.9 K and 4.2 K.

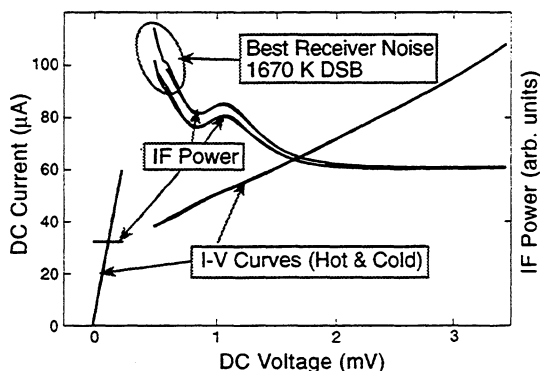


Fig.4; The DC IV curves and IF power versus DC voltage curves with the receiver looking at the 295 K and 82 K calibration loads. These curves were measured at an ambient temperature of 1.9 K, and gave a lowest receiver noise temperature of 1670 K DSB.

Measurement of a Gas Spectral Line

As a verification of the heterodyne response, an absorption line measurement using a gas cell was made. Sulfur dioxide was chosen for this experiment, since this gas has several strong lines around 1100 GHz. Transmission spectra for three different gas pressures were measured by sweeping the BWO frequency and detecting the transmission with a commercial silicon bolometer cooled to 4.2 K. The spectra were normalized by a transmission measurement with an empty gas cell, and are shown in Fig.5 .

A multichannel spectrometer such as an AOS or autocorrelator was not available for the experiment described here, so instead the set-up shown in Fig.6 was used. The IF bandpass filter that was used in the Y-factor measurements was removed to increase the available bandwidth. The intermediate frequency output from the receiver was instead filtered to a 1 MHz bandwidth using a microwave spectrum analyzer, and this filtered signal was measured with a coaxial diode detector and a lock-in amplifier. The lock-in amplifier was synchronized to a 40 Hz chopper, which switched the receiver input between the 295 K and the 82 K calibration loads. This laboratory set-up had a considerably lower signal-to-noise ratio than the back-end spectrometers mentioned above, but was sufficient for the intended demonstration. This measurement was made at an ambient mixer temperature of 4.2 K.

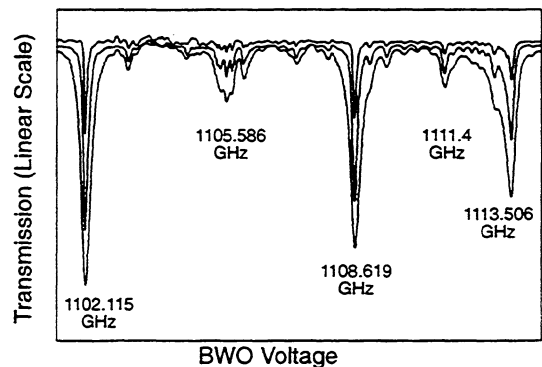


Fig.5; The transmission spectrum of the sulfur dioxide calibration gas, from a direct-detection measurement using a silicon bolometer. The three curves were measured at three different gas pressures.

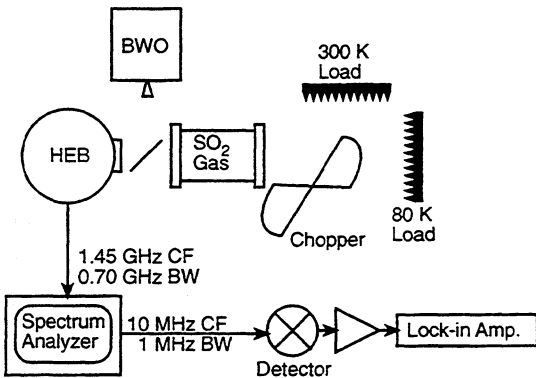


Fig. 6; Block diagram of the laboratory set-up for the gas cell measurement. A spectrum analyzer was used as a tunable IF filter.

Fig.7 shows three IF spectra, where the 1102.115 GHz sulfur dioxide line was detected in the lower sideband of the HEB receiver for different local oscillator frequencies. The spectra were normalized to a measurement with an empty gas cell to cancel out gain variations in the intermediate frequency amplifier chain. The gas line appears as a dip, since the chopped calibration loads are obscured from the mixer right at the line frequency (where the gas is optically thick), while they are visible at frequencies where the gas is optically thin. The frequency of the line shifts through the IF band in the expected way as the local oscillator frequency is changed, which shows that the response is heterodyne. A measurement of the mixer sideband ratio is in progress, which will allow us to fully quantify the heterodyne response, and will be reported at a later date.

During the preparations for the spectral measurement above, a series of measurements were made to accurately calibrate the BWO output frequency as a function of anode voltage and current. This was done by measuring transmission spectra of sulfur dioxide by sweeping the BWO anode voltage for several specific values of the anode current, which was adjustable by changing the cathode heater current. The detector in this measurement was a silicon bolometer. The two strong absorption lines at 1102.115 GHz and 1108.619 GHz were used as frequency references in the calibration. As expected, the

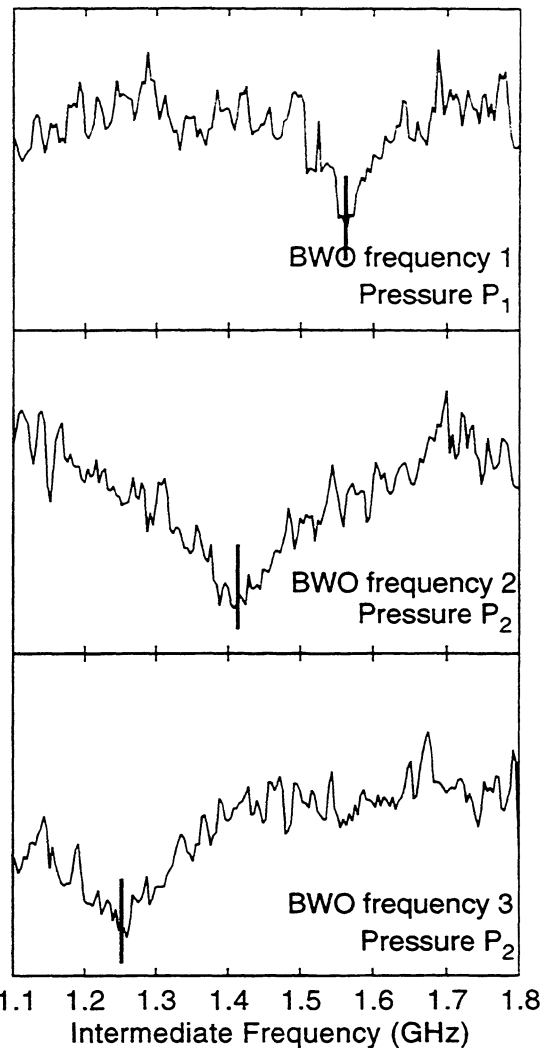


Fig.7; The 1102.115 GHz sulfur dioxide gas line detected in the lower sideband of the HEB receiver for three different local oscillator frequencies.

main factor in determining the frequency was the anode voltage, but the frequency was also found to change in a linear way with the anode current. This shift was almost 2 GHz over the useful range of the anode current (23 to 37 mA). It was therefore necessary to take the anode current into account when calculating frequencies during the mixer measurements, where the cathode heater current was often changed to adjust the amount of local oscillator power.

Intermediate Frequency Bandwidth

The intermediate frequency dependence of the device conversion efficiency can be calculated from the hot/cold response if a correction is made for the frequency dependence of the IF amplifier chain. In this experiment the hot/cold response was measured by the lock-in technique described in the previous section. The IF calibration was done by heating the mixer to the critical temperature of the niobium film and applying a DC voltage of several millivolts. Under these conditions the average temperature in the niobium film, and therefore the thermal noise generated, changes in proportion to (small) changes in bias voltage. This means that the frequency dependence of the IF system gain, excluding the HEB device matching but including the spectrum analyzer and the lock-in amplifier, could be measured through lock-in detection by applying a 40 Hz bias modulation. Fig.8 shows the lock-in detected RF hot/cold response and the response to the DC bias modulation. The "calibrated" conversion efficiency in the figure is calculated by dividing these two curves. As can be seen, the calibrated response is essentially flat over the entire 1.1 to 1.8 GHz band. This indicates that the IF roll-off frequency of this device is well over 1.8 GHz, which is consistent with measurements of similar devices [8-9].

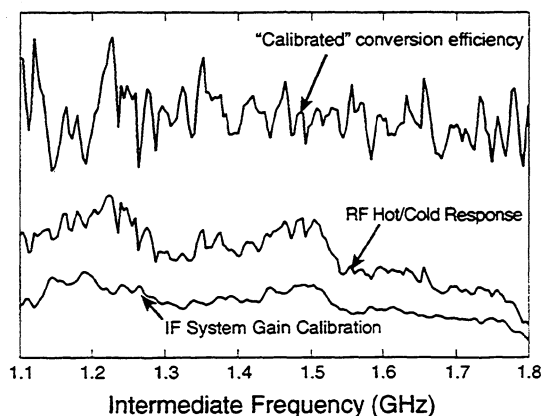


Fig.8: The RF hot/cold response, the IF system gain and the conversion efficiency calculated as the ratio of the two curves. No roll-off in the response is seen. This measurement was made at an ambient temperature of 4.2 K.

Summary

Receiver noise measurements have been made with a niobium hot-electron bolometer, yielding a best receiver noise temperature of 1670 K DSB at a local oscillator frequency of 1103.5 GHz and an ambient temperature of 1.9 K. The total conversion loss in the mixer, including RF coupling losses was 18 dB. The amount of absorbed local oscillator power is estimated at around 40 nW. The IF conversion bandwidth of the bolometer exceeds 1.8 GHz. The best receiver noise measured with this device is slightly lower than in our previous experiments, and showed no evidence of direct detection.

The 1102.115 GHz absorption line in sulfur dioxide gas was detected in the intermediate frequency band of our HEB receiver, showing that the response is heterodyne.

Acknowledgments

The research described in this paper was performed by the Center for Space Microelectronics Technology, Jet Propulsion Laboratory, California Institute of Technology, and was sponsored by the National Aeronautics and Space Administration, Office of Space Science.

References

- [1] E.M. Gershenson, G.N. Gol'tsman, I.G. Gogidze, Y.P. Gusev, A.I. Elant'ev, B.S. Karasik, A.D. Semenov, "Millimeter and submillimeter range mixer based on electronic heating of superconducting films in the resistive state," *Sov. Phys. Superconductivity*, Vol.3(10), pp.1582-1597, 1990
- [2] D.E. Prober, "Superconducting Terahertz Mixer using a Transition-Edge Microbolometer," *Appl. Phys. Lett.*, Vol.62(17), pp.2119-2121, 26 April 1993.

- [3] E.L. Kollberg, "Superconducting mixers for submillimetre wavelength," Book chapter in *New Directions in Terahertz Technology*, J.M. Chamberlain, R.E. Miles (ed.), Kluwer Academic Publishers, Dordrecht, the Netherlands, 1997, ISBN 0-7923-4537-1.
- [4] A. Skalare, W.R. McGrath, B. Bumble, H.G. LeDuc, "Receiver Measurements at 1267 GHz using a Diffusion-Cooled Superconducting Transition-Edge Bolometer," *IEEE Trans. Applied Superconductivity*, Vol.7(2),pp.3568-3571, June 1997.
- [5] B. Bumble, H.G. LeDuc, "Fabrication of a Diffusion Cooled Superconducting Hot Electron Bolometer for THz Mixing Applications," *IEEE Trans. Applied Superconductivity*, Vol.7(2),pp.3560-3563, June 1997.
- [6] P.T. Parrish, T.C.L.G. Sollner, R.H. Mathews, H.R. Fetterman, C.D. Parker, P.E. Tannenwald, A.G. Cardiasmenos, "Printed Dipole-Schottky Diode Millimeter Wave Antenna Array," *SPIE Millimeter Wave Technology*, pp.49-52, Vol.337, 1982.
- [7] A. Skalare, Th. de Graauw, H. van de Stadt, "A Planar Dipole Array Antenna with an Elliptical Lens," *Microwave and Optical Tech. Lett.*, Vol.4, No.1, Jan 5, 1991.
- [8] P.J. Burke, R.J. Schoelkopf, D.E. Prober, A. Skalare, W.R. McGrath, B. Bumble, H.G. LeDuc, "Length Scaling of Bandwidth and Noise in Hot-Electron Superconducting Mixers," *Appl. Phys. Lett.* 68(23), 3 June 1996.
- [9] B.S. Karasik, M.C. Gaidis, W.R. McGrath, B. Bumble, H.G. LeDuc, "Low noise in a Diffusion-Cooled Hot-Electron Mixer at 2.5 GHz," *Appl. Phys. Lett.* 71(11), 15 September 1997.

NbN HOT-ELECTRON MIXER AT RADIATION FREQUENCIES BETWEEN 0.9 THz AND 1.2 THz

Yu.P. Gousev* and H.K. Olsson
Royal Institute of Technology, S-164 40 Kista-Stockholm, Sweden

G.N. Gol'tsman, B.M. Voronov, and E.M. Gershenzon,
Moscow State Pedagogical University, 117 439 Moscow, Russia

We report on noise temperature measurements for a NbN phonon-cooled hot-electron mixer at radiation frequencies between 0.9 THz and 1.2 THz. Radiation was coupled to the mixer, placed in a vacuum chamber of He cryostat, by means of a planar spiral antenna and a Si immersion lens. A backward-wave oscillator, tunable throughout the spectral range, delivered an output power of few μW that was enough for optimum operation of the mixer. At 4.2 K ambient temperature and 1.025 THz radiation frequency, we obtained a receiver noise temperature of 1550 K despite of using a relatively noisy room-temperature amplifier at the intermediate frequency port. The noise temperature was fairly constant throughout the entire operation range and for intermediate frequencies from 1 GHz to 2 GHz.

INTRODUCTION

Astrophysical and stratospherical investigations in the terahertz (THz) frequency range, which are forthcoming events of the next few years, require heterodyne receivers with low-noise mixers. SIS mixers, having lowest noise temperatures up to ≈ 1 THz, have a drastic decrease in performance at higher frequencies. Sensitivity of Schottky diode mixers for THz range is limited by high intrinsic noise level in the diode. A superconductive hot-electron mixer (HEM), proposed in [1] and [2], is presently the only alternative to extend heterodyne spectroscopic measurements up to at least 10 THz, possibly over 30 THz. HEMs demonstrate a noise temperature, comparable to that of SIS receivers at 1 THz, and the lowest noise temperatures at higher frequencies [3]. They have also other advantages, like a small required local oscillator (LO) power, a nearly real impedance, and a relatively simple planar technology.

Two different ways to realize a HEM, with cooling of hot electrons via an out-diffusion of carriers from the sensitive element to contact pads [2], or by means of intensive electron-phonon interaction [1], result either in a smaller local oscillator power [3], or in a larger intermediate frequency (IF) bandwidth [4], respectively. Due to the lack of tunable LO sources in the far-infrared the large IF bandwidth is essentially important for spectroscopic measurements. Though future development of a tunable cw radiation source with a reasonable power at frequencies above 1.5 THz may weaken the latter requirement, IF bandwidth is currently an important issue for the THz mixer.

* E-mail: yuri@ele.kth.se

Large IF signal bandwidths, up to several GHz, of the phonon-cooled HEM have been realized with NbN due to a very short electron-phonon interaction time in this material, which is about 10 ps at 10 K [5]. Even a shorter time has been reported for $\text{Yb}_2\text{Cu}_3\text{O}_{7-\delta}$ [6], which could result in a high-temperature superconducting THz mixer with large IF bandwidth. Since the effective IF bandwidth of the hot-electron mixer is larger than the conversion gain bandwidth due to decrease of temperature fluctuation noise at high IF [7,4], NbN mixers are supposed to have effective IF bandwidths over 10 GHz.

In this paper we report on receiver measurements with an NbN phonon-cooled hot-electron mixer designed for operation in the THz range. Two devices have been investigated, with different sensitive element volumes and, correspondingly, different optimum LO power. We demonstrate that the receiver noise temperature is fairly constant between 0.9 THz and 1.2 THz throughout the IF measurements range.

EXPERIMENTAL SET-UP

35 Å thick NbN films were deposited on 350 μm thick Si substrates by magnetron sputtering of Nb in the atmosphere of Ar and N; a 0.3 μm Ti-Au layer was deposited on top. By means of photolithography and ion milling a NbN microbridge and a gold planar logarithmic spiral antenna were formed (Fig. 1). Since NbN films have large sheet resistance, the microbridge was shaped in a horse shoe form in order to match the normal state resistance of the device to the radiation resistance of the planar antenna which is $377[2(\epsilon+1)]^{-0.5} \approx 75 \Omega$ ($\epsilon = 11.4$ is the dielectric constant of Si). Arms of the planar antenna were connected to a co-planar transmission waveguide [8]. The superconducting transition temperature of NbN film for two devices used in the experiment was 7.5 K (device #1) and 7.9 K (device #2), with a transition width of 1.2 K and 1.1 K, respectively. The normal state resistance, taken at a temperature of 16 K, was 140 Ω for device #1 and 320 Ω for device #2.

A Si synthesized elliptical lens with no anti-reflection coating was used to couple radiation to the mixer. A hybrid antenna, consisting of the planar antenna and the immersion lens, had a nearly rotationally symmetrical radiation pattern (Fig. 2) with a main lobe width Θ_A of 1.7° at the -3 dB level. The radiation pattern was obtained by measuring a direct detection response of the NbN microbridge to a low power radiation at a frequency of 0.97 THz, produced by a backward-wave oscillator. The effective aperture of the hybrid antenna, $\approx 100 \text{ mm}^2$, was about 80 % of the cross-section of the immersion lens, thus approaching a maximum possible value.

Heterodyne measurements were performed with two black body radiation sources; a backward-wave oscillator (BWO), fabricated by ISTOK (Russia), served as a local oscillator at radiation frequencies between 0.9 and 1.2 THz. Maximum total output power, delivered by the BWO, was 10 μW at 0.97 THz. Two black body sources were placed in a vacuum chamber (Fig. 3), connected with a He cryostat, thus eliminating a problem of water vapor absorption in the signal path. One black body was attached to a metal can filled with liquid N_2 and had a temperature of about 90 K; the can was hanging in the vacuum chamber on a stainless steel tube serving also as a filling path for N_2 . The

other black body was fixed to a wall of the vacuum chamber and had a temperature of 290 K.

A TPX lens, installed instead of one window of the vacuum chamber, was matching the diverging beam of the BWO to the hybrid antenna. A wire grid polarizer served as a beam splitter for device #1; a Mylar beam splitter was used when measuring with device #2. A Goly cell, calibrated with a black body radiation, was set in the LO path to control output power of the BWO. Black polyethylene film, cooled to 77 K, blocked the near-infrared background radiation from the vacuum chamber to eliminate parasitic heating of the mixer. A mechanical chopper with a gold-plated blade switched radiation from the two black bodies. IF signal from the mixer at frequencies between 1 GHz and 2 GHz was amplified by a room temperature amplifier (noise temperature 40 K), then integrated with a diode detector, and recorded by a lock-in amplifier. To measure the IF dependence of the noise temperature, we used an internal detector of HP8592L spectrum analyzer, thus having a possibility to measure the signal at different IF frequencies within the amplifier bandwidth; the resolution bandwidth was set to 3 MHz.

HETERODYNE MEASUREMENTS AND DISCUSSION

Current-voltage (IV) characteristics for both mixers with and without LO power applied are presented in Fig. 4. Dc resistance of both devices increased from a constant value of few Ω at bias voltage below 1 mV to about 30 Ω for device #1 and 60 Ω for device #2 at a bias of five millivolt. We apply the constant dc resistance at small bias voltage, R_s , to a dc series resistance of the bias tee (3.8 Ω) and the resistance of the spiral antenna arms. Device #2 demonstrated lower bias currents and higher differential resistance compared to those of device #1 within the bias voltage interval.

Optimum LO power, P_{LO} , absorbed by the mixer at a radiation frequency of 0.97 THz, was obtained as a difference between power, dissipated in the mixer at two operation points, 2 and 1, with and without LO applied, respectively. The dc resistance of the mixer at two points and, consequently, the electron temperature, was the same. We extracted the dc power dissipated in the series resistance R_s , when calculating P_{LO} . Optimum LO power for device #2 (130 nW), was 6 times lower compared to that of device #1 (0.8 μ W), corresponding to a smaller volume for the device #2. Since the available LO power was limited, we used the wire grid polarizer for heterodyne measurements with device #1, thus providing a larger LO power and having additional losses in the signal path. Besides 3 dB polarization loss in the signal path, the wire grid beam splitter added a resistive loss of 0.5 dB.

Double sideband (DSB) receiver noise temperature for different intermediate frequencies, measured with device #2 at 1.025 THz, is presented in Fig 5. Though the noise temperature varies within 10 % in the range of our IF amplifier, we could not observe any pronounced IF dependence. Deviations in the noise temperature should be rather explained by the influence of our IF chain.

Noise temperature versus radiation frequency for device #2 is presented in Fig. 6. The noise temperature is fairly constant throughout the operation range. The largest Y-

factor, 1.122, and a corresponding noise temperature of 1550 K were obtained at 1.025 THz for an IF of 1.1 GHz. We should point out that all measurements were performed with a room temperature IF amplifier, which contributes about 30 % to the total noise temperature of the receiver. Using a cooled amplifier should result a decrease in noise temperature down to ≈ 1000 K.

Device #1 demonstrated a higher noise temperature (Fig. 6). However, unlike device #2, it was used with the wire grid beam splitter, which had much higher losses compared to that of the Mylar beam splitter. Extracting 3.5 dB loss in the grid beam splitter, we obtain a lowest noise temperature of 1170 K at 0.97 THz, which is less than that of device #2 with extracted losses in Mylar. The lower noise temperature of device #1 may be explained by a smaller normal state resistance, resulting in a smaller rf mismatch.

Other rf losses, which contribute to the receiver noise temperature, are listed in Table 1. Extracting reflection loss at the surface of the immersion lens, reflection and transmission loss in the polyethylene filter, and contribution from the IF amplifier, we obtain a 300 K intrinsic noise temperature of the mixer. Better matching a rf and IF impedance would result in even lower noise temperatures.

Table 1. Rf losses

<i>Element</i>	<i>Loss (dB)</i>	
	Device #1	Device #2
Beam Splitter (wire grid)	3.5	-
Beam Splitter (Mylar)	-	1
Black Polyethylene filter	0.5	0.5
Reflection at Si surface	1.5	1.5
Absorption in Si	0.4	0.4
Rf mismatch	0.4	2.1

The measured low value of the system noise temperature of the NbN phonon-cooled hot-electron mixer and obvious possibilities for further improvement demonstrate the advantages of the mixer at THz frequencies. Comparing our present results with those obtained in the first experiments with phonon-cooled HEM at 2.5 THz [9], where the noise temperature was many times higher, one should find a reasonable explanation for a drastic decrease in sensitivity at the higher frequency. We should mention numerous changes in our present experimental setup, such as better quasi-optical alignment of the system, eliminating the problem of water vapor absorption, and much higher power stability of the BWO compared to that of the FIR gas laser used in [9]. As a one more important factor, we should point out a greatly improved quality of NbN films. We believe there is no physical reason for any deterioration in performance at radiation frequencies up to at least 10 THz.

CONCLUSION

We have shown operation of NbN hot-electron mixer in a frequency range between 0.9 and 1.2 THz without any deterioration in performance. The measured DSB receiver noise temperature, about 1550 K, only slightly changes at intermediate frequencies from 1 GHz to 2 GHz, thus proving a suitability of phonon-cooled hot-electron mixers for spectroscopic measurements.

ACKNOWLEDGMENTS

Authors acknowledge financial support from the Swedish Research Council for the Engineering Sciences (TFR) and the Swedish Institute. Yu.P. Gousev is also grateful for technical support provided by KTH staff.

REFERENCES

1. E. M. Gershenzon, G. N. Gol'tsman, I. G. Goghidze, Yu. P. Gousev, A. I. Elant'ev, B. S. Karasik, and A. D. Semenov, The mixer for millimeter and submillimeter wavelengths based on electron heating in the resistive state of superconductive films, *Sov. Phys. Superconductivity* **3**(10), pp. 1582-1597 (1990).
2. D.E. Prober, Superconducting terahertz mixer using a transition-edge microbolometer, *Appl. Phys. Lett.* **62**(17), pp. 2119-2121 (1993)
3. B.S. Karasik, M.C. Gaidis, W.R. McGrath, B. Bumble, and H.G. LeDuc, Low noise in a diffusion-cooled hot-electron mixer at 2.5 THz, *Appl. Phys. Lett.* **71**(11), pp. 1567-1569 (1997).
4. H. Ekström, E. Kollberg, P. Yagoubov, G. Goltsman, E. Gershenzon, and S. Yngvesson, Gain and noise bandwidth of NbN hot-electron bolometric mixers, *Appl. Phys. Lett.* **70**(24), pp. 3296-3298 (1997).
5. Yu.P. Gousev, G.N. Gol'tsman, A.D. Semenov, E.M. Gershenzon, R.S. Nebosis, M.A. Heusinger, and K.F. Renk, Broadband ultrafast superconducting NbN detector for electromagnetic radiation, *J. Appl. Phys.* **75**(7), pp. 3695-3697 (1994).
6. A.D. Semenov, R.S. Nebosis, Yu.P. Gousev, M.A. Heusinger, and K.F. Renk, Analysis of the nonequilibrium photoresponse of superconducting films to pulsed radiation by use of a two-temperature model, *Phys. Rev. B* **52**(1), pp. 581-590 (1995).
7. B.S. Karasik and A.I. Elantiev, Noise temperature limit of a superconducting hot-electron bolometer mixer, *Appl. Phys. Lett.* **68**(6), pp. 853-855 (1996).
8. Yu.P. Gousev, A.D. Semenov, E.V. Pechen, A.V. Varlashkin, R.S. Nebosis, and K.F. Renk, Coupling of THz radiation to a high- T_c superconducting hot electron bolometer mixer, *Appl. Phys. Lett.* **69**(5), pp. 691-693 (1996).
9. A. D. Semenov, Yu. P. Gousev, R. S. Nebosis, K. F. Renk, P. Yagoubov, B. M. Voronov, G. N. Gol'tsman, and E. M. Gershenzon. Heterodyne detection of THz radiation with a superconducting hot-electron bolometer mixer. *Appl. Phys. Lett.* **69**(2), pp. 260-262 (1996).

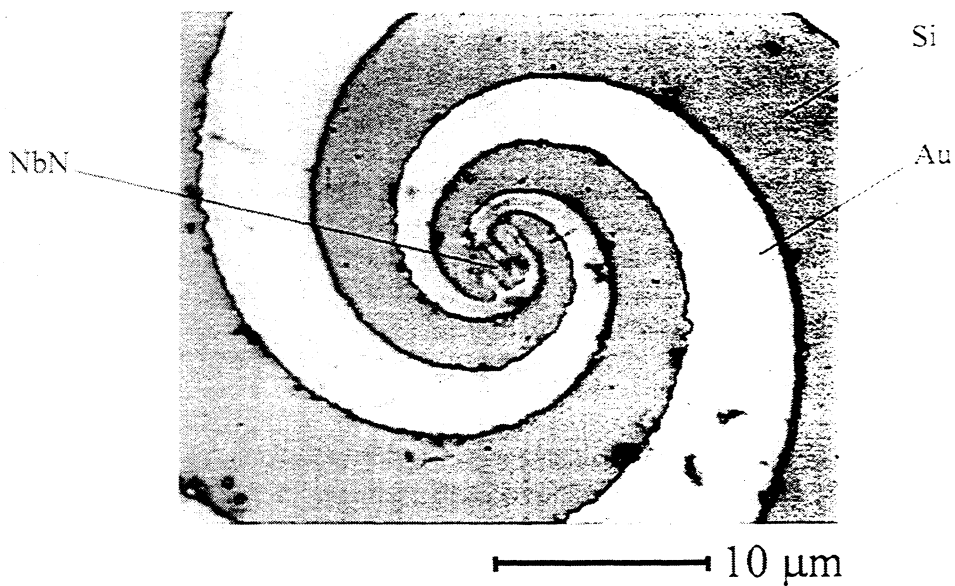


Fig. 1. Inner part of the planar spiral antenna. The NbN film between the antenna arms is transparent and therefore not visible on the picture.

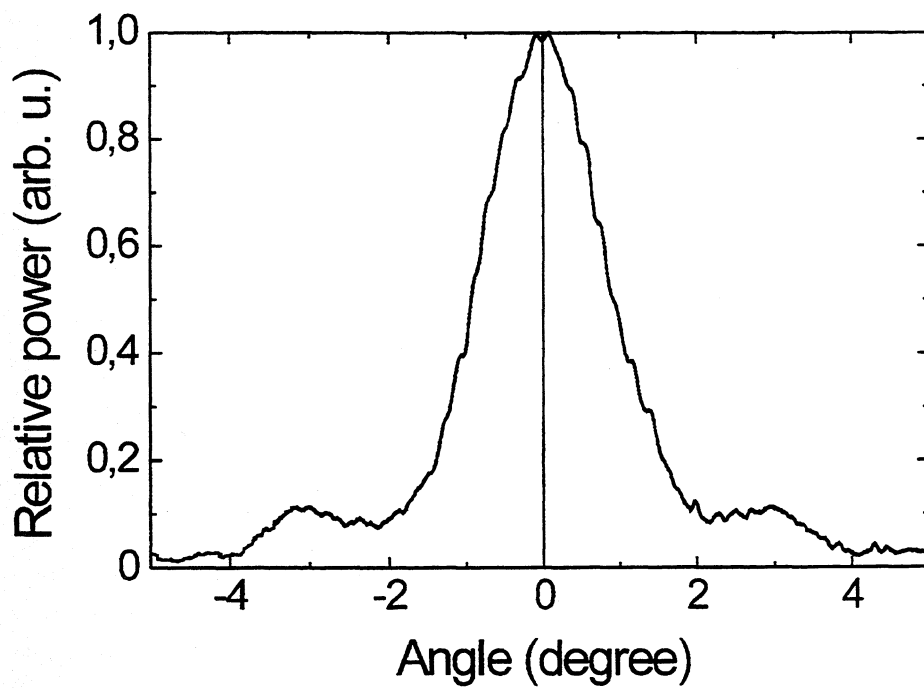


Fig. 2. Radiation pattern of the hybrid antenna at 0.97 THz.

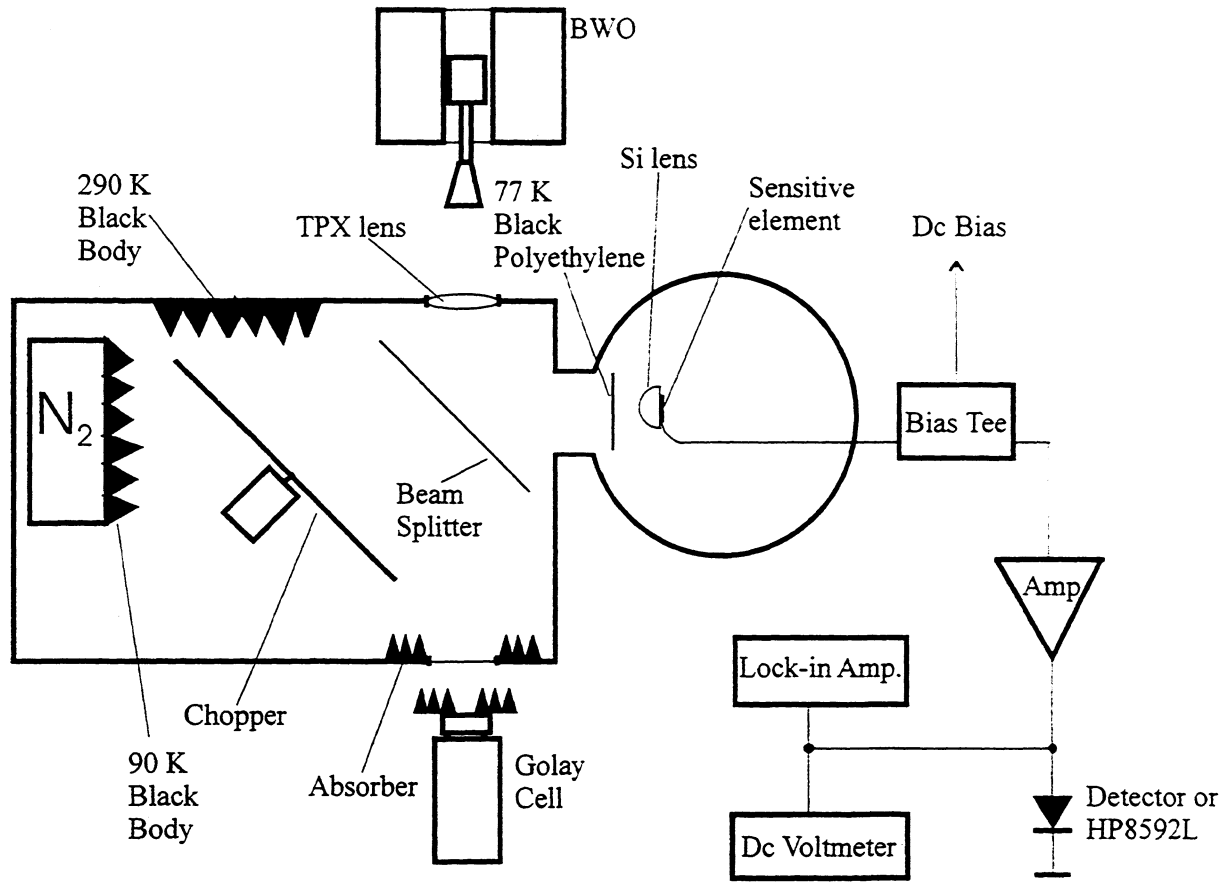


Fig. 3. Block diagram of the experimental set-up.

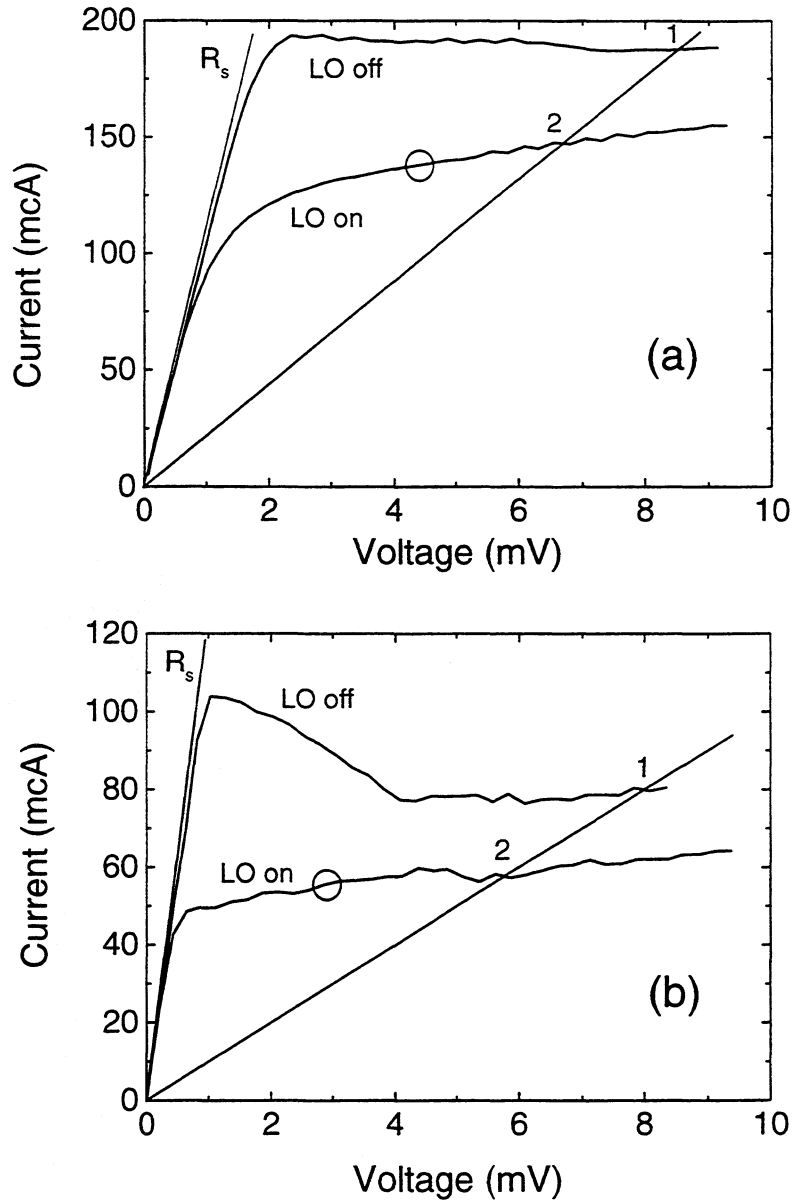


Fig. 4. Voltage-current characteristics for device #1 at an ambient temperature of 3.9 K (a) and device #2 at a temperature of 4.2 K (b). Operation point is marked by a circle.

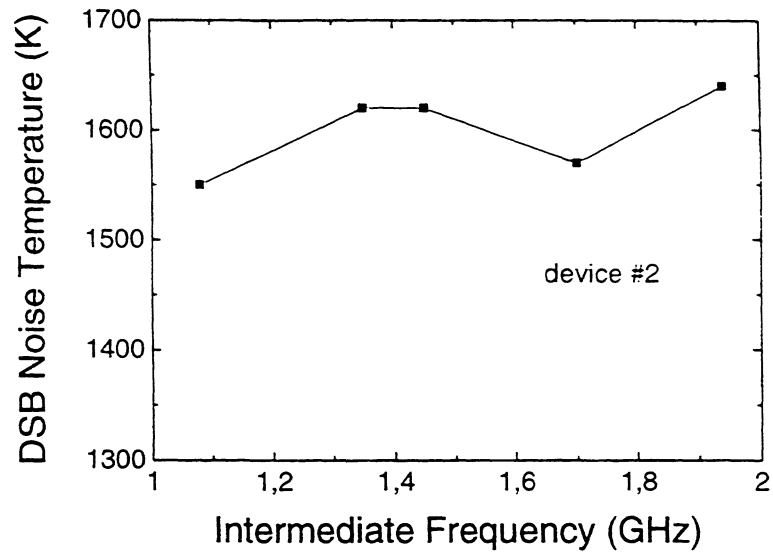


Fig. 5. System noise temperature versus intermediate frequency for device #2.

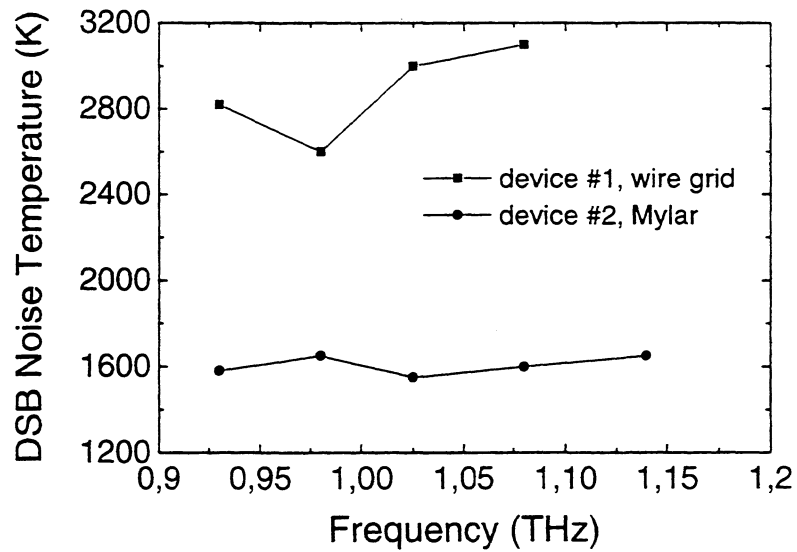


Fig. 6. System noise temperature for different radiation frequencies.

QUASIOPTICAL NbN PHONON-COOLED HOT ELECTRON BOLOMETRIC MIXERS WITH LOW OPTIMAL LOCAL OSCILLATOR POWER

P. Yagoubov*, M. Kroug, H. Merkel, E. Kollberg

Department of Microelectronics
Chalmers University of Technology
Gothenburg S-412 96, Sweden
*E-mail: yagoubov@ep.chalmers.se

G. Gol'tsman, A. Lipatov, S. Svechnikov, E. Gershenzon

Department of Physics
Moscow State Pedagogical University
Moscow 119435, Russia

Abstract

In this paper, the noise performance of NbN based phonon-cooled Hot Electron Bolometric (HEB) quasioptical mixers is investigated in the 0.55-1.1 THz frequency range. The best results of the DSB noise temperature are: 500 K at 640 GHz, 600 K at 750 GHz, 850 K at 910 GHz and 1250 K at 1.1 THz. The water vapor in the signal path causes a significant contribution to the measured noise temperature around 1.1 THz. The required LO power is typically about 60 nW. The frequency response of the spiral antenna+lens system is measured using a Fourier Transform Spectrometer with the HEB operating in a detector mode.

Introduction

In the past years the development of low noise receivers for the THz frequency range has focused on superconducting HEB mixers. Predicted feasible noise figures of HEB are close to the quantum limit and their RF frequency bandwidth is not limited by the superconducting energy gap like in SIS mixers [1].

Two different types of HEB mixers have been developed: The phonon cooled HEB and the diffusion cooled HEB. These mixers employ different cooling mechanisms of the electron subsystem. In the phonon cooled HEB the electron energy relaxes through interaction with phonons [1] while in the diffusion cooled HEB hot electrons are predominately cooled by outdiffusion into metal contact pads [2]. The intermediate frequency (IF) bandwidth of a HEB mixer is determined by an electron energy relaxation time. To realize a wide bandwidth in the phonon-cooled HEB one must use a superconductor with a short electron-phonon relaxation time τ_{e-ph} , e.g. NbN. For the diffusion-cooled HEB a material with rather long τ_{e-ph} as Nb can be used, but the bolometer strip must be short enough to enhance the outdiffusion of electrons to dominate over electron-phonon interaction. Recently reported results show that both mixer techniques yield reasonably broad IF bandwidth of several GHz [3-6].

Which type of HEB mixer is more appropriate is not yet clear. The comparison of mixer technologies shows that at the present stage of the development the phonon cooled HEB mixers exhibit larger gain and noise bandwidths, 3.2 and 8 GHz respectively, measured at 650 GHz [3] and a better noise performance at frequencies up to 1.1 THz [7].

The diffusion cooled Nb HEB mixers have shown better noise performance at 2.5 THz [8]. Gain bandwidth measurements at 20 GHz indicate that for this type of HEB it is possible to achieve a bandwidth of 6 GHz for the 0.1 μm long devices [6]. However, at higher RF frequencies measurements were performed only for 0.3 μm long devices and the noise bandwidth does not exceed 2 GHz [8,9].

Taking a look at the recent results obtained for both types of mixers one can see that the main difference in the characterization of these mixers was the amount of absorbed LO power, P_{LO} , which is basically determined by the bolometer time constant and its volume. It should be noted that the conversion gain of the HEB mixer does not depend on the bolometer volume [1]. Therefore the dimensions of the strip can be in principle chosen to adjust P_{LO} for a particular application. This freedom is limited by the constraint to match the device impedance to the antenna. Moreover there are other limitations restricting the bolometer dimensions for both types of HEB:

For the diffusion cooled devices the length of the strip must be small to provide a short time constant of the mixer. The need to match the device to the antenna makes it necessary to have a small cross-section of the Nb strip due to the low film resistance. These two requirements reduce the device volume leading to a very small P_{LO} . This, in turn, restricts the dynamic range of the mixer.

For the phonon-cooled HEB the film thickness is the only limiting parameter. It must be small enough to provide fast escape of nonequilibrium phonons into the substrate. The strip in-plane dimensions are free parameters. Matching to the antenna requires a certain length-to-width ratio of the strip, but one can scale the strip to adjust the dynamic range of the mixer and meet particular LO power requirements.

In this paper we describe the development of submicron size phonon cooled HEB mixers with low required LO power and present results of heterodyne measurements in the 0.55-1.1 THz frequency range.

Device fabrication and experimental setup

Micrographs of the spiral antenna integrated HEB mixer and the center part of the antenna are shown in Figures 1 and 2. The fabrication procedure consists of 4 main steps (illustrated in Figure 3):

1. Deposition of NbN film;
2. Patterning of Au pads for bolometer strip definition;
3. Patterning of antenna, large contact pads and transmission line;
4. Patterning of the bolometer.

The devices are made out of a 3 nm thick NbN film deposited on a high-resistivity Si substrate. A detailed description of the film fabrication process is found in [4].

The obtained films have a sheet resistance of about 1 $\text{k}\Omega/\square$, a transition temperature around 10 K and a transition width of 0.5 K. After all processing steps the transition temperature drops down to 9 K with a transition width of 1 K. A typical $R(T)$ curve of the device is shown in Figure 4.

In the next process step Au pads are placed in the center of each chip. The spacing between them already defines the dimension of the bolometer, typical is a length 0.2-

0.5 μm and a width of 1-5 μm (depending on the design of the spiral antenna). Applying electron beam lithography for patterning a double layer resist system (Copolymer + PMMA) one gets a lift-off mask which allows metallization of the structure. After evaporating 5 nm titanium (to establish good adhesion) plus by 80 nm Au using e-beam evaporation system the lift-off mask is removed in acetone.

The baseline wiring consists of the spiral antenna and large contact pads. For patterning, the same lithography technique as in the previous step is used with 5 nm titanium plus 200 nm Au.

In the last step the NbN film, which is still left on the whole wafer, has to be removed except between the contact pads. E-beam lithography with negative resist SAL601 is used to define a mask that covers the bolometer part and the Au pads. Etching is done in an argon ion beam system for about 10 min (acceleration voltage 400 V, current 0.2 mA/cm²). The remaining resist is left on the device.

Finally, photo resist is spun on the whole wafer for protection when sawing up into chips of size 2x4 mm (5x5 mm if transmission line is included).

The setup for heterodyne measurements is shown in Figure 5. The mixer chip is clamped to an extended hemispherical silicon lens with a quarter wavelength antireflection coating optimized for 660 GHz. The mixer block is mounted in a LHe-cooled vacuum cryostat equipped with a 380 μm Zitex G115 IR radiation filter. As LO sources we use three BWOs covering the 550-1100 GHz frequency range. The radiation from the LO is focused by a Teflon lens and combined with the signal by a 12- μm -thick Mylar beamsplitter. The noise temperature is measured using the Y-factor technique with hot/cold (295/77 K) loads in the signal path of the receiver.

The device output is connected through a bias-T to a two-stage IF amplifier chain. As a first stage we use a cooled HEMT amplifier with a center frequency of 1.5 GHz, 300 MHz band and a noise temperature of 5 K. The amplified mixing signal is then fed to a scalar network analyzer.

Antenna design and simulations

The antenna used in the quasioptical setup is an equiangular spiral with a 90° arm width, which yields a self-complementary design. The antenna shape is specified by a spiral expansion rate and an antenna terminal size. The expansion rate is optimized for smooth and uniform antenna patterns with small variations in beamwidth with frequency and wide bandwidth. Based on previous experience an expansion rate of 3.2 per turn was chosen for a 1.5 turn antenna. A wide bandwidth is needed at the present stage of the mixer development since it allows to perform mixer measurements and comparison of mixer properties over a wide frequency range.

As follows from Babinet's principle the input impedance of a self-complementary infinite structure should be pure real and equal to $Z_{\text{ant}}=Z_0/[2(1+\epsilon)]^{1/2}$, i.e., 75 Ohm for Si. However, there are several factors like finite antenna arm length, nonideal antenna geometry at the device, finite thickness of the antenna arms, frequency-dependent surface impedance of the metal etc, which in practice influences the impedance of the antenna.

Three-dimensional simulations of the integrated antenna were performed using HFSS (High Frequency Structure Simulator – HP85180A) by Hewlett Packard. The

following setup is investigated: The antenna arms are modeled as a three-dimensional structure with finite resistance which is located on the back plane of silicon extended hemispherical lens. The whole structure is placed in a cavity with absorbing boundaries.

The antenna is modeled in a transmit mode. This requires to replace the bolometer by a voltage source parallel to a surface resistor with the same size. Such a feed port does not allow direct impedance calculations but it produces consistent field distributions. Simulations are performed in a frequency range 0.5-1.5 THz for a 200 nm thick Au antenna. The surface resistor dimensions are $2 \times 0.3 \mu\text{m}$. The conductivity of the Au film was assumed to be $8 \cdot 10^7 \text{ Ohm}^{-1} \cdot \text{m}^{-1}$ - two times larger than its bulk value at room temperature. The calculation results obtained for frequencies above 1.3 THz show strong spurious mode excitations. At frequencies below 1.3 THz the expected field distribution in spiral arms is observed. We have calculated the spot diameter related to current drop off in the antenna arms and compared that to a first order estimation for the minimum required antenna diameter of the ideal spiral (antenna structure is a perfect electric conductor and scaling invariant) [10]. This predicts that the current fades away at an armlength of about one wavelength. The current spot diameter of the calculated structure decreases with frequency faster than predicted. This is due to ohmic losses in the antenna arms which increase with frequency and the change in antenna curvature in the center. The obtained results are preliminary and further work on integrated antenna simulation (antenna impedance and pattern calculations) has to be done.

The integrated antenna frequency response has been investigated experimentally using Fourier Transform Spectroscopy (FTS) technique. In these measurements the HEB is driven to a temperature close to T_c and operated as a detector. Since the HEB response is frequency independent the obtained spectrum is basically determined by the antenna+lens system response. There are also additional optical losses in the signal path (cryostat Teflon window, Zitex IR filter) which were not taken into account so far.

The signal from the FTS is phase modulated (PM) in order to reduce the background noise and increase the detector signal-to-noise ratio. Due to the fact that PM does not modulate all wavelengths equally the modulation amplitude of a vibrator mirror was chosen in such a way to make the spectral power distribution within 50% variations in the frequency range of interest 0.7-2.5 THz. The maximum of FTS output power measured with a Golay cell was found at about 1.5 THz.

The FTS spectrum obtained for the device #2 is show in Figure 6. The antenna extends one and a half turns and has an inner radius of $3 \mu\text{m}$. This gives a crude short wavelength limit of $30 \mu\text{m}$ (3 THz in a free space) [11].

The observed lower cut-off frequency of the measured integrated antenna arises because of the wavelength selective nature of phase modulation and spectral emission function of the FTS Hg lamp. The upper cut off frequency is about 1.25 THz. This is considerably lower than the expected value for the above antenna geometry. Possible explanations for this are:

Destructive interference of the antireflection coating of the lens optimized for a maximum transition at 660 GHz; minimum transition occurs at a double frequency – 1.3 THz;

Chromatic aberration of the lens leading to a shorter focal length at higher frequencies which deteriorates the antenna coupling efficiency. This can be avoided employing elliptical or smaller hemispherical lenses.

Results and discussion

Several mixers made by e-beam lithography have been tested. Most of them have shown excellent noise performance. The noise temperature of three best mixers are plotted as a function of LO frequency in Figure 7. The in-plane dimensions of the bolometer strip are $0.2 \times 4 \mu\text{m}$ for the device #1 and $0.2 \times 2 \mu\text{m}$ for the devices #2 and #3. The best Y-factor of 1.4 dB was measured for the device #1 at 630 GHz, corresponding to 500 K DSB noise temperature. Note that all reported results are not corrected to account for losses. The measurements are performed at 4.5 K ambient temperature, cooling the mixers down to 2.5 K leads to an insignificant drop of the noise temperature.

The optical losses in the signal path are estimated to be at least 3 dB. This includes absorption losses in the cryostat teflon window, Zitex IR filter, beamsplitter and Si lens, and antenna losses (backside radiation and sidelobe losses). Eliminating this from the receiver noise temperature gives the intrinsic mixer noise temperature of about 300 K for all mixers presented in this work.

The observed smooth frequency dependence of the noise temperature for all mixers is probably determined by the antenna-lens system, as discussed above. Another possible reason could be the change of the RF impedance of the superconducting film near the gap frequency. This effect influences the RF matching of the device to the antenna.

A considerable contribution to the measured receiver noise temperature at THz frequencies comes from atmospheric absorption. It can be seen distinctively at 1.1 THz, where the sharp rise in the noise temperature is due to a strong water absorption line. Moving the cold load forth and back in front of the cryostat window at this LO frequency causes the substantial change of the measured Y-factor.

In Figure 8 we plot the pumped IV-curves of the device # 2 as well as results of noise temperature measurements vs. position of the operating point at 0.75 THz. It can be seen that in a quite wide range of the LO power and dc bias variations the noise temperature of the mixer is not changing drastically. This is a special benefit for THz frequency applications where one still has to refer to laser systems as LO sources often suffering from output power instability.

The absorbed LO power was estimated using the isotherm technique assuming that the response to dc and RF power is the same. It is derived from two pumped IV curves with different amounts of LO power which are crossed far from the unstable region by a constant resistance line [7]. This technique gives about 100 nW absorbed LO power for the device #1 and about 60 nW for the devices #2 and #3. These numbers correlate well with the in-plane dimensions of the bolometer. It is important that there is no fundamental limitation to further decrease the bolometer volume and assure even smaller amount of LO power.

Conclusions

A quasioptical phonon-cooled HEB mixer with submicron in-plane dimensions of the superconducting strip has been fabricated and tested in the 0.55-1.1 THz frequency range. The results of the noise temperature measurements show that these mixers have excellent performance, comparable to SIS mixers at frequencies about 1 THz. The small amount of coupled LO power, about 60 nW, is needed to pump the mixer to the optimal operating point.

Acknowledgments

This work has been supported by ESA (ESTEC/No.11738/95/NL/MV), Swedish Research Council for Engineering Sciences, Swedish National Space Board and Russian program on Condensed matter Grant # 96128. The authors are thankful to S.Yngvesson for many useful discussions and B. Voronov for fabrication of NbN films.

References

- [1] E. M. Gershenson, G. N. Gol'tsman, I. G. Gogidze, A. I. Elant'ev, B. S. Karasik and A. D. Semenov, *Sov. Phys. Superconductivity*, **3**, 1582-1597, (1990).
- [2] D. E. Prober, *Appl. Phys. Lett.*, **62**, 2119-2121, (1993).
- [3] H. Ekström, E. Kollberg, P. Yagoubov, G. Gol'tsman, E. Gershenson and S. Yngvesson, *Appl. Phys. Lett.*, **70**, 3296, (1997).
- [4] P. Yagoubov, G. Gol'tsman, B. Voronov, L. Seidman, V. Siomash, S. Cherednichenko and E. Gershenson, *Proceedings of the 7th Int. Symp. on Space Terahertz Technology*, Charlottesville, VA, 290, (1996).
- [5] S. Cherednichenko, P. Yagoubov, K. Il'in, G. Gol'tsman and E. Gershenson, *Proceedings of the 8th Int. Symp. on Space Terahertz Technology*, Cambridge, MA, 245, (1997).
- [6] P. J. Burke, R. J. Schoelkopf, D. E. Prober, A. Skalare, W. R. McGrath, B. Bumble and G. H. LeDuc, *Appl. Phys. Lett.*, **68**, 3344, (1996).
- [7] M. Kroug, P. Yagoubov, G. Gol'tsman and E. Kollberg, presented at the 3rd. European Conference on Applied Superconductivity, Veldhoven, Netherlands, 1997, (Inst. Phys. Conf. Ser. No 158, p.405).
- [8] B. S. Karasik, M. Gaidis, W. R. McGrath, B. Bumble and H. G. LeDuc, *Appl. Phys. Lett.*, **71**, 1567, (1997).
- [9] K. Fiegle, D. Diehl and K. Jacobs, *IEEE Transactions on Applied Superconductivity*, vol 7, No.2, 3552, (1997).
- [10] A. Balanis, *Antenna theory and design*, 1984.
- [11] E. N. Grossman, J. E. Sauvageau, and D. G. McDonald, *Appl. Phys. Lett.*, **59**, 3225, (1991).

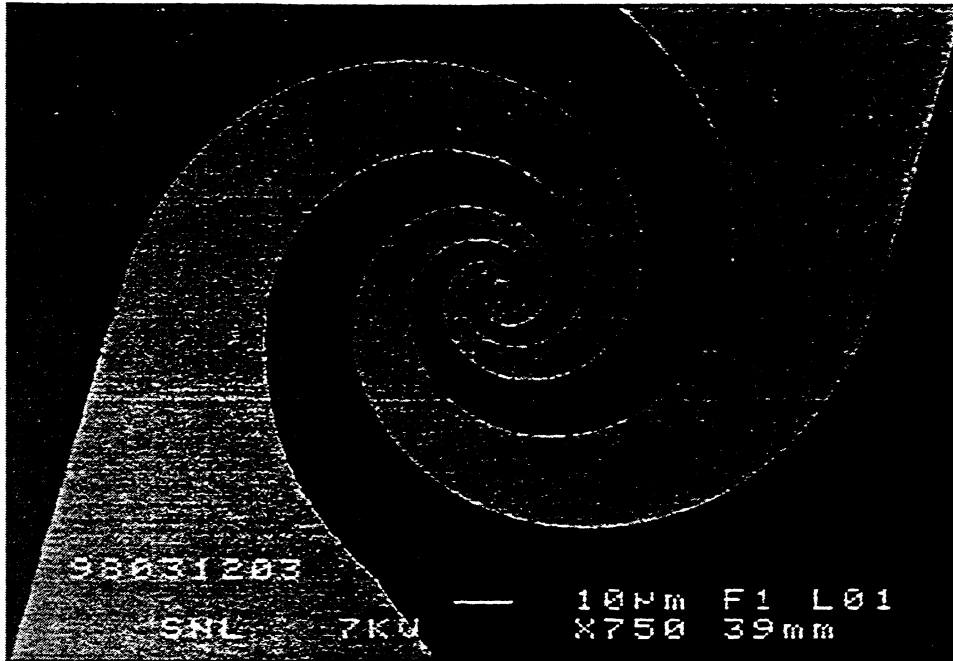


Fig.1. Micrograph of the spiral antenna integrated HEB mixer.

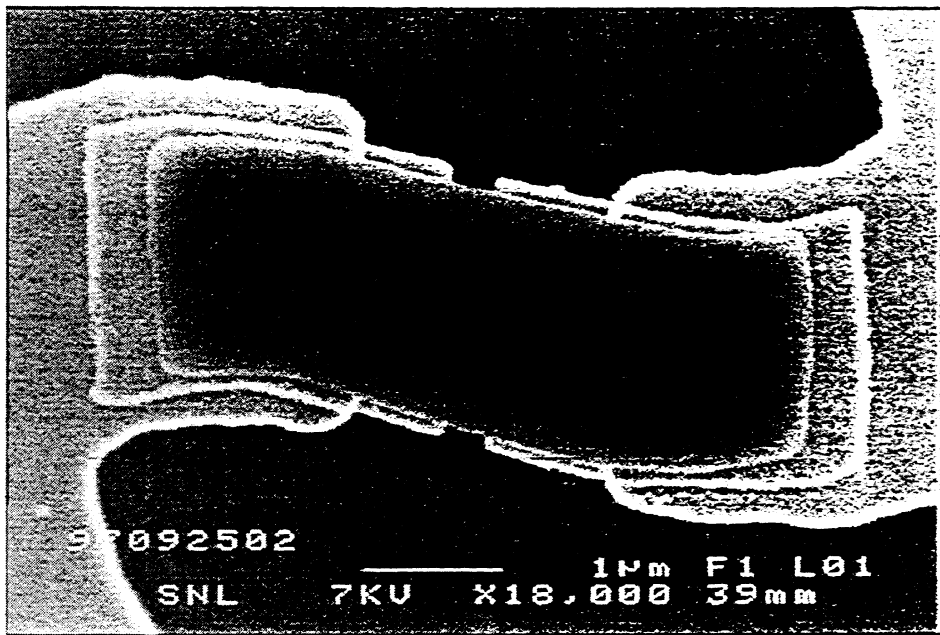


Fig.2. Micrograph of the antenna gap.

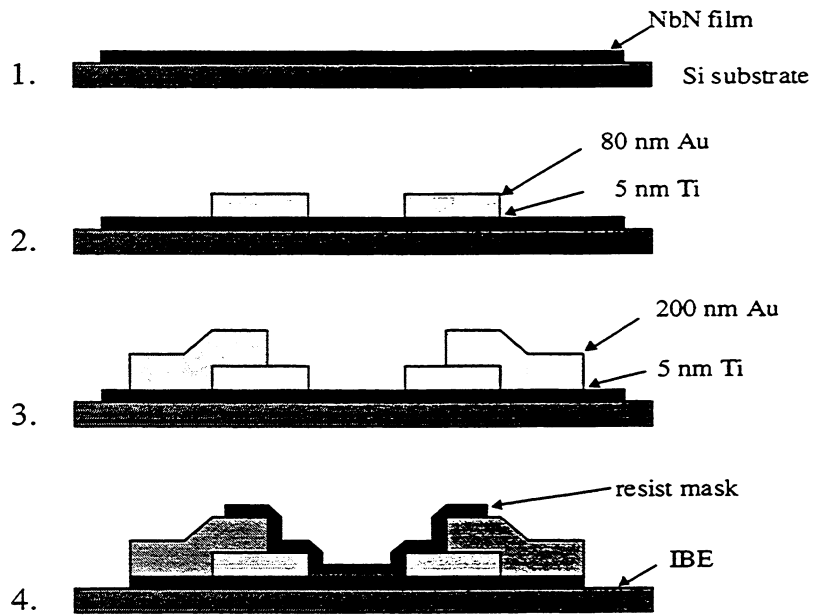


Fig.3. Schematic top of the fabrication process.

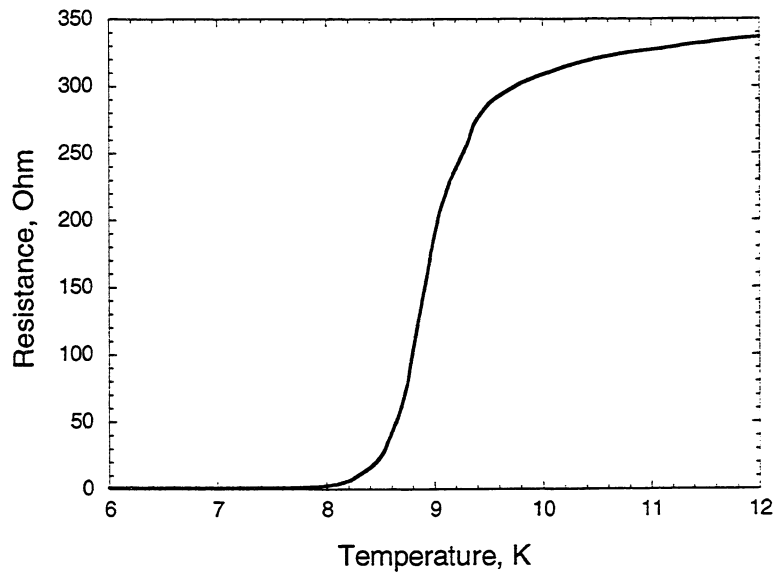


Fig.4. Typical R(T) curve of mixer with submicron dimensions of the bolometer strip.

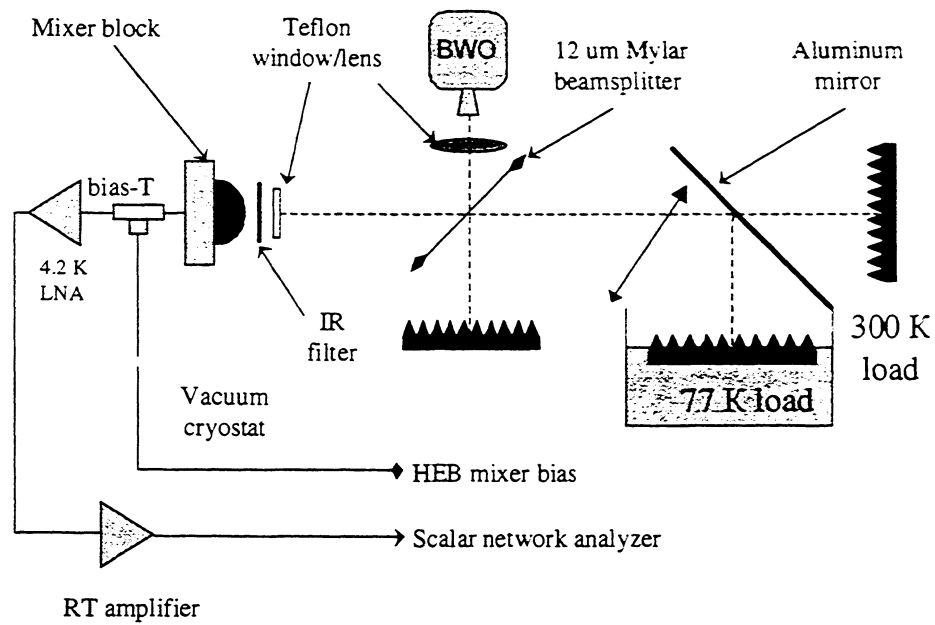


Fig.5. Setup for noise temperature measurements.

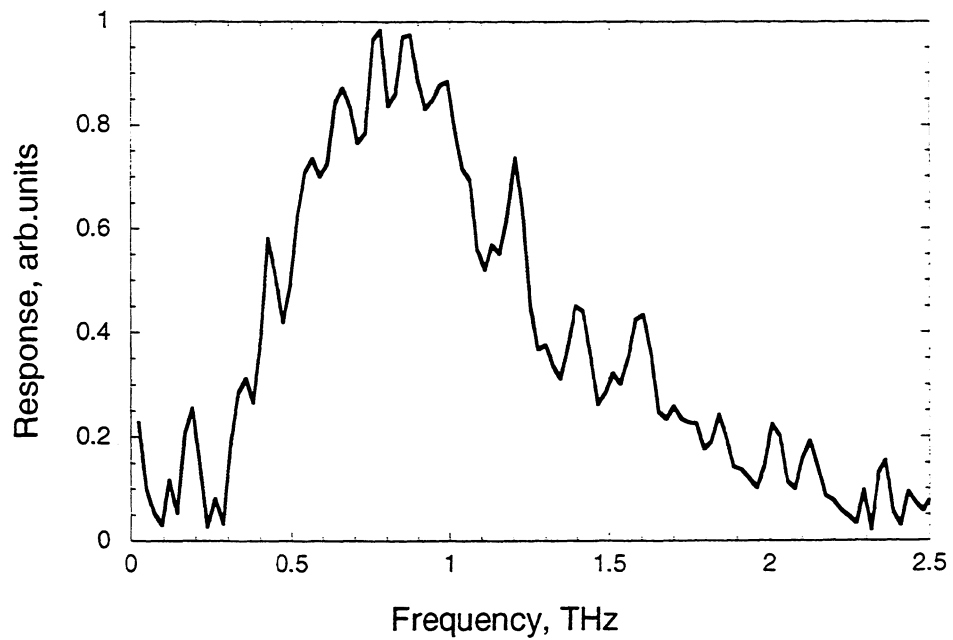


Fig.6. FTS spectrum measured for the device #2. The antenna extends one and a half turns and has an inner radius of 3 μm. The Si lens has an antireflection coating optimized for 660 GHz.

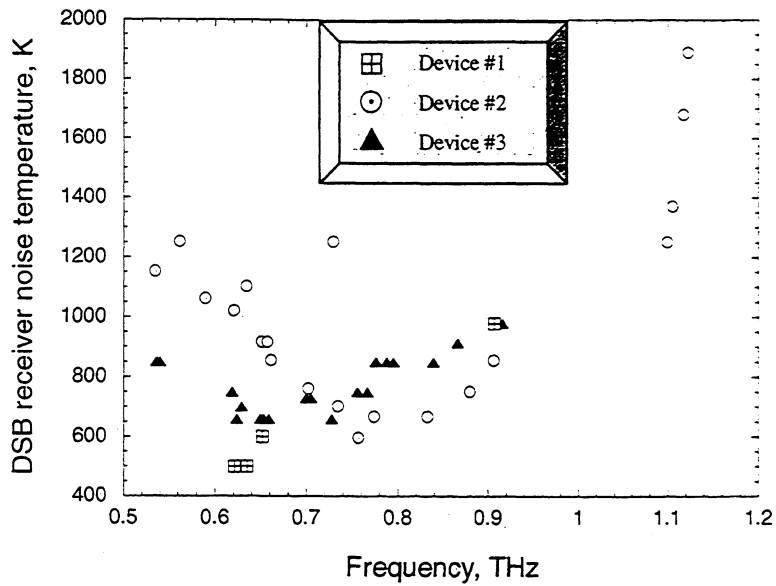


Fig.7. DSB receiver noise temperature as a function of LO frequency for three mixers.

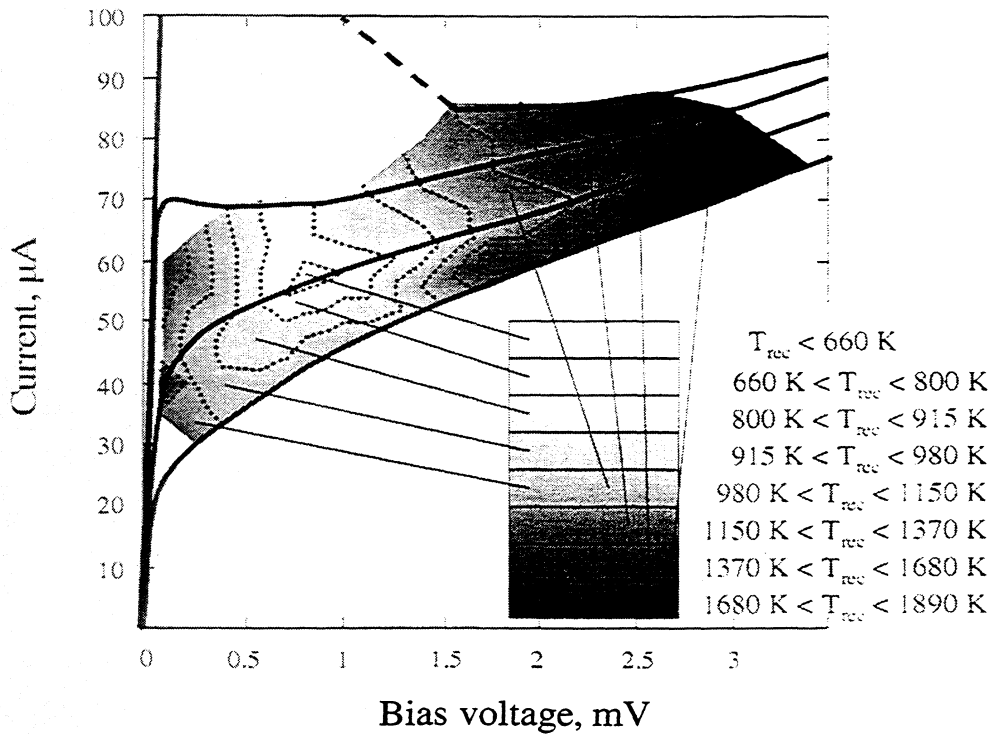


Fig.8. Pumped IV-curves of the device # 2 and results of noise temperature measurements for different positions of the operating point.

GAIN-BANDWIDTH CHARACTERISTICS OF HIGH- T_c SUPERCONDUCTING MILLIMETER-WAVE HOT-ELECTRON BOLOMETER MIXERS

Chao-Te Li, Bascom Deaver Jr., Robert M. Weikle II. and Mark Lee *

University of Virginia, Charlottesville, VA 22903

Rajesh A. Rao and Chang-Beom Eom

Duke University, Durham, NC 27708

ABSTRACT

The conversion gain bandwidth characteristics of millimeter-wave mixers using high- T_c superconducting $\text{YBa}_2\text{Cu}_3\text{O}_7$ (YBCO) thin films are presented. The YBCO films are patterned into lattice-cooled hot-electron bolometers (HEB) coupled to an integrated antenna and transmission line. Direct heterodyne and homodyne down-conversion measurements using local-oscillator frequencies of 75 GHz and 585 GHz show overall conversion gains of -35 dB, which includes a -18 dB coupling loss. The gain bandwidth shows a simple Lorentzian roll-off with -3 dB point of 5 to 8 GHz. No second plateau in the gain spectrum has been observed, in contrast to other reports. The effective volume of the HEB is believed to be significantly smaller than the physical dimensions of the device.

Gershenson, *et al.*¹ first proposed the design of a lattice-cooled superconducting hot-electron bolometer (HEB) for use as a low-power, wide-band-width heterodyne mixer at millimeter and submillimeter-wave frequencies. This idea has been successfully implemented using NbN^2 , which shows a conversion gain as high as -15 dB using 1 μW of pump power at a temperature of 4.2 K. The ultimate speed and bandwidth of the lattice-cooled HEB is determined by the electron-phonon scattering rate. For this reason, Gershenson³ suggested that the high normal-state resistivity of the high- T_c superconductor $\text{YBa}_2\text{Cu}_3\text{O}_7$ (YBCO) could indicate a very fast electron inelastic scattering rate and so make this material an ideal candidate to produce a very wide instantaneous

bandwidth lattice-cooled HEB operating at 77 K. The first reports of such mixers at 1.5 μm (Ref. 4) and 9.6 μm (Ref. 5) wavelengths showed a very low intrinsic conversion gain of -77 dB (excluding coupling losses) using a relatively large 0.3 mW of absorbed LO power. However, the gain bandwidth showed a two-plateau structure. A low frequency plateau near -77 dB rolled off near 1 GHz intermediate frequency (IF) but gave way to a second plateau near -90 dB that extended to at least 18 GHz, the upper limit of the measurement.

Karasik, *et al.*,⁶ have done extensive calculations on the conversion gain properties of lattice-cooled HEB mixers for different mixer dimensions, using a two-temperature model. They found that the conversion gain increases

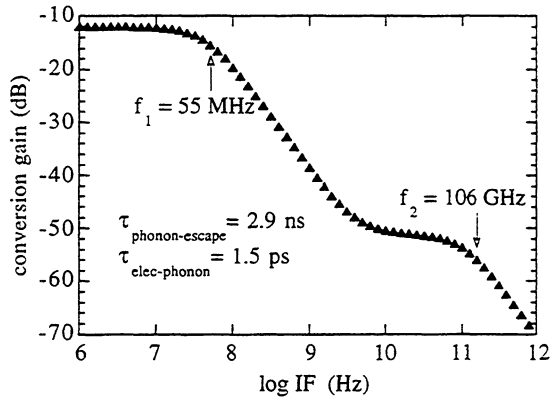


Figure 1: Calculation of the conversion gain bandwidth for a YBCO HEB mixer using the model of Ref. 6. An ideal 100% coupling of power to the HEB is assumed. The parameters used, including the phonon escape lifetime and the electron-phonon scattering time, are appropriate to YBCO with the nominal physical dimensions of the devices discussed in the text.

and noise temperature decreases for smaller bolometer volumes. The conversion gain bandwidth of the HEB is determined by the time it takes to remove heat from electrons via electron-phonon scattering and the escape of phonons from the bolometer. The latter is the slower time scale and is determined primarily by the bolometer thickness, with thinner bolometers leading to faster response times. The first roll-off in the reported two-tiered bandwidth structure was interpreted as a consequence of the phonon escape time from the HEB, and the upper limit of the second plateau interpreted as caused by the electron-phonon relaxation rate. Time-resolved measurements⁷ of the electron-phonon relaxation rate in YBCO show a relaxation time of 1.5 ps, leading to a calculated upper bandwidth limit of order 100 GHz. Fig. 1 shows the calculated two-tiered conversion gain bandwidth for a YBCO HEB with the nominal physical dimensions of our

device, using the model of Ref. 6. The low-frequency plateau shows a maximum intrinsic conversion gain of -12 dB, dropping to -50 dB at the second plateau. Because of the relatively thick (100 nm) films used, the slow phonon escape lifetime leads to a first roll-off point f_1 of only 55 MHz.

We recently reported on the low power responsivity and conversion gain characteristics of small YBCO HEBs operating near 77 K.⁸ A 60 dB improvement over previously reported values in the intrinsic conversion gain near 2 GHz IF demonstrated the potential of the YBCO HEB as a useful mixer. Here we address the conversion gain bandwidth characteristics of these mixers. In contrast to Refs. 4 and 5, we observe a single roll-off conversion gain bandwidth with -3 dB point of 5 to 8 GHz in these high-gain mixers. Based on the analysis of Ref. 6, this relatively high conversion gain, combined with the high resistance of the device, indicates that the effective volume of the HEB is significantly smaller than the nominal physical dimensions of the device.

The HEBs began as YBCO thin films nominally 100 nm thick covered with ~ 2 penetration depths of a gold overlayer, all on MgO substrates. A double-slot antenna and co-planar transmission line were then etched into the YBCO/Au using an ion beam (see Fig. 2). The Au overlayer was removed over the area of the HEB itself, which had nominal physical dimensions $2 \mu\text{m}$ (width) $\times 2 \mu\text{m}$ (length) $\times 100$ nm (thickness), using a non-aqueous iodine-based Au etch which did not affect the superconducting transition temperature or width

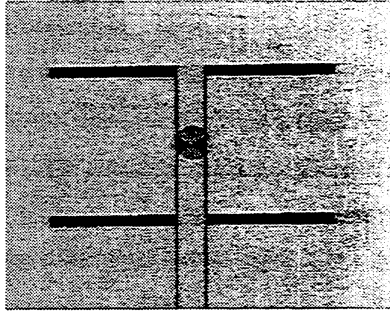


Figure 2: SEM micrograph of a YBCO HEB coupled to a 585 GHz double-slot antenna and a co-planar transmission line. The $2\ \mu\text{m} \times 2\ \mu\text{m}$ HEB itself is at the intersection of the two tapered antenna arms in the center of the picture. The width of the antenna arms is $175\ \mu\text{m}$.

and was found to be more reliable than the timed argon ion beam milling previously used. Finished bolometers had room temperature resistances of 300 to 600 Ω , transition widths of 2 to 3 K at around 85 K, and nominal critical currents at 77 K of ~ 0.1 mA.

Measurements were done quasi-optically. Samples were clamped onto a silicon hyper-hemispherical lens and heat sunk to a copper block. Sample temperature could be varied from 66 to 93 K. For direct heterodyne conversion gain measurements, two tunable Gunn

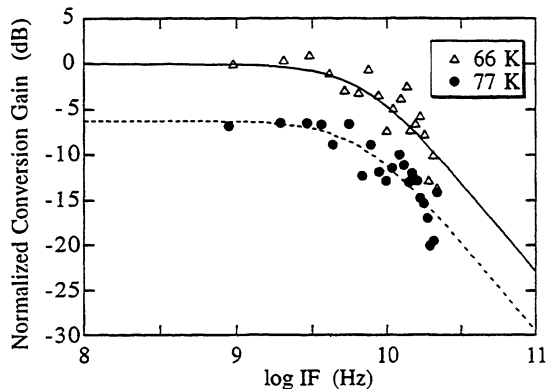


Figure 3: Measured conversion gain bandwidth at two sample temperatures for 75 GHz LO frequency using $2\ \mu\text{W}$ LO power. Data are normalized to the low-frequency gain at 66 K. The fits are simple Lorentzians, with -3dB points of 8 GHz (66 K) and 6.5 GHz (77 K).

diodes (75 to 90 GHz) were used. Attenuators kept the total power ≤ 1 mW in all measurements. The difference frequency generated by the HEB was amplified using a cooled microwave amplifier with bandwidth of 20 GHz. At 585 GHz, homodyne response was measured by using a Schottky diode in a corner cube to generate amplitude modulated sidebands onto the beam from a gas laser. Sidebands could be tuned up to 20 GHz off the laser line. Sideband power (1 to 10 μW) was calibrated using a known Schottky diode receiver.

Fig. 3 shows the measured conversion gain bandwidth at two different temperatures for one of our YBCO HEBs using $2\ \mu\text{W}$ of LO power at 75 GHz. The rf power was kept at $0.1\ \mu\text{W}$ and was tuned upward from the LO. Data are normalized to the low-frequency gain at 66 K. Estimating a coupling loss of 18 dB from pumped and unpumped I - V curves,⁹ the intrinsic conversion gain to be compared with Fig. 1 is approximately -17 dB at the lowest frequencies at 66 K. The conversion gain is slightly lower and has a lower frequency roll-off at the higher temperature. At both temperatures, the data are well fit by a simple Lorentzian with -3 dB roll-off of 6.5 GHz at 77 K and 8 GHz at 66 K. There is no sign of a second plateau in the spectrum up to 20 GHz IF. Similar Lorentzian bandwidths were observed with other samples in the homodyne measurements at 585 GHz LO frequency. Typical -3 dB frequencies measured with 585 GHz were ~ 5 GHz.

There are several important differences between the data shown above and the data of

Refs. 4 and 5 and the calculation of Ref. 6. Most markedly, we do not observe a two-plateau gain-bandwidth structure. Using smaller LO power, the single Lorentzian bandwidth shown in Fig. 3 has an overall conversion gain two orders of magnitude larger, and a -3 dB roll off at frequencies 5 to 8 times higher, than the comparable values reported in Refs. 4 and 5. While we have not observed evidence of a two-plateau structure, it is possible that the restricted frequency range of the measurement allows us to observe only one of the two plateaus. If so, the measured intrinsic conversion gain of -17 dB agrees much more closely with the the calculated low-frequency plateau conversion gain of -12 dB in Fig. 3, rather than the -50 dB gain of the second plateau. This suggests that of the two frequency plateaus, the lower frequency one whose roll-off is set by the phonon escape time is being measured.

However, the bandwidth of the first plateau was calculated to be only 55 MHz given the nominal 100 nm thickness of the YBCO film, compared to the measured bandwidth of 5 to 8 GHz. It is possible that the larger bandwidth we observe pushes out the first plateau far enough to obscure a clear observation of the second plateau within our measurement limits.

The higher than expected bandwidth implies, within the two-temperature model, a faster phonon escape time. This can result from a combination of a thinner HEB than the nominal dimensions indicate, and the presence of effective phonon escape routes from the HEB other than to the substrate. If phonons escaped only to the substrate, to obtain a first roll-off of

5 GHz would require a bolometer thickness of ~ 1.5 nm within the model of Ref. 6. Such a small thickness is inconsistent with the good superconducting transition in the DC resistance of these devices.

The idea of having a smaller effective superconducting bolometer volume is consistent with the high normal-state resistivity of the device. Given the nominal dimensions of the bolometer and an upper bound on the room-temperature resistivity of $300 \mu\Omega\text{-cm}$ for YBCO films showing a good superconducting transition, the device is expected to have a room-temperature resistance of less than 30Ω , while we measure $\geq 300 \Omega$ routinely. Because the entire device shows a DC super-current, the entire length of the bolometer must superconduct. The high resistance must then come from a decrease in the supercurrent-carrying cross-sectional area. Similarly, a good YBCO film should have a critical current density of at least $5 \times 10^5 \text{ A/cm}^2$ at 77 K, while the measured values for our devices indicate critical current densities ten times lower using the nominal width and thickness. Based on the resistivity and the critical current, we estimate the effective superconducting thickness of the HEB to be closer to 15 to 20 nm. It is quite possible that etching damage to the top and edge surfaces can degrade the exposed YBCO and leave only a smaller region in the center of the patterned film with good superconducting properties.

The decrease in sample cross-section is actually fortuitous. Higher resistance makes it easier to obtain a 50Ω impedance match to the antenna and transmission lines when operating

the bolometer in the superconducting transition. Also, the smaller effective thickness and volume gives a faster phonon escape time to the substrate and provide alternate phonon escape paths to the damaged non-superconducting material at the edges and sides. The decrease in the escape time leads naturally to a higher conversion gain bandwidth. Finally, the calculations of Ref. 6 indicate that the mixer noise temperature should decrease with smaller HEB volumes. Preliminary measurements of the mixer noise show an input noise temperature of around 5,000 K for our best (highest conversion gain) samples at the optimal operating point. This noise figure is also much lower than expected for an HEB of the nominal physical dimensions we use, but is consistent with a mixer of significantly smaller superconducting volume.

In summary, we have reported on conversion gain bandwidth measurements for high- T_c superconducting YBCO hot-electron bolometer mixers. Using LO frequencies of 75 GHz and 585 GHz, simple Lorentzian bandwidths were measured with -3 dB IF roll-offs between 5 to 8 GHz. This is in contrast to two-tiered roll-offs reported by others. The larger bandwidths we observe may be due to a faster phonon escape time resulting from a smaller superconducting cross-section than the nominal dimensions of the device indicate, as well as alternate phonon escape routes. The DC resistance of the device, the critical current, and noise temperature measurements also support a smaller effective volume.

This work was supported by NSF grant no. ECS-9623893 and the U.S. Army National Ground Intelligence Center.

* email: marklee@virginia.edu

¹E. M. Gershenzon, G. N. Gol'tsman, I. G. Gogdize, Y. P. Gusev, A. I. Elant'ev, B. S. Karasik, and A. D. Semenov, *Sov. Phys. Supercond.* **3**, 1582 (1990)

²J. Kawamura, R. Blundell, C. E. Tong, G. Gol'tsman, E. Gershenzon, B. Voronov, and S. Cherednichenko, *Appl. Phys. Lett.* **70**, 1619 (1997)

³E. M. Gershenzon, G. N. Gol'tsman, Y. P. Gousev, A. L. Elant'ev, A. D. Semenov, and I. M. Pirogovskaya, *IEEE Trans. Magnetics* **27**, 1317 (1991)

⁴M. Lindgren, M. A. Zorin, V. Trifonov, M. Danerud, D. Winkler, B. S. Karasik, G. N. Gol'tsman, and E. M. Gershenzon, *Appl. Phys. Lett.* **65**, 3398 (1994)

⁵V. A. Trifonov, B. S. Karasik, M. A. Zorin, G. N. Gol'tsman, E. M. Gershenzon, M. Lindgren, M. Danerud, and D. Winkler, *Appl. Phys. Lett.* **68**, 1418 (1996)

⁶B. Karasik, W. R. McGrath, and M. C. Gaidis, *J. Appl. Phys.* **81**, 1581 (1997)

⁷F. Hegmann, D. Jacobs-Perkins, C.-C. Wang, S. H. Moffat, R. A. Hughes, J. S. Preston, M. Curte, P. M. Fauchet, T. Y. Hsiang, and R. Sobolewski, *Appl. Phys. Lett.* **67**, 285 (1995)

⁸C.-T. Li, B. S. Deaver, Mark Lee, R. M. Weikle, R. A. Rao, and C. B. Eom, *Appl. Phys. Lett.* **71**, 1560 (1997)

⁹H. Ekström, B. Karasik, E. Kollberg, and S. K. Yngvesson, *Microwave Guided Wave Lett.* **4**, 253 (1994)

2.5 THz GaAs MONOLITHIC MEMBRANE-DIODE MIXER A NEW PLANAR CIRCUIT REALIZATION FOR HIGH FREQUENCY SEMICONDUCTOR COMPONENTS

Peter H. Siegel, R. Peter Smith, Michael Gaidis, Suzanne Martin, Judy Podosek, Ute Zimmermann
California Institute of Technology, Jet Propulsion Laboratory, Pasadena, CA 91109

ABSTRACT

A novel GaAs monolithic membrane-diode (MOMED) structure has been developed and implemented as a 2.5 THz Schottky diode mixer. The mesa-style planar diode uses a rectangular anode with a T-shaped metalization and a footprint that measures nominally $0.2\mu\text{m}$ by $1\mu\text{m}$. It is integrated onto a $3\mu\text{m}$ thick by $36\mu\text{m}$ wide by $600\mu\text{m}$ long GaAs membrane which bridges across an aperture in a monolithic all GaAs support frame approximately $50\mu\text{m}$ thick. RF filter structures are incorporated on the $600\mu\text{m}$ long membrane. The membrane frame and RF circuit are coupled to an electroformed waveguide mount that places the diode across the center of a 2.5 THz full height rectangular waveguide ($100\times 50\mu\text{m}^2$). The mixer mount contains an integrated Pickett-Potter feed horn and rectangular waveguide transformer, suspended-stripline single-mode RF filter channels to house the membrane, a fixed waveguide backshort for RF matching and a quartz-based transformer for the desired 7-21 GHz IF output. Measurements of receiver performance, in air, yield a T_{receiver} of 20,000 K DSB at 8.4 GHz IF using a 150K commercial Miteq amplifier. The receiver conversion loss measures 17 dB (including air, diplexer, IF filter and horn coupling losses), yielding a derived front-end noise temperature of approximately 12,500K DSB at 2514 GHz. A CO_2 pumped methanol far-IR laser is used as a local oscillator at 2522 GHz and is injected with a Martin-Puplett diplexer. The required local oscillator power is below 3mW for optimum pumping, and no device damage was observed with incident power as high as 22mW. Improvements in noise temperature are expected as the devices and circuits are still being optimized. The mixer is baselined for flight use on the Earth Observing System Microwave Limb Sounder instrument to measure O_2 at 2502 GHz and OH at 2510 and 2514 GHz. EOS-MLS is scheduled for launch in 2002 on the Chem I platform, as part of NASA's Mission to Planet Earth.

I. INTRODUCTION

The THz frequency range offers a unique challenge for both heterodyne circuit and device designers. It represents a cross-over regime where wavelength scales stretch the tolerances of traditional machining as well as the dimensions and geometries accessible through photolithographic processes. In addition, critical device and RF circuit dimensions require submicron resolution to reduce parasitics whereas surrounding circuitry, especially at the intermediate frequencies which lie in the microwave bands, require macroscopic structures with smooth mechanical and electronic transitions to the RF environment. In this paper we report on a process and component design which blends the flexibility of mechanical machining and the tight tolerances and multiple die processing advantages of micro-machining. Although the techniques and circuit concepts described in this paper have been aimed at a specific flight component realization, a 2.5 THz Schottky diode mixer, other millimeter and submillimeter-wave GaAs semiconductor circuits can be enhanced with similar processing: frequency multipliers, detectors, oscillators, antenna coupled devices, planar array circuits, etc. The mixture of semiconductor and mechanical fabrication techniques, the blending of the active device and surrounding passive RF circuitry, the enhanced reliability and ease of handling of the planar circuit and the solid RF performance achieved with the first demonstration circuit, have opened a window of opportunity for submillimeter-wave semiconductor circuitry.

II. GaAs MEMBRANE

IIa. Introduction and Concept:

Due to moding effects, high frequency circuits are often limited by the thickness of the support substrates that must be used to define the active and passive RF structures used for signal processing. After device and circuit processing, microwave semiconductor substrates are generally mechanically lapped to a thickness as small as 50 microns; but even 50 microns is too thick for microstrip cir-

cuits above 300 GHz. Also, III-V semiconductors like GaAs are extremely brittle, and handling is a major problem with these wafer dimensions. Wet chemical etching has been used to thin GaAs-based devices to a thickness of <5 microns, but here again, handling and cracking of the substrate material becomes a major concern.

Silicon micromachining techniques have been used very successfully to make a variety of RF structures and components, including superconducting mixers, with dimensions compatible with THz circuitry [1-6]. However, these components rely on the mechanical, not the electrical properties of the silicon for their applications. At high frequencies, silicon cannot be used to form good quality active devices, i.e., diodes, transistors, etc. For device applications above 50 GHz, III-V semiconductors, especially GaAs, are preferred over silicon. Several research groups [7-10] have recently investigated GaAs membrane structures. These approaches have led to techniques for fabricating GaAs membranes of multiple shapes and sizes for a few assorted mechanical applications. Although some device incorporation has been attempted [8, 11], no one has yet taken advantage of the combined device/RF properties afforded by a GaAs membrane technology, nor realized a membrane fabrication approach that is compatible with existing high frequency circuits and devices.

The GaAs membrane process we have developed is tailored specifically for compatibility with existing RF circuit and two terminal device realizations at THz frequencies. It is a relatively straightforward process, requires no strongly anisotropic etchants, makes use of a simple epitaxial layer structure with two AlGaAs etch stops and is directly compatible with our existing THz planar diode fabrication process [12].

IIIb. Diode and Membrane Fabrication:

The 2.5 THz mesa air-bridge T-anode Schottky barrier diodes used for the mixer circuit described in this paper are fabricated in a process which is similar to one we developed for THz resonant tunneling diodes [13] with a few enhancements and a novel planarization step. In order to allow subsequent membrane formation the GaAs host wafer has the epitaxial structure shown in Fig. 1. The only additional layer structure required over our traditional mesa Schottky diodes are the 3 μ m thick semi-insulating layer and the lower etch stop which define the membrane. All device and surrounding RF circuit processes are completed before membrane definition occurs.

For the 2.5 THz diode definition, the wafer structure consists of a thin (<1000 Å), $10^{18}/\text{cm}^3$ n-type Schottky layer, a heavily doped (5×10^{18}), one micron thick n+ layer for low-resistance ohmic contact and a thin (≈ 600 Å) AlGaAs etch stop layer. Front-side lithography is defined using a combination of tools including a 5x I-line projection mask aligner, a 50 kV electron beam system, and contact lithography. Conventional recessed Au/Ge/Ni/Ag/Au ohmic contacts are used. Two mesas are required for each device because of our anode process [13]. The active mesa is only about a micron larger than the ohmic contact, and it is etched using a selective $\text{BCl}_3/\text{SF}_6/\text{Ar}$ mixture in an electron cyclotron resonance (ECR) reactive ion-etch system (RIE). Mesa edges and the etched field are smooth. A subsequent metalization step is used to provide air-bridges to the tops of the vertical mesa walls and to form the RF filters and the IF and DC bias lines used to connect the diode with off-chip mixer circuitry.

Anodes are formed using a novel PMMA quasi-planarization technique followed by a PMMA/copolymer/PMMA trilayer resist as is commonly used for HEMT or FET T-gates [13]. The PMMA planarization is done by spinning on multiple layers of 495k PMMA to a thickness of approximately 4 to 5 microns, much thicker than the height of the mesas, followed by a sequence of deep-UV blanket exposures and brief acetone spin-develop steps until the mesa tops are exposed. PMMA was chosen for the planarization because more commonly used substances turned out to be incompatible with the PMMA used for the anode lithography. The definition of the Ti/Pt/Au anodes has been described elsewhere [14]. Finally, plasma enhanced chemical vapor deposition (PECVD) silicon nitride is used to passivate the finished devices.

The first membrane-related processing step lithographically defines the membrane strips from the topside of the wafer. CF_4/O_2 RIE is used to remove the silicon nitride device passivation layer. An ECR system using BCl_3/Ar , then $\text{BCl}_3/\text{SF}_6/\text{Ar}$, is used to continue etching down to the lower AlGaAs etch stop layer. Material must be left wherever the membranes themselves are to be formed as well as over the tops of the frames so that there is no step incurred for the metalization layer as it traverses the frame.

The wafer is next mounted topside-down, using wax, onto a suitable carrier wafer, e.g. silicon, glass or sapphire. The backside is then lapped and polished to the desired frame thickness of 50 μm . After lapping, the backside of the wafer is cleaned by subjecting it to a light etch and then protected by a low temperature deposited (ECR) silicon nitride layer. The back of the wafer is then coated with photoresist and, employing a backside aligner, the relative positioning of the membrane and support frame is accomplished. The silicon nitride is then etched from all non-frame areas, including all membrane areas, by reactive ion etching.

The frames are then formed by wet etching in an $\text{H}_2\text{O}_2/\text{NH}_3\text{OH}$ mixture [15] that selectively etches GaAs relative to AlGaAs. A brief non-selective etch (phosphoric acid/hydrogen peroxide/water) is then used to remove the AlGaAs etch stop. An additional lithography step and dry etch can be employed to expose metal beam leads overhanging the edges of the frames when such leads are desired.

The membranes with their associated RF structures and frames are now completely defined. The finished parts can be removed from the carrier wafer by dissolving the wax and any remaining photoresist in an appropriate solvent. The parts can be collected in a fine mesh placed in the bottom of the solvent vessel. No dicing or cleaving of the final parts is required. Process steps are shown in Fig. 2 and SEM micrographs of the finished parts appear in Fig. 3.

III. 2.5 THz MIXER

IIIa. Introduction and Concept:

The lowest order OH doublets at 2510 and 2514 GHz are strong tracers for the reaction rates of key ozone depleting cycles in the Earth's atmosphere. By a fortuitous coincidence of nature, a strong methanol laser line at 2522 GHz can be used as a pump source for heterodyning; producing IF's at 8 and 12 GHz. An O_2 line at 2502 GHz provides a convenient pressure (altitude pointing) calibration at an IF of 20 GHz. A receiver noise temperature of 20,000K single sideband (30K for receivers at both polarizations) provides enough sensitivity to allow daily global stratospheric maps of OH above 35 km and weekly zonal maps above 18 km from a satellite in polar orbit. These requirements are consistent with the performance that can be obtained from state-of-the-art room-temperature Schottky diode mixers.

Whisker-contacted corner cube mixers have been used at frequencies at and above 2.5 THz for many years [16-19 for example]. Although the performance that has been reported [18], can be exceptionally good compared to mixers at other frequencies, as far as space-based remote sensing applications are concerned, the corner-cube suffers from three major drawbacks: (1) low reliability (anyone who has used one will attest to this), (2) poor beam quality and (3) extremely tight assembly tolerances that substantially affect RF performance and beam shape.

Recently, a group at Rutherford Appleton laboratory fabricated a waveguide-based 2.5 THz mixer with a novel "planar-whisker" contact [20]. The reported performance of this mixer was not quite as good as the better corner-cubes, but was very reasonable, and subsequent work has improved the noise temperature substantially [21]. Advantages of the RAL mixer include improved reliability (the planar whisker is more repeatable and reliable than its corner-cube counterpart) and in the improved efficiency obtained from single-mode waveguide-to-horn antennas. Members of the RAL team also proposed [22] a structure, which goes several steps further and integrates the semiconductor diode and whisker contact into a fully planar circuit that can be coupled to a photolithographically defined waveguide.

The technology presented in this paper has the same goals as the Rutherford Appleton work: to increase the reliability and performance of THz diode mixers relative to the traditional corner-cube mixers. We utilize the monolithic membrane diodes (MOMED's) described in the previous section, integrated into a mechanically machined waveguide circuit. This combination affords high reliability, solid performance, and ease of assembly.

IIIb. Mixer Design and Fabrication:

The mixer design is based upon a scaling of lower frequency single-ended mixer circuits with modifications that allow for relatively simple fabrication and assembly at 2.5 THz. Since the intended application is a space-based instrument, special consideration is given to device and circuit reliability and performance repeatability.

The mixer consists of five pieces: (1) the monolithic membrane diode (MOMED), which contains all RF filter circuitry, (2) an electroformed "button-mount" that houses the membrane and a single mode 2.5

THz signal waveguide and feed horn, (3) an interchangeable fixed depth "hobbed" backshort section, (4) a fused quartz suspended-substrate IF transformer, and (5) a split-block housing that holds the RF and IF pieces as well as DC bias resistors and DC and IF connectors. A separate IF amplifier is required as well as an appropriate RF diplexer for LO injection.

The MOMED's unique bridge structure (Fig. 3) allows placement of the diode across the center of the broad wall of the 2.5 THz waveguide. Surrounding the diode on the membrane are low pass filters which both block RF propagation from the waveguide port and provide RF shorts at the waveguide walls. Unlike the configuration described in [2], the thin (36 μm wide, 600 μm long) membrane bridge is actually suspended along the centerline of a sealed single-mode transmission line cavity (60 wide x 40 μm high cross-section, metal on all sides) forming a 3 μm thick GaAs suspended stripline circuit. The membrane support frame lies outside the sealed cavity (active RF area) and is intended to have no effect on the signal coupling. A finite difference time domain (FDTD) analysis [23] of the filter is shown in Fig. 4. An interesting result of the analysis was the appearance, at the center of the stop band, of what we believe is a propagating ridge waveguide mode between the membrane and cavity side. This mode could only be reliably suppressed by reducing the height of the stripline cavity from 60 to <40 μm , hence the resulting asymmetric cross section.

The membrane thickness (3 μm) was chosen as a compromise between ease of fabrication (epitaxial growths of >4 μm are expensive) and mechanical robustness. Careful adjustment of the membrane layer thickness to avoid mechanical stress (a concern in silicon nitride membrane configurations) does not appear to be necessary. In our tests a membrane thickness of 3 μm gave sufficient robustness to a 600 μm long, 36 μm wide beam, for withstanding fairly relaxed handling procedures. No strain related bowing was visible, even after device and metal deposition. Membranes of 1.2 and 2 μm thickness with widths varying between 10 and 80 μm were also fabricated on test wafers and, although they survived routine handling and had no signs of mechanical stress, the thinner membrane structures were deemed a bit too fragile for the repeated handling expected in a flight program.

The length of the membrane bridge was chosen to be as short as possible and still accommodate sufficient high/low impedance filter sections for reasonable RF rejection. The membrane frame size was selected to

be large enough for handling, yet small enough to have a negligible effect at the highest IF frequency (21 GHz). The diode epitaxial layer properties and anode area were selected to minimize parasitic effects without compromising severely the diode non-linearity (ideality factor no higher than 1.5). Initial wafer variations included only anode area (.1x1 and .2x1 microns), anode finger shape (an S-bend was included in case stress on the membrane turned out to be a problem; it didn't) and required process variation bracketing. A membrane variation which included overhanging beam leads (for IF and DC bonding) was also included, but processing of the beam leads was not completed on the first device run.

Upon completion of the membrane fabrication process, the separated circuits are collected on filter paper, transferred en masse to a wafer holder and individually probed and sorted before being inserted into the mixer block. Device yield on the first quarter wafer run was fairly poor with only about 10% of the diodes surviving with good DC performance characteristics (series resistance below 20 ohms, leakage current below 5 microamps). Yields were limited by three problems. The photolithographically defined air-bridges need to be slightly altered on future runs. Also, the e-beam anode formation is quite difficult, and the first wafer's yield was particularly low in this step. Finally, device characteristics appear to have degraded through backside processing, particularly on the devices with smaller anodes. Improvements have been made in the backside process that should eliminate the last problem. A second quarter wafer is now in processing.

Mechanically, almost all the membrane structures survived intact and there is no observed strain or strain related problems (diodes that were processed to completion did not fail during storage or handling although their small area makes them more susceptible to damage from static discharge than our lower frequency diodes). Device reliability appears to be very high, although no Arrhenius tests have as yet been completed. Sample devices were thermally cycled from -50 to +150 C (10 cycles, 15 minute dwell) with no observed changes in their DC characteristics. One mounted device was also subjected to vibration (average 9.2 g's, 10 Hz to 2 kHz) with no mechanical problems. During device mounting, the membrane frames are picked up, dropped into place in the mixer block, glued with cyanoacrylic, probed and finally subjected to ultra-

sonic wire bonding (one bond on each side) while they are in place in the waveguide block, all with no apparent detrimental effects.

The RF coupling circuit, which provides signal and LO to the membrane diode, is formed in a standard copper electroforming operation. This electroformed "button mount" (Fig. 5.) contains a single mode 2.5 THz rectangular waveguide (nominally 100x50 microns), a tapered transition to circular waveguide and a scaled Pickett-Potter dual mode feed horn [24] (aluminum mandrel shown in Fig. 6).

Other than the small waveguide dimensions, no special requirements are placed on the fabrication at this point. Following electroforming, but while the aluminum mandrel still fills the waveguide cavity, the button mount is machined to final size (.187x.075"). A relief cavity to house the membrane frame is then milled into the copper and the suspended stripline filter cavity is machined across the button and through the center of the waveguide using a high speed diamond saw with a cubic boron nitride blade. The depth of the stripline cavity channel is set at this time to precisely locate the membrane bridge and frame below the surface of the button, at a depth determined by two support ledges that have been machined into the frame relief slot. These ledges catch, and support, the bottom of a membrane web left between two dog-ears on the sides of the membrane frame. Since the ledge references the membrane itself, it precisely positions the suspended stripline filter vertically in the enclosed cavity. After dicing the stripline slot, the aluminum mandrel is etched out of the copper button using NaOH.

The button mount is press fit into a brass split-block mount that also contains a much larger stripline cavity to house the IF transformer and the bias and IF connectors. Machining of this portion of the mixer block is straightforward.

In order to provide some degree of adjustable matching to the diode, a fixed depth backshort cavity, aligned with the 2.5 THz waveguide, is added over the top of the membrane. Since the membrane frame support ledges locate the membrane and the top of the frame below the top surface of the button mount, the waveguide and stripline cavity are completely sealed off by the backshort cavity block. The backshort cavity itself is easily formed using a hobbing technique to punch the rectangular hole to depths as great as several mills. A range of cavity depths is readily obtained by repeated "hobbing" to produce random depths and a few finishing strokes on some fine lapping paper.

Alignment of the blind waveguide in the backshort piece with the waveguide in the button mount is accomplished by picking up alignment holes in both parts under an optical microscope. The fixed backshort feature makes tuning rather time consuming, but assures extremely stable and repeatable measurements and requires no changes for flight implementation. Optimal cavity depth so far varies only by a few microns for different diodes of the same nominal anode size.

The final piece of the mixer block is the IF transformer which converts the expected diode output impedance of 200-250 ohms to 50 ohms over the required IF bandwidth of 7-21 GHz. In order to be mechanically and electrically compatible with the tiny membrane structure and at the same time provide a very high impedance at the output of the GaAs filter, a thin (125 μm) fused quartz, suspended stripline transformer design was selected. The stripline cavity is sized to provide the 250-to-50 ohm impedance range and match (at the connector side) to a standard microstrip launcher. Due to some initial moding problems with the connector-to-stripline joint at 20 GHz, the original wide tab (0.050") launcher had to be replaced with a .020" wide tab launcher [25]. A through measurement on two back-to-back 200-to-50 ohm transformers is shown in Fig. 7.

Assembly of the mixer block is fairly simple and can usually be accomplished in less than an hour. The membrane device is carefully placed in position in the provided button cavity and checked for relative height with respect to the provided support ledges (usually not a problem, so long as no particulates have fallen onto the ledge). The frame is then held in place with a wafer probe while cyanoacrylic is generously applied to the frame edges. The quartz stripline is already glued in place at this time. Half mil wire bonds are now added from the frame across to the quartz stripline filter metal on one side, and to the continuation of the stripline channel slot on the far side of the button mount. Bonds are also added for the bias resistors and the tab launcher at this time. The backshort cavity is then lightly screwed in place and optically aligned before being locked down with a set screw on the top half of the split block. A photo of the assembled mixer (without the backshort cavity and with the top half removed) can be found as Fig. 8 and a close up of the membrane mounting is shown as Fig. 9.

IV. PERFORMANCE

IVa. Test System:

Accurate RF noise measurements at 2.5 THz are complicated by several factors: high mixer noise temperatures, variable atmospheric attenuation, poorly calibrated "absolute power" detectors, unavailability of matched attenuators, "gray body" loads, and imperfect Gaussian beams. The measurement test system used here to overcome these difficulties is shown schematically in Fig. 10. Local oscillator power is generated by a CO₂ -pumped methanol gas laser with a maximum output power of more than 100 mW at 2522 GHz. A Martin-Puplett style wire grid diplexer is used to spatially combine the LO and signal beams. An off-axis ellipsoidal mirror matches the beam of the diplexer to that of the Pickett-Potter feed horn. The laser beam profile at 2.5 THz can be coarsely viewed with low thermal response liquid crystal paper, and, when the laser is properly tuned, appears to be circular with a single bright central spot. LO power measurement is provided by a "calibrated" Scientech multimode thermal detector and the numbers reported here should be taken with error bars of at least 3dB, due to beam mode and detector absorber non-idealities.

The noise temperatures are measured using the standard Y-factor technique on the full receiver only. A chopper switches the signal beam between a hot load (wedged Eccosorb CR110) and a cold load (Eccosorb AN74 flat sheet, soaked in liquid nitrogen, and held in the signal beam during the measurement. The assumed hot and cold load temperatures are 300 and 77K respectively, no corrections are made to account for mismatch or non-ideal Rayleigh-Jeans behavior. Note that incorporation of the more accurate Planck law would reduce the noise temperatures reported here by approximately 5%. A lock-in detector at the ≈ 100 Hz chopper frequency is used to extract a hot/cold load power output variation from a crystal diode detector. A correction factor of 0.45 is divided into the lock-in value to convert its RMS output to a peak-to-peak value (the chopper bowtie blade, radius 50 mm, produces a good approximation to a square wave as it switches the relatively small signal beam: waist radius of ≈ 4 mm). This peak-to-peak variation is then scaled by the DC average diode detector value to give the hot and cold powers needed for an accurate Y-factor measurement. This lock-in technique can be used to evaluate receivers with noise in excess of 500,000 K DSB.

For the results reported here, a broadband bias Tee [26] connects the mixer to a low-noise broadband IF amplifier [27]. The IF amplifier provides approximately

65 dB of gain over the frequency range 7 to 21 GHz, with noise at the low frequency end of ≈ 150 K, and at the high frequency end of ≈ 200 K. Coaxial filters [28] limit the detected bandwidth to ≈ 500 MHz about the desired center frequencies of 8.4, 12.8 and 20.4 GHz. Detected power is in the neighborhood of 10 microwatts. Front-end conversion loss is measured using a power meter to calibrate the response of the crystal diode detector, and extract the measured amplifier gain and filter loss (0.9 dB).

Mixer noise temperature can be extrapolated from the receiver measurements after separate IF amplifier calibration, but includes diplexer, atmospheric and horn coupling losses as well as any bias tee losses and IF impedance mismatch that may be present between the mixer output port and the amplifier. We can provide only approximate corrections for these losses until better calibration can be performed. They are distributed as follows: diplexer signal loss: 0.5 dB, mirror-to-horn coupling loss: 0.5 dB, IF mismatch loss: up to 3dB at 20 GHz based on relative IF measurements, atmospheric losses: 1 dB. More accurate values will be obtained in the future. For this paper, we will not attempt to calibrate out these losses, but will refer to "front-end" (rather than mixer) noise and loss as that belonging to all components forward of the IF amplifier.

During measurements, the mixer is current biased so that LO power fluctuations are compensated by a voltage change on the diode. We find that current bias (\approx curvature bias) makes the mixer relatively insensitive to changes of LO power. We observe nominally the same receiver noise temperature at fixed current when we alter the LO power by more than a factor of 5. The fluctuations visible on the graphs of noise temperature (Figs. 11-12) apparently arise from atmospheric fluctuations (variable water vapor content immediately in front of the cold load). In the near future, tests will be performed in vacuum to eliminate the effects of the atmosphere.

The entire RF noise test system is computer controlled and can be programmed to sweep bias current versus time to obtain the plots shown in the figures. Pumped and unpumped IV curves can also be generated (Fig. 11). Typically we operate with a lock-in time constant of 300 msec and 100 data points per curve.

IVb. Receiver/Mixer Noise:

The best measured receiver noise temperatures to date, using the test system described in the prior section, are given in Fig. 11. and are plotted against bias current flowing through the diode. The device which produced these results had a nominal area of $0.2 \times 1 \mu\text{m}^2$, a measured resistance of 16 ohms, an ideality factor of 1.53 and a saturation current of 3×10^{13} A. Smaller area devices have not yet yielded as good performance. A backshort depth between 12 and 25 μm consistently gave the best performance during tests of several different devices of varying resistance. Five devices have so far been measured and two have given performance similar to that shown in Fig 11. Fig. 11. also shows the dependence of receiver noise on LO power, with bias current again a fixed parameter. As can be seen from the figure, the current bias mitigates greatly the effect of LO power variation. In fact we were able to adequately pump the mixer with only 3 mW of measured LO power and could occasionally go as low as 2 mW without noticeably starving the diode. On the other extreme, pump power levels as high as 22 mW did not burn out the device and we could obtain essentially identical noise temperature vs. bias current curves for the two LO power extremes.

The extrapolated "front-end" noise, based upon a measured receiver conversion loss of 17 dB is shown in Fig. 12, again as a function of bias current at fixed LO power. All the data shown is at an IF of 8.4 GHz. At 12.8 GHz the receiver noise is within 5% that of 8.4 GHz, but at 20.4 GHz the noise performance is consistently a factor of two higher for all devices. We are not certain at this time of the origin of this degradation. One might focus on the IF chain, but as can be seen in Fig. 7, the IF transformer does not appear to account for the degradation, nor do the amplifier noise specifications.

We have not measured the mixer at any other LO frequency and the performance is sensitive to the backshort cavity depth. Changes of as little as 10 microns can result in changes of more than 50% in receiver noise. This is consistent with the sensitivity observed in lower frequency mixers that use full height waveguide.

So far we have measured only a small number of membrane devices and have not accumulated enough data to make any conclusions regarding the importance of the device DC parameters on RF performance. A large change in optimal backshort cavity depth was observed between the 0.1×1 and $0.2 \times 1 \mu\text{m}^2$ area diodes, with the smaller diodes requiring more matching inductance (larger cavity depth), but a more de-

tailed analysis on the full RF circuit has not yet been concluded. Only diodes with low leakage current and low series resistance (relative to those in the processed batch) have been measured so far and we cannot put any weights on the relative importance of these DC variables as yet. Further measurements on devices with different doping and epilayer profiles, anode areas and RF circuit configuration are clearly desirable. In the meantime we are preparing the existing mixer mount and membrane structure for use in space and are focussing more on reliability and system level parameters than performance at this time.

IVc. RF Beam Pattern:

As a final characterization measurement, we used the mixer as a direct detector to measure the beam pattern of the Pickett-Potter feed horn. The data is presented in Fig. 13. The laser beam quality allowed us to measure reliably only to the 10 dB level, but the beam widths at this and the 3dB point match those predicted in [24].

V. SUMMARY

A novel GaAs membrane diode circuit concept has been developed and demonstrated. The membrane fabrication process has been combined with our existing submillimeter-wave planar T-anode mesa Schottky diode process to design and fabricate a 2.5 THz waveguide mixer. Early measurements of mixer performance have shown the design to be competitive with alternative corner-cube and whisker contacted waveguide mixer concepts, although not as good as the best reported measurements in the literature. In addition, the required LO power is as low as 3mW (optimal) and 2 mW slightly starved. The membrane devices have proven to be both robust and reliable, having been taken through "shake and bake" at mil-spec levels. The waveguide block, although requiring careful machining and electroforming, is relatively simple to fabricate and assemble. The combination of the narrow membrane bridge circuit containing both the integrated planar diode and the RF filters, allows the implementation of sealed cavity single mode circuitry everywhere, even at wavelengths as short as 100 microns. The membrane fabrication process requires no post processing on the die as chemical etching replaces labor intensive dicing or scribe and break procedures. The lack of induced stress on the completed membrane makes it ideal for circuits where long thin bridging is required.

The circuit and device implementation demonstrated in this application can be employed for other submillimeter and millimeter wave components including multipliers or harmonic mixers (membrane couples to two different sized waveguides), heterodyne arrays (multiple membranes superimposed on a feed horn array), oscillators (cavity coupled membrane strip) or micromachined components (membranes used to span formed waveguides or cavities). The circuit described in this paper is being employed on a NASA flight mission and will undergo extensive lifetime and reliability screening before delivery of finished components.

VI. ACKNOWLEDGEMENTS

The authors would like to acknowledge the many valuable contributions of Pete Bruneau to the mixer block fabrication process. They would also like to thank John Oswald for help in setting up the FDTD analysis of the RF filters, Andrew Pease and Robert Lin for the device thermal cycling, Tracy Lee for the IF transformer processing and the remaining members of the SWAT (Submillimeter-Wave Advanced Technology) team for assorted technical support. Special acknowledgement is also due to Dr. Carl Kukkonen, Dr. Virendra Sarohia and Gary Lau at JPL for financial support of the program. This work was carried out at the California Institute of Technology Jet Propulsion Laboratory under contract with the National Aeronautics and Space Administration's Office of Advanced Concepts and Technology and the Earth Observing System Microwave Limb Sounder project office.

VII. REFERENCES

- [1]. G.V. Eleftheriades, W.Y. Ali-Ahmed and G.M. Rebeiz, "Progress in Integrated Circuit Horn Antennas for Receiver Applications: Part I and II," *Second International Symposium on Space THz Technology*, March 24-26, 1992, pp. 324-344.
- [2]. J.W. Kooi, M.S. Chan, P. Schaffer, B. Bumble, H.G. LeDuc, C.K. Walker and T.G. Phillips, "An 850 GHz Waveguide Receiver Using Tuned Nb SIS Tunnel Junction Fabricated on a 1 μm Si_3N_4 Membrane," *Seventh International Symposium on Space THz Technology*, March 12-14, 1996, pp. 86-102.
- [3]. G. de Lange, B. R. Jackson, A. Rahman, E. Duerr and Q. Hu, "Low-Noise Micromachined SIS Mixers for Millimeter-Wave Imaging Arrays," *Seventh International Symposium on Space THz Technology*, March 12-14, 1996, pp. 29-36.
- [4]. R.F. Drayton, C. Kidner, J. East and L.P.B. Katehi, "Micromachined Detector Mounts for Millimeter-Wave Applications," *Fifth International Symposium on Space THz Technology*, May 10-12, 1994, pp. 796-801.
- [5]. T. Weller, S. Robertson, L.P. Katehi and G.M. Rebeiz, "Millimeter and Submillimeter Wave Microshield Line Components," *Fifth International Symposium on Space THz Technology*, May 10-12, 1994, pp. 802-810.
- [6]. C.-Y. Chi and G.M. Rebeiz, "Planar microwave and millimeter-wave lumped elements and coupled-line filters using micromachining techniques," *IEEE Trans. Microwave Theory and Tech.*, vol. 43, no. 4, April 1995, pp. 730-38.
- [7]. Hjort, Klas, "Sacrificial Etching of III-V Compounds for Micromechanical Devices," *J. Micromech. Microeng.*, 6 (1996), pp. 370-375.
- [8]. Dehe, A., D. Pavlidis, K. Hong and H.L. Hartnagel, "InGaAs/InP Thermoelectric Infrared Sensor Utilizing Surface Bulk Micromachining Technology," *IEEE Trans. Electron Devices*, vol. 44, no. 7, July 1997, pp. 1052-1059.
- [9]. Uenishi, Yuji, H. Tanaka, and H. Ukita, "AlGaAs/GaAs Micromachining for Monolithic Integration of Micromechanical Structures with Laser Diodes," *IEICE Trans. Electron.*, E78-C, #2, 1995, pp. 139-145.
- [10]. Seassal, C., J.L. Leclerc, and P. Viktorovitch, "Fabrication of InP-based Freestanding Microstructures by Selective Surface Micromachining," *J. Micromech. Microeng.*, 6 (1996), pp. 261-265.
- [11]. C.I. Lin, A. Simon, M. Rodriguez-Gironies, H.L. Hartnagel, P. Zimmermann, R. Zimmerman, "Substrateless Schottky Diodes for THz Applications," to appear in *Proceedings of the Eighth International Symposium on Space THz Technology*, Cambridge, MA, April 1997.

- [12]. R.P. Smith, S.C. Martin, Moonil Kim, Jean Bruston, Dexter Humphrey, Neal Erickson, and P. H. Siegel, "Advances In Submillimeter Wave Semiconductor-Based Device Designs And Processes," to appear in *Eighth Int. Symposium on Space THz Technology*, Cambridge, MA, April 1997.
- [13]. T. Allen, M. Reddy, M.J.W. Rodwell, R.P. Smith, S.C. Martin, J. Liu and R. Muller, "Submicron Schottky-collector AlAs/GaAs resonant tunneling diode," *Proceedings Int. Electron Device Sym.*, Wash. D.C., Dec. 1993.
- [14]. R.E. Muller, S.C. Martin, and R.P. Smith, S.A. Allen, M. Reddy, U. Bhattacharya, and M.J.W. Rodwell, "Electron Beam Lithography for the Fabrication of Air-bridged, Submicron Schottky Collectors," *Journal of Vac. Sci. and Tech.*, Nov/Dec, 1994.
- [15]. W. Bishop, K. McKinney, R. Mattauch, T. Crowe, and G. Green, "A Novel Whiskerless Diode for Millimeter and Submillimeter Wave Applications," *1987 IEEE-MTT-S Digest*, June 1987, pp. 607-610.
- [16]. H. Krautle, E. Sauter and G.V. Schultz, Properties of a submillimetre mixer in an open structure configuration," *Infrared Physics*, vol. 18, 1978, pp. 705-712.
- [17]. J. Zmuidzinas, A.L. Betz and R.T. Boreiko, "A Corner-Reflector Mixer Mount for Far Infrared Wavelengths," *Infrared Physics*, vol. 29, no. 1, 1989, pp. 119-131.
- [18]. H.W. Hubers, T.W. Crowe, G. Lundershausen, W. C.B. Peatman and H.P. Roser, "Noise temperature and conversion losses of submicron GaAs Schottky-barrier diodes," *Fourth International Conference on Space THz Technology*, March 30-April 1, 1993, pp. 522-527.
- [19]. A.L. Betz and R.T. Boreiko, "A practical Schottky mixer for 5 THz," *Sixth International Symposium on Space THz Technology*, March 21-23, 1995, pp. 28-33.
- [20]. B.N. Ellison, B.J. Maddison, C.M. Mann, D.N. Matheson, M.L. Oldfield, S. Marazita, T. W. Crowe, P. Maaskant, W. M. Kelly, "First Results for a 2.5 THz Schottky Diode Waveguide Mixer," to appear in *Proceedings of the Eighth International Symposium on Space THz Technology*, Cambridge, MA, April 1997.
- [21]. Dr. Chris Mann, Rutherford Appleton Lab, private communication.
- [22]. S.W. Moon, C.M. Mann, B.J. Maddison, I.C.E. Turcu, R. Allot, S.E. Huq and N. Lisi, "Terahertz waveguide components fabricated using a 3D x-ray microfabrication technique," *Electronics Letters*, vol. 32, no. 19, 12 Sept. 1996, pp. 1794-1795.
- [23]. J.E. Oswald, P.H. Siegel and S. Ali, "Finite Difference Time Domain Analysis of Coplanar Transmission Line Circuits and a Post Gap Waveguide Mounting Structure," *Fifth International Conference on Space THz Technology*, Ann Arbor, Michigan, May 10-12, 1994.
- [24]. H.M. Pickett, J.C. Hardy and J. Farhoomand, "Characterization of a Dual Mode Horn for Submillimeter Wavelengths," *IEEE Trans. Microwave Theory and Techniques*, vol. MTT-32, no. 8, Aug. 1984, pp. 936-8.
- [25]. CDI part numbers 5753 CC or 5763 CC, available from Midwin and Olifson, 2400 Grand Ave., Long Beach, CA 90815.
- [26]. Wiltron model K250 bias Tee, Wiltron Co., 490 Jarvis Drive, Morgan Hill, CA 95037-2809
- [27]. Miteq model JSD2-00010, MITEQ, Inc., 100 Davids Drive, Hauppauge, NY 11788
- [28]. K&L Microwave, Inc., 408 Coles Circle, Salisbury, MD 21804.

FIGURES

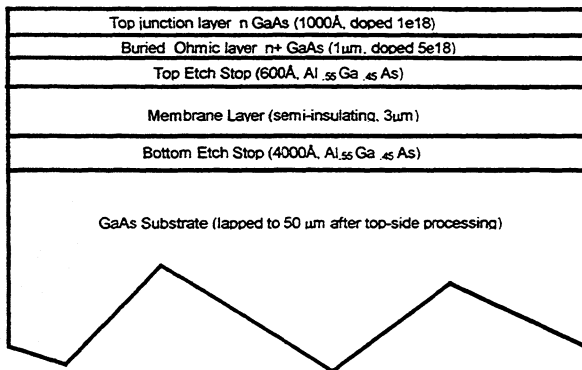


Fig. 1. Wafer profile for membrane and device/RF circuit definition. Layer pattern (from top): n doped GaAs, n+ GaAs, AlGaAs etch stop (device definition) followed by semi-insulating GaAs (membrane layer), AlGaAs etch stop and host wafer (used to form frames).

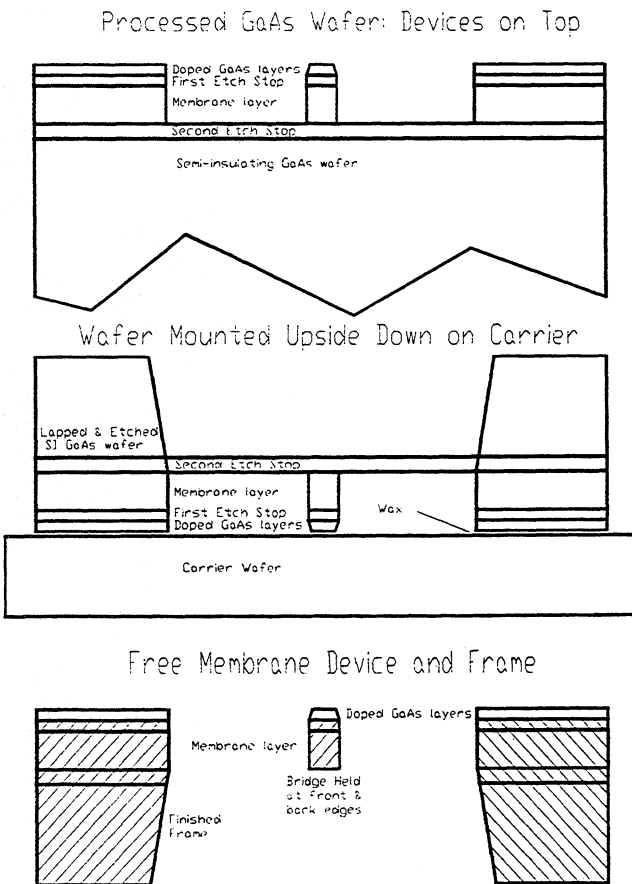


Fig. 2. Membrane fabrication steps. Top: Finished top-side wafer (with devices and RF circuitry) is etched down to lower etch stop, defining membrane region. Middle: Wafer is mounted upside down on carrier using low temperature wax. Wafer is thinned, frame is patterned and etched out to bottom of membrane. Lower: Etch stop is removed, wax is dissolved, individual membranes and frame float off carrier and are collected by filter or screen at bottom of beaker.

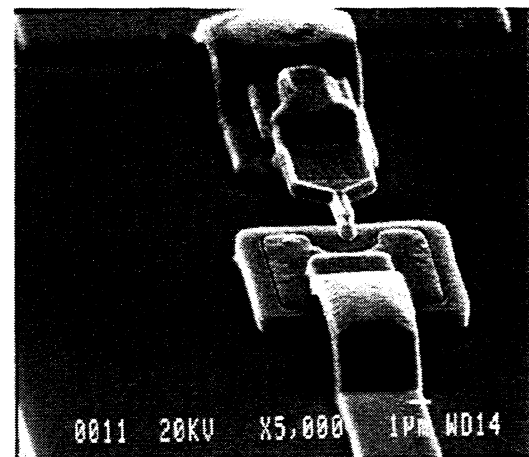
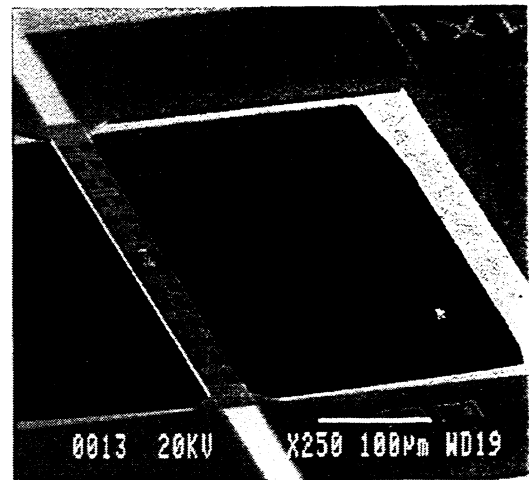
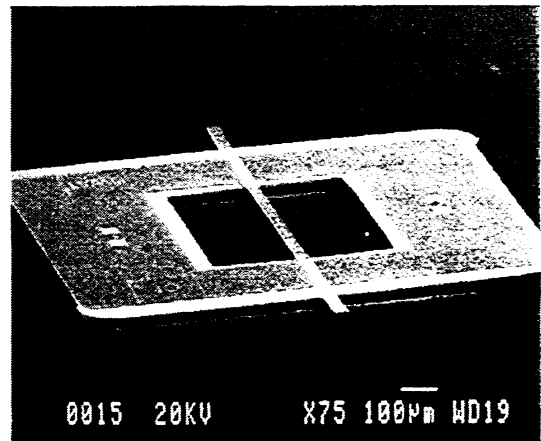


Fig. 3. SEM micrographs of completed membrane and frame with 2.5 THz Schottky diode and RF low-pass filter structure. Frame dimensions are 1x1.4 mm x 50 µm thick. Membrane is 36x600x3 µm thick.

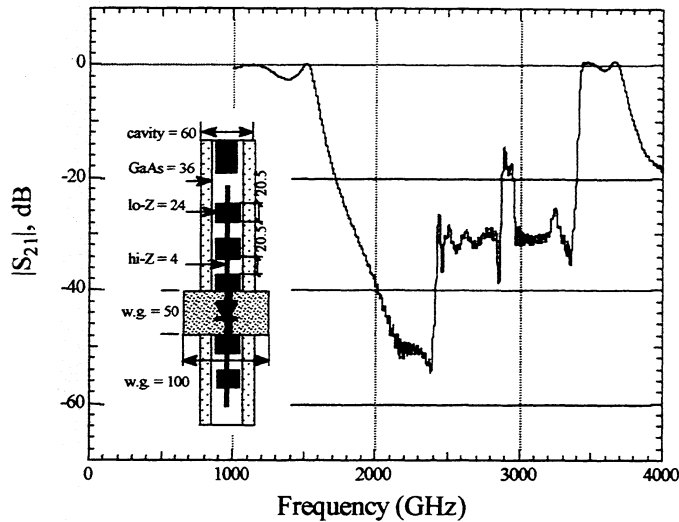


Fig. 4. Calculated finite-difference-time-domain performance of a 4-section RF choke with dimensions equal to those in the existing device. The inset shows a dimensioned (in μm) top view of the membrane strip as mounted. The cavity depth is $40\ \mu\text{m}$. A more ideal configuration would utilize a $30\ \mu\text{m}$ cavity depth and a $30\ \mu\text{m}$ wide GaAs membrane strip, as asymmetries in the membrane mounting would be less likely to induce undesired mode propagation.

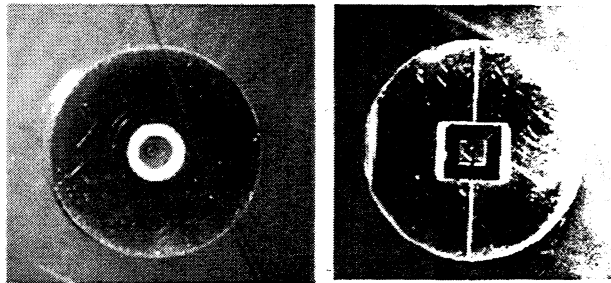


Fig. 5. 2.5 THz electroformed "button-mount" showing horn aperture on one side and 2.5 THz waveguide with inserted membrane mixer, MOMED, on the other.

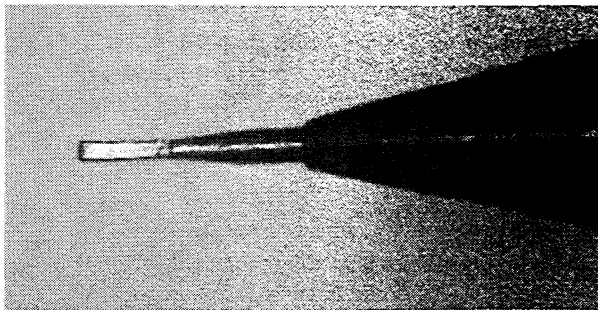


Fig. 6. 2.5 THz Pickett-Potter feed horn mandrel. Tip dimensions are $50 \times 100\ \mu\text{m}$. Mandrel is etched away in NaOH after electroforming.

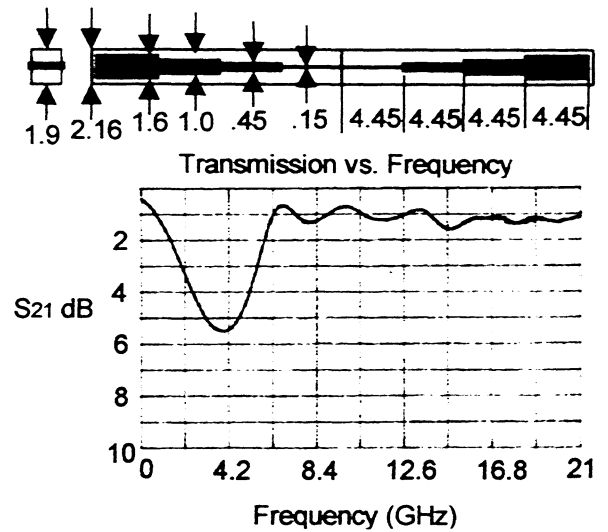


Fig. 7. Dimensioned diagram (in mm) and HP8510 plot of transmission loss for two back-to-back 7-21 GHz suspended-substrate IF transformers ($50\text{-}200\ \Omega$). Quartz = $.15\text{mm}$ thick, cavity = $1.9\ \text{mm}$ square.

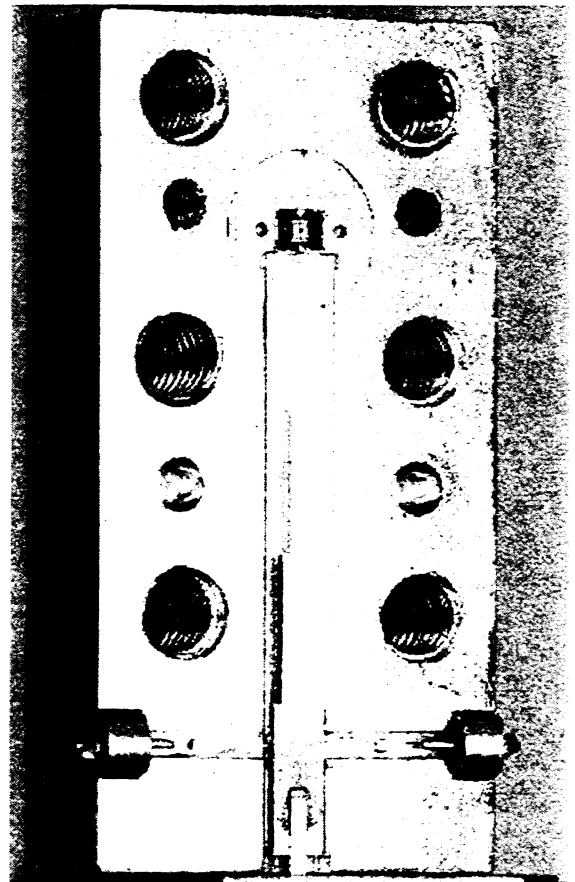


Fig. 8. Photo showing bottom half of complete 2.5 THz mixer block with RF membrane diode, quartz IF transformer and DC bias resistor and sensing taps. A backshort tuner cavity and top block seal the membrane and IF transformer cavities.

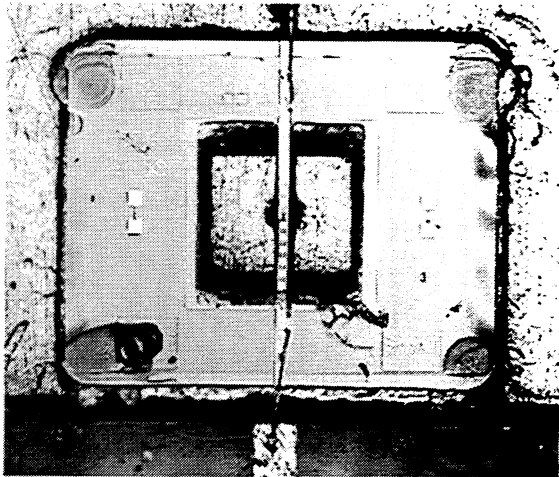


Fig. 9. Close up showing monolithic membrane mixer (MOMED) mounted in "button" with diode suspended across 2.5 THz waveguide (center), DC return (top) and IF transformer wire bond (bottom).

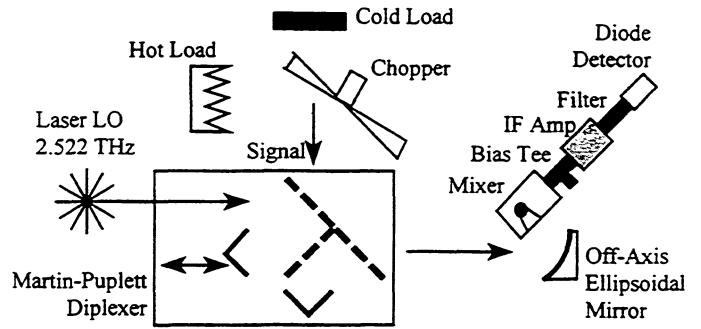


Fig. 10. Schematic of the RF test system used to collect the performance data given in this paper.

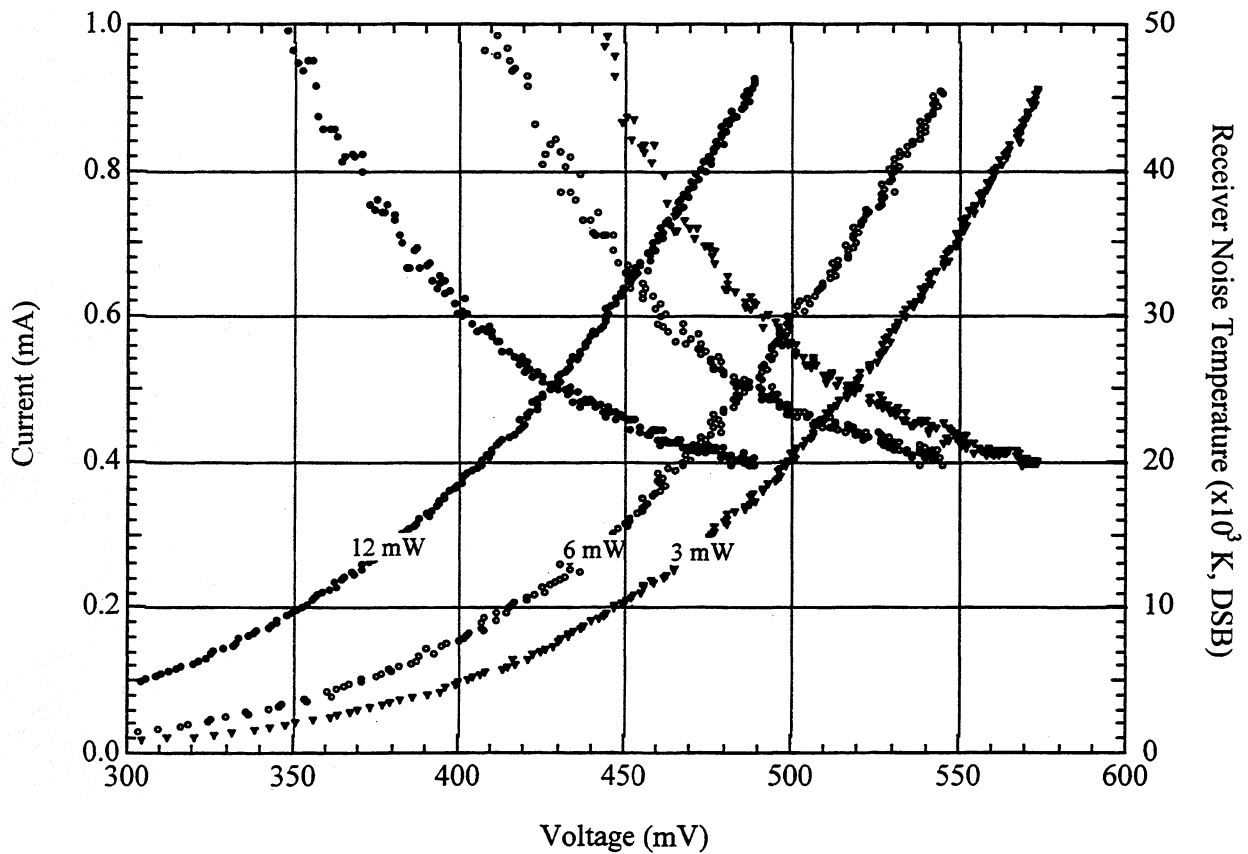


Fig. 11. Measured bias current and receiver noise temperature as a function of bias voltage for LO power levels of ≈ 12 , 6, and 3 mW (left-to-right). The bias current curves exhibit monotonic positive slope, noise temperature curves negative.

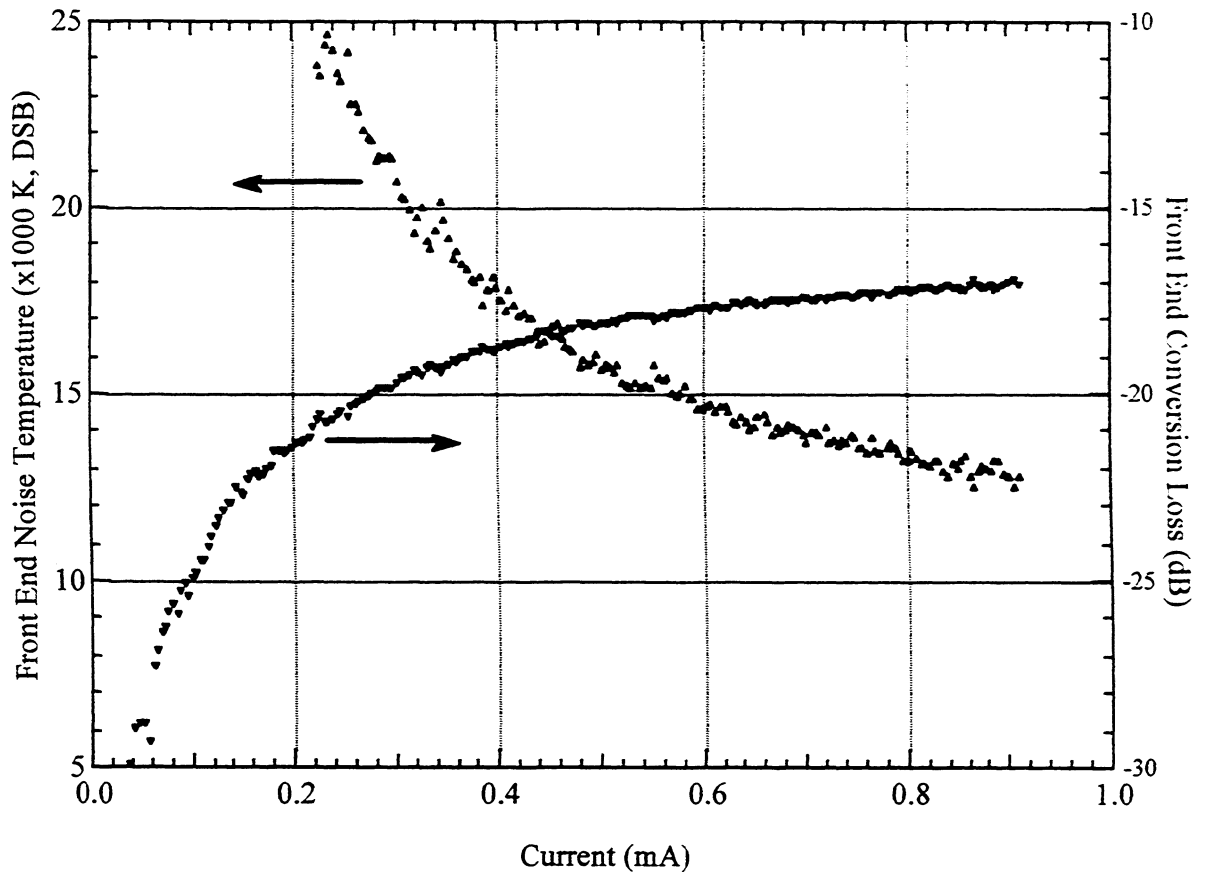
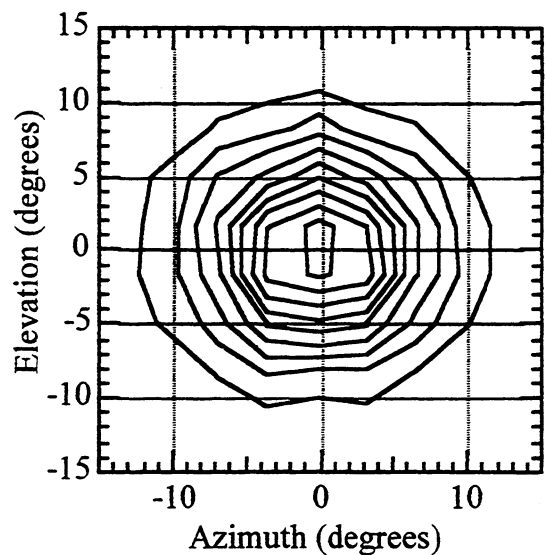


Fig. 12. Extrapolated “front-end” noise temperature and conversion loss. No corrections for diplexer, horn, air, IF mismatch, bias tee, or Rayleigh-Jeans approximation have been included. The minimum noise temperature is $\approx 12,500$ K, DSB, and the minimum conversion loss is ≈ 17 dB. When plotted against bias current as above, noise temperature and conversion loss curves overlap for LO powers between 3 mW and 22 mW.

Fig. 13. Measured beam pattern of 2.5 THz Pickett-Potter feed horn using the LO pump laser as the RF source and the mixer as a direct detector. The contours are linearly spaced in 10% intervals (i.e., the outer contour has 0.1 times the signal strength of the peak).



ON THE DESIGN AND MEASUREMENT OF A 2.5THz WAVEGUIDE MIXER

by C. M. Mann, D. N. Matheson, B. N. Ellison, M. L. Oldfield, B. P. Moyna,
J. J. Spencer, D. S. Wilsher, and B. J. Maddison

Rutherford Appleton Laboratory, Didcot, Oxon. UK.

ABSTRACT

The usefulness of waveguide circuits at frequencies as high as 3THz has now been demonstrated culminating in the realisation of a 2.5THz waveguide mixer implementing Schottky diodes.

For waveguide devices to be optimised at these frequencies it has been necessary to modify the design of the waveguide mount paying particular consideration to areas such as ease of assembly, simplification of machining, reliability and fast adjustment of the RF circuit.

This paper discusses the detailed design and associated RF performance of a new 2.5THz waveguide mixer mount that makes use of the following; an ultrasonically bonded RF circuit, a non-contacting backshort and part fabricated waveguide.

All of these features are aimed at determining the optimum impedance required by the Schottky diode used and thus provide a more ideal circuit in which to place it.

INTRODUCTION

There has been much interest in recent years in the potential use of heterodyne receivers for the observation of stratospheric hydroxyl (OH) at frequencies in the terahertz region. Lines can be observed at 1.8, 2.5 and 3.5THz. Various schemes have been considered including receivers employing a Hot Electron Bolometer mixer pumped via an optically derived local oscillator (LO). Such a system has yet to have been demonstrated at terahertz frequencies although the mixer technology can now be considered mature. Schottky diode mixers have demonstrated the necessary performance required to make the measurement and the use of waveguide as the circuit architecture has also been demonstrated. Waveguide has the advantage of providing excellent radiation properties via use of conventional corrugated feedhorns at frequencies as high as 3.1THz [1] and use of a Schottky diode allows operation at ambient temperatures.

Whilst such mixers have the required sensitivity their LO requirement has to date been excessive. Experience at low frequencies indicates that as the conversion loss of the

mixer is reduced, its LO requirement also falls as does its noise. The waveguide mixers built to date at this frequency have made use of the same intrinsic Schottky diodes that have been used in the more common corner cube mixers but appear to require nearly an order of magnitude more LO. Since the waveguide mixer shows comparable RF performance to the corner cube mixer this implies that there is an additional source of loss within the waveguide circuit. Intuitively it might therefore also be expected that the waveguide mixer will overtake the corner cube mixer once the additional circuit losses have been eradicated.

This paper discusses the design rationale, manufacture and testing of a new waveguide mixer that aims to be able to fully optimise the waveguide mount for a given Schottky diode.

DESIGN RATIONALE

At terahertz frequencies the dimensions of the waveguide circuit shrink to human cell proportions. For example, standard waveguide at 2.5THz is $\approx 100 \times 50\mu\text{m}$ in cross section. For comparison a human ovum is $\approx 120\mu\text{m}$ in diameter. The design discussed here has chosen to eradicate unwanted GaAs from the RF circuit therefore the normal lithography techniques that are used to reduce circuit dimensions to such sizes are largely not available. Instead, use is made of ultra high precision machining to form the waveguide cavity and corrugated feedhorn combined with micromachining techniques to produce the RF filter and whisker that is used to contact the Schottky diode and form the RF circuit. Finally, a combination of micromanipulation and ultrasonic bonding is used to assemble the complete mixer.

The main aim of this work therefore has been to ease the constraints made on all of the above whilst allowing the circuit to be realised with sufficient accuracy that it can be adjusted in controlled way. By taking this approach it is hoped and shown that the resulting mixer can produce state of the art performance and at the same time reduce mixer LO requirement.

THE PLANAR WHISKER

The component of the mixer that makes an RF circuit realisable at these frequencies is the planar whisker. This is a lithographically patterned $0.4\mu\text{m}$ thick gold airline RF filter. The tip is sharpened naturally by the fabrication process such that it is able to make reliable contacts onto an $0.25\mu\text{m}$ diameter Schottky diode anode. The resulting arrangement has the minimum parasitic capacitance that can be attained but has sufficient mechanical flexibility built in that can easily pass the environmental tests

required for a mixer intended for space operation. A picture of a planar whisker is shown below in figure 1.

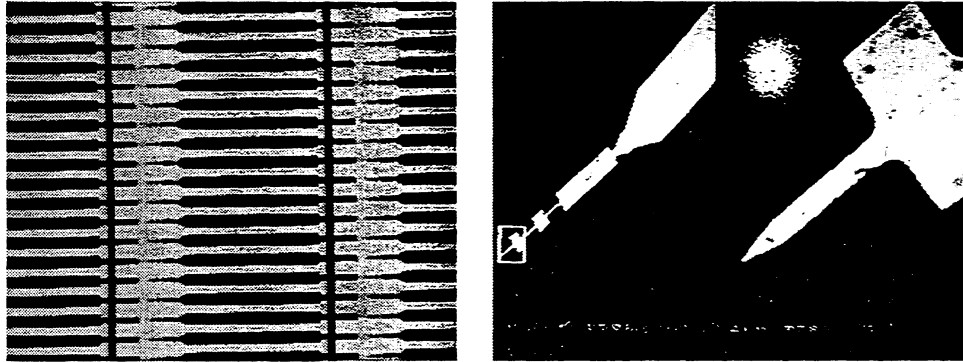


Figure 1: *Pictures of the chrome lithographic mask and a planar whisker*

The RF filter/waveguide probe is adjoined to a bond pad. Directly behind the bond pad there is a weak link to the main carrier which is used to manipulate the whisker. After the whisker has been bonded the main carrier is simply withdrawn leaving the whisker in place.

Sixteen designs of whisker are included on the mask. These have been designed using the approach described in [2] and should allow a full range of embedding impedances to be provided to the diode. It is hoped that each design will be fully characterised so that an understanding can be made as to the true behaviour of the sub micron Schottky diodes used.

A schematic of the mechanical arrangement is shown below in figure 3 alongside a diagram showing the contacting procedure.

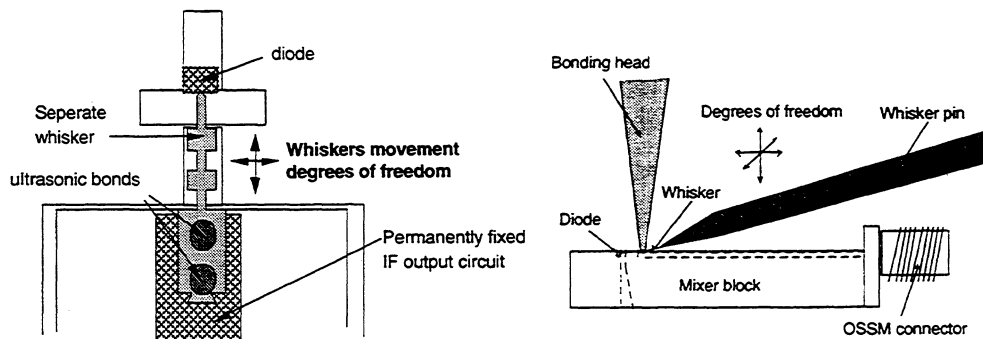


Figure 3: *The mechanical arrangement and contacting technique*

THE MIXER BLOCK DESIGN

Use is made of ultra high precision machining using state of the art mechanical mills and lathes fitted with precision microscopes and measurement slides. Dimensions on drawings are set to the $\pm 0.5\mu\text{m}$ wherever the circuit requires it. Such precision is necessary in order for this potential area of error to be eliminated. However, to ease the machining constraints careful attention has been paid to ensure that overtight tolerances are not specified unnecessarily. Likewise the waveguide mount has been designed so that the machining operations that are most easily carried out are used predominantly. Therefore, the use of electroforming was restricted to the feedhorn only and a novel scheme was devised that enabled the rest of the waveguide cavity to be part assembled. A drawing of the mixer block is shown below in figure 4.

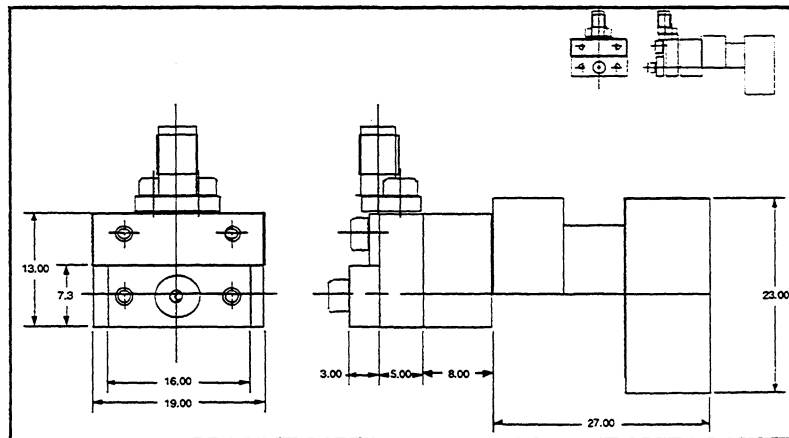


Figure 4: A manufacturing drawing of the 2.5THz mixer (dimensions in millimetres)

A previous design of mixer [3] had relied on the feedhorn being designated to a particular block. This had the disadvantage that comparisons could not be made between different feedhorns for more than one particular configuration of RF circuit. Thus it was not possible to determine if one mixer performed better than another as a result of its feedhorn having lower loss or because its RF circuit was more optimised. For this design feedhorns are aligned optically by viewing down the throat of the horn rather than the use of accurately placed dowels. Feedhorns can then be interchanged between blocks and performance comparisons are easily made.

The section of waveguide in which the diode and backshort lie is fabricated in two parts. This had also been the case in the previous design but rather than relying on a pressure contact between the side walls and the lid of the waveguide, a small machined diode carrying package is soldered to the main mixer body. This ensures

that a good electrical path exists in the region that is most important for low loss waveguide. A machined diode package is shown below in figure 5 alongside an SEM photograph of the assembled mixer block ready for a diode to be soldered in.

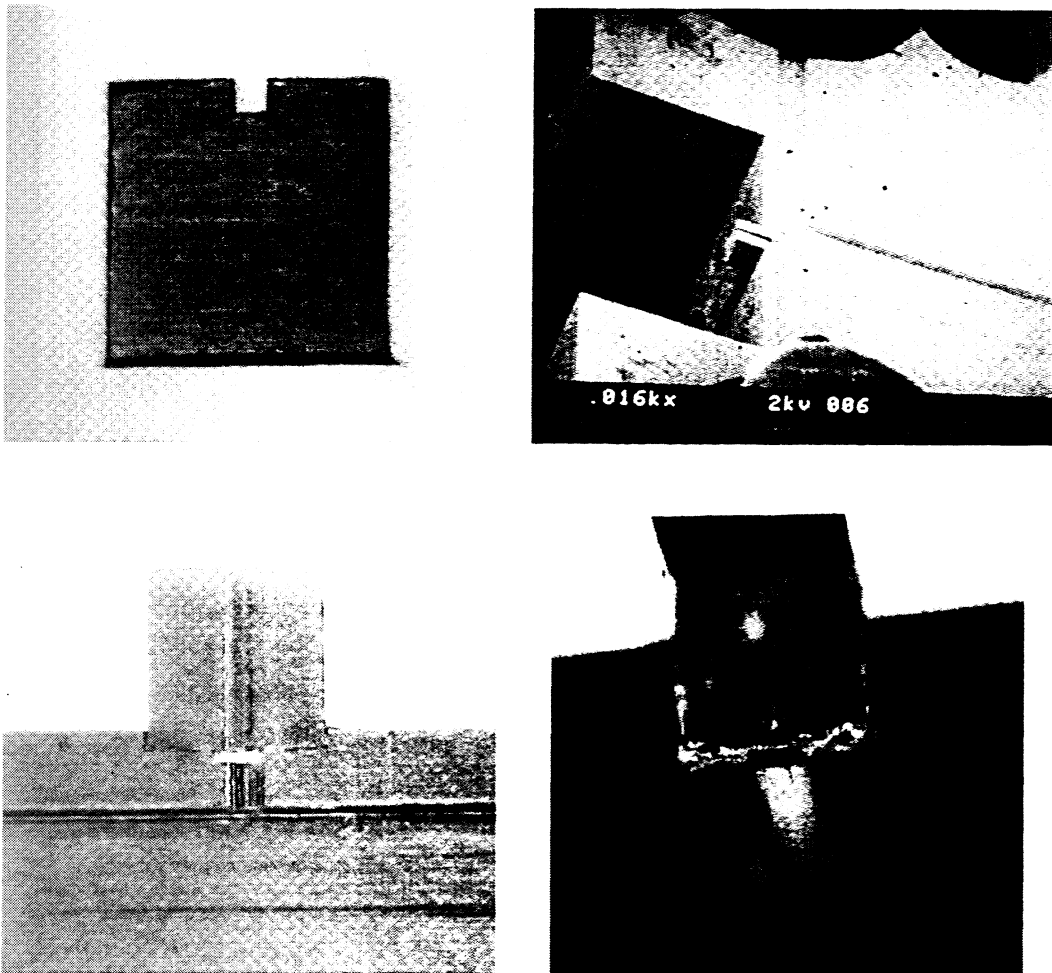


Figure 5: *The machined diode carrier and the mixer block part assembled*

The final stages of assembly required the diode chips to be soldered in followed by the IF substrate and finally the whisker. The two diodes tested so far in this configuration are the X107 and the NF 1T2 both notch front diodes, from the National Microelectronics Research Centre, Cork, Eire and the University of Virginia, Charlottesville, USA, respectively.

Needless to say the process of positioning of the whisker, contacting a diode and eventually ultrasonically bonding it in place took some development but now the process is very repeatable and has the advantage that it is completely 'dry' and 'cold'. Therefore it can be carried out many times with no degradation to the diode chip or

waveguide. A completed circuit is shown below in figure 6 alongside the mixer having just had an NMRC X107 notch front varactor diode soldered in.

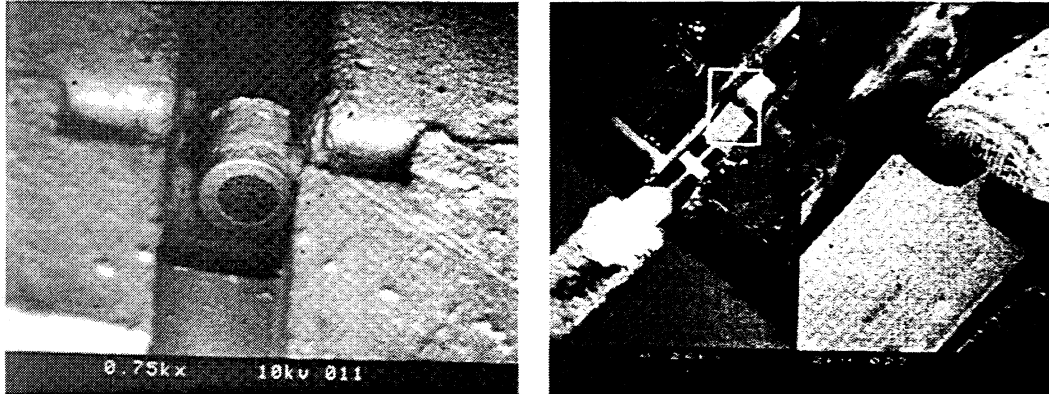


Figure 6: An X107 diode soldered into the mixer and the completed circuit

The final task necessary before RF testing could begin was to insert a tuneable backshort. Initially this consisted of a simple gold ribbon ‘shim’ that could be etched to the approximate size of the waveguide. Later a technique of painting on protective stripes of Crystalbond wax allowed a structured ‘non-contacting’ backshort to be realised. The relative performance of these two types has been determined and the non-contacting backshort is by far better, the results are shown later.

Very recently a lithographically micromachined backshort has been developed [4] that has not yet been testing at RF but looks very promising and should result in a further improvement. Pictures of the fabricated and micromachined backshorts are shown below in figure 7. The cross-section of the signal waveguide is 27 X 105 μ m.

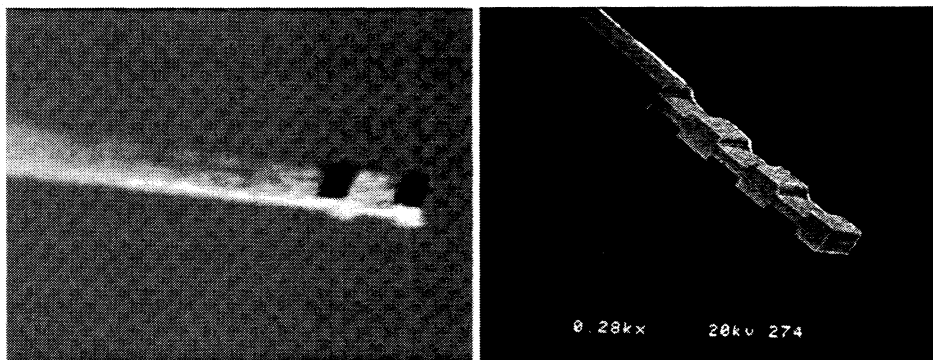


Figure 7: Fabricated and micromachined backshort shims approximated dimensions are 25x100 μ m in cross section

RF MEASUREMENT SET-UP

The mixer has been measured in three ways. Firstly a 3dB beamsplitter formed by projecting a 45 degree wire grid has been used. In order to obtain the corrected mixer performance it is necessary to divide the total receiver noise temperature by two and then correct for the IF contribution again making sure that the conversion loss is also halved. This technique is useful as it gives the intrinsic mixer performance (although Ohmic losses in the grid are still included) and can therefore give insight into the relative performance of an optical coupling circuit such as a diplexer. The correction factor was verified by using a 200GHz subharmonic mixer and rotating the beamsplitter in the signal path to obtain its effective insertion loss as a function of angle. A subharmonic mixer was used as there is no need to inject LO via the polarising grid as is the case for a fundamental mixer. In addition, a 10dB beamsplitter was fabricated using Kapton film membrane and replacing the wire grid. This only became possible when the mixer performance was sufficiently good that the LO requirement was suitably low. Extrapolated values of mixer performance between beamsplitters showed good agreement. This measurement set-up is shown in figure 8. Finally, a Martin Puplett interferometer was used for LO injection, however, this gave only marginally better performance than the 3dB beamsplitter. The reasons for this are not yet clear but poorly aligned optical components appear to be the most likely cause.

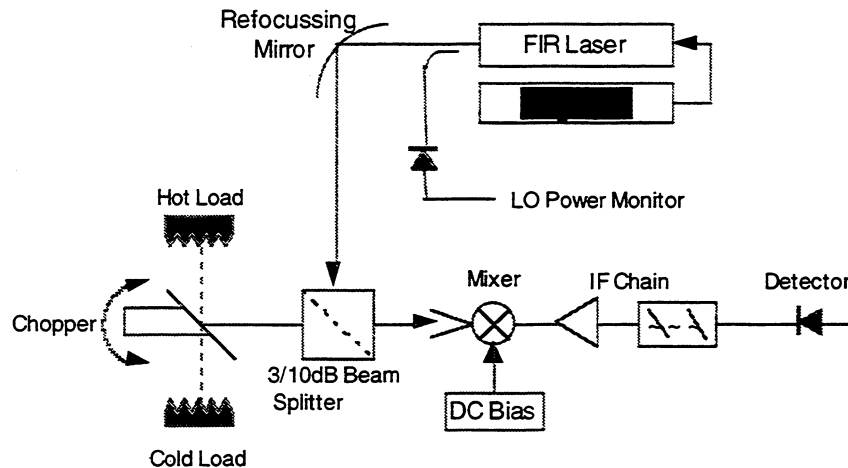


Figure 8: *The measurement set-up*

The chopper was used to remove the instability of the far infrared laser which whilst good, could provide sufficient LO amplitude variations that the total IF noise power was modulated thereby degrading Y-factor measurement accuracy. Therefore, with the

chopper rotating the output from the detector could be displayed on an oscilloscope. The average peak to peak modulated level could then be determined to provide the difference in IF signal power obtained for the hot and cold positions.

RF PERFORMANCE

Of the two diodes tested so far in this configuration the best results have been obtained with the UVA NF 1T2 diodes. These are $\approx 0.5\mu\text{m}$ in diameter and have very good diode IV characteristics.

The NMRC X107 diodes are over five times the area being $\approx 1\mu\text{m}$ square and therefore have five times the parasitic capacitance but also have good IV characteristics. Only two RF filter/waveguide probe configurations have been tried so far for these diodes and so they may yet provide good performance. For the X107 diodes the best corrected mixer noise temperature to date is $\approx 40,000\text{K DSB}$.

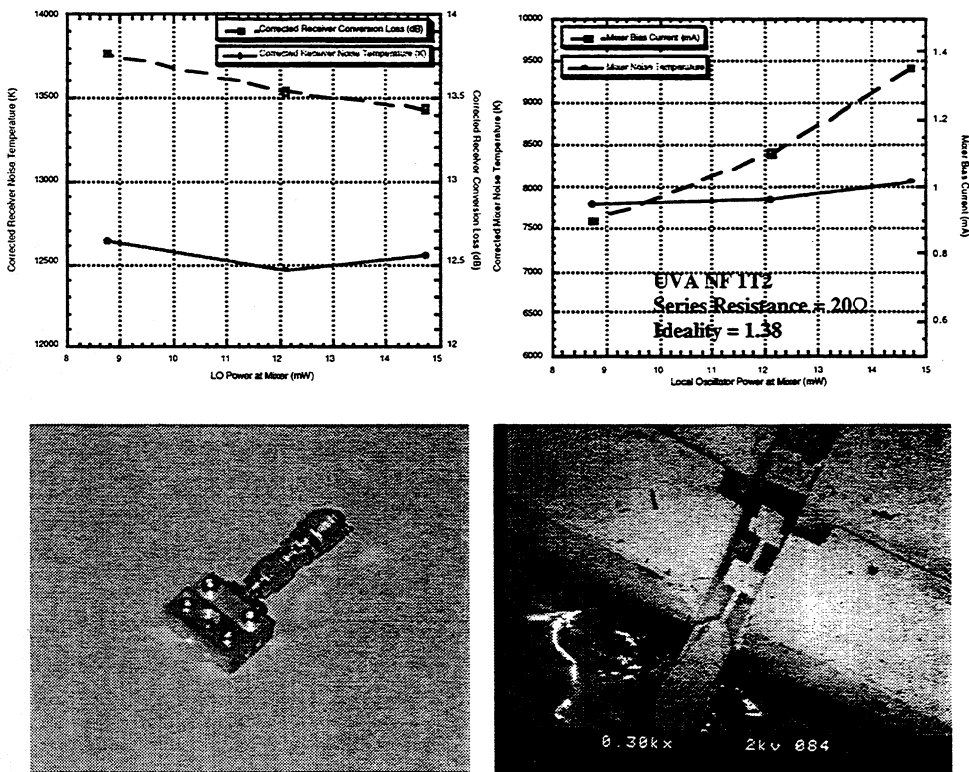


Figure 9: The best RF performance to date and the RF circuit and mixer block.

The UVA NF 1T2 diodes showed very good performance from the first iteration. Figure 9 shows the best performance that has been obtained to date from RAL mixer DW1 measured using the 3dB beamsplitter.

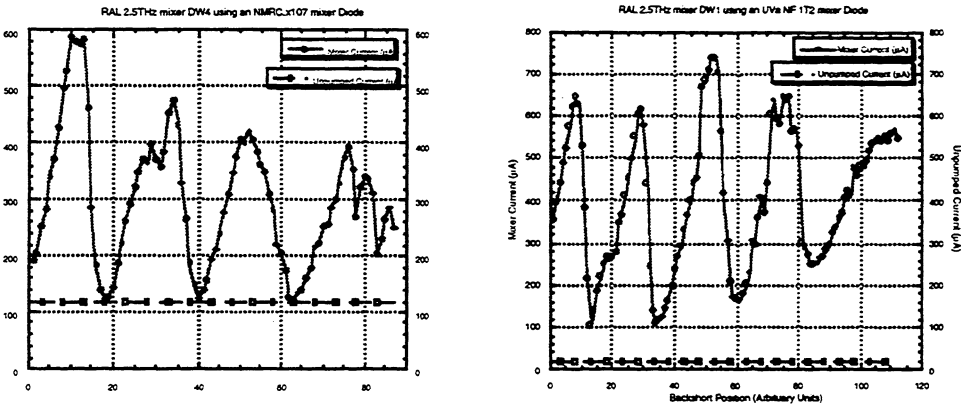
The UVA NF1T2 diode had a series resistance of 20Ω and an ideality factor of 1.38 . The whisker has a waveguide probe width of $19\mu\text{m}$ and first filter section length of $26\mu\text{m}$. An SEM photograph of this structure is shown beneath the plots alongside a photograph of the completed mixer with the backshort drive removed.

The corrected mixer noise temperature is $\approx 7,800$ DSB. Whilst this mixer showed the best performance it had a particularly poor backshort. A comparison is made in figure 10 between the backshort this mixer used, a simple etched shim, and that used by another mixer incorporating a fabricated ‘non-contacting’ backshort. We have defined a intuitive quality factor which relates to how successfully a backshort can tune out coupled LO power. In principle a perfect backshort can prevent any power being coupled to a diode

We define a quality factor, Q , where:-

$$Q = \frac{(I_{\text{peakLO}} - I_{\text{NOLO}})}{(I_{\text{dipLO}} - I_{\text{NOLO}})}$$

I_{peakLO} = Maximum coupled current
 I_{dipLO} = Minimum coupled current
 I_{LO} = Current no LO



Fabricated non-contacting backshort $Q \approx 250$

Simple close fitting shim $Q \approx 8$

Figure 10: Comparison between the two types of backshort tested so far

Unfortunately this particular mixer suffered ESD damage before it could be tested using the 10dB beam splitter and is presently being re-assembled. The best uncorrected system performance has been obtained for a later mixer, DW2. This mixer has a slightly shorter first section length on the RF filter, $20\mu\text{m}$ versus $26\mu\text{m}$ for DW1. However, it still showed good performance. The best uncorrected system

performance was $\approx 16,800\text{K DSB}$ measured using the 10dB beam splitter. The results are shown in figure 11. The corrected mixer performance $\approx 9,500\text{K DSB}$.

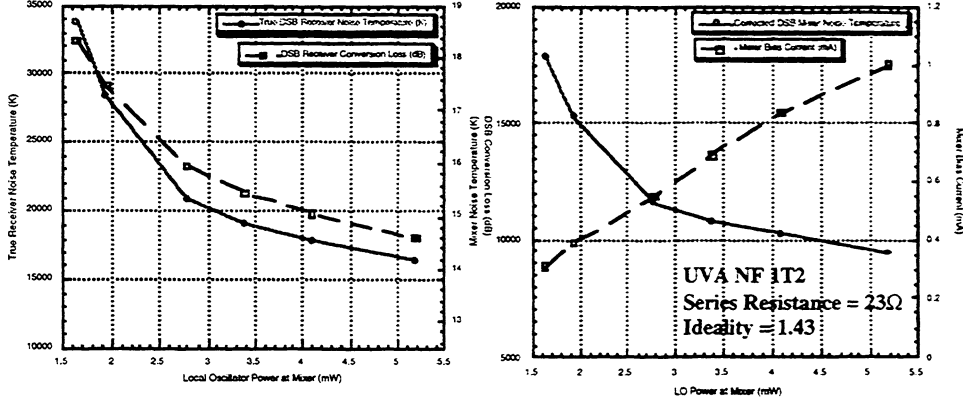


Figure 11: Best uncorrected system receiver performance

CONCLUSIONS

State of the art performance has been demonstrated for a 2.5THz waveguide mixer that makes use of a combination of novel design and assembly. First results indicate that the circuit is by no means fully optimised. The best mixer produced to date had a non-optimum backshort. In addition, only two variations of RF circuit design have been tested. The RF performance for this design of mixer is better by a factor of nearly two compared to that of the previous mixer design in terms of both mixer noise, conversion loss and LO requirement. However, this result has been obtained with the same intrinsic diode, the UVA1T2, implying that it has come about purely as a result of improved waveguide circuit design, fabrication and assembly. Further improvement can be expected in the near future.

ACKNOWLEDGEMENTS

The authors would like to express their thanks to Dr Michael Gaidis and Dr Peter Seigel for their help in making reliable RF measurements and to Dr Victor Lubecke for his work on the fabrication of the micromachined backshorts
This work has been funded by ESA contract :- 8742/90/NL/PB

REFERENCES

- [1] 'Corrugated Feedhorns at Terahertz Frequencies - Preliminary Results', B.N.Ellison, M.L.Oldfield, D.N.Matheson, B.J.Maddison, C.M.Mann and A.F.Smith, The Fifth International Symposium on Space Terahertz Technology, Ann Arbor, May 1994.
- [2] 'A Design Approach for Planar Waveguide Launching Structures', J.Thornton, C.M.Mann, The 7th International Symposium on Space Terahertz Technology, University of Virginia 1996.
- [3] 'First Results for a 2.5 THz Schottky Diode Waveguide Mixer', B.N.Ellison, M.L.Oldfield, D.N.Matheson, B.J.Maddison, C.M.Mann, S.Marazita, T.W.Crowe, P.Maaskant, W.M.Kelly, 7th International Symposium on Space Terahertz Technology, University of Virginia, March 1996.
- [4] 'Practical Micromachining Techniques for High Aspect Ratio Submillimetre Wave Components', V.Lubecke, K.Mizuno, C.M.Mann, , The 8th International Symposium on Space Terahertz Technology, JPL, Pasadena, March 1998

A DISCUSSION OF POWER COUPLING BANDWIDTH LIMITATIONS OF PLANAR SCHOTTKY DIODES AT SUBMILLIMETER WAVELENGTHS

J.L. Hesler and B. Gelmont

Department of Electrical Engineering
University of Virginia
Charlottesville, VA 22903
e-mail: hesler@virginia.edu

Abstract

Planar Schottky diodes can be used to build sensitive, rugged and reproducible mixers that operate at room temperature. Discrete-chip surface-channel planar Schottky barrier diodes have been used in the development of receivers at frequencies up to 700 GHz with performance comparable with that of the best whisker contacted diodes [1]. However, the packaging parasitics of the planar diode geometry have limited the development of such mixers at higher frequencies. The planar diode chip can be modeled as a set of lumped capacitors (representing fringing fields around the diode) and inductors (representing the metal connection lines) that affect the coupling of power to the diode junction. Bode [2] and Fano [3] showed that there is an inherent limit to the bandwidth over which power can be coupled to a complex load of this sort using a lossless passive coupling circuit. We have extended the Bode-Fano theory to circuits with three or more elements, and have used this theory to examine limitations to mixer design caused by planar diode packaging at submillimeter wavelengths. In particular, we have examined the coupling bandwidth limitation for a discrete-chip surface-channel planar Schottky barrier diode mounted in a microstrip channel [4]. The simulations indicate that for diodes chips with semi-insulating GaAs support substrates at frequencies around 500 GHz the coupling of power to the anode is not significantly limited by the chip parasitics. However, at frequencies above approximately 1000 GHz, the packaging parasitics impose tight limits on the power coupling bandwidth, thus complicating mixer design. The bandwidth limitation condition derived here is general and can be used to explore power coupling limitations for a variety of devices and structures.

Introduction

Fig. 1(a) shows a simple equivalent circuit of the whisker-contacted Schottky barrier diode. The capacitance $C_{j,avg}$ is an average value for the junction capacitance over the local oscillator (LO) pump cycle. $R_{d,opt}$ is the RF and LO source resistance that provides optimum mixer performance. Bode showed that there is a fundamental limitation to the bandwidth over which a reasonable transfer of power can be achieved for a parallel RC circuit, given by [2]

$$\int_0^{\infty} \ln \frac{1}{|\rho|} d\omega \leq \frac{\pi}{RC} \quad (1)$$

where ρ is the reflection coefficient looking toward the diode through a lossless matching network. Fig. 2 shows the frequency profile of the reflection coefficient that yields maximum bandwidth given some maximum reflection ρ_a within the band. Using this profile allows the

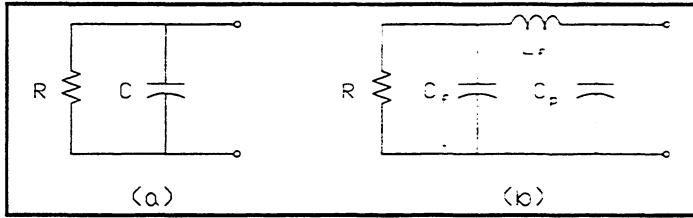


Fig. 1. Simple equivalent circuits of the (a) whisker-contacted and (b) planar Schottky barrier diode.

evaluation of the integral in (1),

$$(\omega_2 - \omega_1) \ln\left(\frac{1}{\rho_a}\right) \leq \frac{\pi}{RC} \quad (2)$$

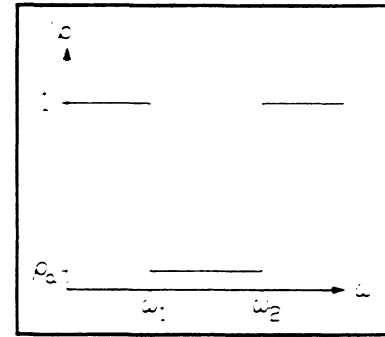


Fig. 2. Impedance matching profile for optimum bandwidth.

that illustrates the tradeoff between power-coupling bandwidth and ρ_a for a parallel RC circuit. As an example, for the UVa-1T15 whisker-contacted diode (epitaxial layer doping $1 \cdot 10^{18} \text{ cm}^{-3}$ and anode diameter $0.25 \mu\text{m}$), some reasonable estimates for $R_{d,opt}$ and $C_{j,avg}$ are $R_{d,opt} = 150 \Omega$ and $C_{j,avg} = 2 \cdot C_{j0} = 0.5 \text{ fF}$. For a center frequency of 3 THz and an in-band reflection coefficient ρ_a of 0.2, the largest obtainable fractional bandwidth for the 1T15 is 140%. Thus, for the whisker-contacted diode, the junction capacitance does not inherently limit the power coupling bandwidth, and the design is instead limited by other issues.

Fig. 3 shows the planar diode chip geometry and the location of the significant parasitic elements near the diode's anode region, which we have reduced to the simple equivalent circuit of Fig. 1(b) for this analysis. C_f represents the parallel combination of $C_{j,avg}$ and the parasitic capacitance from the finger to the ohmic-contact pad, C_{fp} . The other parasitics are the finger inductance L_f and the pad-to-pad capacitance C_p that represents the fringing capacitance between the pads. These parasitics can potentially reduce the achievable bandwidth from that of the whisker-contacted geometry. In order to determine the significance of the planar diode parasitics on the high frequency performance, this article derives an equation similar to (2) for the planar diode equivalent circuit.

Statement of the Problem

The basic setup of the problem is shown in Fig. 4. Z_L represents the load whose power-coupling bandwidth limit is to be determined. Throughout this analysis, the impedances are assumed to be normalized to the source impedance. The goal of the analysis is to determine the fundamental limits to the performance of the matching network that are imposed by the load impedance Z_L . The reflection coefficient looking toward the matching network is taken as the figure of merit by which the bandwidth is judged.

Darlington showed that any physically realizable load can be represented by a purely reactive two-port network with a resistance terminating one of the ports [5]. This

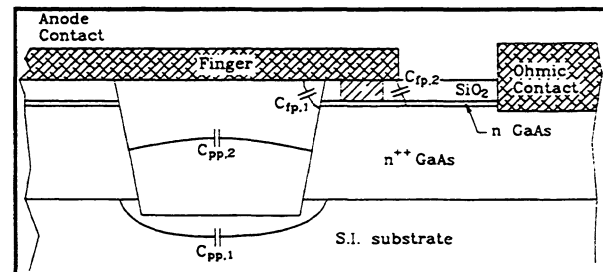


Fig. 3. Schematic of the diode chip near anode indicating physical location of fringing capacitances.

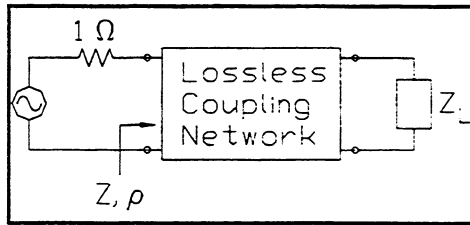


Fig. 4. Basic setup of Bode-Fano problem

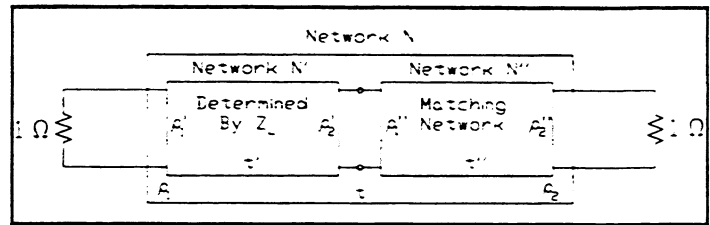


Fig. 5. Division of Bode-Fano circuit into two subcircuits N' and N''

terminating resistance can be made arbitrary by the inclusion of an ideal transformer within the reactive two-port network. Using a Darlington representation of the load impedance allows the problem to be redrawn as shown in Fig. 5.

The goal of this analysis, then, is to determine the limitations to the performance of the entire circuit N caused by the load circuit N' independent of the matching circuit N'' . The relationship between the overall circuit N and the load circuit N' was explored by Fano [3]. Fano showed that at an n^{th} order zero of transmission of N' in the right half of the complex frequency plane (RHP), ρ_1 and its first $2n-1$ derivatives are equal to ρ_1' and its first $2n-1$ derivatives and are thus independent of the circuit N'' . Using this basic insight, Fano showed that by performing a contour integration around the RHP involving the function $F = \ln(1/\rho_1)$, an integral relation can be determined between the frequency response of N and the physical circuit parameters of N' .

One caveat to this analysis is that under certain circumstances the adjacent elements of N' and N'' are of the same type and orientation. The network N is then called degenerate because both N' and N'' have zeros of transmission at the same location. For this degenerate case, only the first $2n-2$ derivatives of ρ_1' are independent of the circuit N'' , and the bandwidth can be improved by increasing the value of the final element of N' . The bandwidth limitation determined by the circuit with $n-1$ elements then determines the behavior, as will be discussed later.

The next section uses the integral relations developed by Fano to derive the relations for the planar diode equivalent circuit. However, Fano's theory was derived for the case of low-pass matching. For many circuits, the low-pass theory can be simply extended to the band-pass case using standard transformation techniques. For the circuit under consideration, this transformation is not applicable because the circuit elements are not accessible for the connection of the requisite parallel elements. Kerr extended Fano's theory to the case of a bandpass matching without the use of this lowpass to bandpass transformation [6]. In addition, Fano's analysis was only valid for circuits with two elements. In [7], we extended the analysis of Fano to the three-element circuit of Fig. 1(b), and we will now use the results of this analysis in deriving the bandwidth limitation equations for this circuit.

Derivation of Equations

The circuit N' in Fig. 6 shows the key parasitics for a typical planar diode chip. The resistor r is an arbitrary resistance that eventually drops out of the calculations. The first step of

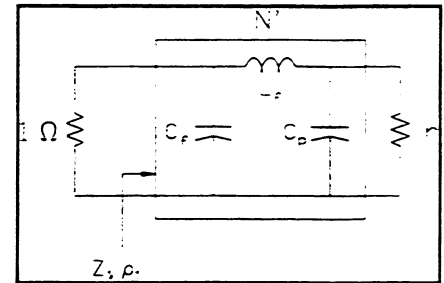


Fig. 6. Equivalent circuit model of planar diode used during derivation of Bode-Fano equations.

the analysis is to determine the coefficients of the Taylor series for the function $F(s) = \ln(1/\rho_1(s))$. The circuit N' has three zeros of transmission at infinity, and it is thus convenient to define the variable $\xi \equiv 1/s$. Because of the three zeros of transmission, the first 5 coefficients of the Taylor series of ρ_1 , and therefore F as well, are determined entirely by the circuit N' for the non-degenerate case. The Taylor series for F is given by

$$F(s) = \ln(1/\rho_1) = jA_0 + A_1\xi + A_2\xi^2 + A_3\xi^3 + \dots \quad (3)$$

where A_0 is either 0 or π depending upon the sign of ρ_1 , and A_n are

$$A_n = \frac{1}{n!} \left. \frac{d^n F(\xi)}{d\xi^n} \right|_{\xi=0} \quad (4)$$

The impedance looking into the circuit N' is given by

$$Z_1' = \frac{s^2 r L_f C_p + s L_f + r}{s^3 r L_f C_f C_p + s^2 L_f C_f + s r (C_f + C_p) + 1} \quad (5)$$

Using (5) to calculate the inverse of the reflection coefficient yields

$$\frac{1}{\rho_1} = \frac{Z_1' + 1}{Z_1' - 1} = - \frac{s^3 r L_f C_f C_p + s^2 (L_f C_f + r L_f C_p) + s (L_f + r (C_f + C_p)) + (1 + r)}{s^3 r L_f C_f C_p + s^2 (L_f C_f - r L_f C_p) - s (L_f - r (C_f + C_p)) + (1 - r)} \quad (6)$$

Finally, the function $F(s)$ in terms of ξ is

$$F(s) = \ln \left[\frac{1}{\rho_1} \right] = \ln \left[- \frac{\xi^3 (1+r) + \xi^2 (L_f + r(C_f + C_p)) + \xi (L_f C_f + r L_f C_p) + r L_f C_f C_p}{\xi^3 (1-r) - \xi^2 (L_f - r(C_f + C_p)) + \xi (L_f C_f - r L_f C_p) + r L_f C_f C_p} \right] \quad (7)$$

Taking the appropriate derivatives of F and evaluating them at $\xi = 0$ yields the coefficients of the Taylor series:

$$\begin{aligned} A_0 &= \pi, & A_1 &= \frac{2}{C_f}, & A_2 &= 0, & A_3 &= \frac{2}{3} \frac{L_f - 3C_f}{L_f C_f^3}, \\ A_4 &= 0, & A_5 &= \frac{2}{5} \frac{5C_f^3 + 5C_f^2 C_p - 5C_f C_p L_f + C_p L_f^2}{C_f^5 C_p L_f^2}. \end{aligned} \quad (8)$$

In Table 1 of Fano's paper, he gives the integral conditions for physical realizability for a circuit with n zeros of transmission at infinity as [3, p. 68]

$$\int_0^{\infty} \omega^{2k} \ln \left(\frac{1}{|\rho_1|} \right) d\omega = (-1)^k \frac{\pi}{2} F_{2k+1} \quad (9)$$

where k runs from 0 to 2 and F_{2k+1} is defined as

$$F_{2k+1} = A_{2k+1} - \frac{2}{2k+1} \sum_i \lambda_{ri}^{2k+1} \quad (10)$$

and where the A_{2k+1} are the coefficients of the Taylor series for $F(\xi)$ and λ_{ri}^{2k+1} are the zeros of ρ_1 in the right hand plane, which are determined by the matching network. Using the reflection coefficient profile shown in Fig. 2, (9) can be simplified to

$$K \Omega_{2k+1} = (-1)^k (2k+1) F_{2k+1} \quad (11)$$

where Ω_{2k+1} is defined as

$$\Omega_{2k+1} = \omega_2^{2k+1} - \omega_1^{2k+1} \quad (12)$$

and K is given by

$$K = \frac{2}{\pi} \ln \left(\frac{1}{|\rho_a|} \right) \quad (13)$$

Substituting the values of k and expanding F_{2k+1} we arrive at a series of three equations

$$\begin{aligned} A_1 - K\Omega_1 &= 2 \sum \lambda_{ri} \\ 3A_3 + K\Omega_3 &= 2 \sum \lambda_{ri}^3 \\ 5A_5 - K\Omega_5 &= 2 \sum \lambda_{ri}^5 \end{aligned} \quad (14)$$

All that remains is to determine the right-half-plane (RHP) zeros λ_n that maximize the coefficient K within the matching band, thus minimizing ρ_a . The zeros λ_n must be real or appear in complex conjugate pairs and must have a real part greater than zero. Fano showed that for a CL circuit in the non-degenerate case, the bandwidth can be maximized by choosing a single real root [3, p. 72]. However, as Fano mentions, his proof for the two element CL circuit could not be extended to circuits with larger numbers of elements [3, p. 73]. In [7], we give a proof for the three element CLC circuit and show that, except for the degenerate case, K is maximized by a single pair of either real or complex conjugate roots. Thus, choosing a pair of roots $\lambda_{r1} = x + \sigma$ and $\lambda_{r2} = x - \sigma$ where $\sigma = y$ for two real roots and $\sigma = iy$ for a pair of complex-conjugate, then the summation of the zeros in (14) becomes

$$\begin{aligned} \sum \lambda_{ri} &= 2x \\ \sum \lambda_{ri}^3 &= 2(x^3 + 3x\sigma^2) \\ \sum \lambda_{ri}^5 &= 2(x^5 + 10x^3\sigma^2 + 5x\sigma^4) \end{aligned} \quad (15)$$

Substituting (15) into (14) yields

$$\begin{aligned} A_1 - K\Omega_1 &= 4x \\ 3A_3 + K\Omega_3 &= 4(x^3 + 3x\sigma^2) \\ 5A_5 - K\Omega_5 &= 4(x^5 + 10x^3\sigma^2 + 5x\sigma^4) \end{aligned} \quad (16)$$

Eliminating the variables x and σ yields the equation

$$\begin{aligned} 144(A_1 - K\Omega_1)(5A_5 - K\Omega_5) + (A_1 - K\Omega_1)^6 \\ - 20(A_1 - K\Omega_1)^3(3A_3 + K\Omega_3) - 80(3A_3 + K\Omega_3)^2 = 0 \end{aligned} \quad (17)$$

Note that this equation is valid for both the real root and complex-conjugate root solutions. If we introduce the fractional bandwidth b and center frequency ω_0 , related to ω_1 and ω_2 by the equations $\omega_1 = \omega_0(1-b/2)$ and $\omega_2 = \omega_0(1+b/2)$, then the Ω_{2k+1} can be rewritten as

$$\begin{aligned} \Omega_1 &= b\omega_0 \\ \Omega_3 &= \frac{b(12+b^2)\omega_0^3}{4} \\ \Omega_5 &= \frac{b(80+40b^2+b^4)\omega_0^5}{16} \end{aligned} \quad (18)$$

Finally, defining the variables $B_{C_f} \equiv \omega_0 C_f$, $B_{C_p} \equiv \omega_0 C_p$, and $X_{L_f} \equiv \omega_0 L_f$ and substituting (8) and (18)

into (17) yields a polynomial in K and b,

$$\begin{aligned}
0 = & 2880 + K^6 b^6 B_{C_f}^3 B_{C_p} X_{L_f}^2 \\
& - K^5 12 b^5 B_{C_f}^2 B_{C_p} X_{L_f}^2 \\
& + K^4 (60 b^4 B_{C_f} B_{C_p} X_{L_f}^2 + 60 b^4 B_{C_f}^3 B_{C_p} X_{L_f}^2 + 5 b^6 B_{C_f}^3 B_{C_p} X_{L_f}^2) \\
& + K^3 (-120 b^3 B_{C_f} B_{C_p} X_{L_f}^2 - 120 b^3 B_{C_f} X_{L_f}^2 - 360 b^3 B_{C_f}^2 B_{C_p} X_{L_f}^2 \\
& \quad - 30 b^5 B_{C_f}^2 B_{C_p} X_{L_f}^2) \\
& + K^2 (720 b^2 B_{C_p} X_{L_f}^2 + 720 b^2 B_{C_f} B_{C_p} X_{L_f}^2 + 60 b^4 B_{C_f} B_{C_p} X_{L_f}^2 \\
& \quad + 240 b^4 B_{C_f}^3 B_{C_p} X_{L_f}^2 + 4 b^6 B_{C_f}^3 B_{C_p} X_{L_f}^2) \\
& + K (-1440 b B_{C_f} - 1440 b B_{C_p} + 2880 b B_{C_f} B_{C_p} X_{L_f} + 240 b^3 B_{C_f} B_{C_p} X_{L_f} \\
& \quad - 440 b B_{C_p} X_{L_f}^2 - 120 b^3 B_{C_p} X_{L_f}^2 - 1440 b B_{C_f}^2 B_{C_p} X_{L_f}^2 \\
& \quad - 720 b^3 B_{C_f}^2 B_{C_p} X_{L_f}^2 - 18 b^5 B_{C_f}^2 B_{C_p} X_{L_f}^2)
\end{aligned} \tag{19}$$

Equation (19) can then be used to generate curves showing the relationship between ρ_a and the fractional bandwidth b for different system parameters. Once we have solved (19) for a given set of values, we can then use (16) to determine whether we have two real roots or a pair of complex-conjugate roots.

Application of the Theory to a Discrete Planar Schottky Diode

Table 1 gives the equivalent circuit values for the SC1T5 type planar diode for 5 μm and 20 μm finger lengths (indicated by -S5 and -S20 respectively). These parameters were generated by matching the equivalent circuit of Fig. 1(b) to the results of finite-element modeling of the mounted diode performed using Hewlett Packard's High Frequency Structure Simulator over frequencies from 450–700 GHz [8]. The capacitance C_f includes both the finger-to-pad capacitance C_{fp} and the time averaged junction capacitance $C_{j,avg}$. The capacitance $C_{j,avg}$ was found by averaging the capacitance waveform (determined using harmonic balance simulations) over an LO cycle. The optimum RF and LO diode resistance, $R_{d,opt}$, was estimated to be 100 Ω based on the results of harmonic balance simulations. These circuit values were then used with (19) to calculate curves of ρ_a versus fractional bandwidth for various planar diode geometries at different frequencies.

Fig. 7 shows the relation between ρ_a and the fractional bandwidth b for an SC1T5 type planar diode [4] with a 5 μm finger length plotted at frequencies from 500 GHz to 2000 GHz. The bandwidth limitation is not a practical limitation at the lowest frequency, and it is only above about 1000 GHz that the bandwidth limitation significantly effects the coupling of power to the

Table 1. Equivalent circuit values used during bandwidth modeling for the SC1T5 diode for various finger lengths.

Diode Type	$C_{pp} \equiv C_p$ (fF)	C_{fp} (fF)	$C_{j,avg} + C_{fp} \equiv C_f$ (fF)	L_f (pH)
SC1T5-S5	2.8	0.4	4.4	20
SC1T5-S20	2.0	0.8	4.8	29

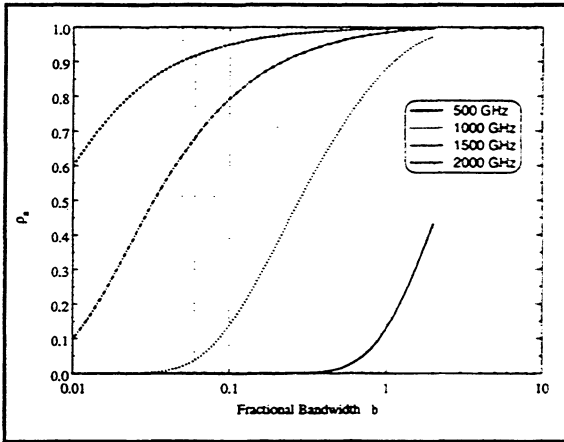


Fig. 7. ρ_a versus fractional bandwidth for the SC1T5-S5 diode for frequencies from 500 GHz to 2000 GHz.

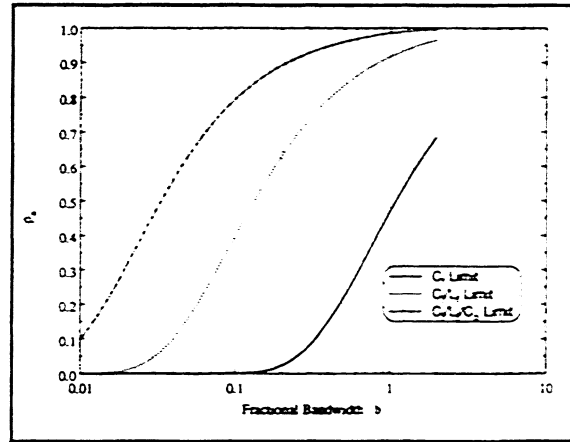


Fig. 8. ρ_a versus fractional bandwidth for the SC1T5-S5 diode at 1500 GHz for C , CL and CLC circuits.

diode. Note that this is a power coupling bandwidth, not a predicted mixer bandwidth. In order to illustrate the relative importance of each circuit element, Fig. 8 compares the bandwidth limitation for an SC1T5-S5 diode at 1500 GHz considering first the effect of C_f only, then both C_f and L_f , and finally for the full three-element circuit. Fig. 9 shows a set of bandwidth limitation curves comparing different finger lengths and different junction capacitances. As the finger length is reduced, L_f decreases while C_p increases; also, the bandwidth increases, thus indicating the importance of L_f in relation to C_p . Also shown is the improvement in bandwidth as the junction capacitance is reduced from 2 fF to 1 fF.

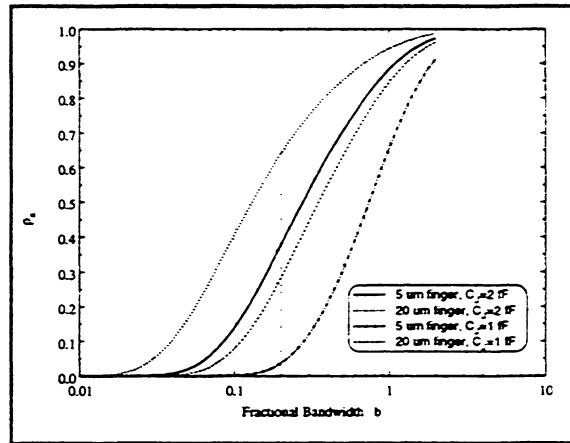


Fig. 9. ρ_a versus fractional bandwidth for various diode at 1500 GHz.

Conclusions

In this paper we have derived the bandwidth limitation equation for the coupling of power to a resistor through a three-element CLC circuit. This derivation was made possible by our extension of the Bode-Fano theory to circuits with three or more zeros of transmission at infinity. The results of this analysis were then used to examine the performance of a fundamental mixer built using discrete planar diode chips with semi-insulating GaAs support substrates. The simulations indicate that at frequencies around 500 GHz the coupling of power to the diode is not significantly limited by the chip parasitics. However, at frequencies above approximately 1000 GHz, the packaging parasitics impose tight limits on the power coupling bandwidth for this diode and mixer geometry, thus complicating mixer design. The bandwidth limitation condition derived here is general, and can be used to explore power coupling limitations for a variety of devices and structures.

Acknowledgments

The authors would like to thank Dr. Anthony Kerr and Dr. John Granlund of the National Radio Astronomy Observatory for their invaluable advice, comments and criticisms of this work.

This research has been supported by the U.S. Army National Ground Intelligence Center through contract DAHC90-91-C-0030.

References

1. J.L. Hesler, W.R. Hall, T.W. Crowe, R.M. Weikle, II, B.S. Deaver, Jr., R.F. Bradley, and S.-K. Pan, "Fixed-Tuned Submillimeter Wavelength Waveguide Mixers Using Planar Schottky Barrier Diodes," *IEEE Trans. Microwave Theory Tech.*, Vol. 45, pp. 653-658, May 1997.
2. H.W. Bode, *Network Analysis and Feedback Amplifier Design*, New York, Van Nostrand, 1945.
3. R.M. Fano, "Theoretical Limitations on the Broadband Matching of Arbitrary Impedances," *J. Franklin Inst.*, vol. 249, pp. 57-83, 139-154, Jan./Feb. 1950.
4. W.L. Bishop, E. Meiburg, R.J. Mattauch, T.W. Crowe and L. Poli, "A Micron-Thickness, Planar Schottky Diode Chip For Terahertz Applications With Theoretical Minimum Parasitic Capacitance," 1990 IEEE MTT-S Int. Mic. Symp. Digest, pp. 1305-1308, May 1990.
5. S. Darlington, "Synthesis of Reactance 4-Poles Which Produce Prescribed Insertion Loss Characteristics", *Journal of Mathematics and Physics*, vol. 18, pp. 275-353, September 1939.
6. A.R. Kerr, "Some Fundamental and Practical Limits on Broadband Matching to Capacitive Devices, and the Implications for SIS Mixer Design," *IEEE-MTT43*, No. 1, pp. 2-13, Jan. 1995.
7. J.L. Hesler, V. Celli, and B.L. Gelmont, "An Extension to Fano's Theory of Broadband Matching of Arbitrary Impedances," submitted to *IEEE Trans. on Circuits and Systems: I - Fund. Theory and Applic.*, Feb. 1998.
8. J.L. Hesler, *Planar Schottky Diodes In Submillimeter-Wavelength Waveguide Receivers*, Ph.D. Dissertation, University of Virginia, Jan. 1996.

**A HIGH PERFORMANCE,
318 GHz SUBHARMONIC (x3)
BALANCED MIXER**

Israel Galin
Aerojet
PO Box 296
Azusa, CA 91702

israel.galin@aerojet.com

ABSTRACT

The 300-3000 GHz sub-millimeter-wave (SMMW) spectrum offers ample opportunities for space-borne remote sensing, as reflected in a partial list of US and European planned space missions—for example, SWAS, MLS, MIRO. Because of these opportunities, the current shortfalls of SMMW receiver technology underscore the need for its further advancement.

Mixer technology leads the way in facilitating SMMW receiver—consistently exhibiting earlier availability and faster maturity—relative to the necessary solid-state local-oscillators (LO), and desirable low-noise amplifiers SMMW technologies. Such an uneven rate of progress has created technology “gaps” in which SMMW receivers often fall victim.

This paper describes the developments of a new class of high performance, higher order subharmonic (>x2) mixers uniquely suitable to accommodate the present underdeveloped state of SMMW LO technology.

I. INTRODUCTION

The 300-3000 GHz sub-millimeter-wave (SMMW) spectrum offers ample opportunities for space-borne remote sensing, as reflected in a partial list of US and European planned space missions—for example, SWAS, MLS, MIRO. Because of these opportunities, the current shortfalls of SMMW receiver technology underscore the need for its further advancement.

Mixer technology leads the way in facilitating SMMW receiver—consistently exhibiting earlier availability and faster maturity—relative to the necessary solid-state local-oscillators (LO), and desirable low-noise amplifiers SMMW technologies. Such an uneven rate of progress has created technology “gaps” in which SMMW receivers often fall victim.

This paper describes a new class of high performance, higher order subharmonic ($>x2$) balanced mixers, uniquely suitable to accommodate the present underdeveloped state of LO technology for SMMW receiver.

Subharmonic ($x2$) mixers, employing readily available up to 150 GHz Gunn LOs, have successfully facilitated space-borne low-noise receivers throughout the 30-300 GHz MMW spectrum [1]. But, similar subharmonic ($x2$) mixers [2] let alone fundamental mixers [3], implemented at SMMW frequencies, presently require Gunn-based LO assemblies, which include efficiency challenged frequency multipliers, or bulky and/or reliability challenged laser based LOs.

Harmonic (xN) mixers with $N>2$ constitute an immediate bridge for matching available up to 150 GHz Gunn LOs, for 450 GHz receivers (harmonic $x3$ mixers) and for 600 GHz receivers (harmonic $x4$ mixers). Furthermore, with a frequency doubler [4] following the LO such harmonic ($>x2$) mixers may facilitate SMMW receivers well above 1 THz.

Unfortunately, harmonic ($>x2$) single-ended mixers exhibit rapid degradation in conversion-loss and noise-figure performance, and present formidable challenges matching to broadband IF amplifiers [5].

This paper describes a new class of even-subharmonic ($x(2N+1)$) balanced two-diode mixers, featuring performance advantages in comparison with single-diode subharmonic (xM) mixers (for $M=2N+1$) at similar SMMW frequencies.

The paper reports the performance of a 318 GHz subharmonic ($x3$) balanced mixer prototype which had been integrated with a 106 GHz LO and an IF amplifier to yield a SMMW receiver. This 318 GHz receiver yields promising performance when tested at narrow-band or wide-band outputs.

II. MIXER DESCRIPTION

Two mixer diodes connected to a mixer ports as shown in Figure 1—in series to RF port, and in anti-parallel to the LO and IF ports—constitute a balanced mixer configuration. We have implemented this mixer configuration, as a SMMW waveguide structure with RF (WR-2) and LO (WR-6) waveguides, and a pairs of whiskerless mixer diodes (University of Virginia) on a suspended printed circuit at the IF mixer port. The feedhorn at the RF port is implemented as an integral part of the mixer structure.

The output current (I) of this mixer generally consists of the following series of low-frequency (IF) current components (i):

$$I_{IF}(\omega) \propto \sum_N i_{(2N+1)} \cdot \{ \cos[(((2N+1) \cdot \omega_{LOt}) - (\omega_{Rft}))] \}$$

For $N=0$, this expression depicts the well known fundamental balanced mixer, but for $N>0$, the same expression highlights a family of odd-subharmonic balanced mixers. Filters at the RF port of the mixer determine the accessible external inputs, the relevant LO harmonic N , and the mixer's output (to the exclusion of other possible outputs).

A paper by Schuppert [6] provides a comprehensive account for the advantages offered by such subharmonic ($\times 3$) balanced mixers, in comparison to a single ended harmonic ($\times 3$) mixers. Among the most notable advantages are: a lower mixer IF impedance facilitated by two diodes in parallel, easier matched to IF amplifiers over wide frequency bands; better conversion-loss, due to the exclusion of all even subharmonic mixing by virtue of symmetry (not filters); and simpler mixer RF circuitry, facilitated by two diode in series, easier matched to a waveguide with height closer to standard.

III. MEASURED DATA

The 318 GHz receiver had been tuned and tested over a variety of wide-band IF outputs: with an instantaneous 2-8 GHz IF output (IF amplifier with ~ 2 dB noise-figure) the receiver features an average DSB noise-figure of 12.2 dB (Figure 3); and with an instantaneous 6-16 GHz output (IF amplifier with ~ 2 dB noise-figure) the receiver yields an average DSB noise-figure of 13 dB (Figure 4). Each one of these two different wide-band receivers represents a mixer with waveguide back-shorts set at different positions. As a narrow band 318 GHz receiver with an instantaneous IF output of 7-8 GHz (IF amplifier with ~ 2 dB noise-figure) the receiver yields 11.5-12 dB DSB noise-figure, with waveguide back-shorts set for optimum performance with this IF amplifier.

In all tested 318 GHz receiver configurations the 106 GHz LO power requirements ranged a modest $+7\pm 1$ dBm, as depicted in Figure 5 for the case of a narrow band receiver.

IV. ACKNOWLEDGEMENTS

The author would like to acknowledge the contributions of Mrs. Cynthia A. Schnitzer for testing the receiver and Mrs. Cuc Nguyen for assembling the mixer.

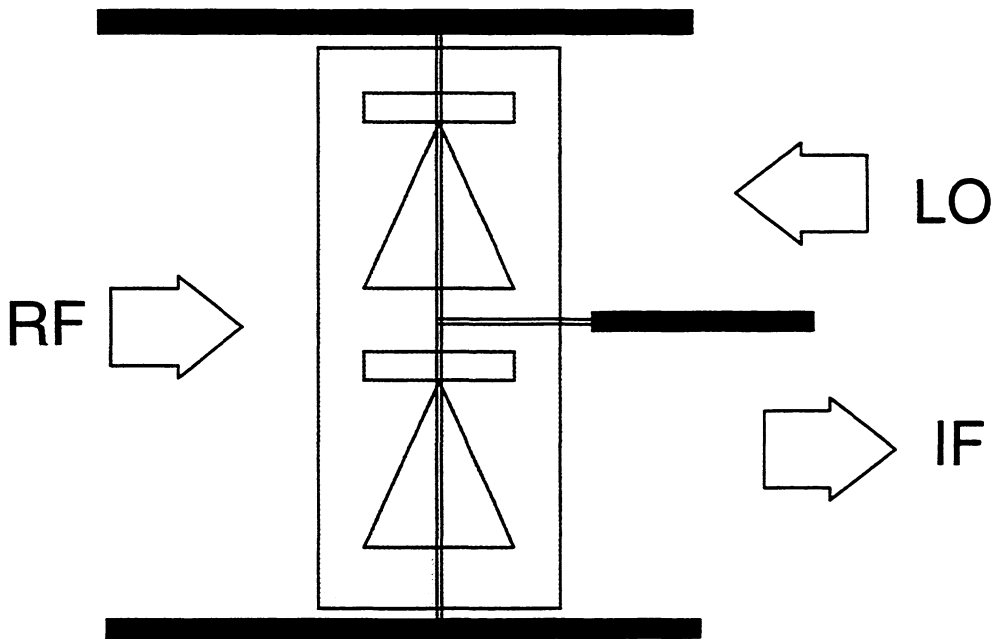


Figure 1. The Electrical Equivalent Circuit For Odd-Subharmonic ($x(2N+1)$) Balanced Mixers (Diodes in Series to RF, And in Anti-Parallel to LO And IF Mixer Ports)

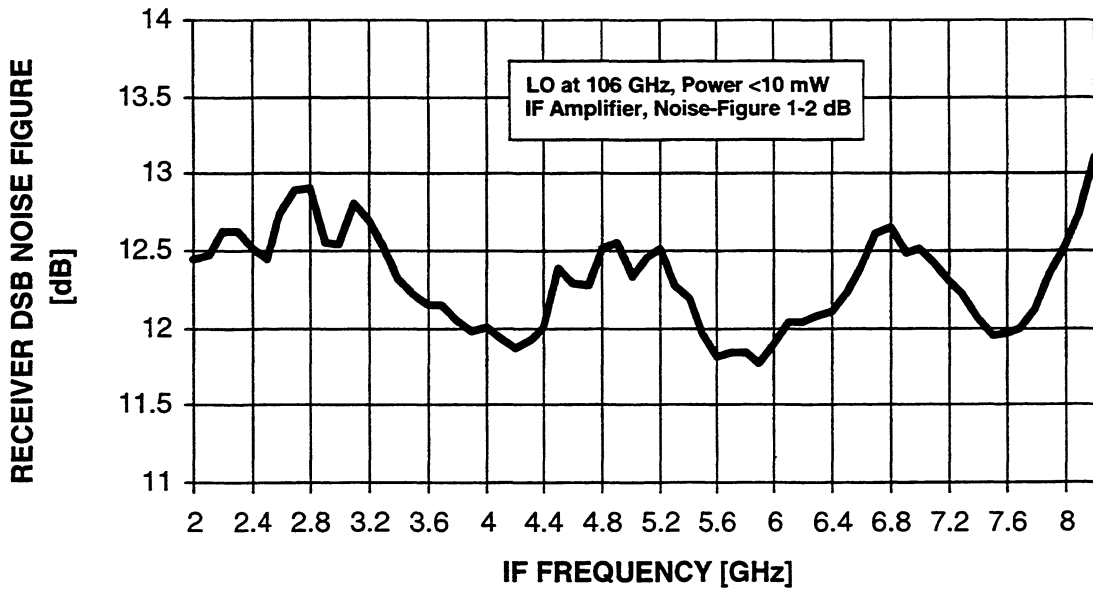


Figure 2. Measured Performance of a 318 ± 8 GHz Wide Band Receiver, with a Subharmonic ($x3$) Balanced Mixer

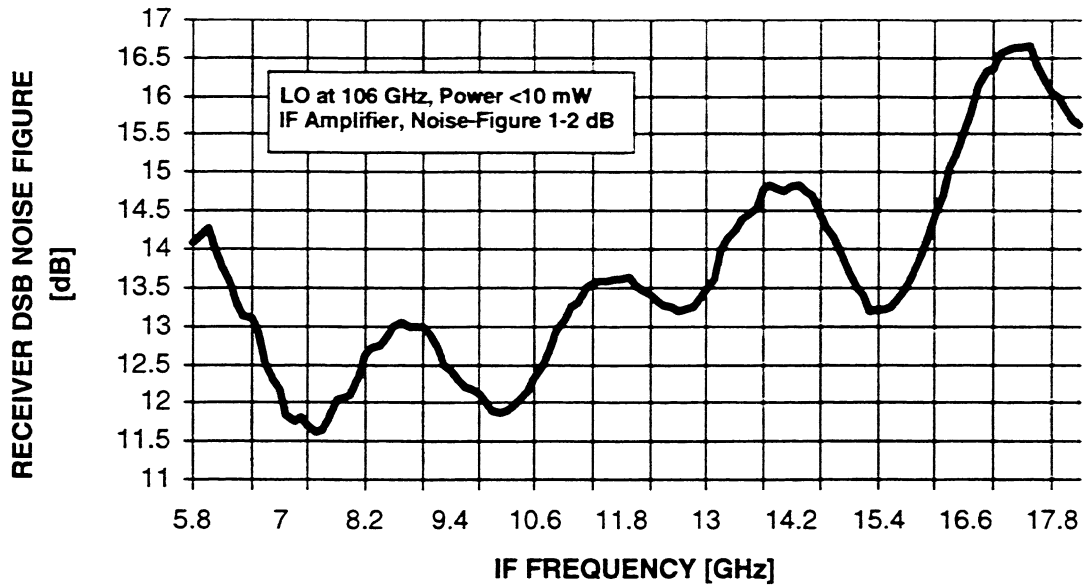


Figure 3. Measured Performance of a 318±18 GHz Wide Band Receiver, with a Subharmonic (x3) Balanced Mixer

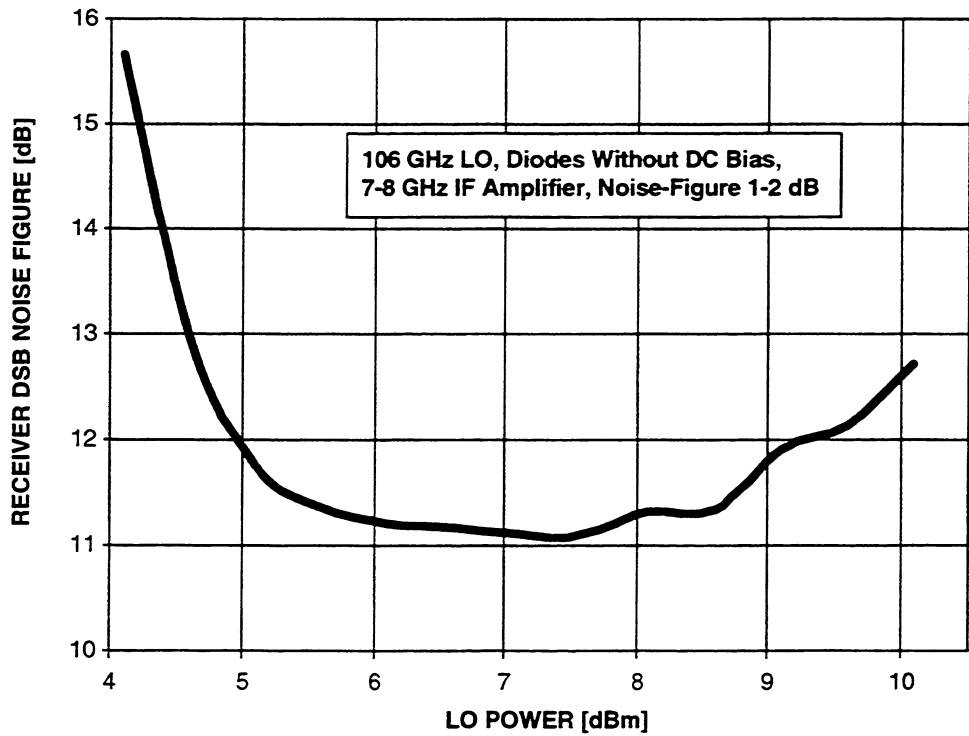


Figure 4. 106 GHz LO Power Requirements for the 318 GHz Narrow Band Receiver, with a Subharmonic (x3) Balanced Mixer, Requiring Low LO Power Drive

REFERENCES

- [1] I. Galin, "A Mixer Up-To 300 GHz With Whiskerless Schottky Diodes For Spaceborne Radiometers", 7th International Symposium on Space Terahertz Technology, Charlottesville, Virginia 1996.
- [2] I. Mehdi, et al, "600 GHz Planar-Schottky-Diode Subharmonic Waveguide Mixers", IEEE MTT-S Digest 1996.
- [3] J.L. Hessler, et al, "The Development of Planar Schottky Diode Waveguide Mixers at Submillimeter Wavelengths", IEEE MTT-S Digest 1997.
- [4] R.P. Smith, et al, "Advances in Submillimeter Wave Semiconductor-Based Device Designs And Processes at JPL", 8th International Symposium on Space Terahertz Technology, Cambridge, Massachusetts 1997.
- [5] N.R. Erickson, "Low-Noise Submillimeter Receivers Using Single-Diode Harmonic Mixers", Proceedings of the IEEE, November 1992.
- [6] B. Schuppert, "Analysis And Design of Microwave Balanced Mixers", IEEE Transactions on MTT, January 1986.

QUASI-INTEGRATED PLANAR SCHOTTKY BARRIER DIODES FOR 2.5 THz RECEIVERS

Tetsu Suzuki^{1,2}, Chris Mann³, Takanari Yasui¹, Hiroto Fujishima¹, and Koji Mizuno^{1,2}

¹Photodynamics Research Center, RIKEN, Sendai 980, Japan

²Research Institute of Electrical Communications, Tohoku University, Sendai 980, Japan

³Rutherford Appleton Laboratory, Chilton, Didcot, United Kingdom

ABSTRACT

Schottky barrier diodes (SBDs) remain an important device for detecting and mixing at terahertz frequencies, particularly in atmospheric remote sensing and plasma diagnostics. The hydroxyl radical (OH), which plays a critical role in all cycles of ozone destruction and also acts as an oxidant for harmful gases in the atmosphere, has first significant spectral emissions at 1.8 and 2.5THz. Here we will present a new SBD configuration called a quasi-integrated planar (QUIP) SBD, to be used in 2.5THz receivers for measuring spatial distribution of the hydroxyl radical.

Submillimetre wave and terahertz applications require sub-micron anode SBDs. Traditionally, whisker-wire contacted diodes, with Schottky and Ohmic contacts at opposite sides of the device, are used in open structures such as corner-cube mixers. Here we propose a “planar” SBD with Schottky and Ohmic contacts on the same side of the device. Instead of mounting a small diode chip on a post, a large chip is used to form the wall of a waveguide which feeds a corrugated conical feedhorn antenna. A small area of this chip consisting of SBD anodes is placed near the feed of the antenna, while the rest of the chip provides the Ohmic contact and acts as a top cover for the waveguide. Thus, the diode is “integrated” into the mixer block. This greatly simplifies mixer block fabrication and assembly, and also minimises losses between the antenna and the diode by allowing the SBD contact to be placed at the feed of the antenna. The diode is then contacted using a planar whisker with an integrated RF/IF filter. QUIP SBDs with anode diameters of 0.25 - 0.3 μ m have been successfully fabricated and mounted into a mixer block for RF performance evaluation.

INTRODUCTION

Waveguide devices are now being used with some success in the terahertz region [1,2] and waveguide mixers are now showing comparable performance to the more common corner cube mixer configuration at frequencies as high as 2.5THz. The waveguide devices have the additional advantages of rugged construction, in-situ tuning capability and radiation properties that are isolated from the diode embedding circuit. However, the specialist fabrication level of machining required combined with

the intricate fabrication procedures adopted make this approach one that is intended for applications where cost and time are not the main drivers.

The 2.5THz waveguide mixers used to date have made use of notch front diodes that have the soldered Ohmic contact on the faces that are perpendicular to the diode array. In order to realise the sub-miniature dimensions required, the chips are separated using deep Reactive Ion Etching (RIE) techniques. The fabrication process is therefore complicated requiring specialist equipment and careful process control. The resulting chips have dimensions in the order of 40 μ m across either as cubes or cylinders [2,3]. This paper describes a new novel approach where the diode chip itself is partially integrated with the waveguide circuit. In addition, the fabrication process is extremely straightforward as all processing steps are carried out on a flat or 'planar' surface.

By taking this approach a number of advantages result. Firstly, the chip becomes very easy to handle as it can be manufactured to be many times the size of the waveguide circuit rather than having to fit within it. Secondly, all unwanted GaAs is removed from the RF circuit itself and the soldering procedure is greatly simplified. Finally, the machining of the waveguide cavity becomes much easier so that when combined with the use of the planar whisker other types of waveguide device can be realised using this circuit architecture, for example, frequency multipliers or RTD oscillators.

BASIC CONCEPT

For a more detailed description of the mixer design see [3] in this proceedings. Use is made of the same circuit architecture. A schematic diagram showing the basic concept of the QUIP SBD chip is shown in figure 1. The mixer consists of three main components. The signal is coupled to the waveguide via a conventional corrugated feedhorn. This can be detached from the main part of the mixer block. The section of waveguide that contains the backshort and diode chip is machined from copper and electroplated in gold. A minimum of 2 μ m of gold is required as the soldering process used to mate the diode chip to the machined section uses a low melting point (130C) Indium solder. If an insufficient thickness of gold is used the solder can form brittle intermetallic compounds that can lead to poor electrical properties and mechanical failure.

The QUIP chip forms the waveguide lid thus completing the RF circuit.

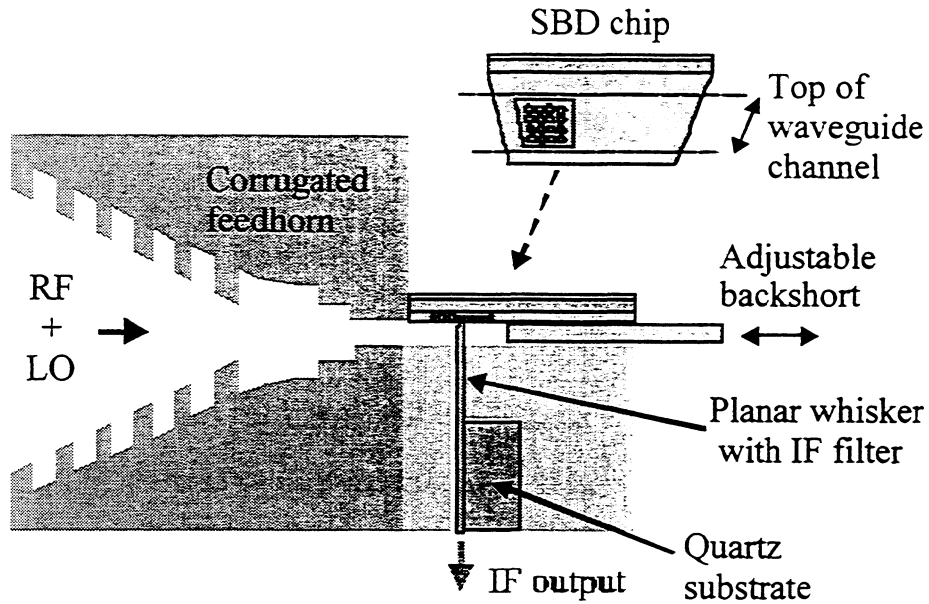


Figure 1: *The basic quasi-integrated planar diode concept*

A working drawing of the QUIP chip showing the relevant dimensions is given in figure 2. The dimensions of the chip can be set very accurately by using a commercial diamond dicing saw.

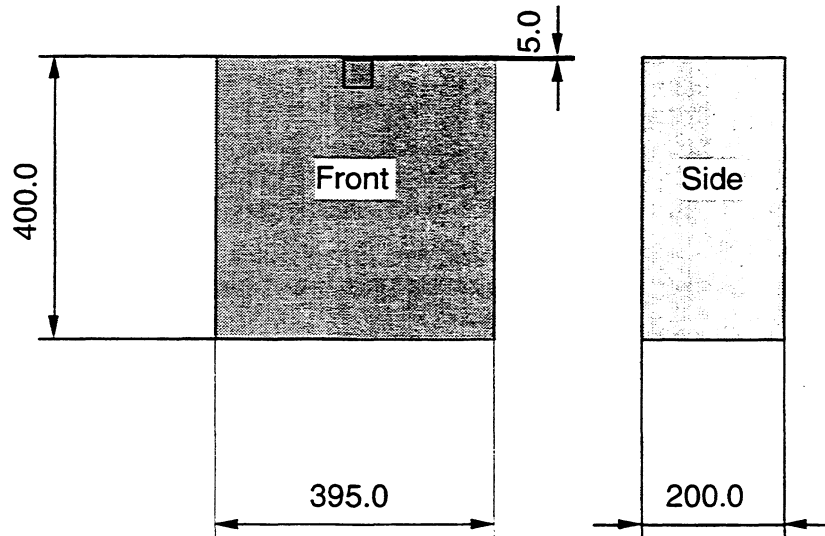
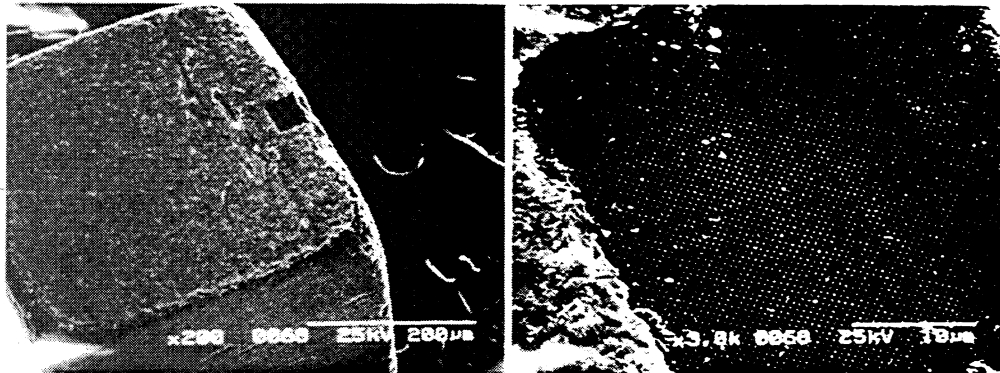


Figure 2: *Dimensions of the quasi-integrated planar diode chip used*

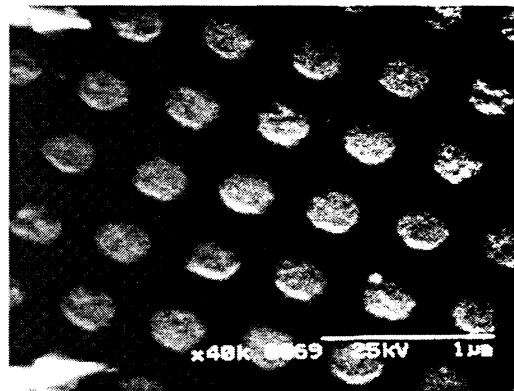
The diode sits in a $400\mu\text{m}$ wide recess machined into the mixer block above the channel which eventually forms the $27\mu\text{m}$ high by $105\mu\text{m}$ wide RF waveguide. This means that the $40\times 40\mu\text{m}$ array of diode anodes automatically aligns to the centre of the RF filter channel in which the planar whisker is housed. The soldering procedure for the QUIP chip is made very straightforward by its large dimensions.

A photograph showing a QUIP chip (X69) soldered into a mixer block is shown in figure 3 (d). The anodes are $\approx 0.25\text{-}0.3\mu\text{m}$ in diameter.

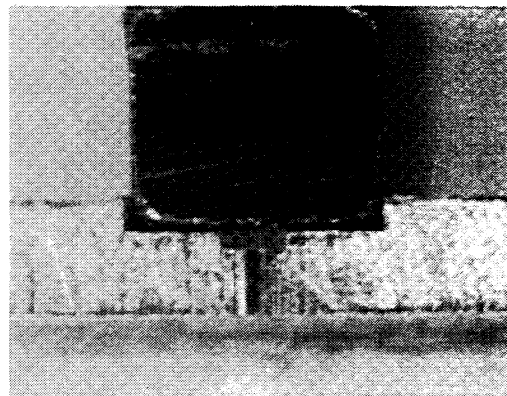


(a)

(b)



(c)



(d)

Figure 3: An X69 QUIP chip and soldered into RAL block DW3

DIODE FABRICATION

The fabrication procedure is very similar to that used for the fabrication of the conventional back contacted Schottky diode chips used in corner cube mixers. Much work has been carried out aimed at reducing the intrinsic diode noise. Various aspects of the fabrication process have been examined to determine if the diode noise can be minimised [4, 5]. For example, it was found that ECR (electron cyclotron resonance) plasma etching reduces the the number of defects when compared with RIE, and thus significantly lowers the $1/f$ noise. This is particularly important for mixers intended for Fusion Plasma Diagnostic applications. These mixers typically operate at IF frequencies of a few tens of megahertz and therefore the $1/f$ noise contribution becomes significant. Comprehensive results of this study will be published elsewhere [6].

A schematic of a QUIP diode chip is shown in figure 4. The Ohmic contact is made on the front side of the wafer. In the case of conventional diode chip, GaAs lies between the diode anode and the Ohmic and hence the bulk GaAs that makes up the chip now has to be included as part of the RF circuit. Even though it is formed from highly doped material it must still add extra loss into the signal path so in general the thickness of the chips has been kept to a minimum, typically $100\mu\text{m}$, making handling difficult. For the QUIP chip the Ohmic contact is on the front face and leaving a minimum amount of exposed GaAs in the RF circuit. The chip can now be made as thick as thought practical with no detrimental effects on mixer performance. The Ohmic contact on the bottom of the QUIP chip is required only to facilitate Au/Pt plating of the anodes, and it does not effect the diode current. The details of the fabrication process will be addressed in [7].

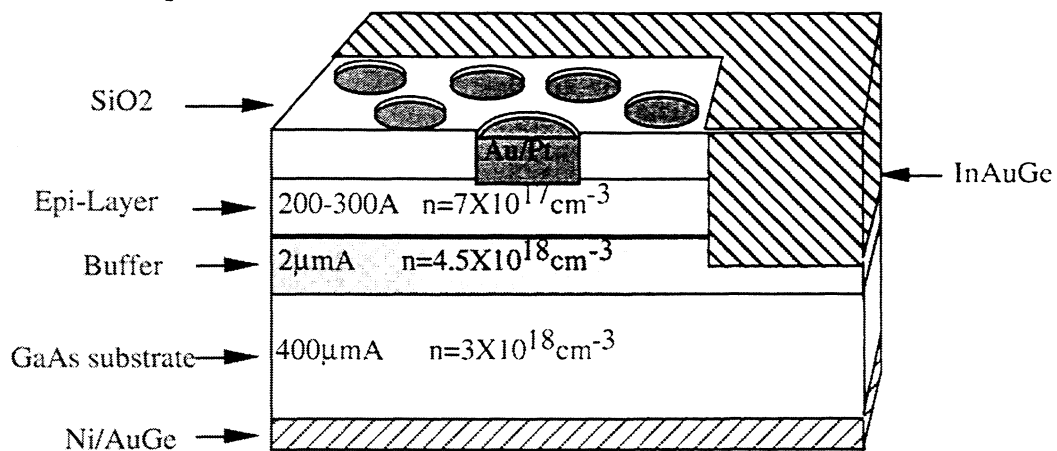


Figure 4 : A *QUIP* diode chip with the Ohmic contact on the front

RF MEASUREMENTS IN A WAVEGUIDE MIXER

The advantages of a waveguide mixer over a corner reflector mixer are particularly apparent when the RF embedding circuit is considered. For the corner reflector, the embedding impedance is theoretically set to be real somewhere in the range 80-200 Ω . Knowledge of the absolute embedding impedance is more or less impossible to obtain and this is mainly because the antenna pattern and embedding impedance both depend on the whisker/antenna/reflector configuration. Small physical changes in the mount can modify the beam pattern adding additional optical coupling losses or alternatively introduce reflections on the whisker/antenna which result in an unknown reactive component in the embedding impedance. In the waveguide mount the radiation properties are isolated from the embedding circuit via the use of a corrugated feedhorn. The signal is matched to the diode via the use of a waveguide matching probe and a movable backshort tuner. Therefore in principle a complete range of embedding impedances can be presented to the diode the aim being to eventually find the optimum value.

RAL mixer DW3 was assembled as described in [3] and tested at 2.5THz. An SEM of a completed mixer assembly is shown in figure 5.

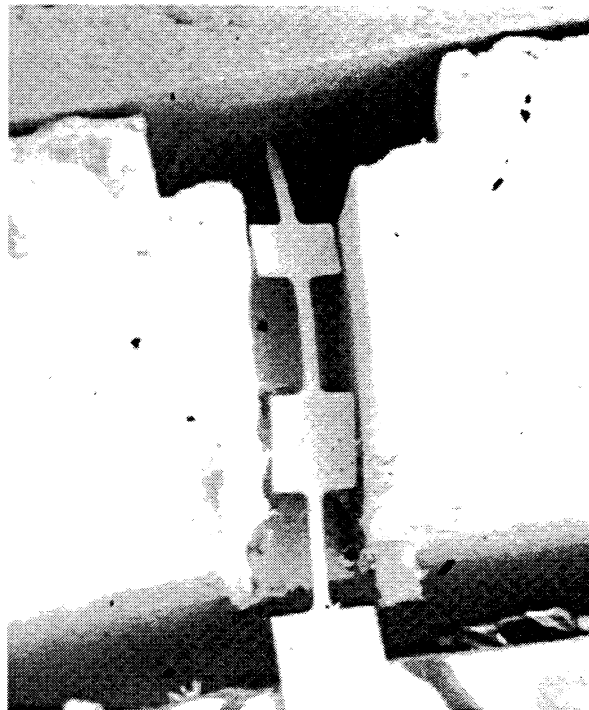


Figure 5: An assembled mixer RF circuit

Preliminary RF results at 2.5THz are very encouraging and are displayed in figure 6. A double sideband receiver noise temperature of 24,000K was obtained at the first iteration. This compares with our best receiver noise performance of $\approx 16,000\text{K}$ DSB obtained using a UVA 1T2 notch front diode. However, these are both very early results. A full empirical optimisation of the RF circuit is now required before accurate comparisons can be made between diodes.

Importantly, for the X69 QUIP diode, the LO requirement has been reduced to levels that are directly comparable to that required by a corner reflector mixer showing that the loss associated with the waveguide mount is not too prohibitive. In addition, this level of LO requirement is approximately 60% lower than for a UVA 1T2 notch front diode mixer. The RF circuit will now be empirically optimised in order to find the best impedance match for the X69 QUIP diode.

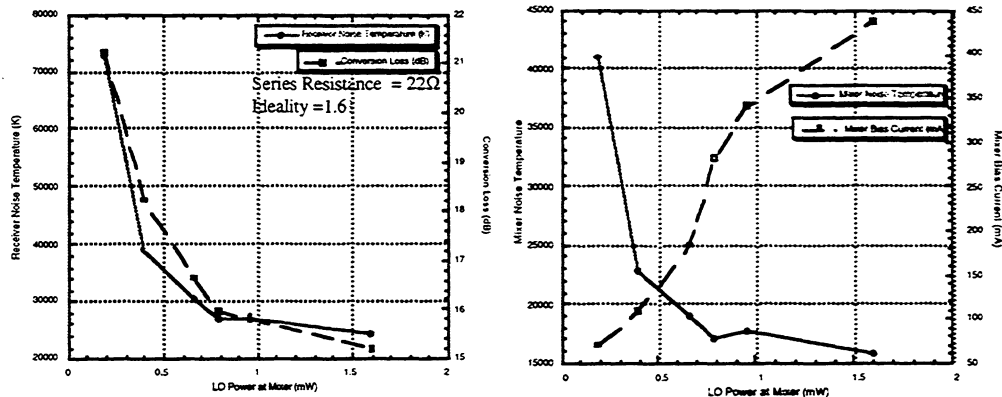


Figure 6: 2.5THz mixer RF performance for Tohoku diode X69 in RAL mixer DW3

CONCLUSIONS

A new RF circuit architecture has been demonstrated. A novel Schottky diode chip configuration that allows it to be partly integrated with a waveguide mount has eased many of the fabrication and assembly problems encountered in previous designs that made use of sub-miniature notch front diodes. Good mixer performance has been obtained at first iteration and the circuit will now undergo further empirical optimisation.

This approach could be easily modified to accommodate different devices such as Schottky varactors, whiskered HBVs or RTDs.

ACKNOWLEDGEMENTS

Thanks are given to Dr J.J.Chang for his input into the early discussions about the QUIP chip diode concept. Part of this work was carried out at the Laboratory for Electronic Intelligent Systems, Research Institute of Electrical Communications, Tohoku University, supported by the Heiwa Nakajima foundation and a Grant-in Aid of Scientific Research from the Ministry of Education, Science and Culture of Japan.

REFERENCES

- [1] 'Corrugated Feedhorns at Terahertz Frequencies - Preliminary Results', B.N.Ellison, M.L.Oldfield, D.N.Matheson, B.J.Maddison, C.M.Mann and A.F.Smith, The Fifth International Symposium on Space Terahertz Technology, Ann Arbor, May 1994.
- [2] 'First Results for a 2.5 THz Schottky Diode Waveguide Mixer', B.N.Ellison, M.L.Oldfield, D.N.Matheson, B.J.Maddison, C.M.Mann, S.Marazita, T.W.Crowe, P.Maaskant, W.M.Kelly, 7th International Symposium on Space Terahertz Technology, University of Virginia, March 1996.
- [3] 'On The Design And Measurement Of A 2.5THz Waveguide Mixer ', C.M.Mann, D.N.Matheson, B.N.Ellison, M.L.Oldfield, B.P.Moyna, J.J.Spencer, D.S.Wilsher, and B.J.Maddison, The 8th International Symposium on Space Terahertz Technology, JPL, Pasadena, March 1998
- [4] T. Suzuki, H. Shinohara, T. Nozokido, Y. Kudo, H. Warashira, and K. Mizuno, "Noise Dependence of Submillimeter Wave Pt/GaAs Schottky Diodes on Interface Defects and Temperature," Proc. of the 16th International Conf. on IR & MMW, pp. 472-473, Lausanne, Switzerland, August 1991.
- [5] "Development of Low Noise Schottky Barrier Diode for the THz Region and Semiconductor Surface Analyses," T. Yasui, T. Suzuki, H. Fujishima, M. Arasawa, T. Nozokido, T. Yamada, S. Tsunekawa, and K. Mizuno, Technical Report of IEICE, ED96-180, MW96-143, ICD96-168 (1997-01), pp. 1-8 (in Japanese).
- [6] "Reduced Low Frequency Noise Schottky Barrier Diodes for Terahertz Applications," T. Suzuki, T. Yasui, H. Fujishima, T. Nozokido, K. Mizuno, O. Boric-Lubecke, and V. M. Lubecke, manuscript in preparation for IEEE Trans. on MTT.
- [7] "Fabrication of Quasi-Integrated Planar Schottky Barrier Diodes for THz Applications", T. Yasui, T. Suzuki, C. Mann, H. Fujishima, and K. Mizuno, submitted to the 23th International Conf. on IR & MMW, Essex, England, September 1998.

A TUNERLESS SIS MIXER FOR 200–280 GHz WITH LOW OUTPUT CAPACITANCE AND INDUCTANCE

A. R. Kerr¹, S.-K. Pan¹,
A. W. Lichtenberger² and H. H. Huang²

¹National Radio Astronomy Observatory*
Charlottesville, VA 22903

²Department of Electrical Engineering**
University of Virginia
Charlottesville, VA 22904

ABSTRACT

The introduction by Padin *et al.* in 1996 of an SIS mixer with an integrated IF amplifier eliminates the need for an IF isolator and makes possible SIS receivers with multi-octave IF's. To realize a wide IF bandwidth, an SIS mixer must be designed with low IF capacitance and inductance. This paper describes an SIS mixer in which the RF circuit is effectively decoupled from the IF circuit, and a compact high-impedance RF choke circuit is used, resulting in low output capacitance and inductance.

INTRODUCTION

If an SIS receiver is operated with a 50-ohm cable between the mixer and IF amplifier, impedance mismatch at the ends of the cable can cause the overall receiver gain and noise temperature to vary substantially across the IF band. This results from two processes: (i) the IF signal from the mixer undergoes multiple reflections between the mixer and amplifier, and (ii) the outgoing noise wave from the input port of the amplifier is reflected at the mixer and returns to interfere with the ingoing noise wave with which it is correlated. An amplifier well matched to the cable eliminates mechanism (i), while a well matched mixer eliminates both (i) and (ii). In practice, SIS mixers do not usually operate with a well matched output, and in many cases matching the output would lead to undesirable behavior — excessive conversion gain with a corresponding reduction of dynamic range, and negative RF input conductance which implies reflection gain at the mixer input. An isolator is often inserted in the cable, and presents a good match to both the mixer and amplifier. The isolator is not without penalty, however, as thermal noise from its internal termination is partially reflected at the mixer and adds to the IF noise; this can add

*The National Radio Astronomy Observatory is a facility of the National Science Foundation operated under cooperative agreement by Associated Universities, Inc.

** This work was supported in part by the National Science Foundation under grant number AST-9618747

significantly to the receiver noise temperature, even when the isolator is at 4 K. A more serious drawback may be the limited bandwidth of an isolator, usually no greater than an octave. To achieve a wide IF bandwidth when using an isolator therefore requires a high IF center frequency. If it is desired to build a receiver with an IF bandwidth of 8 GHz, as is needed for the NRAO's proposed Millimeter Array, the use of an isolator would require an IF of 8-16 GHz IF, or higher.

The introduction by Padin *et al.* [1,2] of an SIS mixer with a built-in IF amplifier makes possible SIS receivers with multi-octave IF's, and eliminates the need for an IF isolator. It is pointed out in [2] that to realize a wide IF bandwidth, the SIS mixer must be designed with low output capacitance, and in general minimizing the output circuit parasitics (capacitance and inductance) will facilitate broadband coupling to the first IF stage. In many SIS mixers most of the output capacitance is associated with the RF matching and choke circuits, and the output inductance is mainly in the RF circuit. In the present paper we describe an SIS mixer in which the RF circuit is decoupled from the IF circuit, and a compact high-impedance RF choke with low capacitance and inductance is used. The mixer operates in the 200-280 GHz range, but the design is suitable for scaling to higher or lower frequencies.

Three RF matching circuits used in SIS mixers are shown in Fig.1. They are: (a) an end-loaded microstrip circuit, as used in several very successful SAO mixers [3]; (b) a microstrip inductor terminated with a $\lambda_{RF}/4$ open-circuit microstrip stub, as used at NRAO [4]; and (c), similar to (b), but with the microstrip inductor terminated in a sectoral stub, as described in [5, 6]. As indicated in the figure, for operation at ~230 GHz, the static (low frequency) capacitance of the three circuits is between 200 and 500 fF.

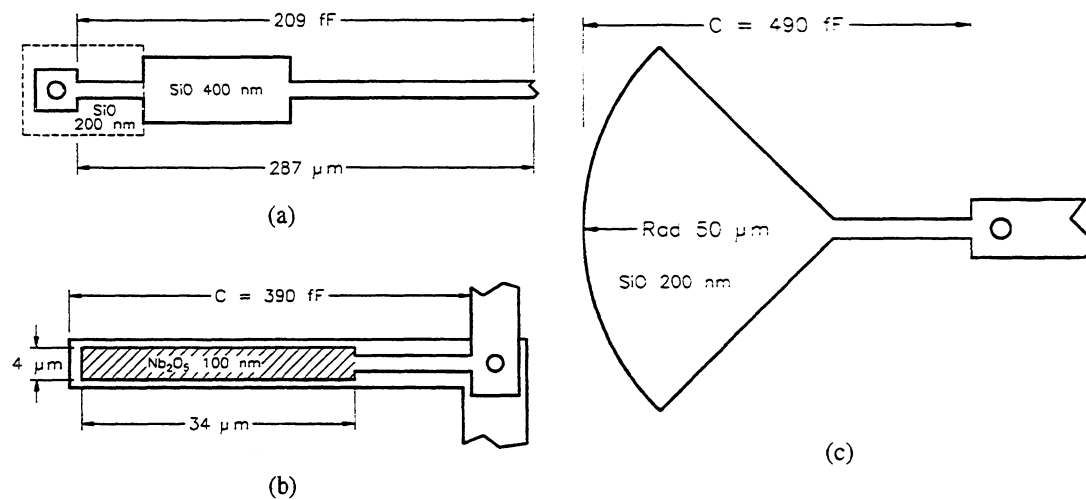


Fig. 1. Three RF tuning circuits used in SIS mixers. Dimensions and capacitances indicated are for a center frequency of ~230 GHz. (a) End loaded matching circuit. (b) Tuning inductor with $\lambda/4$ microstrip stub. (c) Tuning inductor with radial microstrip stub. (Diagrams not to scale.)

For the SAO mixer complete with RF chokes, the static capacitance at the IF port is 470 fF. This consists of 200 fF from the RF choke, 210 fF from the RF matching circuit, and 60 fF from the SIS junction itself. The low-frequency inductance of the IF circuit is 1700 pH, of which only 42 pH is from the RF matching circuit.

A NEW DESIGN

It is clear from the foregoing that to reduce the IF output capacitance of an SIS mixer, the capacitance of the RF matching circuit and/or the RF choke must be reduced. The IF inductance can be reduced by reducing the inductance of the RF choke. A design which attempts to minimize both these components is shown in Fig. 2. The mixer is fabricated on a 0.010" fused quartz substrate, thinned after lithography to 0.0035". A 50-ohm suspended stripline, at the left end of the substrate in Fig. 2(a), is driven by a broadband transition [7] from full-height rectangular waveguide. Near the middle of the substrate is a broadband transition from suspended stripline to capacitively loaded coplanar waveguide (CLCPW) [8]. This transition is almost identical in geometry to the suspended stripline-to-coplanar waveguide (CPW) transition described in [7]. The CLCPW has a characteristic impedance of 63 ohms, and is the first element of the broadband RF matching circuit — see Fig. 2(b). The next matching elements are short sections of microstrip and CPW in series, followed by a parallel pair of quarter-wave short-circuit microstrip stubs of characteristic impedance 3.4 ohms. The series array of four SIS junctions is connected through a capacitor (C_A) to ground, and to a high impedance RF choke (RFC) as shown in Fig. 2(c). Note that all conductors are on the same side of the substrate. The ground plane extends over most of the right half of the substrate and has gold pads along the edges (indicated in Fig. 2 by heavy hatching) which make contact with the shoulders of the substrate channel via 0.001" gold crush wires.

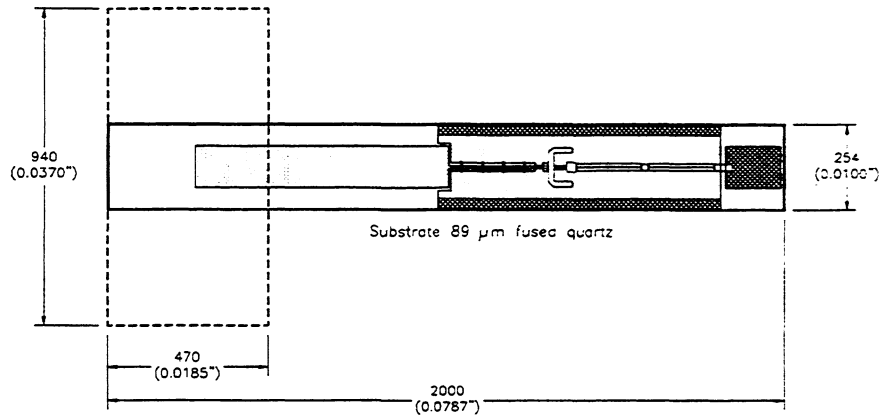
Operation of the RF tuning circuit is as follows: The series array of four SIS junctions is inductive and is resonated by capacitor C_A to ground. Its input impedance, as seen from the stubs, is plotted as a function of frequency in Fig. 3(a). Adding the stubs winds up the impedance locus as in Fig. 3(b). The microstrip MS1 and the coplanar line CPW1 form a resonant LC transformer which increases the impedance level to about 50 ohms, as in Fig. 3(c). Finally, the CLCPW, which has an electrical length of about half a wavelength, transforms the locus as in Fig. 3(d). The parameters assumed in these simulations are: junction diameter $a = 1.5 \mu\text{m}$, critical current density $J_C = 6600 \text{ A/cm}^2$, and specific capacitance $C_S = 85 \text{ fF}/\mu\text{m}^2$, corresponding to a normal resistance $R_N = 15.5 \text{ ohms per junction}$ and $\omega R_N C_J = 3.6$ at 250 GHz.

The RF choke, shown in Fig. 2(c), is designed to present a high RF impedance to the array of SIS junctions and capacitor C_A . It has two sections, each consisting of a CPW of 110-ohm characteristic impedance followed by a capacitor to ground, and has a total static capacitance of 137 fF and inductance of 235 pH. In most applications one section (line + capacitor) can be omitted, which reduces the capacitance to 68 fF and inductance to 118 pH.

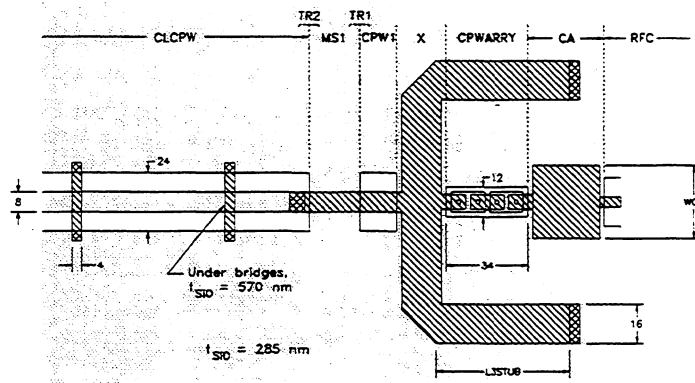
The RF embedding impedance seen by each junction in the array is shown in Fig. 4. The Smith chart is normalized to the optimum source impedance¹ for the junctions, 12.5 ohms (per junction) in the present case. The junction capacitance is included as part of the embedding circuit in this calculation. The circle at $|p| = 0.4$ indicates the range of embedding impedances within which acceptable SIS mixer performance will be obtained [11].

To accommodate variations from wafer to wafer, particularly in J_C , junction area, and SiO thickness, each wafer contains twelve mixer designs with four values of W_{CA} and three values of $L_{S,STUB}$ (see Fig. 2(b)).

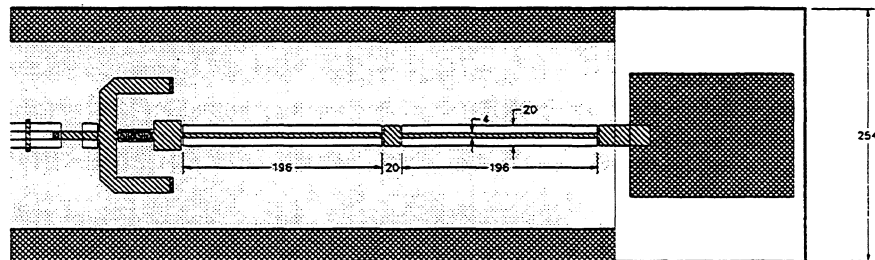
¹ The optimum source impedance is related to the junction's normal resistance R_N by $R_{OPT} = 0.015 R_N f_{GHz}^{0.72}$ [9], which in this frequency range is close to the value of Z_{OPT} given by [10].



(a)



(b)



(c)

Fig. 2. Diagrams of the low-parasitic mixer. (a) The whole mixer, showing the suspended stripline probe which couples to the signal/LO waveguide at the left. The ground plane contacts the mixer block along gold plated contact strips, shown heavily hatched on the upper and lower edges of the substrate. The bonding pad for the IF connection is at the right end of the substrate. (b) The RF tuning circuit, showing the end of the CLCPW (at the left), microstrip and CPW (capacitive and inductive) lines, the pair of microstrip short-circuit stubs, series array of four SIS junctions, and tuning capacitor C_A . (c) The right-hand end of the substrate, showing the RF tuning circuit at the left, the two-section RF choke, and the DC/IF bonding pad.

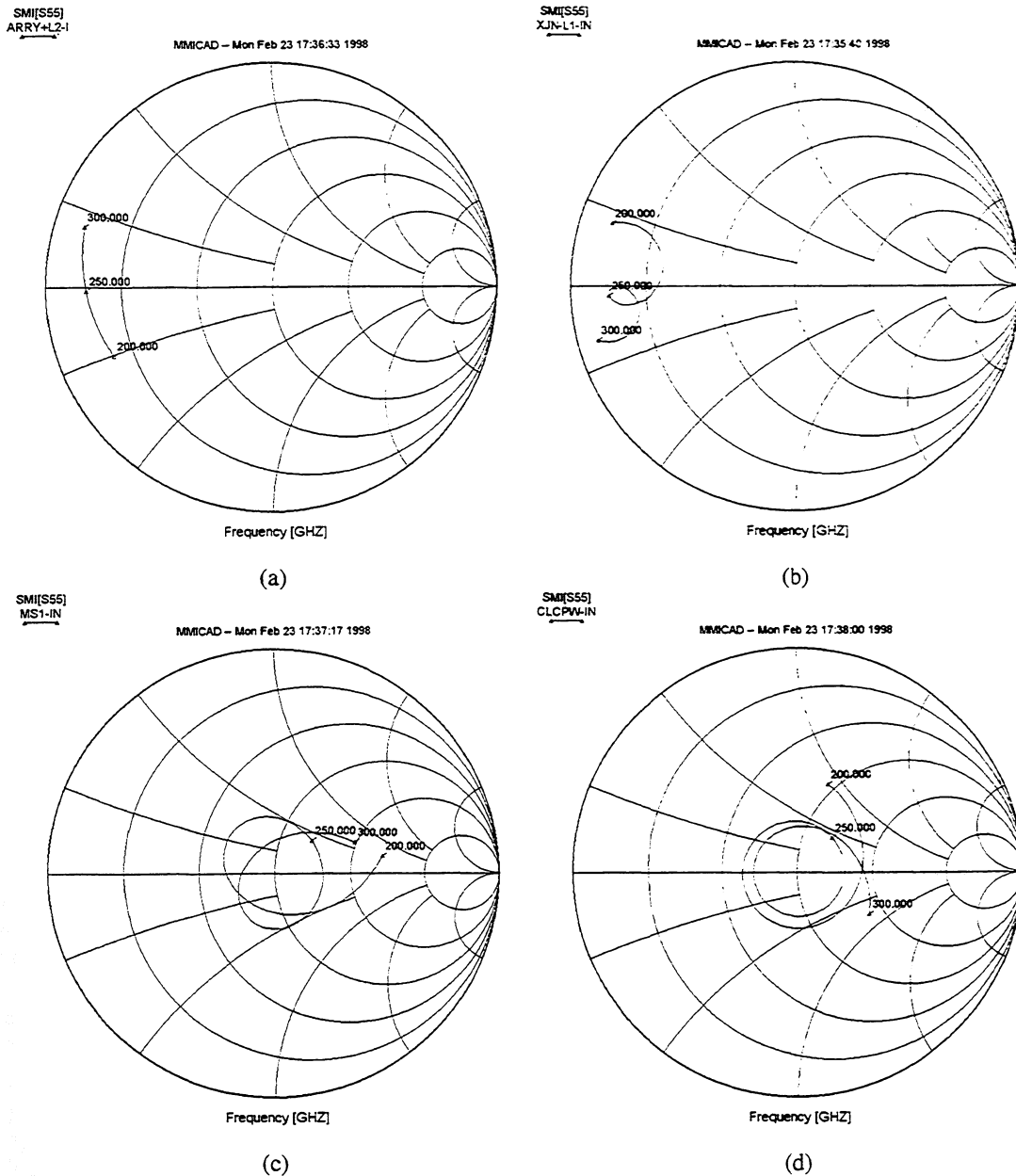


Fig. 3. RF impedance transformation through the broadband matching network. (a) Impedance of the array of junctions and capacitor C_A , (b) including the two stubs, (c) including MS1 and CPW1, and (d) including the CLCPW input line. All Smith charts are normalized to 50 ohms.

At IF, the pair of microstrip stubs has a very low impedance to ground, effectively bypassing the rest of the RF matching circuit. The static capacitance of the whole mixer, seen at the IF port on the substrate, is 241 fF, which consists of contributions from the array of junctions (38 fF), the tuning capacitor C_A (66 fF), and the RF choke (137 fF). The corresponding low frequency inductance is 294 pH of which 59 pH is contributed by the RF matching circuit. If only a single section RF choke is used, the overall static capacitance and inductance are reduced to 172 fF and 174 pH.

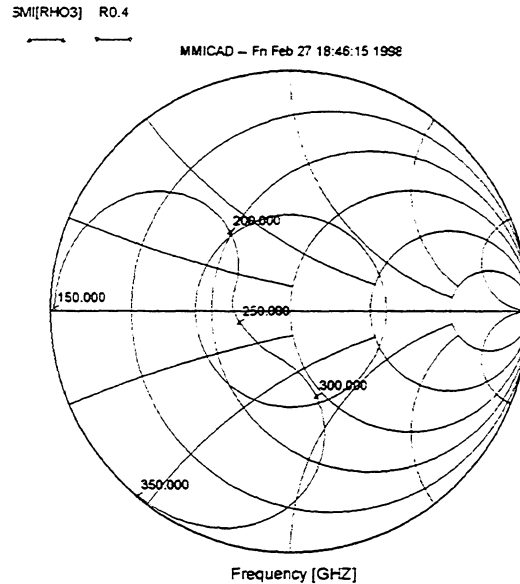


Fig. 4. RF embedding impedance seen by the array. The junction capacitance is taken as part of the embedding circuit. The circle is at $|p| = 0.4$. (The Smith chart is normalized to the optimum source impedance.)

FABRICATION

The mixers were fabricated on chemically polished fused quartz wafers 1" diameter and 0.010" thick. After dicing the individual mixers were thinned to 0.0035" using a dicing saw. The new mixer differs in three ways from those previously made at UVA: (i) the junctions are situated on small islands of trilayer where it is not possible to use removable anodization lines, (ii) an SiO layer 200 nm thick is deposited around the junctions, with a thicker SiO layer in the CLCPW sections, and (iii) vias are required to connect the bridges in the CLCPW section to the base electrode. Our previously established Cr based trilayer resist [12] and Futurex junction anodization [13] processes were inadequate for requirements (i) and (ii). For the present mixers we adapted JPL's Au overlayer technique [14] to our processes. Since Au does not naturally oxidize, an in-situ physical cleaning of the surface of the junction counter electrode is not needed prior to depositing the Nb interconnection layer. Omitting the usual physical cleaning step has two advantageous: any native Nb and Al oxides which have grown after deposition of the junction SiO insulation will remain, and the SiO insulation layer will not be disturbed. Both these factors tend to prevent micro-shorts between the wiring and base electrodes, and we have been able to fabricate junctions with 200 nm insulation layers without resorting to anodization techniques.

In the Au overlayer process we used a separate DC magnetron sputtering system to deposit layers of Au(1-2 nm)/[Cr(4% wt.)-Au](28 nm) on top of the trilayer wafer after an ion gun clean. The Cr-Au mixture was used to increase the physical durability of the over-layer. Prior to the trilayer etch, the Cr-Au layer is etched in a solution of 10 g I, 40 g INH_4 , 400 ml DI water, and 600 ml ethanol, which we have found etches Cr-Au films containing as little as 0.4% (wt.) Cr more repeatably and uniformly than pure Au films. Before the junction etch, the Au/Cr-Au layer is removed with an ion beam inclined at 45° which cleans the surface around the perimeter of the polyimide etch mask. After the junction etch and SiO deposition, a liftoff of the self-aligned trilayer resist is performed. It was found that the $(\text{CH}_3)_4\text{NO}_4$ in our usual 300T resist stripper attacked the counter electrode/overlayer interface, resulting in the loss of the Au/Cr-Au overlayer from the tops of the small junctions. The 300T stripper was replaced with OCG Inc. QZ-3321 or NMP, both of which have been found satisfactory.

The vias, to connect the bridges in the CLCPW section to the base electrode, can be accomplished in two ways. The first is to use large area junctions, and the second uses a direct contact from counter electrode to base electrode. We have chosen the second approach to avoid possible internal resonances in large-area junctions used as vias. Since an in-situ cleaning step is not used in our Nb wiring process, a second Au overlayer was defined on top of the base electrode after removing the Au/Cr-Au and Nb counter electrode from the via sites.

INITIAL RESULTS

The mixer described here had a normal resistance of 93 ohms for the array of four junctions, and the junction diameter, measured by SEM, was 1.6 μm , corresponding to a critical current density of 3900 A/cm² and $\omega R_N C_J = 6.2$. The I-V curve at 4.2 K is shown in Fig. 5 with and without LO power applied. With appropriate choice of tuning elements C_A and $L_{3,STUB}$, the embedding impedance seen by the array is as shown in Fig. 6, in which impedances are normalized to the optimum source impedance for this particular mixer (74 ohms).

The mixer was tested in a liquid helium cooled vacuum cryostat containing 4.2 K IF calibration components, similar to that described in [15]. The incoming RF signal enters the cryostat through a plastic film vacuum window supported by polystyrene foam [16]. It passes through a PTFE infrared filter at 77 K into a scalar feed horn at 4.2 K. LO power is injected through a 20 dB branch-line directional coupler, also at 4.2 K. A 50-ohm 1.4 GHz IF was used with a 50-MHz bandwidth and no IF impedance transformer between the mixer and amplifier. The IF noise temperature, including a coaxial switch, two isolators, and a directional coupler, was 6.3 K. A DC magnetic field was applied to the mixer to suppress the Josephson currents in the junctions.

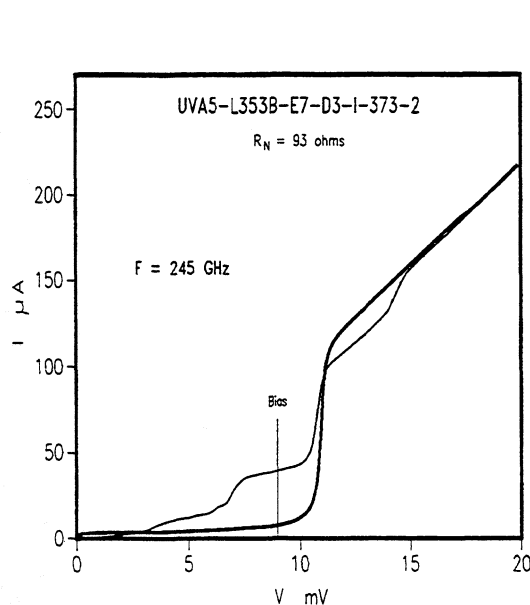


Fig. 5. I-V curve for the mixer at 4.2 K without LO power (heavy line), and with LO power at 245 GHz (light line). The operating bias voltage is indicated by the vertical line.

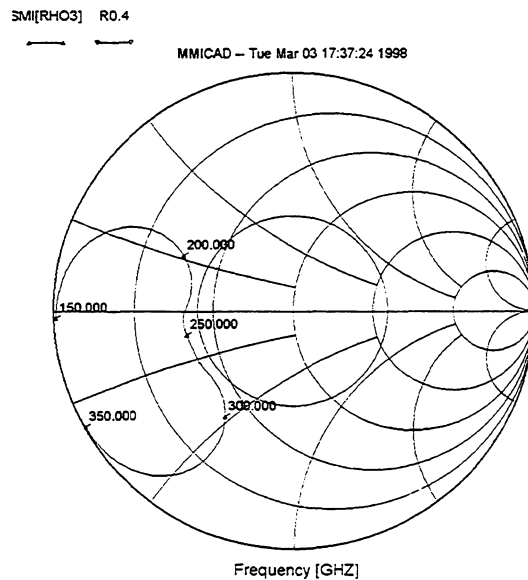


Fig. 6. RF embedding impedance seen by the array. The junction capacitance is taken as part of the embedding network. The circle is at $|\rho| = 0.4$. The Smith chart is normalized to the optimum source impedance (74 ohms).

The overall receiver and mixer noise temperatures are plotted as functions of LO frequency in Fig. 7. The mixer noise temperature includes contributions from the vacuum window, IR filter, horn, and LO coupler, but does not include contributions from the IF amplifier, reflected noise from the termination on the IF isolator, or injected noise from the LO. Fig. 8 shows the mixer conversion loss and VSWR at the IF port of the mixer (with respect to 50 ohms) as functions of LO frequency. The conversion loss includes contributions from the vacuum window, IR filter, feed horn, and LO coupler.

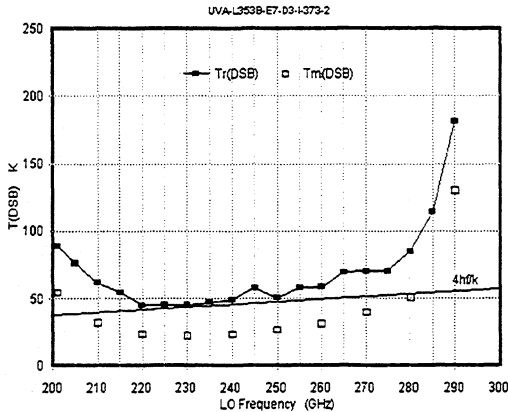


Fig. 7. DSB receiver noise temperature (solid line) and mixer noise temperature (open squares). Shown for reference is the line $4hf/k$.

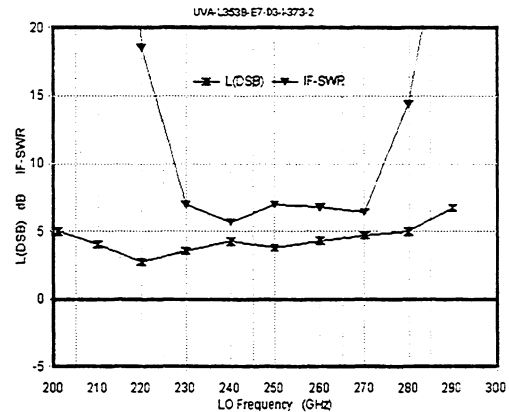


Fig. 8. DSB conversion loss (lower curve) and IF port VSWR.

CONCLUSION

The new mixer has output capacitance and inductance lower by factors of about 2 and 6 than typical SIS mixers in this band. These parasitics could be further reduced by using a single-section RF choke as discussed above. The initial measurements presented here gave overall receiver noise temperatures of 45–89 K (DSB) over the LO range 200–280 GHz, with corresponding mixer noise temperatures of 22–55 K (DSB). By increasing the critical current density of the junctions to $\sim 6600 \text{ A/cm}^2$ we hope to improve the performance and cover the full 200-300 GHz band.

We have not yet operated this type of mixer with an internal wideband IF amplifier, but only with an L-band IF. While the present mixer operates in the 200–300 GHz waveguide band, the design should be suitable for scaling to higher or lower frequencies. Note that, with frequency scaling, the IF output capacitance and inductance will change, both increasing as the design is scaled to lower frequencies.

ACKNOWLEDGMENTS

The authors thank R. Amos for his help in fabricating the niobium circuits, N. Horner, F. Johnson, and A. Marshall for fabricating and assembling the mixer, and K. Crady for his help in testing the mixer.

REFERENCES

- [1] S. Padin, "An Integrated SIS Mixer and HEMT IF Amplifier," National Radio Astronomy Observatory. Millimeter Array Memo No. 114, April 1994.
- [2] S. Padin, D. P. Woody, J. A. Stern, H. G. LeDuc, R. Blundell, C.-Y. E. Tong, and M. W. Pospieszalski. "An Integrated SIS Mixer and HEMT IF Amplifier" *IEEE Trans. Microwave Theory Tech.*, vol. MTT-44, no. 6, pp. 987-990, June 1996.
- [3] R. Blundell, C.-Y. E. Tong, D. C. Papa, R. L. Leombruno, X. Zhang, S. Paine, J. Stern, H. G. LeDuc, and B. Bumble, "A wideband fixed-tuned SIS receiver for 200 GHz operation," *IEEE Trans. Microwave Theory Tech.*, vol. MTT-43, no. 4, pp. 933-937, April 1995.
- [4] A.R. Kerr, S.-K. Pan, and M. J. Feldman, "Integrated tuning elements for SIS mixers," *Int. J. Infrared Millimeter Waves*, vol. 9, no. 2, pp. 203-212, Feb. 1988.
- [5] G. Pance and M. J. Wengler, "Integrated tuning elements for millimeter and submillimeter SIS mixers." *IEEE International Microwave Symposium Digest*, pp. 337-340, June 1992.
- [6] J. Zmuidzinas and H. G. LeDuc, "Quasi-optical slot antenna SIS mixers," *IEEE Trans. Microwave Theory Tech.*, vol. 40, no. 9, pp. 1797-1804, Sep. 1992.
- [7] A. R. Kerr, S.-K. Pan, S. Whiteley, M. Radparvar, and S. Faris, "A Fully Integrated SIS Mixer for 75-110 GHz." *IEEE Int. Microwave Symp. Digest*, pp. 851-854, May 1990.
- [8] A. R. Kerr and S.-K. Pan, "Design of planar image-separating and balanced SIS mixers. Proceedings of the Seventh International Symposium on Space Terahertz Technology, pp. 207-219, 12-14 March 1996. (Also available on the web at <http://colobus.aoc.nrao.edu/memos/memolist.html>. as Millimeter Array Memo. 151.)
- [9] A. R. Kerr, S.-K. Pan, A. W. Lichtenberger and D. M. Lea, "Progress on Tunerless SIS Mixers for the 200-300 GHz Band," *IEEE Microwave and Guided Wave Letters*, vol. 2, no. 11, pp. 454-456, Nov. 1992.
- [10] Q. Ke and M. J. Feldman, "Optimum source conductance for high frequency superconducting quasiparticle receivers," *IEEE Trans. Microwave Theory Tech.*, vol. MTT-41, no. 4, pp. 600-604, April 1993.
- [11] A. R. Kerr, "Some fundamental and practical limits on broadband matching to capacitive devices, and the implications for ShHIS mixer design," *IEEE Trans. Microwave Theory Tech.*, vol. MTT-43, no. 1, pp. 2-13, Jan 1995.
- [12] A.W. Lichtenberger, D. M. Lea, C. Li, F. L. Lloyd, R. J. Mattauch, M. J. Feldman, S.-K. Pan, and A. R. Kerr, "Fabrication of Micron Size Artificially Insulated Nb/Al-Al₂O₃/Nb Junctions with a Trilevel Resist Liftoff Process." *IEEE Trans. Magn.*, MAG-27(20), March 1991.
- [13] D. M. Lea, H. H. Huang, and A.W. Lichtenberger, "Use of a Negative Tone Photoresist to Improve Low-Tc Superconducting Tunnel Junction Fabrication Processes", *IEEE Transactions on Applied Superconductivity*, 1997.
- [14] H. G. LeDuc, B. Bumble, S. R. Cypher, A. J. Judas, and J. A. Stern, "Sub Micron Area Nb/AlO_x/Nb Tunnel Junctions for Submm Mixer Applications," Third International Symposium on Space Terahertz Technology, 1992.
- [15] S.-K. Pan, A. R. Kerr, M. J. Feldman, A. Kleinsasser, J. Stasiak, R. L. Sandstrom and W. J. Gallagher, "A 85-116 GHz SIS receiver using inductively shunted edge-junctions," *IEEE Trans. Microwave Theory Tech.*, vol. MTT-37, no. 3, pp. 580-592, March 1989.
- [16] A. R. Kerr, N. J. Bailey, D. E. Boyd and N. Horner, "A study of materials for a broadband millimeter wave quasi-optical vacuum window," Electronics Division Internal Report No. 292, National Radio Astronomy Observatory, Charlottesville, VA 22903, Aug. 1992. (Also available as Millimeter Array Memo. 90.)

A 350 GHZ FINLINE MIXER FED BY A HORN-REFLECTOR ANTENNA

G. YASSIN, S. WITHINGTON AND M. BUFFEY
*Department of Physics, University of Cambridge,
Madingley Road, Cambridge CB3 0HE, UK*

K. JACOBS AND S. WULFF
*University of Cologne, I. Physikalisches Institut, Zulpicher Str., Koeln
50937, Germany*

ABSTRACT

In this paper we describe the design and preliminary results of testing a tunerless finline mixer over the frequency range of 330-360 GHz. The mixer is fed by a conical horn-reflector antenna, machined into an aluminium split block to ensure that the mixer has low sidelobe level and high aperture efficiency, without the employment of a phase correcting lens. The mixer chip itself comprises an antipodal finline taper and a miniature microstrip line, which contains an Nb/Al-oxide/Nb junction. Our preliminary test of the mixer at 4.7 K yielded receiver noise temperature of about 90 K DSB which includes some IF and RF losses. The measured beam pattern of the conical horn reflector antenna was in excellent agreement with the computed results.

INTRODUCTION

We have already reported the successful operation of an antipodal finline mixer at 230 GHz. We showed that the mixer is easy to use and has a noise temperature which is comparable to best waveguide mixers, despite that it does not have any mechanical tuning (Yassin *et al*, 1997a). Another feature of the finline mixer is that it operates over a remarkably wide band. We have already demonstrated that the finline mixer can operate well over one octave provided the junction tuning remains effective. In this paper we shall describe an improved design and test results of a tunerless finline mixer which is designed to cover the frequency range of 320-390 GHz. The mixer is fed by a horn-reflector antenna, machined into an aluminium split block to ensure that the mixer has low sidelobe level and high aperture efficiency, without the employment of a phase correcting lens. The mixer chip itself comprises an antipodal finline taper and a miniature microstrip line, which contains an Nb/Al-oxide/Nb junction. The two superconducting films are deposited on one side of a 90 μm thick quartz substrate and are separated by 400 nm thick oxide layer. The antipodal finline taper is then transformed into a microstrip line of characteristic impedance of 20-30 ohms which is ideal for SIS junctions. The inductive tuning stub was fabricated as part of the IF microstrip transmission line rather than at right

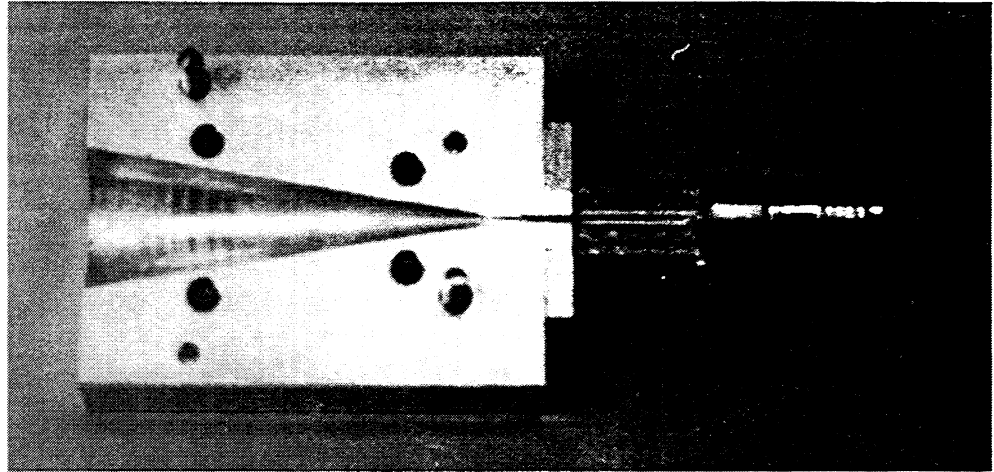


FIGURE I A photograph of the split Aluminium block

angles to it, as in our previous designs. In this way, the stub both tunes out the junction capacitance and also acts as an RF choke.

MIXER DESIGN

The mixer block and antenna: The mixer block comprised a horn-reflector antenna, machined into an Aluminium split block. We have chosen wave guide dimensions of $a= 700\mu\text{m}$ and $b= 350\mu\text{m}$, a horn semiflare angle of 9.46° , a horn diameter of 10.0 mm and a parabolic reflector of focal length of 17.7 mm. This gave a -3 dB beamwidth of about 4.5 degrees depending on polarisation and plane of observation. A photograph of the lower part of the split block including the IF bias board carrier is shown if Fig. 1.

We have chosen to start our first tests employing a horn-reflector antenna which is fed by a smooth-wall (rather than a corrugated) conical horn, keeping in mind that the horn will be corrugated at a later stage. This antenna has four principal copolar radiation patterns of different beamwidths and sidelobe levels, since the field distribution over the aperture of a smooth-wall (unlike the corrugated) horn depends on the input polarisation, and since the radiation pattern of the horn-reflector antenna can be observed either in the longitudinal plane (the plane of symmetry, which includes the horn axis) or in the transverse plane (which is perpendicular to the horn axis). This choice therefore gives us the opportunity to verify the accuracy of our design and the precision of our machining techniques by comparing several computed and measured beam patterns of similar yet distributions. We have computed the far field pattern of the antenna in the usual manner by first projecting the field over the horn aperture into the projected aperture, using conformal mapping (Withington *et al*, 1997). The field distribution of the horn aperture was assumed to be that of a TE₁₁ circular waveguide and the far field of the projected aperture was calculated using either

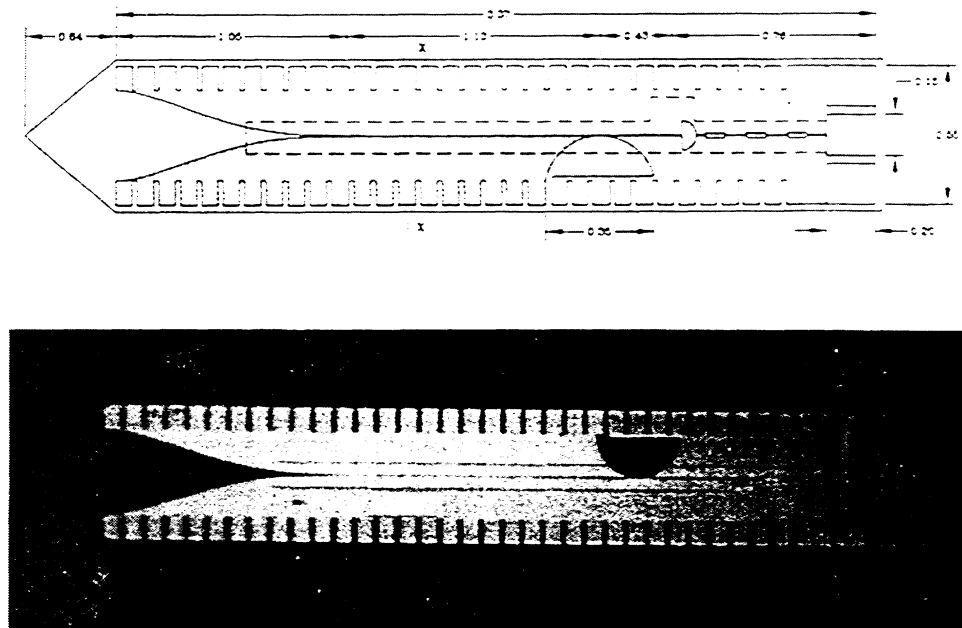


FIGURE II A magnified view and a photograph of the finline mixer chip

the Kirchoff scalar integral or Gaussian modes.

The mixer chip and IF assembly: A magnified view and a photograph of the mixer chip are shown in Fig. 2.

The finline taper and mixer circuits were deposited on a quartz substrate of thickness $d=90 \mu\text{m}$. The transmission-line tapers were designed using quasi-TEM techniques, and the electrical properties of the finline and microstrip were calculated using methods which we have described previously (Yassin *et al*, 1997b). As was mentioned above the tuning radial stub was fabricated as part of the main microstrip transmission line rather than at right angles to it, as in our previous designs. The main reason for this choice is to eliminate the effect of the IF circuit on the junction tuning, and to make the radial stub act as an RF choke. This means that the old RF choke structure (three inductive and three capacitive pads) may now be removed, resulting in a significant decrease in the chip capacitance at IF frequencies. The mixer chip was manufactured at KOSMA, university of Cologne, using four mask layers. The first forms the base finline electrode and the ground plane for the microstrip, the second defines the tunnel junction and a $200 \mu\text{m}$ of SiO, the third allows the addition of an additional $200 \mu\text{m}$ layer of SiO and the fourth forms the wiring finline layer, the microstrip, the RF choke and the tuning stub. The area of the the junction which was employed in our tests (wls3) is $0.6 \mu\text{m}^2$, current density of 14000 A/cm^2 and a normal resistance of 25Ω . The IF signal is extracted by bonding $30 \mu\text{m}$ wires to the three pads on the chip and connecting those wires to the bias

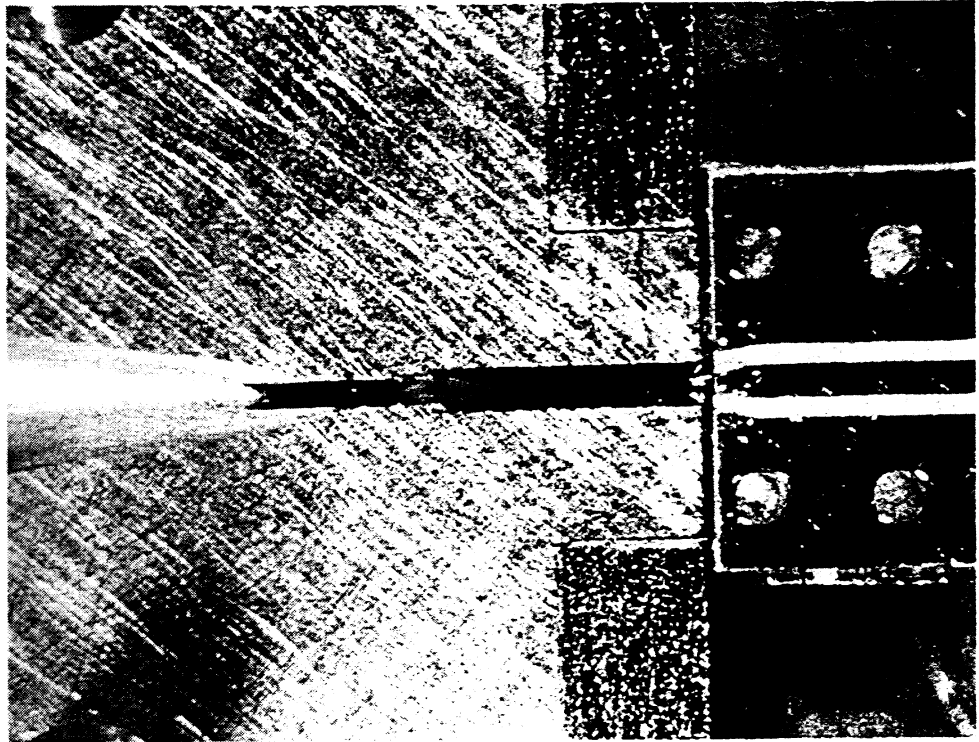


FIGURE III A photograph of the IF assembly

board as shown in Fig. 3.

The bias board itself was a ground plane backed coplanar waveguide which was preferred to the more commonly used microstrip in order to make the bonding pads on the chip level with the IF board metallisation. We designed the coplanar waveguide using the electromagnetic modelling software "Sonnet" in order to take into account the finite width of the ground planes which was made relatively small so that the IF board could be fitted within the coil former. Fig. 4 shows that the measured transmission and return loss of the coplanar waveguide are remarkably good over a wide range of IF frequencies.

EXPERIMENTAL RESULTS

We started our mixer tests by investigating the far field pattern of the horn-reflector antenna. The local oscillator horn was used as a transmitter and its output power was modulated electronically. A radiation pattern was taken by placing the Dewar on a rotary table and rotating the table about a vertical axis which passed through the apex of the horn. Since at this stage we were only interested in measuring the main beam, no special effort was made to increase the dynamic range or to eliminate wide-angle reflections. In Fig. 5 we show a measured pattern when the input polarisation was longitudinal and the observation was made in the longitudinal plane. This configuration yields

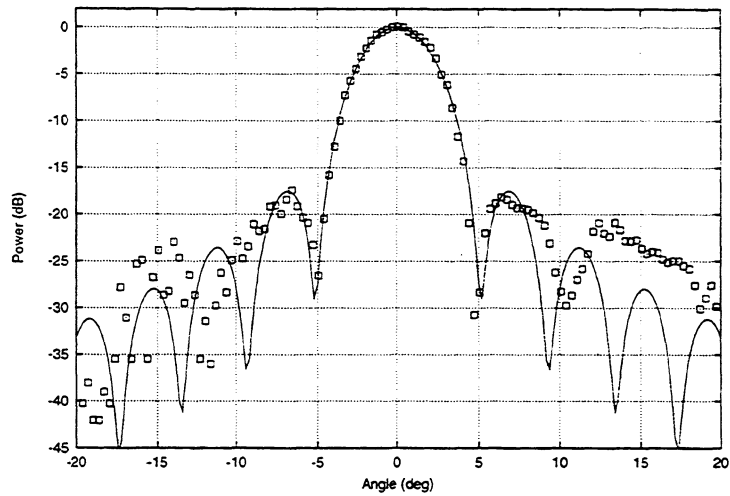


FIGURE V 350GHz conical horn-reflector beam pattern

Josephson effect could easily be suppressed at the first null with a coil current of 88 mA. Although the slope of the photon step at 344 GHz appears to be slightly negative, we did not observe any instabilities in the IF output. Instabilities however may still exist at frequencies below 330 GHz and we shall investigate this later.

We show the IF response of the mixer at 356 GHz in Fig. 9 which gives a noise temperature value of 90 K. Similar values were obtained at all frequencies between 333-360 GHz range which was determined by the availability of local oscillator power. The above quoted values of noise temperature, which are higher than expected at those frequencies, include the losses of the IF amplifier, the Mylar splitter and the cryostat window whose width was in fact designed to test a 500 GHz mixer. In addition, these results represent our first attempt to test the mixer and we expect them to improve on them by modifying the experimental setup and trying different devices.

Finally we intend to modify the finline chip in order to design an image separating mixer. The design will be based on two back-to-back finline tapers, where the signal is fed through one side, and the LO through the other. The IF can be taken from the side, through the waveguide wall without affecting the electrical properties of the transmission line since the electromagnetic field is well confined in the microstrip (Kerr, A. R., and Pan, S-K., 1996). An obvious advantage of this design is that the RF signals are fed to the device without using highly inductive probes. Moreover, there will be enough space on the chip to design the required integrated circuits.

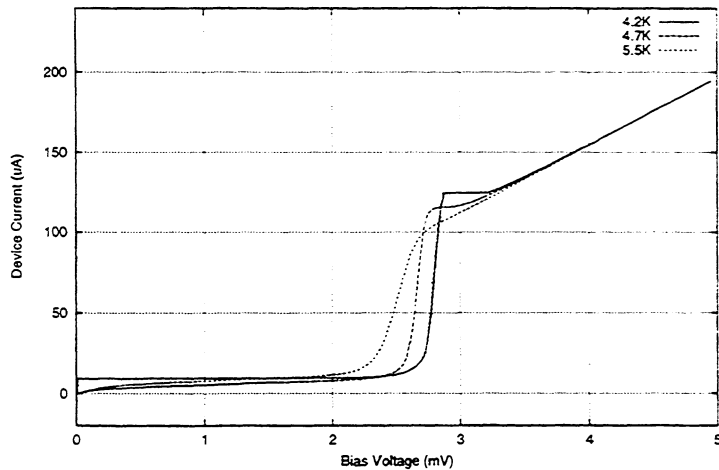


FIGURE VI I-V curves at 3 different temperatures

CONCLUSIONS

We reported the successful operation of an antipodal finline mixer in the frequency range of 330-360 GHz. The preliminary measured results of DSB receiver noise temperature are 90 K which include IF and RF losses in the test system. The measured beam pattern of the horn reflector antenna are in excellent agreement with computed results which illustrates the integrity of both our design and manufacturing techniques of these antennas.

REFERENCES

- Yassin, G., Padman, R., Withington, S., Jacobs, K., and Wulff, S. " Abroad band 230 GHz finline mixer for astronomical imaging arrays," *Electron. Lett.*, vol. 33, pp. 498-500, 1997. MTT-36, PP. 1521-1525, 1988.
- Withington, S., Yassin, G., Buffey, M., and Nordon, C. " A horn-reflector antenna for high performance submillimeter imaging arrays," *International J. Infrared and Millimeter Waves* vol. 18, no. 2, pp. 341-358.
- Yassin, G. , Withington, S., and Padman, R. " Elctromagnetic analysis of finline mixers," *Proc. 8th Int. Symp. on Tetahertz Technology*, pp. 344-354, Harvard, 1997
- Kerr, A. R., and Pan, S-K. "Design of planar image seperating and balanced SIS mixers," *Proc. 7th Int. Symp. on Space Terahertz Technology*, pp. 207-219, Charlottesville, 1996

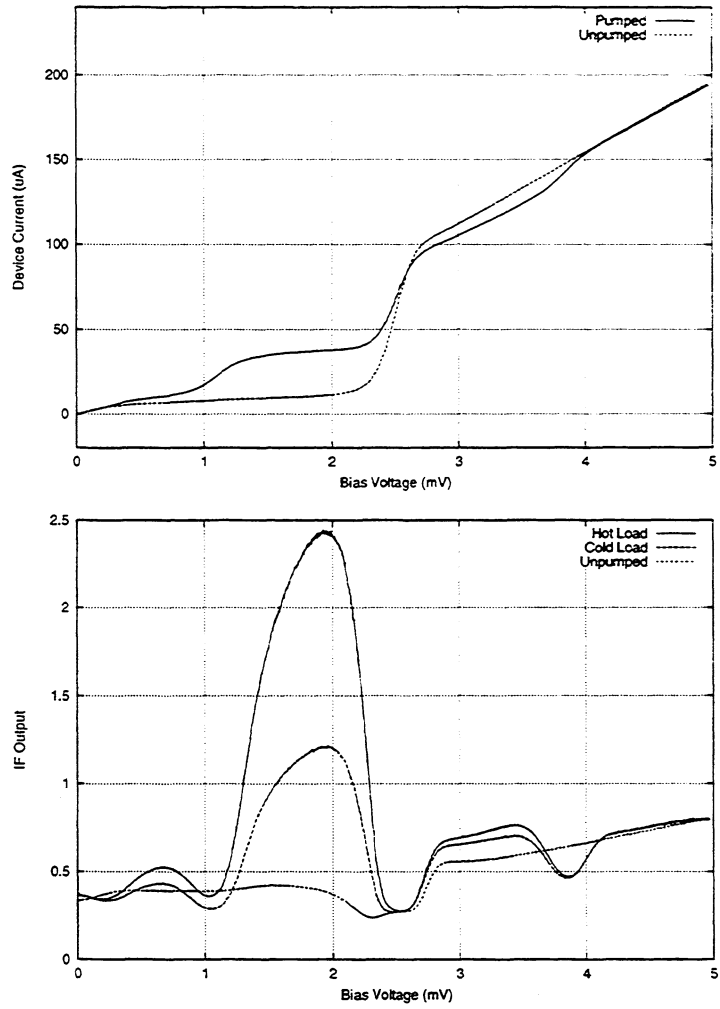


FIGURE VII Pumped I-V curves and the hot/cold IF response at 5.5K

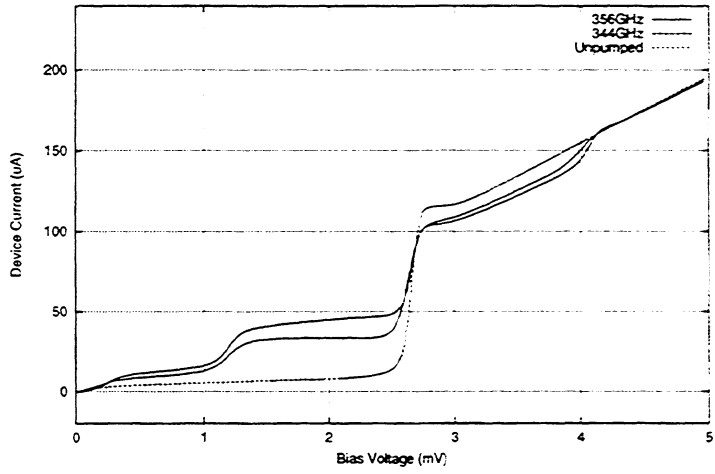


FIGURE VIII Pumped I-V at two different frequencies

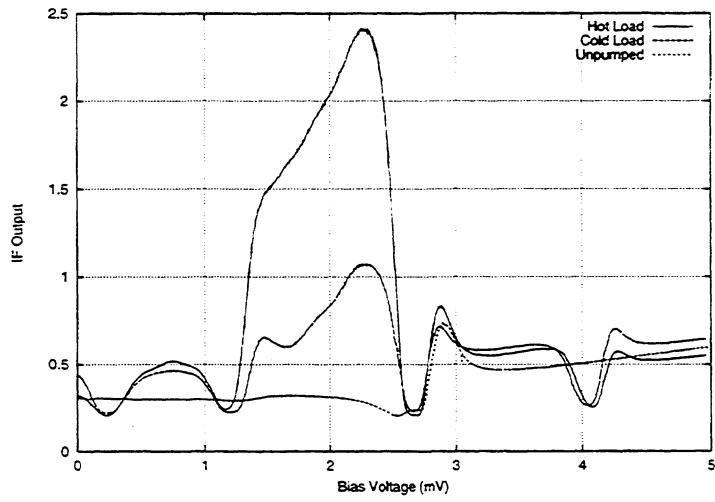


FIGURE IX The IF response at 356GHz

AN INTEGRATED SIDEBAND SEPARATING SIS MIXER FOR 200-280 GHz

A. R. Kerr¹, S.-K. Pan¹, and
H. G. LeDuc²

¹National Radio Astronomy Observatory*
Charlottesville, VA 22903

²Jet Propulsion Laboratory
Pasadena, CA 91109

ABSTRACT

Separate waveguides for the signal and LO are connected via suspended striplines to a 2 x 1 mm quartz substrate which contains all the RF components of the sideband separating mixer: quadrature hybrid, LO power splitter, two LO couplers, and two SIS mixers. These components are realized in capacitively-loaded coplanar waveguide, which minimizes stray coupling between adjacent components and coupling to undesired modes in the thick quartz substrate. Over the 200-280 GHz band, the mixer noise temperature was 50-150 K and the overall receiver noise temperature was 60-200 K (both measured outside the vacuum window). The sideband separation was ≥ 9 dB, which we hope to improve by reducing leakage of LO power under the substrate into the signal port, and by improving the match of the cold termination of the fourth port of the input quadrature hybrid.

INTRODUCTION

With noise temperatures of SIS receivers now in the range 2-4 times the photon temperature (hf/k), the overall sensitivity of radio astronomy measurements can be seriously degraded by atmospheric noise. In spectral line measurements, atmospheric noise in the unwanted (image) sideband can be eliminated by using a sideband separating scheme. The benefits of such a scheme, in the context of interferometers and single-dish radio telescopes have been explored in [1] and [2].

An experimental 100 GHz sideband separating mixer using discrete components — a waveguide magic-T and two SIS mixers, with an adjustable phase-shifter in the LO path to one mixer — was described in [3]. At shorter wavelengths, the signal and LO phasing can be done quasi-optically using various configurations described in [3]-[5], but even at 250 GHz the quasi-optical schemes are physically cumbersome and require a large cryostat if several receivers are to be attached to the same refrigerator. At the 1996 THz Conference we proposed a design for a single-chip sideband separating SIS mixer [5], and the present paper gives our first results.

*The National Radio Astronomy Observatory is a facility of the National Science Foundation operated under cooperative agreement by Associated Universities, Inc.

In the microwave range, sideband separating mixers have been available commercially for many decades. The usual implementation is to divide the signal and LO power between two mixers using a quadrature hybrid in either the signal or LO path; here the former option is used as shown in Fig. 1. The IF outputs from the two mixers are combined in an IF quadrature hybrid, with the result that, ideally, all the downconverted power from the upper and lower sidebands appears separately at the two output ports of the IF hybrid.

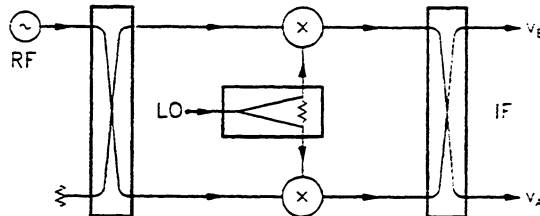


Fig. 1. Schematic diagram of a sideband separating mixer of the type used in this work.

The image rejection of such a sideband separating mixer depends on the amplitude and phase imbalance through the parallel signal and LO paths, including the IF quadrature hybrid, as analyzed in [5]. For radio astronomy applications, the primary reason for using a sideband separating mixer is to reduce atmospheric noise in the unwanted sideband to an acceptable level, and this is accomplished with ≥ 10 dB of image rejection. An amplitude imbalance of 5.7 dB (for the whole circuit) or a phase imbalance of 35° results in an image rejection of 10 dB, so the required tolerance on components should not be a practical obstacle. An image rejection of 20 dB would result from an amplitude imbalance of 1.7 dB or a phase imbalance of 12° , numbers which may well be achievable using Nb integrated circuit technology.

DESIGN

The design of the sideband separating mixer was described in detail in [5]. The complete RF circuit is on a 2×1 mm fused quartz substrate, connected to signal and LO waveguides via suspended striplines on separate substrates, as shown in Fig. 2. Connections between the probes and the main substrate are by thin gold ribbons soldered to the bonding pads. A Nb ground plane extends over most of the upper side of the substrate, and has gold contact pads along all four sides. These pads contact the mixer block through gold crush-wires which are compressed as the block is assembled.

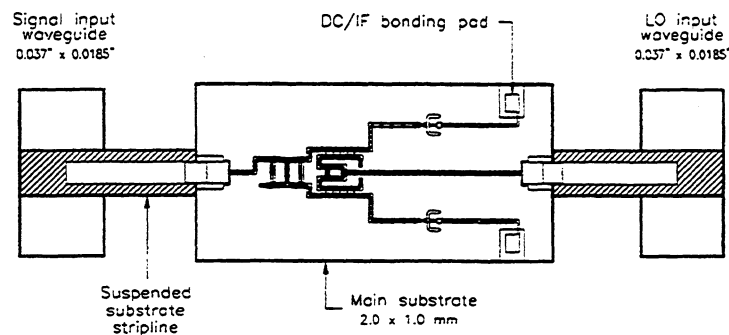


Fig. 2. The image separating mixer, showing the signal and LO waveguides, suspended stripline coupling probes, and the main substrate.

All the components and interconnections on the mixer chip are realized using capacitively loaded coplanar waveguide (CLCPW) — see Fig. 3. CLCPW has several advantages over microstrip and

coplanar waveguide (CPW): On a quartz substrate it can have characteristic impedances in the range 10-100 ohms with dimensions convenient for standard optical lithography. All conductors are on the same side of the substrate and the energy is confined to a region close to the center conductor, which allows the use of a conveniently thick substrate. The periodic bridges are grounded at their ends, which effectively suppress coupling to the odd-mode which can occur in long CPW lines, and reduces coupling between adjacent components.

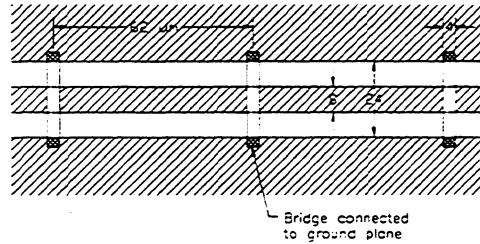


Fig. 3. A length of capacitively loaded coplanar waveguide (CLCPW). Dimensions are in microns.

A detailed view of the mixer substrate is shown in Fig. 4. The RF signal enters at the left CPW which makes a broadband transition to CLCPW. It is divided in the quadrature hybrid and passes into the mixers via the LO couplers. Similarly, the LO enters at the right CPW, then passes through a Wilkinson power divider to two ~ 17 dB LO couplers and into the SIS mixers. The individual components were designed using an electromagnetic simulator (Sonnet *em*) and a microwave circuit simulator (MMICAD) as described in [5].

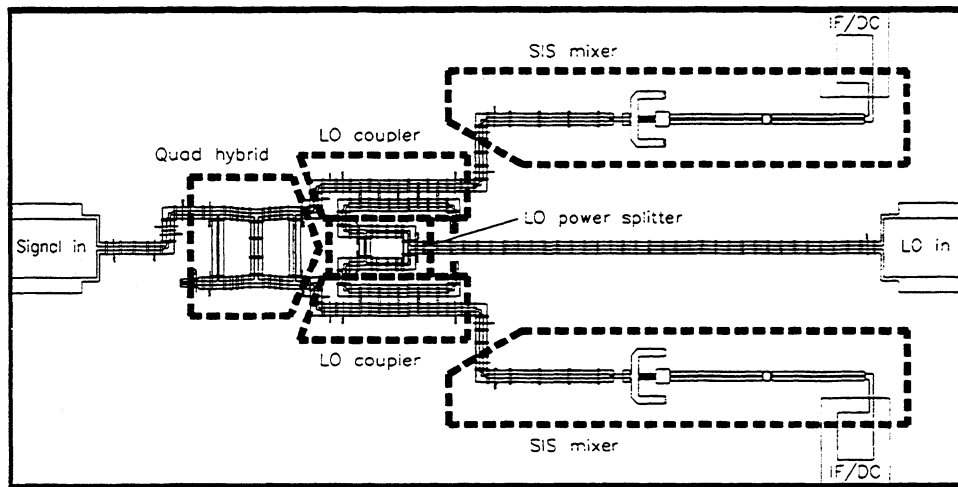


Fig. 4. Substrate of the sideband separating mixer, showing the main components. Most of the surface is covered by a ground plane.

To facilitate (eventual) operation with a wide IF bandwidth, the individual mixers are designed to have low output capacitance and inductance, and are similar to those described in a companion paper [6]. Target parameters for the tunnel junctions were a diameter of $1.6 \mu\text{m}$ and critical current density of 6000 A/cm^2 , corresponding to a normal-state resistance of 15 ohms and $\omega R_N C_J = 4$ at 250 GHz. To allow for uncertainties and variation in the processing, twelve designs were included on the masks — three tuning stub lengths and four series capacitor widths.

FABRICATION

The mixers were fabricated on 0.010" thick, chemically polished Infrasil 301 fused quartz wafers 3" in diameter. A five mask Nb/AlO_x/Nb trilayer process was used, similar to those described in the literature. All photolithography was performed with a 5x i-line wafer stepper.

The resistors — needed to terminate the quadrature hybrid, LO power splitter, and the LO couplers — were fabricated by liftoff prior to depositing the trilayer. The resistor material was Au(53 wt%)Pd(47 wt%) deposited using a technique similar to that described in [7]. To achieve the target sheet resistance of 12.5 ohm/square required films approximately 25 nm thick.

The tunnel junctions were patterned using reactive ion etching in a mixture of CCl₂F₂, CF₄, and O₂, and electrically isolated using 200 nm thermally evaporated SiO. The vias between the wiring layer and the ground plane, required at the ends of the RF tuning stubs and CLCPW bridges, were actually large-area tunnel junctions fabricated simultaneously with the smaller mixer junctions. A second SiO layer, of thickness 270 nm (for a total two-layer thickness of 570 nm), was deposited and patterned by lift-off to achieve the appropriate capacitance for the bridges. The final wiring layer of Nb was deposited in the same system as the trilayer and patterned using RIE.

After lithography the wafers were diced into approximately 1" squares which were lapped to a thickness of 0.0035", and then diced into the final 2 x 1 mm chips.

We had difficulties in achieving the target sheet resistance due to poor thickness control. As a result we have performed several experiments that suggest substoichiometric NbTiN may be a better resistor material for this application. Its base resistivity is approximately six times larger than AuPd, and thickness control is less of an issue.

INITIAL RESULTS

In the particular sideband separating mixer described here, each of the component mixers has four SIS junctions in series, with a total normal resistance of 70 ohms and a critical current density ~ 7000 A/cm² corresponding to $\omega R_N C_J = 3.4$. The I-V curves of the two component mixers at 4.0 K are shown in Fig. 5 with and without 225 GHz LO power applied. Note the difference between the curves with LO applied.

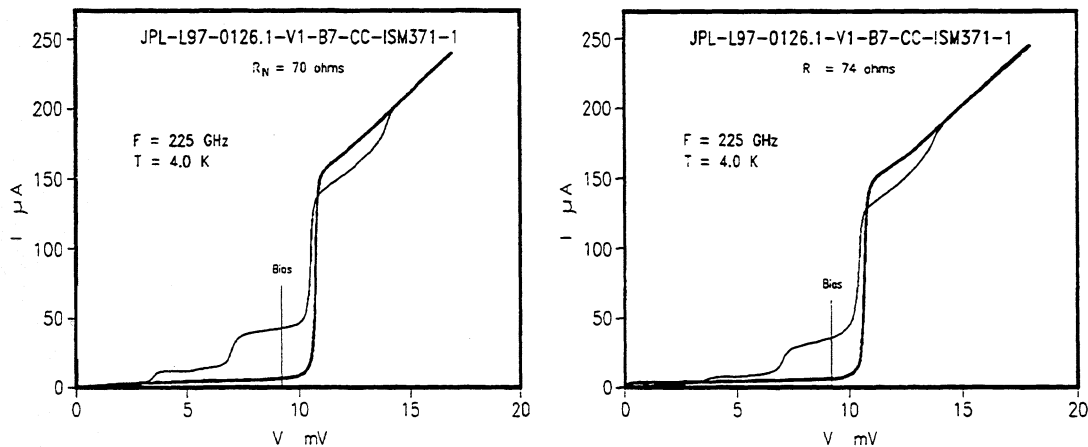


Fig. 5. I-V curves of the component mixers at 4.0 K without LO power (heavy lines), and with LO power (light lines) at 225 GHz. The operating bias voltage is indicated by the vertical line.

The mixer was tested in a vacuum cryostat cooled to ~ 4 K by a Joule-Thompson refrigerator. The incoming RF signal enters the cryostat through a plastic film vacuum window [8] supported by a 0.125" sheet of expanded PTFE [9]. It passes through a 50-K infrared filter, also made of 0.125" expanded PTFE, a PTFE lens at 4 K, and into a scalar feed horn, also at 4 K. LO power is connected to the mixer through an (overmoded) stainless steel waveguide. A 4-K IF plate containing a coaxial switch and 50-ohm IF calibration components, similar to that described in [10], enables the noise temperature at either port of the sideband separating mixer to be measured. The IF noise temperature, including the coaxial switch, two isolators, and a directional coupler, was 3.6 K at 1.4 GHz.

The sideband separating mixer has separate SMA DC/IF connectors for each component mixer. These were connected through cables of equal length to the 4 K IF quadrature hybrid [11]. Bias-T's [12] on the other side of the hybrid were connected through isolators to the IF switch. No IF impedance transformer was used between the junctions and the 50-ohm IF plate. A DC magnetic field was applied to the mixer to suppress the Josephson currents in the junctions.

Measurements were made using RF hot and cold loads (room temperature and liquid nitrogen) in front of the receiver, with the IF switch connected in turn to each mixer output. The calibrated IF plate enables the mixer noise temperature and conversion loss in each channel to be deduced, and also the overall receiver noise temperature; these are all DSB quantities. The image rejection was determined using a CW input signal, first in one sideband then in the other, and measuring the relative IF output levels in both channels with a spectrum analyzer. From the DSB measurements it was then possible to deduce the SSB conversion loss and noise temperatures. These quantities are plotted in Figs. 6-8 as functions of LO frequency. Fig. 9 shows the DC mixer currents as a function of frequency. Note that the noise temperatures and conversion losses include all the input components (vacuum window, IR filter, etc.).

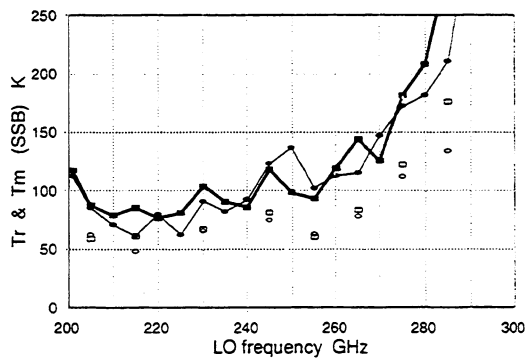


Fig. 6. SSB receiver and mixer noise temperatures.

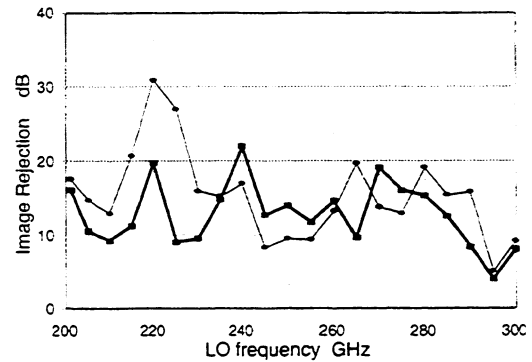


Fig. 7. Image rejection (dB).

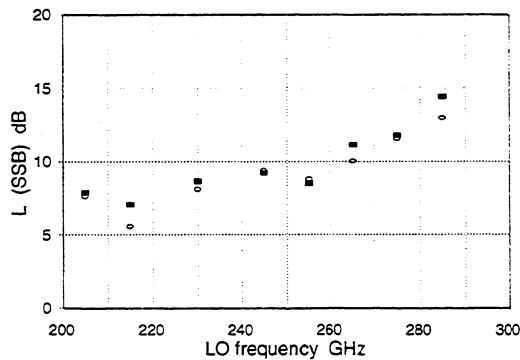


Fig. 8. SSB conversion loss (dB).

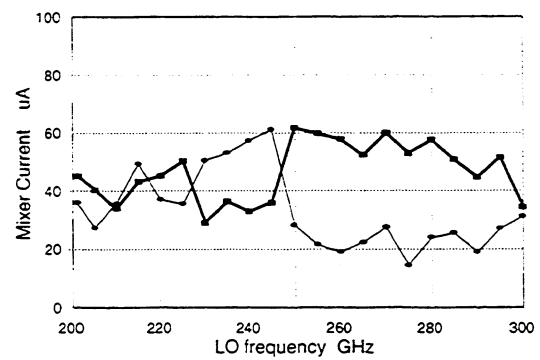


Fig. 9. DC currents in the component mixers (μ A).

DISCUSSION

The SSB receiver noise temperatures in Fig. 6 are, as expected, approximately twice the DSB values obtained by a simple mixer similar to one of the component mixers of the sideband separating mixer. With some improvement in tuning it should be possible to obtain a flatter noise temperature over the desired frequency band. The image rejection is ≥ 9 dB, which is sufficient to remove image frequency atmospheric noise in radio astronomy applications, but is lower than expected. The variation of the image rejection with frequency suggests that LO leakage entering the signal port of the mixer may be spoiling the LO phasing at the component mixers. Because ~ 17 dB LO couplers are used, LO leakage to the signal port at the -20 dB level would appear at the individual mixers only ~ 3 dB below the desired LO and could account for the poor image rejection. We believe this LO leakage is through a mode under the quartz substrate, excited by the suspended stripline to CPW transition at the LO end of the substrate, and coupling into the similar transition at the signal end. To suppress such leakage, the present mixer contains a small piece of absorbing material. After the mixer measurements described here, it was realized that this absorber was too small and remote from the mixer substrate to have a significant effect. We are in the process of replacing it with a larger piece positioned closer to the substrate, and made of material with a higher attenuation constant [13].

An additional contribution to the poor image rejection arises from the (image) termination on the input quadrature hybrid. Because of the difficulty of achieving a given sheet resistance using AuPd, resistors on the present wafer were 36% too high — 68 ohms rather than 50 ohms. SIS mixers are seldom well matched to the LO, nor to signals in either sideband, and a mismatched termination on the hybrid can spoil the phasing of those waves at the two mixers through multiple reflections. Assuming identical component mixers with signal reflection coefficient ρ_s , the effect of a mismatch ρ_H at the input hybrid is to produce an output at the IF image port corresponding to an image rejection $|\rho_s \rho_H|^2$. Hence the present 68 ohm termination can contribute an image rejection no worse than 16 dB. LO power reflected at identical mixers, arriving at the mismatched termination, returns to the mixers with a phase ϕ_{MH} , dependent on the electrical distance between mixer and termination, plus a $\pi/2$ difference (between mixers) contributed by the quadrature hybrid. ϕ_{MH} changes with LO frequency, causing the amplitude and phase of the LO at the mixers to vary. We expect the phase variation to have the more substantial effect on the image rejection. For the 68 ohm termination the maximum phase error between mixers is $\sim 9^\circ$, corresponding to an image rejection of ~ 22 dB. We deduce that the high resistance of the termination on the quadrature hybrid is unlikely to account for more than about half the measured minimum image coupling.

The DC currents in the two mixers exhibit unexpected frequency dependence, as evident in Fig. 9. Above ~ 250 GHz, the currents differ by almost a factor of two. We do not yet know whether this is a characteristic only of the particular chip measured here, or whether it is caused by some error in the design.

An interesting and potentially useful property of this type of sideband separating mixer occurs when the mixer elements have anti-symmetrical I-V curves, as do SIS junctions. Then, reversing the polarity of the bias on one of the component mixers interchanges the sideband outputs. Hence a sideband separating mixer connected to a *single* IF channel can be used to receive signals in *either* sideband.

ACKNOWLEDGMENTS

The authors thank N. Horner, F. Johnson, and A. Marshall for fabricating and assembling the mixer, and K. Crady for his help in testing the mixer.

REFERENCES

References marked with an asterisk () are available on the web at <http://colobus.aoc.nrao.edu/memos/memolist.html>

- [*1] A. R. Thompson and A. R. Kerr, "Relative sensitivities of single and double sideband receivers for the MMA," Millimeter Array Memo. 168, National Radio Astronomy Observatory, Charlottesville VA, April 1997.
- [*2] P. R. Jewell, J. G. Mangum, "System Temperatures, Single Versus Double Sideband Operation, and Optimum Receiver Performance," Millimeter Array Memo. 170, National Radio Astronomy Observatory, Charlottesville VA, April 1997.
- [3] R. L. Akeson, J. E. Carlstrom, D. P. Woody, J. Kawamura, A. R. Kerr, S.-K. Pan, and K. Wan, "Development of a sideband separation receiver at 100 GHz," Proceedings of the Fourth International Symposium on Space Terahertz Technology, pp. 12-17, March 1993.
- [4] C.-Y. E. Tong and R. Blundell, "A Quasi-Optical Image Separation Scheme for Millimeter and Submillimeter Waves," *IEEE Trans. Microwave Theory Tech.*, vol. MTT-42, no. 11, pp. 2174-2177, Nov. 1994.
- [5] A. R. Kerr and S.-K. Pan, "Design of planar image-separating and balanced SIS mixers," Proceedings of the Seventh International Symposium on Space Terahertz Technology, pp. 207-219, 12-14 March 1996.
- [6] A. R. Kerr, S.-K. Pan, A. W. Lichtenberger and H. H. Huang, "A Tunerless SIS mixer for 200–280 GHz with low output capacitance and inductance," Proceedings of the Ninth International Symposium on Space Terahertz Technology, 17-19 March 1998.
- [7] R. L. Sandstrom, A. W. Kleinsasser, W. J. Gallagher, and S. I. Raider, "Josephson Integrated Circuit Process for Scientific Applications," *IEEE Transactions on Magnetics*, vol. MAG-23, no. 2, pp. 1484-1488, March 1987.
- [8] Hercules HR500-2S film is 0.00075" thick. It consists of 0.0005" biaxially oriented polypropylene coated both sides with polyvinylidene chloride. The plastic film division of Hercules is now operated by Applied Extrusion Technology Inc., Covington, VA. HR500-2S is now obsolete and has been superceded by a similar material called UBS-2.
- [9] Gore RA-7957 expanded PTFE has a submicroscopic open-cell structure. It has a density 25% of that of solid PTFE.
- [10] S.-K. Pan, A. R. Kerr, M. J. Feldman, A. Kleinsasser, J. Stasiak, R. L. Sandstrom and W. J. Gallagher, "A 85-116 GHz SIS receiver using inductively shunted edge-junctions," *IEEE Trans. Microwave Theory Tech.*, vol. MTT-37, no. 3, pp. 580-592, March 1989.
- [11] MAC Technology Inc., Klamath Falls, OR. Model C-7203.
- [12] A. R. Kerr, "The NRAO Type-2B 1-2 GHz SIS Bias-T," Electronics Division Technical Note No. 173, National Radio Astronomy Observatory, Charlottesville, VA, 15 Feb. 1996.
- [13] Emerson and Cuming, Canton, MA. Eccosorb 110. See H. Hemmati, J. C. Mather, and W. L. Eichhorn, "Submillimeter and millimeter wave characterization of absorbing materials," *Applied Optics*, vol. 24, no. 24, pp. 4489-4492, 15 December 1985.

EXPERIMENTAL RESULTS OF SIS MIXERS WITH DISTRIBUTED JUNCTION ARRAYS

Sheng-Cai Shi¹, Takashi Noguchi¹, Junji Inatani², Yoshihisa Irimajiri³, and Toshimi Saito⁴

1. Nobeyama Radio Observatory, Nobeyama, Minamisaku, Nagano 384-13, Japan

2. Tsukuba Space Center, National Space development Agency of Japan

3. Communication Research Laboratory, Ministry of Posts & Telecommunications, Japan

4. Mitsubishi Electric Logistics Support Co., Ltd., Kamakura, Japan

e-mail: shencai@nro.nao.ac.jp; noguchi@nro.nao.ac.jp;

Inatani.Junji@nasda.go.jp; irimaji@crl.go.jp; tsaito@nro.nao.ac.jp

Abstract — The heterodyne mixing performances of three distributed junction arrays (i.e., a number of SIS junctions distributed along a thin-film transmission line) involving two, five, and ten junctions, respectively, are experimentally investigated in the frequency range of 320-540 GHz, and are compared to their Fourier-Transform-Spectroscopy detecting responses. In addition, the Josephson resonance effects of the three distributed junction arrays are examined. Finally, other possible applications of distributed junction arrays, such as harmonic mixing and direct detecting, are addressed.

1. Introduction

SIS mixers have exhibited as low a receiver noise temperature as three times the quantum limit at submillimeter wavelengths [1]. In developing submillimeter-wave SIS mixers, ones usually adopt SIS junctions of a relatively large $\omega R_n C_j$ product (R_n and C_j are junction's normal-state resistance and geometric capacitance, respectively), say four, to avoid the limitation of the junction's critical current density (J_c , approximately 10 kA/cm² for Nb junctions), which is proportional to the ratio of $\omega/\omega R_n C_j$. Hence, submillimeter-wave SIS mixers with a single junction, a junction array in series, or twin junctions in parallel have a limited bandwidth according to such a relation $\omega/\Delta\omega = \omega R_n C_j$. On the one hand, broadband junction devices are highly desirable for tuneless SIS mixers, are suitable to direct-detecting applications, and are beneficial to some complex systems such as millimeter-/submillimeter-wave interferometer arrays in reducing the cost and complexity.

Theoretical simulations have demonstrated that like non-linear transmission lines [2], distributed junction arrays, which are a number of SIS junctions connected in parallel with every two junctions separated by a short thin-film transmission line like a conventional tuning inductance, have a bandwidth performance nearly independent of the junctions' $\omega R_n C_j$ product [3]. While adopting

low- J_c (say less than 4 kA/cm²) SIS junctions, distributed junction arrays are still applicable to submillimeter-wave SIS mixers. In this paper, the bandwidth performance of distributed junction arrays is experimentally studied.

2. Distributed junction arrays and a 470-GHz SIS mixer

Three distributed junction arrays involving two, five, and ten SIS junctions, respectively, have been fabricated to investigate the bandwidth performance of such a type of junction device experimentally. Their photographs are displayed in Fig. 1. The SIS junctions in the three arrays were designed to be identical for simplicity and for convenience of comparison. The junctions' critical current density was taken as 4 kA/cm² (relatively low for submillimeter-wave applications), while the junction area and the normal-state resistance for a single junction were 1.5 μm² and 31 Ω. With the assumption of a junction specific capacitance of 60 fF/μm², the junctions' $\omega R_n C_j$ product is equal to 8.2 at 470 GHz. The transmission line housing the SIS junctions was a Nb-based thin-film superconducting microstrip line of a 4.5-μm width and of an insulator layer as Nb₂O₅(1000 Å)/SiO₂(2700 Å)/Al₂O₃(900 Å). The length of each section separating every two junctions of the thin-film microstrip line was optimized in connection with a 470-GHz waveguide SIS mixer, which was employed to measure these junction arrays. The optimum microstrip-line lengths for the ten-, five-, and two-junction arrays were equal to 17, 22, and 26 μm (approximately $\lambda_g/13.2$, $\lambda_g/10.2$, and $\lambda_g/8.6$ at 470 GHz), respectively. It is understandable that these lengths do not differ significantly, considering that the resonance frequency of the circuit made up of two junctions and the microstrip line between them approximately defines the upper frequency limit of a distributed junction array.

The 470-GHz waveguide tuneless mixer mount used here is similar to that described in [4,5], but has a larger waveguide and a larger SIS-chip slot to fit the broadband characteristic of distributed junction arrays. Its detailed structure, together with the integrated circuits on the SIS chip, is displayed in Fig. 2a. The RF and LO signals are transmitted to the distributed junction array through a diagonal horn, a waveguide-to-microstrip transition, and a quarter-wavelength impedance transformer. The diagonal horn [6], of a feed waveguide just as the mixer's input waveguide, has an aperture measuring 3.5 mm x 3.5 mm and a length of 16 mm. The waveguide-to-microstrip transition, featuring a 'built-in' DC/IF return path and an offset probe (for larger bandwidth) [7], transforms the waveguide impedance (~289 Ω at 470 GHz) to an output impedance of 75 Ω, which is just equal to the characteristic impedance of the output microstrip line. Transforming the 75-Ω output impedance to the input impedance of the distributed junction array (approximately equal to R_n/N , here N is the number of junctions), the quarter-wavelength impedance transformer is composed of three sections, with one being a conventional microstrip line of a 44.7-Ω characteristic impedance and the other two a thin-film microstrip line (of different characteristic impedances for

the three distributed junction arrays). The calculated RF embedding impedance seen before the distributed junction array is demonstrated in Fig. 2b for the three instances. The IF signal is outputted through the IF choke filter, which has an RF impedance nearly equal to zero at 470 GHz and is not followed by any IF impedance transformers whereas distributed junction arrays may have an output impedance around 50Ω owing to a small equivalent normal-state resistance (several ohms).

3. Experimental results and discussions

3.1 Josephson resonance effects

The fabricated junction arrays have a critical current density of about 3.4 kA/cm^2 (slightly lower than the desired value, 4 kA/cm^2), while their normal-state resistances are equal to 2.2, 4.4, 11 Ω , being apparently smaller than the respective design values of 3.1, 6.2, 15.5 Ω . The resistance difference, together with a lower junction current density, suggests that the actual junction area is 66% larger than the designed one. An over-estimated margin for junction shrinking (in photomask design) and imperfect fabrication process might account for the enlargement of the junction area. Nevertheless, it appears that the junctions have been identically defined because the arrays' equivalent normal-state resistances scale exactly with the number of junctions.

In case of twin SIS junctions connected in parallel (with a tuning inductance between them), it has already known that two Josephson resonance steps will appear on the junction I-V curve [5]. The resonance steps are the dc responses of the Josephson ac currents through the two SIS junctions, indeed indicating two resonance frequencies for two respective circuits — one consists of the tuning inductance and one junction, and the other the tuning inductance and the two junctions. Here we have examined the I-V characteristics of the three fabricated junction arrays (from the same batch). Their resonance effects are shown in Figs. 3a-c with respective I-V curves (enlarged for Figs. 3b and 3c). Note that the resonance steps for both the five- and the ten-junction array are not completely exhibited because they are very sensitive to magnetic field. It can be observed from Figs. 3a-c that for the two-junction array a resonance step (higher one) occurs around 0.7 mV (corresponding to 339 GHz, a low frequency obviously due to an enlarged junction area), whereas for the five- and ten-junction arrays multi-steps (>2) occur with the highest voltage being around 0.9 mV. Apparently, the more the junctions, the more the resonance steps. Such a multi-step structure, indeed arising from the multi-resonance loops of a distributed junction array, suggests that distributed junction arrays can perform over a large bandwidth, which will increase with the number of junctions. This conclusion is coincident with the simulation results plotted in Fig. 3d, which are the calculated input S_{11} parameters for the three distributed junction arrays with the assumption of that each junction is a parallel combination of its actual normal-state resistance and geometric capacitance (i.e., 22 Ω and 90

fFx1.66). Notice that for S_{11} -parameter simulations, the parameters of the thin-film microstrip line are kept the same as the design values.

It should be pointed out that for mixing applications with distributed junction arrays, especially in the terahertz regime, the Josephson current must be completely suppressed as the resonance steps may extend to a relatively high voltage so as to affect the IF response of the mixing considerably.

3.2 FTS responses and heterodyne mixing performances

Prior to measure the heterodyne mixing performances of the three distributed junction arrays, we have studied their Fourier-Transform-Spectroscopy responses with the aid of the 470-GHz waveguide mixer (acting as a direct detector here), in which the distributed junction array is mounted. The measured direct-detecting responses are presented in Fig. 4a. The upper- and lower-frequency limits of these responses are caused mainly by the adopted mixer mount, while the dips in the response curves are partly the intrinsic behaviors of the distributed junction arrays and partly due to the measurement system (i.e., spectrometer itself). These direct-detecting curves predict the RF-coupling behaviors of the three distributed junction arrays, though not exact ones. As can be clearly observed from Fig. 4a, the response curve for the two-junction array is peaked around 375 GHz, which is very close to the displaced center frequency due to an enlarged junction area (i.e., $470 \text{ GHz}/1.66^{1/2} \approx 365 \text{ GHz}$). Note that the difference between this frequency and the two-junction-array's resonance frequency (i.e., 339 GHz) is caused by the embedding impedance (of a negative susceptance around 339 GHz, refer to Fig. 2b) of the adopted 470-GHz mixer mount. In addition, its 3-dB bandwidth is approximately 60 GHz, apparently defined by the junctions' $\omega R_n C_j$ product (i.e., $470 \text{ GHz}/8.2 \approx 57 \text{ GHz}$). On the contrary, the response curves for the five- and ten-junction arrays have a larger bandwidth and are centered around 450 GHz, even though the junction area in the two instances is similarly enlarged. Obviously, the frequency responses of distributed junction arrays become less sensitive to the junction area and the junctions' $\omega R_n C_j$ product with the increase of the number of junctions. Being in good agreement with the simulation results described in [3], the direct-detecting results are very encouraging for the development of SIS mixers with distributed junction arrays.

Using the conventional Y-factor method, we have measured the noise performance of the 470-GHz waveguide SIS mixer for the three distributed junction arrays. The measured receiver noise temperatures (DSB) are plotted in Fig. 4b. Notice that the noise contribution due to the quasi-optical system for measurement, which is located just in front of the measured SIS mixer and consists of a 25- μm thick Mylar vacuum window, and an elliptical mirror and a 25- μm thick Mylar beam splitter both angled at 45 degrees, were not calibrated out, and that the equivalent noise temperature of the IF-chain following the 470-GHz SIS mixer was found to be about 15 K. The noise performance in the

frequency range of 360–470 GHz was not measured for lack of LO sources. Nevertheless, the general trends of the three noise-temperature curves should not be changed if looking into the results shown in Fig. 4a. Of the three measured instances, the ten-junction array has the best noise performance, giving a minimum noise temperature of 150 K at 470 GHz and being less than 400 K from 320–540 GHz. The frequency response of the receiver noise temperature for the two-junction array is clearly centered at a frequency of lower than 360 GHz, in like manner proving that the actual junction area is larger than the desired one. This frequency displacement attributes to a high receiver noise temperature in case of the two-junction array, as the junction device and the mixer mount were optimized at completely different frequencies (~365 and 470 GHz). The results shown in Fig. 4b are generally in good agreement with those in Fig. 4a.

Another five- and ten-junction arrays of a critical current density and equivalent normal-state resistances equal to 3.8 kA/cm² and 6.6/3.3 Ω (very close to the respective design values), have been fabricated with an improved fabrication process. As demonstrated in Fig. 5, their measured noise performances are improved considerably compared to those given in Fig. 4b. The receiver noise temperature for the ten-junction array is less than 220 K from 325–535 GHz (namely, of a relative bandwidth approximately equal to 50%), and has a minimum value of around 95 K at 485 GHz, which is four times as large as the quantum limit. It should be pointed out that the LO pumping power level was insufficient around 425 GHz somehow in the case of the ten-junction array. Similarly, the ten-junction array has shown a larger bandwidth than the five-junction array.

3.3 Discussions

Both the five- and the ten-junction array have demonstrated a relative bandwidth of much larger than $1/\omega R_n C_j$ (~12% for the two instances), namely, the relative bandwidth for a single junction or twin junctions. In fact, their bandwidths might be even larger if eliminating the effect of the adopted waveguide mixer mount, which has a smaller bandwidth. Therefore, the RF bandwidths of distributed junction arrays (for $N > 5$) are nearly independent of the junctions' $\omega R_n C_j$ product (the more the junctions, the less the dependency). Accidentally, it has been observed that for distributed junction arrays the junction area is no longer as critical to the mixing performance as for a single junction or twin junctions. This conclusion is similar to such a simulation result that the performance of SIS mixers with distributed junction arrays is insensitive to the tuning inductance [3] (not experimentally confirmed here). The measured receiver noise temperature is already quite low, but could be further reduced if using an IF chain of a lower noise temperature.

Regarding the LO power level necessary for distributed junction arrays, it has been found that the optimum LO pumping current for the ten-junction array is typically one-tenth of the current at the gap voltage, a level lower than for a single junction (i.e., of a smaller reduced LO voltage). Hence, the

necessary LO power level may not increase to some degree with the increase of the number of junctions. Moreover, it has been observed that though the junctions in a distributed junction array are quite separated, suppressing the Josephson current is just as easy as in case of a single junction.

As distributed junction arrays can offer a very large bandwidth, it is likely to have a good matching at the fundamental and harmonic frequencies simultaneously, thereby being possible to use distributed junction arrays for harmonic mixing, which requires both the fundamental and the harmonic frequency port well matched [unpublished simulation results]. It is already known that there are some ripples in the RF-response curves of distributed junction arrays. Increasing the number of junctions may reduce the ripples, but will make RF matching difficult (or degrade the RF-matching bandwidth) because of a smaller equivalent normal-state resistance. Adopting non-identical junctions (i.e., of different areas) and non-uniform separations between every two junctions might be a good alternative. Additionally, distributed junction arrays should be applicable to direct-detecting applications as far as the bandwidth is concerned.

4. Summary

The noise performance of distributed junction arrays has been experimentally investigated with the help of a 470-GHz waveguide mixer mount. Measurement results clearly demonstrated that the more junctions the array has, the larger the bandwidth is. Though adopting junctions of a relatively low current density (i.e., 3.8 kA/cm²), the ten-junction array has exhibited a good performance, giving a minimum receiver noise temperature of 95 K at 485 GHz ($\sim 4 \hbar\omega/k$) and as large a relative bandwidth as 50%. It has also been found that in comparison to a single junction, distributed junction arrays have a frequency response much less dependent on the junction area. Good agreement between FTS responses and heterodyne mixing responses has also been observed. Distributed junction arrays should be of good use for heterodyne mixing (either fundamental or harmonic) and direct detecting in the terahertz frequency regime.

Acknowledgment

Hiroshi Matsuo of NRO and Akahori of Shinshu University are thanked for their help in measuring the FTS responses of distributed junction arrays.

References

1. J.E. Carlstrom and J. Zmuidzinas, "Millimeter and submillimeter techniques," in *Reviews of Radio Science 1993 - 1995*, W. R. Stone, ed., The Oxford University Press, Oxford, 1996.

2. C.E. Tong, R. Blundell, B. Bumble, J.A. Stern, and H.G. LeDuc, "Quantum limited heterodyne detection in superconducting non-linear transmission lines at sub-millimeter wavelengths," *Appl. Phys. Lett.*, vol.67, pp.1304-1306, Aug. 1995.
3. S.C. Shi, T. Noguchi, and J. Inatani, "Analysis of the bandwidth performance of SIS mixers with distributed junction arrays," *Proc. 8th Int. Symp. on Space Terahertz Tech.*, Boston, USA, Mar. 1997, pp.81-90.
4. S.C. Shi, T. Noguchi, and J. Inatani, "A fixed-tuned 100-GHz SIS mixer exhibiting broad bandwidth and very low noise temperature," *IEEE Trans. Appl. Supercond.*, vol.7, no.4, pp.3850-3857, Dec. 1997.
5. S.C. Shi, T. Noguchi, and J. Inatani, "Development of a 500-GHz band SIS mixer," *IEEE Trans. Appl. Supercond.*, vol.7, no.2, pp.2587-2590, June 1997.
6. A.W. Love, *Electromagnetic Horn Antennas*, IEEE Press, New York, 1976.
7. S.C. Shi and J. Inatani, "A waveguide-to-microstrip transition with DC/IF return path and an offset probe," *IEEE Trans. Microwave Theory Tech.*, vol.45, no.3, pp.442-445, Mar. 1997.

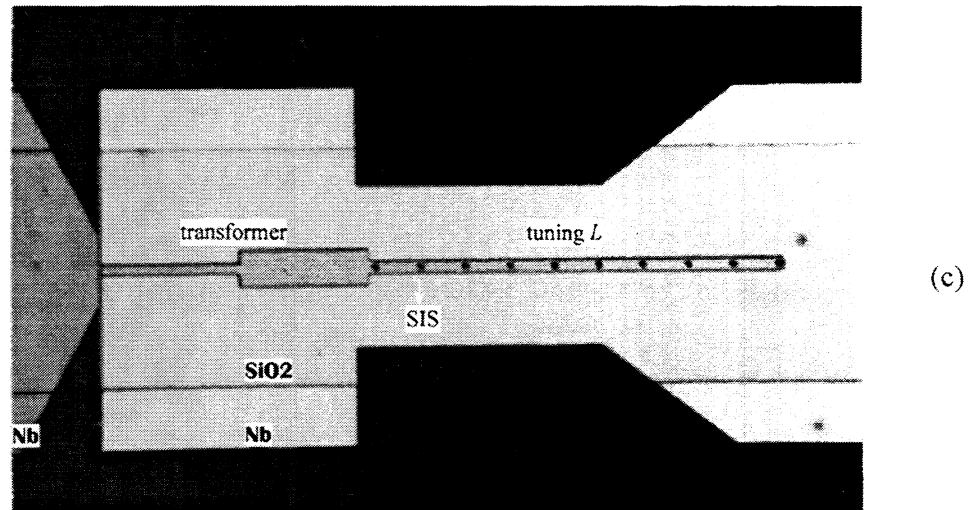
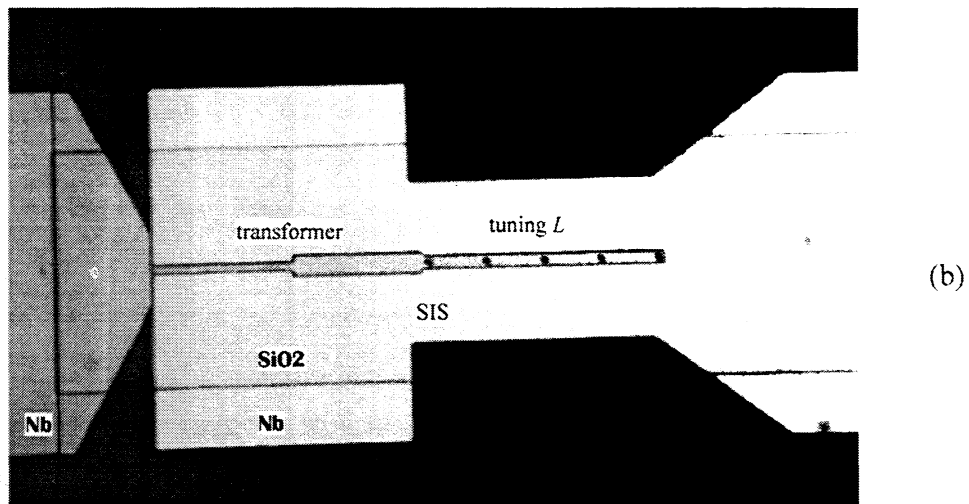
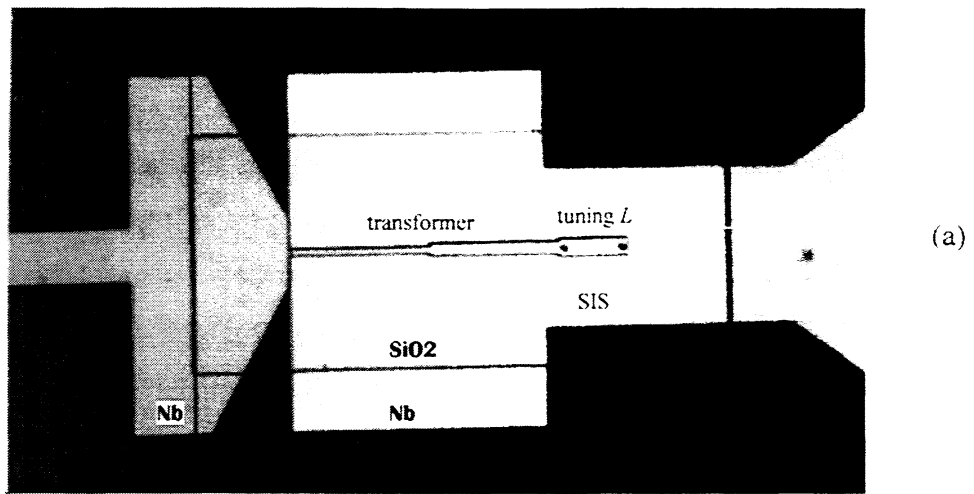


Fig. 1 Photographs of three distributed junction arrays, with (a) two junctions, (b) five junctions, and (c) ten junctions.

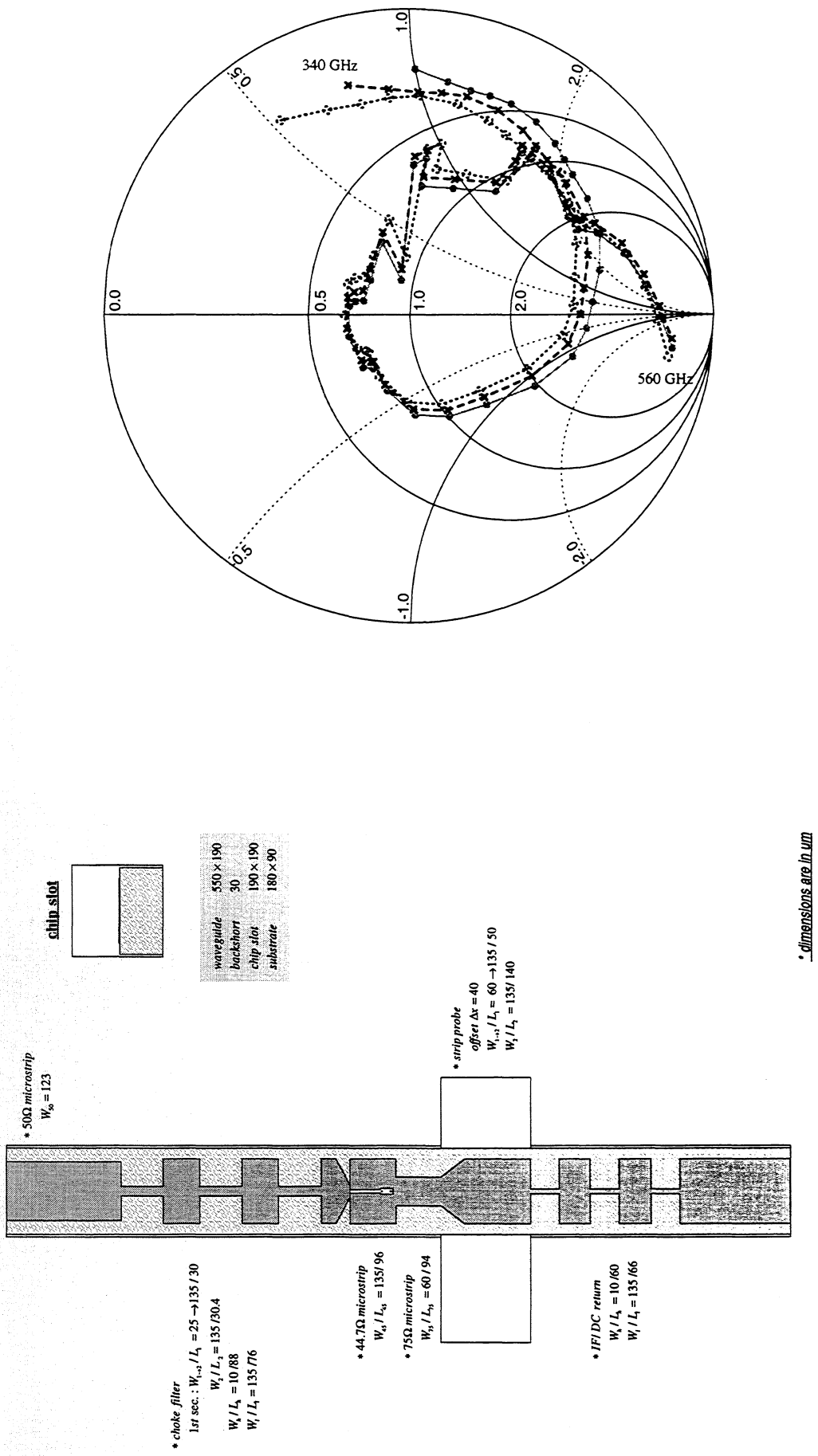
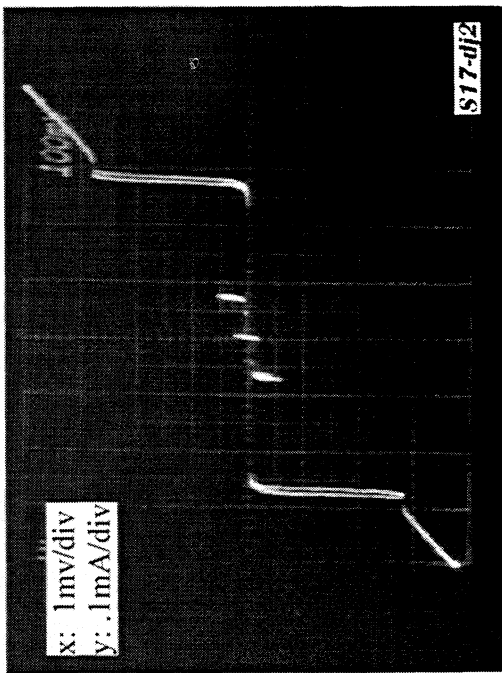
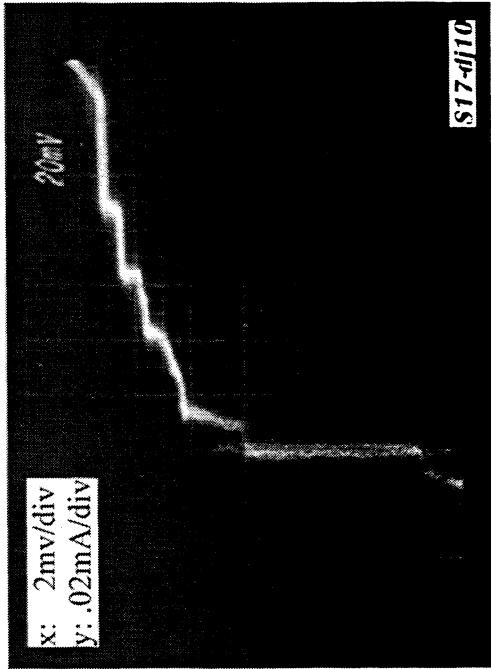


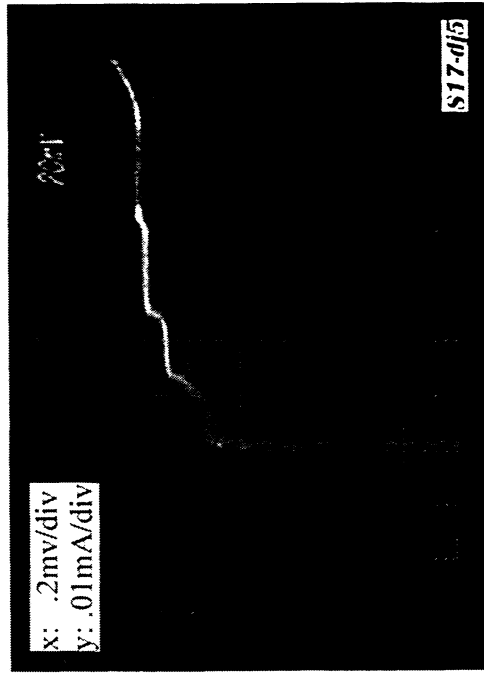
Fig. 2 (a) Cross-sectional view of a 470-GHz tuneless waveguide SIS mixer; (b) Embedding impedance of the 470-GHz mixer mount (seen from the distributed junction array), plotted on a Smith impedance chart for the two-, five-, and ten-junction arrays.



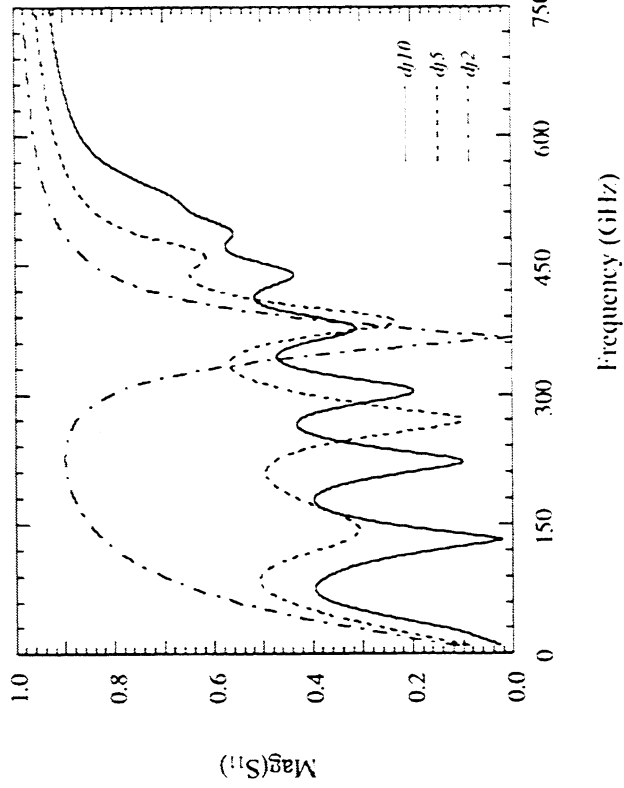
(a)



(c)



(b)



(d)

Fig. 3 Josephson resonance effects of three distributed (a. two-, b. five-, and c. ten-) junction arrays of a $\sim 66\%$ enlarged junction area and a current density of 3.4 kA/cm^2 ; (d) Simulated S_{11} parameters for the three junction arrays, shown as a function of frequency. Note that each SIS junction is assumed as a parallel combination of its normal-state resistance and geometric capacitance (i.e., $22 \text{ } \Omega$ and $90 \text{ fF} \times 1.66$).

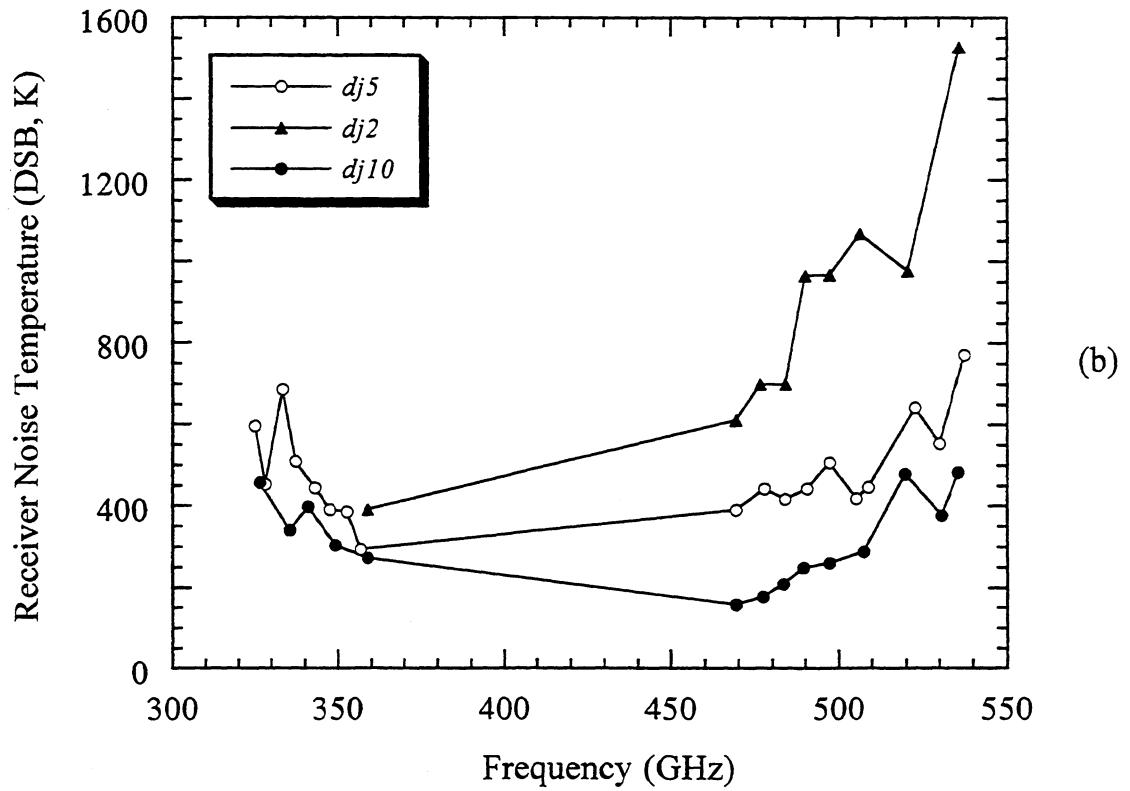
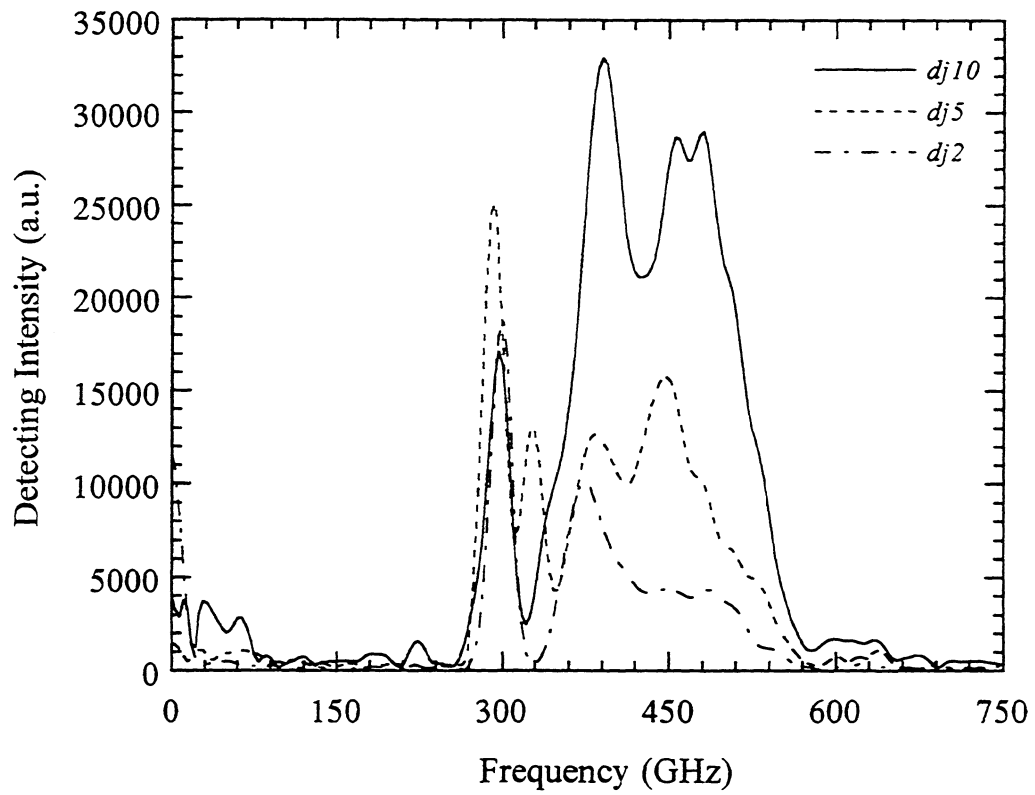


Fig. 4 (a) Measured FTS responses and (b) measured receiver noise temperatures (DSB), for the two-, five-, and ten-junction arrays of a $\sim 66\%$ enlarged junction area and a current density of 3.4 kA/cm^2

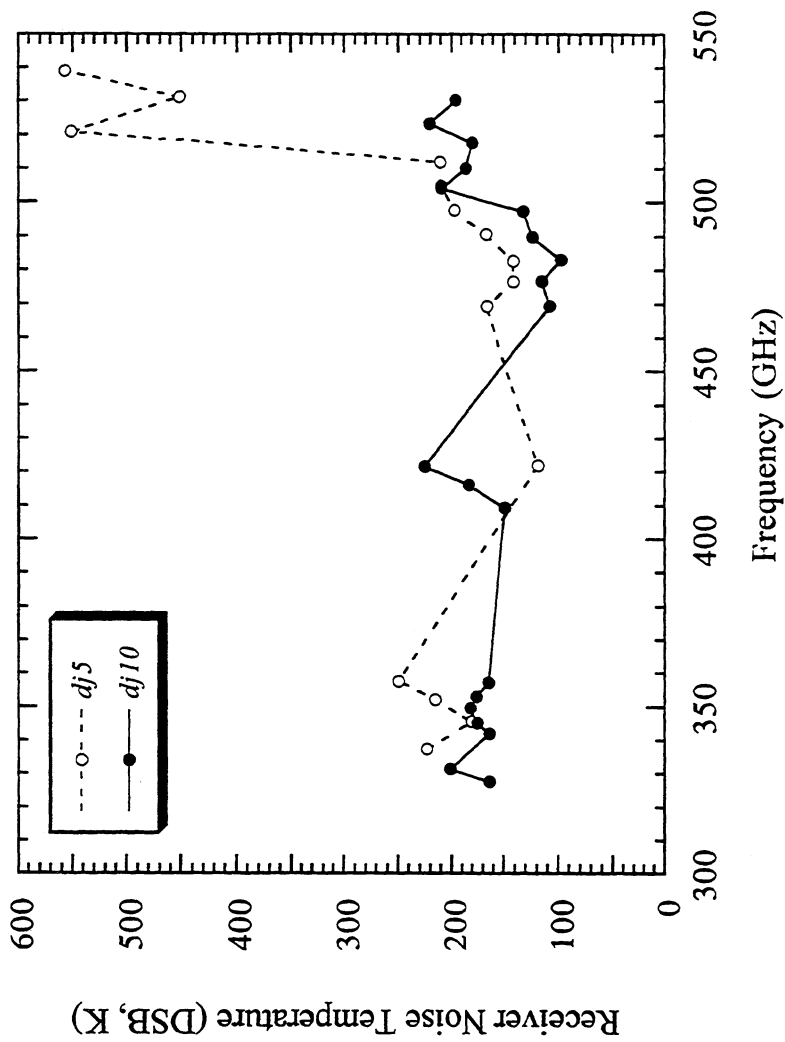


Fig. 5 Measured receiver noise temperature (DSB) as a function of frequency. Results are shown for a five- and a ten-junction array of a corrected junction area and a critical current density equal to 3.8 kA/cm².

DOUBLED SHOT NOISE IN NIOBIUM SIS MIXERS¹

P. Dieleman², J.R. Gao^{†3}, and T.M. Klapwijk

University of Groningen, Department of Applied Physics and Materials Science Center (MSC) Nijenborgh 4, 9747 AG Groningen, The Netherlands.

† Space Research Organisation of the Netherlands. Landleven 12, 9747 AD Groningen, The Netherlands.

Abstract

The electrical and shot noise characteristics of high current density niobium superconductor - insulator - superconductor tunnel junctions suitable for heterodyne detection of THz radiation are studied. It is found that a significant part of the current at voltages $V < 2\Delta/e$ is carried via barrier defects (pinholes). Due to the transport mechanism in these pinholes, the shot noise is considerably increased. The data presented clarifies an often-observed discrepancy between measured and expected heterodyne mixer noise temperatures and predicts a 25 % increase in the receiver noise temperature of Nb SIS heterodyne detectors at 1 THz.

1 Introduction

The standard procedure to calculate the gain and noise of Superconductor - Insulator - Superconductor (SIS) heterodyne detectors is by means of the Tucker theory[1]. A fundamental assumption of this theory is that the current transport mechanism is single - electron tunneling through the insulator. It has recently been shown that this assumption does not hold for high current density NbN SIS junctions[2]. Consequently the measured noise can be more than twice as large as theoretically predicted. This discrepancy is also of interest for Nb junctions for two reasons. First, a discrepancy of equal magnitude has often been observed in Nb junctions but has never been understood[3, 4, 5, 6]. Second, since junctions with progressively thinner oxide barriers are used to improve the ωRC product at THz frequencies[7]. An intrinsic

¹This work has been accepted for publication in Applied Physics Letters

²e-mail: Dieleman@phys.rug.nl

³e-mail: Gao@phys.rug.nl

dependence exists between the oxide thickness and the current carried by barrier imperfections (pinholes). This is shown in Fig. 1 in which values for the subgap current in junctions fabricated by several groups are normalized to the theoretically expected thermal current[8]. Fig. 1 demonstrates that at a commonly used current density (J_c) of 10 kA/cm² the subgap current is at least 4 times larger than the expected thermal current, indicating that 80 % or more of the current is carried via higher order processes⁴. The charge transport mechanism in these pinholes is multiple Andreev reflection (MAR)[9, 10], which causes the current to flow in multiply charged quanta (Andreev clusters). Therefore, with increasing current density the generated shot noise increases as the current flowing through pinholes increases. Moreover, the shot noise associated with this current is much larger than theoretically expected[2]. To investigate the impact of this effect on the heterodyne mixing performance of Nb SIS junctions we measure the shot noise as a function of bias voltage and compare it with the theory of Ref. [2].

2 Junction characteristics

The tunnel junction used is fabricated by sputtering 100 nm of Nb and 8 nm of Al. The Al is oxidized *in situ*, after which a top electrode of 100 nm Nb is deposited. The junction size is defined by optical lithography. Fabrication details are described in Ref. [11]. The junction has an area of 0.8 μm^2 and a resistance of 20.5 Ω , corresponding to a critical current density of 13 kA/cm². The current-voltage characteristic measured at 3.6 K is plotted in Fig. 2(a), together with the differential conductance curve. The subharmonic gap structure indicated by the arrows is clearly visible, showing that a considerable part of the subgap current is carried by MAR.

3 Measurement setup

The junctions are connected via an integrated low-pass filter, a circulator with 0.5 dB loss, to the amplifier chain with a noise temperature of 3.2 K and a gain of 80 dB at 1.5 GHz with 85 MHz bandwidth. The output power is given by[16]:

$$P_{out} = G_{amp}B \left(\frac{1}{4} S_I R_{dyn} (1 - \Gamma^2) G_{iso} + k_B T G_{iso} \Gamma^2 + k_B (1 - G_{iso}) T + T_{amp} \right) \quad (1)$$

in which G_{amp} is the amplifier gain, B is the bandwidth, I , V and R_{dyn} are the current, voltage and the differential resistance dV/dI of the junction respectively, T is the measurement temperature, Γ is the reflection coefficient $|R_{dyn} - R_{amp}| / (R_{dyn} + R_{amp})$, G_{iso} is the isolator gain, and T_{amp} stands for the noise temperature of the amplifier chain.

⁴The slope of the line is most likely influenced somewhat by the fabrication techniques used, but the general trend clearly is an increase of the subgap current with increasing J_c .

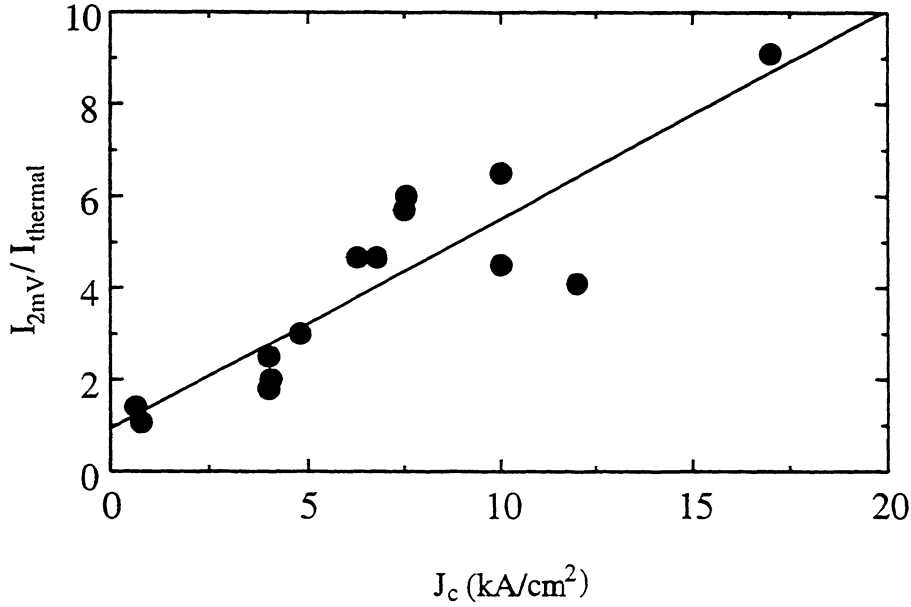


Figure 1: Subgap current at 2 mV (I_{2mV}) as a function of the current density J_c . The current is normalized to the thermal current theoretically expected at 4.2 K. The solid line shows a linear least squares fit to the data. (Data extracted from Refs. [4, 5, 12, 13, 14, 15]).

4 Noise measurements

In Fig. 2(b) and (c) the measured and calculated junction noise contribution after amplification, $P_{noise} = \frac{1}{4} S_I \cdot R_{dyn} (1 - \Gamma^2) G_{iso} G_{amp} B$, is plotted as a function of voltage for temperatures of 3.6 and 6 K, respectively. The dotted lines show the shot noise of the junction if the subgap current is attributed to single - electron tunneling.

5 Shot noise calculation

The dashed noise curve is calculated as follows. Two conduction channels exist in parallel; the tunnel barrier carrying I_{tun} and the pinholes carrying I_{MAR} via higher-order processes. Hence, the shot noise spectral density S_I is the sum of two contributions:

$$S_I(V) = 2e I_{tun}(V) + 2q(V) I_{MAR}(V) \quad (2)$$

The effective charge of an Andreev cluster is approximately given by $q(V) = (1 + \frac{2\Delta}{eV})e$ [2]. The pinhole transmission is measured to be 0.2 from the relative magnitude of the current steps at the subharmonics[17, 18]. The corresponding shot noise suppression calculated from this transmission value is a mere 1 % [2, 19], hence Eq. 2.

The tunnel current, I_{tun} , is calculated[8] and subtracted from the measured current, yielding the pinhole current, I_{MAR} . The shot noise is obtained by using I_{tun} and I_{MAR} as inputs for Eq. 2. The magnified currents in Fig. 2(a) give an impression of the ratio of those currents.

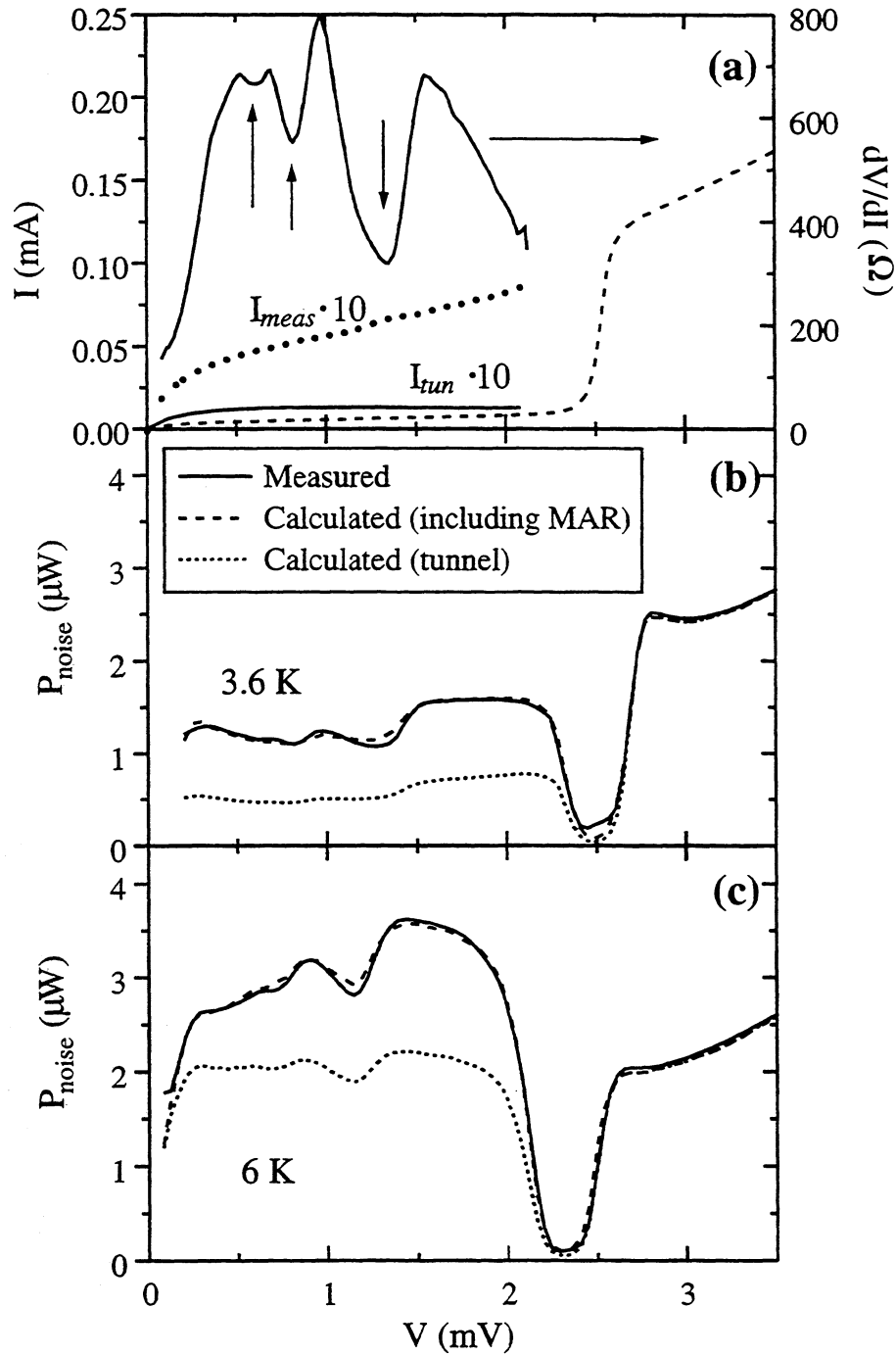


Figure 2: (a). I - V curve and differential resistance dV/dI at 3.6 K. The subharmonic gap structure in dV/dI is indicated by the arrows at $V = 2\Delta/ne$, $n = 2, 3, 4$. The solid line labeled $I_{tun} \cdot 10$ is the theoretical thermal current, to be compared to the actual measured current $I_{meas} \cdot 10$ shown by the solid circles. (b). Shot noise contribution at 3.6 K, at which temperature 80 % of the current is carried via pinholes. The solid line gives the power derived from the measurements, the dotted line indicates the noise calculated assuming all current is tunnel current, and the dashed line is calculated as explained in the text. (c). Shot noise contribution of the same junction at a temperature of 6 K, at which temperature 50 % of the current is carried via pinholes.

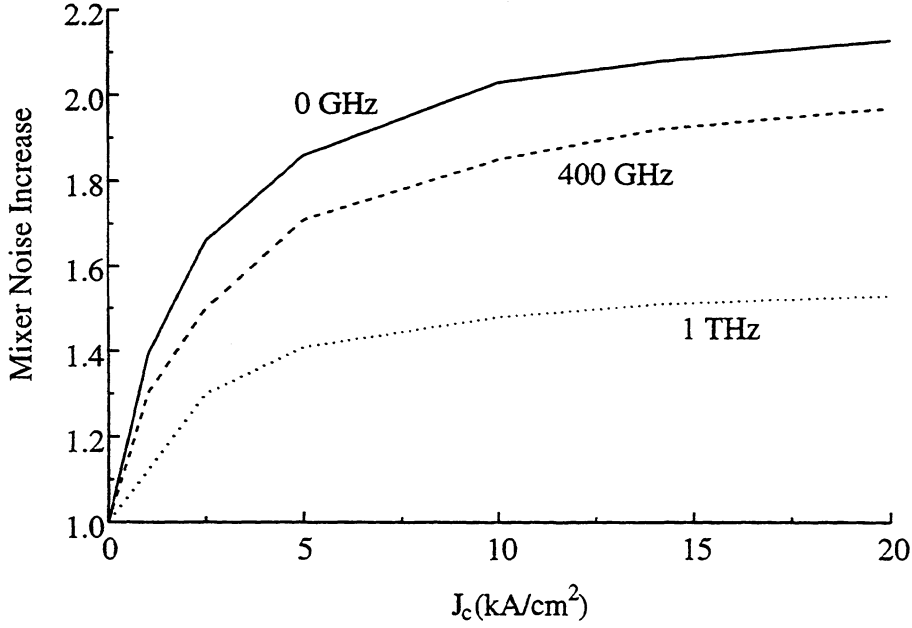


Figure 3: Correction factors to the Tucker[1] mixer noise due to the presence of MAR as a function of critical current density. At low frequencies the mixer noise is close to the shot noise at the bias voltage (the solid line). At higher frequencies the correction factor decreases because the contribution from voltages $V_{bias} + \hbar\omega/e$ becomes important where single electron transport is dominant.

The shot noise is increased by 63 % at a voltage just below $2\Delta/e$ when half of the current is tunnel current (See Fig. 2(c)) and the noise is doubled when only 20 % is tunnel current, as shown in Fig. 2(b). Clearly, high current density junctions exhibit single and multiple electronic charge transport mechanisms which have to be treated separately to obtain the total junction noise contribution.

6 Implications for the noise temperature

The noise temperature of a device when operated as heterodyne mixer is calculated by modifying the Tucker equations[1] to include noise arising from multiply charged current transport. The current correlation matrix element H_{00} becomes:

$$H_{00} = 2 \sum_{n=-\infty}^{n=\infty} J_n^2(\alpha) q I_{MAR} \coth \frac{qV}{k_B T} + 2 \sum_{n=-\infty}^{n=\infty} J_n^2(\alpha) e I_{el} \coth \frac{eV}{k_B T} \quad (3)$$

The remaining matrix elements, H_{10} , H_{11} and H_{1-1} , are rewritten similarly by substituting q for e in the noise calculation of I_{MAR} . The ratio of the mixer noise temperatures calculated with the modified theory and the original theory is plotted in Fig. 3. The relation between J_c and the pinhole current contribution of Fig. 1 is used to obtain the input currents for Eqs. 2 and 3. The values shown are calculated for an optimized radiation power level at 4.2 K.

A common method to improve the mixer noise temperature is to lower the operating temperature from 4.2 to 2 K. As a result the thermal current becomes nearly negligible, but the pinhole current remains unaffected. Therefore the shot noise correction factor is increased when the temperature is lowered.

7 Effects on the receiver characteristics

With the results of Fig. 3 the receiver noise temperature can be calculated to obtain an optimum design value for the current density. In the calculation we assume a double junction aluminum coupling circuit[12] with a resonance frequency of 1 THz, junctions with areas of $0.8 \mu\text{m}^2$ and I - V curves as modeled in [20]. The receiver noise is given by

$$T_{REC} = T_{opt} + \frac{T_M + 2T_{qf}}{2G_{opt}} + \frac{T_{amp}}{2G_M G_{iso} G_{opt}} \quad (4)$$

in which T_{opt} and G_{opt} , respectively, stand for the total noise and gain of the dewar window, heat filter and aluminum stripline together, the vacuum fluctuations T_{qf} contribute 24 K at 1 THz, the mixer gain G_M and noise T_M are calculated from the model I - V curve. The resulting receiver noise temperature is shown in Fig. 4 with, and without, a correction for the Andreev reflection enhanced shot noise. The initial improvement in the noise with increasing J_c is due to a lower loss in the Al stripline. The minimum noise is clearly shifted towards lower J_c because of the increased influence on the noise of MAR at high J_c , where the mixer noise dominates.

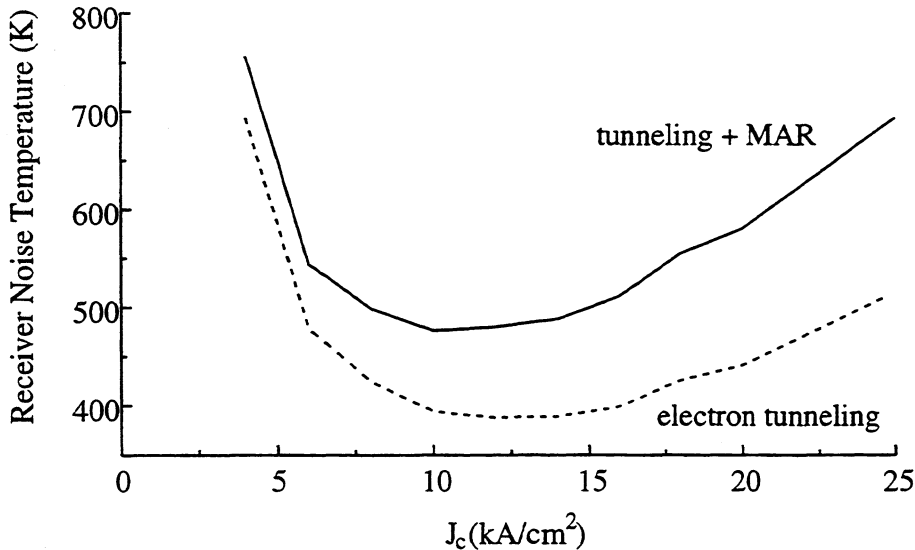


Figure 4: Receiver noise temperature calculated for a Nb junction at 1 THz with an Al tuning structure. The dashed line is calculated ignoring MAR.

8 Conclusions

In conclusion, Nb tunnel junctions with moderate critical current densities exhibit subgap currents which are much larger than the thermal current due to the presence of pinholes in the tunnel barrier. Since the pinhole current is carried in Andreev clusters with charge $q \gg e$ the associated shot noise is significantly enhanced. Due to this effect, the mixer noise can be more than twice as large as expected from the Tucker theory. This causes a 25 % increase in the receiver noise temperature at THz frequencies.

9 Acknowledgement

Helpful discussions and general assistance of N.D. Whyborn, J.J. Kuipers, H. van de Stadt, D. Nguyen, H. Golstein, W. Hulshoff, and H.H.A. Schaeffer are acknowledged. This work was supported by the European Space Agency under contract No. 7898/88/NL/PB(SC) and the Stichting voor Technische Wetenschappen.

References

- [1] J.R. Tucker and M.J. Feldman, *Rev. Mod. Phys.* **57**, 1055 (1985).
- [2] P. Dieleman, H.G. Bukkems, T.M. Klapwijk, M. Schicke, and K.H. Gundlach, *Phys. Rev. Lett.* **79**, 3486 (1997).
- [3] W.R. McGrath, P.L. Richards, D.W. Face, D.E. Prober, and F.L. Lloyd, *J. Appl. Phys.* **63**, 2479 (1988).
- [4] C.E. Honingh, J.J. Wezelman, M.M.T.M. Dierichs, G. de Lange, H.H.A. Schaeffer, T.M. Klapwijk, and M.W.M. de Graauw, *J. Appl. Phys.* **74**, 4762 (1993).
- [5] G. de Lange, C.E. Honingh, J.J. Kuipers, H.H.A. Schaeffer, R.A. Panhuyzen, T.M. Klapwijk, H. van de Stadt, and M.W.M. de Graauw, *Appl. Phys. Lett.* **64**, 3039 (1994).
- [6] S. Withington, K.G. Isaak, S.A. Kovtonyuk, and R.A. Panhuyzen, *European SIS user meeting*, 1994, Cologne, Germany.
- [7] F. Schäfer, P. van der Wal, E. Kreysa, and K.H. Gundlach, *Eighth Int. Symp. on Space THz Techn.*, 1997, Cambridge, MA, USA.
- [8] E.L. Wolf, *Principles of Electron Tunneling Spectroscopy*, (Oxford University Press, New York, 1985).
- [9] A.W. Kleinsasser, R.E. Miller, W.H. Mallison, and G.B. Arnold, *Phys. Rev. Lett.* **72**, 1738 (1994).

- [10] T.M. Klapwijk, G.E. Blonder, and M. Tinkham, *Physica* **109- 110B,C**, 1657 (1982).
- [11] M.M.T.M. Dierichs, R.A. Panhuyzen, C.E. Honingh, M.J. de Boer, and T.M. Klapwijk, *Appl. Phys. Lett.* **15** 774 (1993).
- [12] M. Bin, M.C. Gaidis, J. Zmuidzinas, T.G. Phillips, and H.G. LeDuc, *Appl. Phys. Lett.* **68**, 1714 (1996).
- [13] A.W. Kleinsasser, F.M. Rammo, and M. Bushan, *Appl. Phys. Lett.* **62**, 1017 (1993).
- [14] D. Maier, H. Rothermel, K.H. Gundlach, and R. Zimmerman, *Physica* **268 C**, 26 (1996).
- [15] P. Dieleman, T.M. Klapwijk, J.R. Gao, and H van de Stadt, *IEEE Trans. Appl. Supercond.* **7**, 2566 (1997).
- [16] N.B. Dubash, G. Pance, and M.J. Wengler, *IEEE Trans. Microwave Theory Tech.* **42**, 715 (1994).
- [17] N. van der Post, E.T. Peters, I.K. Yanson, and J.M. van Ruitenbeek, *Phys. Rev. Lett.* **73**, 2611 (1994) and N. van der Post, Ph.D. Thesis, University of Leiden, 1997.
- [18] The transmission value of 0.2 agrees with the value obtained in Ref. [9] when the difference in definition of the transmission is taken into account.
- [19] M.J.M. de Jong and C.W.J. Beenakker, *Phys. Rev. B* **49**, 16070 (1994).
- [20] W.C. Danchi and E.C. Sutton, *J. Appl. Phys.* **60**, 3967 (1986).

LOW NOISE FIXED TUNED 490 GHZ SIS MIXERS MADE OF EPOXY RESIN

M. Sahr, D. Hottgenroth, S. Haas, K. Jacobs, C. E. Honingh

Abstract:

We developed a method to make identical copies of a master mixer block, using a simple molding technique [1]. A 490 GHz copper mixer block with a fixed backshort [2] was used as the molding form. The structures with critical dimensions in the mixerblock, the waveguide cavity and the substrate channel, are copied into a silicone negative. An epoxy resin is used to mold these structures from the negative. The resin is placed as an inlet in a copper block. After sputtering a 1 μm gold layer onto the resin, we thicken this layer to 3 μm using a standard galvanic gold bath. Both the silicone and the resin show detailed reproduction of the original mixer block down to 1 μm dimensions. Experiments show that the copper block with the gold plated epoxy inlet stands multiple cooling to 4.2 K. The thermal conductivity of the resin proves to be sufficient for cooling SIS junctions. We achieve receiver noise temperatures of about 110 K DSB in the frequency range of 440-500 GHz, which compares well to our results with copper mixer blocks [2]. The method presented here is a promising technique to manufacture mixer blocks for imaging array applications in submm wave astronomy.

References:

- [1] T. W. Crowe et al. Compilation of Abstracts of the 8. International Symposium on Space Terahertz Technology, March 1997
- [2] S. Haas et al. International Journal of Infrared and Millimeter Waves Vol. 17, No. 3, 1996

A low-noise, 9-element Micromachined SIS Imaging Array.

Gert de Lange, Konstantinos Konistis and Qing Hu

Department of Electrical Engineering and Computer Science
Research Laboratory of Electronics,
Massachusetts Institute of Technology, Cambridge, Massachusetts 02139.

Ray Robertazzi and David Osterman

Hypres Inc.
175 Clearbrook Rd. Elmsford, NY 10523

Results from a 3×3 micromachined millimeter-wave focal-plane imaging array with superconducting tunnel junctions as mixing elements are presented. The array operates in the 170-210 GHz frequency range. The array uses 9 μm², low impedance (3.5 – 4.5 Ω) junctions, commercially available from Hypres Inc. Integrated tuning structures are implemented to match the devices to the antenna impedance. Noise measurements show a lowest DSB noise temperatures of 52 K (@190 GHz) (for the central element). Lowest noise temperatures from the off-axis elements are in the range of 60-100 K DSB, with a uniform bandwidth of 30 GHz. Antenna beam patterns with a high Gaussian profile have been measured for on- and off-axis elements.

1 Introduction

Imaging arrays of SIS-receivers are of great benefit for the observation of spatially extended sources in astronomy, but the high cost and mechanical difficulties of building an array of waveguide mixers and the poorer beam-quality of open-structure antennas have thus far limited the efforts of actually developing such arrays [1, 2, 3, 4, 5]. SIS-mixers made with micromachined horn antennas offer a relatively easy, low cost fabrication, excellent Gaussian beam properties, and compactness, and are therefore well suited for the development of imaging arrays. Because of the specific structure of the micromachined horn antenna, interference of IF and DC-bias lines with RF antenna is avoided and also there is no limitation on the element spacing, which are problems of concern in waveguide and open structure antennas. Further advantages for the use of micromachined horn antennas in high frequency imaging arrays are the absence of substrate losses, and the possibilities of integrating a mixing element with super- or semi-conducting electronics (e.g. SQUID IF-amplifiers or Flux-Flow oscillators) [6, 7, 8]. To demonstrate the feasibility of micromachined horn antennas in imaging arrays, we have developed a 3×3 focal plane SIS imaging array for the 170-210 GHz frequency range (the choice of the frequency range is mainly determined by the availability of the Local Oscillator and the dimensions of the cryostat). In parallel we have developed two room-temperature imaging arrays with thin-film Nb as bolometers for the 70-110 GHz and 170-210 GHz frequency range [9].

Micromachined horn antennas consist of a dipole antenna fabricated on a thin ($\sim 1 \mu\text{m}$) Si_3N_4 dielectric membrane inside a pyramidal cavity etched in silicon (see Fig. 1)[10, 11]. We previously developed a single-element micromachined SIS receiver for the W-band frequency range, which showed a sensitivity comparable to the best waveguide and quasi-optical open-structure receivers [12].

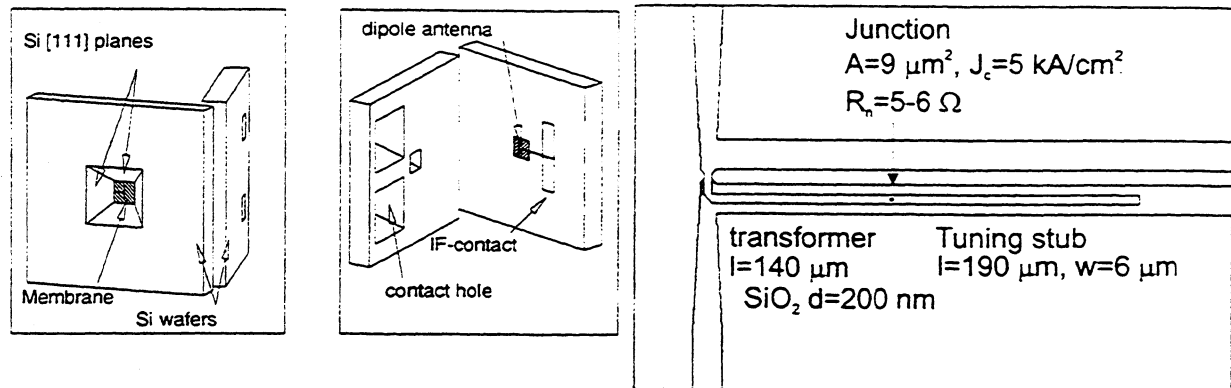


Figure 1: (a) Details of a single element of the micromachined array, showing the pyramidal cavity, the membrane, the through holes for the IF/DC connections, and the dipole antenna. (b) Details of the central region of the dipole antenna. The junction and tuning structure are located on the DC/IF coplanar bias lines.

This paper describes the design and fabrication of a 3×3 170–210 GHz imaging array receiver, and the DC and noise characterization of the array performance.

2 Receiver Design

An expanded view of the receiver and some details of the individual elements are shown in Figs. 1 and 2. A detailed description of the receiver is given in [13]

The micromachined array is made of a stack of 4 Si wafers with a total thickness of 1.7 mm. The dipole antenna on the membrane is 0.58 mm long (0.37λ). In order to have access to the contact pads on the device wafer, through holes are etched in the two wafers forming the apex of the horn (see Fig. 1a). A detailed description of the individual micromachined antenna elements and the quasi-integrated horn antenna is given in [14, 15].

A single Nb/Al₂O₃/Nb SIS junction is used as mixer element. The device has an area of $9 \mu\text{m}^2$ and a current density of 5 kA/cm^2 . The coupling of the relatively large-area and low impedance ($3.5\text{--}4.5 \Omega$) junction to the 35Ω antenna impedance is optimized by an on-chip tuning circuit, shown in Fig. 1b. The tuning circuit uses an inductive length of microstrip to tune out the junction capacitance, and a $\lambda/4$ microstrip impedance transformer to match the junction impedance to the antenna impedance. The microstrip is $6 \mu\text{m}$ wide and its characteristic impedance is 8.5Ω . Devices with a microstrip length of $190 \mu\text{m}$ for the inductive stub and $140 \mu\text{m}$ for the impedance transformer show a maximum coupling around 190 GHz, which is the center frequency of the dipole antenna.

The geometry of the machined horn section is similar to the diagonal horn described in Ref [16]. Arrays of diagonal horns can be made with a high packing density and are relatively easy to fabricate on a milling machine with a split block technique. The array is formed by a stack of six gold plated tellurium copper blocks and fabricated at MIT Lincoln Laboratory

As shown in Fig. 2, the minimum spacing of the individual elements of the array is determined by the aperture dimensions of the machined diagonal horn section. For the 200 GHz array the element spacing is 6.5 mm, which is ~ 3.5 beam waist (the $1/e^2$ beam angle of the horn is 16°). The angular separation θ_r of the parallel beams from the array, separated by a distance d , in combination with a lens or reflector of focal length f is $\approx d/f$, whereas the 3dB beam angle θ_{3dB} of a beam with input beam waist w_{in} is $0.59 w_{in}/f$. A maximum sampling of the sky requires a 3 dB beam overlap and thus $\theta_r = 2 \theta_{3dB}$ which gives an element separation of $d = 1.18 w_{in}$. Our array

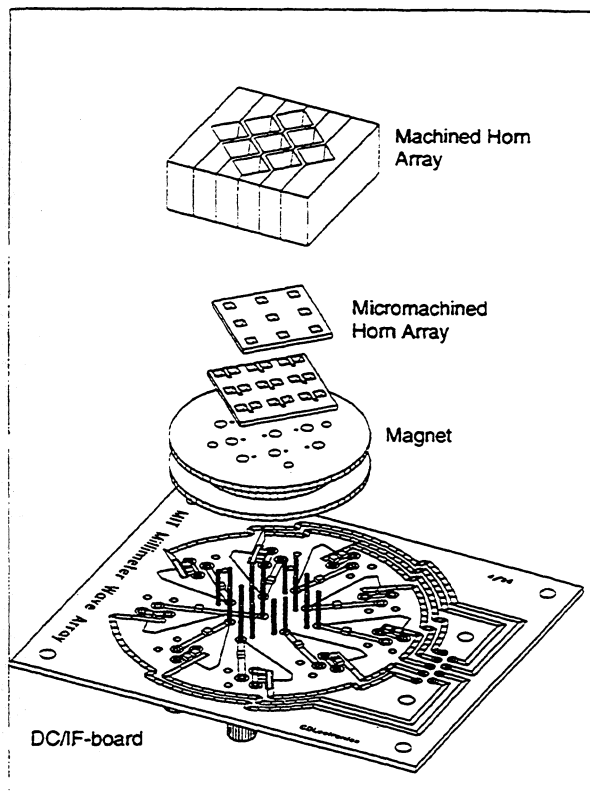


Figure 2: Expanded view of the array receiver showing the machined horn array, the micromachined array, the magnet, and the DC/IF-board

therefore undersamples the sky, as any horn array will do since the beam waist of the horn is always considerably smaller than the aperture dimensions of the horn [2]. Quasi-integrated horn antennas can be used as a feed for reflector antennas without additional lenses. Because of the limited diameter (5 cm) of the 77 K radiation filter (a 5 mm thick PTFE disk) and the dewar window (a 25 μm thick sheet of polypropylene) in the measurement set-up, a PTFE lens with a focal length of 37 mm is used in our set-up, to avoid truncation of the array beams. This lens is at 4.2 K.

A single magnet coil (made of copper) with approximately 2500 turns of superconducting 100- μm thick Nb wire (Supercon T48B) is used to suppress unwanted Josephson effects. The geometry of the micromachined array allows the magnet to be in very close proximity of the junction (~ 1.5 mm). Although the positioning of the magnet (with the magnetic field lines perpendicular to the junction surface) is not preferable, a magnet current of 200-300 mA is sufficient to suppress the Josephson effects

In order to have local access to the array elements, through holes are etched in the backing wafers. This avoids the use of long coplanar lines on the device wafer (to bring the signals to the border of the wafer) and thereby increases the available space for mixer elements, reduces possible cross-talk between different elements, and increases the flexibility of the receiver design. Contact between the array elements and the DC/IF board is made by Servometer bellow contacts (type 2510), mounted on top of a miniature screw. The screws are mounted either directly in the core of the magnet (for the ground contact) or as the center conductor of a short section of semi-rigid cable which is also mounted in the core of the magnet. This allows individual adjustment of all contacts

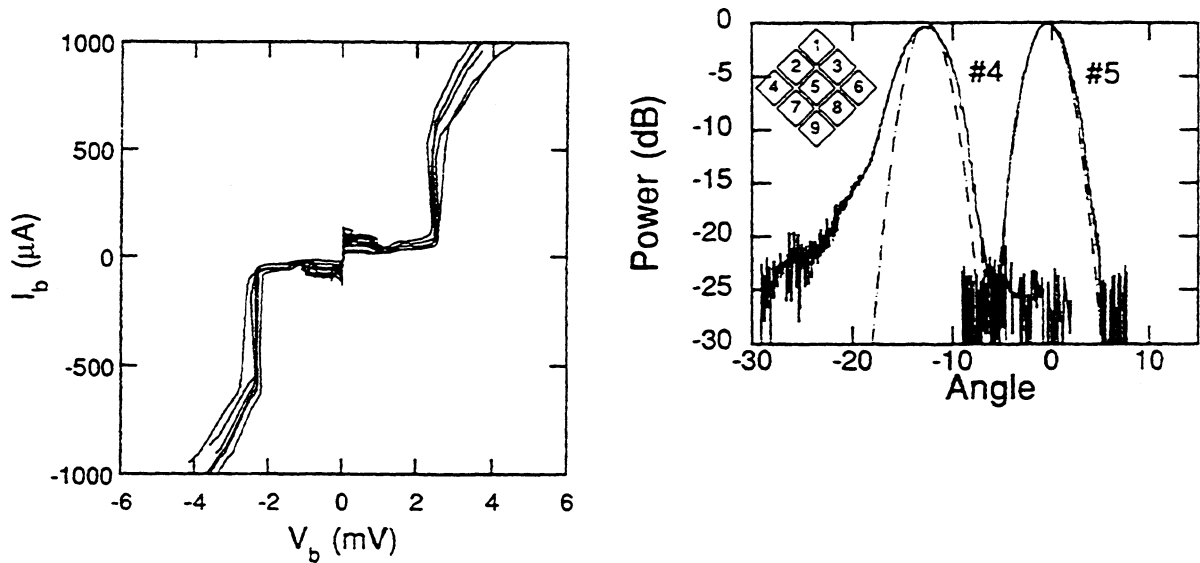


Figure 3: (a) DC I-V curve of 5 SIS devices of the 9 element array. (b) Measured antenna beam patterns for two elements on the diagonal of the imaging array. The inset shows the device numbering.

and has proven to be a reliable contact at cryogenic temperatures.

The IF/DC-board is made of Duroid 6010 material and contains a T-bias circuit for each array element. Contact between the contact screws and the IF board is made by using tight fitting sockets, soldered on the IF-board.

The array operates with a single IF-amplification stage. Noise measurements on different elements of the array are done by connecting the IF-amplifier to the different IF-ports on the DC/IF Board. The cold stage of the IF-chain consists of a Pamtech LTE 1268K isolator, and a Berkshire Technologies L-1.5-30HI IF-amplifier (40 dB). A further amplification of 60 dB is provided by room-temperature amplifiers outside the dewar. The IF-power is measured in a 35 MHz bandwidth with an HP-436A power sensor at a center frequency of 1.5 GHz (set by a tunable bandpass filter).

3 Device fabrication

The micromachined SIS arrays are made partially at Hypres and partially at MIT Lincoln Lab. The SIS devices are fabricated on 0.38 mm thick (100)-oriented silicon wafers, covered on both sides with a 1- μm thick, low-stress Si_3N_4 layer. The junctions and antennas are defined with the standard Hypres fabrication procedure. The freestanding membrane is formed by etching the silicon in a solution which contains 20% KOH by weight at 80 $^{\circ}\text{C}$ for 4-5 hours and another hour at 60 $^{\circ}\text{C}$. The last step is used to create smooth sidewalls of the aperture. The final fabrication step is the deposition by E-beam evaporation of a 400-nm Ti/Au layer on the sidewalls of the aperture through a ceramic shadow mask.

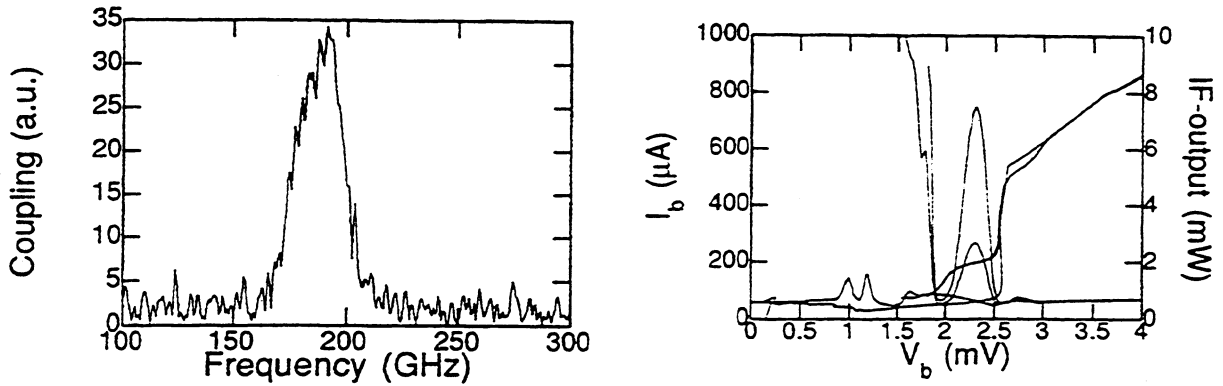


Figure 4: (a) FTS Measurement of an array element with a tuning structure as shown in Fig. 1b. (b) Pumped I-V characteristics of element #5 at a LO frequency of 190 GHz and the measured IF-output power with a 295 and 77 K input load.

4 Results

4.1 DC measurements

Results of typical DC I-V measurements of 5 SIS devices in the array are shown in Fig. 3a. The measurements are performed with the mixerblock mounted in the vacuum dewar (at a bath temperature of 4.2 K). As shown in Fig. 3a the I-V characteristics show 'back bending' at voltages above the 2.5 mV gap voltage. This is not observed if the devices are measured on a dip-stick submerged in liquid helium and therefore it indicates heating of the devices due to the poor thermal conductance of the membrane. Previous measurements with smaller ($2.5 \mu\text{m}^2$, $R = 40 \Omega$) devices did not show this heating effect. Although the back bending does not severely deteriorate the mixer performance, future designs can have an improved cooling by extending the tuning structure (with an extra length of $\lambda/2$), which will locate the devices on the solid silicon region. The device resistance ranges from 3.5 to 4.5 Ω . A drawback of SIS arrays fabricated on one single chip is the possible failure of one of the elements, which then cannot be replaced. We have measured the I-V characteristics of several arrays and always found all 9 elements operating.

4.2 Antenna Pattern Measurement

As a preliminary test of the antenna patterns of different array elements, we previously measured the 45-degree antenna patterns of two elements at a frequency of 182 GHz. The 45-degree plane antenna are obtained by measuring the video response of the elements while rotating the dewar with a rotation stage. Due to the 45 degree angle of the array with respect to the optical table, a combined co- and cross-polarisation is measured. The two elements are at the center and outermost position on the diagonal of the array, with the antenna beams parallel to the optical table. This measurement includes the cold lens inside the dewar. The measured antenna patterns are shown in Fig. 3b, together with a Gaussian beam profile. The measured radial separation of the beams is 12.5° , and the 10 dB beamwidth of the central beam is 6.8° . Calculated values (using a thin lens approximation) for the beam separation and beam width are 14.4° and 5.2° , respectively. The off-axis element has a wider beam and it has an asymmetric shoulder at -17 dB, which we attribute to aberrations caused by the lens. Previous measurements of single element quasi-integrated horn antennas [11] and single element [17] and arrays of diagonal horns with waveguide feeds [16] have shown excellent Gaussian antenna beam profiles at frequencies close to 1 THz. Recent

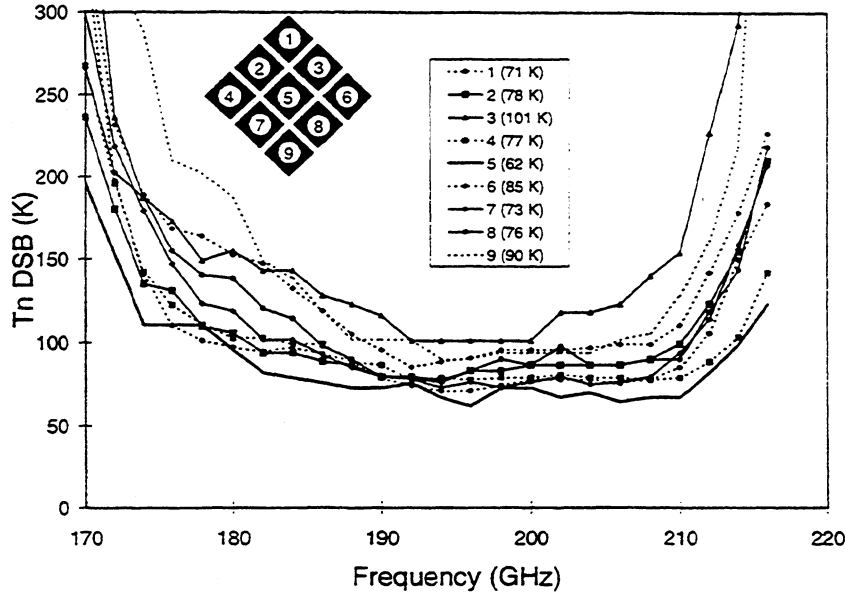


Figure 5: Measured DSB noise temperatures of the different elements in the array. The inset shows the minimum noise temperature for the individual elements.

measurements on our 95 GHz room-temperature bolometer also show excellent beam properties [18].

4.3 FTS measurements

The frequency response of the integrated tuning structures is measured with a Fourier Transform Spectrometer (FTS). The FTS uses a Hg-arc lamp as a broadband millimeter wave source, and is operated in the step-and-integrate mode. In these measurements the devices are biased at a voltage just below the gap voltage and used as a video detector. Fig. 4a shows the result of a measured frequency dependent coupling of a device with a tuning stub length of 190 μm and a transformer length of 140 μm . The calculated bandwidth for this tuning structure (assuming a frequency independent antenna impedance) is about 60 GHz. The measured bandwidth of 30 GHz is therefore limited by the 15 % bandwidth of the dipole antenna.

4.4 Noise measurements

Results of a heterodyne measurement on the central element (device # 5, see inset of Fig. 3b) of the array are shown in Fig. 4b. The signal and LO-power are combined by a 97% transmission beam splitter and the IF-power is measured in a 35 MHz bandwidth at a center frequency of 1.5 GHz. Fig. 4b shows the pumped DC I-V curve and IF-output power measured at a 190 GHz LO frequency. The minimum uncorrected receiver noise temperature is 52 K DSB, measured at a bath temperature of 2.7 K. Although the device shows some heating effects above the gap-voltage, this noise temperature is still comparable to the best results obtained in tunable waveguide mixers [19, 20, 21].

The measured noise temperatures as functions of frequency for 9 elements of another array are shown in Fig. 5. In this array the minimum noise temperature of the central element is 62 K (see the inset). The measured noise temperature of the different elements is fairly uniform, with minimum noise temperatures for 8 elements ranging from 62 to 90 K and one element with a somewhat elevated noise temperature of 101 K. The 3-dB noise bandwidth of the elements has a uniform value of around 30 GHz across the array. We contribute the differences in the noise

temperature across the array partly to the effect of the limited size of our dewar window and the need of using a rather thick lens inside the dewar. Measurements of different arrays always showed a lowest noise temperature for the central element. As shown in Fig. 4b, the lens deteriorates the off-axis beam pattern and because the 9 beams enter the dewar under different angles, it complicates the coupling of the LO and the Hot/Cold source. The LO and signal coupling is now optimized by tilting and rotating the beam splitter or the dewar. Further optimization of the optical coupling will most likely make the noise temperature across the array more uniform.

Our measurements therefore indicate the feasibility of compact, low-cost micromachined SIS focal plane imaging arrays, with competitive noise temperatures. Furthermore, the scalability of the machined and micromachined sections show the promising prospect for the use of micromachined focal plane imaging arrays for frequencies up to 1 THz.

5 Summary

We have described the design, fabrication, and testing of a SIS micromachined 3×3 focal-plane imaging array for the 170-210 GHz frequency range. Heterodyne noise measurements on the array elements showed a lowest DSB noise temperature of 52 K for a central element, with a 3-dB bandwidth of 30 GHz. The noise temperature of the off-axis elements ranges from 71 to 101 K, with a uniform bandwidth of 30 GHz.

6 Acknowledgement

We would like to thank Earle Macedo, Dan Baker, Rich Ralston, Gerry Sollner, Rick Magliocco, Lewis Tedstone, Glenn Willman and William Cummings at MIT Lincoln Laboratory for their help during the fabrication of the devices and the fabrication of the machined horn section. Richard Bradley and Anthony Kerr are acknowledged for their useful suggestions on the dewar and IF-board design. We thank Erik Duerr and Arifuh Rahman, for their useful suggestions and help during the measurements. This work was supported by the National Science Foundation under grant No. 9423608-AST, and by NASA under grant No. NAGW-4691.

References

- [1] J.M. Payne, *Multibeam Receiver for millimeter-wave radio astronomy*, Rev. Sci. Instrum. **59**, 1911 (1988).
- [2] Neal R. Erickson, Paul F. Goldsmith, G. Novak, Ronald M. Grosslein, P.J. Viscuso, Ronna B. Erickson, and C. Read Predmore, *A 15 element Focal Plane Array for 100 GHz*, IEEE Trans. on MTT **40**, 1 (1992).
- [3] Philip A. Stimson, Robert J. Dengler, Peter H. Siegel, and Henry G. LeDuc, in *Proc. of the Third Int. Symp. on Space Terahertz Techn.*, Univ. of Michigan (Univ. of Michigan, Ann Arbor, 1992), pp. 235-242.
- [4] P.F. Goldsmith, C.-T Hsieh, G.R. Huguenin, J. Kapitzky, and E.L. Moore, *Focal Plane Imaging Systems for Millimeter Wavelengths*, IEEE Trans. MTT **41**, 1664 (1993).
- [5] M.A. Scherschel, G.A. Ediss, R. Güsten, K.H. Gundlach, H. Hauschildt, C. Kasemann, A. Korn, D. Maier, and G. Schneider, in *Proceedings of the Sixth International Symposium on Space Terahertz Technology*, Caltech (Caltech, Pasadena, 1995), pp. 338-343.
- [6] John A. Wright, Svetlana Tatic-Lucic, Yu-CHong Tai, William R. McGrath, B. Bumble, and H. LeDuc, in *Proceedings of the Sixth International Symposium on Space Terahertz Technology*, Caltech (Caltech, Pasadena, 1995), pp. 387-396.
- [7] J.W. Kooi, M.S. Chan, M. Bin, Bruce Bumble, H.G. LeDuc, C.K. Walker, and T.G. Phillips, *The Development of an 850 GHz Waveguide Receiver Using Tuned SIS Junctions on 1 μm Si_3N_4 Membranes*, Int. J. of IR and MM waves **16**, 1 (1995).

- [8] S.V. Shitov, V.P. Koshelets, A.M. Baryshev, I.L. Lapitskaya, L.V. Filippenko, Th. de Graauw, H. Scaeffler, H. van de Stadt, and W. Luinge, in *Proceedings of the Sixth International Symposium on Space Terahertz Technology*, Caltech, (Caltech, Pasadena, 1995), pp. 324–337.
- [9] Arifur Rahman, Gert de Lange, and Qing Hu, *Micromachined room-temperature microbolometers for millimeter-wave detection*, Appl. Phys. Lett. **68**, 1 (1996).
- [10] G.M. Rebeiz, D.P. Kasilingam, Y. Guo, P.A. Stimpson, and D.B. Rutledge, *Monolithic millimeter-wave two-dimensional horn imaging arrays*, IEEE Trans. Antennas and Propagation **AP-38**, 1473 (1990).
- [11] G.V. Eleftheriades, W.A. Ali-Ahmad, L.P. Katehi, and G.M. Rebeiz, *Millimeter-wave integrated horn antennas: Part I: Theory*, IEEE Trans. Antennas and Propagation **AP-39**, 1575 (1991).
- [12] Gert de Lange, Brian R. Jacobson, and Qing Hu, *A low-noise micromachined millimeter wave heterodyne mixer with Nb superconducting tunnel junctions*, Appl. Phys. Lett. **68**, 1862 (1996).
- [13] G. de Lange, Qing Hu, Howard Huang and Arthur Lichtenberger in *Proc. of the Eighth Int. Symp. on Space Terahertz Techn.*, Harvard University (Harvard, Cambridge, Massachusetts, 1997), pp. 518–529
- [14] G. de Lange, B.R. Jacobson, and Qing Hu, *Micromachined millimeter-wave SIS-mixers*, IEEE Trans. Appl. Supercond. **5**, 1087 (1995).
- [15] G. de Lange, B.R. Jacobson, A. Rahman, and Qing Hu, in *Proc. of the Sixth Int. Symp. on Space Terahertz Techn.*, Caltech (Caltech, Pasadena, California, 1995), pp. 372–386.
- [16] Joakim F. Johansson and Nicholas D. Whyborn, *The diagonal horn as a sub-millimeter wave antenna*, IEEE Trans. MTT **40**, 795 (1992).
- [17] H. van de Stadt, A. Baryshev, P. Dieleman, Th. de Graauw, T.M. Klapwijk, S. Kovtonyuk, G. de Lange, I. Lapitskaya, J. Mees, R.A. Panhuyzen, G. Prokopenko, and H. Schaeffer, in *Proceedings of the Sixth International Symposium on Space Terahertz Technology*, Caltech, (Caltech, Pasadena, 1995), pp. 66–77.
- [18] Arifur Rahman, Erik Duerr, Gert de Lange, and Qing Hu, *Micromachined room-temperature microbolometers for millimeter-wave detection and focal plane imaging arrays*, submitted for the Proceedings of the SPIE's 11th International Symposium on Aerospace/Defense Sensing, Simulation, and Controls, Orlando, April 1997.
- [19] J.W. Kooi, M. Chan, T.G. Phillips, B. Bumble, and H.G. LeDuc, *A low noise 230 GHz Heterodyne Receiver Employing .25 μm^2 Area Nb/AlO_x/Nb Tunnel Junctions*, IEEE Trans. MTT **40**, 812 (1992).
- [20] J.W. Kooi, M. Chan, B. Bumble, H.G. LeDuc, P.L. Schaeffer, and T.G. Phillips, *180–425 GHz low-noise SIS waveguide receivers employing tuned Nb/AlO_x/Nb tunnel junctions*, Int. J. IR and MM Waves **15**, 783 (1994).
- [21] A.R. Kerr, S.-K. Pan, A.W. Lichtenberger, and D.M. Lea, *Progress on Tunerless SIS Mixers for the 200–300 GHz Band*, IEEE Microwave and Guided Wave Lett. **2**, 454 (1992).

RESULTS OF THE PIROG 8 BALLOON FLIGHT WITH AN EMBARKED EXPERIMENT BASED ON A 425/441 GHz SIS RECEIVER FOR O₂ SEARCH

by (alphabetical order):

A. Deschamps¹, P. Encrenaz¹, P. Febvre^{1*}, H.G. Florén², S. George¹, B. Lecomte¹, B. Ljung³, L. Nordh², G. Olofsson², L. Pagani¹, J.R. Pardo¹, I. Peron¹, M. Sjökvist³, K. Stegner³, L. Stenmark⁴, J. Tauber⁵, and C. Ullberg⁴

¹ DEMIRM - PARIS OBSERVATORY - 75014 PARIS - FRANCE - E-mail: Pascal.Febvre@univ-savoie.fr

² STOCKHOLM OBSERVATORY - S-13336 SALTSJÖBADEN - SWEDEN

³ SWEDISH SPACE CORPORATION - P.O. Box 4207 - S-17104 SOLNA - SWEDEN

⁴ ACR ELECTRONIC AB - BOX 99 - 61922 TROSA - SWEDEN

⁵ ESTEC - ASTROPHYSICS DIVISION - 2200 AG - NOORDWIJK - THE NETHERLANDS

CNES - AIRE-SUR-L'ADOUR - FRANCE

* New address: LAHC - UNIVERSITE DE SAVOIE - 73376 LE BOURGET DU LAC CEDEX - FRANCE

Abstract. The swedish-french PIROG 8 project (Pointed InfraRed Observation Gondola) has been developed in 1996/1997 in order to try to detect the presence of molecular oxygen in two molecular clouds of the interstellar medium: NGC7538 and W51. PIROG 8 consists of a 500 kg gondola carrying a 60 cm diameter Cassegrain telescope equipped with a 425/441 GHz SIS heterodyne receiver at its focus. This balloon-borne submillimeter SIS experiment successfully flew in september 1997 from the south-west of France. An overview of the technical experiment behaviour during flight is presented along with some performed measurements.

I - Introduction

The scientific goal of the PIROG 8 project (Pointed InfraRed Observation Gondola) was to observe simultaneously the O₂ line at 425 GHz and the ¹³CO line at 441 GHz in the molecular clouds of the interstellar medium by heterodyne spectrometry. The main scientific interest is to detect molecular oxygen which has never been observed in the interstellar medium so far. The theoretical models predict¹ that the line emissivity is weak: about 500 mK.km.s⁻¹ in dark molecular clouds. Consequently, it is necessary to use a sensitive receiver with a good spectral resolution. The simultaneous observation of the ¹³CO line allows to verify the correct operation of the receiver and the pointing of the telescope.

In order to be free from the Earth atmosphere, the experiment must observe at high altitude so it has been embarked on the PIROG gondola, run by

the Swedish Space Corporation, which flew 7 times in the past.

The heterodyne receiver developed for the PIROG 8 project consists of a sensitive front-end cooled at liquid helium temperature which feeds an autocorrelator spectrometer (back-end). The cryostat used to cool the receiver front-end operates at ambient pressure ($p \approx 3$ mbar at 39 km altitude) so that the SIS mixer is at a physical temperature of about 1.5 K. The cryostat has been provided by ESTEC along with the autocorrelator spectrometer. Both have been successfully used during former flights.

The PIROG 8 instrument has been developed at the Observatory of Paris between september 95 and june 96 in order to be ready for a flight initially scheduled for september 96 and postponed to may 97. This delay has allowed some additional tests to be performed on the instrument: in particular some tests of the receiver behaviour in the real low-pressure environment (measurements of cryostat hold time, receiver noise temperature and of physical temperature profiles of most sub-systems) have been made during winter 96 at the Observatory of Paris. The integration of the instrument on the PIROG 8 gondola took place in march 97 in Trosa (Sweden) at the ACR facility where the gondola was designed and built. Final integration including control of the receiver by the PIROG ground station has been made at the CNES balloon base in Aire-sur-l'Adour (France) during april and early may 97. Payload check and flight simulations procedures have been defined and tested during the same period. The flight, planned in may 97 has been delayed to september 97 due to bad weather conditions and balloon-flight safety regulations. Payload check procedures and flight simulations have been fine-tuned in early september

and the flight occurred on september 25th, 1997. The flight duration was 11 hours from take-off to cut-down with more than 8 hours at the ceiling altitude of about 39.5 km.

II - Technical features of the PIROG heterodyne SIS instrument

II.1. General design

The PIROG 8 receiver is based on the technology of SIS mixers. The mixer block² uses a reduced-height waveguide and has an integrated Potter horn³. It is sensitive to signals of horizontal polarization at frequencies of 425 and 441 GHz on an instantaneous bandwidth of 320 MHz. The SIS mixer uses one mechanical contacting backshort which has been fixed after proper optimization in the laboratory. It is cooled in a cryostat at liquid helium temperature, along with the HEMT amplifier placed at the mixer output. The cryostat has one helium tank of about 2 liters and one intermediate thermal shield, at a physical temperature of ≈ 20 K, screens the helium tank from external thermal radiations. A block diagram of the receiver is shown in figure 1.

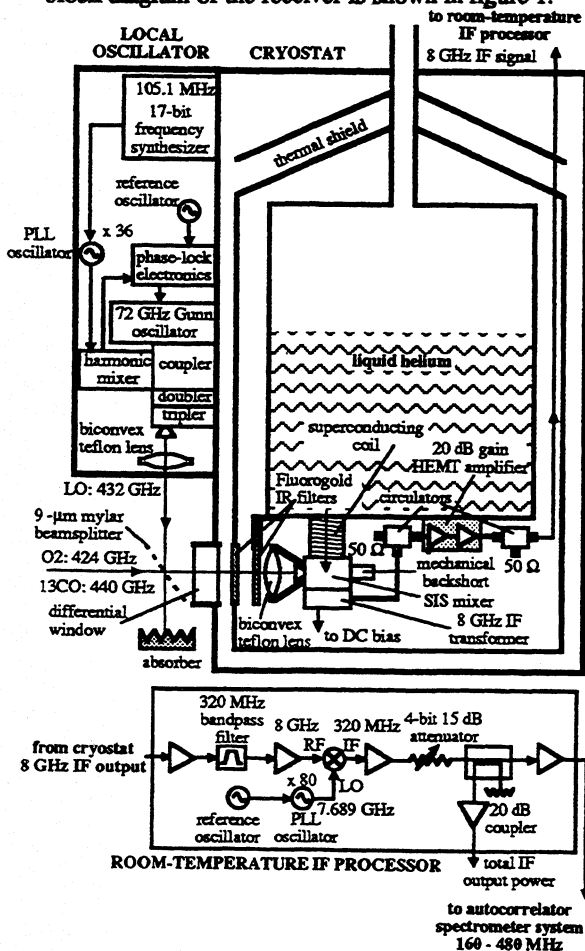


Fig. 1: General block diagram of the PIROG 8 receiver

The signal coming from the secondary mirror of the 60 cm Cassegrain telescope is directly injected in the cryostat through a quartz window with an antireflexion coating. Then it meets a biconvex teflon lens cooled at liquid helium temperature which couples the secondary mirror with the mixer horn. The quasi-optical coupling has been calculated so that the beam-waist is located in the plane of the cryostat window in order to reduce the window size and increase the hold time of the cryostat. Two one-wavelength-thick ($450 \mu\text{m}$) infrared filters made with fluorogold are installed on the beam path to prevent infrared radiations from heating the mixer. The first one is installed on the intermediate thermal shield at about 20K, the second one is directly fixed in front of the lens and mixer on the stage at liquid helium temperature. A beamsplitter, made with a $9\text{-}\mu\text{m}$ -thick mylar sheet, is located at room-temperature in front of the cryostat window to allow the coupling of a few % of the local oscillator (LO) power in the cryostat. The remaining LO power is absorbed by a submillimeter absorber.

II.2. Controlled phase-locked Local Oscillator

The local oscillator consists of a Gunn oscillator at 72 GHz stabilized in frequency by a dedicated electronics with a phase-lock loop. The frequency of the Gunn output signal is multiplied by 6 by a doubler followed by a frequency tripler² in order to generate a few hundreds μW around 433 GHz. The center frequency of the Gunn oscillator is electrically controlled as follows: a 17-bit frequency synthesizer, centered at about 105.3 MHz, tunable from the ground, drives a PLL oscillator at about 3.8 GHz ($\times 36$). The PLL oscillator output signal is injected with a tiny fraction of the Gunn signal in an harmonic mixer. The signal at the intermediate frequency of the harmonic mixer is generated at about 100 MHz by mixing the Gunn signal with the 19th harmonic of the PLL oscillator signal. It is compared with a reference oscillator at 100 MHz by a dedicated electronics which reacts on the Gunn voltage. The phase-lock electronics works over a 600 MHz bandwidth centered at the LO frequency of 433 GHz. This frequency allows the simultaneous detection in the double side-band mode of the O_2 line at 425 GHz and the ^{13}CO line at 441 GHz with a receiver intermediate frequency of 8 GHz. The local oscillator power is also tunable from the ground through the bias voltage of the whisker-contacted varactor diode of the frequency doubler. The local oscillator with its phase-lock electronics is installed on a plate directly fixed on the cryostat in order to simplify and ease the quasi-optical coupling. Moreover, this allows to make the receiver quite compact which is necessary for a balloon-borne experiment where constraints in mass and volume are strong (see figure 1).

II.3. SIS mixer and SIS junction

The mixer uses a $2 \mu\text{m}^2$ round-shaped superconducting tunnel junction made in Nb/Al- Al_2O_3 /Nb⁴. This junction has a high current density (about 13 kA/cm^2) which corresponds to an $\omega R_N C$ product of 6 at 433 GHz and eases the coupling of the junction with its microwave environment. The associated normal resistance is $R_N = 12 \Omega$. Moreover, the subgap leakage current is low: the leakage resistance at 2 mV is $R_{sg} = 150 \Omega$, which corresponds to a ratio $R_{sg}/R_N = 12.5$ and a factor of merit $V_m = 35$.

A tuning circuit⁵, using niobium superconducting electrodes, is integrated to the junction in order to resonate out, at the frequency of operation, the high intrinsic capacitance of the junction estimated⁶ to $95 \text{ fF}/\mu\text{m}^2$. The tuning circuit is made of a microstrip line terminated by a 90-degree radial stub and provides, at the frequency of operation, an inductance in parallel with the SIS junction to compensate for its capacitance (see figure 2). The SIS junction, with its integrated tuning circuit, has been fabricated with a low-pass microstrip filter which propagates the mixer output signal at the intermediate frequency of 8 GHz but rejects the mixer input signals at 425, 433 and 441 GHz. All these elements are deposited on a quartz substrate polished at a thickness of $50 \mu\text{m}$ and diced at the final dimension of $200 \mu\text{m}$ by 2 mm. The substrate is installed transversally in the waveguide of dimensions 120 by $700 \mu\text{m}$.

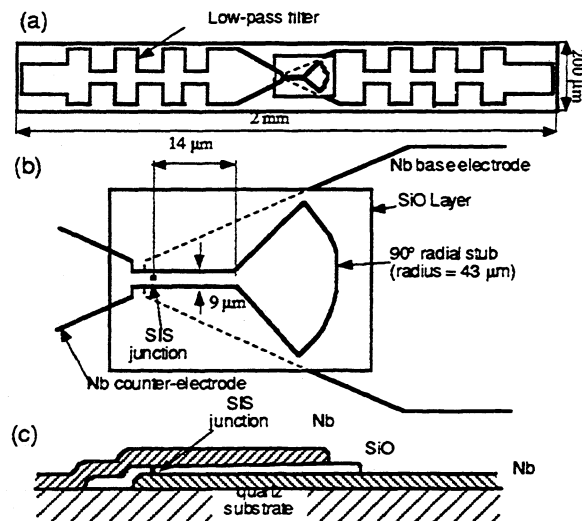


Fig. 2: SIS tunnel junction with an integrated parallel microstrip tuning circuit and low-pass filter. a) general view showing quartz substrate, low-pass filter, SIS junction and tuning circuit. b) Top view showing tuning circuit dimensions. c) Cross section view showing film topology.

The low-pass filter, connected at one end to the mixer ground, is wire-bonded to the input of an

impedance transformer at the intermediate frequency. The transformer is realized in microstrip technology on a 1.27 mm-thick Duroïd substrate (relative dielectric constant = 10.2), it is used to transform the mixer output impedance to 50Ω . It also allows the SIS junction to be DC biased.

On the other hand, a Helmholtz coil, made with niobium-titane superconducting wire, is able to produce a tunable magnetic field in the plane of the SIS junction (up to 1000 Gauss). This is in order to suppress the Josephson currents which add some noise and create instabilities on the receiver. The magnetic field is also tunable from the ground.

II.4. SIS junction fabrication process

The SIS junction has been fabricated⁴ by sputtering a trilayer of Nb/Al- Al_2O_3 /Nb on a fused quartz substrate. The thickness of the niobium electrodes is about 2000 \AA . Then, the low-pass filter is shaped by Reactive Ion Etching of the trilayer in a plasma of SF_6 . In a third step, the shape of the junction is defined by photolithography and etched by Reactive Ion Etching in a plasma of SF_6 and O_2 . Two gold pads are deposited by evaporation on the ends of the low-pass filter in order to ensure good electrical contacts with the mixer. Then, a 2000 \AA -thick SiO layer is evaporated so that the junction perimeter is electrically insulated, this layer is also used as a dielectric for the integrated tuning circuit of the junction. At last, a niobium counter-electrode, which connects the top electrode of the junction to the low-pass filter, is sputtered. This counter-electrode is also used as the top electrode of the integrated tuning circuit.

II.5. Processing of the mixer output signal

The signal coming out of the impedance transformer at the intermediate frequency is amplified by about 20 dB by a low-noise two-stage cryogenic HEMT amplifier located on the cold stage of the cryostat (at the temperature of liquid helium). The average noise temperature of the amplifier is 9 K over a 320 MHz bandwidth centered at 8 GHz. The output signal of the amplifier propagates through a coaxial cable out of the cryostat and is amplified at room-temperature, filtered over a 500 MHz bandwidth and down-converted to the center frequency of the spectrometer, which is 320 MHz. The room-temperature amplification is tunable from the ground from 55 to 70 dB by steps of 1 dB in order to obtain an output level of about -7 dBm, which is the optimal level for the autocorrelator. A telemeasurement of the total output power is also made to control the correct behaviour of the receiver from the ground during the flight and to determine the beam pattern with moon measurements.

II.6. Control electronics

A specific control electronics has been developed to interface the receiver with the gondola electronics. It consists of 5 boards which allow on one hand to telecommand the different modules of the receiver: SIS junction bias voltage, superconducting coil current, HEMT amplifier status (on/off), gain of the room-temperature chain at the intermediate frequency and gain and frequency of the local oscillator.

On the other hand, some telemeasurements are made through this electronics: current and voltage of the SIS junction, total output power, control of the state (on or off) of every module and check of the local oscillator phase-lock status. A portable computer allows to telecommand and control the status of the receiver during the flight.

II.7. Autocorrelator spectrometer

The spectrometer used was an autocorrelator of the hybrid type, and was developed and built at Onsala Space Observatory in Gothenburg for the Astrophysics Division of the European Space Agency. "Hybrid" refers to the fact that the IF band is initially split into several subbands by a set of downconversions using tunable local oscillators. Each subband is then fed to an autocorrelator based on the chip developed⁷ by the Netherlands Foundation for Research in Astronomy (NFRA). The maximum bandwidth of the IF is 320 MHz in the range 160-480 MHz; the user may select configurations with bandwidths of 20, 40, 80, 160 and 320 MHz, covered by either 200 or 400 channels. The spectrometer is built into a vessel pressurized with nitrogen gas at 0.5 bar, and cooled by a circulating liquid system. Its mass is around 9 kg, and it consumes about 120 W at peak power. It is controlled by telemetry commands from a dedicated PC (on the ground), which also processes the data from the level of lags up to that of a spectrum.

II.8. Thermal control

Several temperature sensors have been fixed on different subsystems of the receiver to monitor receiver components during flight. Two heating resistors have been installed in order to warm up the receiver if necessary during the balloon ascent when air temperature drops below -50°C .

II.9. Power, volume and mass budgets

The total receiver consumption has been measured to be about 45 watts, the receiver mass, excluding spectrometer, was lower than 28 kg. The front-end is 60 cm high x 23 cm x 30 cm and the electronics boxes overall volume is 19 cm x 18 cm x 18 cm.

III. Ground measurements

III.1. Noise temperature & cryostat hold time

The cryostat hold time has been measured on the ground ($T_{\text{helium}} = 4.2 \text{ K}$) and was about 20 hours with receiver off and longer than 14 hours with receiver on. A 180 K DSB receiver noise has been measured using the Y-factor technique between room and liquid nitrogen temperatures (see figure 3).

At a helium temperature of 1.5 K, obtained on the ground by pumping on the cryostat helium tank to simulate an external pressure of about 3 mbar, the cryostat hold time was longer than 11.5 hours with ≈ 8.5 hours at ceiling. The best measured DSB receiver noise temperature was 130 K in the laboratory.

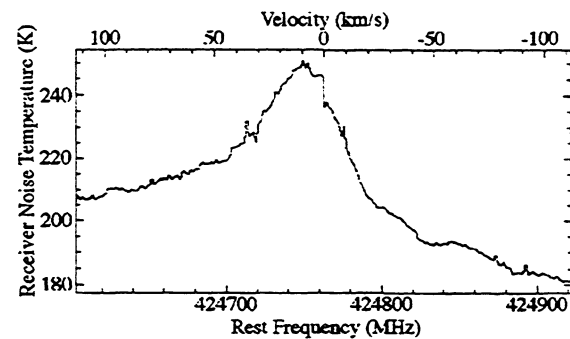


Fig. 3: DSB receiver noise temperature versus lower sideband frequency at 4.2 K helium temperature.

Remark: the variation of the receiver noise temperature in the useful bandwidth, seen in fig. 3, is due to an unfortunate resonance in the impedance transformer at the intermediate frequency, which appears only at low physical temperatures. This does not pose any problem during operation since the lines to observe are located "in the edges" of the bandwidth and take advantage of the lowest receiver noise.

A DSB receiver noise temperature of about 270 K has been measured on the ground before flight. And a noise temperature of about 200 K DSB was expected during flight from the measurements at low pressure (≈ 3 mbars) performed in the laboratory.

Note: The increase of the receiver noise temperature (from about 180 K to 270 K) has been observed in the end of 1996 and is likely due to some slight change of the mixer backshort position caused by repeated thermal cycles between 4 K and room-temperature.

III.2. Sideband ratio

Measurements in the laboratory have shown that the average resonance frequency of the SIS junction with its microwave environment (at which the mixer is supposed to better work) is about

400 GHz, i.e. lower than the normal 433 GHz center frequency of operation.

Some measurements of DC I-V curves pumped at frequencies in the lower and upper mixer sidebands have been performed. The I-V curves have been compared with theoretical predictions based on Tucker's theory in order to determine the mixer gain in each sideband. It appeared that the sensitivity of the mixer is better in the lower side-band where the weak O₂ signal is supposed to be seen. But the sideband gain ratio could not be determined accurately and has been estimated to be between 0.5 dB to 3 dB (gain ratio between 1.1 and 2).

III.3. In-flight calibration setup

A hot and cold load calibration setup has been installed between the telescope and the cryostat to calibrate the receiver in flight. The "cold" load is at ambient temperature and the "hot" load is heated at about 70 °C by a resistor fixed on its backside. Both are made of a submillimeter absorber and can be inserted in the beam path any time during the flight. The low temperature difference (≤ 50 K) between the two loads did not allow us to make accurate noise calibrations but was sufficient to verify the correct behaviour of the receiver. Moreover, ground calibrations showed that the measured hot load temperature had to be decreased by 12 K to account for the "real" receiver noise temperature (measured more accurately with a 77 K liquid nitrogen and a 300 K room temperature set of loads and always used in the past to calibrate the receiver).

III.4. Influence of Josephson currents

One of the main problems encountered with SIS mixers is the presence of Josephson currents⁸ in the SIS junction. Also, they depend on the magnetic flux trapped inside the junction. The phenomenon of flux trapping is random and can be provoked by electromagnetic or electrical perturbations. When Josephson currents are present in the junction, some additional Josephson noise add to the receiver noise and some instabilities in the output signal make the operation difficult or impossible. Usually, a magnetic field is applied in the plane of the junction in order to suppress the Josephson currents and make the receiver less noisy and more stable. Nevertheless, the currents reappear randomly and the magnetic field needs to be reajusted, which is done on ground or airborne receivers by the operator. In our case, for a balloon-borne experiment, or for some future space applications, this problem becomes overwhelming since there is no operator aboard. It becomes necessary to fully understand the interaction of Josephson currents with the quasiparticle mixing in order to suppress them in a safe way. Consequently, PIROG 8 is a good test bed for such an objective.

Figure 4 displays unpumped and pumped I-V

curves along with DSB receiver noise temperature versus the SIS junction bias voltage at 4.2 K physical temperature.

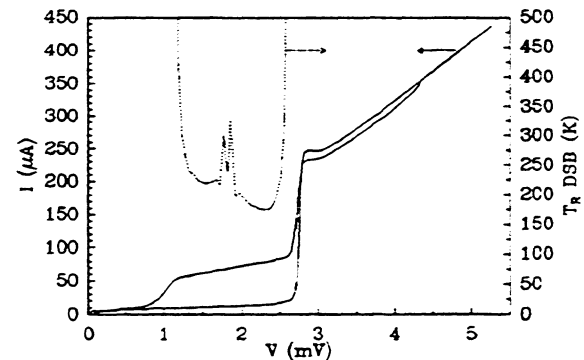


Fig. 4: Unpumped and pumped I-V curves and DSB receiver noise temperature versus bias voltage

Though the Josephson currents have been suppressed the best we could by applying the proper magnetic field of about 250 Gauss, one clearly sees that the noise is higher by about 100 K around 1.8 mV. Moreover, the receiver is unstable around this voltage which corresponds to the second Shapiro step at 433 GHz. It turns out that, at 433 GHz, the optimum voltage for lowest receiver noise temperature is about 2.3 mV, i.e. not too close to the Shapiro step. Consequently, the presence of Josephson currents does not hurt too much the operation of the receiver for this particular bias voltage and we observed a very good stability with low receiver noise for more than 8 hours in the laboratory. Nevertheless, the stability depends on the perturbations around the receiver and may be different during the flight due to the different receiver environment (motors, RF transceivers on the gondola, ...)

III.5. Problems with telemetry

Full experiment has exhibited correct behaviour on the ground EXCEPT in presence of real TeleMetry antenna which caused a big perturbation on the front-end and the back-end. Front-end was unstable and could not be operated properly. A few tests with microwave absorbers close to the antenna and with gondola outside the building lead to the conclusion that the receiver should work at ceiling due to the absence of TM power reflected on the experiment.

III.6. Telescope alignment and attitude control

The telescope was aligned with the two TV cameras (a fixed one with a 2° field of view and a movable one with a 0.5° field of view) using a laser and remote light sources. The radioastronomical (RA) focus ('waist') of the telescope was defined using the

optical focus as a reference and then relying on the calculated difference. The optical/radio alignment of the telescope was done using a 30 cm collimator. The set-up was not fully satisfactory and the alignment was judged to be within 2 arcminutes. The RA beam was measured using the 30 cm collimator and it was in agreement with expectations - basically determined by the small size of the collimator (it was planned to use the 1m collimator at Toulouse, but it was occupied by ODIN). The angular position of the sun sensor relative to the telescope was measured using a theodolite. The software and hardware controlling the azimuth position of the gondola were checked by daytime "observations" of Polaris. The elevation software and hardware were checked by guiding on a star for a couple of hours. The gondola reference horizontal plane deviates from the true one, and two inclinometers are used to measure this deviation. The software is constructed to take care of this effect and this was confirmed by looking at a double star, while tilting the gondola.

IV - Test procedures

Some payload check procedures have been defined during the integration period to verify the correct operation of the receiver, including backend. Some specific routines have been implemented in the software which controls the front-end PC: calibration routines, routines to digitize I-V curves of SIS junctions, routines to use the frequency switch observation mode.

Receiver noise calibrations were performed both by the autocorrelator PC, using power levels measured by the correlator, and the front-end PC, measuring the total output power versus hot and cold loads. Also, a cold against sky calibration routine has been implemented.

Payload check procedures have been defined to verify the correct receiver operation at different frequencies of interest and for different resolutions and bandwidths of the autocorrelator: mainly for observation of O_2 for all scheduled astronomical sources, for observation of ozone lines in order to calibrate the mixer sideband gain ratio, and with frequency offset for sky dip.

Also, routines for frequency switch and position switch modes of observation have been implemented. Several flight simulations have been performed to verify the correct operation of the entire experiment including ground control station and "human interfaces".

V - PIROG 8 flight

V.1. General considerations

The preparations before launch went smoothly, but due to a delay we decided to refill the

cryostat in order not to run out of helium in case of a long-duration flight. The launch was smooth.

The duration of the flight was unexpectedly long, leaving 8 hours of observation at ceiling. But, because of repeated TM drop-outs caused by the long distance between gondola and ground base in the end of the flight, the last hour of observations at altitude was essentially lost.

Launch occurred at 5:38 am on september 25th, 1997 from Aire-sur-l'Adour, ceiling was reached at about 8:30 am. Cut-down was decided by CNES at 4:48 pm. Gondola landed in the trees in Massif Central 45 mn after cut-down and was brought back to the base the day after in fairly good conditions.

V.2. Receiver behaviour in flight

The cryostat stayed cold up to the end of the flight. It started to warm up during the descent after cut-down of the balloon. The hold time, higher than 11.5 hours, was a little longer than expected and just enough not to shorten the long flight.

The receiver, front-end and back-end, behaved very well during the entire flight and the fact that it was fully remote-controlled was totally unharmed during the whole flight. Nevertheless a few problems have been observed, fortunately they caused only very minor troubles. First, there has been a few unexpected total power shut-down of the receiver on the ground pad (gondola on batteries) before launch, during the ascent and during the flight when an I-V curve was being digitized. The origin of the shut-down is not known so far but it seems to be correlated with a big number of commands sent to the receiver in a row. Hopefully, the receiver was powered again every time with no damage for the SIS junction.

An expected failure of the phase-lock loop of the synthesized local oscillator happened during the ascent during 1 hour and 40 mn between 10 km altitude (6:20 am local time) and 31 km altitude (08:00 am local time). The outside air temperature was between -40°C and -60°C . The outer shield of the gondola went down to -50°C and the local oscillator plate, which was heated during the ascent, went down to 0°C . The phase-lock stopped functioning below $+8^{\circ}\text{C}$ at 10 km altitude and worked again when it reached $+7^{\circ}\text{C}$ at 31 km altitude. Consequently, the phase-locked system behaved better than expected and made the operation of the receiver possible before reaching ceiling. Figures 5 and 6 show the general temperature variations during flight for different parts of the receiver and gondola. In particular, one can see in figure 6 that heating of the Local Oscillator base plate during ascent has been quite helpful in preventing the phase-lock electronics from cooling down below 0°C , which could have harmed the receiver operation at the beginning of the observations.

At last, the total output power value at the intermediate frequency was corrupted during the same period, very likely by a malfunction of the associated ambient temperature electronics (different gain for operational amplifiers, etc...). It recovered at about 08:15 am local time, again before reaching ceiling.

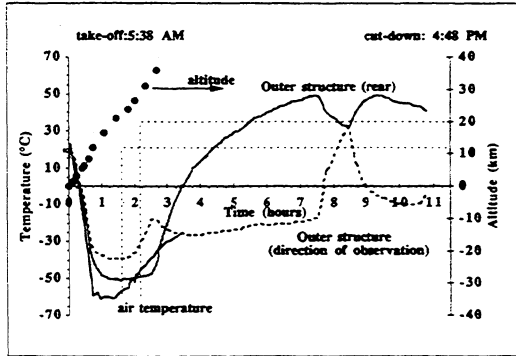


Fig. 5: Temperature variations on different gondola places and altitude profile during PIROG 8 flight.

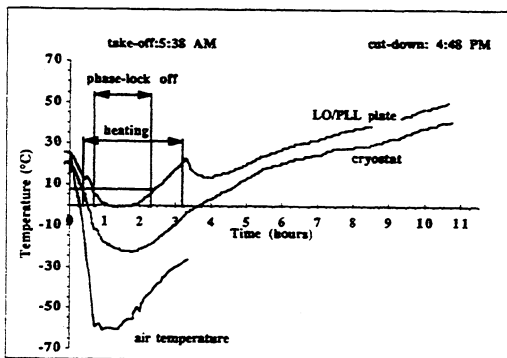


Fig. 6: Temperature variations of receiver components during PIROG 8 flight.

V.3. Stabilizing at altitude

The azimuth stability was achieved as planned and a bright star was quickly found. However, a pendulum motion - not seen in previous flights - was noted. As the inclinometers were useless to trace this motion it could not be compensated for by the control system. We had just to wait for a slow decline. Post-flight analysis with statistical methods of the fine pointing phase shows that pointing was achieved with a RMS value of 0.4 arcminute.

V.4. Alignment

Once the gondola was stabilized, the guide camera was confirmed to be aligned with the fixed camera.

V.5. In-flight receiver calibration

Calibration in flight between sky and ambient calibration load showed that T_r (DSB) was about 295 K. The system DSB noise temperature (including the telescope) was about 500 K. The receiver noise temperature, higher than expected, is likely due to the presence of additional Josephson currents which were hard to suppress. Also, one pumped I-V curve has been digitized at ceiling, it shows that there is a low frequency noise on the SIS junction which smooths the I-V curve non-linearity, hence reducing the performance of the mixer (see figures 7 and 8). Moreover, this noise, which is likely due to the TM power emitted by the antenna and reflected on the gondola structure, may increase the influence of the remaining Josephson currents and, then, contribute to the lower mixer sensitivity. We had to increase the magnetic field in the plane of the SIS junction to about 500 Gauss during flight, to be compared to 250 Gauss on the ground.

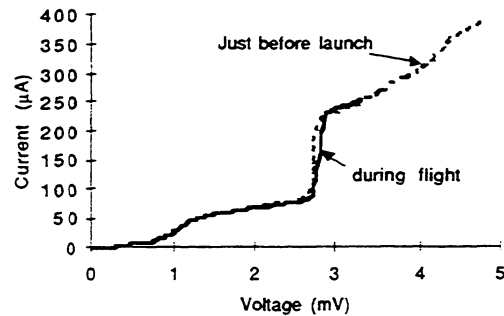


Fig. 7: Experimental pumped I-V curves digitized on ground and during flight.

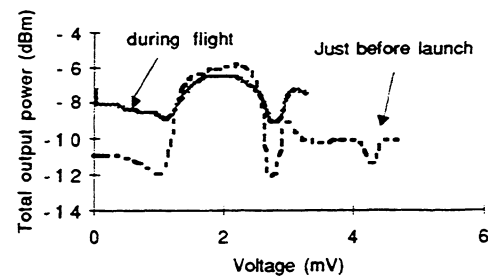


Fig. 8: Experimental output power versus bias voltage curves digitized on ground and during flight. Smoothing of I-V curve is clearly seen. It resulted in degraded performance of the SIS mixer.

V.6. Dip scan.

As planned, the atmospheric emission was measured at a few different elevations. The expected lines were seen, verifying the frequency calibration of the receiver. The dip scan confirms that there is no continuous atmospheric extinction, which means that the low elevation of our main target (down to 18

degrees) does not imply any additional damping of the signal to that given by the telluric O₂ line wing.

V.7. Ozone line fit

Another way of measuring the sideband gain ratio in order to improve the accuracy obtained by laboratory measurements has been suggested⁹. It is based on the observation of two atmospheric ozone lines, one in each sideband, for which emission temperatures are known (or at least for which the ratio of their emission temperatures is known). It turns out that the tunability of the local oscillator allows the observations of two ozone lines, respectively centered at about 425.16 and 441.34 GHz. With this technique, the sideband ratio has been estimated to range between 1.2 and 1.25 which is a big improvement compared to the 1.1-2 range obtained in the laboratory. A fit of observations of measured ozone lines at ceiling with theoretical models based on different sideband ratios is shown in figure 9.

```

3292: 4 OZONE 03(425+441) PIROG8 C9 SX 0: 25-SEP-1997 R: 4-MAR-1999
RA: 00:00:00.000 DEC: 00:00:00.00 (1850.0) Off: 0.0 0.0 E:
Unknown Tau: 0.0000E+00 Tays: 12.00 Time: 8.1237E-02 El: 34.59
N: 400 I0: 200.5 VD: -45.84 Dv: 5640 LSR
FD: 425222.775 DF: -.8000 FI: 441240.775

```

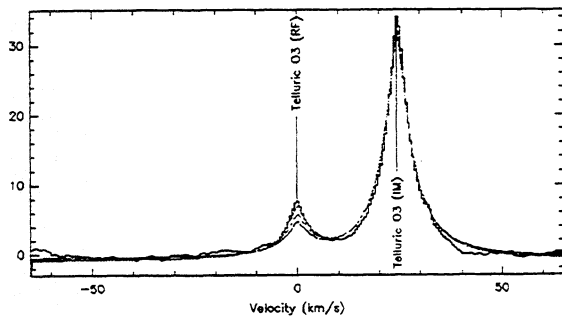


Fig. 9: Experimental spectrum obtained with PIROG 8 receiver at ceiling altitude. Three theoretical fits with different LSB/USB sideband ratios (0.8, 1 and 1.25) are also shown (dashed lines). Best fit is for LSB/USB gain ratio of 1.25

In fact, when the Local Oscillator is tuned to observe the two ozone lines, the ratio is in the range 1.2-1.25 but, once the receiver is tuned at the O₂ frequency, the sideband ratio seems to change but we have no direct evidence of this (no O₃ line in the upper sideband). Indeed, we need a ratio of 1 to explain the telluric O₂ line intensity. The discrepancy may come from the ATM model being not precise enough, from the receiver behaviour itself or from some other reason we could have overlooked. Thus, the overall uncertainty is between 1 and 1.25. It is not due to the method but on the way we can interpret the results in this particular case.

V.8. Calibrations on the moon.

The purpose of the moon observation was to determine the beam efficiency, the beam profile and if possible, to confirm the alignment of radio/optical beams. For some reason - not yet identified - it took a while to find the moon and then in order to gain time, the planned step-by-step scan across the moon was replaced by a few continuous scans, leaving the optical/radio correlation for the post-analysis. The total output power at the intermediate frequency of the receiver has been measured versus moon position. In order to relate the observations with a model, the brightness temperature variation (at 0.7 mm wavelength) across the moon has been derived and convolved with a gaussian beam with a width of 5 arcminutes. The observed data agrees very well with the observations (see figure 10).

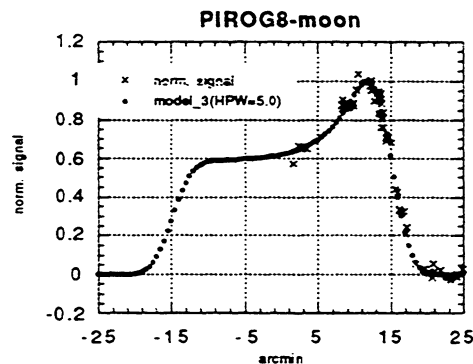


Fig. 10: Experimental and theoretical data of normalized brightness temperature of the moon versus moon position. Data agrees very well with observations.

From this observation, it is also possible to derive the main beam efficiency. If one assumes that the brightness temperature of the hot load is 12 K less than the measured one (as was found on the ground) one calculates a main beam efficiency equal to 0.42. This is slightly lower than our goal (0.6), but in view of our crude ways to align and focus the system, it is not bad. The most probable reason for the low efficiency is that the secondary mirror is a bit over-illuminated (half of the integrated beam from the receiver passing the edge of the mirror). This is in fact not so bad as the sky is transparent and one only sees the cosmic background outside the mirror. This would also mean a slightly lower tapering than usual (10 dB at the edge), which in turn would give a slightly worse side-lobe situation.

VI - Astronomical observations

Two sources have been observed: NGC7538 and W51. A map of the 441 GHz 4-3 13CO line of NGC7538 in the upper sideband has been made. Molecular oxygen has not been detected. Observations will be detailed elsewhere.

Some attempts to observe W51 have been made in the end of the flight but, because of repeated TM drop-outs, the observations were essentially lost. We could, however, confirm the presence of the 13CO line (brighter than in the case of NGC7538), and it may become possible to recover something from the analog recordings of the TM data.

VII. Conclusion

The SIS heterodyne receiver developed for the PIROG 8 balloon project is the first fully remote-controlled submillimeter SIS receiver to have successfully flown on a balloon gondola. It behaved very well during the flight (except for 1 hour and 40 mn during the ascent), which is above expectations. The receiver noise temperature was slightly degraded compared to what was expected from measurements performed on the ground (≈ 300 K instead of 200 K DSB). Some investigations are necessary to safely assess the real causes of this degradation but they seem to be partly due to low-frequency noise in the SIS mixer generated by the TeleMetry antenna.

Project organization - Acknowledgements. PIROG 8 has been developed in the frame of a swedish-french collaboration between the Observatory of Stockholm (PI: Lennart Nordh, Instrument Scientist: Göran Olofsson) and the Observatory of Paris (coPI: Pierre Encrenaz, Instrument Scientist: Laurent Pagani). The project has been managed by Bo Ljung from the Swedish Space Corporation (SSC). The SIS instrument development has been managed by P. Feuvre from Paris Observatory. The swedish company ACR was in charge of the gondola and of the interfaces with the receiver. The french space agency (CNES) was in charge of the flight campaign. The Observatory of Paris has developed the instrument with some contributions of the Observatory of Stockholm. The receiver development has been funded by CNES (2/3) and by SSC (1/3). We are very grateful to S. Lebourg and F. Pelletier from Meudon Observatory for their decisive contribution by micromachining the most sensitive parts of this receiver. We also wish to thank J.P. Ayache, V. Thévenet, P. Barroso, J.M. Munier, A. Maestrini and G. Santarelli, from Paris Observatory, for the technical support that they brought to the development of the receiver. Also, we are very grateful to Philippe Goy: indeed, the determination of the sideband ratio in the laboratory has been made possible by using a tunable local oscillator of AB Millimètre.

References

- ¹ P. Maréchal, Y.P. Viala, and J.J. Benayoun, *Astronomy and Astrophysics*, vol. 324, pp. 221-236, 1997.
- ² Made by Radiometer Physics, Bergerwiesenstraße 15, 5309 Meckenheim, Germany.
- ³ H.M. Pickett, J.C. Hardy, J. Farhoomand, *IEEE Trans. Microwave Theory Tech.*, vol. MTT-32, pp. 936, 1984.

⁴ P. Feautrier, M. Hanus and P. Feuvre, *Supercond. Sci. Technol.*, vol. 5, pp. 564-568, 1992.

⁵ P. Feuvre, C. Boutez, S. George and G. Beaudin, *Proceedings of the International Conference on Millimeter and Submillimeter Waves and Applications II*, vol. SPIE 2558, pp. 136-147, San Diego Convention Center, 9-14 July 1995.

⁶ P. Feuvre, W.R. McGrath, P. Batelaan, B. Bumble, H.G. LeDuc, S. George, P. Feautrier, *International Journal of Infrared and Millimeter Waves*, vol. 15, no. 6, pp. 943-965, June 1994.

⁷ A. Bos, "The NFRA correlator chip", *NFRA ITR* 176, 1986.

⁸ B.D. Josephson, *Phys. Lett.*, vol. 1, pp.251-253, July 1962.

⁹ Jose Cernicharo (private communication).

RECENT PROGRESS ON THE SUPERCONDUCTING IMAGING RECEIVER AT 500 GHz

Sergey V. Shitov¹⁾, Andrey B. Ermakov¹⁾, Lyudmila V. Filippenko¹⁾, Valery P. Koshelets²⁾,
Willem Luinge²⁾, Andrey M. Baryshev²⁾, Jian-Rong Gao^{2),3)},
and Petri Lehtikoinen⁴⁾.

¹⁾Institute of Radio Engineering and Electronics, Russian Academy of Sciences, Mokhovaya 11, Moscow 103907, Russia. ²⁾Space Research Organization of the Netherlands, P.O. Box 800, 9700 AV Groningen, the Netherlands. ³⁾Department of Applied Physics and Materials Science Center, University of Groningen, Nijenborgh 4, 9747 AG Groningen, the Netherlands. ⁴⁾Helsinki University of Technology, Radio Laboratory, Otakaari 5A, FIN 02150 Espoo, Finland.

New integrated receiver chips with a superconducting FFO on a Si substrate are designed in order to match silicon optics. A solution for the problem of spatial mismatch between the silicon-immersed double-dipole antenna and the SiO₂-based microstrip tuning circuit is found and tested experimentally. A number of single mixer pixels for the imaging array receiver are fabricated and tested. Preliminary results of a balanced SIS mixer are given. The integrated lens antenna was tested with a reference SIS mixer showing sidelobes at approximately -17.5 dB and a DSB receiver noise temperature $T_{RX} = 130$ K. A $T_{RX} = 200 - 300$ K and $110 - 150$ K is obtained at 480-520 GHz for the single and balanced mixers respectively using the internal LO. A prototype of the FFO shield was tested with the magnet of 1000 Gauss. A computer system "IRTECON" is developed based on LabWindows for precise computer control of the chip device and the receiver complete characterization.

Introduction

A low-noise imaging array receiver (IAR) for the radio astronomy or monitoring of the atmosphere pollution is of general interest since it may save observation time and most of related technical and financial resources. IAR may contain pixels based on the Superconducting Integrated Receiver (SIR) chip which consists of a low-noise planar antenna SIS mixer and a flux-flow oscillator (FFO) as a local oscillator [1, 2]. This concept of chip-size, light-weight and low-power consuming SIR is very attractive for most imaging applications because dense packaging of such chips is possible. The independent control of each pixel seems to be an advantageous feature either for optimization of LO power or for multi-frequency operation of the array receiver.

We present here results of the experimental study of recently developed SIR device intended for a nine-pixel IAR [2] with silicon optics. The goal of the study is to demonstrate that each pair of pixels can work at about 500 GHz independently and equally good. The detailed study of the phase-lock (or frequency-lock) loops [3] for the integrated LO is the last option that has to be accomplished for the practicable receiver.

A few problems were found in going from quartz to the silicon substrate. The design principles developed for SIR on a silicon substrate/lens are discussed below. The main optical cryostat with a large (array) input window is being assembled. Test data reported

here were obtained with a special single-pixel assembly cryostat.

I. Design of New Silicon Device

The simplified electrical diagram of the new SIR on silicon and a photograph of the chip are shown in Fig. 1 and Fig. 2 respectively.

a) Antireflection coated optics

Each pixel of IAR has its own elliptical silicon lens ($R_1 = 5$ mm, $R_2 = 5.228$ mm). This lens has to be the only optical element providing a beam $f/10$ at 450 - 550 GHz [4, 5]. The silicon lenses with antireflection (AR) coating from Stycast epoxy have been fabricated by diamond turning. Two epoxy compounds art. 2850 FT and art. 1264 were tested for the AR-coating using FTS technique. We have found for a number of different tests that AR-coating made from epoxy 2850 FT has 5.2 instead of 4 reported in [6]. Extra absorption was also suspected because of unspecified carbon filler in this epoxy. The AR-coating of 87 m fits the requirements [7] for epoxy 1264 (2.9). However, the data reported here were measured only for the lenses with the 75 m AR-coating from 2850 FT epoxy.

b) Antenna mixer

We continue with the concept of a quasi-optical double-dipole antenna SIS mixer [1, 2, 4]. This kind of integrated lens antenna must have a back reflector installed at the quarter-wave distance to achieve the

¹⁾ e-mail: sergey@hitech.cplire.ru, sergey@sron.rug.nl

beam of good symmetry. The back reflector is a silicon chip (800 μ m \times 800 μ m, thickness 44 μ m) which is one-side covered with a film of Nb/Au. To install the back reflector onto the SIR chip, a tiny drop of the vacuum oil was used. A double-dipole antenna with the back reflector could be treated as a four-dipole array immersed into a homogeneous silicon medium ($\epsilon_r = 11.7$). Center of the antenna array has to be placed in the focus of the elliptical lens. Because of homogeneity of the medium surrounding the antennas, one may hope that the relatively simple analytical formulas developed for a thick wire dipole antenna are accurate enough to estimate the main properties of the real device. The beam inside the silicon media was estimated analytically taking into account the mutual interference of all four antennas. The calculated main lobe was found to be consistent with the results obtained via the method of moments. Since the microstrip feeders connecting the antennas may somewhat change the impedance of the dipoles, the experimental samples are designed with three slightly different lengths of their antenna (84 μ m, 92 μ m and 100 μ m).

c) SIS mixer tuning

To achieve a low noise performance of the receiver, the mixing SIS junction has to be tuned to cancel its capacitance. A modified concept of the end-loaded stub is used in the tuning structure. The mixing junction can be treated as a shared load placed in the center of a microstrip line half-way from two antennas. Each half of the microstrip feeder is acting as an inductive tuner which cancels capacitance of the half-junction at the specified frequency of about 500 GHz.

The insulation film of SiO₂ ($\epsilon_r = 3.8$) is currently used that defines an optimal length of the tuning lines as 260 μ m while the optimal distance between the antennas is 235 μ m ($\epsilon_r = 11.7$). Unlike a double-slot antenna [8], it seems not possible to bend the tuning lines freely in the space available between two dipole antennas. This problem was solved by tuning each dipole antenna with an additional capacitive tuner (Fig. 1 and Fig. 3). To make length of the complete tuning structure as short as possible, thinner insulation of 150 nm is used for the tuners instead of 250 nm for the rest of the chip circuitry. The same tuning microstrip is used for supplying the magnetic field to the junction. A strip of narrower width can give a stronger magnetic field in the vicinity of the junction. The width of 3 μ m is chosen

for the tuning strip because of the limited mask alignment accuracy. A fabrication misalignment not more than 0.5/1 μ m is desired/allowed for the proper operation of the device. A microphotograph of the double-dipole antenna SIS mixer is shown in Fig. 3.

d) LO power coupling

To couple the LO power from FFO with an estimated output impedance of about 0.4 Ω [1, 2], the two-stage impedance transformer has been synthesized empirically as a stair-type microstrip connection. The SiO₂ insulation of 150 nm is used for the widest section of the transformer. The LO power is supplied from FFO to the mixing junction via a microstrip transmission line of about 900 μ m long and 4 μ m wide. The characteristic impedance of the line is about 14 Ω . A dc/IF break in both leads [9] is inserted at about half-way between the LO and the mixer (Fig. 1 and Fig. 2).

To couple the LO power from FFO to the mixing junction, a microstrip T-connection working similar to a cold beamsplitter is implemented. The LO port is presented by a 1 μ m wide strip which acts as a section of a quarter-wave transformer providing high impedance of the LO path ($Z_0 = 60 \Omega$) in parallel to the mixing SIS junction. The impedance of the LO port allows about 20-30 % of the signal to be lost.

To avoid the signal loss, the concept of a balanced SIS mixer have been developed [2]. The balanced device can use 100 % of both signal and LO power that may result in the lower noise temperature of the receiver.

II. Single Pixel Test Unit

A special unit is developed to test each pixel for the array separately (Fig. 4). The SIR chip device (4 mm \times 4 mm \times 0.5 mm) is centered within an accuracy of 10 μ m and then glued to the lens at the corners with soft epoxy art. 2216 from "3M". All electrical contacts are provided by the wire bonding (Al wire 50 μ m) to a printed circuit board which presses the lens down against a cold metal frame. The pentagonal frame of the pixel is mounted on a copper "leg" which is holding the chip far enough from the opening of the shielding can. The shield of the test unit is made similar to one described in [2], but smaller in size. The shield and the "leg" are thermally isolated from each other having independent heat contacts to the bottom of the liquid helium bath. The external layer of the shield is bent from -metal; internal one is made from copper galvanically covered with 100 μ m layer of lead. Both the internal superconducting shield and the chip can be heated independently above their superconducting transition temperature point to remove trapped magnetic flux. All wiring of the chip (including IF cable) is made through the same and only opening of the shielding can.

III. Experimental Data and Discussion

a) Magnetic shield test

A shield around the integrated receiver chip is necessary because any current or magnetic field noise

influences the LO frequency of integrated FFO. The magnetic shield (Fig. 4) was tested qualitatively by placing a magnet with strength 1000 Gauss near the cryostat window at the distance of 5 cm from the opening of the shield. The effect of about 4 V shift of the FFO bias point has been measured that is equal to the LO frequency shift 2 GHz. This effect can be compensated by the FFO control line current of approximately 50 A that in terms of magnetic field means a suppression factor of $10^3 - 10^4$. As a consequence the flux trapping only seldom occurred for the experimental chips.

b) SIS mixer control line test

It is known that superconducting strips of a few microns most efficiently generate a local magnetic field. However, it has been found experimentally that for the Nb film of 3 m wide and 0.6 m thick, the critical current can be reduced to about 10 mA due to the non-rectangular (diffused) profile of the film fringe. To get the rectangular profile of the fringe, the fabrication procedure for the wiring layer has been improved. Third minimum of $I_c(H)$ is achievable now with the control line current of 80 - 100 mA for 1 - 2 m^2 junction.

c) FTS test

To learn about the instantaneous bandwidth, a FTS test is performed for each SIR chip assembled into the cryostat. The preliminary dipstick test does also show a frequency response of the SIS mixer since the internal FFO is emitting approximately equal *rf* power within the 450 - 650 GHz frequency range [9]. However, this estimate is usually a bit higher than one made in the cryostat because the installation of the backing reflector is decreasing the antenna resonant frequency 15 - 20 GHz. The FTS experiments have demonstrated the central frequency of the new silicon SIRs within 490 - 520 GHz and the instantaneous bandwidth of 70 GHz and 90 GHz for the single and balanced mixers respectively that agrees well with the design values.

d) Antenna beam test

The typical antenna beam pattern of the new silicon SIR is shown in Fig. 5. The SIS mixer was operating in the video-detection mode that limits the dynamic range to 25 - 30 dB. Taking into account the radiation pattern of the 2 mm aperture used to obtain the wide-angle illuminating, the following data are obtained for the SIR chip H7341 at 490 GHz: the sidelobe level of about -16 dB, the full 3 dB beamwidth of about 3.7 and the full 10 dB beamwidth of about 6.7. The first minima in the radiation pattern occurs approximately at 4.5. This corresponds roughly to a $f/9.4$ beam with a waist size w_0 3.6 mm.

The antenna beam of a reference SIS mixer *without* LO path was similar, indicating that LO circuitry has

a minor effect. The choke filters are connected now to the capacitive tuners at more distant position that may reduce the distortion of the antenna beam pattern. To minimize the space occupied by the choke filters without reducing their quality, the high-impedance section is designed as a coplanar two-wire line while the low-impedance sections are made as overlaps (microstrip line) that provides desirable discontinuity (variation) of impedance. The antenna beam had a gaussian profile with sidelobes at the level of about -17.5 dB that is close to the theoretical prediction [5]. The receiver DSB noise temperature measured for the reference SIS mixer is about 130 - 140 K at 490 - 495 GHz (corrected to the 20 m Mylar beamsplitter). The goal of the study is to achieve the same noise temperature with the complete Integrated Receiver.

IV. "IRTECON" System for Data Acquisition and Receiver Control

The experimental study of the Integrated Receiver devices was started with manually controlled bias supply comprising four floating *dc* sources adjusted separately (Fig. 1). It took hours even for the short *dc* check. A data acquisition system called IRTECON was developed for the Integrated Receiver Test and Control (Fig. 6). It collects *dc* and *rf* data automatically. The program is written under LabWindows. Two computer cards from "National Instruments" are used: 16 bit resolution card for FFO and 12 bit resolution card for the SIS mixer. The GPIB interface for SR510 lock-in amplifier, 4 DAC and 10 ADC are used in the system to hookup the analogue bias supply and HP436 power meter to the computer. The complete test run takes now about 45 minutes per device including mounting into dipstick and printing the selected data-graphs (Fig. 7).

One of the routines does optimization of magnetic field for the FFO and the best bias for the SIS mixer providing minimum of the receiver noise temperature, T_{RX} , at particular frequency, f_{LO} , related to the FFO voltage, V_{FFO} , with the Josephson's relationship

$$f_{LO} = 2eV_{FFO}/h.$$

Here e and h are the charge of electron and Planck's constant respectively.

The LO power supplied to the SIS mixer is varied via FFO bias current while the LO frequency is kept constant being adjusted via magnetic field (control current of the FFO). The Y-factor is measured at IF 1.5 GHz with a fast *rf* detector, lock-in amplifier and running "hot/cold" chopper. Since the traces of T_{RX} versus mixer bias are *not* usually crossing each other, the lowest noise figure always belongs to the lowest curve. It means that optimum pump level can be found using any bias voltage, V_{SIS} , within the range of about 1-2.5 mV. The data on the receiver

DSB noise temperature at the level of 250 K optimized by IRTECON are presented in Fig. 8. For the balanced SIS mixer [2] a noise temperature of 110 - 150 K at 515 GHz has been measured recently.

Conclusion

The performance of the Superconducting Integrated Receiver (SIR) with a silicon lens/substrate has been demonstrated as following: center frequency is about 500 GHz, instantaneous bandwidth 15 %, DSB receiver noise temperature 200 - 250 K at the center frequency, the antenna beam $f/10$ with sidelobes below - 16 dB.

The shielding of FFO was tested and found to be sufficient at the magnetic field about 1000 Gauss.

Recent results of a balanced SIS mixer [2] are promising: T_{RX} 110-150 K at 515 GHz and instantaneous bandwidth 20 % (FTS data).

The system IRTECON is proven to be a useful tool in selection and operation of Superconducting Integrated Receiver.

Acknowledgment

Authors thank M. J. M. van der Vorst for calculating the optimal parameters for our double-dipole antenna, J. Evers for testing the Stycast coatings and D. van Nguyen for mounting samples.

The work was supported in parts by Russian Program for basic Research, the Russian State Scientific Program "Superconductivity", and ESA TRP contract No. 11653/95/NL/PB/SC.

References:

[1] V. P. Koshelets, S. V. Shitov, L. V. Filippenko and A. M. Baryshev, H. Golstein, T. de Graauw, W. Luinge, H. Schaeffer, H. v.d. Stadt. *First Implementation of a Superconducting Integrated Receiver at 450 GHz*, Appl. Phys. Lett. **68** (9), pp. 1273-1275 (February 1996).

[2] S. V. Shitov, V. P. Koshelets, A. M. Baryshev, L. V. Filippenko, J.- R. Gao, H. Golstein, Th. de Graauw, W. Luinge, H. van de Stadt, N. D. Whyborn, P. Lehtokainen. *Study of a quasioptical superconducting integrated receivers for imaging applications at 400-700 GHz*. Proc. of 8th Int. Symp. on Space Terahertz Technology. Harvard Univ., Cambridge, MA, pp. 281-290 (March 1997).

[3] V. P. Koshelets, S. V. Shitov, A. V. Shchukin, L. V. Filippenko, J. Mygind, A. V. Ustinov. *Self-pumping effects and radiation linewidth of Josephson flux-flow oscillators*. Phys. Rev. B, **56**, No. 9, pp. 5572-5577 (September 1997).

[4] A. Skalare, Th. de Graauw and H. van de Stadt. *A planar dipole array antenna with an elliptical lens*. Microwave and Optical Technology Letters, vol. 4, pp. 9-12, 1991.

[5] M. J. M. van der Vorst. *Design and Analysis of integrated lens antennas*, Graduation report, Fac. of Electrical Engin., Eindhoven Univ. of Tech., 1995.

[6] J. Zmuidzinas, N. G. Ugras, D. Miller, M. Gaidis, H. G. LeDuc, J. A. Stern. *Low-Noise Slot Antenna SIS Mixers*. IEEE Trans. on Appl. Superconductivity, vol. 5, No. 2, p. 3053, June 1995.

[7] M. J. M. van der Vorst, P. J. I. de Maagt and M. H. A. J. Herben, *Matching layers for integrated lens antennas*, Proc. of the Int. Symp. on Antennas, (JINA '96), pp. 511-515, 1996, Nice, France.

[8] J. Zmuidzinas, and H. G. LeDuc, *Quasi-optical slot antenna SIS mixers*, IEEE Trans. on Microwave Theory and Tech., vol. 40, pp. 1797-1804, 1992.

[9] S. V. Shitov, V. P. Koshelets, A. V. Shchukin, A. M. Baryshev, I. L. Lapitskaya, L. V. Filippenko, Th. de Graauw, J. Mees, H. Schaeffer, H. van de Stadt. *Experimental Study of a Superconducting Integrated Receiver at Submillimeter Wavelengths*. Digest of 19th Int. Conf. on Infrared and Millimeter Waves, Report M7.11, pp. 122-123, Sendai, Japan, (October 17-20, 1994).

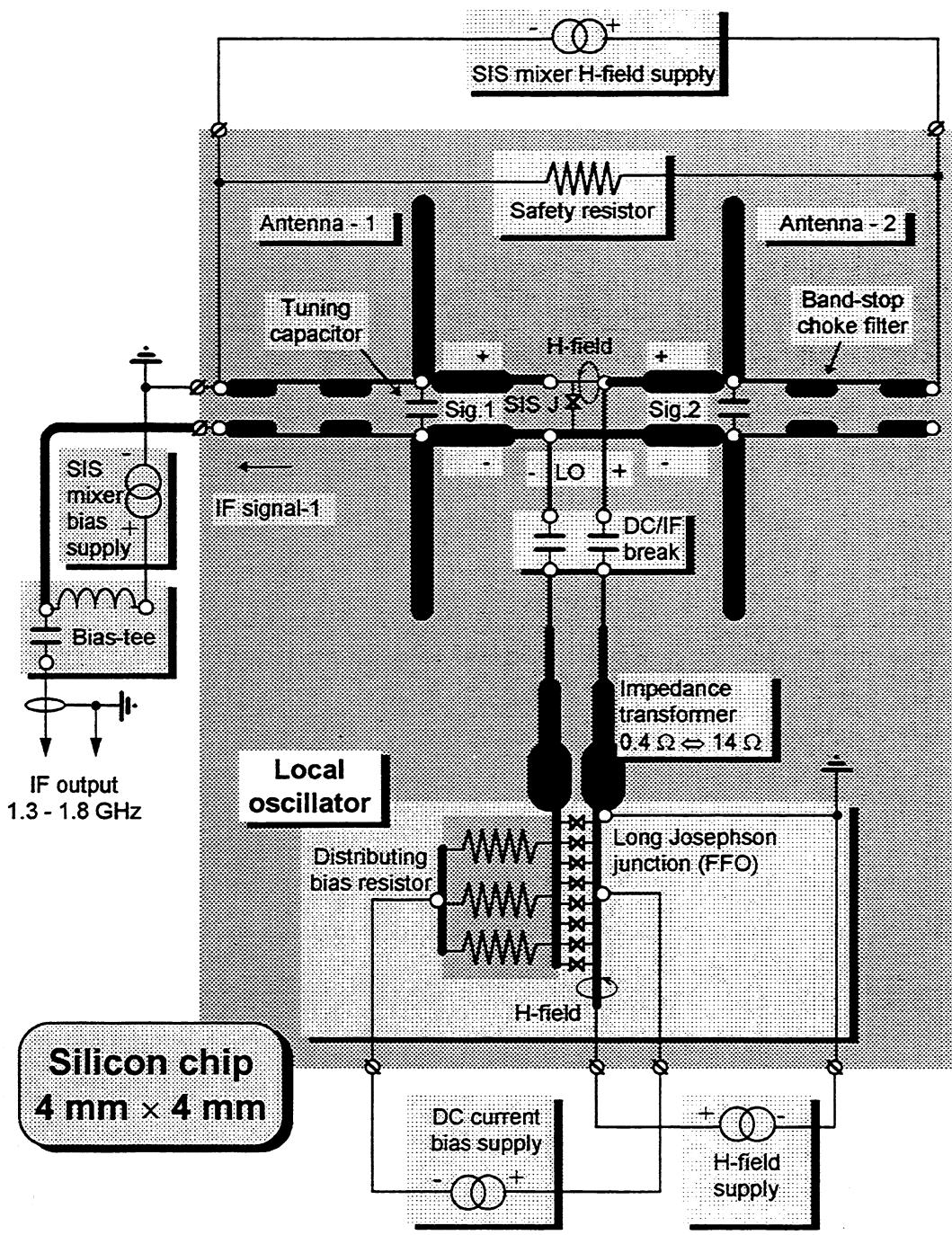


Fig. 1. Simplified equivalent diagram of the single mixer Integrated Receiver chip for 500 GHz; SISJ presents the mixing junction. Typical power consumption of the chip is defined mainly by FFO and estimated as 20 - 40 μW.

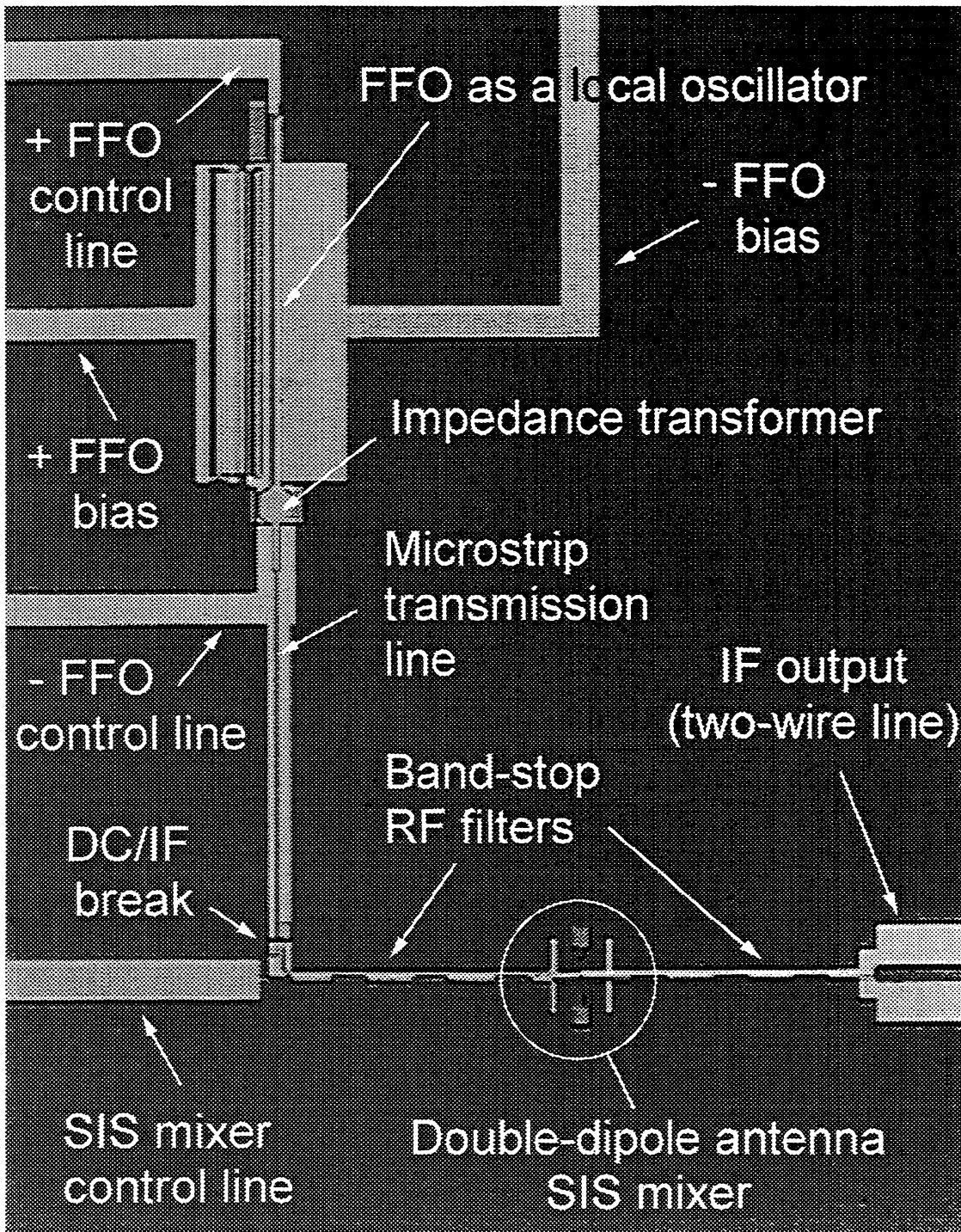


Fig. 2. Microphotograph of central part of the silicon Integrated Receiver chip; all main elements presented; the backing reflector is not installed; some details of wiring and contact pads are out of the field of view which is about 1 mm × 1.5 mm.

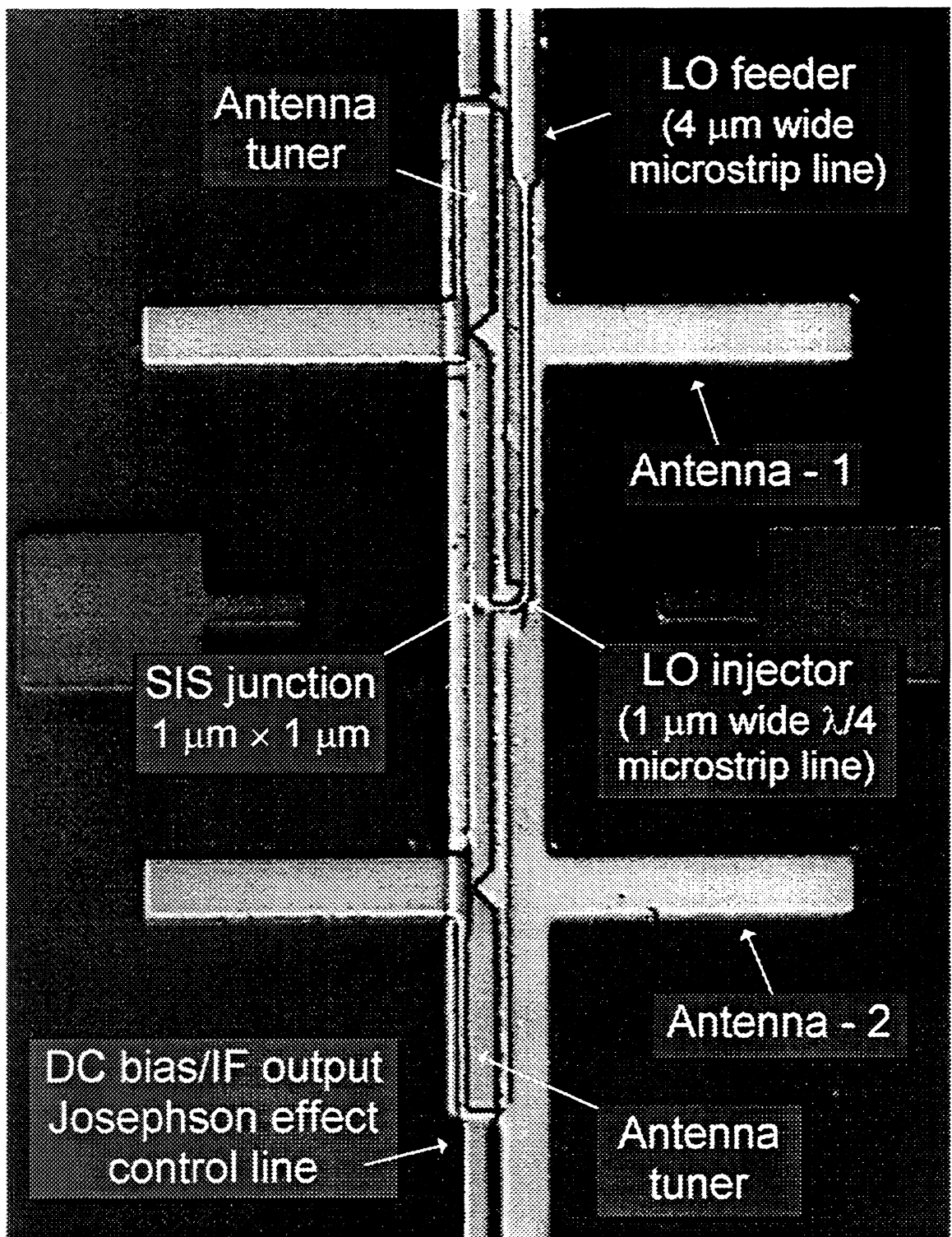


Fig. 3. Microphotograph of the double-dipole antenna SIS mixer of the Integrated Receiver; both antennas are tuned by special microstrip tuners; the local oscillator feed is shown. Complete field of view is about 100 μm × 150 μm.

Shield section A - A

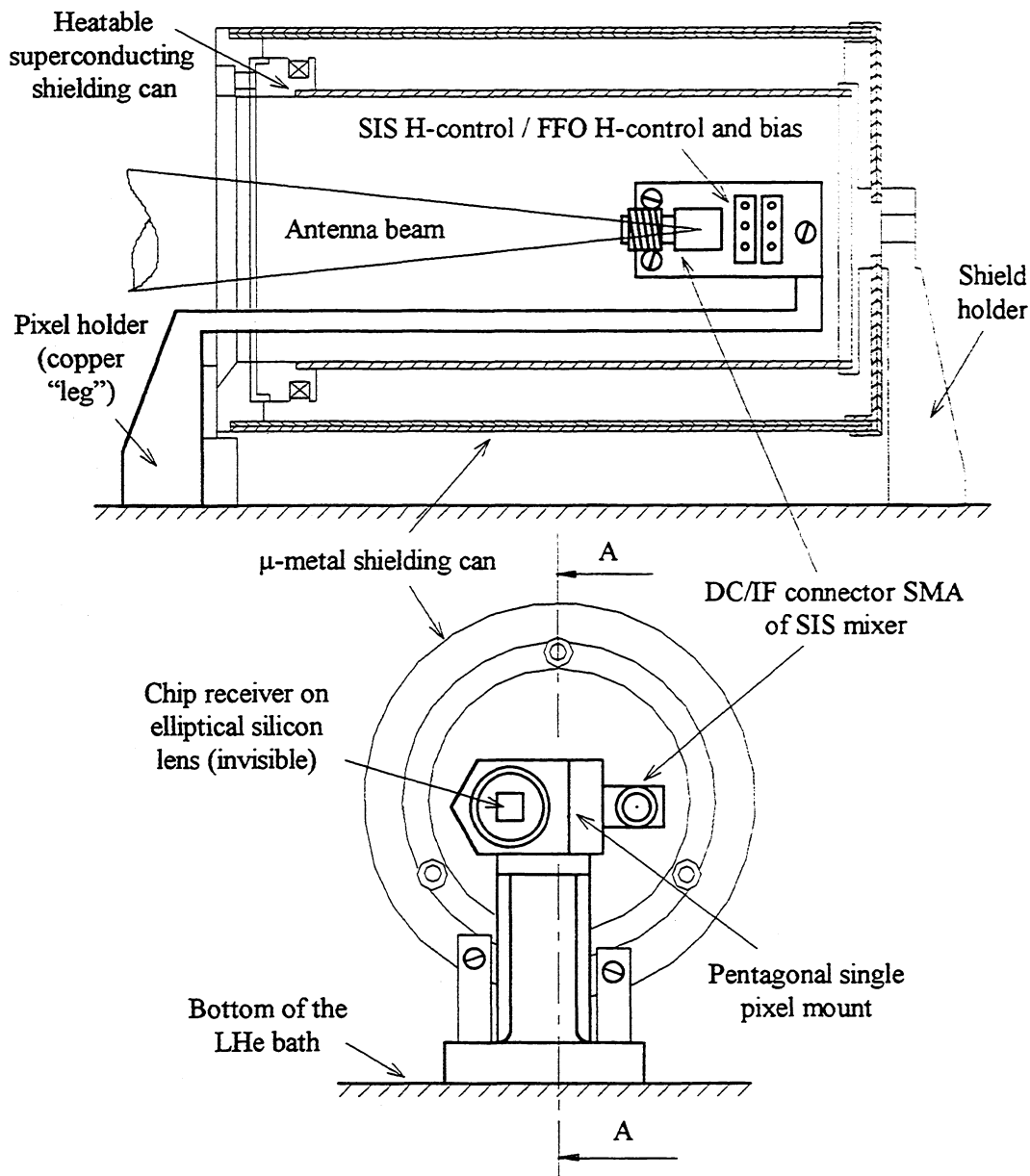


Fig. 4. Schematic drawing of the test mount for single pixel measurement. Note that the optical axis of the silicon lens is not centered in respect to the shielding can. This configuration should simulate the antenna beam conditions for a side pixel of the array receiver. Coaxial IF cable and bias wiring are not shown for simplicity.

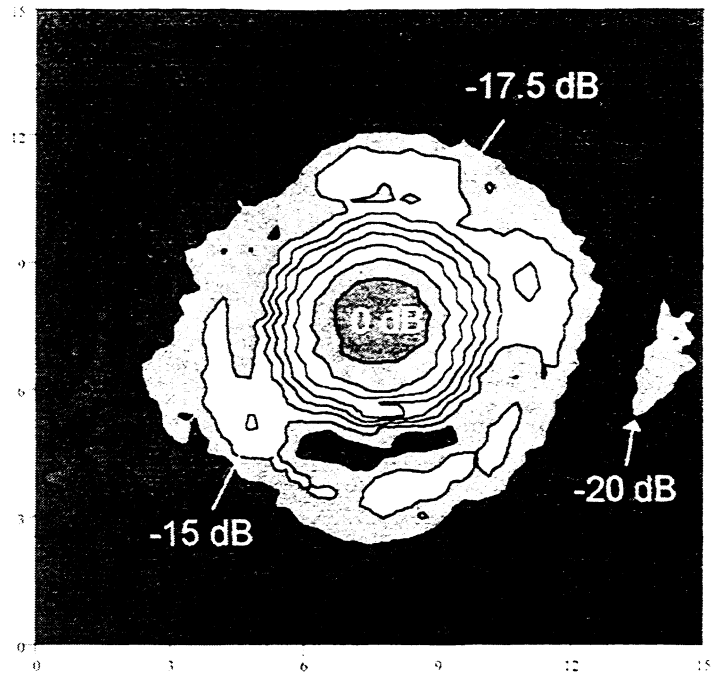


Fig. 5. Far field beam pattern of the Integrated Receiver sample with 92 μm long antenna: contour step is 2.5 dB: covered area is 150 mm \times 150 mm: distance from the chip is 33 cm.

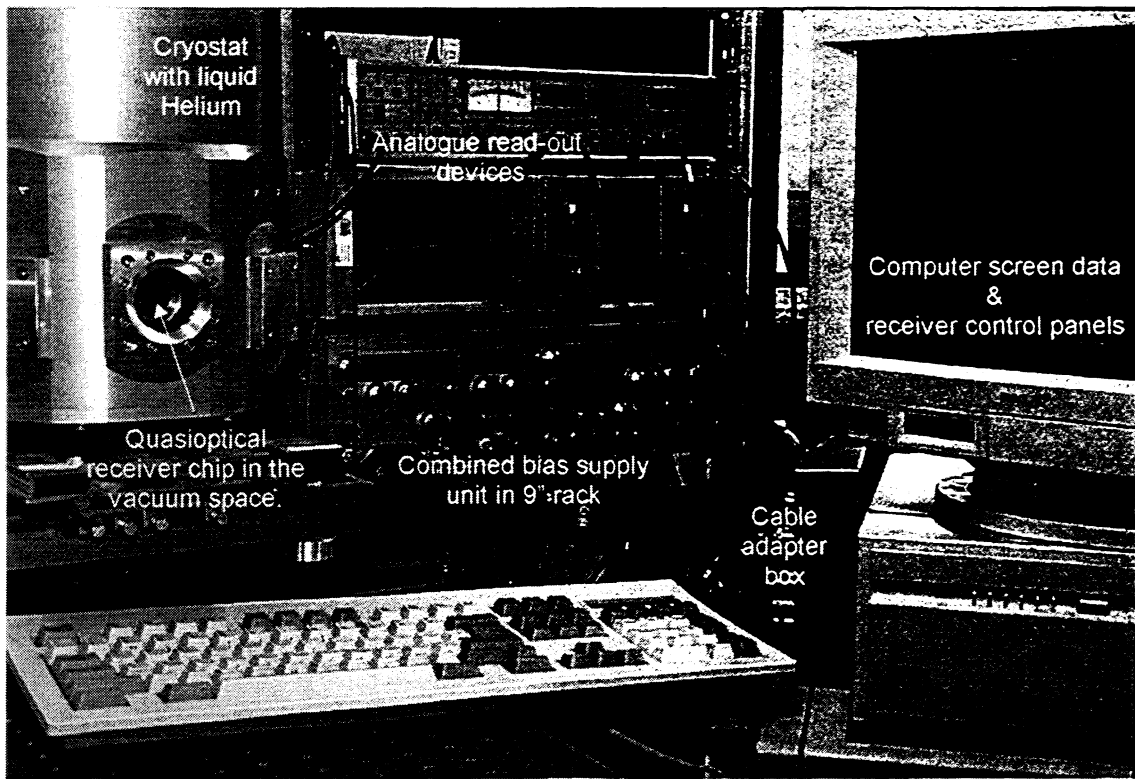


Fig. 6. Photo of the experimental setup: optical liquid Helium cryostat with the receiver, bias supply unit and controlling computer are shown.

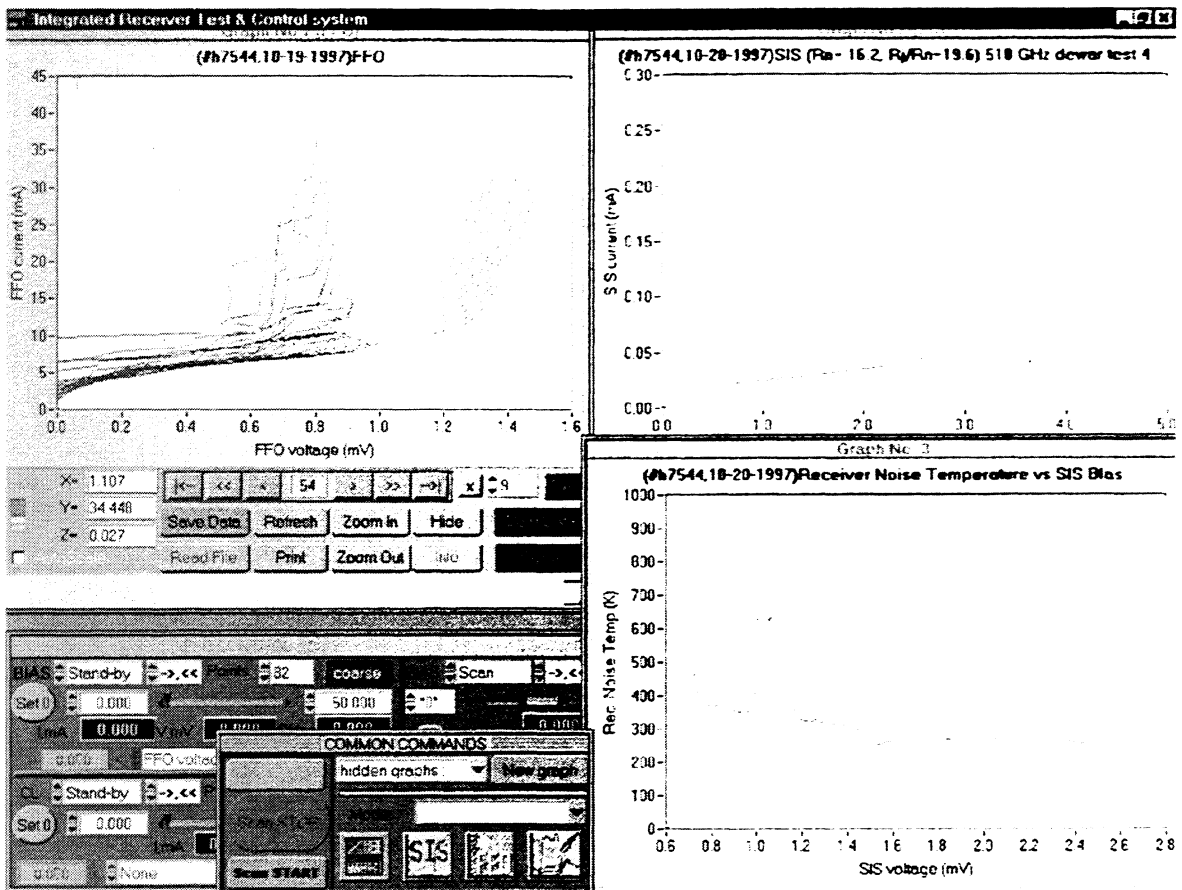


Fig. 7. Computer screen of "IRTECON" - Integrated Receiver Test & Control system: FFO IV-curves (top-left); un pumped and pumped IV-curves of SIS mixer (top-right); receiver noise temperature vs. mixer bias voltage (bottom-right); receiver control panels (bottom-left).

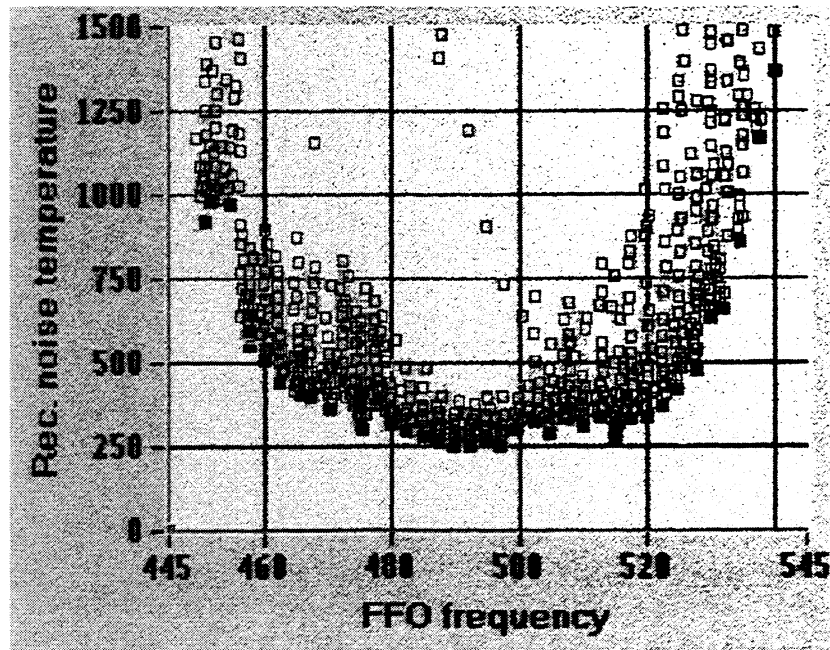


Fig. 8. Receiver noise temperature optimized by IRTECON (print-screen colored copy). The search process is presented by the light "bubbles" of intermediate (non-optimal) points.

TERAHERTZ NbN/AlN/NbN MIXERS WITH Al/SiO/NbN MICROSTRIP TUNING CIRCUITS

Yoshinori UZAWA, Zhen WANG, and Akira KAWAKAMI

Kansai Advanced Research Center, Communications Research Laboratory,
Ministry of Posts and Telecommunications, 588-2 Iwaoka, Iwaoka-cho, Nishi-Ku,
Kobe, 651-2401 JAPAN
e-mail: uzawa@crl.go.jp

Abstract

We have developed a low-noise quasi-optical NbN/AlN/NbN SIS mixer that operates at terahertz frequencies. The mixer uses a MgO hyperhemispherical lens with an anti-reflection cap, a single-crystal NbN log-periodic antenna, and two-junction tuning circuits which employ Al/SiO/NbN microstriplines. The NbN/AlN/NbN junction size was about 0.9 μm in diameter, and the current density was about 45 kA/cm^2 . The frequency-dependence of the receiver noise temperature was investigated by using an optically pumped far-infrared laser and a backward-wave oscillator as a local oscillator at several frequencies from 670 GHz to 1082 GHz. The experimental results showed that the center frequency was around 800 GHz, and the receiver noise temperature measured by the standard Y-factor method was 457 K(DSB) at 783 GHz including a 9 μm -thick Mylar beam splitter loss and other optical losses at the physical bath temperature of 4.2 K. This is the first SIS mixer based on NbN with low-noise performance ($12h\nu/K_B$) above the gap frequency of Nb.

1. Introduction

Until now, the most sensitive elements in heterodyne mixers are the superconductor-insulator-superconductor (SIS) tunnel junctions. Both high RF-to-IF conversion efficiency and low noise are predicted for these mixers from theory [1], and ultra-low noise SIS mixers using Nb/AlO_x/Nb tunnel junctions approach $\sim h\nu/k_B$ in the millimeter and submillimeter wave regions [2]. This good performance is mainly a result of using an Nb SIS junction with a ideal current-voltage (I-V) curve and a low-loss Nb tuning circuit to resonate out the junction capacitance. However, the low gap frequency of Nb (about 700 GHz) essentially limits its application as an ultra-low noise SIS mixer in the sub-terahertz band because the onset of pair breaking above the gap frequency results in a rapid increase in RF loss in the superconducting electrodes and tuning circuits. Therefore, the mixer noise performance is greatly degraded at frequencies above the gap frequency [3]. In order to develop a low-noise SIS mixer at the terahertz band, it is necessary to make SIS junctions based on materials which have energy gap higher than that of Nb. In addition, tuning circuits have to be high-quality superconducting films with a higher gap frequency of Nb, or high-conductivity normal-metal films.

NbN is the best candidate for developing a low-noise terahertz SIS mixer because it has large gap frequencies up to 1.4 THz. We have recently developed a process to grow single-crystal NbN thin films on MgO substrates [4] and to fabricate high-quality NbN/AlN/NbN tunnel junctions that have high current densities, up to 54 kA/cm², for high-frequency device applications [5]. Excellent noise characteristics in the 300-GHz band have been obtained using these junctions with low-loss Nb/SiO/NbN microstrip tuning circuits [6]. However, an all-NbN SIS mixer designed for 1 THz operation has shown poor noise performance that was much worse than the value calculated using Tucker's quantum theory of mixing with measured I-V curve of the NbN SIS junction [7]. The large amount of noise was possibly caused by the large RF losses in the tuning circuits of polycrystalline NbN on the SiO. In this paper, we report on the fabrication and testing of a quasi-optical NbN/AlN/NbN SIS mixer with Al/SiO/NbN microstrip tuning circuits that is capable of terahertz frequency operation. The low-noise operation above the gap frequency of Nb was the best ever reported for SIS mixers based on NbN.

2. Mixer Design

In our mixers, a quasi-optical structure employing a substrate lens was used to couple the RF radiation to the junctions. An optical micrograph of our mixer chip is shown in Fig. 1. Four NbN/AlN/NbN junctions and an Al wiring were integrated with a single-crystal NbN log-periodic antenna on a 0.3-mm-thick single-crystal MgO substrate. The tuning circuit consisted of two junctions separated by an inductor for tuning out the junction capacitance and a $\lambda/4$ impedance transformer for matching the resistance of the two-junction circuit to the antenna impedance [8]. A mirror-symmetrical-circuit pattern at the feed point of the antenna was employed in order to reduce the antenna source impedance of about 80 Ω . We designed the tuning circuit at the center frequency of 900 GHz for the NbN/AlN/NbN tunnel junctions with the size of 0.9 μm in diameter and the current density of 30 kA/cm^2 . Because the $J_C R_N A$ product is about 350 for such a NbN SIS junction, the normal state resistance is 18 Ω . Here, J_C is the current density in kA/cm^2 , R_N is the normal state resistance in Ω , and A is the area of the junction in μm^2 . The capacitance of the junction was 78 fF. This value was calculated from the following expression that was obtained from measurements on our high current density NbN SIS junctions ;

$$\text{Log}C_S = 1.85 + 0.16\log J_C,$$

where C_S is the specific capacitance in $\text{fF}/\mu\text{m}^2$ [9]. Al/SiO/NbN microstriplines were utilized for tuning circuits. The ground plane of the microstripline which is the arm of the antenna was a 200-nm-thick single-crystal NbN base electrode, while the microstripline was a 120-nm-thick Al wiring layer. A 250-nm thick insulator layer of SiO was used to electrically isolate the NbN/AlN/NbN tunnel junctions. The loss, slow wave factor, and characteristic impedance of the microstripline were calculated from incremental inductance considerations described in Ref. [10]. The calculation included the surface impedance of the superconducting NbN thin-film and the normal metal Al thin-film as given by the Mattis-Bardeen theory and the theory of the skin effect. Figure 2 shows the calculated loss per wavelength as a function of frequency for the Al/SiO/NbN and Al/SiO/Al microstriplines that have widths of 3- μm . The

parameters used for the calculation are described in Table 1. Our calculations showed that the loss of the Al/SiO/NbN microstripline at 900 GHz was 0.86 dB/wavelength which is about 2.5 dB better than the Al/SiO/Al microstripline. This result suggests that the power coupling efficiency of the Al/SiO/NbN microstrip tuning circuits from the feed point to the junctions should be approximately twice as good as that of Al/SiO/Al microstrip tuning circuits at frequencies below the gap frequency of NbN. The calculated coupling efficiency is shown in Fig. 3. The maximum coupling efficiency achieved was about 70 % at a center frequency of 900 GHz.

3. Results and Discussion

The mixer devices were prepared by the fabrication process described in Ref. [11]. The thickness of the NbN, SiO, and Al was 180 nm, 230 nm, and 300 nm, respectively. The Al wiring layer was deposited by thermal evaporation. The conductivity of the Al film at 4.2 K was able to be estimated from the slope of the supercurrent branch of the I-V curve. We obtained a high conductivity of about $2.8 \times 10^8 \Omega^{-1}\text{m}^{-1}$, which is better than the design value by a factor of 1.4. The Josephson critical current of two junctions in parallel was 570 μA , and the junction size was about 0.9 μm in diameter. This gave a current density of about 45 kA/cm^2 for these junctions.

The heterodyne receiver noise measurements were made using the standard Y-factor method for room-temperature (295 K) and liquid-nitrogen-cooled (77 K) loads. The receiver set-up was basically the same as described in Ref. [7]. The incoming radiation entered the dewar through a 0.5-mm-thick Teflon vacuum window and Zitex infrared filters cooled to 77 K and 4.2 K, respectively. Local oscillator (LO) power was introduced into the signal path through a 9- μm or 25- μm -thick Mylar beam splitter. No corrections were made for losses in front of the receiver. Figure 4 shows I-V characteristics of the receiver at 783 GHz with and without local oscillator (LO) power. The LO source was an optically pumped CH_2F_2 laser and the 9- μm -thick Mylar beam splitter was used. The receiver IF output in response to hot and cold loads is also shown in Fig. 4 as a function of bias voltage. The gap voltage was 4.9 mV, corresponding to a gap frequency of 1.19 THz. The normal state resistance was about 13 Ω . Photon-assisted tunneling steps were clearly observed when LO power was applied. The

distinct IF responses to hot and cold loads showed a maximum Y-factor of about 1.41, which corresponded to a double sideband (DSB) receiver noise temperature of 457 K. This value is the best ever reported for SIS mixers based on NbN at frequency above the gap frequencies of Nb.

The frequency dependence of the receiver noise temperature was investigated at several frequencies from 670 GHz to 1082 GHz by using the optically pumped far-infrared laser and a backward-wave oscillator (BWO) as the local oscillator. A CH₃I laser was used for the 670 GHz measurement, and the CH₂F₂ laser was used for 760 and 783 GHz measurements, respectively. The other measurements were made by using the BWO. At all measured frequencies, the 25- μ m-thick Mylar beam splitter was used. Figure 5 shows the receiver noise temperature as a function of frequency. Although it can be seen from the figure that the center frequency of the receiver is around 800 GHz, which is slightly lower than the design frequency of 900 GHz, the experimental results are in good agreement with the designed tuning properties. The main reason for the shift of the center frequency can be attributed to the lower gap voltage of the fabricated device. Since the thickness of the NbN film was comparable to the London penetration depth, the slow-wave factor of the microstripline was strongly affected by the effective penetration depth near the gap frequency. In fact, the calculated center frequency of the power coupling efficiency using the actual parameters including the microstrip size, the NbN gap, the current density, and the Al conductivity, was almost the same as the experimental result. This indicates that the properties of the NbN junction and the tuning circuits were well characterized in our design process, and that the parameters of the fabricated mixer were also well controlled.

4. Conclusion

We have designed, fabricated, and tested a quasi-optical NbN/AlN/NbN SIS mixer that has low-loss Al/SiO/NbN microstrip tuning circuits and is capable of operating at terahertz frequencies. A double sideband receiver noise temperature of 457 K has been achieved at 783 GHz (above the gap frequency of Nb). The frequency dependence of the receiver noise agreed well with the calculated frequency dependence. These results suggest that our well controlled NbN SIS mixer is capable of low-noise operation at frequencies

below the NbN gap frequency of about 1.4 THz. We are developing a process to fabricate NbN/AlN/NbN tunnel junctions with low-loss NbN tuning elements or self-tuned NbN SIS junctions with the hope of obtaining even better performance.

Acknowledgments

We thank Dr. C.E. Tong and Dr. R. Blundell of Harvard-Smithsonian Center for Astrophysics for valuable discussions on the tuning circuits. This work was supported in part by the Joint Research Fund of National Astronomical Observatory.

References

- [1] J. R. Tucker, *Appl. Phys. Lett.* 36, 477 (1979).
- [2] J. Carlstrom and J. Zmuidzinas, *Review of Radio Science 1993-1996*, edited by W. Ross Stone (The Oxford University Press, Oxford, 1996).
- [3] J. Zmuidzinas, H.G. LeDuc, J.A. Stern, and S.R. Cypher, *IEEE Trans. Microwave Theory Tech.*, 42, 698 (1995).
- [4] Z. Wang, A. Kawakami, Y. Uzawa, and B. Komiyama, *J. Appl. Phys.*, 79, 7837 (1996).
- [5] Z. Wang, A. Kawakami, and Y. Uzawa, *Appl. Phys. Lett.*, 70, 114 (1997).
- [6] Y. Uzawa, Z. Wang, and A. Kawakami, *IEEE Trans. Appl. Supercond.*, 7, 2574 (1997).
- [7] Y. Uzawa, Z. Wang, and A. Kawakami, *Eighth Intern. Symp. Space THz Technology*, Boston, MA, 301 (1997).
- [8] Y. Uzawa, Z. Wang, and A. Kawakami, *IEICE Trans. Electron.* E-79-C, 1237 (1996).
- [9] Z. Wang, Y. Uzawa, and A. Kawakami, *IEEE Trans. Appl. Supercond.*, 7, 2797 (1997).
- [10] C. E. Tong, R. Blundell, S. Paine, D. C. Papa, J. Kawamura, X. Zhang, J. A. Stern, and H. G. LeDuc, *IEEE Trans. Microwave Theory Tech.*, 44, 1548 (1996).
- [11] Z. Wang, A. Kawakami, Y. Uzawa, and B. Komiyama, *Appl. Phys. Lett.*, 64, 2034 (1994).

Table. 1 Parameters used in the design process.

NbN gap frequency:	1.27 THz
NbN film thickness:	200 nm
NbN conductivity at 20 K:	$1.5 \times 10^6 \Omega^{-1} \text{m}^{-1}$
SiO film thickness:	250 nm
SiO dielectric constant:	5.5
Al film thickness:	120 nm
Al conductivity at 4.2 K:	$2.0 \times 10^8 \Omega^{-1} \text{m}^{-1}$

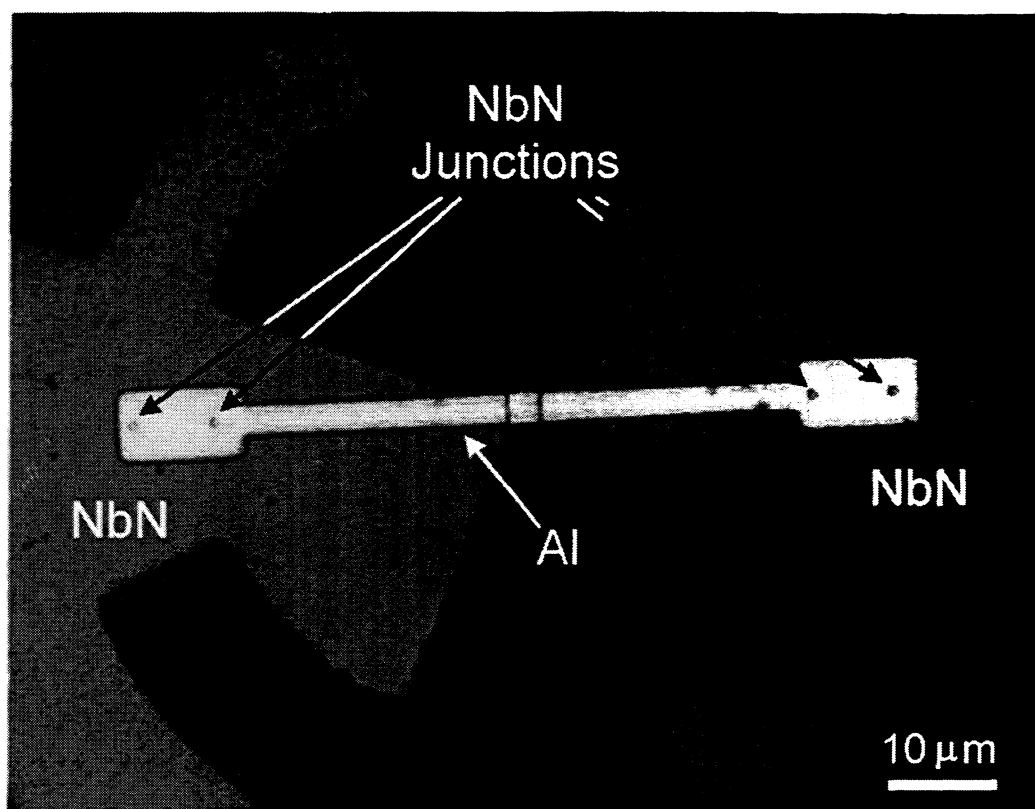


Fig. 1. An optical micrograph of the NbN/AlN/NbN mixer. NbN junctions with integrated Al/SiO/NbN microstrip tuning circuits are fabricated with a self-complementary log-periodic antenna as their ground plane. Each junction is approximately $0.9 \mu\text{m}$ in diameter.

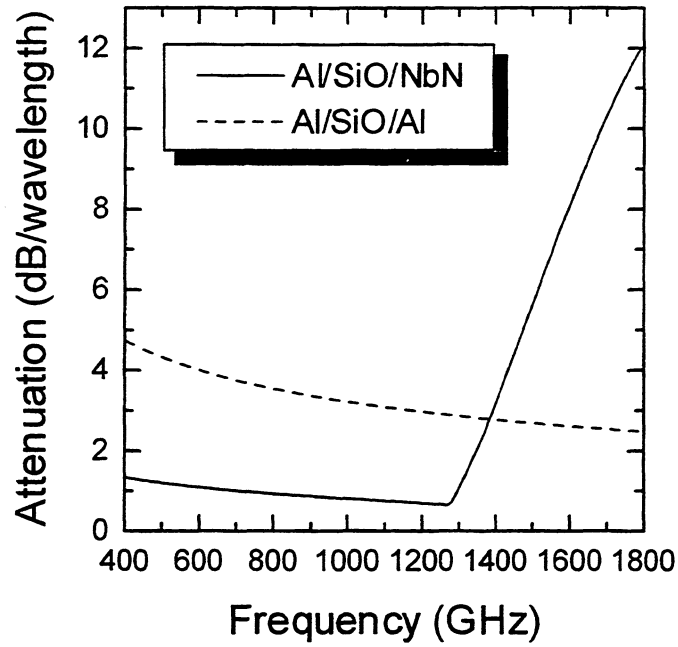


Fig. 2. The calculated frequency dependence of the loss per wavelength for the 3- μ m-wide Al/SiO/NbN microstripline and the Al/SiO/Al microstripline.

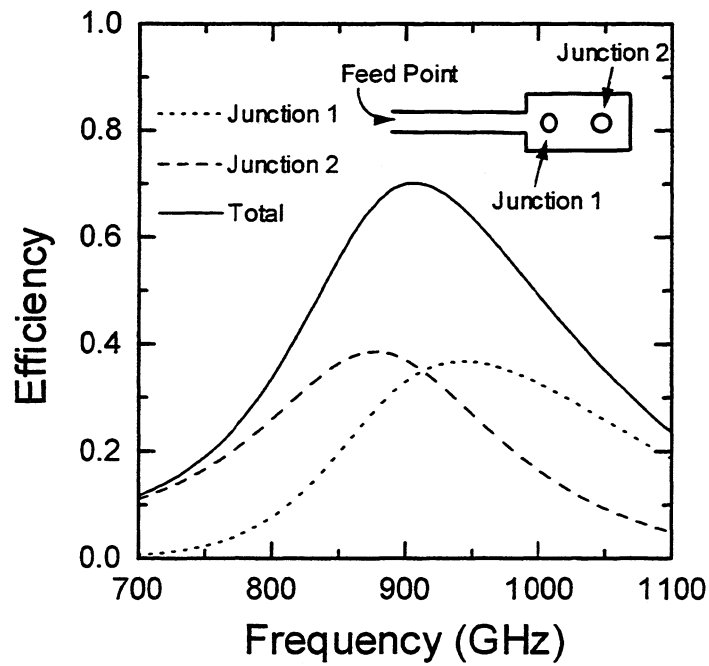


Fig. 3. The calculated power coupling efficiency from the feed point to the two-junction.

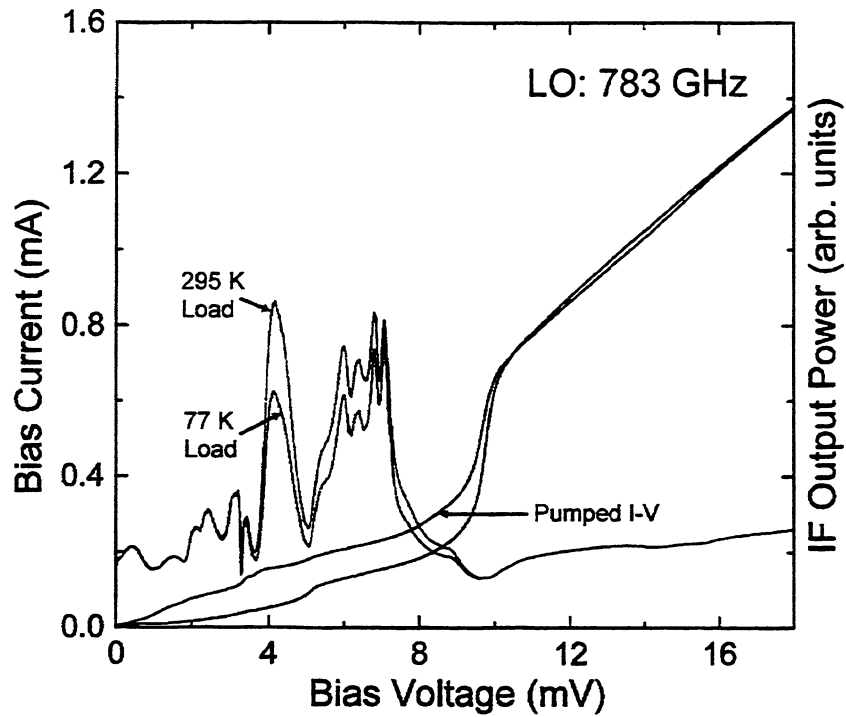


Fig.4 Heterodyne response of the receiver at 783 GHz. Shown are the I-V characteristics of the mixer device with and without LO power. Also shown is the IF power as a function of bias voltage for hot (295 K) and cold (77 K) loads.

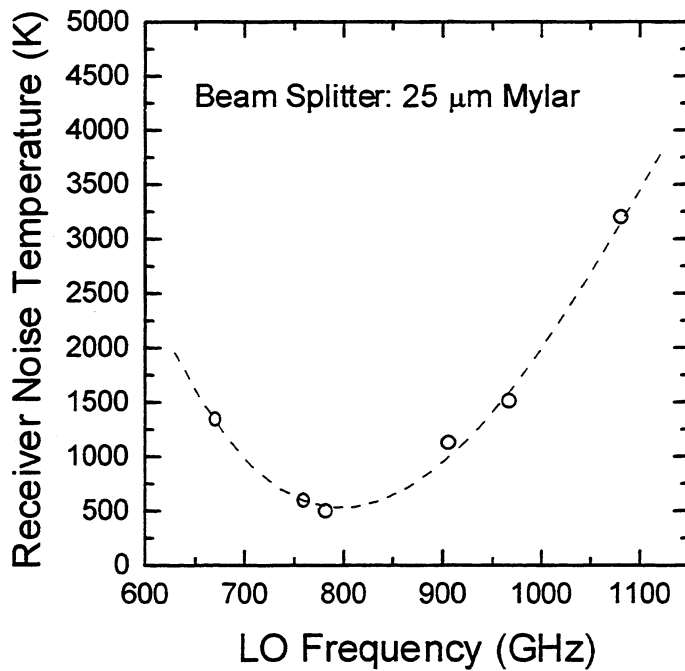


Fig. 5 DSB receiver noise temperature as a function of LO frequency.

LOW-LOSS NbTiN FILMS FOR THz SIS MIXER TUNING CIRCUITS

J. W. Kooi¹, J. A. Stern², G. Chattopadhyay¹,
H. G. LeDuc², B. Bumble², J. Zmuidzinas¹

¹ California Institute of Technology, MS 320-47, Pasadena Ca 91125

² Center for Space Microelectronics Technology/JPL, Pasadena, CA 91108

1998-1

Accepted for publication in the Infrared and Millimeter Waves Journal
Vol. 19, No. 3, March 1998

Abstract

Recent results at 1 THz using normal-metal tuning circuits have shown that SIS mixers can work well up to twice the gap frequency of the junction material (niobium). However, the performance at 1 THz is limited by the substantial loss in the normal metal films. For better performance superconducting films with a higher gap frequency than niobium and with low RF loss are needed. Niobium nitride has long been considered a good candidate material, but typical NbN films suffer from high RF loss. To circumvent this problem we are currently investigating the RF loss in NbTiN films, a 15K T_c compound superconductor, by incorporating them into quasi-optical slot antenna SIS devices.

Keywords: NbTiN superconducting films, SIS junctions, Niobium bandgap

I. Introduction

There is a strong astronomical interest to construct sensitive heterodyne receivers above 700 GHz, which is the bandgap energy of niobium. Niobium is the material of choice in nearly all Superconducting-Insulating-Superconducting tunnel junction (SIS) mixers.

Niobium has a bandgap energy of (2Δ) of 700 GHz. Above this frequency the photons have enough energy to break Cooper pairs within the superconductor. This results in a very steep increase in the absorption loss of niobium films, as is shown in Figure 1. To circumvent this problem, up to 1.2 THz at least, we are developing quasi-optical SIS devices with NbTiN films[1]. Many of these devices show I-V resonances up to 1 THz, indicating that the loss continues to be low up to the gap frequency (1.2 THz).

Comparison of circuit simulations and FTS measurements indicate that the resistivity of the NbTiN just above T_c is about 60 $\mu\Omega$ -cm, which computes to a phase velocity of 0.21c for NbTiN microstrip lines with a 200 nm SiO₂ dielectric. The critical temperature of the NbTiN films is around 15K and the gap voltage about 5.2 mV. Several different devices have been tested up to 650 GHz, all of which can be categorized in the following three groups.

- NbTiN ground plane, Nb wiring and Nb/Al-O_x/Nb junctions
- NbTiN ground plane and wiring, NbTiN/MgO/NbTiN junctions
- NbTiN/Nb ground plane and wiring, Nb/Al-N_x/NbTiN junctions

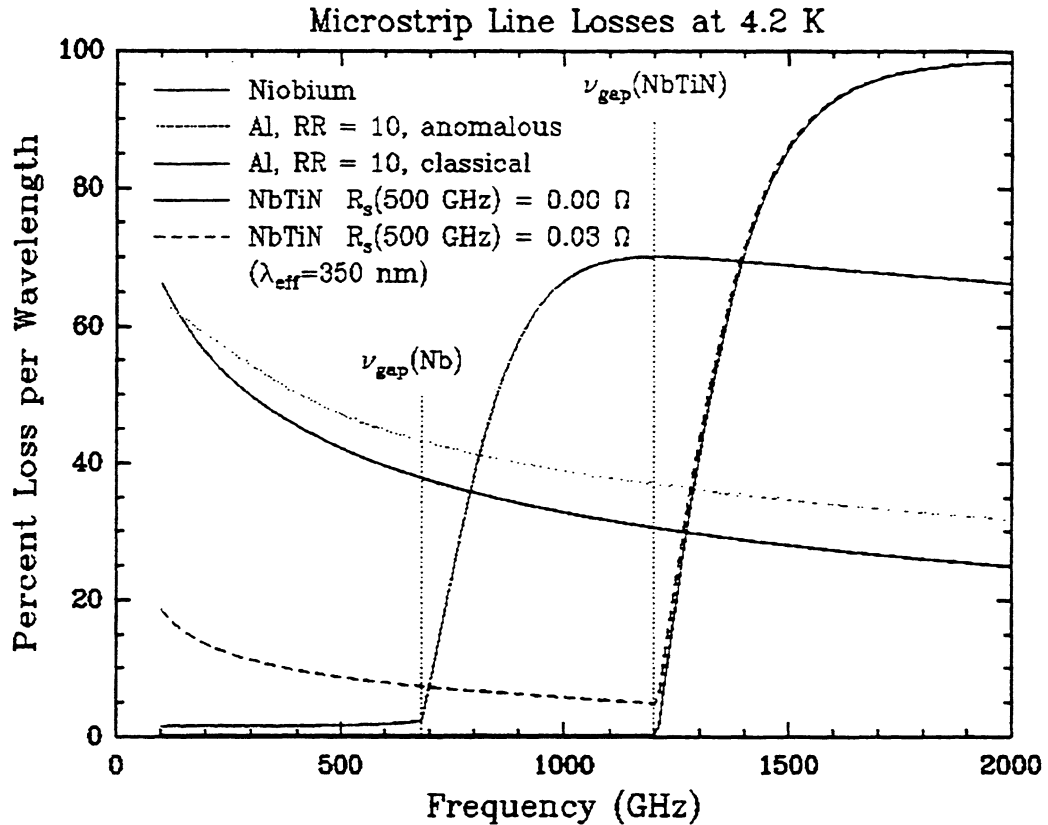


Fig. 1 RF loss of microstrip lines made with several different materials.

II. NbTiN Ground Plane, Nb Wiring and a Nb/Al-O_x/Nb Junctions

Since we did not know the material properties (mechanical and electrical) of the NbTiN superconducting films, we first fabricated double slot antenna devices with an existing mask designed for niobium [1, 2]. The devices had a NbTiN ground plane, Nb/Al-O_x/Nb junction, and niobium wiring. We have made direct detection Fourier Transformer Spectrometer (FTS) measurements and hot/cold heterodyne measurements near the peak

of the FTS response, at 639 GHz. The frequency response measured with the FTS fits quite well with our circuit calculation if we assume that the NbTiN films have essentially no loss. Significant discrepancies arise between theory and experiment if the surface resistance of the NbTiN film is assumed to be $0.1 \Omega/\text{square}$. We also deduce from our circuit simulations a phase velocity of about $0.21c$ and a penetration depth on the order of 230 nm . For comparison, niobium films have a penetration depth of 80 nm . As an interesting side note, the heterodyne result of 110K at 639 GHz proved to be one of the most sensitive un-corrected receiver measurements at this frequency to date. Clearly the loss in the NbTiN ground layer is very low. A $9\mu\text{m}$ mylar LO injection beamsplitter was used during the duration of the heterodyne measurement.

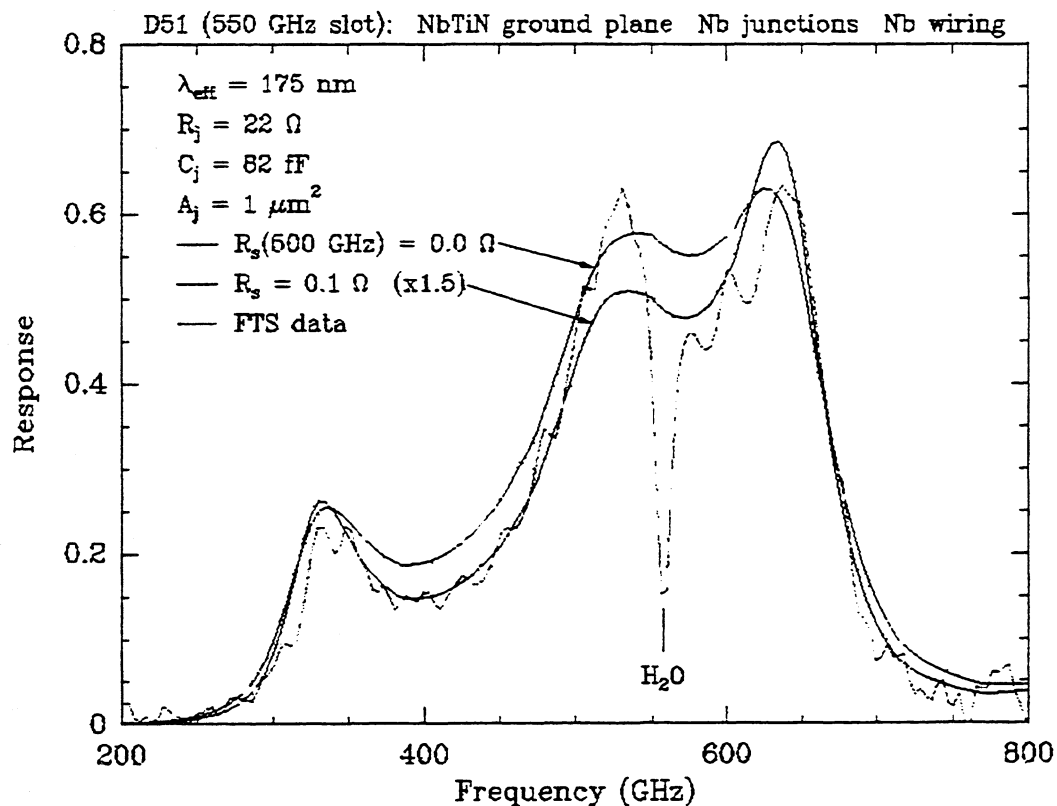


Fig. 2 FTS measurement of a Nb/Al-Ox/Nb junction with NTiN groundplane.

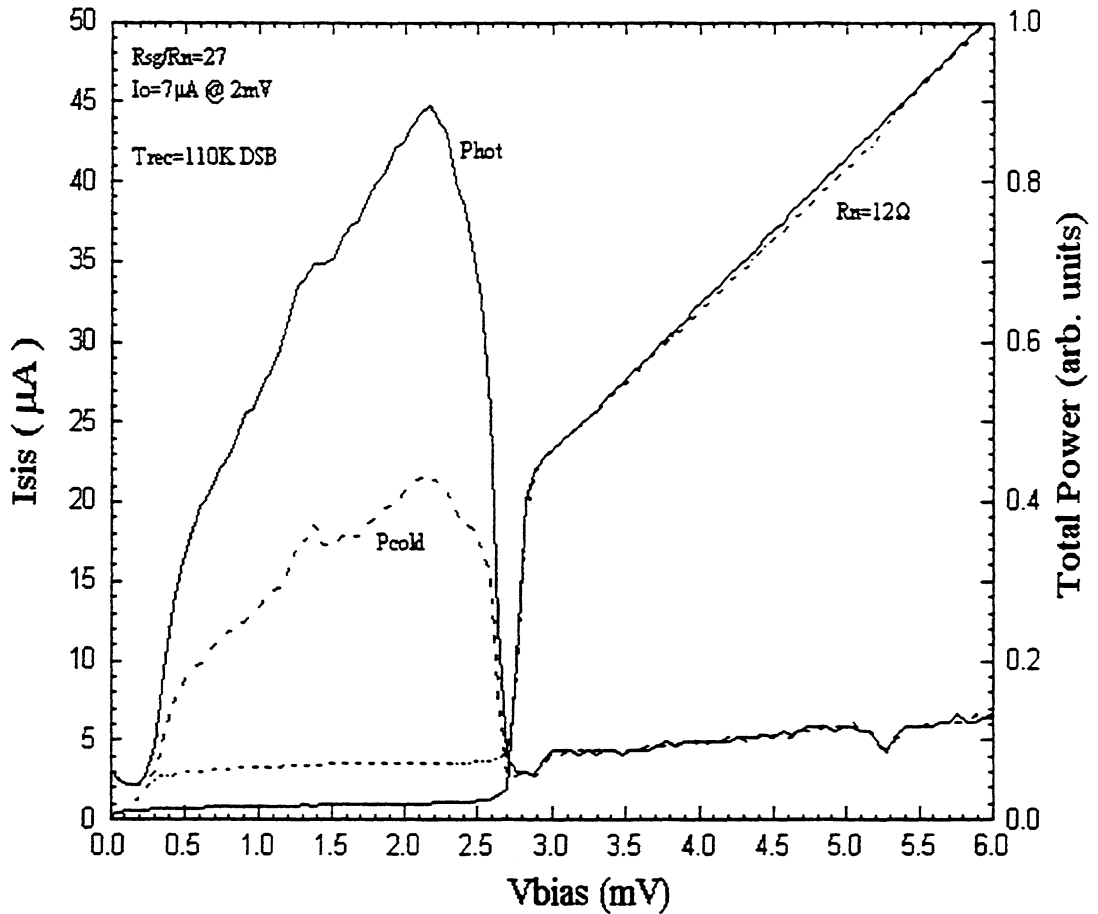


Fig. 3 Heterodyne response of a Nb/Al-O_x/Nb junction with NTiN groundplane at 639 GHz.

Once an understanding of the phase velocity and penetration depth of the NbTiN films was gained, we designed two different double slot antenna circuit layouts for further experimentation.

The first design was for an all NbTiN device with a NbTiN/MgO/NbTiN junction, and the second design was optimized for an Nb/Al-O_x/Nb junction. The difference being that, according to our computer simulations to FTS fits, the specific capacitance of a MgO barrier is on the order of 140-160 fF/µm². Nb/Al-O_x/Nb junctions with similar current density have a specific capacitance around 85 fF/µm².

The RF capacitive impedance of a $0.5 \mu\text{m}^2$ NbTiN/MgO/NbTiN SIS junction at 1 THz is less than 2 Ohm, which makes it very difficult to match. Due to its lower capacitance, Al-O_x would be a preferred barrier except that we were not successful in fabricating high quality NbTiN junctions with Al-O_x barriers. A third barrier was used, Al-N_x, which has a reported specific capacitance similar to that of Al-O_x but is better suited to the fabrication process. There are good indications that Al-N_x has a lower barrier height than Al-O_x, and is thermally more stable.

III. NbTiN Ground Plane and Wiring, NbTiN/MgO/NbTiN Junction

As discussed, a $0.5\mu\text{m}^2$ NbTiN/MgO/NbTiN SIS junction at 1 THz presents a mere 2 Ohm of reactance and the I/V characteristics are similar to the well known “washed-out” NbN I/V curves. Nonetheless, these devices are still of interest because of the relatively high energy gap, $(2\Delta) = 1200$ GHz, and low RF loss. To verify that these films do indeed show improved performance over NbN devices, we have measured several of these devices over a wide range of current densities. Figure 4 shows the FTS response with three different circuit simulation fits for a junction with a RnA product of $42 \Omega\text{-}\mu\text{m}^2$. Though the fits are not perfect, it does enable us to put an upper limit on the loss (0.03-0.06Ω/square), get an estimate for the junction capacitance ($132\text{fF}/\mu\text{m}^2$ for a RnA product of $42 \Omega\text{-}\mu\text{m}^2$) and resistivity ($60\mu\Omega\text{-cm}$). We have also measured MgO devices with RnA products as low as 8 and as high as $60 \Omega\text{-}\mu\text{m}^2$. The specific capacitance, according to circuit simulations fits to the FTS data, for these particular device were $163 \text{fF}/\mu\text{m}^2$ and $125 \text{fF}/\mu\text{m}^2$ respectively.

The NbTiN/MgO/NbTiN SIS junction heterodyne measurement presented in Figure 5 has a receiver noise temperature of 250K DSB. This is several factors better than results reported with NbN devices at similar frequencies.

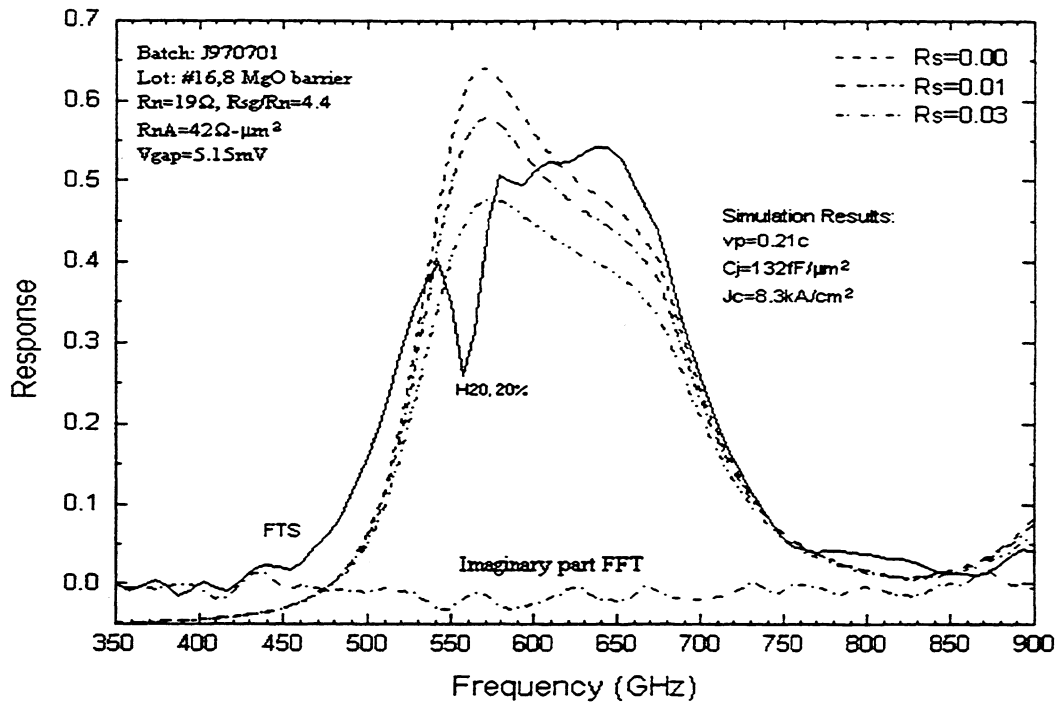


Fig. 4 FTS response of an All NbTiN junction with MgO barrier.

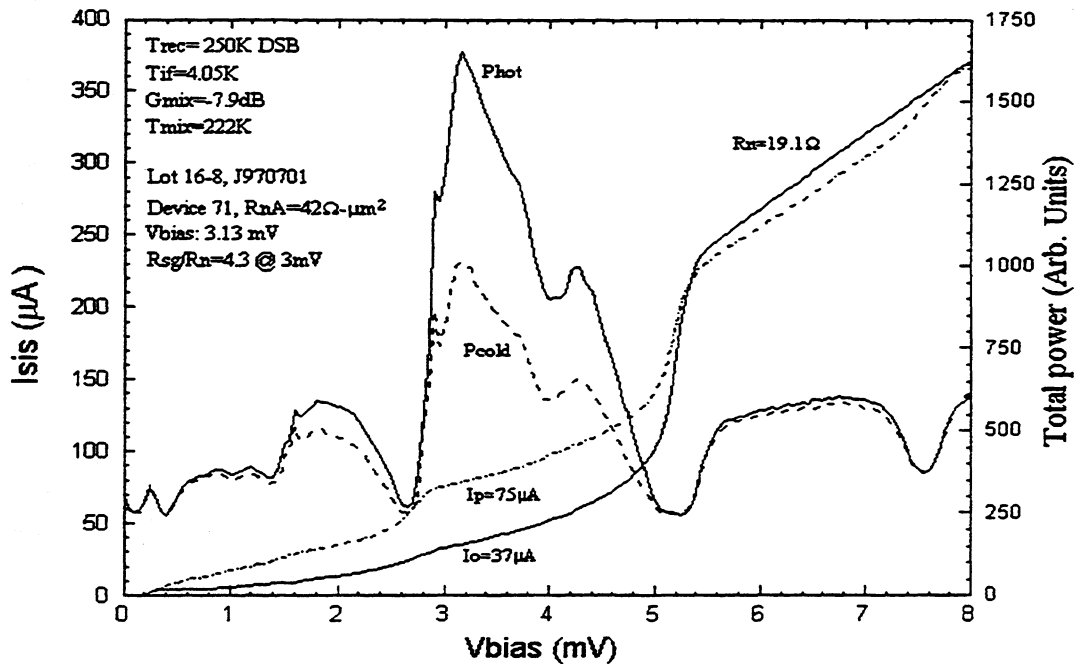


Fig. 5 Heterodyne response of an All NbTiN junction with MgO barrier at 638 GHz.

IV. NbTiN/Nb Ground Plane, NbTiN Wiring, Nb/Al-N_x/NbTiN Junction

A promising technology for THz applications is the use of an Al-N_x barrier rather than MgO barrier. This should result in a reduced specific capacitance, making the RF match to these devices at 1 THz more realistic. Josephson resonances in the I/V curve of many of these devices show resonances up to 2.1 mV. In Figure 6 we present a device that shows a rather nice resonance at 800 GHz. Unfortunately the I/V curve showed a weak-link break around 5 mV, and no heterodyne data is available for this particular device. Note that the junction gap voltage is at 3.5 mV. The devices discussed here were fabricated with a 100 Angstrom niobium layer on top of the NbTiN ground plane. This was done because Aluminum can readily be deposited on top of a niobium base electrode, but not easily on NbTiN. The sum gap of the 100 Angstrom niobium and NbTiN counter electrode is 3.5 mV as shown in Figure 6. Our calculations show that the absorption loss in the very thin niobium film is significant enough to effect the RF performance above 700 GHz, the gap frequency of niobium.

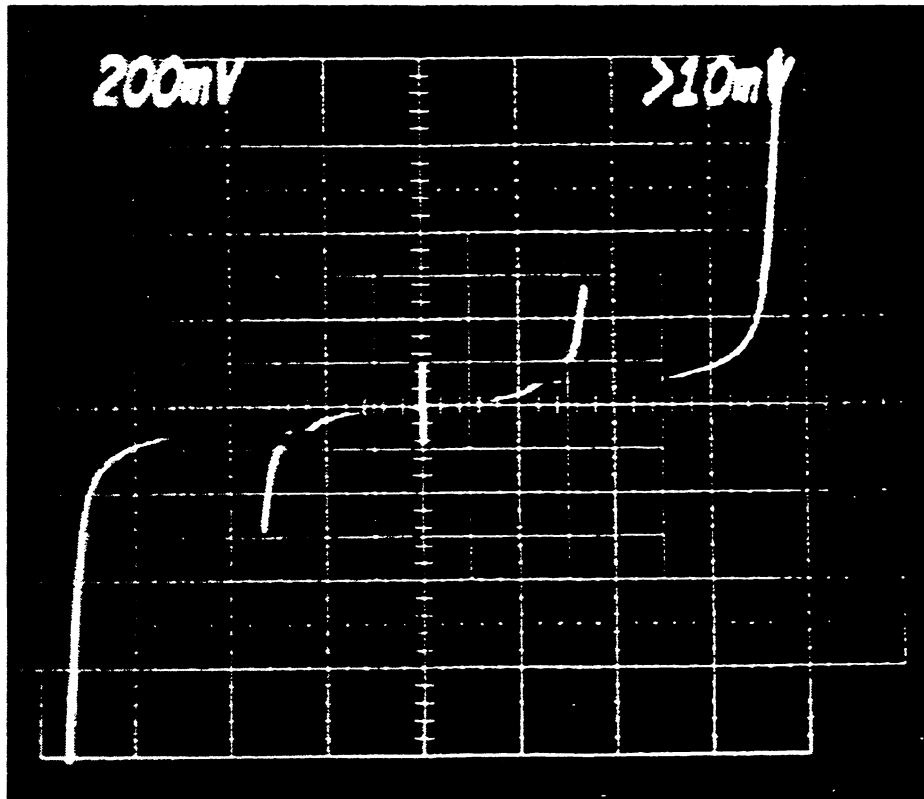


Fig. 6. Josephson resonance at 800 GHz of a Nb/Al-N_x/NbTiN junction
Horizontal scale: 1mV/division, Vertical scale: 20μA/division

A new process is currently under development at JPL which will etch completely through the 100 angstrom niobium layer on top of the NbTiN base electrode, except for where the junction is patterned. This should solve the RF loss issue in the niobium film, yet still allow good quality IV curves with gap voltages around 3.5 mV. This technology is therefore particularly interesting for THz applications.

RF circuit simulations show a 3 dB bandwidth of about 120 GHz for these devices, which is in good agreement with the measured FWHM bandwidth of 115 GHz on our FTS. The small RF bandwidth is indicative of a low loss RF tuning circuit. In fact the 3 dB bandwidth of a similar device with aluminum wiring is 450 GHz [3].

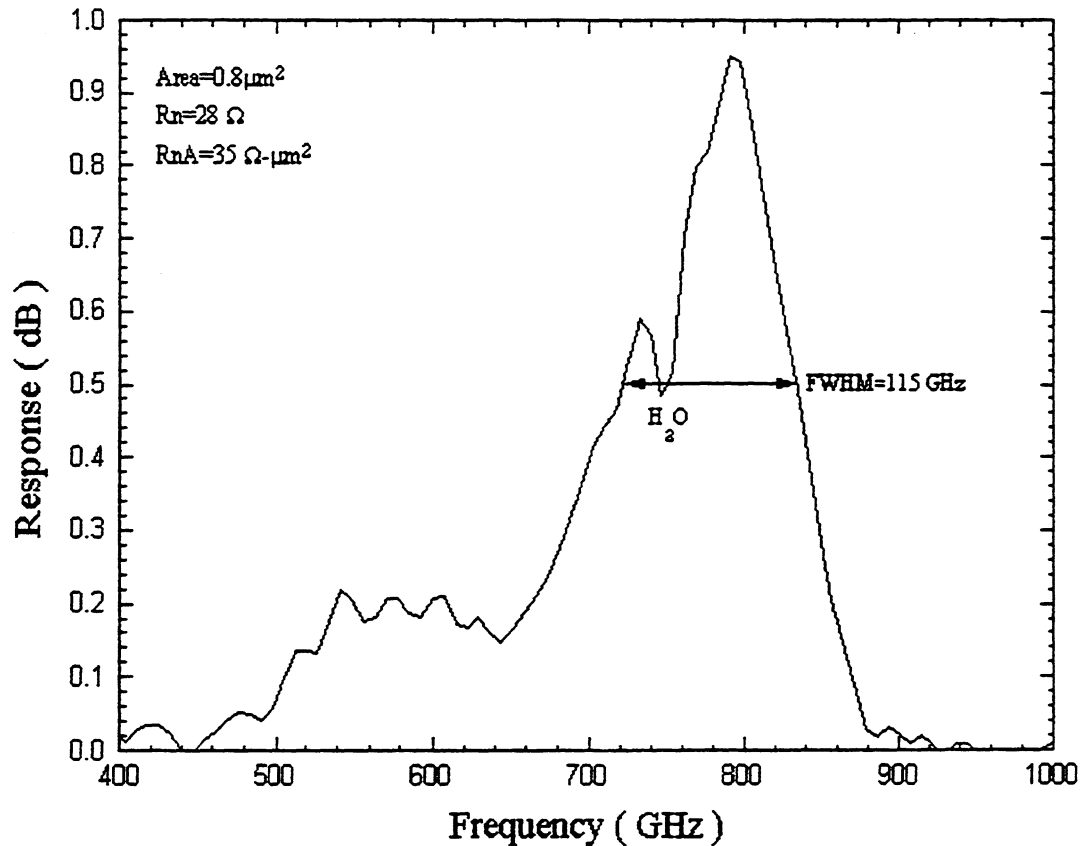


Fig. 7 Direct Detection response of a 950 GHz designed Nb/Al-N_x/NbTiN junction with NbTiN groundplane and wire layers.

Since no more high quality 950 GHz devices were available for this fabrication run, we turned our attention to a 650 GHz device. The direct detection response is shown in Figure 8. The measurement was made at two different resolutions and it shows a resonance that is shifted down from the 650 GHz design frequency to 590 GHz, approximately 10%. Heterodyne measurements at 588 GHz gave a 195K DSB noise temperature.

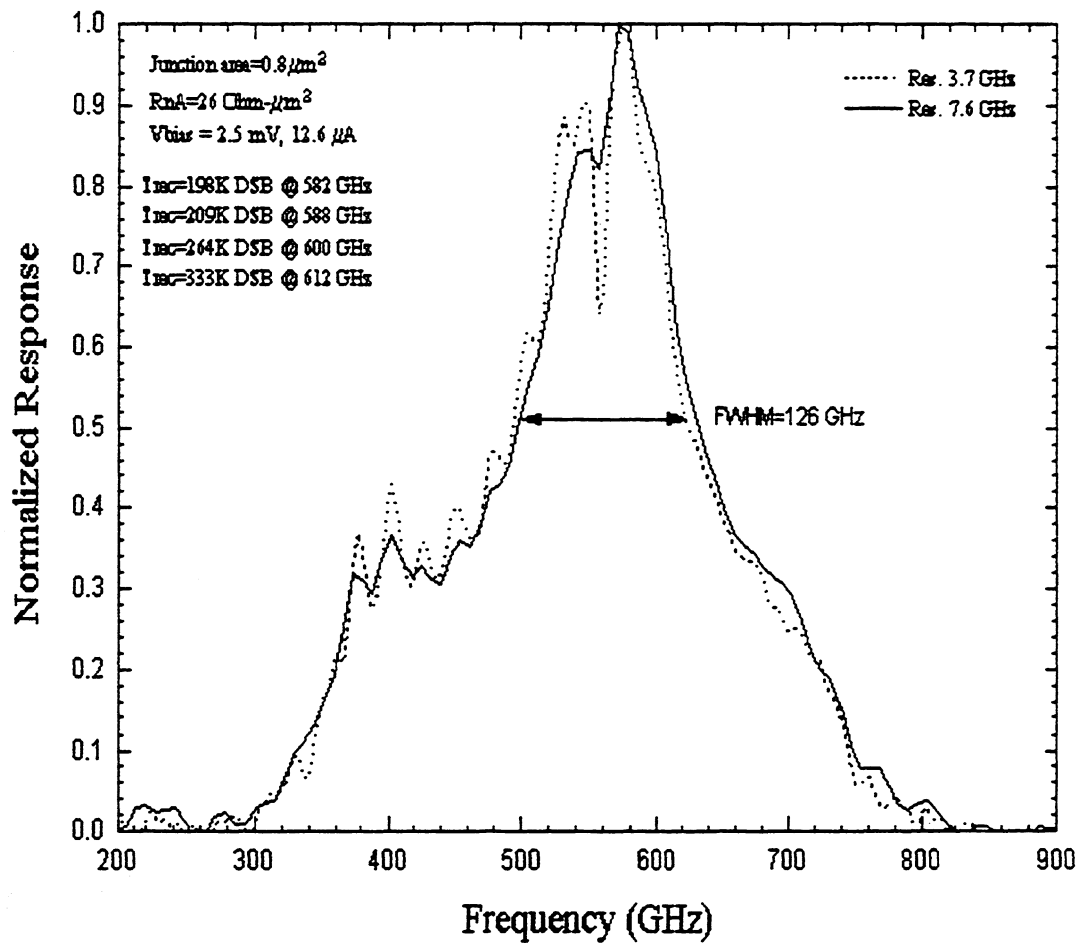


Fig 8 FTS response of an Al-N_x barrier junction designed to resonate at 650 GHz. $R_nA = 26 \Omega\text{-}\mu\text{m}^2$

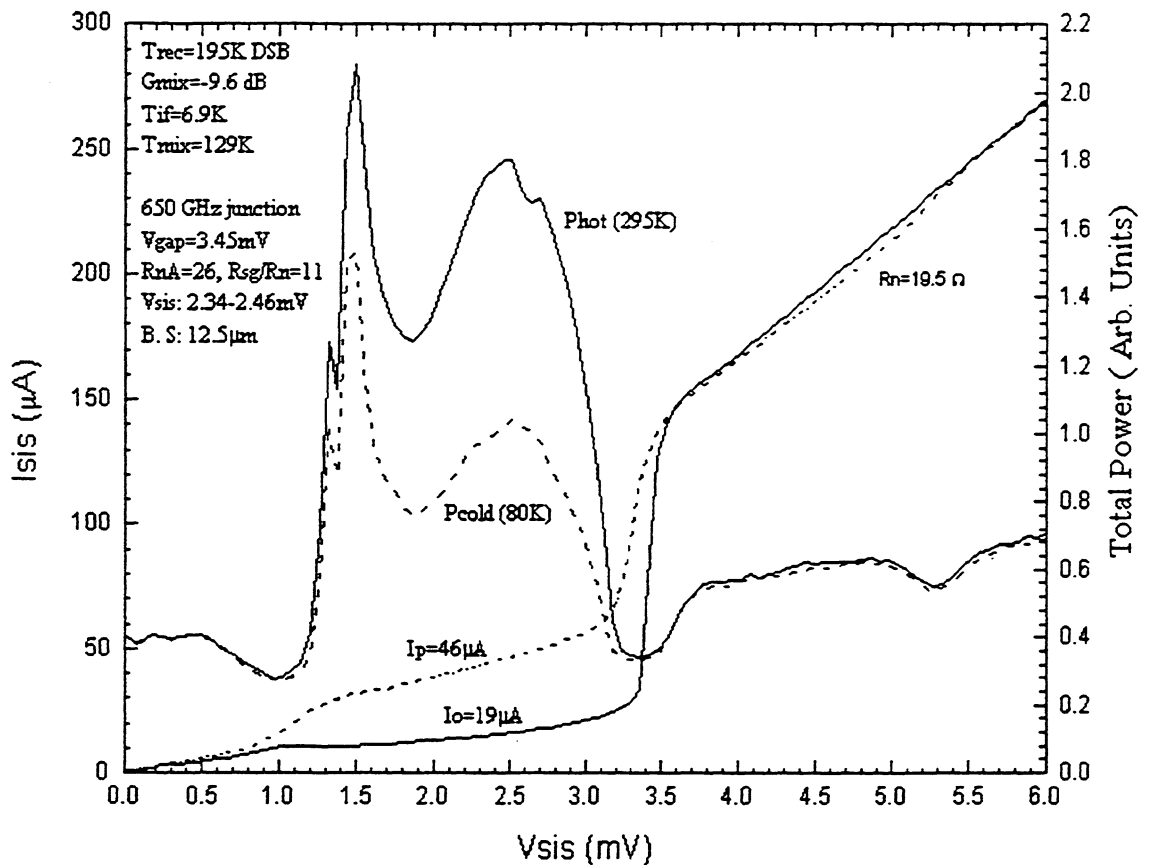


Fig 9 Heterodyne response if an Al-N_x barrier junction at 588 GHz.

The standard IF shot noise calibration technique[4] gave a mixer noise temperature of 129K and a mixer gain of -9.6 dB. The mixer conversion loss is somewhat higher than expected. The reason for this is not very clear since we are below the gap frequency of niobium. However if the loss in the NbTiN tuning circuit were significant would have expected a broadened RF response.

V. Conclusion

Clearly, our preliminary measurements demonstrate that NbTiN films show great promise for use in low-loss tuning circuits for SIS mixers at 1 THz. However, much work remains to be done to turn this promise into reality. Numerous technical difficulties must be

overcome before a stable, reproducible fabrication process is available, which is necessary for the production of optimized devices. Several different junction configurations are currently under investigation as it is not clear which one will perform best up to 1.2 THz.

New devices have recently become available, and we anticipate testing them at 800 GHz in the very near future.

VI. Acknowledgments

This work was supported in part by NASA grants NAG5-4890 and NAGW-107, NAG2-1068, the NASA/JPL Center for Space Microelectronics Technology and the Caltech Submillimeter (NSF grant AST-9615025).

VII. References

1. **J. Zmuidzinas and H.G. LeDuc**, "Quasi-Optical Slot Antenna SIS Mixers", *IEEE transactions on Microwave Theory and Techniques*, Vol. 40. No. 9, pp. 1797-1804, Sept 1992.
2. **M. Gaidis, H. G. LeDuc, M. Bin, D. Miller, J. A. Stern and J. Zmuidzinas**, "Characterization of low noise quasi-optical SIS mixers for the Submillimeter Band", *IEEE transactions on Microwave Theory and Techniques*, Vol. 44, No. 7, pp. 1130-1139, July 1996.
3. **M. Bin, M. C. Gaidis, J. Zmuidzinas, T. G. Phillips and H. G. Leduc**, "Quasi-Optical SIS mixers with Normal-Metal Tuning Structures", *IEEE Transactions on Applied Superconductivity*, Vol. 7 (2), Part 3, pp 3584-3588, Jun. 1997.
4. **D.P. Woody, R.E. Miller, and M.J. Wengler**, "85-115 GHz Receivers for Radio Astronomy," *transactions on Microwave Theory and Techniques*, Vol. 33, pp.90-95, Feb. 1985.

FABRICATION OF Nb / Al-N_x / NbTiN JUNCTIONS FOR SIS MIXER APPLICATIONS ABOVE 1 THZ

B. Bumble, H. G. LeDuc, and J. A. Stern
Center for Space Microelectronics Technology, Jet Propulsion Laboratory,
California Institute of Technology, Pasadena, CA 91109, USA

ABSTRACT

We discuss the material processing limits of superconductor-insulator-superconductor (SIS) junctions with an energy gap high enough to enable THz heterodyne mixer detection. The focus of this work is a device structure which has Nb as a base layer, a tunnel barrier formed by plasma nitridation of a thin Al proximity layer, and NbTiN as a counter-electrode material. These SIS junctions typically exhibit 3.5 mV sum-gap voltages with the sub-gap to normal state resistance ratio $R_{sg} / R_N = 15$ for resistance - area products $R_N A = 20 \Omega \mu\text{m}^2$. This process is developed such that junctions will be integrated to mixer antenna structures incorporating NbTiN as both ground plane and wire circuit layers. Run-to-run reproducibility and control of the $R_N A$ product is addressed with regard to the conditions applied during plasma nitridation of the Al layer. RF plasma nitridation of the aluminum is investigated by control of DC floating potential, N₂ pressure, and exposure time. Processing is done at near room temperature to reduce the number of variables. Stress in the metal film layers is kept in the low compressive range. Recent receiver results will be discussed in another work presented at this symposium. [1]

INTRODUCTION

High quality Nb/Al-Ox/Nb Josephson junctions have produced the lowest noise temperatures in heterodyne receivers up to 1 THz.[2] Low noise temperatures have been achieved above the energy gap frequency of Nb ($2\Delta/h \sim 700\text{GHz}$) by using high conductivity normal metal (Al) tuning circuits. However, the ideal superconductor-insulator-superconductor (SIS) junction for THz heterodyne receivers should incorporate a high transition temperature (T_c), low-loss superconductor. Applications of tunnel junctions fabricated with NbN/ MgO/NbN and NbN/AlN/NbN have been reported, but performance seems to be limited by either gap rounding in the current- voltage (I-V) characteristic or surface resistance in the NbN. [3,4]. Thin films of NbTiN used in RF accelerator cavities have shown an improvement in surface resistance over NbN.[5] Recent measurements from mixers fabricated with NbTiN have shown that losses can be quite low. [6] However, the integration of Nb/Al-Ox/Nb junctions with NbTiN ground planes and wires suffers from gap reduction due to quasiparticle trapping at the Nb/NbTiN interfaces on both sides of the junction. There is also a problem with getting an insulator - NbTiN interface clean enough such that the superconducting energy gap does not degrade over the distance of its coherence length. Junctions which have deposited

barrier layers are prone to tunneling irregularities due to thin spots or “pin-holes.” Transmission electron microscope (TEM) images of Nb/Al-Ox/Nb junctions clearly show that aluminum smoothes out over the granular niobium surface. [7] Thermal oxidation of the aluminum surface produces a dense and uniform insulator. The niobium counter-electrode may degrade slightly at the interface, but not over the distance of its relatively long coherence length.

Below is a table of the enthalpy of formation for some compounds of interest for this work: [8] The information is useful in that it helps to predict the direction of surface reactions which may occur. Note that the oxides tend to be more stable than the nitrides. Thus, excess oxygen on an Al₂O₃ surface will tend to react with a deposited NbTiN layer to degrade the superconductor at the interface. Depositing NbTiN on a layer of AlN should have less of an ill effect on the superconductor. However, depositing pure Al on a NbTiN base depletes the superconductor of nitrogen at the interface. We also want to point out that thermal oxidation of Al is much easier than thermal nitridation because the triple bond of N₂ is harder to break than the double bond in O₂. Producing a nitride requires either higher temperatures or creating a plasma to break the N₂ molecule. Another method is to get free nitrogen from a gas such as NH₃ which is more reactive.

Compound	ΔH (Kcal/mol)
AlN	-76
NbN	-56
Al ₂ O ₃	-401
Nb ₂ O ₅	-454
N element	+113
O element	+60
NH ₃	-11

Figure 1. Heats of Formation

The work presented here deals only with plasma nitridation at near room temperature by driving the substrate with an RF generator. AlN is an insulator of similar properties to Al₂O₃ with band gap energy ~4 eV and dielectric constant of 8.5. [8] Nb/Al-Nx/Nb Josephson junctions produced by plasma nitridation of aluminum have been previously investigated by Shiota, et al and shown to exhibit improved annealing stability over oxide barriers. [10] Replacing the counter-electrode with NbTiN has the advantage of moving the sum-gap voltage out by 0.6 mV. Thus, a THz receiver would have a substantial improvement in bias range. Figure 2 shows a comparison of a

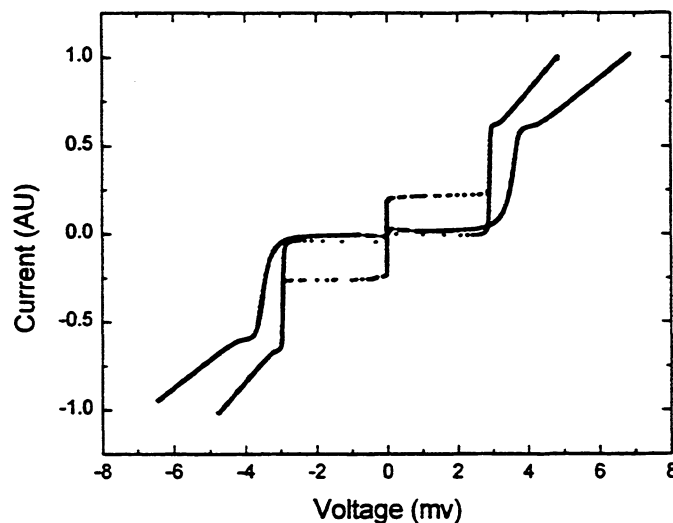


Figure 2. Nb/Al-Ox/Nb compared to Nb/Al-Nx/NbTiN

Nb/AlO_x/Nb junction with 2.9 mV gap to a Nb/Al-N_x/NbTiN junction with 3.5mV gap. Both junctions have $R_{N,A} \sim 20 \Omega\text{-}\mu\text{m}^2$ and are plotted with arbitrary units for the current scale so that the gap voltages and step features can be compared.

EXPERIMENTAL TECHNIQUE

Junctions for this set of experiments are fabricated by a trilayer deposition and self-aligned processing technique. Details of the pattern and etch steps of this technique are reported in another paper in these proceedings.[11] The point of focus presented here is on trilayer deposition which involves plasma nitridation of the Al proximity layer. A brief description and illustration of the process steps for trilayer deposition are given below:

1. DC magnetron sputter deposition of 150 nm of Nb.
2. DC magnetron sputter deposition of 7 nm of Al.
3. Growth of nitride barrier using pure N₂ plasma exposure of Al layer.
4. DC magnetron reactive sputtering 50 nm NbTiN in Ar + N₂ gas mixture.

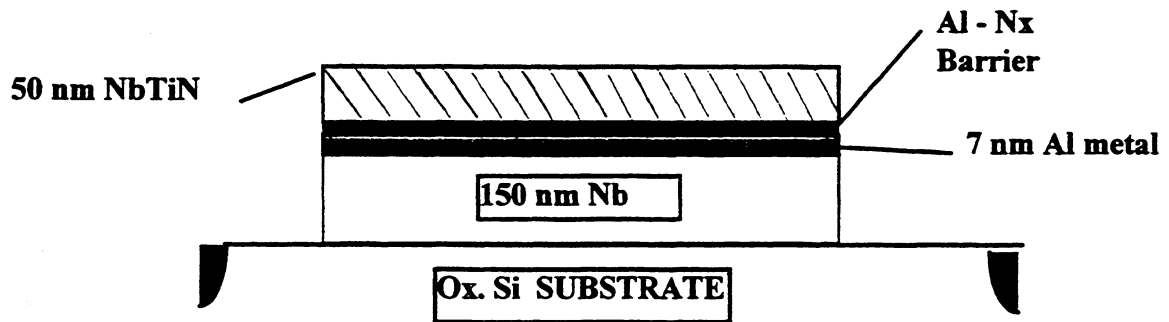


Figure 3. Diagram of Nb/Al-N_x/NbTiN layered structure as studied.

Our process development is investigated for two separate vacuum systems. We have produced devices for receiver testing in system #1 and are currently attempting to transfer the process to system #2. Although the two cylindrical chambers are similar in many respects, system #1 is 46 cm in diameter and 36 cm high whereas system #2 is 76 cm in diameter and 48 cm high. Sputtering sources are all DC magnetrons with 7.6 cm diameter targets which are positioned to sputter upward with a target to substrate throw distance of about 6 cm. Samples are inserted through a vacuum load-lock chamber. A manipulator arm rotates about the chamber center to place the sample over the various sources located around the circumference. All depositions are done without extra heating such that substrate temperature is between 30-60 °C. Samples are held on a metal platform which is grounded for all process steps except the plasma nitridation.

Trilayers are deposited in-situ with a base pressure lower than 10^{-5} Pa. Substrates used in this experiment were thermally oxidized Si wafers. They were cleaned in-situ

prior to film deposit with mild Ar ion beam exposure of 150eV, 20mA for 45 seconds in system #2 and Ar plasma cleaned with comparable conditions in system #1. The base layer of Nb is deposited under sputter conditions which produce slight compressive stress in the film of $2-5 \times 10^9$ dynes/cm². Typical deposition rates are 50 nm/min. in 10 mTorr Ar ambient. These conditions have resulted in the best results for Nb/Al-Ox/Nb junctions and we have seen indications that it is desirable for junctions with subsequent nitride layers as well.

The aluminum layers are deposited by oscillating the sample over the target such that a 7 nm thick film is grown with about 75 passes for system #1 and about 10 passes for system #2. This method produces a more uniform thickness distribution than by remaining stationary over the target.

Plasma nitridation of the aluminum layer is done at a chamber location which allows about 15 cm of free space between the wafer face and the grounded chamber bottom. The substrate manipulator is a grounded cylindrical assembly with capabilities for 13 MHz RF biasing of the bottom chuck which the substrate is held to. Nitrogen gas of 99.999 % purity is flowed into the chamber at ~10 sccm and the pressure is controlled by throttling a turbomolecular pump. RF power of less than 10 W is applied through an impedance matching network to the substrate platform. The DC floating potential developed on the substrate is feedback controlled for the required exposure time.

Counter-electrode deposition of 50 nm thick NbTiN is done by reactive DC magnetron sputtering from a Nb₇₈ Ti₂₂ (wt. %) target in an ambient of Ar and N₂. The flow ratio for optimum properties of NbTiN is integrally related to deposition rate, total gas pressure, target and substrate temperature, and plasma dynamics which involve fixture geometry. Furthermore, there is a compromise to be made between the properties of film stress, T_c, and resistivity. Typical values for films in this study are T_c = 14-15 K, $\rho_{20K} = 75-85 \mu \Omega \text{ cm}$, and compressive stress (σ) = $5-10 \times 10^9$ dynes/cm². A more detailed description of the NbTiN film deposition process is given in a separate paper in these proceedings. [11]

PROCESS VARIATIONS AND RESULTS

Junctions are characterized by low frequency electrical testing in liquid He at near 4.2 K in temperature. Test chips each have 12 various sized square junctions with side dimensions on the lithography mask designed from 0.8 μm up to 5 μm . We have chosen to use the parameter $R_N A$ (product of normal state resistance and junction area) rather than current density because this value is derived by statistically fitting the measured R_N with the junction dimensions. Since the gap voltage (V_g) is typically 3.5 mV, current density (J_c) can be calculated by the Ambegaokar-Baratoff relation $J_c R_N A = \pi V_g / 4$. [12]

a. Bias variation

Figure 4 is a plot of junction $R_N A$ product for DC floating potential values ranging from -35 to -80 V. This data only exists for system #2 at the present time. The background nitrogen pressure is held constant at 20 mTorr and exposure time is between 1-2 minutes. Corresponding junction quality is also plotted as the ratio of sub-gap resistance at 2 mV to normal state resistance (R_{sg}/R_N). Increasing the floating potential means that both ion energy and density will be increased. The $R_N A$ value does increase and it is inferred that AlN thickness grows faster by increasing bias. Junction quality (R_{sg}/R_N) improves up to the point near 75eV where sputtering thresholds cause surface damage. The $R_N A$ values presented in Figure 4 are rather low, therefore, this apparent improvement could also simply result from reducing "pin-hole" density as the AlN_x grows.

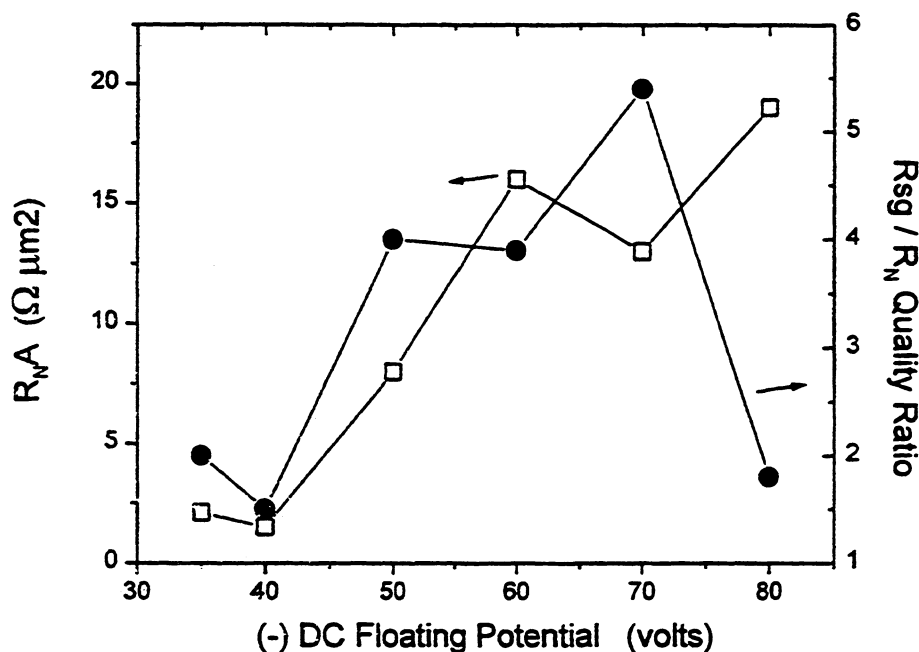


Figure 4. (a) $R_N A$ and corresponding (\bullet) R_{sg}/R_N as bias voltage is varied. 1-2 minutes at 20mTorr N_2 in System #2

b. Exposure time

We also investigated the effect of the duration of plasma exposure as a control parameter for $R_{N}A$. Figure 5 shows how $R_{N}A$ varies with exposure times from 30seconds up to 5 minutes for two different vacuum systems. Nitrogen pressure is again held at 20 mTorr for both systems. DC floating potential is held at -35V for system #1 and -25V for system #2. Lines are drawn to guide the eye only. Data for system #1 seems to show a higher rate of AlN_x formation than for system #2. Both systems were driven by low energy plasmas, but the substrates did come out of system #1 at a hotter temperature. Scatter in the data for 60 second exposure times demonstrates the difficulty with run-to run reproducibility. Corresponding R_{sg}/R_N is not plotted, but it should be noted our highest quality junctions ($R_{sg}/R_N \sim 20$) were produced with exposures between 1 to 2 minutes in system #1.

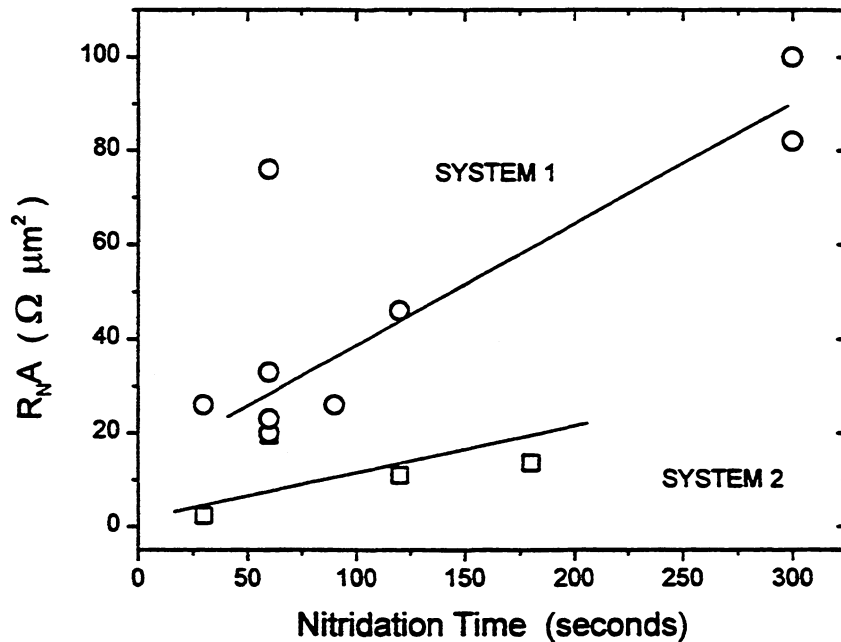


Figure 5. Junction $R_{N}A$ vs plasma exposure time for (o) system #1 and (□) system #2, 20mTorr N_2 and approximately -30V.

c. N₂ Pressure variation

Figure 6 demonstrates the result of nitrogen pressure variation between 5 to 25 mTorr for system #1 and between 20 to 40 mTorr for system #2.. Pressure ranges were determined by plasma constraints and a desire for R_{NA} values near $20 \Omega \mu\text{m}^2$. Here the DC floating potential is held constant at approximately -30V and exposure time is fixed to 1 minute since those conditions seemed to be optimum from previous data sets for the current density of interest. R_{NA} is presented on a logarithmic scale because of its range. Data for system #1 is inconclusive since there is so much scatter, but data for system #2 does exhibit a trend between 25-37 mTorr. A value at 35 mTorr was reproduced once. Here the general trend of increasing R_{NA} with nitrogen pressure is expected thermodynamically since the nitride growth should increase with pressure.

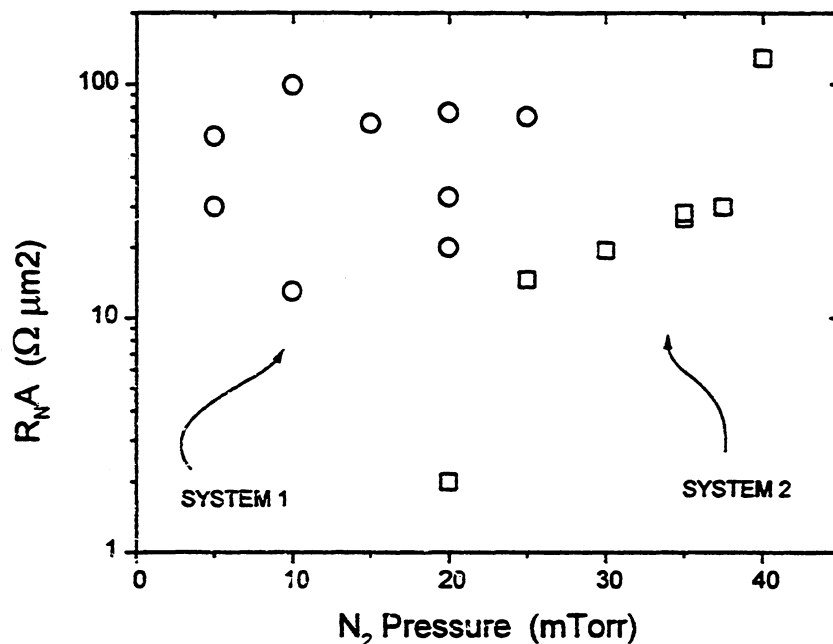


Figure 6. N₂ pressure effect on RNA product for (o) system #1 and (□) system #2 60second exposure, approximately -30V.

d. Junction quality

Quality of junctions produced under many different nitridation conditions is plotted in Figure 7 as the resistance ratio R_{sg}/R_N against junction $R_N A$ product. Most of the data for both vacuum systems is clustered around $R_N A = 20 \Omega \mu m^2$ since that is the current design target for mixer applications. Values plotted for R_{sg}/R_N are obtained from statistics on 10 or more junctions of the size range given above which do not have extraneous processing flaws. System #1 produced the best junctions with the highest average ratio of 18 for $R_N A = 69 \Omega \mu m^2$. Larger $R_N A$ junctions may show higher quality, but processing is not optimized around high $R_N A$ in this set of experiments. System #2 has never produced a junction with R_{sg}/R_N above about 10. There is a trend exhibited in both systems to rapidly change junction quality in the range between 10 to $30 \Omega \mu m^2$. Junctions down to $4 \Omega \mu m^2$ have been made with resistance ratio of more than 5.

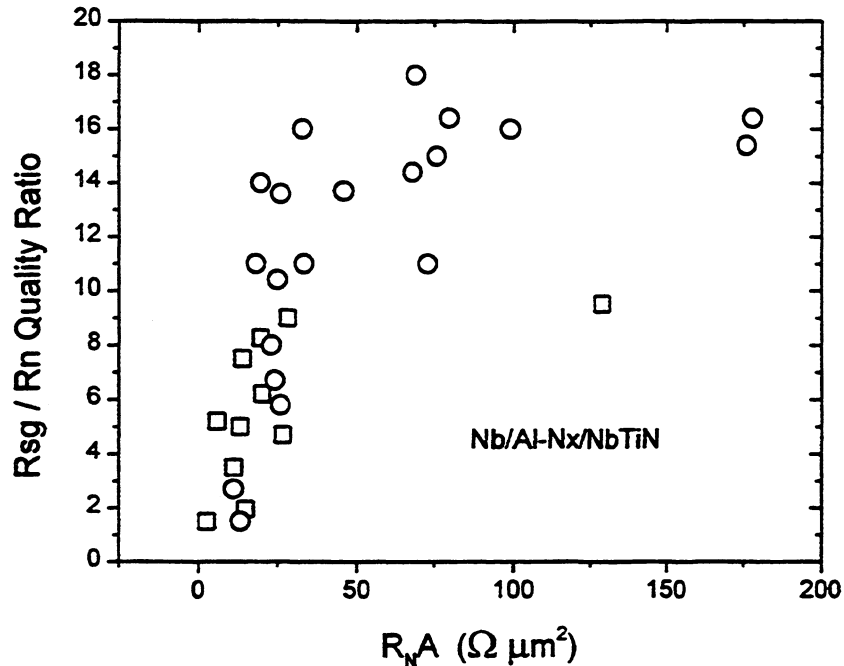


Figure 7. Resistance ratio vs $R_N A$ for (o) system #1 and (□) system #2 for various RF plasma nitridation conditions.

CONCLUSIONS

We have presented our results from process development of Nb/Al-N_x/NbTiN junctions which is focused on RF plasma nitridation of the aluminum proximity layer. System #1 is shown to produce the higher quality junctions, but system #2 seems to have more controllable and reproducible results. SIS mixers with $R_{N/A} = 20 \Omega \mu\text{m}^2$ and resistance ratios of 15 can be fabricated by this method if run-to-run variations are acceptable. Other experimental data on temperature control are needed. It is anticipated that nitride junctions will benefit from higher temperature processing because of improvement in the NbTiN quality, but there is still a question of control for $R_{N/A}$ values of interest. Another avenue of investigation is to thermally nitride the aluminum with NH₃. We think that the voltage gap of 3.5mV will bring a significant improvement in bias range for THz SIS receivers. Low noise temperatures should result from low-loss NbTiN tuning circuits combined with the junction's sharp I-V behavior.

ACKNOWLEDGEMENTS

This research was performed by the Center for Space Microelectronics Technology, Jet Propulsion Laboratory, California Institute of Technology, and was sponsored by the National Aeronautics and Space Administration, the Office of Space Science.

REFERENCES

- [1] J.W. Kooi, J.A. Stern, G. Chattadpadhyay, H.G. LeDuc, B. Bumble, and J. Zmuidzinas, "Low-loss NbTiN films for THz SIS mixer tuning circuits," *Int. J. IR and MM Waves* **19**, 1998 (in press).
- [2] M. Bin, M.C. Gaidis, J. Zmuidzinas, T.G. Phillips, and H.G. LeDuc, "Low-noise 1 THz niobium superconducting tunnel junction mixer with normal metal tuning circuit," *Appl. Phys. Lett.* **68**, pp.1714-1716, 1996.
- [3] A. Karpov, B. Plather, and J. Blondel, "Noise and gain in frequency mixers with NbN SIS junctions," *IEEE Trans. Applied Superconductivity* **7**, pp.1077-1080, 1997.
- [4] Z. Wang, A. Kawakami, Y. Uzawa, and B. Komiyama, "High critical current density NbN/AlN/NbN tunnel junctions fabricated on ambient temperature MgO substrates," *Appl. Phys. Lett.* **64**, pp. 2034-2036, 1994
- [5] R. Di Leo, A. Nigro, G. Nobile, and R. Vaglio, "Niobium- titanium nitride thin films for superconducting rf accelerator cavities," *J. Low Temp. Phys.* **78**, pp. 41-50, 1990

- [6] J. Zmuidzinas, J. Kooi, J. Kawamura, G. Chattopadhyay, B. Bumble, H.G.LeDuc, J.A. Stern, "Development of SIS mixers for 1 THz," Proceedings of SPIE (to be published), 1998.
- [7]] T. Imamura and S.Hasuo, "Cross-sectional TEM observation of Nb/Al-Ox - Al/Nb Junction structures," IEEE Trans. Mag. **27**, No.2, pp.3172-3175, 1991.
- [8] O.Kubaschwski and C.B. Alcock, *Metalurgical Thermochemistry*, 5th Ed., Pergamon Press, 1979.
- [9] G. Lewicki and C.A. Mead, "Currents through thin films of aluminum nitride," J. Phys. Chem. Solids **29**,pp.1255-1267, 1968.
- [10] T. Shiota, T. Imamura, and S. Hasuo, "Nb Josephon junction with an AlN_x barrier made by plasma nitridation," Appl. Phys. Lett. **61**, pp. 1228-1230, 1992.
- [11] J. Stern, B. Bumble, H. LeDuc, "Fabrication and DC characterization of mixers for use between 600 and 1200 GHz," (these proceedings)
- [12] Ambegakor and A. Baratoff,. "Tunneling between superconductors," Phys. Rev Lett. **10**, pp. 486-491, 1963.

FABRICATION AND DC-CHARACTERIZATION OF NbTiN BASED SIS MIXERS FOR USE BETWEEN 600 AND 1200 GHz*

J. A. Stern, B. Bumble and H. G. LeDuc, Center for Space Microelectronics Technology--
Jet Propulsion Laboratory, Pasadena CA 91109.

J.W. Kooi and J. Zmuidzinas, California Institute of Technology, Pasadena, CA 91106.

SIS mixers incorporating two-junction, NbTiN tuning-circuits have been designed and fabricated using two different types of tunnel-junctions. The first type of tunnel junction--NbTiN/MgO/NbTiN--has the advantage of a large gap voltage (5 mV), but has a relatively soft I-V characteristic and high specific capacitance as compared to Nb/Al-O_x/Nb tunnel-junctions. The second type of junction--Nb/Al-AlN_x/NbTiN, is a hybrid structure, which has many of the advantages of Nb junctions, with a slightly larger energy gap voltage (3.5 mV) and more robust thermal properties. A detailed description of the deposition techniques used in making the AlN_x devices will be given in a separate paper¹. In this paper, we discuss the deposition of high-quality NbTiN films, and the trade-off between stress and quality in these films. We also discuss the deposition details for the NbTiN/MgO/NbTiN junctions. We measured the magnetic-penetration-depth of our NbTiN films with SQUID circuits. Using long resonators coupled to Josephson junctions, we measured propagation velocities for our microstrip-line circuits; this measurement gave us an independent estimate of the NbTiN magnetic-penetration-depth and a qualitative measure of RF-losses in the microstrip-lines.

Introduction

With the upcoming construction of the Far Infrared Space Telescope (FIRST) and of NASA's new airborne observatory (SOPHIA), low-noise heterodyne receivers are needed for the frequency band of 700 to 1200 GHz^{2,3}. For frequencies below 700 GHz, niobium-based SIS mixers provide nearly quantum limited performance.⁴ However, above 700 GHz, Nb has significant RF-losses, so although Nb-based SIS tunnel junctions are still viable mixer elements, the Nb-tuning circuits used to tune out the junction capacitance do not perform well.

One alternative is to use Nb tunnel-junctions with normal metal tuning circuits.⁵ A better solution is to use a superconductor with a larger energy-gap that will be nearly lossless, for the tuning circuit. Previously we demonstrated that NbTiN was an excellent candidate for low loss tuning circuits at these high frequencies, and we achieved state-of-the-art mixer results at 649 GHz, with a hybrid Nb-mixer using a NbTiN ground-plane.⁶ Our next step is to fabricate SIS mixers with all NbTiN tuning circuits. If we use all Nb tunnel junctions in these structures, the NbTiN layers will trap quasi-particles in the junction region,

* This work is supported by the NASA Office of Space Science through the Center for Space Microelectronics Technology

which will degrade our mixer I-V characteristics. We would like to replace one or both of the junction electrodes with NbTiN to reduce or eliminate this quasi-particle trapping. To accomplish this, we are fabricating SIS mixers using two distinct junction-technologies (NbTiN/MgO/NbTiN and Nb/Al-AlN_x/NbTiN.)

NbTiN Film Deposition and Characterization

NbTiN films are deposited by reactive DC-magnetron sputtering from a Nb-Ti alloy target in a mixture of argon and nitrogen. The vacuum chamber used is pumped by an 20 cm diameter cryopump and typically has a base pressure of 1×10^{-8} Torr. 7.6 cm diameter MAC sputter sources from US Thin Films Inc. are used, and the target to substrate separation is approximately 6 cm. A constant Ar flow of 150 sccm was used for all of our depositions; the N₂ flow was varied between 9 and 15 sccm (typically 13) to optimize the NbTiN's properties. High-purity Nb and Ti starting materials are vacuum-arc-remelted to make the Nb-Ti alloy targets.⁷ Despite this, we had some difficulty with metal impurities in some of our targets, and x-ray photoemission spectroscopy was necessary to determine the "good" quality targets. We have evaluated several different ratios of Nb to Ti, however, all of our device work was done with 78% Nb to 22% Ti by weight. There are many ways to characterize our NbTiN films, however, we are primarily interested in is the RF-losses of our films in the terahertz frequency range. Since it is extremely difficult to measure RF-losses at these frequencies, we instead focus on two DC properties to evaluate

our film quality. The transition temperature of the films should be above 15 K, so the energy gap will be greater than 2.5 meV; this is a minimum requirement for use at 1.2 THz. In addition, the resistivity of the films just above the transition temperature (typically measured at 20 K) is also a good indicator of film quality with lower resistivities being desirable.

The highest quality NbTiN films are under compressive stress. Since excessive stress is a problem in device fabrication, it is important to measure stress in our films. Film stress was measured by observing the deflection in long, narrow glass or silicon "beams" with NbTiN films deposited on them⁸. The deflection is measured over several millimeters using a Tencor profilometer. Although this method is only accurate to 20 or 30%, it does give us an adequate way to screen out bad films, which would cause a problem in device processing.

The best quality NbTiN films are made by applying an RF-bias at 13.56 MHz to the substrate during the film growth. We believe this increases the quality of our films through added ion-bombardment and electron heating of the film surface. This technique increases the film T_c by a small amount, and it lowers the low-temperature resistance of the films significantly. The disadvantage of this technique is that these films have higher compressive-stress than films deposited with a grounded substrate. Table 1 shows typical deposition conditions and properties for some of our NbTiN films. Also listed in this table are several films with higher titanium concentrations. These films are interesting because they have lower resistivities, but their lower T_cs mean their energy gaps will be too low

for use at 1200 GHz. As our targets erode, the sputter conditions need to be continually optimized, however, several general statements seem to hold: the deposition rate should be approximately 40 nm/min for bias sputtered films and 50 nm/min for unbiased films. If the RF-bias is too large ($V_{DC} < -75$ V), nitrogen is resputtered from the film. High quality films can be grown with higher RF-bias

levels, however the optimal nitrogen level is then a strong function of the RF-bias level. To avoid this complication, most of our films are grown with a DC-bias of -50 V, which corresponds to roughly 4 or 5 Watts of absorbed power. Finally, lower pressures and/or higher deposition rates lead to higher quality films, but also to greater compressive stress.

Table 1

Substrate/ Temp.	Pressure (mTorr)	DC-bias (Volts)	Sputter Current (Amps)	Sputter Voltage (Volts)	Rate (nm/min)	σ (dynes/ cm ²)	T _c (K)	ρ_{20K} ($\mu\Omega$ -cm)
Oxidized Si	6.0	0	1.06	-230	50	6×10^9	15.2	81
Glass	5.0	-50	0.90	-246	38	2.5×10^{10}	16.3	56
Oxidized Si	5.0	-50	0.85	-261	45	5×10^9	15.3	63
Mgo/450° C	5.0	-50	1.25	-266	52	-	17.0	37
Si (Nb-Ti 70-30%)	6.0	-40	1.10	-226	44	-	14.6	46
Si (Nb-Ti 65-35%)	5.0	-50	1.20	-295	68	-	13.8	40

Tunnel Junction Fabrication

Fabrication of NbTiN-based tunnel junctions is similar to that of NbN based junctions⁹. There are several differences however. The biggest difference is in controlling the effects of compressive stress in NbTiN. Bias-sputtered NbTiN has the higher compressive stress, and we use it only as a ground plane. If the stress in the ground plane is less than 5×10^{10} dyne/cm² and the substrate surface is clean, we have no problems getting our films to adhere to the substrate. Before depositing our films we typically use an RF Ar-ion clean at -150 V and then deposit a thin MgO buffer layer. Stress in the counter electrode can also cause

problems. The counter electrode must be kept thin (50 nm) to avoid stress relief after the junction-etch. Finally, to make electrical contact to the tunnel junction and to avoid the wiring layer from deadhering from the devices, we use an Ar-ion clean at -150 V. Stress in the wiring layer is kept below 1×10^{10} dyne/cm².

Our tunnel junctions are patterned using photolithography and reactive ion etching (RIE). Three different gas mixtures are used in our processing. The first step is generally an Ar pre-clean at 30 mT and 120 Watts. With one exception, Nb and NbTiN films are etched in a mixture of CF₂C₂ (16 sccm) CF₄ (4 sccm) and O₂ (3 sccm), at 30 mT and 133 Watts. This mixture of gases provides an anisotropic

etch of both Nb and NbTiN. After using this mixture, the wafer is rinsed in water to remove chlorine salts, which can degrade the device's properties over time. For the last minute of the wire etches, we use a different mixture (CF_4 --15 sccm and O_2 --2 sccm); this is also done to reduce problems with chlorine-salts.

For the hybrid mixers, the junction etch is extremely important because it must go through the Nb counter-electrode, but not the underlying NbTiN ground plane. A similar problem exists for the Nb/Al- O_x /Nb hybrid junctions with the Al tuning circuits. We use a pair of etch monitor samples to accurately control the etch times during the junction etch. The first monitor has only the NbTiN counter electrode, and the second has the complete tunnel-junction without the ground-plane. The junction etch consists of an Ar preclean, followed by the counter-electrode etch, which is terminated as soon as the first monitor clears. It is important to stop this step promptly, or an aluminum-fluoride layer is formed, which is difficult to remove. The Al- AlN_x barrier is removed with an Ar etch followed by the Nb counter-electrode etch; this etch is terminated when the second monitor clears. The final etch step is a 1 minute Ar clean to ensure the SiO layer adheres well to the ground plane.

NbTiN/MgO/NbTiN Deposition

Trilayer

Trilayer deposition for NbTiN/MgO/NbTiN junctions is virtually identical to that of NbN/MgO/NbN junctions. The base-electrode of our NbTiN/MgO/NbTiN mixers was typically 280 nm and is deposited with an RF bias. Next, the MgO barrier was RF-sputtered from a pressed MgO target. To reduce the

deposition rate and promote more uniform coverage, the substrate is swept over the source in a circular arc. After the MgO deposition, the substrate is exposed to a brief oxygen-plasma glow discharge to cure pinholes in the barrier. Finally a thin (50 nm) NbTiN counter-electrode is deposited with the substrate holder grounded.

NbTiN/Nb/Al- AlN_x /NbTiN Hybrid-Junction Deposition

The ground plane of the hybrid-junctions is identical to the NbTiN/MgO/NbTiN junctions. The Nb base-electrode (typically 30 nm) is deposited immediately following the ground plane. The deposition conditions for this layer are optimized for T_c and to yield a slight compressive stress ($2\text{-}5 \times 10^9$ dynes/cm²). As is the case with Nb/Al- O_x /Nb junctions, this small amount of compressive stress seems to give smoother Nb films and better quality devices¹⁰. A thin (6-9 nm) Al layer is deposited on top of the Nb; to promote uniform coverage, the substrate holder is swept over the Al target during deposition. The aluminum-nitride barrier is formed by applying an RF-bias to the substrate for approximately 1 minute while it is in a nitrogen ambient (20 mT.) The DC-bias voltage during the nitridation is typically -50 V. This process is discussed in greater detail elsewhere in these proceedings¹. Finally the 50 nm NbTiN counter-electrode is deposited with the substrate grounded. In some cases, we heated the substrate to approximately 250° C before depositing the counter-electrode. The quality of these devices seemed to be slightly better than

the conventional ones, but the results were not conclusive.

Twin-Slot Mixer Design and Fabrication

We have fabricated a number of mixer chips for use in Caltech's twin-slot receiver.¹¹ The first mixers we fabricated used a mask set designed for hybrid Nb/Al-O_x/Nb tunnel junctions and Al wiring. Fabrication of these junctions went very well, but the mask was not designed properly, so mixer results were not optimal. As a result, a new mask set was designed with several changes. We went from a contact mask-aligner to an I-line stepper. The stepper allowed us to reduce the junction size from 1.1, 1.3 and 1.5 μm to 0.7, 0.8 and 0.9 μm , which was deemed necessary to push the operating frequency above 1 THz. The improved layer-to-layer alignment of the stepper (approximately 0.5 μm) also allowed us to reduce our line widths from 2 to 1 μm , thus reducing the parasitic capacitance at the IF-frequency. Because we were concerned about the adhesion of the wiring layer, the second SiO insulation layer was not used. Figure 1 is an optical photograph of an 1150 GHz mixer chip. An unfortunate result of the above changes was an increased chance of open circuits or series weak-links at places where the narrow (2 μm) wire crossed over the edge of the trilayer. This is particularly a problem because a series link in the second crossover does not show up in the DC I-V characteristic because the $\frac{1}{4}$ wavelength-short is an open circuit at DC frequencies. In past designs, the second SiO layer, which was deposited while rotating the substrate at a

slight angle, made the step edge smoother. The second SiO layer reduced parallel shorts at these crossovers. In addition, Nb-based trilayers are defined with a liftoff stencil, so the trilayer edge is tapered, thus reducing step-edge problems. A new mask using wider lines at the crossovers and a second SiO layer is now being designed. We also intend to increase the thickness of our wiring layer from 400 to 600 nm to reduce this problem.

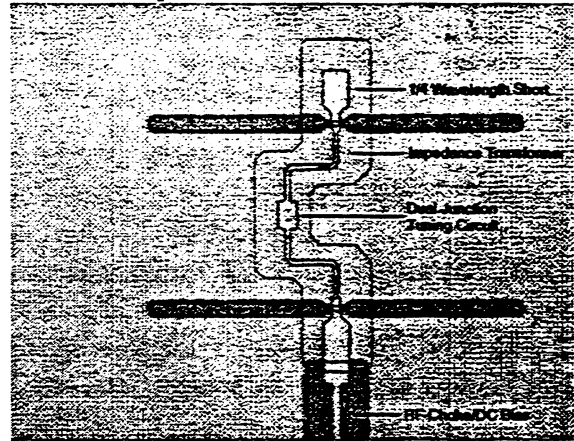


Figure 1: 1150 GHz Twin-Slot Mixer.

Current-Voltage Characteristics of Mixers

Despite the problems we encountered in fabricating mixers using the new mask design, we were able to deliver many devices. Most of these devices exhibited lead switching somewhere between 5 and 10 mV. These devices could be tested in an FTS, where the DC bias is well below the switching threshold, however, the switching-level shifts down in voltage as LO power is applied, so these devices made poor mixers. Detailed mixer and FTS results are given elsewhere in this proceeding.¹²

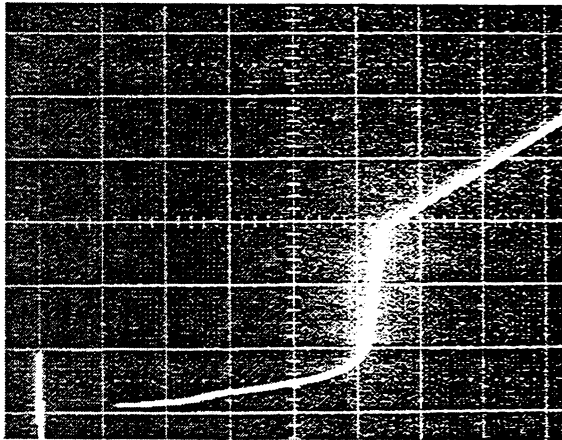


Figure 2: I-V characteristic of a 650 GHz NbTiN/MgO/NbTiN mixer (20 μ A, 1mV/div).

Figure 2 is an I-V characteristic of a NbTiN/MgO/NbTiN mixer (two 0.8 μ m junctions in parallel). The I-V characteristic is nearly identical to an all-NbN device. In high R_{NA} (100 $\Omega \mu\text{m}^2$) devices, the sum-gap voltage is typically 5.2-5.3 mV. As R_{NA} decreases, the gap voltage decreases due to self-heating. These I-Vs are fairly “soft” in comparison to a Nb/Al-O_x/Nb device, having excess leakage above half the gap voltage, and a broad turn on at gap voltage. Nonetheless we have achieved respectable mixer results with these devices ($T_R=250$ K at 638 GHz)¹³. The largest disadvantage these mixers suffer is their increased capacitance as compared to Nb mixers⁹, which causes significantly narrower RF-bandwidths, and makes it more difficult to properly design mixer circuits.

Figure 3 is an I-V characteristic of a NbTiN/Nb/Al-AlN_x/NbTiN test junction. As compared to the NbTiN/MgO/NbTiN device, this I-V characteristic has much lower leakage and a sharper current-rise at the gap-voltage. In addition, the gap voltage (3.35 mV in this case and typically 3.5 mV) is significantly larger

than that of a Nb/Al-O_x/Nb mixer (2.9 mV). An increase in gap voltage of 0.6 mV corresponds to an increase in available DC-bias range of 1.2 mV, which is significant for a THz mixer. The best mixer performance with NbTiN/Nb/Al-AlN_x/NbTiN mixers is $T_R=195$ K at 582 GHz⁶, however the conversion loss was 9.6dB, so there may have been some other problem with this mixer.

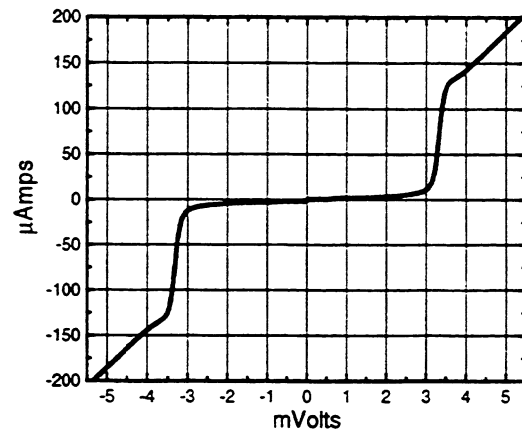


Figure 3: I-V characteristic of a 1.1 μ m NbTiN/Nb/AlN/NbTiN test device ($R_{NA}=29 \Omega\mu\text{m}^2$)

One additional advantage of aluminum-nitride barriers over aluminum-oxide barriers is that they survive much higher temperatures. Niobium/aluminum-oxide junctions begin to degrade at temperatures as low as 130° C. We have baked our completed NbTiN/Nb/Al-AlN_x/NbTiN junctions at temperatures up to 294° C in air with only a 10% increase in R_N . The gap voltage of the devices did not change, and the subgap leakage-current did not increase. As a result of the temperature insensitivity, wiring layers can be deposited at elevated temperatures to improve their properties; however, this was not typically done.

Josephson Resonances in NbTiN Circuits

A Josephson junction oscillates at a frequency that is proportional to the voltage applied to it ($\nu = V \times 484 \text{ GHz/mV}$, where ν is the frequency and V is the voltage). When a Josephson junction is connected to an electrical circuit with a high-Q resonance, steps will appear in the I-V characteristic at voltages corresponding to the frequency of the resonance. We can use this phenomenon to determine the resonance-frequency of our mixer tuning-circuits. By making circuits with long micro-strip line resonators, we can also measure the propagation velocity of our micro-strip lines^{14,15}. Also, since these lines are long, the circuit will not be high-Q, if there is significant loss in the NbTiN films. Thus the presence of a high frequency resonance is an indication of low loss in our NbTiN films.

Figure 4 is an I-V characteristic of a NbTiN/Nb/Al-AlN_x/NbTiN mixer with the subgap region expanded to 2 $\mu\text{A}/\text{div}$. There is a resonance at 2.05 mV, which corresponds to 990 GHz. The current rise at the resonance is roughly 10% or the current rise at the gap-voltage, indicating the tuning circuit is low loss.

Figure 5 is an I-V characteristic of a hybrid-junction connected to a 500 μm long NbTiN/SiO/NbTiN microstrip-line. Clear resonances are observable up to 1.9 mV with weaker resonances also observable up to 2.2 mV; this corresponds to frequencies of 920 and 1060 GHz respectively. At 1 THz, the microstrip-line is approximately 20 wavelengths long. Therefore, based on these resonances we are fairly confident our NbTiN films have reasonably low loss at 1 THz. Using

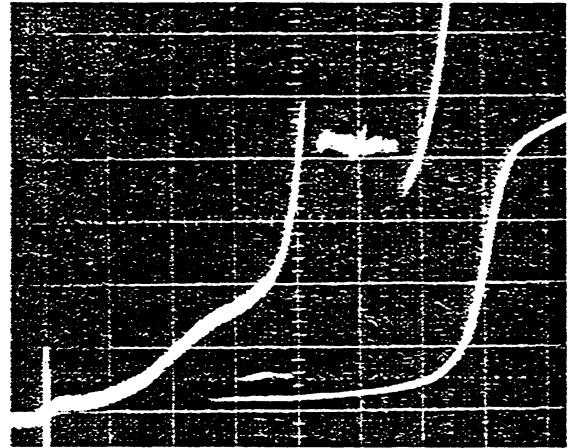


Figure 4: I-V characteristic of an 1150 GHz, 0.7 μm , NbTiN/Nb/Al-AlN_x/NbTiN mixer (20 μA , 500 $\mu\text{V}/\text{div}$)

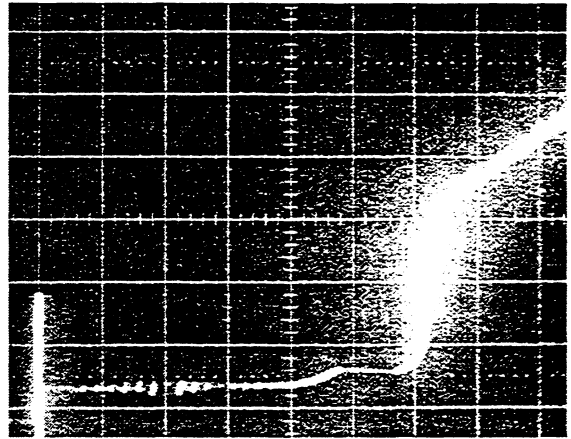


Figure 5: I-V characteristic of a hybrid junction connected to a 500 μm , open-ended microstrip-line stub (20 μA , 500 $\mu\text{V}/\text{div}$.)

on this device and others we estimate the magnetic penetration-depth of our films to be between 200 and 250 nm. It should be noted that this measurement assumes the penetration depth of the base and wire-electrodes are equal, which is not true in general. As a result, the penetration depth we calculate is an average value for the ground-plane and wiring layer. Nonetheless, this data agrees well with calculations using the BCS relation between magnetic penetration-depth, resistivity and T_c .

$$\lambda \approx 100nm \times \sqrt{\frac{\rho(\mu\Omega cm)}{T_c(K)}}$$

Using typical values of $T_c=15.2$ K and $\rho=70 \mu\Omega$ cm implies that $\lambda=215$ nm.

SQUID Measurement of NbTiN Magnetic Penetration-Depth

We can also measure the penetration depth of our films using DC-SQUIDS.¹⁶ The geometry of our SQUIDS is a microstrip-line with two junctions connecting the microstrip-line to the ground-plane. By running a control current along the microstrip-line and observing the periodicity of the SQUID modulation, we obtain the inductance of the microstrip-line. We can then calculate the penetration depth of the NbTiN films, although again we are assuming the ground-plane and wiring electrode have the same penetration-depth. These SQUID measurements yield a magnetic penetration-depth of 200-230 nm, which agrees well with our other data. We had hoped to measure the specific capacitance of our devices using these same SQUIDS, but we did not have sufficient time.

Conclusions and Future Work

Mixer results at 600 GHz, and Josephson resonances indicate that NbTiN has very low RF-losses for frequencies below 1 THz. We anticipate excellent mixer performance with both NbTiN/MgO/NbTiN and Nb/Al-AlN_x/NbTiN SIS tunnel junctions at 1 THz. However, we would like to use SIS mixers for frequencies up to 1.2 THz. Based on our all-NbTiN junctions, The gap voltage of our NbTiN films is at least 2.6 mV, so in theory we will be able to get low-loss structures up to 1260 GHz. At

this time, we have no data on what our losses are above 1.0 THz. If necessary, we can heat our substrates during the deposition of our NbTiN and we can grow our ground planes on single-crystal MgO substrates to reduce the losses of our NbTiN microstrip-lines:

We are just beginning to design and test Terahertz mixers. One of our primary goals is to get agreement between our theoretical models and our experimental results, so we can design future receivers more accurately. From a fabrication standpoint, we need to produce many devices with identical I-V characteristics, so RF results from several different tuning circuits can be directly compared. In addition, we need to have good DC characterization of R_{NA} , magnetic penetration-depth and junction capacitance. Thus far, we were not able to fabricate NbTiN mixers using our new mask set, which had the correct R_{NA} , high yields and without series weak-links. We are currently redesigning our mask set to reduce problems at ground-plane crossovers. We are also having great difficulty controlling run-to-run variation in the R_{NA} of Nb/Al-AlN_x/NbTiN junctions¹, and we are looking at a number of possible solutions to this¹.

¹ B. Bumble, H.G. LeDuc, and J.A. Stern "Fabrication of Nb/Al-N_x/NbTiN Junctions for SIS Mixer Applications Above 1 THz," *This Proceedings*, 1998.

² J. Zmuidzinas, G. Blake, J. Keene, T. Phillips, N. Erickson, P. Goldsmith, A. Harris, M. Morris, W. Langer, H. LeDuc, and W. McGrath, "A submillimeter/far-IR heterodyne receiver for SOFIA," #09.06, *Bull. American Astron. Soc.* **191**, Dec. 1997.

³ T.G. Phillips, J. Zmuidzinas, W.D. Langer, C. Lawrence, and J. Pearson, "The FIRST mission," #41.21, *Bull. American Astron. Soc.* **191**, Dec. 1997.

-
- ⁴ J. Carlstrom and J. Zmuidzinas, "Millimeter and submillimeter techniques," in *Review of Radio Science 1993-1996*, W.R. Stone, ed., pp. 839-82, Oxford University Press, 1996.
- ⁵ M. Bin, M. C. Gaidis, J. Zmuidzinas, T. G. Phillips, and H.G. LeDuc, "Low-Noise 1 THz niobium superconducting tunnel junction mixer with normal metal tuning circuit," *Appl. Phys. Lett.* **68**, pp. 1714-16, 1996.
- ⁶ J.W. Kooi, J.A. Stern, G. Chattopadhyay, H.G. LeDuc, B. Bumble, J. Zmuidzinas, "Low-Loss NbTiN Films for THz SIS Mixer Tuning Circuits," *J. IR and MM Waves*, **19**, 1998 (in press).
- ⁷ Targets were supplied by Angstrom Sciences, 1200 Lebanon Rd, W. Mifflin, PA 15122.
- ⁸ G.G. Stoney, *Proc. R. Soc. London Ser., A* **82**, p. 172, 1908.
- ⁹ J.A. Stern, B.D. Hunt, H.G. LeDuc, A. Judas, W.R. McGrath, S.R. Cypher, and S.K. Khanna, "NbN/MgO/NbN SIS Tunnel Junctions for Submm Wave Mixers," *IEEE Trans. Magn.*, **MAG-25**, 1989.
- ¹⁰ T. Imamura, "Fabrication of high quality Nb/AlO_x-Al/Nb Josephson junctions: Sputtered Nb films for junction electrodes," *IEEE Trans. Appl. Superconductivity*, **2**, March 1992.
- ¹¹ J. Zmuidzinas and H.G. LeDuc, "Quasi-optical slot antenna SIS mixers," *IEEE Trans. Microwave Theory Tech.*, **MTT-40**, 1797-1804, 1992.
- ¹² J.W. Kooi, J. Kawamura, G. Chattopadhyay, J. Zmuidzinas, J.A. Stern, H.G. LeDuc, and B. Bumble, "Low-loss NbTiN films for THz SIS mixer tuning circuits," *these proceedings*.
- ¹³ J. Zmuidzinas, J. Kooi, J. Kawamura, G. Chattopadhyay, B. Bumble, H.G. LeDuc, and J.A. Stern, "Development of SIS mixers for 1 THz," *submitted to the proceedings of the SPIE*, 1998.
- ¹⁴ R.L. Kautz, "Picosecond Pulses on Superconducting Striplines," *J. Appl. Phys.*, **49**, pp.308-314, 1978.
- ¹⁵ A.V. Räisänen, W.R. McGrath, P.L. Richards, and F.L. Lloyd, "Broad-Band RF Match to a Millimeter-Wave SIS Quasiparticle Mixer," *IEEE Trans. Microwave Theory and Tech.*, **MTT-33**, 1985.
- ¹⁶ J.H. Magerlein, "Specific Capacitance of Josephson Tunnel Junctions," *IEEE Trans. Magn.*, **MAG-17**, pp. 286-289, 1981.

A 4×1 GHz Array Acousto-Optical Spectrometer for air- and spaceborne observations in the submm-region

J. Horn^{(2),(1)}, C. Macke⁽¹⁾, F. Schlöder⁽¹⁾, F. Schmülling⁽¹⁾, O. Siebertz⁽¹⁾
and R. Schieder⁽¹⁾

⁽¹⁾: I. Physikalisches Institut, Universität Köln,
Zülpicher Str. 77, 50937 Köln, Germany

⁽²⁾: University of California at Los Angeles,
405 Hilgard Av, CA 90024 Los Angeles, USA
email: horn@jupiter.astro.ucla.edu

March 17, 1998

Abstract

In this paper an array acousto-optical spectrometer (AOS) with four 1 GHz bands and a frequency channel spacing of 1 MHz is presented. The test results of the array AOS are comparable to those of the space-qualified AOS for the Submillimeter Wave Astronomy Satellite (SWAS). Allan variance tests, longtime integration tests and investigations of the relative stability between the four bands are presented. The Allan variance minimum time was found to be at least 1000s, which is one of the best results observed for broadband AOSs so far. Performance tests of the different bands revealed an identical frequency response. Therefore the relative stability of two simultaneous measured baselines is extraordinary, so that correlated noise can be eliminated efficiently. Recently the Array AOS has been in operation for 2 months at the IRAM 30m telescope. From this test-run, several results present the competitiveness of AOSs compared to filterbanks and hybrid autocorrelators. In an upgraded design concept the second generation array AOS will be more compact and reliable. This version will be operated not only on ground-based observatories like KOSMA or AST/RO, but also on airborne and spaceborne facilities like SOFIA and FIRST.

Keywords: Radio Astronomy, Acousto-Optical Spectrometer, Backends, Radiometers, Heterodyne Instrumentation, Array Receivers

1 Introduction

In the recent years the worldwide development of large bandwidth, multi-frequency or multi-beam receivers has incited a demand on corresponding backends. In the submillimeter wavelength range and of course in the THz region, the requirements in bandwidth increase drastically. At the same time it might be necessary to have relatively high resolution at the same time, for frequency surveys e. g. Such requirements hold for atmospheric observations as well, because most atmospheric lines tend to have extended line wings together with rather narrow peaks at the center of the lines. Future airborne or spaceborne observatory projects like SOFIA¹ or FIRST² depend crucially on versatile backend developments in order to achieve a most economic usage of the available equipment with optimum scientific return. At KOSMA³ a new superconducting mixer array frontend with 2×4 channels at 490 and 810 GHz is under development, so that the number of backends needed grows accordingly.

In this paper, the recent development of an array acousto-optical spectrometer (AOS) with 4×1 GHz bandwidth is presented. Its optical layout is discussed with respect to the required specifications for normal operation at radio observatories. The laboratory test results have proven that the specifications have been achieved. To check the performance of the array AOS during observations at a telescope, it has been installed at the IRAM 30m telescope for a two-month test period this early summer. The outcome of these tests did also show an excellent agreement with the expected performance.

¹Stratospheric Observatory for Infrared Astronomy

²Far InfraRed Space Telescope

³Kölner Observatorium für SubMm Astronomie

2 System Design

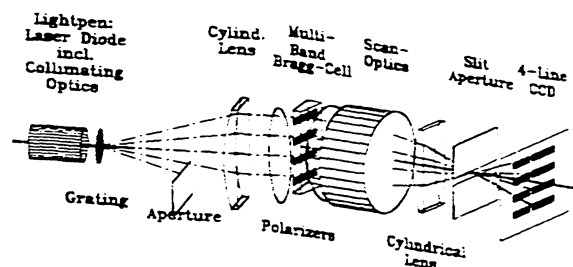


Figure 1: *The principal optical design of the KOSMA 4×1 GHz array AOS*

The principal design of the array AOS is similar to those of the standard KOSMA single-band AOSs such as the one for the Submillimeter Wavelength Astronomy Satellite (SWAS), (Klumb et al., 1994). As shown in Fig. 1, four intermediate frequency (IF) signals, are fed to the array Bragg cell which is made out of a single LiNbO₃ crystal. Through the piezoelectric transducer, an acoustic wave inside the crystal is induced. The acoustic wave produces a periodically

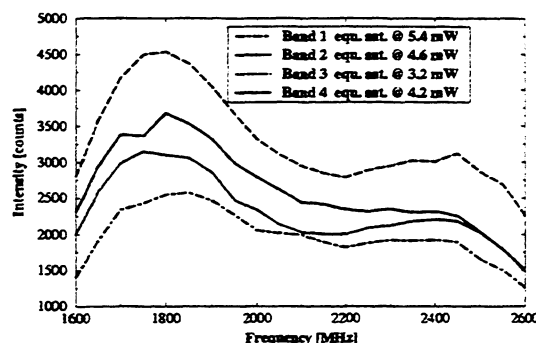


Figure 2: *The bandpasses of the four bands of the array AOS measured with a synthesizer*

varying diffraction index inside the crystal. At the associated phase grating, monochromatic laser light, four beams for each acoustic

active zone produced by means of a holographic grating, is diffracted under the Bragg condition. The first order diffracted laser light is then imaged onto the CCD by means of a scan optics and a cylindrical lens. The Bragg cell is operated in shear wave mode, enabling efficient light scatter reduction by means of two crossed polarizers. The deflected light beams are then imaged onto four independent and parallel CCD lines. Especially the second cylindrical lens is responsible for the exact matching of the beams onto the corresponding CCD line.

With this setup, a high efficiency has been achieved, as can be seen in Fig. 2. The IF power, which is necessary to bring all pixels equalized in saturation, is well below 6 mW for all four bands, yielding a maximum total power level on the crystal of less than 20 mW, which is comparable to the amount of one of our single-band AOSs. Furthermore, the bandpasses have a 3 dB shape over the 1 GHz band, which could be further smoothed by means of an r. f. equalizer if necessary. The problem in such an efficient optical layout is the increasing amount of light scatter collected on the CCD. Former studies have shown, that a strong light scatter level decreases the spectroscopic stability of a spectrometer, which is measured by the maximum total power integration time as a result of the so-called Allan-variance plot (Schieder et al., 1989). By introducing a slit aperture at the beam crossing point, the scattered light could be nearly eliminated in all four bands simultaneously. As a result, extraordinary spectroscopic stabilities have been achieved with the array AOS, as is described in the next section.

To avoid any overlap of the acoustic beams, which would cause unwanted crosstalk between the bands, the transducers are spaced by 1.6 mm. The residual crosstalk measured

is below -30 dB between the bands and purely of electrical origin. This has been confirmed with measurements done by the supplier of the cell, measuring the electrical crosstalk of the IF matching circuit (GEC Marconi, 1995).

3 Performance Tests

3.1 Laboratory tests

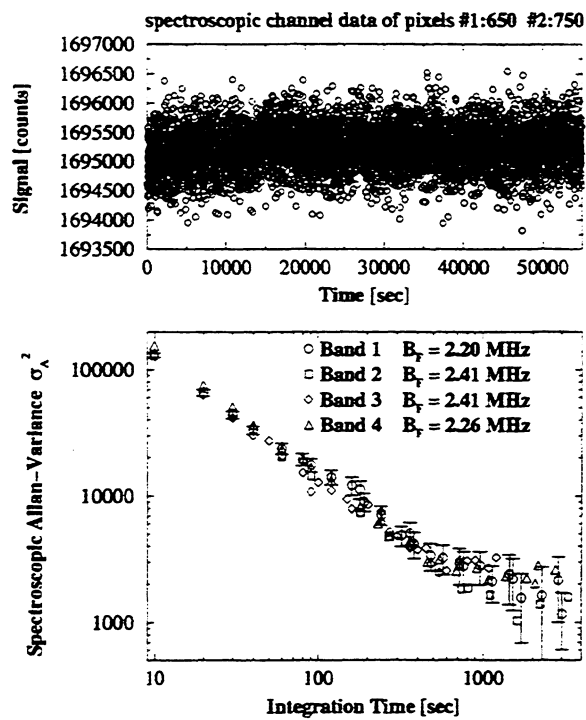


Figure 3: Data of one spectroscopic channel and the spectroscopic Allan-variance plot

One important test parameter is the minimum time of the Allan-variance plot, or the maximum total power integration time, which has been found to be up to 1000 s using a noise source under thermally stable conditions, see Fig. 3. Compared with normal operation, where a minimum time of above 100 s

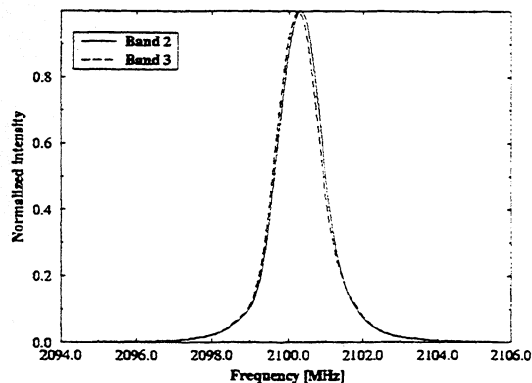


Figure 4: *The filtercurves of two vertically adjacent pixels (in two adjacent AOS bands)*

is enough to guarantee proper measurements, the array AOS is therefore not limiting the measurements.

The identical performance of the different bands has been tested in various ways. First, the bandpasses have shown, that the IF power response of the bands is equal within 2 dB. The differences are partly due to the grating and partly to alignment tolerances. The frequency response has been tested to be identical for two bands as well. Therefore, filtercurves of the same pixel in two adjacent bands have been measured, see Fig. 4. The strong overlap of these curves indicates high radiometric correlation, which can be calculated to be 99.8 %, (Horn, 1997).

To make sure, the filtercurves show such strong overlap along the whole frequency band, the frequency nonlinearity, which typically exist in AOSs, has to be taken into account. This nonlinearity has been measured in all four bands to be identical over the whole 1 GHz bandwidth. Furthermore, although it is very low about 1 frequency channel along the full bandwidth it can be further reduced to about 0.1 channels by means of a prism. This identical frequency response of the

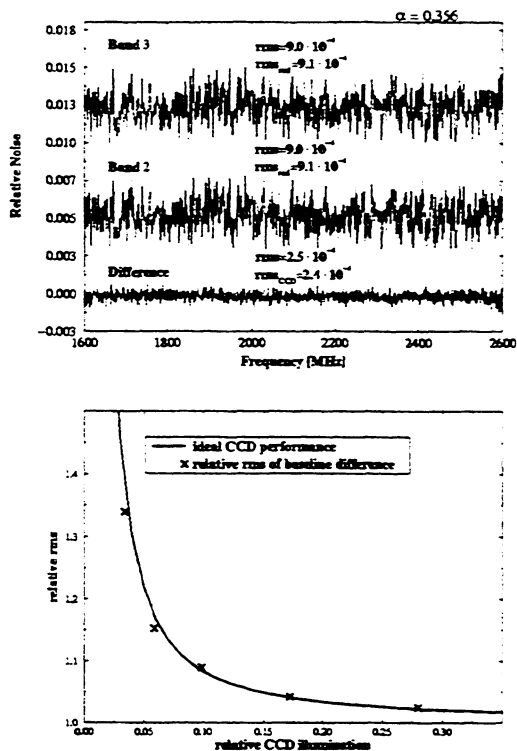


Figure 5: *The top graph shows simultaneously measured noise spectra in both AOS bands at high illumination level together with the difference spectrum. The noise of such difference spectra, measured at various illumination levels, has been scaled down to the contribution of one single CCD relative to radiometric noise, as shown in the lower graph*

various bands is a precondition, to eliminate identical noise apparent in two different bands. To check this performance, the output of a noise source has been split up and fed into two bands of the array AOS. Subtracting both simultaneously measured noise spectra, only the detector resides. The theoretical noise of the CCD has been calculated to be identical to the noise of the difference spectrum. The difference spectrum in Fig. 5 directly reflects the identical frequency response of the 1 GHz bands.

Decreasing the illumination level, that is, the IF drive power level at the Bragg cell the detector noise of the AOS, which consists mainly of shot- and dark-noise of the CCD, should increase. In that sense, one can define a noise dynamic range as the illumination level, where the CCD adds less than 1 dB noise to the radiometric noise.

The noise spectra described above have been repeated at various IF drive power levels of the noise source. The lower plot in Fig. 5 shows the noise contribution of the CCD relative to radiometric noise. One can see, that the noise is increased by 1 dB at an illumination level of about 5-6 %, yielding a noise dynamic range of at least 12 dB. If the CCD is illuminated below this level, the noise increases drastically, as is indicated by the steep slope of the curve.

3.2 Astronomical measurements

```

1907: 1 IRC+10216 13CO(2-1) IRAM-30M-B31 O: 15-MAY-1997 R: 15-MAY-1997
RA: 9:45:14.800 DEC: 13:30:40.00 (1950.0) Offr: 0.0 E1
Unknowns Tau: 0.2670 Tsys: 462.0 Time: 15.00 El: 32.54
N: 512 IQ: 256.5 VO: -27.00 Dr: 1.360 LSR
FO: 220398.682 DI: -1.000 FI: 228262.941

```

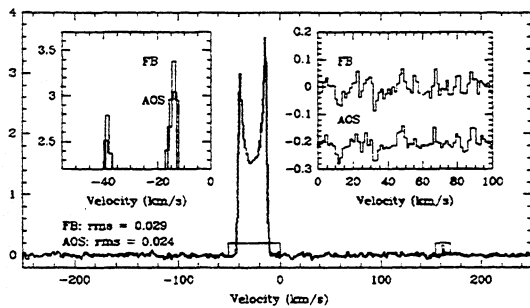


Figure 6: A measurement of $^{13}\text{CO}(1-0)$ in IRC+10216 to test the calibration scale of the AOS compared to the filterbank

The calibration of the array AOS has also been checked, using well known sources, like IRC+10216, where the line peak tempera-

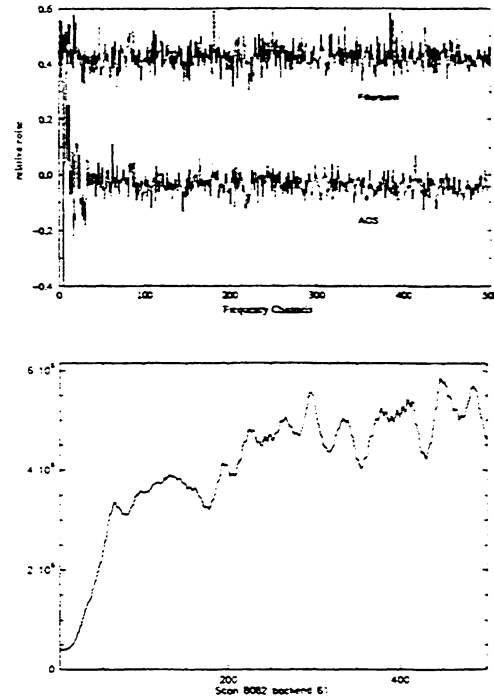


Figure 7: The baseline quality at illumination levels below the specified range for the AOS; the lower spectrum is measured with the AOS, the upper one with the filterbank. The bandpass shows a 500 MHz band measured with the AOS, on Hot Load. Saturation is reached at about $25 \cdot 10^6$ counts, the 12 dB noise dynamic range limit is therefore reached at roughly $2 \cdot 10^6$ counts.

ture is known. The IRAM filterbanks have been used in parallel to directly compare the results. For an interpretation, one has to take into account, that the AOS has a lower resolution (resolution bandwidth 1.5 MHz) than the filterbank (resolution bandwidth 1.0 MHz). In AOS spectra, narrow line features must therefore be frequency diluted and show a lower peak response as lines measured with the filterbank. This is nicely visible in Fig. 6, where the curve with the lower peak response has been measured with the array AOS. The identical response in the flat part

of the line center demonstrates on the other hand that the calibrations are identical, as can be seen in the left zoom. The velocity range from 0 to 100 km s⁻¹ zoomed, shows that features in the baselines are also nearly identical. The ratio of the RMS values is consistent with the ratio of the fluctuation bandwidths, which is 2.3 MHz for the array AOS and 1.4 MHz for the filterbank (Wild, 1995). For the calculation of the RMS values, line window have been set as are indicated in Fig. 6, so that the bad filterbank channel is not regarded.

During normal observations after installation of the array AOS, B. Lazareff et al. have generated some radiometric test data at 500 MHz bandwidth on Venus, again using the filterbanks in parallel, see Fig. 3.2. One can see excess noise at the left edge of the array AOS spectrum, whereas the Filterbank has only little of this excess noise.. The reason, that this only becomes visible at the edges of the spectra is due to the low IF power at the edges of the spectrum, which is fed into the AOS as is shown in Fig. 3.2. The bandpass for the 500 MHz band is shown in the lower graph. The 12 dB noise dynamic range limit is reached at about 2 10⁶ counts. This limit has been calculated, assuming 3 dB difference between Hot Load and sky and about 25 10⁶ counts for saturation. The excess noise indicates the limits of the CCD, which has to be illuminated above the 12 dB noise dynamic range limit, in the way it is operated at the moment. One could think of improvements in the CCD itself, in terms of looking for a device with better noise characteristics. But then the 12 Bit Analog to Digital Converter (ADC) used is the limiting factor, as the inherent differential non-linearity (DNL) then contributes to the noise. The effect of the DNL is already obvious at the very left edge, below 1 10⁶

counts of the bandpass. or within the first 20 frequency channels, due to the power difference between On- and Off-position on Venus. (Jarnot R.F., 1988). The effect of DNL can easily be reduced by inserting 14 or 16 Bit ADCs instead of the 12 Bit ADC used in this prototype version. A detailed discussion of the impact of the DNL on the noise performance at low illumination levels will be published soon. Furthermore, the DNL affects the baseline only when there are power offsets between the On and the Off position. Depending on how strong these offsets are, the DNL might already become a significant contributor to excess baseline noise next to the CCD. Sensitive measurements therefore require higher Bit resolution ADCs. When using 14 or 16 Bit ADCs, it would also make sense to improve the CCD characteristics or the readout speed, so that a noise dynamic range of 15 dB or more could be achieved. Furthermore one

```

2836: 1 SGRCAOS 13CO: (-0) IRAM-30M-B81 0: 17-MAY-1997 R: 17-MAY-1997
RA: 17:41:23.66: DEC: -29:14:22.00 (1950.0) Offs: -0.250 0.0 Eq
Unknown Tau: 7.5166E-02 Tsys: 302.2 Tobs: 10.00 El: 23.79
N: 50: IC: 251.0 VO: 0.0000E+00 Dr: -2.829 LSR
FO: 110201.370 DS: 1.040 FS: 113197.118

```

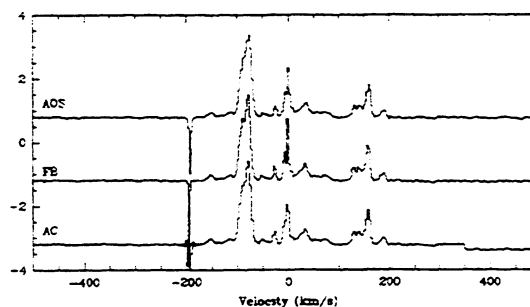


Figure 8: *Simultaneous measurements at 500 MHz bandwidth with the array AOS, filterbank, and hybrid autocorrelator*

can think of introducing an r.f. equalizer to reduce the bandpass variation of the AOS from 3 dB at the moment to about 1 dB. Filterbank spectra would also be affected

by DNL if the digitization is done with ADCs. At the IRAM filterbanks however, Voltage Controlled Oscillators with following Counters are in use. The excess noise at the edges is therefore only detector noise.

Further measurements on SgrC using 500 MHz bandwidth have been performed with the array AOS, filterbank, and hybrid autocorrelator in parallel, see Fig. 8. As in Fig. 6, one can see the frequency dilution of the array AOS due to its lower resolution compared with the filterbank. This becomes visible in the absorption feature at 0 km s^{-1} as well as at the IF spike at -200 km s^{-1} . Besides platforming, the autocorrela-

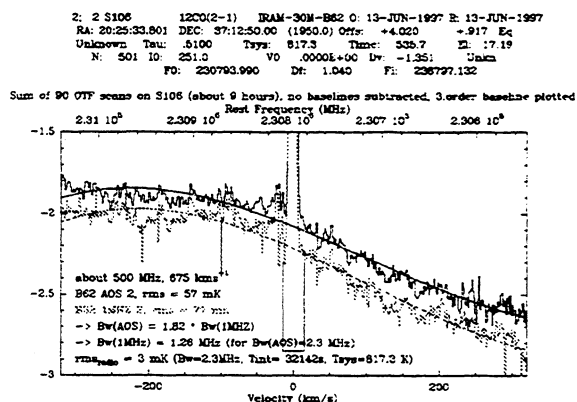


Figure 9: *Simultaneous On-the-fly (OTF) measurements at 500 MHz bandwidth with the array AOS (top) and the filterbank (bottom)*

tor shows much lower resolution as the nominally expected 1.25 MHz. One can see this at the absorption feature, which does not become visible in this spectrum, as well as at the absorption spike. This is probably caused by the process of smoothing the data with some apodization to suppress the sidelobes, which become visible if narrow lines are observed.

Schneider et al. mapped S106 on-the-fly (OTF). Summing up all 90 OTF scans, yields

to the spectrum shown in Fig. 9. After a total integration time of about 9 hours, the filterbank spectrum shows several bad channels. The AOS spectrum shows some excess noise at the right edge, where the illumination level is below the specified 12 dB, otherwise, the baselines would be exactly identical at this edge as they are for the rest of the baseline.

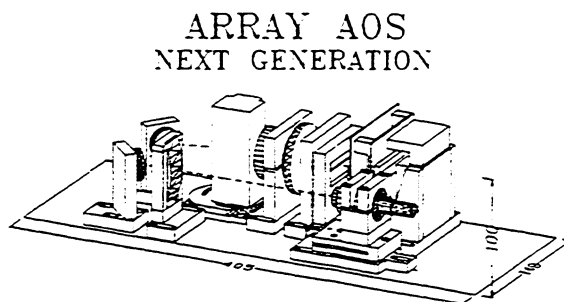


Figure 10: *The mechanical concept of the next generation array AOS. The optical parameters are the same as with the first version.*

The array AOS presented herein served as a prototype and showed already very good results. Nevertheless, the next versions e.g. for AST/RO or KOSMA, are being redesigned to make them more compact and to have already a kind of 'engineering model' for missions like FIRST or SOFIA. The principal optical setup of the next generation AOS is shown in Fig. 10. It differs from the first version only in the folded optical layout and some means to facilitate the alignment.

4 Conclusions

The performance tests have shown, that the concept of the KOSMA array AOS is suitable for radio astronomical applications at millimeter and submillimeter observatories. Even for heterodyne receiver arrays in the

THz region, which can be implemented at SOFIA, the array AOS provides sufficient frequency coverage to allow the detection of extragalactic signals. At 2 THz, the bandwidth of 1 GHz corresponds to 150 km s^{-1} , which is still sufficient for most galactic observations. If the velocity range needs to be larger, the AOS bands could also be joint together as done with hybrid autocorrelators. The identical noise performance of the different bands, if illuminated properly, are a decisive precondition to avoid different noise levels in the hybrid band. As there are no obvious different drifts within the two bands, platforming should not arise. At the moment, an IF processor is under development, to split a 2 GHz IF band and to feed the signals into two AOS bands. The performance of hybrid spectra can then directly be tested.

To improve the noise dynamic range of the AOS from now 12 dB to at least 15 dB are on the way, enhancing the Bit resolution of the analog to digital converter and the readout speed of the CCD.

5 Acknowledgements

We like to thank IRAM and the 30m staff to realizing the test-run with the array AOS, especially B. Lazareff and G. Paubert as well as N. Schneider, C. Kramer et al. and H. Wiesemeyer for providing additional test data. The array AOS has partly been financed through grant SFB 301 of the DFG (Deutsche Forschungsgemeinschaft).

6 References

GEC-Marconi, *Test Results of the array Bragg Cell*, Device Identity: Y-36-7436-02, Serial No.: MRQ IS001 (1995)

Horn J., *The development of an array acousto-optical spectrometer*. Ph.D. thesis. Univ. Köln (1997)

Jarnot R. F., Technical Note 1. JPL Microwave Atmospheric Sciences Group (Aug. 18., 1988)

Klumb M., Frerick J., Tolls V., Schieder R., Winnewisser G., *The SWAS Acousto-Optical Spectrometer*, SPIE Vol. 2268, p305 (1994)

Schieder R., Tolls V., Winnewisser G., *The Cologne Acousto-Optical Spectrometers*, Exp. Astron. 1: 101-121 (1989)

Schneider N., Kramer C. et al., *IRAM project 39/97* (1997)

Wild W., *The 30m Manual*, Version 1.0. IRAM Granada (1995)

COMPARATIVE STUDY OF THE BANDWIDTH OF PHONON-COOLED NbN HOT-ELECTRON BOLOMETERS IN SUBMILLIMETER AND OPTICAL WAVELENGTH RANGES

K. S. Il'in, S. I. Cherednichenko, and G. N. Gol'tsman,

Physics Department, Moscow State Pedagogical University, Moscow 119435, Russia

M. Currie and R. Sobolewski

Department of Electrical Engineering and Laboratory for Laser Energetics

University of Rochester, Rochester, NY 14627-0231, USA

Abstract

We report the results of the bandwidth measurements of NbN hot-electron bolometers, performed in the terahertz frequency domain at 140 GHz and 660 GHz and in time domain in the optical range at the wavelength of 395 nm. Our studies were done on 3.5-nm-thick NbN films evaporated on sapphire substrates and patterned into μm -size microbridges. In order to measure the gain bandwidth, we used two identical BWOs (140 or 660 GHz), one functioning as a local oscillator and the other as a signal source. The bandwidth we achieved was 3.5-4 GHz at 4.2 K with the optimal LO and DC biases. Time-domain measurements with a resolution below 300 fs were performed using an electro-optic sampling system, in the temperature range between 4.2 K to 9 K at various values of the bias current and optical power. The obtained response time of the NbN hot-electron bolometer to ~ 100 -fs-wide Ti:sapphire laser pulses was about 27 ps, what corresponds to the 5.9 GHz gain bandwidth.

Introduction

The bandwidth of hot-electron bolometer (HEB) mixers has reached values which are record for bolometers. The gain bandwidth for phonon-cooled NbN HEB mixers of 4 GHz for 140 GHz and 650 GHz frequencies [1, 2] and the noise bandwidth of 8 GHz for 650 GHz [2] have been demonstrated. For diffusion-cooled Nb HEB mixers, the bandwidth has reached 6 GHz, when measured at 20—40 GHz [3]. However, there is a definite practical interest to even further extend the bandwidth of these devices. The possibilities of the HEB mixer technology in this direction are far from being exhausted. For example, the future of the NbN HEB technology requires that critical temperature $T_c > 10$ K and critical current density $j_c > 10^6$ A/cm² at 4.2 K are simultaneously obtained for $d < 3$ nm-thick films [1]. The reduction of the optimal power of the local oscillator P_{LO} below 100 nW leads to the decrease of the device length down to $L < 0.2$ μm , which, in turn, should bring an additional cooling channel for hot electrons—diffusion into metal contacts and a further bandwidth extension.

Once the very wide gain bandwidth of the mixer is achieved, one must face problems associated with the device characterization, since it is difficult to provide the necessary wide bandwidth connection for the output of the IF signal from the cryostat. In order to ensure the sufficient precision of the measurements, the bandwidth of the output line must be substantially (several times) greater than the mixer bandwidth with minimal losses and spurious resonances. Further problems arise when the device is operated at THz frequencies, since there is no data published about the gain bandwidth of HEB mixers at or above 1 THz, apparently due to the difficulty of smooth re-tuning of both the LO and the signal source in the sufficiently large frequency range. Some of the above difficulties can be avoided by measuring the noise bandwidth of the mixers, since it requires no tunable source and the Y-factor is measured as a noise ratio for the hot and cold loads. However, the noise bandwidth for HEB mixers usually does not coincide with the gain bandwidth, causing new technical problems—very low-noise amplifiers are needed for sufficiently high frequencies (in the range of 4-12 GHz).

The aim of this work is to study the gain bandwidth of NbN HEB mixers using a time-domain optical method, namely an electro-optical (EO) sampling technique [4]. EO sampling not only does not require output of the signal to be transmitted out of the cryostat, but the signal is measured in the close vicinity (below 100 μm) to the hot-electron bolometer connected into a coplanar waveguide. Thus, far larger bandwidth can be measured (the limit of the measurements is moved into the femtosecond/THz range) and the measurements are performed at optical frequencies, giving an independent comparison with the results obtained at hundreds GHz, and increasing our confidence that the bandwidth estimations for the terahertz range.

Experimental Techniques and Results

Ultrathin NbN films have been deposited on sapphire substrates by reactive dc magnetron sputtering in the Ar+N₂ gas mixture [5]. The maximum values of the critical film parameters (T_c and j_c) are reached at the discharge current value of 300 mA, the partial N₂ pressure of 1.7×10^{-4} mbar and the substrate temperature 850°C. The Ar pressure proved to have no substantial impact on the film deposition rate or film composition. For this reason, the pressure level is chosen in such way as to maintain a stable discharge, namely 4.5×10^{-3} mbar. The deposition rate is 0.5 nm/s, defined as the ratio between the film thickness, measured with a Talystep profilometer/profilograph and the deposition time. Structures of NbN HEB mixers for the frequency-domain measurements consist of several parallel strips 1- μm wide and 1- μm spaced. For patterning, a standard photolithography followed by ion milling was used. The strips were placed between Ti-Au contact pads 2-3 μm apart from each other. The number of NbN strips varied between 1 and 16, depending on the film thickness, to ensure that the normal-state resistance of the bolometer stayed within the 200-300 Ω range.

The device was mounted on a waveguide flange, as shown in Fig. 1. The experimental setup used for bandwidth measurements is presented in Fig. 2. Two BWOs operating at 120-145 GHz were used as the LO and signal sources. The LO and signal beams were coupled by a beam splitter and a beamguide into the cryostat. Two attenuators included in the quasioptical path allowed to adjust independently the signal and LO power, and to maintain the optimum LO power during re-tuning. The IF signal received from the mixer was amplified by a room temperature wideband amplifier (0.1-6 GHz) and sent to the input of the spectrum analyzer.

The results of the frequency domain investigations of the bandwidth of NbN HEB mixers are presented in Fig. 3. It must be noted that the obtained bandwidth values for ultrathin ($d = 2.5$ - 3.5 nm), high quality films. For films of lower quality, characterized by lower values of T_c and j_c at $T = 4.2$ K, the bandwidth was narrower than for the high quality films of the same thickness. At the same time, the data on the mixer bandwidth obtained at the 140 GHz frequency are fully confirmed by the measurements done at higher frequencies (660 GHz). In the latter experiments, a quasi-optical mixer was used, which was made of a spiral-antenna-coupled NbN HEB on a sapphire substrate.

For EO sampling measurements [6], we designed a simple, single-line, 5- to 10- μm long microbridge structure, in order to be treated as a point source of the photogenerated signal, so its resistance did not have to be matched to the impedance of our coplanar waveguide (CPW) transmission line. Since it is difficult to accurately terminate the transmission line for broadband signals such as a picosecond electrical pulse and our CPW line was not long enough, we had only a 40-ps-long reflection-free time window for the EO measurements and had to deal with waveforms containing reflections from the transmission line ends.

The actual experimental structure for our EO sampling measurements (shown in Fig. 4) consisted of a 4-mm-long CPW with a 30- μm -wide center line and 5- μm -wide gaps to the ground planes. Gold contact pads for wirebonding were deposited on both ends. Typically, after processing, the bridges exhibited $T_c \approx 10.6$ K, a transition width 0.8 K, and a critical current $I_c \approx 800$ mA at 4.2 K. The sample was mounted on a gold-plated alumina substrate, attached to a copper block inside an exchange-gas, liquid-helium dewar, with optical access through a pair of fused-silica windows. During measurements, the sample was in He exchange gas and the temperature was regulated in the 2- to 10-K range and stabilized to below 0.1 K by adjusting the intensity of the stream of He exchange gas and the temperature controller heater. One end of the CPW was wirebonded directly to a semirigid, 50- Ω coaxial cable, which was used to bring the signal out the dewar and, together with an 18-GHz-bandwidth amplifier and bias-tee, allowed us to observe the bridge response on a fast oscilloscope. As shown in Fig. 4, the entire sample structure was overlaid with an electro-optical LiTaO₃ crystal to facilitate the EO sampling measurements.

The complete experimental setup of the EO system is shown in Fig. 5. A commercial Ti:sapphire laser, pumped by an Ar-ion laser, was used to excite picosecond pulses in the microbridge and electro-optically measure the propagating transient. The laser provided ~ 100 -fs-wide optical pulses with 800-nm wavelength and 76-MHz repetition rate, at an average power of 1 W. The beam was split into two paths by a 70/30 beamsplitter. The first (excitation) beam (700 mW) was frequency doubled in a nonlinear β -Bariumborate (BBO) crystal, and a reflective filter was used to eliminate the remaining 800-nm light. The excitation beam was intensity modulated by an acousto-optic modulator and focused by a microscope objective to a 10- μm -diameter spot on the microbridge. The microscope objective is also a part of the viewing and beam positioning arrangement. The average optical power of the 400-nm light, measured at a position just outside the dewar, was ~ 0.75 mW. By measuring the amount of light absorption/reflection in the two dewar windows and the LiTaO_3 crystal, we found that the incident power was further reduced to ~ 0.37 mW at the NbN detector surface, corresponding to a fluency of $8.5 \mu\text{J}/\text{cm}^2$. Taking the geometry as well as the reflectance and transmittance of NbN into account, we estimate the power actually absorbed by the microbridge was only $\sim 3.5 \mu\text{W}$, which could result in only minimal, well below 0.1 K increase in the bridge temperature.

Figure 6 shows the photoresponse of an NbN sample, obtained using the EO sampling technique. The measurements were performed at 8.9 K ($T_c = 10.6$ K), with the bridge bias current $I = 200$ mA. The fine line in Fig. 6 represents the experimentally recorded transient, while the thick one is the computed average. Since our reflection-free window was only 40 ps, the observed response is a superposition of the main signal and the end reflections. This may explain the relatively long (30 ps) time of the signal build-up. A comparative study of several response waveforms showed that the signal decay time had approximately the same duration of 27 ± 5 ps, which we can associate with the cooling time of the electron subsystem in thin NbN films. The calculated corresponding IF bandwidth is 5.9 ± 0.9 GHz, a bit wider than that obtained in frequency domain measurements. The discrepancy between the two results is, however, not drastic and seems to be caused by limitations of both techniques. In the frequency-domain technique, the measurements above 4 GHz are complicated by the resonances which appear in the IF signal tract, while the EO sampling technique in the above 10-ps-time range is hampered by signal reflections. In fact, the latter technique works better for considerably shorter response signals [4], or specially designed, reflection-free test beds are needed. In future, we plan to manufacture samples imbedded in a long CPW, which in addition will contain matched loads on both ends of the line, helping to reduce (ideally, suppress completely) the reflected signals. Such arrangement should enable us to obtain the intrinsic relaxation time of NbN HEBs.

Conclusions

We have conducted comparative measurements of the gain bandwidth of NbN HEB mixers. The results obtained by the two techniques—frequency-domain measurements in the 140-650 GHz range and time-domain measurements in the optical range—allow one to give a very accurate estimate of the bandwidth attainable by the HEBs at this stage of NbN thin-film technology. This bandwidth is 4 to 5 GHz and, as EO sampling technique indicates, it could be substantially further extended, as well as should not decrease for HEB mixers operating in the THz frequency range.

Acknowledgment

This work has been supported by Russian Program on Condensed Matter (Superconductivity Division) under Grant N 98062 and by the US Office of Naval Research Grant (project N00014-97-1-0696). The authors wish to thank B. M. Voronov and E. M. Menstchekov for their assistance in fabrication of the devices.

Referencies

- [1] S. Cherednichenko, P. Yagoubov, K. Il'in, G. Gol'tsman, and E. Gershenson, "Large bandwidth of NbN phonon-cooled hot-electron bolometer mixers on sapphire substrate," Proc. of the 8th Int. Symp. on Space Terahertz Tech., 245-257, Cambridge, MA, USA, 1997.
- [2] H. Ekstrom, E. Kollberg, P. Yagoubov, G. Gol'tsman, E. Gershenson, S. Yngvesson, "Gain and noise bandwidth of NbN hot-electron bolometric mixers," Appl. Phys. Lett. **70**, 24, 3296, 1997.
- [3] P.J. Burke, R.J. Schoelkopf, D.E. Prober, A. Scalare, W.R. McGrath, B. Bumble, and H.G. LeDuc, "Length scaling of bandwidth and noise in hot-electron superconducting mixers," Appl. Phys. Lett. **68**, 23, 3344, 1996.
- [4] M. Lindgren, M. Currie, C. Williams, T.Y. Hsiang, P.M. Fauchet, R. Sobolewski, S.H. Moffat, R.A. Hughes, J.S. Preston, F.A. Hegmann, "Ultrafast Photoresponse in Microbridges and Pulse Propagation in Transmission Lines Made from High-Tc Superconducting Y-Ba-Cu-O Thin Films," IEEE J. Sel. Top. Quantum Electron. **2**, 668, 1996.
- [5] P. Yagoubov, G. Gol'tsman, B. Voronov, L. Seidman, V. Siomash, S. Cherednichenko, and E. Gershenson, "The bandwidth of HEB mixers employing ultrathin NbN films on sapphire substrate", Proc. of the 7th Int. Symp. on Space Terahertz Tech., 290, Charlottesville, VA, 1996.
- [6] M. Lindgren, M. Currie, W.-S. Zeng, R. Sobolewski, S. Cherednichenko, B. Voronov, G.N. Gol'tsman, "Picosecond response of a superconducting hot-electron NbN photodetector," Proc. of the 6th Int. Superconducting Electronics Conf., 405, Berlin, Germany, 1997, and Appl. Supercon., in print.

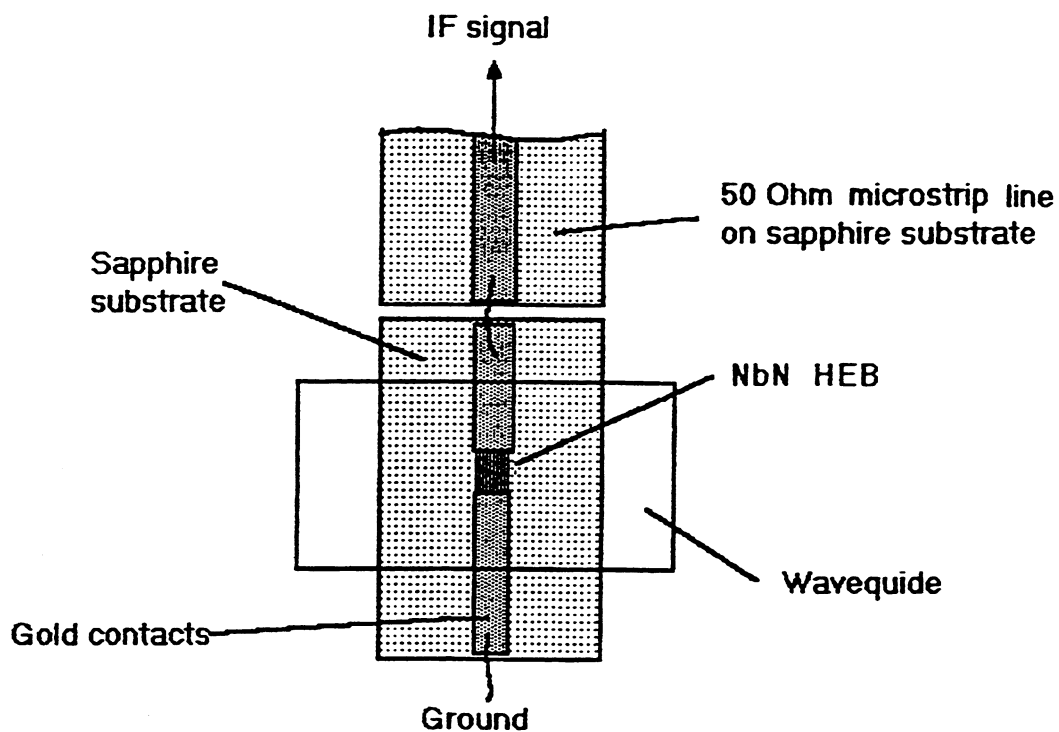


Fig.1 View of the mixer chip on the waveguide flange.

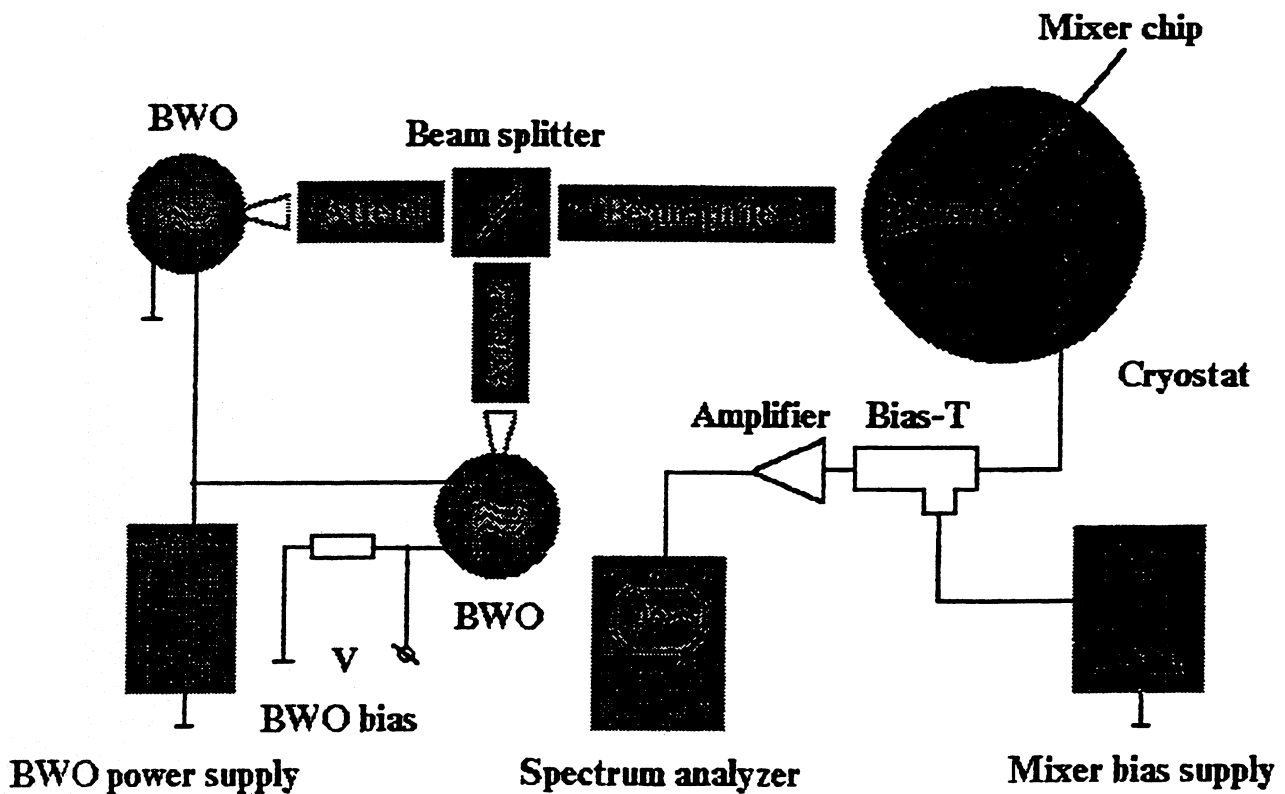


Fig. 2 Set-up for bandwidth measurements.

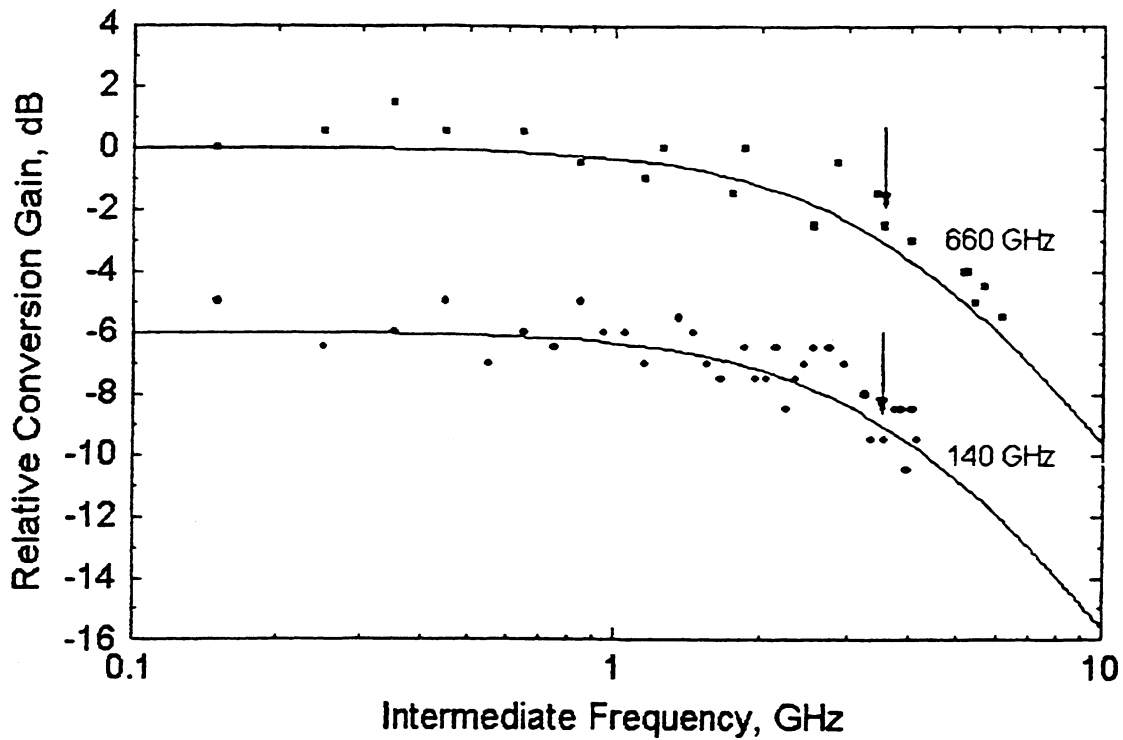


Fig. 3 Relative conversion gain for NbN device measured at 140 and 660 GHz under optimal LO and dc bias.

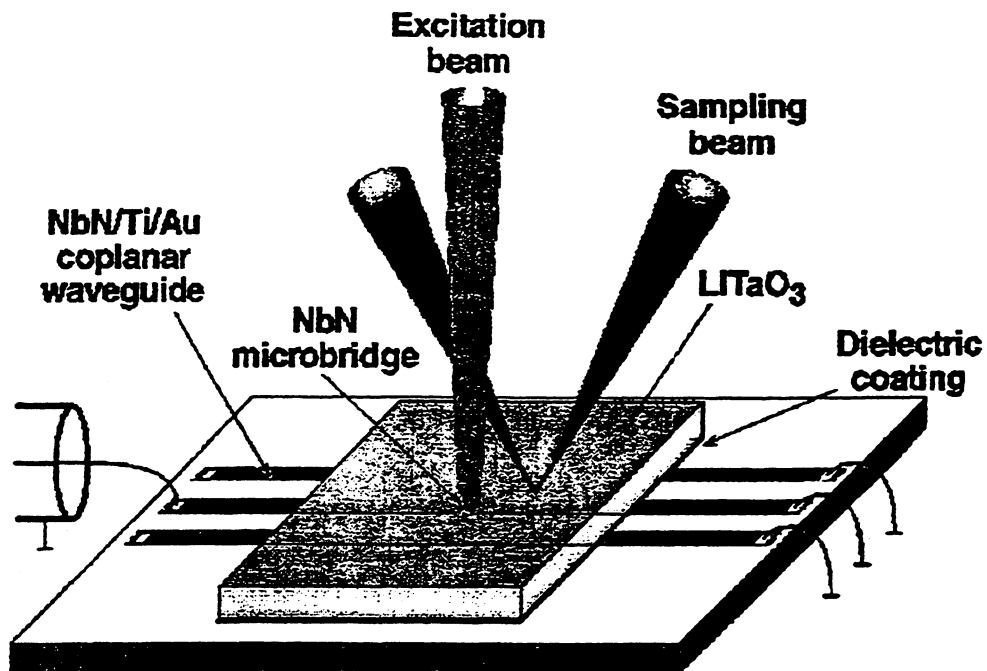


Fig. 4 Electro-optic sampling is performed by covering the NbN microbridge with LiTaO₃ crystal.

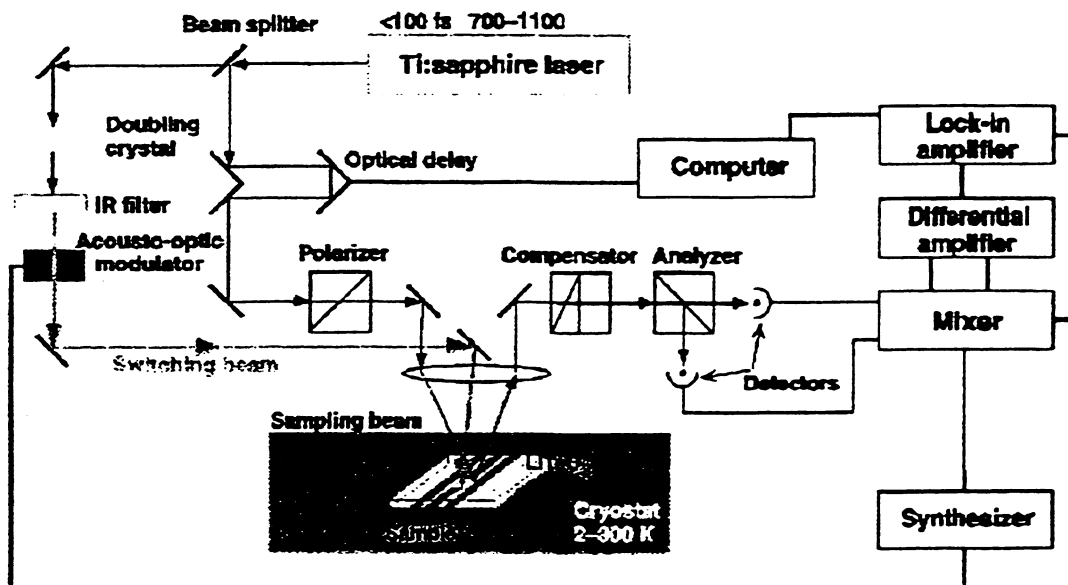


Fig.5 The cryogenic electro-optic sampling system measures ultrafast electrical transients.

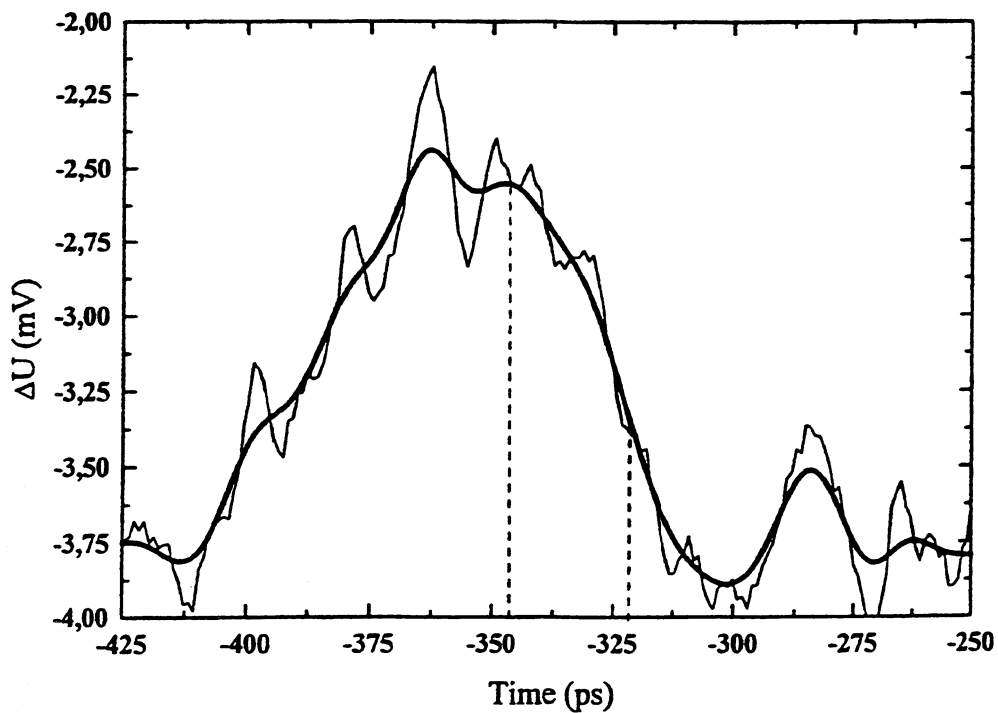


Fig. 6 Photoresponse of a NbN film at 8.9K measured with an EO sampling system.

NORMAL METAL HOT-ELECTRON MICROBOLOMETER WITH ANDREEV MIRRORS FOR THZ SPACE APPLICATIONS

D. CHOUVAEV, L. KUZMIN, M. TARASOV*, P. SUNDQVIST, M. WILLANDER, AND T. CLAESON

DEPARTMENT OF MICROELECTRONICS AND NANOSCIENCE, CHALMERS UNIVERSITY OF TECHNOLOGY, S-412 96 GOTHENBURG, SWEDEN

* INSTITUTE OF RADIOENGINEERING AND ELECTRONICS OF RUSSIAN ACADEMY OF SCIENCES, MOKHOVAYA 11, 103907 MOSCOW, RUSSIA

Abstract

We present a concept and experimental development of an ultrasensitive normal metal hot-electron microbolometer with Andreev mirrors and electronic cooling by superconductor-insulator-normal metal (SIN) tunnel junctions. A value $NEP = 5 \cdot 10^{-18} \text{ W/Hz}^{1/2}$ for the temperature fluctuations component of noise and the thermal time constant $\tau = 0.2 \mu\text{s}$ at 300 mK have been estimated for one of the realized devices with thermal conductance $G \approx 6 \cdot 10^{-12} \text{ W/K}$. Such microbolometer is intended as a detector of millimeter and sub-millimeter wave radiation.

1. Introduction

The normal metal hot-electron microbolometer (NHEB) with Andreev mirrors has been developed and demonstrated earlier [1][2]. It has shown very high power sensitivity at operating temperatures around 100 mK. NHEB is designed as a normal metal strip with a very small volume, connected to superconducting electrodes at both ends. A signal current from an antenna fed through those electrodes warms up the electron gas in the strip by dissipated power. The electrons can not give out their energy back to the electrodes because of the Andreev reflection at the NS-interface. They can loose energy by interacting with the lattice, but the thermal coupling gets very weak at temperatures below 1 K. This weak thermal coupling characterized by the heat conductance G is mainly responsible for a

substantial temperature rise for very low input power (so-called hot-electron effect).

To detect the changes in temperature of the electrons, an SIN tunnel junction in contact with the normal metal strip forming its N-electrode is used (fig. 1). The shape of IV curve of this junction depends on the electron temperature in the normal part, and by biasing the junction with a constant current and measuring voltage on it we can get a response $\Delta V(T)$ linear in a rather wide range.

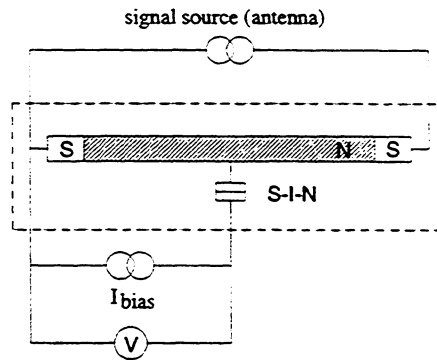


Fig. 1. Schematic of the microbolometer: an SIN junction is biased at a small constant current. A junction voltage depends on the smearing of the IV-curve, which is used to measure the electron temperature in the normal metal absorber (hatched).

An important feature of the NHEB with Andreev mirrors is that the thermal time constant τ equals the electron-phonon relaxation time τ_{e-ph} . The typical values of τ (10 μs at 100 mK and 0.4 μs at 300 mK) are much smaller than it is usually required for applications [1][3].

Since ultrasensitive detectors of submillimeter wave radiation are mostly needed for space radioastronomy, a very sensitive device working at a temperature around 300 mK, which can be reached in relatively simple and low-weight He³-cryostats, seems to be an attractive choice. European Space Agency (ESA) has formulated requirements for bolometer detectors to be used in future far infrared and submillimeter astronomy satellite missions [3]. Such a detector should operate at 300 mK and have the noise equivalent power $NEP < 1 \cdot 10^{-17} \text{ W/Hz}^{1/2}$ and the time constant $\tau < 1 \text{ ms}$.

There are three major components contributing to the NEP of NHEB according to the expression

$$NEP = \left[4k_B T_e^2 G + \frac{V_j^2}{S^2} + \frac{V_n^2}{S^2} \right]^{1/2}, \quad (1)$$

where T_e is the temperature of electrons in the absorber, $G = dP/dT$ is the thermal conductance for the outflow of signal-induced heat, $S = dV/dP = dV/dT \cdot G^{-1}$ is the power responsivity of the detector, V_j is voltage noise of the SIN junction and V_n is voltage noise of an amplifier. The first term describes the electron temperature fluctuations in the absorber and sets the fundamental noise limit for a given device at a given temperature. It is clear from the expression above, that it is mostly the small G that provides comparatively low NEP in this type of bolometer.

We suggest using an already demonstrated [4] mechanism of electronic cooling to decrease the NEP further by decreasing the temperature T_e of the electron gas in the absorber of the microbolometer while leaving the physical temperature of the lattice above 300 mK [5]. Such a device would balance the heating power transfer from phonons to electrons and the cooling power transfer by high-conductive tunnel junctions biased around the gap voltage, thus removing the most energetic electrons (fig. 2).

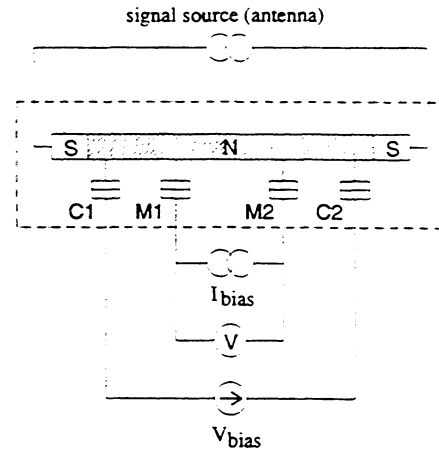


Fig. 2. Schematic of the microbolometer with electronic refrigeration. Two low-resistive SIN junctions (C1 & C2) are voltage-biased and used to decrease the effective electron temperature of the normal metal absorber element (hatched). Two high-resistive SIN junctions (M1 & M2) are biased with a small current and used to measure the resulting electron temperature.

According to the preliminary estimates [5] the total thermal conductance G can not be decreased by the electronic cooling even though it is very temperature dependent, since an additional channel for heat sink is then added. The electronic cooling should improve the overall performance of NHEB by reducing T_e in the first term in (1) and by increasing the temperature responsivity dV/dT (giving higher S) in the second and third terms of the NEP [5].

2. The power detector

We have made several experimental steps in realization of an NHEB and developing it further by attaching SIN junctions for cooling. First, we have made a microbolometer with a single tunnel junction for measuring the electron temperature in the absorber [6]. The absorber has been fabricated together with the superconducting electrode of the junction using electron beam lithography and the shadow evaporation technique. The superconducting electrode (40 nm-thick aluminum film) has been evaporated first and oxidized in $4 \cdot 10^{-2}$ mbar of O₂ for 2 min

to form the tunnel barrier. Subsequently 3 nm of chromium and 35 nm of silver have been evaporated to form the 6 μm long 0.25 μm wide absorber strip. Two superconducting leads (120 nm of lead) were then attached using one more lithography and deposition cycle. An ion etching *in situ* before the deposition was used to remove any oxide or contamination, which could otherwise make the Andreev reflection at the interface inefficient.

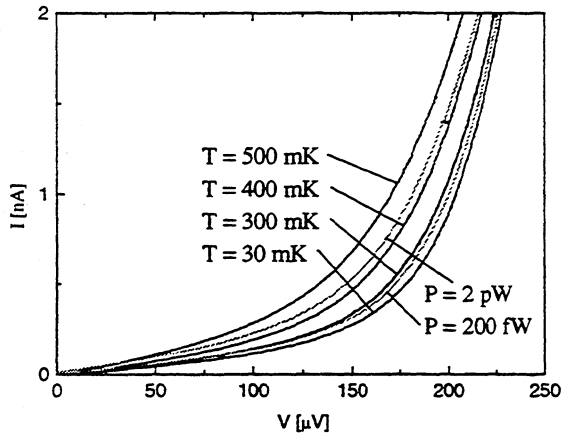


Fig. 3. IV curves of the SIN junction measured for different temperatures without any signal current and for two different powers dissipated by the signal current at the base temperature of 30 mK.

We performed measurements of IV curves of the SIN junction at different temperatures and with different dissipated power from the signal current (fig. 3). The dependence of the voltage V at constant bias current through the junction on the signal current I_{ABS} in the absorber was measured at constant temperature for two devices with different absorber lengths. The corresponding curves $V(I)$ for the two devices almost overlapped (fig. 4). The derivative dV/dI_{ABS} directly related to the form of the curve can be expressed via temperature responsivity, inverse thermal conductivity, and dP/dI_{ABS} :

$$\frac{dV}{dI_{ABS}} = \frac{dV}{dP} \cdot \frac{dP}{dI_{ABS}} = \frac{dV}{dT} \cdot \left(\frac{dP}{dT} \right)^{-1} \cdot \frac{dP}{dI_{ABS}}$$

One can find from the Joule law

$$P = P_{Joule} = I_{ABS}^2 R \Rightarrow \frac{dP}{dI_{ABS}} = 2R I_{ABS}$$

The inverse thermal conductivity can be found from the expression for the heat exchange in case of the hot-electron effect:

$$P_{e \rightarrow ph} = \Sigma U (T_e^5 - T_{ph}^5) \Rightarrow \quad (2)$$

$$\Rightarrow \frac{dP}{dT} = 5\Sigma U T^4,$$

where Σ is a material-specific parameter and we assume equilibrium, $P_{Joule} = P_{e \rightarrow ph}$. After substitution we get

$$\frac{dV}{dI_{ABS}} = \frac{dV}{dT} \cdot \left(\frac{2I_{ABS}R}{5\Sigma T^4 U} \right) \propto \frac{R}{U} \quad (3)$$

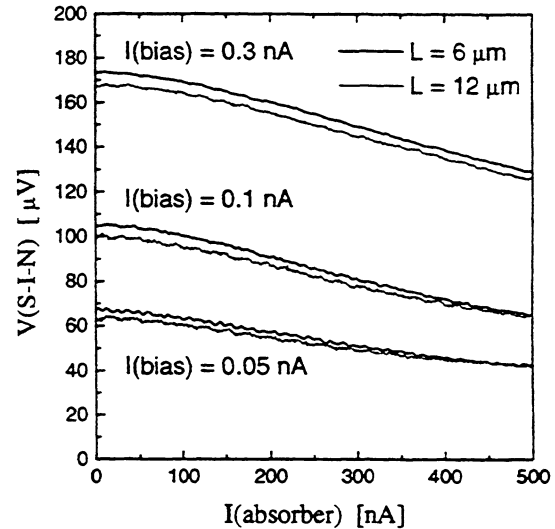


Fig. 4. The junction voltage V at constant bias current $I(\text{bias})$ through the junction as a function of the signal current $I(\text{absorber})$ for two devices with different absorber length 6 μm and 12 μm at $T = 30$ mK.

The overlapping of the curves means then, that increase of dissipated power (P) due to higher resistance (R) has been exactly compensated by increase of heat conductance due to larger volume (U), i.e. no substantial thermal transport through the NS-contacts has been present. The dependence $V(I_{ABS})$ was then re-calculated to give $V(P)$. Maximal power responsivity at an optimal $I_{bias} = 0.3$ nA was found to be

$S_{max} = |dV/dP| = 3 \cdot 10^7$ V/W. Combining the data $V(I_{bias}, T)$ and $V(I_{bias}, P)$ the dependence $P(T_e)$ could be calculated (fig.5).

From a fit to the expression (2) we could determine the material parameter $\Sigma \approx 3 \cdot 10^{-9}$ nW·K⁻⁵·μm⁻³ and, consequently, the thermal conductance $G \approx 6 \cdot 10^{-12}$ W/K at 300 mK. This value is twice as low as the one, which can be calculated using the data from [2]. This decrease was due to the smaller volume of the absorber in our case. The thermal fluctuation component of the NEP calculated for this value of G is about $5 \cdot 10^{-18}$ W/Hz^{1/2}, which is well below the ESA requirements for the total NEP for future spaceborn bolometers [3].

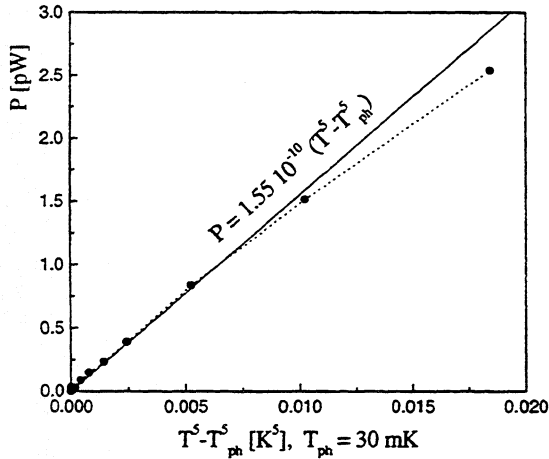


Fig. 5. Power dissipated in the absorber vs. $(T^5 - T_{ph}^5)$, where T is temperature of electrons deduced from measurements $V(I_{bias}, T)$, and $T_{ph} = 30$ mK is temperature of the lattice (measured temperature of the sample holder). Linear fit corresponds to the relation (2).

The thermal time constant can be computed as $\tau = C/G$, where C is the electron heat capacity. For the obtained value of Σ we get $\tau \approx 5T^{-3}$ ns. At $T = 300$ mK the time constant $\tau \approx 0.2$ μs, which is considerably shorter as what is typically required.

When operated at temperature 100 mK and below the NHEB did not show significantly better power sensitivity. The performance was apparently limited by the quality of the measuring tunnel junction, which has had an

IV curve changing its shape substantially only above 300 mK. We believe that such a behavior can be due to the thermal treatment while making the second layer lithography.

3. The electronic cooling

Using similar routines we have also fabricated an NHEB with four tunnel junctions as shown in fig. 2 and fig. 6. The absorber has been in this case a 40 nm thick 0.25 μm wide and 7 μm long copper strip. Junctions used for cooling need to have normal resistance of the order of 1 kΩ each to make this process efficient. At the same time, the junctions used for measuring the electron temperature should have normal resistance at least over 10 kΩ to keep the biasing current low. To get this combination we used junctions with very different areas (0.2 μm² for large and 0.01 μm² for small ones). In practice we have got the ratio of normal resistances much larger than 20, presumably because of oxidation from the edges affecting the small junctions much more than the large ones.

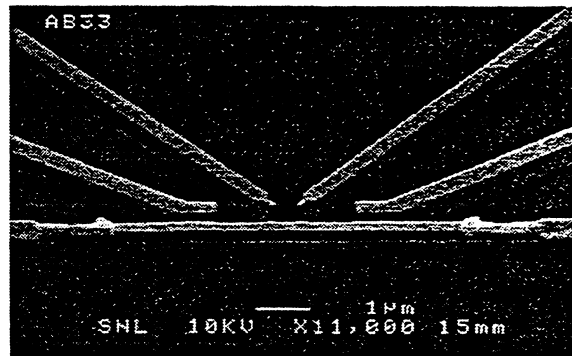


Fig. 6a. SEM picture of a microbolometer with electronic microrefrigeration fabricated by double shadow evaporation. The upper strip is made of copper and forms the absorber. The darker layer is aluminum; two large and two small tunnel junctions are formed where the absorber strip covers the oxidized aluminum electrodes. The ends of the absorber are contacted to aluminum electrodes, which has been fabricated using a separate lithography process.

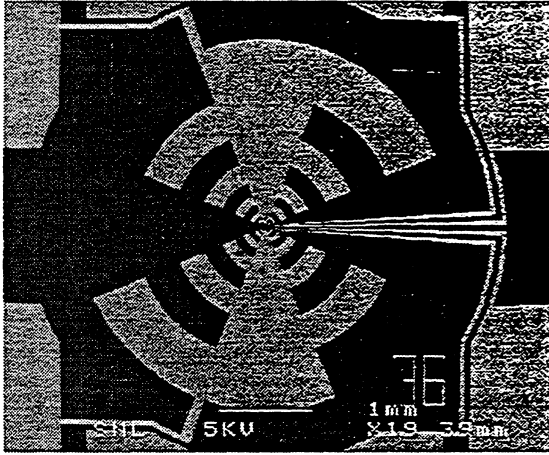


Fig. 6b. View of a chip with a planar log-periodic antenna designed for device tests at 100-1000 GHz.

To demonstrate the electronic cooling action in the microbolometer we measured the voltage drop over the small junctions at a constant biasing current as a function of voltage over the large junctions. Then we calibrated this voltage drop as a function of temperature in a cryostat with the large junctions not connected.

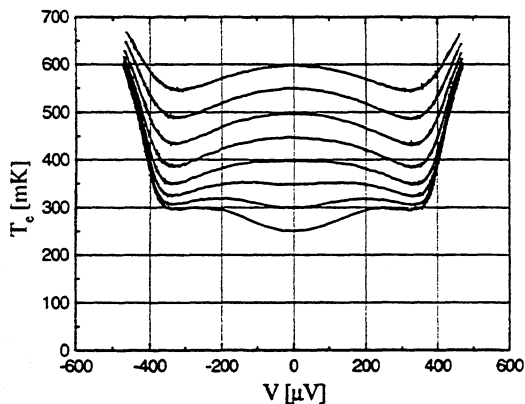


Fig. 7. Temperature of electrons T_e in the absorber as a function of voltage applied over two large SIN junctions ($R_n[M1] + R_n[M2] = 62 \text{ k}\Omega + 116 \text{ k}\Omega$) at various starting temperatures. T_e is computed from the voltage drop over two smaller tunnel junctions ($R_n[C1] + R_n[C2] = 625 \Omega + 645 \Omega$) biased at a small constant current using a calibration curve obtained in a separate measurement.

The resulting curves with different starting temperatures $T_{ph} = T_e$ at $V = 0$ are presented in the fig. 7. We can see both the cooling action and its unexpected suppression below

400 mK. At present we do not have a clear understanding of this contradiction to the previous results from [4]. We had a suggestion that this effect could be due to the Joule heating from the bias current flowing between the tunnel junctions. To check this we had put those large junctions as close as only $0.5 \mu\text{m}$ from each other, but the behavior of the system remained the same.

4. Conclusion

We have fabricated a normal metal hot-electron bolometer (NHEB) with an absorber of very small volume, connected to an antenna by the Andreev NS-contacts. Experiments where the absorbers have had different lengths show that the thermal conductance is mainly determined by the electron-phonon interaction and almost no heat losses through the NS-contacts have been present. The thermal conductance of $6 \cdot 10^{-12} \text{ W/K}$ has been measured for the microbolometer with the shorter absorber at 300 mK. It gives the time constant $\tau = 0.2 \mu\text{s}$ and $NEP = 5 \cdot 10^{-18} \text{ W/Hz}^{1/2}$ for the temperature fluctuation noise component. These parameters, especially the time constant, are considerably better than similar parameters of a voltage-biased superconducting transition edge bolometer [7]. We have fabricated also an extended version of NHEB where the electronic cooling by two SIN tunnel junctions has been applied to eventually be able to decrease the total NEP of the detector.

References

- [1] M. Nahum, P.L. Richards, C.A. Mears, IEEE Trans. Appl. Supercond. **3**, 2124 (1993)
- [2] M. Nahum, J.M. Martinis, Appl. Phys. Lett, **63** (22), 3075 (1993)
- [3] ESA tender AO3288 Hot-electron microbolometers, opened Oct.2, 1997
- [4] M.M. Leivo, J.P. Pekola, D.V. Averin, Appl. Phys. Lett., **68** (14), 1996 (1996)
- [5] L. Kuzmin, I. Devyatov, 4th Int. conf. on mm and submm waves, San Diego, July 1998 (submitted)
- [6] D. Chouvaev *et al.*, 4th Int. conf. on mm and submm waves, San Diego, July 1998 (submitted)
- [7] A.T. Lee, S-F. Lee, J.M. Gildemeister, and P.L. Richards, Proc. of the 7th Int. workshop on Low Temperature Detectors, Munich, July-Aug 1997

SINGLE SIDEBAND MIXING AT SUBMILLIMETER WAVELENGTHS

Junji Inatani ⁽¹⁾, Sheng-Cai Shi ⁽²⁾, Yutaro Sekimoto ⁽³⁾,
Harunobu Masuko ⁽⁴⁾, and Satoshi Ochiai ⁽⁴⁾

(1) National Space Development Agency, Tsukuba, Ibaraki 305-8505, Japan

(2) Nobeyama Radio Observatory, National Astronomical Observatory,
Nobeyama, Nagano 384-1305, Japan

(3) University of Tokyo, Hongo, Tokyo 113-0033, Japan

(4) Communications Research Laboratory, Ministry of Posts and
Telecommunications, Koganei, Tokyo 184-8795, Japan

Abstract

Two quasi-optical circuits are proposed and compared for single sideband mixing at submillimeter wavelengths. First one is a quasi-optical version of the conventional microwave technique for image rejection. Two mixers are combined by means of a single wire-grid polarizer, which works as an RF and LO hybrid simultaneously and also as an RF/LO diplexer. A reflecting-type circular polarizer is used at the LO input port to generate a 90-degree phase-difference between two perpendicular components.

Second approach is a dual polarization usage of the well-known Martin-Puplett Interferometer (MPI). We propose a pair of mixers be used in combination with a single MPI for receiving the upper sideband (USB) and lower sideband (LSB) at the same time. Another MPI is coupled to this configuration for LO injection and image termination to a cold load.

The first approach is superior in realizing a broader RF bandwidth without necessity of mechanical tuning, while the second gives a higher coupling efficiency for LO injection.

Introduction

Low-noise mixers at millimeter and submillimeter wavelengths usually receive signals in upper sideband (USB) as well as in lower sideband (LSB). In astronomical and atmospheric molecular line observations, this property may result in several troubles such as (i) difficulty in precise calibration of line intensity, (ii) increase of the system noise temperature, and (iii) complexity of the IF band due to superposition of signals from both sidebands. To remove these troubles, Martin-Puplett interferometers (MPI) have been used as an image-rejection filter [1]. Since MPI is a high-Q filter, fine mechanical tuning is often required to optimize MPI for each observation frequency. Such mechanical tuning is, however, not desirable for the receiver system which is remotely operated in space or other places of difficult accessibility. Here we would like to propose two quasi-optical circuits for sideband separation, which have no mechanical tuners and are available at submillimeter wavelengths.

Quasi-optical Image-Rejection Circuit

Principle

Operational principle of our first circuit is exactly the same as the conventional microwave image-rejection mixer, which is shown in Fig.1 [2]. If we apply this principle to the submillimeter mixer, the critical problem is what kind of transmission lines and RF hybrids are available without increasing the insertion loss in the RF path. We propose here to use a quasi-optical Gaussian beam and a polarization beam-splitter. Such quasi-optical image-rejection circuit is shown in Fig.2. A piece of wire-grid is used in common as an RF in-phase hybrid and as an LO 90-degree hybrid. If precisely described, there is an additional phase slip of 180 degrees between the transmitted and reflected field, but that does not affect the operation of this circuit. A reflecting-type circular polarizer is used to generate a 90-degree phase-difference between vertical and horizontal components of LO field. The wire-grid used as the RF/LO hybrid also has a role of RF/LO diplexer, although the RF polarization plane is perpendicular to that of LO in both branches. But this is not a problem. If the polarization plane of the mixer input port is slightly tilted from that of the RF beam, the mixer will be coupled efficiently with the RF beam and partially with the LO beam.

As for the IF hybrid, the Lange coupler has been designed to realize a broad

IF bandwidth. Calculated coupling loss and phase difference are shown in **Fig.3** for a center frequency of 2 GHz. This IF circuit could be installed in a single mixer-mount which involves two mixers back-to-back in the geometrical configuration of **Fig.2**.

Characteristics

This new quasi-optical image-rejection mixer is expected to have a very broad bandwidth in RF as well as in IF, in spite of that there is no mechanical tuners. RF bandwidth of a wire-grid for RF/LO hybrid will be sufficiently broad. So a band-limiting factor should be a wire-grid circular polarizer for LO injection. At this device, phase-difference between two perpendicular components is determined by a gap between a wire-grid plane and a flat reflecting mirror. The phase difference therefore changes linearly as LO frequency.

In **Fig.4 (a)** and **(b)**, the coupling efficiencies between RF and IF are calculated for SIGNAL band and IMAGE band separately. The designed IF characteristics of the Lange coupler is included in this calculation. This efficiency is normalized to the ideal one which is realized when the RF and LO are divided in precise amplitude and phase, the two mixers have the same conversion gain, and the IF coupler is perfectly balanced. Changes of IF characteristics are shown with six different curves in each panel of **Fig.4**, which correspond to different LO frequencies from 400 GHz to 500 GHz. The LO circular polarizer is optimized at 500 GHz. So this result shows that the relative RF bandwidth of this quasi-optical image-rejection circuit is more than 30-40 %.

More practical factor of deterioration will be imbalance between two mixers. When the two conversion gains are different by 0.5 dB, for example, the IF characteristics of SIGNAL band suffer about 0.3 dB loss, as shown in **Fig.4 (c)**. But the IMAGE band is not affected by this level of imbalance.

Another possible factor of deterioration is a difference in optical path-length between two branches. However, in this quasi-optical configuration, both the RF and LO beam propagate along the same path between the RF/LO hybrid and the mixer device. So if there is an additional phase in RF due to some path-length difference between two branches, it would be canceled by the similar additional phase in LO. Such path-length difference could affect the image-rejection only when it is large enough compared with the IF wavelength. Actually the IF characteristics shown in **Fig.4** are not affected even if there exists a path-length difference as large as 1 % of the IF wavelength. This means that a fine mechanical tuning of the path-

length is not necessary. A fixed configuration which is finished by usual mechanical engineering will be enough to realize a good performance.

Dual-Polarization MPI Circuit

Principle

Our second approach is to use a pair of Martin-Puplett Interferometers in combination with two mixers and a single LO source (Fig.5). One MPI works for sideband separation, and the other for LO injection and image termination. Since two mixers receive perpendicular polarizations each other, MIX-1 looks at the Antenna Port in USB and at the Cold Load Port in LSB, while MIX-2 looks at the Antenna Port in LSB and at the Cold Load Port in USB. LO power is delivered into two mixers through two MPIs with the insertion loss of 3 dB.

Characteristics

RF characteristics of this dual-polarization-utilized MPI can be calculated based on the well-known MPI's formula. However, if we want to evaluate the image rejection level, we have to take a non-ideal property of a wire-grid into our consideration. An ideal wire-grid in MPI should have a perfect transmission efficiency for electric field perpendicular to its wire direction, and at the same time, a perfect reflection efficiency for electric field parallel to the wire direction. Even if we optimize geometrical parameters of the wire-grid, there will still remain undesirable reflection for perpendicular field and undesirable transmission for parallel field, which is estimated to be about 1 % in power [3].

We have designed a dual-polarization MPI as shown in Fig.5 for JEM/SMILES, a submillimeter mission on the International Space Station, where the LO frequency is 638.5 GHz and the nominal IF band is 9-15 GHz. So the LSB is 623.5-629.5 GHz, and the USB is 647.5-653.5 GHz. Fig.6 shows several insertion losses of this dual-polarization MPI system, which are calculated by assuming 1 % undesirability for the wire-grid. Fig.6 (a), (b), (c), (d) show the insertion losses between the Mixer Port (MIX-1 and MIX-2) and the Antenna Port (main polarization and cross polarization). This result shows that there appears some loss even at the center of LSB for MIX-2, and at the center of USB for MIX-1, due to the undesirable transmission and reflection of the wire-grid. Fig.6 (b), (d) also show that the image-rejection level is affected by a more efficient coupling between the Mixer Port and the cross polarization at the Antenna Port.

Fig.6 (e), (f), (g), (h) show the insertion losses between the Mixer Port and the Cold Load Port (main polarization and cross polarization). The insertion loss is larger than that for the Antenna Port due to two MPIs used in series. This is not negligible, because it increases the thermal noise injected into the image band, which results in the increase of the SSB system noise temperature. From these calculations, we find it is important to keep the undesirability of the wire-grid less than 1 % in power.

Comparison

Two kinds of quasi-optical sideband separation techniques described above have several advantages and disadvantages. They are summarized in **Table 1**. The quasi-optical image-rejection circuit is superior in broad instantaneous RF bandwidth, which is realized without necessity of mechanical tuning. It is possible to use the dual-polarization MPI in a fixed setting, but in that case we have to fix the LO frequency, so the RF bandwidth is also fixed within the IF bandwidth. The image-rejection circuit also has a broader IF bandwidth, if a broad IF hybrid such as the Lange coupler is available. The IF bandwidth of the dual-polarization MPI is limited by the cosine function of MPI.

As for the LO injection loss, the dual-polarization MPI is superior. Its theoretical value is only 3 dB, which is inevitable because the LO power is supplied to two mixers. But in the quasi-optical image-rejection circuit, the LO power is divided into two components at first (3 dB), and then each component is only partially coupled to the mixer. We have to keep this coupling efficiency less than about 5 % (13 dB loss), in order not to sacrifice the more important RF coupling to the mixer.

There is also an important difference in mixer operation mode. Two mixers should be well balanced in the image-rejection circuit, but they are operated independently in the dual-polarization MPI. Even in an extreme case when one of the two mixers had a failure, the other mixer could work properly in the single sideband mode in the latter circuit. This is of practical importance in space applications, to avoid a complete damage of the system.

Conclusions

We have proposed two techniques of quasi-optical sideband separation which

could be available for submillimeter mixing. One is a quasi-optical version of the conventional microwave image-rejection circuit, and the other is a dual polarization usage of the well-known Martin-Puplett interferometer. The former technique is superior in realizing a broader RF bandwidth without necessity of mechanical tuning, while the latter gives a higher coupling efficiency for LO injection. Further experimental investigations are needed for both techniques.

References

- [1] D. H. Martin and E. Puplett, *Infrared Physics*, 10, 105-109, 1970
- [2] e.g. S. A. Maas, "Microwave Mixers," Artech House, Inc., 1986
- [3] W. G. Chambers, A. E. Costly and T. J. Parker, *International Journal of Infrared and Millimeter Waves*, 9, No.2, 157-172, 1988

	Quasi-Optical Image-Rejection Circuit	Dual-Polarization MPI Circuit
RF Bandwidth (Instantaneous)	Broad [Limited by LO circular polarizer.]	Narrow [Limited by MPI.]
RF Bandwidth (Tuning Coverage)	N/A	Broad [Limited by wire-grid and beam diversion.]
IF bandwidth	Broad [Limited by IF hybrid.]	Moderate [Limited by MPI.]
RF Insertion Loss (N wire-grids inserted)	Small [Three wire-grids]	Small [Four wire-grids]
LO Injection Loss	> 16 dB	3 dB
Mechanical Tuning	None	Necessary for broad RF coverage.
Two Mixers	should be balanced.	are independent.

Table 1 Comparison of two quasi-optical circuits for sideband separation.

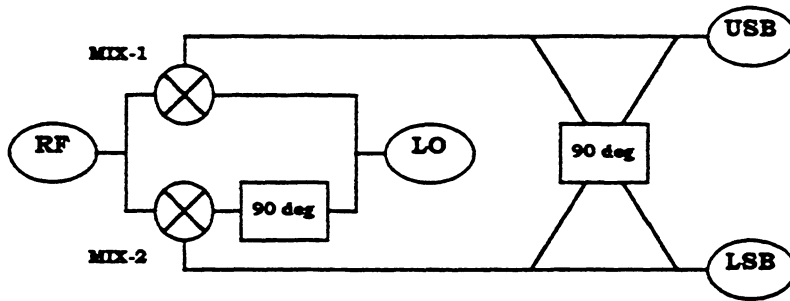


Fig.1 Principle of the conventional microwave image-rejection mixer circuit.

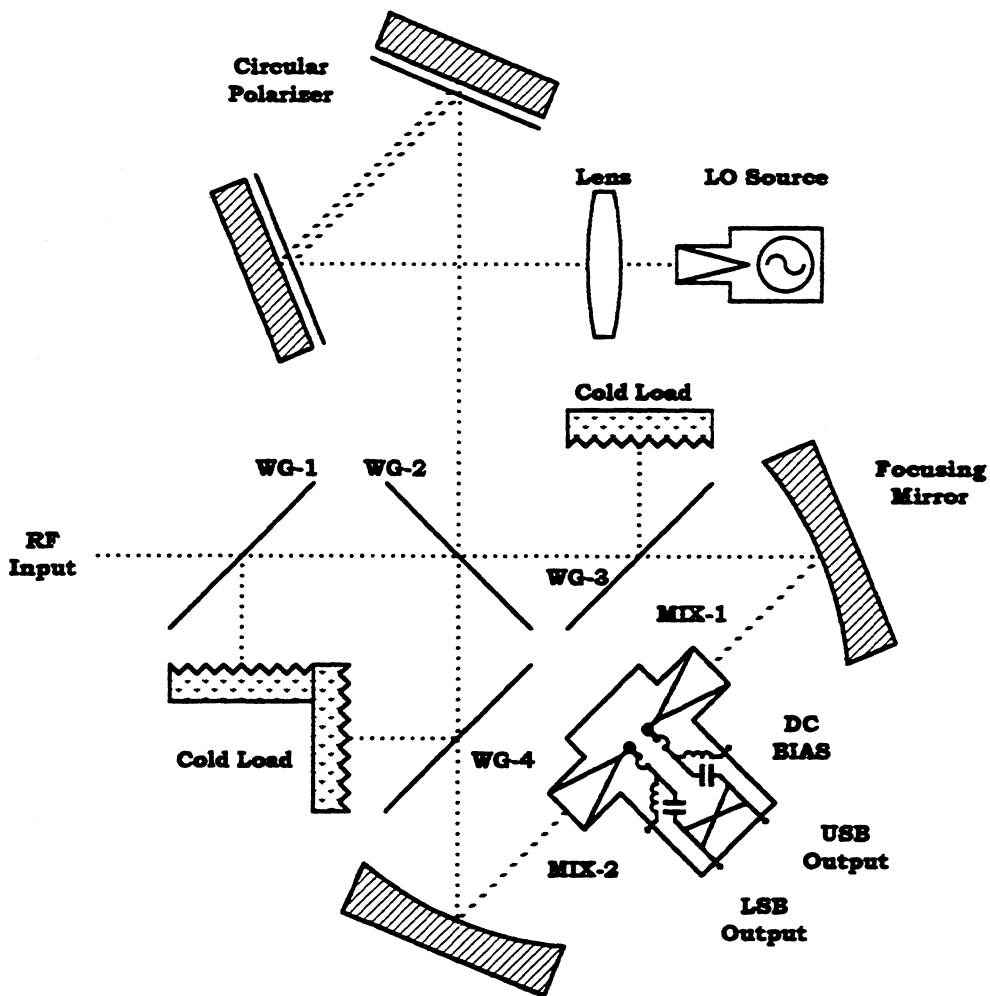


Fig.2 Quasi-optical image-rejection circuit. Role of each wire-grid (WG) is as follows: WG-1 to define the RF input polarization (cross polarization is terminated to a cold load), WG-2 to split RF as well as LO, WG-3 and WG-4 to define the mixer input polarization. Reflected LO power is terminated to absorbers.

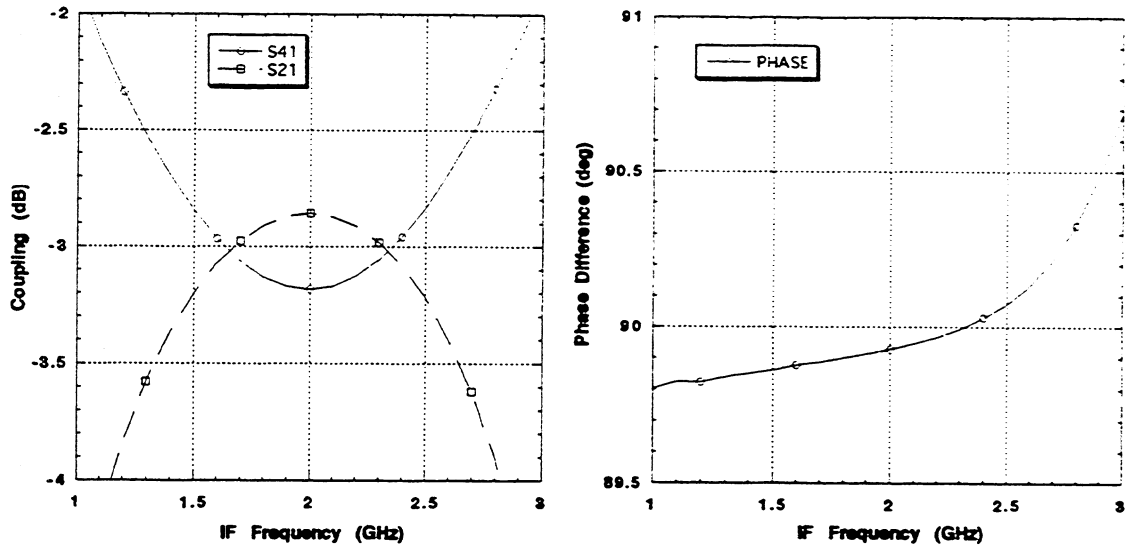


Fig.3 Calculated coupling and phase-difference of the Lange coupler which is designed for a center frequency of 2.0 GHz.

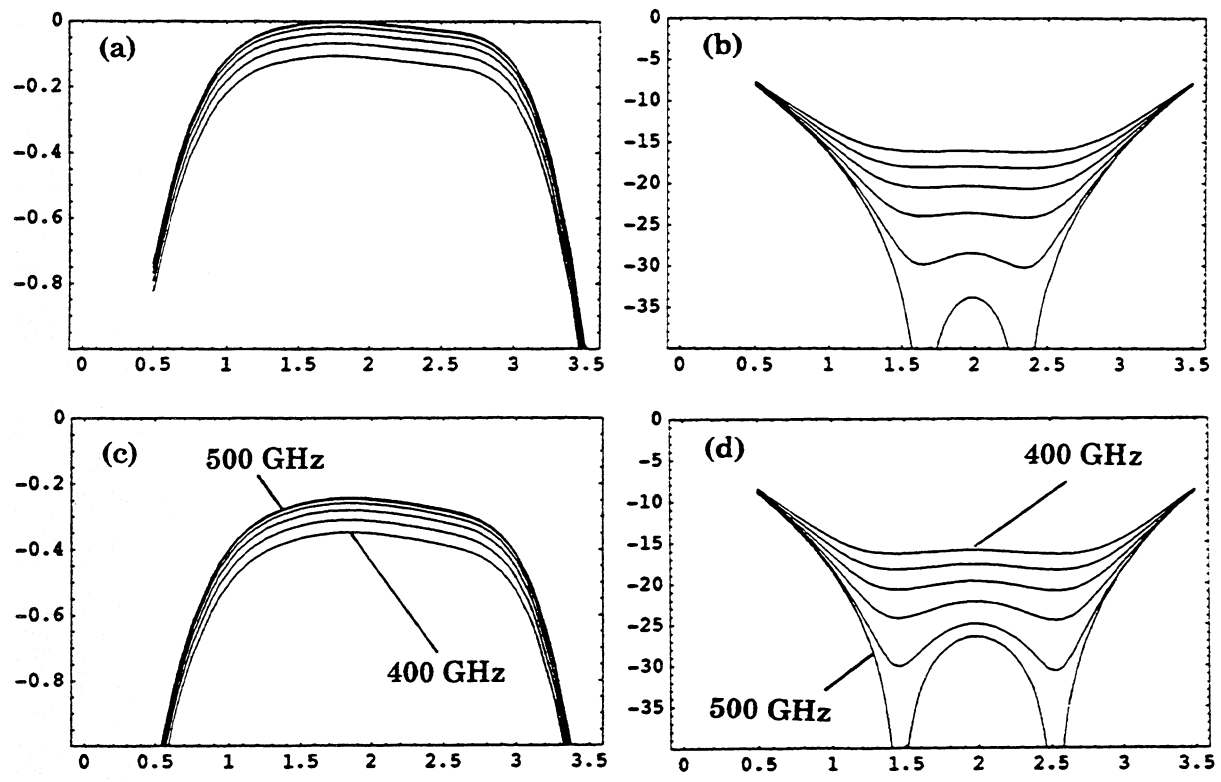


Fig.4 (a) Coupling efficiency in the SIGNAL band between RF and IF through the quasi-optical image-rejection circuit in Fig.2. (b) Same in the IMAGE band. (c) Same in the SIGNAL band when 0.5 dB gain difference exists between two mixers. (d) Same in the IMAGE band for 0.5 dB difference.

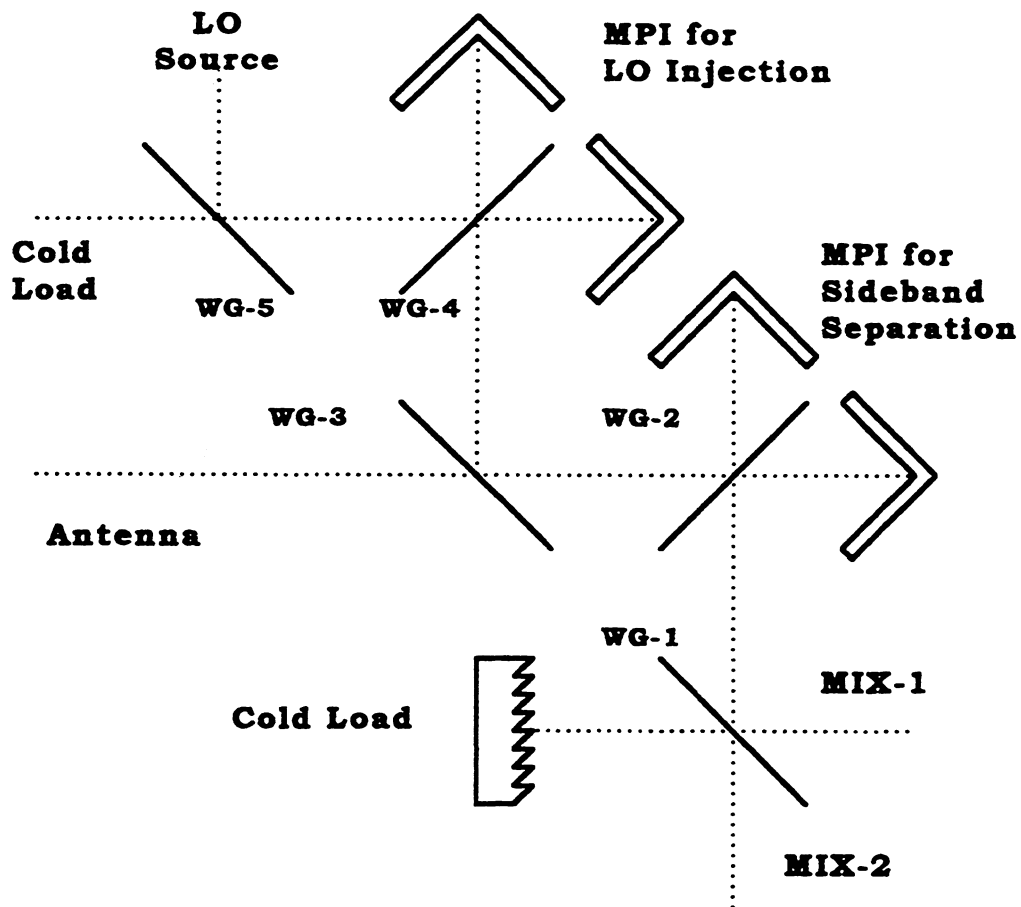


Fig.5 Dual-polarization-utilized MPI circuit. WG-1 to WG-5 are wire-grids. MIX-1, receiving a horizontal polarization, looks at the Antenna Port in the USB and at the Cold Load in the LSB, while MIX-2, receiving a vertical polarization, looks at the Antenna Port in the LSB and at the Cold Load in the USB.

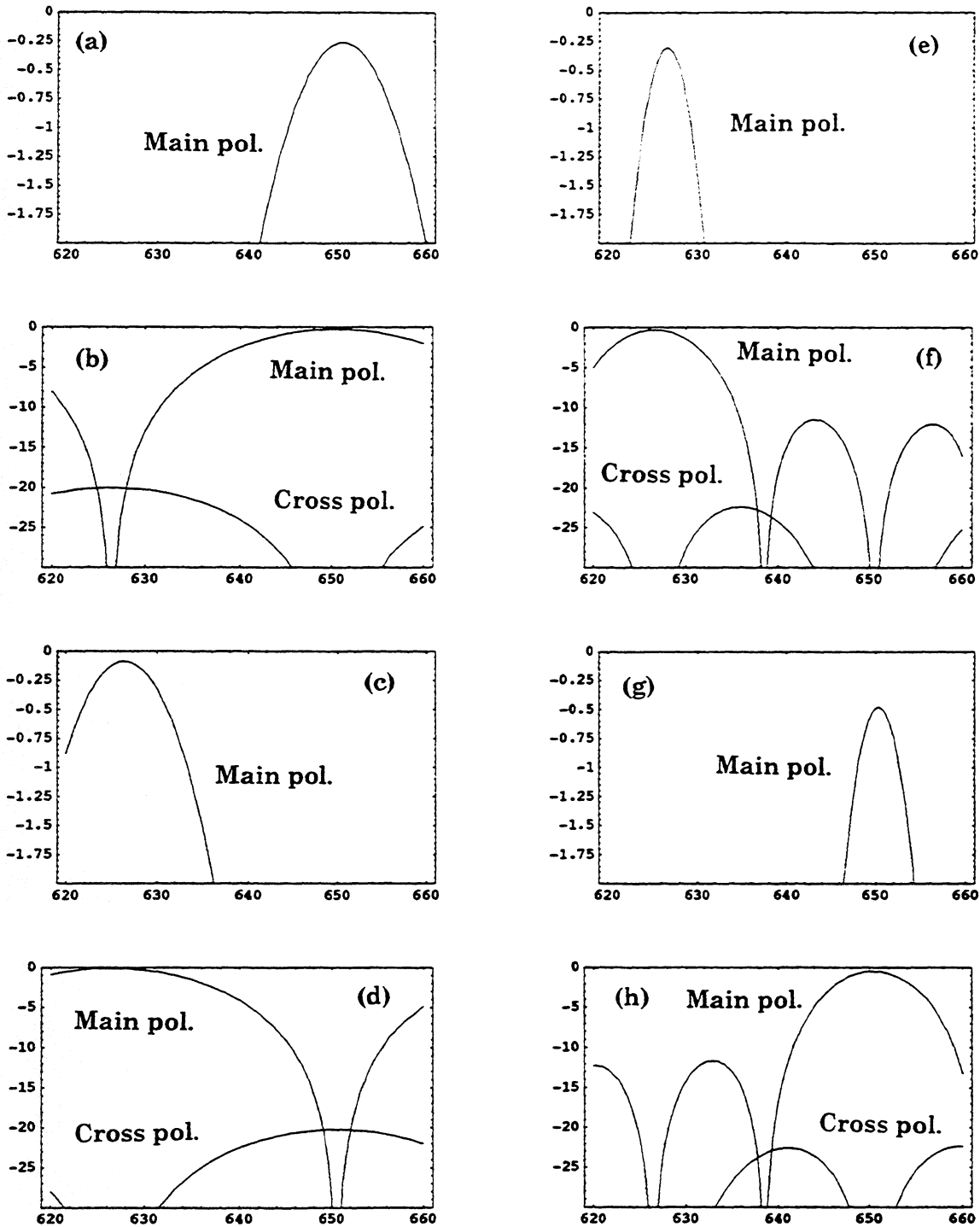


Fig.6 (a),(b) Insertion losses (dB) between MIX-1 and the Antenna Port in its main and cross polarizations. (c),(d) Same for MIX-2. (e),(f) Insertion losses (dB) between MIX-1 and the Cold Load Port in its main and cross polarizations. (g),(h) Same for MIX-2.

NOISE AND CONVERSION EFFICIENCY OF HIGH- T_c SUPERCONDUCTOR JOSEPHSON MIXERS

O. Harnack¹, S. Beuven, M. Darula, H. Kohlstedt

Institute for Thin Film and Ion Technology, Research Center Jülich, D-52425 Jülich, Germany

M. Tarasov, E. Stepantsov, Z. Ivanov

Physics Department, Chalmers University of Technology, S-41296 Gothenburg, Sweden

Abstract

We report on experimental studies of the noise performance and conversion efficiency of high- T_c Josephson mixers at frequencies between 90 GHz and 550 GHz. The heterodyne mixing experiments have been performed by using $\text{YBa}_2\text{Cu}_3\text{O}_{7-\delta}$ step-edge junctions and bicrystal junctions on MgO ($\epsilon \approx 9.6$) substrates. We studied the Josephson mixer performance for the case of internal pumping (self-pumping) and external pumping. Receiver noise measurements in a waveguide setup for the case of external pumping at 90-94 GHz gave formally calculated double-side-band (DSB) mixer noise temperatures (T_m) of about 2000 K at physical temperatures of 10 K. Similar measurements in a quasioptical setup at 4.2 K and at operation frequencies of 430 GHz and 546 GHz yielded mixer noise temperatures of 1200 K and 1100 K, respectively. Using the internal pumped mode, i.e. mixing without external local oscillator signal, we also obtained clear IF response in hot/cold-measurements. The formally calculated T_m were between 580 K and 2300 K.

I. Introduction

Mixers based on the Josephson effect have been shown to have low local oscillator power consumption and high conversion efficiencies in the millimeter-wave range. In contrast to classical resistive mixers, the conversion efficiency of a Josephson mixer can be higher than -3 dB, i.e. conversion gain is possible. Beyond this, a large bandwidth up to several tens of GHz at the intermediate frequency (IF) is expected. Conventional low- T_c superconductor-isolator-superconductor (SIS) mixers which utilize the quasi-particle tunneling effect are known to have the highest sensitivity, but their mixing performance degrades above 0.7 THz. High-temperature superconductor (HTS) Josephson junctions (JJ) are expected to operate as heterodyne mixers up to some THz due to the relatively high energy gap of the HTS materials. High transition temperatures of HTS materials promise operation temperatures above 20 K. In addition, the low local oscillator power consumption makes the HTS Josephson mixer an attractive candidate for air- and spaceborne receiver applications.

¹ E-Mail: o.harnack@fz-juelich.de

It is known that the sensitivity of Josephson mixers is limited by the intrinsic junction noise and excess noise from Josephson oscillations. Theoretical studies of the noise properties of Josephson mixer were performed by Likharev et al. [1]. Their analysis predicts for normalized frequencies $\Omega > 1$ a minimum noise temperature of $T_n = 10.5T(\omega/\omega_c)^2$, where $\Omega = \omega/\omega_c$ with $\omega_c = 2I_c R_n e/\hbar$ is the characteristic frequency of the Josephson junction (I_c is the critical current, R_n the normal-state resistance of the Josephson junction). An even more optimistic prediction of $T_n = 6T$ was given for signal frequencies ω equal to ω_c ($\Omega = 1$). In the selfmixing mode, i. e. the junction is pumped by the intrinsic Josephson oscillations, the noise temperature was predicted to be equal to T for $\omega > 0.2\omega_c$.

Schoelkopf et al. [2] have recently clarified the origin and the magnitude of this noise by simulations based on the macroscopic resistively shunted junction (RSJ) model. They showed that the linewidth of the internal Josephson oscillation is comparable with the frequency at bias points near the critical current, yielding an excess noise floor at low voltages. Following this analysis the mixer noise temperature depends on the working temperature, the embedding impedances, and the normalized frequency Ω . Their result for the minimum DSB mixer noise temperature was $T_n = 20T$ for $\Omega = 0.5$. These calculations were done for a fixed RSJ fluctuation parameter, $\gamma = 0.01$, which is defined by $\gamma = 2ek_B T/\hbar I_c$. This parameter is the ratio of the thermal energy, $k_B T$, to the Josephson coupling energy, $\hbar I_c/2e$. In general, the noise temperature of a Josephson mixer increases with increasing γ .

Several groups have studied experimentally the mixing properties of HTS Josephson junctions in [3]-[5]. Chen et al. [6] have recently demonstrated frequency downconversion of relatively strong signals at terahertz frequencies using $\text{YBa}_2\text{Cu}_3\text{O}_{7-x}$ (YBCO) bicrystal junctions (BCJ). Noise measurements on YBCO Josephson mixers were performed by Shimakage et al. [5]. They measured a receiver noise temperatures T_r (DSB) of 1800 K in the 100 GHz band and 1200 K in the 300 GHz band.

In this paper we present our experimental study of the noise and mixing properties of two different types of HTS grain-boundary junctions (GBJ): step-edge junctions (SEJ) and bicrystal junctions prepared on MgO substrates. The results of measurements of the mixer noise temperature and the conversion efficiency will be presented. The experiments were performed using a waveguide based setup for W-band frequencies and a quasioptical mixer for frequencies between 300 GHz and 600 GHz.

II. Fabrication of High- T_c Superconductor Josephson Junctions

GBJs, based on intrinsic barriers/interfaces, are specific for high- T_c superconductors and not known for conventional metallic superconductors. This class of Josephson junctions includes different GBJs like SEJs and BCJs. The former junction type can be realized by fabricating GBs at steep substrate steps. In the latter case, a grain boundary which is present in a bicrystal

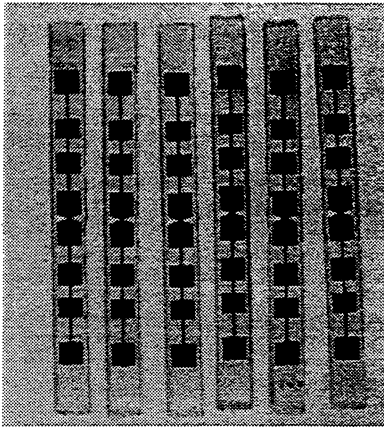


Fig. 1a: Step-edge Josephson junction mixers on MgO for waveguide mount

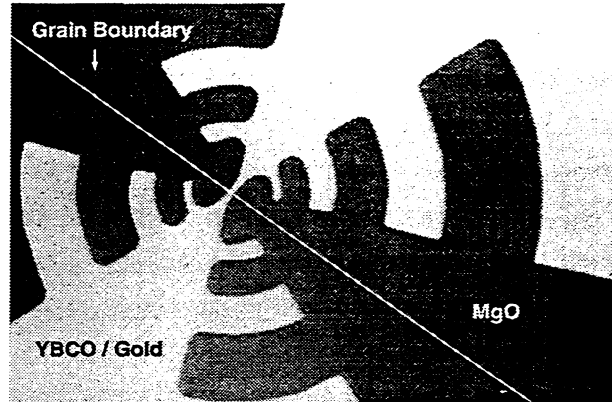


Fig. 1b: Logarithmic-periodic antenna for quasioptical mount with bicrystal junction in the center

substrate grows through the epitaxial HTS film during the deposition. A detailed review on HTS-JJs is given in [7].

For our studies, SEJs and BCJs were fabricated on (100) MgO substrates ($\epsilon_r = 9.6$). Laser deposition method was used for fabrication of thin YBCO films with different thicknesses from 50 nm to 100 nm. After the deposition of the superconductor a approximately 50 nm thick gold layer was sputtered in-situ on the YBCO film. This layer is utilized as a low-loss antenna material and it is also used for electrical contacts. We used standard photolithographic processes and ion beam etching for patterning of the junction and the antenna structure. The Josephson junction consist of a 1 μm wide bridge which crosses a grain boundary (bicrystal junction) or a substrate step (step-edge junction). For step-edge junctions the standard step height was 250 nm and the thickness of the YBCO film was 200 nm. In order to remove the gold shunt from the top of the bridge we opened a window in the gold layer using ion beam etching. The junctions were integrated into bow-tie and logarithmic-periodic antenna layouts for measurements in a waveguide and a quasioptical setup, respectively (see Fig. 1a,b).

III. Waveguide Setup

A waveguide setup for measurements in the W-band was assembled as follows. The LO signal from a Gunn oscillator is combined with a broadband noise signal from an absorber using a two grid diplexer. The combined signals are focussed through the teflon window of a cryostat. The mixer chip is mounted across a section of a rectangular waveguide inside a mixer block which feeds a circular, conical horn. A backshort and an e-plane tuner allow adjustment of the RF embedding impedance. The IF signal output of the mixer is connected to a bias-tee and a circulator which is located outside the cryostat. The IF signal is amplified by a 1.4 GHz IF HEMT amplifier with gain of 34 dB, followed by an amplifier with gain of 35 dB. The amplified signal passes a bandpass filter with a center frequency of 1.4 GHz and bandwidth of 400 MHz. The filtered signal is detected by a power meter. In order to introduce a broadband noise signal towards the mixer, we connected a noise diode to the circulator. The noise temperature T_F of the IF chain was measured to be 230 K using the standard hot/cold load technique (Y-factor method).

IV. Quasi-Optical Setup

For heterodyne mixing experiments in the frequency range between 300 GHz and 600 GHz a quasioptical setup was assembled at Chalmers University of Technology. A backward wave oscillator (BWO) generated the LO signal, and a broadband signal from a black body absorber was combined with the LO signal by using a simple polyethylene beam splitter. The beam was formed by a teflon lens and focussed thru the windows of a LHe cryostat. For filtering of infrared signal contributions we used black polyethylene and fluorogold filters. The mixer chip was mounted on the rear side of a hyperhemispherical MgO lens. The IF signal was connected to a matching circuit and amplified by a cooled amplifier with a circulator at the input.

V. Experimental Results

A. Response to External Pumping

The Josephson junction response to external pumping was investigated in the millimeter and the sub-millimeter wavelength range. Fig. 2 shows the response of a MgO bicrystal junction,

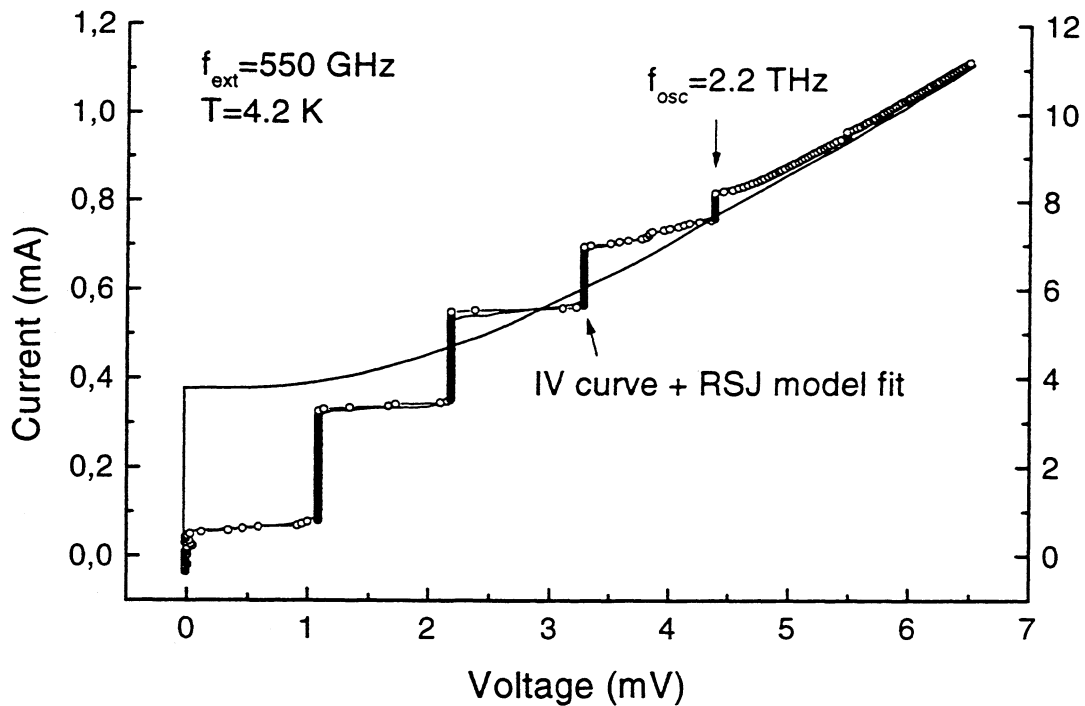


Fig. 2: External pumping of a BCJ on MgO at 550 GHz, with and without external pumping irradiated by 550 GHz radiation using the quasioptical configuration. In this experiment it was possible to suppress the critical current completely to zero (lack of excess current) and we obtained oscillation of the Shapiro step height with increasing power in accordance with RSJ model predictions. The calculated RSJ-model fit ($\Omega=0.5$, $\beta_c=0.8$, $\gamma=0.01$) showed nearly perfect correlation with the experimental data. This means that the junction behavior can be completely described by the RSJ model - also at frequencies above 1 THz. Therefore we can assume that no parasitic effects, e.g. Cooper-pair breaking, occur.

B. Mixer Noise Temperature

Receiver and mixer noise temperatures have been measured by using standard hot/cold load technique (Y-factor method) with 300 K (hot) and 77 K (cold) absorber loads.

1. Waveguide Mixer

For noise measurements in the waveguide setup, we fabricated SEJs on thin MgO substrates in order to reduce the high frequency losses. After the fabrication of several junctions on $10 \times 10 \text{ mm}^2$

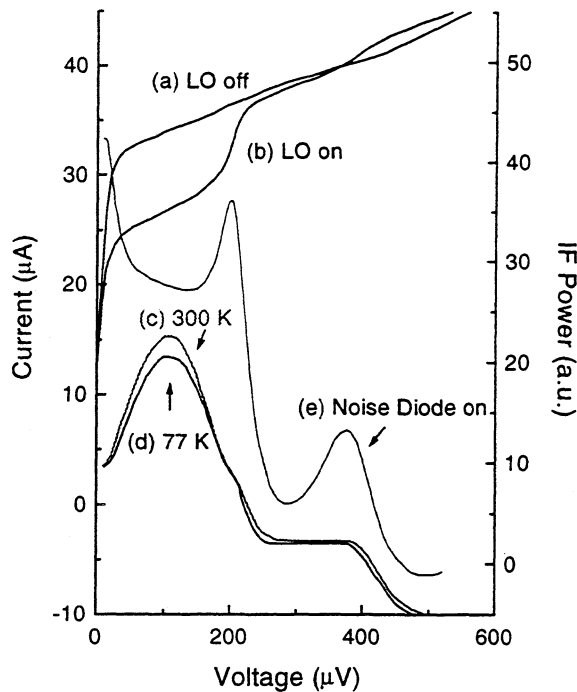


Fig.3: Waveguide mixer noise measurement

substrates, we reduced the substrate thickness down to approximately 150 μm and cutted each junction into a small $0.9 \times 10 \text{ mm}^2$ strip (see Fig. 1 a).

The output noise of the mixer was measured at different current biaspoints. The best sensitivity of the receiver was obtained by maximizing the IF output power at biaspoints between the zeroth and the first Shapiro step with respect to tuner positions and local oscillator level. It is important to note that only a very narrow range of the tuner positions allowed a response of the mixer output to a change of the input absorber load temperature.

The results at a physical temperature of 10 K and 90-94 GHz LO frequency are displayed in Fig. 3. Curve (a) and (b) show the unpumped and the pumped IVC of the mixer, respectively.

The characteristic voltage of this step-edge junction was 450 μV at 10 K corresponding to a characteristic frequency of 218 GHz and $\Omega_{90}=0.41$. Curve (c) and (d) in Fig. 3 show the output noise of the mixer with a 300 K and a 77 K absorber load in front of the receiver, respectively. From this measurement, the calculated receiver noise temperature T_R was 3300 K. The mixer's conversion loss could also be determined using a reflection measurement method in order to get a measure of the reflection coefficient Γ which implies the impedance mismatch between mixer and IF amplifier. For this measurement, a broadband (DC-18 GHz) noise signal was introduced into one port of the circulator to be launched towards the mixer and reflected from the mixer into the input of the IF line. From the difference in IF power with and without the noise diode applied we can derive Γ [8]-[9].

Curve (e) in Fig. 3 displays the result of a reflection measurement. The differential resistance which determines the real part of the mixer's IF impedance was very close to the normal resistance R_n of 15 Ω of the junction at biaspoints between Shapiro steps. The best matching was obtained between the zeroth and the first Shapiro step with a Γ of approximately 0.47.

Knowing Γ and T_{IF} , we calculated a conversion loss of approximately -7.6 dB and an IF contribution to the receiver noise temperature of approximately 1300 K. The DSB mixer noise temperature is then estimated to be 2000 K including all front-end losses at the receiver input.

The fact that the differential resistance was close to R_n can be related to a high noise smearing of the IV curve. We expect a infinite (if noise current is zero) or high dynamical resistance between the Shapiro steps, since $\Omega_{90} < 1$ (unseparated steps). In contrast, in our experiment the noise current was 5 times larger than the thermal noise current at 10 K. We attribute this to a high external noise contribution, which also increased the mixer noise temperature.

2. Quasi-Optical Mixer

Measurements in the quasi-optical configuration showed DSB mixer noise temperatures of 1200 K at 430 GHz (Fig. 4a) and 1100 K at 546 GHz (Fig. 4b) including all front-end losses. The operation temperature was 4.2 K. The critical current of the BCJ on MgO was 300 μA and the normal resistance was about 10 Ω . This yields a formally calculated $I_c R_n$ product of 3 mV and normalized frequencies of $\Omega_{430}=0.29$ and $\Omega_{546}=0.37$. The conversion efficiency was estimated by dividing the variation of the input temperature 300-80 K = 220 K by the related IF output power variation of about 10 K (compared to the IF amplifier noise temperature measured separately). This yields a uncorrected conversion efficiency of -13.4 dB and a mixer input noise temperature of approximately 50-54 K.

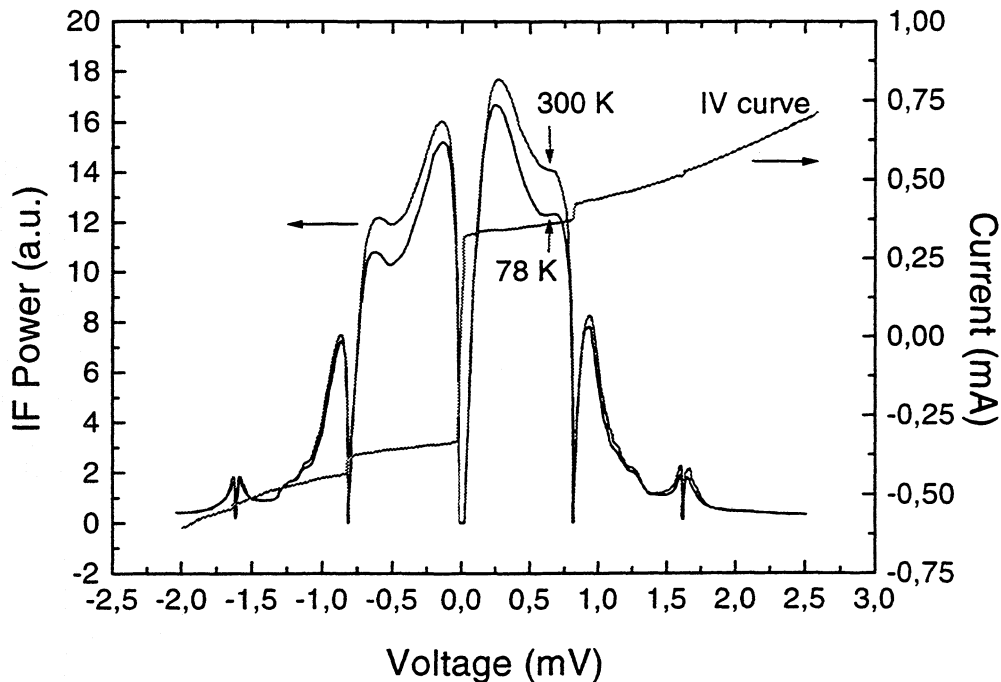


Fig. 4 a: Hot/Cold noise measurement at **430 GHz** using a bicrystal HTS Josephson junction, T_m , $T_{DSB} \approx 1200$ K.

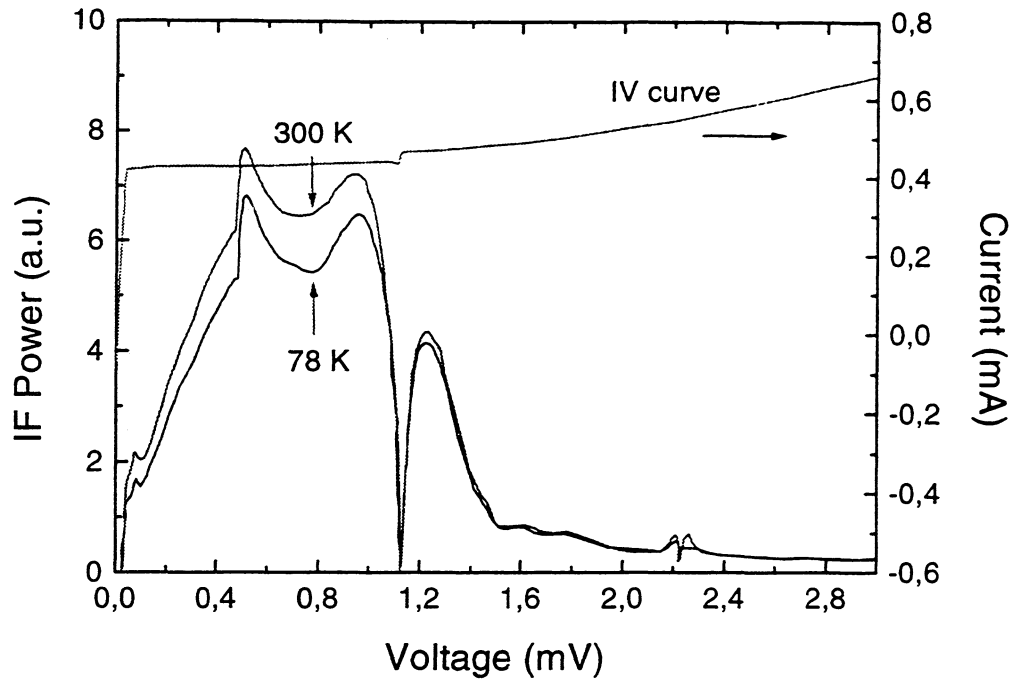


Fig. 4 b: Hot/Cold noise measurement at **546 GHz** using a bicrystal HTS Josephson junction, $T_{m, DSB} \approx 1100$ K.

C. Selfpumped Mode

We also performed mixer noise measurements in the self-pumped mode. For these measurements we closed the input window of the cryostat by hot and cold absorber. It is important to exclude any direct detection effects, i.e. the IV curve of the mixer should not respond to the absorber load. Fig. 5 shows the result of a noise measurement in the self-pumped mode at 4.2 K. The mixer is the same device as in the experiments with external pumping. From this data we extract a mixer noise temperature of 580 - 2300 K in the dc bias range 0.1-0.5 mV. Interesting features are the clearly visible minima and maxima in the IF output signal which are related to geometrical resonances of the “teeth” of the logarithmic-periodic antenna (Fig. 1b). The differential resistance is reduced at the point of a resonance what results a change of the mixer impedance matching selfpumped mode.

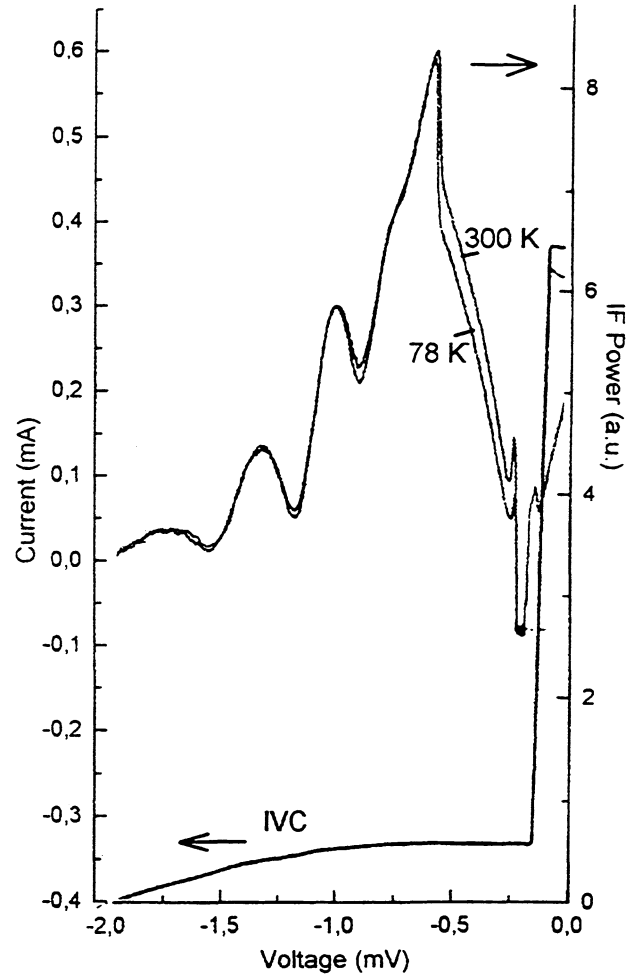


Fig. 5: Hot/Cold-measurement in the to the IF amplifier.

VI. Discussion and Conclusion

The experimental results show that with high- T_c grain boundary Josephson junctions frequency conversion is possible at large IF bandwidths, high working temperatures, and low LO power levels which are important requirements for mixer applications in the mm and sub-mm wavelength range.

Following the analysis of Likharev et al., the best expectable mixer noise temperature should be approximately 26 K and 60 K at a physical temperature of 4.2 K and 10 K, respectively. In fact, the condition $\Omega < 0.5$ was satisfied in all of our experiments. The analysis of Schoelkopf predicts

a best DSB mixer noise temperature of 84 K at 4.2 K and 200 K at 10 K for $\gamma=0.01$. The measured noise temperatures differ by a large factor from the theoretical predictions. However, we have to keep in mind that the measured values were not corrected for any kinds of receiver input losses. For the quasi-optical experiments, these losses include all losses of the beam splitter, window, and lens. The impedance mismatch between the mixer and the logarithmic-periodic antenna was quite large, since the required junction impedance was about 60 Ohm for this antenna on MgO. In contrast, the normal resistance of the mixer used in the quasi-optical measurement was 10 Ohm.

Additionally, the beamwidth was not optimized and consisted of two comparable lobes what gives about 2-4 dB losses. The broaden beam and the tilted polarization of the antenna with variation of frequency gave also 300 K influence from the sidelobes (3-4 dB losses). In fact, we have reflections from the MgO-vacuum interface, from the fluorogold-vacuum, and from the teflon window-air interface that gives about 2 dB losses in summary. The back lobe of the antenna on MgO gives about 1 dB more losses. These simple calculations of about 8-11 dB input losses, which can be reduced, show that our experimental results underestimate the performance of the Josephson mixer.

Other sources of noise are more of physical nature: $1/f$ noise which includes a number of different noise mechanisms (telegraph-like noise, fluctuations of critical current and resistance) could contribute to the overall mixer noise. In the RSJ model simulations only the presence of thermal noise was assumed and up to now, no other sources of noise were included. Indeed, at present we have no clear understanding how the intrinsic junction noise influences the mixer performance.

However, the experimental results demonstrate, that the Josephson mixer noise temperature is more or less independent of the operation frequency. We expect this behaviour as long as the normalized frequency $\Omega=\omega/\omega_c$ can be held constant for higher operation frequencies. The characteristic frequency ω_c is connected to the energy gap of the superconducting material. Due to the high energy gap of HTS material we expect that HTS Josephson mixers will prove to be useful for receiver applications at high working temperatures in the THz frequency range.

Acknowledgement

This work is supported by the German Ministry of Education and Research (BMBF) and in part by the European Community under Grant No. IC15-CT96-0806 (INCO-Copernicus project). We would also like to thank P. Zimmermann from Radiometer Physics GmbH, K. Jacobs from KOSMA/University of Cologne, and E. Tong for useful help and fruitful discussions.

References

- [1] K. K. Likharev, V. V. Migulin, Josephson effect millimeter range receivers, *Radio Engineering and Electron Physics*, v. 25, June 1980, pp. 1-18
- [2] R. J. Schoelkopf, J. Zmuidzinas, and T. G. Phillips; R.J. Schoelkopf, Ph.D. dissertation, California Institute of Technology, 1995 (unpublished)
- [3] J. P. Hong, H. R. Fetterman et al., *Appl. Phys. Lett.*, **62**, 22, 1993
- [4] Y. Fukumoto, R. Ogawa and Y. Kawate, *Jpn. J. Appl. Phys.*, **32**, 1993
- [5] H. Shimakage, Y. Uzawa, M. Tonouchi, Z. Wang, *ASC'96*, Pitsburg 1996
- [6] J. Chen, H. Myoren, K. Nakajima, T. Yamashita, P. H. Wu, *Appl. Phys. Lett.*, **71** (5), 1997
- [7] R. Gross, L. Alff, A. Beck, O. M. Froehlich, D. Koelle, A. Marx, *IEEE Trans. on Appl. Supercon.*, Vol. 7, No. 2, June 1997
- [8] R. J. Schoelkopf, J. Zmuidzinas, T. G. Phillips, H. G. LeDuc, and Jeffrey A. Stern, *IEEE Trans. on Microw. Theor.*, Vol. 43, No.4, April 1995
- [9] R. J. Schoelkopf, T. G. Phillips, and J. Zmuidzinas, *IEEE Trans. on Appl. Supercon.*, Vol. 3, No.1, 1993

Design of 100-900 GHz AlGaAs/GaAs Planar Heterostructure Barrier Varactor Frequency Triplers

¹Jan Stake, ¹Lars Dillner, ²Stephen H. Jones, ³Chris Mann, and ¹Erik Kollberg

¹Microwave Electronics Laboratory, Chalmers University of Technology, SE-412 96 Göteborg,

²University of Virginia, Charlottesville, VA 22903, USA

³Rutherford Appleton Laboratory, Chilton, Oxon, UK

Email: stake@ep.chalmers.se

Abstract—In this paper we offer a simple set of accurate frequency-domain design equations that can be used to calculate optimal embedding impedances and tripling efficiency. These equations can be used for a wide range of device and circuit parameters. The effects of parasitic resistance and operating temperature on device performance, and how these parameters vary with device design are explored. Comparisons to experiment are made for planar HBVs demonstrating at least 3% efficiency at 78 GHz input frequency and 50 mW of input power.

Index Terms—HBV, varactor frequency tripler.

I. INTRODUCTION

The Heterostructure Barrier Varactor (HBV) diode [1, 2] is ideally suited for frequency tripling in the millimeter wave and sub-millimeter wave regime. The symmetric capacitance-voltage characteristic of the HBV allows for tripler design without requiring second-harmonic idler circuits or DC bias. In principle, this should make HBV triplers easier to design and implement; however, the complex device structure and device physics can make the overall tripler design process more difficult. In particular, the design and fabrication of the devices are more difficult than Schottky diode structures used in similar applications. Subsequently, the output power and efficiency from Schottky diode varactor multipliers are still somewhat superior to HBV

multipliers [3-5]. In this paper we describe the basic design concepts, equations, and parameters related to GaAs-AlGaAs-GaAs planar HBVs.

II. HBV MULTIPLIER ANALYSIS

A. Intrinsic device model

A generic layer structure of an HBV is shown in table i. For N epitaxially stacked barriers, the layer sequence 2-5 is repeated N times. The intrinsic part of the HBV consists of layer 2-6, where a high band-gap material (layer 4) prevents electron transport through the structure and the diode capacitance is modulated due to depletion of carriers in layers 2 and 6.

TABLE I: HBV GENERIC LAYER STRUCTURE

Layer No.		Thickness [Å]	Doping level [cm ⁻³]
7	Contact	~ 3000	n ⁺⁺
6	Depletion	1 ~ 3000	N _d ~ 10 ¹⁷
5	Spacer	s ~ 50	Undoped
4	Barrier	b ~ 200	Undoped
3	Spacer	s ~ 50	Undoped
2	Depletion	1 ~ 3000	N _d ~ 10 ¹⁷
1	Buffer		n ⁺⁺
0	Substrate		n ⁺⁺ or SI

In our analysis, we use a two element model for the intrinsic part of the HBV: a non-linear differential elastance, $S(V) = dV/dQ = 1/C(V)$, in series with a non-linear parasitic resistance, $R(V)$. Varactor mode of operation for HBVs is

preferred and therefore large conduction currents should be reduced as much as possible for optimal performance.

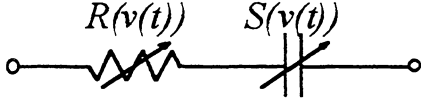


Figure 1: Intrinsic equivalent circuit of a pure varactor diode (i.e. no leakage current).

Elastance model

The minimum differential elastance of an HBV is determined by the effective separation distance between the charge on each side of the barrier. For a typical HBV structure (see table i) the minimum elastance per barrier can be estimated as

$$S'_{\min} = \frac{b}{\epsilon_b} + \frac{2s}{\epsilon_d} + \frac{2L_D}{\epsilon_d} [\text{m}^2/\text{F}] \quad (1)$$

$$S_{\min} = \frac{N}{A} S'_{\min}$$

where N is the number of barriers, A is the device area, and L_D is the Debye length:

$$L_D = \sqrt{\frac{kT\epsilon_d}{q^2 N_D}} \quad (2)$$

During a pump-cycle, the differential elastance is modulated due to depletion of carriers and the overall elastance can, therefore, be expressed as the sum of the above linear term and a non-linear part as:

$$S(t) = \frac{N}{A} \left(S'_{\min} + \underbrace{S'_d(t)}_{\text{depletion}} \right) [1/\text{F}] \quad (3)$$

$$S'_d(t) \in \left[0, A \frac{S_{\max} - S_{\min}}{N} \right]$$

where S_{\min} and S_{\max} are the minimum and maximum elastance during a pump cycle

respectively. The maximum differential elastance is determined by the maximal extension of the depletion region, w_{\max} , as:

$$S'_{\max} = \frac{b}{\epsilon_b} + \frac{2s}{\epsilon_d} + \frac{w_{\max}}{\epsilon_d} [\text{m}^2/\text{F}] \quad (4)$$

For an HBV, the depletion length limit is determined by at least one of three “breakdown” conditions each giving a different value for w_{\max} . These are: 1) depletion layer punch-through and $w_{\max}=l$, 2) large electron conduction across the barrier region at large voltage, V_{\max} , or 3) large currents from avalanche breakdown at large voltage. To maintain varactor efficiency the conduction current should be minimized. For relatively large band gap materials such as GaAs-AlGaAs-GaAs conditions 1 and 2 appear to dominate. In order to calculate w_{\max} used in equation 4 it is necessary to estimate the peak operating voltage. For optimal performance, $w_{\max} = l$. If the punch-through voltage is greater than the voltage at the onset of large conduction current the maximum depletion width cannot be achieved. For this case, w_{\max} will be reduced and its value must be estimated. This is particularly important when the device temperature is increased and conduction current across a moderate HBV barrier is increased.

It is possible to estimate w_{\max} by calculating the voltage at which the conduction current through the device is nearly equal to the displacement current. For HBVs, the conduction current is approximately

$$I(E_b) = A \cdot a T^2 \text{Sinh} \left(\frac{E_b}{E_o} \right) e^{-\frac{\phi_b}{kT}} \quad (5)$$

where a , ϕ_b , and E_o are fitting parameters and E_b is the electric field in the barrier and can be estimated as:

$$E_b = qN_d \frac{b\varepsilon_d + 2s\varepsilon_b}{\varepsilon_b^2} \cdot \left(\sqrt{1 + \frac{2\varepsilon_d \varepsilon_b^2 V_{\max}}{NqN_d (b\varepsilon_d + 2s\varepsilon_b)^2}} - 1 \right) \quad (6)$$

Taking the derivative of equation (5) (device conductance) and given:

$$\left. \frac{dI(V, T)}{dV} \right|_{V=V_{\max}} \ll \omega_p C_{\max}. \quad (7)$$

For strong conduction, one can solve for V_{\max} and w_{\max} where conduction is dominant.

Intrinsic Series Resistance

The parasitic series resistance is the sum of the resistance of undepleted active layers, the spreading resistance, and the ohmic contact resistance. However, only the resistance of undepleted layers contributes to the intrinsic varactor model shown in figure 1. All extrinsic impedances can be regarded as a part of the embedding circuit, see figure 2. If the depletion layer, No. 2,6 in Table I, is homogeneously doped and an abrupt space charge is assumed, the resistance of undepleted layers can be expressed as a function of the length of the depleted region, w , as

$$R(t) = \frac{\rho_d}{A} (l + N(l - w(t))) \quad (8)$$

$$w(t) \in [0, l]$$

where l is the length of the depletion layer and ρ_d is the corresponding resistivity. For simplicity, the extension of the depletion region, $w(t)$, is assumed to be proportional to the elastance as

$$w(t) = \varepsilon_d S'_d(t) \quad (9)$$

which in combination with (8) gives:

$$R(t) = \frac{\rho_d}{A} (l + N(l - \varepsilon_d S'_d(t))) \quad (10)$$

B. The frequency tripler circuit

The time-dependent voltage, $v(t)$, across the diode terminals in figure 1 can with the above proposed HBV model (3,10) be written as:

$$v(t) = \frac{\rho_d l}{A} (1 + N)i(t) - \frac{N\rho_d \varepsilon_d}{A} S'_d(t)i(t) + \int S(t)i(t)dt \quad (11)$$

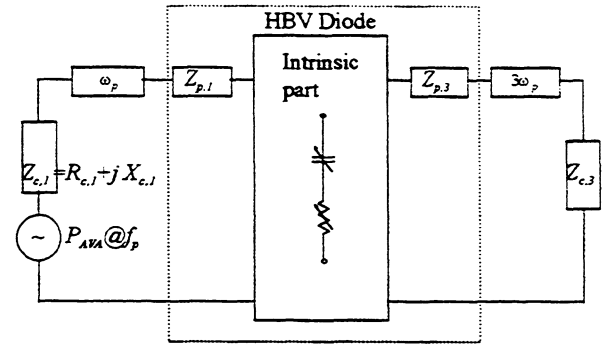


Figure 2: Schematic view of an HBV tripler circuit.

Since we are interested in the periodic steady-state solution of the above circuit equation (11), we represent the voltage-, current- and the elastance-waveforms in the frequency domain and the time-domain equation takes the following form for the kt harmonic [7,11]:

$$V_k = \frac{\rho_d l}{A} (1 + N)I_k + \frac{N}{A} \frac{S'_{\min}}{jk\omega_p} I_k + \frac{N}{A} \left(\frac{1}{jk\omega_p} - \rho_d \varepsilon_d \right) \sum_{l=-\infty}^{\infty} I_l S'_{d,k-l} \quad (12)$$

The two first terms are linear but the last term accounts for the complex movement of the depletion edge. The current and the elastance

harmonics can be found by imposing embedding circuit conditions

$$V_k = V_k^{source} - (Z_{c,k} + Z_{p,k})I_k \quad (13)$$

where $Z_{c,k} = R_{c,k} + jX_{c,k}$ is the embedding circuit impedance and $Z_{p,k} = R_{p,k} + jX_{p,k}$ is the extrinsic parasitic impedance, see figure 2. Furthermore, define the complex modulation ratio as $M'_k = S'_k / (S'_{max} - S'_{min})$ and a general form of the large-signal device impedance, $Z_{d,k}$, within our varactor circuit model can be written as:

$$Z_{d,k} = \frac{\rho_d I}{A} (1 + N) + \frac{N S'_{min}}{A jk\omega_p} + \frac{N(S'_{max} - S'_{min})}{A} \left(\frac{1}{jk\omega_p} - \rho_d \varepsilon_d \right) \frac{1}{I_k} \sum_{l=-\infty}^{\infty} I_l M'_{d,k-l} \quad (14)$$

Optimal embedding impedances

The summation over all current and elastance harmonics in (14) is a complex value which depends slightly on circuit conditions (13) and on physical details of the HBV itself. However, for maximum conversion efficiency when all available pump-power is absorbed and the third harmonic power delivered to the load is maximized, we assume that this complex summation is independent on external conditions and HBV layer structures. Consequently, the optimal embedding impedances, $Z_{c,n}$, close to any operating point can be expressed as

$$\begin{aligned} R_{c,1} &\approx R_{p,1} + \frac{\rho_d I}{A} (1 + N) \\ &\quad + \frac{N}{A} (S'_{max} - S'_{min}) \left(\frac{A_1}{\omega_p} - \rho_d \varepsilon_d C_1 \right) \\ X_{c,1} &\approx -X_{p,1} + \frac{N S'_{min}}{A \omega_p} \\ &\quad + \frac{N}{A} (S'_{max} - S'_{min}) \left(\frac{B_1}{\omega_p} - \rho_d \varepsilon_d D_1 \right) \\ R_{c,3} &\approx R_{p,3} + \frac{\rho_d I}{A} (1 + N) \\ &\quad + \frac{N}{A} (S'_{max} - S'_{min}) \left(\frac{A_3}{3\omega_p} - \rho_d \varepsilon_d C_3 \right) \\ X_{c,3} &\approx -X_{p,3} + \frac{N S'_{min}}{A 3\omega_p} \\ &\quad + \frac{N}{A} (S'_{max} - S'_{min}) \left(\frac{B_3}{3\omega_p} - \rho_d \varepsilon_d D_3 \right) \end{aligned} \quad (15)$$

where A_n , B_n , C_n , and D_n are fitting coefficients. If these parameters are extracted for realistic operating conditions and with accurate large-signal device simulator, the above optimal embedding impedances can be calculated for a wide range of device and circuit parameters.

Dynamic cut-off frequency

The dynamic cut-off frequency of a pure varactor device (i.e. no leakage current) is defined as:

$$f_c = \frac{S_{max} - S_{min}}{2\pi R_s} \quad (16)$$

With the proposed intrinsic varactor model in Section IIa, define the series resistance as the sum of the maximal value of the intrinsic resistance (8) and the real part of the extrinsic parasitic impedance at the fundamental harmonic. If the equations for maximal and minimal elastance and the series resistance are

inserted in (16), the dynamic cut-off frequency for an HBV can finally be calculated as:

$$f_c = N \frac{w_{max} - 2L_D}{2\pi\epsilon_d (AR_{p,1} + \rho_d(1+N))} \quad (17)$$

As shown above, it is very important to reduce the parasitic resistance as much as possible relative to the intrinsic device resistance. Also, w_{max} should be large relative to L_d to insure significant capacitance modulation and tripling. As described above, to optimize f_c the conduction current should be minimized and $w_{max}=l$.

Pump power and conversion efficiency

The conversion efficiency is defined as the power delivered to the load at the third harmonic divided by the available input power and for a pure varactor multiplier, the efficiency is determined by the ratio of the pump-frequency and the dynamic cut-off frequency [6, 7]. A quick and fast estimation of the maximum conversion efficiency can be achieved from the following empirical expression

$$\eta \approx \frac{100}{1 + \alpha \left(\frac{f_p}{f_c}\right)^\beta} [\%] \quad (18)$$

where α and β are extracted from detailed large-signal simulations for a wide range of devices and circuit conditions, see table ii. For maximum possible efficiency f_c should be increased to its maximal value as described in equation 17.

Finally, it is necessary to estimate the input power needed to modulate the elastance of an HBV from S_{min} to S_{max} . The pump-power can be estimated as

$$P_{AVA} = \frac{|V_s|^2}{8R_{c,1}} = \frac{R_{c,1}}{2|Z_{d,1}|^2} |V_1|^2 \quad (19)$$

$$\approx \gamma \frac{R_{c,1}}{2|Z_{c,1} - Z_{p,1}^*|^2} |V_{max}|^2$$

where γ is also a fitting coefficient, see table ii. Equation 19 insures that reasonable device parameters and required input powers are designed for a particular application.

III. RESULTS AND DISCUSSION

A. Parameter extraction

All the coefficients were extracted by analyzing two four-barrier HBVs with an integrated Drift-Diffusion Harmonic Balance (DDHB) simulator [8, 9]. The pump frequency was 90 GHz and the device area $66 \mu\text{m}^2$. All simulations were performed by assuming a homogenous temperature of $T = 300 \text{ K}$ across the active device region. A field-independent (low field) electron mobility of $4375 \text{ cm}^2/\text{Vs}$ in the GaAs region and a calculated extrinsic parasitic series resistance of $R_{p,1} = 4.9 \text{ ohm}$ were used. Intrinsic losses, e.g. ohmic losses in layers (No. 2,6), are fully taken into account by the DDHB simulator. The conversion efficiency was maximized by tuning the embedding impedances at the first and the third harmonic respectively. Finally, coefficients for the design equations (15,18,19) were extracted, see table ii. These coefficients allow the optimal embedding impedances and efficiency to be easily calculated.

TABLE II: HBV DESIGN COEFFICIENTS

Extraction conditions: $f_p/f_c \sim 0.05$			
$A_1 = 0.047$	$B_1 = 0.33$	$C_1 = -0.17$	$D_1 = -2.5$
$A_3 = 0.24$	$B_3 = 0.66$	$C_3 = -1.3$	$D_3 = 4.9$
$\alpha = 200$	$\beta = 1.4$	$\gamma = 0.7$	

Comparison to experimental results

Device structure and measured performance

The epitaxial layer structure in table iii has been fabricated into a planar HBV configuration, see figure 4.

TABLE III: UVA-NRL-1174

Layer	Material	Doping [cm ⁻³]	Thickness [Å]
9	InAs	5×10 ¹⁸	100
8	In _{1-x} GaAs	5×10 ¹⁸	400
7	GaAs	5×10 ¹⁸	3000
6	GaAs	8×10 ¹⁶	2500
5×4	GaAs	Undoped	35
4×4	Al _{0,7} GaAs	Undoped	200
3×4	GaAs	Undoped	35
2×4	GaAs	8×10 ¹⁶	2500
1	GaAs	5×10 ¹⁸	40000
0	GaAs	SI	-

An HBV device with an anode area of 89 μm² was mounted and tested in a tripler waveguide block (RAL DB2a). A flange-to-flange peak-efficiency of 3.1 % was achieved at an output frequency of 234 GHz. The maximal output power was 3.6 mW, see figure 3. The estimated loss at the input- and output circuit are approximately 1 dB and 2 dB respectively.

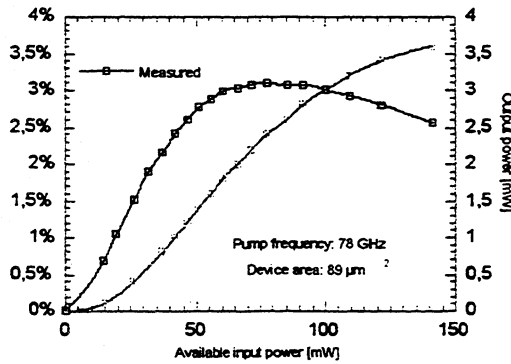


Figure 3: Measured output power and efficiency at an output frequency of 234 GHz.

Estimated thermal and parasitic resistance

In order to explain the lower than expected efficiency shown in figure 3, the effect of self-

heating must be taken into account. This has been described in section IIA. For a 8 μm diameter device and by assuming a point heat-source in the middle of the active region, Jones [10] has estimated the thermal resistance through the finger and the GaAs substrate to $R_t = 2$ K/mW for this device geometry. Furthermore, if we assume that the thermal resistance is inversely proportional to the anode diameter and an input circuit loss of 1 dB, the device temperature can be as high as 400 K for the 10 μm (89μm²) HBV used and an available pump power of 80 mW.

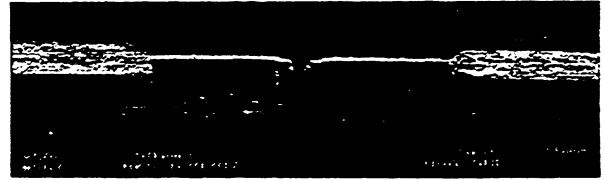


Figure 4: Planar HBVs (UVA-NRL-1174-17).

The extrinsic parasitic series resistance consists of the ohmic contact resistance and the spreading resistance in the n⁺⁺ island that connects the two diodes. By using standard expressions for these losses, we can approximate the temperature dependent parasitic series resistance as

$$Z_{p,1} = Z_{p,3} = \frac{200}{A} + \left(4 + \frac{20}{\sqrt{A}} + \frac{100}{A}\right) \frac{T}{298} \quad (20)$$

where A is the anode area in μm². The first term represents the contact resistance and the second term estimates the spreading resistance in the n⁺⁺ island.

Conversion efficiency

The negative effect of heating on the dynamic cut-off frequency (17) results from the temperature dependence of the series resistance (20) and the Debye-length (2), as well as the reduction in maximal depletion length, w_{max} , as the temperature increases.

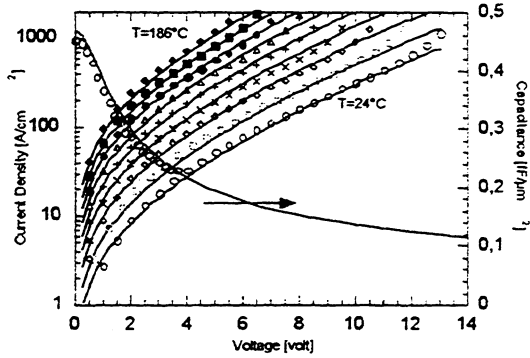


Figure 5: Measured C-V (RT) and I-V (RT-186°C) characteristics of the UVA-NRL-1174 HBV material.

The conversion efficiency increases with pump power as long as the conduction current through the barrier is negligible compared to the displacement current. The measured I-V characteristic versus temperature and C-V characteristic for the UVA-NRL-1174 device are shown in Figure 5. The parameters: $\alpha = 170 \text{ A}/(\text{m}^2\text{K}^2)$, $E_o = 4.2 \times 10^6 \text{ V}/\text{m}$, and $\phi_b = 0.17 \text{ eV}$ in (5) provides an excellent fit with measured I-V characteristic at different temperatures. As a guideline, to ensure varactor mode of operation, the maximum voltage, V_{max} , can be estimated versus temperature as:

$$\left. \frac{dI(V,T)}{dV} \right|_{V=V_{max}} = \frac{1}{10} \omega_p C_{max} . \quad (21)$$

The value of 1/10 can be adjusted significantly and only have a minor effect on the overall value of the efficiency.

Using the analysis outline in IIA w_{max} was calculated for temperatures ranging from 250-500 K. Then, the predicted efficiency over this range was calculated using equations (17,18) with the coefficients in Table II. The results are shown in Figure 6 (including 3 dB of circuit loss). The experimental results are shown. As seen, the efficiency is reduced at higher temperatures as the conduction current increases and $w_{max} < 1$. Also, if the parasitic

resistance is reduced the entire curve will shift up. For Figure 6 the parasitic resistance is approximately 12 ohms and calculated using equation 20.

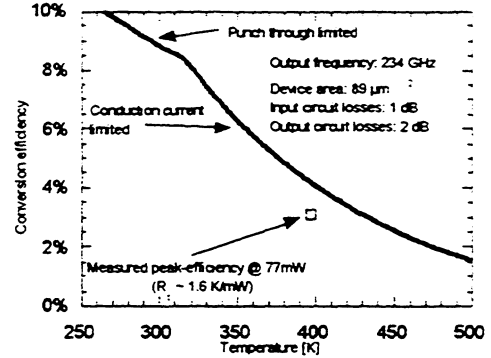


Figure 6: Maximal efficiency versus device temperature.

Finally, with the design-coefficients in table ii and equations (1-2,4,15,20) the optimal embedding impedances for a device temperature of 400 K can be estimated: $Z_{c,1} = 21 + j97$ and $Z_{c,3} = 27 + j36$.

IV. CONCLUSIONS AND SUMMARY

We have described a complete model that can be used to predict the optimal embedding impedances and efficiency for HBVs. The important effects of self heating and the need to minimize parasitic resistance have been described. Comparisons to experimental results are favorable. Based on the analysis described here a new set of HBVs have been designed and will be tested in the near future.

V. ACKNOWLEDGMENT

Jan Stake was supported during this work by the SSF High Speed Electronics program. The work was also partly sponsored by grants from LM Ericsson and the Royal Swedish Academy of Sciences. Thanks are due to William L. Bishop, Art Lichtenberger, Benjamin Sarpong, Steven Marazita, and Tom Crowe of the Semiconductor Device Laboratory at the

University of Virginia for their support during device fabrication.

Theoretical Investigation of the Heterostructure Barrier Varactor." in *School of Electrical Engineering*. Charlottesville: University of Virginia, 1996.

REFERENCES

- [1] E. L. Kollberg and A. Rydberg, "Quantum-barrier-varactor diode for high efficiency millimeter-wave multipliers," *Electron. Lett.*, vol. 25, pp. 1696-1697, 1989.
- [2] A. Rydberg, H. Grönqvist, and E. L. Kollberg, "Millimeter- and Submillimeter-Wave Multipliers Using Quantum-Barrier-Varactor (QBV) Diodes," *IEEE Trans. Electron Devices*, vol. 11, pp. 373-375, 1990.
- [3] N. R. Erickson, "High Efficiency Submillimeter Frequency Multipliers," presented at IEEE MTT-S, Dallas, 1990.
- [4] N. R. Erickson, "A High Efficiency Frequency Tripler for 230 GHz," presented at 12th European Microwave Conf, Helsinki, 1982.
- [5] J. Thornton, C. M. Mann, and P. d. Maagt, "A High Power 270 GHz Frequency Tripler Featuring a Schottky Diode Parallel Pair," presented at IEEE-MTT Int. Microwave Symp. Digest, Denver, USA, 1997.
- [6] L. Dillner, J. Stake, and E. L. Kollberg, "Analysis of Symmetric Varactor Frequency Multipliers," *Microwave Opt. Technol. Lett.*, vol. 15, pp. 26-29, 1997.
- [7] P. Penfield and R. P. Rafuse, *Varactor Applications*. Cambridge: M.I.T. Press, 1962.
- [8] J. R. Jones, G. B. Tait, S. H. Jones, and S. D. Katzer, "DC and Large-Signal Time-Dependent Electron Transport in Heterostructure Devices: An Investigation of the Heterostructure Barrier Varactor," *IEEE Trans. Electron Devices*, vol. 42, pp. 1393-1403, 1995.
- [9] J. Stake, S. H. Jones, J. R. Jones, and L. Dillner, "Analysis of Carrier Transport in a Heterostructure Barrier Varactor Diode Tripler," presented at 1997 International Semiconductor Device Research Symposium, Charlottesville, 1997.
- [10] J. R. Jones, "CAD of Millimeter Wave Frequency Multipliers: An Experimental and
- [11] R. E. Lipsey, S. H. Jones, and T. W. Crowe, "Accurate Circuit and Device Equations for Designing 50-600 GHz GaAs Schottky Diode Varactor Frequency Doublers", presented at Eight International Symposium on Space Terahertz Technology, Boston, 1997.

A COMPACT 500 GHz PLANAR SCHOTTKY DIODE RECEIVER WITH A WIDE INSTANTANEOUS BANDWIDTH

B J Maddison¹, R J Martin², M L Oldfield¹, C M Mann¹, D N Matheson¹, B N Ellison¹, J Thornton¹, W J Hall² and D M Lamarre³.

(1) Rutherford Appleton Laboratory, Chilton, Didcot, Oxon, OX11 0QX

(2) Matra Marconi Space UK Ltd., P.O.Box 16, Filton, Bristol, BS34 7YB

(3) ESTEC, Postbus 299, 2200 AG Noordwijk

Abstract

Microwave Limb Sounding has proved to be an important technique for probing the Earth's atmosphere. Studies of proposed atmospheric chemistry instruments have shown a requirement for single sideband heterodyne radiometers which operate at frequencies up to ~900 GHz, with wide instantaneous bandwidth (up to 20 GHz), good sensitivity and high beam efficiency.

Here we report results from a very compact, solid state sub-harmonically pumped planar diode mixer receiver operating in a broad frequency band around 500 GHz. LO power is supplied by an ~87 GHz fundamental Gunn diode oscillator multiplied by a whisker contacted Schottky varactor diode tripler, and the signal band is selected by a low loss frequency selective surface (FSS) filter positioned in the signal path. The receiver has a simple configuration and good sensitivity over a wide instantaneous bandwidth; total SSB system noise is about 10,000K when measured in a band from 498.5 - 505 GHz.

Introduction

The need to measure atmospheric processes involved in ozone depletion and global climate change has highlighted the potential of microwave limb sounding in the lower stratosphere and upper troposphere. Successful measurements in the stratosphere can be made with receivers which have instantaneous bandwidths similar to those generally employed in radio astronomy receivers, typically ~1 GHz (e.g., UARS MLS [1]). However, because of pressure broadening, at lower altitudes an instantaneous bandwidth of several GHz may be needed to properly establish the line shape of even a single emission feature. Further receiver design constraints include the requirement for very high efficiency optical coupling to the detector (to avoid confusing signals from directions away from the intended field-of-view) and a simple, reliable design (because of the remote, often hostile environment encountered in aircraft and satellite operation).

For these reasons the design of sub-millimetre receivers most commonly encountered in ground based telescopes may not be appropriate. Specifically, it is difficult to inject signal and Local Oscillator (LO) power into a single ended fundamental mixer whilst maintaining a wide bandwidth. Here we describe a receiver based on a planar double

diode mixing structure, pumped by a Schottky varactor diode tripler. Designs of this type have been specified for a number of instruments at millimetre wavelengths (e.g., MAS, AMSU-B, MHS) and have been demonstrated at frequencies up to 300 GHz. This paper describes preliminary results from a receiver designed to operate in the band 498.5 to 505 GHz, a region of the atmospheric spectrum which includes ClO and a potentially accessible transition of BrO.

Receiver Design

Heterodyne receivers utilising waveguide sub-harmonic mixers (that is, double diode mixers pumped at half the signal frequency) have a number of attractive features from a system design point of view. First, signal and LO frequencies are well separated and can be isolated by simple filters within the waveguide cavity, thus avoiding the requirement for a low loss LO injection network. Not only does this remove an important bandwidth limiting element, it also simplifies the receiver optics and removes a potential cause of baseline instability (that is, lack of spectral flatness across the band when viewing thermal noise of uniform power density). Second, it allows a simpler LO configuration (since power need only be generated at half the signal frequency). Third, and most important, sub-harmonic mixers utilise double diode mixer structures in which two diodes are seen in parallel at the IF. This considerably simplifies IF matching problems, and allows the simple implementation of receivers with wide instantaneous bandwidths; at frequencies up to 300 GHz, sub-harmonic receivers are well known to demonstrate both good sensitivity (approaching that of a good fundamental mixer receiver) and signal bandwidths in excess of 10 GHz.

Consequently, the receiver described here is based on a sub-harmonic pump architecture. Recent improvements in planar diode technology indicate that “flip-chip” diodes can be used at frequencies approaching one terahertz: we have therefore chosen planar diode technology (because of its obvious benefits), and waveguide cavities for both mixer and frequency tripler.

In order to avoid possible confusion from unwanted emission lines it is highly desirable to filter the image sideband. Following a systematic study of optional filtering methods, a frequency selective surface filter (FSS) has been chosen on grounds of performance (insertion loss and filtering characteristics) and mechanical convenience. This is simply positioned in the mixer field of view, in front of a focusing mirror. However, in order to obtain adequate isolation between the signal and image sidebands, it is necessary to operate the mixer at a high IF frequency; a frequency of 19.0 to 25.5 GHz has been selected.

Mixer

The mixer is based on a design developed at RAL for millimetre wavelengths [2] and extended to higher frequencies for the present application. The mixer utilises a crossed waveguide cavity with a reduced height signal waveguide coupled to the optical field of view by a waveguide transformer and a corrugated feedhorn. An anti-parallel “flip-

chip” planar diode pair (type SD1T7 manufactured by the University of Virginia) is soldered onto a quartz substrate which spans the signal waveguide and incorporates necessary signal filtering: LO power (at half the signal frequency) is introduced into the diodes through a waveguide transformer at one end of the filter, and from the opposite end the down converted signal is passed to the IF pre-amplifier.

In order to ensure that signal is coupled to the IF in the 19 to 26 GHz band, a ‘K’ connector has been implemented which efficiently transforms the 50 Ω microstrip filter to a coaxial line with good return loss. Filtering between the LO and signal frequency is achieved with a simple $\lambda/4$ high-low impedance transmission line filter, whilst the IF filter is an empirical hammerhead design, scaled from lower frequencies. Non-contacting, fixed position waveguide backshorts are used to optimise performance. The mixer design has been verified by extensive modelling.

Multiplier

The tripler incorporates a crossed waveguide cavity and is based on a design reported by Archer [3], in which the output waveguide supports both the second and third harmonic of the pump at the diode, before transforming to single moded waveguide supporting the third harmonic at the multiplier output. An optimum embedding circuit for the dot-matrix Schottky varactor type (University of Virginia type 5M4) has been calculated using a non-linear analysis programme [4] and realised through a simple stripline filter in a rectangular enclosure designed to present a near short circuit to the second and third harmonic frequencies at the wall of the output waveguide, and a novel planar probe which straddles the waveguide and includes an integral whisker for contacting the diode. This “planar whisker” technology [5] is simpler to analyse than a wire whisker, and, by varying its width, can be used as a convenient circuit tuning element. Minimal time has been spent characterising the multiplier on its own; rather, performance of the receiver (including the multiplier) has been optimised.

Receiver

Mixer and multiplier have been designed mechanically to fit neatly together with minimal lengths of waveguide, and a custom designed waveguide coupler allows the Gunn source to be phase locked (results presented here, however have been made with a free running Gunn). Waveguide blocks, with other receiver components (focusing mirror, FSS filter and IF amplifiers) are mounted directly to a simple receiver plate.

Although the mixer and frequency multiplier have adjustable tuning shims for receiver optimisation, their drive mechanisms are removable. Consequently, the receiver has been mounted on a plate to which the backshort drive mechanisms are fixed; the waveguide shims are glued to these. Once optimised, the tuning shims can be locked in position, and the adjusters removed.

Results

Receiver performance has been measured at a number of IF frequencies, including 1, 8 and 19 - 25.5 GHz. Allowing for the effect of IF amplifier chains with differing noise characteristics, receiver performance is encouragingly uniform across the complete 1 to 26 GHz frequency band. Near optimum zero biased mixing performance is noted when a Gunn power of $\sim 70 - 100$ mW is applied to the multiplier through a variable attenuator; the varactor diode is typically biased at 5.5 volts and draws a current of 3 to 7 milliamps at these drive levels. Mixer IF return loss is typically greater than ~ 7 dB.

Noise performance has been characterised by measuring the receiver Y factor, using simple CV3 thermal loads (assumed to be at hot and cold temperatures of 295 and 80 K respectively) in the receiver field of view.

Figure 1 illustrates DSB receiver performance measured in a 1 GHz bandwidth at an IF of 8 GHz. In this example, the receiver was optimised with the FSS optical filter removed. A total receiver noise of $\sim 4,800$ K is measured, in spite of an IF amplifier chain of noise temperature ~ 200 K. De-embedded mixer noise performance and conversion loss (including an IF mismatch loss of ~ 0.7 dB) are estimated to be $\sim 2,300$ K and 9.6 dB respectively.

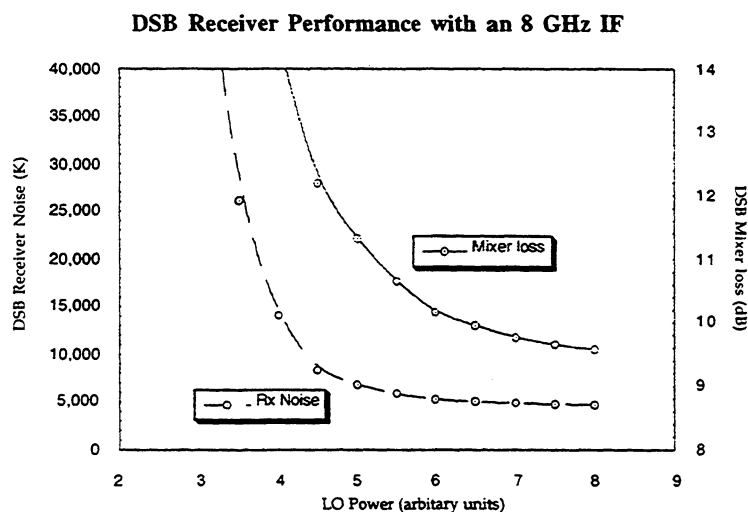


Figure 1: Plot of receiver noise and mixer loss as a function of LO power

Figure 2 illustrates the SSB receiver performance, including the FSS sideband filter, across an integrated IF band 19 to 25.5 GHz (that is, a signal band extending from 498.5 to 505 GHz). In this case the receiver has been tuned to minimise receiver noise in the signal band; we have used an interferometer to investigate the mixer sideband ratio in this configuration and at the optimum backshort tuning point a gain ratio of 2 to 3 was observed. The FSS has been separately characterised using a Fourier transform spectrometer (FTS), which indicated a signal insertion loss of 0.8 dB and sideband rejection of >20 dB. This is consistent with a radiometric measurement of its loss,

though this measurement is potentially confused by uncertainties in the mixer sideband ratio.

Equivalent SSB receiver performance, mixer performance and conversion loss in the 19 to 25.5 GHz band is calculated to be 10,800K, ~3,700 K and 12.8 dB respectively. As in the 8 GHz case, mixer conversion loss includes an IF mismatch loss of ~0.7 dB.

As can be noted from the illustrations, the receiver behaves in a similar manner to sub-harmonic receivers measured at lower frequencies. That is, as LO pump power increases, noise and conversion loss drop rapidly. Further increasing LO power has little effect on performance, until eventually diode noise begins to slowly increase.

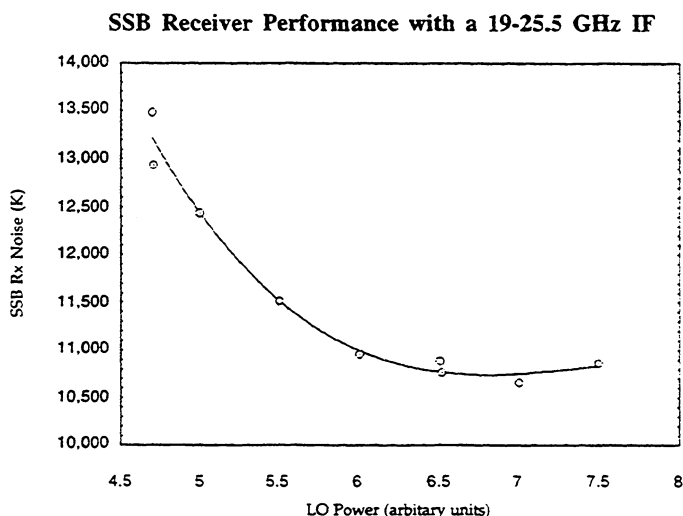


Figure 2: Plot of receiver noise as a function of LO power

The complete front end receiver, including Gunn oscillator, mixer, frequency multiplier and other waveguide and IF amplifier components is very compact, and can easily be accommodated within a volume of approximately $20 \times 12 \times 10 \text{ cm}^3$.

Conclusions

A very compact, 500 GHz sub-harmonic diode mixer receiver pumped by a Gunn diode oscillator and varactor frequency tripler has been demonstrated to have good sensitivity, and a well matched IF which spans ~0.5 to 26 GHz. A DSB mixer noise temperature and conversion loss of 2,300 K and 9.6 dB respectively has been measured at an IF of 8 GHz, and a SSB mixer noise temperature and conversion loss of 3,700 K and 12.8 dB respectively has been measured in an IF band from 19 - 25.5 GHz. An SSB receiver system with greater than 20 dB sideband rejection and total system noise ~10,800 K has been demonstrated for an instantaneous signal band extending from 498.5 - 505 GHz.

Since it is clearly possible to scale the waveguide and diode circuitry by a further factor of at least 1.5, it is likely that this technology will be applicable to receivers operating at frequencies up to one terahertz.

References

1. Barath, et al., 'The Upper Atmosphere Research Satellite Microwave Limb Sounder Experiment', *J. Geophys. Res.*, Vol. 98, No. D6, pp 10,751-10,762, 1993.
2. C. M. Mann, D. N. Matheson and M. R. B. Jones, '183 GHz Double Diode Subharmonically Pumped Mixer', *Int. J. of IR. and MM. Waves*, Vol. 10, No. 9, 1989.
3. J. W. Archer, 'An efficient 200 - 290 GHz Frequency Tripler Incorporating A Novel Stripline Structure'. *IEEE-MTT*, Vol. 32, No. 4, 1984
4. P. H. Siegel, A. R. Kerr and W. Hwang, 'Topics in the Optimisation of Millimetre Wave Mixers', *NASA Technical Paper 2287*, March 1984.
5. J. Thornton, C. M. Mann, and P. de Maagt, 'A high power 270 GHz frequency tripler featuring a Schottky diode parallel pair', *IEEE Symposium Digest*, Denver, 1997.

COMPUTER CONTROLLED, PHASE-LOCKED 126-147 GHz TRANSFERRED ELECTRON OSCILLATOR SYSTEM

TAO YE , STEPHEN JONES, JOHN CARLSTROM*, ROBERT WEIKLE

DEPARTMENT OF ELECTRICAL ENGINEERING, UNIVERSITY OF VIRGINIA, CHARLOTTESVILLE, VA

*DEPARTMENT OF ASTRONOMY AND ASTROPHYSICS, UNIVERSITY OF CHICAGO, CHICAGO, ILL

Abstract- A digitally controlled phased-locked 126-147GHz Transferred Electron Oscillator (TEO) system is described. This agile solid-state source is compact and easily integrated into existing RF systems. The system can be used as a bench top source for testing millimeter wave systems, or as a low noise broadband local oscillator for heterodyne receivers. The general specifications include a continuously tunable output frequency of 126-147 GHz, maximum output power of 30-50mW over the band, frequency accuracy and resolution of at least ± 10 Hz when phase-locked, and a set and phase-lock time of about 60 seconds. The system can be operated in sweep mode, a fixed frequency output mode, or a programmable output-frequency mode.

I. INTRODUCTION

The millimeter and submillimeter wave range has long been of vital interest to radio astronomers and atmospheric scientists, and is becoming increasingly important for commercial receiver, transceiver, and radar applications. Progress in the development of such systems will depend critically on the availability of reliable, low noise, and compact solid state sources. Solid state oscillators such as Transferred Electron Oscillators (TEO) have demonstrated excellent reliability, low noise, and medium power in 50-200GHz regime [1-5]. In this paper we will discuss the design, construction, and testing of a digitally controlled, phased-locked, 126-147 GHz TEO that can be used as a bench top source to develop high frequency radar and receiver systems.

II. OVERVIEW OF THE SYSTEM DESIGN

The block diagram of the system is shown in Figure 1. The interchangeable heart of this system is the Stable Depletion Layer (SDL) Transferred-Electron Device (TED) [3,5] and resonant cavity [1]. The TEO is a mechanically tuned Carlstrom style cavity [1] incorporating one mechanical back-short tuner for power and one back-short tuner for frequency. The back-shorts are positioned throughout a 40-mil range using digitally controlled micro-stepping motors. The performance of the oscillator has been manually characterized in terms of backshort positions and DC bias to optimize output power over the frequency range of 126-147GHz. This characterization provides the initial, crude

source of reference for the digital controller to adjust the power and frequency back-short positions appropriately.

The digitally controlled phase-lock loop operation is straightforward and functions in two steps, coarse and fine frequency lock, respectively. During coarse tuning, the user enters the operating frequency using a convenient Labview [6] PC interface. Then both the frequency and power back-shorts are crudely set according to a look-up table. A fraction of the oscillator output signal is sampled through a -10db coupler. The sampled signal is sent to both the r.f. input of the harmonic mixer, and a fast power-detection diode. The detector diode and IF output from the mixer are used to feedback frequency and power values to the digital controller. The harmonic mixer local oscillator (LO) (8-18GHz) is provided by a phase-locked frequency-agile X-band YIG oscillator. The LO frequency is set by the PC according to the RF output frequency set point. The power back short is controlled and adjusted by the PC until peak power is measured by the fast power-detection diode. At this point, the RF output frequency is only approximately set to within about 70 MHz, and the peak power point has been achieved.

After this first frequency capture step, all back-short adjustments are set and the XL phase-lock unit is activated. Within the XL phase-lock unit, the sweep bias circuit injects a current into an integrator amplifier in a manner that sweeps the operating voltage (0.4 volts above and below the nominal operating voltage set by the bias circuit (9 volts). If the resultant IF frequency becomes equal to the 10 MHz reference frequency and the IF level is large enough, locking will occur. After the phase-lock is on, the output frequency of the TEO will be maintained at a value, which is given by the following equation (1):

$$FRF=9*FLO+FIF \text{ (GHz)} \quad (1)$$

where FRF is the frequency of the TEO, FLO is the frequency of the YIG oscillator, and FIF is the system 10 MHz reference frequency. This reference signal is provided by an oven controlled crystal oscillator (OCXO) which is a built-in part of the XL source locking counter. The temperature stability of the OCXO is 1×10^{-8} for a temperature range of 0°C to 50°C. An external reference source can be used if needed. A source locking counter [7] is used to phase lock the YIG oscillator. The locking resolution is 1Hz and the accuracy is ± 1 Hz. So the frequency accuracy of 126-147 GHz RF output is ± 9 Hz after phase-lock. After the frequency and power are set and locked, the system look-up table containing the back-short position versus frequency and power is updated. Hence the look-up table is dynamic and the system control of frequency and power is intelligent.

The Labview software of National Instruments, Inc., and the programming language G are used as control, display, and interface software. The system front panel and interface is shown in Figure 2. After the lock is on, an indicator on the front panel will light. The output frequency and power, as well as the positions of the frequency and the power backshorts are also displayed on the front to the user.

The system can also work in the sweep mode and program output mode. When working in the sweep mode, the stepper motors move to their prescribed positions according to the look up table at a given sweep speed. When working in program output mode, the system can maintain a frequency output for a given period time on any day of

the year. So after you set times and dates, the system will intelligently set and change the RF output frequency over an extended period of time.

III. TESTING RESULTS

The RF output has been measured using a Tektronics 2784 spectrum analyzer with an accompanying 90-140 GHz WM782F waveguide mixer. The Tektronics system is capable of measuring signals in the 90-140 GHz band, but with limited resolution. The minimum resolution bandwidth of the Tektronics system is 300 kHz and therefore this instrument is not capable of resolving the phase-locked TEO output. None-the-less, direct measurement of the TEO output signal is possible as the system is set to different frequencies between 126-140 GHz. For this band, the TEO system was observed to set the output frequency correctly and with a resolution finer than the resolution of the Tektronics spectrum analyzer system.

In order to more carefully measure the resolution and accuracy of the TEO set point, the YIG LO input and 10 MHz IF output from the Pacific Millimeter Wave mixer were measured using an HP 8562A (9 kHz –50GHz) higher resolution spectrum analyzer. The resolution bandwidth of this spectrum analyzer is approximately 1 Hz. Figures 3a-c show the measured 14.998888889 GHz YIG LO signal to the 9th harmonic mixer, the 10.0 MHz IF signal output by the 9th harmonic mixer, and 135.0 GHz RF output spectrum after system phase lock. As shown, the resolution and accuracy of the LO and the IF are 1Hz which indicate that the RF output resolution and accuracy are better than 10 Hz.

As indicated, the resolution and accuracy of the XL microwave source locking counter is specified as 1Hz. When the RF frequency is set to 135 GHz the frequency counter indicates the LO frequency is appropriately set to 14.998888889 GHz. However, at this set point the HP8562A indicates the LO frequency is 14.998888724 GHz. We believe the XL frequency counter has greater accuracy than the HP8562A and the frequency is accurately set to within 1Hz (since the minimum resolution bandwidth of the Tektronics spectrum analyzer is 300 kHz, the bandwidth of the RF output can not be directly resolved and incorrectly appears to be about 300 kHz in Figure 3c).

IV. CONCLUSIONS AND ACKNOWLEDGMENTS

A digitally controlled, phase locked 126-147 GHz TEO source has been described. Approximately 30-50 mW of output power is available across the band and the system frequency resolution and accuracy are better than 10 Hz. The system is relatively compact and includes a Labview interface for easy use and integration with other RF systems. This system can be used as bench top source for developing and testing millimeter and sub-millimeter wavelength components and systems as well as a low noise source for heterodyne receivers. The described system can be expanded to include multiple TEO outputs for situations where broader bandwidth or arrays of sources are required. For this case one controller unit is needed, but multiple TEO and phase locked YIGs are required.

This research is funded by Nation Science Foundation grant ECS-9202037. The authors thank Robert Ross and Chris Mann for many helpful discussions.

V REFERENCES

- [1] J.E. Carlstrom, R.L. Plambeck, and D.D. Thornton, "A Continuously Tunable 65-115GHz Gunn Oscillator", IEEE Trans. On Microwave Theory and Techniques, Vol. 33, No. 7 (1985) pp.610-619. Also, these style cavities for the 60-147 GHz band are manufactured by J.E. Carlstrom Company, Chicago, IL.
- [2] A. Rydberg, IEEE Electron Device Letters, vol. 11, no. 10, (1990).
- [3] J.D. Crowley, C. Hang, R.E. Dalrymple, D.R. Tringali, F.B. Frank, L.Wandinger, H.B. Wallace, Electronic Letters, 30, 499 (1994).
- [4] H. Eisele, G. Haddad, IEEE Trans. On Microwave Theory and Techniques, vol. 43, 210 (1995).
- [5] M.F. Zybura, S.H. Jones, J.E. Carlstrom, J.D. Crowley, and B.Lim, "120-145GHz Stable Depletion Layer Second-Harmonic Transferred Electron oscillators", Solid- State Electronics, Vol. 39, No. 4(1996), pp. 547-553.
- [6] National Instruments, Austin Texas, (512) 794-0100, offers both instrumentation hardware and software. See <http://www.natinst.com> for more information. The system described in this paper makes use of Labview software, data acquisition boards, GPIB boards, and Nulogic motion control boards that are all offered by National Instruments.
- [7] XL Microwave, Oakland California, (510) 428-9488, offers phase lock units and frequency counters for microwave systems. The system described here makes use of the XL TEO phase lock unit and the YIG source locking counter. More information regarding phase lock circuits for TEOs can be found in reference 3.

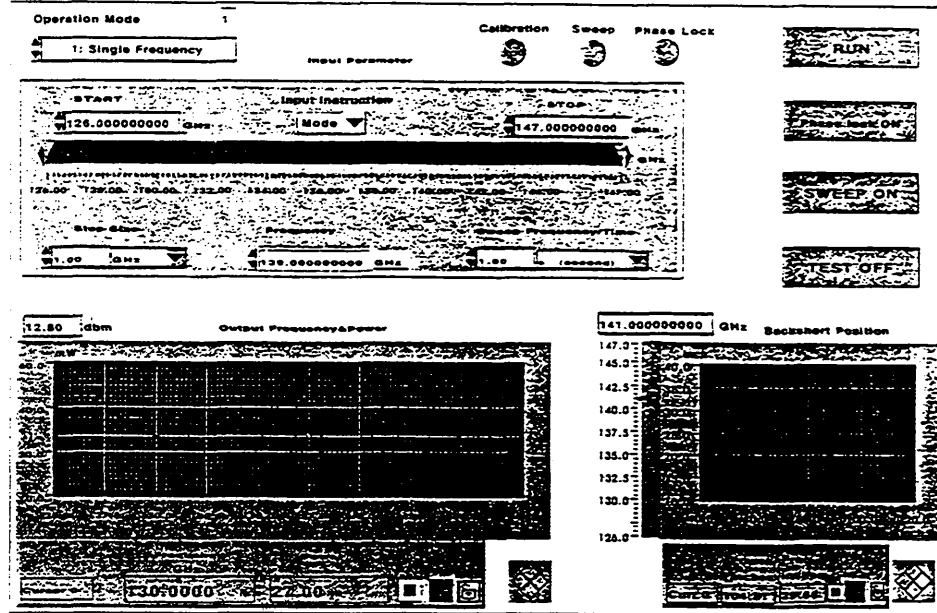


Figure 2 Diagram of the LabView front panel used by the user.

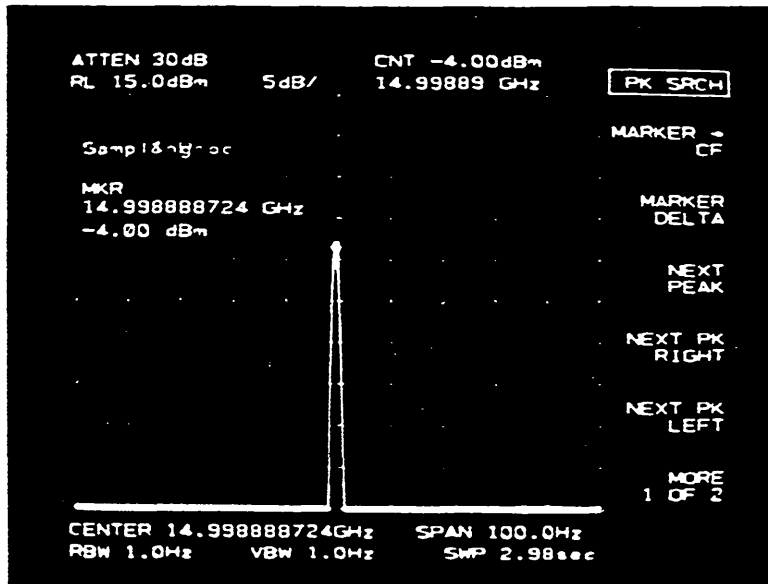


Figure 3a Output spectrum for the YIG LO that is driving the harmonic mixer used to down convert the 135 GHz RF output.

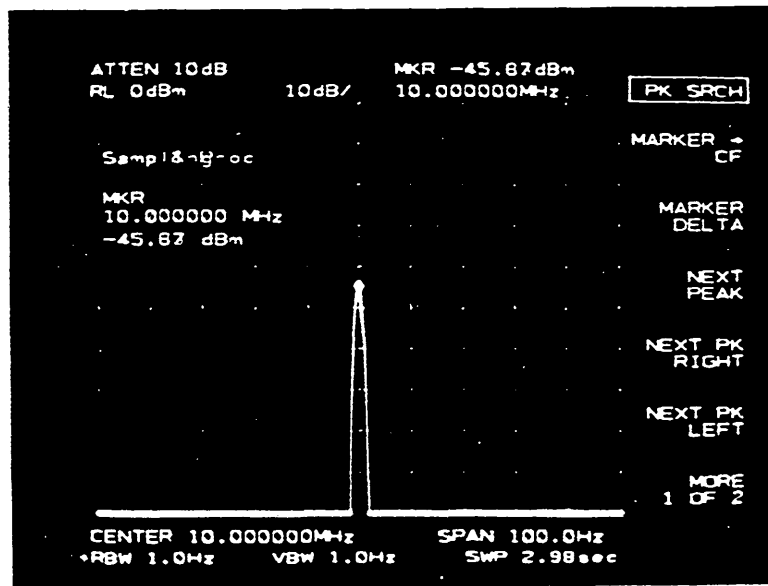


Figure 3b Output spectrum for the harmonic mixer IF down converted from the 135 GHz RF output.

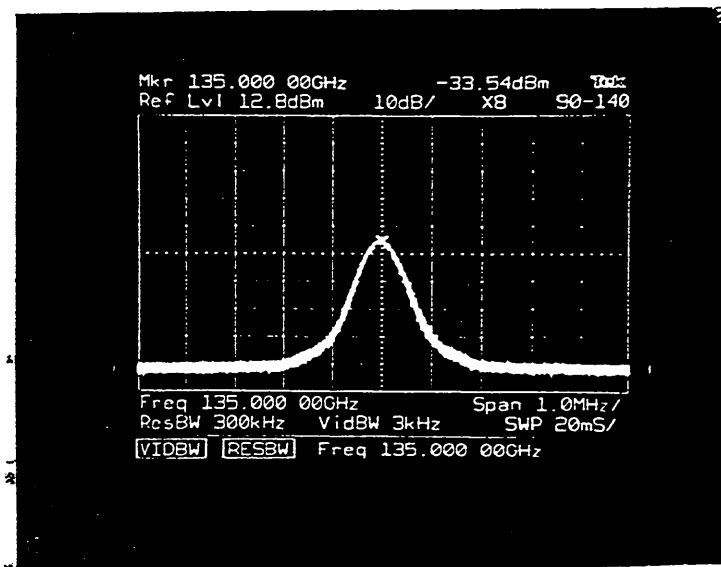


Figure 3c The output spectrum at 135 GHz is shown. The minimum resolution bandwidth of the spectrum analyzer is only 300 KHz and unable to accurately display the narrow band phase-locked TEO.

SERIES CONNECTION OF RESONANT TUNNELING DIODES FOR ELIMINATING SPURIOUS OSCILLATIONS

Tetsu Fujii^{1,2}, Olga Boric-Lubecke¹, Jongsuck Bae^{1,2}, and Koji Mizuno^{1,2}

¹ *Photodynamics Research Center, The Institute of Physical and Chemical Research, 19-1399 Aza-Koeji, Nagamachi, Aoba-ku, Sendai 980, Japan*

² *Research Institute of Electrical Communications, Tohoku University, 2-1-1 Katahira, Aoba-ku, Sendai 980-77, Japan*
kotetsu@riec.tohoku.ac.jp

Abstract

Removal of spurious oscillations produced by RTD oscillators, using series connection, has been investigated. It has been shown experimentally that tunnel diode oscillators with two or more diodes do not produce the unwanted low frequency oscillations, which occur in a corresponding single-diode circuit. Preliminary experiments with the series connection of two RTD's have also been carried out, demonstrating possibility to construct such oscillators.

Introduction

Resonant tunneling diode (RTD) oscillators offer significant potential for submillimeter wave generation. However, the RTD's inherently broad-band negative differential resistance usually leads to undesirable low frequency spurious oscillations which are related to bias circuitry. Several methods for suppressing spurious oscillations have been proposed so far, including lossy line stabilization [1], and on wafer stabilization with an integrated Schottky diode [2]. Unfortunately, these methods introduce additional losses, and thus decrease oscillator efficiency. Here we propose using a series combination of two RTD's to eliminate unwanted low frequency oscillations, without affecting the efficiency of the oscillator.

It has been shown experimentally that the output power of tunnel diode oscillators can be increased by connecting multiple devices in series [3]. Additionally, this series-connection exhibits low frequency cutoff, and a minimum oscillation amplitude, which make oscillator circuits less prone to spurious oscillations. The increased stability of such oscillators has previously been investigated theoretically [4]. Here, we will present experimental results that show the elimination of spurious oscillations through the series-connection of tunnel diodes, and also some preliminary results with RTD's. The effect of differing I-V characteristics between two series connected diodes will be discussed as well.

Series Connection

When two identical diodes, which exhibit a negative differential resistance (NDR) region in their DC I-V curves, are connected in series and biased with a single battery with sufficient voltage to have bias both in the NDR region, there are three possibilities for the bias voltage distribution (Fig. 1): both diodes can be biased in the NDR region and have the same DC voltage (solution I), or both diodes can be biased in the positive differential resistance (PDR) region, one at a voltage lower than the peak voltage V_p , and the other at a voltage higher than the valley voltage V_v (solutions II and III). If there is no RF signal present in the circuit, solution I is unstable, and will move towards solutions II

or III in a very short time. This phenomenon is due to the nature of the NDR, and has been previously described as the DC instability [4]. It is analogous to the case of a single tunneling diode biased with the constant current source: the device always seeks the stable alternative, which is a bias outside of the NDR region. When an RF signal is present across the series connection, solution I might be stable if oscillation amplitude (V_{rf}) and frequency are above the minimum values (V_{rfmin} , f_{min}), which can be calculated from the device parameters [4].

If the diode I-V curves are not identical (Fig. 2), the lower current diode (diode 1) cannot achieve the peak current I_p of the higher current diode (diode 2) at the voltage V_p (Fig.). Initially, diode 1 will cross the peak current I_{p1} and enter the NDR region. Only when V_{d1} exceeds the valley voltage V_v , can diode 2 cross the peak current I_{p2} and become biased in the NDR region. As a result of either DC instability or difference in DC I-V curves, the series connection DC I-V curve will exhibit multiple peaks (Fig 5a, 6a) if there is no oscillation. When an RF signal is present, it is possible to bring both bias points in the NDR region, and achieve stable oscillation. However, similar to the case of identical diodes, certain oscillation amplitude and frequency constraints must be satisfied. Displacement currents through the parasitic capacitance of the device must “compensate” for the difference between the conductive current at the current peak I_{peak} , and from this requirement a simple way to estimate minimum oscillation frequency f_{min} can be deduced:

$$f_{min} = \Delta I_{peak} / 2\pi \Delta V_{rf} C, \quad (1)$$

where C is the capacitance of a single diode, and V_{rf} the difference between diode oscillation amplitudes. Since V_{rf} must be above the minimum value V_{rfmin} , determined by the DC instability, we must assure V_{rf} is sufficiently small to keep this condition satisfied. A reasonable estimate is that V_{rf} should be less than 10% of the voltage amplitude of one diode. If the following condition is satisfied at the oscillation frequency f ,

$$\Delta I_{peak} \ll 2\pi f V_{rf} C, \quad (2)$$

the previously described DC instability will be the prevailing phenomena for determining f_{min} .

Single RTD low frequency spurious oscillations, usually associated with a resonance in bias circuitry, occur due to the absence of a low frequency cutoff f_{min} , and a broad range of device impedances for which oscillation condition can be satisfied. In the case of the series connection, minimum oscillation frequency and amplitude impose further constraints on the oscillation condition, and therefore unwanted oscillations, even though theoretically possible, are not very likely to occur.

Tunnel Diode Experimental Results

Oscillators with series connected tunnel diodes have been successfully demonstrated in the past [3,4]. Recently, such circuits have been revisited to examine oscillator stability in more detail. The tunnel diodes and circuit topology were the same as described in [3,4]. These are very low current diodes, with a peak current of about 0.5 mA, and the I-V curves for different diodes vary by less than 10%. At the 2 GHz design frequency, equation (2) is satisfied, which means that the DC instability is the prevailing reason for the existence of f_{min} and V_{rfmin} , which were estimated to be 20 MHz and 0.125 V respectively [4].

Low NDR current results in a small negative differential conductance, and therefore a somewhat limited impedance range for which oscillation condition can be

satisfied, even in the case of a single diode oscillator. Still, most one diode circuits exhibited spurious oscillations to some degree. Typically, such oscillations occurred for the bias voltage near V_p , and gradually disappeared as bias voltage was increased closer to the V_v . On the other hand, while one diode spurious oscillations were also observed in multiple diode circuits for similar bias conditions, such oscillations ceased once all diodes were biased in the NDR region, and a clean signal appeared at the design frequency of 2 GHz. Fig. 3a shows the spectrum of a single diode oscillator, for a bias voltage range of 0.07-0.09 V. Even though there is a signal at 2 GHz, a low frequency oscillation occurs as well, and produces higher harmonics and mixing components close to the design frequency. Two (and more) diode oscillators always produced only a single line (Fig. 3b), which clearly indicated that series connection can effectively suppress the unwanted oscillations.

Series Connection of RTD's

Mesa type GaAs/AlAs RTD's, with the doping profile described in [5], were also used for the experiments. Mesas were formed using two types of dry etching: reactive ion etching (RIE) in a PCl_3 environment, and electron cyclotron resonance reactive beam ion etching (ECR-RIBE) in a Cl_2 environment. It was found that ECR etching produced better quality diodes, with straight mesa side walls, and twice as high peak-to-valley current ratio (about 4).

Previously, millimeter wave oscillations were achieved with these RTD's [5] in a quasi-optical resonator, using 9 μm diameter mesas, and very short whisker wires. However, it would be very difficult to create a series connection for two diodes in this configuration, without integrating them monolithically. Therefore, microstrip oscillator circuits were designed using the procedure described in [3]. Diodes were contacted with whisker wires attached to the microstrip. This resulted in fairly long whiskers, about 1-1.5 mm long, and due to the corresponding inductance, the oscillation frequency range was limited to under 20 GHz. Since it was anticipated that an external RF source would be necessary for triggering oscillation [3], an oscillation frequency was chosen in the range of 2-5 GHz, to be compatible with the available circulators and signal sources.

Initially, a "back-to-back" connection of two RTD's was attempted (Fig. 4a). An RTD chip was mounted on a simple microstrip circuit, and diode contacts were made with two whisker wires attached to the microstrip. While such a configuration offered easy assembly and small distance between the diodes, individual diode I-V curves were quite different (Fig. 4b), and it was not possible to achieve simultaneous oscillation. A small difference in the width of the spacer layer on the mesa and substrate sides of the double barriers may partially account for this variation in I-V curves. Symmetric doping profile wafers are being processed to check the influence of this asymmetry. However, physical asymmetry of the diode orientation could also contribute to the difference in I-V curves. It might be possible to overcome this problem by etching most of the highly doped GaAs substrate in between the mesas.

Next, two chips were connected in cascade (Fig. 5a), and diode contacts were repeated until it was assured that the best uniformity in the I-V curves was achieved. The DC I-V curve for the series connection was measured while individual diode voltages were monitored using a small whisker probe in between the chips (Fig. 5b). The diodes were then biased with sufficient voltage to bring them both to the middle of the NDR region, and an external RF signal was applied through the circulator to switch the bias points from the PDR regions to the NDR region. It was possible to have both diodes biased in the NDR region while the external signal was present (Fig. 6), and diodes were clearly oscillating. These results indicate that RTD DC instability may be removed using

an external source for a short amount of time, similarly to the case of tunnel diodes [3]. However, after the external RF signal was turned off, the bias points switched back to the PDR region and there was no oscillation. Careful examination of the I-V curves showed that even though the diode difference appeared very small (less than 5%), it was still significant according to equations 1 and 2, due to the very small device capacitance (about 80 fF), and thus possibly responsible for the absence of oscillations. Shunting the diodes with capacitors of about 1 pF might help to solve this problem, and we are currently investigating oscillators with shunt capacitors.

Conclusions

Benefits of the series connection of tunneling diodes for the removal of spurious oscillations have been discussed. It was demonstrated experimentally that the series connection of tunnel diodes has improved performance over a single diode oscillator. Series connection of RTD's has also been investigated. So far, we have experimentally demonstrated RF switching of the bias points to the NDR region in the case of two series connected RTD's, and are presently working on the further oscillator development.

Acknowledgments

We would like to thank H. Sakaki, T. Noda, and M. Narihiro from the University of Tokyo for supplying MBE grown GaAs wafers. Part of this work was carried out at the Laboratory for Electronic Intelligent Systems, Research Institute of Electrical Communications, Tohoku University, supported by a Grant-in Aid of Scientific Research from the Ministry of Education, Science and Culture of Japan.

References

- [1] K. D. Stefan and S. C. Wong, "Lossy-Line Stabilization of Negative-Resistance Diodes for Integrated-Circuit Oscillators," *Proc. of the Second International Symposium on Space Terahertz Technology*, pp. 154-162, February 26-28, 1991.
- [2] M. Reddy, R. Y. Yu, H. Kroemer, M. J. W. Rodwell, S. C. Martin, R. E. Muller, and R. P. Smith, "Bias Stabilization for Resonant Tunnel Diode Oscillators," *IEEE Microwave and Guided Wave Letters*, vol. 5, pp. 129-221, July 1995.
- [3] O. Boric-Lubecke, D. S. Pan and T. Itoh, "Fundamental and Subharmonic Excitation of an Oscillator with Several Tunneling Diodes in Series", *IEEE Trans. on Microwave Theory Tech.*, vol. 43, no. 4, pp. 969-976, April 1995.
- [4] O. Boric-Lubecke, D. S. Pan and T. Itoh, "DC Instability of the Series Connection of Tunneling Diodes" , *IEEE Trans. on Microwave Theory Tech.*, vol. 44, no. 6, pp. 936-943, June 1996.
- [5] T. Fujii, H. Mazaki, F. Takei, J. Bae, M. Narihiro, T. Noda, H. Sasaki, and K. Mizuno, "Coherent Power combining of Millimeter Wave Resonant Tunneling Diodes in a Quasi-Optical Resonator," *1996 IEEE MTT-S Digest*, pp. 919-922.

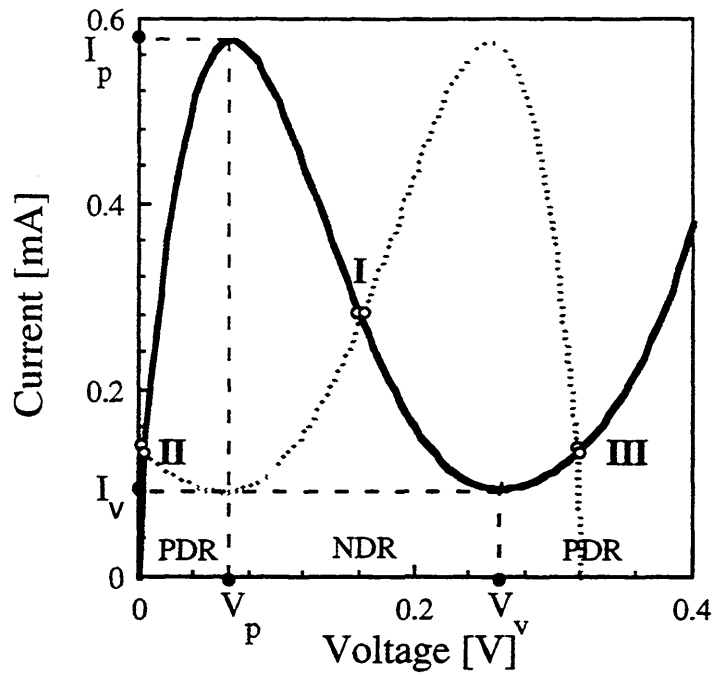


Fig. 1 Three solutions for the bias voltage distribution of tunneling diodes: both diodes can be biased in the NDR region (I), or in the PDR region, one at the voltage lower than the peak voltage V_p , and the other at the voltage higher than the valley voltage V_v (II and III).

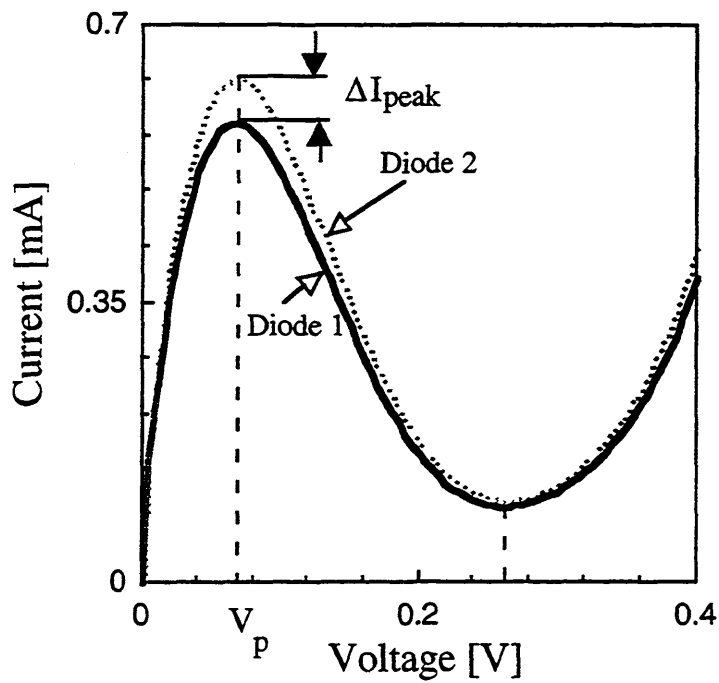
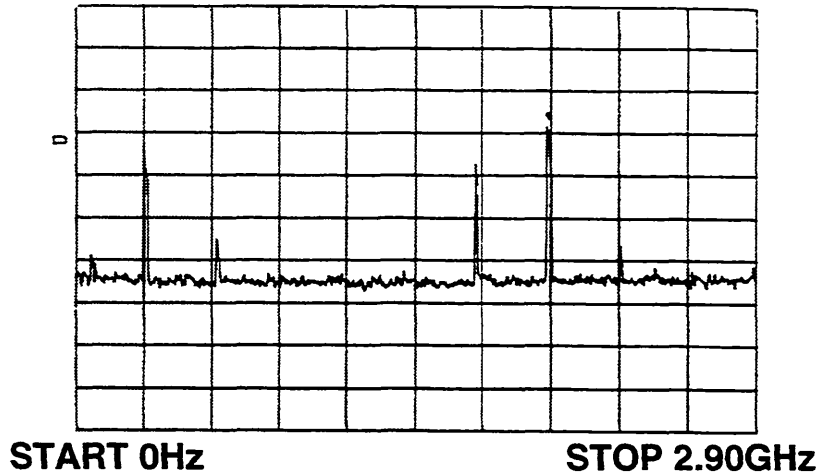


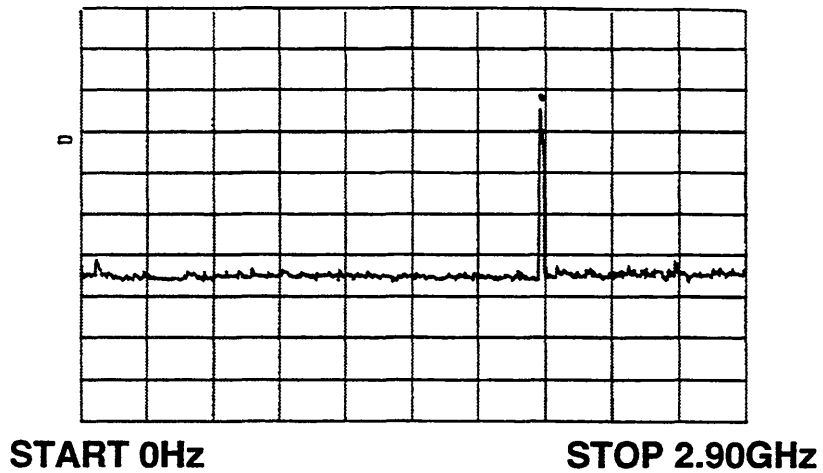
Fig. 2 If the diode I-V curves are not identical, a lower current diode (diode 1) cannot achieve the peak current I_p of the higher current diode (diode 2) at the voltage V_p .

ATTEN 10dB MKR -36.67dBm
RL -10.0 dBm 10dB/div. 2.020GHz



(a)

ATTEN 10dB MKR -32.67dBm
RL -10.0 dBm 10dB/div. 2.011GHz



(b)

Fig. 3 Output spectrum of one diode oscillator (a), and a two diode oscillator (b). One diode oscillator produces spurious components, whereas two diode circuit oscillates only at the design frequency of 2 GHz.

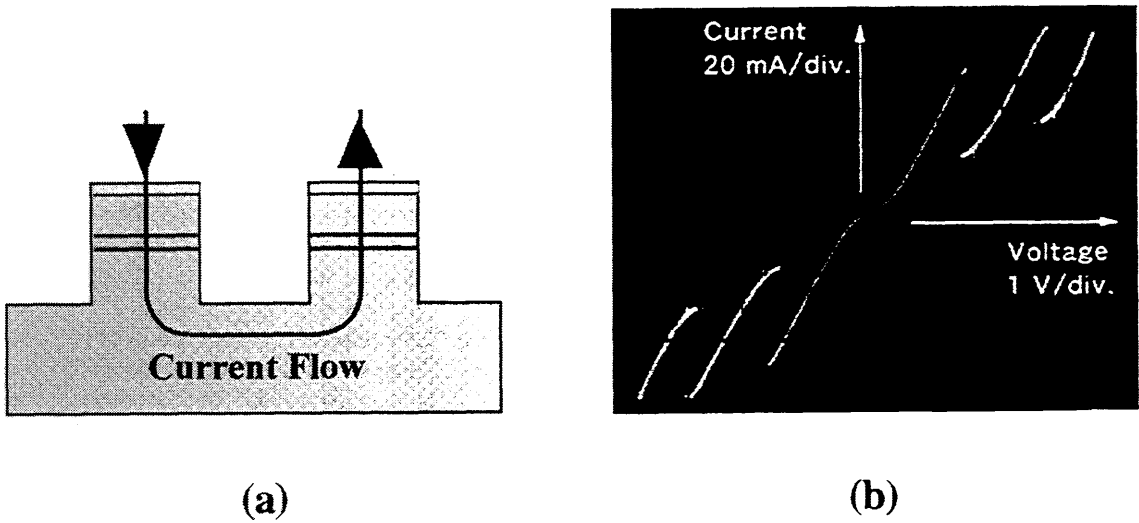


Fig. 4 Schematic of a "back-to-back" configuration (a), and measured DC I-V curve (b). Due to the large difference in peak current, it was not possible to construct an oscillator with this configuration.

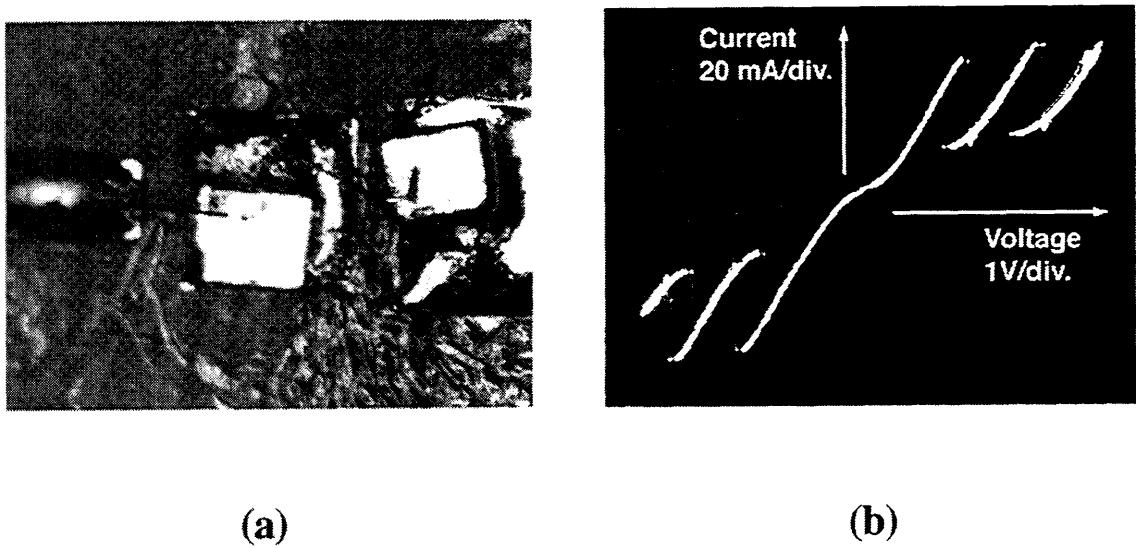
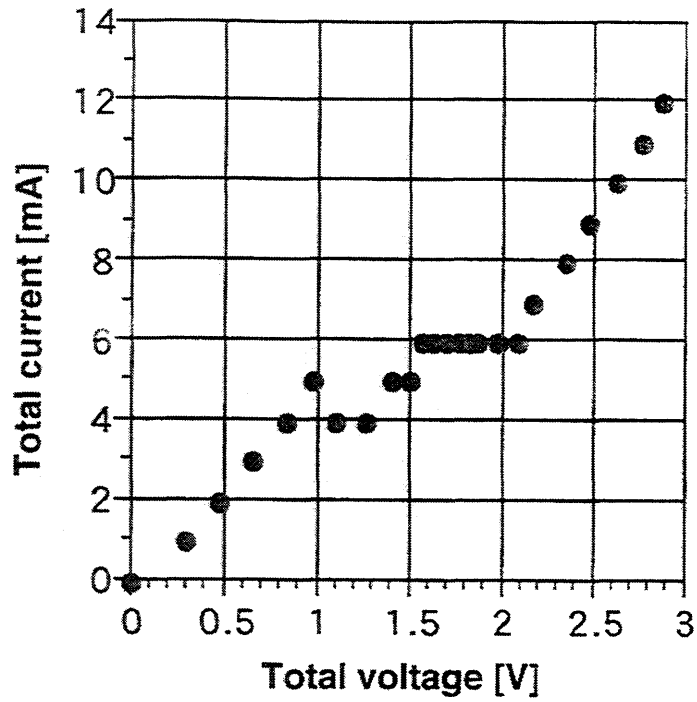
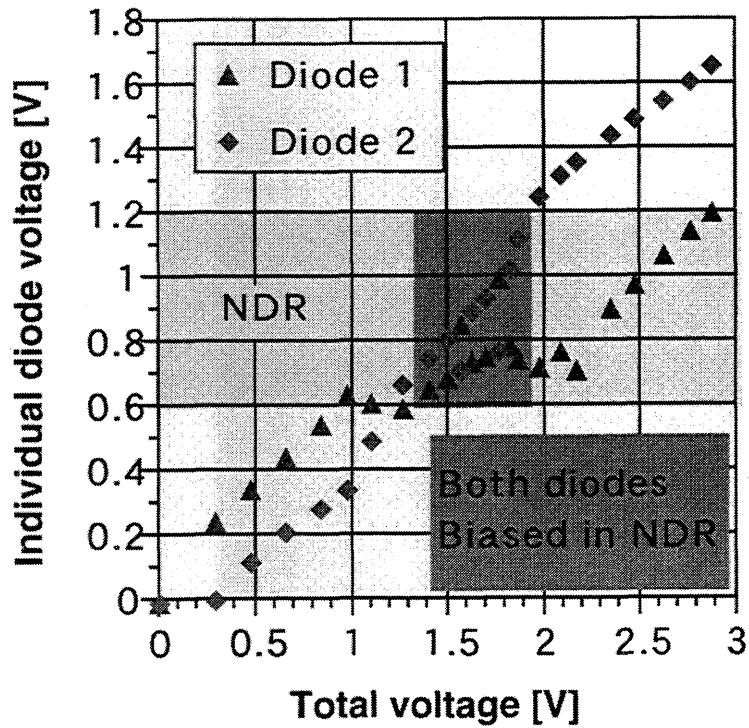


Fig. 5 Photograph of the microstrip cascade connection (a), and measured DC I-V curve (b). Very good uniformity of individual diodes I-V's can be achieved in this case.



(a)



(b)

Fig. 6 DC I-V curve of a series connection during RF triggering (a), and the individual between diode voltages (b). Both RTD's can be biased simultaneously in the NDR region.

ELECTROMAGNETIC MODELING OF OBJECTIVE LENSES IN COMBINATION WITH INTEGRATED LENS ANTENNAS

Maarten J.M. van der Vorst, Peter J.L.de Maagt* and Matti H.A.J. Herben

Eindhoven University of Technology, Faculty of Electrical Engineering P.O. Box 513,
5600 MB Eindhoven, The Netherlands, e-mail: M.J.M.v.d.Vorst@ele.tue.nl

*European Space Agency ESTEC, P.O. Box 299, 2200 AG Noordwijk, The Netherlands

Abstract—In this paper the electromagnetic modeling of an integrated (eye) lens antenna with an additional objective lens is described. Two different field calculation methods, Geometrical/Physical Optics (GO-PO) and Physical/Physical Optics (PO-PO), are compared for various diameter over wavelength ratios of the integrated lens antenna. The main difference between both methods is that in case of PO-PO, the entire eye-lens contributes to the PO currents at a point on the outer objective lens surface, while only one GO ray contributes in case of the GO-PO method. The comparisons show that the GO-PO method can be used as a good first-order approximation. However, if a more accurate prediction of the beam pattern is required, then the PO-PO method should be applied.

ward way of modeling the objective/integrated lens antenna combination is by means of Geometrical Optics (GO) from the planar feed of the HILA to the outer objective lens surface and subsequently Physical Optics (PO) to obtain the far-field pattern. However, the GO analysis does not include the wave diffraction due to the limited lens size of the HILA. To improve the accuracy of the modeling, a PO method will be described which takes the radiation from the entire eye-lens surface into account to calculate the PO currents on the outer surface of the objective lens. A Fourier decomposition is applied to the second PO integral to speed up the calculations.

I. INTRODUCTION

IT IS OBVIOUS that with the availability of integrated planar antenna technology extremely compact receivers can be made. This technology is quite suitable for imaging arrays which are of great interest for both space astronomy and atmospheric research. Particularly in astronomy most of the spectral line emitting regions are usually spatially extended over many observing beams in the sky and therefore mapping is required to understand the astrophysics of these regions. In atmospheric research, imaging is used for profiling, rain sounding, etc.

For imaging purposes the hyperhemispherical integrated lens antenna (HILA) is often applied in combination with an objective lens, because of the nearly aberration free performance. Another reason for using an objective/integrated lens antenna combination is the matching of the beam of the HILA to the beam required to properly feed a typical Cassegrain or Gregorian telescope.

Usually, the objective lens is placed in the Fresnel zone of the integrated lens antenna and this does not validate the use of the far-field radiation pattern of the HILA in the analysis of the combined quasi-optical system. Then, the most straightfor-

II. DESIGN

A. General Aspects

For certain applications, like imaging and quasi-optical beam transformers, it is needed to include an objective lens in front of the integrated lens antenna, and the resulting configuration is shown in Fig. 1. Here the objective lens is placed in the Fresnel zone of the lens antenna which is generally the case.

When the objective lens is used as a beam transformer, the incoming Gaussian beam (first order) is changed into another Gaussian beam with a different beam waist or phase center. For imaging it is important that a sharp image of a certain object is obtained and this means that an incoming plane wave has to be focused to the planar feed of the lens antenna. In the next section it will be shown that a number of different objective lenses can be applied for this purpose.

B. Lens Types

For imaging applications the shape of the objective lens is designed as to produce a spherical or nearly spherical phase front at the eye-lens aperture. To achieve this two different surface-lens types can be used [1]:

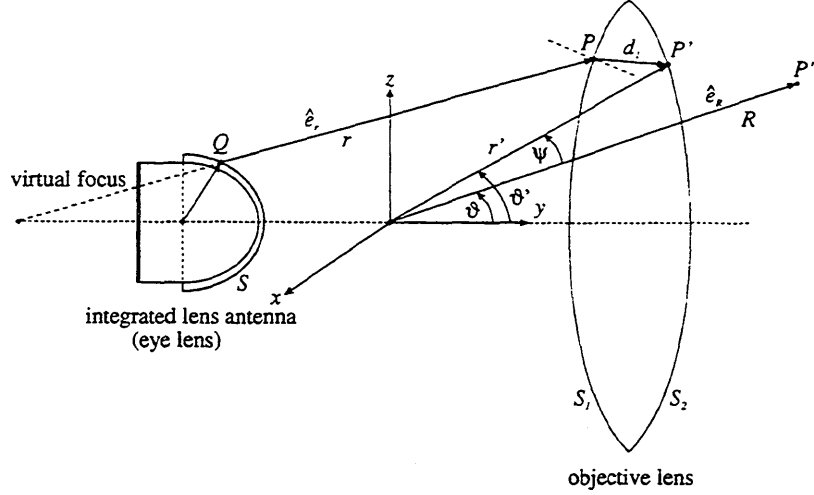


Fig. 1. Geometry of integrated lens antenna (with matching layer) in combination with an objective lens.

- single-surface lenses
 - hyperbolic inner and flat outer surface
 - spherical inner and flat outer surface
 - meniscus lens
- dual-surface lenses
 - flat inner and curved outer surface
 - curved inner and outer surface

For the single-surface lenses refraction of the incident wave only takes place at one surface of the objective lens, while for the dual-surface lenses both surfaces change the direction of propagation.

For imaging applications it is required that the side lobes of the quasi-optical system are low and this cannot be achieved by means of a flat field distribution in the aperture. The meniscus lens will give a nearly uniform field distribution and therefore this lens type is not preferred. A disadvantage of the dual-surface lenses is that their fabrication is somewhat more elaborate than that of the single-surface ones. In practice the spherical lens is more often used than the hyperbolic one, and therefore in this paper emphasis will be put on the spherical single-surface lens. This means that in, Fig. 1, surface S_1 is part of a sphere and S_2 is flat. It is noted that the spherical single-surface lens does not transform an incoming plane wave into a spherical one, but in the thin lens approximation (thickness of lens negligible to focal distance) it does.

III. ELECTROMAGNETIC MODELING

A. PO-PO

When the objective lens is placed in the Fresnel region of the integrated lens antenna, the far-field

approximations can not be used and it becomes necessary to start with the original Physical Optics integrals. Silver [2] showed that for the electric and magnetic fields in any observation point P the following equations hold:

$$\underline{E}(P) = \frac{-j}{4\pi\omega\epsilon_0} \iint_S \left[(\underline{J}_s \cdot \nabla) \nabla + k^2 \underline{J}_s + j\omega\epsilon_0 (\underline{M}_s \times \nabla) \right] \frac{e^{-jkr}}{r} dS \quad (1)$$

$$\underline{H}(P) = \frac{-j}{4\pi\omega\mu_0} \iint_S \left[(\underline{M}_s \cdot \nabla) \nabla + k^2 \underline{M}_s - j\omega\mu_0 (\underline{J}_s \times \nabla) \right] \frac{e^{-jkr}}{r} dS \quad (2)$$

In the integrands of these equations, the operator ∇ acts on the source element coordinates and therefore the following results are valid [2]:

$$\nabla \left(\frac{e^{-jkr}}{r} \right) = \left(jk + \frac{1}{r} \right) \frac{e^{-jkr}}{r} \hat{e}_r \quad (3)$$

and

$$\begin{aligned} (\underline{J}_s \cdot \nabla) \nabla \left(\frac{e^{-jkr}}{r} \right) &= \left[-k^2 (\underline{J}_s \cdot \hat{e}_r) \hat{e}_r + \right. \\ &\left. \frac{3}{r} \left(jk + \frac{1}{r} \right) \hat{e}_r (\underline{J}_s \cdot \hat{e}_r) - \frac{\underline{J}_s}{r} \left(jk + \frac{1}{r} \right) \right] \frac{e^{-jkr}}{r} \end{aligned} \quad (4)$$

If the fields are evaluated in the Fresnel and Fraunhofer region of the integrated lens antenna ($r > 0.62\sqrt{D^3/\lambda}$), the terms with $1/r$ and $1/r^2$ can be

neglected and the fields of (1) and (2) become:

$$\underline{E}(P) = \frac{-jk^2}{4\pi\omega\epsilon_0} \iint_S \left[\underline{J}_s - (\underline{J}_s \cdot \hat{e}_r) \hat{e}_r + \frac{1}{Z_0} (\underline{M}_s \times \hat{e}_r) \right] \frac{e^{-jkr}}{r} dS \quad (5)$$

$$\underline{H}(P) = \frac{-jk^2}{4\pi\omega\mu_0} \iint_S \left[\underline{M}_s - (\underline{M}_s \cdot \hat{e}_r) \hat{e}_r - Z_0 (\underline{J}_s \times \hat{e}_r) \right] \frac{e^{-jkr}}{r} dS \quad (6)$$

These equations show that the fields in point P can be treated as an infinite summation of spherical waves (spherical wave expansion) originating from the lens antenna surface. The complex excitation of these waves is given by the equivalent electric (\underline{J}_s) and magnetic (\underline{M}_s) current densities, which can be calculated from the pattern of the planar feed in the dielectric lens by using:

$$\begin{aligned} \underline{J}_s &= \hat{n} \times \underline{H}(Q) \\ \underline{M}_s &= -\hat{n} \times \underline{E}(Q) \end{aligned} \quad (7)$$

Because the H -field of each individual spherical wave is related to the E -field according to:

$$\underline{H} = \frac{\hat{e}_r \times \underline{E}}{Z_0} \quad (8)$$

only the E -field will be considered in the remainder of this analysis. If the objective lens is included in the design, the refracted wave in point P on the inner surface propagates to point P' on the outer surface. To describe the fields and currents at the outer side of the lens, the influence of the lens has to be modeled. By means of Geometrical Optics each spherical wave can be traced through the lens, which means inclusion of the transmission coefficients, the spreading factor from the inner to the outer surface and an additional phase change. Finally, if all effects are accounted for, the following integral is obtained:

$$\underline{E}(P') = \frac{-jk^2}{4\pi\omega\epsilon_0} \iint_S \left[\underline{J}_s - (\underline{J}_s \cdot \hat{e}_r) \hat{e}_r + \frac{1}{Z_0} (\underline{M}_s \times \hat{e}_r) \right] \bar{\bar{T}}_1 \bar{\bar{T}}_2 D_F \frac{e^{-jkr - jk_d d_1}}{r} dS \quad (9)$$

with D_F the divergence factor, $\bar{\bar{T}}_1$ and $\bar{\bar{T}}_2$ the dyadic Fresnel transmission coefficients at S_1 and S_2 respectively, and d_1 the length of a ray inside the objective lens.

To obtain the far-field radiation pattern of the objective/integrated lens antenna combination, the Physical Optics equivalent current densities have to be computed at the outer objective lens surface and then the standard PO integrals can be determined.

B. GO-PO

In the previous section the PO-PO method was described, where the entire eye-lens surface is taken into account in the calculation of the fields in P' . Another method, which is extensively used in optics, is GO-PO and here only one ray from the planar feed to P' is used. This means that GO is applied from the feed to the outer surface of the objective lens. The validity of this method depends on the size of the eye lens, the distance between eye and objective lens and the frequency. The larger the eye lens is in terms of a wavelength, the more accurate the method will be.

Because the transmitted ray passes through two refraction points from feed to objective lens, the ray-tracing is more complex for this method than for the PO-PO method. In this paper hyperhemispherical eye lenses will be used, which offer the possibility of tracing the rays from the virtual focus to the objective lens (see Fig. 1). It should be noted that when this method is applied, the small lateral shift of the ray due to the matching layer will be neglected in the ray-tracing procedure [3].

C. Ray-tracing Procedure

In Sections III.A and III.B the electromagnetic fields were described on the outer objective lens surface (S_2). For an efficient PO integration scheme the equivalent currents, corresponding to these fields, must be defined in a regular grid. Of course this requires a ray-tracing procedure to find, for each grid point on S_2 , the refraction points on the first lens surface (S_1) that correspond to the source points on the integrated lens antenna (see Fig. 1). In Fig. 2 the configuration for the ray-tracing and the symbols used are depicted.

First a center of the curved inner surface of the objective lens is defined (point C). For the spherical lens this corresponds to the real center of surface S_1 . The cross-section plane that is shown in Fig. 2 contains the incident ray, the refracted ray and the normal vector in B , because the normal vector equals the unity vector from C to B . It contains also the vectors from C to P' and from C to Q . It should be clear that the wanted refraction

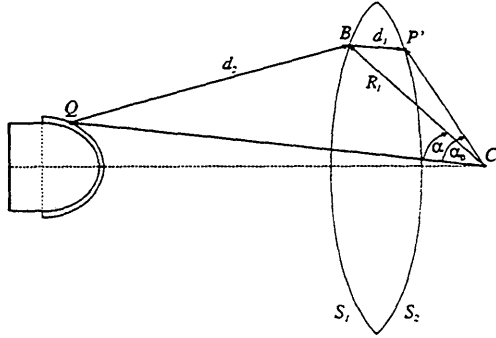


Fig. 2. Ray-tracing from source point Q to grid point P' on second objective lens surface.

point is to be found in this plane. The phase from source point to observation point is determined by the distances d_1 and d_2 which are given by:

$$d_1 = \sqrt{(CP')^2 + R_l^2 - 2(CP')R_l \cos(\alpha_0 - \alpha)} \quad (10)$$

$$d_2 = \sqrt{(CQ)^2 + R_l^2 - 2(CQ)R_l \cos \alpha} \quad (11)$$

with (CQ) and (CP') the distances from C to Q and from C to P' , respectively. Refraction point B is found for an angle α , that corresponds to a minimum of the function $n_d d_1 + d_2$ (shortest electrical path length).

D. Far-field and Fourier Decomposition

Now that the fields at the second objective lens surface (S_2) are known, it is possible to compute the far-field of the total system (eye plus objective lens). For this PO is used and Eqs. (5) and (6) describe the fields in any observation point. However, because in this paper we are only interested in the far-field of the antenna system, a few approximations can be made [2] and these result in:

$$\underline{E}(P'') = \frac{-j\omega\mu_0 e^{-jkR}}{4\pi R} \iint_{S_2} \left[\underline{J}'_s - (\underline{J}'_s \cdot \hat{e}_R) \hat{e}_R + \frac{1}{Z_0} (\underline{M}'_s \times \hat{e}_R) \right] e^{jk r' \cos \psi} dS_2 \quad (12)$$

with \underline{J}'_s and \underline{M}'_s the equivalent current densities on the second objective lens surface (S_2). Every far-field pattern, beam and Gaussian beam efficiency calculation requires many of these double-integral computations to be performed, which are very time-consuming. Therefore, it would be elegant to rewrite (simplify) Eq. (12) and speed up the calculations. By using a similar expansion as

mentioned in Ref. [4], Eq. (12) is rewritten as:

$$\underline{E}(P'') = c_1 \iint_{S_2} \underline{N}(x', z') e^{jk r' \cos \psi} dS_2 \quad (13)$$

with c_1 and $\underline{N}(x', z')$ defined as:

$$c_1 = \frac{-j\omega\mu_0 e^{-jkR}}{4\pi R} \quad (14)$$

$$\underline{N}(x', z') = \underline{J}'_s - (\underline{J}'_s \cdot \hat{e}_R) \hat{e}_R + \frac{\underline{M}'_s \times \hat{e}_R}{Z_0} \quad (15)$$

The next step is to transform the integration over the, generally curved, surface S_2 to an integration over a plane aperture with diameter D . To do so, the normal vector of S_2 is needed and the Cartesian coordinates (x', z') of point P' are transformed to polar coordinates (ρ', φ') . Then Eq. (13) changes to:

$$\underline{E}(P'') = \int_0^{2\pi} \int_0^{D/2} \underline{G}(\rho', \varphi') e^{jk r' \cos \psi} d\rho' d\varphi' \quad (16)$$

with

$$\underline{G}(\rho', \varphi') = \frac{\underline{N}(x', z') c_1 \rho'}{\sqrt{1 + \left(\frac{\partial S_2}{\partial x'}\right)^2 + \left(\frac{\partial S_2}{\partial z'}\right)^2}} \quad (17)$$

To calculate \underline{G} in (17), x' and z' have to be substituted by $\rho' \sin \varphi'$ and $\rho' \cos \varphi'$, respectively.

By describing P' and P'' with their spherical coordinates, $(r', \vartheta', \varphi')$ and (R, ϑ, φ) , and inserting these into (16), the next equation is found:

$$\underline{E}(P'') = \int_0^{2\pi} \int_0^{D/2} e^{jk r' \cos \vartheta \cos \vartheta'} \underline{G}(\rho', \varphi') e^{jk \rho' \sin \vartheta \cos(\varphi - \varphi')} d\rho' d\varphi' \quad (18)$$

In the following only one component (x) of the electric field will be considered, because the others can be treated similarly. A new variable is defined and directly decomposed into its Fourier series:

$$K(\rho', \varphi') = e^{jk r' \cos \vartheta \cos \vartheta'} G_x(\rho', \varphi') = \sum_{m=-\infty}^{\infty} k_m(\rho') e^{jm\varphi'} \quad (19)$$

The coefficients k_m can be found simply by taken a Fast Fourier Transform (FFT) of the function K . By substituting the Fourier series of K into (18)

the following expression for the x -component of the electric field is obtained:

$$E_x(P'') = \int_0^{2\pi} \int_0^{D/2} \sum_{m=-\infty}^{\infty} k_m(\rho') e^{jm\varphi'} e^{jk\rho' \sin\vartheta \cos(\varphi-\varphi')} d\rho' d\varphi' \quad (20)$$

Interchanging the integration variables and using the known relation for the m^{th} -order Bessel function J_m [5]:

$$J_m(u) = \frac{1}{2\pi} \int_0^{2\pi} e^{j(u \sin\varphi' - m\varphi')} d\varphi' \quad (21)$$

gives:

$$E_x(P'') = 2\pi \int_0^{D/2} \sum_{m=-\infty}^{\infty} k_m(\rho') J_{-m}(k\rho' \sin\vartheta) d\rho' \quad (22)$$

if the observation point P'' is located in the plane $\varphi = \pi/2$. It should be mentioned that in the integral of Eq. (22) the original integration interval $[-\pi, \pi]$ is changed to $[0, 2\pi]$. Of course also other observation planes can be chosen, but then an extra phase term should be added:

$$E_x(P'') = 2\pi \int_0^{D/2} \sum_{m=-\infty}^{\infty} k_m(\rho') J_{-m}(k\rho' \sin\vartheta) e^{jm(\pi/2-\varphi)} d\rho' \quad (23)$$

In principal an infinite number of terms need to be included in the Fourier series decomposition. However, computer simulations showed that, depending on the value of ρ' , 11-15 Fourier terms are sufficient to describe the function K . However, to numerically evaluate Eq. (23) the integral from 0 to $D/2$ has to be written as a finite summation. In the software that is used to generate the results for this paper, the integral is carried out by applying Gaussian quadratures. Then only a small number, compared to conventional integration procedures, of fixed ρ' are needed.

The CPU-time saving by using this decomposition was tested for an integrated lens antenna without objective lens. It was found that the computation time can be decreased by more than 50% if the number of observation points is larger than 80.

Of course the time saving will be less for the complete quasi-optical system, because the calculation of the PO-currents on the outer objective lens surface is more elaborate than the calculation of the PO currents on the eye lens. Nevertheless, usually not only the far-field patterns are computed but also the efficiencies and then the Fourier decomposition will result in a more efficient use of the CPU time.

IV. SIMULATION RESULTS

In the examples in this section the two different methods will be compared for various operating frequencies. To test the accuracy of the GO-PO method, the co- and cross-polar radiation patterns are computed and compared with the results from the more accurate PO-PO method. In Fig. 3 the patterns are depicted for an antenna system operating at 500, 1000 and 2000 GHz, where the diameter of the eye and objective lens are 6 and 30 mm, respectively. The hemispherical eye lens is made of silicon ($\epsilon_r = 11.7$) and has an extension length of 0.877 mm (hyperhemispherical condition). To minimize the reflection losses, a quarter-wavelength matching layer is put on top of the silicon lens. For the 4.35 mm thick objective lens, with a spherical inner and flat outer surface, high density polyethylene ($\epsilon_r = 2.3$) is used and this lens is placed at a distance of 36.7 mm from the center of the eye lens. The radius of curvature of the inner surface of the objective lens is taken 28 mm, which results in an optimized directivity of more than 41 dBi at 500 GHz. As planar radiator a double slot is chosen with a length of $0.28\lambda_0$ and a separation between the slots equal to $0.16\lambda_0$. This feed design results in a good rotationally symmetric pattern within the eye lens.

It can be seen from Fig. 3 that the results obtained by the GO-PO and the PO-PO methods become more alike, observing the main lobe and the first side lobes, for increasing frequencies. This is expected as GO is a high-frequency technique. For the lower frequencies however the discrepancies are significant and therefore it can be said that the use of the more elaborate PO-PO method is necessary if an accurate prediction of the far-field patterns is needed. Furthermore, it should be noted that GO-PO method can be very useful to get a first-order approximation of the beam pattern, because the computation time is negligible compared to the PO-PO method.

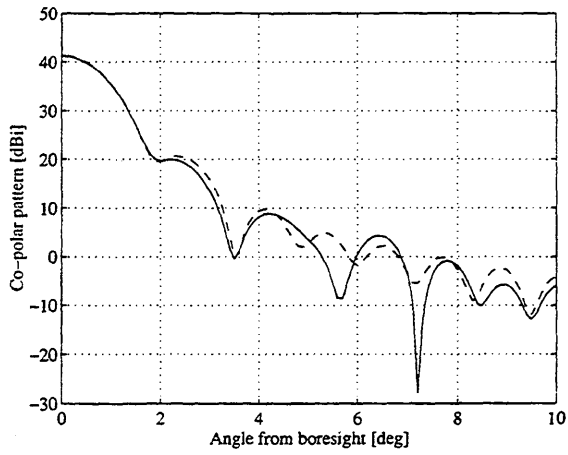
V. CONCLUSIONS

Quasi-optical systems, consisting of a feed with an additional objective lens, can play an important role in applications like imaging. The modeling of these systems becomes more complex due to this extra lens. In this paper two calculation methods are compared with each other, GO-PO and PO-PO, of which GO-PO is the more traditional and PO-PO the more accurate. The analysis showed that GO-PO can be used as a good first-order approximation of the main lobe and the first sidelobe. However, if a better prediction of the far-field pattern is required, then the field contribution of the entire eye-lens surface has to be included into the modeling and this is done by means of the PO-PO method.

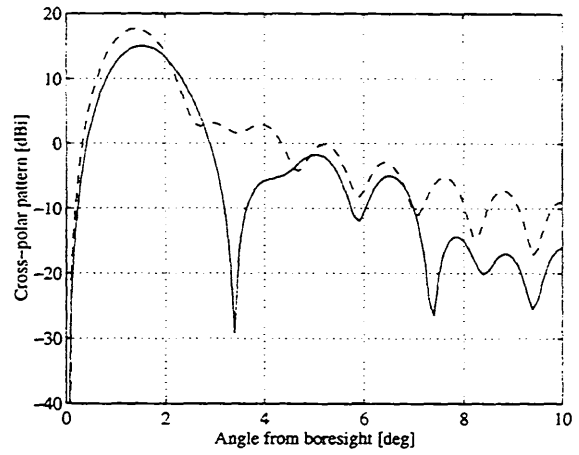
Also in this paper, a time-efficient procedure is described for computing the far field of the entire quasi-optical system. The PO integrals are rewritten in such a way that a Fourier decomposition of the integrands can be made and this can decrease the computational effort by more than 50% if the far fields in many observation points are needed.

REFERENCES

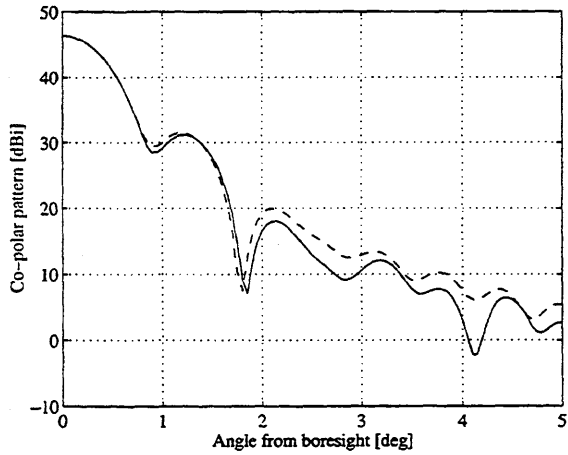
- [1] A.D. Olver et al., *Microwave horns and feeds*, New York: IEEE Press, Ch. 11, 1994.
- [2] S. Silver, *Microwave antenna theory and design*, McGraw-Hill, Ch. 3, 1949.
- [3] M.J.M. van der Vorst, P.J.I. de Maagt and M.H.A.J. Herben, *Matching layers for integrated lens antennas*, Proceedings of the International Symposium on Antennas (JINA '96), pp. 511-515, 1996, Nice, France.
- [4] V. Galindo-Israel and R. Mittra, *A new series representation for the radiation integral with application to reflector antennas*, IEEE Trans. Antennas and Propagat., vol. 25, pp. 631-641, 1977.
- [5] F. Lösch, *Tables of higher functions*, Stuttgart: Teubner Verlagsgesellschaft, p. 145, 1966.



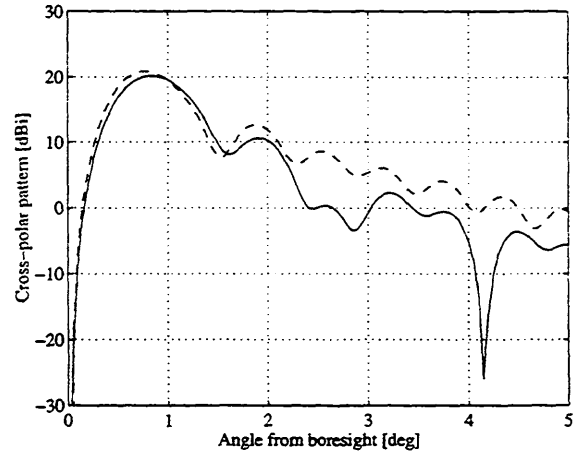
(a) $f = 500$ GHz



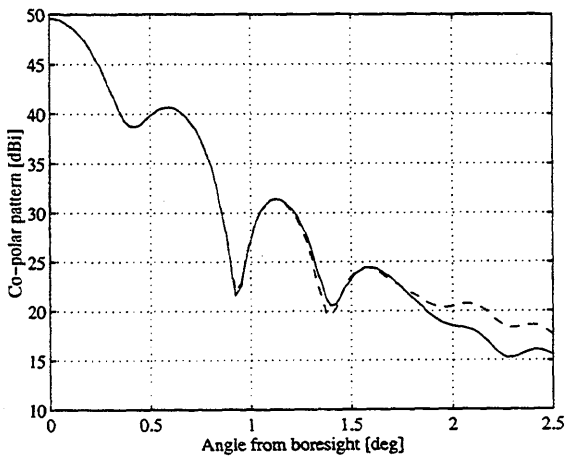
(b) $f = 500$ GHz



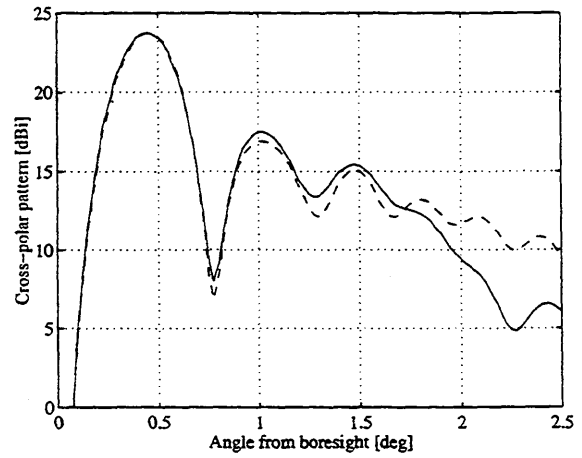
(c) $f = 1000$ GHz



(d) $f = 1000$ GHz



(e) $f = 2000$ GHz



(f) $f = 2000$ GHz

Fig. 3. Co- and cross-polar patterns for various frequencies (solid: PO-PO; dashed: GO-PO).

A NOVEL RADIO-WAVE ALIGNMENT TECHNIQUE FOR MILLIMETER AND SUB- MILLIMETER RECEIVERS

C. -Y. E. Tong¹, M. T. Chen², D. C. Papa¹, and R. Blundell¹

¹Harvard-Smithsonian Center for Astrophysics,
60 Garden St., Cambridge, MA 02138

²Institute of Astronomy and Astrophysics
Academia Sinica, Taipei, Taiwan 115

ABSTRACT

We report on a novel radio-wave alignment technique for millimeter and sub-millimeter wavelength receiving systems of radio astronomy. The technique employs a near-field scanning system to map out the 2-D amplitude and phase beam profile of a receiving system under test. Next, small scatterers, such as a pair of cross-wires or small absorbers, are introduced at known locations between the transmitting scanner and the receiver. The resultant beam pattern is measured again. These small scatterers ideally do not introduce substantial perturbation in the measured amplitude pattern. A full-wave, numerical method is then applied to transform the measured field onto the plane of the scatterers. By comparing the transformed field distributions with and without the scatterers, we can determine whether the beam is physically displaced or tilted in some ways, thereby, providing diagnosis to the alignment of different optical components in a receiving system. We will describe the application of this technique to verify the alignment of the receiver optics of the 200 GHz receivers of the Sub-Millimeter Array. The limitations of the method will also be discussed.

Keywords: Radio-wave alignment, near-field measurement, near-field numerical simulation, the Sub-millimeter Array.

I. INTRODUCTION

Aligning receiver and optical components is one of the most basic tasks in telescope operation. A well-aligned receiving system will yield optimal coupling to the incoming signal beam while a poorly aligned system will cause degrade overall system efficiency and performance. Compared to optical telescopes, aligning components of a radio telescope is more difficult because non-optical devices are commonly used in radio systems. For example, wire grids can be used as polarizer or diplexer and they are not good reflectors for visible light. Teflon is used in vacuum windows or lenses for its transparency to mm and sub-mm wavelength signal, but it is opaque to visible light. The presence of such components in a receiving system makes it rather difficult to carry out a complete system alignment using standard optical alignment techniques with laser beams.

In this report, we demonstrate a radio-alignment technique useful for millimeter and sub-millimeter receiving system. This technique employs a near-field scanning system to map out the 2-D power and phase beam profiles. Unlike optical alignment with laser system, near-field scanning is slow. It is therefore not possible to perform real-time alignment using near-field scanning data. In order to make maximum use of the measured data, we have developed a novel diagnostic procedure. Scatterers, such as a pair of cross-wires or small absorbers, are introduced at known locations between the receiver and the near-field scanner. The measured vector field at the scanning plane is transformed onto the plane of scatterers using a full-wave, numerical Kirchhoff integral. By comparing the transformed field with and without the scatterers we can determine the degree of alignment of the receiving system-- beam tilt, lateral displacement of the beam from the optical axis, and longitudinal displacement due to change in focal length. Using different scatterers placed at different locations, it is possible to infer the source of misalignment and devise ways to correct it.

This paper reports on the application of such technique to verify the alignment of the receiver optics of the 200 GHz receivers of the Sub-Millimeter Array (SMA). It firstly describes the SMA receiver optics, along with the near-field measurement setup. The Kirchhoff integral is introduced next. Then the measured beam pattern and subsequent data analysis are presented. Finally, the accuracy and limitation of this method is discussed.

II. RECEIVER OPTICS & SCANNING SETUP

The Submillimeter Array (SMA), currently under construction by the Smithsonian Astrophysical Observatory (SAO) and the Institute of Astronomy and Astrophysics of Academia Sinica in Taiwan, will function as a fully automated radio interferometer of eight 6-m antennas. Fixed-tuned receivers incorporating superconductor-insulator-superconductor (SIS) mixers are being developed to cover the major submillimeter atmospheric windows from 176 GHz to 900 GHz.^[1-6] Figure 1 shows the optics layout for the receiver system in lower frequency bands. The design of the lens and feed combination in different frequency bands creates an identical virtual feed at a distance 780mm behind the lens.^[6] The lens is located at the 80K shield, and the mixer is at the 4K stage of the cryostat.

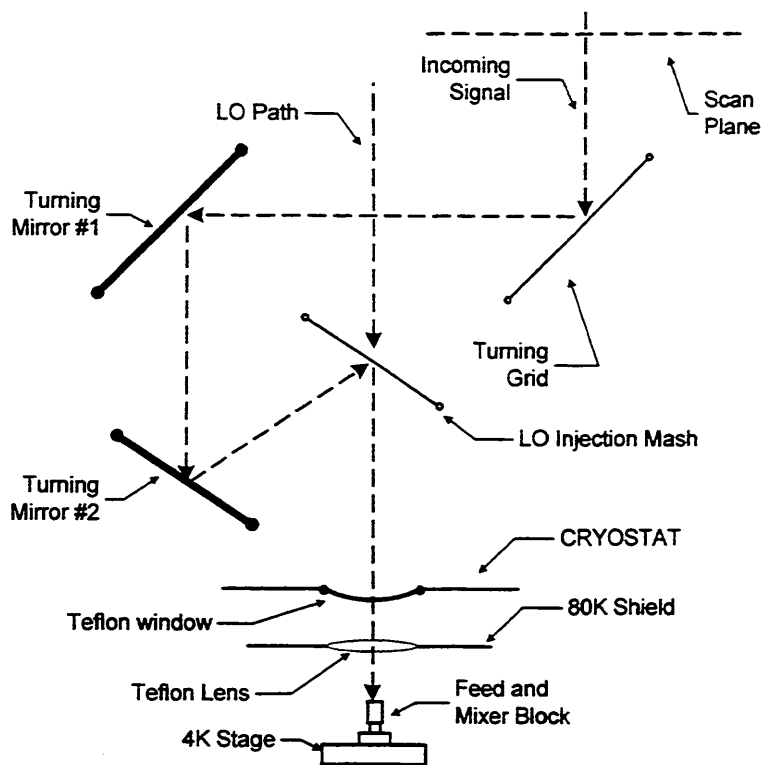


Figure 1: Schematic diagram of the SMA receiver optics.

Initial system alignment is performed optically with lasers by replacing the grid and the mesh with optical beam splitters. Once the optical alignment is done, we set up a near-field measurement system to map out the beam patterns of each receiver insert under test. The scanner consists of an XY translation stage mounted on top of the receiver system perpendicular to the signal path. A high-frequency transmitter set up on the translation stage is used as a signal source. Total radiated power coupled to the SIS junction is well below the saturation level of the mixer. The master reference signal for the entire system is the 10 MHz internal reference of a signal synthesizer.

The transmitter is tuned to operate at 242 GHz for the 200 GHz band receiver. A dynamic range of more than 50 dB, and short-term phase fluctuation of less than 5 degrees are achieved with the current setup. The scan area is typically 120 mm X 120 mm. The scanning time is mainly limited by the speed of the stepper motor. In a typical scan with sampling points 1.5 mm apart on an 81 X 81 mesh, total scan time is around 100 minutes. No probe correction has been applied to the measured data because the beams are essentially paraxial.

Special precautions have been taken to ensure that the scan plane is normal to the optical axis of the receiver assembly. We have measured that the scan plane is parallel to the top plate of the receiver assembly to within 50 μm over a distance of 150 mm. Long-term phase fluctuation has also been measured and it is typically less than 3

degrees RMS at 240 GHz over a measurement period. This is equivalent to about 10 μm , over a distance of 150 mm. This error is considered as an additional alignment error. Combined with the positioning error of the probe, we have a total misalignment budget of 60 μm over the 150 mm scan plane, equivalent to a maximum pointing error of 1.4 arc minutes.

III. NUMERICAL METHOD

The numerical calculation is based on a Kirchhoff integral in the following form:^[7]

$$\vec{E}(\vec{r}) = \frac{1}{2\pi} \int_S \frac{e^{ikR}}{R^2} \left[jk - \frac{1}{R} \right] \cdot \vec{R} \times [\hat{z} \times \vec{E}(\vec{r}_0)] \cdot dS \quad (1)$$

where k is the propagation constant, \hat{z} the unit normal vector of the plane defined by \vec{r}_0 , and $\vec{R} = \vec{r} - \vec{r}_0$. Using the above formalism, we have developed a computer code to calculate the electric field, $\vec{E}(\vec{r})$, on a target plane of interest (scatter plane) from an initial plane with known field distribution, $\vec{E}(\vec{r}_0)$.

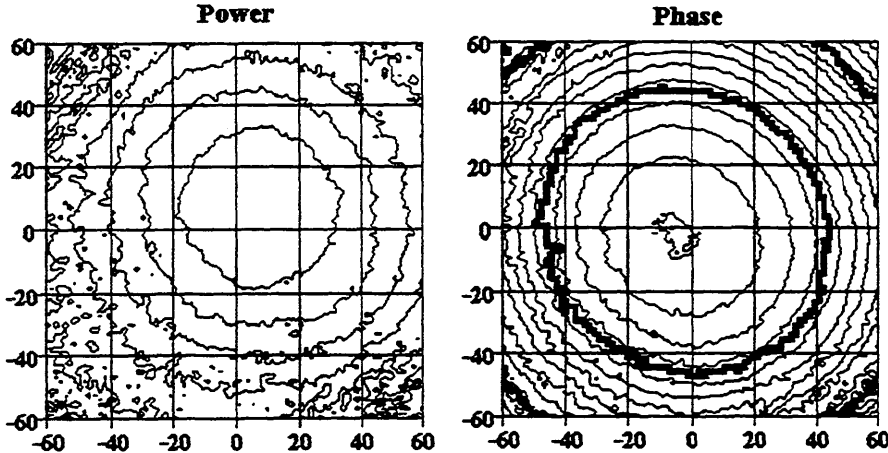


Figure 2: Beam pattern of the 200 GHz receiver measured at 242 GHz. The power contours are every 5 dB descending from the origin, while the phases are every 50 degrees. The dimensions are in millimeters.

IV. BEAM PATTERNS AND ALIGNMENT

In Fig. 2 we show the beam patterns of the 200 GHz receiver measured at 242 GHz. Obviously, the beam is misaligned with the beam center being displaced by about 10mm from the optical axis. The fact that the power and the phase maxima locate at different positions implies that the beam is actually tilted. It is not clear from this data set where the misalignment is introduced. To solve this problem, we have

performed a second scan with a cross-wire introduced at a location between the turning grid and the turning mirror #1, at a distance of 370mm from the scan plane. The diameter of the wire is 1.2 mm. The measured fields, with and without the cross-wire, are then transformed back to the scatterer plane. The difference of the 2 amplitude patterns on the scatterer plane reveals the cross-wire (see Figure 3). From this 2-D differential amplitude map, we can clearly see the center of the cross, which is about 1 mm away from the optical axis. This slight deviation is due to the thickness of the cross-wire. Since this error is small compared to the 10mm offset of the beam center shown in Fig.2. We can therefore conclude that the rotating grid is not the cause of the displacement of the beam.

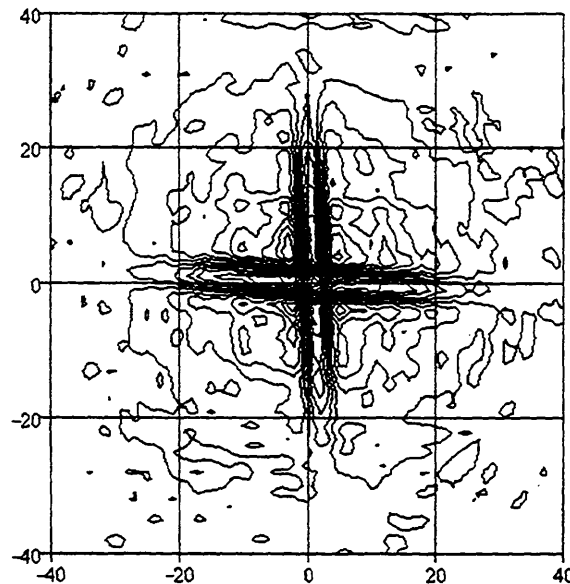


FIGURE 3. Differential amplitude contours showing a cross-wire in the signal path.

We have attempted to inspect the entire room temperature optics by placing the cross-wires right at the vacuum window, about 1400 mm away from the scan plane. However, in this case the cross-wire is not well resolved, and its center remains undetermined. The reason is that the scan area is not sufficiently large considering the long distance between the scan plane and the scatterer. A small measurement area means that part of the evanescent wave generated by the scatterer falls outside the scan area. In order to determine the relation between the scan area and the scan distance, we have simulated numerically a case in which an absorber strip 4 mm wide is introduced at the vacuum window of the cryostat. The blocked field is transformed to several planes at different distances from the window. These data sets are calculated over finite area, corresponding to a limited scan size in the near-field measurement data set. The size of the scan area is initially chosen to cover the first side lobe of the beam. The simulated measurements are then transformed back to the absorber strip plane again to reconstruct the image of the absorber strip. The results of

these simulations are shown in Fig. 4 as a cross-sectional view through the center of the window. Figure 4A shows that when the scan plane is more than 500 mm from the scatterer plane, we would not be able to resolve the absorber strip. We further explore the size effect of the scan area. In a second simulation, the scan distance is fixed at 500mm, while the scan area is increased from 100 mm square to 200 mm and 300 mm square. The result shows that a larger scan area indeed improve the image resolution. The cross-sectional view of the simulated images are shown in Fig. 4b.

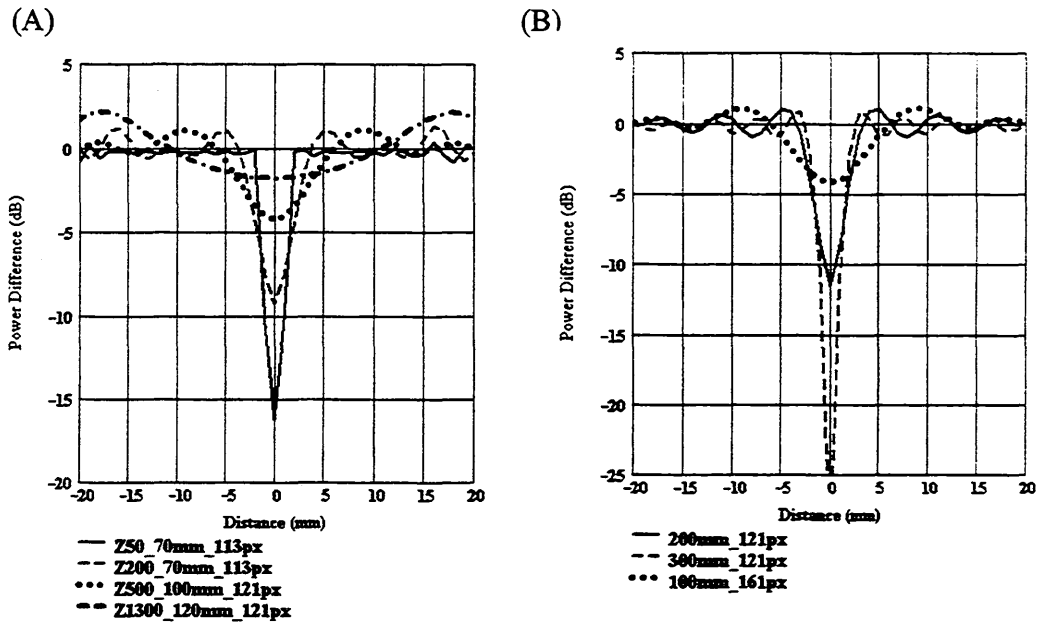


Figure 4: Cross-sectional view of the reconstructed absorber strip at the vacuum window. The traces are labeled according to the distance and size of the "scan" planes: "Z" indicates distance from the window to the scan plane, "mm" the width of the scan area, and "px" the number of sample points along one side. Figure (B) is generated from a plane located 500 mm from the window in the optical path.

Owing to the limitation of our measurement equipment and the physical system layout, a larger scan area is not achievable. Thus we have tried a different scheme of scatterer arrangement. A pair of small absorbers are introduced at diametrically positions about the center of the vacuum window which is also the optical axis. They are placed in a region of moderate beam power, about -10 to -15 dBc. Once again we measure the beam profile with and without the absorbers, and compute a differential amplitude map at the plane of the absorbers. Two such maps are shown in Fig. 5. The centers of the scatters are determined by fitting the image contours to a bi-quadratic function. The intersection of the lines connecting each pair of absorbers gives the mechanical center of the vacuum window in the image. From these images, the mechanical center

is found to be 2mm ($\sqrt{0.5}$ mm) from the beam center at the dewar window. This result verifies the alignment of the receiver optics between the vacuum window and the turning wire-grid to be within 5 arc-minutes. This small error may be due to uncertainties introduced in the fitting process. From this result, we conclude that the cause of the beam misalignment is inside the cryostat.

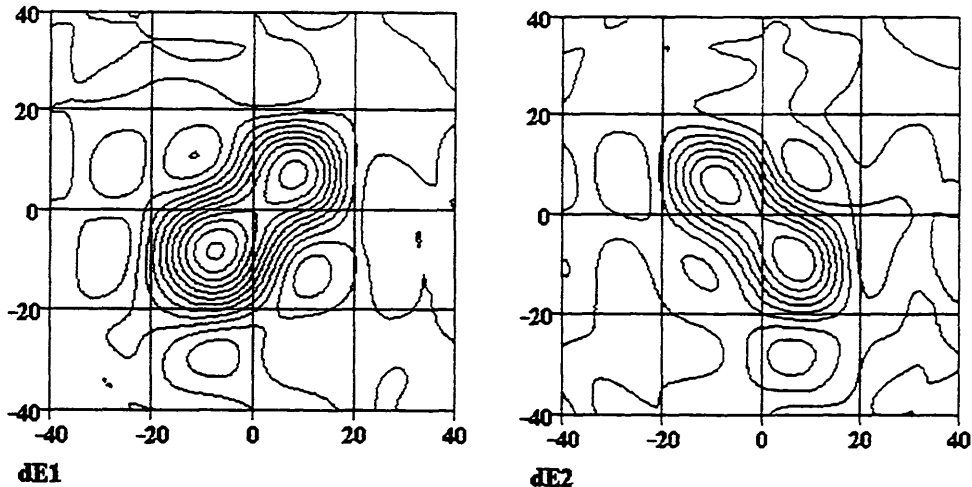


Figure 5: Differential amplitude maps showing a pair of absorbers placed at the vacuum window. The two most prominent peaks in each image correspond to the pair of small, circular absorbers. The amplitude contours are in 0.01 steps. The dimensions are in millimeters.

V. SUMMARY

We have demonstrated a radio-wave alignment technique for mm and sub-mm wavelength receiver system. This method is very useful in the alignment of mm and sub-mm telescope and receiver system with complicated optics design. We have applied the technique to verify the alignment of the SMA receiver optics. This technique has the advantage of providing an *in situ* access to individual component in a complex, radio-wavelength receiving system. With careful design, we believe that we can perform a precise radio alignment diagnosis.

VI. ACKNOWLEDGMENT

The authors would like to thank Dr. Scott Paine for valuable discussion and Mr. Michael Smith for his superior technical assistance in aligning the receiver optics. Funding for MTC is supported in part by the National Science Council of Taiwan under a grant NSC-87-2213-E-001-028.

VII. REFERENCES

1. R. Blundell, C.-Y. E. Tong, D. C. Papa, R. L. Leombruno, X. Zhang, S. Paine, J. A. Stern, H. G. LeDuc, and B. Bumble, "A Wideband Fixed-Tuned SIS Receiver for 200-GHz Operation," *IEEE Trans. Microwave Theory Tech.*, **MTT-43**, pp.933-937, 1995.
2. R. Blundell, C.-Y. E. Tong, J. W. Barrett, J. Kawamura, R. L. Loembruno, S. Paine, D. C. Papa, X. Zhang, J. A. Stern, H. G. LeDuc, and B. Bumble, "A Fixed Tuned Low Noise SIS Receiver for the 450 GHz Frequency Band," *Proc.6th Int. Symp. Space Terahertz Tech.* 1995.
3. C.-Y. E. Tong, R. Blundell, S. Paine, D. C. Papa, J. Kawamura, X. Zhang, J. A. Stern, and H.G. LeDuc, "Design and Characterization of a 250-350 GHz Fixed-Tuned Superconductor-Insulator-Superconductor Receiver," *IEEE Trans. Microwave Theory Tech.* **MTT-44**, pp. 1548-1556, 1996.
4. C.-Y. E. Tong, R. Blundell, D. C. Papa, J. W. Barrett, S. Paine, X. Zhang, J. A. Stern, and H. G. LeDuc, "A Fixed Tuned Low Noise SIS Receiver for the 600 GHz Frequency Band," *Proc. 6th Int. Symp. Space Terahertz Tech.* 1995.
5. M. T. Chen, C. E. Tong, S. Paine, and R. Blundell, "Characterization of Corrugated Feed Horns at 216 and 300 GHz", *International Journal of Infrared and Millimeter Waves*, Vol. 18, No.9, pp. 1697-1710, 1997.
6. S. Paine, D. C. Papa, R. L. Leombruno, X. Zhang, and R. Blundell, "Beam Waveguide and Receiver Optics for the SMA," *Proc. 5th Int. Symp. Space Terahertz Tech.* 811-823, 1994.
7. Thorkild B. Hansen and Arthur D. Yaghjian, "Planar Near-Field Scanning in the Time Domain, Part 1: Formulation," *IEEE Tans. Antennas Propagat.*, **AP-42**, No.9, pp. 1280-1291, 1994.

SPECTROSCOPIC MEASUREMENTS OF OPTICAL COMPONENTS AROUND 1 TERAHERTZ

D. J. BENFORD, J. W. KOOI AND E. SERABYN

California Institute of Technology, Pasadena, CA 91125, USA.

contact: dbenford@tacos.caltech.edu

ABSTRACT

Recent advances in submillimeter SIS receivers necessitate the use of very-low-loss components in order to achieve their theoretical performance. Additionally, as HEB and thermal bolometer instruments become more sensitive, better infrared blocking filters are needed. Often these optical elements will be cooled to 4K, where their properties are less well measured. We present measurements of the effectiveness of dielectric antireflection coatings on quartz at 4K over the frequency range 0.3 to 1.6 THz. Absorption coefficients for materials used as infrared blocks are presented. Studies of the transmission of other optical components are discussed.

1. INTRODUCTION

In the design of optical systems for submillimeter wavelengths there is a variety of materials available with properties suitable for windows, filters, infrared blocks, and lenses. Advanced SIS receivers are achieving nearly quantum-limited performance: at 492GHz, Kooi et. al.^[1] measured a receiver total noise temperature of 74K, of which 52K stems from optical losses. Modern bolometric instruments such as SHARC^[2] have a total optical efficiency of only $\sim 30\%$, far from ideal. Clearly, choosing materials with the optimum dielectric constants, lowest loss, and best cryogenic performance is critical.

With this in mind, we have characterized optical elements using a Fourier Transform Spectrometer (FTS). The instrument was initially developed to test the response of SIS junctions^[3], and consists of a Michelson interferometer with a movable mirror on a 2 meter translation stage as shown in figure 1. A glowing coil is used as a source, with an optical chopper modulating the beam between the source and a 77K blackbody at roughly 150 Hz. The source illuminates an off-axis paraboloid with an effective $f/2.5$

beam, where it is collimated in a $10''$ diameter beam. A Mylar beamsplitter separates and recombines the two beams, which are focused onto a detector. The entire optics setup is contained in an acrylic dry box which is purged using nitrogen gas to a relative humidity of $< 2\%$, reducing the contribution from the strong absorption features of water in the submillimeter. The moving stage is actively controlled to keep the two beams coincident over the long path length. A Macintosh computer running LabVIEW is used both to control the FTS and to collect and reduce the data.

The instrument used in this work was a 2K bolometer with a Winston cone providing a $f/4$ beam looking into the FTS. Also at 2K is a filter wheel with spaces for several materials under examination. An off-axis paraboloid (not shown in figure 1) is used to collimate the FTS beam into the dewar, providing an image of the collimated portion of the FTS inside the dewar at the position of the samples in the filter wheel. Because of the collimation, variations in the beam as a result of increasing optical path in the samples is not a problem. In addition to the samples, there is a clear aperture which

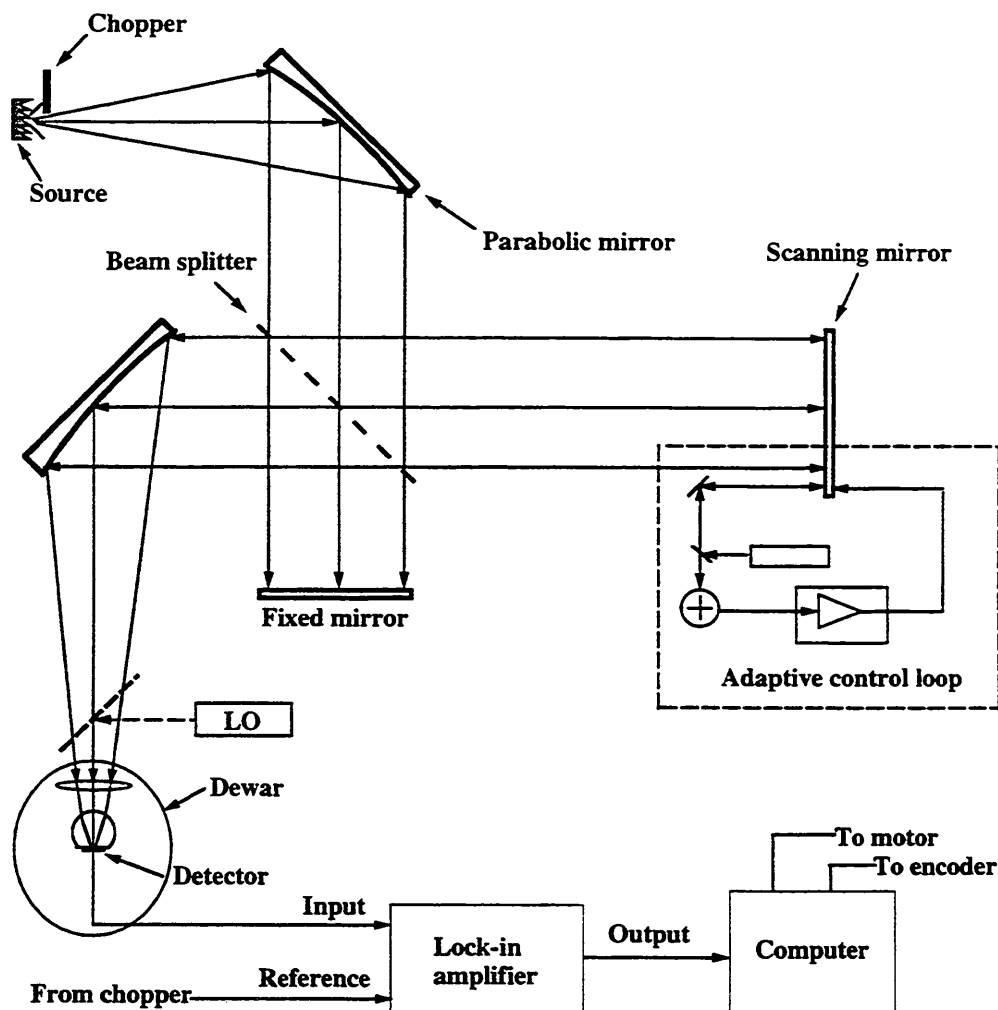


Fig. 1.— Block diagram of the FTS with a heterodyne receiver in place; the results presented in this paper used a bolometer, hence there was no LO.

permits the use of ratios to remove instrumental sensitivity and yield the calibrated transmission of the sample.

2. GERMANIUM

The spectral resolution of a grating spectrometer is linearly dependent on the optical path length (depth) of the grating. If the grating is immersed in a material of medium n , the grating depth increases by this factor. Hence, for a given spectral resolution, the grating volume can be reduced by a factor of n^3 . We have designed an immersion grating spectrometer^[4] in which the grating will be immersed in germanium since its index of

nearly 4 is among the highest available. The desired resolution of ~ 1500 , chosen to minimally exceed the width of extragalactic line emission, requires a grating almost 10cm in length. In order to be feasible, the absorption coefficient must be very small.

Several samples of germanium between 2 and 17mm thickness were measured in the FTS, and the absorption coefficient estimated for every possible pair. The refractive index at 2K is found to be $n = 3.90 \pm 0.01$. No absorption could be detected, allowing us to place a limit on the absorption coefficient at all frequencies below 1500GHz of $\alpha \leq 0.01 \text{ cm}^{-1}$. Assuming the absorption

goes as ν^2 , the absorption coefficient at ~ 750 GHz is $\alpha \leq 0.003$. Thus the absorption in our germanium slab will be $\lesssim 5\%$.

3. FLUOROGOLD

Fluorogold, a form of glass-filled Teflon, is a material which has been measured at liquid helium temperatures in the past^[5]. It is often used as an infrared blocking filter, but its absorption coefficient must be known precisely to yield the best transmission in the submillimeter band of interest.

Using three samples of Fluorogold at 2K, cut from sheets of thicknesses 0.79, 1.6 and 2.2mm, we measured the transmission of each with respect to an open port. The samples were also ratioed with each other to remove any error in the absorption coefficient induced by surface reflections. An excellent agreement was found between the

samples, as is illustrated in figure 2. An approximate expression for the absorption coefficient of Fluorogold over the 300-1400 GHz range is $\alpha = 6\nu^4 \text{ cm}^{-1}$, where the frequency ν is in THz. This value is close to the previous measurements of Halpern et. al.^[5], $\alpha = 9\nu^{3.6} \text{ cm}^{-1}$ at 4.8K over the 60-900 GHz range. As they suggest, the difference probably derives from differences in the manufacture of sheets versus disks cut from rods.

4. ZITEX

Zitex has recently enjoyed a surge of popularity as an inexpensive, low-loss infrared-blocking filter. Zitex^[6] is a sintered Teflon material with voids of 1-50 μm and a filling factor of $\sim 50\%$. Several different varieties are available, divided into two categories by manufacturing process: Zitex A is designed to reproduce filter paper, and so has many

Absorption Coefficient of Fluorogold

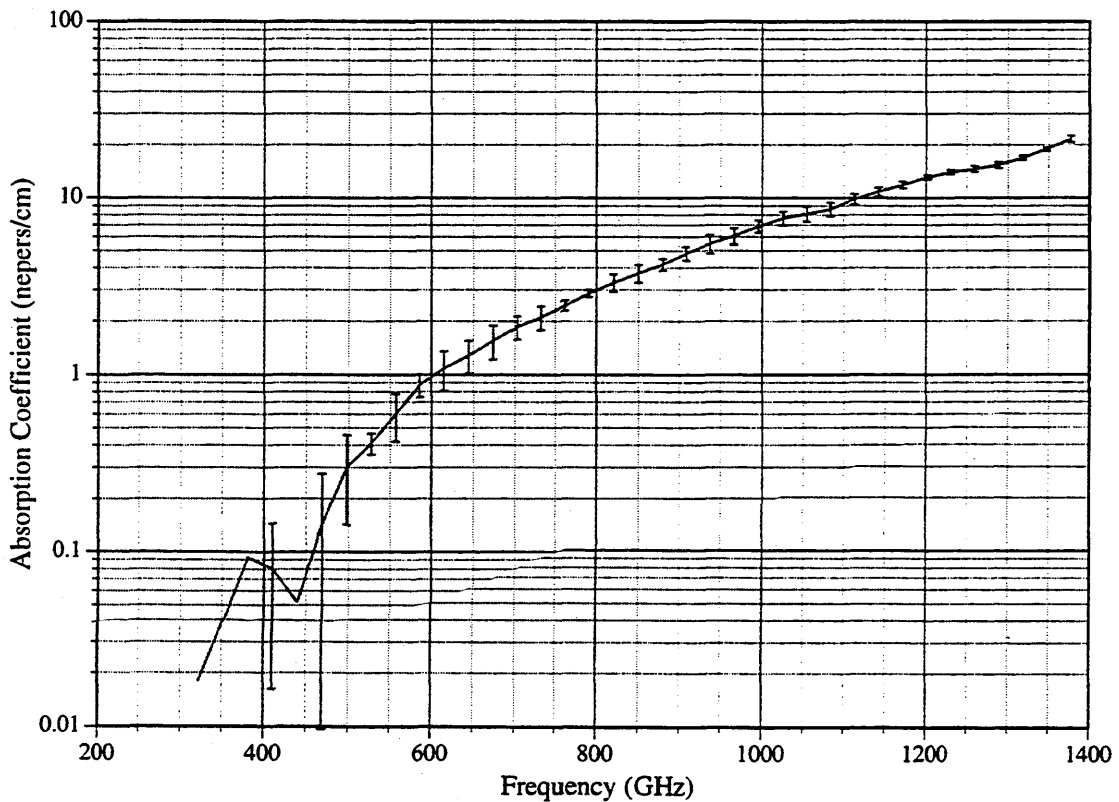


Fig. 2.— Absorption coefficient of Fluorogold sheets at 2K.

narrow linear paths through it and is a rough but soft sheet; Zitex G is made of sintered Teflon spheres of small sizes, resulting in a denser, smoother material. The grades of Zitex of each class differ primarily in the size of the voids in the Teflon; this affects the IR to Mid-IR scattering characteristics. A study of this material has been undertaken to understand its transmission properties from $1\mu\text{m}$ to 1mm wavelengths^[7].

Whereas Zitex is typically available in thicknesses of 0.10mm (0.004") to 0.38mm (0.015"), we have measured a sample of Zitex G-125 3.53mm (0.139") thick. Being this

thick, it is possible to measure both the loss, as shown in figure 3, and the refractive index, which is $n = 1.20 \pm 0.07$. Despite the scatter in the data, a power law fit to the data (excluding the absorption band at 1400 GHz) of $\alpha \simeq 0.25\nu^{3.1} \text{ cm}^{-1}$ with ν in THz is quite good. This fit and the absorption band agree well with the results of Kawamura et. al.^[8] in Teflon. Since this implies the submillimeter loss is from the bulk Teflon rather than the scattering in the near-infrared, extrapolation to other thicknesses at frequencies below ~ 2 THz should be valid.

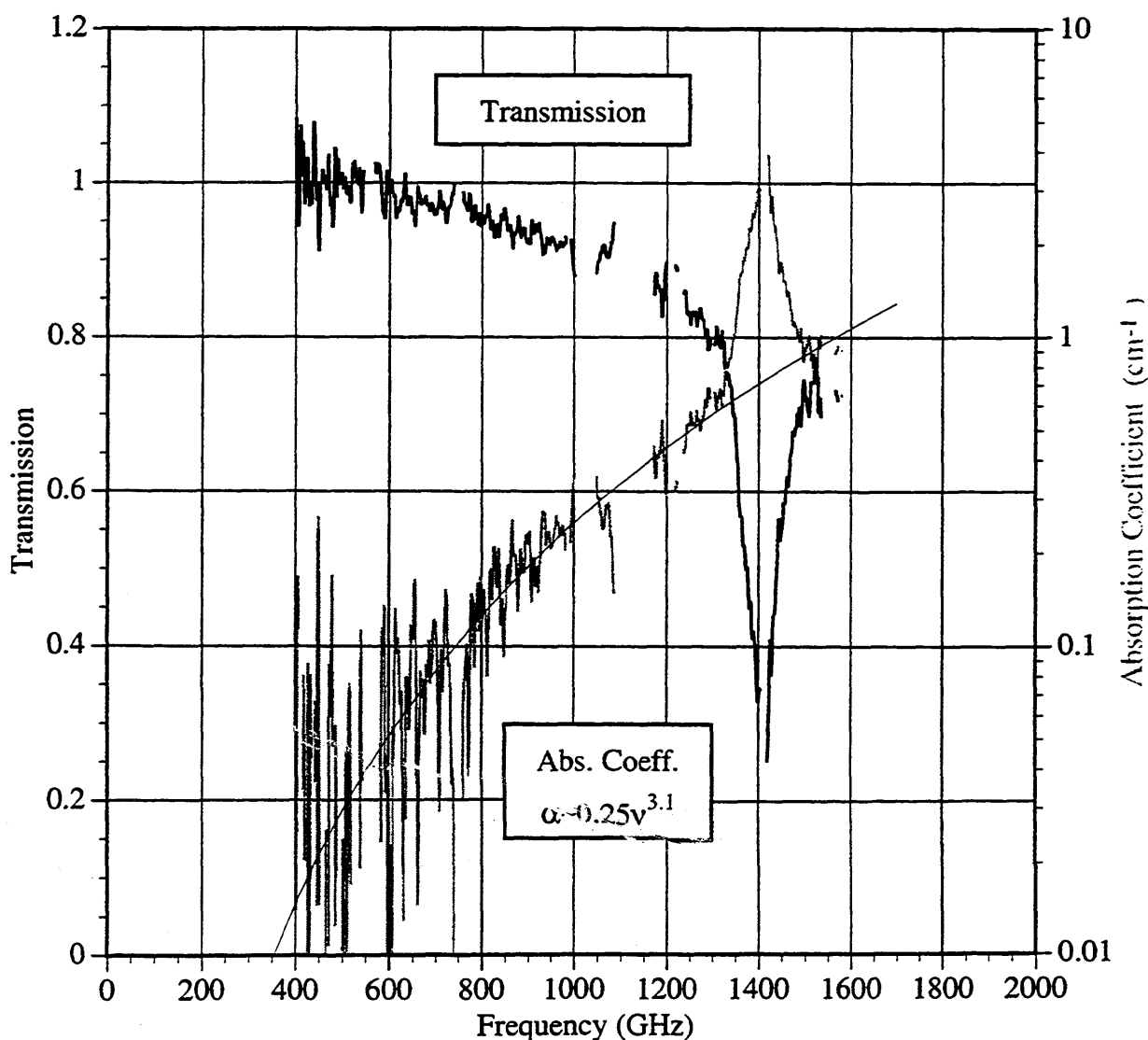


Fig. 3.— Transmission and absorption of Zitex at 2K.

5. QUARTZ WINDOWS

Quartz is a useful material both for vacuum windows and for infrared-blocking filters, because of its high transparency in the submillimeter and its relatively poor transmission in the infrared. However, its refractive index is high enough to cause substantial ($\sim 20\%$) reflection losses; for this reason, it is worthwhile to antireflection coat the quartz substrate with a layer of a material with index $n \sim 1.4$ such as Teflon. We have measured the transmission of numerous windows and infrared blocks with Teflon antireflection coatings of various manufacturers (e.g. Francis Lord Optics). Figure 4 is one such measurement: a 230 GHz antireflection coated window (heavy curve) compared with the theoretical design curve (light). The difference between the two most likely results from the generally poor uniformity of the thickness of the Teflon coatings, each roughly 0.2mm (0.008") thick but visible quite rough. Even so, the loss around 230 GHz is decreased by a factor of ~ 5 , a substantial improvement.

6. QUARTZ LENSES

As quasioptical receivers become more common, the use of quartz lenses has increased. We have measured the improvement in transmission of a quartz lens when antireflection coated with Teflon. Using two lenses designed for CHAMP, the 16-element 492 GHz SIS array of the MPIfR^[9], we ratioed the transmission of one with a coating and one without. Figure 5 shows the data (heavy curve) over the complete region while a calculated model (light curve) is plotted only for $\nu < 1000$ GHz to enable a clearer view of the measure transmission. Since an accurate calculation of the antireflection coating of a nonplanar surface is difficult, we have merely made an estimate of the ratio assuming a planar geometry; the two agree well in shape. This again shows the improvement found with a dielectric antireflection coating, improving the transmission by $\sim 20\%$ at the design frequency.

7. METAL MESH FILTERS

Resonant metal mesh filters have been used as optical filters for some time^[10]. We evaluated the transmission of several bandpass and long wavelength-pass filters, commercially available from Cochise Instruments^[11], in figure 6. These are fabricated by depositing copper layers onto very thin mylar sheets which are stacked to improve rejection of out-of-band signal. In order to determine their effectiveness as blocking filters, we have measured the average attenuation of the signal in the out-of-band regions below 1 THz. The long wavelength-pass filters' out-of-band transmission is everywhere $\lesssim 0.001$ while the bandpass filters are typically ~ 0.002 with some variation as a function of frequency.

8. DOUBLE FABRY-PEROT FILTER

We have developed a double Fabry-Perot filter constructed from two precise silicon disks with a thin air gap between them^[12]. The filter was designed to have transmission peaks approximately every 115GHz, the fundamental rotational transition of CO. Doubling the Fabry-Perot increases the width of the transmissive region of the spectrum while increasing the rejection of the reflective region. When used with a Fourier transform spectrometer, this filter will transmit only the wavelengths of interest while reducing the loading on the detector.

In order to characterize this filter before use at the Caltech Submillimeter Observatory, we performed careful measurements of the silicon disks. A computer model of a double Fabry-Perot was used to determine the optimum optical depth of each silicon disk, the product of its index and thickness. The thickness was measured interferometrically in the near-infrared, while we measured the index in the Terahertz region at 2K to be $n = 3.385 \pm 0.01$, somewhat lower than the room temperature value. After completion, the filter transmission was measured (figure 7); the data is shown by the solid line

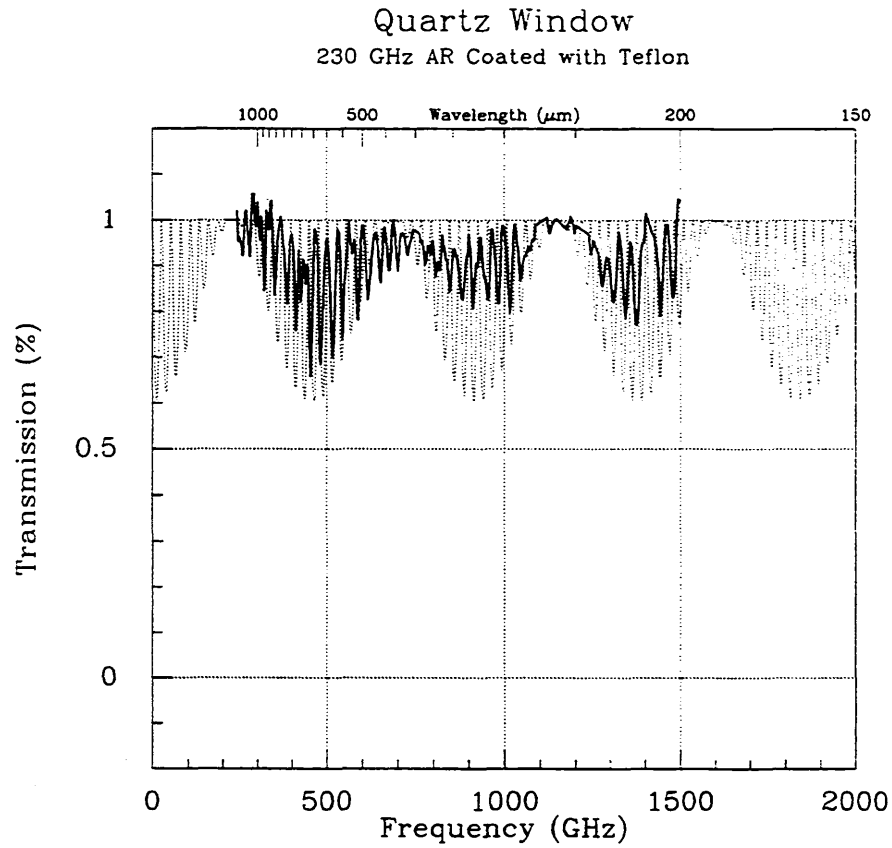


Fig. 4.— Transmission of an antireflection coated quartz window designed for the 230 GHz region.

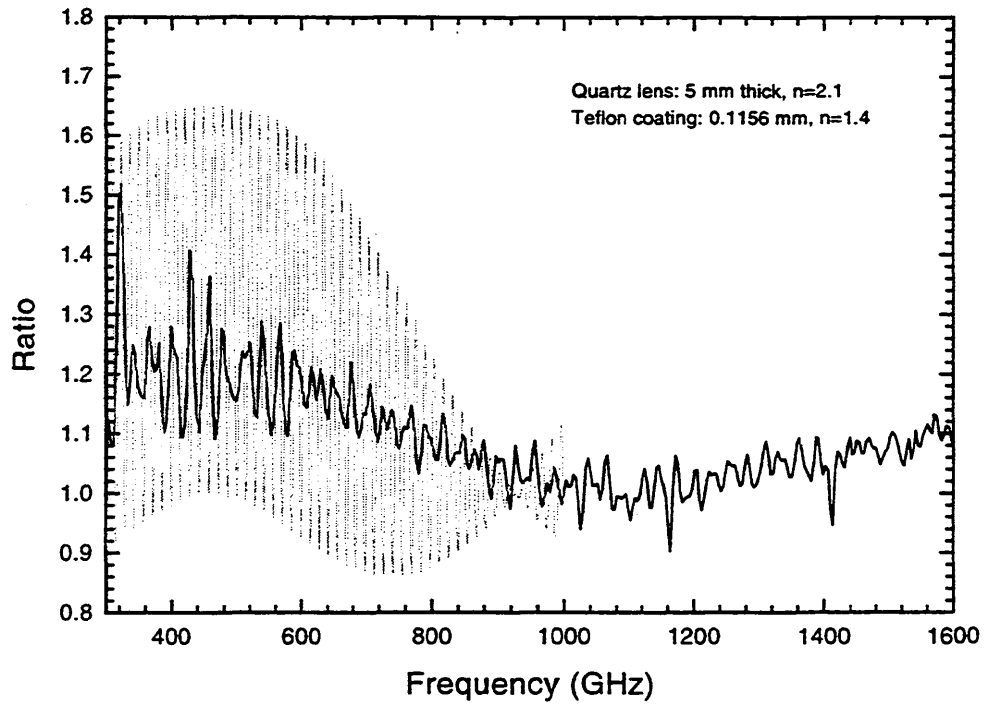


Fig. 5.— Transmission ratio of an antireflection coated quartz lens and an uncoated lens.

Metal Mesh Filters
(supplied by Cochise Instruments)

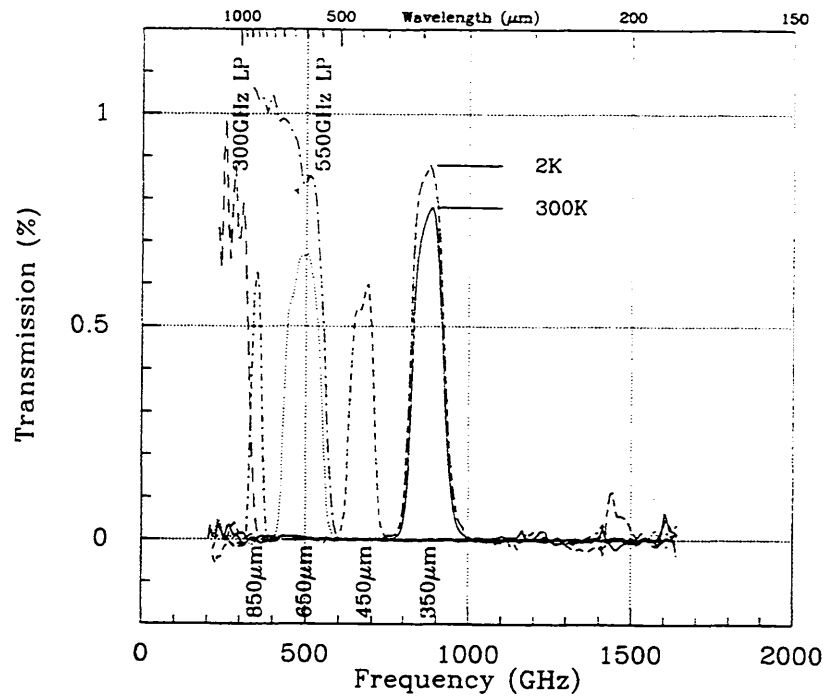


Fig. 6.— Transmission of resonant metal mesh bandpass and lowpass filters. All measurements but one are at 300K; the 350 μ m filter was also tested at 2K.

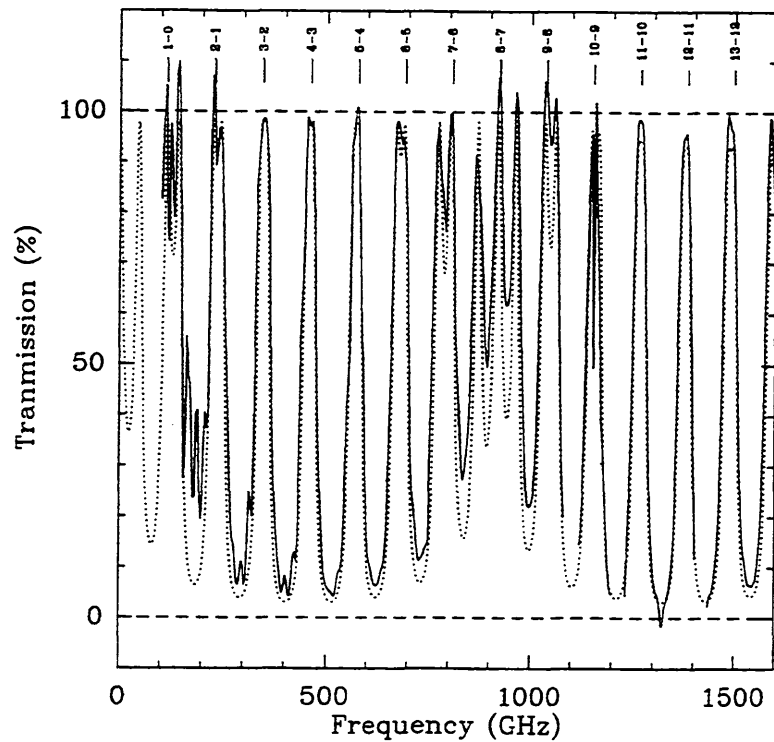


Fig. 7.— Double Fabry-Perot filter with CO transitions marked above the transmission curve.

while the theoretical spectral transmission is shown as a dotted line. The transmission in the bands of interest is > 90% while the rejection is around 10%. This filter is being used at the CSO to detect all available rotational transitions of CO in nearby galaxies.

9. RESTSTRAHLEN FILTER

Transmission filters made from polyethylene sheets loaded with varieties of powdered crystals have been fabricated for decades^[13]. Each crystal scatters strongly in its reststrahlen band (in the 10-100 μ m range), so that combinations produce a broad region of near-zero transmission. Coupled with a small amount of carbon, these become good long-wavelength filters. However, the width of each crystal's scattering region increases with increasing temperature, so that the properties of this kind of filter changes drastically with temperature. We tested at 2K and 300K a commercially-available filter^[14] with a nominal cutoff at 1650 GHz. The transmission from 300 to 1650 GHz is shown in figure 8. While our coverage does not provide any information about the rejection of higher frequencies, we do see a substantial decrease in transmission when the filter is warm compared to the relatively good cold transmission. Unfortunately, while the cutoff is sharp around 1600 GHz, the transmission at frequencies near 1 THz is far from ideal.

10. AEROGEL AND LIQUID NITROGEN

Aerogel is well-known as the least dense solid. Being made of an exceptionally low-density glass matrix, it might be useful as a scattering filter in the far-infrared and therefore its absorption coefficient might be a steep function of frequency. However, the absorption coefficient as shown in figure 9 goes as $\nu^{1.7}$ and is therefore unsuitable as a low-pass filter.

Liquid nitrogen is used by most experimenters as a cold load; often, fixed setups use a dewar flask of cryogen with a piece of eccosorb floating or submerged in it. We had wondered what would take place if the eccosorb were fully submerged: would the radiation penetrate into the liquid at all? The absorption coefficient (figure 9) is high enough that near 1 THz, a depth of a few centimeters is sufficient to attenuate the beam; therefore, eccosorb is not needed provided that surface reflection does not terminate at a different temperature.

11. CONCLUSION

We have measured the optical properties of a variety of materials and components useful in the submillimeter range using an FTS. Knowledge of these properties should be useful in the design of low-noise, high-efficiency instruments in the Terahertz region.

REFERENCES

- [1] J.W. Kooi, M. Chan, B. Bumble, H.G. LeDuc, P. Schaffer & T.G. Phillips, *Infrared & Millimeter Waves*, 16 (1995)
- [2] N. Wang, T.R. Hunter, D.J. Benford, E. Serabyn, D.C. Lis, T.G. Phillips, S.H. Moseley, K. Boyce, A. Szymkowiak, C. Allen, B. Mott & J. Gyax, *Applied Optics* 35, 6629 (1996)
- [3] M. Bin, M.C. Gaidis, D.J. Benford, T.H. Buttgenbach, J. Zmuidzinias, E. Serabyn and T.G. Phillips, *Infrared & Millimeter Waves*, to be submitted
- [4] D.J. Benford, E. Serabyn, S.H. Moseley & T.G. Phillips, *Proc. SPIE 3357* (1998)
- [5] M. Halpern, H.P. Gush, E. Wishnow & V. De-Cosmo, *Applied Optics* 25, 565 (1986)
- [6] Norton Co., Wayne, New Jersey. 201-696-4700
- [7] D.J. Benford, M.C. Gaidis & J.W. Kooi, *Infrared & Millimeter Waves*, to be submitted
- [8] J. Kawamura, S. Paine & D.C. Papa, *Seventh International Symposium on Space Terahertz Technology*, Charlottesville, 349 (1996)
- [9] R. Güsten et al., *Proc. SPIE 3357* (1998)
- [10] R. Ulrich, *Infrared Physics* 7, 37 (1967)
- [11] Cochise Instruments, Hereford, AZ. 602-378-6321
- [12] D.J. Benford, E. Serabyn & S. Wu, *Applied Optics*, to be submitted
- [13] Y. Yamada, A. Mitsuishi & H. Yoshinaga, *JOSA* 52, 17 (1962)
- [14] Supplied by S. E. Church

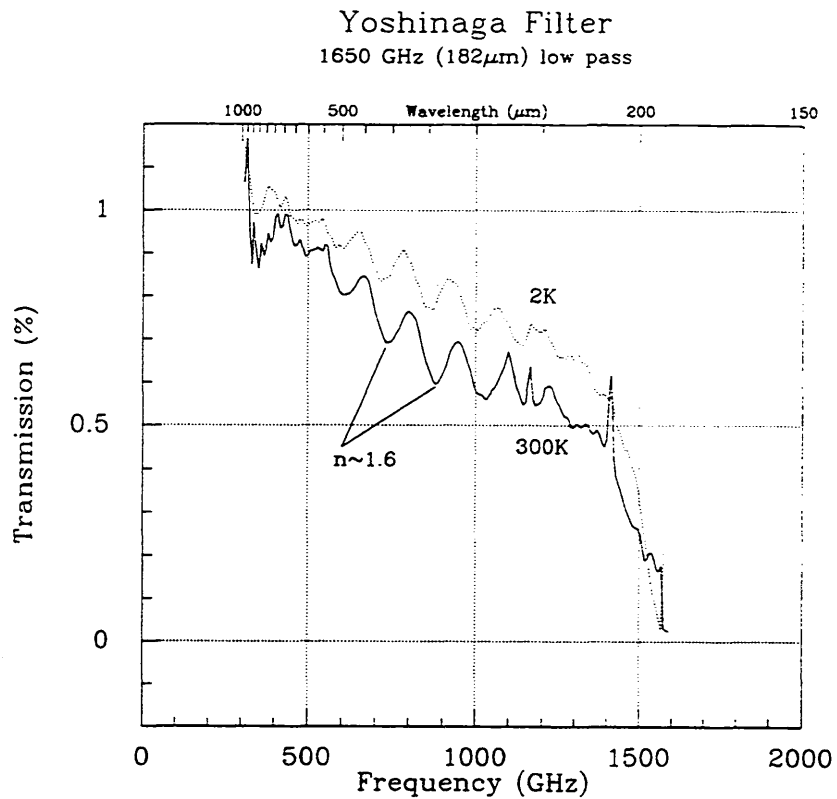


Fig. 8.— Transmission of a Yoshinaga-type reststrahlen crystal lowpass filter at 300K and 2K.

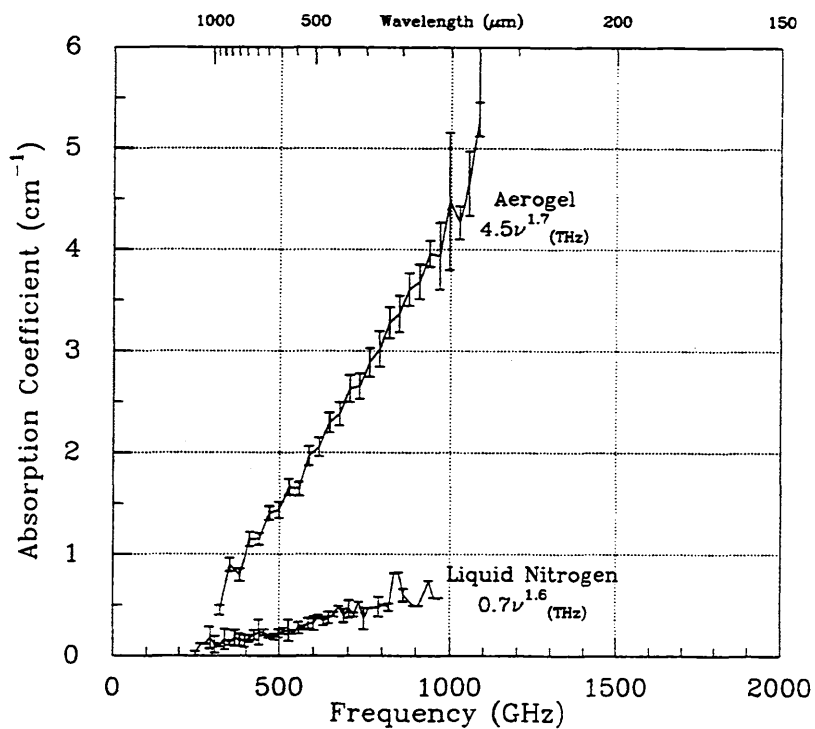


Fig. 9.— Absorption coefficient of aerogel and liquid nitrogen.

A SIMPLE MILLIMETER/SUBMILLIMETER-WAVE BLACKBODY LOAD SUITABLE FOR SPACEBORNE APPLICATIONS

Peter H. Siegel

California Institute of Technology Jet Propulsion Laboratory, Pasadena, CA

Robert H. Tuffias
Ultramet, Pacoima, CA

Philippe Goy
AB Millimetre
52 Rue Lhomond, Paris, France

ABSTRACT

A very simple black body calibration target is described for millimeter and submillimeter wavelengths. The target combines random scattering, impedance matching and power absorption to produce a low return loss to incident radiation over a broad range of wavelengths. The design uses a unique light-weight silicon carbide based open cell foam [1] coated with a commercially available ferrite absorbing resin [2] to provide both high thermal conductivity and a high absorption coefficient. The cell size of the foam can be used to tailor the frequency range of operation. Materials other than silicon carbide can be used to form the foam base if different thermal or mechanical properties are desired without greatly affecting the absorption coefficient. This design is an alternative to much more difficult to fabricate periodic scatterers/absorbers [3-7] which perform a similar function.

INTRODUCTION

At millimeter and submillimeter wavelengths high quality absorbing loads are typically fabricated from flat sheet carbon loaded polyurethane foams [8]. These foam absorbers provide low return loss and easy-to-contour surfaces for a wide variety of applications, including room temperature or cooled black body calibration targets, absorbing apertures, anechoic chambers etc. Unfortunately, the base material for these absorbers degrades and crumbles over time periods as short as a few years, the thermal conductivity is only moderate, and for vacuum applications, the material outgasses significantly. Absorbers based on silicone have recently become popular [6,9] but these are unsuitable for vacuum applications due to outgassing and typically are more resonant (frequency dependent) than the open cell foam absorbers. One company [10] produces a polypropylene based carbon loaded absorber which is suited for very high frequencies, but which has so far proven unacceptable for spaceborne applications (again due to outgassing) and for producing black bodies which rely on thermal conductivity to keep the gradient through the material low. Alternative rigid absorbers are available [3,5,11 for example] in an assortment of cast or machined shapes

which don't have outgassing, thermal conductivity or lifetime problems. However, these rigid absorbers, which generally rely on ferrite loading for their absorbing properties, are extremely heavy and, for millimeter or submillimeter wave applications, must be very precisely machined or cast into finely pointed periodic surfaces so as to present the proper dielectric match to the incident RF fields. This usually entails one of two techniques: (1) machining or casting the surface of the material so as to form tapered cones, ridges or pyramids which are sized and spaced on a period akin to a half wavelength or less at the desired frequency of operation or (2) molding or coating the material on a very large aperture structure with a slow geometric taper (slowly tapering cone for example) that allows multiple bounces of the incident RF energy before it can emerge or scatter from the absorbing body.

In this short paper we propose a load composed of a base similar in structure to the polyurethane foam, but with high thermal conductivity, no degradation over time, and no outgassing. The load is made from a sheet of specially prepared silicon carbide open cell foam which is simply dip coated with a layer of commercially available castable ferrite absorber. The coating increases the absorption coefficient of the base material without significantly changing the matching/scattering properties of the open cell foam. The impedance match to the RF field is accomplished through judicious choice of the base material cell size, which can be fabricated with a lattice constant from a few millimeters to less than a tenth of a millimeter and thereby cover a frequency range from below 100 GHz to at least 1 THz and probably higher. The load is extremely easy to fabricate, once the base material and castable resin are in hand, and, although flat sheets are the simplest to implement, more complicated geometries are not excluded.

FABRICATION

The load is based upon the availability of large, fairly thin (0.5-1 inch thick) sheets of the silicon carbide (or similar structured) open cell foam [1] and medium viscosity castable resin absorber [2]. The silicon carbide sheet is placed in a disposable tray or on top of a permanent metal plate (if it is to be used in reflection) and the castable resin absorber is simply poured through the cell structure allowing it to pool at the bottom of the tray. In our samples we used Emerson and Cuming CR117, which has the viscosity of syrup when heated to 65C, and is easily cured in an oven under standard atmospheric pressure. To improve the uniformity of the coating the foam sheet (9x12x0.5 inches thick in this case) was actually soaked in a tray of resin, flipped several times and then transferred to a metal pan where the resin was allowed to drip naturally through the material and pool to a thickness of approximately one-quarter inch at the bottom of the pan. After curing in an oven for one hour at 150C, the load was permanently adhered to the metal pan. In the measurements to follow, two sheets were fabricated and then joined together to form a rather large wedge (Figure 1) providing a large aperture for the incident RF beam and several bounces off the material to mimic the arrangement described in [5]. A cell spacing of 10-15 pores/inch was chosen to optimize the load performance around 200 GHz. The large pore size (near a half wavelength) provides both a randomly rough (on the wavelength scale) surface to enhance non-preferential scattering and a low impedance (average of CR117 and open area) to better match to free space.

RF PERFORMANCE

The RF performance of the new SiC coated load, used both as a wedge and in flat sheet was measured using the arrangement shown in Fig. 2. A special vector network analyzer [12], with a very wide dynamic range at submillimeter wavelengths, was used to measure the return loss off the metal backed load and compare it to a similar load made of rigid absorber (also CR117) cast in a periodic arrangement of 0.15 inch high pyramids (Fig. 3) and flat sheet foam absorber (Eccosorb AN74). Photographs showing the surfaces of each measured load and their performance over frequency are displayed in Figs. 4 and 5. As is apparent from Fig. 5, the silicon carbide load worked as well or better than the much more difficult and expensive to fabricate pyramidal absorber in flat sheet form and almost as well in the wedge arrangement. In addition, the silicon carbide absorber had little (if any) polarization dependence whereas any periodic absorber must be designed so as to eliminate large reflections at specific angles due to diffraction lobes. The foam absorber was superior to both rigid absorbers at the higher frequencies but comparable or poorer performing below 200 GHz, as might be expected from the smaller cell size compared to a wavelength at these frequencies. Flat sheet CR117 (with no surface roughness machined in) performs very poorly with return loss above -10dB at most frequencies. The measurements also indicate the performance enhancement that occurs with frequency when the cell size (or periodicity in the case of the pyramids) is appropriately chosen. This feature was chosen to be best suited to a measurement frequency near 200 GHz for both of these loads. Additional frequency tailoring can be accomplished by altering the surface contour of the silicon carbide foam on a scale large compared to the cell size, like the arrangement often used at lower frequencies with the polyurethane and silicone based absorbers found in anechoic chambers. Finally, although thermal conductivity measurements on the load were not made, the inherent thermal conductivity of the silicon carbide base material is very high compared to polypropylene, silicone or even the castable absorbing resin, so it is expected that this load will perform at least as well as the rigid pyramidal type absorber and better than absorbers based on other materials.

OTHER APPLICATIONS

Uses for the proposed black body absorber are not limited to millimeter and submillimeter wavelengths. The principle of operation, i.e. scattering and impedance matching at the surface of the material, apply to any frequency and the foam base can be cast in any geometric arrangement desired. This means much lower frequency operation is possible and less costly base materials might be employed for large coverage areas. Obvious benefits of the silicon carbide base material are imperviousness to high temperatures, resistance to physical loading and high thermal conductivity. Pure carbon foam has also been coated successfully, but does not have the resistance to breakage and flaking inherent with the silicon carbide. Non absorber related applications for the material may exist but are not a concern here.

SUMMARY

A simple absorbing black body load can be formed by combining an open cell silicon carbide based foam and a castable ferrite absorbing resin. The resulting structure is easy to fabricate and performs as well as much more expensive and difficult to build periodic absorbing surfaces. Applications are not confined to high frequencies if the base material is formed into geometric shapes compatible with the frequency of application. The cell size of the base material can be adjusted to peak the absorption at a particular wavelength if desired.

ACKNOWLEDGEMENT

This work was performed at the California Institute of Technology Jet Propulsion Laboratory under contract with the National Aeronautics and Space Administration.

REFERENCES

- [1]. The silicon carbide foam is available in sheet or custom shaped form from Ultramet, Pacoima, California, 91331, 818-899-0236. It is produced using a proprietary process employing CVD deposition and can be produced with base materials other than silicon carbide.
- [2]. A variety of microwave absorbing resins are available from Emerson and Cuming Microwave Products, 28 York Avenue, Randolph, Massachusetts 02368 781-961-9600. The resin used to make the loads described in this report is Eccosorb CR117, which has one of the highest absorption coefficients, but any of the CR series resins could be used depending on the application.
- [3]. J.M. Stacey, "Microwave Blackbodies for Spaceborne Receivers," JPL report 85-10, March 1, 1985, 40 pages.
- [4]. P. Goldsmith, R. A. Kot and R.S. Iwasaki, "Microwave radiometer black body calibration standard for use at millimeter wavelengths," Review of Scientific Instruments, vol. 50, no. 9, pp 1120-1122, Sept. 1979.
- [5]. D.A. Hills, "Reflection response of the MLS Radiometer Calibration Load," IOM DLH-8606-02, June 6, 1986.
- [6]. R.H. Giles and T.M. Hogan, "Silicone-Based Wedged-Surface Radiation Absorbing Material," US Patent No. 5,260,513, Nov. 1993.
- [7]. S.Janz, D.A. Boyd and R.F. Ellis, "Reflectance Characteristics in the Submillimeter and Millimeter Wavelength Region of a Vacuum Compatible Absorber," Int. Journal of Infrared and Millimeter Waves, vol. 8, no. 6, pp. 627-635., 1987.

[8]. Emerson and Cuming, as well as other companies, produce a variety of polyurethane foam based broadband carbon loaded absorbers. The most common example of which is the Eccosorb AN series.

[9] Silicone based absorbers loaded with absorbing ferrite generally come in flat sheets (Eccosorb FDS or GDS) or can be molded into wedges like the material referred to in [6].

[10]. A polypropylene based molded pyramidal absorber for millimeter and submillimeter wavelength operation "Tessalating Terahertz RAM" is available from Thomas Keating Ltd., Station Mills, Billinghamurst, West Sussex, RH14 9SH, England. This material has so far proven to be unsuitable for space application due to outgassing (probably fixable) and has a low thermal conductivity (not fixable), making it less desirable for high quality black body calibration loads which must have front-to-back surface thermal gradients which are extremely small.

[11]. Emerson and Cuming MF series for example.

[12]. AB Millimetre MVNA with ESA1 and ESA2 extensions.

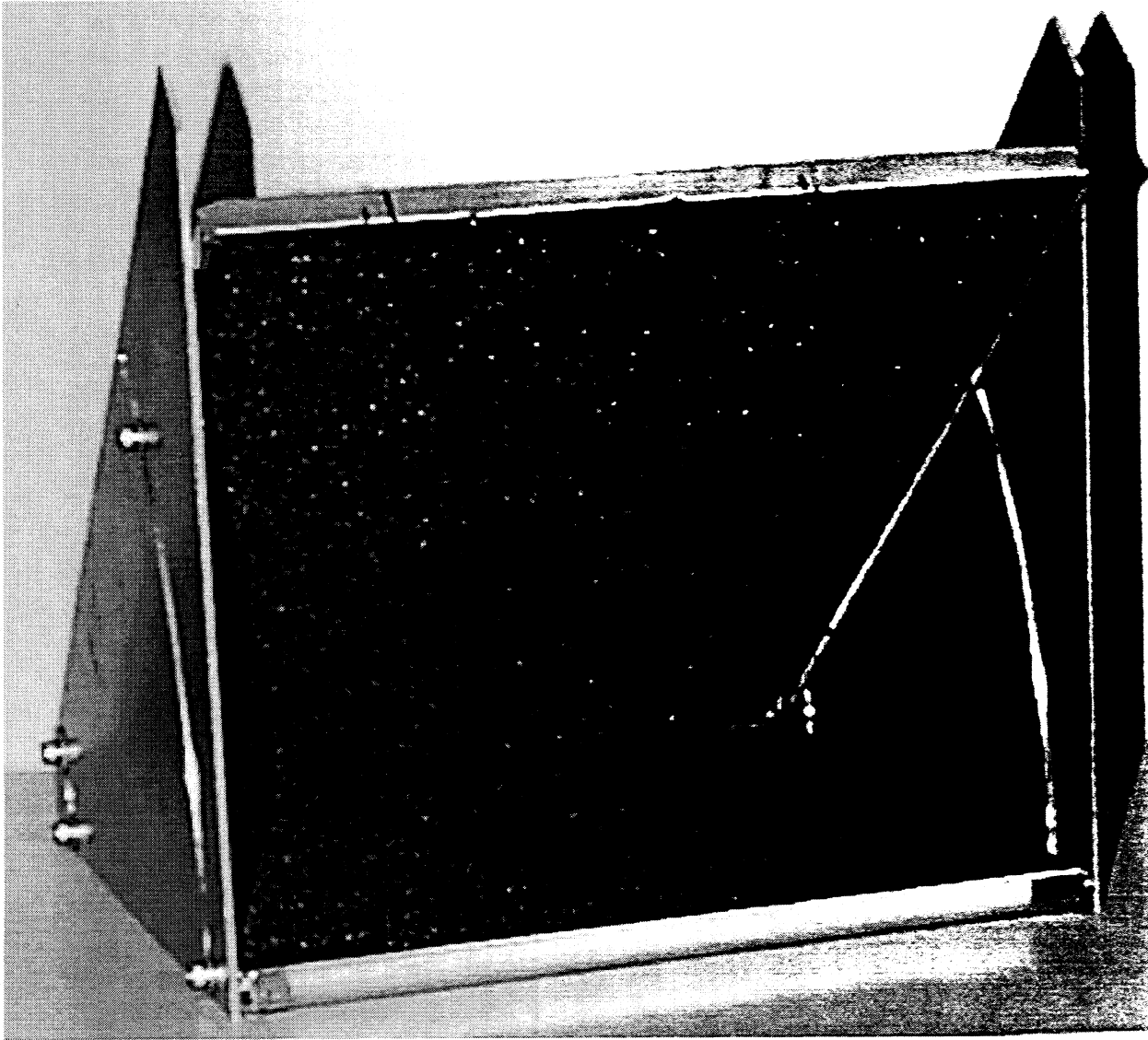


Figure 1. CR117 coated Silicon Carbide load formed from two sheets of material (9x12 and 9x9 inches by 0.5 inches thick) joined together to form a wedge. The wedge allows multiple bounces of the incident RF energy, enhancing absorption. No material is present on the sides of the wedge. Incident RF energy is contained within a beam which fits within the projected aperture of the angled absorbing sheet. The wedge can handle a large beamwidth but the absorber thickness (0.5 inches) limits the lower frequency of operation to about 100 GHz. Slots on the sides allow the wedge angle to be altered between about 20 and 45 degrees to achieve the best performance for a given beam diameter.

Measurement Set-Up

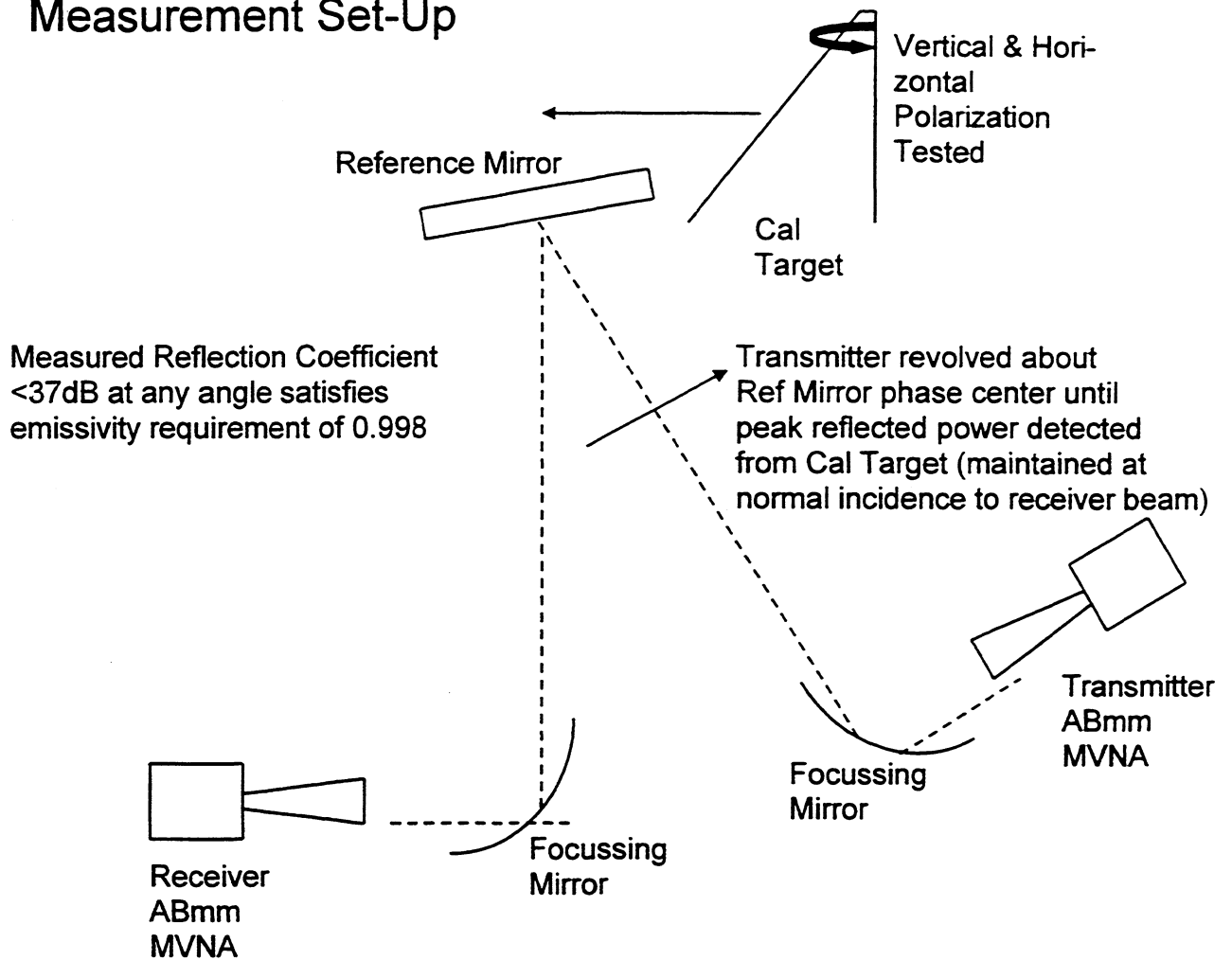


Figure 2. Measurement set up used to determine the reflection coefficient (and derived emissivity) of the load material at any incident angle. During measurements the wedge and flat sheet absorbers were fixed while the transmitter was rotated through angles from 20 to 60 degrees. The maximum received power was recorded with reference to a reflecting mirror. The absorber based on a periodic grid of small pointed pyramids showed specific angles with peak power reflection (due to grating lobes) whereas the foam absorbers showed sinusoidally varying power versus angle related to the standing wave structure set up by the varying penetration depth of the RF energy into the load.

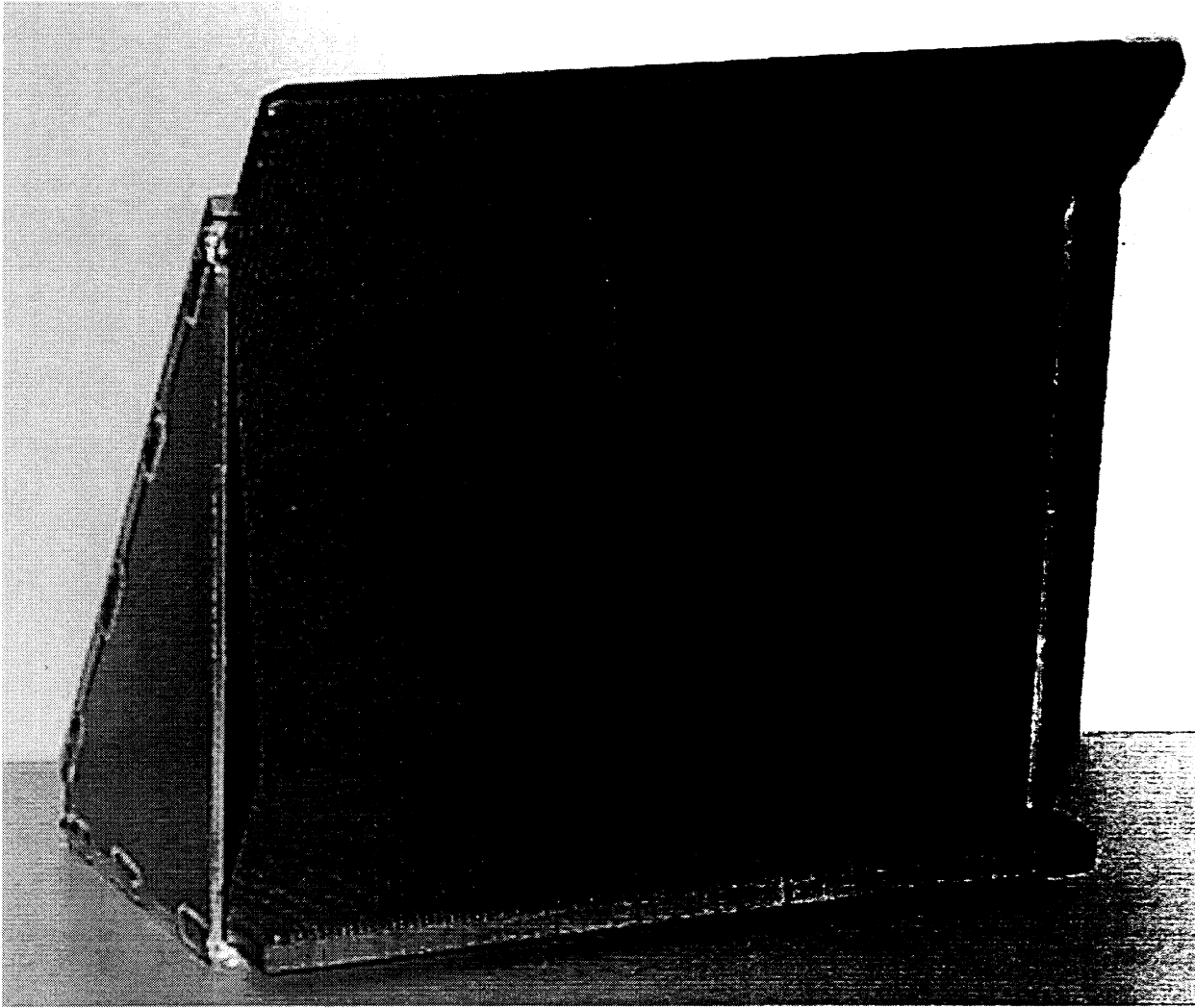


Figure 3. CR117 cast periodic pyramidal absorber formed in the same wedge geometry as the silicon carbide foam load. The pyramids are barely visible, but are roughly .15 inches high and .1 inch apart with a 25 degree taper angle. The wedge angle is approximately 42 degrees. The incident beam is parallel to the table and hits the angled plate of the wedge near the center before bouncing off the lower plate and into the apex of the wedge. Both the wedge and single flat sheet were measured. The material at the base of the pyramids (which give the load considerable weight, but bind the cones together and is equivalent to the pooled CR117 at the bottom of the silicon carbide foam load) is about .2 inches thick.

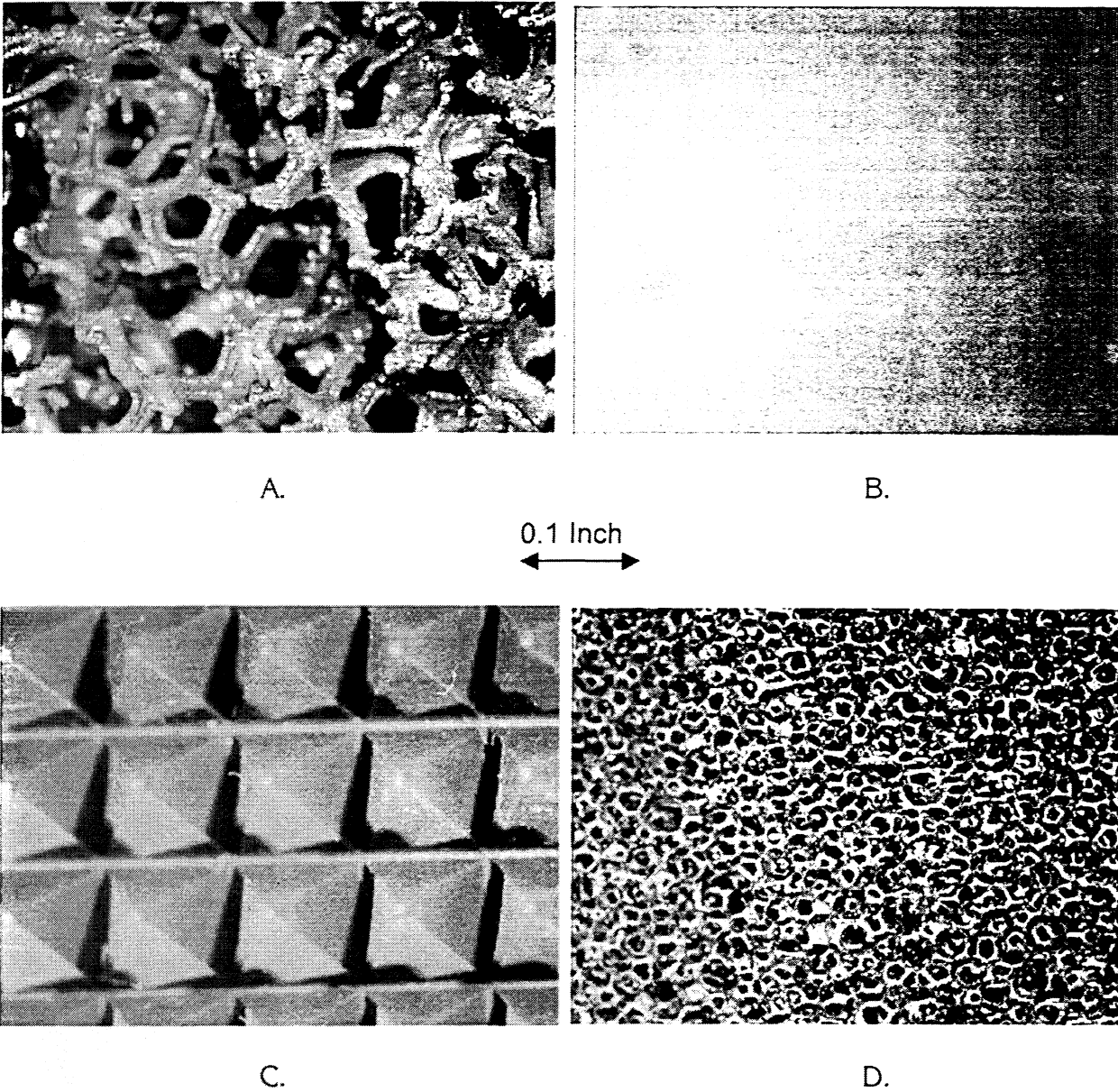


Figure 4. Photographs showing each of the loads tested, at the same scale.
(A). New CR117 coated Silicon Carbide foam.
(B). CR117 cast in a flat sheet.
(C). CR117 cast into pyramids and arranged in a periodic pattern suitable for 200 GHz. (D). Typical carbon loaded polyurethane foam absorbing sheet – AN74.

Load Measurements: Worst Case Return Loss

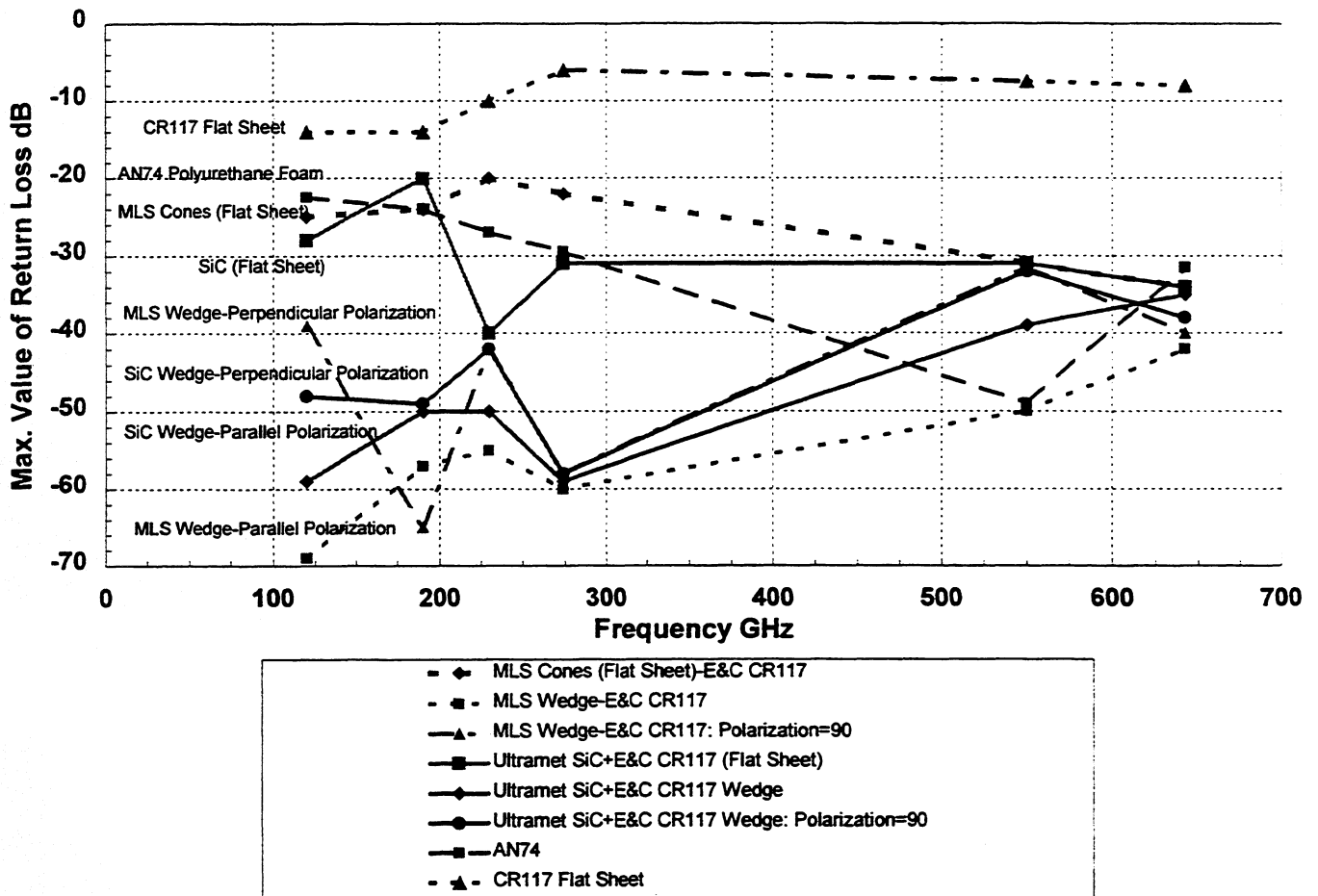


Figure 5. RF measurements showing the peak reflected power as a function of transmitter angle off the wedge and flat sheet absorbers at different RF frequencies and two polarizations (E field vertical and horizontal). Note that the AN74 performs better than either the pyramidal cones or SiC flat sheet load at higher frequencies but similarly near the resonant wavelength of 200 GHz. Flat sheet CR117 is very poor by comparison. The dynamic range of the test set limits the load performance at 600 GHz.

PRACTICAL MICROMACHINING TECHNIQUES FOR HIGH ASPECT RATIO SUBMILLIMETER WAVE COMPONENTS

Victor M. Lubecke ¹, Chris M. Mann ², and Koji Mizuno ^{1,3}

¹ Photodynamics Research Center, The Institute of Physical and Chemical Research (RIKEN)
19-1399 Koeji, Nagamachi, Aoba-ku, Sendai 980, Japan
victor@postman.riken.go.jp

² Rutherford Appleton Laboratory
Chilton, Didcot, Oxfordshire, OX11 0QX, The United Kingdom

³ Research Institute of Electrical Communication, Tohoku University,
2-1-1 Katahira, Aoba-ku, Sendai 980-77, Japan

Abstract- High-performance submillimeter wave circuits often require the use of extremely small three-dimensional waveguide and antenna components. While such components can be difficult and very costly to produce through conventional machining, cost-effective micromachining techniques offer an attractive alternative. The fabrication of 2.5 THz waveguide backshorts and 640 GHz dichroic plates through the use of thick UV-sensitive resin, are described. The technique is suitable for fabricating a wide range of submillimeter wave components, with aspect ratios in excess of 10:1.

INTRODUCTION

Waveguide technology has been used to produce a variety of high-performance millimeter and submillimeter wave circuits, such as sensitive mixers and efficient multipliers. Various scientific applications including radio astronomy and atmospheric remote sensing, have driven the demand for extending the application of this technology to increasingly higher frequencies. As the wavelength for these circuits reduces however, so do the critical dimensions for waveguide components. While such circuits can sometimes be realized through precision conventional machining and painstaking assembly, their usefulness is thus limited to specialty applications where high cost and limited production can be justified. Micromachining provides an attractive alternative, where highly developed photolithographic integrated circuit fabrication techniques are used for the cost-effective batch-production of components with three-dimensional characteristics.

The anisotropic etching, or *bulk micromachining*, of silicon has been used to form limited three-dimensional submillimeter wave antenna and waveguide structures [1-2], and forms of sacrificial layer, or *surface micromachining*, techniques used for semi-planar hollow millimeter-wave waveguide structures [3] and micromechanically adjustable submillimeter wave integrated circuit tuning elements [4]. Recently, the use of thick UV-sensitive curable resin has been proposed for the formation of waveguide channels of significant height and varied shape is a submillimeter wave mixer block [5]. Here the application of such a resin, the main ingredient of which is EPON SU-8 [6], is extended to the fabrication of ten-micron scale three-dimensional

waveguide backshorts for a 2.5 THz mixer developed for atmospheric remote sensing [7], and relatively large diameter frequency selective mirrors, or *dichroic plates*, featuring a uniform pattern of hundred-micron scale holes, designed to quasi-optically isolate 640 GHz signals from 230 GHz signals in a multi-receiver radiometer system. Both have been proposed for the NASA EOS Microwave Limb Sounder [8].

2.5 THZ BACKSHORTS

A waveguide backshort consists of a conducting shaft, which when inserted in a waveguide will establish an effective RF short circuit near its tip. A non-contacting backshort achieves this function through a patterned shape which alternately fills and empties the guide for quarter wavelength sections, to produce high/low impedance transitions. Signals incident at a transition are largely reflected, with the transmitted portion being coherently reflected at subsequent transitions. While this design does not depend on establishing or maintaining DC contact, it does depend on critical dimensions which become exceedingly small and difficult to realize for increasing frequency of operation. At 2.5 THz, the wavelength is 120 μm , and a half-height TE_{10} waveguide is 25 μm tall and 100 μm wide. A backshort for such a guide must nearly fill the guide for one section, and then significantly reduce in height for the next, with a repeating pattern.

The batch-process for fabricating the backshorts is shown on Fig. 1. A 120- μm coating of resin is spun onto a silicon substrate, and exposed to UV light through a shadow mask in close proximity to its surface. The unexposed resin is then dissolved in solvent, and the remaining structures and substrate are RF sputter-coated with 2000 \AA of gold. The substrate and resin structures are then wax-bonded to a silicon superstrate, and the substrate and unwanted resin are removed with a dicing saw. Once

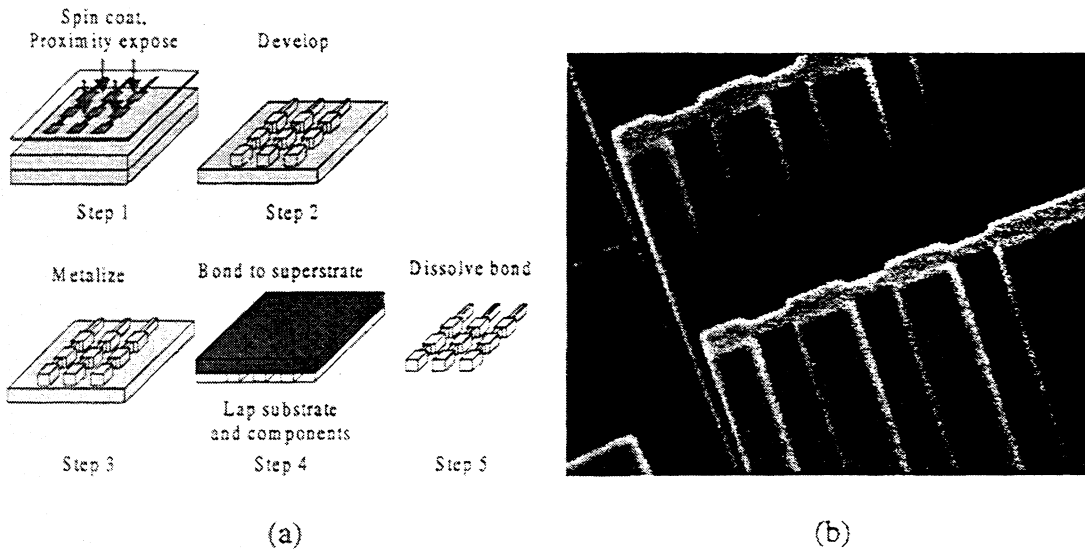


Fig.1. Fabrication overview for the 2.5 THz waveguide backshorts (a), and SEM photograph of the process after developing. Cost-effective photolithographic techniques are used to batch process the three-dimensional high aspect ratio submillimeter components.

the desired *width* has been achieved, the backshorts are washed off in acetone and recovered in filter paper.

Examples of the resulting backshorts are shown in Fig. 2. The side-features of the backshorts accurately reproduce the mask pattern, with dimensions on the order of 10 μm , and the width is trimmed to about 90 μm . Manual assembly is required for integration with the mixer block, and RF tests are in progress.

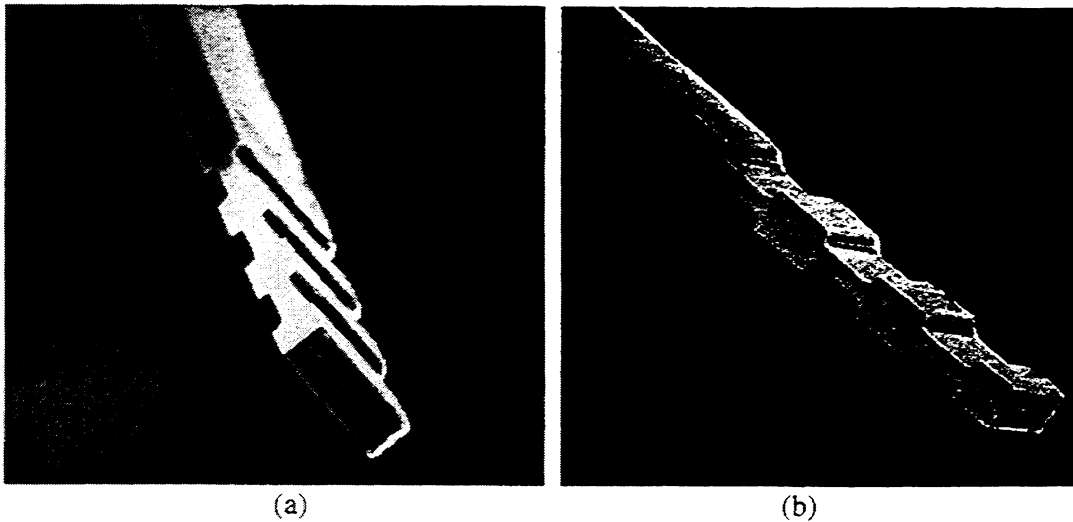


Fig. 2. SEM photographs of end (a) and side (b) views of the completed 2.5 THz waveguide backshorts. The surface of the backshort tip is approximately 25 μm by 90 μm .

640 GHz DICHROIC PLATES

A submillimeter wave dichroic plate typically consists of a semi-thick conducting mirror, perforated with a closely packed array of waveguide apertures. The aperture dimensions determine the modes and frequencies that will be supported in the plate, and thus transmitted. The thickness of the plate determines the attenuation and rejection of signals below the cut-off frequency of the waveguide apertures. As the frequency of operation increases, the apertures become smaller, yet maintaining adequate thickness is critical for proper signal rejection. It may also be necessary to provide a relatively wide diameter to allow the plate to accommodate a broad beam over a range of incidence angles. The dichroic plates described here feature thousands of apertures with dimensions of 360 μm by 180 μm , and were designed to pass signals at 640 GHz (95% at up to 40° incidence), and reject signals at 230 GHz (~30 dB attenuation). The plate is 250 μm thick, and the perforated surface is 3.5 cm by 3.5 cm.

The procedure for fabricating the dichroic plates is shown in Fig. 3. While the same process used for the backshort fabrication could be applied, this modified process better accommodates the resolution requirements by minimizing process dependence on a highly collimated UV source. A 250- μm thick coating of resin is spun onto a transparent quartz substrate/mask, on the same side as the chrome mask pattern. The

resin is exposed to UV light through the transparent parts of the mask, and the unexposed resin subsequently dissolved. The structure is then heat-cured, and the substrate is removed through etching or other convenient means. The resulting structure can be metallized through RF sputter-coating and additionally through electroplating if necessary.

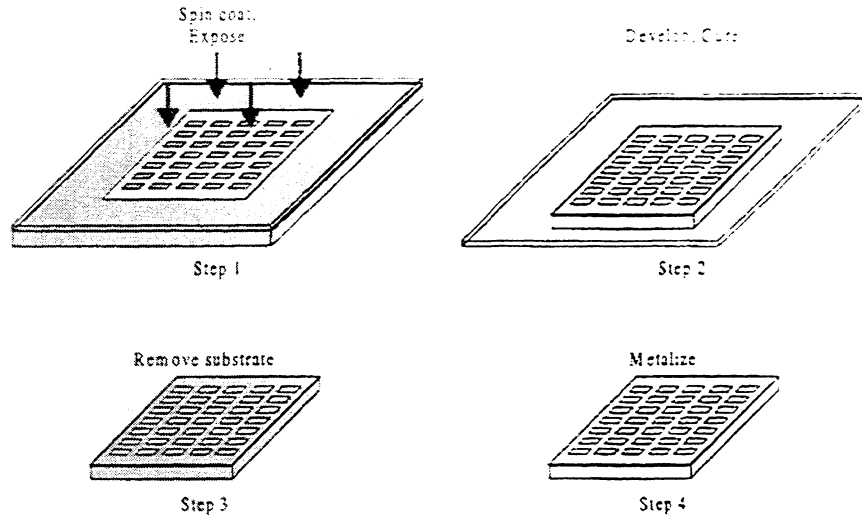


Fig. 3. Fabrication overview for the 640 GHz dichroic plates. The structure is formed directly on the mask to optimize resolution through the full thickness.

A dichroic plate fabricated by this technique is shown in Fig. 4 (a), and an SEM photograph of the aperture detail appears in Fig. 4 (b). To facilitate its application in a quasi-optical submillimeter wave system, the delicate plate can be clamped in an appropriate support structure. It is also possible to selectively remove only the center portion of the substrate, leaving the remainder to support metallized resin structure.

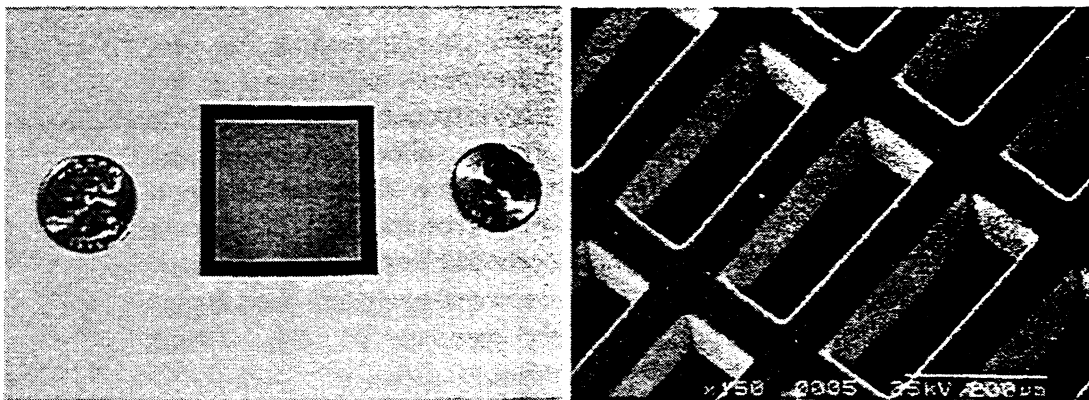


Fig. 4. Photograph of the metallized dichroic plate (a), and SEM of the hole-pattern detail. The plate, shown in comparison with American (quarter) and Japanese (100 yen) coins, is about 4 cm by 4 cm, 250 μm thick, with 360- μm by 180- μm holes.

CONCLUSIONS

The fabrication of submillimeter wave three-dimensional waveguide components through cost-effective micromachining techniques has been demonstrated. Waveguide backshorts for 2.5 THz, with all three dimensions on the order of tens of microns, were formed from a curable UV-sensitive resin. A similar technique was also employed to form a 250- μm thick 640 GHz dichroic plate, several centimeters in diameter and uniformly perforated by patterned holes on the order of a few hundred of microns. This fabrication approach is suitable for producing a wide range of millimeter and submillimeter wave discrete and integrated components, directly from the resin or in combination with electroforming techniques.

ACKNOWLEDGMENTS

The authors would like to thank Peter Siegel of the NASA Jet Propulsion Laboratory for providing the pattern design for the dichroic plate. This work was supported by the Frontier Research Program of the Institute of Physical and Chemical Research (RIKEN), Japan.

REFERENCES

- [1] W.Y. Ali-Ahmad and G.M. Rebeiz, Gordon Chin and Hermant Davee, "802 GHz integrated horn antennas imaging array," *International Journal Infrared Millimeter Waves*, vol. 12, pp. 481-486, May 1991.
- [2] W.R. McGrath, C.K. Walker, M. Yap, and Y.-C. Tai, "Silicon Micromachined Waveguides for Millimeter-wave and Submillimeter-wave Frequencies," *IEEE Microwave and Guided Wave Letters*, vol. 3, pp. 61-63, 1993.
- [3] J. W. Digby, C.E. Collins, B.M. Towlson, et al., "Integrated Micro-Machined Antenna for 200 GHz Operation," *IEEE MTT-S International Microwave Symposium*, pp. 561-564 June 1997.
- [4] V.M. Lubecke, W.R. McGrath, P.A. Stimson, and D.B. Rutledge, "Micromechanical Tuning Elements in a 620 GHz Integrated Circuit," submitted to the *IEEE Transactions on Microwave Theory and Techniques*, December 1997.
- [5] T.W. Crowe, P. J. Koh, W.L. Bishop, C. M. Mann, et al., "Inexpensive Receiver Components for Millimeter Wavelengths," *Eighth International Symposium on Space Terahertz Technology*, pp. 377-384 March 1997.
- [6] K.Y. Lee, N. LaBianca, S.A. Rishton, et al., "Micromachining Applications of a High Resolution Ultrathick Photoresist," *J. Vac. Sci. Technol. B* 13(6), pp. 3012-3016, Nov/Dec 1995.
- [7] C. M. Mann, D. Matheson, B. Ellison, M. Oldfield, B. Moyna, J. Spencer, D. Wilsher, B. Maddison, "On the Design and Measurement of a 2.5 THz Waveguide Mixer", *Ninth International Symposium on Space Terahertz Technology*, March 1998.
- [8] J.W. Waters, "Submillimeter-Wavelength Heterodyne Spectroscopy and Remote Sensing of the Upper Atmosphere," *Proceedings of the IEEE*, vol. 80, no. 11, pp. 1679-1701, November 1992.

A SUPRATHz SIS HETERODYNE RECEIVER USING WAVEGUIDE / MEMBRANE TECHNOLOGY.

M. Salez¹, Y. Delorme, I. Peron, J.-M. Munier
DEMIRM-Observatoire de Paris, 61 avenue de l'Observatoire, 75014 Paris, France

D.Rovera
DANOF-Observatoire de Paris, 61 avenue de l'Observatoire, 75014 Paris, France

J.-C. Villégier², V. Larrey
CEA-Grenoble, DRFMC/SPSMS, 17 rue des Martyrs, F-38054 Grenoble, France

ABSTRACT

Among the top priority scientific goals of ESA's FIRST mission is the heterodyne detection of interstellar water via its information-rich submm transitions above 1 THz. While 'classical' SIS receivers using the now well-mastered niobium technology will fail to match this goal, cautiously designed SIS receivers with good-quality NbN junctions offer a potential solution.

As part of a european research and technology effort led by ESA, an heterodyne receiver based on waveguide/membrane technology has been developped for use in the range 1.2 -1.6 THz, using $\sim 1\text{-}\mu\text{m}^2$ NbN/AlN/NbN and NbN/MgO/NbN high current density SIS tunnel junctions. The process to fabricate these junctions on thin ($\sim 1\text{-}\mu\text{m}$) SIMOX membranes is described, and DC characteristics of the junctions are presented.

Al/SiO₂/Al microstrip circuits are used to tune the junctions and to match a waveguide-to-suspended-microstrip transition over a broad bandwidth, in association with a dumbell non-contacting backshort. The 1.5-mm square membrane is wet-etched in the silicon chip which supports both the IF and DC circuits and is reliably suspended 5-7 μm away from the injection and backshort sections of waveguide. A novel design for the mixer block allows to reach (with relatively low cost) an accuracy better than 1 μm on the waveguide dimensions and the ground to strip spacings. To carry out accurate receiver noise measurements above 1 THz, an automated calibration apparatus was constructed and a CO₂-pumped FIR laser is used as an LO.

In this paper, DC characteristics of the NbN junctions and preliminary results from RF measurements are presented and discussed.

¹*salez@mesiob.obspm.fr*

²*villégier@chartreuse.cea.fr*

DESIGN OF MIXER ELEMENTS FOR THE HHT 345 GHz HETERODYNE ARRAY RECEIVER

G. Narayanan^{1,2}, C. K. Walker, H. Knoepfle, and J. Capara
Steward Observatory, University of Arizona, Tucson, AZ 85721

ABSTRACT

We present the design of mixer elements for a 7-element SIS heterodyne array receiver for operation in the 870 μm atmospheric window. The focal plane array receiver will be a facility instrument on the 10-meter University of Arizona/Max Planck Institute for Radioastronomy (MPIfR) Heinrich Hertz Telescope (HHT). The array will have a tuning range from 315 to 380 GHz. Due to prevailing physical conditions in the interstellar medium, this wavelength range is one of the richest in the submillimeter portion of the spectrum. We use results of scaled model measurements and detailed electromagnetic modeling of the mixer block to arrive at an optimum design for the individual mixers. We describe an iterative technique of optimizing mixer design in linear microwave circuit simulators, using results of finite element analysis of the waveguide embedding impedance.

1 Introduction

The 870 μm atmospheric window (see Figure 1) has the highest transmission of any submillimeter band, and due to prevailing physical conditions in the interstellar medium is also one of the richest spectroscopically. Figure 1 shows some of the important molecular transitions in this atmospheric window. The noise performance of submillimeter receivers is improving dramatically every year and is approaching limits set by quantum mechanics and/or the sky background, especially in the lower end of the submillimeter frequency band. A large increase in the speed of spectroscopic astronomical observations can be obtained by using a heterodyne array receiver. There are two approaches to obtaining a real improvement in the speed of imaging using arrays. It is possible to develop an array with a large number of elements each of which has less than optimum performance in terms of noise temperature and optical coupling. A better approach in terms of cost and speed is to build a moderate sized array without compromising mixer performance.

The seven element 345 GHz focal plane array receiver we are building for the Heinrich Hertz Telescope (HHT) will have a tuning range between 315 and 380 GHz and will make excellent use of the telescope and available atmospheric transmission. The HHT is a joint development between Steward Observatory, University of Arizona, and the Max-Planck-Institut of Radioastronomie. The overall design of the optics and cryogenic systems of the array will be outlined in a future paper [1]. In this paper we describe the design of individual mixer elements that will make up the final array.

Technical, scientific and budgetary issues dictate the following objectives for the mixer design:

¹Five College Radio Astronomy Observatory, University of Massachusetts, Amherst, MA 01003

²e-mail: gopal@fcrao1.phast.umass.edu

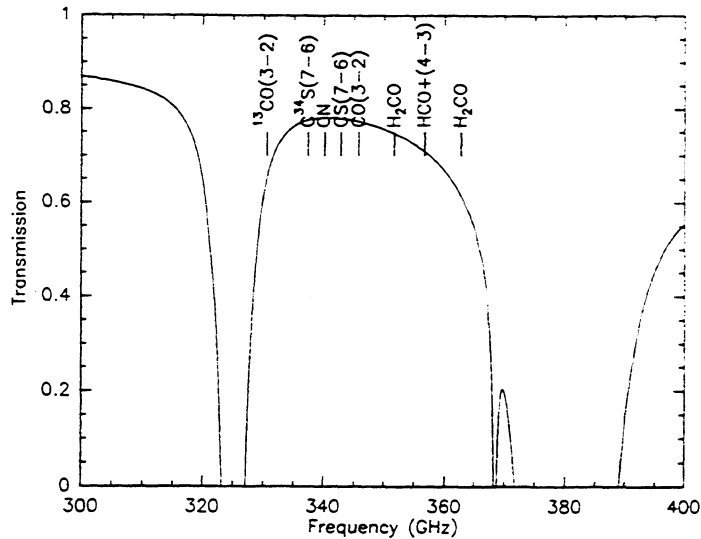


Figure 1: Model Atmospheric transmission in the 870 μm window (Mount Graham 1mm water). The frequencies of important molecular transitions are marked.

- State-of-the-art performance of the individual elements. In particular we require receiver temperatures $T_R \leq 100$ K over the band, a tuning range of 315 to 380 GHz to make full use of the atmospheric band, an IF bandwidth of 4 – 6 GHz, and good antenna efficiencies and clean beams.
- Since the array will be a facility instrument, the mixers should be robust and easy to use. Therefore, no mechanical tuners will be used.
- To keep the costs down, the mixer blocks should be designed for easy fabrication.

2 Mixer Block Design

Figure 2 shows a schematic side view of the designed mixer block. The first section is the horn block and consists of a diagonal feedhorn [2] that transitions from a full-height rectangular waveguide. The full-height rectangular waveguide is then transformed to a half-height waveguide through a three-section transformer. Diagonal feedhorns have been chosen over corrugated feeds, because of their relative ease of construction using split-block techniques. Although their Gaussian coupling efficiency is $\sim 13\%$ smaller than corrugated horns, diagonal horns have been shown to be a good candidate for use in submillimeter focal-plane arrays [3]. We follow the design outlined in [3] by making a direct transition from rectangular to diagonal feed. The half-opening angle of the feedhorn is 10.2° , with a slant length of 8.26 mm. The analytical designs of the full-height to half-height transformer and the rectangular to diagonal horn transition were verified using Ansoft's High Frequency Structure Simulator (HFSS) [4]. The half-height waveguide dimensions are 0.7 by 0.175 mm.

The second section is the junction block, which also houses the IF matching network. The fused quartz substrate carrying the SIS junction sits in a suspended microstrip line configuration, which

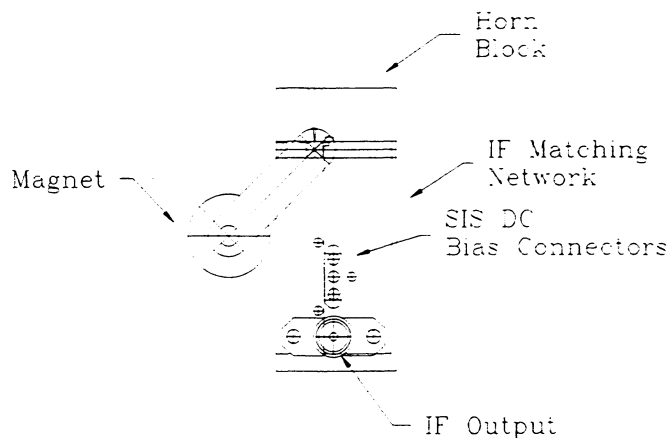


Figure 2: Schematic side-view of the mixer block.

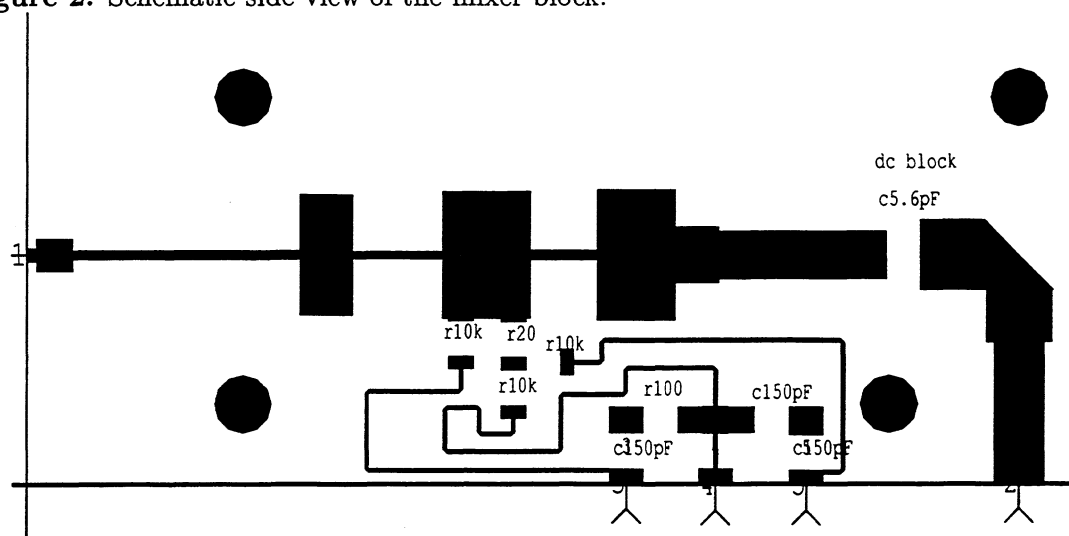


Figure 3: Layout of the 4 to 6 GHz IF matching network.

is parallel to the E-field of the waveguide. Using the suspended strip configuration considerably eases tolerances in mounting the junction on the mixer block. The junction substrate is designed to be $0.309 \times 0.078 \times 3.48$ mm. The dimensions of the suspended microstrip line channel are derived from the successful CfA designs [5, 6]. The channel has a 0.222×0.038 mm airgap behind the junction substrate and a similar airgap above the substrate in the horn block (also see Figure 7). When the junction is placed in the channel, it is oriented such that the junction lies within the waveguide. The IF output and DC bias inputs are made through the matching network circuit. The matching network is orthogonal to the junction substrate. The magnetic field for suppressing Cooper pair tunneling is brought into the mixer via magnetic field concentrators embedded in the junction block [7]. The ground side of the junction will be held in place with silver paint, and the “hot” side of the junction will be connected to the IF matching network by wire-bonding.

The designed normal state resistance of the junction is expected to produce an IF output

impedance of $> 100 \Omega$. The IF output impedance of the mixer is transformed to 50Ω through a 4-6 GHz IF matching network. A prototype IF matching network has been designed, built and tested. Figure 3 shows the layout of the matching network that was designed using HP's Microwave Design System circuit simulator program [8]. The value of the DC bias resistors and chip capacitors used for RF chokes are shown in the layout. A 5.6 pF capacitor is used as DC block. The substrate used in the microstrip design is Rogers Duroid 6002 with a thickness of 30 mils and $\epsilon_R = 2.94$ [9]. The overall dimensions of the matching network is 1.25×0.5 inches. The IF output of the SIS junction is wire-bonded to the $\sim 160 \Omega$ line to the left of the layout. The DC bias traces shown in the bottom portion of the layout are part of a 4-wire SIS bias circuit. IF output at 50Ω is brought out in the lower right of the layout in Figure 3 through an SMA connector (see Figure 2). The fabricated matching networks were tested against predictions using a special purpose fixture constructed for this purpose. For an input impedance range of 100 to 180Ω , the match to a 50Ω output is found to be better than -10 dB throughout the 4-6 GHz band. The IF output of each mixer then passes through an isolator before entering the first amplifier. Low-noise 4-6 GHz amplifiers have been ordered from Miteq [10]. The amplifier specifications are a noise temperature requirement of ~ 5 K, a gain of ~ 30 dB, and a power dissipation of ~ 50 mW.

The fabrication of waveguide structures at submillimeter wavelengths tends to be difficult and expensive. For higher frequencies, wet etching or laser micro-machining [11] methods may be required. At lower frequencies, conventional machining has been successful. The so-called "split-block" technique has often been used [12]. In an effort to keep the cost of machining down, the array mixer blocks will be fabricated using this approach. The mixer blocks will be machined at the University of Massachusetts (UMass), in return for which UMass astronomers will receive a proportional amount of observing time on the HHT. A new numerically-controlled precision milling machine has been constructed at UMass using Aerotech positioners [13] that will allow the fabrication of waveguide components to a few microns of accuracy at low cost.

3 Scale Model Tests

SIS quasiparticle tunnel junction mixers have a rather large geometric capacitance that has been traditionally tuned out using high quality non-contacting backshort and E-plane tuners [7]. The reliance on waveguide tuners alone has two major disadvantages. The large capacitance and small normal state resistance of the SIS junction typically places a severe demand on the waveguide tuners and results in a relatively small frequency band over which an adequate match can be achieved. In addition, the process of tuning with waveguide tuners becomes very complicated and time consuming from the point of view of an astronomer using the full array. To improve the junction match to the embedding impedance of the waveguide circuit and to increase the instantaneous bandwidth of the mixer, a variety of inductive tuning circuits fabricated along with the junction have been used [14]. For such designs, a knowledge of the waveguide embedding impedance is essential. Scaled model tests are a traditional technique to obtain the embedding impedance of a probe in a waveguide. In this section, we describe the results of scaled model tests of the half-height 345 GHz mixer block presented in Section 2. In the next section, we discuss finite element analysis (FEA) methods to obtain embedding impedances.

We constructed a half-height scale model (see Figure 4) with a center frequency of 5 GHz (scale factor of ~ 68) and measured three different RF choke structures to determine a favorable

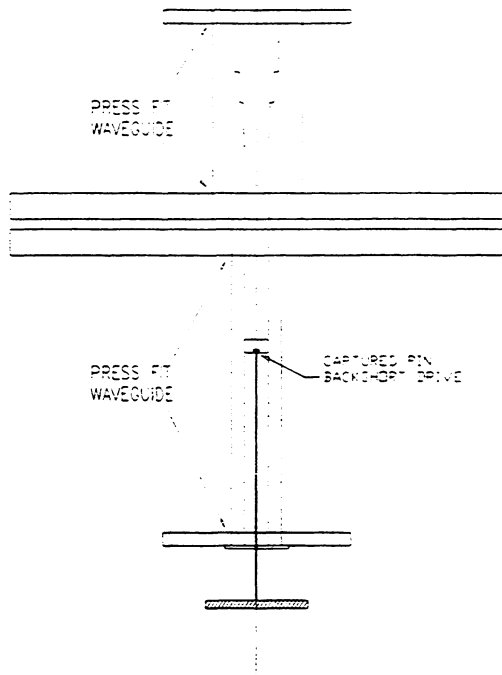


Figure 4: Schematic of the Scaled Model Test Jig. The backshort drive was constructed with a captured pin and a precision screw to ensure smooth and repeatable motion inside the waveguide.

embedding impedance. Acetyl was used as the substrate to approximate fused quartz. The real and imaginary parts of the embedding impedance for one of the choke structures is shown in Figure 5(a) for a backshort distance of 0.2 mm. Shown in Figure 5(b) is the input match of this waveguide-probe combination to a tuned junction with an effective impedance of $40 + j20 \Omega$. This impedance value is being considered for one of the baseline designs of the 345 GHz array junction to be fabricated by JPL [15]. As can be seen from Figure 5, this combination of embedding impedance and junction design is able to provide a broadband match for the desired band of the array.

4 Finite Element Analysis

Typically, accurate scale model measurements are difficult, time-consuming and prone to uncertainties for the following reasons: (1) the wide range of sizes ($> 1000:1$) in an SIS mount are difficult or impossible to achieve in a model (2) The iterative process of modifying the scale model to study the effect of changes involves re-machining and/or re-layout of probe circuits and (3) the problem of providing small coaxial probes to the location of the SIS junction involves uncertainties in the scale model measurements due to calibration errors and the fact that the probe itself is disturbing the field at the measurement point.

We have performed numerical electromagnetic simulations of the waveguide mount. The advantages of numerical analysis are that one may study the effects of the dielectric, optimize the SIS

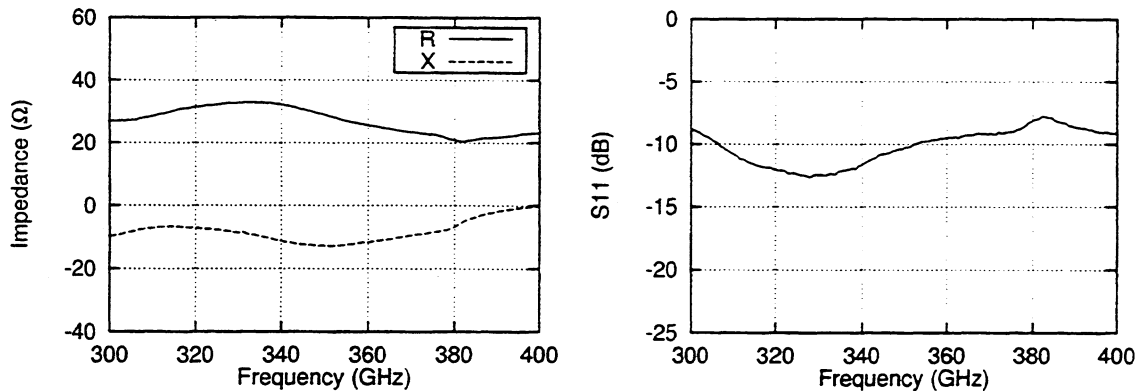


Figure 5: (a) Scale model test results. Real and imaginary parts of embedding impedance of half-height waveguide in combination with RF choke and probe in a suspended microstrip configuration for a backshort distance of 0.2 mm at 345 GHz. (b) Input match scaled back to the frequency of operation for an impedance of $40 + j20 \Omega$ looking into the tuned junction.

tuning circuit using the embedding impedance, and modify the structure easily. Other advantages include the ability to study the small size scales of the junction mount with the antenna probe, and the ability to reduce the complexity of the problem by exploiting symmetry considerations. The finite element analysis was done using Ansoft’s HFSS [4]. The accuracy of HFSS in predicting embedding impedances has already been demonstrated in the design of multipliers [16].

We tried several different approaches in the numerical analysis. Initially, voltage sources were used at the location of the gap between the two antenna probes in the center of the waveguide. The field-calculator in the post-processor of HFSS was then used to determine impedance by calculating the Poynting power flow through the gap and using the Z_{PV} definition to determine the impedance. This technique gave reasonable results in measuring the embedding impedance, but was slow and laborious. It also suffers from the fact that these impedances are time-dependent, and hence care must be taken to set the phase of the excitation right. The next method was to “subtract” the RF choke and antenna structure from the waveguide structure. Subtraction in HFSS is an “exclusive-or” operation, and results in a new structure that contains one of the two objects but not both. This has the effect of bringing the buried gap in the center of the waveguide to the outside world, thereby allowing us to define a port and excite the gap with a TEM-type transmission line. In Figure 6, we show the comparison of the scale model from the previous section to an HFSS model configured using this technique. The backshort distance in the HFSS model was set to 0.2 mm, and is the same as the scale model. It can be seen that although their location is in the same general vicinity in the Smith Chart, the agreement between the scale models and finite element analysis is not very good. We modeled the antenna structure as a perfect conductor, and this could account for some of the discrepancy. However, since the HFSS model is performed at the frequency of operation, much of the discrepancy is attributed to uncertainties in the scaling and calibration of the scaled model measurements.

A third approach to the numerical analysis is to reproduce as faithfully as possible, the actual

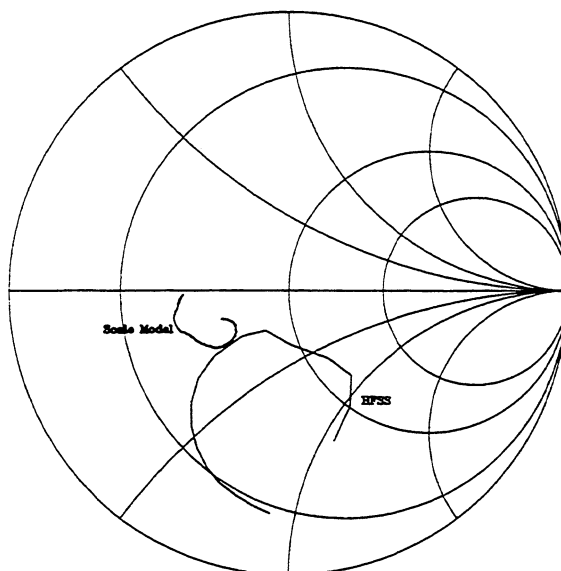


Figure 6: Comparison of the embedding impedance of the scale model with HFSS analysis. The equivalent back-short distance of the scale-model at the frequency of operation is 0.2 mm, and is the same for the HFSS model. The HFSS results are shown after renormalizing to 50Ω . The two plots are for an equivalent frequency range of 300 to 400 GHz.

layout of the junction with relation to the antenna probe. Figure 7 shows the view of the HFSS model used. The model is a 4-port network with port 1 being the SIS junction, port 2 the IF port and ports 3 and 4 the input and the output waveguide ports respectively. The output port is deembedded at a later stage and a backshort attached to it using analysis outside HFSS. The zoomed-in view of the antenna-probe to junction transition shows the junction defined as a square area. The insulator gap of the junction for this problem is a virtual object to help with creating an adequate mesh for the problem. The actual port for the TEM transmission line is capped off at the end with a perfect conductor. The capped feed ensures that the field propagates only into the junction area, which is the area of interest. Once the problem is analyzed in HFSS, the four-port S-parameter is exported (after renormalization to 50Ω and deembedding) to a linear circuit simulator (MDS) and optimized there. Figure 8 shows the MDS equivalent circuit model. The backshort is modeled with a shorted half-height rectangular waveguide transmission line in the circuit simulator. For the purpose of this analysis, the tuned SIS junction was replaced with an equivalent impedance of $40 + j20 \Omega$. The circuit was then optimized for the best backshort distance, resulting in the best case input RF match shown in Figure 9. In practice, the SIS junction and tuning circuit as well as the backshort can be optimized *together* with the embedding impedance S-parameter set derived from HFSS for the best optimization. It can be seen from Figure 9 that the input match is much better than that shown in Figure 5 using the scale-model measurements, and that one backshort setting covers the entire band of interest. Another advantage of this analysis is that the coupling of RF to the IF port and the effectiveness of the RF choke is easily calculated, and any transverse resonance modes in the substrate channel can be studied carefully.

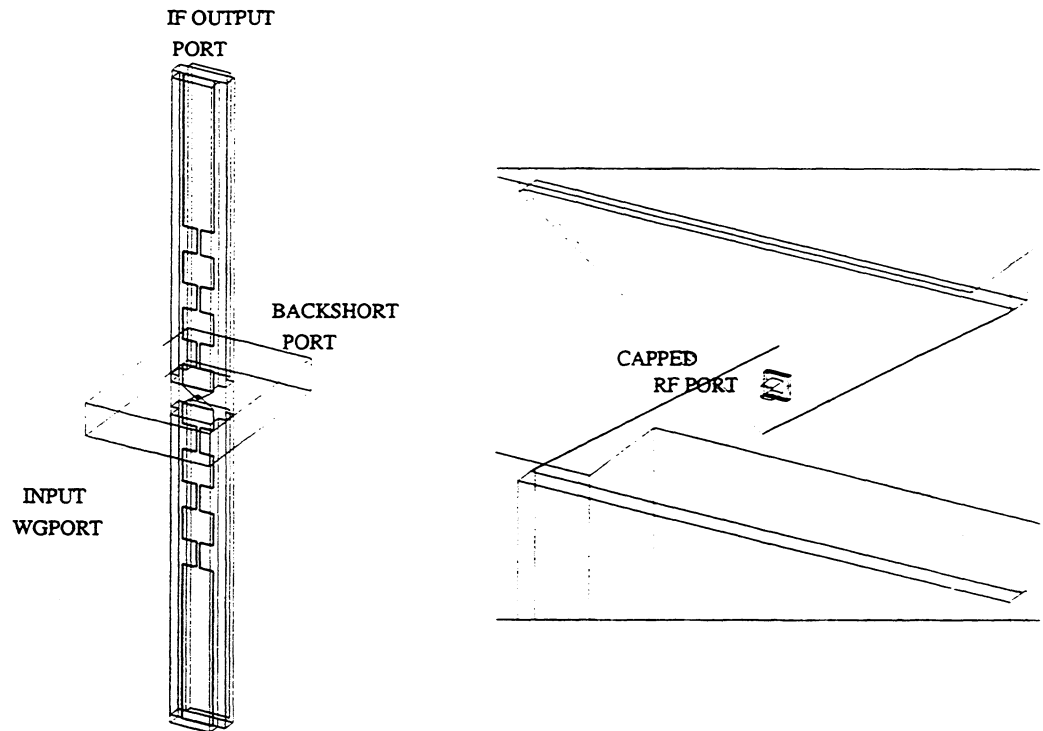


Figure 7: View of the HFSS model and the defined ports of the 4-port model. The zoomed-in view to the right shows the definition of the SIS junction as a square gap, with a TEM port and a capped feed.

5 Conclusion

We have described the mixer block design for a 7-element SIS heterodyne array being built for the HHT. The mixers employ half-height tunerless waveguide mounts with the junctions mounted in a suspended microstrip configuration. Details of the feed horn, IF matching network and fabrication issues were discussed. Scale model measurements were made of the embedding impedance offered by the waveguide mount and compared with numerical simulations using state-of-the-art electromagnetic simulators. A technique to combine FEA with optimizing circuit simulators was used to arrive at a design that provides a broad-band match for the entire frequency range of interest.

We wish to thank Neal Erickson for useful discussions on HFSS, and Jacob Kooi for discussions and help with the design of the SIS junctions.

6 References

- [1] C. K. Walker, G. Narayanan, A. Hungerford, C. Groppi, J. Capara, and H. Knoepfle, 1998, in preparation.
- [2] A. W. Love, "The Diagonal Horn Antenna", *Microwave Journal*, vol V, pp 117-122, Mar.

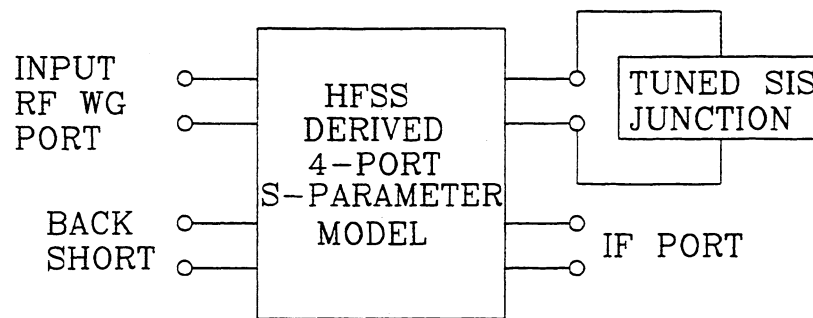


Figure 8: Equivalent MDS circuit model. The backshort is treated as a short-circuited transmission line.

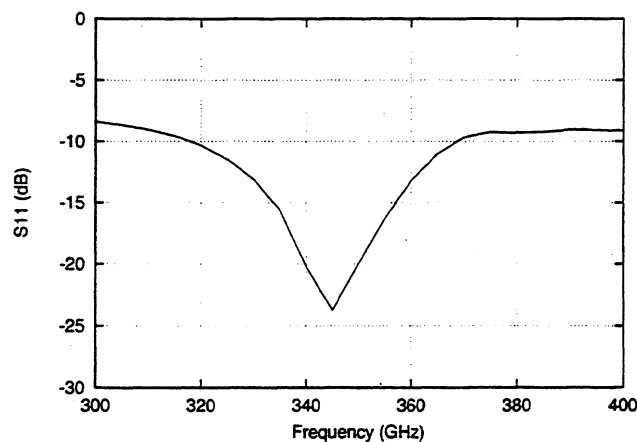


Figure 9: Optimized input RF match into a tuned SIS junction of impedance $40 + j20 \Omega$ using embedding impedance model from HFSS and optimization in MDS. The equivalent backshort distance is 0.25 mm.

1962.

- [3] J. F. Johansson, and N. D. Whyborn, "The Diagonal Horn as a Submillimeter Wave Antenna", IEEE Trans. on Microwave Theory and Techniques, vol 40, No. 5, pp 795-800, May 1992.
- [4] "High Frequency Structure Simulator (HFSS) v 5.0", Ansoft Corporation, Pittsburgh, PA 15219 USA.
- [5] R. Blundell, C. E. Tong, D. C. Papa, R. L. Leombruno, X. Zhang, S. Paine, J. A. Stern, H. G. Leduc, and B. Bumble, "A Wideband Fixed Tuned SIS Receiver for 200 GHz Operation", IEEE Trans. on Microwave Theory and Techniques, vol 43, No. 4, pp 933-937, April 1995.
- [6] C. E. Tong, R. Blundell, S. Paine, D. C. Papa, J. Kawamura, X. Zhang, J. A. Stern, and H. G. Leduc, "Design and Characterization of a 250-350 GHz Fixed-Tuned SIS Receiver", IEEE Trans. on Microwave Theory and Techniques, vol 44, No. 9, pp 1548-1555, Sep. 1996.

- [7] C. K. Walker, J. W. Kooi, M. Chan, H. G. Leduc, P. L. Schaffer, J. E. Carlstrom, and T. G. Phillips, "A Low Noise 492 GHz SIS Waveguide Receiver", *Int. J. IR and MM Waves*, V 13, pp 785-798, June 1992.
- [8] HP85150B Microwave Design System (MDS), Hewlett-Packard, Westlake Village, CA.
- [9] RT/Duroid 6002, Rogers Corporation, Chandler, AZ 85226.
- [10] Miteq JS Series LNAs, Miteq, Hauppauge, NY 11788.
- [11] C. K. Walker, G. Narayanan, H. Knoepfle, J. Capara, J. Glenn, A. Hungerford, T. M. Bloomstein, S. T. Palmacci, M. B. Stern, and J. E. Curtin, "Laser Micromachining of Silicon: A New Technique For Fabricating High Quality Terahertz Waveguide Components", Eighth Intl. Symp. on Space Terahertz Technology, March 1997.
- [12] N. R. Erickson, P. F. Goldsmith, G. Novak, R. M. Grosslein, P. J. Viscuso, R. B. Erickson, and C. R. Predmore, "A 15 Element Focal Plane Array for 100 GHz", *IEEE Trans. on Microwave Theory and Techniques*, vol 40, No. 1, pp 1-11, January 1992.
- [13] ATS1500 Series Linear Positioning Stages, Aerotech, Inc., Pittsburgh, PA 15238.
- [14] T. H. Büttgenbach, H. G. LeDuc, P. D. Maker, T. G. Phillips, "A Fixed Tuned Broadband Matching Structure for SIS Receivers", *IEEE Trans. Applied Supercond.*, vol 2., no. 3., pp 165-175, 1992.
- [15] J. W. Kooi, personal comm.
- [16] J. Tuovinen, and N. R. Erickson, "Analysis of a 170 GHz Frequency Doubler with an Array of Planar Diodes", *IEEE Trans. on Microwave Theory and Techniques*, vol 43, No. 4, pp 962-968, April 1995.

LOW NOISE SINGLE SIDEBAND SIS MIXERS FOR MM AND SUBMILLIMETER RADIO ASTRONOMY

A. Karpov, J. Blondel, M. Voss, D. Billon-Pierron, P. Pasturel, K. H. Gundlach

Institut de Radioastronomie Millimétrique,
300, rue de la Piscine, F-38406 St. Martin d'Hères, France

We present our experience of the last years in development of the practical single sideband SIS receivers for the 80 GHz - 400 GHz band and their operation at the IRAM radio telescopes.

The receivers with a sideband rejection and extremely low noise, approaching the quantum limit, are required for optimisation of the spectral observations at the modern radio telescopes in the mm and sub millimetre bands. The tuning using a single backshort for rejection of the image sideband inside of a mixer allow to obtain a minimum degradation of the SIS receiver noise temperature.

The different types of the wave guide single sideband SIS mixers are developed for the 0.8 mm, 1.3 mm and 3 mm bands. The minimum SSB receiver noise ranges from 30 K at 85 GHz to 48 K in the 0.8 mm band. For the first time the SSB receiver noise as low as $3h\nu/k$ with the is demonstrated at the radio telescope with an SIS mixer.

After an analysis of the requirements for optimisation of the receivers for the radio astronomy applications the mixer design and operation will be presented. We discuss the HEMT/SIS problem in application to the 3 mm band and present the first laboratory results with 25 K SSB mixer in the 3 mm band.

A HIGH-POWER FREQUENCY-STABILIZED TUNABLE TWO-FREQUENCY DIODE LASER SYSTEM FOR GENERATION OF COHERENT TERAHERTZ-WAVE BY PHOTOMIXING

Shuji Matsuura and Geoffrey A. Blake

Division of Geological and Planetary Sciences, California Institute of Technology, Pasadena, CA 91125
E-mail: matsuura@gps.caltech.edu

Pin Chen

Division of Chemistry and Chemical Engineering, California Institute of Technology, Pasadena CA 91125

J. C. Pearson and Herbert M. Pickett

Jet Propulsion Laboratory, California Institute of Technology, Pasadena, CA 91109

Abstract

A tunable two-frequency high-power diode laser system at 850 nm for terahertz (THz)-wave generation by photomixing in low-temperature-grown GaAs photo-conductors has been developed. The difference frequency is obtained through a three laser system, where two lasers are locked to different orders of a Fabry-Perot cavity and a third is offset-locked to the first. The difference-frequency signal is generated by the offset laser and the other cavity-locked laser. The spectral purity of the beat note is better than 1 MHz. The maximum output power of ~500 mW was obtained by using the master oscillator power amplifier (MOPA) technique, simultaneous injection of two seed frequencies with a single semiconductor optical amplifier. Here we report the generation of THz waves and spectroscopy of acetonitrile as proof of concept.

1. Introduction

The difference-frequency generation, or the frequency down-conversion, by photomixing using nonlinear optical materials and photoconductors has been long investigated as a promising technique to develop widely tunable coherent sources in the terahertz (THz) region. Photomixing in low-temperature-grown (LTG) GaAs photoconductors with

planer antennas is the most attractive method in terms of conversion efficiency¹⁻³, and LTG-GaAs photomixer sources have already been applied to laboratory spectroscopy by several authors⁴⁻⁶. However, the frequency stability and calibration of these sources have not been sufficient for high-resolution spectroscopic applications. The frequency control and calibration of pump laser system is the key issues for the next generation of such THz sources.

Diode-laser-based systems are suitable for space-borne fiber-coupled instruments because of their compactness, low power consumption, and long lifetime.^{2,3} Wide frequency tunability of diode lasers is also an important advantage for applications in the THz-wave generation. The advances in frequency stabilization of diode lasers locked to cavity modes allows us to define the frequency of the THz-wave precisely. We have developed a fiber-coupled, tunable, two-frequency diode laser system at 850 nm using such frequency-stabilization scheme.

The THz-wave output power generated by photomixing with a photoconductor has a quadratic dependence on the photocurrent oscillation induced by the pump lasers. Up to now, the THz-wave output power generated with LTG-GaAs photomixers have been limited to 0.1-1 μ W level corresponding to the ac-photocurrent of ~0.1 mA, dc-photocurrent of ~1 mA.^{6,7} The photocurrent is proportional to the pump laser power, but conventional type

photomixers cannot handle the incident power over ~50 mW because of thermal failure.⁷ Large dimension devices allow high-power laser input and provide much higher photocurrent by avoiding the thermal problem. In order to drive these devices, the development of high-power (>>50 mW) tunable diode laser is required. Unfortunately, the output power of our fiber-coupled diode laser system was not sufficient for this purpose.

The master oscillator power amplifier (MOPA) technique solve the dilemma between narrow linewidth and high power. The master laser with narrow linewidth is injected into the power amplifier, and the laser power is amplified while preserving the spectral purity. Although the MOPA has been normally used for single-frequency operation, simultaneous two-frequency injection seeding to a single power amplifier is achievable⁸. The two-frequency MOPA operation has an advantage

in spatial overlap of the two frequency beams, which is essential to achieve an efficient photomixing.

We developed a high-power, narrow-linewidth, tunable two-frequency diode laser system at 850 nm based on the two-frequency MOPA with the fiber-coupled tunable master laser and a single optical amplifier. In this paper, design and performance of this system and its application to the THz-wave generation and spectroscopy are presented.

2. Laser system design and performance

2-1. Frequency-stabilized tunable diode laser

The fiber-coupled tunable two-frequency diode laser system to synthesize a precise difference-frequency consists of three external

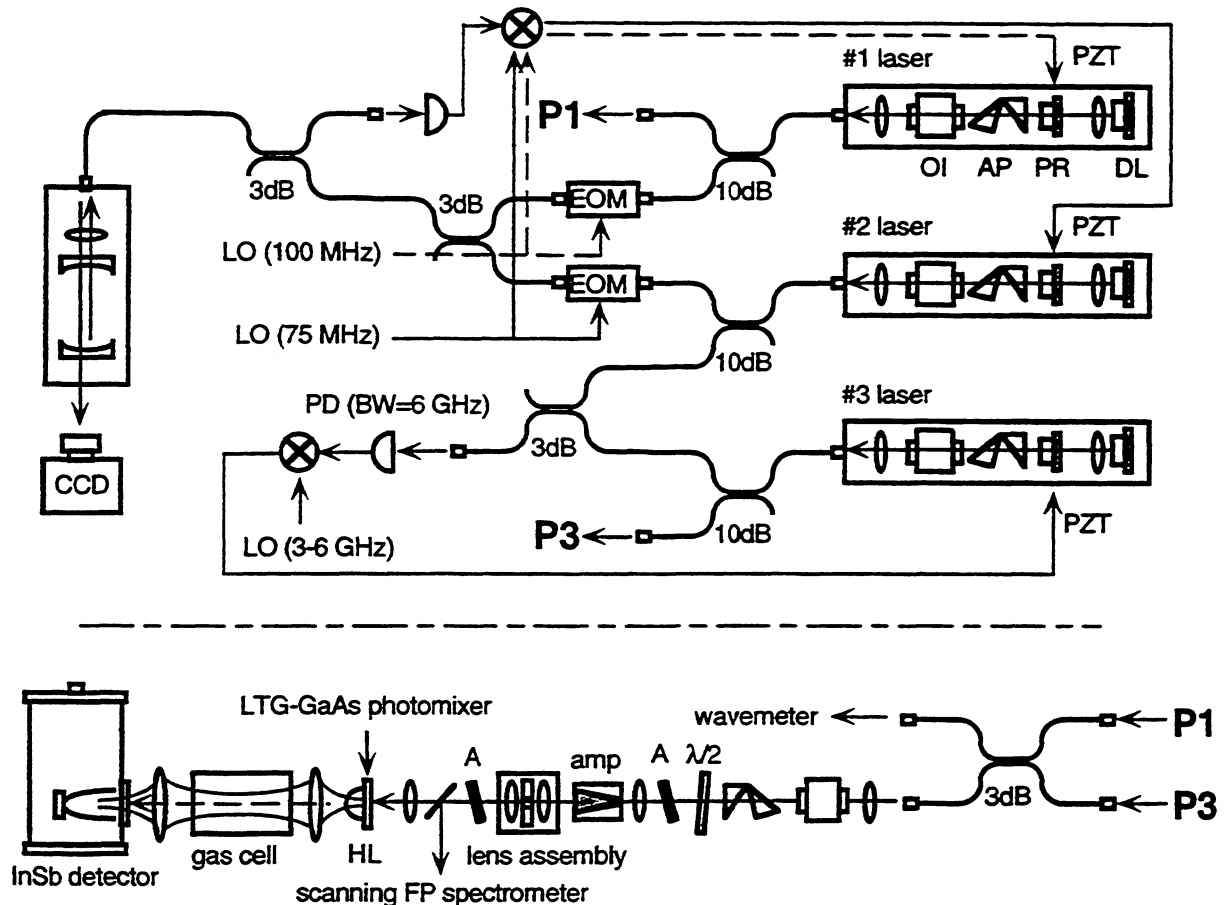


Fig. 1: Schematic diagram of the laser system and experimental setup of the spectroscopy. DL, DBR diode laser; PR, partial reflector; AP, anamorphic prism pair; OI, optical isolator; $\lambda/2$, half-wave plate; A, attenuator; HL, hyper-hemispherical lens; PD, photodetector.

cavity diode lasers as depicted in Figure 1. Two of these lasers (#1 and #2) are locked to different longitudinal modes of a Fabry-Perot (FP) cavity with a free spectral range (FSR) of 3 GHz. The third laser (#3) is locked to one of the cavity-locked lasers (#2) with a 3-6 GHz tunable offset, which can be continuously swept over the FSR. The difference frequency between the #1 and #3 is precisely determined by the sum of integral multiples of the FSR and the offset frequency. All the components are connected with single-mode polarization-maintained fiber optics.

Each external cavity laser assembly consists of an 852 nm distributed Bragg-reflector (DBR) semiconductor laser diode (SDL5722), an $f=4$ mm collimating lens, a 20% partial reflector mounted on piezoelectric transducer (PZT), an anamorphic prism pair, a 60-dB optical isolator, an $f=4$ mm focusing lens, and a FC-connecterized fiber mount. These components were assembled in an aluminum rail assembly as shown in Figure 1. The temperature of the diode laser is controlled by a thermo-electric (TE) cooler with an accuracy better than 1 mK. The injection current is supplied by a low noise ($7 \text{ nA}/\sqrt{\text{Hz}}$) current driver. The partial reflector and the DBR in the laser chip constitute an external cavity with FSR of ~ 3 GHz. The optical feedback induced by the external cavity narrows the linewidth of ~ 500 kHz, while typical linewidth of DBR lasers is several megahertz. The laser frequency was continuously tunable within the FSR of the external laser cavity by changing the cavity length. The continuous tunable range could be expanded to 5 GHz, which corresponds to the voltage limit applied to the PZT (± 15 V), by tracking the laser temperature to maximize the laser gain at the external cavity mode frequency.

To improve the long-term frequency stability, the laser frequency was locked to longitudinal modes of the ULE (Ultra Low Expansion: $\alpha = -2 \times 10^{-10} \text{ }^\circ\text{C}^{-1}$) FP-cavity with a finesse of 750 and FSR of 3 GHz. The FP-cavity is installed in a sealed box filled with dry nitrogen to prevent from refractive index change caused by variations in surrounding pressure. To lock the laser frequency to the FP-cavity mode, we used the Pound-Drever-Hall method. The FM sidebands of the laser are generated at ~ 100 MHz with a fiber-coupled electro-optic phase modulator (EOM), and the

modulated signal is injected into the FP-cavity. The reflected signal from the FP-cavity is detected and fed back to the PZT of the laser cavity. The feedback loop bandwidth was limited to 500 Hz by acoustic resonance of the PZT. The dc-drift of the frequency caused by thermal expansion of the external laser cavity is canceled by tracking the PZT voltage with the integrated error signal through the computer control system. In the laboratory environment the drift was so large that the feedback voltage to the PZT reaches to the 15-V limit in a few minutes. The drift was considerably reduced by putting the whole laser system on a temperature-controlled thick aluminum plate, and the all-day-long cavity-lock of the laser frequency was achieved.

Combined output power of the #1 and #3 lasers from the final 3-dB fiber coupler was approximately 30 mW, while the output power of each DBR laser was originally 150 mW. The total power loss of the present system consisted of the transmission loss in the free-space optics in the laser assembly (1.5dB), the insertion loss to the fiber (4dB), and the loss in fiber directional couplers and at fiber connectors (1.5dB).

2-2. Two-frequency MOPA system

The two-frequency MOPA system was constructed using a single traveling-wave 850 nm semiconductor tapered optical amplifier, which was a component of a commercial external-cavity single-mode laser (SDL8630). The two-frequency fiber-coupled output beam from the tunable laser system, a master oscillator, is launched into the free-space through a collimating lens. The circular beam passed through an optical isolator and a half-wave plate for fine adjustment of the polarization, and is reshaped to elliptical beam by an anamorphic prism pair to match the spatial mode to the amplifier facet spot. After appropriate attenuation, the beam is injected into the optical amplifier chip through an $f=8$ mm focusing lens. The output beam from the amplifier is spatially filtered and collimated to ~ 3 -mm size Gaussian beam by a lens assembly. After passing through an attenuator and a beam divider for monitoring the spectrum, the beam is focused on the photomixer.

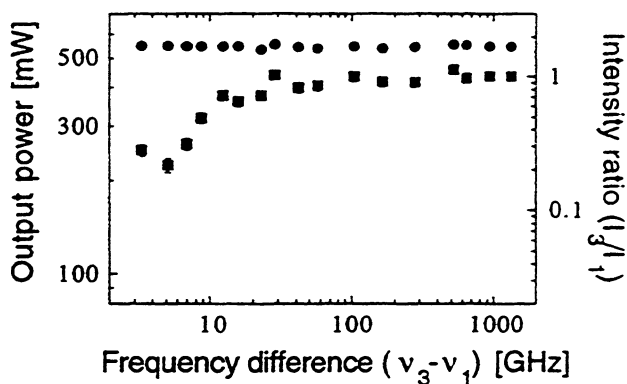


Fig. 2: The output power of the laser system (circles) and the intensity ratio between the two frequency components (squares) as a function of the difference frequency.

Under the conditions of the temperature of 22 °C and the injection current of 1.9 A, the optical amplifier provides the saturated output power of ~500 mW for the input power of approximately 4 mW. Since we set the input power to ~10 mW, the amplifier was operated under highly saturated conditions. Therefore, the output power is insensitive to the input power and the frequency.

2-3. Spectral properties

In Figure 2 the amplified output power as a function of the frequency difference between #1 and #3 lasers is shown by the circles. According to the highly saturated condition, the output power was constant within 5% over the entire difference frequency range.

The intensity ratio between the two frequency components in the amplifier output, I_3/I_1 , measured with a scanning FP-spectrometer is also plotted in Figure 2 as a function of the difference frequency. The intensity ratio was close to unity over a wide range of difference frequencies from ~10 GHz to 1.3 THz. Unbalanced amplification occurred at difference frequencies lower than 10 GHz due to the two-frequency interaction driven by the refractive index change induced by the carrier density modulation at the difference frequency⁷. The lower frequency limit of the well-balanced two-frequency amplification is determined by the carrier lifetime of the

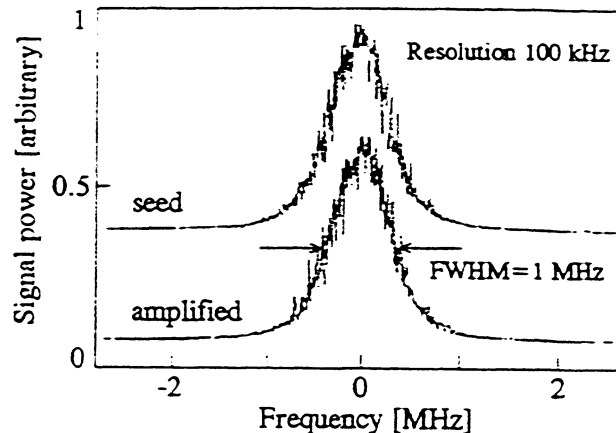


Fig. 3: The spectrum of the beat signal between the two frequency components before amplification (upper) and after amplification (lower).

amplifier.

Since the amplifier used in this system is a component of a commercial external-cavity single-mode laser, an amplifier chip facet was anti-reflection coated ($R=0.1\%$) but the other facet was not coated ($R=30\%$). Small variation in the output power and the intensity balance seen in Figure 2 are caused by the chip mode with a spacing of ~15 GHz. Therefore, these frequency dependence can be considerably reduced by AR-coating both of the amplifier chip facets.

The spectral purity of the beat signal at the difference frequency was measured with the 25-GHz bandwidth photodetector. Figure 3 represents the beat signal spectrum at 12.6 GHz for both the amplified output and the master laser. The linewidth of the beat signal was approximately 1 MHz and completely preserved through the amplification process.

3. Generation of THz-wave and application to spectroscopy

3-1. Experimental setup

The laser system described above was used for the THz-wave generation with a LTG-GaAs photomixer, and the absorption spectroscopy of acetonitrile (CH_3CN) was carried out using this THz source. The experimental setup of the spectroscopy is shown in Figure 1. The two-frequency output

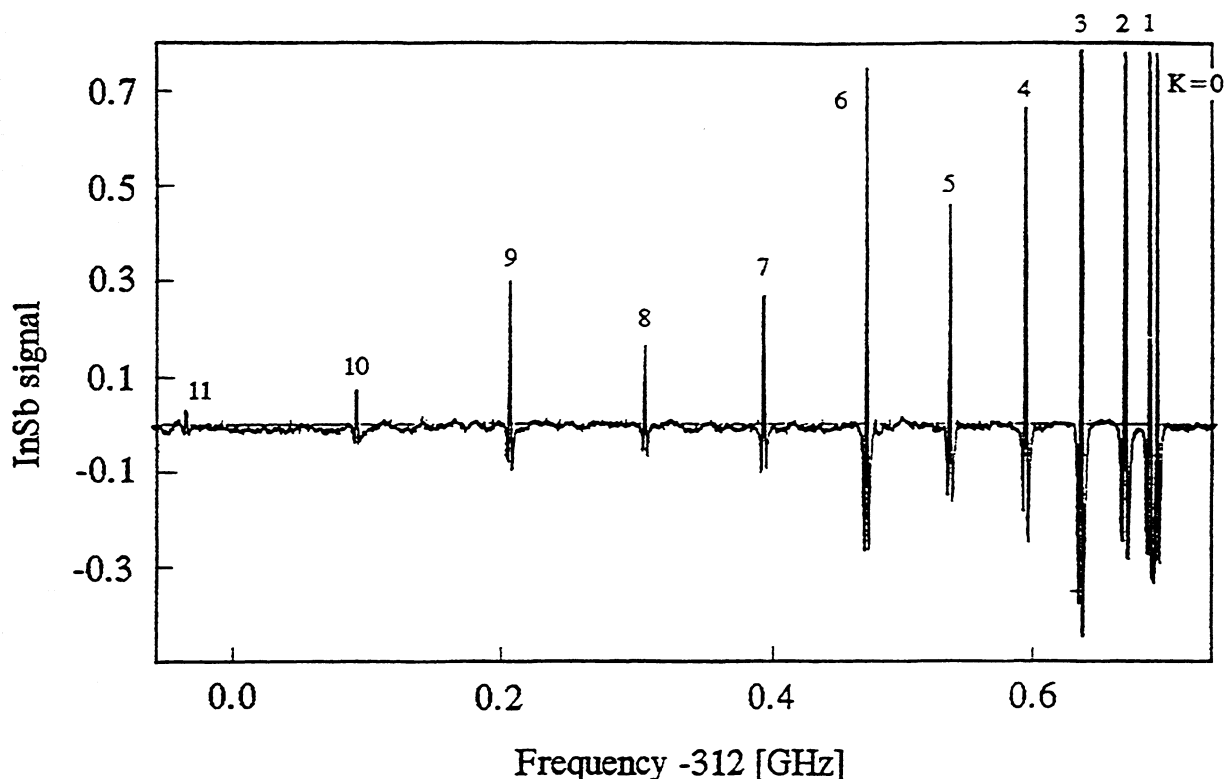


Fig. 4: The measured rotational spectrum of acetonitrile.

beam from the MOPA is attenuated and focused on the LTG-GaAs photomixer. The THz-wave output beam is collimated with a combination of a hyper-hemispherical lens put on a backside of the photomixer and a Teflon lens. The collimated beam passes through a 8-cm long 1-inch diameter gas cell with polyethylene windows. The transmitted beam was weakly focused with a Teflon lens and fed into a 4.2-K InSb hot-electron bolometer.

3-2. Generation of THz-wave by photomixing

The photomixer used in this experiment was fabricated at Minnesota University. The LTG-GaAs wafer was grown on a 0.5-mm-thick semi-insulating GaAs substrate, and a planar log-spiral antenna with 1- μm -wide interdesitated electrodes and 1- μm -wide gaps in a $10 \times 10 \mu\text{m}^2$ active area was etched on the wafer. The bandwidth of the photomixer determined by a combination of the carrier

lifetime of the LTG-GaAs and the RC time constant of the electrode is estimated to be approximately 300 GHz. The dc bias voltage was applied to the electrode by a constant current supply of -0.5 mA for the laser power of 30 mW.

Before carrying out the spectroscopy, the THz-wave power was measured without the gas cell. The pump laser beam was modulated at 400 Hz by a mechanical chopper, and the output signal of the InSb detector was measured. The $\times 100$ -amplified detector signal at 300 GHz was $\sim 100 \text{ mV}$ that corresponds to the radiation power of $\sim 1 \mu\text{W}$.

3-3. Spectroscopy

The tone-burst FM spectroscopy method⁹ was used to obtain the spectrum. The injection current of the #1 cavity-locked laser of the master laser system was modulated at 2 MHz above the cavity-lock loop bandwidth, and the

modulation input was switched on and off at a 10-kHz rate. The detected signal was demodulated by a lock-in amplifier at 10-kHz switching rate. The spectrum was obtained by sweeping the offset frequency. The lock-in signal traces the second derivative of the absorption spectrum.

Figure 4 presents the absorption spectrum of CH_3CN $J=16$ rotational transitions near 312 GHz. The lock-in amplifier signal taken by a single frequency sweep with a rate of 2 MHz/sec was plotted against the offset frequency between #2 and #3 lasers. The data sampling rate was 7 sample/sec which corresponds to the frequency resolution of 0.3 MHz, while the time constant of the lock-in amplifier was 0.3 sec. The spectrum shows a K -structure of a symmetric-top molecule that was assigned to $K=0-11$ lines as depicted in the figure. The $K=0$ and 1 lines separated by ~ 6 MHz are clearly resolved. The width of the absorption lines was pressure-limited, while the gas pressure was 60 mTorr. To evaluate the instrumental linewidth, further measurements by changing the gas pressure are required.

The lock-in amplifier outputs for the absorption lines were ~ 100 mV, while the noise amplitude was ~ 5 $\mu\text{V}_{\text{p-p}}$, and the detection limit of the absorption is estimated to be $\sim 10^{-4}$. The spectrum of the C^{13} -isotopomer of acetonitrile, which has the natural abundance of $\sim 1\%$, was detected with a signal-to-noise ratio of ~ 20 according to the detection limit. Unfortunately, the noise originated mainly from an electronic pick-up at the A/D input, and the detection limit was determined by neither the detector noise nor the source noise. The detection limit of 10^{-5} level can be achieved with the present system by reducing this noise. Although the present measurement was carried out at ~ 300 GHz, the source intensity is sufficiently high for the spectroscopy at higher frequencies if only the detector is replaced to that for high-frequency use; the output power at 1 THz is estimated to be ~ 10 dB down.

For further spectroscopic measurements such as the search for unknown molecular lines and the use for astronomical observation, the absolute frequency calibration of the system is necessary. The frequency calibration is carried out by measuring the FSR of the FP-cavity. Once the exact value of the FSR was obtained, the THz-wave frequency can be determined

with an accuracy of $\sim 10^{-10}$, even if there exists a fluctuation of the cavity temperature of ~ 1 °C, because of an extremely low thermal expansion coefficient of the cavity material which is equivalent to the crystal used as a microwave oscillator. The FSR was measured by detecting the beat signal between the two cavity-locked lasers (#1 and #2). The accuracy of the measurement was ~ 10 kHz, while the FSR is 3 GHz. Well-known strong molecular lines in the THz region such as rotational transitions of carbon monoxide (CO) are usable for more accurate calibration. Frequencies of such molecular lines in the THz range that corresponds to ~ 300 times of the FSR are known with an accuracy of $\sim 10^{-7}$, and the resultant accuracy of the FSR measurement is expected to be $\sim 3 \times 10^{-10}$ or ~ 300 Hz. The cavity calibration with CO lines is in the process.

4. Conclusions

A 850 nm tunable two-frequency diode laser system based on the three-laser frequency control scheme and the two-frequency MOPA technique was developed, and the output power of 500 mW and the linewidth of < 1 MHz were achieved. The laser system was applied to the THz-wave generation using the LTG-GaAs photomixer, and the absorption spectroscopy of acetonitrile with this source was demonstrated. The present THz-wave source system is usable for actual spectroscopy, only if the frequency calibration is carried out. The system will be useful not only for spectroscopy but also for the application in development of local oscillators for future space-borne heterodyne receivers.

The photomixer used in the present experiment provided the output power of ~ 1 μW for the pump laser power of 30 mW. According to a straightforward calculation by the quadratic dependence of the THz-wave power on the pump laser power, the sub-mW level output power is achievable by using the present laser system with the maximum power of 500 mW. In order to use such high-power laser effectively, the development of new type of the photomixer with high thermal-damage threshold such as the large dimension device is required.

Since the gain bandwidth of the semiconductor optical amplifier is over 10 THz, the two-frequency MOPA system is applicable to the difference-frequency generation of the mid-infrared radiation. At higher frequencies, even at several THz, the optical down-conversion method using nonlinear optical materials¹⁰ or recently developed quantum-well devices could be more efficient than the electro-optical conversion method using the photomixer. Further development of nonlinear optical materials and novel devices with large $\chi^{(2)}$ at the diode laser frequency and the phase matching condition at the THz frequency is expected.

We thank T. J. Crawford of Jet Propulsion Laboratory for his technical support. This work was supported by the National Aeronautics and Space Administration.

References

1. E. R. Brown, K. A. McIntosh, K. B. Nichols, O. B. McMahon, W. F. DiNatale, and T. M. Lyszczarz, *Appl. Phys. Lett.* **67**, 3844 (1995).
2. K. A. McIntosh, E. R. Brown, K. B. Nichols, and C. L. Dennis, *Appl. Phys. Lett.* **66**, 285 (1995).
3. S. Matsuura, M. Tani, and K. Sakai, *Appl. Phys. Lett.* **70**, 559 (1997).
4. A. S. Pine, R. D. Suenram, E. R. Brown, and K. A. McIntosh, *J. Mol. Spectrosc.* **175**, 37 (1996).
5. P. Chen, G. A. Blake, M. C. Gaidis, E. R. Brown, K. A. McIntosh, S. Y. Chou, M. I. Nathan, and F. Williamson, *Appl. Phys. Lett.* **71**, 1601 (1997).
6. S. Matsuura, M. Tani, H. Abe, K. Sakai, H. Ozeki, and S. Saito, *J. Mol. Spectrosc.* **187**, 97 (1998).
7. S. Verghese, K. A. McIntosh, and E. R. Brown, *IEEE Trans. Microwave Theory and Tech.* **45**, 1301 (1997).
8. S. Matsuura, P. Chen, G. A. Blake, J. C. Pearson, and H. M. Pickett, *Opt. Lett.*, submitted.
9. H. M. Pickett, *Appl. Optics* **19**, 2745 (1980).
10. Y. R. Shen, *The Principles of Nonlinear Optics* (John Wiley and Sons, 1984).

THE FOCAL PLANE UNIT OF THE HETERODYNE INSTRUMENT FOR FIRST: *HIFI*

N. D. Whyborn^a, Th. de Graauwa^a, H. van de Stadt^a
V. Belitsky^b, R. Krusinga^c, S. Torchinsky^b, H. Visser^c, K. Wildemana^a

^a Space Research Organisation Netherlands (SRON), PO Box 800, 9700 AV Groningen, The Netherlands
E-mail: nick@sron.rug.NL; Tel: +31 50 363 4074; Fax: +31 50 363 4033

^b Onsala Space Observatory, Chalmers University of Technology, S-412 96 Göteborg, Sweden

^c TNO-TPD, Stieltjesweg 1, 2600 AD Delft, The Netherlands

ABSTRACT

ESA's Far-IR and Sub-millimetre-wave Telescope, *FIRST*, is an astronomy space mission which will provide an unobstructed view of the universe in the last major unexplored region of the electromagnetic spectrum. The satellite is planned to be launched in mid 2006 and will carry a payload of three instruments spanning the wavelength interval 80 and 800 μm . ESA has recently released an Announcement of Opportunity (AO) asking for interested parties to make proposals to provide these instruments and this paper will describe our proposed front-end for a Heterodyne Instrument for FIRST - *HIFI*. *HIFI* will be built by a large consortium of European, American and Canadian institutes which began work defining a heterodyne instrument in 1996.

HIFI will cover the frequency interval 480 - 1250 GHz in 5 bands using pairs of SIS tunnel junction mixers to receive both polarisations. The frequency ranges 1600 - 1900 GHz and 2400 - 2700 GHz will also be covered using single hot-electron bolometer mixers. A modular construction will be used with 6 mixer assemblies, one for each of the 5 lower bands and one for the two high-frequency bands. Each mixer assembly will contain optics for local oscillator injection and the first stage of IF amplification. The local oscillator signals are generated outside the cryostat in a separate unit and pass through dedicated windows in the cryostat wall. The local oscillator unit is described elsewhere. Low noise InP HEMT's with very low power consumption will be used in the IF preamplifiers and will provide a 4 GHz IF bandwidth. A suite of spectrometers in the warm service module of the spacecraft will analyse the IF signals with frequency resolutions ranging from 100 kHz to 1 MHz.

The mixer assemblies slot into a housing containing the optics common to all bands. The common optics performs the functions of refocusing the beam from the telescope, splitting the focal plane amongst the 6 mixer assemblies, chopping, and calibration.

1 INTRODUCTION

The proposed Heterodyne Instrument for FIRST, *HIFI*, has been optimised to address a number of key themes in modern astrophysics related to understanding the cyclical interrelation of stars and the interstellar medium of galaxies. This interplay between stars and the ISM drives the evolution and, thus, the observational characteristics of the Milky Way and other nearby and far away galaxies, all the way back to the earliest protogalaxies at high z .

By combining the high spectral resolving power capability of the radio heterodyne technique with quantum noise limited detection from super-

conductor physics and with the state-of-the-art in microwave technology, *HIFI* will provide unrivalled spectral resolution and ultimate sensitivity over the frequency ranges 480 to 1250 GHz (in 5 bands), 1410 to 1910 GHz, and 2400 to 2700 GHz. The instrument will be able to perform rapid and complete spectral line surveys with resolving powers from 10^3 up to 10^7 (300 - 0.03 km/s) and, will complement the spectroscopy capabilities of the two incoherent instruments on FIRST.

This instrument will fully exploit the recent rapid pace of development in sub-mm wavelength mixer technology to give sensitivity close to the theoretical limit. The first five frequency bands

will each contain a pair of mixers using superconductor-insulator-superconductor (SIS) tunnel junctions. Both polarisations of the astronomical signal will be received for maximum sensitivity. Channel 6 will contain two mixers based on the recently-developed fast hot-electron bolometers (HEB) using thin superconducting films – each mixer will cover one of the sub-bands. The instrument will operate at one frequency at a time, i.e. only one of the frequency bands will be active.

HIFI will have an instantaneous IF bandwidth of 4 GHz analysed in parallel by two types of spectrometers: a pair of wide-band spectrometer (WBS), and a pair of high resolution spectrometer (HRS). The wide-band spectrometer will use acousto-optic technology with a frequency resolution of 1 MHz and a bandwidth of 4 GHz for each of the two polarisations. The HRS will employ either a digital auto-correlation spectrometer (ACS) or a chirp transform spectrometer (CTS) and will provide two combinations of bandwidth and resolution: 1 GHz bandwidth at 200 kHz resolution, and at least 500 MHz at 100 kHz resolution. The HRS will be divided into 4 or 5 sub-bands each of which can be placed anywhere within the full 4 GHz IF band.

HIFI will consist of three major sub-systems and an instrument controller:

1. The focal plane sub-system comprises the focal-plane unit (HFPU) inside the cryostat, containing relay optics, mixers, low-noise IF HEMT pre-amplifiers, a focal plane chopper, and a calibration source; and the HFPU control unit (HFCU) which supplies the bias voltages for the mixers and IF preamplifiers in the HFPU and controls the frequency diplexers, the focal plane chopper mechanism and the calibration source.
2. The local oscillator sub-system comprises: the local oscillator unit (HLOU) located on the outside of the cryostat generating the LO signal which is coupled into the HFPU via a window in the cryostat wall; and the local oscillator control unit (HLCU) in the service module (SVM) which controls the frequency of the local oscillator with a precision of 1 part in 10^8 .
3. A back-end sub-system (HBES) within the SVM. This contains the IF processor, WBS, HRS, and backend control system (BCS).
4. An instrument control unit (HICU) within the SVM which interprets commands from the

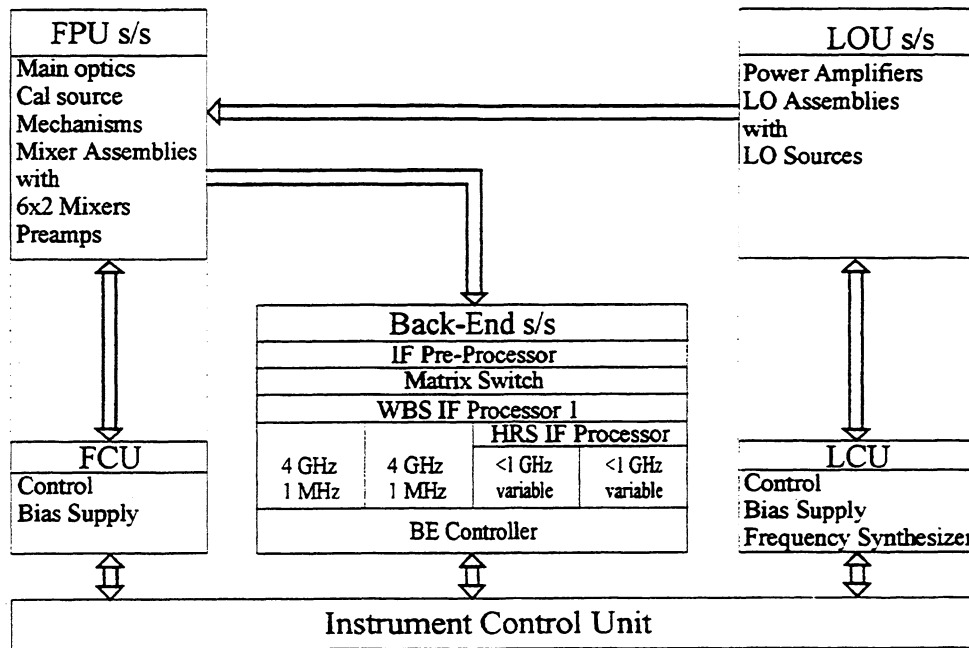


Figure 1. Block diagram of the *HIFI* instrument

satellite telecommand system, controls the operation of the instrument, and returns science and housekeeping data to the satellite telemetry system.

Figure 1 is a block diagram of the *HIFI* showing the relationship between the various units of the instrument.

2 FOCAL PLANE SUB-SYSTEM

2.1 General Description

In the HFPU the sub-mm wavelength signal from the telescope is mixed with radiation from a local oscillator and the "beat frequencies" are generated in a cryogenically cooled mixer. The instrument measures radiation in two polarisations in 5 contiguous bands covering the frequency interval 480 to 1250 GHz and in a single polarisation in two sub-bands around 1.7 THz and 2.5 THz. There are 6 optical beams coming from the telescope, one for each of the 5 dual-polarisation bands and one for the two high-frequency sub-bands.

The HFPU employs a highly modular design consisting of:

- a common optics assembly (COA) which serves as the support structure for the other HFPU modules and contains the optical elements which are common to the 6 optical beams,
- 6 mixer assemblies (MA) containing the optical elements, mixers and IF components specific to each of the 6 instrument bands,
- a chopper assembly containing a nutating mirror and drive mechanism,
- a calibration assembly containing a black-body calibration source and refocusing optics.

These elements are described in the following sections.

Extremely flat and stable spectral baselines are a stringent requirement for the *HIFI* instrument in order to be able to study the very weak broad emission and absorption lines of distant galaxies and to perform broadband spectral surveys. Thus, special emphasis is placed on the design of the optics in the HFPU to avoid generation of standing waves. It also includes a chopper mechanism to switch between two positions on the sky, and will allow the standard dual beam switch techniques for standing wave elimination. In addition, the specification of the intermediate frequency processing from the first IF amplifiers down to the spectrometer backends are driven by these requirements, resulting in particular in the necessity of mounting the first IF amplifiers very close to the mixers (see below) and carefully controlling the thermal environment of critical components with regard to stability.

2.2 Common Optics Assembly

The functions of the instrument optics and their order of implementation are indicated in Figure 2. The first function is calibration (CAL) followed by focal plane chopping (CHOP), band splitting (CHAN), polarisation separation (POL), and LO injection (LO).

The Common Optics Assembly (COA) contains the optics from mirror M3 in the telescope focal plane through to but excluding the Mixer Assemblies (MA) which are described in Section 2.5 (see Figure 3). The COA also includes the calibration assembly.

The telescope focal plane mirror (M3) acts as a folding mirror and also as a field mirror to reduce the optical path length towards the pupil image (= image of the telescope secondary mirror) for packaging reasons. The telescope focal plane is re-imaged in the main optics by means of a Gaussian telescope at unit magnification implemented by a collimating mirror and an imaging mirror, both with a focal length of 280 mm. Between these two

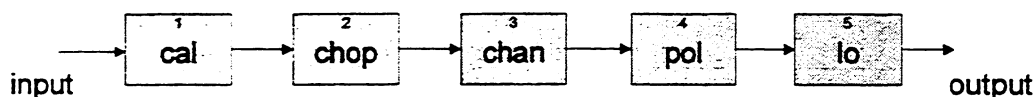


Figure 2. *HIFI* Common Optics functional block diagram

mirrors a flat chopper mirror is positioned in the pupil plane. This mirror implements the second function mentioned above.

After the imaging mirror a flat mirror folds the beam towards a stack of 6 beam splitting mirrors placed at an image of the focal plane. The centres of these mirrors are located on a line oriented perpendicular to the plane shown in Figure 3. These 6 mirrors differ in orientation so that the six resulting beams are separated in direction, thus implementing the function of beam separation. The focal length of the individual band splitting mirrors can be chosen to alter the system exit pupil location while keeping the focal plane image in the same position. Finally the images on the band splitting field mirrors (6x) are re-imaged into the mixer assemblies, which are mounted onto the Main Optics structure in a stack.

The housing of the COA and the mirrors will be machined from a single block of aluminium giving rigidity and dimensional stability. Mirrors will be

bolted to flanges in the housing using 3 fixation points and if necessary shims will be used to adjust the alignment. The mirrors can be added sequentially to allow the alignment to be checked optically at each stage. This construction technique was used very successfully in the Short Wavelength Spectrometer (SWS) flown on ISO.

2.3 The chopper-mechanism

Most observations with *HIFI* will be made using beam switching. A focal plane chopper within the instrument will switch the telescope beam between the astronomical source and a nearby reference position. The spectrometer system will measure the difference in emission between the two positions. The focal plane chopper in *HIFI* will have a beam throw (separation between source and reference position) of 3 arcmin. on the sky and will chop at frequencies up to 1 Hz. The mechanism is similar to the scanning mechanism flown in SWS and LWS on board ISO. The mechanism moves a mirror between three positions: two sky positions

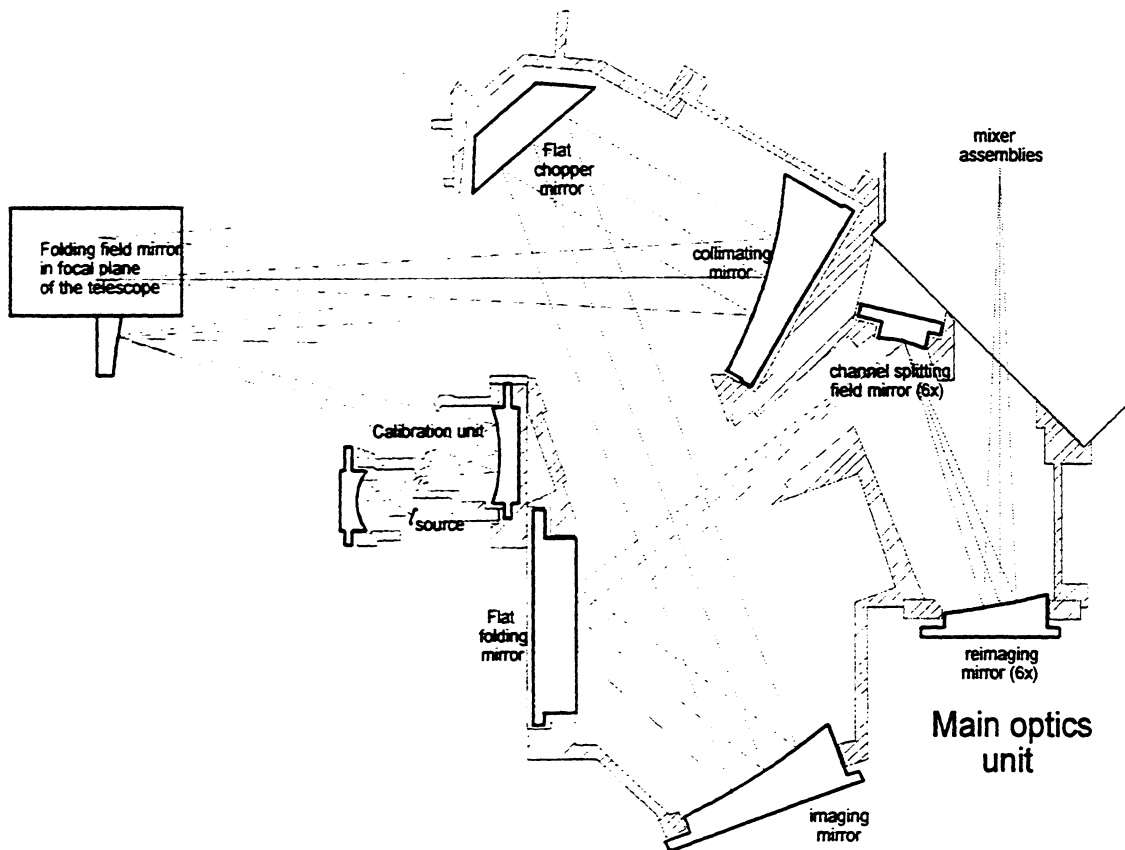


Figure 3. *HIFI* Common Optics layout

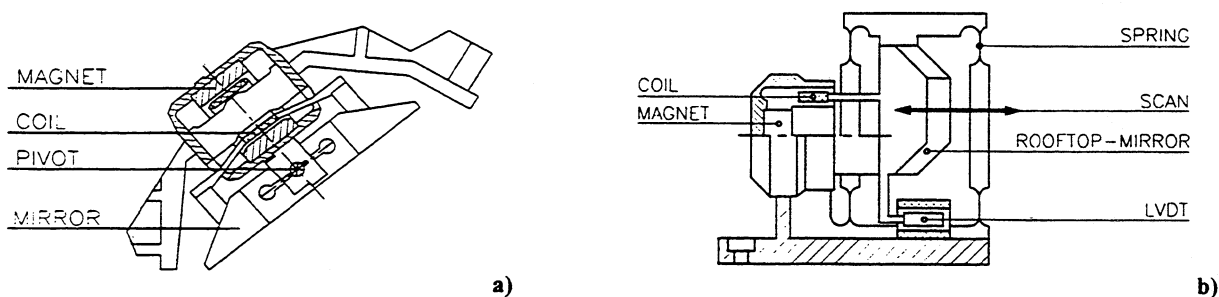


Figure 4. Drawing showing the *HIFI* mechanisms: a) chopper; b) diplexer

and a third calibration position. The required scan angle for the present optical design is 4.6° (pk-to-pk).

The mirror is supported by two flexural pivots. A copper coil carrying a current moving in a radially-oriented magnetic field from SmCo permanent magnets provides the drive force (Figure 4a). The dissipation in the motor coil is estimated to be 0.5 mW on average for square wave chopping of 1 Hz. An LVDT position sensor (also flown on SWS-ISO) provides position feedback for the drive electronics. The dissipation in this sensor is about 0.6 mW.

Because of the vital position of the chopper in *HIFI*, redundant wiring, drive coils and drive electronics will be used for the motor. Additionally, the neutral position of the mechanism will be a sky position allowing *HIFI* to execute most of the scientific observations using telescope position switching and frequency switching in case of failure of the chopper; external astronomical sources would have to be used as calibrators.

2.4 Calibration Assembly

The calibration assembly, located just above the input opening of the main optics housing, provides the instrument with a black body source having an adjustable temperature in the range 15–100 K. This unit couples to the instrument via a part of M3 and is selected for calibration measurements by suitably positioning the chopper mirror. The auxiliary optics in the calibration unit minimises the surface area of the source so as to reduce the heat load on the cryostat.

The goal is to achieve an instrumental calibration accuracy of 3 %. The end-to-end calibration of the system including the telescope will be accomplished by observation of astronomical sources of known strength. The accuracy achieved will depend upon pointing accuracy but should be better than 10 %.

2.5 Mixer Assemblies

The *HIFI* mixers are located in Mixer Assemblies (MA). The MA's contain mechanical supports, mixers, diplexers and polarisers as well as IF amplifiers, and are mechanically mounted on the HFPU. Thermal straps connect the mixers and 1st stages of the IF amplifiers to the "1.7 K level", and the 2nd stage IF amplifier to the "15 K level". A connection to the "4.3 K level" is used to heat-sink an internal wiring harness. A 0.5 K adsorption cooler will be included for the aluminium HEB mixers proposed for band 6.

There will be 6 MA's, each covering a certain frequency range with two mixers, only one MA will operate at any time. The pair of mixers in individual MA's will operate on orthogonal polarisations and are described in Section 2.7.

The optical input to an MA consists of a signal beam and a LO beam. In the MA box the signal beam will be split into 2 polarisations for the 2 mixers. The LO beam will also be split into 2 beams with suitable linear polarisations to be coupled to the mixers. The combining of the signal and LO beams will be by a beamsplitter for the lower frequency two bands, and by tuneable diplexers in the higher bands where less LO power is available. This gives rise to two different optics

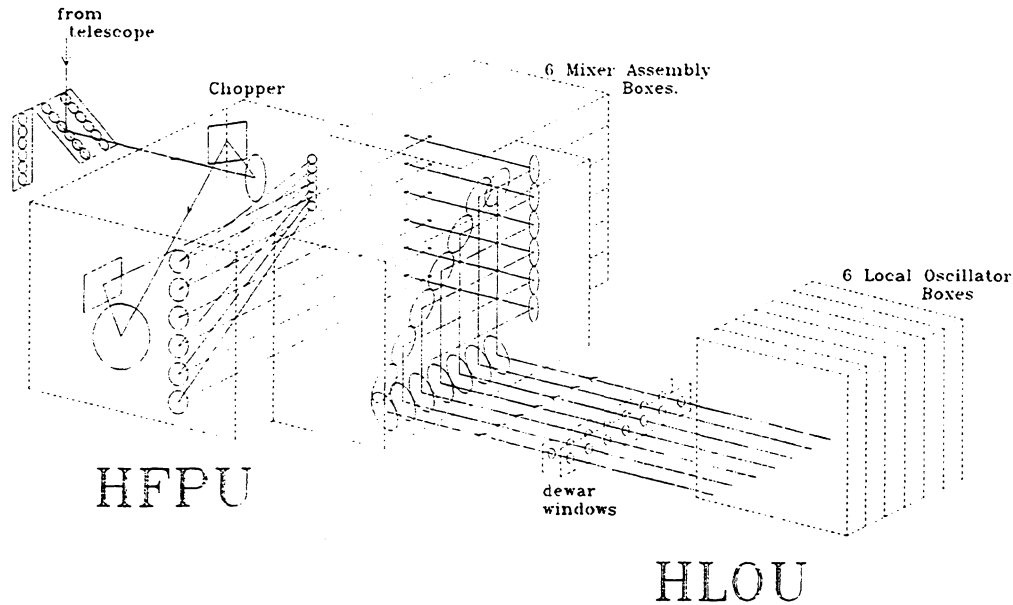


Figure 5. Perspective view showing the LO beam disposition

layouts for the MA boxes, but they will be identical externally.

2.5.1 The Diplexer Mechanisms

The function of the mechanism in the diplexer is to translate a rooftop mirror over about 0.2 mm full stroke. An aluminium rooftop mirror is supported by four leaf springs and driven by a moving coil in a static magnetic field (Figure 4b). A similar mechanical concept was used for the Fabry-Perot mechanism in SWS on ISO. The dissipation is 0.6 mW in the drive coil and about 0.7 mW in the LVDT position sensor. The mechanism is used in bands 3–6 in *HIFI*.

2.5.2 0.5 K Adsorption Cooler

For the 0.5 K level we will include a dedicated ^3He adsorption cooler of a type similar to that flown on IR Telescope in Space (IRTS). This is a sealed device which can provide the necessary small cooling power at 0.5 K and rejects the heat to the "1.7 K level" of the cryostat through a thermal strap. The cooler requires recycling every 48 hours by an electrical heater and when operating will result in a time-averaged dissipation of about 2.4 mW, peak dissipation is expected to be about 50 mW.

2.6 Local Oscillator Optics

The HLOU is located outside the dewar at an optical distance of more than 650 mm from the *HIFI* HFPU. The LO beams are coupled through vacuum windows in the dewar wall and directed into the respective MA's by a set of folding mirrors (Figure 5). We have chosen to use 7 separate sub-windows each optimised for transmission of its LO band. The sub-windows will be small to reduce the thermal load on the cryostat due to radiation and this is accomplished by focusing each beam to a minimum waist at the window location.

2.7 Mixers

Existing technologies for fabricating sensitive heterodyne mixers favour the use of waveguide mixers for the lower frequency bands, while the higher frequencies will use lenses and planar antennas such as double slot lines. However both solutions are compatible with the chosen mechanical and optical configurations.

The proposal for the MA's, mixers and junctions is based on the following assumptions.

- Fixed tuned, double sideband (DSB) mixers in dual polarisation for optimum sensitivity and redundancy.

Table 1. HIFI DSB receiver noise temperature for 3 cases and probable mixer types: (i) State-Of-the-Art Performance (SOAP), (ii) Baseline values and (iii) Goal values. The last column indicates the baseline mixer type: WG – waveguide, QO – quasi-optical.

band	range, GHz	DSB noise temperature, K			mixer technology			mixer type
		SOAP	Baseline	goal	SOAP	Baseline	goal	
1	480	80	70	70	Nb-SIS	Nb-SIS	Nb-SIS	WG
	640	130	110	110				
2	640	130	110	110	,,	NbTiN-SIS	NbTiN-SIS	WG
	800	500	150	130				
3	800	500	150	130	,,	,,	,,	WG
	960	700	190	160				
4	960	700	190	160	,,	,,	,,	WG
	1120	1600	230	190				
5	1120	1600	230	190	,,	,,	,,	WG
	1250	1900	510	210				
6a	1410	2100	650	300	Nb-HEB	Nb-HEB	Al-HEB	QO
	1910	2100	650	300				
6b	2400	2500	800	450	,,	,,	,,	QO
	2700	2500	800	450				

- Continuous frequency coverage of 480–1250 GHz split into 4 sub-bands of 160 GHz bandwidth and one of 130 GHz with an overlap of 2 GHz between bands.
- 2 sub-bands covering 1410–1910 GHz and 2400–2700 GHz without dual polarisation.

The proposed frequency bands, sensitivities and foreseen detector types are given in Table 1. Sensitivity values are given for three cases: (i) presently achieved values with state-of-the-art performance (SOAP); (ii) Baseline values to be achieved after the development years from 1998 to 2000; (iii) Goal values, expected to be achievable after further improvements before delivery of the

FM in 2004. The use of new detector materials such as NbTiN makes the expected improvement in sensitivity possible.

The SIS mixers need an adjustable magnetic field of a few hundred Gauss which is provided by small superconducting electromagnet coils. These magnets are integrated in or close to the mixers. To occasionally remove unwanted trapped flux from the junction, a heater resistor, either on chip or close to the chip, is used to warm up the mixer chip just beyond the superconducting transition temperature of the SIS junction materials momentarily. The HEB mixers of band 6 do not need a magnetic field.

Table 2. Cryogenic IF preamplifier performance

Centre frequency	10 GHz for SIS mixers, 4 GHz for HEB mixers	IF system noise temperature	10 K – baseline 5 K – goal
Bandwidth	4 GHz	Passband ripple	± 1.5 dB
IF power level at SVM	-90 ± 5 dBm W/MHz	Amplitude non- linearity	< 1 %

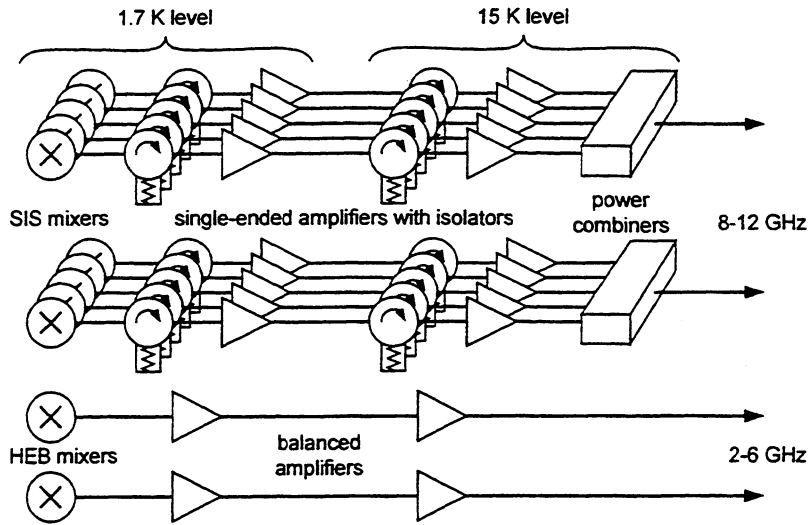


Figure 6. Block diagram of IF pre-amplification scheme.

2.8 IF Preamplifiers

The function of the IF preamplifiers of the *HIFI* instrument is to amplify the IF signals from the mixers with the minimum of additional noise. Other aims are to achieve flat gain over the band, low power dissipation, stability and reliability. The IF preamplifiers will be as close as possible to the mixers and operate at 1.7 K to maximise sensitivity. The preamplifier outputs will be connected to the IF processor in the SVM by coaxial cables in the spacecraft cryoharness. One mixer assembly with two mixers and their associated IF preamplifiers, one set for each polarisation, will operate at a time. A summary of the cryogenic IF system is given in Table 2.

The basic IF pre-amplification scheme is shown in Figure 6. Each mixer is followed by a dedicated IF

preamplifier – 6 bands times 2 polarisations giving 12 preamplifiers in total. For the SIS mixers of bands 1 to 5, these operate with an IF of 10 GHz, while band 6 will use HEB mixers and have an IF centre frequency of 4 GHz. Since only one pair of mixers will operate at any time, we propose to use power combiners to feed the signals from bands 1 to 5 into a single pair of coaxial cables – the choice of band is made by activation of the required pair of preamplifiers. The IF signals from band 6 will be fed into a second pair of IF cables. This reduces the number of coaxial cables between the front-end and the IF processor to four, with a consequent reduction in thermal load.

Cryogenic isolators at 1.7 K will be used to suppress reflections between the mixers and 10 GHz preamplifiers, but balanced amplifiers will be necessary for the 2-6 GHz band. Fixed

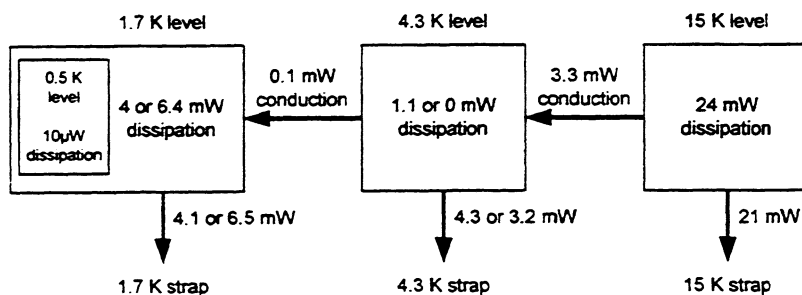


Figure 7. Diagram showing the HFPU thermal interface with the spacecraft.

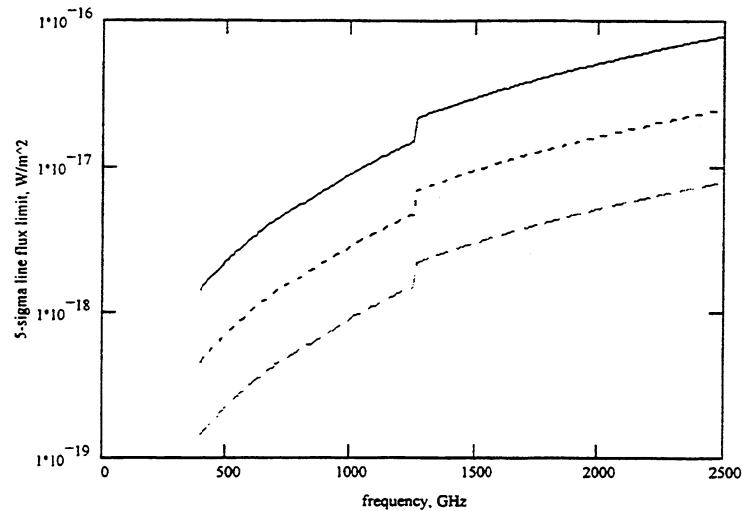


Figure 8. 5-sigma point-source line flux detection limits for a 1 hour integration and for three velocity resolutions starting from the top: 300, 30, and 3 km/s

attenuators after each preamplifier will be used to set the correct IF output levels and band-pass filters in each chain will suppress out-of-band signals.

A total IF gain of 38 dB or more is required in the HFPU to overcome cable and other losses and to render the noise contribution of the back-end system insignificant. To avoid problems with feedback and instability the desired amplification will be achieved by a cascade of two amplifiers. The baseline is to cool the 1st stages of the IF preamplifiers to 1.7 K with the second stages operating at 15 K where there is a higher heat-lift capacity. An option to integrate the first preamplifier stage into the mixer to obtain the maximum possible sensitivity will be studied. If the cooling capability at 1.7 K is insufficient for the expected 4 mW dissipation of the 1st stages of the preamplifier, then a back-up option is to operate them at 4.3 K.

2.9 Focal Plane Unit Control Electronics

The Focal plane unit Control Unit (HFCU) will contain electronics to perform the following functions:

- control the mechanisms, the calibration source, and the 0.5 K adsorption cooler,

- provide suitable bias voltages and currents to the mixers, mixer magnets, de-flux heaters and IF preamplifiers,
- interface with the Instrument Controller Unit (HICU) to allow it to control all functions and to return housekeeping data.

The digital interface controller forms the heart of the HFCU. Implemented in an FPGA or ASIC, it will communicate with the HICU via balanced serial digital interfaces. It will store in volatile memory all settings relevant to the above functions, as received from the HICU. These settings will be fed to D/A converters, thus generating reference levels that are translated into accurate mechanism positions, bias currents/voltages or temperature levels. The HFCU will also periodically recycle the 0.5 K adsorption cooler by passing current through a heater.

The HFCU will also contain a data acquisition system to collect analogue housekeeping information on all relevant parameters of HFCU and HFPU: mechanism positions, bias current/voltage, temperature levels etc. This analogue housekeeping circuitry will include signal conditioning (filtering, amplification), multiplexing and A/D conversion. The HFCU will also provide digital housekeeping: information on unit status and settings. All housekeeping

information will be available to the HICU upon request, through the interface controller.

The HFCU will obtain secondary power from a dedicated section of the DC/DC converter in the HICU. In order to support stand-by and sleep modes, parts of the HFCU electronics can be switched off.

2.10 Thermal Interface

The thermal interface of the HFPU is shown schematically in Figure 7. The housing, optical components, and 2nd stage IF preamplifiers are cooled to 15 K by thermal straps to the S/C. There is only limited heat transfer from the HFPU housing to the optical table. A strap to the 4.3 K level provides a heat-sink for the cables to the mixers. The SIS mixers operate at 1.7 K being cooled by a strap to the helium tank. Heat rejected from the 0.5 K adsorption cooler is also removed through a strap to the 1.7 K level.

3 PREDICTED PERFORMANCE

We present the baseline observing performance of *HIFI* for three illustrative cases: a deep, point-source integration, a frequency survey, and mapping is shown below. We have not made any allowance for calibration and other overheads.

3.1 Deep Integration

For this case taking a spectral resolution of $R=10^4$ (30 km/s velocity resolution), 1 hour integration time gives the 5σ flux detection limits shown in Figure 8.

3.2 Line survey

In Table 3 we list the expected $1-\sigma$ noise levels for a complete 24-hour line survey over various frequency intervals and at a resolution of 1 MHz.

3.3 Mapping

In Table 4 we list the expected speed in mapping a region to the given noise levels using the on-the-fly technique.

Table 3. Spectrum $1-\sigma$ noise level for 24 hour line survey at 1 MHz resolution

Frequency range	spectrum $1-\sigma$ noise level
480-1250 GHz	18 mK
1410-1900 GHz	52 mK
2400-2700 GHz	73 mK

Table 4. The mapping speed in arcmin² per hour to achieve the stated noise level in a fully sampled map

Frequency, GHz	noise level, $\sigma T^* / K$	mapping speed $((\text{arcmin}^2 \text{hr}^{-1})$
500	0.1	530
1000	0.3	290
2500	1	41

4 SUMMARY

We have described the focal plane unit of *HIFI* as proposed for FIRST. According to the current mission schedule, the instrument will be launched at the end of 2005 and will provide the first high resolution view of the sub-mm universe unaffected by absorption in the Earth's atmosphere.

5 ACKNOWLEDGEMENT

We gratefully acknowledge the contributions of the following people:

- M. Carter, K-F. Schuster: IRAM, France.
- G. Beaudin, M. Gheudin, M. Salez: Observatoire de Paris, France.
- F. Lura, G. Schwaab: DLR Berlin, Germany.
- K. Jacobs, C. Honingh, R. Schieder, J. Stutzki: Köln University, Germany.
- P. Zimmermann: Radiometer Physics, Germany.
- A. Murphy: St. Patrick's College Maynooth, Ireland.
- E. Natale: CNR Firenze, Italy.
- R. Orfei: Frascati, Italy.
- D.A. Beintema, J.R. Gao, B-J. van Leeuwen: SRON, The Netherlands.
- J.D. Gallego-Puyol, J. Martin-Pintado: Centro Astronomico Yebes, Spain.
- J.P. Stursky: Chalmers Univ. of Technology, Sweden.
- S. Withington: MRAO Cambridge, UK.
- B. Ellison, D. Matheson: RAL, UK.
- T. Phillips, J. Zmuidzinas: CALTECH, USA.
- N. Erickson: FCRAO UMass, USA.
- T.C. Gaier, R. McGrath, J.C. Pearson: JPL Pasadena, USA.

A LOCAL OSCILLATOR SYSTEM FOR THE FIRST HETERODYNE INSTRUMENT

Gerhard W. Schwaab^a, John C. Pearson^b, Nicholas D. Whyborn^c

^aDLR Institute of Space Sensor Technology,
Rudower Chaussee 5, D-12489 Berlin, Germany
e-mail: gerhard.schwaab@dlr.de

^bJet Propulsion Laboratory
4800 Oak Grove Drive, Pasadena, CA 91109, USA

^cSpace Research Organisation of the Netherlands
P.O. box 800, NL-9700 AV Groningen, The Netherlands

Abstract

The Heterodyne Instrument for FIRST (HIFI) shall cover the full frequency range from 480 to 1250 GHz plus two additional parts of the spectrum around 1.6 and 2.6 THz. To be able to cover this frequency range, the Focal Plane Unit and the Local Oscillator Unit of HIFI will be split into 6 channels. The Local Oscillator Unit will be located at the outside of the satellite's LHe dewar and will be operated at a temperature of about 100 K. Each of the channels 1 to 5 consists of 2 chains of wide bandwidth HEMT power amplifiers in the 60 to 110 GHz range feeding wide-band planar multipliers. To provide enough output power to pump two mixers at perpendicular polarizations wire grid beam splitters will be used. The amplifiers are fed by an actively multiplied tunable YIG oscillator which is located in the ambient temperature service module part of the satellite. The 6th channel is split into a 1.6 and a 2.6 THz part. Here, optical mixing in LTG GaAs will provide the LO power to feed a set of HEB mixers. The overall LO system design as well as the necessary development program are described.

Introduction

The ESA cornerstone mission 'Far-Infrared and Submillimeter Telescope' (FIRST)^{1,2} will consist of a 3.5 m telescope that is mounted on a LHe cryostat. It will give the first opportunity to cover a large part of the submillimeter and far-infrared wavelength range with a sensitivity close to the quantum noise limit at high angular and spectral resolution and without damping absorption of atmospheric water vapor and trace gases. A heterodyne instrument on FIRST will allow to study the complex chemistry and dynamics in a variety of astronomical sources ranging from comets to distant galaxies³. Essential to achieve this goal will be a complete coverage of a wide frequency range. Therefore, (HIFI) shall cover the full frequency range from 480 to 1250 GHz plus the astronomically important spectral regions from 1410 to 1910 GHz and from 2400 to 2700 GHz. HIFI consists of four sub units, the Focal Plane Unit inside the cryostat, the local oscillator system, the IF section, and the control electronics. This paper describes the current baseline for the LO system.

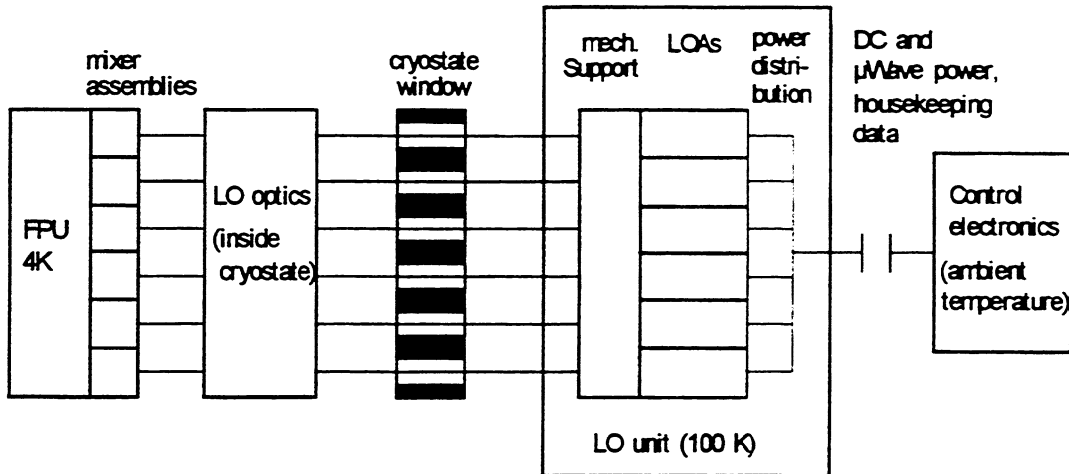


Figure 1: Schematics of the LO system with respect to the focal plane unit (FPU)

General Description

The design of the LO system is driven by the choice of mixer frequency bands and mixer properties, and by the spectroscopic requirements, i.e. maximum resolution and bandwidth. The HIFI frequency range is split into 6 mixer bands which are operated in double sideband (DSB) mode⁴. The lower five mixer bands are equipped with SIS mixers with an IF range from 8-

12 GHz. Band 6, which is called the ultra-high frequency channel (UHF) will be equipped with hot electron bolometric mixers (HEBMs) with an IF range from 2-6 GHz.

The HIFI backend will consist of a high resolution spectrometer with a resolution of 0.1 MHz at a minimum bandwidth of 500 MHz and a wideband spectrometer with a resolution of 1 MHz and a bandwidth of 4 GHz.

An overview of the local oscillator part of

Table 1. Proposed mixer, local oscillator and amplifier frequency bands (* for band 6 the baseline is to use a photomixer LO source)

mixer band	operating range, GHz	LO band	tuning range, GHz	multiplier stages	LO amplifier frequency band, GHz
1	480–642	1a	492–550	x2x2x2	61.5–68.8
		1b	572–630	x2x2x2	71.5–78.8
2	640–802	2a	652–710	x2x2x2	81.5–88.8
		2b	732–790	x2x2x2	91.5–98.8
3	800–962	3a	812–870	x2x2x3	67.7–72.5
		3b	892–950	x2x2x3	74.3–79.2
4	960–1122	4a	972–1030	x2x2x3	81.0–85.8
		4b	1052–1110	x2x2x3	87.7–92.5
5	1120–1250	5a	1132–1174	x2x2x3	94.3–97.8
		5b	1196–1238	x2x2x3	99.7–103.2
6	1410–1910 2400–2700	6a	1414–1906	x2x2x2x3*	58.9–79.4
		6b	2404–2696	x2x2x2x3*	100.2–112.3

the HIFI instrument is given in Figure 1. It consists of a coupling optics part inside the LHe vessel, the Local Oscillator Unit and the LO control electronics.

The Local Oscillator Unit will be arranged in 6 local oscillator assemblies (LOA's) with a spacing of about 50 mm between the optical axes of adjacent LOAs yielding one optical plane per mixer band which eases alignment and gives a high degree of modularity. The LOAs are fixed to a mechanical support structure. Each LOA feeds both polarizations of the Focal Plane Unit's mixer bands.

The LO control electronics, which is sited in the service module of the satellite and which also supplies the electrical and microwave signals needed by the Local Oscillator Unit, monitors the LO system, and reports its status to the instrument control unit.

For bands 1 to 5 the high IF frequency and DSB mixer operation is used to reduce the tuning range required from the LO, but to ensure a smooth transition between adjacent mixer bands a band overlap of 2 GHz

was assumed. Further, due to the restricted tuning ranges of sub-mm LO sources, we have chosen to use two LO sources to cover each mixer band. Only one LO source is operational at any given time. This LO pumps two mixers operating on orthogonal polarizations.

Assuming equal tuning ranges for the upper and lower LO sources for each mixer band, the above leads to minimum LO tuning ranges of 58 GHz for bands 1 to 4 and 42 GHz for band 5. We expect that the tuning range of LO sources will be increased in which case we can use any overlap between the coverage of upper and lower LO sources for each band to increase the redundancy. An overview of the different frequency bands applicable to HIFI is given in Table 1.

LO Sources

For bands 1 to 5, the listed tuning ranges can only be achieved if a broadband, high-power mm-wave source is available to drive the varactor frequency multiplier chain. In our baseline design we propose

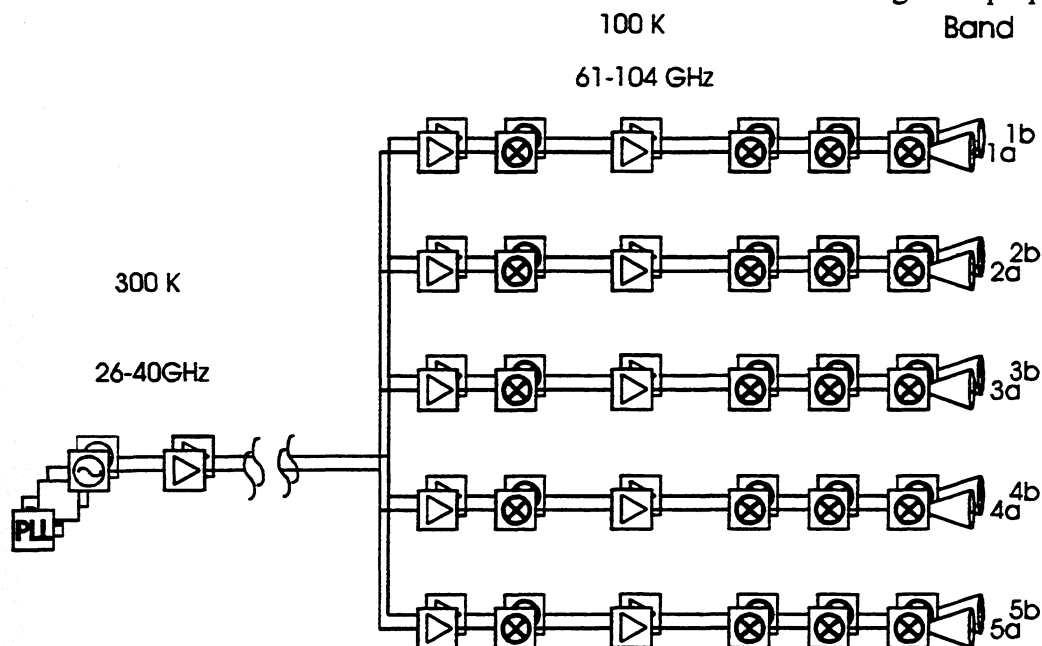


Figure 2: Schematic diagram of bands 1-5 of the LO system using power amplifiers

Table 2: Current performance of whisker-contacted and planar frequency multipliers

Type	Multiplication	Output Frequency GHz	Output Power mW	Efficiency %
planar	x2	160	77	22
whisker	x2	167	30	30
whisker	x2	190	15	15
planar	x2	240	6	15
planar	x2	320	9	13
whisker	x3	334	7	10
whisker	x2	384	1.5	10
whisker	x2	500	2 (est.)	20 (est.)
whisker	x3	800	0.04	4
whisker	x3	1000	0.06	1

to use custom high-power mm-wave amplifiers manufactured by TRW⁵ to drive cascaded frequency multipliers. Such an LO source has already been demonstrated to work well at 500 GHz. A possible backup solution using mm-wave Gunn oscillators to drive the multiplier chains (as used in almost all ground-based sub-mm receivers) is unlikely to have the required electrical tuning range. In this case we would either have to resort to mechanically tuned Gunn oscillators or use 4 LO sources per mixer band and a more complex optical setup employing fixed tuned diplexers. For band 6 laser photomixers are under development. A schematic diagram of the LO channels 1 to 5 is shown in Figure 2.

LO Sources for Bands 1 to 5

High Frequency Power Amplifiers

The successful development of GaAs p-HEMT MMIC power amplifiers in the 60-110 GHz frequency range makes it feasible to use them as the broadband sources to drive the frequency multiplier chains. Units manufactured at TRW have demonstrated output powers of 350 mW, an output power far exceeding what is

available with Gunn devices. Presently, instantaneous bandwidths of 10 GHz are available but with modest further development this is expected to increase to 15 GHz.

Frequency Multipliers

An overview of state-of-the-art varactor frequency multiplier performance is given in Table 2. Generally, at lower frequencies, planar and whisker-contacted multipliers show rather similar performance. However, considering the reproducibility needed for a satellite project, the high power-handling capability and the wide bandwidth needed for the HIFI LOs, planar Schottky diodes will be used for at least the first stage of the varactor multiplier chains^{6,7}. As backup, particularly for the high-frequency multiplier stages, whisker-contacted multipliers will be used⁸. Although the whisker contact is difficult to manufacture, it presents an important 'free' parameter for matching the diode to the embedding circuitry. Due to its extremely low mass it is not very vulnerable to vibration and such devices have flown on various satellites (e.g. MLS on UARS, MAS on the Space Shuttle). For the final design, several LO chain and technology options will be considered.

Various multiplication schemes are feasible to generate an LO signal at THz frequencies. Best results are obtained with a cascade of multipliers with small multiplication factors ($\times 2$ or $\times 3$), since they provide the highest efficiency and are easier to make broad band. A design goal is to cover a full mixer band with a single multiplier chain. This way we obtain full redundancy with the second chain.

As baseline we have chosen an amplifier driving a cascade of 2 planar frequency doublers followed by a whisker contacted final stage of frequency multiplication. As an option we will actively pursue a goal of integrating the first 2 doublers into an MMIC since development work in this area has already shown very promising results. This goal will open up the possibility of combining the amplifier and MMIC multiplier in a single package with consequent benefits of improved performance, reduced mass and smaller volume.

Band 6: Laser Photomixer Local Oscillator

In the Laser Photomixer Local Oscillator⁹ two near-IR laser beams are combined in a photomixer to generate a difference frequency in the THz region. The current system concept is composed of four different components; the laser sources, the optical processing hardware, the control electronics, and the photomixer assembly (see Figure 3).

Two laser sources are currently under evaluation: a Distributed Bragg Reflector (DBR) laser diode with external optical feedback, and an external cavity diode laser. In both cases the laser source includes a laser with its respective optical feedback mechanism and the necessary isolation and optics to couple the radiation into Polarization Maintaining (PM) single mode fiber.

The optical processing unit is assembled from fiber-optic components, and includes two Electro Optic Modulators (EOM), a number of directional couplers, a wave-meter, a Cs reference cell, a number of photo detectors, an Ultra Low Expansion (ULE) high finesse cavity and an optical amplifier (MOPA). A MOPA amplifier has demonstrated the ability to amplify two laser signals separated by more than 10 GHz.

The control electronics supply the current and feedback to the lasers, and provide all the necessary signal processing to control the laser source frequencies. A microprocessor controls the operation of the laser frequency locking system. To date, a line width (FWHM) of 500 kHz has been demonstrated along with all-day lock times using 852 nm DBR lasers. The ability to generate any offset frequency to 100 kHz within the 1.5 THz tuning range of the lasers has been demonstrated. Optical feedback experiments at Caltech have demonstrated that a 100 kHz line width is possible.

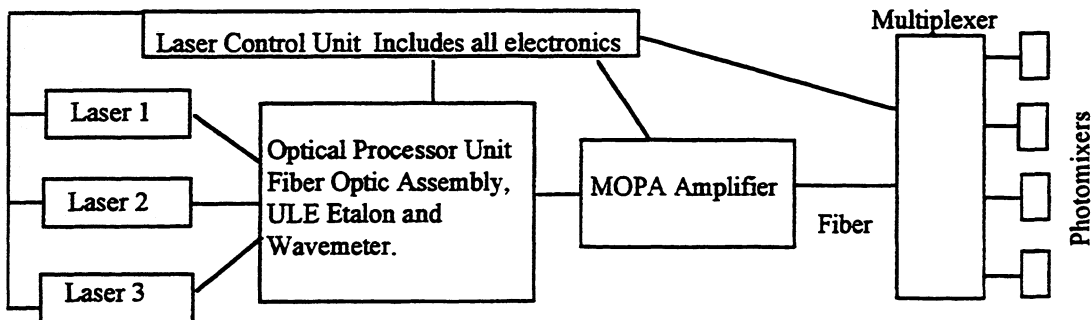


Figure 3. Laser photomixer LO source block diagram

Current etalons have free spectral ranges of ~3 GHz. The current baseline is to use a system with three external-cavity lasers. The reference laser and the offset laser would be fixed tuned gratings (tuning bandwidth ~60 GHz), while the second cavity locked laser would be a tuned grating device (tuning bandwidth ~10 THz). The two fixed tuned devices would lie near the 371 THz Cs line and would use that to determine the cavity order for the reference laser and tune the microwave frequency offset around the cavity order picked. The cavity order of the second laser would be determined by a wavemeter with better than a free spectral range resolution. The free spectral range of the etalon will be measured to better than the required part in 10^8 accuracy. Several suitable calibration methods are known and the actual calibration procedures will be developed and evaluated this year.

LO Assemblies

There are two types of local oscillator assemblies (LOA), the standard version for bands 1-5 using frequency multiplier chains, and a photomixer version for band 6.

LO Coupling Optics

The design drivers for the calculation of the detailed optical parameters of the LO beam-guide are the geometrical f/D ratio of the beams entering the mixer assemblies, the locations of the relevant components as defined by the satellite set-up (e.g. position of the Focal Plane Unit, position of cryostat window, etc.), and the requirement to minimize the IR heat load through the cryostat windows. In addition, the LO coupling shall be wavelength independent within a mixer band, and the optical path between the first mirror outside the dewar and the LO source has to be large enough to accommodate for the nec-

essary optical components. This is especially important in the case of the backup solution with four LO sources per band that are coupled by fixed tuned diplexers. In that case, a third focusing element will have to be implemented.

To minimize diffraction effects, aperture diameters of the optical elements are chosen as four times the $1/e^2$ beam radius within the element.

A detailed study of the different design criteria resulted in the need of a minimum of 2 focusing elements along the optical path, one inside and one outside the cryostat. However, there is some flexibility in the choice of beam sizes and this will be exploited, for example, to reduce the size of the LO window in the cryostat or to relax the lateral alignment tolerances between the local oscillator unit and the focal plane unit.

Local Oscillator Assembly for Bands 1 to 5

The LOA for bands 1 to 5 (see Figure 4) consists of a small optics part with a focusing mirror and a wire grid beam combiner and two essentially identical LO sources oriented with orthogonal polarization. Together these two sources provide full frequency coverage of the particular mixer band. The chosen arrangement of two LO sources (one operational) pumping two mixers on orthogonal polarizations can be implemented with minimal

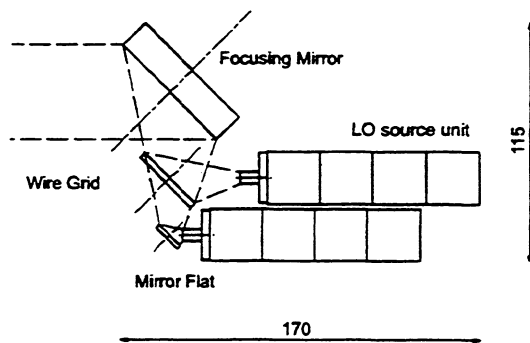


Figure 4. Layout of the local oscillator assembly for bands 1 to 5

loss.

Local Oscillator Assembly for Band 6

The photomixer assembly will include a fiber multiplexer feeding a set of fiber-coupled photomixers. Each photomixer will be integrated with a planar antenna on high resistivity Si lens to couple out the sub-mm radiation efficiently. Photomixers have been demonstrated to provide output power at 1.6 and 2.6 THz. However, this power is still not enough to drive the HEB mixers at the frequencies needed for band 6. Further photomixer development is currently focused on improving device performance and reliability by research in the areas of faster materials, increased output power and efficiency, and increased input power handling. The current plan is to use local heaters to warm the photomixers to above 250 K so that 852 nm lasers can be used.

All of the laser system except the photomixers will reside in the service module of the FIRST satellite. Transmission of the signal to the photomixer will take place in PM fiber which has a loss of less than 3 dB/km.

To minimize optical losses in the bands 6a and 6b, the two beams will be conducted separately through the window section of the satellite's LHe vessel and combined again inside the cryostat to feed the mixer assembly of band 6.

The LO Control Unit

The LO control unit will perform several functions. It will allow the selection of the proper LO band, provide the drive frequency for the local oscillator unit and adjust the power level to the LO to the mixers. In addition, the LO control unit will supply and monitor the bias for the multipliers and amplifiers and provide the DC/DC power conversion.

The LO control unit will provide the microwave signal to drive the power amplifiers (see Figure 2). The high stability oscillator will provide the reference frequency for a synthesizer which will have an output in the 26 to 40 GHz range. The output of this oscillator will be amplified, and fed to the Local Oscillator Unit via low loss coaxial cable. The step size of the synthesizer has to be small enough to have two steps within the 500 MHz minimum bandwidth of the high resolution spectrometer backend. With a maximum overall multiplication factor of 36 in bands 1 to 5 this leads to a step size in the order of a few MHz to a few tens of MHz. Within the Local Oscillator Unit, the 26 to 40 GHz signal will be distributed to the different LO assemblies. The feed signal will be further amplified and, depending on the frequency range of the LO assemblies, doubled or tripled for each band separately. With a second chain full frequency coverage and a high degree of

Table 3. Local oscillator spectral purity and stability.

Parameter	value	notes
Frequency accuracy	1 part in 10^8	
Linewidth	25 kHz	
Carrier-to-noise ratio	70 dB	0.1 MHz offset
	90 dB	1 MHz offset
	139 dB	2 GHz offset
	155 dB	10 GHz offset

redundancy will be obtained.

In order not to compromise the frequency resolution or sensitivity afforded by the instrument it is necessary that the LO signal is of high spectral purity and stable in frequency. Table 3 lists the necessary requirements.

The Interface to the Satellite

The local oscillator unit will be bolted to a plate or space-frame on the side of the satellite's payload module over 3 fixation points. The mechanical interface will mechanically support the Local Oscillator Unit and will be used to maintain its alignment with respect to the Focal Plane Unit. The LO unit is thermally insulated from the payload module by a low heat conductivity mounting structure and, optionally, by a thermal radiation shield. The heat generated by the LO unit will be radiated into deep space to achieve an operating temperature of 100–150 K.

Discussion

The HIFI LO system described above has some intriguing features. It is compact, shows a high degree of modularity, and is relatively simple considering the complexity of functions it has to perform.

To ensure the feasibility of the described LO system and to increase the redundancy, several items need further development. For channels 1 to 5, this holds especially for the MMIC power amplifiers and the planar and whisker contacted multipliers. The efficiency and output power of both items have to be increased as well as their bandwidth and reproducibility.

For the multipliers the development goal is broad band operation without mechanical tuners. To save cost, scaled planar doublers will be developed at least for the first multiplication stage. We hope to be able to

integrate up to the first two multiplier stages into the power amplifier module.

Concerning channel 6, the efficiency and output power of the laser photomixer LO has to be increased even considering the low power levels requested by the HEB mixers.

Finally, the layout of the LO optics will have to be refined to be able to relax alignment tolerances of the LO unit relative to the focal plane unit at minimized window losses and to further reduce the size and mass of the LO unit.

Summarizing, a compact LO system for the HIFI instrument is within reach. Current estimates of the size and mass of the most critical part of the LO system, the LO unit, yield dimensions of $200 \times 130 \times 300 \text{ mm}^3$ and a mass of less than 10 kg. Since only one LO chain will be operational at any given time, the power consumption of the LO unit can be kept below the 6 W limit, that has been specified by ESA.

Acknowledgments

It is a pleasure to acknowledge the contributions of the members of the HIFI LO group, who are:

A.Räisänen, Finland,

M.Carter, IRAM, France

G.Beaudin, M. Salez, A. Maestrini,
DEMIRM, France

F.Lura, H.-W. Hübers, H.P. Röser, R.

Bauer, DLR, Germany

P.Zimmermann, R. Zimmermann, RPG,
Germany

A.Murphy, St. Patrick's College
Maynooth, Ireland

M.W.M. de Graauw, H. van de Stadt, K,
Wildeman, H. Aarts, SRON, Netherlands

E.Kollberg, V. Belitsky, S. Torchinsky,
Chalmers University of Technology, Sweden

U.Frisk, SSC, Sweden

A.Emrich, OMNISYS, Sweden

S.Withington, R. Hills, MRAO, UK

B.Ellison, D.Matheson, RAL, UK
 T.Phillips, J.Zmuidzinas, G. Blake, Cal-
 Tech, USA
 N.Erickson, FCRAO, UMass, USA
 M.Mahoney, E. Cohen, M. Frerking,
 W.Gray, C.Lawrence, H.LeDuc,
 R.MacGrath, P.Siegel, JPL, Pasadena,
 USA
 C.Cunningham, S. Claude, HIA, Canada

References

1. G. Pilbratt, „The FIRST Mission: Baseline, Science Objectives and Operations“, Proc. Of the ESA symposium on The Far Infrared and Submillimeter Universe held at Grenoble, France from 15-17 April 1997, ESA SP-401, pp. 7-12, 1997
2. J.A. Steinz, „The FIRST Project“, Proc. Of the ESA symposium on The Far Infrared and Submillimeter Universe held at Grenoble, France from 15-17 April 1997, ESA SP-401, pp. 13-17, 1997
3. E. van Dishoeck, „The Importance of High-Resolution Far-Infrared Spectroscopy of the Interstellar Medium“, Proc. Of the ESA Symposium on The Far Infrared and Submillimeter Universe held at Grenoble, France from 15-17 April 1997, ESA SP-401, pp. 81-90, 1997
4. see: N. Whyborn, M. de Graauw, H. van de Stadt, „The Focal Plane Unit of the Heterodyne Instrument for FIRST (HIFI)“ in this volume
5. P.-P. Huang, T.-W. Huang, E. W. Lin, Y. Shu, G. S. Dow, R. Lai, M. Biedenbender, J. H. Elliott, „A 94-GHz 0.35 W Power Amplifier Module“, IEEE Trans. MTT 45 (12), pp. 2418-2423, 1997
6. J. Bruston, R.P. Smith, S.C.Martin, A. Pease, P.H. Siegel, „Progress Towards the Realization of MMIC Technology at Submillimeter Wavelengths: A Frequency Multiplier to 320 GHz“, submitted to IEEE-MTTS International Microwave Symposium, Dec. 1, 1997
7. see N. Erickson, „Wideband High Efficiency Planar Diode Doublers“ in this volume
8. R. Zimmermann, T. Rose, T. W. Crowe, T. W. Grein, Proc. of the Fifth Int. Space Terahertz Symposium, Pasadena, March 1995
9. see S. Verghese, K. McIntosh, S. Duffy, E. Brown, S. Calawa, K. Molvar, W. Dinatale, T.Lyszczarz, „Photomixing in Low-Temperature Grown GaAs for Generating Coherent Radiation Above 1 THz“ in this volume

WIDEBAND HIGH EFFICIENCY PLANAR DIODE DOUBLERS

Neal Erickson
Department of Physics and Astronomy
University of Massachusetts
Amherst, MA 01003
Email: neal@fcrao1.phast.umass.edu

ABSTRACT

Very wideband heterodyne receiver systems are planned for many astronomical applications during the next 5-10 years extending up to 2.7 THz for space and airborne applications. At present the only means to provide sufficient local oscillator power for these submillimeter receivers is the Schottky varactor diode frequency multiplier. Using these devices in a chain of multipliers will require high output power with high efficiency in the early stages. This paper describes two new designs for planar varactor doublers which cover wide bandwidths with fixed tuning. A doubler for 150 GHz has 28% peak efficiency with a 3 dB bandwidth of 130-168 GHz. Room temperature output is 25-40 mW and the efficiency increases to a peak of 37% with ~55 mW output when cooled to 80 K. A similar doubler has been designed for 270-340 GHz.

INTRODUCTION

Very wideband heterodyne receiver systems are planned for many astronomical applications during the next 5-10 years. These include the SOFIA airborne observatory, the FIRST spacecraft, the Millimeter Array (MMA), the Submillimeter Array and numerous single antenna ground based observatories. Of these, the requirements for FIRST and SOFIA are the most demanding in terms of frequency coverage although the MMA will require by far the most receiver systems. At present, there are plans to include receiver systems on FIRST which may extend up to 2.7 THz, and on SOFIA up to 1.9 THz. Currently the only means of supplying this LO is the Schottky varactor frequency multiplier. All of these systems require the maximum bandwidth in all of their LO components, and it is desired that the LO components use planar technology wherever possible. This paper describes work on frequency doublers which demonstrate the potential to build wideband fixed tuned planar diode doublers centered at frequencies of 150 and 300 GHz, with sufficient power output to drive subsequent multiplier stages.

Planar diodes have shown the potential to replace whisker contacted diodes throughout the mm and submillimeter range, with performance in many types of devices which is as good or better than the whiskered diodes they replace. Planar diode arrays have been used in balanced doublers for 160 and 320 GHz [1,2], achieving very high power output and efficiencies at both frequencies. However, planar diodes include higher parasitic capacitance than is usually present in whiskered diodes, and this extra capacitance tends to limit the matching bandwidth that is possible with fixed tuning. Planar diodes also open up many additional circuit concepts that are not practical with whisker contacts, and this additional circuit flexibility in many cases more than compensates for the higher parasitics. The doublers described here have fixed tuned bandwidths which are larger than has been accomplished with whiskered designs, and are very efficient. They also are fairly easy to fabricate and are sufficiently robust that they can survive and operate at 77K.

CIRCUIT DESIGN

The doubler circuits are based on balanced designs using 4 diodes, which have been previously built for 160 and 300 GHz. Earlier models have achieved high efficiencies, with a maximum power output at 160 GHz of 63 mW, and a maximum output of 7.5 mW at 320 GHz. These results were obtained with a circuit originally designed for whiskered diodes, which could deliver high efficiencies only when tuned for narrow bandwidths [1,2,3]. The new 150 GHz doubler uses the same four diode arrays that were used previously (UVa batch SC6T6) and achieved an efficiency of 40% in doubling to 158 GHz, while the 300 GHz doubler uses the same diode arrays (UVa batch SB3T2) that were used in the previous 300 GHz design, and gave doubling efficiencies of 18% at 280 GHz and 13% at 320 GHz. However, the actual circuits have been extensively changed to maximize the bandwidth, and also to make machining and assembly as easy as possible. The configurations of these diodes are shown in Fig. 1.

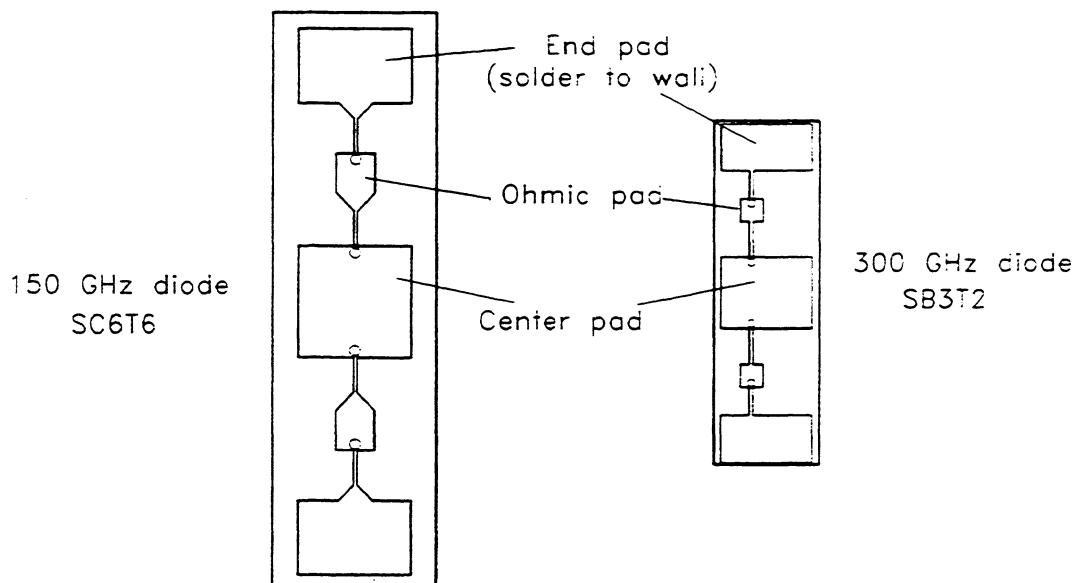


Figure 1. Planar varactor diodes used in the two doublers. The dimensions of the 150 GHz chip are $800 \times 224 \mu\text{m}$ and those of the 300 GHz chip are $490 \times 135 \mu\text{m}$. Circles mark locations of the anodes.

The diodes were designed somewhat conservatively several years ago, and their relatively large pad sizes, particularly of the intermediate ohmic contacts, would appear to add serious parasitic capacitance. The overall lengths of the diodes were chosen to match the existing whisker contacted doubler designs and had nothing to do with optimized matching for a planar diode. It was believed at the time that the thickness of the GaAs substrate should also be minimized, since it increases the parasitics. However, the studies performed for this design show that the bandwidth of a complete doubler circuit is not critically dependent on any of these concerns, although all of them do have an effect on the final design. As an aid to the building of circuits which should be relatively easily fabricated, we assumed for this design that the GaAs thickness was $37 \mu\text{m}$, although thinner diodes are available. For future layouts, we investigated modifications to the diodes which would improve the power balance between the anodes and also the modification of

the center pads to facilitate wideband matching. The goal of this work is ultimately to make a planar diode where much of the circuit would be incorporated onto the GaAs wafer, but this design is intended as a demonstration based on currently available diodes.

The circuit design is based entirely upon an HFSS [4] analysis of the planar diode as embedded in a waveguide. Experience has shown that this finite element simulator is sufficiently accurate that the results may be used for detailed circuit design without the need for prototyping or scale modeling. The diode is modeled including details of all of the metal pads, but with minimum fidelity to the areas around the anodes. The GaAs substrate is modeled as a uniform slab, without the region of high doping found under the metal pads, and with no channel under the fingers connecting the anode pads with the ohmic pads. The anodes are modeled as very short square coaxial lines which enter into the metal pads and then end. Ports are defined at the ends of these lines and are used as the diode terminals in later circuit simulation. All of the omitted detail makes the diode much easier to draw and very much quicker to simulate, and its effect on the final solution is too small to justify the effort to include it, given a number of more important parameters which are not so well known. All materials are assumed to be lossless, since the effect of losses is expected to be fairly small, and should have little effect on the design so long as inherently high loss geometries are avoided.

For simplicity, the circuit is split in half along the symmetry plane of the waveguide H-plane midline. At the input frequency the symmetry plane is a perfect electric conductor, and the waveguide is extended in both directions for a distance from the diode sufficient to attenuate higher modes, and is then ended with two ports. For the output, the symmetry plane is a magnetic conductor. The center pad of the diode connects to a metal strip extending to one of the waveguide ports, which forms the output TEM port, and the other waveguide port is not used. This method of analysis is essentially the same as that used in reference 5.

The S parameter files created with HFSS are imported into a linear simulator (HP MDS [6]) and the remainder of the circuit is initially designed using ideal circuit elements. In this simulation the diode itself is modeled as a linear element consisting of a series resistor and capacitor. The effective values of these elements were determined using a nonlinear simulation of the diode to be used, with the diode biased to the lowest voltage for which nearly optimum doubling efficiency is obtained. This bias minimizes the diode Q, which is found to be about 5.9 for the input circuit and 2.9 for the output circuit. The assumed zero bias junction capacitance of 45 fF used in the 150 GHz doubler gives an effective capacitance in the simulation of 22 fF, and an effective resistance of 16 Ω at midband. At the output frequency the capacitance is 19 fF while the midband resistance is 20 Ω .

The complete circuit for the 150 GHz doubler can be viewed with a number of simplifications in the following way. At the input the diode has significantly less than optimum inductance to resonate out the diode capacitance. As a result the diode load is quite capacitive, and this reactance is tuned out by placing the input backshort quite close to the diode. The long section of reduced height waveguide, which is necessary for TM₁₁ mode suppression, also acts as an impedance transformer to the higher impedance waveguide. The remaining waveguide lengths were empirically chosen for the best wideband match, using series elements only, and may not represent the best input matching solution. More general forms of a matching circuit, including stubs or irises, may work better, but are more difficult to design. At the output frequency, the diode has too much inductance, and it is necessary to place a semi-lumped capacitor as close as possible to the center pad to tune it out. This capacitance is produced by the initial wide line,

which might work even better if wider, except that it is entirely within the input waveguide and would affect the input circuit. Following this element, the impedance is quite high and a quarter wave high impedance line consisting of a free standing 120 μm wide ribbon is used for matching. Finally, a half wave long mismatched (low impedance) line in coax is used to improve the broadband match. The transition to waveguide was initially designed to have no effect except as a mode transition, but the actual transition used was found to enhance the match after optimization. The output circuit was developed by working outward from the diode, adding circuit elements one at a time with each succeeding length and impedance optimized for the best match into a arbitrary resistive load. This approach ensures that the circuit has some logical structure that is likely to be close to a global optimum. In the end, all of the circuit elements were reoptimized, leading to some significant changes but the same basic concept.

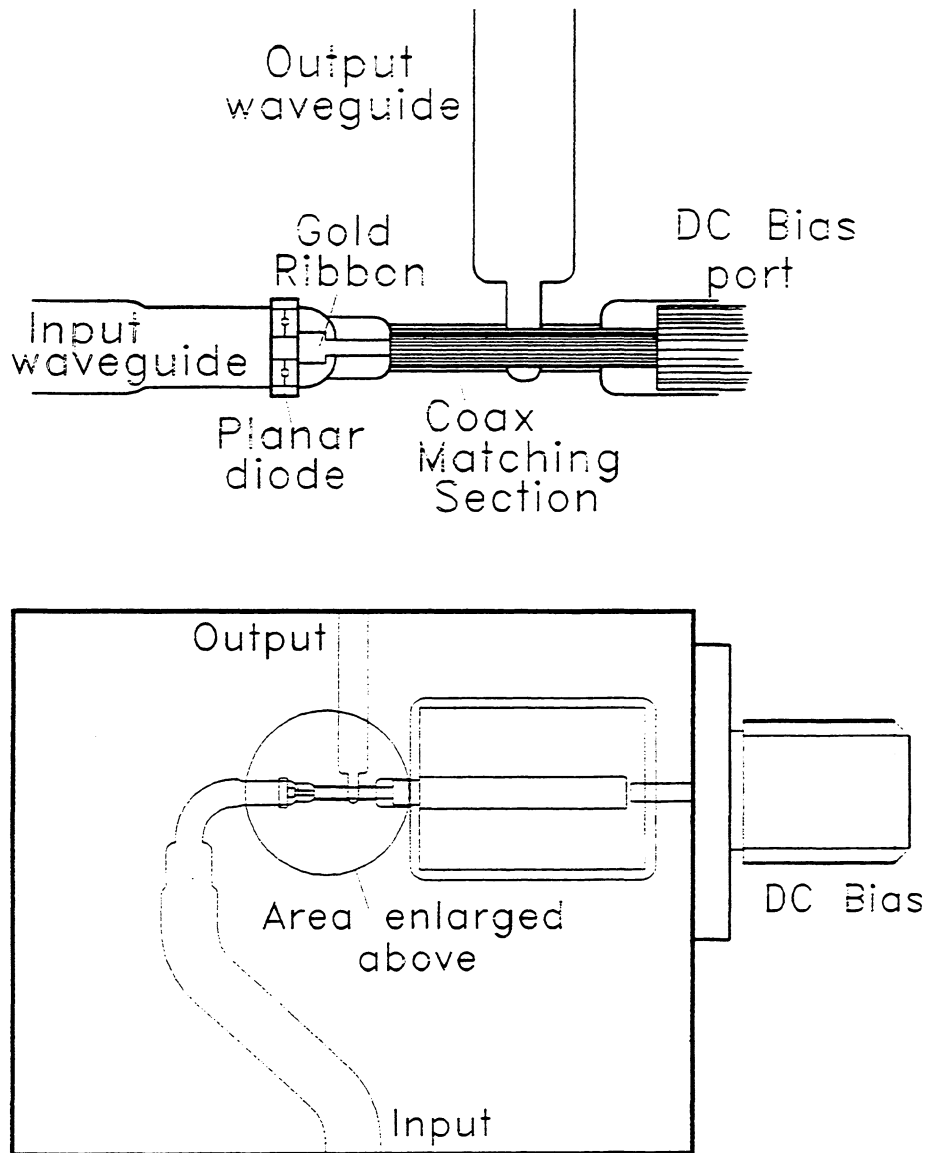


Figure 2. Internal detail (top) and overall view of 150 GHz balanced doubler.

The maximum practical bandwidth was desired, and a circuit was designed covering 135-170 GHz, with an input return loss of 7-8.5 dB over the full band and an output return loss of 9-10 dB. The resulting mismatch losses seemed to be acceptable, and predicted very flat performance over the band. The complete circuit that resulted is shown in Fig 2. The doubler is designed with the input and output directly in line, which requires bending the input waveguide tightly. To save length, one right angle bend occurs within one of the impedance matching sections. The overall size of the block is determined by flange dimensions, with a length of 1.5 cm to accommodate internal flange screws. In this design all circuit elements were constrained to be easily machined, with very high and low impedances eliminated, and both backshorts were machined in place with no provision for adjustment. The only free parameter remaining is the varactor bias voltage, and it is fairly tightly constrained (to 4-5 V per anode) in order for the diode to work well. The design is quite sensitive to varactor capacitance, and adjusting the bias voltage to compensate for errors is not very successful for more than a 10% variation. Diode thickness is also fairly critical as well, although $\pm 12\mu\text{m}$ variation can be tolerated, particularly if the diode capacitance is changed to compensate.

The circuit assembly began by soldering in the coaxial pin which is attached to an insulating pad of an expansion matched circuit board [7]. Then a gold ribbon was cut to the correct shape to form both the low and high impedance sections, and this ribbon was soldered to the diode center pad. The diode and ribbon were laid into the block with the end of the ribbon resting in a cutout in the coaxial pin, and the two outside pads of the diode were soldered to the doubler block. The ribbon was attached to the pin by filling the cutout with conductive epoxy.

The 300 GHz doubler was designed in much the same way except that only the input circuit was designed for maximum bandwidth, with an expected matching band of 270-340 GHz. The output circuit was not designed for such a wide band except with backshort tuning, but is expected to cover the upper half of the band with a fixed setting. This doubler is still being machined so no results are available, but assuming this design is successful, a full bandwidth output circuit would be a straightforward next step. However, a problem with the diode design was noted in this process, which is that the power division between the pair of series diodes is poor in the output band, differing by over 1 dB at the highest frequencies, and is accompanied by a phase shift as well. These problems are particularly apparent if the GaAs thickness exceeds 37 μm , which is desired for the best strength of the chips. The amplitude and phase imbalance decrease the maximum efficiency of the chip and also may lead to unequal bias voltage division, further degrading the efficiency. This problem led to a redesign of the diode chip for future fabrication, with the overall size scaled downward slightly, and the finger lengths adjusted. To facilitate a wideband output match, and also to increase the bonding or soldering area on the chip, the center pad was increased in area significantly. This should allow the output connection to the diode to be simply a high impedance line, while at the input these changes have little effect.

TEST RESULTS

Testing of the 150 GHz doubler was somewhat difficult because its bandwidth exceeds that of any source with sufficient power to drive it. This is a high power doubler and can not be properly tested with an input power below 100 mW. The plan for FIRST and other upcoming systems is to use MMIC power amplifiers to drive the complete LO multiplier chain, but these amplifiers at present are available at only 94 GHz with relatively narrow bandwidths. The purpose of these doublers are largely to demonstrate that such sources are indeed practical, and to justify the effort required to develop the power amplifiers, and other related components. At this time the

only alternative is to use several high power narrow band oscillators, and these limit test frequencies to only a few values. We used IMPATT oscillators at 75, 80 and 85 GHz with power outputs >250 mW, and Gunn oscillators with 80-130 mW output to cover the other parts of the band. Input powers for frequencies above 75 GHz, and all output powers, were calibrated with a well matched, stable calorimeter in WR10 waveguide [8] with an accuracy of 5%. At lower frequencies a commercial WR12 power sensor was assumed to be accurate.

Initially the doubler input and output return loss were measured with a small signal reflectometer to determine the general matching band. This type of measurement is useful because while the resistive part of the diode load under small signal conditions consists only of the series resistance of the diode, the varactor can be biased to simulate the actual large signal capacitance, and the reactive part of the match is much more critical. The resultant return loss curves show very poor match but the bandwidth of the match is representative of the actual large signal match. The measured input return loss showed a fairly flat return loss of 2-3 dB over the band of 65-85 GHz, with a varactor bias of 4.5 V, and a very poor match more than 3 GHz to either side of the band. The band could be shifted significantly through a change in bias, but no other bias produced a flat response. This method may be used to estimate the actual rf series resistance and the fit to this data is 4.5 Ω , as compared to a dc value of 1.7 Ω . At the output the match was measured from 135-170 GHz, and appeared to correspond to the design band, but the match was much better toward the low frequency end, and near 170 GHz was quite poor. These tests showed no narrow features, and served to justify the rather sparse sampling of the band under large signal pump.

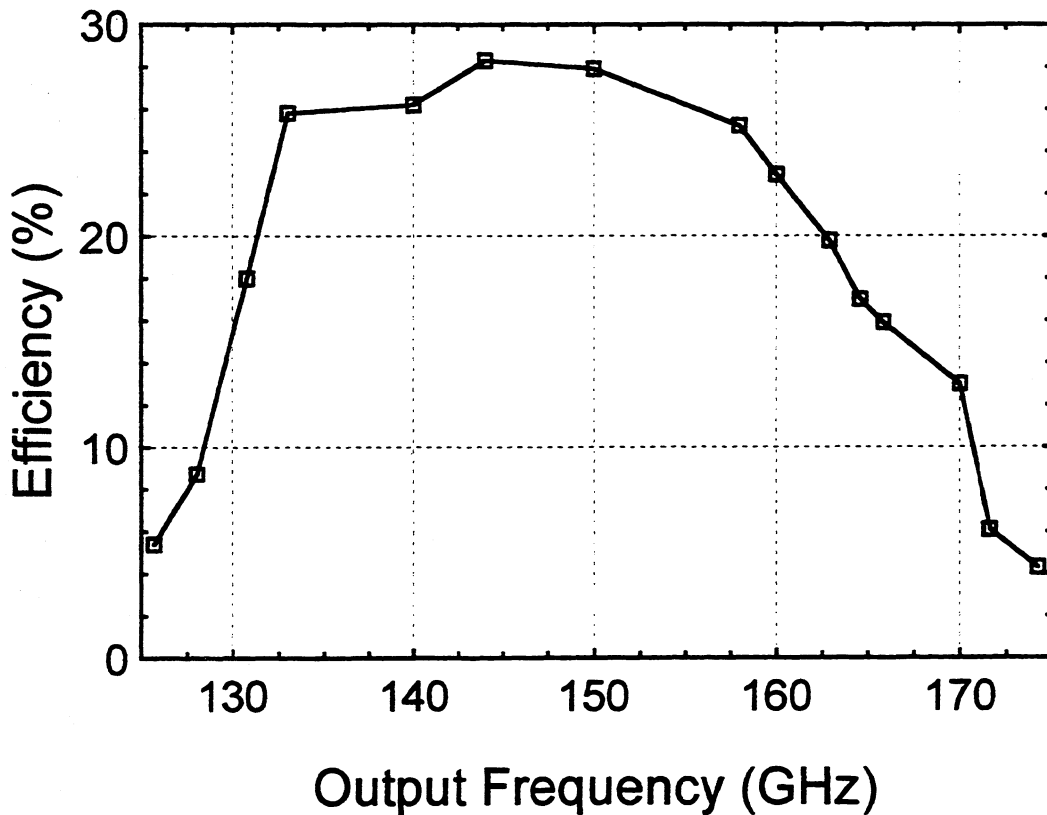


Figure 3. Maximum efficiency of the planar diode doubler. The input power for the best efficiency is 100-150 mW, with the maximum safe input power about 180 mW.

Large signal tests provided the data shown in Fig. 3 which shows the efficiency at optimum input power (or at the highest available power where input power is limited). At all frequencies, the maximum safe input power could be as large as 180 mW, with the efficiency slowly decreasing up to this power. The optimum bias voltage varies from 7 to 11 V across the band, depending on both power and frequency. Bias current is less than 1 mA for an input power below 120 mW. The operating band is shifted slightly lower than the design by about 5 GHz, while the total bandwidth meets expectations. The input return loss was measured at peak efficiency at 70, 75, 80 and 85 GHz and was found to be $6 \text{ dB} \pm 0.2 \text{ dB}$ at all frequencies. While this is less than predicted, the very flat match is as designed. The poorer match is probably due to interactions between the input and mismatched output impedances that were not considered in the design. Other contributions may be small differences between the design and the actual circuit that was fabricated, and diode properties different from those of the design. It is not possible to directly measure the output match of a doubler, but it may be inferred from the improvement possible by adding an output tuner. With an input of 80 GHz, we added a Teflon quarter wavelength plug into the output waveguide and adjusted its position for the greatest output. The power increased by only 10%, indicating that the output return loss is $\sim 10 \text{ dB}$, which is comparable to what is expected. The small signal measurements predict that the output match is better at lower frequencies, and this would appear to be the case based on the flat input match and the higher efficiencies at lower frequencies. Errors in the construction of the TEM line almost exclusively affect the output match, and can easily produce this response. There is no way to be certain of the power that a given varactor is capable of producing, since the dc series resistance is a poor predictor, but using the small signal fitted value of 4.5Ω for R_s , an efficiency of 52% is predicted at 150 GHz. The best previous results with this batch of diodes gave 40% efficiency at 158 GHz output, with 120 mW input, and optimized input and output matching. The best results with this doubler, 28% at 150 GHz, if corrected for the input mismatch alone would give 37% efficiency, and the output loss due to the widebanding circuit is certain to be somewhat greater than that of the previous narrow band circuit, so it appears that this doubler's performance is consistent with expectations.

COOLED OPERATION

The increasing mobility of GaAs with decreasing temperature leads to a reduction of the series resistance and increased efficiency, as well as improved power handling. This makes cooling a multiplier chain an attractive option since each of its stages will improve [9], and at frequencies above 500 GHz the improvement in a single stage may be a factor of three. For this reason this doubler was tested at 77 K by cooling over a bath of liquid nitrogen. A single frequency of 150 GHz was measured, with an input power of 140 mW. The output power increased by a factor of 1.31, bringing the efficiency up to 36%, and the output power to 51 mW. This improvement is comparable to that measured previously in a similar doubler using whisker contacted varactors [10], and is consistent with the known mobility increase in GaAs. The improvement can not be due to a changing impedance match since the bias was unchanged, and the varactor capacitance is very nearly independent of temperature. It should be noted that the diode in this doubler is installed by soldering it in with 96C melting solder, so its operational temperature range is extremely wide. No special effort was made to ensure the survival of the diode over this temperature range except to use a thin gold ribbon as the contact to the center pad of the diode. The doubler block itself is brass with a thermal expansion coefficient very poorly matched to GaAs, but the differential expansion over the length of the diode is only $\sim 2 \mu\text{m}$, and the indium solder has considerable compliance.

CONCLUSIONS

A new frequency doubler has been built with 25% bandwidth to 3 dB points, centered at 150 GHz. The frequency response is flat to within 1 dB over 20% bandwidth and the minimum power output over this range is 40 mW, with ~25% efficiency. The design, using planar diodes, is quite robust mechanically and operates with 30% higher power and efficiency when cooled to 77K. A second doubler for 300 GHz has been designed with comparable bandwidth, but is still under construction. Both doublers were designed with the aid of HFSS, and it appears that this computer program is sufficiently accurate to be the sole tool needed for the design of these devices without additional prototyping or modeling. This circuit is a hybrid construction of waveguide, coax, stripline and a free standing GaAs circuit, which is a bit complex to assemble. The TEM portion of the circuit could be redesigned as a microstrip circuit on quartz as has been done with a wideband 80 GHz doubler [11], which would simplify the assembly. Designing a diode specifically for a wideband circuit should improve the input and output match, and some work in this direction has been done in recent designs, particularly to help the output match. Doublers of these types could form the first stages of a multiplier chain to the THz range.

ACKNOWLEDGMENTS

This work was supported by NASA under grant NAG5-4272 and by JPL under contract 959206.

REFERENCES

1. B.J. Rizzi, T.W. Crowe and N.R. Erickson, "A High-Power Millimeter-Wave Frequency Doubler Using a Planar Diode Array," *IEEE Microwave and Guided Wave Lett.*, pp. 188-190, June 1993.
2. N.R. Erickson, J. Tuovinen, B.J. Rizzi and T.W. Crowe, "A Balanced Doubler Using a Planar Diode Array for 270 GHz," *Fifth Int'l Symposium on Space THz Technology*, pp. 409-413, 1994.
3. P.J. Koh, W.C.B. Peatman, T.W. Crowe and N.R. Erickson, "Novel Planar Varactor Diodes," *Seventh Int'l Symposium on Space THz Technology*, pp 143-156, 1996.
4. Hewlett Packard High Frequency Structure Simulator
5. N.R. Erickson, "Wideband Fixed-Tuned Submillimeter Frequency Multipliers," *Eighth Int'l Symposium on Space THz Technology*, 1997.
6. Hewlett Packard Microwave Design System
7. Circuit board material TMM-3, Rogers Corporation, Chandler, AZ
8. N.R. Erickson and J. Tuovinen, "A Waveguide Tripler for 720-880 GHz," *Sixth Int'l Symposium on Space THz Technology*, pp 191-198, 1995.
9. J.T. Louhi, A.V. Raisanen, and N.R. Erickson, "Cooled Schottky Varactor Frequency Multipliers at Submillimeter Wavelengths," *IEEE Trans. Microwave Theory Tech.*, vol 41, pp. 565-571, 1993.
10. N.R. Erickson, "High Efficiency Submillimeter Frequency Multipliers," 1990 IEEE Int'l Microwave Symposium Digest, pp 1301-1304, Dallas.
11. D.W. Porterfield, T.W. Crowe, R.F. Bradley and N.R. Erickson, "A High-Power, Fixed-Tuned, Millimeter-Wave Balanced Frequency Doubler," preprint of submitted paper.

A BROADBAND FREQUENCY TRIPLER FOR SIS RECEIVERS

by, S. Mahieu, C. M. Mann, J. Stake*, L. Dillner*, S. H. Jones**,
E. Tong***, and J.Thornton****

Rutherford Appleton Laboratory, Didcot, Oxon, UK.

*Department of Microwave Technology, Chalmers University of Technology, Göteborg, Sweden.

**University of Virginia, Charlottesville, VA 22903 USA.

***Smithsonian Institution, Astrophysical Observatory, Cambridge, Massachusetts 02138, USA.

****University of Oxford, Oxford, UK.

ABSTRACT

Considerable success has recently been gained in the design and production of high powered frequency triplers incorporating Schottky varactor diodes. The design approach that was used for this goal has now been turned to the design of fixed tuned, broadband frequency triplers specifically intended for use in SIS receivers.

The tripler reported here makes use of a Heterostructure Barrier Varactor or HBV. A waveguide circuit has been designed that provides more than $50\mu\text{W}$ of output power for an input power of 10mW over a frequency range of 250 - 300GHz completely fixed tuned and without the need for bias.

Further modification of the waveguide circuit should extend the useful fixed tuned bandwidth to greater than 100GHz centred at 300GHz.

INTRODUCTION

Future space missions such as FIRST have a requirement for fixed tuned frequency multipliers. Also, there are now a number of large millimetre and submillimetre astronomical arrays both planned and under construction. These will not be able to rely on tuneable frequency multipliers as the receiver local oscillator source because of the increased system complexity that would result. Consequently the requirement for fixed tuned, ultra broadband sources is now becoming urgent.

When considering the design of broadband frequency sources intended for use with SIS receivers it is important to note that high levels of local oscillator power are not required even though most of the available power is dumped via a 20dB beamsplitter. A design study for a broadband Schottky varactor tripler shows that the idler termination of the second harmonic provides the limitation to bandwidth. This is where the HBV has a considerable advantage. HBV frequency triplers have been demonstrated and are now showing performance levels [1, 2] that are very respectable compared with conventional varactor triplers. Possessing an anti-symmetric capacitance versus voltage (CV) characteristic ensures that only odd order harmonics are produced. In addition, unlike an antiseriess arrangement of varactor diodes, a HBV tripler does not even require a particular configuration of the external RF circuit to cancel out unwanted harmonic products, as is the case for a balanced doubler or quadrupler. Cancellation of unwanted harmonics for a HBV is carried out within the intrinsic device.

In many ways therefore the design of a tripler based on a HBV is similar to that of a fundamental mixer with the added complication of providing a broadband input circuit. This paper discusses the design of a fixed tuned unbiased HBV tripler that has been specifically targeted as an LO source for a fixed tuned SIS receiver operating in the frequency range 250 -300GHz.

TRIPLER DESIGN

The tripler has been designed to provide a minimum of 20 μ W for an input power of 10mW over a frequency range of 250-300GHz. This amount is perceived to be adequate for a well designed SIS receiver, however, in the event this specification was easily surpassed.

As no available custom made tripler mount was available for this work an obsolete varactor waveguide doubler block, NB-6, was used. This doubler was originally designed (in 1978) to operate in a tuned manner from 180-220GHz and so includes both E and H plane tuners on the input but only an E-plane tuner on the output. In addition, the waveguide is standard size (reduced height) for the band below that at which the HBV tripler was intended to work. This choice of block was therefore by no means ideal but was the only one available at the time.

For the design of the block a modified version of the Eisenhart and Khan [3] analysis was used [4]. The Eisenhart and Khan (E & K) analysis models the waveguide configuration shown in figure 1.

The analysis allows the waveguide arms to be terminated in any complex reflection coefficient, the position of which is again arbitrary. In this way it can be used to model the output circuit of the proposed HBV tripler. The code has been modified to take into account the effect of placing a contacting probe across the gap between the end of the post and waveguide wall. This structure is realised in practice by the use of a flat $2\mu\text{m}$ thick gold probe integrated with the quartz microstrip filter. The probe is suspended in air, spanning the waveguide.

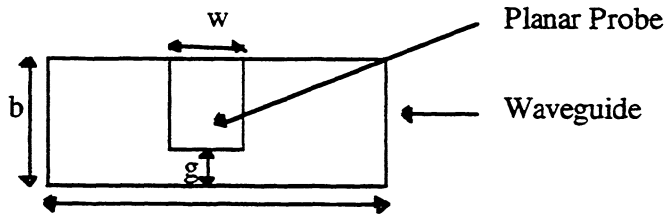


Figure 1: *The Eisenhart and Khan geometry*

The HBV device is then soldered between the end of the probe and the waveguide wall which is formed by the end of the now redundant whisker post. A schematic of this arrangement is shown in figure 2 with a photograph of the inside of the NB-6 doubler block and an SEM of a planar HBV diode chip (UVA-NRL-1174-17).

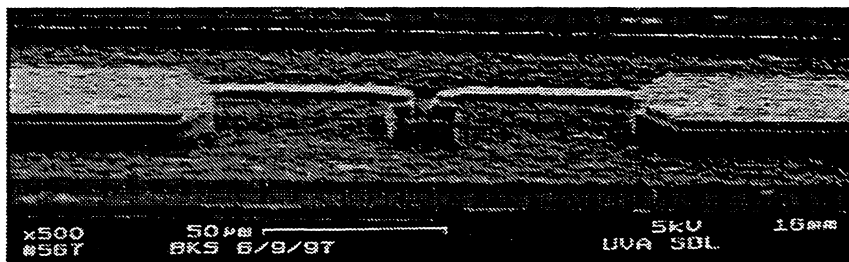
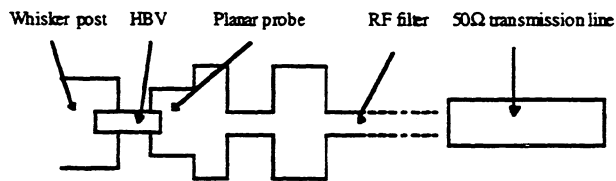
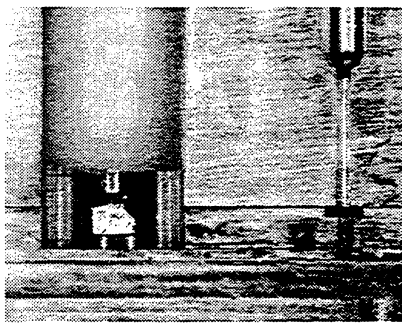
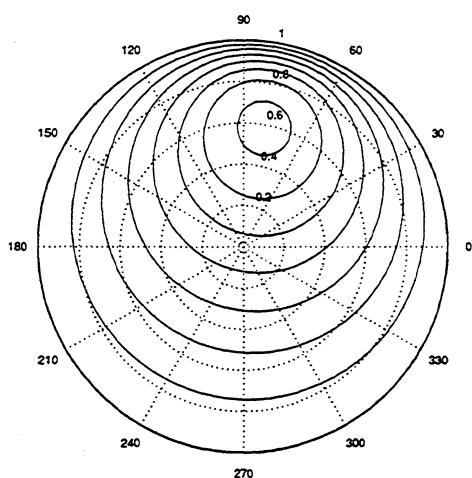


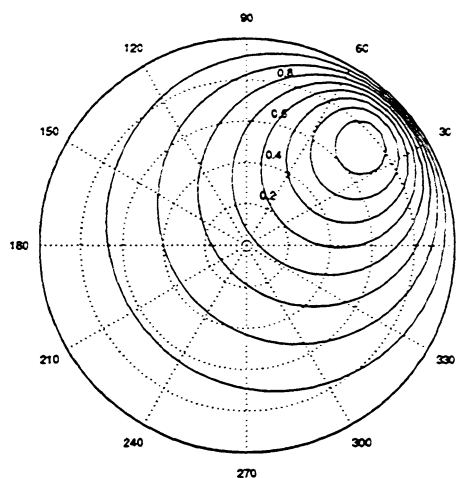
Figure 2: *A schematic of the HBV assembly, and the inside of the NB-6 doubler block*

In order for the tripler mount to be designed accurately (that is the dimensions of the waveguide probe and the microstrip RF filter), a target impedance is required.

An analytical model for a HBV device has been derived [5] and used to produce a two dimensional map of predicted performance (efficiency) as a function of output impedance. This is then plotted on a Smith chart. Two such plots are shown below in figure 3 for $6\mu\text{m}$ and $8\mu\text{m}$ diameter HBVs operating under the conditions indicated.



Contour plot for the $8\mu\text{m}$ diode pumped at 87 GHz and 50 mW input power. The contours corresponds to 1, 2, 3, 4, 5, 6, 7% efficiency respectively. The simulated peak efficiency was 7.8 %.



Contour plot for the $6\mu\text{m}$ diode pumped at 78 GHz and 30mW input power. The contours corresponds to 2, 4, 6, 8, 10, 12, 14 and 16 % efficiency respectively. The simulated peak efficiency was 17.5 %.

Figure 3: *Predicted efficiency as a function of output embedding impedance for a HBV tripler.*

These plots can then be compared with similar plots of predicted embedding impedance as a function of frequency and backshort position, produced using the E & K analysis. Optimisation of the waveguide probe for the NB-6 block was restricted to the variation of the probe width and gap only, as the waveguide dimensions **a** and **b** were not adjustable. Figure 4 shows a series of embedding impedance plots for a frequency range of 200-300GHz as a function of backshort position. The final circuit parameters that gave the most broadband response for the NB-6 mount are, $w = 0.176\text{ mm}$, $g = 0.111\text{ mm}$. It is important to note that the final frequency response available is limited purely by the choice of waveguide dimensions which are fixed. It will be shown later that once the waveguide dimensions **a** and **b** are adjusted a much more broadband device is obtained.

An analytical model for a HBV device has been derived [3] and used to produce a two dimensional map of predicted performance (efficiency) as a function of output impedance. This is then plotted on a Smith chart. Two such plots are shown below in figure 3 for $6\mu\text{m}$ and $8\mu\text{m}$ diameter HBVs operating under the conditions indicated.

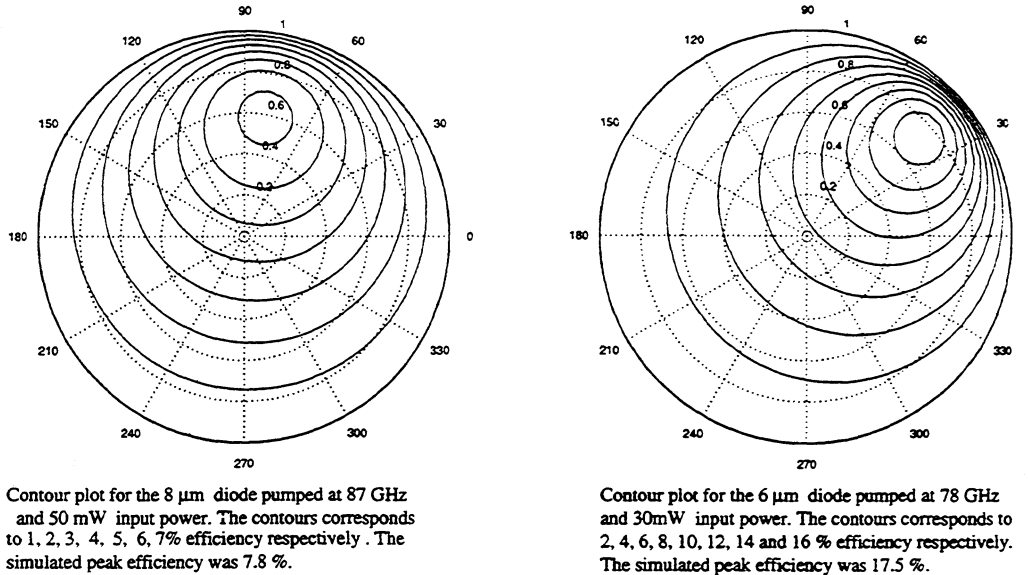


Figure 3: Predicted efficiency as a function of output embedding impedance for a HBV tripler.

These plots can then be compared with similar plots of predicted embedding impedance as a function of frequency and backshort position, produced using the E & K analysis. Optimisation of the waveguide probe for the NB-6 block was restricted to the variation of the probe width and gap only, as the waveguide dimensions **a** and **b** were not adjustable. Figure 4 shows a series of embedding impedance plots for a frequency range of 200-300GHz as a function of backshort position. The final circuit parameters that gave the most broadband response for the NB-6 mount are, $w = 0.176\text{ mm}$, $g = 0.111\text{ mm}$. It is important to note that the final frequency response available is limited purely by the choice of waveguide dimensions which are fixed. It will be shown later that once the waveguide dimensions **a** and **b** are adjusted a much more broadband device is obtained.

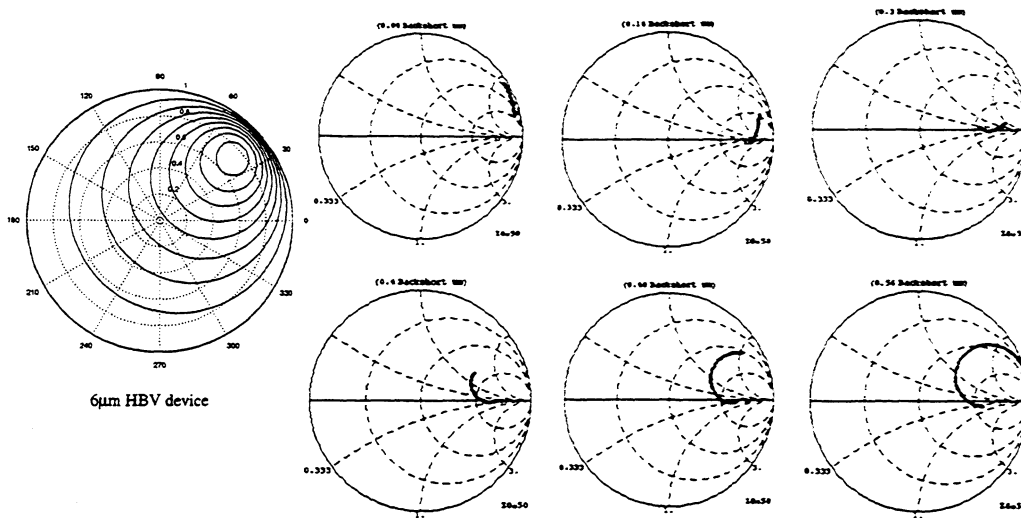


Figure 4: Fixed tuned output embedding impedance as a function of backshort position. For comparison, the efficiency contour plot for a 6 μm HBV is shown on the left.

This series of plots show that for a fixed backshort position it is not possible to provide the optimum embedding impedance over the frequency range 200 - 300GHz. Variation of the probe and HBV position within the waveguide was attempted but a more broadband response could not be obtained. The plots indicate that as the backshort is moved away from the HBV the frequency response would shift. This trend was observed in the real tripler. Further evidence as to the accuracy of the E & K predictions came about by accident when upon insertion into the waveguide the output backshort became trapped at a position of 4.45mm from the HBV instead of a position 0.45mm (the position corresponding to the best broadband response).

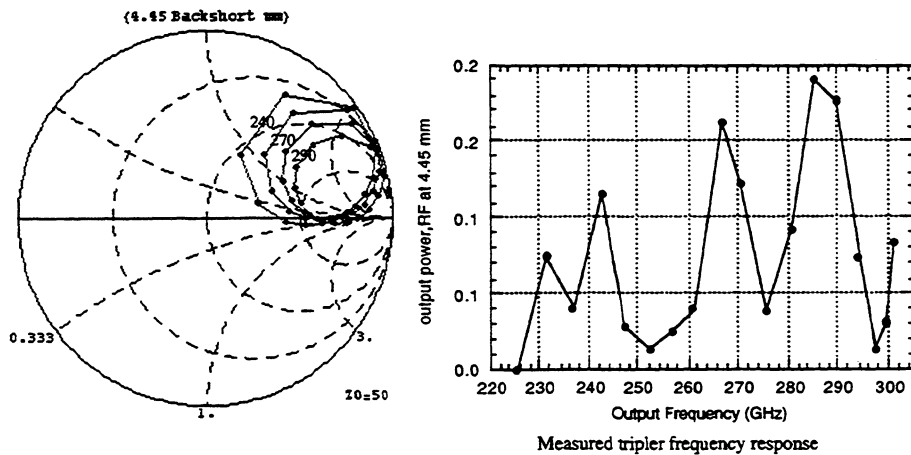
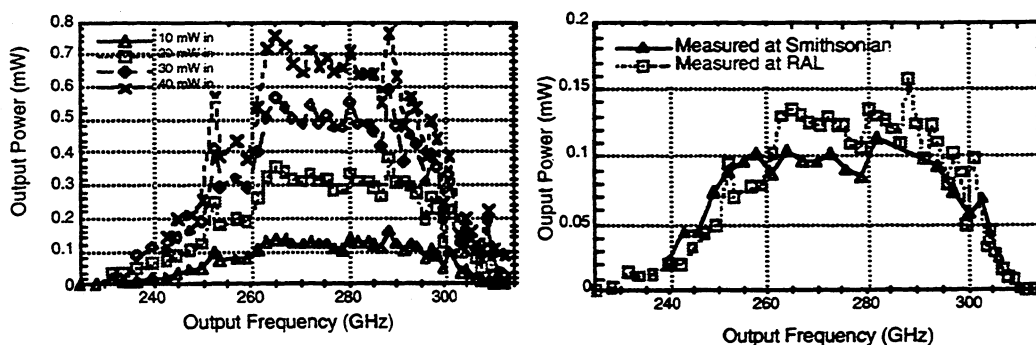


Figure 5: Effect of misplacement of backshort on the broadband frequency response.

This occurred during the first iteration of RF testing. Disappointingly, the tripler showed a far from broadband response, rather a series of resonances. However, once the error with the output backshort was found the E & K analysis was re-run for this backshort position. The results are shown in figure 5. From the E & K analysis a series of resonances is predicted for a backshort fixed this far back from the HBV. Due to dispersion, the frequency response follows a series of loops. As the loops move inside the Smith chart a sharp improvement would be observed followed by a rapid degradation as the output impedance moves towards the open circuit position. Whilst initially a source of some disappointment this exercise did, however, give some indication as to the validity of the design approach.

Once the correct backshort position was obtained the tripler produced a smooth broadband response as expected. The optimisation process was then simply to move the backshort in small increments and measure the frequency response. This was carried out iteratively until the desired response was obtained. The most flat frequency response was obtained for a backshort position of 0.45mm.

The final frequency response, after the backshorts had been locked is displayed in figure 6. For comparison purposes the triplers performance has been measured at the Smithsonian Institute. The output levels measured at both establishments agree well. In addition, the harmonic frequency response of the tripler has been investigated using a Fourier Transform Spectrometer at RAL and no unwanted second or fourth harmonics were observed measured to within the sensitivity of the system.



Final measured frequency response as a function of input power (Backshort fixed at 0.45mm)

Final fixed performance for 10 mW input. Comparison of measures made at RAL and the Smithsonian Institute

Figure 6: Final fixed tuned frequency response for the NB-6 'tripler'.

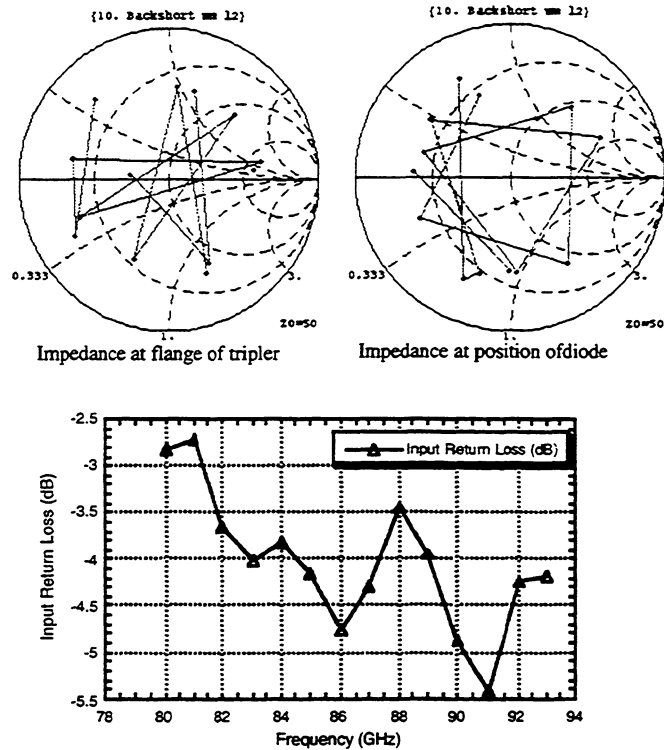


Figure 7: Measured and de-embedded reflection coefficients for the finished tripler.

DISCUSSION

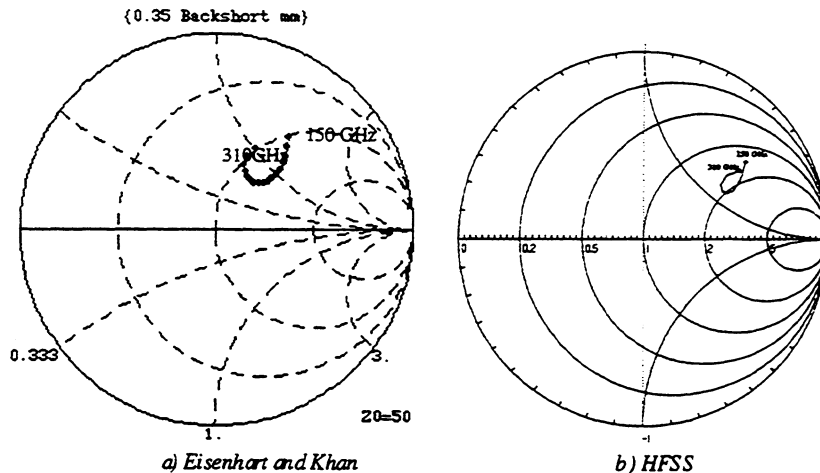
The HBV tripler provides a minimum of $50\mu\text{W}$ for a frequency range of 250 - 350GHz, however, the efficiency is very low, only $\approx 1\%$ over most of the band. The efficiency improves slightly for harder pump power which would imply that this diode is too large in area for the intended 10mW input power available for this application. Another design parameter that could be improved is the input circuit impedance. No attempt has been made to optimise this aspect of the design. The input return loss and reflection coefficients have been measured at the Smithsonian Institute. The results are displayed in figure 7. It can be seen that there are substantial gains to made with regard to this aspect of the device.

However, the area in which most gains are likely to be made involve the complete redesign of the waveguide mount this time including the waveguide dimensions **a** and **b**.

FUTURE POTENTIAL FOR THIS WORK

Before the waveguide mount was completely redesigned a comparison between HFSS and the E & K analysis was first carried out in order to determine the level of

agreement attainable. A simple waveguide structure was modelled for both cases and then compared. Figure 8 shows how the two approaches both predict the same trend. However, the absolute values for the embedding impedances differ but because of the speed advantages (5 seconds for the E & K verses \approx 1 day for HFSS) it was decided that the E & K analysis would be used to obtain the approximate dimensions for the mount and HFSS to be used for final verification.



HFSS and Eisenhart and Khan results for the same waveguide structure i.e.
 $a = 1.35$ mm; $b = 0.1$ mm; $g = 0.035$ mm; backshort at 0.35 mm; width = 0.2 mm
 frequency range: (150 - 310 GHz)

Figure 8: A comparison between Eisenhart and Khan and HFSS

A complete sweep of the waveguide circuit was then carried out to determine the most optimum values for the variable parameters, a , b , w , g and the optimum backshort position. The following figures show the embedding impedance as a function of two of these parameters over a fixed tuned frequency range of 150Ghz -350Ghz.

Similar plots could be shown for the variation of a and b .

Finally the optimised waveguide configuration is shown in figure 10 overlaid on the efficiency contour plot for a $6\mu\text{m}$ HBV and the RF backshort fixed at a distance of 0.35mm. It can be seen from this figure that the output impedance of a fixed tuned waveguide cavity can provide the optimum embedding impedance over a frequency range of 150 - 310 GHz .

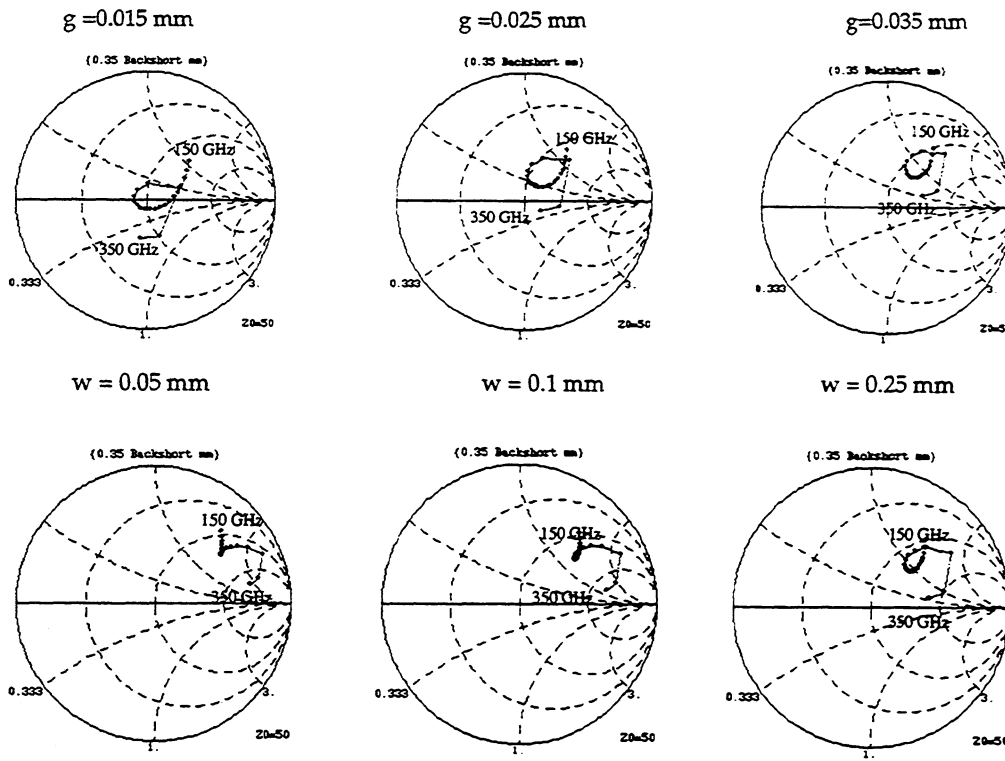


Figure 9: Embedding impedance as a function of g and w is shown.

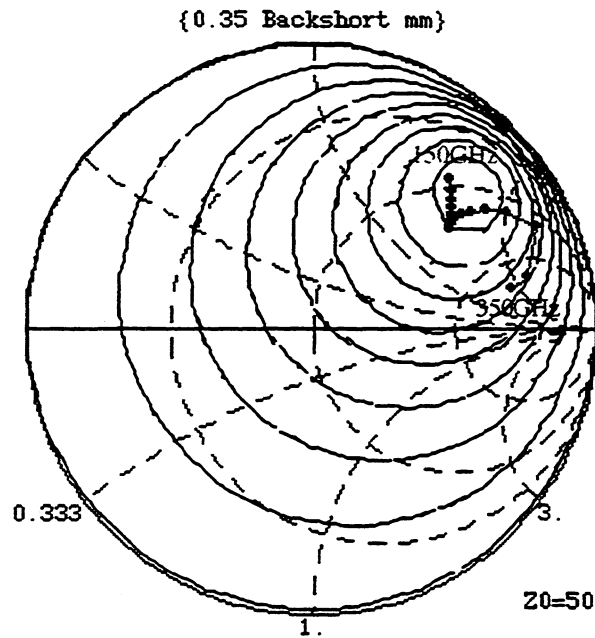


Figure 10: View of the contour plot for the $6 \mu\text{m}$ diode together with the E & K simulated response, for $a = 1.35 \text{ mm}$, $b = 0.1 \text{ mm}$, $g = 0.035 \text{ mm}$ and $w = 0.1 \text{ mm}$.

CONCLUSION

An obsolete doubler block has been turned into a very useful HBV frequency tripler that has broadband performance completely fixed tuned and unbiased. This has been achieved via the use of accurate analytical models and a planar HBV diode. The tripling behaviour makes the HBV an ideal device for ultra broadband frequency triplers particularly where high powers and efficiency are not the ultimate driver.

REFERENCES

- [1] 'A High Power 270 GHz Frequency Tripler Featuring A Schottky Diode Parallel Pair', J.Thornton, C.M.Mann, P.de Maagt, IEEE-MTT Conference, Denver, 1997.
- [2] 'Design of 100-900GHz GaAs/Al/GaAs/GaAs Planar Heterostructure Barrier Varactor Frequency Triplers', J.Stake, L.Dillner, S.H.Jones, T.O'brien, C.M.Mann. E.Kollberg, 9th International Conference on Space Terahertz Technology, JPL, Pasadena, 1998.
- [3] 'Theoretical and Experimental Analysis of a Waveguide Mounting Structure', R.L.Eisenhart, P.J.Khan , IEEE Transactions on Microwave Theory and Techniques VOL. MTT-19 no.8 August 1971, pp706 - 719.
- [4] 'A Design Approach For Planar Waveguide Launching Structures', J. Thornton, C. M. Mann, 7th Int. Symposium. Space THz Technology, Charlottesville, March 96.
- [5] 'Analysis of Carrier Transport in a Heterostructure Barrier Varactor Diode Tripler', J Stake , S H Jones, J R Jones, L Dillner, Proceedings. of the 1997 International Semiconductor Device Research Symposium, Charlottesville, December, 1997

A 430.5 GHz QUASI-OPTICAL HBV FREQUENCY TRIPLER

P. Arcioni¹, M. Bozzi¹, G. Conciauro¹, H. L. Hartnagel²,
L. Perregrini¹, E. Sacchi¹, M. Shaalan², and J. Weinzierl³.

¹ University of Pavia, Department of Electronics, Via Ferrata 1, 27100, Pavia, Italy.

Phone +39-382-505223 Fax +39-382-422583 Email p.arcioni@ele.unipv.it

² Darmstadt University of Technology, Merckstr. 25, 64283, Darmstadt, Germany.

³ University of Erlangen, Cauerstr. 9, 91058, Erlangen, Germany.

ABSTRACT – In this paper, we present the design and the fabrication of a quasi-optical frequency tripler at 430.5 GHz. The multiplier consists in a 10×10 slot array, on a GaAs substrate, integrated with Hetero-structure Barrier Varactors. A specialized CAD tool, based on the infinite array approximation, has been developed for the design of the antenna and for the optimization of the embedding system (external filters and matching slabs).

1. INTRODUCTION

Quasi-optical frequency multipliers in the millimeter and submillimeter wave range have been recently investigated as an alternative to the conventional waveguide devices [1, 2]. The multiplier (Fig. 1) consists of a planar antenna array integrated with non-linear devices, embedded in a quasi-optical gaussian system together with input/output filters and dielectric matching slabs [3, 4].

For an overall optimized design, two different components have to be carefully accounted for [5]: *i*) the non-linear device should be fed with a sufficient pump power, and connected to an impedance that maximizes the conversion efficiency; *ii*) the antenna and the embedding system should provide the device with the required impedance, and, at the same time, fulfil the best power coupling with the quasi-optical gaussian beam.

In this paper we discuss the use of Hetero-structure Barrier Varactors (HBVs) for the design of a frequency tripler at 430.5 GHz. We present the physical structure of the HBV, the measured $C_j(v)$ and $I_j(v)$ characteristics and the estimation of the efficiency performance and of the optimal

embedding impedance, using an algorithm based on the Harmonic Balance technique.

With regards to the analysis of planar antennas we have developed a specialized code [4], based on the simplifying approximation of an infinite array, which permits to take into account the effect of external filters and matching slabs. Using this code, we designed a 10×10 slot antenna array, which allows to closely approach the estimated optimal impedance. We discuss the tuning of the embedding system and its effect on the conversion performance.

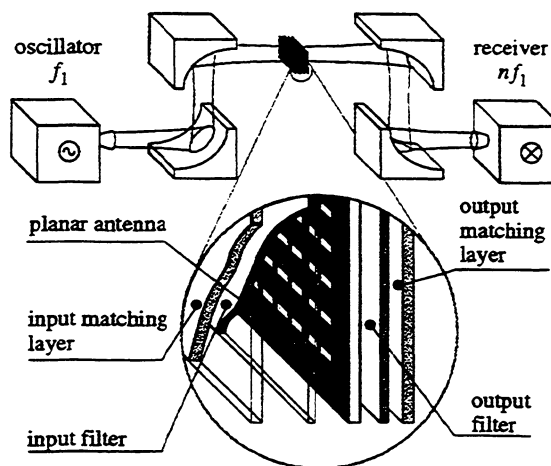


Fig. 1 – Schematic of a quasi-optical frequency multiplier, embedded in a gaussian system.

2. DEVICE ANALYSIS

In the recent years, the Hetero-structure Barrier Varactors have been largely investigated as promising devices for efficient high frequency triplers [6, 7]. In fact, these varactor devices require less design complexity compared to Schottky diode tripler circuits. This is attributed to the device characteristics, leading to the formation of only odd harmonics and hence no idler circuits are required for the even harmonics. Furthermore, since the HBV exhibits the highest non-linearity around zero bias voltage, no DC bias circuitry is required. Moreover, multiple-barrier HBV has a large degree of design flexibility in barrier number, layer thickness and doping profile; it allows for "tailoring" the device

characteristics which are particularly suitable to a specific application.

In this section we consider a multiple-barrier HBV, which has been fabricated and tested at the Darmstadt University of Technology. The layered wafer structure is shown in Fig. 2: a total of four GaAs/Al_{0.7}Ga_{0.3}As hetero-structure barriers have been used in the device (see the SEM photograph in Fig. 3a). The diameter of the structure amounts to approx. 15 μ m.

The device characteristics have been measured, using the test structure shown in the photo of Fig. 3b. We have obtained the quasi-static $C_j(v)$ and $I_j(v)$ curves (Fig. 4) by fitting the measurement results. A series resistance $R_S = 5 \Omega$ was measured.

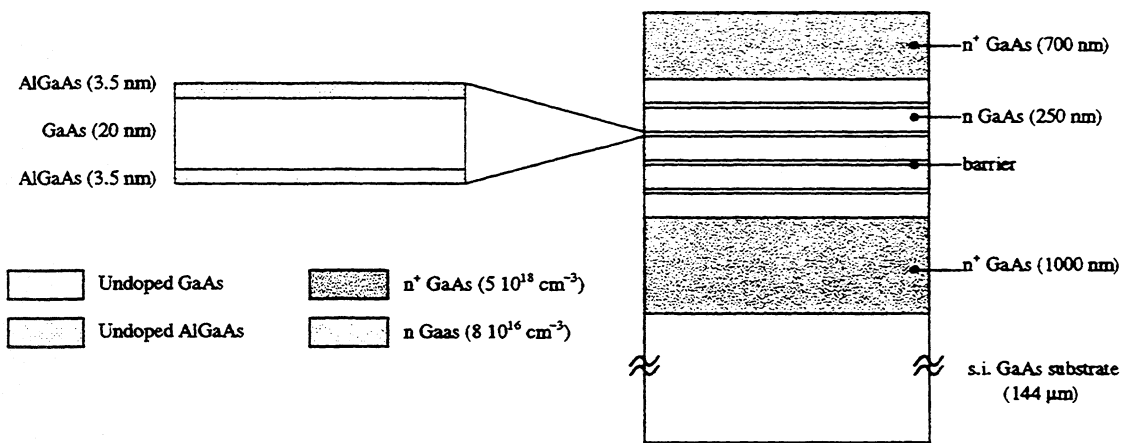


Fig. 2 – Structure of the HBV fabricated at the Darmstadt University of Technology.

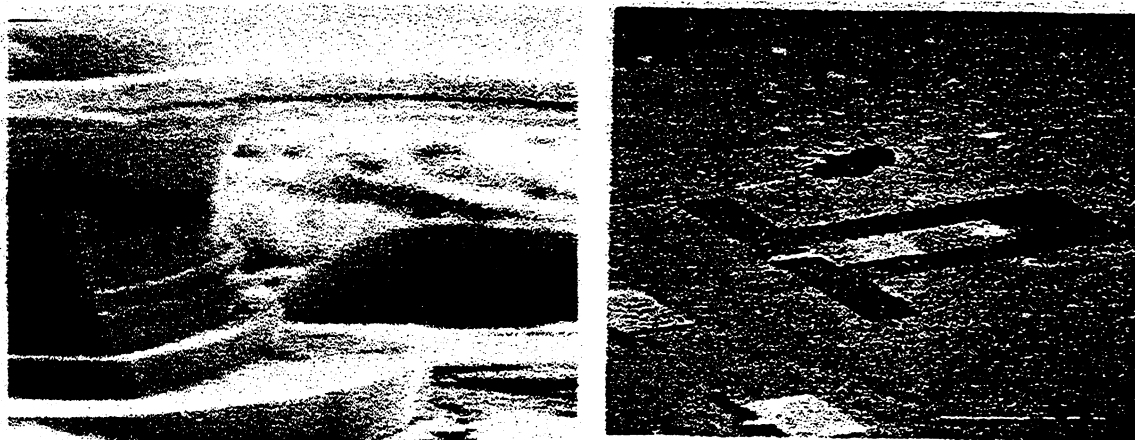


Fig. 3 – SEM photographs of the four-barrier HBV (left) and of the test structure (right).

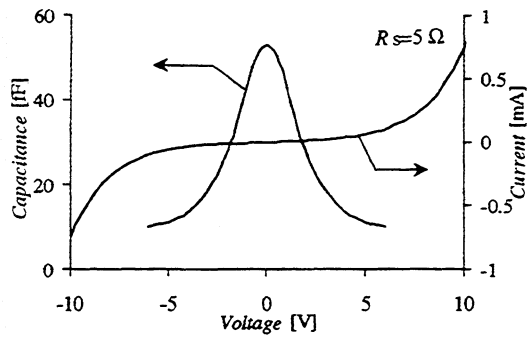


Fig. 4 – $C_j(v)$ and $I_j(v)$ characteristics of the HBV, deduced from measurements.

For the simulations, we have used the equivalent circuit of Fig. 5, where V_0 represents the open circuit voltage of the (receiving) antenna at the fundamental frequency f_1 , and $Z(f_n)$ is the input antenna impedance at f_n , for all the frequencies of interest. The total device current as a function of the voltage $v(t)$ is given by

$$i(v) = C_j(v) \frac{dv}{dt} + I_j(v)$$

The numerical analysis of the non-linear circuit is based on the Harmonic Balance technique. We have developed an algorithm, which is a modified version of the one presented in [8]. This algorithm resulted in a more robust routine for the analysis of circuits including HBVs.

The input data for the circuit analysis are the device characteristics and the available pump power P_0 at the device terminals at f_1 . While the behavior of the non-linear device mainly depends on the technological process, the power P_0 is related to the total power P_{TOT} carried by the gaussian beam and to the antenna geometry. For a given non-linear device (modeled through $C_j(v)$, $I_j(v)$ and R_s), and an available power P_0 , our code is able to find the optimal embedding impedance $Z(f_n)$ at the frequencies of interest.

An extensive use of this code allowed us for deeply investigating the HBV behavior for the operation in a frequency tripler at 430.5 GHz. We have calculated the device conversion efficiency versus the power P_0

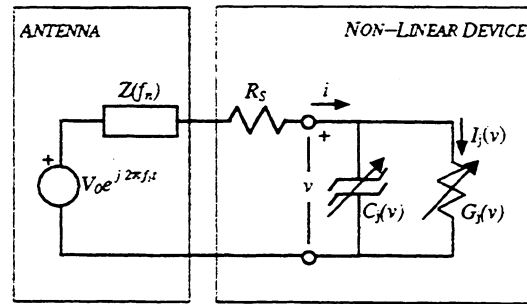


Fig. 5 – Equivalent circuit representing the elementary cell of the array.

and versus the impedance $Z(f_n)$.

The first result is that the value of P_0 has a strong impact on the maximum conversion efficiency (obtained with the optimal impedance at all the harmonic frequencies): Fig. 6 shows that the device conversion efficiency is quite poor at low pump power levels. Furthermore, different impedance values are required, in order to maximize the conversion efficiency at different pump power levels (Fig. 7).

If the embedding impedance is not the required one, the performance of the device deteriorates. We found that the impedance at the fundamental frequency is the most critical, while the efficiency has a minor sensitivity versus the impedance at the output harmonic. We experienced that the impedance at higher harmonics has a negligible effect on the efficiency up to large power levels.

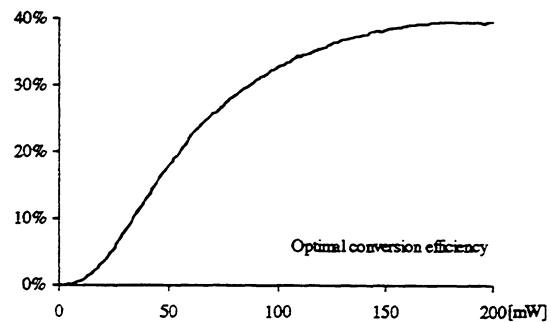


Fig. 6 – Optimal conversion efficiency of the HBV versus available pump power at the fundamental frequency ($f_1=143.5$ GHz).

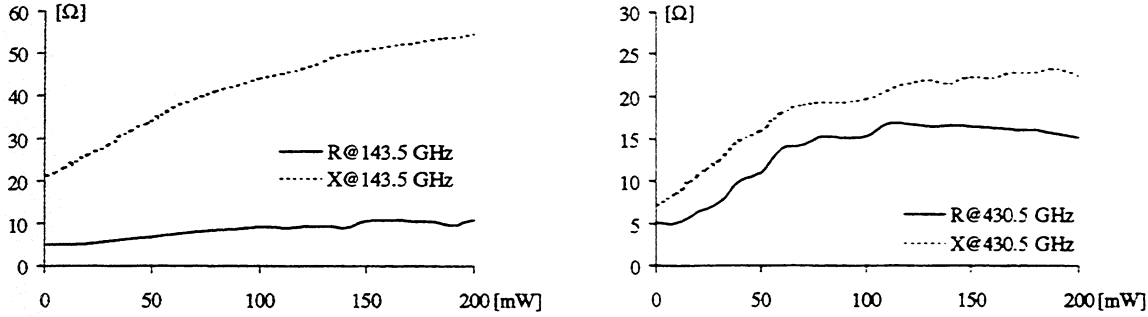


Fig. 7 – Optimal embedding impedance of HBV versus P_0 at the f_1 (left) and at $3f_1$ (right).

These considerations lead to the conclusion that the embedding circuit (*i.e.* the antenna, in our case) should be designed, carefully considering the total available pump power of the source P_{TOT} and the number of elements in the antenna array. In other words, since we consider the approximation of the infinite array, the estimation of the available power per unit cell P_0 is required. On the other hand, the number of elements of the array should be large enough to allow for a good power coupling with the quasi-optical gaussian beam and, at the same time, sufficiently limited to ensure an adequate power level to each non-linear device.

These constraints determine the array size, and consequently the available P_0 , once the total power P_{TOT} is fixed.

In our design, the source at 143.5 GHz is a BWO, which can provide the system with about $P_{TOT}=400$ mW. We estimated that the most satisfactory number of elements of the array is 100. As a consequence, the (average) P_0 is 4 mW, at the best. With this power level, the maximum conversion efficiency which can be achieved is approx. 0.1%. The required impedance values are

$$Z_{OPT}(f_1) = 5.0 + j21.7 [\Omega]$$

$$Z_{OPT}(3f_1) = 5.0 + j7.4 [\Omega]$$

where $f_1=143.5$ GHz is the fundamental frequency of the system.

In the following section, we will show how these impedance values can be obtained, by means of a careful design of the antenna and the embedding system.

3. ANTENNA ANALYSIS

In this section we describe the design of the antenna array and of the embedding system, which provide the non-linear device with the required impedance at all the harmonic frequencies. In our design, the antenna consists in a 10×10 slot array on a GaAs substrate.

For the analysis of layered structures, we have developed a novel specialized computer code, which is able to simulate the non-linear device, the planar antenna and the layered embedding structure as a whole. The analysis of the multiplier is performed making the simplifying approximations of an infinite array excited by a uniform plane wave incident from the broadside direction.

Under these assumptions, the study of the structure reduces to the analysis of the unit cell of the array, which, in turn, leads to the equivalent circuit of Fig. 5. The aperture, as seen by the non-linear device, is represented by an equivalent generator at f_1 and by equivalent loads $Z(f_2)$, $Z(f_3)$, ... at the harmonic frequencies f_2 , f_3 , Either the open circuit voltage V_0 and the impedances $Z(f_n)$ are deduced from a full-wave analysis, based on the Method of the Moments (MoM) in the spectral domain, of the multi-layered structure embedding the antenna at frequencies f_1, f_2, \dots . The effect of the filters is taken into account by their plane-wave reflection / transmission coefficients at the harmonic frequencies. The number and the type of the dielectric layers, the shape, the size and the separations of the apertures

and the frequency response of the filters can be given arbitrarily. Once the equivalent circuit has been determined, the frequency spectrum of the current flowing in each non-linear device is found by the Harmonic Balance method. These results permit to find the scattered field at the fundamental frequency and at the harmonic of interest, thus leading to the calculation of the overall conversion efficiency of the multiplier. A careful dimensioning of the whole structure allows to obtain an efficiency very

close to the maximum one, that can be deduced from circuit analysis, as described in the previous section.

To this aim, we have integrated the analysis code into an optimization routine (Fig. 8). Using this routine, we have optimized the aperture dimensions, the array geometry, the characteristics and the position of the dielectric matching slabs, together with the positions of the input and output filters, in order to approach the maximum conversion efficiency.

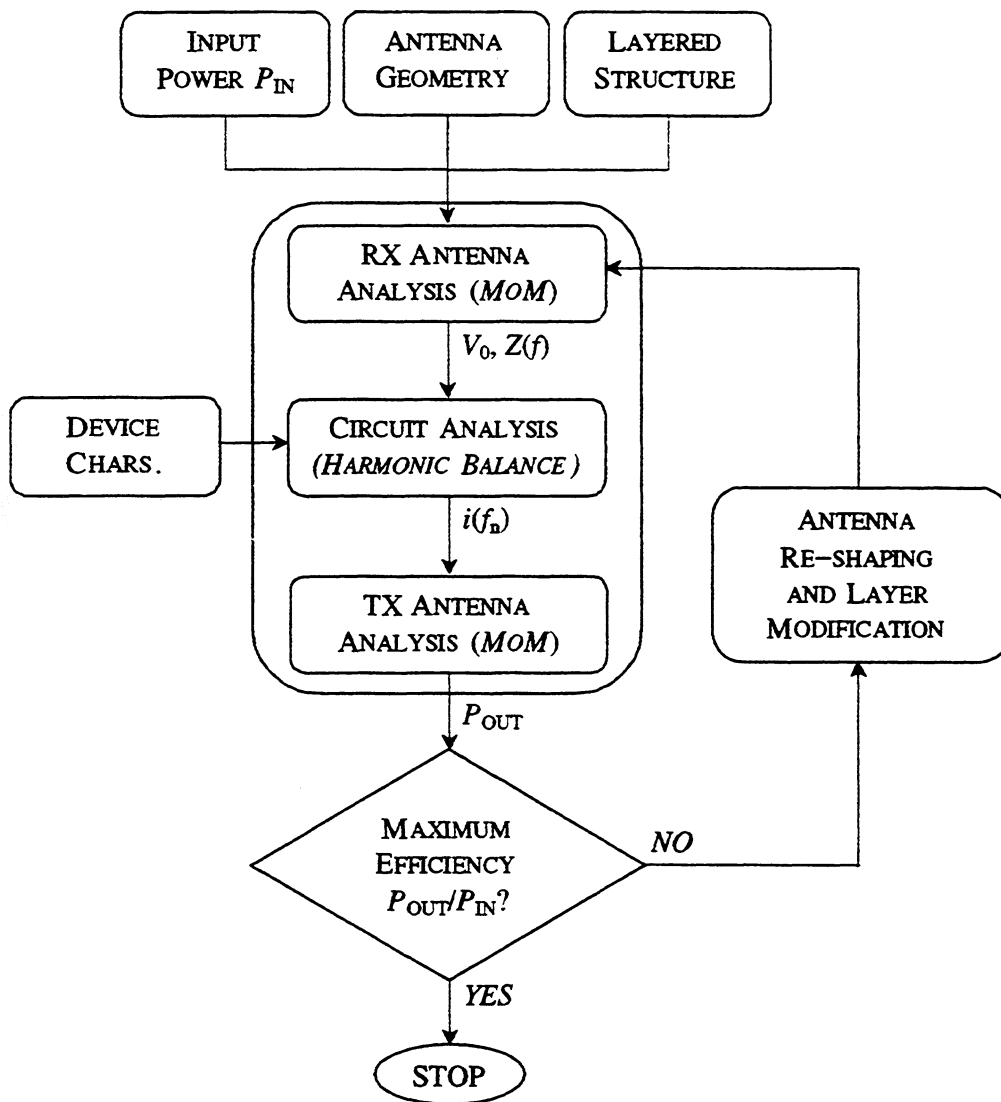


Fig. 8 – Block diagram of the computer code for the analysis and the optimization of the multiplier.

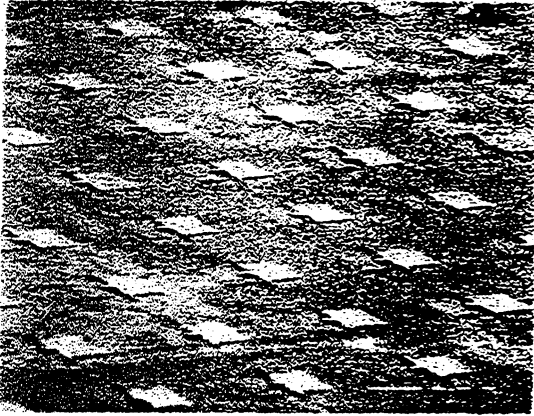


Fig. 9 – Photograph of the 10×10 slot array

In our design, we used a 144 μm thick GaAs substrate ($\epsilon_r=12.9$, $\tan \delta_E=0.002$); as shown in [3], the chosen thickness is effective against the substrate wave propagation.

The optimal dimension of the slot antenna resulted 175×20 μm², while the 10×10 array element spacing was 300 μm in both directions. The tripler chip has been fabricated at the Darmstadt University of Technology (see Fig. 9)

From the simulations resulted that the input matching structure should consist of two alumina slabs, with a relative dielectric permittivity $\epsilon_r=9$ and a thickness of 170 μm; the optimal simulated spacing was 5.54 mm. Similarly, the output matching structure consists of two alumina slabs, with a

thickness of 56.7 μm, with a spacing of 4.94 mm. For the input and output filters (band-pass at 143.5 GHz and 430.5 GHz, respectively) we considered free-standing metal layers, with a power transmission coefficient of approx. 95%. The complete measurement setup is sketched in Fig. 10.

With the layer spacing reported in the caption of Fig. 10, we found the following impedance values:

$$Z(f_1) = 4.7 + j27.0 [\Omega]$$

$$Z(3f_1) = 5.3 + j6.5 [\Omega]$$

These values are very close to the optimal ones, reported in the previous section. With these impedance values, the estimated efficiency closely approaches the maximum theoretical efficiency of the HBV (see Fig. 6).

Performing the optimization, we found that the most important parameters that must be controlled to maximize the efficiency are the position of the input matching layers and the one of the output filter.

On the basis of these simulations, the measurement setup has been prepared. Its actual optimization is still under way: this is a quite critical and time consuming task, due to the low output power.

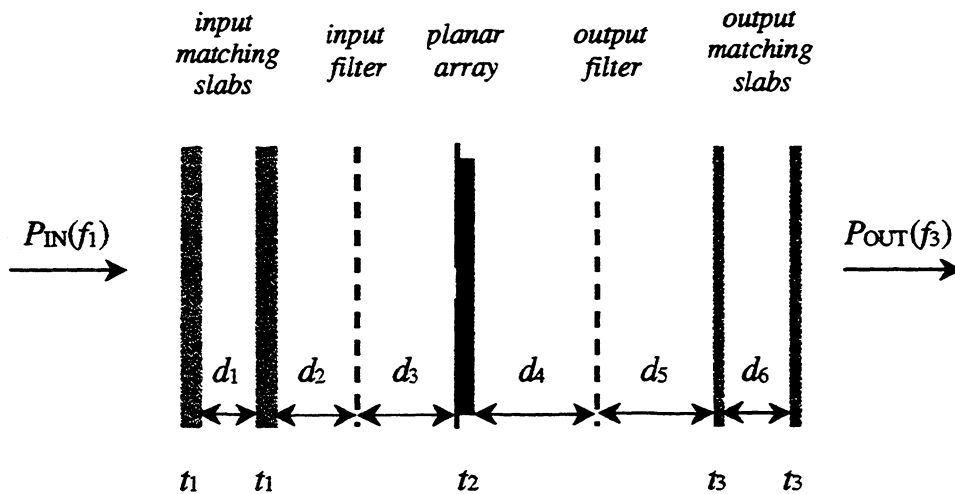


Fig. 10 – Optimized setup for the multiplier embedding system.
 Dimensions: $d_1=5.54$ mm, $d_2=4.56$ mm, $d_3=4.87$ mm, $d_4=5.84$ mm, $d_5=4.39$ mm, $d_6=4.94$ mm, $t_1=170$ μm, $t_2=144$ μm, $t_3=56.7$ μm.

4. FUTURE DEVELOPMENTS

The main factor which limits the conversion performance of the presented HBV frequency tripler is the low power P_0 delivered to each non-linear device. In order to overcome this drawback, the obvious solution could be the use of a more powerful source. Such a solution, nevertheless, leads to cumbersome systems, which are not suitable to space-borne applications.

An other possibility is represented by the integration of non-linear devices, which exhibit a satisfactory conversion efficiency at a low power level. It is interesting to observe that different devices, with the same cutoff frequency (defined like in [9]) but with different $C_j(v)$ characteristic, may have very different conversion efficiency at low power levels.

In this section, we present a comparison of the conversion performance of different HBVs, to be used in a frequency tripler at 430.5 GHz. The device named HBV#1 is the one fabricated at the Darmstadt University of Technology, and previously discussed. The characteristics of HBV#2 and HBV#3 are derived from theoretical considerations, progressively reducing the area of the devices. In a first-order approximation, a reduction of the device area leads to a proportional decrease of the junction capacitance C_j and a corresponding increase of the series resistance R_s (Fig. 11).

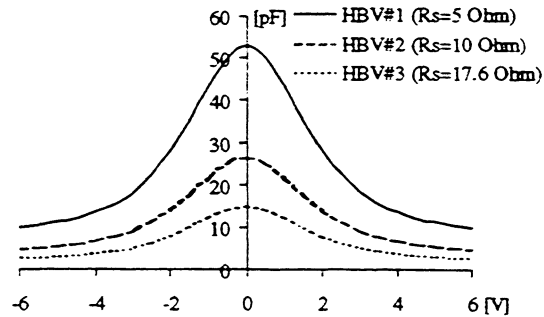


Fig. 11 – Capacitance vs. voltage characteristic of different HBVs.

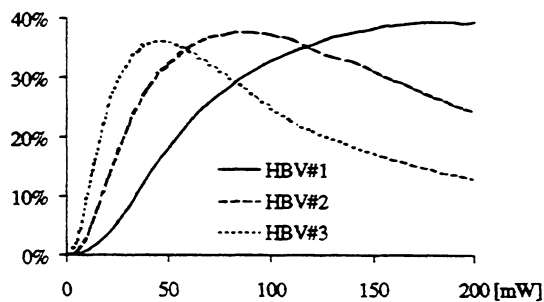


Fig. 12 – Maximum conversion efficiency versus P_0 for different HBVs.

Fig. 12 shows the maximum conversion efficiency for the three HBVs versus P_0 . It is apparent that reduced area devices are to be used when P_0 is small. Unfortunately, up to now, technological limitations prevented us from fabricating, in a reliable and repetitive way, four-barrier HBVs with diameter smaller than 15 μm .

ACKNOWLEDGEMENTS

This work is supported by the European Commission under the TMR Programme contract n. ERBFMRXCT960050 and by the University of Pavia under F.A.R. 1996/97 Funding.

REFERENCES

- [1] A. Moussessian *et al.*, "A Terahertz Grid Frequency Doubler," *1997 IEEE IMS Digest*, Denver, CO, pp. 683–686, June 8–13, 1997.
- [2] M. Shaalan *et al.*, "A 300 GHz Quasi-Optical Schottky Frequency Doubler," *Intern. Journal on Infrared and Millimeter Waves*, Vol. 18, No. 12, Dec. 1997.

- [3] M. Shaalan *et al.*, "Design of a Planar Antenna Array for Quasi-Optical Frequency Triplers," *Proc. of 5th Intern. Workshop on Terahertz Electronics*, IRAM, Grenoble, France, Sept. 18-19, 1997.
- [4] P. Arcioni *et al.*, "Numerical Modeling of Quasi-Optical Frequency Multipliers," *to be presented at the 4th International Conference on Millimeter and Submillimeter Waves Applications*, S.Diego, California, USA, July 20-22, 1998.
- [5] J. R. Jones *et al.*, "DC and Large-Signal Time-Dependent Electron Transport in Heterostructure Devices: An Investigation of the HBV," *IEEE Trans. Electron Devices*, Vol. 42, No. 8, pp. 1393-1403, Aug. 1995.
- [6] E. Kollberg and A. Rydberg, "Quantum-barrier varactor diodes for high-efficiency millimeter-wave multipliers," *Electron. Lett.*, Vol. 25, No. 25, pp. 1696-1698, Dec. 1989.
- [7] J. R. Jones *et al.*, "Planar Multibarrier 80/240-GHz Heterostructure Barrier Varactor Triplers," *IEEE Trans. Microwave Theory Tech.*, Vol. MTT-45, No. 4, April 1997.
- [8] R. J. Hicks and P. J. Khan, "Numerical Analysis of Nonlinear Solid-State Device Excitation in Microwave Circuits," *IEEE Trans. Microwave Theory Tech.*, Vol. MTT-30, No. 3, March 1982.
- [9] M. A. Frerking and J. R. East, "Novel Heterojunction Varactors," *Proc. of the IEEE*, Vol. 80, No. 11, Nov. 1992.

PLANAR SCHOTTKY MIXER DEVELOPMENT TO 1 THz AND BEYOND

Steven M. Marazita, Jeffrey L. Hesler, Roland Feinäugle[†],
William L. Bishop, and Thomas W. Crowe

Applied Electrophysics Laboratories
Department of Electrical Engineering
University of Virginia
Charlottesville, VA 22901

[†]German Aerospace Research Establishment
Institute of Space Sensor Technology
Rudower Chaussee 5
D-12489 Berlin

Abstract

Highly robust submillimeter wavelength heterodyne mixers are required for a variety of remote sensing missions. These mixers must exhibit sufficient spectral sensitivity, wide bandwidth, low noise, and reduced LO power requirements. Planar GaAs Schottky diodes are currently the most promising technology for radiometers where cryogenic cooling is not an acceptable option. This discussion emphasizes integration of planar mixer structures as operating frequencies approach 1 THz and beyond.

We present a new mixer fabrication technique MASTER as a viable integrated technology. The first batch of 640 GHz MASTER devices demonstrates comparable performance to QUID-style mixers. Preliminary modeling and design of fundamental fixed-tuned mixers using these integrated structure at 1 THz is discussed. For a 1 THz mixer the modeling predicts that integrated devices allow for fixed-tuned coverage of nearly a full waveguide band which is not possible using discrete devices.

I. Introduction

Detection of submillimeter-wave radiation is of great interest to scientists studying electromagnetic signatures in interstellar space. These signatures provide a better understanding of interstellar chemistry, star formation, and galactic structure. In addition, radiation emitted from a number of molecules in the Earth's atmosphere such as O₃, ClO, and OH are critical to the study of ozone depletion and greenhouse warming. The Microwave Limb Sounder (MLS) on NASA's Earth Observing System (EOS), for example, will employ heterodyne receivers operating from 240 GHz to 2.5 THz to study these molecules. These remote sensing missions require highly robust millimeter and submillimeter wavelength radiometers which can survive the rigors of launching and the lifetime of the satellite. Heterodyne mixers based around planar GaAs Schottky diodes are currently the most promising technology since cryogenic cooling is not an acceptable option.

II. Prior Schottky Mixer Developments

GaAs Schottky diodes are a mature technology. Devices based upon whisker-contacted geometries have achieved record sensitivity at frequencies up to 2.5 THz [1]. However, the fragile whisker-contact is difficult to space qualify and integration with surrounding circuitry is extremely difficult. The University of Virginia developed a planar Schottky mixer diode with

good RF performance, inherent mechanical ruggedness, and adaptability to higher levels of integration [2]. Several groups have successfully used the planar diode structure in receivers [3][4]. We have demonstrated good fundamental mixer performance in the 500-700 GHz range using a discrete planar diode flip-chip soldered into a quartz microstrip circuit [5]. However, simulations at these frequencies indicate that higher packaging parasitics and difficulties in controlling chip alignment and soldering limit discrete mixer performance as compared to a fully integrated device [6]. A first step in this direction was taken in 1990 with the demonstration of a planar diode integrated on a quartz substrate [7]. This process removed the high dielectric, lossy GaAs substrate and replaced it with lower dielectric quartz, thereby reducing the parasitic capacitance and improving RF performance [8].

In 1993 NASA's Jet Propulsion Laboratory (JPL) further integrated the planar diode on quartz structure by incorporating the mixer RF/LO and IF microstrip filter circuitry with the diode using their QUID process [9]. This permits perfect alignment of the diode to the surrounding filter circuitry and eliminates flip-chip soldering. A disadvantage is that the upside-down device bonding fills the surface channel area with epoxy ($\epsilon_r \approx 3.0$) which increases parasitic capacitance and potentially degrades mixer performance as compared to an upside-up device configuration. At UVA an epoxy etching technique was developed which can reduce the parasitics and improve mixer performance by 20-30% [10][11]. The epoxy also sits between the filters and the quartz substrate and is lossy at these wavelengths. Even so, these devices exhibit good subharmonic performance at 640 GHz with DSB $T_{\text{mix}} = 2500$ K and $L_{\text{mix}} \approx 9$ dB [12]. The DSB T_{mix} remains less than 3500 K over a 1.5 to 14 GHz IF band.

III. MASTER - Method of Adhesion by Spin-on-dielectric Temperature Enhanced Reflow

Many different types of semiconductor-substrate bonding techniques exist in the literature: bonding by Van der Waal forces [13], silicate spin-on-glass [14], electrostatic forces [15], reactive sputtered oxides [16], UV curing glue [7], epoxy [9], and others. Van der Waal, electrostatic, and reactive sputtered oxide bonding all rely on very close proximity (on the order of 50 angstroms) of the two surfaces to be bonded. Silicate spin-on-glass must be applied in a liquid state which could leave large voids in the bonding when the two surfaces are heated to evolve solvents and cure the glass to a hard film. UV curing glue and epoxy are typically thicker than 2 microns which may affect RF performance due to losses in the films at submillimeter wavelengths. In addition, they are incompatible with many chemicals necessary for semiconductor fabrication.

We have developed a novel bonding technique which overcomes all of the aforementioned deficiencies. The bonding agent is an organic spin-on-dielectric (SOD) originally developed as a low dielectric planarizing agent between CMOS metal interconnect levels [17][18]. It is applied by a spin-on technique and becomes a solid film less than 0.5 microns thick after baking at 200°C. This step evolves most of the solvents out of the film. When the film is re-baked in excess of 150°C, it softens greatly and actually reflows. This reflow phenomenon is responsible for its adhesive properties. After a 200°C cure it remains resistant to most solvents and chemicals but can be etched in a $\text{CF}_4 + \text{O}_2$ plasma. Because the adhesive film is so thin after baking, it should not degrade RF performance. We are currently performing FTIR measurements on this material and will report the results at a later time.

Our new fabrication procedure is called MASTER - Method of Adhesion by Spin-on-dielectric Temperature Enhanced Reflow [19]. Using this process we have fabricated 640 GHz subharmonically pumped integrated mixers for EOS-MLS. The microstrip filter design was given to us by NASA-JPL's SWAT group. Figures 1 and 2 show a device wafer after the GaAs epilayer has been bonded to quartz, and a GaAs mesa with 45 degree sloped sidewalls has been etched down to the bare quartz substrate. After a brief wet etch to reveal the Schottky anode contact, a blanket Ti/Pt/Au evaporation is performed. This step forms the Schottky contact for the device and provides a seed layer for subsequent electroplating of the finger and microstrip filter sections [20]. Figure 3 is an SEM photo after the fingers and microstrip filters have been plated and the seed layer has been removed. Note the excellent metal step coverage from the quartz substrate up onto the GaAs mesa. The surface channel isolation etch is then performed, as shown in Figure 4, and the diodes are ready for DC I-V testing. For the 640 GHz devices typical I-V parameters for the first two batches are $R_s=11-15$ ohms, $V_{knee}=520$ mV, and $\Delta V=78-85$ mV ($\eta=1.33-1.45$). The epi doping is 4×10^{17} cm⁻³ n-type and anode diameters range from 0.8 to 0.9

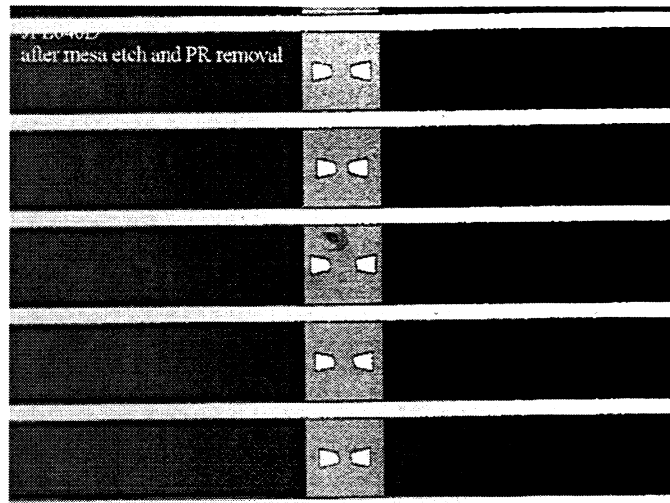


Figure 1: Top view after mesa etch

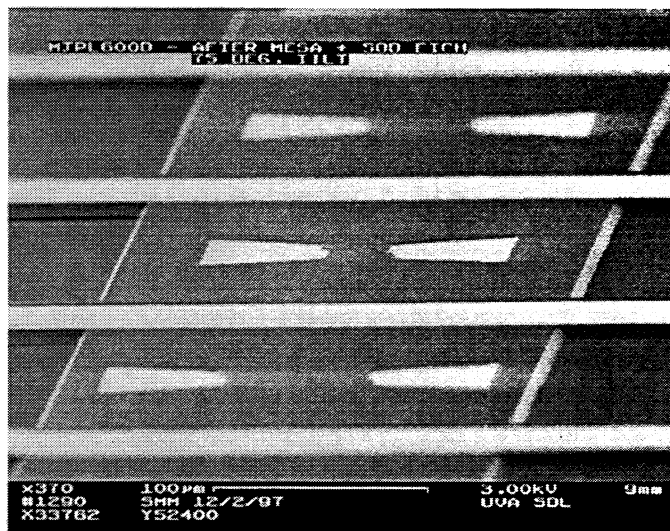


Figure 2: MASTER device wafer after mesa etch

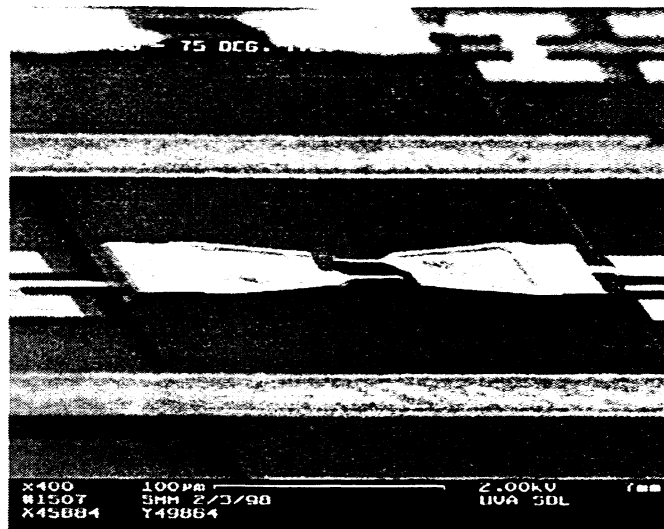


Figure 3: Devices after finger and filter formation

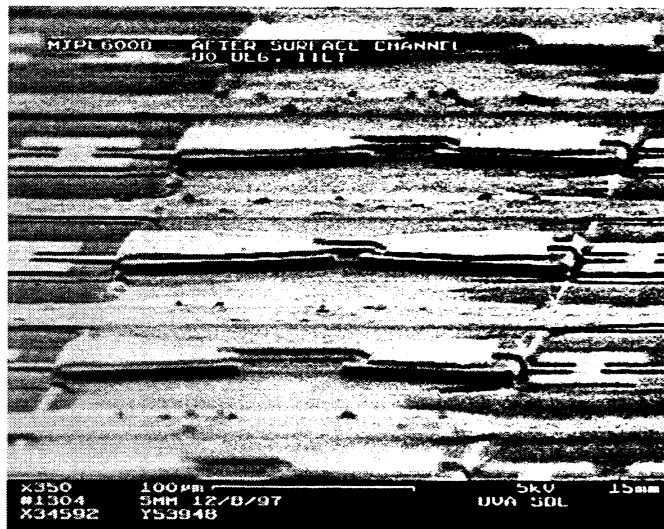


Figure 4: Devices after surface channel isolation

μm . After I-V testing, the wafer is mounted to a silicon carrier, and the fused quartz substrate is thinned to its target thickness of 50 microns (2 mils). The wafer is then diced into individual devices and the DC I-V is tested again. Capacitance measurements at 1 MHz are also performed. QUID 640 GHz mixers typically have 5-6 fF of parasitics after subtracting out the anode junction capacitance [12]. The second batch of MASTER devices have parasitic capacitances of 2.3-2.7 fF for an open circuit device, a 50% improvement over QUID. The microstrip filters on quartz contribute about 1 fF to the parasitics. The remaining 1.4 fF is due to the device structure sitting on the GaAs mesa. These capacitance numbers are measured with chips mounted in black wax on a silicon carrier which sits on a grounded probe station stage.

RF testing is performed at JPL. The local oscillator (LO) source is a BWO operating at 310.7, 320, and 324.6 GHz. One of the first devices tested is demonstrating respectable performance. It has a 60 micron finger length. Table 1 summarizes its best noise temperature

and conversion loss at various LO frequencies:

LO freq. (GHz)	Mixing freq. (GHz)	IF freq. (GHz)	LO power (mW)	DSB T_{mix} (K)	DSB L_{conv} (dB)
310.7	621.4	4	8.24	3681	13.24
320	640	4	4.67	2396	10.98
324.6	649.2	4	10.11	2762	11.3

Table 1: Measured MASTER mixer RF performance

This device also shows good IF bandwidth. At 320 GHz LO, the DSB T_{mix} remains less than 3500 K as the IF frequency is swept from 1.5 to 13 GHz. As mentioned in Section II, typical measurements for QUID 640 GHz subharmonic mixers give DSB $T_{\text{mix}}=2500$ K and $L_{\text{conv}}=9$ dB with $T_{\text{mix}} < 3500$ K for an IF bandwidth of 1.5 to 14 GHz [12]. The first MASTER devices, therefore, are very competitive with state-of-the-art subharmonic mixers in this frequency range. This performance is achieved in a mixer block designed for QUID devices without optimizing the diode's finger length. Also, the ideality factor of this device is 1.45. We can now fabricate junctions with ideality factors of about 1.35. We are confident that these results should improve with a new optimized batch of mixers. With their low parasitic capacitance, the MASTER devices also could perform better than QUID-type structures as frequencies are pushed towards 1 THz and higher.

IV. Simulations of a 1 THz Integrated Schottky Mixer

At 585 and 690 GHz UVA demonstrated excellent performance with a fixed-tuned waveguide fundamental mixer using a flip-chip mounted SC1T5-S10 diode soldered into a microstrip circuit [5]. The best DSB T_{mix} and L_{conv} were 1800 K, 7.6 dB with $P_{\text{LO}}=1.16$ mW at 585 GHz and 2240 K, 8.8 dB with $P_{\text{LO}}=1.04$ mW at 690 GHz. The mixer was designed using the computed aided simulation tools HFSS and MDS from Hewlett Packard. Because of the great success of this design we decided to scale it to 1 THz.

Early in the process it was determined that a flip-chip soldered diode may not be appropriate for this frequency range. For optimum performance of the microstrip filter and matching circuitry, the waveguide channel should be 75 μm wide and 63 μm high. The quartz substrate needs to be 25 μm thick. A typical planar diode chip has a thickness of 20-30 μm . These specifications only leave about 10-15 microns for soldering the diode onto the circuit. The bulk GaAs substrate would be very close to the top channel wall. The position of the diode both laterally and vertically could not be precisely controlled to the tolerances required at these wavelengths. Uncertainties in the solder thickness and higher parasitic capacitance of flip-chips also would make the prediction of the diode embedding impedance difficult.

We decided to compare a flip-chip design to a MASTER integrated mixer to determine which structure would perform better around 1 THz. The diode parameters in both simulations were SD1T7-type with $R_s=10$ -12 ohms, $\Delta V=77$ mV ($\eta=1.32$), $I_{\text{sat}}=6 \times 10^{-17}$ A, and $C_{j0}=1.2$ fF. Using harmonic balance simulation routines in MDS the predicted noise temperature and conversion loss were calculated versus the embedding impedance presented to the diode. The

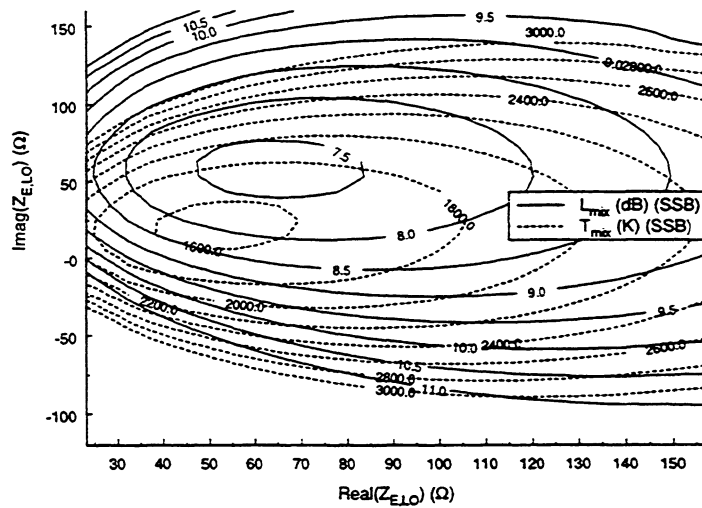


Figure 5: Contour plot of T_{mix} and L_{conv} based on simulations for diode SD1T7 with LO power of 1.2 mW

contour plot for an SD1T7-type diode pumped at 1.2 mW LO power is shown in Figure 5. The two structures, integrated and flip-chip, were drawn in HFSS inside a microstrip channel. The diode finger length for both structures was 5 μm . A simulation was run to determine the 3-port s-parameters for each structure versus frequency from 700 to 1200 GHz. The diode on the microstrip was modeled with a port at each end of the structure and a small coaxial port at the device anode location. The coaxial probe s-parameters were de-embedded, normalized to 50 ohms, and a 3-port device in MDS was created from the full set of s-parameters. This 3-port device was used to optimize the microstrip circuits. A frequency sweep was performed in MDS to determine the range of embedding impedances that each mixer structure would present to the diode. Using Figure 5 the mixers' noise temperatures and conversion losses were calculated for embedding impedances at different RF frequencies. Figures 6 and 7 show the RF behavior of both a discrete flip-chip and integrated mixer. At the design frequency of 1037 GHz, both devices achieve SSB $T_{\text{mix}}=1700$ K and $L_{\text{conv}}=8.25$ dB. However, the integrated device shows a significant increase in RF bandwidth over discrete without trading off performance at the design frequency. One integrated mixer design therefore covers nearly a full waveguide band.

The 1 THz integrated device design using a MASTER structure has been completed. In the next several months we will begin mask design and fabrication of these mixers. Its simulated predictions are encouraging although factors not incorporated into the analysis will certainly degrade measured performance. Unknown losses at submillimeter wavelengths and inaccuracies in the harmonic balance modeling and embedding impedance calculations are thoroughly discussed in [21]. With its wider frequency response than discrete mixers, the integrated structure should be more tolerant of unknown factors which might cause shifts in the design frequency.

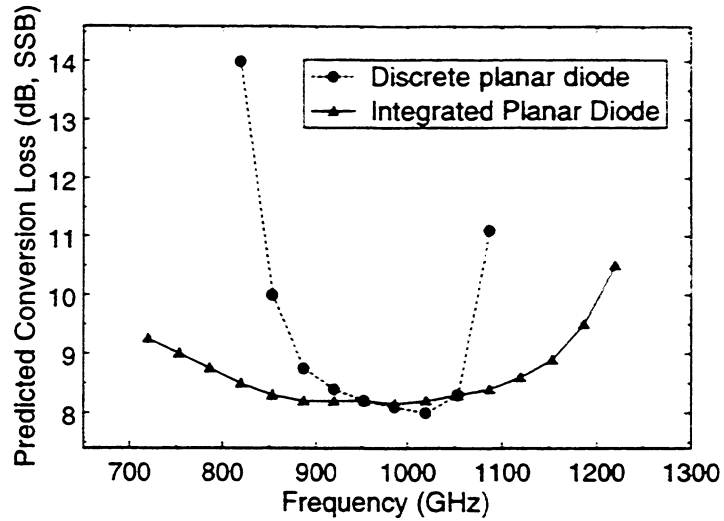


Figure 6: Simulated L_{conv} vs. frequency for integrated and discrete mixers

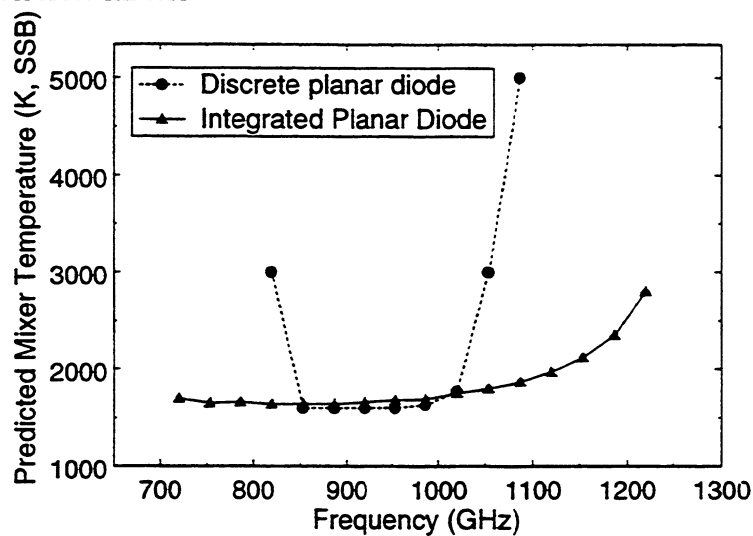


Figure 7: Simulated T_{mix} vs. frequency for integrated and discrete mixers

V. Summary

A new integrated fabrication process, MASTER, has produced devices which perform very competitively at 640 GHz compared to QUID-style mixers. Their low parasitic capacitance suggests that they also could work well at higher frequencies. Preliminary modeling around 1 THz indicates that integrated structures should outperform discrete. Issues such as higher parasitic capacitance, diode misalignment, and unknown solder effects limit discrete mixer bandwidth as operating frequencies are increased. In addition, waveguide channel dimensions are becoming too small for soldered devices to fit comfortably.

Studying the composition of the Earth's atmosphere is essential to understanding phenomena such as ozone depletion and greenhouse warming. Developing more sensitive receivers to detect the presence of important molecules such as O₃, ClO, and OH is critical to this understanding. Integrated THz mixers should satisfy the requirements of sufficient spectral sensitivity, wide bandwidth, low noise, and reduced LO power necessary for the next generation remote sensing radiometers. GaAs Schottky diodes will continue to be the dominant technology in this arena while cryogenic cooling is not an acceptable option.

VI. Acknowledgments

The authors would like to acknowledge NASA-JPL's SWAT group for their assistance during the 640 GHz mixer testing. This work was supported by NASA-NGT-51396, JPL-960017, and ARL/UMD-Z847301.

VII. References

- [1] W.L. Bishop, Steven M. Marazita, Perry A.D. Wood, Thomas W. Crowe, "A Novel Structure and Fabrication Process for Sub-Quarter-Micron THz Diodes", Proceedings of the 7th Int. Symp. on Space THz Tech., Charlottesville, VA, March, 1996, p. 511-524.
- [2] W. Bishop, K. McKinney, R. Mattauch, T. Crowe, and G. Green, "A Novel Whiskerless Diode for Millimeter and Submillimeter Wave Applications," 1987 IEEE Int. Microwave Symposium Digest, pp. 607-610, June 1987.
- [3] I. Galin, "A Mixer up to 300 GHz with Whiskerless Schottky Diodes for Spaceborne Radiometers," 7th Intl. Symp. Space THz Tech., Charlottesville, VA, pp. 474-476, March 1996.
- [4] S.S. Gearhart and G.M. Rebeiz, "A Monolithic 250 GHz Schottky-Diode Receiver," IEEE Trans. Microwave Theory Tech., Vol. 42, No. 12, pp. 2504-2511, Dec. 1994.
- [5] J.L. Hesler, W.L. Hall, T.W. Crowe, R.M. Weikle II, B.S. Deaver Jr., R.F. Bradley, and S.K. Pan, "Fixed-Tuned Submillimeter Wavelength Waveguide Mixers Using Planar Schottky-Barrier Diodes", IEEE Transactions on Microwave Theory and Techniques, Vol. 45, No. 5, May 1997.
- [6] J.L. Hesler, T.W. Crowe, W.L. Bishop, R.M. Weikle II, R.F. Bradley, and S.K. Pan, "The Development of Planar Schottky Diode Waveguide Mixers at Submillimeter Wavelengths," IEEE MTT-S International Microwave Symposium Digest, Volume 2, Denver, CO, June 8-13, 1997, pp. 953-6.
- [7] W.L. Bishop, E.R. Meiburg, R.J. Mattauch and T.W. Crowe, "A Micron Thickness, Planar Schottky Barrier Diode Chip for Terahertz Applications with Theoretical Minimum Parasitic Capacitance," 1990 IEEE MTT-S Int. Microwave Symp., Dallas, TX, pp. 1305-1308, May 1990.

- [8] Peter H. Siegel, Robert J. Dengler, Imran Medhi, John E. Oswald, William L. Bishop, Thomas W. Crowe, and Robert J. Mattauch, "Measurements on a 215 GHz Subharmonically Pumped Waveguide Mixer Using Planar Back-to-Back Air-Bridge Schottky Diodes," *IEEE Transactions on Microwave Theory and Techniques*, Vol. 41, No. 11, Nov. 1993, pp. 1913-1921.
- [9] I. Medhi, P. Siegel, M. Mazed, "Fabrication and Characterization of Planar Integrated Schottky Devices for Very High Frequency Mixers", in *Proceedings of the IEEE/Cornell Conference on Advanced Concepts in High Speed Semiconductor Devices and Circuits*, August 2-4, 1993.
- [10] S.M. Marazita, W.L. Bishop, T.M. Cunningham, P.J. Koh, T.W. Crowe, and R.M. Weikle II, "Planar GaAs Schottky Barrier Diodes", presented at 8th Intl. Symp. on Space THz Tech., Boston, March, 1997.
- [11] I. Medhi, S. Marazita, D. Humphrey, T. Lee, R. Dengler, J. Oswald, A. Pease, S. Martin, W. Bishop, T. Crowe, and P.H. Siegel, "Improved 240 GHz Subharmonically Pumped Planar Schottky Diode Mixers for Space-Borne Applications", November, 1997, to be submitted to *IEEE Transactions on MTT*,
- [12] I. Medhi, P.H. Siegel, D.A. Humphrey, T.H. Lee, R.J. Dengler, J.E. Oswald, A. Pease, R. Lin, H. Eisele, R. Zimmerman, and N. Erickson, "An All Solid-State 640 GHz Subharmonic Mixer", submitted to *International Microwave Symposium*, Baltimore, June, 1998.
- [13] E. Yablonoitch, T. Gmitter, J.P. Harbison, and R. Bhat, "Extreme selectivity in the lift-off of epitaxial GaAs films", *Applied Physics Letters* 51 (26), Dec. 28, 1987.
- [14] Hans J. Quenzer, Wolfgang Benecke, *Direct Substrate Bonding*. U.S. Patent No. 5,407, 856.
- [15] Qing-An Huang, Shi-Ji Lu, and Qin-Yi Tong, "Gallium Arsenide on Insulator by Electrostatic Bonding", *IEEE SOS/SOI Technology Conference*, p. v+178, 62-3, Oct. 1989.
- [16] James A. Folta, Charles E. Hunt, and Shari N. Farrens, "Low-temperature Wafer Bonding of Surfaces Using a Reactive Sputtered Oxide", *J. Electrochem. Soc.* Vol 141, No. 8, Aug. 1994.
- [17] Y. Homma, K. Kusukawa, T. Furusawa, H. Miyazaki, and N. Kobayashi, "An Approach to Realize Deep Submicron Multilevel Interconnection Using Low-Resistance and Low- ϵ Materials", *Electronics and Communications in Japan, Part 2*, Vol. 78, No. 10, 1995, pp. 52-64.
- [18] T. Furusawa, Y. Homma, Y. Shimamura, H. Morishima, Y. Yamamoto, and H. Satoh, "New Reflowable Organic Spin-On Glass for Advanced Interlevel Dielectric Planarization", *Electronics and Communications in Japan, Part 2*, Vol. 78, No. 10, 1995,

pp. 65-72.

- [19] S. Marazita, W. Bishop, T. Crowe, "An Improved Method of Integrating Semiconductor Device Structures with Alternative Substrates using Spin-on-Dielectric Bonding", Patent Disclosure submitted to University of Virginia Patent Foundation, October 16, 1997.
- [20] W.L. Bishop, T.W. Crowe, P.J. Koh, "An Improved Method For The Formation Of Electrical Contacts Used In The Manufacture Of Planar Schottky Diodes," Invention Disclosure (unpublished internal document), University of Virginia Patent Foundation, October, 1997.
- [21] J.L. Hesler, "Planar Schottky Diodes in Submillimeter-Wavelength Waveguide Receivers", Ph.D. dissertation, University of Virginia, January, 1996.

QUARTZ-BASED GaAs SCHOTTKY DIODES — LIFETIME AND FAILURE ANALYSIS

R. Lin, A. Pease, R. Dengler, D. Humphrey, T. Lee, S. Kayali, I. Mehdi

California Institute of Technology
Jet Propulsion Laboratory
4800 Oak Grove Drive
Pasadena, CA 91109

ABSTRACT

A previously reported technology that allows for the fabrication of semiconductor devices based on quartz (or other dissimilar substrates) has resulted in state-of-the-art mixer performance at frequencies up to 640 GHz. The present work will discuss the procedure that has been used to quantify the reliability of such devices for space-borne missions. A number of accelerated lifetime tests have been conducted. It is concluded that these devices exhibit lifetimes that are consistent with other GaAs devices for space applications. Our accelerated lifetime data, analyzed with the Arrhenius-lognormal model, predict a room temperature MTTF on the order of 10^{10} hours, a value that is comparable to conventional high-frequency planar Schottky diodes. This result demonstrates that the use of an appropriate epoxy to obtain GaAs devices on quartz substrates does not reduce the lifetime of the devices.

I. INTRODUCTION

For very high frequency applications, quartz is a desirable substrate material, because it has lower loss and lower dielectric constant than GaAs. One possible method of obtaining semiconductor devices on quartz substrates is to use a bonding agent such as epoxy. A technique, named QUID (for Quartz-substrate Upside-down Integrated Device), has been developed to produce GaAs Schottky diodes on quartz substrates for millimeter- and submillimeter-wave applications [1,2]. With this technique, planar GaAs Schottky diodes are mounted upside-down onto quartz substrates operating as low noise mixers at frequencies up to 640 GHz. After successful performance demonstration, it is now desirable to study the lifetime and failure mechanisms associated with such structures.

Figure 1 shows a cross-sectional schematic of the QUID structure. The anode of the Schottky diode is made with a T-anode structure similar to the T-gate technology used for HEMTs. Two such diodes are arranged in an antiparallel configuration to provide subharmonic mixing. Following the integration of the diode with the RF microstrip filter circuitry, the entire circuit is bonded upside-down onto a 50 micron thick quartz substrate with a heat-cured epoxy [3]. This bonding agent also fills the air gap under the fingers, which may affect the device's reliability. Finally, all of the GaAs substrate is etched except for two small mesas around the active region with the two planar diodes. The thin 4000Å AlGaAs layer that was used as the etch

stop layer can be either removed or left in place without affecting RF performance. However, it does have reliability consequences which will be discussed later.

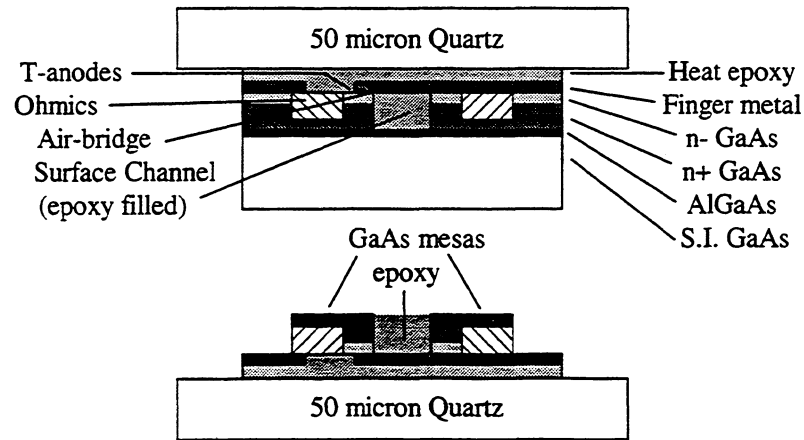


Figure 1: Cross-sectional schematic of the starting and ending point of the QUID process. (not to scale)

II. ACCELERATED LIFETIME TESTING

The accelerated lifetime tests are based on the Arrhenius-lognormal model which is widely used for GaAs MMICs [4]. It states that the failure times for a batch of devices have a lognormal distribution about the median time to failure (the time for 50% of the devices to fail). This median time to failure, in turn, is related to absolute temperature by

$$t = t_0 \exp(E_a/kT),$$

where t is the median time to failure (MTTF), E_a is the activation energy measured in eV, k is Boltzmann's constant, and T is the absolute temperature. A number of studies have been done in the past to determine lifetimes of Schottky diodes. In particular, two studies that investigate the lifetime of high frequency planar diodes made at the University of Virginia have been reported [5,6]. An important goal of this study is to determine whether the QUID process degrades the lifetime of the devices compared to conventional high frequency planar diodes.

A. Failure Criteria and Test Procedure

In defining what constitutes a failure for the QUID structures, we use a failure criteria based on the DC I-V characteristics that may help us predict the device's performance degradation at RF. These devices are being developed for a particular application, so the failure criteria is based on a quantitative degradation in the noise temperature of the subharmonic mixer. Using the procedure outlined in [7], a number of simulations were carried out with a 640 GHz subharmonic mixer. The pad-to-pad and pad-to-finger capacitance of the device were assumed to

be fixed at 4 and 2 fF, respectively [7]. A nominal device was taken to have series resistance of 6 ohms, ideality factor of 1.2 and knee voltage (voltage where current is equal to 1 μ A) of 512 mV. These three parameters are then varied one by one, and the resulting mixer noise temperature is compared to the noise temperature obtainable from the nominal device. The simulation results are shown in Table 1.

% change in mixer	% change in η			% change in R_s					% change in V_0			
	4	17	21	8	17	25	33	50	-4	-10	-14	-39
T_{mix}	2.7	14.6	20.1	5.5	11.3	17.0	22.8	34.1	1.0	2.0	4.0	15.0
L_s	0.0	0.4	0.5	1.8	3.4	5.2	6.8	9.9	0.5	1.3	2.0	6.5

Table 1: Results of harmonic balance simulation of mixer RF performance, as a function of changes in η , R_s , and V_0 .

It is further assumed that a 15% degradation in the noise temperature of the mixer will constitute failure. Based on this information, an anode is considered to have failed if any of the following conditions are met:

1. ideality factor, η , changes by more than 15%,
2. series resistance, R_s , changes by more than 20%,
3. knee voltage, V_0 (voltage where current is 1 μ A), changes by more than 40%,
4. a combination of changes in η , R_s , V_0 results in mixer noise temperature degrading by more than 15%.

The baseline value for each of these three parameters is calculated by averaging a diode's parameter during the first few measurements at the test temperature. This is to smooth out some of the noise due to measuring errors. Further reduction of noise in the acquired data is done by local averaging of the diode's properties over time. For each device, when the device parameters meet the failure criteria, the time since the beginning of the test temperature period is recorded. The failure times are plotted on a lognormal graph paper, and an apparent linear regression line is constructed to determine the median time to failure and the standard deviation at each temperature. Infant mortalities, or devices that failed significantly earlier than the rest of the sample, were not considered in the apparent linear fit.

B. Experimental Setup

An automated system was designed to conduct the accelerated lifetime tests [8]. The QUID structures were placed unbiased in a nitrogen-purged high-temperature oven for an extended period of time. The temperature was slowly increased from room temperature with the devices already mounted inside the oven. Device I-V characteristics were monitored in situ, once every hour, with a computer-controlled data-acquisition system. Nominally fifteen devices, or thirty anodes, were tested at each temperature. The temperature range used extends from 170°C to 240°C. The devices were mounted onto ceramic chip carriers using two-part epoxy and gold wire bonds (Figure 2), and subsequently placed in a high-temperature wiring fixture designed to withstand at least 250°C. Recently we have developed a macor-based mounting that does not involve the use of solder and can withstand temperatures up to 340°C (Figure 3).

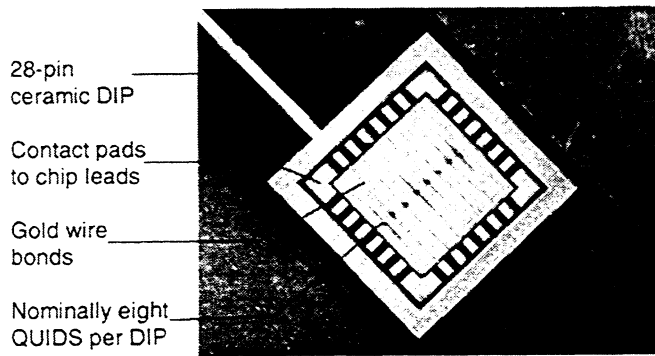


Figure 2: Devices mounted on ceramic chip carrier for thermal lifetime tests.

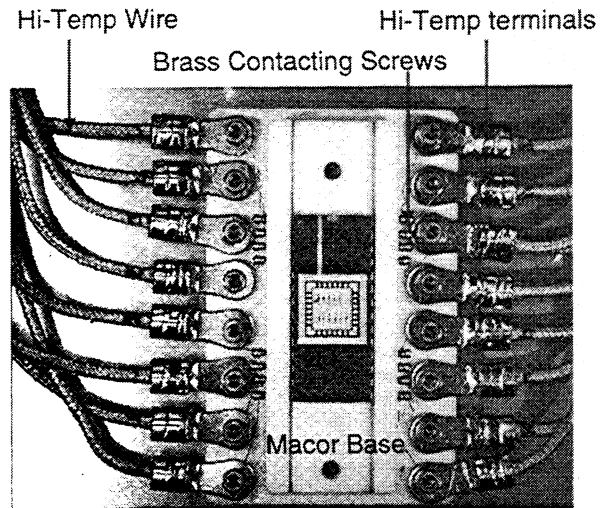


Figure 3: Macor-based solder-less mounting fixture rated to 340°C.

III. EFFECT OF PROCESSING VARIATIONS ON DEVICE LIFETIME

A nominal QUID structure and three processing variations, as shown in Figure 4, were investigated. Their effects on device lifetime are detailed below.

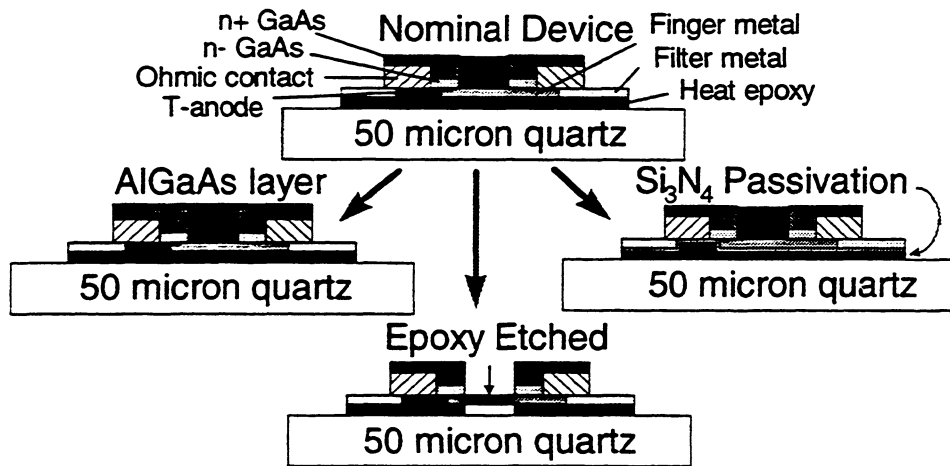


Figure 4: Device Processing Variations: (1) AlGaAs etch-stop layer, (2) epoxy-etched channel, (3) Si₃N₄ passivation. (Figures not drawn to scale)

A. Effect of the AlGaAs etch stop layer

The AlGaAs etch-stop layer, with 55% aluminum mole fraction, is a critical component that enables uniform back etching of the substrate. In earlier devices, the AlGaAs layer was left intact in order to reduce one processing step and to reduce yield loss during dicing. However, once RF measurement results made it clear that the epoxy within the channel would have to be etched, it became necessary to etch the AlGaAs layer. To investigate if this would have an effect

on the device reliability, a number of lifetime tests were conducted both on devices with the AlGaAs and devices without the AlGaAs. The results are shown in Figure 5.

Interestingly, some of the devices with the AlGaAs layer used in the tests failed catastrophically while no device without the AlGaAs layer failed catastrophically. A catastrophic failure is defined as one in which the device meets the failure criteria abruptly rather than gradually. The data shown in Figure 5 includes the devices that failed catastrophically. However, if that data is removed from the test sample, then both types of devices have identical activation energies (that is, the lines are parallel) with the AlGaAs devices having a slightly higher MTTF.

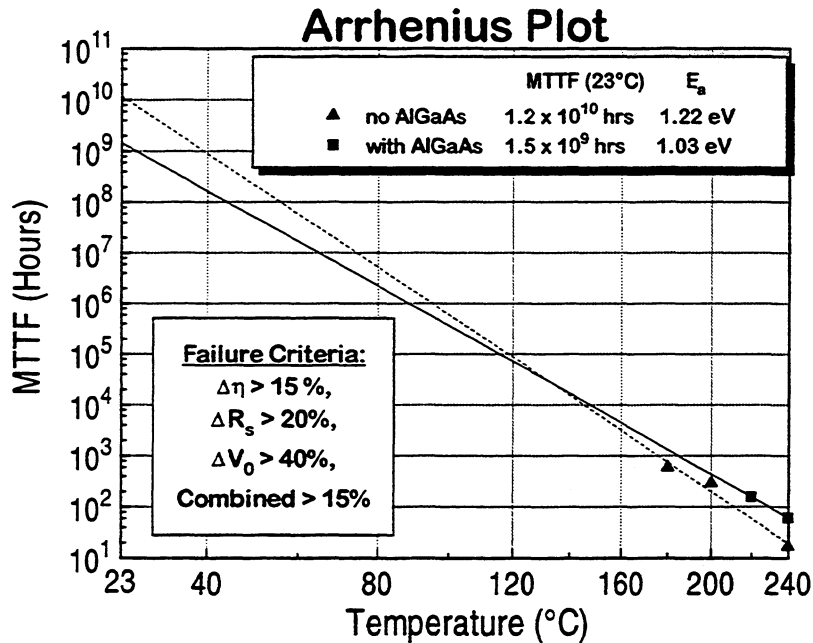


Figure 5: Arrhenius Plot for devices with and without AlGaAs etch-stop layer.

An attempt was made to determine the mechanisms that were responsible for device failures. Following the accelerated lifetime test, devices were inspected with an optical microscope and a scanning electron microscope (SEM). The SEM analysis showed that there are at least two types of failure mechanisms, and that they are related to different failure paths. Figure 6 shows a device with AlGaAs that failed catastrophically, and Figure 7 shows a device without AlGaAs that failed gradually (that is, its I-V parameters slowly degraded before it met the failure criteria).

Several observations can be made about Figure 6. The 4000Å AlGaAs layer is prone to severe cracking. This particular device experienced a catastrophic failure, and further inspection of the top finger revealed that it was broken near the right end. The high-temperature stress possibly caused a structural stress buildup before it was released in the form of a catastrophic crack. Figure 7 shows a device with no AlGaAs layer, and this device does not have signs of cracking. Currently we are investigating other non-structural failure mechanisms that might be responsible for the devices that failed with gradual degradation.

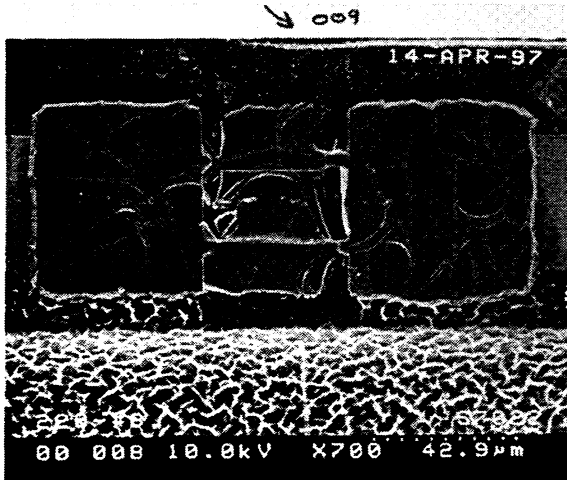


Figure 6: SEM photo of a device with AlGaAs etch-stop layer after 220°C lifetime test. This device failed catastrophically, and there is a break near the right end of the top finger.

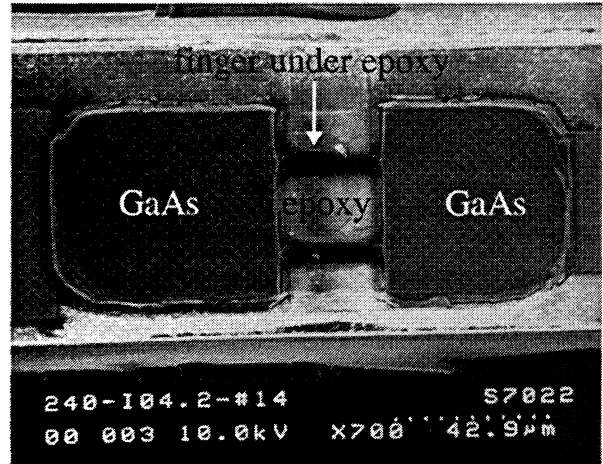


Figure 7: SEM photo of a device without AlGaAs layer, after 240°C lifetime test. This device degraded gradually, and shows no sign of cracks in the GaAs mesas.

B. Effect of epoxy inside the channel

During the procedure for bonding GaAs onto a quartz substrate, an epoxy layer is applied to the wafer, and fills the channel region underneath the metal fingers. Removing this epoxy with an oxygen plasma etch causes a 20% reduction in parasitic capacitance, and enhances the mixer RF performance. To investigate the effect of the epoxy-etch on device reliability, lifetime tests were performed on a batch of epoxy-etched devices and results compared to those without the epoxy-etch. Both batches have the AlGaAs layer already removed. Lifetime tests were conducted at three different temperatures for each type of device. The Arrhenius plots are shown in Figure 8.

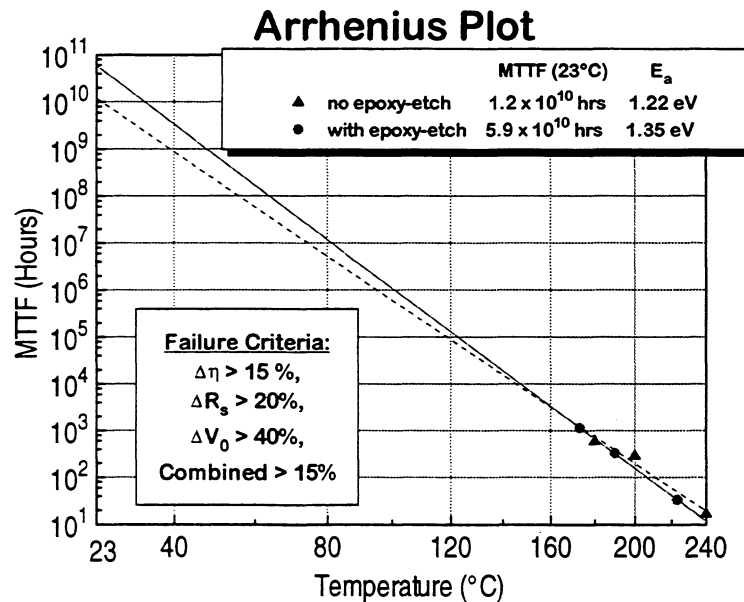


Figure 8: Arrhenius Plot for devices with and without epoxy-etch procedure.

The data collected in these tests fall on nearly the same Arrhenius line. The extrapolated MTTF values at 80°C are equal to within a factor of two, and even at room temperature, they differ by less than an order of magnitude. The activation energies differ by 0.13eV, or about 10%.

Figures 9 and 10 show the images of the two types of devices under a SEM. Both of these devices failed gracefully, although the epoxy in the channel region for Figure 9 seems to have a crack parallel to the fingers. We have already seen a correlation between cracks perpendicular to the fingers and catastrophic failures, but it appears that devices are less affected by cracks parallel to the fingers. Removing the epoxy completely from the channel, however, would reduce the risk of any epoxy cracks around the finger pair, thus reducing the risk of a catastrophic failure due to a mechanical break. This is shown in Figure 10, where the fingers are visible after the epoxy has been etched away.

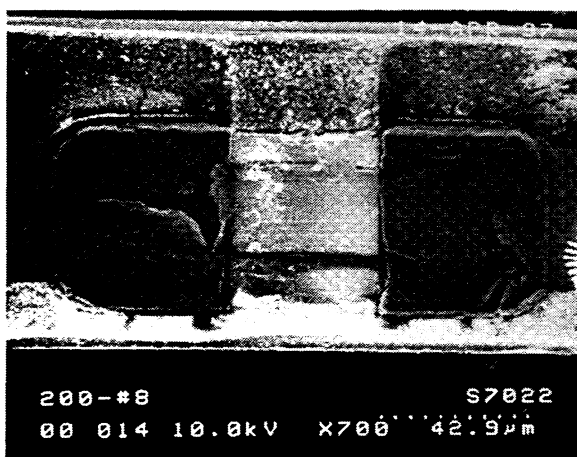


Figure 9: SEM photo of a QUID device after 200°C lifetime test.

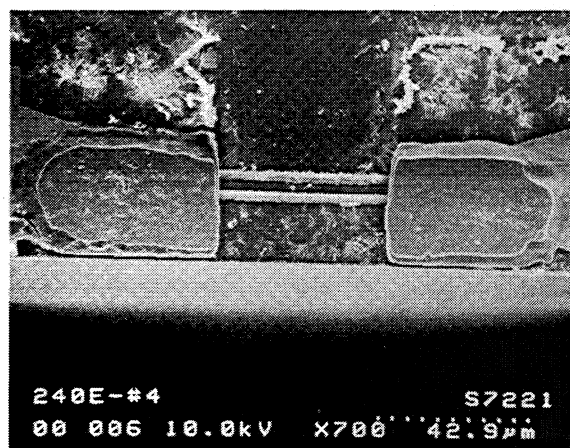


Figure 10: SEM photo of an epoxy-etched QUID device after 240°C lifetime test.

C. Effect of Si₃N₄ passivation

Prior to bonding the GaAs wafer upside-down onto a quartz substrate, a Si₃N₄ passivation layer can be put down around the anodes by a PECVD (plasma enhanced chemical vapor deposition) system. The effect of this procedure on device RF performance is currently being investigated, and its effect on device reliability is reported below.

The Arrhenius plots comparing devices with and without nitride passivation are shown in Figure 11. Both types of devices do not have an AlGaAs layer, and the epoxy inside the channels were not etched. Figure 11 clearly indicates that the nitride passivated devices have a much better lifetime than unpassivated devices. In fact, we had to tighten our failure criteria in order to keep the test from extending too long. The failure criteria in calculating the failure times are reduced by 50%. That is, the new failure criteria is $\Delta\eta > 7.5\%$, $\Delta R_s > 10\%$, $\Delta V_0 > 20\%$, or any combination of these changes that causes the mixer noise temperature to degrade by 7.5%. For a

proper comparison, the same failure criteria was applied to the batch of devices without nitride passivation.

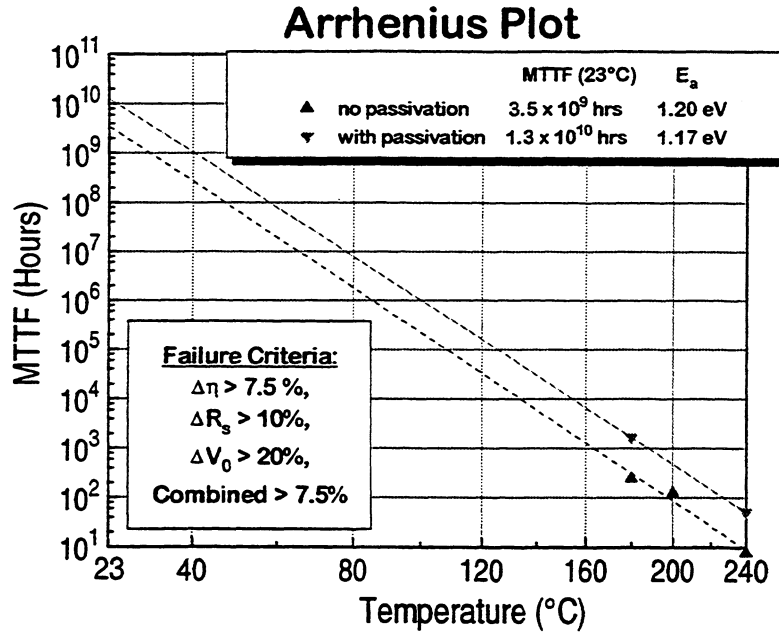


Figure 11: Arrhenius Plot for devices with and without Si_3N_4 passivation layer. Note that the failure criteria was tightened to obtain 50% sample failure from the nitride passivated devices.

Another difference that was observed in the data for passivated devices is the direction of change in the I-V characteristics. Figure 12 compares the device I-V characteristics taken at 180°C at the beginning and end of the test (after 1336 hours) for two devices, one from the unpassivated batch, and the other from the passivated batch. These two devices underwent the same test conditions at the same time, and yet their I-V curves shifted in different directions. The knee voltage for passivated devices increases, while it decreases for unpassivated devices. Currently we are investigating possible causes for this effect.

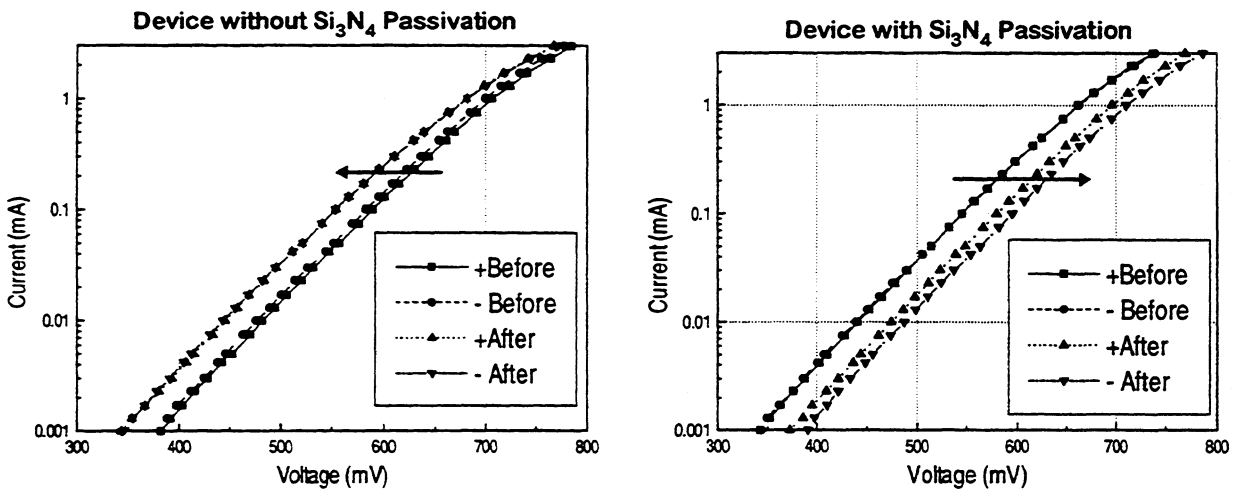


Figure 12: I-V Characteristics of devices before and after lifetime testing. These measurements were made at 180°C, at the beginning of the lifetime test and after 1336 hours.

D. Causes of failure

So far, we have observed that severe cracking in the AlGaAs layer and the channel epoxy region can cause catastrophic failures. Other mechanisms responsible for the gradual degradation could not be observed under the SEM. At this time, we have not made a complete failure analysis of QUID devices in order to determine these mechanisms. From the collected data, however, it is observed that almost all devices failed due to the series resistance meeting the failure criteria. Only the nitride passivated devices differ in that a number of passivated devices failed due to a combination of the three diode parameters.

IV. CONCLUSIONS

Based on results from numerous accelerated lifetime tests, the 640 GHz QUID circuits were determined to have a room temperature MTTF on the order of 10^{10} hours, with an activation energy of 1.2 to 1.3 eV. This value is more than three orders of magnitude higher than the five year mission that QUID devices must meet.

The effects of device processing variations on device lifetime were studied. It was found that the presence of an AlGaAs etch-stop layer can cause severe cracking under high temperature stress, thus increasing the likelihood of a catastrophic failure. The presence of the epoxy in the surface channel region was found to have little or no effect on device lifetime. The presence of a silicon nitride passivation layer, however, significantly enhanced device lifetime by nearly an order of magnitude. Observations of the changes in device I-V characteristics showed that the passivated devices have a failure mechanism different from the unpassivated devices.

Results from a more thorough failure analysis will enable us to better understand these mechanisms. The acceptable MTTF values obtained from this work show that the QUID process can be a useful technique to obtain GaAs devices on non-semiconductor substrates. This technique could also be useful for other applications where a dissimilar substrate is required.

ACKNOWLEDGMENTS

The authors would like to acknowledge S. Martin for help in device fabrication, K. Evans for SEM analysis, and B. Fujiwara for wire bonding. We are also grateful to Dr. Peter Siegel and Karen Lee for technical discussion and for the support of this investigation.

REFERENCES

- [1] I. Mehdi, S. C. Martin, R. J. Dengler, R. P. Smith, and P. H. Siegel, "Fabrication and performance of Planar Schottky Diodes with T-Gate-Like Anodes in 200-GHz

- Subharmonically Pumped Waveguide Mixers,” in *IEEE Microwave and Guided Wave Letters*, Vol. 6, No. 1, January 1996, pp. 49-51.
- [2] I. Mehdi, T. H. Lee, D. A. Humphrey, S. C. Martin, R. J. Dengler, J. E. Oswald, A. Pease, R. P. Smith, and P. H. Siegel, “600 GHz Planar-Schottky-diode subharmonic waveguide mixers,” in *IEEE MTT-S 1996 Digest*, pp. 377-379.
 - [3] The epoxy used is EPOTEK 301-2, from Epoxy Technology, Inc.
 - [4] S. Kayali, G. Ponchak, R. Shaw, ed., *GaAs MMIC Reliability Assurance Guidelines for Space Applications*, JPL Publication 96-25, Dec 1996, pp. 6-14.
 - [5] S. M. Marazita, “A Reliability and Failure Mechanism Analysis of Planar and Whisker-contacted GaAs Schottky Diodes,” *B.S. thesis*, University of Virginia, 1994.
 - [6] J. L. Bowers, “Reliability of Planar GaAs Schottky Diodes,” *M.S. Thesis*, University of Virginia, 1993.
 - [7] I. Mehdi and P. H. Siegel, “Effect of Parasitic Capacitance on the Performance of Planar Subharmonically Pumped Schottky Diode Mixers,” in *Fifth International Symposium on Space Terahertz Technology*, May 1994, pp. 379-393.
 - [8] R. Lin, “Reliability and Failure Analysis of Sub-micron T-anode GaAs Schottky Diodes with Quartz Substrates,” *B.S. Thesis*, California Institute of Technology, 1997.

PHYSICAL PROPERTIES OF THE POTENTIAL BARRIER OF Pt/n-GaAs SCHOTTKY MIXER DIODES

H.-W. Hübers, H. P. Röser
DLR Institute of Space Sensor Technology
Rudower Chaussee 5
12489 Berlin, Germany
heinz-wilhelm.huebers@dlr.de

Abstract

The temperature dependence of the current-voltage characteristic of Pt/n-GaAs Schottky diodes which are used as mixers in low noise THz heterodyne receivers is investigated. Two different groups of diodes are identified. While the barrier height and temperature dependence of the diodes of one group are determined by the energy gaps of GaAs they are determined by defects at the metal-semiconductor interface for the diodes of the other group. For a defect free interface the barrier height has no influence on the noise performance of the diode. The influence of spatial inhomogeneities at the interface on the noise temperature is investigated. It was found that the noise temperature increases with increasing magnitude of the spatial inhomogeneities.

1. Introduction

It is well known that the electronic properties of Schottky diodes for example their current-voltage (I-V) characteristic and their noise performance depend critically on the microphysical structure of the metal-semiconductor contact [1,2]. Interface defects can pin the Fermi-level and consequently change the barrier height of the diode compared to a defect free interface [3]. Spatial inhomogeneities at the potential barrier can lead to a drastic increase of noise when the standard deviation of their magnitude exceeds a critical value of $2kT$ [4].

In the course of this study we have investigated the influence of defects on the height and temperature dependence of the potential barrier in Pt/n-GaAs Schottky diodes with different doping densities of the epitaxial layer. All diodes are used as mixers in low noise THz heterodyne receivers. For the

diode which currently yields the lowest noise temperature in the frequency range from 1 to 5 THz (diode 1T15 from the University of Virginia [5, 6,7]) it was studied if the barrier height has any significant influence on the noise performance of the diode. In addition, for different contacts of this type of diode the magnitude of the spatial inhomogeneities at the metal semiconductor transition was determined and correlated to the measured noise temperature. Evidence is presented that with increasing magnitude of the spatial inhomogeneities the noise performance of the diode degrades.

2. Experimental Setup

The Schottky contact of all diodes is a submicron-size dot of Pt on a GaAs (100) epitaxial layer which has a doping density between $0.5\text{-}10 \times 10^{17} \text{ cm}^{-3}$. The I-V curves

were measured at temperatures varying from 300 K to 80 K. Cooling was performed with a closed cycle He refrigerator. The temperature was measured with a Si temperature diode mounted close to the Schottky contact. In order to make sure that the temperature of the Schottky diode under investigation is the same as the temperature measured by the Si diode a delay of 15 minutes between two measurements was kept. This procedure was checked by replacing the Schottky diode with a Si temperature diode and measuring the temperature with both Si diodes. The difference in the measured temperature between the two Si diodes was always less than 0.2 K. The temperature could be held constant within ± 0.1 K by the use of stabilization loop. The loop consisted of the temperature diode, a heating resistance and a temperature controller, which regulates the temperature to a preset value. All measurements were performed in the dark. The voltage was supplied by a Keithley 236 voltage source, which at the same time measured the current.

As an example, the I-V curves of a Schottky diode 1I7 at different temperatures are plotted in Fig 1. As one can see the I-V curves shift to higher bias voltages and are getting steeper with decreasing temperature.

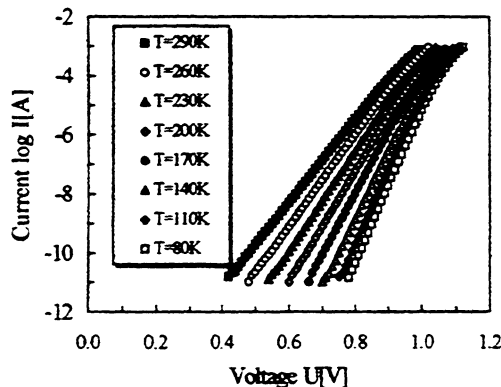


Fig. 1: Current voltage characteristics of the diode 1I7 as a function of temperature.

In order to correlate the microphysical properties of the Schottky contact to the noise performance of the diode when used as a THz mixer in a heterodyne receiver we measured the noise temperature of different diodes at 1.47 THz. A FIR gas laser was used as the local oscillator with $^{13}\text{CH}_3\text{OH}$ as the lasing medium (CO₂ pump laser line 10R16). The diodes were whisker contacted with a standard 4λ antenna in a corner cube mounting. The noise temperatures were measured by the Y factor method with Eccosorb™ immersed in a liquid nitrogen bath as the cold load and Eccosorb™ at ambient temperature as the hot load. Signal beam and laser beam were superimposed by the use of a Martin-Puplett diplexer. A single stage $\lambda/4$ impedance transformer was used. The noise temperatures were measured at an intermediate frequency of 11.1 GHz with a bandwidth of 1 GHz. The first amplifier was cooled to 77K and had a noise temperature of about 100 K. The presented data are double sideband (DSB) noise temperatures and are not corrected for atmospheric losses or losses in the optics.

3. Defects at the Metal-Semiconductor Transition

In the case that the current transport in the Schottky diode is dominated by thermionic emission it can be described by [2]

$$I = I_s \exp(qV/nkT) [1 - \exp(-qV/kT)]. \quad (1)$$

Here q is the electronic charge, k is Boltzmann's constant, T is the temperature, V the applied forward bias and n the empirical ideality coefficient. I_s is the saturation current given by

$$I_s = A^{**} S T^2 \exp(-q\Phi_{b0}/kT), \quad (2)$$

where A^{**} is the effective Richardson constant taken as $8.6 \times 10^4 \text{ A m}^{-2} \text{ K}^{-2}$, S is the anode area and Φ_{b0} is the zero-bias barrier

height. n and I_s were deduced from a least squares fit of eq. 1 to the data while Φ_{b0} is determined from I_s with the help of eq. 2. For a given n and Φ_{b0} it is possible to calculate the height of the potential barrier when the semiconductor bands are flat. This is the so called flat-band barrier height. It is worth noting that the flat-band barrier height is independent of the current transport mechanism [8]. Therefore it can also be determined for the highly doped diodes where tunneling contributes significantly to the total current. According to Wagner et al. [8] the flat-band barrier Φ_{bf} is given by

$$\Phi_{bf} = n\Phi_{b0} - (n-1) (kT/q) \ln(N_C/N_D), \quad (3)$$

where N_C is the effective density of states in the conduction band and N_D is the ionized donor density. Both are functions of the temperature. This is taken into account in our analysis. It has been shown that the flat-band barrier height is the same as the barrier height determined by the capacitance-voltage method [9].

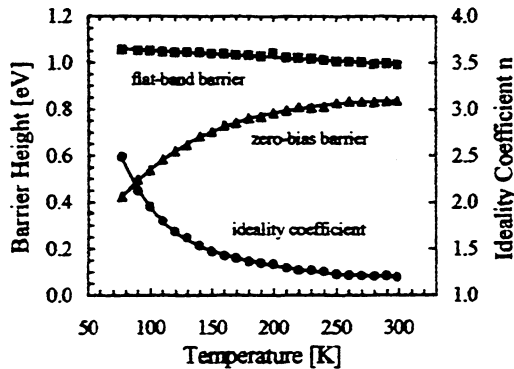


Fig. 2: Ideality coefficient, zero-bias barrier height and flat-band barrier height as a function of temperature for the diode 117c.

Fig. 2 shows the ideality coefficient, the zero-bias barrier height and the flat-band barrier height as a function of temperature. While the ideality coefficient decreases with increasing temperature the zero-bias barrier height increases. Especially at temperatures

below about 150 K this dependence is quite pronounced. In contrast, the flat-band barrier height decreases weakly with increasing temperature. This decrease can be expressed by

$$\Phi_{bf}(T) = \Phi_{bf}(T=0K) + \alpha T. \quad (4)$$

Here $\Phi_{bf}(T=0K)$ is the flat-band barrier height extrapolated to 0 K and α is the temperature coefficient. We have analyzed 11 Schottky diodes with different doping densities by this method. The results are given in table 1 (see appendix). For a further analysis the flat-band barrier height is plotted as a function of the temperature coefficient (fig. 3). Obviously there are two groups of contacts. The Schottky diodes of group 1 have a flat-band barrier height of 1.018 ± 0.008 eV. Their temperature coefficient varies between -0.17 meV/K and -0.30 meV/K with a mean value of -0.23 ± 0.02 meV/K. The diodes of the second group have a mean barrier height of 0.922 ± 0.021 eV and a temperature coefficient close to zero (-0.002 ± 0.004 meV/K). It is worth noting that even diodes which are nominally the same can belong to the different groups (e.g. diode 117 a-c).

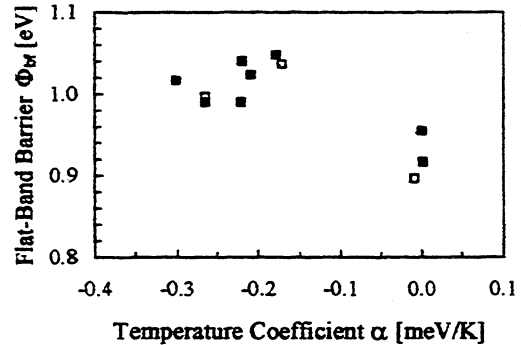


Fig.3: Flat-band barrier height as a function of the temperature coefficient. Two groups of diodes are discernible. It is worth noting that even diodes which are nominally the same can belong to the two different groups (diode 117 open symbols).

These findings can be interpreted on the basis of recent models of Fermi-level pinning and barrier formation in Schottky diodes. According to a model developed by Tersoff [10] the barrier height for a metal on n-type GaAs is given by

$$\Phi_{bn} = E_g^{-1/2} (E_g^i - \Delta/3) - \delta_m, \quad (5)$$

where E_g is the direct energy gap (1.42 eV [11]), E_g^i is the minimum indirect energy gap (1.81 eV [11]), Δ is the spin orbit splitting (0.34 eV [11]) and δ_m is an adjustable parameter which takes into account the dependence of the barrier height on the metal. From our measurements of the flat-band barrier height it follows $\delta_{Pt} = -0.45$ eV. This value is reasonable, since the value for gold is -0.33 eV and Pt is more electronegative than Au if one considers the electronegativity values given by Miedema [1].

The temperature dependence of the potential barrier can be easily deduced from eq. 5

$$d\Phi_{bn}/dT = dE_g/dT - 1/2 dE_g^i/dT. \quad (6)$$

The linearized temperature dependence of the direct energy gap is -0.39 meV/K [11] while for the indirect gap it is -0.43 meV/K [11]. From this a temperature coefficient of -0.18 meV/K is calculated in good agreement with our measurements.

The close to zero temperature coefficients of the Schottky diodes of group 2 are understandable on the basis of a combined model where metal induced gap states as well as defects at the metal semiconductor interface have to be considered. As shown in Ref. [1] defects at the interface result in a decrease of the potential barrier $\delta\Phi_b$ by

$$\delta\Phi_b \approx N_i / D_{MIGS}, \quad (8)$$

where N_i is the density of interface states and D_{MIGS} is the density of metal induced gap states ($\approx 3.7 \times 10^{14} \text{ eV}^{-1} \text{ cm}^{-2}$ for GaAs [1]). For the diodes of group 2 $\delta\Phi_b$ is about 0.1

eV which results in a density of interface states of $N_i \approx 3.7 \times 10^{13} \text{ cm}^{-2}$. This is about one fiftieth of the total density of sites of a GaAs (100) plane. In addition, as Revva et al pointed out [12], the temperature coefficient of a potential barrier which is pinned by defects is close to zero. This is due to the fact that the temperature dependence is governed by the ionization entropy of the defects which is almost independent of temperature.

In fig. 4 the DSB receiver noise temperature measured with a diode 1T15 is shown as a function of the flat-band barrier height. It is worth noting that all measurements were made with Schottky contacts from one diode chip in order to have well defined experimental conditions. No dependence of the noise temperature on the flat-band barrier height is discernible. However, for all diodes the flat-band barrier height is around 1 eV. In this case the barrier height is not determined by defects. If the influence of defects is negligible the noise temperature of the Schottky diodes does not depend on the barrier height. Since this study does not include contacts where the barrier height is determined by interface defects the question if and how they affect the noise performance is still open.

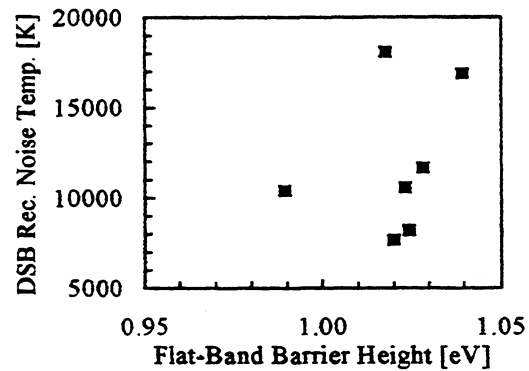


Fig. 4: DSB receiver noise temperature as a function of the flat-band barrier height for the diode 1T15. All contacts are from the same diode chip.

4. Spatial Inhomogeneities at the Metal-Semiconductor Transition

The interface between a metal and a semiconductor is not flat but rough on an atomic scale. These roughness may have different origins. Defects, atomic steps, dislocations, grain boundaries in the metal or irregular distributed donor atoms are a few of them. Spatial inhomogeneities cause a deviation of the measured ideality coefficient of a Schottky diode from the theoretical expected value. In addition, spatial inhomogeneities cause differences between the flat-band barrier height and the zero-bias barrier height of a Schottky diode. It has been shown previously that the noise performance of a Schottky diode depends on the magnitude of the spatial inhomogeneities [4]. In the analysis of our data we follow the approach of Werner and Güttler [3]. They assume that the spatial distribution of the barrier height Φ_b at the metal-semiconductor transition can be modeled by a Gaussian distribution with a standard deviation σ_s around the flat-band barrier height Φ_{bf}

$$P(\phi_b) = (\sigma_s \sqrt{2\pi})^{-1} \exp(-(\Phi_{bf} - \Phi_b)^2 / 2\sigma_s^2). \quad (8)$$

From this it follows that the difference between the flat-band barrier height and the zero-bias barrier height is given by

$$\Phi_{bf} - \Phi_{b0} = q\sigma_s^2 / 2kT. \quad (9)$$

Because of the high doping density of the diode 1T15 the lowering of the potential barrier is not only due to inhomogeneities. Tunneling currents and image force cause a barrier lowering with respect to the flat-band. In order to determine the barrier lowering due to inhomogeneities their contributions are subtracted from the flat-band barrier height. Other effects such as generation-recombination currents in the space charge region or defects are negligible for the 1T15 diodes in this study. By taking into account the barrier lowering due to tunneling and

image force the standard deviation σ_s of the spatial distribution of the Schottky barrier heights was calculated. Fig. 5 shows the receiver noise temperature as a function of kT/σ_s^2 . There is a correlation between both. For all contacts the thermal energy kT of the electrons is smaller than $0.5 \sigma_s$. It is worth noting that in this case where the standard deviation σ_s exceeds a critical value of $2kT$ a drastic increase of noise was observed for different silicide/Si Schottky diodes [4].

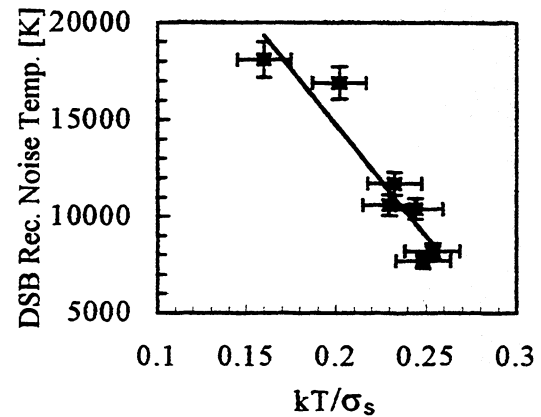


Fig. 5: The DSB receiver noise temperature increases with increasing standard deviation σ_s of the spatial inhomogeneities.

5. Summary

From the analysis of the temperature dependence of the I-V curves of different Pt/n-GaAs Schottky diodes two different groups could be identified. While the diodes of group 1 have a barrier height of about 1 eV which increases with decreasing temperature the diodes of group 2 have a barrier height of about 0.9 eV which is almost independent of the temperature. These findings are interpreted on the basis of recent models of Fermi-level pinning in Schottky diodes. The barrier height and the temperature dependence of the diodes of the first group are determined by the direct and indirect energy gap of GaAs. For the diodes of

the second group defects pin the Fermi-level. Since their ionization entropy is almost independent of the temperature the barrier height is also temperature independent. The density of the defects is about one fiftieth of the total density of sites in a GaAs (100) plane. The results indicate that problems with impurities may have occurred during the processing of the devices. Furthermore it was found that the noise temperature is independent of the barrier height for a defect free Schottky contact while it depends on the magnitude of the spatial inhomogeneities at the Schottky contact. This study demonstrates that I-V-T measurements are useful not only to characterize the physical properties of a metal semiconductor transition but also to give useful information about the processing.

Acknowledgement

The authors would like to thank T. W. Crowe and J. L. Hesler for providing the computer program which was used for data acquisition.

Appendix: table 1 see next page

References

1. W. Mönch, *Semiconductor Surfaces and Interfaces*, 2nd ed. (Springer, Berlin, 1995).
2. E.H.Rhoderick, R.H. Williams, *Metal Semiconductor Contacts*, 2nd ed. (Clarendon Press, Oxford, 1988).
3. J.H. Werner, H.H. Güttler, *J. Appl. Phys.* **73**, 1315 (1993).
4. H.H.Güttler, J.H. Werner, *Appl. Phys. Lett.* **56**, 1113 (1990).
5. A. L. Betz, R. Boreiko, *Proc. 7th Intl. Symp. Space THz Technol.*, 503, Charlottesville, (1996).
6. H. P. Röser, H.-W. Hübers, T.W. Crowe, W.C.B. Peatman, *Infrared Phys. Technol.* **32**, 385 (1991).
7. R. Titz, M. Birk, D. Hausamann, R. Nitsche, F. Schreier, H. Küllmann, H. P. Röser, , *Proc. 6th Intl. Symp. Space THz Technol.*, 1, Pasadena (1995).
8. L.F. Wagner, R.W. Young, A. Sugarman, *IEEE Electron Dev. Lett.* **EDL-4**, 320 (1983).
9. V.W.L. Chin, M.A. Green, J.W.V. Storey, *J. Appl. Phys.* **68**, 3470, (1990).
10. J. Tersoff, *Phys. Rev. B* **32**, 6968 (1985).
11. J.S. Blakemore, *J. Appl. Phys.* **53**, R123 (1982).
12. P.Revva, J.M. Langer, M. Missous, A.R. Parker, *J. Appl. Phys.* **74**, 416 (1993).

Appendix

Tab. 1: Parameters of the investigated Schottky diodes.

Diode	Manufacturer	Doping Density [10^{17}cm^{-3}]	Ideality Coeff.	Zero-Bias Bar- rier Height [eV]	Flat-Band Bar- rier Height [eV]	Temperature Coefficient [meV/K]
SDO 20	Farran Tech.	0.5	1.28	0.830	1.048	-0.18
DA499	TU Darmstadt	1.0	1.12	0.917	1.017	-0.30
HSD3S	Tohoku U..	1.0	1.16	0.827	0.954	0.00
1T6	U. of Virg. (UVa)	1.0	1.39	0.758	1.040	-0.22
1I7 a	UVa	3.0	1.16	0.780	0.896	-0.01
1I7 b	UVa	3.0	1.34	0.777	1.037	-0.17
1I7 c	UVa	3.0	1.20	0.836	0.997	-0.27
1T12	UVa	3.0	1.22	0.821	0.990	-0.22
1I12	UVa	4.5	1.23	0.833	1.023	-0.21
1T14	UVa	10.0	1.67	0.544	0.917	0.02
1T15	UVa	10.0	1.57	0.628	0.990	-0.27

PHOTOMIXING IN LOW-TEMPERATURE-GROWN GaAs

S. Verghese,¹ K. A. McIntosh, S. M. Duffy, E. R. Brown,² S. Calawa,

K. Molvar, W. F. Dinatale, and T. M. Lyszczarz

Lincoln Laboratory, Massachusetts Institute of Technology

244 Wood Street, Lexington, MA 02173

ABSTRACT

Photomixing occurs in epitaxial low-temperature-grown GaAs between two voltage-biased metal electrodes on which two laser beams are focused and are detuned to a desired difference frequency. Compared with pulsed THz-radiation emitters such as time-domain photoconductive switches, the photomixer is useful when a constant wave source is needed with high spectral brightness and narrow linewidth. Also, a general technique has been demonstrated at microwave frequencies for photoconductive sampling in the frequency domain using two photomixers driven by a single pair of diode lasers. A terahertz implementation would compare favorably to time-domain sampling for narrow-linewidth spectroscopy.

Heterodyne measurements in the region 30–1000 μm can reveal the spectroscopic signatures of molecules that are important for atmospheric sensing and for astrophysical measurements. Recent advances in superconducting THz receivers [1, 2] have created a compelling need for a tunable single-frequency local oscillator with output power $> 1 \mu\text{W}$ from roughly 1 to 3 THz.

The photomixer generates a THz difference frequency by photoconductive mixing of two tunable single-frequency lasers in low-temperature-grown (LTG) GaAs [3, 4]. In one design, the combined laser beams are focused on an $8 \times 6\text{-}\mu\text{m}$ area with interdigitated $0.2\text{-}\mu\text{m}$ -wide electrodes that are separated by a $1.8\text{-}\mu\text{m}$ gap and are voltage biased at approximately 30 V. The electrodes are at the drive point of either a log-spiral or a dipole antenna [5] that radiates through the GaAs substrate that is mounted on a Si hyperhemisphere lens. Compared to other fast photoconductors, high-quality LTG GaAs is well suited to this application because of its short carrier lifetime (< 0.25 ps), high electrical breakdown field ($> 5 \times 10^5$ V/cm), and its relatively high mobility ($> 100 \text{ cm}^2/\text{Vs}$).

Our recent efforts have focused on increasing the maximum THz power available from the photomixer. The available THz power is approximately proportional to P_i^2 , where P_i is the total optical power incident on the photomixer. Our room-temperature photomixers

¹simonv@ll.mit.edu

²On leave of absence to DARPA/ETO, 3701 N. Fairfax Dr., Arlington VA 22203-1714

can withstand a total optical power of $P_i \approx 60 \text{ mW}$ ($9 \times 10^4 \text{ W/cm}^2$) when biased at 30 V. Above that power, a combination of optical and ohmic heating causes catastrophic failure of the device. Cryogenic operation at 77 K was shown to increase the optical power handling to $\sim 90 \text{ mW}$ which increased the emitted THz power by approximately $\times 2$ —because of the increased thermal conductance of the GaAs substrate [6]. Recently, LTG-GaAs layers with carrier lifetime less than $\sim 300 \text{ fs}$ were grown by molecular-beam epitaxy on a high-resistivity silicon substrate. Photomixers that were fabricated from this wafer sustained incident optical power of 120 mW without failing. Also, the output THz power increased commensurately with the optical pump power and THz absorption losses in the silicon substrate degrade the signal at 1.1 THz by only $\sim 20\%$. At present, photomixers with log-spiral antennas are being used for comparison of the THz output power with photomixers on GaAs substrates over a wide range of operating frequencies. Photomixers with resonant antennas have also been fabricated on the silicon substrate. An example of a 1.5-THz full-wave dipole is shown in Fig. 1. The scanning electron micrograph shows the metal electrode pattern that defines the photomixer. The Smith chart shows design calculations that were obtained with a commercial planar-structure solver [7]. Preliminary measurements show a peak output power at 1.4 THz with a 3-dB bandwidth of approximately 15%. By comparing the output power from this antenna with a spiral-antenna from the same wafer, the measured radiation resistance of the dipole will be estimated.

Photomixers show promise for use as local oscillators [4] and for high-resolution gas spectroscopy when coupled to a cryogenic detector such as a bolometer [8]. A recent development is the demonstration of photoconductive sampling in the frequency domain using a pair of photomixers. This technique is analogous to time-domain photoconductive sampling where two photoconductive switches are illuminated by a mode-locked laser. Such a technique, in principle, would use the second photomixer as the receiver rather than a helium-cooled bolometer. For spectroscopy applications that require narrow-resolution linewidth ($< 1 \text{ MHz}$), this technique can offer significant improvement over time-domain sampling in spectral brightness ($\sim 10^6$ times higher). Furthermore, the system is coherent, widely tunable, and can be compact—using inexpensive diode lasers that are fiber coupled to photomixer-transmitter and receiver chips.

Figure 2a shows a block diagram of how narrow-linewidth spectroscopy could be performed coherently and at room temperature using antenna-coupled photomixers as the transmitter and receiver. Figure 2b shows the experimental setup that was used to test the concept at microwave frequencies. The combined light from a pair of distributed-Bragg-reflector laser diodes is split in half and fiber coupled to each photomixer. Each LTG-GaAs photomixer consists of a $20 \times 20\text{-}\mu\text{m}$ active region with $0.2\text{-}\mu\text{m}$ wide interdigitated electrodes spaced by

0.6 μm for the transmitter and by 0.4 μm for the receiver. The transmitter is dc biased through a broadband bias tee and therefore develops an ac current across the electrodes when the photoconductance is modulated at the difference (beat) frequency of the two laser beams. Some of the resulting microwave power is launched onto a coplanar waveguide which transitions into a 50- Ω coaxial line that is connected in similar fashion to the receiver. At the receiver end, the optical beating periodically raises the photoconductance such that a small amount of unipolar current flows into the dc current amplifier. This action is equivalent to homodyne detection of the rf electric field.

Two experiments have been performed to verify that homodyne detection is occurring. First, the transfer characteristic of a narrow bandpass filter has been measured and agrees with that measured using a microwave spectrum analyzer. Second, as shown in Fig. 3, the homodyne signal scales linearly with the dc-bias voltage (or incident electric field) while the transmitted power measured with a spectrum analyzer scales quadratically. The magnitude of the receiver photocurrent is in good agreement with predictions from a theoretical model that accounts for the impedance mismatch between the photomixers and the transmission line.

In summary, photomixers fabricated from low-temperature-grown GaAs deposited on a silicon substrate show improved optical power handling and increased THz output power. Resonant antennas are being evaluated that should further increase the output power. Compared to time-domain sampling, the most important advantages of frequency-domain photoconductive sampling are spectral brightness and the use of compact inexpensive lasers. The disadvantages including longer acquisition times for measuring very broad spectra and standing waves introduced by the high level of coherence. This work was supported by the National Aeronautics and Space Administration, Office of Space Access and Technology, through the Center for Space Microelectronics Technology, Jet Propulsion Laboratory, California Institute of Technology.

References

- [1] D. E. Prober, *Appl. Phys. Lett.*, **62**, 2119 (1993); A. Skalare, W. R. McGrath, B. Bumble, H. G. LeDuc, P. J. Burke, A. A. Verheijen, and D. E. Prober, *IEEE Trans. Appl. Supercond.* **5**, 2236 (1995).
- [2] G. N. Gol'tsman, B. S. Karasik, O. V. Okunev, A. L. Dzardanov, E. M. Gershenzon, H. Ekstroem, S. Jacobsson, and E. Kollberg, *IEEE Trans. Appl. Supercond.* **5**, 3065 (1995).
- [3] K. A. McIntosh, E. R. Brown, K. B. Nichols, O. B. McMahon, W. F. Dinatale, and T. M. Lyszczarz, *Appl. Phys. Lett.* **67**, 3844 (1995).

- [4] S. Verghese, K. A. McIntosh, and E. R. Brown, *IEEE Trans. Microwave Theory Tech.* **MTT-45**, 1301 (1997).
- [5] K. A. McIntosh, E. R. Brown, K. B. Nichols, O. B. McMahon, W. F. Dinatale, and T. M. Lyszczarz, *Appl. Phys. Lett.* **69**, 3632 (1996).
- [6] S. Verghese, K. A. McIntosh, and E. R. Brown, *Appl. Phys. Lett.* **71**, pp. 2743-2745 (1997).
- [7] MomentumTM, in Hewlett-Packard's EESOF electronic-design application suite.
- [8] A. S. Pine, R. D. Suenram, E. R. Brown, and K. A. McIntosh, *J. Mol. Spectrosc.* **175**, 37 (1996).

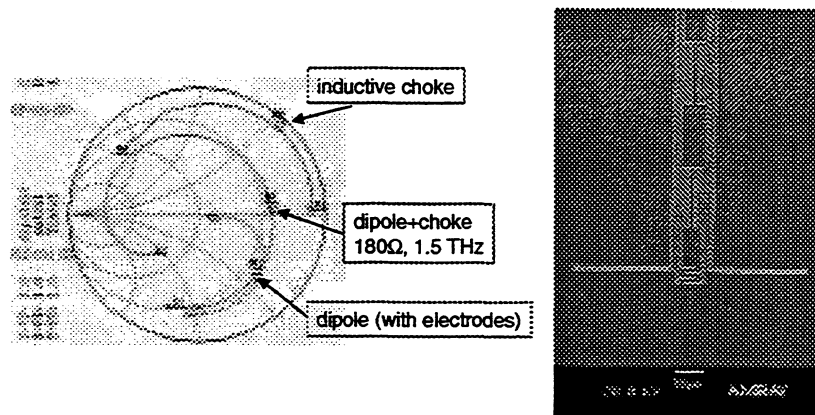


Figure 1: Calculated drive-point impedance for a 1.5-THz full-wave dipole with inductive tuning built into the choke. Also shown: scanning electron micrograph of such an antenna fabricated on LTG-GaAs on a GaAs substrate.

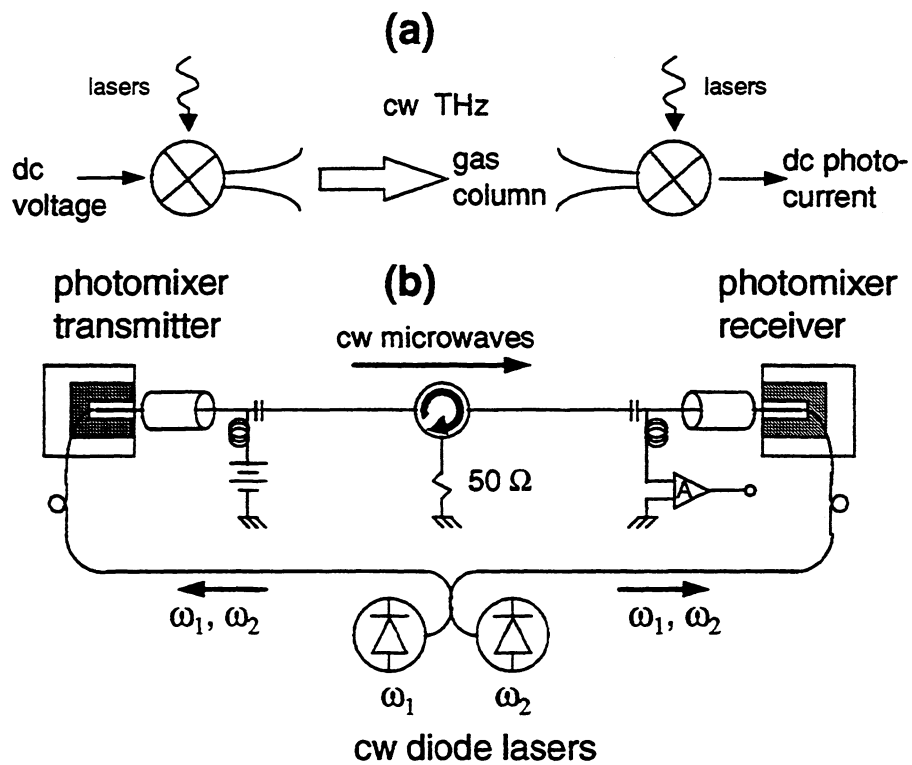


Figure 2: (a) Block diagram for frequency-domain photoconductive sampling. (b) LTG-GaAs photomixers used as transmitter and receiver in proof-of-concept measurements at microwave frequencies (0.05–26.5 GHz).

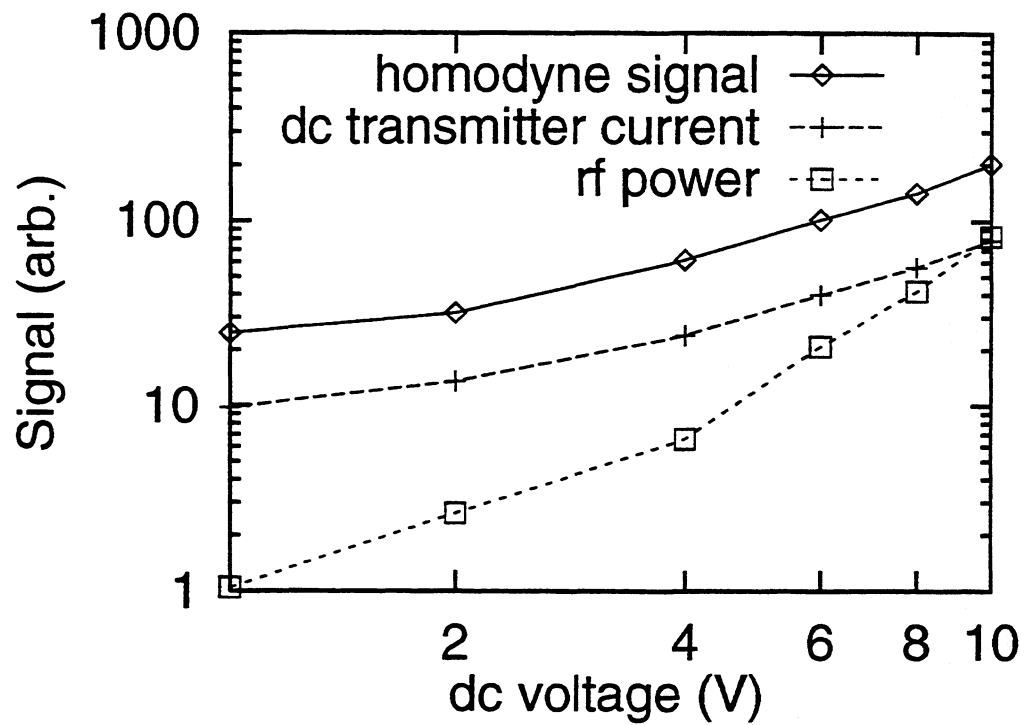


Figure 3: 4.5-GHz homodyne signal detected by the receiver as a function of voltage bias on the transmitter. The coherent signal scales linearly with voltage while the power scales quadratically with voltage. The dc photocurrent in the transmitter is also shown ($300 \mu\text{A}$ at 10V).

A COHERENT, TUNABLE, FIR SOURCE

J.H. Brownell, M.F. Kimmitt, J.C. Swartz and J.E. Walsh

Department of Physics and Astronomy, Dartmouth College, Hanover, New Hampshire 03755-3528

(March 18, 1998)

A tunable coherent source which operates in the THz-FIR region of the spectrum has been developed. The device, termed a grating-coupled oscillator (GCO) uses the beam in a scanning electron microscope (SEM) and a diffraction grating placed in the e-beam's focal region to generate the radiation. Distributed feedback is provided by the grating itself and the e-beam is focused and positioned using the microscope's internal control system. A summary of operating characteristics of the present device and a survey of the scaling relations which will determine the spectral coverage is presented. Comments on what will be required in order to develop a very compact device are also included.

I. INTRODUCTION

The region of the electromagnetic spectrum which falls in the approximate band of wavelengths between 10 and 1000 μm , the so-called far-infrared (FIR) spectral region, is relatively devoid of tunable, coherent, radiation sources. Until quite recently, and relative to the range of options available at longer and shorter wavelengths, this assertion would be almost indisputable. However, the challenge presented by the lack of sources together with the existence of a broad range of interesting research puzzles and opportunities has led to a renewed interest in providing access to this spectral region. The present note deals with one promising approach to a means of producing tunable THz or FIR radiation.

The beam in a scanning electron microscope (SEM) and a diffraction grating mounted in the e-beam focal region has been used to produce coherent radiation [1] over a range of wavelengths that extends from approximately 250 μm out to 1000 μm . Termed a grating-coupled oscillator (GCO), the device is a new variation on an old theme.

Observation of radiation produced by electrons skimming over a diffraction grating was first reported by Smith and Purcell [2] in 1953. Even earlier, Salisbury had filed a patent application [3] on a device based on the coupling of moving electrons and a diffraction grating although Salisbury apparently did not conduct experiments until somewhat later [4]. Others [5-8] have also followed up on the early work.

The radiation mechanism described in reference [1], which has become associated with the authors'

names, was essentially an incoherent or shot noise process. Individual rulings on the grating contributed coherently to the passage of a single electron but the contributions of each electron in the beam added incoherently. This was a consequence of the fact that in the early experiments, the focus was on short wavelengths, visible, and the size of the beam was large relative to the wavelength. The relative beam energy which is also a factor in the dimensionless coupling parameter was also low. A quantitative discussion of this point is presented further along in the manuscript.

Coherent radiation at mm [9-12] and sub-mm [13,14] wavelengths has been introduced in grating-coupled devices. Termed either Orotrons [9,11-14] or the Ledatron [10], these devices used gratings embedded in Fabry-Perot resonators and electron beam technology similar to that used in other microwave tubes to produce the radiation. The name Ledatron, introduced by Mizuno [10], was an acronym that was chosen in order to emphasize the dual nature of the surface modes and the importance of both the bound and radiative space harmonics in the coupling and emission process.

In the present device it is the distributed feedback on the grating itself that leads to bunching of the electron beam and the growth of coherent radiation. The beam voltages are modest (10-50 kV) but higher than those used in any but high-power tubes. Beam current density is high (100 A/cm² or greater), but the total currents are modest (100's μA). The "quality" of the electron beam, energy spread and emittance are critical factors. Thus, overall, the "brightness" of the beam is very high. The "open" nature of the resonator together with the extremely bright electron beam are the essential features of the device.

The remainder of the paper is divided as follows: A survey of device performance will be given in Section II and a summary of basic scaling relations that govern device operation is contained in Section III. These sections are followed by brief remarks on possible means by which very compact GCO devices might be realized, and by concluding remarks.

II. SURVEY OF EXPERIMENTAL RESULTS

Given the importance of beam quality and brightness, an SEM is the ideal device for exploring the potential of the GCO. The beam quality is excellent and the microscope's own focusing and transport elements may be used to shape and position the beam. The beam column of the SEM used in the present experiments is illustrated in Fig. 1. Electrons are emitted from a Tungsten "hairpin" cathode and focussed by a Wehnelt electrode and a series of magnetic lenses. The waist of the beam is placed at approximately the midpoint of the grating and at present the lower limit to the waist diameter is approximately 25 μm . This however is a machine-design imposed but not an absolute limit. The beam may also be swept either in and out along the grating normal or across the grating surface. This provides a convenient temporal reference modulation. Operation in fixed spot temporally pulsed mode is also an option.

The grating is placed on a miniature "optical bench" which is mounted on the microscope stage. At present the FIR optical system limits observation to the normal direction and the grating parameters are chosen to optimize normal emission. Designs that circumvent this limitation are under evaluation.

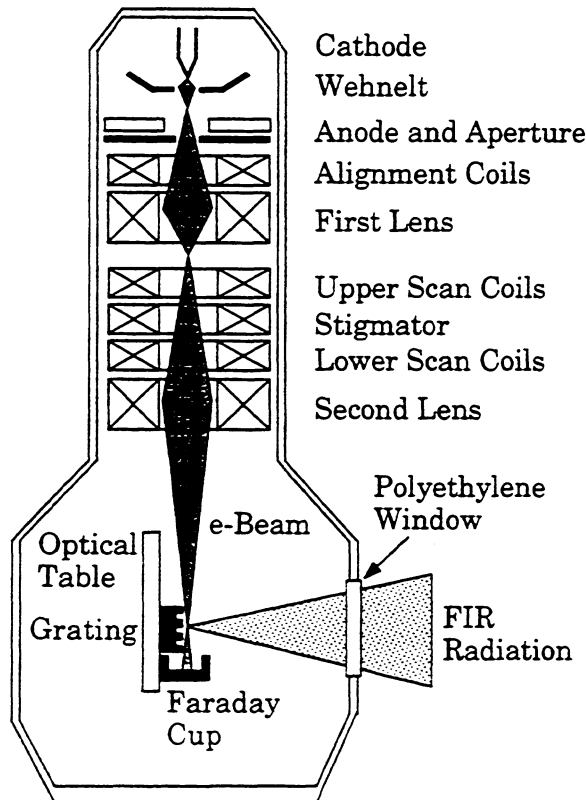


FIG. 1. Diagram of the SEM optical system.

A typical example of a plot of observed power versus electron beam current is shown in Fig. 2. It has two characteristic regions. When the current is relatively low and/or the beam diameter is comparatively large, the observed power increases linearly with current. This is characteristic of a shot noise or spontaneous emission process. In this region, a detailed analysis of the emission process has been carried out [15]. The emitted power in W/sr is given by:

$$\frac{dP}{d\Omega} = eI \frac{Nn^2}{2\ell\epsilon_0} F |R_n|^2 \exp(-x_0/\lambda_e) \quad (1)$$

where e is the electron charge, I is the beam current, N is the number of grating periods, n is the order of emission, ℓ is the grating period, and ϵ_0 is the permittivity of free space. Other parameters which appear in Eq. (1) are:

$$F = \frac{\sin^2 \theta}{(1/\beta - \cos \theta)^3} \quad (2)$$

$$\begin{aligned} \lambda_e &= \frac{\gamma\beta\lambda}{4\pi} \\ &= \frac{\gamma\beta\ell}{4\pi|n|} \left(\frac{1}{\beta} - \cos \theta \right) \end{aligned} \quad (3)$$

Eq. (2) is the variation of the emission with polar angle. The symbols β and γ are respectively the electron velocity relative to the speed of light and the relative electron energy. Angles are measured with respect to the electron beam axis and x_0 is the distance of the infinitesimally thick beam above the grating. When observed power is compared with the prediction of Eq. (1), the measured beam profile is folded together with the evanescent field length given by Eq. (3). The remaining factor in Eq. (1), $|R_n|^2$, is in effect an antenna gain and the notation is that first introduced by van den Berg [16]. A detailed discussion that is adapted to the conditions of this experiment may be found in Urata [17].

When evaluated for parameters used in producing Fig. 2 and assuming an interaction length of 5 mm, Eq. (1) would predict emitted power levels of the order of 100 pW/ $\mu\text{A}\cdot\text{sr}$. The effective field of view of the collection optics is approximately 0.07 sr. The FIR emission is detected with a silicon composite bolometer placed between 0.5 and 1.0 m distant from the grating. Although the loss in the collection system is not accurately known, the theoretical predictions and estimated geometrical factors are consistent with the sub-nW power levels observed in the range where $P \propto I$.

The focused beam will support fast and slow space charge modes. As the beam plasma frequency is increased, those modes become resolved on the scale

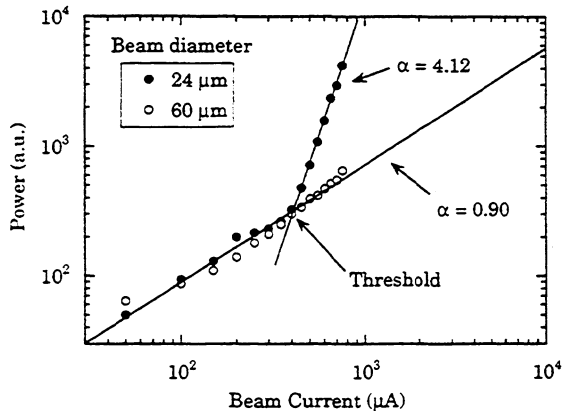


FIG. 2. Detected power vs. beam current. Fits of the form $y = Ax^\alpha$ are shown for the linear and superlinear regimes.

of the free spectral range which is determined by the beam velocity and the interaction length (i.e. the transit time). When, by increasing the beam current, this regime is reached, it is expected that coupling of the “negative energy” slow space charge wave with a co-propagating space harmonic component could result in a bunching of the beam. In this case, growth of the component of the emitted radiation will occur. While the details of the theory in this regime are still under development, such a transition is indeed observed. The transition occurs when the beam plasma frequency times the transit time exceeds 0.2-0.25. Beyond the transition point, the radiated power grows rapidly as a power of the current exceeding the expected spontaneous emission by 1 to 2 orders of magnitude. The exponent in this power law relation typically ranges from 3 to 6 and is sensitive to the operating conditions. With the present operating parameters, the system does not appear to have reached saturation.

It is clear that the finite length grating is functioning as a relatively high quality surface resonator but the details are yet to be understood. A similar caveat applies to the non-linear regime but Eq. (1) provides a basis for some interesting estimated. Since it is proportional to the product of the electron charge and the current, it has the characteristic form of a shot noise formula. If it is multiplied and divided by a spectral interval, $d\omega$, and the product eI factored out, what remains is a “radiation resistance”. The spectral width of the spontaneous emission “Smith-Purcell line” has been deduced from both grating spectrometer and Fourier transform interferometer measurements. In either case the spectral width is about $\Delta\nu \approx 1\text{cm}^{-1}$. Converting this to an angular frequency, $d\omega$, and using a beam current of 100 μA , the factors

$$eId\omega = 3.2\text{pW}/\Omega \quad (4)$$

Thus the measured power near the upper limit of the spontaneous emission regime indicates that the radiation resistance lies between 1 and 10 $\text{k}\Omega$. The interaction length and the exact value of the beam profile – evanescent wave overlap are not determined precisely. However the 1–10 $\text{k}\Omega$ range for a radiation resistance is also consistent with an independent evaluation of Eq. (1) (after factoring out eI and evaluating $d\Omega/d\omega$).

A bunched beam with 100 μA rms current would be expected to generate between 10 and 100 μW . A beam with approximately one order of magnitude greater current ($\approx 1\text{mA}$) would produce power levels in the mW range.

These arguments are qualitative but they are also based on fundamental constraints. The estimates probably represent reasonable upper limits to what can be expected from SEM electron optical system based e-beam technology.

III. SCALING OF GCO DESIGN CONSTRAINTS

A discussion of the constraints governing GCO operation is facilitated by first examining the dispersion plane associated with the electromagnetic fields above a grating. A schematic dispersion plane is illustrated in Fig. 3. The vertical axis is the angular frequency measured in units of 2π times the speed of light divided by the grating period. The horizontal axis is the wave number along the grating in a direction perpendicular to the rulings. Again, the units are normalized.

The plane is divided into two principal regions, “fast” and “slow”. These designations are relative to

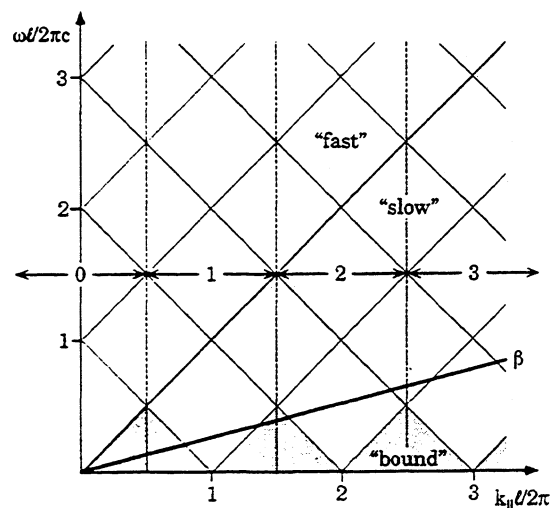


FIG. 3. Schematic of GCO dispersion plane.

the speed of light, the lines with slope ± 1 on the diagram. Each Fourier component of the field above the grating will contain a complete set of space harmonic whose axial wave numbers differ by $2\pi/\ell$. Space harmonics with phase velocities that fall within the "light cone", the region labeled fast, satisfy radiative boundary conditions. The points in the fast region represent components of either incident and scattered waves or an outgoing wave generated by the beam.

Points on the plane which fall outside the light cone have phase velocities less than the speed of light. Space harmonic components in this region are non-radiative but they do serve as a coupling mechanism for the electron beam. A "beam line" is also shown on the figure. Along this line the relation

$$\omega = k_{\parallel}v \quad (5)$$

is satisfied (ω is the angular frequency, k_{\parallel} is the axial wave number in dimensional units, and v is the velocity of the beam. In the current discussion only waves which have at least one space harmonic component in this light cone are of interest. Thus, the darker shaded areas, marked bound, may be ignored. The wavenumber which appears in Eq. (5) may be broken down into two components

$$k_{\parallel} = k_0 + 2\pi|n|/\ell \quad (6)$$

where

$$k_0 = (\omega/c) \cos \theta \quad (7)$$

is the axial component of the wavenumber along the grating that would be associated with an outgoing radiative wave. Combining Eqs. (5 - 7) and choosing $|n| = 1$ yields

$$\frac{\omega}{c} = \frac{2\pi/\ell}{1/\beta - \cos \theta} \quad (8)$$

or

$$\lambda = \ell(1/\beta - \cos \theta) \quad (9)$$

which is the well-known relation discussed by Smith and Purcell in Ref. [2]. It can also be deduced using the Huygens construction.

The choice $|n| = 1$ is not necessarily the dominant mode. It is interesting to note that if, for instance, the depth of the grating is chosen in order to optimize the spontaneous emission for $|n| = 3$ that mode will also dominate above threshold (Fig. 4). Small variations in voltage will also lead to $|n| = 1$ and $|n| = 3$ operating simultaneously (Figs. 5 and 6). The potential for operation on higher-order modes of the grating provides an important degree of freedom for grating design.

Another important constraint is related to the evanescent scale length of the slow space harmonics. Outside the light cone, the square of the perpendicular component of the total wavenumber is less than

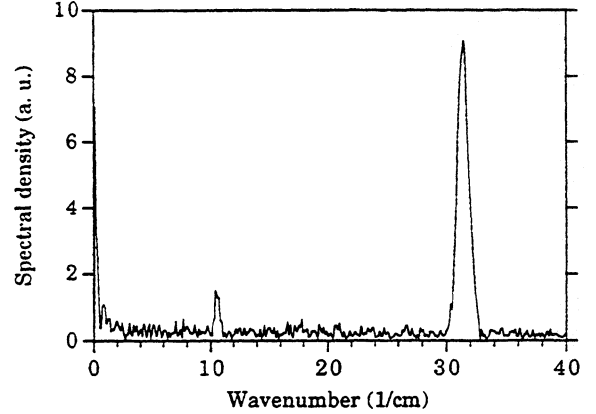


FIG. 4. Power spectrum of GCO operating at $|n| = 3$.

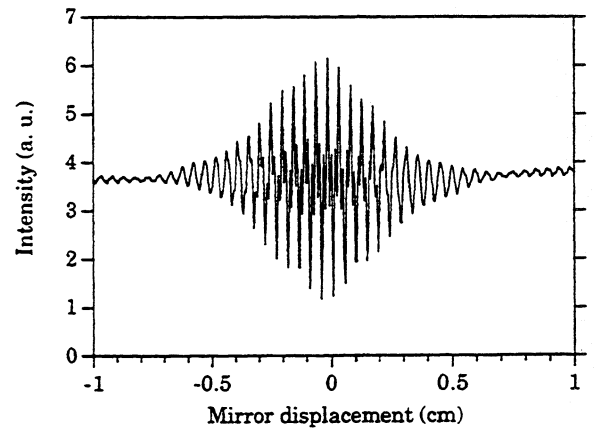


FIG. 5. Interferogram of GCO radiation while operating simultaneously at $|n| = 1$ and $|n| = 3$.

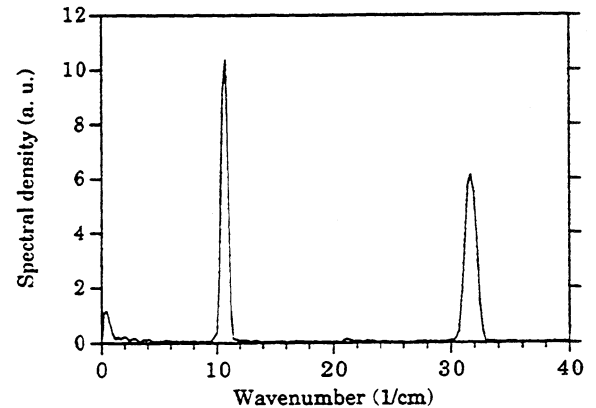


FIG. 6. Power spectrum inferred from the interferogram in Fig. 5.

zero and the wavenumber itself is pure imaginary and has a magnitude

$$|k_{\perp}| = \sqrt{k_{\parallel}^2 - \omega^2/c^2} \quad (10)$$

Since energy transfer is through the nearly-synchronous co-propagating space harmonic the relation $k_{\parallel} = \omega/v$ can be used to infer that

$$|k_{\perp}| = \omega/v\gamma \quad (11)$$

where $\gamma = 1/\sqrt{1 - \beta^2}$. Thus,

$$|k_{\perp}| = 2\pi/\gamma\beta\lambda \quad (12)$$

or

$$|k_{\perp}|^{-1} = \lambda_e \quad (13)$$

the evanescent scale length introduced in Section II. In general, good coupling will require the beam diameter to be

$$d \leq \lambda_e \quad (14)$$

or

$$\lambda \geq 2\pi d/\gamma\beta \quad (15)$$

Using the values associated with a 25 kV beam gives the relation

$$\lambda \geq 20d \quad (16)$$

Good coupling at 300 μm (1 THz) would be achieved with a beam parameter of the order of 15 μm . This is consistent with data obtained in the proof-of-principle experiments. Experiments designed to test the lower limits of d are currently in progress. Much smaller values of d are achievable and operation well above 1 THz may be expected. Further extension of the evanescence scale length may also be achieved by increasing the beam voltage.

A final pair of scaling relations follow if it may be assumed that the depth of field of the beam focus is emittance dominated and that this limits the effective interaction length. In this case the interaction length L is related to the beam diameter by the expression

$$L \simeq \frac{\gamma\beta d^2}{\epsilon_N} \quad (17)$$

where ϵ_N is the normalized emittance. Since d and λ_e are comparable, the relation

$$L \simeq \frac{\gamma\beta\lambda_e^2}{\epsilon_N} \quad (18)$$

also follows.

Threshold occurs when the beam plasma frequency ω_b times the transit time of a beam electron through the interaction length exceeds about 0.25. Operation well above threshold will require

$$\frac{\omega_b L}{\gamma^{3/2} v} > 1 \quad (19)$$

(where the factor $\gamma^{3/2}$ has been included since the bunching is longitudinal; it has, of course, a negligible numerical effect for non-relativistic beams).

With the aid of the usual expression for the beam plasma frequency and multiplying and dividing by additional factor of beam velocity yields the constraint

$$\frac{JL^2}{(\epsilon_0 mc^3/e)(\gamma\beta)^3} > 1 \quad (20)$$

where J is the beam current density. If the relation between the interaction length and the evanescent scale are invoked, the constraint becomes

$$\frac{J\lambda_e^4}{(\epsilon_0 mc^3/e)\gamma\beta\epsilon_N^2} > 1 \quad (21)$$

Finally, if re-written in terms of wavelength, the result

$$\lambda > 2\pi \left[\frac{(\epsilon_0 mc^3/e)\epsilon_N^2}{(\gamma\beta)^3 J} \right]^{1/4} \quad (22)$$

is obtained. Evaluating this last expression using typical parameters for the present electron optical system indicates that we are operating near the lower wavelength limit of that apparatus.

IV. TOWARD A COMPACT GCO

The GCO described in the preceding sections is already compact by some standards. As is evident from the scaling relations discussed in Section III, increase of beam energy as well as a decrease of beam emittance can be used to lower the limiting wavelength. Increasing the beam energy is, of course, the route taken in relativistic electron-beam-driven, free-electron lasers (FEL). The present GCO is already far smaller than these devices. The GCO's output power is much smaller than the levels produced by a relativistic beam-driven FEL. However, it is already sufficient for application in spectroscopy or as a local oscillator.

Straightforward engineering and elimination of the non-essential features of the SEM would lead immediately to a much smaller device. It is also interesting to speculate on more dramatic options.

The beam voltage required for GCO operation probably need never exceed 50 kV and in the present device, THz operation is achieved with only 20 kV of beam voltage. This range is well within the scope of modern dc-dc converter-based power supply technology. The beam currents required are also modest and well within the scope of current converter-based power supplies. These supplies can now be obtained in very compact packages.

A second major reduction in size might be obtained if modern field emission cathode technology were employed. The primary motivation for much work on the field emission cathode is for use in flat panel displays. However, use in microwave tubes has also been a factor. The GCO is an ideal place to use this technique. A ribbon beam a micron thick and about a millimeter wide propagating a distance no more than a few centimeters would be ideal. Power consumption and heat load would be reduced dramatically.

The GCO is also a linear device and standard energy recovery technology is probably applicable. Implementation of energy recovery would improve terminal efficiency. If done in a way such as to also reduce beam intercept at high voltages the already-modest x-ray production could be further reduced.

Finally, although the grating is a simple and reliable means of converting electron beam kinetic energy to coherent radiation, other photonic band gap structures might be employed. The present GCO uses only the distributed feedback on the grating. More complex structures, particularly ones with well-defined high-quality factor modes, may offer significant advantages.

V. CONCLUSIONS

A potentially very useful THz-FIR source has been developed. Based on a novel variation of an old theme, the device is simple and versatile. Power output levels and tuning range are already of interest in some applications and fundamental scaling arguments support the claim that considerable extension of the tuning range and output power is possible. If operated near the limit of established electron beam optical art it will be possible to access the challenging 10-1000 μm wavelength range.

Support from ARO Contract DAAH04-95-1-0640, DoD/AF DURIP Contract F49620-97-1-0287, and Vermont Photonics, Inc., is gratefully acknowledged.

- [1] J. Urata, M. Goldstein, M.F. Kimmitt, A. Naumov, C. Platt and J.E. Walsh, *Phys. Rev. Lett.* **80**, 516 (1998).
- [2] S.J. Smith and E.M. Purcell, *Phys. Rev.* **92**, 1069 (1953).
- [3] W.W. Salisbury, US Patent 2,634,372, filed October 26, 1949, granted April 7, 1953.
- [4] J.P. Bachheimer, *Phys.Rev. B* **6**, 2985 (1972).
- [5] W.W. Salisbury, *Science* **154**, 386 (1966).
- [6] E.L. Burdette and G. Hughes, *Phys. Rev. A* **14**, 1766 (1976).
- [7] A. Gover, P. Dvorkis and U. Elisha, *J. Opt. Soc. Am. B* **1**, 723 (1984).
- [8] I. Shih, D.B. Chang, J.E. Drummond, K.L. Dubbs, D.L. Masters, R.M. Prohaska and W.W. Salisbury, *J. Opt. Soc. Am. B* **7**, 351 (1990).
- [9] F.S. Rusin and G. Bogomolov, *Proc. IEEE* **57**, 720 (1969).
- [10] K. Mizuno and S. Ono, *The Ledatron, Infrared and Millimeter Waves 1: Sources of Radiation*, ed. K. Button (Academic Press, Inc., 1979), Ch. 5, pp. 213-233.
- [11] D.E. Wortman, H. Dropkin and R.P. Leavitt, *IEEE Journ. Quant. Elect.* **QE-17**(8), 1341 (1981).
- [12] V.P. Shestapov, *Diffraction Electronics* (Kharkov: 1976).
- [13] E.J. Price, *Appl. Phys. Lett.* **61**, 252 (1992).
- [14] J.H. Killoran, *IEEE Trans. Pl. Sci.* **22**, 530 (1994).
- [15] M. Goldstein, J.E. Walsh, M.F. Kimmitt, J. Urata and C.L. Platt, *Appl. Phys. Lett.* **71**, 452 (1997) and A Far-Infrared Smith-Purcell Micro-Radiator, Ph.D. thesis, 1994, available from Department of Physics and Astronomy, Dartmouth College, Hanover, NH 03755.
- [16] P.M. van den Berg, *J. Opt. Soc.* **63**, 1588 (1973).
- [17] J. Urata, Spontaneous and Stimulated Smith-Purcell Radiation Experiments in the Far-Infrared, Ph.D. thesis, 1997, pp. 19-20, available from Department of Physics and Astronomy, Dartmouth College, Hanover, NH 03755.

ELECTRICAL GENERATION OF TERAHERTZ CURRENT OSCILLATIONS IN BALLISTIC DEVICES

Alexander N. Korshak and Vladimir V. Mitin

Wayne State University, Detroit, MI 48202, USA

Abstract

A theoretical study of ballistic transport of current carriers with negative differential effective mass is presented. A symmetric double-heterostructure p-type quantum well is considered as a realistic system with current carriers (holes) which have the required dispersion relation. A ballistic current of quantized holes in a short doped p-type quantum well generates current oscillations. This generation is a result of a negative effective mass part in the hole dispersion relation. An oscillation frequency is in the terahertz range and depends on the inner parameters of the diode structure with quantum well base. It is approximately determined by a carrier transit time through the diode base. GaAs quantum wells of about 8 nm width, 0.1÷0.3 μm length, and 10^{11} cm^{-2} acceptor doping may be used for generation in the range of 0.5÷1.5 THz.

1 General principle of generation

We consider current carriers with a special non-parabolic dispersion relation. The peculiarity of this dispersion is that the differential effective mass becomes negative in a some region of wavevectors, and it is positive outside of this region. Figure 1 shows an example of the dispersion relation, ε , with a negative differential effective mass (NEM) part. A group velocity, $v = \partial\varepsilon/\partial p$, and an inverse effective mass, $1/m = \partial^2\varepsilon/\partial p^2$, as the functions of wavevector, $k = p/\hbar$, are shown in Fig. 1, b, c. We do not assume that the velocity of the carriers is negative for a positive

momentum as would be in the case of a negative mass everywhere. Negative differential effective mass means that an increment in momentum results in a decrement in velocity.

A ballistic plasma with current carriers having negative differential effective mass (NEM-carriers) is convectively unstable [1]. It can be easily confirmed by finding a spectrum of excitation in the quasineutral plasma with carriers having negative mass, m_c . For a frequency of excitation ω with a wavevector k we have

$$\omega = v_c k \pm i\omega_c,$$

where v_c is a velocity of the NEM-carriers, $\omega_c^2 = e^2 n_0 / \kappa_d |m_c|$ is the plasma frequency for the NEM-carriers, n_0 is a concentration of ions, and κ_d is a dielectric constant. We see that the frequency is complex with a positive imaginary part. This means that any fluctuation in the plasma is increasing, and therefore, the homogeneous state of the quasineutral plasma with the NEM-carriers is unstable.

2 NEM carriers

To implement this instability for generation we should find a system with the required dispersion relation for current carriers. We have considered three different systems which allow the carrier dispersion relations with a NEM part. They are: 1) electrons in an asymmetrical double quantum wells formed by materials with considerably different electron masses, or electrons in a composite ΓX -quantum well [2], 2) holes in uniaxially compressed semiconductor [3], and 3) holes in a heterostructure quantum well [4]. The later system seems to be the most realistic for fabrication of the proposed generator.

Quantization of holes in a double heterostructure quantum well is a reason of mixing of light and heavy hole states. Spin-orbit interaction between them results in a complicated dispersion relation shown in Fig. 2, and the lowest subband of

the quantized hole spectrum is exactly what we need. A position of the NEM part depends on the well width and depth. Therefore changing a well width or choosing another material system allow one to obtain the hole dispersion with a desired position of the NEM part.

3 Ballistic diode

To exploit the instability associated with the NEM of quantized holes we should form a quasineutral ballistic plasma region with NEM-holes as current carriers. The simplest way is to accelerate holes ballistically to the energy where they have NEM. In the ballistic diode with a p-type quantum well as a base holes enter into the base from the heavily doped anode, are accelerated in the electric field, and finally reach another contact (cathode) with energy eV_D , where V_D is a voltage across the diode base. It is important that no scattering occurs in the diode base and the energy of these carriers is exactly determined by the potential difference between the initial and final states. The distribution function of the ballistic carriers is overstretched in the current direction and the energy width of the ballistic beam is determined by the Fermi energy of the injected carriers. Therefore, the Fermi energy should not be greater than the energy width of the NEM part in the hole dispersion relation.

Here we consider a ballistic diode with parallel equipotential plates — cathode and anode, which are connected by current-conducting channels of length L . These channels form a spatial periodic system with a spatial period a .

A solution of a stationary problem of space charge limited ballistic currents for holes which have a dispersion relation with a NEM part shows that the electric field distribution in the diode base is nonuniform [5]. The diode base can be divided into three parts: a dipole space charge region near the cathode with comparatively light holes which have energy below the energy of the NEM part, then a wide quasineutral region with moving NEM-carriers (NEM-region), and the second dipole space charge

region near anode with comparatively heavy carriers which have energy higher than the energy of the NEM part. The widest region is the quasineutral NEM-region where the electric field is small. Stationary current-voltage characteristics show saturation of the current as a function of the voltage V_D in the voltage interval when this NEM-region exists in the base. The voltage, when the current saturation begins, corresponds to the energy of the NEM part. Instability in the NEM-plasma results in the current oscillations [6] which are accompanied by the plasma waves propagating in the NEM-region. The oscillation frequency is determined by the transit time, and this frequency is in the terahertz range for submicron ballistic structures. Numerical simulations indicate that in most cases spectrum of these oscillations is characterized by the main frequency which depends on the applied voltage. Figure 3 shows a relation between the current oscillations with a single main frequency and the dispersion relation of the carriers. The oscillation regime appears in the voltage interval where the current saturation for stationary characteristics would be expected. For a long diode base when the NEM-region becomes sufficiently long the oscillation spectrum becomes complicated due to excitation of modes with higher frequencies.

4 Ballistic regime

Ballistic transport regime in the base of the diode holds if a carrier transit time, τ_{tr} , through the base is sufficiently smaller than a mean scattering time, τ_{sc} . Since the transit time determines a frequency of the oscillations we get a fundamental restriction for the lowest attainable frequency of oscillations. It is determined by the scattering time in the diode base, $f_{min} = 1/\tau_{sc}$. So to obtain oscillations with the frequency 1 THz we have to guarantee scattering time longer than 1 ps.

Let us make some simple estimations to determine the ballistic length which corresponds to that time. To estimate the mean velocity of the carriers in the base,

we take the velocity of the NEM-carriers. For the particular dispersion relation in Fig. 1, this velocity is about $0.1 \mu\text{m/ps}$ or 10^7 cm/s and the ballistic length must be greater than $0.1 \mu\text{m}$.

How can the ballistic length be increased? To have a scattering time in the range of a few picoseconds carriers should not reach the energy of the optical phonon. For GaAs this energy is about 36 meV . Therefore the energy position of the NEM part in the hole dispersion relation is chosen below the optical phonon energy, near 20 meV , to obtain oscillations in a sufficiently long voltage interval.

Below the optical phonon energy the main contribution to the scattering comes from ionized impurity scattering. To decrease this contribution one usually uses a modulation doping with spacer width of about 10 nm or greater. Reported hole mobilities in p-type GaAs quantum wells on $\langle 311 \rangle$ -A-GaAs substrates are greater than $100,000 \text{ cm}^2/\text{Vs}$ for helium temperatures. This mobility seems to provide the scattering time of longer than 5 ps .

5 Characteristics of the oscillation regime

Frequency. For a sufficiently high doping the length of the space charge region is small and the length of the NEM region is approximately equal to the base length. Oscillations of about 1 THz are expected in the $0.1 \mu\text{m}$ base for the velocity of the NEM carriers of 10^7 cm/s . For $0.2 \mu\text{m}$ base the oscillation frequency is decreased to 500 GHz .

To increase the frequency of the oscillations we have to decrease the base length. When shortening the base length becomes of the order of the width of the space charge region, Λ . For a bulk ballistic diode this width is given by

$$\Lambda = v_c \frac{\pi}{e} \sqrt{\frac{m\kappa}{n_0}},$$

where m is a positive effective mass near the bottom of the subband. For bulk doping of 10^{17} cm^{-3} this width can be estimated as 40 nm. For a shorter base the NEM region shrink and no oscillations occurs. The base length when the oscillations disappear is about 60 nm for that doping. Increased doping shortens the width of the space charge region and allows oscillations for shorter base lengths with higher oscillation frequencies.

When the base doping is increased, the Fermi energy of the injected carriers (or the cathode doping) should be increased to hold a space charge limited current regime in the ballistic diode. This regime is necessary because it provides a nonuniform electric field distribution in the diode base with a long quasineutral NEM-region. An increased Fermi energy causes an increased energy width of the ballistic beam. If this width becomes greater than the energy width of the NEM part in the hole dispersion relation the oscillations weaken because only a part of the carriers has the NEM while the other part has a positive mass. The current carried by the holes with the positive mass shorten the oscillations. For the given dispersion relation and for the given injection scheme we have a fundamental limitation for the maximum attainable frequency of about 2 THz. This frequency is expected for the base of 60 nm length, $3 \cdot 10^{11} \text{ cm}^{-2}$ doping, and 12 meV Fermi energy of injected carriers. The dispersion is supposed to have the NEM part near 20 meV.

To get frequencies higher than 10 THz we have to shorten the base length to 30 nm and to increase the energy of NEM carriers to 0.1 eV. In this case even optical phonon scattering with scattering time of about 0.2 ps will not prevent the ballistic transport in the base. The velocity of the NEM carriers is then about $2.5 \cdot 10^7 \text{ cm/s}$ and the ballistic length is about 50 nm. We have to sufficiently increase doping to shorten the space charge region to about 20 nm. Therefore, the doping in the range of $(2 \div 3) \cdot 10^{12} \text{ cm}^{-2}$ is required.

Output power. The input power of the ballistic diode with p-GaAs/AlAs quantum wells of ~ 9 nm width is about 5 mW cm^{-1} . The efficiency and output power of the generator depend on the load resistance. Our estimates show that the output power is expected to be about $5 \cdot 10^{-5} \text{ W cm}^{-1}$ and the efficiency — about 1 %, when the load resistance is equal to $0.2 \Omega \text{ cm}$. If the length of the structure in the third direction is about $200 \mu\text{m}$ (the in-plane size is $0.1 \times 200 \mu\text{m}^2$) the microwave power is about $1 \mu\text{W}$ per quantum well at the load resistance of 10Ω . We can significantly increase the output using multiwell structures grown layer by layer.

Required structure. For our goals we need a symmetrical p-type double heterostructure rectangular quantum well with sharp and flat sidewalls. The well width should be smaller than 9 nm. Symmetrical (double-side) modulation doping of $\geq 10^{11} \text{ cm}^{-2}$ is required to reduce ionized impurity scattering. To provide a sufficient depth of the hole quantum well one has to use heterostructures: 1) GaAs/ $\text{Al}_x\text{Ga}_{1-x}\text{As}$ with $x > 0.6$ (up to $x = 1.0$), or 2) $\text{In}_{0.53}\text{Ga}_{0.47}\text{As}/\text{InP}$. In the case of GaAs/AlGaAs-structure, higher hole mobilities are observed for the structures grown on $\langle 311 \rangle$ A-GaAs-substrates with Si as acceptor. Multiwell structures are desirable to increase output power. Parallel p^+ -contacts to the quantum well are regions enriched by diffusion or implantation. They have to be spaced by $0.1 \div 0.5 \mu\text{m}$ or even smaller.

References

1. Z. S. Gribnikov, A. N. Korshak. *Semiconductors* **28**, 1445 (1994).
2. Z. S. Gribnikov, A. N. Korshak, N. Z. Vagidov. *J. Appl. Phys.* **80**, 5799 (1996).
3. N. Z. Vagidov, Z. S. Gribnikov, A. N. Korshak. *Semiconductors* **31**, 150 (1997).
4. A. N. Korshak, *et al.*, *Phys. Stat. Sol. (b)*, **204**, 80 (1997); A. N. Korshak, *et al.*, *Microelectronic Eng.*, accepted (1998); Z. S. Gribnikov, *et al.*, *ICPS-23 Proc.*,

Berlin, 4, 3287 (1996).

5. N.Z.Vagidov, Z.S.Gribnikov, A.N.Korshak. *Semiconductors* **29**, 286 (1995).

6. N. Z. Vagidov, Z. S. Gribnikov, A. N. Korshak. *Pis'ma ZhETF*, **61**, 38 (1995).

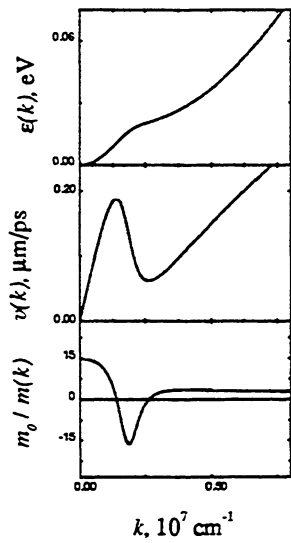


Figure 1. Dispersion relation, $\epsilon(k)$, with differential negative effective mass domain, velocity, $v(k)$, and differential effective mass, $m_0/m(k)$.

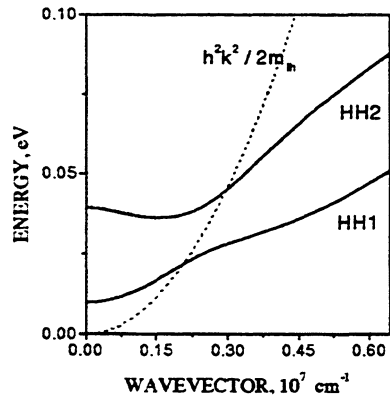


Figure 2. Quantized hole spectra for p-GaAs/AlAs quantum well of 8 nm.

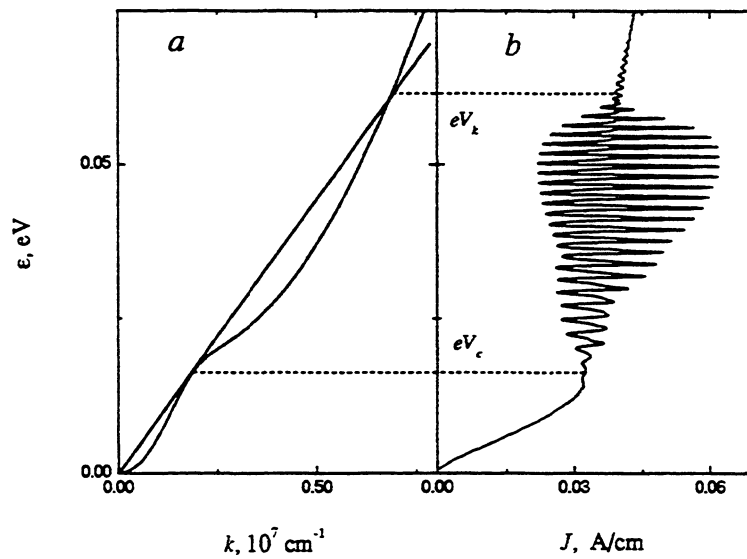


Figure 3. Dispersion relation, $\epsilon(k)$, and corresponding current oscillations as a function of applied voltage $eV_0 = \epsilon$ for p-GaAs QW of 0.5 μm length, 9 nm width, and $2 \cdot 10^{10} \text{ cm}^{-2}$ doping.

GENERATION OF CW-TERAHERTZ RADIATION USING A TWO-LONGITUDINAL-MODE LASER DIODE

PING GU, MASAHIKO TANI, KIYOMI SAKAI AND TAKEHIKO HIDAKA¹

KANSAI ADVANCED RESEARCH CENTER, COMMUNICATIONS RESEARCH
LABORATORY, MINISTRY OF POSTS AND TELECOMMUNICATIONS, JAPAN

588-2 IWAOKA, KOBE-SHI, HYOGO 651-2401, JAPAN

E-MAIL: guping@crl.go.jp

¹DEPARTMENT OF ELECTRIC ENGINEERING

SHONAN INSTITUTE OF TECHNOLOGY

1-1-25 TUJIDO-NISHIKAIGAN, FUJISAWA, KANAGAWA 251, JAPAN

ABSTRACT

A coherent 163.5 GHz radiation has been generated by photomixing in a photoconductive antenna fabricated on the low-temperature-grown (LTG) GaAs film using a two-longitudinal-mode distributed Bragg reflector (DBR) laser diode (LD). The frequency of the emitted radiation corresponds to the difference frequency between the two modes of the excitation laser. We have found that the linewidth of the radiation is much narrower than that of the each laser mode. The narrowed linewidth is due to the common-mode rejection effect between the two modes oscillating in the

identical cavity. This property of the two-mode DBR laser, as well as the compactness and the ease for the optical alignment, make the device promising as an excitation laser source for the photomixing.

INTRODUCTION

For the high-resolution THz spectroscopy, a compact coherent cw-THz source is highly desired due to the restriction of the payload. Recently, the technique to generate coherent cw-THz radiation by using photomixing in low-temperature-grown (LTG) GaAs was exploited by several groups.^{1,2,3} This technique enables to build a compact cw-THz source. For the photomixing, two independently tunable lasers were used, and by changing the difference frequency of the lasers, the oscillator frequency in a very wide range (0-5THz) could be tuned. However, the use of two lasers requires stabilization and the precise spatial mode matching of the two lasers. More optics and electrical components should be to the system added, thus, resulting in a larger system. A simultaneous two-frequency oscillation in the same laser cavity is a good alternative when we restrict ourselves to the fixed frequency sources. It simplifies the experimental set up and does not require the elaborate optical alignment for the spatial mode matching. In addition, a narrowing of the radiation linewidth is expected from the common-mode rejection effect between the two modes, by which a large part of the frequency fluctuations of the two laser modes in the same cavity is canceled out and the beat frequency of the laser is stabilized.

In this paper we report generation of the coherent 163.5 GHz radiation by photomixing in low-temperature-grown GaAs using a two-longitudinal-mode

distributed Bragg reflector (DBR) laser. We also confirm the narrowing of the oscillator linewidth due to the common-mode rejection effect from an interferometric measurement.

PRINCIPLE OF THE GENERATION OF CW-THz RADIATION

When two lasers with powers P_1 and P_2 , and frequencies ν_1 and ν_2 are mixed, the power detected by a photoconductive device is given by

$$P(t) = P_0 + 2[\eta_m P_1 P_2]^{1/2} [\cos(2\pi(\nu_1 - \nu_2)t) + \cos(2\pi(\nu_1 + \nu_2)t)] \quad (1),$$

$P_0 = P_1 + P_2$ is the total power of the two lasers, η_m the mixing efficiency arising from the spatial overlap of the two laser beams. The η_m , ranging between 0 and 1, approaches unity when the beams have the same polarization and are completely spatially overlapped. Since material can not respond to the sum frequency ($\nu_1 + \nu_2$), the second term in Eq.(1) can be neglected. Thus, the photocurrent is modulated at the difference frequency of the two lasers, and the electromagnetic wave with the same frequency ($\nu_1 - \nu_2$) will be generated.

We used low-temperature-grown (LTG) GaAs as a photoconductive device material. This device, as compared to other semiconductors, has the short (sub-ps) photocarrier lifetime, the high photocarrier mobility ($200\text{cm}^2\text{V}^{-1}\text{s}^{-1}$) and the high DC breakdown field larger than $5 \times 10^5 \text{V/cm}$. These properties satisfy the requirements for a THz photomixer. ⁴ Figure 1 shows the photomixer, which consist of a bow-tie antenna fabricated on the LTG-GaAs film. The radiation of the optical beat of the two laser

modes illuminates the gap of the antenna biased with voltage V . The operation of such a device is described by an equivalent electric circuit shown in Fig.2. The capacitance across the antenna gap is expressed by C , which depends on the electrode geometry and the dielectric constant of the photoconductive material. A photoconductance is denoted by $G(t)$, a function of the absorbed optical power. Z indicates antenna radiation impedance. The time-dependent conductance modulates the bias current (i) at the frequency $\nu = \nu_1 - \nu_2$ and thus delivers power to Z at the given frequency.

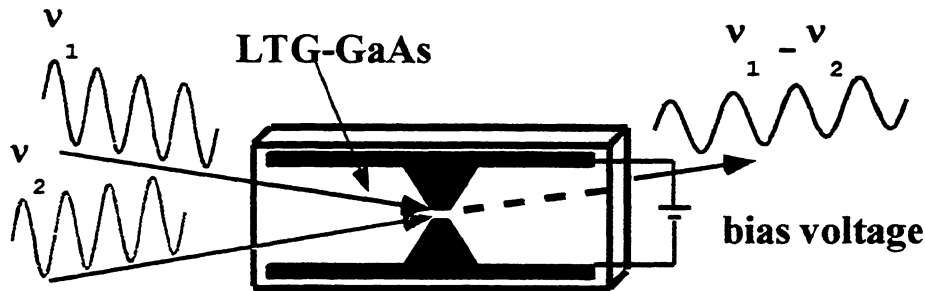


Fig.1. Schematic diagram of a photoconductive antenna device.

The power is found by solving the dynamic current equation for the circuit shown in Fig.2. From the Kirchoff current law, we write the time varying voltage v across the photoconductive gap as

$$\frac{dv}{dt} = \frac{V - v}{ZC} - \frac{v}{C}G(t) \quad (2),$$

where $G(t) = G_0 [1 + \sin(\omega t) / \sqrt{1 + (\omega\tau)^2}]$

is the conductance modulated at the

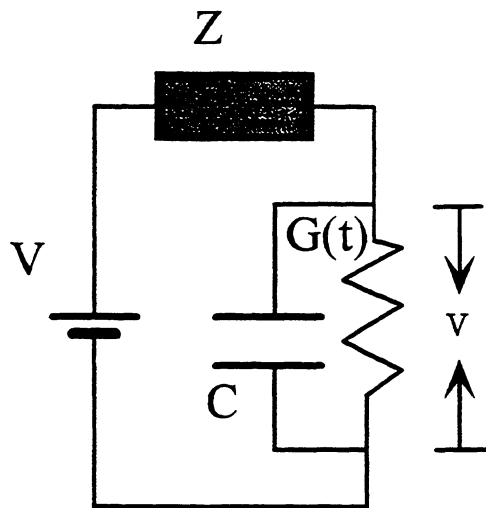


Fig.2. Equivalent circuit of the photoconductive antenna device.

frequency ω , and τ is the carrier lifetime. The power emitted from the antenna at frequency ν is written as ⁵

$$P(\omega) \approx \frac{(G_o V)^2 Z / 2}{[1 + (2\pi\nu\tau)^2][1 + (2\pi\nu Zc)^2]} \quad (3).$$

$$(Z \ll 1/G_o(t))$$

From this equation we see that the output power is proportional to the square of the excitation bias voltage and laser power since G_o is proportional to P_o . If the impedance Z does not depend on the frequency, the carrier lifetime and capacitance of the gap limit the spectral bandwidth. That means if we want to generate the high power and wide band THz radiation, we should make a mixer with the carrier lifetime as short, and the capacitance of the antenna gap as small as possible.

TWO-LONGITUDINAL-MODE LASER DIODE

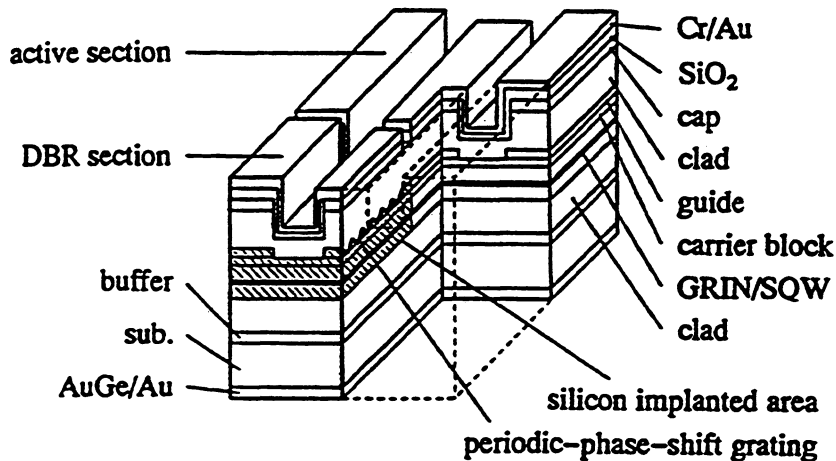


Fig.3. Schematic diagram of a two-longitudinal-mode DBR LD.

The grating in the DBR section has periodic phase shifts.

A simultaneous two-mode-oscillation DBR laser diode is a two-section DBR LD with a periodic-phase-shift grating adopted at DBR section.⁶ The period of the grating and the interval of the phase shifts determine the center wavelength and the separation of the two modes, respectively. Figure 3 shows the structure of the two-mode DBR LD used in the experiment. Figure 4 shows the emission spectra of the two-mode LD. The diode power was about 10mW measured at 191mA bias current and at 19°C by a double-monochromator with a resolution of 0.06cm^{-1} (1.8GHz). The difference of the center wavelength between the two modes was 0.39 nm (163.5 GHz). The full width at half maximum of the spectral width for each mode, estimated by a scanning Fabry-Perot interferometer with 50 MHz resolution, was 240 MHz as shown in Fig.5.

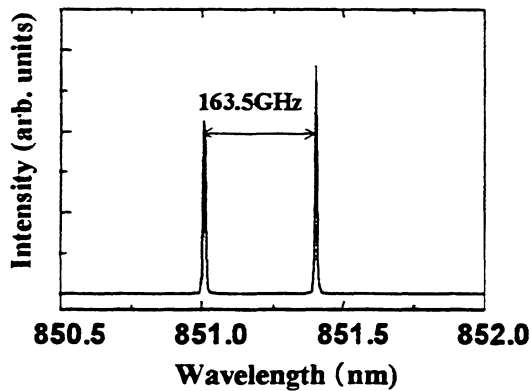


Fig.4. Emission spectrum of the LD.

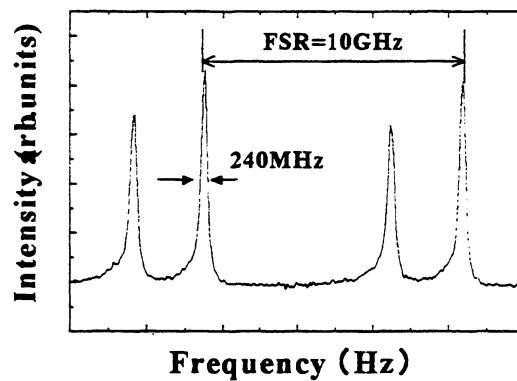


Fig.5. Spectral linewidth measured using a scanning Fabry-Perot interferometer.

EXPERIMENTS AND RESULTS

Figure 6 shows the experimental set-up to generate coherent cw-THz radiation using the two-mode DBR LD as an excitation source. The two-mode laser beam (15

mW) goes through an isolator and an optical chopper for lock-in detection. The beam was focused on a gap of the 1mm-long dipole antenna fabricated on the LTG-GaAs film. The radiation from the antenna was fed into a Martin-Puplett polarizing interferometer, which consisted of the two wire-grid polarizers with 45° polarization with respect to each other, a fixed mirror and a scanning mirror.

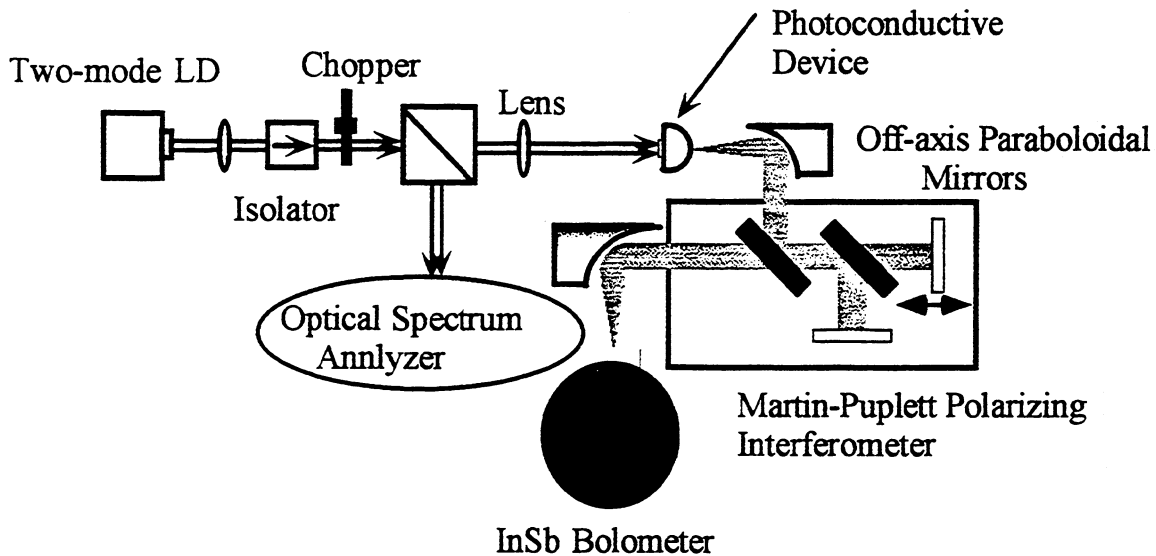


Fig.6. The experimental set-up to generate coherent cw-THz radiation and to measure the radiation properties.

The interference signal measured with an InSb hot-electron bolometer at 4.2 K is shown in Fig.7. The power of the radiation from the antenna is several nW. The conversion efficiency of this system is about 10^{-6} . The Fast Fourier Transform (FFT) of the interferogram is shown in Fig.8. The frequency of the main peak of the spectrum is 163.5GHz. The generation of radiation with the same frequency as the beat frequency of the two-mode LD (Fig.4) indicates that the radiation originates from the current

modulated by the two-mode LD. The double and triple frequencies of the main peak also are observed shown in Fig.8. We suggest that the overtones may come from a nonlinearity of the antenna device.

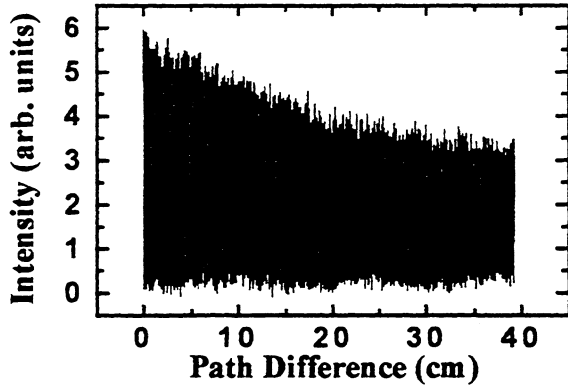


Fig.7. Interferogram of the radiation.

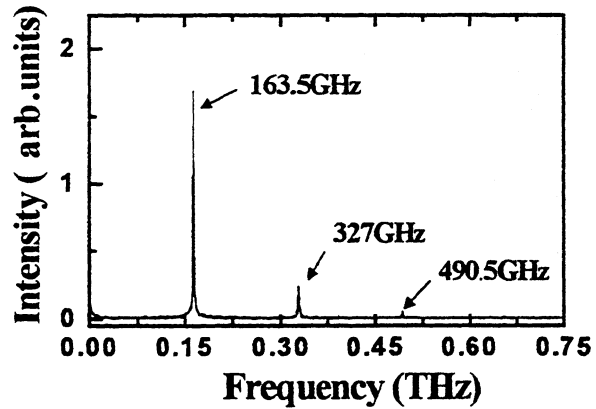


Fig.8. FFT spectrum of the interferogram

The scanning mirror of the interferometer could move only about 18 cm, limiting the spectral resolution to 0.8 GHz. Thus, we could not directly measure the coherence length of the radiation. However, from the decay of the interferometric component against the average detected power with increasing path difference, we can estimate the coherence length. First, we should subtract the average detected power from the interferogram shown in Fig.7 and then, fit to a damped cosinoidal function

$$I(t) = A \exp(-2x/l_0) \cos(\pi x \nu) \quad (4).$$

Here, x is the path difference between the two arms, l_0 the coherence length of the radiation, ν and A the frequency of the interferogram and the interferogram intensity

at $x = 0$, respectively. We estimated the coherence length of the radiation to be larger than 230 cm. This number means that the linewidth of the radiation is smaller than 130 MHz. The linewidth is 2 times narrower than that of each mode of the excitation laser. A large part of the frequency fluctuations of the two laser modes are canceled out and the beat frequency of the laser is more stable than that of the individual two-laser mode. This confirms the common-mode rejection effect of the two-mode oscillation in the same cavity.

SUMMARY

The coherent cw-THz radiation was generated by exciting photoconductive switch with a two-mode DBR LD. The linewidth of the radiation is narrower than that of the pump laser modes due to the common-mode rejection effect in the identical laser cavity. The system is more simple and compact than that with two individual lasers. Our results indicate that the two-longitudinal-mode diode laser is an excellent source for the generation of a stable THz wave by photomixing. We believe that by continuously changing the beat frequency of the two-mode laser in the same cavity tunable THz oscillations can be generated using the same technique as described in this paper.

REFERENCES

1. E. R. Brown *et al.*, Photomixing up to 3.8THz in low-temperature-grown GaAs, *Appl. Phys. Lett.* 66, 285 (1995).

2. S. Matsuura *et al.*, Generation of coherent terahertz radiation by photomixing in dipole photoconductive antennas, *Appl. Phys. Lett.* 70, 559 (1997).
3. E. R. Brown *et al.*, Milliwatt output levels and superquadratic bias dependence in a low-temperature-grown GaAs photomixer, *Appl. Phys. Lett.* 64, 3311 (1994).
4. M. Tani *et al.*, Spectroscopic characterization of low-temperature-grown GaAs Epitaxial films, *Jpn. J. Appl. Phys.* 33, 4807 (1994).
5. E. R. Brown *et al.*, Coherent millimeter-wave generation by heterodyne conversion in low-temperature-grown GaAs photoconductors, *J. Appl. Phys.* 73, 1480 (1993)
6. T. Hidaka *et al.*, Simultaneous two wave oscillation LD using biperiodic binary grating, *Electron. Lett.* 27, 1075 (1991).

2.5 THZ LASER LOCAL OSCILLATOR FOR THE EOS CHEM 1 SATELLITE

Eric R. Mueller, William E.
Robotham, Jr., Richard P. Meisner,
Richard A. Hart, John Kennedy, and
Leon A. Newman
DeMaria ElectroOptics Systems, Inc.
1280 Blue Hills Ave.
Bloomfield, CT 06002
(806) 243-9557

Abstract

The EOS CHEM I satellite will have a channel at 2.5 THz to perform a global mapping of OH in the atmosphere. The OH data is vital to modeling of O₃ processes in the atmosphere and, in fact, OH is thought to dominate a number of cycles in the mid-latitude lower stratosphere. The OH channel will utilize two Schottky diode receivers pumped by an optically-pumped FIR laser system. DeMaria ElectroOptics Systems is presently under contract to design, fabricate, and deliver this space-based FIR laser local oscillator. The specifications, design, and modeling of this 2.5 THz laser local oscillator will be presented here, along with some of the important early design validation results.

This work is supported by Jet Propulsion Laboratory (JPL) under contract number 961080.

Introduction

In order to provide a global mapping of OH (and also -O₂), the Microwave Limb Sounder (MLS), on the Chem I satellite, will have channels with a LO at 2.52 THz (these channels will be collectively referred to as the THz channel). The Local Oscillator for the THz channel is a methanol laser pumped by a CO₂ laser. DeMaria ElectroOptics

Systems (DEOS) leads the team that is going to deliver this laser system to JPL for integration into the MLS.

The THz channel is one of five radiometer channels on the MLS. While DEOS is providing the Laser Local Oscillator (LLO) system for the THz channel, JPL is fabricating the receivers, performing the systems integration, and conducting the atmospheric data evaluation. The spacecraft will be integrated by TRW. All of the receivers for the MLS, except the 118 & 190 GHz channels, are being fabricated by JPL.

The IF's for the THz channel are indicated in Table 1. The spectrometer for processing the IF's from all of the receivers is being developed by JPL.

Table 1: Table of IF's for the 2.52 THz Channel.

IF	Constituent
8.4 GHz	-OH
12.8 GHz	-OH
20.4 GHz	-O ₂

While many readers may have experience with moderate-to-low reliability optically-pumped FIR lasers, high-reliability FIR lasers may not be familiar. Starting with the pump laser technology: the LLO will utilize the same high-reliability, sealed-off, RF-excited, CO₂ laser technology found in DEOS's commercial lasers and in numerous high-sophistication systems DEOS has delivered over the years. Specifically, this technology has demonstrated: operating life in excess of 35,000 hrs, shelf life of over 10 years, operation in high-performance aircraft environments, spectral purity and stability sufficient for LIDAR applications, and all within a very compact and rugged package.

Applicable vacuum and optical techniques from the CO₂ laser design are being incorporated into the FIR laser design. Thus while DEOS staff have constructed ultra-high-stability and spectral purity FIR lasers which have operated for years with only periodic gas refills, the sealing and mirror mount technologies adopted from the

CO₂ laser designs are expected to yield FIR lasers which operate for years without refilling or service of any kind.

In the design of a system as intricate, efficient, and autonomous as the LLO, a number of complex interactions, which may not be imperative for a laboratory-based system, must be considered to assure a robust design. The remainder of this paper will present the LLO design, with limited details, in the sections that follow: LLO Specifications, LLO Configuration, High-Efficiency Pump Laser, Pump Laser Frequency Control, FIR Laser, and Conclusions.

It should be pointed out that DEOS is merely the leader of the LLO team. The other team members are: Teledyne Brown Engineering – electronics fabrication, Aerospace Structural Research – mechanical/thermal design and analysis, Supplier-Based Manufacturing – quality assurance, National Technical Systems – compliance testing, and JPL – general system design guidance. The team also relies a network of vital suppliers too numerous to mention.

LLO Specifications (abbreviated)

The LLO has a long list of specifications. In the interests of brevity only those specifications which relate to topics covered in this paper will be presented.

The LLO must autonomously operate and produce sufficient output power to optimize two Schottky diode receivers. The output power specification is 20 mW. The required lifetime is 5 years on-orbit plus 2200 hrs of ground testing. All specifications are required to be met over the entire lifetime of the LLO and thus constitute the definition of lifetime.

There are significant constraints on available prime power, mass, and envelope. The entire LLO (including all control electronics) must fit in a box no larger than 75 x 30 x 10 cm. The allowed total mass is 20 kg, and the total available 28 V DC prime power is 120 W. The size/mass/efficiency

portion of the specification drives a large part of the LLO design.

Further mechanical constraints are in force via the launch survival specification. While the LLO does not have to operate during launch, it must of course survive launch. With the LLO's position on the Delta II launch vehicle, this amounts to 15.8 G RMS for 1 min on all three axes. Further, with the launch platform's acceleration profile, the time from atmospheric pressure to 1 torr is ~ 20 seconds. Therefore adequate venting must be provided to prevent rupture of non-pressure enclosures.

The frequency stability requirement is 100 kHz/s (FWHM), long-term drift not to exceed 2 MHz from line-center, and spectral purity - sidebands < -30 dBc (> 200 kHz off carrier). Since a SuperInvar structure would not be compatible with the mass budget, DEOS has devised a novel method of active frequency control for the FIR laser.

The required amplitude stability is 1% over 30 s. System level Rigrod modeling has shown this to be dominated by feedback interaction with the diplexer/receiver system. DEOS has devised a novel method to mitigate this effect as well.

The output spatial mode specification is that: only power in the specified TEM₀₀ mode is counted, and the LLO output beam waist must be 4.1 mm located 465 mm from the LLO-radiator interface.

The output polarization specification is equal parts horizontal and vertical (within 10%) with any phase relationship. Thus circular polarization or 45 degree linear polarization is acceptable. 45 degree linear is the baseline for the LLO.

All of the performance specifications must be met in the presence of feedback from the diplexer/receivers. This is expected to be less than 20 %. Accordingly the specification is robustness to up to 20% FIR feedback of arbitrary phase and polarization. DEOS has devised a method to mitigate the FIR feedback, as will be presented in the FIR Laser section.

The temperature range specification for the LLO is non-trivial as well. The system will be tested from -10 to 50 C

(operational), and from -35 to 60 C (non-op survival).

LLO Configuration

The LLO block diagram is shown in Figure 1. The LLO electronically interfaces with the MLS via three main connections: prime power, RS-422 communications, and mixer bias signal.

To illustrate the operation of the LLO, "follow-the-power". Prime power is converted into RF power in the RF Power Supply. The RF power propagates through coaxial hard-line to the pump laser and excites the Pump Laser. The emitted 9.69 μm light propagates through the Pump Beam Delivery Optics and Photoacoustic Cell into the FIR Laser. Included in the

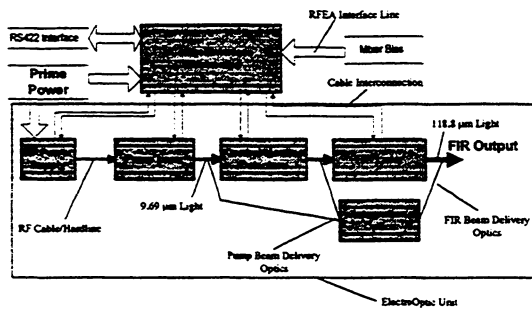


Figure 1: Block diagram of LLO.

pump beam optics are beam sample mirrors which send a very small portion of the pump power into a locking pyro and health-and-status thermopile. The FIR laser converts the pump light to FIR light at 118.83 μm (2.52 THz). Finally the FIR Beam Delivery Optics transform the laser output mode to match the specified output profile.

A drawing of the LLO is presented in Figure 2. The control/interface electronics reside in the upper portion of the housing (Control/Interface Electronics Unit), and the RF power supply and all optical components are located in the lower portion of the housing (ElectroOptic Unit). A radiator plate is mounted to the ElectroOptic unit and radiates the waste heat created by the LLO. The radiator is not structural; in fact the LLO provides the support for the radiator. The LLO's mechanical interface with the MLS is through three bipod struts (not

shown) which mount to tabs shown in Figure 3.

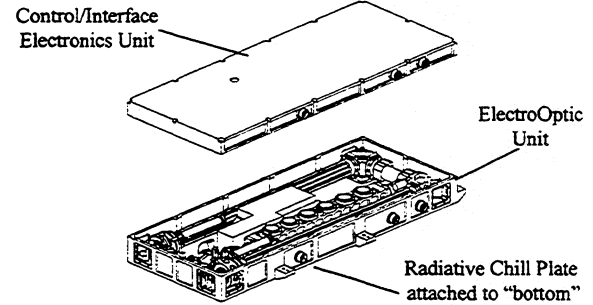


Figure 2: LLO system, enclosure opened.

The optical path for the LLO is presented in Figure 3. As shown there, the available space is quite constrained. The pump beam propagates through the Photoacoustic Cell (PA Cell) and then through the lens which focuses the beam into the FIR laser. Using crossed-Brewster-pairs to "pick-off" small portions of the

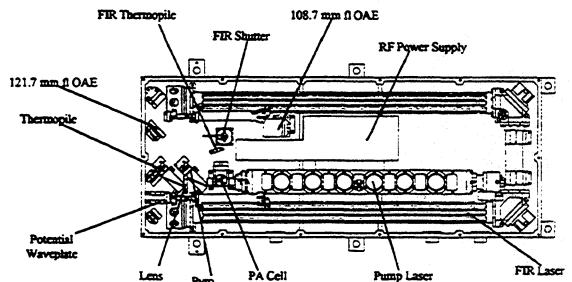


Figure 3: LLO optical path.

pump beam, beam samples are sent to the pyroelectric detector (which is used by the pump laser frequency/amplitude control electronics), and to the thermopile (pump power, health & status). Provision has been made for a $\frac{1}{4} \lambda$ plate, if more pump isolation is required. While this approach will yield circularly-polarized FIR output, this is compatible with the specifications.

The output from the FIR laser will be transformed to match the specified beam profile via a Newtonian telescope. This telescope is formed by two off-axis elliptical mirrors. The fastest $f\#$ in the telescope is ~ 7 . The mirrors will be diamond-turned Al, fabricated as part of their respective optical mounts.

The FIR shutter is included to prevent a gain-switched FIR spike, possible during initial turn-on (note that if conditions

are right, the pump laser can put out a ~ 500 W pulse at turn-on), from damaging the receivers. The back of the shutter is mirrored, so that when the shutter is closed the FIR beam will propagate into the FIR thermopile (health & status). As the output telescope for the FIR beam is Newtonian, the focal spot from the telescope is an ideal location for coupling into the thermopile. This obviates the need for any additional FIR focussing element.

High-Efficiency Pump Laser

The first requirement for a high-efficiency pump laser is a high-efficiency RF power supply. In this case DEOS has already demonstrated 75 W of RF out with 100 W of DC in. The RF power supply is a conductively-cooled device that uses a class-C power amplifier stage.

While this demonstration was performed with target specifications from a Demonstration Program, DEOS now has the total LLO system design. Accordingly DEOS has reallocated power within the LLO providing 110 W of DC power to the RF power supply. With this level of input power, 85 W of RF has been demonstrated. Thus the pump laser will now have 85 W of RF pump.

Effective use of the available RF power is also key to high-efficiency operation. Through a number of patented techniques, DEOS is able to very efficiently couple the RF power into the discharge.

Diagrams of the high-efficiency pump laser are shown in Figure 4. This

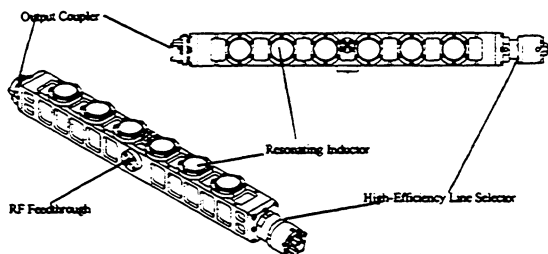


Figure 4: High-efficiency pump laser.

laser is very compact and low in mass (~ 1.5 kg). The RF circuit of the laser is formed by the combination of the electrode/waveguide/enclosure capacitance,

and the resonating inductors. The RF power is admitted through a RF feedthrough in the side of the laser. The cavity is formed by the output coupler, on one end, and the high-efficiency line selector, on the other. This line selector greatly increases the efficiency of the laser, as it has an effective reflectivity at 9P36 of > 99%.

As with the entire LLO project, extensive mathematical modeling of the pump laser has been utilized. In particular, DEOS has measured Rigrod parameters for a complete distributed-loss Rigrod model¹ of the pump laser.

In the Demonstration Program, DEOS delivered an integrated pump laser/RFPS which had an output power of > 9 W @ 9P36 with 100 W of DC input. This laser also exhibited single mode operation, a property DEOS has found to be important for highest efficiency FIR operation.

It should be noted that, due to time and available optics constraints, the cavity optics in the delivered demonstration laser were not optimal. Based on the Rigrod model for the pump laser, with an optimized cavity DEOS is projecting 10 W out with 75 W of RF in. With the new internal LLO power allocations, 85 W of RF is expected – thus the projected output power from the pump laser is now 11 W.

At this time the LLO team has exposed a pump laser, of very similar design, to the launch environment and found no degradation in performance.

Pump Laser Frequency Control

Precise control of the pump frequency is essential for the LLO to meet all specifications. During the Demonstration Program the effects of operating the pump laser at its line-center were studied, as this could significantly simplify the frequency control. However it was found that operation at 9P36 line-center causes a 2 dB loss in FIR efficiency. Therefore it was decided that this would not be acceptable.

Another possible frequency control scheme would involve trying to lock the pump frequency by observing the FIR output. Careful analysis and modeling showed this to be a poor approach,

entangling numerous physical effects and making the frequency control non-robust at best.

To obtain an absolute frequency reference to lock the pump laser against, a photoacoustic cell (see Figure 5) which uses the FIR Laser vibrational pump transition in methanol,² was designed and tested.

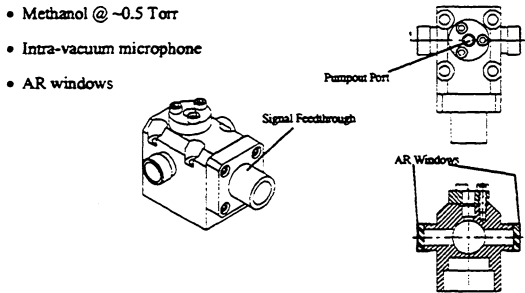


Figure 5: Photoacoustic molecular frequency standard.

The PA Cell is a very simple device. Essentially it is a sealed cavity which contains methanol at ~ 500 mtorr, a pre-polarized microphone, and AR windows. At this time the LLO team has exposed a PA Cell to the launch environment and have had

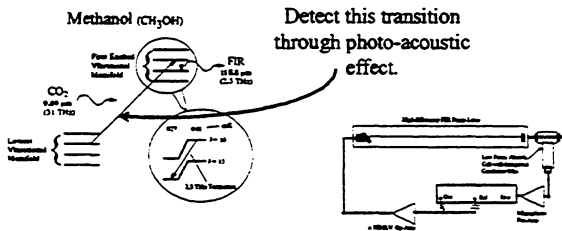


Figure 6: Pump-laser frequency locking method.

it sealed-off for over 5 months, and have observed no performance degradation.

The physical basis for the PA Cell-based pump frequency locking method is presented, graphically, in Figure 6. The pump laser is dithered about the center of the methanol absorption peak producing an acoustic signal as the amount of absorbed power is modulated. The pressure of the cell is set to be low enough that no more than 200 mW of pump power is absorbed.

While the pump laser FM will couple into the FIR output spectrum, this effect should be due to primarily two sources. The first of these, Doppler coupling induced by

velocity memory effects, is given, in worst case, by

$$FM_{FIR} = FM_{pump} \cdot \frac{v_{FIR}}{v_{pump}} \quad \text{Eq. 1}$$

where FM_{FIR} is the Doppler-coupling-induced FIR frequency modulation, FM_{pump} is the FM dither impressed on the pump laser, v_{FIR} is the FIR operating frequency, and v_{pump} is the pump frequency. With the parameters for the LLO's FIR laser, the Doppler-coupling factor is $\sim 1/12$. Therefore the induced FIR dither will be down by a factor of 12 with respect to the pump dither. As DEOS has already demonstrated this lock with < 1 MHz of pump dither, this does not appear to be a problem with respect to the 100 kHz short-term frequency noise specification.

The above does not exhaust sources of frequency noise induced by this locking technique. There is an effect known as the two-photon-light-shift (TPLS), for standing-wave FIR lasers.³

This is a high-frequency, Autler-Townes,⁴ Stark effect, where the Stark field is the pump field. A number of papers on this effect have been published. The LLO team has used the results in these papers to construct a model of the TPLS. While this model is not complete, it does give good agreement with the measured results for other FIR lines (there do not appear to be any direct measurements of the TPLS for the 2.52 THz line but authors⁵ have indicated that the TPLS appears to be anomalously small for this transition).

The general form of the TPLS effect is given by³

$$\Delta v_{FIR} = \frac{\Delta f \cdot \frac{\beta^2 \cdot \Delta p}{2 \cdot \Delta p^2 + \frac{\gamma^2}{8}}}{1 + 2 \cdot \pi \cdot \frac{\gamma}{c \cdot \alpha}} \quad \text{Eq. 2}$$

where Δ_f is the FIR cavity offset from FIR line-center, γ is the vibrational & rotational (assumed same) homogenous linewidth, Δ_p is the pump laser frequency offset from the vibrational transition (in methanol) line-

center, β is the Rabi frequency for the pump transition, α is the FIR gain per unit length, and the factor in the denominator is the FIR gain-reduced pulling factor. It should be noted that β is in general proportional to the pump field magnitude (which is proportional to the square root of pump field density), and $\Delta\nu_{\text{FIR}}$ is proportional to pump power density.

As there is noticeable uncertainty in published values for the dipole matrix element,⁶ and considerable inaccuracy in estimating the circulating pump intensity,⁷ we estimated β from a combination of a model for circulating pump field,⁸ and data obtained during the Demonstration Program.

The results of the TPLS modeling are presented in Figures 7 and 8. As shown

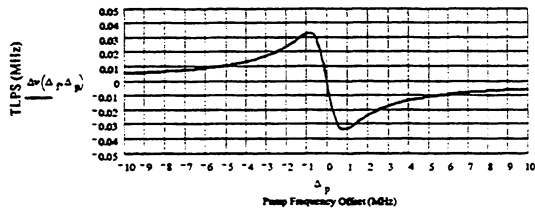


Figure 7: Two-photon light shift vs pump offset.

there the expected TPLS is 60 kHz, worst case @ 1 MHz of pump dither, and the TPLS can be minimized by operating the pump laser only slightly off of the methanol line-center. Further, as indicated earlier, an

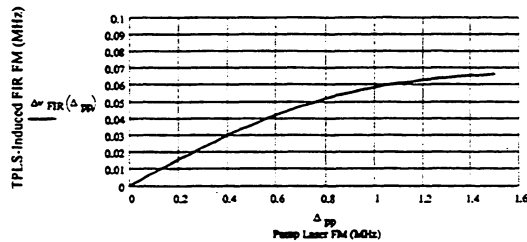


Figure 8: Worst case two-photon light shift vs pump dither amplitude.

anomalously small TPLS has been reported for the 2.52 THz laser transition.

FIR Laser

For reasons of risk⁹ and schedule, the option of a ring FIR laser was dropped from the LLO early in the program. A drawing of the standing-wave FIR laser for the LLO is shown in Figure 9.

Both the input and output mirrors are mounted on PZT-actuated flexure stages. The corner mirrors are mounted on diaphragm flexure alignment mounts. The housing is aluminum with the dielectric waveguides supported inside with flexible wavesprings.

The input coupler and turn mirrors are diamond-turned copper and the input coupling is through a hole in the input mirror. The output coupler is a uniform

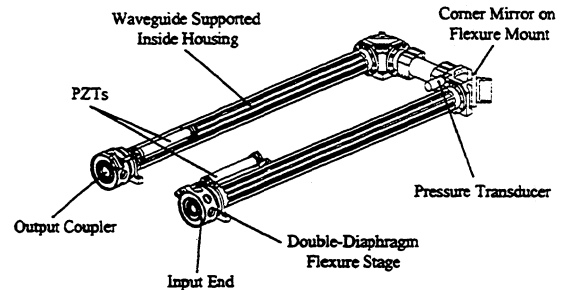


Figure 9: Standing-wave FIR laser.

capacitive mesh type coupler,¹⁰ fabricated by the University of Massachusetts Lowell, STL & POD laboratories. Modeling of the mesh output couplers was accomplished using the GLAYERS program of CSIRO.¹¹

Both the FIR modeling, and the demonstration program results showed optimal uniform output coupling to be necessary to achieve high-efficiency operation. Some of the output power vs pump power results obtained during the Demonstration Program are presented in Figure 10. All of that data was obtained

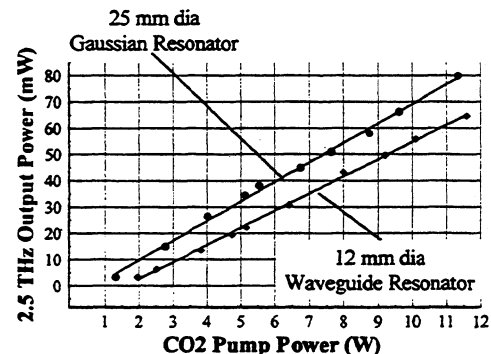


Figure 10: 1.5 m straight-guide Demonstration Program FIR results.

with the pressure held fixed at the optimal pressure for 5 W of pump power, to more accurately simulate flight conditions (ie. once sealed the FIR pressure cannot be

center, β is the Rabi frequency for the pump transition, α is the FIR gain per unit length, and the factor in the denominator is the FIR gain-reduced pulling factor. It should be noted that β is in general proportional to the pump field magnitude (which is proportional to the square root of pump field density), and Δv_{FIR} is proportional to pump power density.

As there is noticeable uncertainty in published values for the dipole matrix element,⁶ and considerable inaccuracy in estimating the circulating pump intensity,⁷ we estimated β from a combination of a model for circulating pump field,⁸ and data obtained during the Demonstration Program.

The results of the TPLS modeling are presented in Figures 7 and 8. As shown

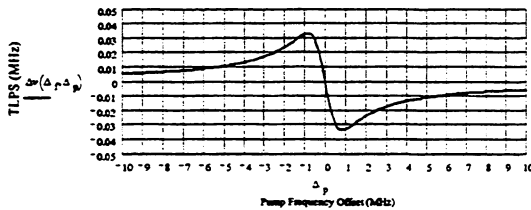


Figure 7: Two-photon light shift vs pump offset.

there the expected TPLS is 60 kHz, worst case @ 1 MHz of pump dither, and the TPLS can be minimized by operating the pump laser only slightly off of the methanol line-center. Further, as indicated earlier, an

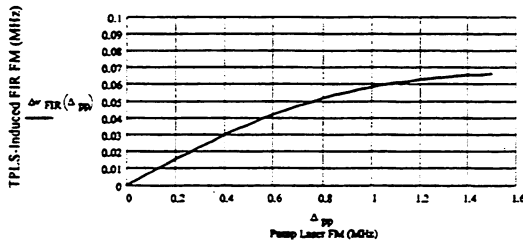


Figure 8: Worst case two-photon light shift vs pump dither amplitude.

anomalously small TPLS has been reported for the 2.52 THz laser transition.

FIR Laser

For reasons of risk⁹ and schedule, the option of a ring FIR laser was dropped from the LLO early in the program. A drawing of the standing-wave FIR laser for the LLO is shown in Figure 9.

Both the input and output mirrors are mounted on PZT-actuated flexure stages. The corner mirrors are mounted on diaphragm flexure alignment mounts. The housing is aluminum with the dielectric waveguides supported inside with flexible wavesprings.

The input coupler and turn mirrors are diamond-turned copper and the input coupling is through a hole in the input mirror. The output coupler is a uniform

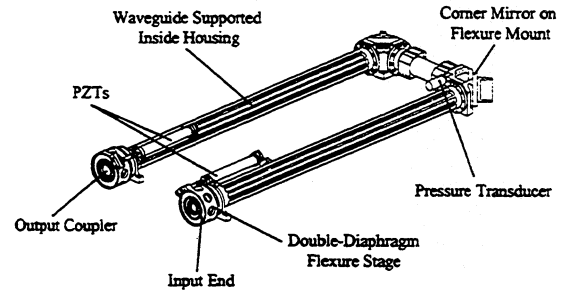


Figure 9: Standing-wave FIR laser.

capacitive mesh type coupler,¹⁰ fabricated by the University of Massachusetts Lowell, STL & POD laboratories. Modeling of the mesh output couplers was accomplished using the GLAYERS program of CSIRO.¹¹

Both the FIR modeling, and the demonstration program results showed optimal uniform output coupling to be necessary to achieve high-efficiency operation. Some of the output power vs pump power results obtained during the Demonstration Program are presented in Figure 10. All of that data was obtained

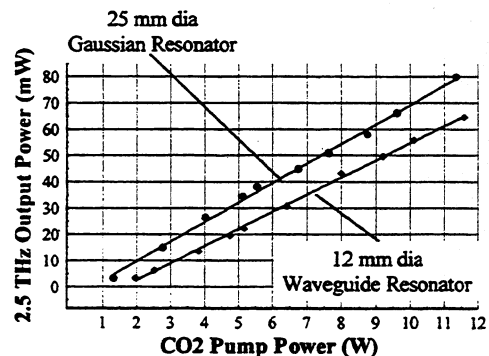


Figure 10: 1.5 m straight-guide Demonstration Program FIR results.

with the pressure held fixed at the optimal pressure for 5 W of pump power, to more accurately simulate flight conditions (ie. once sealed the FIR pressure cannot be

adjusted therefore optimization at the low end of pump power is prudent). The results in Figure 10 bracket the cavity geometries required to meet the initial internal goal of 20 mW out with 5 W of pump power. In looking at Figure 10, it should be remembered that the delivered pump laser actually had an output power of > 9 W – thus a great deal of margin was demonstrated.

The results of Figure 10 are for a straight-guide laser and the losses associated with cavity turns are expected to reduce efficiency and improve mode selection. DEOS developed a distributed-loss Rigrod model for the FIR laser. The results of this model with 5 W of pump are summarized in Figures 11 –13.

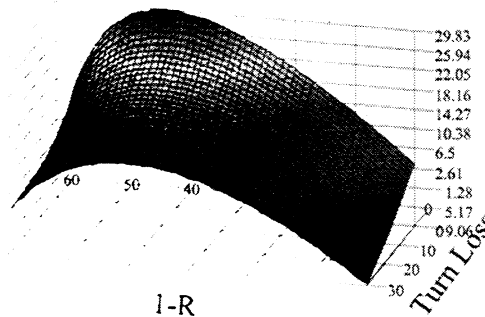


Figure 11: Rigrod prediction for FIR output vs turn loss and output coupling. Pump power fixed @ 5 W.

Figures 11 and 12 plot the output power vs output coupling and turn loss, with

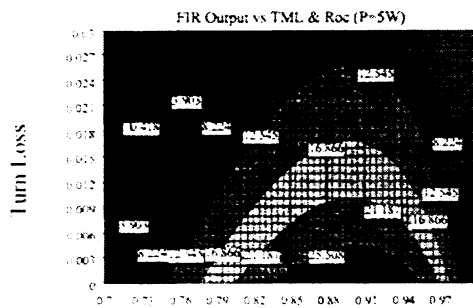


Figure 12: Rigrod prediction for FIR output vs turn loss and output coupling. ("Plan View") Pump power fixed @ 5 W.

the pump power fixed at 5 W. Figure 13 presents the output power vs turn loss with the output coupling fixed at 9 %, and the pump power fixed at 5 W.

All of the parameters for the Rigrod model were determined experimentally during the Demonstration Program. There were no adjustable parameters at this stage of the modeling effort. The most important conclusion of these figures is that turn loss is the key to high-efficiency operation. The LLO's FIR laser operates in the low-gain low-loss regime, thus any loss is significant. Although not shown in this paper, the experimental results for a folded FIR laser show the threshold regime to be below 5 W of pump power – thus the LLO's FIR laser will not be operating in the threshold regime.

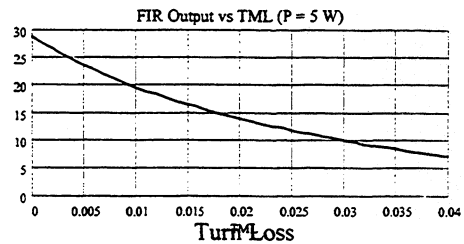


Figure 13: Rigrod prediction for FIR output vs turn loss. Output coupling fixed at 9%, pump power fixed @ 5 W.

The issue of FIR feedback from the diplexer/receivers, combined with the schedule & performance risks of associated with a ring laser, has directed the LLO program towards a novel method for feedback mitigation. Figure 14 illustrates the basis for the approach.

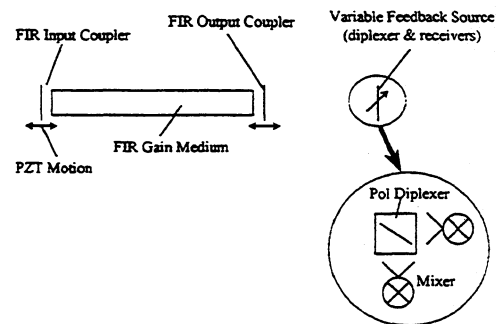


Figure 14: FIR feedback mitigation approach.

The feedback can be considered as a part of the FIR output coupler. This is effectively an etalon output coupler whose reflectivity and effective phase shift are given by

$$E_r(L_{cc}, R_{oc}, R_{fb}) = \sqrt{R_{oc}} \frac{e^{-i 4\pi \frac{L_{cc}}{\lambda}} \sqrt{(1 - R_{oc})^2} \sqrt{R_{fb}}}{1 - \sqrt{R_{oc}} \sqrt{R_{fb}} e^{-i 4\pi \frac{L_{cc}}{\lambda}}}$$

Eq. 3

$$\phi = \arg(E_r) \quad \text{Eq. 4}$$

where E_r is the reflected complex E field seen at the output coupler, L_{cc} is the “coupled-cavity” length, R_{oc} is the reflectivity of the output coupler, R_{fb} is the feedback reflectivity, λ is the FIR wavelength, and ϕ is the effective phase seen at the output coupler.

A signal from one of the mixer bias lines will be fed into the LLO control electronics and used to optimize the output power at all times. Since the LLO control electronics have the ability to command both cavity end mirrors, and the pump laser is locked to an absolute reference, the FIR frequency can be assured to be at line-center.

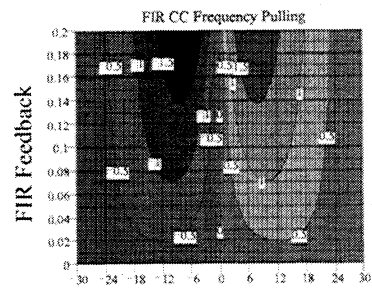
Effects of this control strategy have been modeled and are presented in Figure 15. Figure 15 (a) shows the frequency pulling as a function of change in “coupled-cavity” length (Δl , distance between the diplexer/receivers and the FIR output coupler) and feedback percentage. Figure 15 (b) shows the effective reflectivity vs Δl and feedback percentage. Figure 15 (c) shows the FIR output power vs Δl and turn loss at a fixed pump power of 5 W.

These figures demonstrate:

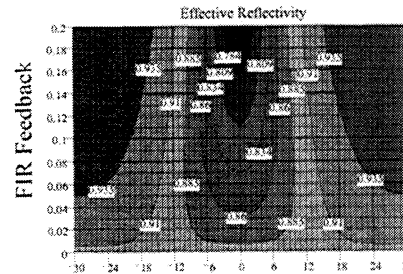
- FIR feedback results in both frequency and amplitude pulling
- Reflectivity pulling drives the efficiency
- The magnitude of the effects increase rapidly with increasing feedback percentage

Further analysis also reveals that the FIR feedback acts most strongly in amplitude and second in frequency.

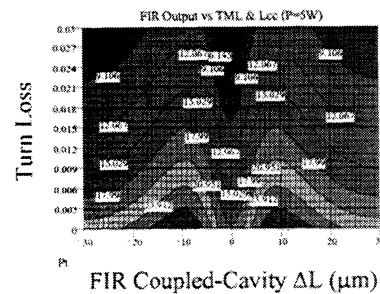
The LLO control design is using the results of the feedback modeling in both design and modeling of the control system (loop margins, etc.).



(a)



(b)



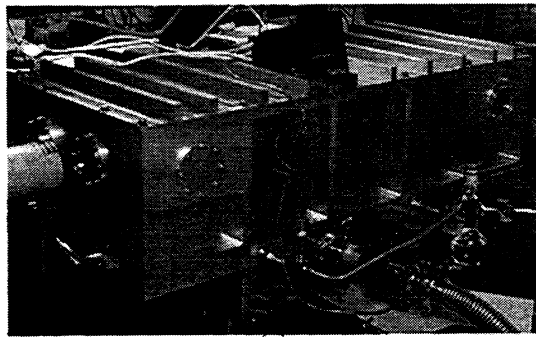
(c)

Figure 15: FIR feedback control effects. (a) FIR frequency pulling [MHz] vs FIR feedback and change in “coupled-cavity” length (Δl), (b) effective output coupling vs FIR feedback Δl , (c) predicted FIR output vs turn loss and Δl , pump fixed @ 5 W.

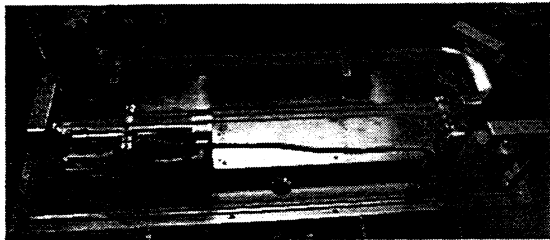
To test the FIR models, and then later to improve them, a high versatility testbed laser was constructed. Figure 16 shows the external and internal view of the testbed laser. Figure 17 shows some more detailed views of the internal workings of the laser.

The testbed is an aluminum enclosure housing a SuperInvar plate on which all of the optical stages are mounted. Cavity translation is accomplished via a 180 μm PZT mounted in a vacuum-tight “can” (see Figure 17 (c)). The inside of this can is kept at atmospheric pressure to avoid discharge problems.

A wide range of waveguide diameters can be used in this laser and easily changed, as they are not involved in the vacuum seal.



(a)



(b)

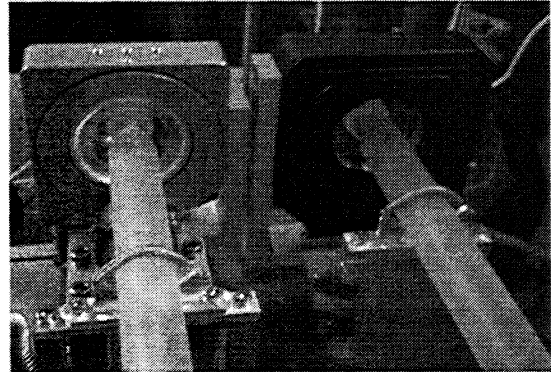
Figure 16: FIR testbed laser. (a) external view, (b) internal view.

The testbed laser also has two ports at each corner to enable virtually any cavity configuration. In a different hardware program, where DEOS is developing a compact high-power FIR laser for another application, the testbed laser will be used to test different ring laser options.

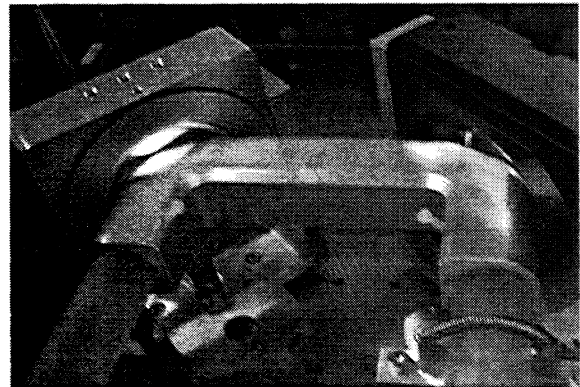
The miter, which holds the three guide pieces together, is shown in Figure 17 (b). As seen there and in Figure 17 (a), the waveguide sections are held in precision-machined V-blocks by standard coil springs stretched across the guide sections. All four of the gimbal stages are slightly modified commercial units.

The testbed laser has sufficient vacuum integrity to permit sealed off operation for many hours and in fact the pressure is typically observed to decrease with time as a result of methanol adsorption onto the internal surfaces. The pressure is monitored by a standard Pirani gauge. While this gauge's calibration is a function of gas composition, it is not prone to drift, and is quite hardenable for flight applications. The LLO will use a custom Pirani gauge to monitor the FIR laser pressure.

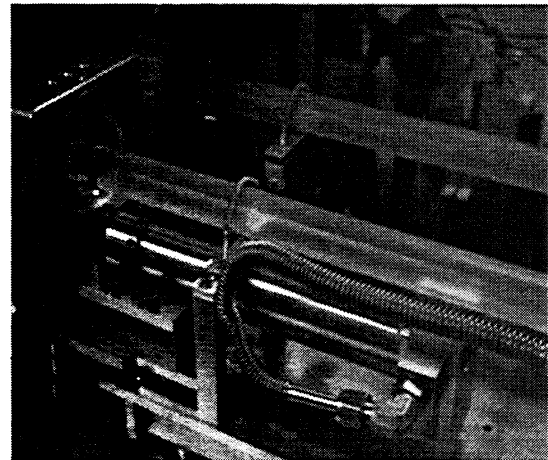
The results obtained with the testbed laser are presented in Figure 18 along with a comparison to the model results that were included in our LLO proposal. As observed in Figure 18, the experimental results are within 9 % of the original prediction. This



(a)



(b)



(c)

Figure 17: FIR testbed laser internal details. (a) input/output end, (b) turn end, (c) PZT "can" cavity length adjustment.

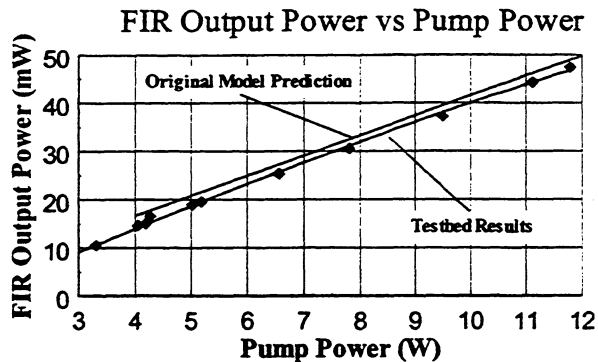


Figure 18: Testbed results: comparison with original model.

prediction was based on an estimate for the turn loss of 0.8 %/turn (reflectivity loss + guide-guide loss around the turn as a result of the unguided region of the mitered corner). If one now takes the Rigrod model and treats the turn loss as an adjustable parameter, then with a turn loss of 1.2 %/turn the model falls directly over the experimental data.

To provide lifetime confidence, DEOS is constructing a simple straight-guide FIR laser system, which uses identical stages, materials, and sealing techniques to those employed in the LLO. This laser system will be operated continuously up to, and possibly after, launch of the Chem I satellite. Thus at the time of launch, there will be > 2 years of lifetime data accumulated.

As a backup option, if any long-term FIR gas degradation issues arise, the LLO design is carrying an optional pump-fill molecular-sieve system. This system uses space proven molecular-sieve technology where one sieve is to be used as a exhaust-free pump, and the other as a source sieve. Calculations indicate that such a system should provide >1000 laser refill cycles (once every 2 days over the total required life). With the assistance of Rutherford Appleton Laboratory, the LLO team is presently designing the molecular sieves.

Conclusions

The LLO will utilize high-reliability laser technology to meet the needs of the MLS for Chem I. There will be substantial performance margin at delivery and

thorough modeling for the entire LLO including control electronics. At the time of launch, >2 years of lifetime data for the LLO will have been accumulated.

FIR feedback effects will be mitigated through the use of a "coupled-cavity" control architecture.

Based on already demonstrated results, the LLO team is projecting 43 mW of FIR output at system delivery.

Acknowledgements

The authors wish to acknowledge the vital contributions of the network of suppliers, and of the other team members, to this work. This work is supported by NASA's Jet Propulsion Laboratory under contract number 961080.

¹ W. W. Rigrod, IEEE JQE, Vol. QE-14(5), 377 (1978)

² G. Busse, E. Basel, and A. Pfaller, Appl. Phys., Vol. 17, 387 (1977)

³ C. R. Pidgeon, W. J. Firth, P. A. Wood, A. Vass, and B. W. Davis, Int. J. IR & MMW, Vol. 2(2), 207 (1981); S. T. Shanahan, and N. R. Heckenberg, Opt. Commun. Vol. 50(6), 393 (1984)

⁴ S. H. Autler, and C. H. Townes, Phys. Rev., Vol. 100, 703 (1955)

⁵ P. M. Plainchamp, IEEE JQE, Vol. QE-15(9), 860 (1979)

⁶ J. Heppner, C. O. Weiss, U. Hubner, and G. Schinn, IEEE JQE, Vol. QE-16(4), 392 (1980); S. T. Shanahan, and N. R. Heckenberg, Opt. Commun. Vol. 50(6), 393 (1984)

⁷ A. Harth, Int. J. of IR & MMW, Vol. 12(3), 221 (1991)

⁸ J.-M. Lourtioz, and R. Adde, J. Physique, Vol.41, 251 (1980)

⁹ J. H. Lee, C. L. Rettig, N. C. Luhmann, JR., and W. A. Peebles, Rec. Sci. Instrum. Vol. 63(10), 4678 (1992)

¹⁰ R. Densing, A. Erstling, M. Gogolewski, H-P Gemund, G. Lundershausen, and A. Gatesman, Infrared Phys., Vol. 33(3), 219 (1992)

¹¹ P. A. Stimson, and L. B. Whitbourn, "GLAYERS, A Program for the IBM PC which Calculates the Properties of Metal Grids in Dielectric Stacks," (1989)

A W-band HEMT based power amplifier module for millimeter-wave LO multipliers

Imran Mehdi ^a, Todd Gaier ^a, Jacob Kooi ^b, Bert Fujiwara ^a, and Richard Lai ^c

^a Jet Propulsion Laboratory, California Institute of Technology, Pasadena, CA

^b Dept. of Applied Physics, California Institute of Technology, Pasadena, CA

^c TRW Inc., One Space Park, Redondo Beach, CA

ABSTRACT

We report on the performance of power amplifiers as local oscillator drivers for millimeter and submillimeter-wave heterodyne receivers. The noise properties of the MMIC amplifier in multiplied local oscillator chains are characterized by pumping a low noise superconductor-insulator-superconductor double slot heterodyne mixer at 386 GHz in the laboratory. A more sensitive measurement of noise contribution from the amplifier was performed with a 278 GHz SIS waveguide receiver at the Caltech Submillimeter-Wave Observatory by means of astronomical observations. It is concluded that the MMIC amplifier does not add noise to the radiometer system.

1. INTRODUCTION

A critical component of all heterodyne receiver systems is the local oscillator (LO) source that enables the mixing device to produce the intermediate frequency (IF) signal. Traditionally, in submillimeter-wave receivers a Gunn diode oscillator followed by the appropriate frequency multiplier has been used to provide the LO source. While this combination has worked well and technology development of Gunn devices [1], multiplier

devices[2], and multiplier circuits[3] continues to improve LO sources, there are compelling reasons to look beyond Gunn oscillators as the fundamental source of power in the LO chain. One inherent limitation of Gunn diode circuits and transit-time device circuits is the very limited achievable electronic tuning bandwidth. For space-borne applications, it is desirable to have all frequency tuning performed electronically, without the potential of mechanical failure. There has been some effort in extending voltage tuning bandwidth of Gunn devices at W-band, but this has resulted in severely degrading the output power. Voltage controlled W-band Gunn oscillators with 10% bandwidth have been demonstrated, with output power degraded to 10 mW [4]. Moreover, each Gunn diode oscillator circuit requires individual tuning making it difficult to produce them in large quantities.

Recent advances in the upper frequency limit and output power of three terminal devices have now made it possible to consider them as an alternative to fundamental oscillator sources [5,6,7]. 50 micron thick substrate, 0.1 micron GaAs high electron mobility transistor (HEMT) technology has now yielded state-of-the-art MMIC power amplifiers at W-band that have output power as high as 0.3W [8]. Use of this technology as

the highest frequency power generation source in a LO chain, raises questions about the noise contributions of the amplifier to the receiver by means of the LO injected signal. We examine the noise properties of low noise receivers pumped by a W-band MMIC power amplifier.

2. TECHNOLOGY

The W-band power amplifier was fabricated with a 0.1 μm gate length pseudomorphic AlGaAs/InGaAs/GaAs HEMT MMIC process on a 50 μm thick GaAs substrate. The process details are described in references [5] and [6] for the 0.1 μm GaAs HEMT and 50 μm substrate processes, respectively. 0.1 μm GaAs HEMT devices achieve cutoff frequencies as high as 200 GHz and up to 10 dB small signal gain at 94 GHz, suitable for W-band power operation [8]. 50 μm GaAs substrate thickness improves thermal conductivity, reduces device source inductance and compacts devices cells and matching structures to minimize circuit losses. The power amplifier was designed with a 64 finger output device cell and a total output periphery of 1.28 mm. This amplifier also includes on-chip bias networks and was matched to 50 ohm input/output lines. A photograph of the chip is shown in Figure 1.

The chip, 2300x1800 μm^2 in size, has been packaged in a split-waveguide block housing, based upon a University of Massachusetts [9] design. E-plane probes are used for input and output coupling between the waveguide and microstrip. Simple wire-bonds are used to connect the probes, which are fabricated on 75 μm thick Teflon, to the chip. Appropriate bypass capacitors are used to enable biasing of the chip without oscillations. Figure 2 shows the lower half of the split block with the MMIC chip in place.

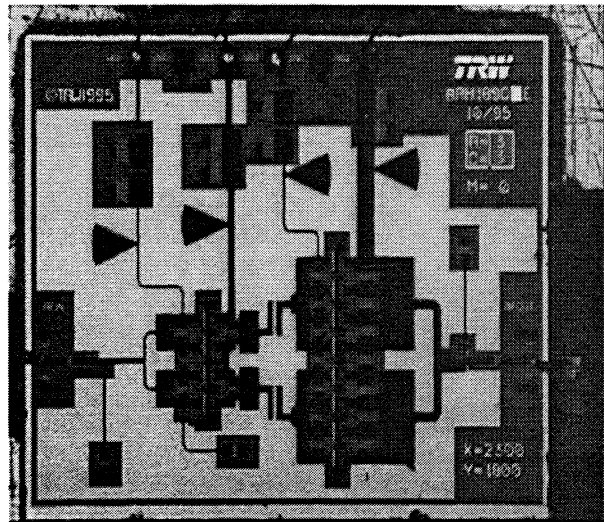


Figure 1: Photograph of the W-band monolithic power amplifier.

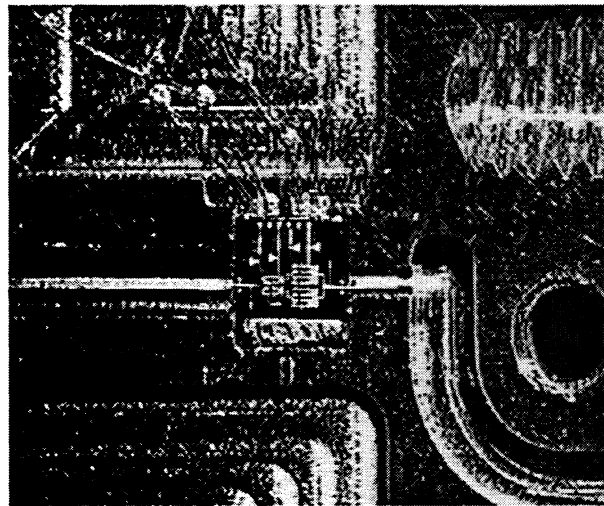


Figure 2: Photograph of the PA inside the lower half of the waveguide block.

The measured available small signal gain of the packaged PA is shown in Figure 3. The drains were biased at 3 volts with 280 mA of current while the gate voltages were held at 0 V for this particular measurement. The measurement was performed on a Hewlett-Packard 8510 vector network analyzer with custom millimeter-wave heads fabricated by Oleson Microwave labs.

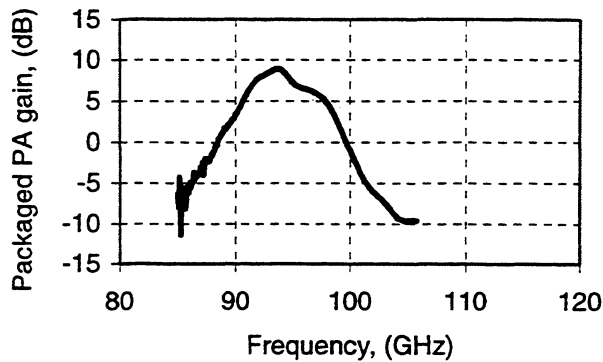


Figure 3: Measured small signal gain of the PA. Drain bias for both stages was 3 Volts at 280 mA total current. The gate voltage was 0 V.

A 75-110 GHz Backward Wave Oscillator (BWO) tube was used to provide an input signal to measure the frequency response of the PA under large signal conditions. The BWO was used because of the easy availability, wide bandwidth and high output power. However, for space borne applications a commercially available YIG based active multiplier will be used. The output power was measured with an Anritsu power meter and is shown in Figure 4.

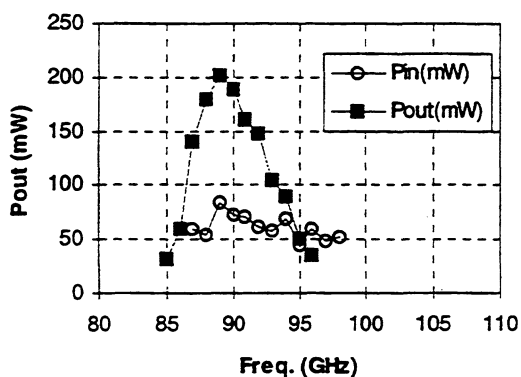


Figure 4: Measured output power of the PA as a function of frequency. For maximum output power $V_{d1}=1.5$ V, $I_{d1}=170$ mA, $V_{d2}=4$ V and $I_{d2}=400$ mA.

3. NOISE CHARACTERISTICS

For low noise millimeter and submillimeter-wave radiometers, the noise added by the LO can cause serious degradation in the receiver sensitivity. Both AM and FM noise can be added by the LO source into the IF signal by means of the mixing process specifically, in the case of interferometers phase noise on the input of the mixer will result in degradation

The noise of HEMT transistors has been characterized as an input Johnson noise from input resistors at the quiescent operating temperature, and an output Johnson noise due to the drain-source resistance at an effective temperature proportional to the drain-source current density [10]. For the PA in the LO chain, both amplified input and output noises contribute to the total source noise. Typical values for the equivalent thermal noise at the output of the W-band PA could be higher than 5000 K. Propagation of this noise through the multiplication chain is difficult to calculate. A comparison of this noise relative to the noise of the high-Q cavity stabilized Gunn oscillator could be a critical design issue for low-noise receiver systems.

In addition to the thermal noise component, HEMT devices are well known to exhibit $1/f$ noise in the device transconductance. While unlikely, this noise can extend to high enough frequency to enter the receiver IF band (1-2 GHz or higher), fluctuations in the LO power could reduce the sensitivity of the receiver in an observing situation. The purpose of our initial investigation is to understand the noise properties of the MMIC PA applied to sensitive heterodyne receivers. Two experiments have been carried out.

In the initial experiment, a laboratory version of a superconductor-insulator-superconductor

(SIS) double slot antenna quasi optical mixer operating at 386 GHz was used [11]. The mixer LO utilizes a free running Gunn diode at 96.7 GHz followed by a Schottky diode quadrupler. The mixer noise temperature was measured with two different LO configurations as shown in Figure 5.

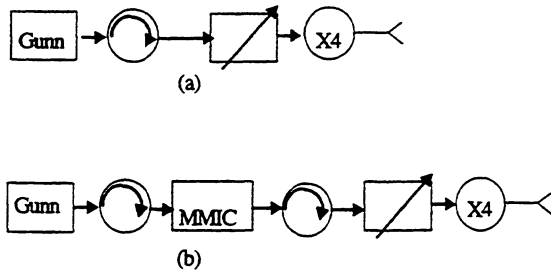


Figure 5: LO chain configuration (a) with the Gunn diode oscillator, (b) with the MMIC PA inserted into the LO chain.

In both cases, the pumped current through the SIS junction was monitored and kept constant. In configuration (a), the standard operating mode, a receiver noise temperature of 219-222 K was measured. In configuration (b), inserting the PA with level setting attenuators and isolators between the Gunn oscillator and multipliers, a noise temperature of 217-214 K was measured. Additionally, in a third configuration, a waveguide bandpass filter (92-96 GHz) was added between the MMIC amplifier and the second isolator for the purposes of limiting the amplifier noise available to the RF passband. This resulted in a possible marginal reduction in the noise temperature, measured to be 208-210 K. In either case, the application of a driver amplifier does not appear to degrade the noise temperature of the SIS receiver. In fact we consistently measured (by going back and forth between A and B) a very slight receiver noise reduction when the power amplifier is inserted.

With this encouraging result we continued our investigation with a more sensitive waveguide receiver at the Caltech submillimeter-wave observatory at Mauna Kea, Hawaii. This also provided us the opportunity to examine the effect of putting an amplifier in the LO chain for astronomical observations. A 278 GHz SIS receiver [12] was used to observe the Methanol (CH_3OH) line in the Orion-South Nebula. The initial LO chain configuration is shown in Figure 6 (a). The Gunn was phase locked and a receiver noise temperature of 22.5 K \pm 1 K (double side band) was measured using hot and cold loads. The observation was done with an integration time of 400 seconds and a number of scans were taken for accuracy. The telescope was then pointed off the source for calibration and to get a measure of the noise floor. The MMIC amplifier was then inserted into the LO chain as shown in Figure 6 (b). The measured noise temperature of the receiver was 21.3 K \pm 1K double side band while keeping identical SIS current to the measurement with the Gunn diode. The same observation of the Orion Nebula with identical integration time and scans was carried out. Figure 7 shows the measurement of the Methanol line, both with and without the power amplifier. As can be seen there is no discernible line broadening and the noise floor in both cases is the same. Figure 8 shows the noise floor fluctuations from the two different LO configurations, again indicating no major discrepancy.

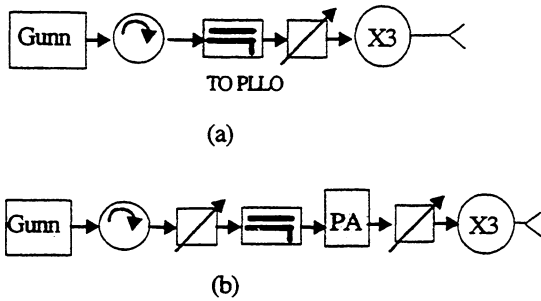


Figure 6: LO chain configuration at the CSO with and without the PA. A second isolator between the PA and the multiplier would have been desirable since some standing wave problems were observed. However given the mounting mechanics, we were unable to do so.

4. CONCLUSION

Sensitive heterodyne receivers have been used to investigate the noise properties of an HEMT based power amplifier as a driver for LO chains. Based on the measured receiver noise temperatures and the amplitude and shape of the measured signal from the Orion Nebula it is concluded that the noise added to the local oscillator chain by the use of a MMIC solid state power amplifier is insignificant for single dish operation.

5. ACKNOWLEDGMENTS

We wish to thank Peter Siegel (JPL) and Jonas Zmuidzinas (Caltech) for the use of their lab facilities and encouragement to pursue this work. We would also like to thank Barry Allen (TRW) and Sander Weinreb (UMass) for technical discussions regarding LO noise. This work was supported by NASA under grant UPN 632 for the Center for Space Microelectronics Development. The MMIC devices were designed and fabricated under TRW IR&D funds.

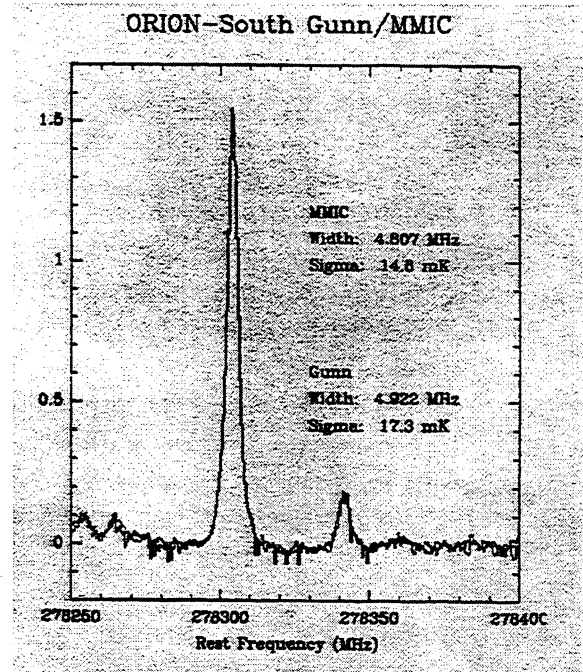


Figure 7: Observation of the Methanol line in the Orion Nebula with the two different LO chains as shown in Figure 6. Addition of the PA does not deteriorate the observation.

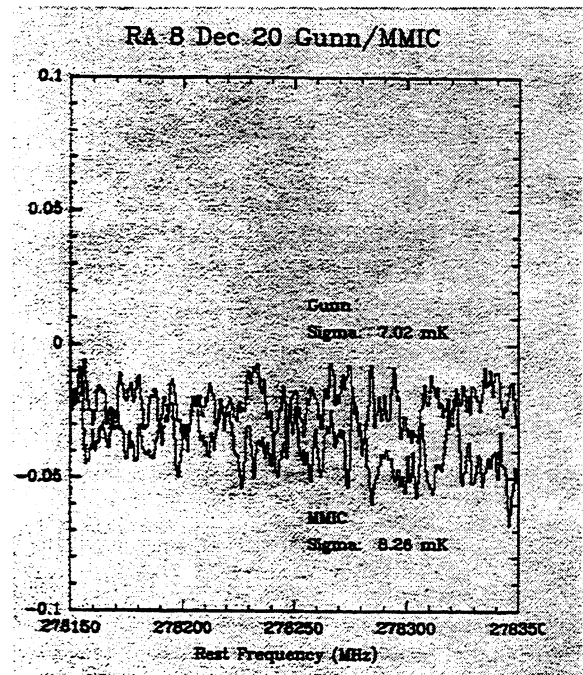


Figure 8: The above signals are obtained when the telescope is pointed to a dark sky target.

6. REFERENCES

1. H. Eisele and G. I. Haddad, "Two-Terminal Millimeter-Wave Sources," to appear in MTT-46, 1998.
2. R. Peter Smith, et. al, "Advances in Submillimeter Wave semiconductor-based device designs and processes at JPL," 8th International Space Terahertz Symposium, Boston 1997.
3. N. Erickson, work to be presented at the 9th International Space Terahertz Symposium, Pasadena, 1998.
4. N. N. (Watkins-Johnson Co.): "W-band Varactor-Tuned Oscillators with 10 GHz Bandwidth", Microwave Journal, Vol. 33, no. 10, 1988, pp. 137-140.
5. M. D. Biedenbender et al., "A 0.1-um W-band HEMT production process for high yield and high performance low noise and power MMIC's," in 16th Annul. IEEE GaAs IC Symposium Digest, Philadelphia, PA, Oct. 1994, pp. 325-328.
6. R. Lai et. al. "A High Efficiency 0.15 μm 2-mil Thick InGaAs/AlGaAs/GaAs V-band Power HEMT MMIC", IEEE GaAs IC Symposium Digest, pp. 225-227, Orlando, FL, Nov. 1996.
7. H. Wang et al., "A W-band monolithic 175 mW power amplifier," in 1995 IEEE MTT-S Int. Microwave Symposium Digest, Vol. 2, Orlando, FL, pp. 419-421.
8. P. P. Huang, et. al, "A 94-GHz 0.35-W Power Amplifier Module," IEEE-MTT vol. 45, no. 12, December 1997, pp. 2418-2423.
9. Y. C. Leong and S. Weinreb, "Design and simulation of W-band microstrip-waveguide transition using HFSS and MDS," University of Massachusetts technical report, May 30th, 1997.
10. M W. Pospieszalski, "Modeling of Noise Parameters of MESFET's and MODFET's and their frequency and temperature dependence," IEEE-MTT Vol. 37, number 9, September 1989, p. 1340.
11. J. Zmuidzinas and H. G. LeDuc, "Quasi-Optical Slot Antenna SIS Mixers," IEEE MTT-40, No. 9, September 1992.
12. J. Kooi, M. Chan, B. Bumble, H. G. LeDuc, P. Schaffer, and T. Phillips, "230 and 492 GHz Low-noise SIS wave-guide receivers employing tuned Nb/AlOx/Nb Tunnel-junctions," International Journal of Infrared and Millimeter Waves, v16 912), pp. 2049-2068, December 1995.

TRANSIENT SIMULATION OF HARMONIC TEO CIRCUITS

Gregory B. Tait and Stephen H. Jones*

Electrical Engineering, Virginia Commonwealth University, Richmond, VA 23284
Email: gbtait@saturn.vcu.edu

*Dept. of Electrical Engineering, University of Virginia, Charlottesville, VA 22903

ABSTRACT

A fast, convolution-based computer algorithm is employed to simulate the fully autonomous operation of a complete millimeter-wave, harmonic transferred electron oscillator (TEO), and an investigation of harmonic power generation is presented. Unlike previous combined harmonic-balance/device simulations of oscillator circuits, the nonlinear physical device/circuit response evolves in time to its natural steady-state mode of operation which permits insights into harmonic energy exchange, stability, load pulling, and frequency tuning effects. A second-harmonic 150 GHz TEO is simulated using both conventional Gunn and novel stable-depletion-layer (SDL) InP devices. The SDL device prohibits the formation of accumulation layers and dipoles. The integrated device/circuit simulations in the time-domain enable us to investigate the formation and build-up of this stable mode in detail.

I. INTRODUCTION

At present, the lack of reliable, high-power, and compact solid-state sources is the single greatest obstacle to achieving an accessible submillimeter-wave technology. Advanced research is needed to create the next generation of THz sources suitable for scientific and commercial applications.

The role of device and circuit simulation is critical to understanding the operation of transferred-electron oscillators (TEO), frequency multipliers, and metal-semiconductor-metal (MSM) photomixers, and to designing a monolithic integrated circuit incorporating the complete THz circuit. In turn, only with fast, robust, and accurate numerical algorithms can computer-aided design (CAD) and analysis tools become practical to the design engineer. This work will help develop the necessary efficient and accurate computational algorithms to be used in future integrated device/circuit CAD.

Although harmonic-balance methods are successful in determining the steady-state behavior of millimeter-wave circuits, there are many important high-frequency and high-speed circuits that require full time-dependent simulation, including transients under discontinuous operating conditions (at start-up and other times) and

the mixing and parametric effects of multiple and possibly non-commensurate-frequency signals. The simulation of low-frequency nonlinear circuits is commonplace (e.g. SPICE simulations), but application of pure time-domain techniques to large-scale nonlinear microwave and millimeter-wave circuits is generally more complex [1]. In particular, any time-domain solution algorithm based on Newton-Raphson or optimization iterations of the nonlinear system virtually precludes the use of a physics-based numerical solid-state device simulator, since the necessary derivatives in the Jacobian matrix can not be practically generated from a purely numerical, "black-box" description of the nonlinear solid-state device.

Seminal work in convolution-based solution algorithms appeared in early literature[2], but has been largely neglected since that time, owing to unacceptably inefficient computer algorithms and lengthy compute times. Currently, with the widespread availability of high-speed workstations, interest in revisiting this approach has surfaced [3, 4]. However, efficient algorithmic implementation and applications to new devices and circuits have been lacking. Presently, a very large number of sample points in the discrete convolution, well over 10^5 , and time steps not exceeding a few femtoseconds need to be used. For a millimeter-wave oscillator circuit of moderate Q, it can take well over 10^6 time steps to reach a steady-state operation [3]. Another approach that allows steady-state operation to be reached much sooner requires the use of an additional time-integration scheme at each time step [4]. This is acceptable if the device can be modeled by an equivalent circuit, but highly undesirable if the device must be simulated by its physics-based numerical model. Clearly, a new approach is needed to

improve computational speed, thus permitting the investigation and co-design of new devices and circuits.

II. SIMULATION METHOD

To meet the unique requirements of efficiency and accuracy in an integrated device/circuit simulator, an improved time-domain convolution-based algorithm must be developed. Specifically, the proposed new approach consists of applying advanced concepts from the fields of digital signal processing and nonlinear iteration theory to the discrete-time impulse response of the linear embedding circuit. The proposed solution method follows these steps:

- 1.) The complex, frequency-dependent embedding impedances as "seen" by each port of the solid-state device in its mount must be accurately determined. Care must be exercised in the sampling of the frequency-domain impedances to insure sufficient resolution and to avoid unwanted aliasing effects in the associated time-domain impulse response. Complex embedding impedances of novel, state-of-the-art waveguide and coplanar mounts can be determined with the use of electromagnetic field simulators, such as the Hewlett-Packard High-Frequency Structure Simulator [5], a 3-D finite element code solving Maxwell's equations.
- 2.) The associated size of the discrete impulse response obtained from an inverse FFT of the complex impedance samples must be reduced by truncation if we are to achieve our goal of efficient simulation. Unfortunately, the nearly discontinuous structure of some embedding impedances (caused by waveguide cut-off and high-Q behavior) will lead to the familiar Gibbs-phenomenon ripples in the embedding impedance function that is reconstructed

from the discretized impulse response. Hence, both truncation and the Gibbs phenomenon will limit the accuracy of the derived impulse response. From the field of digital signal processing, finite-impulse-response digital filters can be designed to reshape the truncated impulse time samples in such a manner that ripples in the corresponding frequency-domain samples have been smoothed [6]. A large volume of literature has explored the optimal reshaping for the causal, linear-phase filters used in signal processing applications. It is unknown at the present time what kinds of reshaping functions will work best for impulse responses derived from the millimeter-wave circuits of interest. We can, however, create a whole new class of asymmetric filter, as we are only interested in maintaining the real, causal property of the impulse response (i.e., we are not constrained by linear-phase considerations). A new filter was used to generate the reshaped impulse response samples, retaining only 8000 terms from the original 2×10^5 . Figure 1 shows a comparison of the impedance samples reconstructed from the digitally filtered impulse response with the original embedding impedances of the model harmonic oscillator cavity.

3.) The discrete convolution used in the device/circuit solution algorithm is placed in an advantageous form suggested by the theory of nonlinear iteration:

$$v_k = \sum_{j=k-N+1}^{k-1} h_{k-j} i_j(v_j) + h_{0k} i_k(v_k) \quad (1)$$

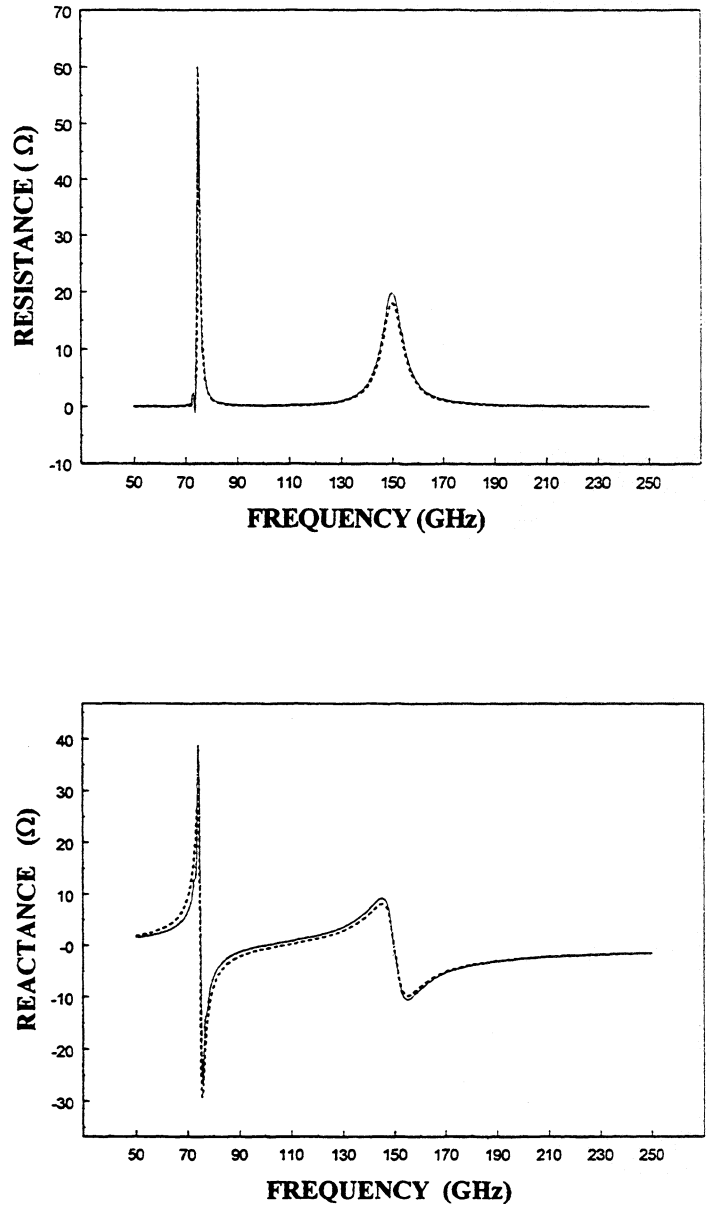


Figure 1. Reconstructed (solid line) and Original (dashed line) TEO Circuit Impedances

where k indicates the time step level ($k\Delta t$) in the simulation, h_n are the impulse response samples, v and i are voltages and currents at the nonlinear device terminals. Equation (1) is in fixed-point iteration form.

If the time step Δt is very small, the “unknown” i_k can be approximated by $i_k \cong i_{k-1}$, and no iteration is needed. However, it may require well over 10^6 time steps until steady-state is achieved, and, at each step, the numerical solution to the device nonlinear differential equations and the convolution integral must be performed. The fixed-point iteration form, on the other hand, allows us to use the maximum-sized time step consistent with the stability and accuracy of the numerical device simulator. Although we may need to iterate on Eq. (1), as $i_k \cong i_{k-1}$ is not necessarily a good approximation, the under-relaxation and Steffensen acceleration schemes employed by us previously make the iteration subject to rapid convergence[7]. The semi-implicit time discretization scheme of our TED device simulator allows stable and accurate time steps such that steady-state oscillator operation is acquired after only 10^4 time steps, a savings in computational effort of two orders of magnitude. The combination of the very efficient convolution calculation performed at each time step with the reduced number of time steps necessary to reach steady-state operation leads to significant reduction in computer execution time.

4.) Since the summation term in the convolution, Eq.(1), contains all known values at time step k , it may be calculated in parallel with the solid-state device equations, yielding a further improvement in efficiency. We plan to implement the device/circuit solution algorithm in a massively parallel and distributed processing environment. Several high-performance

UNIX workstations will collectively solve the complex device/circuit co-design problem.

A critical part of the success of the integrated device/circuit numerical approach is the efficiency and suitability of the physics-based numerical device simulator. The TED device used here is a modified version of a previously developed code [8]. The equations governing TED electron transport are the continuity equation, temperature dependent drift-diffusion equation, and Poisson’s equation:

$$\frac{\partial n(x,t)}{\partial t} = \frac{1}{q} \frac{\partial J_n(x,t)}{\partial x} \quad (2)$$

$$J_n(x,t) = q\mu[\xi(x,t), T(x)]n(x,t)\xi(x,t) + qD[\xi(x,t), T(x)]\frac{\partial n(x,t)}{\partial x} + qn(x,t)D\tau(x)\frac{\partial T(x)}{\partial x} \quad (3)$$

$$\text{and } \frac{\partial^2 \psi}{\partial x^2} = \frac{q}{\epsilon} [n(x,t) - N_D(x)] \quad (4)$$

where n , q , and J_n are electron density, electron charge, and electron particle current density, respectively. In Eq. (3), the field- and temperature-dependent mobility and diffusivity modeling parameters were extracted from three-valley Monte Carlo simulations. Lattice temperature in the device is calculated from a self-consistent solution to the heat equation for the packaged diode. These equations are discretized and solved using an accurate and efficient half-implicit Crank-Nicolson technique. Ohmic and fluid outflow boundary conditions are used at the cathode and anode of the device, respectively. The total device terminal current is given by:

$$I = \frac{A}{l} \int_0^l J_n dx + \frac{\epsilon A}{l} \frac{dV}{dt} \quad (5)$$

where A , l , and ϵ are the area, length, and material dielectric permittivity of the device. A fully self-consistent treatment of the displacement current term requires an accurate, second-order backward finite-difference calculation of the time derivative of terminal voltage in cases where a fully autonomous simulation is executed.

III. SIMULATION RESULTS

Two circuits were simulated - one with a "conventional" notch-doped Gunn diode and one with a novel current-limiting-contact diode. Both devices have $1.8 \mu\text{m}$ InP active regions doped at $1 \times 10^{16} \text{cm}^{-3}$ and are $60 \mu\text{m}$ in diameter. The Gunn diode has a $0.15\text{-}\mu\text{m}$ -long doping notch of $7 \times 10^{15} \text{cm}^{-3}$ near the cathode. The current-limited diode has a shallow barrier ($\sim 110\text{meV}$) cathode contact that prohibits the formation and propagation of accumulation layers and/or dipole domains. This device was experimentally developed by Litton Solid-State, and operates in a Stable Depletion Layer (SDL) mode characterized by the modulation of a stable depletion region [9]. Both diodes are inserted in a model second-harmonic, half-height WR-8 cavity. The embedding impedances presented to the diodes are modeled from representative data obtained from a combination of HP-HFSS and mode-matching simulations with equivalent circuit models. The transient simulations are shown in Figures 2 and 3.

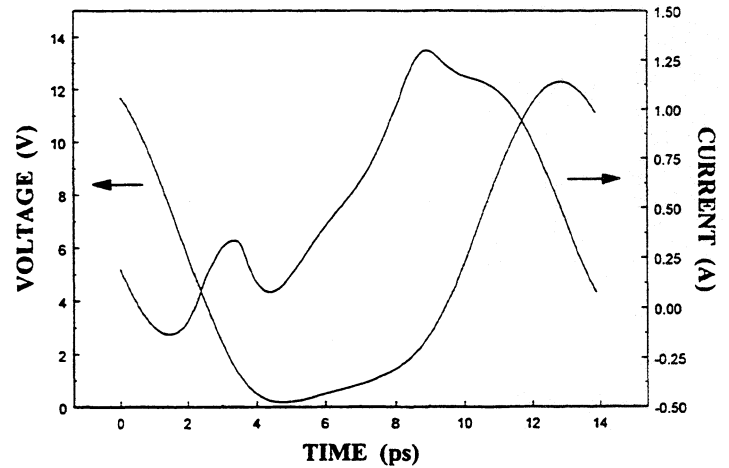
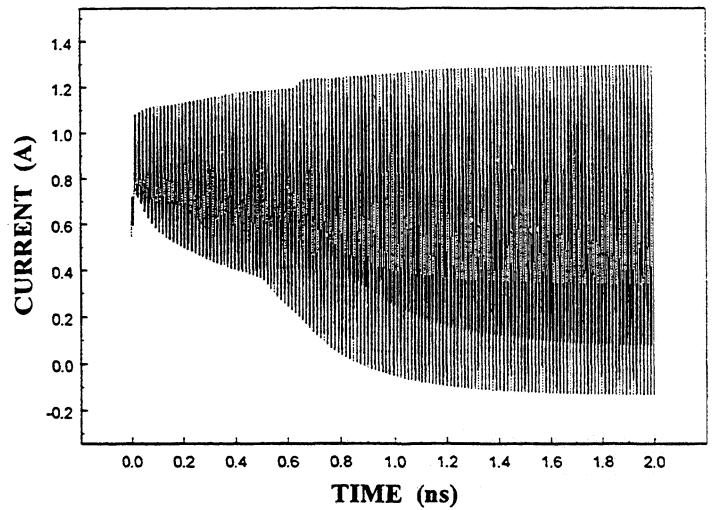


Figure 2. Transient and steady-state simulation of Gunn device terminal voltage and current in TEO circuit. Operating conditions are 5 VDC and 400 °K. Steady-state second-harmonic frequency settles at $f_2 = 144 \text{GHz}$.

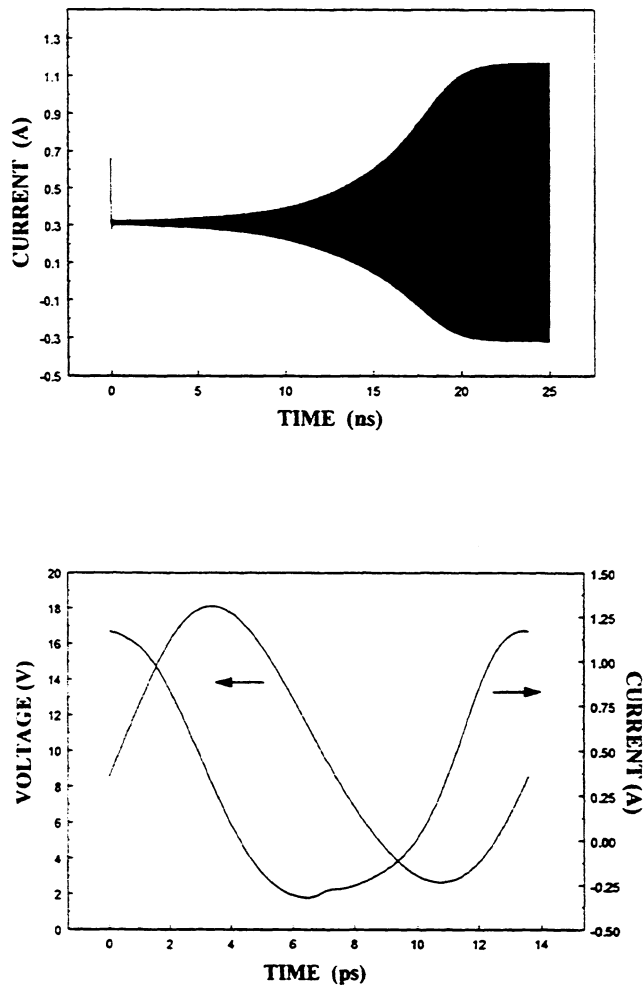


Figure 3. Transient and steady-state simulation of SDL device terminal voltage and current in TEO circuit. Operating conditions are 10 VDC and 400 °K. Steady-state second-harmonic frequency settles at $f_2 = 147$ GHz.

Both circuits exhibit a very large fundamental voltage oscillation near 73 GHz within the coaxial mount section of the cavity. The cut-off frequency of the output waveguide is at 75 GHz, so the diodes are terminated in a nearly pure reactance at the fundamental. Fourier analyses of the voltage and current waveforms show that

very small amounts of power are actually dissipated at the fundamental frequency in the small series resistances of the diodes. In Fig. 2, we can actually see the rapid growth of the second harmonic current component, leading to considerable power generated at 144 GHz. A strong voltage oscillation at the fundamental frequency appears necessary to maintain this operation. We can understand this effect as energy conversion through the diode nonlinearity, much like the idler function in a frequency multiplier circuit. The second-harmonic is coupled to the output waveguide, while a backshort is adjusted to maximize output power. With proper design of the cavity dimensions, the real impedance seen at the second harmonic frequency is easily tuned to 1-20 Ω and the reactance is also tuned to 1-20 Ω . Since the fundamental frequency is in cut-off, impedance tuning at the second harmonic using the backshort should have little influence on the fundamental operation, with possible small parametric effects observed. Hence, a design is feasible with broad frequency tuning at the fundamental using a coaxial backshort and stable power tuning at the second harmonic using a waveguide backshort, with minimal coupled effects between the two tuners.

In Fig. 3, the transient solution for the SDL device indicates a much longer time to build-up a strong oscillation. Physically, the SDL device does not support strong unstable accumulation or dipole modes of operation, like the Gunn diode, but instead supports modulation of a steady electron density depletion. Through a combination of transferred electron effect, depletion layer transit time effect, and back-diffusion of carriers from the anode, the resultant asymmetric current waveform produces appreciable power generation at the second-harmonic. It may be possible to design for

increased harmonic content in the current waveform by tailoring the doping profile in the active region of the SDL device.

Table 1 demonstrates the effect of backshort tuning on the performance of the TEO circuit. A small diode series resistance (0.1Ω) is included in the circuit impedances shown. The simulated output power at the second harmonic frequency compares well with experimental data [10]. In a WR-6 test cavity, output powers at a nominal 150 GHz ranged from 15-30 mW for several diodes in various package configurations.

IV. CONCLUSION

A time-domain technique has been developed that integrates numerical solid-state device simulation with complete nonlinear circuit simulation using an efficient convolution-based algorithm. This technique should aid in advancing the available CAD tools for submillimeter-wave components, especially harmonic TEOs, Schottky diode mixers, and MSM photomixers. Future developments will include implementation in a massively parallel and distributed computing environment, and the creation of Web-based CAD tools available to the THz community.

Backshort (degrees)	DC Power (W)	Z_1^{ckt} (Ω)	Z_2^{ckt} (Ω)	P_2 (mW)
+16	3.2	$0.1 + j 10.0$	$7.7 - j 4.5$	9.2
+6	3.2	$0.1 + j 10.1$	$7.7 + j 3.6$	18.0
+2	3.2	$0.1 + j 10.2$	$3.7 + j 4.5$	24.7
0	3.2	$0.1 + j 10.2$	$3.1 + j 4.2$	25.3
-2	3.2	$0.1 + j 10.2$	$2.7 + j 4.0$	25.1
-8	3.2	$0.1 + j 10.1$	$1.5 + j 3.1$	19.1
-14	3.2	$0.1 + j 10.0$	$0.8 + j 2.3$	10.9

Table 1. 147 GHz Second-Harmonic TEO Circuit Operation with $1.8 \mu\text{m}$ InP SDL Device

V. REFERENCES

1. R.J.Gilmore and M.B.Steer, "Nonlinear Circuit Analysis Using the Method of Harmonic Balance. A Review of the Art," *International Journal of Microwave and Millimeter-Wave Computer-Aided Engineering*, vol. 1, no. 1, pp. 22-37, Jan. 1991.
2. W.J.Evans and D.L.Scharfetter, "Characterization of Avalanche Diode TRAPATT Oscillators," *IEEE Trans. Electron Devices*, Vol. ED-17, No. 5, pp. 397-404, May 1970.
3. M. Curow, "New Insight in Operating Modes and Optimum Design of Harmonic TED Oscillators for W-Band Applications," *IEEE Trans. Electron Devices*, vol. 43, no. 6, pp. 861-870, June 1996.
4. M.B.Steer, "Oscillator Analysis," Workshop on Recent Advances in Microwave and Millimeter-Wave Oscillator Design, 1995 IEEE MTT-S International Microwave Symposium (Orlando, FL), May 16-20, 1995.
5. High-Frequency Structure Simulator, Release 5.0, Hewlett-Packard Company, Santa Rosa, CA, 1997.
6. A.V.Oppenheim and R.W.Schafer, *Discrete-Time Signal Processing*. Englewood Cliffs, NJ: Prentice-Hall Inc., 1989.
7. G.B.Tait, "Efficient Solution Method for Unified Nonlinear Microwave Circuit and Numerical Solid-State Device Simulation," *IEEE Microwave and Guided Wave Lett.*, vol. 4, no. 12, pp. 420-422, Dec. 1994.
8. G.B.Tait and C.M.Krowne, "Efficient Transferred Electron Device Simulation Method for Microwave and Millimeter-Wave CAD Applications," *Solid-State Electronics*, vol. 30, no.10, pp. 1025-1036, Oct. 1987.
9. M.F.Zybura, S.H.Jones, B.W.Lim, J.D.Crowley, and J.E.Carlstrom, "125-145 GHz Stable Depletion Layer Transferred Electron Oscillators," *Solid-State Electronics*, vol. 39, no. 4, pp. 547-553, April 1996.
10. M.F. Zybura, *A Theoretical and Experimental Contribution to the Design of 100-200 GHz Transferred Electron Oscillators*. Ph.D. Dissertation, University of Virginia, Jan. 1996.

GAAS TUNNETT DIODES AND INP GUNN DEVICES FOR EFFICIENT SECOND-HARMONIC POWER GENERATION ABOVE 200 GHz

Heribert Eisele

Solid-State Electronics Laboratory
Department of Electrical Engineering & Computer Science
1246B EECS Building
The University of Michigan
Ann Arbor, Michigan 48109-2122

Abstract

Low-noise operation and significant RF power levels were demonstrated recently with GaAs TUNNETT diodes and InP Gunn devices in fundamental-mode operation at W-band (75-110 GHz) and D-band (110-170 GHz) frequencies. State-of-the-art RF power levels of 100 ± 5 mW at 100-107 GHz from TUNNETT diodes as well as > 200 mW at 103 GHz, > 130 mW around 132 GHz, and > 80 mW at 152 GHz from Gunn devices were measured, which correspond to dc-to-RF conversion efficiencies of 5.8-6.1 % at 100-107 GHz, > 2.3 % at 103-132 GHz, and > 1.4 % at 152 GHz. As shown with the first experimental results, *e.g.*, RF power levels of > 0.3 mW at 283 GHz from Gunn devices and > 0.6 mW at 210 GHz from TUNNETT diodes, both two-terminal devices exhibit strongly nonlinear characteristics. Therefore, second-harmonic power generation was investigated further theoretically and experimentally. State-of-the-art RF power levels of 9 mW at 209 GHz and > 4 mW at 235 GHz from TUNNETT diodes as well as more than 1 mW at 280 GHz from Gunn devices were measured with a submillimeter-wave dry calorimeter. Corresponding dc-to-RF conversion efficiencies were > 1 % at 209 GHz and > 0.6 % at 235 GHz. Simulations revealed a large modulation in the depletion width of the TUNNETT diodes and explained the high up-conversion efficiencies observed. The results from TUNNETT diodes compare favorably with those from Schottky varactor diode frequency multipliers that are driven by transferred-electron oscillators. As expected from the excellent noise performance in the fundamental mode, these free-running oscillators showed clean spectra with a low phase noise of, *e.g.*, well below -94 dBc/Hz at a frequency off the carrier of 500 kHz.

1. Introduction

Low-noise operation of free-running oscillators and significant RF power levels were demonstrated recently with GaAs TUNNETT diodes and InP Gunn devices in fundamental-mode operation at W-band (75-110 GHz) [1] and D-band (110-170 GHz) [2] frequencies. Improved heat dissipation of devices on diamond heat sinks resulted in state-of-the-art RF power levels of 100 ± 5 mW at 100-107 GHz from TUNNETT diodes [1,3] as well as more than 200 mW at 103 GHz, more than 130 mW around 132 GHz, and more than 80 mW around 152 GHz from Gunn devices [2,3]. These RF power levels correspond to

dc-to-RF conversion efficiencies of 5.8-6.1 % at 100-107 GHz [1,3], more than 2.3 % at 103-132 GHz, and more than 1.4 % at 152 GHz [2,3]. Figure 1 summarizes these experimental results from TUNNETT diodes and Gunn devices. Tunneling as the injection mechanism in TUNNETT diodes or the formation of domains in Gunn devices causes inherently nonlinear device properties with respect to the RF voltage across the device terminals. In addition, a modulation in the width of the active region corresponds to a capacitance variation and generation of higher harmonics similar to that of Schottky varactor diodes. Second-harmonic power extraction was initially investigated, mainly to confirm fundamental-mode operation, and first experimental results, *e.g.*, RF power levels of more than 0.3 mW at 283 GHz [4] and more than 0.6 mW at 210 GHz [1], indicate that both Gunn devices and TUNNETT diodes hold strongly nonlinear characteristics. As a consequence, second-harmonic power extraction was investigated further experimentally using different waveguide configurations and theoretically using diode simulations.

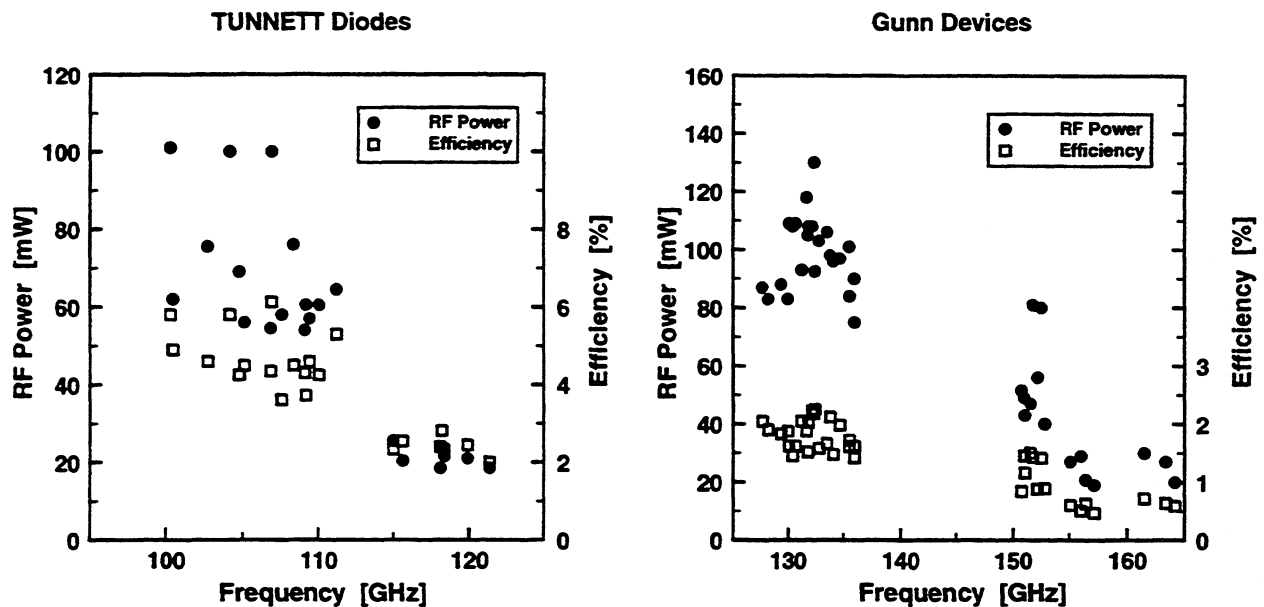


Figure 1: RF performance of GaAs TUNNETT diodes at W-band and InP Gunn devices at D-band frequencies, all on diamond heat sinks.

2. Experimental setups

All GaAs TUNNETT diodes were tested in the same type of a full-height WR-10 waveguide cavity as in fundamental-mode operation [1,3], where a resonant cap coarsely determined the oscillation frequency. A standard noncontacting back short for frequency and power fine-tuning was mounted on one flange of the cavity. Different configurations for reactively terminating the diode at the fundamental frequency were investigated. In all experiments with TUNNETT diodes and Gunn devices, a 1-inch-long WR-3 wave-

guide section cut off all signals below 173 GHz, which includes the signal at the fundamental frequency. Examples of configurations for TUNNETT diode oscillators are a tapered transition from the WR-10 waveguide of the cavity to the WR-3 waveguide or a discontinuity with a step from the WR-10 to the WR-3 waveguide. The configuration shown in Figure 2 resulted in the highest RF power levels from all tested TUNNETT diode oscillators. A tapered transition from the WR-6 to the WR-3 waveguide was connected directly to the WR-10 waveguide output flange of the cavity and introduced a small step discontinuity at this flange.

Most of the InP Gunn devices were tested in the same type of a full-height WR-6 waveguide cavity as in fundamental-mode operation [2,3], where, similar to the cavity for TUNNETT diodes, a resonant cap coarsely determined the oscillation frequency. Gunn devices in this type of cavity yielded the highest RF power levels with a sharp discontinuity from the WR-6 waveguide output flange to the WR-3 waveguide. For the experiments with the InP Gunn devices, also a scaled version of a Carlstrom-type [5] cavity with coaxial-line frequency short, a power back short in a WR-5 waveguide and a transition to the output WR-6 waveguide [6] was successfully employed.

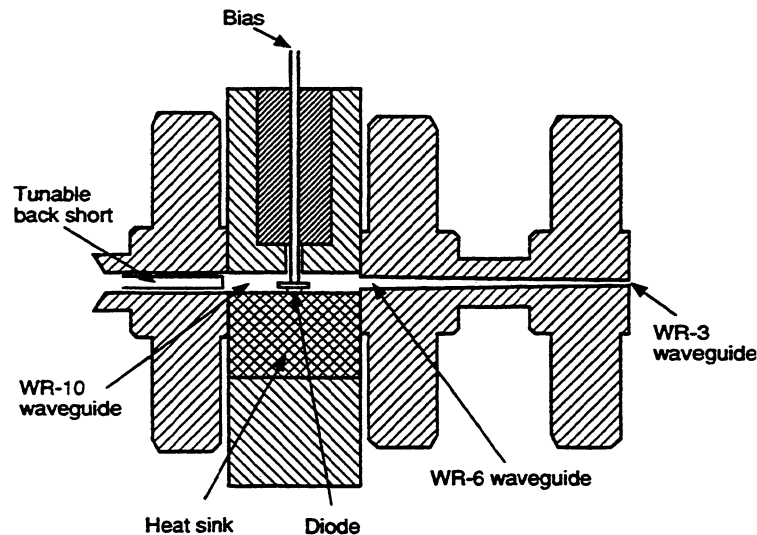


Figure 2: Schematic of the WR-10 waveguide cavity and waveguide transition for second-harmonic power extraction from GaAs TUNNETT diodes.

At first, a 140-220-GHz power sensor in a WR-5 waveguide or a D-band thermistor power meter with a WR-6 waveguide input flange was used to measure the RF power levels. Their sufficiently fast response time (compared to that of a calorimeter) allowed tracking of power changes quickly as the back short was tuned for maximum RF output power at the second-harmonic frequency. Tapered transitions from the WR-5 to WR-4 and WR-4 to WR-3 waveguides or from the WR-6 to WR-3 waveguide provided adequate impedance matching in the WR-3 waveguide at the second-harmonic frequency. Subsequently, a

submillimeter-wave dry calorimeter with a WR-8 waveguide input flange and two tapered transitions, one from the WR-8 to WR-6 waveguide and the other from the WR-6 to WR-3 waveguide, each approximately 1-inch-long, was employed to confirm the RF power levels. An attenuation of 0.85 dB, for example, was measured at 234 GHz for the 1-inch-long WR-3 waveguide section in the setups, which is slightly higher than the predicted attenuation for a gold-plated waveguide. As a consequence, an attenuation of 0.55 dB was estimated for the two waveguide transitions to the calorimeter. The attenuation in either the WR-6 to WR-3 or the WR-10 to WR-3 waveguide transition at the oscillator output flange was not factored in in any of the experiments as such a transition was considered part of the oscillator circuit.

3. Experimental results

The measurements with the dry calorimeter verified all RF power levels from the TUNNETT diodes except for one result with an RF output power of more than 10 mW at 209 GHz. This minor discrepancy is attributed to changes that were introduced as oscillators were partly disassembled and reassembled between the measurements with power sensor or thermistor head and the measurements with the calorimeter. As a result, the conditions for generation of the RF power of more than 10 mW could not be reproduced. Figure 3 summarizes the best results measured with the calorimeter. As examples, RF power levels up to 9 mW and more than 4 mW were measured at second-harmonic frequencies of 209 GHz and 235 GHz, respectively, which correspond to dc-to-RF conversion efficiencies of more than 1.0 % and more than 0.6 %. Contrary to operation in the fundamental mode at 104-118 GHz, bias currents for optimum second-harmonic power extraction were in the range from 60 % to 85 % of the respective maximum bias currents. Therefore, operating junction temperatures were estimated [1] to be well below 150 °C, and reliable long-term operation can be expected from these diodes. As a further consequence, up-conversion efficiencies, which were determined as the ratios of RF power generated in a second-harmonic mode to RF power generated in the fundamental mode at the same bias current and fundamental oscillation frequency, always exceeded 9 % and were more than 20 % for the best results at 209 GHz and 235 GHz.

Second-harmonic power extraction with a Gunn device in Rydberg's cavity [6] yielded RF power levels of more than 2 mW at various frequencies between 220 GHz and 223 GHz as measured with the calorimeter. Tuning of the frequency short appeared to be critical since the cavity supported fundamental-mode operation of the same device very easily at numerous D-band frequencies around, *e.g.*, 150 GHz, but was not designed for efficient second-harmonic power extraction around, *e.g.*, 300 GHz. Furthermore, resulting RF power levels in the fundamental mode turned out to be below well-established state-of-the-art results from the same batch of InP Gunn devices [2,3] and, as a matter of fact, fundamental-mode operation was not within the scope of this work. Therefore, this mode of operation had to be avoided in this cavity.

RF power levels of 0.7 mW at 269 GHz, 1 mW at 279 GHz, and 1.2 mW at 280 GHz were obtained from InP Gunn devices in the WR-6 waveguide cavity and measured with the calorimeter. These RF power

levels and those from the GaAs TUNNETT diodes are the highest reported to date for any other Gunn device and any GaAs transit-time diode, respectively. Second-harmonic RF power levels from the TUNNETT diodes and corresponding dc-to-RF conversion efficiencies, in particular, compare favorably with high-efficiency frequency multipliers, where Schottky varactor diodes are driven by low-noise Gunn device oscillators [7,8]. Lower than expected RF power levels from the Gunn devices in a second-harmonic mode indicate that optimum embedding impedances as seen by the diode at the fundamental and second-harmonic frequency have not yet been fully established.

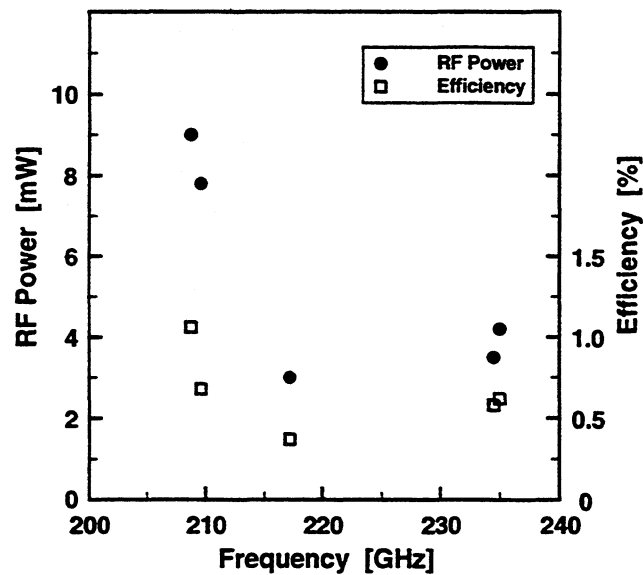


Figure 3: RF performance of GaAs single-drift TUNNETT diodes in a second-harmonic mode for the frequency range 200-240 GHz.

The spectra of free-running oscillators with Rydberg's cavity [6] and with all tested TUNNETT diodes in a WR-10 waveguide cavity were recorded at significant RF power levels by disconnecting the calorimeter and connecting a harmonic mixer to the WR-3 waveguide section. The phase noise determined at a frequency off the carrier of 500 kHz typically remained below - 87 dBc/Hz and was always at or below the noise floor of the employed spectrum analyzer and harmonic mixer. Therefore, actual phase noise levels were estimated to be considerably lower and correctly reflected the excellent noise performance known already from fundamental-mode operation [1-4]. Figure 4 shows an exemplary spectrum with a phase noise of < - 94 dBc/Hz at a frequency off the carrier of 500 kHz for the TUNNETT diode that yielded the RF power of 9 mW at a second-harmonic frequency of 209 GHz. Operation at a higher harmonic number causes much higher conversion loss in the harmonic mixer of the spectrum analyzer and prevents meaningful phase noise measurements for Gunn devices tested in the WR-6 waveguide cavity above 260 GHz.

4. Device simulations

Accurate predictions from diode simulations typically require prior knowledge of the embedding impedances seen by the diode at the frequencies of interest. However, GaAs TUNNETT diodes terminated with a matched load at the fundamental frequency were operated at 20-25 % lower bias voltages than measured without RF oscillations at the same maximum bias currents [9]. As shown in Figure 5 for a fundamental frequency of 107 GHz, this strong back bias effect reflects RF voltage amplitudes of 6.5-7.0 V, which were predicted by a large-signal simulation program [10]. This simulation program uses a two-valley energy-momentum model for electrons and a drift-diffusion model for holes, takes interband tunneling into account and was described in greater detail elsewhere [10]. Predicted RF power levels for fundamental-mode operation at the above-mentioned RF voltages and corresponding dc-to-RF conversion efficiencies including those of Figure 5 agree well with the experimental results of Figure 1.

For second-harmonic power extraction, the diodes were terminated mainly reactively at the fundamental frequency. At the RF power levels of Figure 3 and optimum bias current densities of 60-85 % of the maximum values in fundamental-mode operation, 25-30 % lower bias voltages than those without RF oscillations were observed and corresponded to predicted RF voltages of 7.0-8.0 V. Such large voltage swings are similar to those in second-harmonic transferred-electron devices, and, as illustrated with Figure 6, result in waveforms with a relatively sharp turn-on and a higher harmonic content of the current densities injected into the drift region of the diode than in the fundamental mode. Since RF voltages at the second-harmonic frequency were always less than 15 % of those at the fundamental frequency, no significant impact on the back bias effect could be observed in the simulations. In Figure 7, the electric field profiles in the active region of the diode are plotted for phases $\omega t = 0^\circ, 90^\circ, 180^\circ,$ and 270° , whereas the inset shows the three waveforms of the RF voltage across the diode, the injected and the total current densities of the diode as a function of time for one RF cycle at a fundamental frequency of 104 GHz. The bias current density was set to 35 kAcm^{-2} , and RF voltage amplitudes were adjusted to 7.3 V at 104 GHz and 0.6 V at 208 GHz.

As can be seen from Figure 7, the drift region shown as the n^- region in the inset becomes nearly undepleted and neutral when the RF voltage approaches its minimum. When the RF voltage rises again and more of the drift region becomes depleted, a steep increase in the total current density ensues and corresponds to a high harmonic content. This large modulation of the depleted region in the diode resembles that of Schottky varactor diodes in high-efficiency frequency multipliers and explains the observed up-conversion efficiencies in excess of 20 % much better than just a sharp turn-on in the injected current density. All the above simulations took a total specific series resistance from ohmic contacts of $1.5 \times 10^{-6} \Omega\text{cm}^2$ into account and indicated that the RF output power at the second-harmonic strongly depends on the termination at the fundamental frequency, but is a relatively weak function of the impedance at the second-harmonic frequency. The simulations for Figures 6 and 7 predicted an RF output power of 16 mW with a corresponding dc-to-RF conversion efficiency of 1 % for a load impedance of $(1.5 + j 4.0) \Omega$ at 208 GHz. These predicted values agree very well with the measured results of Figure 3.

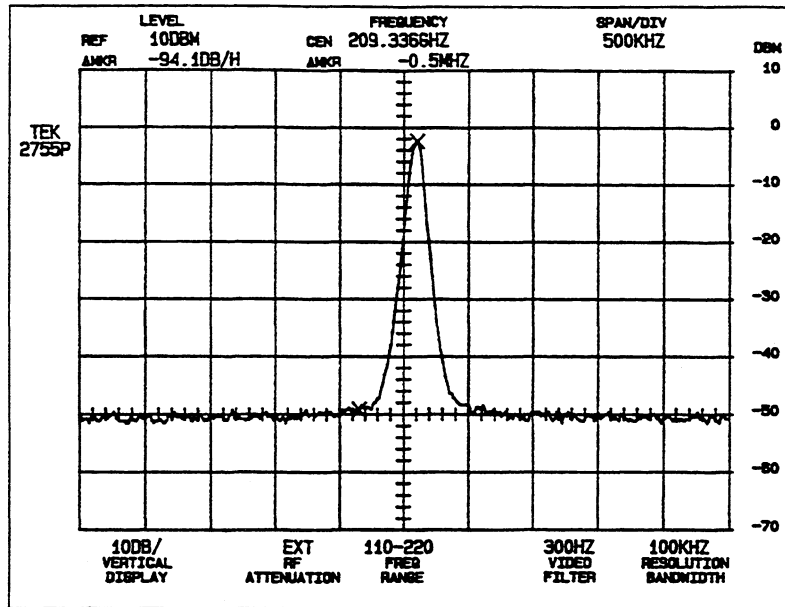


Figure 4: Spectrum of a free-running TUNNETT diode oscillator in a second-harmonic mode. RF power level 9 mW, center frequency 209.377 GHz, vertical scale 10 dB/div, horizontal scale 500 kHz/div, resolution bandwidth 100 kHz, video bandwidth 3 kHz.

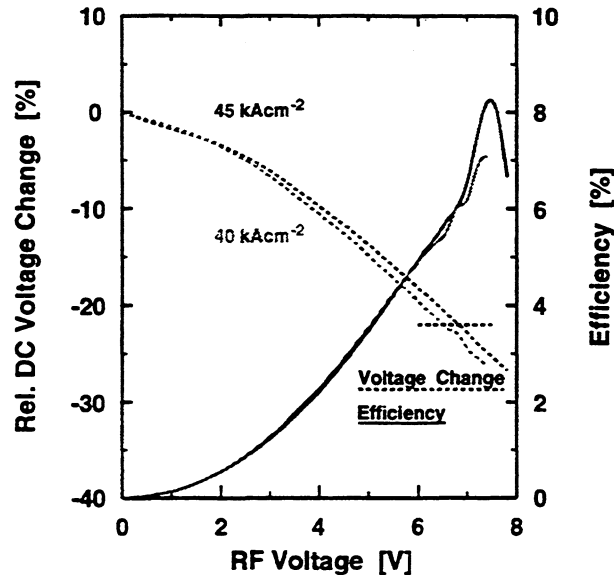


Figure 5: Predicted back bias effect and dc-to-RF conversion efficiency as a function of RF voltage amplitude for a GaAs TUNNETT diode in the fundamental mode at 107 GHz.

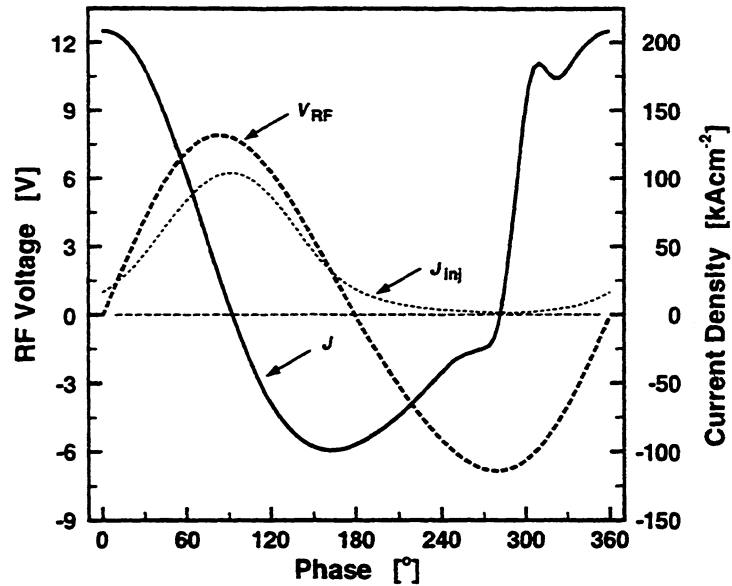


Figure 6: Waveforms of RF voltage V_{RF} , injected and total current densities J_{inj} and J of a GaAs TUNNETT diode as a function of time during one RF cycle at the fundamental frequency of 104 GHz.

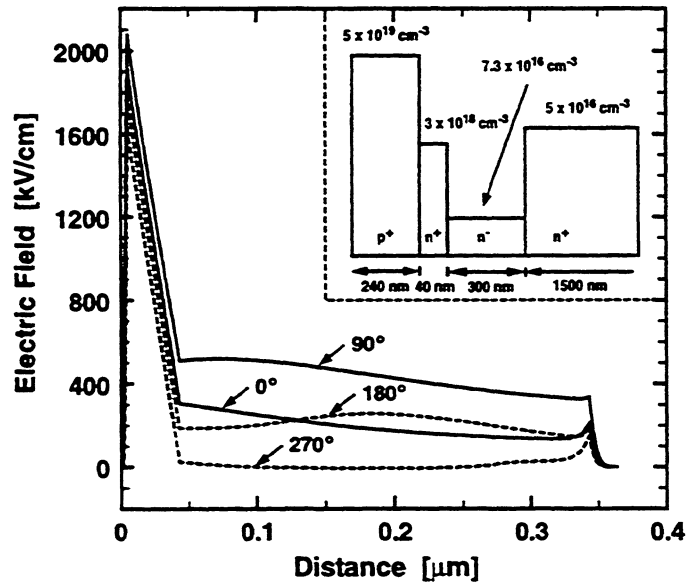


Figure 7: Electric field profiles of a GaAs TUNNETT diode in a second-harmonic mode at phases of 0°, 90°, 180°, and 270° during one RF cycle at the fundamental frequency of 104 GHz. Inset: Nominal doping profile of the TUNNETT diode.

5. Conclusion

Second-harmonic power extraction was demonstrated successfully with GaAs TUNNETT diodes and InP Gunn devices at frequencies above 200 GHz. To the author's knowledge, RF power levels up to 9 mW and dc-to-RF conversion efficiencies of more than 1 % are the highest reported to date from any GaAs transit-time diode, and RF power levels of more than 1 mW at 280 GHz are the highest reported to date from any GaAs or InP Gunn devices. In particular, results from GaAs TUNNETT diodes compare favorably with results from low-noise all-solid-state RF sources with frequency multipliers [7,8]. Simulations revealed a mode of operation similar to the large modulation in the width of the depleted region as seen in Schottky varactor diodes. Therefore, the high up-conversion efficiencies observed are attributed much more to this large capacitance modulation of the diode than to a high harmonic content in the injected and the resulting induced diode currents. Performance parameters predicted for TUNNETT diodes agree well with measured results. In InP Gunn devices, the interaction of circuit and device, *i.e.*, the impedance levels at the fundamental and the second-harmonic frequencies, must be studied in greater detail to increase the RF power levels that can be extracted in a second-harmonic mode.

Acknowledgment

Thanks go to Anders Rydberg at the University of Uppsala for making the cavity available as well as to Imran Mehdi with the Jet Propulsion Laboratory and Michael Coulombe with the University of Massachusetts at Lowell for providing the submillimeter-wave power meter and calorimeter, respectively.

References

- [1] Eisele, H., Haddad, G. I.: "Enhanced Performance in GaAs TUNNETT Diode Oscillators Above 100 GHz Through Diamond Heat Sinking and Power Combining", *IEEE Transactions on Microwave Theory and Techniques*, **MTT-42**, 1994, pp. 2498-2503.
- [2] Eisele, H., Haddad, G. I.: "High-Performance InP Gunn Devices for Fundamental-Mode Operation in D-Band (110-170 GHz)", *IEEE Microwave and Guided Wave Letters*, **MWGL-5**, 1995, pp. 385-387.
- [3] Eisele, H., Haddad, G. I.: "Two-Terminal Millimeter-Wave Sources", to appear in *IEEE Transactions on Microwave Theory and Techniques*, **MTT-46**, 1998.
- [4] Eisele, H., Haddad, G. I.: "D-Band InP Gunn Devices with Second-Harmonic Power Extraction up to 290 GHz", *Electronics Letters*, **30**, 1994, pp. 1950-1951.

- [5] Carlstrom, J. E., Plambeck, R. L., Thornton, D. D.: "A Continuously Tunable 65-115-GHz Gunn Oscillator", *IEEE Transactions on Microwave Theory and Techniques*, **MTT-33**, 1985, pp. 610-619.
- [6] Rydberg, A.: "High Efficiency and Output Power from Second- and Third-Harmonic Millimeter-Wave InP-TED Oscillators at Frequencies above 170 GHz", *IEEE Electron Device Letters*, **EDL-11**, 1990, pp. 439-441.
- [7] Räisänen, A. V.: "Frequency Multipliers for Millimeter and Submillimeter Wavelengths", *Proceedings of the IEEE*, **80**, 1992, pp. 1842-1852.
- [8] Crowe, T. W., Grein, T. C., Zimmermann, R., Zimmermann, P.: "Progress Toward Solid-State Local Oscillators at 1 THz", *IEEE Microwave and Guided Wave Letters*, **MWGL-6**, 1996, pp. 207-208, **and**, Crowe, T. W., Grein, T. C., Zimmermann, R., Zimmermann, P.: Correction to "Progress Toward Solid-State Local Oscillators at 1 THz", *IEEE Microwave and Guided Wave Letters*, **MWGL-6**, 1996, pp. 383.
- [9] Eisele, H., Chen, C-C., Mains, R. K., Haddad, G. I.: "Performance of GaAs TUNNETT Diodes as Local Oscillator Sources", *Proceedings of the Fifth International Symposium on Space Terahertz Technology*, May 10 - May 13, 1994, Ann Arbor, Michigan, pp. 622-628.
- [10] Chen, C-C., Mains, R. K., Haddad, G. I., Eisele, H.: "Numerical Simulation of TUNNETT and MITATT Devices in the Millimeter and Submillimeter Range", *Proceedings of the Fourth International Symposium on Space Terahertz Technology*, March 30 - April 1, 1993, Los Angeles, California, pp. 362-376.

A NON-BOLOMETRIC MODEL FOR A TUNABLE ANTENNA-COUPLED INTERSUBBAND TERAHERTZ (TACIT) DETECTOR

C. L. Cates^{a,b,d}, G. Briceño^a, M. S. Sherwin^{a,b}, K. D. Maranowski^c, A. C. Gossard^c

^aCenter for Terahertz Science and Technology, UCSB, Santa Barbara, CA 93106

^bPhysics Department, UCSB, Santa Barbara, CA 93106

^cMaterials Department, UCSB, Santa Barbara, CA 93106

^disabel@physics.ucsb.edu

Abstract

A number of Terahertz applications require detectors with time constants around 1 ns or less and with a certain minimum sensitivity. Detectors are still being developed to fill this niche in the few Terahertz frequency range. We propose a tunable antenna-coupled intersubband Terahertz (TACIT) detector that is expected to be more sensitive than available fast detectors.

When Terahertz radiation is incident on the device, a planar metal antenna couples the oscillating electric field from free space to the quantum well heterostructure, with the field polarization perpendicular to the plane of the quantum wells. Electrons in the active region of the channel quantum wells absorb the far-infrared radiation, exciting them from the ground to the first excited subband. The subbands are engineered to have different electron mobilities. As absorption alters the proportion of the electrons that are in the excited subband, the effective mobility of the device changes. A current is applied to the active area of the channel quantum well through source and drain contacts, and the change in effective mobility is detected as a change of the in-plane resistance of the device.

The device is sensitive to a narrow band of frequencies centered on the intersubband transition frequency. This center absorption frequency can be tuned by applying a bias voltage between the front and back gate contacts of the device.

The intrinsic speed of the TACIT detector is limited only by the excited subband lifetime, or intersubband relaxation time, which has been measured to be about 1 ns at a temperature of 10 K for several heterostructures with unbiased intersubband transitions near 3 THz.

The detector sensitivity can be estimated by calculating the change in population of the excited subband under illumination. In such a model, it is expected that a TACIT detector could be made to have 300K background limited performance (BLIP) while operating at 10 K. Such a device could be made with feasible device parameters. The theoretical model for the TACIT detector is presented.

1 Introduction

Intersubband transitions in quantum wells have enabled the development of sensitive quantum well infrared photoconductors (QWIPs) at frequencies greater than 15 THz. The potential of quantum well-based detectors in the range of 1-5 THz has not been realized For these

frequencies. composite bolometers and Ga:Ge photoconductors are currently the most sensitive THz detectors for low-background astrophysical applications. The response times of these devices is $1 \mu\text{s}$ at best, typically much longer. Superconducting hot-electron bolometers are less sensitive but may have time constants of order 10 ps. For astrophysical applications, superconducting HEBs are used as mixers with noise temperatures an order of magnitude above the quantum limit for frequencies less than 2.5 THz. Both superconducting hot-electron bolometers and composite bolometers absorb radiation over a very broad band of frequencies.

We propose a tunable antenna-coupled intersubband Terahertz (TACIT) detector. Based on modeling presented in this paper and a previous paper[1], we expect it to be at least as sensitive as superconducting hot-electron bolometers and to have a response time variable from 1 ns to 10 ps by operating at different electron temperatures. The TACIT detector is narrowband, absorbing Terahertz radiation only in a small band of frequencies which can be tuned by applying small DC voltages

In the device section of the paper, an overview of the TACIT detector mechanism and structure will be presented. Intersubband absorption and two ideas for subband-dependent electron mobility will be discussed. In the following section, the calculation of the TACIT detector's expected performance will be outlined and the parameters in the model will be discussed. Calculations for predicted performance of a TACIT detector operating in a hot-electron bolometric mode are described elsewhere. [1] Work on making these devices has just recently begun, and will be discussed in a future paper.

2 Device

TACIT detectors can be patterned from a variety of quantum well heterostructures. Our samples are grown in the Molecular Beam Epitaxy (MBE) facilities at UCSB. The precise control of epitaxial layer growth possible through MBE allows clean interfaces between materials to be grown, and so gives the ability to truly tailor heterostructures. Quantum wells are used in the active region of TACIT detectors, such as the heterostructure shown in Fig. 1. Electrons in a quantum well are confined in the direction perpendicular to the plane of the well, and have quantized momenta in this direction. In the plane of the well, the electrons are free to move with any momentum. The combination of the discrete perpendicular-to-well confinement energy, and the in-plane kinetic energy gives rise to energy subbands within the quantum well. The TACIT detector heterostructure shown in Fig. 1 has a quantum well channel for the active region, and another quantum well for a back gate. The wells are filled by electrons from the silicon delta-doping layers. The doping levels and spacings are chosen such that the channel well only has electrons in the ground subband prior to illumination. The back gate quantum well is also designed such that electrons only occupy the ground subband.

When Terahertz radiation is coupled to the channel quantum well with the polarization of the electric field in the direction perpendicular to the plane of the well, electrons in the well can absorb the light, raising them from the ground subband to an excited subband. This intersubband absorption is a resonant process and can have a narrow linewidth, such as that shown in Fig. 2. In previous experiments, absorption peaks with a full-width-at-half-

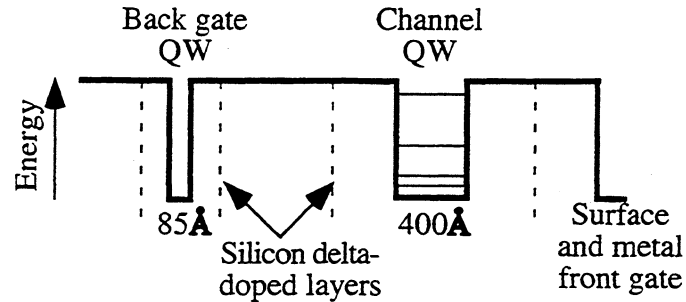


Figure 1: Schematic of one GaAs/Al_{0.3}Ga_{0.7}As heterostructure being used for a prototype TACIT detector.

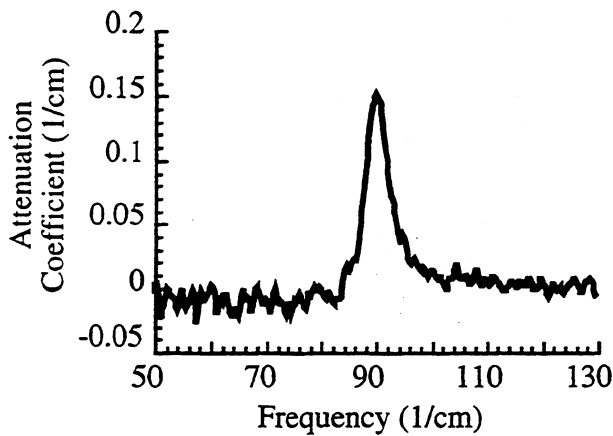


Figure 2: Attenuation measured as a function of frequency for the heterostructure shown in Fig. 1

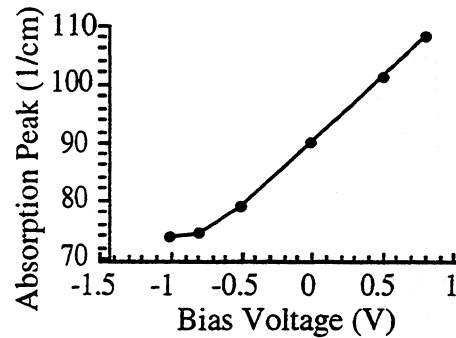


Figure 3: The frequency of peak absorption can be tuned by applying a bias voltage across the detector heterostructure.

maximum (FWHM) as small as $4 \text{ cm}^{-1} = 120 \text{ GHz}$ have been measured. There are many subbands in the channel quantum well, but only transitions between the ground subband and the first excited subband are considered here. The transitions to and among higher subbands are larger energy transitions, and so are not affected by light at the absorption frequency of the first two states.

A schematic of a TACIT detector is shown in Fig. 4. A planar metal broadband antenna couples the Terahertz radiation from free space to the active region of the detector, with the electric field polarized perpendicular to the plane of the quantum wells. Electrons in the channel quantum well absorb the radiation, which changes the percentage of electrons in each subband, which in turn changes the resistance of the active area. A current is sourced through metal ohmic source and drain contacts, and the change in resistance is measured as a change in voltage across the device. The two antenna leaves also serve as a front and a back gate, which are used to apply a DC voltage bias across the active region. The front antenna leaf makes a Schottky contact for the front gate, and the back antenna leaf is connected to the back gate quantum well through an ohmic contact.

A DC voltage bias is applied across the channel quantum well in order to change the

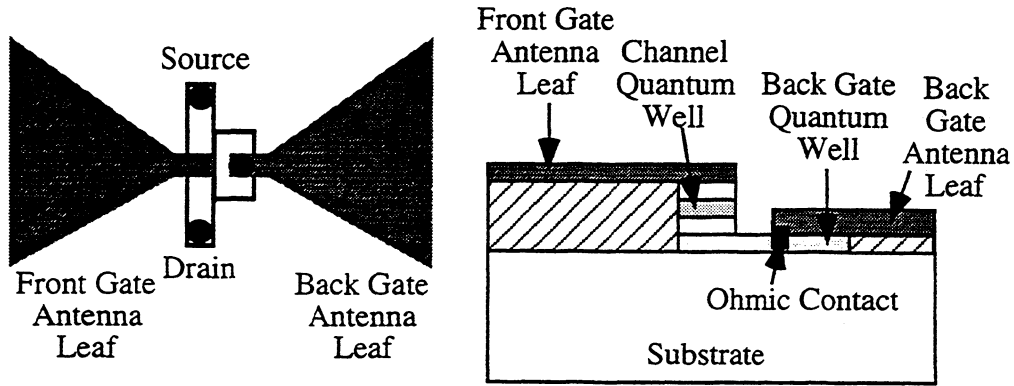


Figure 4: Top-down and cross-section views of a TACIT detector. Ohmic contacts electrically connect the back gate antenna leaf with the back gate quantum well, and the source and drain contacts to the channel quantum well. The active region of the device is defined by making the material outside, indicated by diagonal lines, electrically insulating.

subband energy spacing, and thereby tune the frequency of peak absorption. By applying moderate voltages, the resonant absorption frequency can be tuned over a range that is a significant portion of the original frequency, as shown in Fig. 3 for a typical TACIT heterostructure. Tuning the absorption frequency is simple and can be done while the detector is operating. TACIT detectors could then be used for a wide array of applications, including, in certain situations, to record spectra without the use of a bulky spectrometer. Additionally, the electron density in the channel quantum well can be tuned by applying a DC voltage to the source and drain contacts to the channel. This flexibility allows for fine-tuning the impedance of the device to match the antenna. Independent control of the front gate, back gate, and channel DC voltages allow simultaneous tuning of the intersubband absorption frequency and electron sheet density.

The channel quantum well subbands are engineered to have different electron mobilities, so as absorption alters the proportion of the electrons that are in the excited subband, the effective mobility of the device changes. Many different mechanisms could be used to give the two subbands different mobilities. Two that are currently being pursued are to use the electrons' wavefunctions in the quantum well to alter their scattering profiles, and to use a low enough electron sheet density such that the electrons in the ground subband are localized. In both cases, the current effort involves making the ground subband mobility, μ_0 less than the excited state mobility, μ_1 . In the absence of illumination, all the electrons are in the ground subband, and the device has a high resistance. If the subband mobility ratio, μ_1/μ_0 , is large, then when electrons are promoted to the excited subband, they can effectively short out transport in the lower subband. The device would thus have a sharply dropping resistance when just a small fraction of the channel electrons are raised to the excited subband. It is also possible to make the ground subband mobility higher than the excited subband mobility ($\mu_1/\mu_0 < 1$), but the resulting changes in resistance would be harder to measure.

The first mechanism for differentiating the subband mobilities takes advantage of the

different spatial probability amplitudes of the two subband wavefunctions. For the heterostructure shown in Fig. 1, a spike of electrically-compensated impurities is grown in the center of the channel quantum well. Ionized impurities are used to give a larger scattering cross section than neutral ions, and two types of dopants are used so that the resultant spike is electrically neutral, and should not change the quantum well potential. The ground subband is symmetric in the well, and has its maximum in the center of well, where the impurity spike is, so the electrons in the ground subband should scatter strongly from the impurities. The first excited subband wavefunction is antisymmetric in the well, and has a node in the center of the well. The electrons in the excited subband should spend most of their time away from the impurity spike, and so should scatter far less and have a much higher mobility than the electrons in the ground subband. This mechanism has been studied analytically by Hai and Studart.[2]

The second mechanism for differentiating the subband mobilities is a transition from localized electron states to non-localized states. The electron sheet density in the channel quantum well can be made low enough, a few times $1 \times 10^{10} \text{cm}^{-2}$, so that the ground subband is comprised of localized electron states, but the first excited subband has non-localized electron states. Conduction in the ground subband would be through hopping from one localized puddle to the next, and could be made very low by decreasing the electron density or lowering the temperature. When electrons absorb Terahertz light and are excited to the first excited subband, these electrons would be promoted to non-localized states, and could conduct without hopping. In this manner, the first excited subband would have a much larger mobility than the ground subband. The mobility of electrons undergoing a transition from an insulating state to a metallic state has been measured by Finkelstein et al[3] for quantum well structures similar to those being used for TACIT detectors.

In the calculations of the expected TACIT detector performance, both the impurity spike and localization mechanisms are considered together. The value used for the subband mobility ratio, μ_1/μ_0 , is taken from the data presented by Finkelstein et al.

3 Expected Figures of Merit

The relevant characteristics of an incoherent detector are the sensitivity, speed, and frequency response. These characteristics can be expressed in terms of the noise equivalent power (NEP), response time, and the corner frequency f_c respectively. We assume that the electrons in the ground subband can be described by a thermal distribution with an electron temperature, T_e . The detector will generally be operated at a low bias power so all the electrons are assumed to be in the ground state in the absence of illumination. The system is also assumed to have a single energy relaxation time, T_1 . We consider coupling the incident light to the antenna and coupling from the antenna to the device. We do not, however, include effects associated with coupling the detector to an outside sample mount or electronic circuit, such as heat diffusion or amplifier noise.

The noise equivalent power, NEP, is the root mean square amplitude of sinusoidally modulated radiation power incident on the detector required to produce a unity signal to noise ratio ($S/N = 1$) in a 1 Hz bandwidth. The NEP can be expressed as the ratio of the rms noise voltage, V_n (in V/Hz^{-1}), to the responsivity, \mathcal{R} (in V/W). The responsivity, \mathcal{R} , is

the change in output voltage per unit incident power. A constant current is sourced to the device, and the change in voltage comes from variations in the source-drain resistance, R_{SD} .

$$\mathcal{R} = \frac{dV}{dP_{inc}} = \eta_{FA}\eta_{AD}I_{SD} \frac{dR_{SD}}{dP_{abs}} \quad (1)$$

η_{FA} is the coupling efficiency from free space to the antenna, and η_{AD} is the coupling efficiency from the antenna to the active area of the device. I_{SD} and R_{SD} are the applied source-drain current and source-drain resistance respectively. P_{abs} is the signal power that is absorbed in the detector active region.

The device resistance changes as electrons absorb the Terahertz radiation, raising them from the ground subband to the excited subband. In the absence of inter-valley scattering, conduction in the two subbands can be considered to occur independently and in parallel. [4] The effective resistance of the active area is then the resistances of the two subbands added in parallel. Resistance is inversely proportional to mobility, so an effective mobility can be defined,

$$\mu_{eff} \equiv \frac{N_0}{N_{Total}}\mu_0 + \frac{N_1}{N_{Total}}\mu_1 \quad (2)$$

where N_0 and N_1 are the number of electrons in the ground and excited subbands, and $N_{Total} = N_0 + N_1$. The total number of electrons in the channel quantum well does not change in operation, but how many are in each subband does. The differentiation in the responsivity expression, Eq. 1 can be carried through to variations in the effective mobility with incident light.

$$\begin{aligned} \mathcal{R} &= \eta_{FA}\eta_{AD}I_{SD}\mathcal{G}_{SD} \frac{d\mu_{eff}}{dP_{abs}} \\ &= \eta_{FA}\eta_{AD}I_{SD}\mathcal{G}_{SD} \frac{1}{eN_{Total}} \frac{d(1/\mu_{eff})}{dP_{abs}} \\ &= \eta_{FA}\eta_{AD}I_{SD}R_{SD} \left(\frac{-1}{\mu_{eff}} \frac{d\mu_{eff}}{dP_{abs}} \right) \end{aligned} \quad (3)$$

with \mathcal{G}_{SD} being a geometric factor of the dimensions of the source-drain region.

A photon has a certain probability of being absorbed by an electron in the ground subband. With a sufficiently low incident power, the number of electrons will be much larger than the number of photons arriving in the intersubband relaxation time. Assuming all electrons are initially in the ground subband, the number of electrons in the excited state will then be simply the number of photons at the resonance frequency, f_0 , arriving in the detector within the intersubband relaxation time, T_1 .

$$N_1 = \frac{P_{abs}T_1}{hf_0}$$

An electron in the excited subband has several ways of relaxing back to the ground subband. The excited electron can spontaneously emit a photon, or it can undergo stimulated emission. We assume, however, the detector will be looking at weak signals, so the photon density will be small, and the rate of stimulated emission will be negligible compared to

other relaxation mechanisms. An excited electron can also release energy and momentum by emitting a phonon. If the electron has sufficient energy to emit a longitudinal-optical (LO) phonon, 36 meV in GaAs, it will rapidly do so, for LO phonons are strongly coupled to the electrons. A few picoseconds is a typical relaxation time constant for LO phonon emission in GaAs/AlGaAs quantum well heterostructures. If the excited electron does not have enough energy to emit a longitudinal-optical phonon, it can still emit an acoustical phonon. These acoustical phonons have no minimum energy, and are less strongly coupled to the electrons than LO phonons. For greatest sensitivity, the TACIT detector is operated such that the electrons excited to the upper subband cannot emit a LO phonon, and so have a longer lifetime in the excited state. The intersubband relaxation time constant has been measured for samples similar to the heterostructures being used for prototype TACIT detectors.[5] The time constant $T_1 = 1ns$ for an electron temperature $T_e = 10 K$, where the electrons effectively cannot emit LO phonons. For an electron temperature $T_e = 50 K$, $T_1 < 10 ps$. At $T_e = 50 K$, the electrons still have an average energy far below the LO phonon energy, but the tail of the electrons' Fermi energy distribution is large enough that a small fraction of the excited electrons can emit an LO phonon. Energy relaxation by emission of a LO phonon is significantly faster than by acoustic phonons, so that even with only a small fraction of electrons with sufficient energy, emission of LO phonons becomes the dominant energy relaxation mechanism. The intersubband relaxation time, T_1 , includes all these mechanisms.

As the total number of electrons in the channel quantum well is constant and $N_{Total} = N_0 + N_1$, the population change of the excited subband is simply negative that of the population change of the ground subband,

$$\begin{aligned}
\frac{d\mu_{eff}}{dP_{abs}} &= \frac{1}{N_{Total}} \left(\mu_0 \frac{dN_0}{dP_{abs}} + \mu_1 \frac{dN_1}{dP_{abs}} \right) \\
&= \frac{1}{N_s A_{SD}} \left(\mu_0 \frac{-T_1}{hf_0} + \mu_1 \frac{T_1}{hf_0} \right) \\
&= \frac{T_1(\mu_1 - \mu_0)}{hf_0 N_s A_{SD}}
\end{aligned} \tag{4}$$

The responsivity is proportional to the change in effective mobility with varying signal power, which is in turn proportional to the changes in the relative subband populations. Combining Eqs. 3 and 4, the responsivity for low signal powers can be expressed,

$$\mathcal{R} = -\eta_{FA}\eta_{AD}I_{SD}R_{SD} \frac{(\mu_1 - \mu_0)}{\mu_0} \frac{T_1}{hf_0 N_s A_{SD}} \tag{5}$$

The responsivity is proportional to the ratio of the difference between subband mobilities to the ground subband mobility. It is also inversely proportional to the active region area and resonance frequency.

This expression of the responsivity also includes the two antenna coupling factors, η_{FA} from free space to the antenna, and η_{AD} from the antenna to the active region of the device. Using a transmission line model, η_{AD} is the fraction of of the power delivered through the transmission line to the active region of the device. On resonance, with $f = f_o$, the detector active region can be modeled as a resistance in parallel with a parasitic capacitance. This

resistance is not the source-drain resistance of the device, but rather is the resistance sensed by the radiation-induced Terahertz voltages between the front and back antenna leaves.

$$R_{\perp} = \frac{d}{A_{SD}\sigma_{3-D}} = \frac{2\pi c m^* d^2 \text{FWHM}}{e^2 A_{SD} N_S f_{osc}}$$

where d is the distance between the gates and the channel quantum well and A_{SD} is the area of the active region. FWHM is the full width at half maximum of the intersubband absorption peak (in cm^{-1}), m^* is the conduction band effective mass of the electrons, N_S is the sheet density of electrons in the channel well, and f_{osc} the oscillator strength of the transition between the ground and first excited subbands. This expression is for a low signal power regime, where there are no saturation effects. When this resistance ‘perpendicular’ to the plane of the quantum wells is matched to the antenna impedance, $R_{ant} = 71\Omega$ for our log-periodic antenna, η_{AD} simplifies to,

$$\eta_{AD} = \frac{1}{1 + (f/f_c)^2}$$

with a corner frequency,

$$f_c = \frac{1}{\pi R_{\perp} C} = \frac{e^2}{2\pi^2 c m^* \epsilon} \frac{N_S f_{osc}}{d \text{FWHM}}$$

The corner frequency, along with the intersubband absorption lineshape and tunable resonance frequency, specify the spectral characteristics of a TACIT detector.

Having now an expression for the responsivity, the expected noise equivalent power for a TACIT detector can be computed. Considering Johnson noise, generation-recombination noise, and fluctuations in the thermal background, the detector’s NEP can be written,

$$\text{NEP}^2 = \frac{4K_B T_e R_{SD}}{\mathcal{R}^2} + \frac{4e I_{SD} R_{SD}^2}{1 + (2\pi f T_1) \mathcal{R}^2} + \left(\frac{h f c \text{FWHM}}{\exp\left[\frac{hf}{K_B T_{Bkgnd}}\right] - 1} \right)^2 \frac{1}{c \text{FWHM}} \quad (6)$$

To estimate the performance possible for a TACIT detector using the subband-dependent mobility mechanism, device parameters were taken from the heterostructure design, device processing considerations, and, where applicable, from related experiments. Several factors constrain the choice of parameters. The primary constraints are to match the impedance of the detector active region to that of the antenna, and to consider signal and bias Joule-heating powers to yield an electron temperature that is consistent with the desired subband relaxation time constant. The first constraint relates the active area A_{SD} , gate to channel distance d , and the sheet density of electrons in the channel quantum well N_S . The corner frequency also involves the separation d and electron sheet density, and this frequency should ideally be much larger than the operation frequencies of interest. The responsivity is inversely proportional to the device active area, A_{SD} , as shown in Eq. 5, so to get the highest sensitivity, minimizing the area must be balanced against the corner frequency and impedance-matching criteria. The second constraint limits the total power that can be considered for a given intersubband relaxation time constant, T_1 . The total power absorbed, both signal power and bias Joule heating power, $I_{SD}^2 R_{SD}$, absorbed within the relaxation time will heat the electrons above the semiconductor lattice temperature, T_L ,

$$(P_{Signal} + I_{SD}^2 R_{SD}) T_1 = C_v(T_e)(T_e - T_L)$$

Sourced current I_{SD}	0.1 μ A	Area A	2 μ m ²
Source-drain resistance R_{SD}	1 k Ω	Gate separation d	0.17 μ m
Resistive impedance R_{\perp}	70 Ω	Absorption FWHM	4 cm ⁻¹
Intersubband relaxation T_1	1 ns	Electron temp. T_e	12K
Electron sheet density	4 $\times 10^{10}$ cm ⁻²	Lattice temperature T_L	10K
Free space-antenna coupling η_{FA}	0.5	Oscillator strength f_{osc}	0.9
Subband mobility ratio μ_1/μ_0	300		

Table 1: Parameters used in calculating TACIT detector operating characteristics.

Parameter	f = 1.0 THz	f = 1.8 THz	f = 5.0 THz
Responsivity [V/W]	-2.6 $\times 10^7$	-1.2 $\times 10^7$	1.9 $\times 10^6$
NEP, 300 K bkgnd [$W/Hz^{1/2}$]	1.3 $\times 10^{-15}$	1.2 $\times 10^{-15}$	1.0 $\times 10^{-15}$
NEP, 77 K bkgnd [$W/Hz^{1/2}$]	2.7 $\times 10^{-16}$	2.1 $\times 10^{-16}$	4.4 $\times 10^{-16}$
NEP, 10 K bkgnd [$W/Hz^{1/2}$]	3.1 $\times 10^{-17}$	6.6 $\times 10^{-17}$	4.4 $\times 10^{-16}$

Table 2: Expected responsivities and noise equivalent powers for a TACIT detector operating at 1.0 THz, 1.8 THz, and 5.0 THz, with thermal background noise from a 300 K, 77 K, and 10 K blackbody source. Entries in bold type indicate background-limited sensitivity.

where $C_v(T_e)$ is the specific heat of the electrons. The resulting electron temperature must be consistent with the relaxation time used to calculate it.

The parameters used to estimate the performance of a TACIT detector are given in Table 1. The parameters are design characteristics, with the ratio of subband mobilities, μ_1/μ_0 , and the coupling constant η_{FA} taken from the literature.[3, 6]. These parameters are all feasible to achieve. The responsivities and noise equivalent powers for such a TACIT detector under various conditions is summarized in Table 2. With these experimentally-feasible parameters, a TACIT detector operating at its resonant absorption frequency of 1.8 THz is expected to have 77 K-background-limited sensitivity and 300 K-limited performance for frequencies to and beyond 5 THz with a intersubband relaxation time constant of 1 ns.

4 Summary

Intersubband transitions in quantum wells are a unique system for making detectors for the 1-5 THz frequency range. TACIT detectors are narrowband, with an absorption peak linewidth FWHM = 4cm⁻¹ = 120GHz measured for similar heterostructures, and are tunable by applying a moderate bias voltage. Using quantum well heterostructures designed to give a large subband mobility ratio, absorbing a low signal power is expected to dramatically change the effective mobility of the device active region. This change in mobility is measured as a change in source-drain resistance of the detector. A parallel-current-path model is used to calculate the expected performance of the TACIT detectors. With a set of experimentally-feasible device parameters, TACIT detectors are expected to have background-limited sensitivity for a 300 K background, and for some frequencies, even for a 77 K background. The

intrinsic speed of TACIT detectors is predicted to be limited only by the intersubband relaxation time, which is variable, and is in the range of 1 ns to less than 10 ps. This expected performance compares favorably to other detector technologies.

Acknowledgments

This work has been supported by the NSF Science and Technology Center for Quantized Electronic Structures (QUEST) DMR 91-20007, NSF DMR 9623874, AFOSR91-0214, NPSC (CC), and the Ford Foundation (GB).

References

- [1] C. Cates, G. Briceño, M. S. Sherwin, K. D. Maranowski, K. Campman, A. C. Gossard, to be published in *Physica E*.
- [2] G-Q. Hai, N. Studart. To be published.
- [3] G. Finkelstein, H. Strikman, I. Bar-Joseph, *Phys. Rev. Lett.* **74**, (6), 976-9 (1995).
- [4] T. Ando, A. B. Fowler, F. Stern, *Rev. Mod. Phys.* **54**, (2), 437-672 (1982).
- [5] J. N. Heyman, K. Unterrainer, K. Craig, B. Galdrikian, M. S. Sherwin, K. Campman, P. F. Hopkins, A. C. Gossard, *Phys. Rev. Lett.* **74**, (14), 2682-5 (1995).
- [6] M. Nahum, P. L. Richards, C. A. Mears, *IEEE Trans. on Appl. Supercond.* **3**, (1 pt.4) 2124-27 (1993).

SUPERCONDUCTING CORRELATORS FOR RADIO ASTRONOMY

Marc J. Feldman

Department of Electrical Engineering
University of Rochester
Rochester, New York 14627

The proceedings of this conference attest to the striking progress in front-end receiver technology during the last ten years. This puts great demands on back-end technology. Because of this, high-speed low-power superconducting correlator technology is an attractive alternative to the complex hybrid semiconductor correlators currently employed. It is described how superconducting autocorrelators can be used today and in the next few years. Large scale superconducting correlators have the potential to replace semiconductor correlators to the benefit of future millimeter array observatories.

I. INTRODUCTION

Autocorrelation spectroscopy is widely used in radio astronomy to take a time series of a very small signal buried in noise and produce a time-averaged frequency spectrum. Many single-dish observatories still use acousto-optical spectrometers or even filter banks as they provide high resolution and bandwidth at reasonable cost [1]. Today, digital autocorrelators are becoming more prevalent as their benefits outweigh their cost. The autocorrelator for a modern single-dish telescope such as the Green Bank Telescope (GBT) consists of very many equipment shelves filled with VLSI semiconductor correlator chips, connected by intricate cabling. This is the current state-of-the-art.

Nevertheless it is evident that much more correlation throughput could be profitably employed. A focal-plane array receiver with M independent pixels requires a multi-bank autocorrelator M times as large as the single-pixel receiver. Consider the millimeter array observatories (BIMA, IRAM, OVRO, NRO, SMA), which use digital correlators exclusively for spectral observations. To take full advantage of an N -dish array each baseline must be separately correlated, and so $N(N-1)/2$ times the correlator throughput is required compared to the single dish [2]. Therefore the correlators under design for future large arrays (MMA, LMSA) which will have 40, 50, or more dishes must push the current state-of-the-art, but must also make severe compromises.

The proceedings of this conference attest to the striking progress in front-end receiver technology for millimeter-wavelength astronomy during the last ten years; however the standard design of heterodyne receivers has changed little during this time. It consists of an externally pumped SIS (and lately, HEB) mixer operated at 4.2 K followed by a cooled semiconductor IF amplifier, room-temperature postamplifiers, an analog-to-digital converter (ADC), and some spectrometer. This scheme has been very successful, and such receivers are responsible for most of the recent striking achievements in this spectral range [1].

Nevertheless, this scheme has several limitations. First, SIS receivers are single-pixel devices, with few exceptions (such as [3]). Among other reasons for this [4] are that multichannel spectrometers are complex and expensive. Second, the instantaneous bandwidth of almost all SIS receivers has been limited to 1 GHz. This is not due to the SIS mixers themselves, which are capable of 20% to 30% fractional bandwidth [5]. One problem is that SIS mixers operate at 4.2 K while the HEMT IF amplifiers are usually mounted some distance away with an isolator in between. A great improvement on this, to 4 GHz bandwidth, was demonstrated when Padin et al. [6] positioned a HEMT much closer to the SIS junction. Padin's 1994 accomplishment has been widely cited in plans for future observatories, for example, the Millimeter Array specification calls for **8 GHz** bandwidth per sideband based on Padin's work [7]. This is a striking indication of the thirst for greater bandwidth.

Thus one might say that the correlator is the limiting instrumental subsystem for radio astronomy today. Here we consider using high-speed low-power superconducting technology to replace the complicated hybrid semiconductor correlators currently employed. Is this worth the effort? -- in principle, any size correlator can be built with today's semiconductor technology by further multiplexing. In practice however the limitations are reliability, power dissipation, cost, and complexity of interconnections. The largest correlators today fall comfortably within these constraints, but not by a large margin. Also, semiconductor VLSI appears to be approaching its maximum clock speed according to the authoritative semiconductor industry "Roadmap" [8].

After introducing superconducting correlators we will describe how these can be used today (Sec. IV, Large Focal Plane Arrays), in the near future (Sec. V, Protogalaxy Search Receiver), and if a state-of-the-art fabrication facility becomes available (Sec. VI, General Correlators for Radio Astronomy).

II. SUPERCONDUCTING DIGITAL ELECTRONICS

The potential virtues of superconducting digital electronics are impressive. The intrinsic switching time is very short, on the order of a picosecond. Perhaps even more important is the low power dissipation, on the order of a microwatt per gate, a thousand times less than CMOS circuits. There has been a long and significant research effort in this area, most notably the IBM supercomputer project ending in 1983 and the MITI project (Japan) in the 1980's. These projects and most others chose to emulate semiconductor technology in using a "voltage state" logic -- data is represented by steady voltage levels. This choice was unfortunate. Superconducting voltage state logic cannot operate faster than a few GHz (10 GHz with considerable error rate) for reasons that are intrinsic, in fact topological [9], and the maximum speed can be little increased by better technology.

Today there is a renewed research effort in superconducting digital electronics based on RSFQ (rapid single flux quantum) logic, first proposed in 1985 [10]. Among the accomplishments of this technology are a simple digital circuit operating up to 370 GHz [11], a 64-bit circular shift register with data clocked around at 18 GHz [12], and an oversampling ADC with 18-bit decimation filter composed of 2100 Josephson junctions operating above 10 GHz clock frequency [13]. Note that this combination of digital speed and complexity cannot be approached in any other technology.

It must be stated that no Josephson junction digital devices have yet left the laboratory. One limitation is the requirement to operate at 4 K, a severe disadvantage for many applications. Also, high-speed output from an SFQ circuit is difficult because of the small energy scale. The best result to date is output to room temperature of 8 GHz RSFQ data [14]. Likewise, chip-to-chip SFQ transmission has not yet been demonstrated; the emphasis has been to develop multi-chip modules [15], which is much harder. Perhaps the most severe problem has

been integration scale. A useful digital circuit should require many Josephson junctions with well-controlled properties and complex interconnections. To realize such a circuit puts great demands on fabrication tolerances.

III. SUPERCONDUCTING CORRELATORS

During the past few years there have been a number of designs advanced for superconducting digital correlators, but no concerted development effort. An early 256-lag 1-bit correlator used 4350 Josephson junctions and operated at a clock frequency of 10 GHz [16]. There was no prescaler, however, and the output from the correlator was analog. A fully digital RSFQ correlator was proposed in [17], and different modifications of this [18-20] have converged to a common design. In one of these projects [19] a 16-lag RSFQ autocorrelator complete with on-chip ADC, high-speed clock, and counters (1650 Josephson junctions total) was successfully demonstrated at a clock frequency of 11 GHz [21]. It resolved a sinusoid buried in -40 dB signal/noise.

These are 1-bit autocorrelators with double-Nyquist sampling. The basic architecture is well-known, identical to [22], for instance. 1-bit correlator schemes were a standard tool in early days of radio astronomy [23] and are appropriate for an immature technology where device-count is a greater limitation than switching speed.

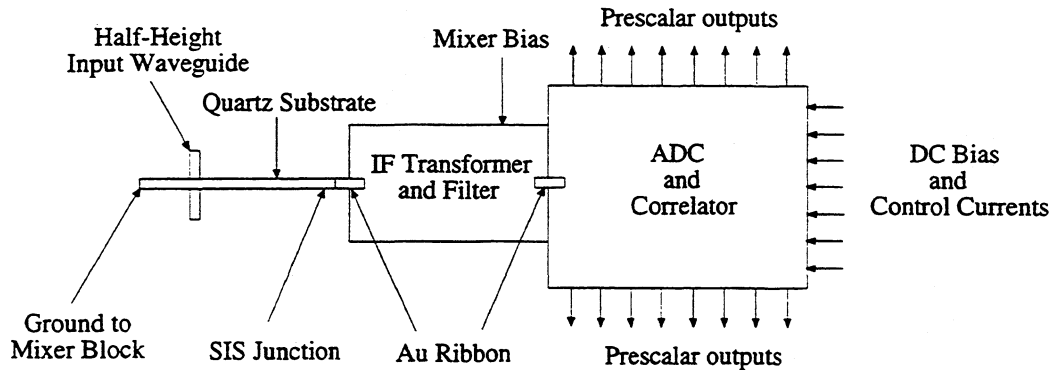


Fig. 1. Possible scheme for an integrated superconductor mixer / back end.

Figure 1 is a sketch of a possible heterodyne receiver. A 1-bit ADC measures the sign of the (almost) random signal $X(t)$ coming from the SIS mixer at intervals $\tau = 1/f_c$, where f_c is the clock frequency; it gives the data stream $\text{sign}(X(t_i))$, where i is the sample number. In double-Nyquist sampling the nominal bandwidth is $f_c/4$. The autocorrelator lag number k must compute the product of $\text{sign}(X(t_i))$ and $\text{sign}(X(t_i+2k\tau))$, which is the sample taken $2k$ clock periods later, and accumulate the result over many samples $i = 1$ to N . Since the SFQ ADC codes $\text{sign}+$ as "1" and $\text{sign}-$ as "0", this product is simply the XNOR function of a given sample and another sample delayed by $2k\tau$. In practice, the XOR function provides the same information.

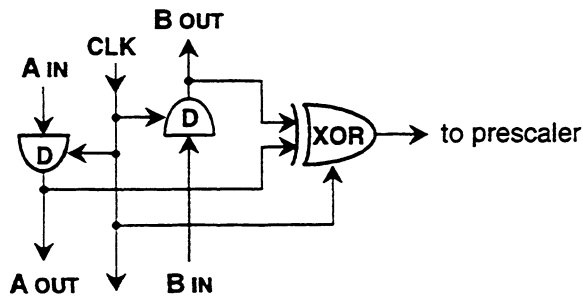


Fig. 2. A single correlator lag.

A single lag stage of this autocorrelator is shown in Fig. 2. The clocked delay line consists of RSFQ destructive read-out (DRO) cells ("D"), which are the simplest RSFQ gates. After the $k=1$ stage the A_{out} is connected back to the B_{in} (with a single delay). The XOR is a standard, and the prescaler is an SFQ T-flip-flop binary counter whose length (8-13 stages) depends on the clock rate, integration time, and desired output rate. This is an extremely simple RSFQ circuit.

The only "interesting" challenge in this circuit is the timing requirements. The A arm uses concurrent clocking (clock flows with data) while the B arm uses counterflow clocking (clock flows opposite data), and as drawn the circuit suffers from the worst aspects of both: susceptibility to race faults in the A arm and low speed because of the B arm [24]. It is likely that this circuit can be made considerably more robust and also faster by an optimization of the timing interconnections [25]. This basic design however is an excellent trade-off between speed and circuit area. It can be made with very few Josephson junctions, and the accuracy lost by the one-bit digitization is partially compensated by the oversampling [26].

III.1 Circuit area and power dissipation

The major design constraint for superconducting correlators today is the necessity to use only a single chip. The correlator design described above will require roughly 100 Josephson junctions per lag. A literature survey shows that current RSFQ design practices use about 2000 μm^2 area per junction. This implies that a 256-lag autocorrelator will fit on a standard 1 cm^2 chip. The area requirements of RSFQ circuits have never been pushed and could be reduced by perhaps 4x today with an aggressive design. They certainly will be reduced with future fabrication improvements. Note that a future specification (Sec. VI) is 100 μm^2 per junction.

A literature survey shows that current RSFQ circuits dissipate on the order of 0.2 μW per junction. Therefore a 256 lag correlator will dissipate about 5 mW at 4.2 K, and so one hundred such chips would require only a standard 1 W cryocooler. This power dissipation is entirely due to static loss in the dc bias resistors and can certainly be reduced. A preliminary estimate is that 0.03 μW per junction is possible with little decrease in reliability [19]. (Note that a future specification from Sec. III.4 is 7.5 nW per junction.) Thus the cryogenics capacity should not limit the ambitions of future superconducting correlators.

IV. LARGE FOCAL PLANE ARRAYS

Recent technological advances have put the construction of a large focal plane array of submillimeter-wave mixers within technical and financial feasibility. It is now standard to incorporate tuning structures directly on the same substrate as the SIS junction, alleviating the need for cumbersome adjustable tuners. Micromachining technology offers the possibility of fabricating large numbers of waveguide / mixer blocks in a single unit [27, 28, 29]. A new laser milling technique has been developed to fabricate high quality submillimeter waveguide components and feedhorns with almost any cross section [30]. Under computer control, the construction of high performance large-format ($\sim 10 \times 10$) waveguide array receiver front ends becomes tractable.

Unfortunately, there is no backend technology to efficiently process the vast quantity of a data that would be gathered by such an array. Using current correlator or acousto-optical components, an entire room of equipment would be required. Superconducting correlators are ideal for this application. A 256-lag single-chip version of the autocorrelator described above, clocked at 1 to 10 GHz, gives a frequency resolution of 1 to 10 MHz. The size of the array would be limited by the requirements for the multiple low-noise HEMT amplifiers. It may however be possible to use superconducting ADC's to digitize the SIS mixer output without intervening amplification, as sketched in Fig. 1. Superconducting ADC's have been the focus of much research for many years, as reviewed in [31, 32]. For instance, a fully SFQ "quasi-one-junction SQUID" ADC [33] consists of only several Josephson junctions. The superconducting mixer / ADC / autocorrelator combination would enable an entire 10 x 10 array receiver (frontend + correlators) to be housed in a standard 1 W cryostat.

V. PROTOGALAXY SEARCH RECEIVER

Last year at this conference it was suggested that observations of protogalaxies are "THE future of millimeter-wavelength astronomy" [34]. It is likely that there is a large class of early objects which are heavily obscured by dust [35],[36]. For instance, Charlot and Fall maintain that there is only a brief period at the beginning of star formation between the generation of Ly α emission and complete attenuation by dust [37]. Protogalaxy model light curves fall within the sensitivity limit of the Hubble Space Telescope (HST) only because of the extended ultraviolet brightness of the irregular galaxy spectrum; for high- z objects the HST sees the flux of a few naked O stars which do not represent the stellar population as a whole -- most of the luminosity appears in the submillimeter [35]. To resolve these issues, some sort of submillimeter-wave search is needed.

The $^2P_{3/2} \rightarrow ^2P_{1/2}$ line of C $^+$ at $\lambda = 158 \mu\text{m}$ is long recognized as a sensitive probe of protogalaxies [38, 39]. This CII line will be most prominent in protogalaxies undergoing a burst of star formation. Cold-dark-matter galaxy formation models (i.e. [40]) predict such bursts occur at $z \sim 2.2$ and decay afterward at a roughly exponential rate. Adopting this redshift, one finds the most promising frequency range to detect protogalaxies in the CII line is between ~ 500 and 700 GHz. Atmospheric absorption narrows this window to 620 - 710 GHz.

To locate such protogalaxies, a sensitive sub-millimeter SIS receiver is desirable. The instantaneous bandwidth of the receiver should be as large as possible, but high resolution is *not* required. The integrated superconducting receiver described above and sketched in Fig. 1 is just such a receiver, if the back-end is operated at a high clock rate. In fact, the bandwidth is limited by the maximum clock rate of the autocorrelator.

All RSFQ circuits use the same material system as SIS mixers -- Nb/Al $_2$ O $_3$ /Nb Josephson junctions. Although more than 10 laboratories in the world fabricate superconducting digital circuits (as reviewed in [41]), few make both competitive SIS mixer junctions and also digital circuits. SIS mixers commonly use junctions with $1 \mu\text{m}^2$ area and critical current density (j_c) 10 kA/cm^2 . Digital circuits however are generally made with $3.5 \mu\text{m}$ linewidth, minimum junction area $10 \mu\text{m}^2$, and $j_c = 1 \text{ kA/cm}^2$. These parameters are more conservative for good reason; it is because the fabrication-induced parameter variations, the differences between design and chip, are by far the limiting factor which determines the maximum clock rate of complex RSFQ circuits. Were it not for this, one could design complex RSFQ circuits which run at almost 100 GHz, today [42].

The correlator is a very simple RSFQ circuit and so a clock rate of 20 GHz is probably possible today using the $j_c = 1 \text{ kA/cm}^2$ specification. Almost all of the most successful complex RSFQ circuits to date have been fabricated at the Hypres, Inc., foundry [43]. Hypres is now in the process of upgrading their fabrication facility and anticipate a $1.0 \mu\text{m}$ linewidth with $j_c = 10 \text{ kA/cm}^2$ by Summer 1999 [44]. This should allow the construction of an autocorrelator clocked at 64 GHz, giving an IF bandwidth of 16 GHz. 256 lags implies a spectral resolution of 62.5 MHz, and the broad ~ 600 MHz emission lines expected from protogalaxies at 680 GHz will be easily resolved. It is seen that superconducting correlator technology is an ideal match to the spectrometer requirements of a protogalaxy search.

VI. GENERAL CORRELATORS FOR RADIO ASTRONOMY

In light of the strong need for greater correlation throughput presented in the Introduction, one asks whether high-speed low-power superconducting correlators can ever compete with the massive semiconductor correlators used at radio astronomy observatories. In fact, future plans for RSFQ logic are far beyond the needs of radio astronomy!

For instance, a large DARPA-sponsored trial project has recently begun development of a petaflops computer (10^{15} floating point operations per second) based on RSFQ logic, under the title "Hybrid Technology Multithreaded (HTMT) Architecture." Many believe that this can not be accomplished with future CMOS technology. One HTMT specification projected 10,000 RSFQ processors, each providing 100 gigaflops. Each processor will consist of about 30 chips in a multi-chip module. Each 2 cm x 2 cm chip will have 4,000,000 Josephson junctions ($0.8 \mu\text{m}$ linewidth with $j_c = 20 \text{ kA/cm}^2$), run at a clock speed of 100 GHz, and dissipate 30 mW at 4 K. The plan is to complete this in ten years. Most recent results and specifications are given in [45].

This is a breathtakingly ambitious project. For comparison, one design for the Millimeter Array correlator requires 204,800 256-lag sub-correlators with a clock rate of 125 MHz [46]. To realize this in RSFQ with 100 Josephson junctions per lag at 125 MHz would require 5 Billion junctions, more than two orders of magnitude less than the HTMT specification. And of course a 1000 x increase in clock rate would simplify the MMA correlator enormously.

One can be certain that superconducting correlators will be widely used in radio astronomy long before other large-scale superconducting digital electronics applications receiving intense interest, such as the HTMT project; for three reasons. First, there is less competition. A large hybrid autocorrelator can provide a correlation bandwidth of perhaps 16 GHz using semiconductor chips with clock rate of only several hundred MHz. It does this by subdividing the input and taking the cross-correlation functions of all the subdivisions. This means that the complexity of a hybrid correlator decreases as the *square* of the clock speed, and so superconducting correlators compete with much more complex semiconductor correlators. Second, the correlator functions without frequent communication to the (room temperature) external world, unlike the other large projects. Third, superconducting correlators have the advantage of a much simpler architecture than other large superconducting circuits, without need of contingent high-speed decisions. Computer circuits are much more difficult to design and to realize.

Many technical advances will be required before this can occur, in particular a large improvement in superconductor circuit fabrication. However, any progress towards the HTMT or other ambitious project goals will require a large investment in Josephson junction fabrication technology, to the benefit of future superconducting correlators for radio astronomy.

VII. CONCLUSION

Single-chip superconducting autocorrelators can enable large focal plane array and/or very wide bandwidth submillimeter wavelength receivers for radio astronomy. This is an extremely simple superconducting digital circuit, the 4 K operating temperature requirement is an advantage rather than a liability, and high-speed output is not required. In the future, large superconducting correlators may allow the information throughput of millimeter array observatories to be fully utilized.

Let us define a figure of merit for a correlator chip $F = (\text{number of lags}) \cdot (\text{clock rate})$. Then the GBT chips have $F = 128 \text{ lag-GHz}$ [46]. Superconducting correlator chips of this performance have already been demonstrated [21]. In several years it should be possible to realize superconducting correlator chips suitable for a protogalaxy search receiver (Sec. V), for which F will be 128 times higher than this. The HTMT specifications (Sec. VI) imply F can be 30,000 times higher than the GBT chips.

The author gratefully acknowledges the substantial contributions of Chris Walker and Tony Kerr to this paper.

- [1] J.E. Carlstrom and J. Zmuidzinas, "Millimeter and Submillimeter Techniques," in *Reviews of Radio Science 1993 - 1995*, ed. W.R. Stone (Oxford University Press, Oxford, 1996).
- [2] R. Hayward, "A Survey of Digital Correlation Spectrometers," in Proc. New Generation Digital Correlators Workshop (NRAO, Tucson, 1993) pp. 203-227.
- [3] M.A. Scherschel et al., "A 16-Element SIS-Receiver for 455-495 GHz for the Heinrich Hertz Telescope," in Proc. Sixth International Symp. Space THz Tech., Pasadena CA, March 1995, pp. 338-343.
- [4] R. Hills, "Cost-Effectiveness of Array Detectors," in Proc. NRAO Workshop on Imaging Arrays, Tucson, Arizona, May 1994.
- [5] S.-K. Pan and A.R. Kerr, "SIS Mixer Analysis with Non-Zero Intermediate Frequencies," in Proc. Seventh International Symp. Space THz Tech., Charlottesville, Virginia, March 1996, pp. 195-219.
- [6] S. Padin, D.P. Woody, J.A. Stern, H.G. LeDuc, R. Blundell, C.-Y.E. Tong, and M.W. Pospieszalski, "An Integrated SIS Mixer and HEMT IF Amplifier," *IEEE Trans. Microwave Theory Tech.* **44**, 987 (1996); and similarly in Proc. Sixth International Symp. Space THz Tech., Pasadena CA, March 1995, pp. 134-139.
- [7] J.E. Carlstrom, "The Millimeter Array," in Proc. Seventh International Symp. Space THz Tech., Charlottesville, Virginia, March 1996, pp. 17-28.
- [8] *The National Technology Roadmap for Semiconductors*, 1994 revision, Semiconductor Industry Association (SEMATECH, Austin, 1995). Also at <http://www.sematech.org/public/roadmap/doc>.
- [9] M.J. Feldman, "Digital Applications of Josephson Junctions," to be published in *Progress of Theoretical Physics, Supplement (Japan), "Physics and Applications of Mesoscopic Josephson Junctions"* 1998.
- [10] K.K. Likharev and V.K. Semenov, "RSFQ Logic/Memory Family: a New Josephson-Junction Technology for Sub-Terahertz-Clock-Frequency Digital Systems," *IEEE Trans. Appl. Supercond.* **1**, 3 (1991).
- [11] P.I. Bunyk, A. Oliva, V.K. Semenov, M. Bhushan, K.K. Likharev, J.E. Lukens, M.B. Ketchen, and W.H. Mallison, "High-Speed Single-Flux-Quantum Circuit using Planarized Niobium-Trilayer Josephson Junction Technology," *Appl. Phys. Lett.* **66**, 646 (1995).
- [12] A.M. Herr, C.A. Mancini, N. Vukovic, M.F. Bocko, and M.J. Feldman, "High Speed Operation of a 64-Bit Circular Shift Register," accepted for publication in *IEEE Trans. Applied Superconductivity*.
- [13] V.K. Semenov, Yu. Polyakov, and D. Schneider, "Implementation of Oversampling Analog-to-Digital Converter Based on RSFQ logic," *Extended Abstracts 6th International Superconductive Electronics Conference (PTB, Braunschweig)*, Vol. 1, pp. 41-43, June 1997.
- [14] O.A. Mukhanov, S.V. Rylov, and D.V. Gaidarenko, "Josephson Output Interfaces for RSFQ Circuits," *IEEE Trans. Appl. Supercond.* **7**, 2826 (1997).
- [15] L.A. Abelson, R.N. Elmadjian, G.L. Kerber, and A.D. Smith, "Superconductive Multi-chip Module Process for High Speed Digital Applications," *IEEE Trans. Appl. Supercond.* **7**, 2627 (1997).
- [16] P.F. Yuh and E. Stebbins, "256-Stage Superconducting Digital Correlator with Analog Output," *IEEE Trans. Appl. Supercond.* **5**, 14 (1995).
- [17] E.B. Goldobin, P.G. Litskevitch, and V.P. Koshelets, "Superconducting Digital Correlator for Integrated Sub-mm Receiver for Space Applications," *Applied Superconductivity 1995*, ed. D. Dew-Hughes (Institute of Physics, Bristol UK, 1995) pp. 1697-1700.
- [18] A. Kidiyarova-Shevchenko and P. Litskevitch, "Design of RSFQ Correlator," Preprint 96-21/428, Nuclear Physics Institute, Moscow State University, July 1996.
- [19] A.V. Rylyakov, "New Design of Single-Bit All-Digital RSFQ Autocorrelator," *IEEE Trans. Appl. Supercond.* **7**, 2709 (1997).
- [20] P.G. Litskevitch and A.Yu. Kidiyarova-Shevchenko, "Design of an RSFQ Correlator," *Extended Abstracts 6th Int'l. Superconductive Electronics Conf. (PTB, Braunschweig)*, Vol. 2, pp. 356-358, June 1997.
- [21] Alexander Rylyakov, SUNY Stony Brook, private communication.
- [22] C. Timoc, "Development of a 1 GHz, 256-Channel, CMOS, Digital Correlator Chip," in Proc. New Generation Digital Correlators Workshop (NRAO, Tucson, 1993) pp. 93-99.

- [23] J.B. Hagen and D.T. Farley, "Digital-Correlation Techniques in Radio Science," *Radio Science* **8**, 775 (1973).
- [24] K. Gaj, E.G. Friedman, and M.J. Feldman, "Timing of Multi-Gigahertz Rapid Single Flux Quantum Digital Circuits," *Journal of VLSI Signal Processing* **16**, 247-276 (1997).
- [25] K. Gaj, Q.P. Herr, and M.J. Feldman, "Parameter Variations and Synchronization of RSFQ Circuits," *Applied Superconductivity 1995*, ed. D. Dew-Hughes (Institute of Physics, Bristol UK, 1995) pp. 1733-6.
- [26] A.R. Thompson, J.M. Moran, and G.W. Swenson, Jr., *Interferometry and Synthesis in Radio Astronomy* (Krieger, Malabar Florida, 1994) p. 220.
- [27] G.M. Rebeiz, D.P. Kasilingam, Y. Guo, P.A. Stimpson, and D.B. Rutledge, "Monolithic Millimeter-Wave Two-Dimensional Horn Imaging Arrays," *IEEE Trans. Antennas and Propagation* **38**, 1473 (1990).
- [28] W.R. McGrath, C.K. Walker, M. Yap, and Y.C. Tai, "Silicon Micromachined Waveguides for Millimeter-Wave and Submillimeter-Wave Frequencies," *IEEE Microwave and Guided Wave Lett.* **3**, 61 (1993).
- [29] G. de Lange, B.R. Jacobson, A. Rahman, E. Duerr, and Q. Hu, "Low-Noise Micromachined SIS Mixers for Millimeter-Wave Imaging Arrays," in *Proc. Seventh International Symp. Space THz Tech.*, Charlottesville, Virginia, March 1996, pp. 29-36.
- [30] C.K. Walker, G. Narayanan, H. Knoepfle, J. Capara, J. Glenn, A. Hungerford, T.M. Bloomstein, S.T. Palmacci, M.B. Stern, and J.E. Curtin, "Laser Micromachining of Silicon: A New Technique for Fabricating High Quality Terahertz Waveguide Components," in *Proc. Eighth International Symp. Space THz Tech.*, Cambridge, Massachusetts, March 1997, pp. 358-376.
- [31] G.S. Lee and D.A. Petersen, "Superconducting A/D Converters," *Proc. IEEE* **77**, 1264 (1989).
- [32] J.X. Przybysz, "Josephson Analog-to-Digital Converters," in *The New Superconducting Electronics*, ed. H. Weinstock and R.W. Ralston (Kluwer, Dordrecht, 1993), chapter 11.
- [33] D.K. Brock, S.S. Martinet, M.F. Bocko, and J.X. Przybysz, "Design and Testing of QOS Comparators for an RSFQ Based Analog to Digital Converter," *IEEE Trans. Appl. Supercond.* **5**, 2244 (1995).
- [34] K. Menten, "Submillimeter Astronomy - The Next Steps," opening address at the Eighth International Symp. Space THz Tech., Cambridge, Massachusetts, March 25, 1997.
- [35] A.A. Stark, "Potential Measurement of the Luminosity Function of 158 Micron [C II] at High Redshifts: A Test of Galaxy Formation Models," *Astrophys. J.* **481**, 587 (1997).
- [36] S.D.M. White, "The Nature and Observability of Protogalaxies," in *Proc. ESO Workshop on Large Millimeter Arrays*, ed. P. Shaver (1996).
- [37] S. Charlot and S.M. Fall, "Lyman-Alpha Emission from Galaxies," *Astrophys. J.* **415**, 580 (1993).
- [38] V. Petrosian, J.N. Bahcall, and E.E. Salpeter, "Fine-Structure Transitions and the Background Microwave Radiation," *Astrophys. J. Lett.* **155**, L57 (1969).
- [39] A. Loeb, "Finding Protoquasars at High Redshifts," *Astrophys. J. Lett.* **404**, L37 (1993).
- [40] N. Katz, "Dissipational Galaxy Formation. II. Effects of Star Formation," *Astrophys. J.* **391**, 502 (1992).
- [41] Lynn A. Abelson, "Superconductive Electronics Process Technologies," *Extended Abstracts 6th International Superconductive Electronics Conference (PTB, Braunschweig)*, Vol. 1, pp. 1-4, June 1997.
- [42] K. Gaj, E.G. Friedman, M.J. Feldman, and A. Krasniewski, "A Clock Distribution Scheme for Large RSFQ Circuits," *IEEE Trans. Appl. Supercond.* **5**, 3320 (1995).
- [43] "HYPRES Niobium Process Flow and Design Rules," available from Hypres, Inc., 175 Clearbrook Road, Elmsford, NY 10523.
- [44] Masoud Radparvar, Hypres, Inc., private communication.
- [45] P. Bunyk, M. Dorojevets, K. Likharev, and D. Zinoviev, "RSFQ Subsystem for HTMT PetaFLOPS Computing," *Stony Brook HTMT Technical Report 03*, found at <http://gamayun.physics.sunysb.edu/RSFQ/Projects/PetaFLOPS>.
- [46] R. Escoffier, "A Possible MMA Correlator Design," *NRAO Memorandum*, August 16, 1995.

WASP: A WIDEBAND ANALOG AUTOCORRELATION SPECTROMETER

K.G.Isaak ^{1,2,4}, A.I. Harris ^{1,2} and J. Zmuidzinas ³

¹Astronomy Department, University of Maryland, College Park, MD 20742

²Formerly with FCRAO, University of Massachusetts, Amherst, MA 01003

³Caltech, Downes Laboratory 320-47, Pasadena, CA 91125

⁴ isaak@astro.umd.edu

Abstract

We describe the design and realization of a new type of wideband, moderate resolution backend spectrometer for heterodyne spectroscopy. WASP, a Wideband (analog) Autocorrelation SPectrometer, combines direct analog multiplication with transmission line delays to achieve a bandwidth of 3250 MHz at a resolution of 33 MHz. This combination of bandwidth and resolution is well matched to the requirements of submillimeter-wave studies of interacting galaxies, active galactic nuclei and high redshift objects. The spectrometer is compact, low-power (75 W) and integrates stably for many hours.

1 Introduction

Improvements in the sensitivity of millimeter and submillimeter-wave heterodyne SIS receivers permit observations of spectral line emission from increasingly distant objects (Brown & Vanden Bout 1991, Ohta et al. 1996, Omont et al. 1996, Guilloteau et al. 1997). As one moves to near-submillimeter-wavelengths it is, however, the bandwidth rather than the sensitivity of the receiver that becomes the limiting factor in observations of several classes of object (eg. Harris et al. 1991). Spectral line widths are set by physical conditions of the emitting gas within an astronomical object. Current receivers and backend spectrometers have analysis bandwidths of 1 GHz. At 1 THz this corresponds to a velocity bandwidth of only 300 km/s, sufficient for studies of many galactic objects but inadequate for observations of astronomically interesting objects such as interacting galaxies, ultraluminous galaxies and active galactic nuclei, and more locally planetary atmospheres. Large bandwidths are also important in searches for molecular and atomic line emission from objects at very high redshifts (quasars and their host galaxies), where uncertainties in the optically determined redshifts as well as systemic redshift offsets can be more than a few hundred km/s. A new generation of wideband receivers and spectrometers is thus required.

We have designed and built a prototype wideband analog autocorrelation spectrometer at the Universities of Massachusetts and Maryland. Known as WASP (the Wideband Analog Autocorrelation SPectrometer), the spectrometer has a contiguous bandwidth of 3250 MHz, with a modest resolution of 33 MHz. WASP has been designed to match the bandwidth and resolution requirements of submillimeter-wave and far-infrared line observations of molecular and atomic gas in local and distant galaxies. WASP will be used in conjunction with the new generation of wideband receivers to make high-frequency observations of a range of extra-galactic objects. The contiguous bandwidth is essential for line searches in the most distant objects, where baseline structure introduced by stitching together narrower band spectrometers can mimic the weak and wide spectral line emission features that are being sought. Wideband correlators can also be used

effectively in studies of the terrestrial atmosphere and in interferometer phase correction spectrometers (eg. Ruf & Swift 1992, Staguhn et al. 1998), and as cross-correlation spectrometers for aperture synthesis arrays.

2 Backend Spectrometers

Observations of line emission and absorption at millimeter- and submillimeter-wave lengths are in general made using heterodyne detection techniques. The down-converted signal may be analyzed in one of two domains: the frequency domain, where the signal power spectrum $S(f)$ is subdivided into narrow frequency bins prior to analysis, and the time (lag) domain, where the autocorrelation function of the signal, $R(\tau)$, is determined by multiplying the signal with time-delayed versions of itself, $V(t).V(t + \tau)$. The signal power spectrum and the autocorrelation function are related by the Fourier transform relationship known as the Wiener Khinchin Theorem:

$$S(f) = \int_{-\infty}^{\infty} R(\tau) \cos(2\pi f\tau) d\tau \quad (1)$$

The instrument used to analyse the signal is colloquially referred to as the backend, of which there are several different types in common use.

Filter banks and acousto-optical spectrometers (AOS) operate in the frequency domain. Filter banks are made up of many contiguous filters, and can have large bandwidths with high spectral resolution. They are, however, often massive, and can be difficult to stabilize over long integrations. An AOS is compact, however the bandwidth for a single spectrometer is limited to approximately 1 GHz. Hybrid spectrometers made up of multiple 1 GHz subbands are under development at the University of Köln (see poster contribution by Horn et al. in this volume).

Digital autocorrelation spectrometers (DAS) are the most common form of backend in use at millimeter and submillimeter telescopes today. The signal delay and cross-multiplication is performed in digital circuitry, with the maximum operation bandwidth of a single DAS determined by the clock rate used. Bandwidths as large as 200 MHz have been achieved (communication, Lavera), again with larger bandwidths realized by stitching together multiple subbands. Digital correlators are typically used where high to medium spectral resolution is required.

The recent introduction of wideband microwave monolithic integrated circuit (MMIC) multipliers has meant that wideband analog autocorrelation spectrometers can now be built. WASP combines the wideband MMIC multipliers with analog delays introduced by sections of microstrip transmission line. The maximum achievable contiguous bandwidth is set by the shortest length of delay between two channels, and the maximum response frequency of the MMIC multiplier.

3 WASP: A Wideband Analog Autocorrelation Spectrometer

3.1 The Signal Path Through WASP

A schematic of the signal path through WASP is shown in Figure 1. The input signal is split into two. The two counter-propagating signals pass through anti-aliasing filters and power amplifiers before being correlated in one of 8 multiplier modules. Each module contains 16 multipliers and signal delays. The modules are connected in parallel using cable delays, spaced to realize a near-equally spaced chain of 128 lags. The signal is phase-switched by 180 deg at 770 Hz - synchronous

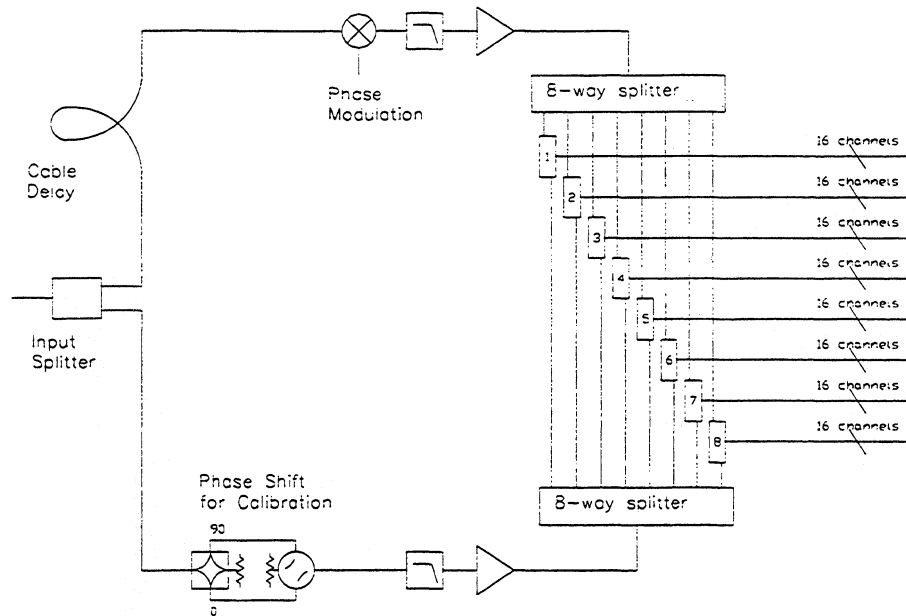


Figure 1: A schematic of the signal path through WASP.

detection is used in the low-frequency signal-processing electronics to recover the multiplier signal, reducing the effects of drift in the DC electronics. The electrical length of a microwave connector is longer than the spacing between adjacent multipliers, and so at least two strings of multipliers are required to achieve equal lag spacing. Each half of the initial signal is in fact further split into eight to minimize the difference in power at the ends of the modules, the splitters in addition providing isolation between modules. Given that the autocorrelation function of a real signal is symmetric in time, it is necessary to measure only either positive or negative lags. An additional signal delay is therefore inserted in one arm of the spectrometer, placing the zero path difference lag at one end of the lag chain. A transfer switch and 90 deg hybrid combination is used to change the phase in one arm, enabling the signal delay at and amplitude response of each multiplier to be measured.

3.2 The Multiplier Modules

Each module houses 16 MMIC multipliers, spaced uniformly along microstrip transmission lines (Figure 2). The multipliers are MMIC active mixers (Hewlett Packard IAM-81008), based on a classical Gilbert multiplier core (Gilbert, 1968). The mixers are consequently good analog multipliers when LO-starved. Measurements suggest that the multipliers are very linear below an input power level of -15 dBm, over a power range of at least 50 dB power for equal-power signals as well as power differences of up to 10 dB between inputs.

The Nyquist sampling criterion requires that a signal is measured at least once per half wavelength. The counter-propagating signals in the two arms of WASP are delayed by equal amounts at the two inputs of the multiplier (Figure 2) and one quarter of the wavelength of the highest frequency signal that can be fully sampled is equal to the spacing between adjacent multipliers. The physical size of the packaged multipliers limits this spacing to 0.265 inches which, on the 0.05 inch thick Duroid circuit board ($\epsilon_r=10$), sets the maximum frequency at just over 4200 MHz. A short tab extending from the transmission line demarks the position of

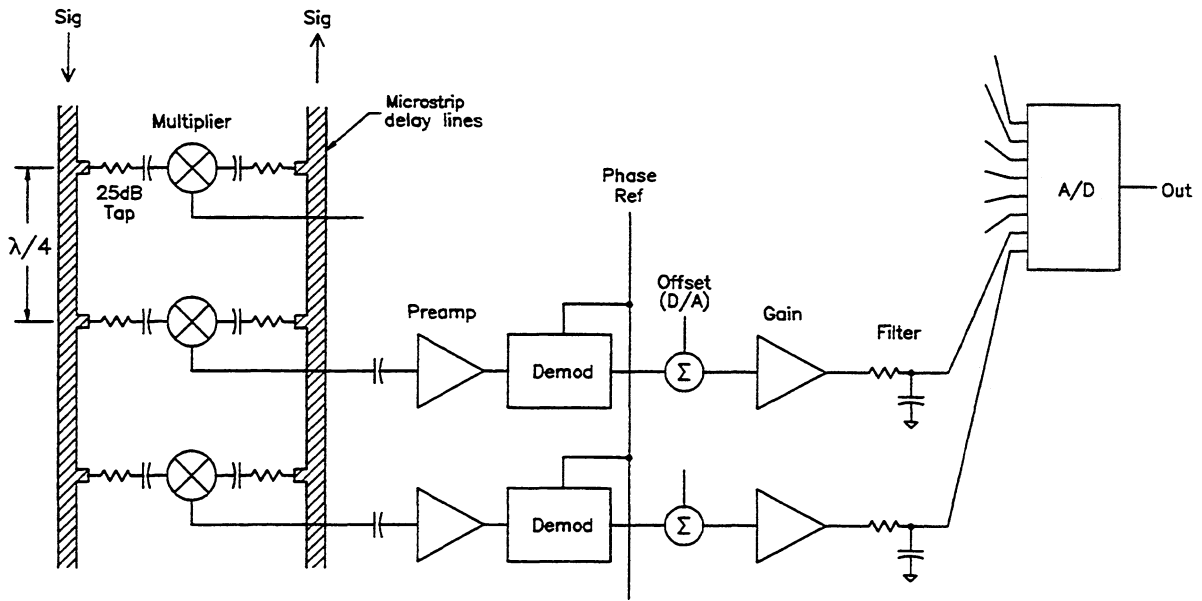


Figure 2: A schematic view of a section of the multiplier/delay chain and the low-frequency signal-processing electronics.

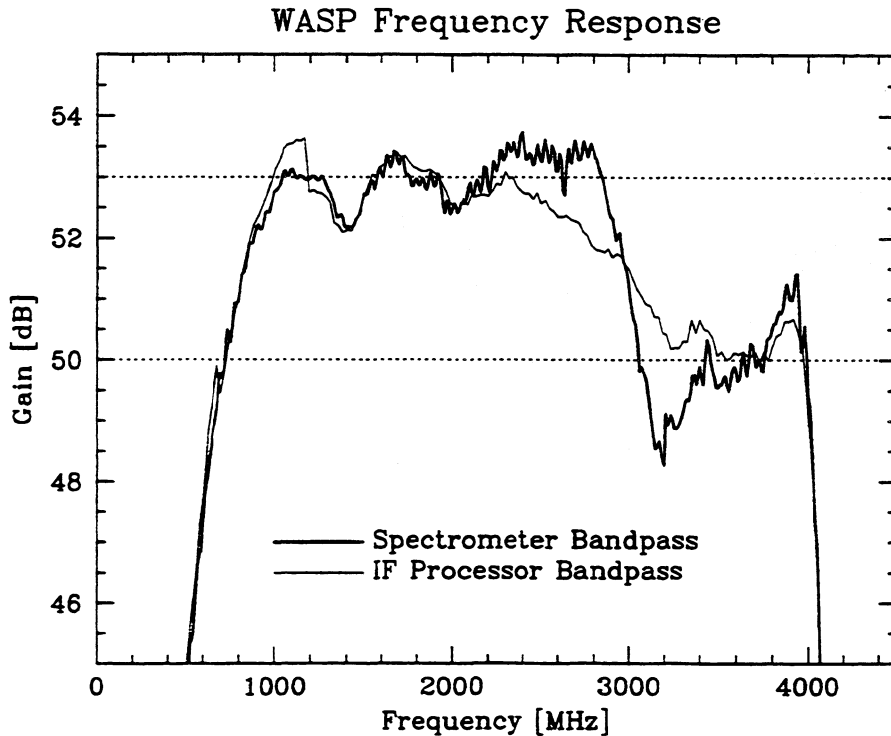


Figure 3: A plot of the WASP passband (heavy line) superposed on the passband of the IF processor (all electronics preceding the 8-way power splitters). A ratio of the two indicates that the response of the multiplier modules is quite flat, except in the region near 3000 MHz.

each multiplier. This tab accurately locates one end of a chip capacitor that forms a broadband resistive power divider that weakly connects the line and multiplier input. The coupling between the transmission line and the multiplier input is around -25 dB at low frequencies, rolling up by 8 dB at the top of the frequency band. This roll-up, caused by the shunt capacitance in the chip resistors, compensates nicely for fall-off in multiplier sensitivity with increasing frequency.

3.3 Signal Processing Electronics

Circuitry at the IF output of each multiplier blocks the DC bias level, and then amplifies, demodulates and low-pass filters the correlated signal. The resultant DC signal is then digitized prior to digital averaging in a PC (Figure 2). The whole spectrometer is read out at a rate of just over 13Hz, keeping the aliased DC noise of the two-pole low-pass filter to below one percent. This data rate is compatible with those attainable using serial input/output analog-to-digital (A/D) converters, and requires a clock frequency that is low enough that connections between the correlator boards and the computer can be made using ribbon cable.

The required dynamic range of the spectrometer readout-electronics is determined by the intrinsic dynamic range of the input signal, and the internal noise floor of the spectrometer. For a bandwidth of 3250 MHz and a sampling interval of 73 ms, the minimum dynamic range needed is just over 14 bits. Further range is required to allow for variations in multiplier sensitivity, differences in power level along the delay line and to sample the noise more finely than the minimum level. This translates to a total range of 17 or 18 bits, achieved using the combination of a 12-bit analog-to-digital converter and a programmable offset (digital-to-analog converter) (Figure 2). The dynamic range requirement relaxes with increasing lag as the size of the correlated signal decreases, and so offsets are included on the first 64 lags only.

3.4 Mechanical Structure

WASP is fully contained within a half-height rack. Each multiplier module is mounted onto a correlator board that also contains the low-frequency signal-processing electronics for all 16 channels. The eight correlator boards are mounted in a standard 3U VME crate which in turn sits in the half-height rack along with the IF processor, power supplies and the rack-mounted PC.

4 Spectrometer Performance

4.1 Amplitude and Phase Response

The amplitude response of the spectrometer is shown in Figure 3. The passband of the IF electronics in front of the 8-way splitters (IF processor) shows a fair amount of structure (Figure 3 light line), due in the main to the mixer used to phase modulate the signal prior to correlation. The multipliers and their coupling circuits also introduce some structure, particularly noticeable around 3000 MHz (a comparison of the light and heavy lines). This dip in response is seen in each multiplier, and is tentatively attributed to a roll-off in amplifiers at the LO-input of the multipliers. Detailed measurements of the multiplier and coupling circuit properties are being made to investigate this.

The phase response of the spectrometer can also be readily determined. This is done using two measurements (at each frequency) of the autocorrelation function, with and without a known phase inserted into one of the two arms of the spectrometer. In an ideal correlator, with perfectly

uniform sampling, the phase difference between adjacent multipliers would increase linearly with increasing frequency. In general this is not the case in WASP, as dispersion and roll-off in the multiplier amplifiers as well as low-level reflections within the module affect the measured phases: at low frequencies the averaged phase difference does increase linearly, however at higher frequencies, and particularly around 3000 MHz, the phase shift per lag deviates quite markedly. The Nyquist frequency of the spectrometer, given by the frequency at which the phase change between adjacent multipliers is π , can be determined from an extrapolation to phase change measurements made at the low-end of the band. This suggests a maximum frequency of just over 4200 MHz, above the cutoff of the anti-aliasing filters included in the IF processor.

4.2 Stability

WASP has proved to be very stable, due mainly to the internal phase switching and subsequent synchronous detection of the input signal. There are, however residual drifts that occur at a low level. Temperature changes are the dominant cause of drift. In particular, small temperature changes produce changes in multiplier sensitivity and the delays between multipliers: a change of 4 K in temperature results in a 1% change in responsivity and delay. The modules are temperate-regulated using heaters, though both the delay change and multiplier responsivity can be corrected for. The temperature sensitivity of the digital-to-analog converters used to increase the dynamic range of the low-frequency signal processing electronics is a more significant source of drift. The drift time scales, however, are long compared to typical sky-chop frequencies used during observing. Again, heaters are used to stabilize the temperature of the programmable offsets. A small change in the layout of the low-frequency signal processing electronics would produce an order of magnitude reduction in the sensitivity to temperature.

Very low-frequency noise in the multiplier power supply manifests itself as small offsets in the measured autocorrelation function. The offset at any time is the same for all channels and therefore transforms to δ -function at zero frequency, without affecting the power spectrum within the spectrometer passband.

Long integrations on the noise diode simulating sky-chop observations at 0.25 Hz show that spectrometer noise integrates down as the square root of the integration time over periods in excess of 10 hours. These time scales agree with measurements of the Allan variance of individual channels.

5 The Recovery of Power Spectra

5.1 The Method

The power spectrum of a correlation spectrometer input signal can be obtained by the inversion of its autocorrelation function (ACF). An ACF that is uniformly sampled in delay may be inverted using a Fourier transform (Equation 1). The small deviations in sampling caused by phase errors in the multipliers and dispersion in the microstrip transmission line distort the sampling of the WASP ACF, with the result that a WASP ACF cannot be inverted analytically. A linear technique has been developed to reconstruct the power spectra from WASP ACFs. Calibration measurements are made of the spectrometer response to a series of monochromatic signals spanning the input band of WASP, spaced at 10 MHz intervals. These ACF measurements are then used to determine a set of basis functions which are then used to reconstruct the power spectrum. The ACF at each

lag, $R(\tau)$, though a function of frequency and non-uniformly sampled, changes very little with time and temperature, and so occasional calibrations only are needed.

The linear reconstruction scheme is described in more detail in Isaak, Harris and Zmuidzinas (in prep.). Nonlinear, iterative inversion techniques are also being developed that will be used when WASP is operating in cross-correlation mode.

5.2 Power Spectra

A variety of different power spectra have been recovered from various WASP autocorrelation functions using the linear reconstruction technique.

Figure 4 is the laboratory spectrum of a 1000 MHz bandpass filter and noise source, normalized by the passband of the spectrometer. The spectrum has a dynamic range of greater than 100 (20 dB), sufficient for extra-galactic astronomy.

WASP has also been used for preliminary observations at the Caltech Submillimeter Observatory. Shown in Figure 5 are two superposed CO $J = 4-3$ spectra of the star-burst galaxy, M82, taken with the 1000 MHz bandwidth 460 GHz facility receiver. The spectra have been binned to a resolution of 30 MHz. The heavy line traces the line profile measured with WASP, while the light line traces the line profile measured using the facility AOS backend - the agreement between the two spectra is good, and the origin of the small differences between the two spectra is currently being investigated.

WASP will be used in conjunction with a wideband 700 GHz SIS receiver that is being built at Caltech. It is intended that the instantaneous bandwidth of the receiver will match the input bandwidth of WASP. This wideband combination will be used to study the warm and dense gas in external galaxies.

6 Conclusions

We have designed and built a wideband analog autocorrelation spectrometer. WASP has a contiguous bandwidth of 3250 MHz with a resolution of 33 MHz, a bandwidth that is a factor of a few larger than other spectrometers. WASP is stable over integration periods of greater than 10 hours, and produces spectra with dynamic range of greater than 100. The spectrometer is compact, physically robust and, in spite of not being optimized at all for low power consumption, consumes only 75 W excluding computer. Prototype low-power correlator boards are being designed to explore the possibilities of power reduction.

7 Acknowledgements

We thank Jeff Gottschalk, formerly at FCRAO at the University of Massachusetts, the "Technical Team from the 8th Floor" also at FCRAO and Jim Morgan at the University of Maryland for their significant contributions to and work on this project. We also thank John Ward and Dave Miller for their contributions, and Tom Phillips and the staff of the Caltech Submillimeter Observatory for their support of this project.

This work has been supported by NASA grant NAG5-6044 to the University of Maryland, USRA funds to Caltech for SOFIA heterodyne spectroscopy, and by the Universities of Maryland and Massachusetts.

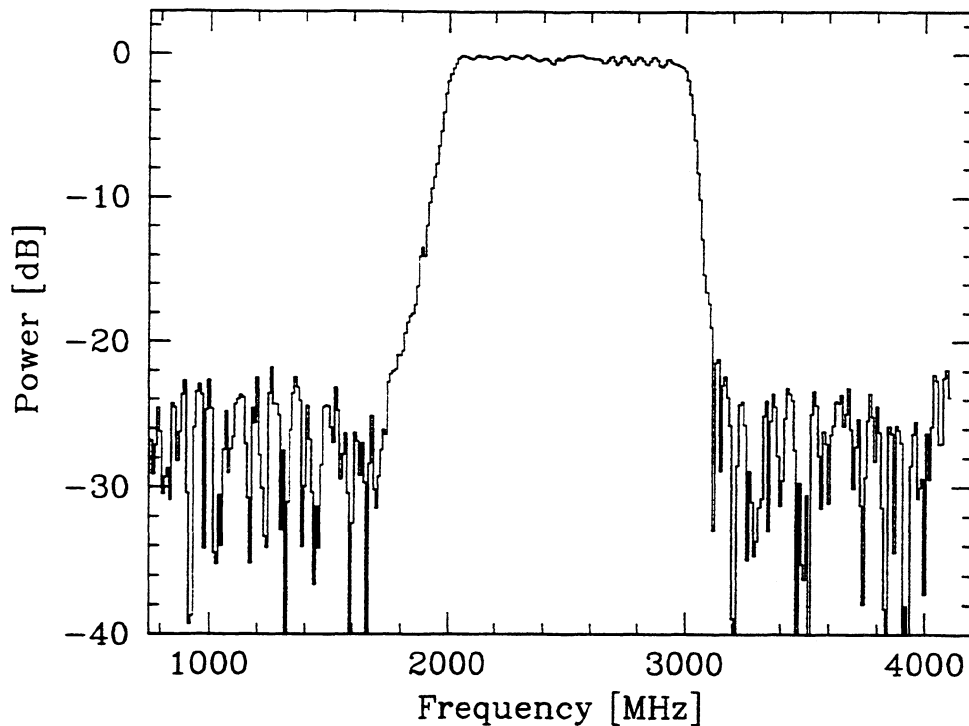


Figure 4: A WASP spectrum of a 1000 MHz-wide bandpass filter and noise diode. A measure of the dynamic range of WASP, the noise level in the power spectrum is a factor of more than 100 lower than the peak signal. The spectrum was reconstructed using the linear scheme.

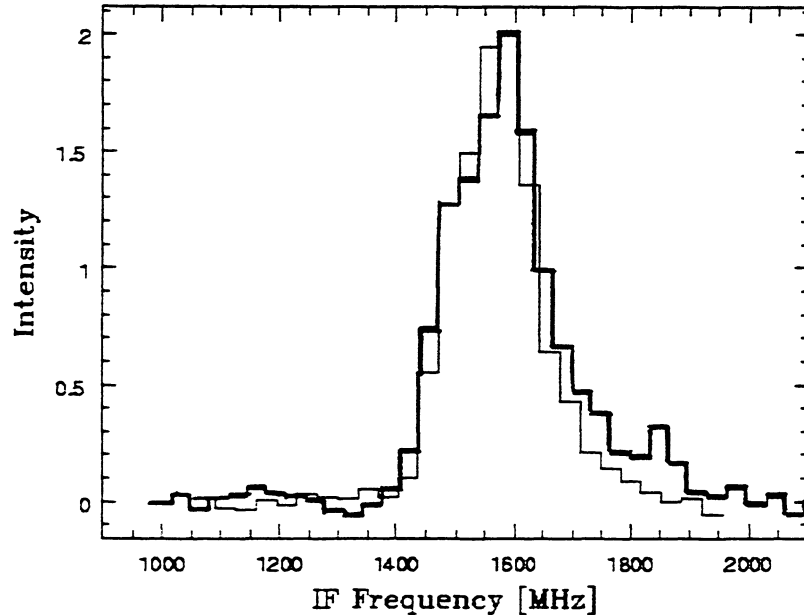


Figure 5: Spectra of the star-burst galaxy M82, taken in the CO(4-3) transition at the Caltech Submillimeter Observatory in January 1998. The heavy line traces the spectrum measured using WASP, and the light line the spectrum measured using the facility AOS backend: the two spectra show good agreement. The bandwidth of the spectra was limited by the receiver and IF bandwidth. The WASP spectrum is an average of two observations, totaling 4 minutes in integration time, and was reconstructed using the linear scheme. The AOS spectrum represents a single, 2 minute observation.

8 References

- Brown, R.L., Vanden Bout, P.A. 1991, AJ, 102, 1956
Gilbert, B. 1968, IEEE J. Solid-State Circuits, 3, 365
Guilloteau, S., Omont, A., McMahon, R.G., Cox, P., Petit-Jean, P. 1997 A&A, 328, L1
Harris, A.I., Stutzki, J., Graf, U.U., Russell, A.P.G., Genzel, R., Hills, R.E 1991, ApJ, 382, L75
Horn, J., Macke, C., Mockel, C., Schloder, F., Sibertz, O., Schieder, R. 1998, this volume
Ohta, K., Yamada, T., Nakanishi, K., Kohno, Akiyama, M., Kawabe, R. 1996, Nature, 382, 426
Omont, A., PetitJean, P., Guilloteau, S., McMahon, R.G., Solomon, P.M., Pecontal, E. 1996, Nature, 382, 428
Ruf, C.S., Swift, C.T. 1988, J, Atmospheric and Oceanic Technol., 4,539
Staguhn, J., Harris, A.I., Plambeck, R.L., Welch, W.J., Sutton, E.W., 1998, In Proceedings of the SPIE, Vol. 3357.

Ninth International Symposium On Space Terahertz Technology

Authors & Registered Participants Mailing List

March 17-19, 1998

PAOLO ARCIONI

University of Pavia
Dept. Electronics; Microwave Lab.
Via Ferrata, 1-127100 Pavia
ITALY
+39 382 505223
+39 382 422583 (FAX)
arcioni@ele.unipv.ic

JEFF BARNER

Jet Propulsion Laboratory
4800 Oak Grove Dr.
M/S 302-306
Pasadena, CA 91109
818-354-7353
818-393-4540 (FAX)
jbarner@serverbeast.jpl.nasa.gov

PAUL BATELAAN

Jet Propulsion Laboratory
4800 Oak Grove Dr.
M/S 168-314
Pasadena, CA 91109
paul.batelaan@jpl.nas.gov

VICTOR BELITSKY

Chalmers Univ. of Technology
Radio & Space Science Dept.
Gothenburg, 541296
SWEDEN
+46 31 7721000
+46 31 164513 (FAX)
belitsky@oso.chalmers.se

DOMINIC BENFORD

Caltech
Mail Code 320-47
Pasadena, CA 91125, USA
626-395-3741
626-796-8806 (FAX)
dbenford@tacos.caltech.edu

PIERRE BERTRAM

Jet Propulsion Laboratory
4800 Oak Grove Dr.
M/S 168-314
Pasadena, CA 91109
818-354-0990
818-393-4683 (FAX)
pbertram@mail1.jpl.nasa.gov

OLGA BORIC-LUBECKE

RIKEN Photodynamics Res. Ctr.
Inst. Physical & Chemical Res.
19-1399 Koeji, Nagamachi
Aoba-Ku, Sendai 980
JAPAN
+81-22-228-2124
+81-22-228-2128 (FAX)
olga@postman.riken.go.jp

MAURIZIO BOZZI

University of Pavia
Dept. Electronics
Microwave Lab
Via Ferrata, 1-127100 Pavia
ITALY
+39 382 505223
+39 382 422583 (FAX)
bozzi@ele.unipv.it

BRUCE BUMBLE

Jet Propulsion Laboratory
4800 Oak Grove Dr.
M/S 302-231
Pasadena, CA 91109
818-354-5117
818-393-4540 (FAX)
bbumble@vaxeb.jpl.nasa.gov

MICHAEL BURNS

Jet Propulsion Laboratory
4800 Oak Grove Dr.
M/S 302-306
Pasadena, CA 91109
818-354-2568
818-393-4540 (FAX)
michael.j.burns@jpl.nasa.gov

TERRY CAFFERTY

Jet Propulsion Laboratory
724 North West Knoll Dr., #308
West Hollywood, CA 90069
213-653-4725
213-653-4726 (FAX)
tctech@earthlink.net

CAREY CATES

UCSB
Quantum Institute
Physics Dept.
Santa Barbara, CA 93106
805-893-2423
805-893-4170 (FAX)
isabel@physics.ucsb.edu

GOUTAM CHATTOPADHYAY

Caltech
Mail Code 136-93
Pasadena, CA 91125, USA
626-395-4246
626-796-8806 (FAX)
goutam@cco.caltech.edu

MING-TANG CHEN

Academia Sinica
Nankang, P.O. Box 1-87
Taipei, 115
TAIWAN
886-2-2652-2020
886-2-2788 1106 (FAX)
mchen@biaa.sinica.edu.tw

SERGEY CHEREDNICHENKO

Dept. Physics
Moscow State Pedagogical Univ.
Moscow 119882
RUSSIA

DENIS CHOUVAEV

Chalmers University of
Technology
Dept. Radio & Space Science
S-416 96 Goteborg
SWEDEN

TOM CROWE

University of Virginia
Dept. Electrical Engineering
Charlottesville, VA 22903
804-924-7693
804-924-8818 (FAX)
twc8u@virginia.edu

C. T. CUNNINGHAM

Herzberg Institute of Astrophysic
5071 West Saanich Road
Victoria V8X 4M6
CANADA
250-363-6937
250-363-0045 (FAX)
charles.cunningham@hia.nrc.ca

LARRY D'ADDARIO

NRAO
2015 Ivy Road, Suite 219
Charlottesville, VA 22903
804-296-0245
804-296-0324 (FAX)
ldaddari@nrao.edu

THIJS DE GRAAUW

SRON
P.O. Box 800
Groningen 9700 AV
THE NETHERLANDS
31 0 50-3634074
31 0 50-3634033 (FAX)
tlijdsd@srn.rug.nl

PIET DE KORTE

Space Research Organisation
Netherlands
Sorbonnelaan2
Utrecht 3584 CA
THE NETHERLANDS
31 20 2535710
31 30 2540860 (FAX)
p.dekorte@srn.ruu.nl

GERHARD DE LANGE

MIT
77 Massachusetts Avenue
Cambridge, MA 02139-4307
gert@mit.edu

PETER DE MAAGT

ESTEC
P.O. Box 299
2200 AG
THE NETHERLANDS
+31 71 565 5906
+31 71 565 4999 (FAX)
pdemaagt@estec.esa.nl

ROBERT DENGLER

Jet Propulsion Laboratory
4800 Oak Grove Dr.
M/S 168-314
Pasadena, CA 91109
818-354-6465
818-393-4683 (FAX)
nogb@nogb.jpl.nasa.gov

PIETER DIELEMAN

University of Groningen
Dept. Applied Physics
Nijenborgh 4
9747 AG Groningen
THE NETHERLANDS

DARREN DOWELL

Caltech
Mail Code 320-47 Downs
Pasadena, CA 91125, USA
626-395-6610
626-796-8806 (FAX)
cdd@socrates.caltech.edu

ERIK DUERR

MIT
Lincoln Laboratory
105 Memorial Dr.
Cambridge, MA 02139
617-225-9782
617-258-7864 (FAX)
duerr@mit.edu

JACK EAST

University of Michigan
2301 EECS Building
Ann Arbor, MI 48109
313-763-0212
jeast@eeecs.umich.edu

PIERRE ECHTERNACH

Jet Propulsion Laboratory
4800 Oak Grove Dr.
M/S 302-231
Pasadena, CA 91109
818-393-3563
818-393-4540 (FAX)
pierre@squid.jpl.nasa.gov

HERIBERT EISELE

University of Michigan
1301 Beal Avenue
Ann Arbor, MI 48109-2122
734-764-3354
734-647-1781 (FAX)
heribert@engin.umich.edu

NEAL ERICKSON

University of Massachussetts
Lederle 619
Radio Astronomy
Amherst, MA 01003
413-545-1873
413-545-4223 (FAX)
neal@fcrao1.phast.umass.edu

RONNA ERICKSON

University of Massachussetts
Five College Radio Astronomy Obs.
619 LGRT
Amherst, MA 01003
413-545-2764
413-545-4223 (FAX)
erickson@fcrao1.phast.umass.edu

PASCAL FEBVRE

Universite De Savoie
Campus Scientifique
Le Bourget Du Lac Cedex,
73376
FRANCE
(33) 4 7975 8864
(33) 4 7975 8742 (FAX)
pascal.febvre@univ-savoie.fr

MARC FELDMAN

University of Rochester
Hopeman Hall - EE
Rochester, NY 14627
716-275-3799
716-473-0486 (FAX)
feldman@ee.rochester.edu

MARGARET FRERKING
Jet Propulsion Laboratory
4800 Oak Grove Dr.
M/S 306-451
Pasadena, CA 91109
818-354-6990
818-393-6869 (FAX)
margaret.frerking@jpl.nasa.gov

TETSU FUJII
RIKEN Photodynamics Res.
Center
Inst. Physical & Chemical Res.
19-1399 Koeji, Nagamachi
Aoba-Ku, Sendai 980
JAPAN
+81-22-228-2124
+81-22-228-2128 (FAX)
kotetsu@riec.tohoku.ac.jp

MICHAEL GAIDIS
Jet Propulsion Laboratory
4800 Oak Grove Dr.
M/S 168-314
Pasadena, CA 91109
818-354-9775
818-393-4683 (FAX)
michael.gaidis@jpl.nasa.gov

TODD GAIER
Jet Propulsion Laboratory
4800 Oak Grove Dr.
M/S 168-314
Pasadena, CA 91109
818-354-4402
todd.gaier@jpl.nasa.gov

ISRAEL GALIN
Aerojet Corp.
P. O. Box 298
1100 West Holyvale Street
Azusa, CA 91702
galini@ms1.aes.com

W. GANZEVLES
University of Groningen
Nijenborghy 9747 AG
Groningen
THE NETHERLANDS
+31 50 363 4880
+31 50 363 3990 (FAX)
ganzevles@phys.rug.nl

J. R. GAO
Space Research Organisation
Netherlands
Dept. Applied Physics
Nijenborgh, 4
Groningen 9743 AG
THE NETHERLANDS
31-50-3634866
31-50-3633900 (FAX)
gao@phys.rug.nl

MATTHEW GARDNER
Caltech
Mail Code 320-47
Pasadena, CA 91125
626-395-3741
626-796-8806 (FAX)
mgardner@socrates.caltech.edu

EYAL GERECHT
Univ. Massachussetts, Amherst
Dept. Electr. & Computer Eng.
Amherst, MA 01003
413-545-0591
413-545-4611 (FAX)
gerecht@kira.ecs.umass.edu

JAN GILDEMEISTER
UC Berkeley
110 Leconte Hall
Berkeley, CA 94720
510-642-4359
510-643-5204 (FAX)
jmg@physics.berkeley.edu

GREGORY GOLTSMAN
Moscow State Pedagogical Univ.
29 M. Piragovskaya
Moscow 119435
RUSSIA
011-7-095-246-12-02
011-7-095-248-0162 (FAX)
goltsman@rpl.mpgu.msk.su

YURI GOUSEV
Royal Institute of Technology,
Stockholm
Dept Electronics, Electronics
229
16440 Kista-Stockholm
SWEDEN
+46-8-752-1242
+46-8-752-1240 (FAX)
yuri@ele.kth.se

PING GU
Kansai Advanced Res. Center
588-2 Iwaoka, Iwaoka-Cho,
Nishi-Ku Kobe-Shi
Hyogo 651-2401
JAPAN
+81 78 969 2198
+81-78-969-2219 (FAX)
guping@crl.go.jp

KARL HEINZ GUNDLACH
IRAM
300 Rue De La Piscine
Domain Universit. De Grenoble
38406 Saint Martin D'Herès
Cedex
FRANCE
(33) 4 76 82 49 00/ 49 85
(33) 4 76 51 59 38 (FAX)
gundlach@iram.fr

ROBERT HAAS
TRW
1 Space Park
M/S 2154B
Redondo Beach, CA 90278
310-812-7419
310-812-5878 (FAX)
r.haas@trw.com

OLIVER HARNACK
Institut Fur Schicht Und
Ionentechnik
Forschungs Zentrum Juelich
Juelich, 52425
GERMANY
+49 2461 61 2367
+49 2461 61 2940 (FAX)
o.harnack@fz-juelich.de

JEFFREY HESLER
University of Virginia
Dept. Electrical Engineering
Thornton Hall
Charlottesville, VA 22903
804-924-4576
hesler@virginia.edu

JOCHEN HORN
UCLA
405 Hilgard Ave.
8318 Math Science Bldg.
Los Angeles, CA 90024
310-825-4782
310-206-2096 (FAX)
horn@jupiter.astro.ucla.edu

HEINZ-WILHELM HUBERS

DLR Inst. Space Sensor Tech.
Rudower Chaussee 5 Techn.
Berlin 12489
GERMANY
+49-30-67055596
+49-30-67055507 (FAX)
heinz-wilhelm.huebers@dlr.de

JUNJI INATANI

National Space Development
Agency of Japan
World Trade Center Bldg. 2-4-1
Hamamatsu-cho, Minato-ku
Tokyo 105-806
JAPAN
inatani.junji@nasda.go.jp

YOSHIHISA IRIMAJIRI

Communication Research Lab
4-2-1, Nukui-Kita-Machi,
Koganei-Shi, Tokyo 184
JAPAN
+81-423-27-6089
+81-423-27-6110 (FAX)
irimaji@ch.go.jp

HIROYUKI IWASHITA

Nobeyama Radio Observatory
411 Nobeyama Minamimaki-Mura
Minamisaku-Gunn
Nagano-Ken, 384-1305
JAPAN
+81-267-98-4374
+81-267-98-2927 (FAX)
iwashita@nro.nao.ac.jp

KARL JACOBS

Cologne University
Zulicher Strasse 77
50937 Koln
GERMANY
49-221-4703484
49-221-4705162 (FAX)
jacobs@ph1.uni-koeln.de

STEPHEN JONES

University of Virginia
Dept. Electrical Eng.
Charlottesville, VA 22903
804-924-6080
804-924-8818 (FAX)
shjan@virginia.edu

BORIS KARASIK

Jet Propulsion Laboratory
4800 Oak Grove Dr.
M/S 168-314
Pasadena, CA 91109
boris.karasik@jpl.nasa.gov

A. KARPOV

Institut de Radioastronomie
Millimetrique
300, rue de la Piscine,
F-38406 St. Martin d'Herès
FRANCE
karpov@iram.fr

AKIRA KAWAKAMI

Kansai Advanced Res. Center,
CRL
588-2 Iwaoka,
Iwaoka-Cho, Nishi-Ku
Kobe Hyogo, 651-2401
JAPAN
+81-78-969-2193
+81-78-969-2199 (FAX)
kawakami@crl.go.jp

JONATHAN KAWAMURA

Caltech
Mail Code 320-47 Downs
Pasadena, CA 91125
626-395-4601
626-796-8806 (FAX)
kawamura@socrates.caltech.edu

A. R. KERR

National Radio Astronomy Obs.
2015 Ivy Rd., Ste. 219
Charlottesville, VA 22903
804-296-0363
804-296-0324 (FAX)
akerr@nrao.edu

POURYA KHOSROPANAH

Chalmers University of
Technology
Dept. Microelectronics &
Microwave Electr. Lab.
Goteborg SE 412 96
SWEDEN
+46 31 772 1931
+46 31 16 45 13 (FAX)
pourya@ep.chalmers.se

TEUN KLAPWIJK

University of Groningen
Nijenborgh 4.13
Groningen, 9721WP
THE NETHERLANDS
31-50-3634932
31-50-3633900 (FAX)
klapwijk@phys.rug.nl

ALAN KLEINSASSER

Jet Propulsion Laboratory
4800 Oak Grove Dr.
M/S 302-231
Pasadena, CA 91109
818-354-9186
818-393-4540 (FAX)
kleins@vaxeb.jpl.nasa.gov

TIMOTHY KOCH

Jet Propulsion Laboratory
4800 Oak Grove Dr.
M/S 168-314
Pasadena, CA 91109
818-354-8469
818-393-4683 (FAX)
timothy.c.koch@jpl.nasa.gov

SATOSHI KOHJIRO

Electrotechnical Laboratory
1-1-4 Umezono
Tsukuba, Ibaraki 3050045
JAPAN
+81-298-54-5561
+81-298-54-5531 (FAX)
kohjiro@etl.go.jp

JACOB KOOI

Caltech
Mail Code 320-47 Downs
Pasadena, CA 91125
626-395-4286
626-796-8806 (FAX)
kooi@tacos.caltech.edu

OLEKSANDR KORSHAK

Wayne State University
5050 Anthony Wayne Dr. #3153
Dept. ECE
Detroit, MI 48202
313-577-5507
313-577-1101 (FAX)
korshak@ciao.eng.wayne.edu

MATTHIAS KROUG
Chalmers Univ. of Technology
Dept. Microelectronics & Nano-
Science
Goteborg SE 412 96
SWEDEN
+46 31 772 3319
+46 31 772 3471 (FAX)
kroug@fy.chalmers.se

CARL KUKKONEN
Jet Propulsion Laboratory
4800 Oak Grove Dr.
M/S 180-604
Pasadena, CA 91109
818-354-4814
818-393-5269 (FAX)
carl.kukkonen@jpl.nasa.gov

LEONID KUZMIN
Chalmers Univ. of Technology
Radio & Space Science Dept.
Gothenburg, 541296
SWEDEN

RICK LE DUC
Jet Propulsion Laboratory
4800 Oak Grove Dr.
M/S 302-231
Pasadena, CA 91109
818-354-2209
818-393-4540 (FAX)
rleduc@vaxeb.jpl.nasa.gov

ADRIAN LEE
UC Berkeley
Cfpa 301 Leconte Hall
Berkeley, CA 94720
510-642-5721
510-643-5204 (FAX)
atl@physics.berkeley.edu

KAREN LEE
Jet Propulsion Laboratory
4800 Oak Grove Dr.
M/S 168-314
Pasadena, CA 91109
818-354-3863
818-393-4683 (FAX)
karen.lee@jpl.nasa.gov

TRACY LEE
Jet Propulsion Laboratory
4800 Oak Grove Dr.
M/S 168-314
Pasadena, CA 91109
818-354-1537
818-393-4683 (FAX)
thlee@serpent.jpl.nasa.gov

CHAO-TE LI
University of Virginia
110 Carrolton Ter #5
Charlottesville, VA
804-924-7520
cl5g@virginia.edu

ROBERT LIN
Jet Propulsion Laboratory
4800 Oak Grove Dr.
M/S 168-314
Pasadena, CA 91109
818-354-7092
818-393-4683 (FAX)
robert.lin@jpl.nasa.gov

VICTOR LUBECKE
RIKEN Photodynamics Res. Ctr.
Inst. Physical & Chemical Res.
19-1399 Koeji, Nagamachi
Aoba-Ku, Sendai 980
JAPAN
+81-22-228-2124
+81-22-228-2128 (FAX)
victor@postman.riken.go.jp

WILLEM LUINGE
SRON
P.O. Box 800
Groningen
THE NETHERLANDS
31-503634022
31-503634033 (FAX)
w.luinge@sron.rug.nl

CHRIS MANN
Rutherford Appleton Laboratory
Chilton, Didcot
Oxon, OX11 00X
UNITED KINGDOM
+44-1235-446435
+44-1235-446421 (FAX)
c.m.mann@rl.ac.uk

STEVEN MARAZITA
University of Virginia
Thornton Hall, C-112
Charlottesville, VA 22903
804-924-6089
804-924-8818 (FAX)
smm7k@virginia.edu

SUZANNE MARTIN
Jet Propulsion Laboratory
4800 Oak Grove Dr.
M/S 302-306
Pasadena, CA 91109
818-354-7076
818-393-4540 (FAX)
suzanne.martin@jpl.nasa.gov

SHUJI MATSUURA
Caltech
M/S 150-21, GPS
Pasadena, CA 91125
626-395-3377
626-585-1917 (FAX)
matsuura@gps.caltech.edu

WILLIAM MC GRATH
Jet Propulsion Laboratory
4800 Oak Grove Dr.
M/S 168-314
Pasadena, CA 91109
818-354-8542
818-393-4683 (FAX)
rob@rob-mac.jpl.nasa.gov

KRIKOR MEGERIAN
Jet Propulsion Laboratory
4800 Oak Grove Dr.
M/S 302-306
Pasadena, CA 91109
818-354-1628
818-393-4540 (FAX)
krikor.g.megerian@jpl.nasa.gov

IMRAN MEHDI
Jet Propulsion Laboratory
4800 Oak Grove Dr.
M/S 168-314
Pasadena, CA 91109
818-354-2001
818-393-4683 (FAX)
imran.mehdi@jpl.nasa.gov

ROBERT MENZIES

Jet Propulsion Laboratory
4800 Oak Grove Dr.
M/S 168-214
Pasadena, CA 91109
818-354-3787
818-393-6984 (FAX)
rtm@lrs.jpl.nasa.gov

HARALD MERKEL

Chalmers Univ. of Technology
Rannvagen 6, Microelectronics
Dept.
Gothenburg, 41296
SWEDEN
+46-31-772 1848
+46-31-164-513 (FAX)
harald@nt.chalmers.se

DAVE MILLER

Caltech
Mail Code 320-47 Downs
Pasadena, CA 91125, USA
626-395-3668
626-796-8806 (FAX)
davem@Ocat.caltech.edu

MARK MORRIS

UCLA
405 Hilgard Ave., Box 951562
Div. of Astronomy
Los Angeles, CA 90095-1562
310-825-3320
morris@astro.ucla.edu

ERIC MUELLER

Demaria Electrooptics Sys., Inc.
1280 Blue Hills Ave.
Bloomfield, CT 06002
860-243-9557
860-243-9577 (FAX)
deos@snet.net

GOPAL NARAYANAN

Univ. Massachusetts, Amherst
GRC Tower, FCRAO
Amherst, MA 01003
413-545-0925
413-545-4223 (FAX)
gopal@fcrao1.phast.umass.edu

TAKASHI NOGUCHI

Nobeyama Radio Observatory
Nobeyama, Minami-Saku
Nagano 384-1305,
JAPAN
+81-267-98-4364
+81-267-98-2927 (FAX)
noguchi@nro.nao.ac.jp

JOHN OSWALD

Jet Propulsion Laboratory
4800 Oak Grove Dr.
M/S 168-314
Pasadena, CA 91109
818-354-3519
818-393-4683 (FAX)
john.oswald@jpl.nasa.gov

SHING-KUO PAN

National Radio Astronomy
2015 Ivy Rd., Ste. 219
Charlottesville, VA 22903
804-296-0262
804-296-0324 (FAX)
span2@nrao.edu

JOHN PAYNE

National Radio Astronomy Obs.
949 N. Cherry Ave.,
Campus Bldg. 65
Tucson, AZ 85721-0566
520-882-8250 X. 118
520-882-7955 (FAX)
jpayne.nrao.edu

JOHN PEARSON

Jet Propulsion Laboratory
4800 Oak Grove Dr.
M/S 183-301
Pasadena, CA 91109
818-354-0822
818-354-8460 (FAX)
jcp@spec.jpl.nasa.gov

TONY PEEBLES

UCLA
66-127J Eng. IV, EE Dept.
Los Angeles, CA 90095
310-825-4068
310-206-5816 (FAX)
peebles@ee.ucla.edu

GERNOT POMRENKE

DARPA
3701 North Fair(FAX) Drive
Electronics Technology Office
Arlington, VA 22203-1714
703-696-4470
703-696-2206 (FAX)
gpomrenke@darpa.mil

DAVID PORTERFIELD

University of Virginia
Department of Electrical
Engineering
Semiconductor Device
Laboratory
Charlottesville, VA 22903

DAN PROBER

Yale University
P.O. Box 208284
New Haven, CT 06520-8284
203-432-4280
daniel.prober@yale.edu

ANTTI RAISANEN

Helsinki University of Technology
P.O. Box 1000
FIN-02015
FINLAND
+358-9-451-2004
+358-9-451-2063 (FAX)
antti.raisanen@hut.fi

FRANK RICE

Caltech
Mail Code 320-47 Downs
Pasadena, CA 91125, USA
626-395-4246
626-796-8806 (FAX)
rice@cco.caltech.edu

PAUL RICHARDS

UC Berkeley
Dept. Physics
Berkeley, CA 94720
510-642-3027
richards@physics.berkeley.edu

LANCE RILEY

Jet Propulsion Laboratory
4800 Oak Grove Dr.
M/S 246-101
Pasadena, CA 91109
818-354-0401
818-354-4341(FAX)
lriley@pop.jpl.nasa.gov

CLAUDIA ROESCH
IRAM
300 Rue De La Piscine
St. Martin D' Heres, 38406
FRANCE
+33 4 76 82 49 16
+33 4 76 51 59 38 (FAX)
roesch@iram.fr

PAVEL ROTT
University of Rochester
204 Hopeman Bldg.
Rochester, NY 14627
716-275-8135
716-473-0486 (FAX)
pasha@ee.rochester.edu

KIYOMI SAKAI
Kansai Advanced Res. Center
588-2, Iwaoka, Iwaokacho,
Nishiku
Kobe-Shi, Hyogo 651-2401
JAPAN
+81-78-969-2150
+81-78-969-2154 (FAX)
sakai@crl.go.jp

MORVAN SALEZ
DEMIRM-Observatoire de Paris
61 avenue de l'Observatoire
75014 Paris
FRANCE

LORENE SAMOSKA
Jet Propulsion Laboratory
4800 Oak Grove Dr.
M/S 168-314
Pasadena, CA 91109
818-354-0849
818-393-4683
lorene.samoska@jpl.nasa.gov

VIRENDRA SAROHIA
Jet Propulsion Laboratory
4800 Oak Grove Dr.
M/S 180-604
Pasadena, CA 91109
818-354-6758
818-393-5269 (FAX)
virendra.sarohia@jpl.nasa.gov

PAT SCHAFFER
Caltech
Mail Code 320-47 Downs
Pasadena, CA 91125
626-395-6620
626-796-8806 (FAX)
pls@socrates.caltech.edu

GERHARD SCHWAAB
DLR
Rudower Chaussee 5
D-12489 Berlin
GERMANY
+49 (0)30 67055597
+49-(0)30 67055502 (FAX)
gerhard.schwaab@dlr.de

MARK SHERWIN
UCSB
Physics Dept.
Santa Barbara, CA 93106
805-893-3774
805-893-4170 (FAX)
sherwin@physics.ucsb.edu

SHENG-CAI SHI
Nobeyama Radio Observatory
Nobeyama, Minamisaku
Nagano, 384-1305
JAPAN
+81-267-98-4364
+81-267-98-2927 (FAX)
shencai@nro.nao.ac.jp

WILLIAM SHILLUE
National Radio Astronomy Obs.
949 N. Cherry Ave.
Campus Bldg. 65
Tuscon, AZ 85721-0655
520-882-8250 X.142
520-882-7955 (FAX)
bshillue@nrao.edu

SERGEY SHITOV
Russian Academy of Science
Institute Radio Engr. & Electron.
Mokhovaya 11, 103907 Moscow
RUSSIA
+(095) 2032784
+(095) 2038414 (FAX)
sergey@hitech.cplire.ru
sergey@sron.rug.nl

IRFAN SIDDIQI
Yale University
Dept. Applied Physics
Rm. 405 Becton Center
15 Prospect St.
New Haven CT, 06520
203-432-4285/203-624-3778
203-432-4285 (FAX)
irfan.siddiqi@yale.edu

PETER SIEGEL
Jet Propulsion Laboratory
4800 Oak Grove Dr.
M/S 168-314
Pasadena, CA 91109
818-354-9089
818-393-4683 (FAX)
peter.siegel@jpl.nasa.gov

ANDERS SKALARE
Jet Propulsion Laboratory
4800 Oak Grove Dr.
M/S 168-314
Pasadena, CA 91109
anders.skalare@jpl.nasa.gov

PETER SMITH
Jet Propulsion Laboratory
4800 Oak Grove Dr.
M/S 302-306
Pasadena, CA 91109
818-354-4424
818-393-4540 (FAX)
petersSmith@jpl.nasa.gov

JAN STAKE
Chalmers University of
Technology
Dept. Microelectronics &
Microwave Electr. Lab.
Goteborg SE 412 96
SWEDEN
+46 31 772 1836
+46 31 16 45 13 (FAX)
stake@ep.chalmers.se

JEFF STERN
Jet Propulsion Laboratory
4800 Oak Grove Dr.
M/S 302-306
Pasadena, CA 91109
818-354-0029
818-393-4540 (FAX)
jstern@vaxeb.jpl.nasa.gov

JURGEN STUTZKI

Universitat Zu Koln
Zulpicher Strasse 77
I. Physikalisches Institut
D-50937 Koln,
GERMANY
stutzki@ph1.uni-koeln.de

KAZUYOSHI SUNADA

Nobeyama Radio Observatory
Nobeyama, Minamimaki,
Minamisaku
Nagano, 384-1305
JAPAN
81-267-98-4384
81-267-98-2927 (FAX)
sunada@nro.nao.ac.jp

S. I. SVECHNIKOV

Moscow State Pedagogical Univ.
Dept. Physics
29 M. Pirogovskaya Str.
Moscow 1119882
RUSSIA

GREGORY TAIT

Virginia Commonwealth
University
P.O. Box 843072
Richmond, VA 23284
804-828-1281
gbtait@vcu.edu

EDWARD TONG

Harvard-Smithsonian Center for
Astrophysics
60 Garden St., MS 42
Cambridge, MA 02138 USA
617-496-7641
617-495-7345 (FAX)
etong@cfa.harvard.edu

YOSHINORI UZAWA

Kansai Advanced Research
Center, CRL
588-2 Iwaoka, Iwaoka-Cho
Nishi-Ku, Kobe Hyogo, 651-
2401
JAPAN
+81-78-969-2195
+81-78-969-2199 (FAX)
uzawa@crl.go.jp

HERMAN VAN DE STADT

SRON
P.O. Box 800
Space Research Org.
Netherlands
Groningen, 9700 AV
THE NETHERLANDS
+31-50-3634035
+31-50-3634033 (FAX)
herman@sron.rug.nl

M. J. M. VAN DER VORST

Eindhoven University
Technology
P.O. Box 513
Eindhoven 5600 MB
THE NETHERLANDS
0031-402473458
0031-402455107 (FAX)

SIMON VERGHESE

MIT Lincoln Lab
LL-E-124
Cambridge, MA 01239
simonv@ll.mit.edu

IGOR VERNIK

University of Rochester
Hopeman Hall
Dept. Electrical Engineering
Rochester, NY 14627
716-275-2099
716-473-0486 (FAX)
vernik@ee.rochester.edu

JOHN WALSH

Dartmouth College
6127 Wilder Laboratory
Hanover, NH 03755
603-646-3262
603-646-1446 (FAX)
john.e.walsh@dartmouth.edu

JOHN WARD

Caltech
Mail Code 320-47
Pasadena, CA 91125
626-395-3740
626-796-8806 (FAX)
ward@socrates.caltech.edu

NICK WHYBORN

SRON
P.O. Box 800
Space Research Org.
Netherlands
Groningen, 9700 AV
THE NETHERLANDS
+31-50-363-4074
+31-50-363-4033 (FAX)
nick@sron.rug.nl

DANNY WILMS-FLOET

University of Groningen
Ngenborghy 9747 AG
Groningen,
THE NETHERLANDS
+31 50 363 4880
+31 50 363 3990 (FAX)
wilms@phys.rug.nl

ROLF WYSS

Jet Propulsion Laboratory
4800 Oak Grove Dr.
M/S 168-314
Pasadena, CA 91109
rolf.wyss@jpl.nasa.gov

PAVEL YAGOUBOV

Chalmers Univ. of Technology
Dept. Microelectronics &
Microwave Electr. Lab.
Goteborg SE 412 96
SWEDEN
+46 31 772 1848
+46 31 16 45 13 (FAX)
yagoubov@ep.chalmers.se

CHIEKO YAMAGUCHI

Nobeyama Radio Observatory
411 Nobeyama Minamimaki-Mura
Minamisaku-Gunn
Nagano-Ken, 384-1305
JAPAN
+81-267-98-4394
+81-267-98-2927 (FAX)
chieko@nro.nao.ac.jp

SHIMPEI YAMASHITA

Caltech
Mail Code 320-47
Pasadena, CA 91125
626-395-3741
626-796-8806 (FAX)
dbenford@tacos.caltech.edu

GHAFFAN YASSIN

MRAO Cambridge University
Radio-Astronomy Cavendish Lab.
Hadingley Rd.
Cambridge CB3 0HE
UNITED KINGDOM
+44 1223 337309
+44-1223-354599 (FAX)
ghassan@mrao.cam.ac.uk

SIGFRID YNGVESSON

University of Massachusetts
Electrical & Computer Eng. Dept.
Amherst, MA 01003-5110
413-545-0771
413-545-4611 (FAX)
yngvesson@ecs.umass.edu

PETER ZIMMERMAN

Radiometer Physics
Bergermeisen Str. 15
Meckenheim 53340
GERMANY
2225-999810
2225-9998199 (FAX)

JONAS ZMUIDZINAS

Caltech
Mail Code 320-47 Downs
Pasadena, CA 91125
626-395-6229
626-796-8806 (FAX)
jonas@socrates.caltech.edu